

Yuji Mochizuki
Shigenori Tanaka
Kaori Fukuzawa *Editors*

Recent Advances of the Fragment Molecular Orbital Method

Enhanced Performance and Applicability

 Springer

Recent Advances of the Fragment Molecular Orbital Method

Yuji Mochizuki · Shigenori Tanaka ·
Kaori Fukuzawa
Editors

Recent Advances of the Fragment Molecular Orbital Method

Enhanced Performance and Applicability

 Springer

Editors

Yuji Mochizuki
Department of Chemistry
Faculty of Science
Rikkyo University
Tokyo, Japan

Shigenori Tanaka
Graduate School of System Informatics
Kobe University
Kobe, Japan

Kaori Fukuzawa
School of Pharmacy and Pharmaceutical
Sciences
Hoshi University
Tokyo, Japan

ISBN 978-981-15-9234-8

ISBN 978-981-15-9235-5 (eBook)

<https://doi.org/10.1007/978-981-15-9235-5>

© Springer Nature Singapore Pte Ltd. 2021

This work is subject to copyright. All rights are reserved by the Publisher, whether the whole or part of the material is concerned, specifically the rights of translation, reprinting, reuse of illustrations, recitation, broadcasting, reproduction on microfilms or in any other physical way, and transmission or information storage and retrieval, electronic adaptation, computer software, or by similar or dissimilar methodology now known or hereafter developed.

The use of general descriptive names, registered names, trademarks, service marks, etc. in this publication does not imply, even in the absence of a specific statement, that such names are exempt from the relevant protective laws and regulations and therefore free for general use.

The publisher, the authors and the editors are safe to assume that the advice and information in this book are believed to be true and accurate at the date of publication. Neither the publisher nor the authors or the editors give a warranty, expressed or implied, with respect to the material contained herein or for any errors or omissions that may have been made. The publisher remains neutral with regard to jurisdictional claims in published maps and institutional affiliations.

This Springer imprint is published by the registered company Springer Nature Singapore Pte Ltd.

The registered company address is: 152 Beach Road, #21-01/04 Gateway East, Singapore 189721, Singapore

Foreword

As electronic structure theory advances and computer performance improves, ab initio quantum mechanical (QM) calculations have steadily increased their usefulness for studying structures, properties, and reactions of molecules and molecular assemblies. However, even simple ab initio QM theories such as the Hartree–Fock method (HF) and density functional theory (DFT) require a computation time proportional to the third or fourth power of the system size. The computational scaling becomes even steeper in more reliable electron correlation theories such as Møller–Plesset perturbation theory or coupled cluster theory. The steep scaling of the computational cost hinders ab initio QM calculations of large systems such as biomolecules. To overcome this obstacle, lower (ideally linear) scaling computational methods are required.

A number of fragment-based QM methods have been proposed for large molecular systems. In these methods, a system is divided into small fragments, QM calculations are performed on the fragments (and in some methods their multimers), and properties of the entire system are calculated using the properties of fragments (multimers). Fragments (multimers) can be calculated independently, making fragment-based methods suitable for modern massively parallel computers. The computational cost of most fragment-based methods scales almost linearly with the system size through the introduction of some approximations.

The fragment molecular orbital (FMO) method is one such fragment-based method. The distinguishing feature of the FMO method is that the total energy of a system is computed as the sum of fragment energies and inter-fragment interaction energies. The two-body inter-fragment interaction energy defined in the FMO method effectively includes higher body effects. By using this approach, the ab initio total energy of the system is accurately reproduced. If need arises, the contributions of explicit three-body and higher body interactions can be computed to further increase accuracy. The properties of systems other than the total energy are calculated in a similar fashion. In some fragment-based methods, fragments generated by covalent bond cleavage are capped with hydrogen atoms or appropriate functional groups, but the FMO method does not introduce such arbitrary atoms. This is another distinguishing feature of the FMO method. A description of the FMO method and a comparison of various fragment-based methods are given in Part I.

Commonly used electronic structure theories have been incorporated into the FMO method; namely the Hartree-Fock method and density functional theory, Møller-Plesset perturbation theory, coupled cluster theory, configuration interaction, multi-configuration SCF, time-dependent density functional theory, and so forth. Energy gradients and Hessian calculations have been developed in some of these methods that enable geometry optimization and vibrational analysis of very large molecules. For modeling solvent effects, continuum solvent models such as the polarizable continuum model (PCM) can be interfaced with the FMO method. A hybrid method of FMO and molecular mechanics (FMO/MM) has been developed for simulating chemical and thermodynamical properties of molecular systems. Several computer programs for FMO calculations have been developed. Part II describes currently available ab initio programs that can perform FMO calculations.

At the beginning of its development, the FMO method was intended to calculate the electronic structure of proteins and protein-ligand complexes. A number of FMO studies of protein-ligand binding aimed at drug design have been conducted so far. In these works, the inter-fragment pair interaction energy (called IFIE or PIE), which is a property obtained from FMO calculations, has been extensively used to understand intermolecular interactions between proteins and ligands. Applications of the FMO method in drug discovery are discussed in Part III. Parts IV and V describe new FMO applications and the development of new FMO-related methods that extend the scope of FMO applications.

The various FMO approaches described in this book are expected to be useful for studying the structures and properties of very large and complex molecular systems and for designing drugs and materials in industrial applications.

Kobe, Japan
February 2020

Kazuo Kitaura

Preface by Editors

The fragment molecular orbital (FMO) method has been one of promising ways to calculate the electronic state of large-scale molecular systems such as proteins in a quantum mechanical framework. The highly efficient parallelism deserves the principal advantage of FMO calculations. Additionally, the FMO method can be used as analysis tools by evaluating the inter-fragment (pairwise) interaction energies and so on, and this feature has been utilized well in the fields of biophysical and pharmaceutical chemistries. In recent years, the methodological developments of FMO have been made remarkably, by which both reliability and applicability have been enhanced even for inorganic systems. Actually, there have been a number of realistic applications using several FMO-customized programs which are highly parallelized.

This book covers recent advances of the FMO method, consisting of the following five parts. Historical review of FMO and comparison to other fragmentation methods are provided in Part I, and FMO programs are described in Part II. Part III is dedicated to a wide range of drug discovery activities. A variety of new applications with methodological breakthroughs are introduced in Part IV. Finally, computer and information science-oriented topics are addressed in Part V. Many color figures and illustrations are compiled as well.

The editors would like to sincerely thank all the contributors in this book, who provided their own important and fruitful work in the respective chapters. They are very sorry for the delay of publication of this book due to a couple of reasons, while some contributions were submitted in 2018.

Finally, the editors would hope that this book will induce interests in FMO method for a wide range of people who are involved in not only computational chemistry but also experimental chemistry.

Tokyo, Japan
Kobe, Japan
Tokyo, Japan
August 2020

Yuji Mochizuki
Shigenori Tanaka
Kaori Fukuzawa

Contents

Positioning of FMO

Fragment Molecular Orbital Method as Cluster Expansion	3
---	---

Shigenori Tanaka

Comparison of Various Fragmentation Methods for Quantum Chemical Calculations of Large Molecular Systems	15
---	----

Shigenori Tanaka

Programs

Recent Development of the Fragment Molecular Orbital Method in GAMESS	31
--	----

Dmitri G. Fedorov

The ABINIT-MP Program	53
------------------------------------	----

Yuji Mochizuki, Tatsuya Nakano, Kota Sakakura, Yoshio Okiyama, Hiromasa Watanabe, Koichiro Kato, Yoshinobu Akinaga, Shinya Sato, Jun-inchi Yamamoto, Katsumi Yamashita, Tadashi Murase, Takeshi Ishikawa, Yuto Komeiji, Yuji Kato, Naoki Watanabe, Takashi Tsukamoto, Hirotochi Mori, Koji Okuwaki, Shigenori Tanaka, Akifumi Kato, Chiduru Watanabe, and Kaori Fukuzawa

PAICS: Development of an Open-Source Software of Fragment Molecular Orbital Method for Biomolecule	69
---	----

Takeshi Ishikawa

Open-Architecture Program of Fragment Molecular Orbital Method for Massive Parallel Computing (OpenFMO) with GPU Acceleration	77
--	----

Hiroataka Kitoh-Nishioka, Hiroaki Umeda, and Yasuteru Shigeta

Pharmaceutical Activities

How to Perform FMO Calculation in Drug Discovery	93
Kaori Fukuzawa, Chiduru Watanabe, Yoshio Okiyama, and Tatsuya Nakano	
FMO Drug Design Consortium	127
Kaori Fukuzawa, Shigenori Tanaka, Yoichiro Yagi, Noriyuki Kurita, Norihiro Kawashita, Kenichiro Takaba, and Teruki Honma	
Development of an Automated FMO Calculation Protocol to Construction of FMO Database	183
Chiduru Watanabe, Hirofumi Watanabe, Yoshio Okiyama, and Daisuke Takaya	
Application of FMO to Ligand Design: SBDD, FBDD, and Protein– Protein Interaction	205
Tomonaga Ozawa and Motoyasu Ozawa	
Drug Discovery Screening by Combination of X-ray Crystal Structure Analysis and FMO Calculation	253
Midori Takimoto-Kamimura and Noriyuki Kurita	
Cooperative Study Combining X-ray Crystal Structure Analysis and FMO Calculation: Interaction Analysis of FABP4 Inhibitors	267
Uno Tagami and Kazutoshi Takahashi	
Application of FMO for Protein–ligand Binding Affinity Prediction	281
Kenichiro Takaba	
Recent Advances of In Silico Drug Discovery: Integrated Systems of Informatics and Simulation	295
Teruki Honma	
Pharmaceutical Industry—Academia Cooperation	307
Alexander Heifetz, Peter V. Coveney, Dmitri G. Fedorov, Inaki Morao, Tim James, Michelle Southey, Kostas Papadopoulos, Mike J. Bodkin, and Andrea Townsend-Nicholson	
Elucidating the Efficacy of Clinical Drugs Using FMO	323
Sundaram Arulmozhiraja, Hiroaki Tokiwa, and Hitoshi Shimano	
Application of Fragment Molecular Orbital Calculations to Functional Analysis of Enzymes	341
Shogo Nakano, Sohei Ito, and Hiroaki Tokiwa	
AnalysisFMO Toolkit: A PyMOL Plugin for 3D-Visualization of Interaction Energies in Proteins (3D-VIEP) Calculated by the FMO Method	357
Takaki Tokiwa, Shogo Nakano, Hiroaki Tokiwa, and Yasuteru Shigeta	

New Methods and Applications

FMO Interfaced with Molecular Dynamics Simulation	373
Yuto Komeiji and Takeshi Ishikawa	

Linear Combination of Molecular Orbitals of Fragments (FMO-LCMO) Method: Its Application to Charge Transfer Studies	391
Hirotaka Kitoh-Nishioka, Ryuma Sato, Yasuteru Shigeta, and Koji Ando	

Modeling of Solid and Surface	407
Koichiro Kato, Aya Hashimoto, Eiichi Tamiya, Kaori Fukuzawa, Yuichiro Ishikawa, and Yuji Mochizuki	

Development of the Analytic Second Derivatives for the Fragment Molecular Orbital Method	425
Hiroya Nakata and Dmitri G. Fedorov	

The FMO-DFTB Method	459
Yoshio Nishimoto and Stephan Irle	

Self-Consistent Treatment of Solvation Structure with Electronic Structure Based on 3D-RISM Theory	487
Norio Yoshida	

New Methodology and Framework

New Methodology and Framework Information Science-Assisted Analysis of FMO Results for Drug Design	511
Tatsuya Takagi	

Extension to Multiscale Simulations	529
Koji Okuwaki, Taku Ozawa, and Yuji Mochizuki	

FMO-Based Investigations of Excited-State Dynamics in Molecular Aggregates	547
Takatoshi Fujita and Takeo Hoshi	

Application of the Fragment Molecular Orbital Method to Organic Charge Transport Materials in Xerography: A Feasibility Study and a Charge Mobility Analysis	567
Ikuro Fujino, Dmitri G. Fedorov, and Kazuo Kitaura	

Group Molecular Orbital Method and Python-Based Programming Approach	589
Tomomi Shimazaki	

Multi-Level Parallelization of the Fragment Molecular Orbital Method in GAMESS	601
Vladimir A. Mironov, Yuri Alexeev, Dmitri G. Fedorov, Hiroaki Umeda, Spencer Pruitt, Alexander Gaenko, and Mark S. Gordon	

Positioning of FMO

Fragment Molecular Orbital Method as Cluster Expansion



Shigenori Tanaka

Abstract In this chapter, the energy increment scheme employed in the fragment molecular orbital (FMO) method is systematically analyzed and validated in terms of a cluster expansion in the framework of the cumulant expansion. Some relationships and similarities among various theoretical approaches concerning the cluster expansion for fragments are comprehensively addressed.

Keywords Fragment molecular orbital method · Energy increment scheme · Cluster expansion · Cumulant expansion · Green's function

1 Introduction

The fragment molecular orbital (FMO) method [1, 2] provides a computational framework by which *ab initio* electronic state calculations for large molecular systems are made feasible with the calculation cost of approximately order- N ($O(N)$) of electron or fragment number. The energy expansion scheme in the FMO method, which is nowadays called FMO2, FMO3, *etc.* [3], is an essential device to realize the drastic reduction in computational time with keeping high accuracy in the evaluations of energy and other molecular properties. In this article, an overview is given to illustrate the physical background for this FMO energy expansion scheme.

First, let us review the original FMO2 energy expansion scheme proposed by Kitaura et al. [1, 2]. Consider a molecular system composed of electrons with electric charge $-e$ and coordinates \mathbf{r}_i and nuclei with electric charge $Z_A e$ and coordinates \mathbf{R}_A . Then the whole system is divided into a collection of N_f fragments (monomers) with index I . In the FMO2 method, one accounts for the FMO calculations up to the fragment pairs (dimers). Using the atomic units hereafter, the Hamiltonians for the fragment monomer (I) and the fragment dimer (IJ) are given by

S. Tanaka (✉)
Graduate School of System Informatics, Kobe University,
1-1 Rokkodai, Nada-ku, Kobe 657-8501, Japan
e-mail: tanaka2@kobe-u.ac.jp

$$\hat{H}_I = \sum_{i \in I} \left[-\frac{1}{2} \Delta_i - \sum_A \frac{Z_A}{|\mathbf{r}_i - \mathbf{R}_A|} + \sum_{J \neq I}^{N_f} \int d\mathbf{r}' \frac{\rho_J(\mathbf{r}')}{|\mathbf{r}_i - \mathbf{r}'|} \right] + \sum_{i \in I} \sum_{i < j \in I} \frac{1}{|\mathbf{r}_i - \mathbf{r}_j|}, \quad (1)$$

$$\hat{H}_{IJ} = \sum_{i \in I, J} \left[-\frac{1}{2} \Delta_i - \sum_A \frac{Z_A}{|\mathbf{r}_i - \mathbf{R}_A|} + \sum_{K \neq I, J}^{N_f} \int d\mathbf{r}' \frac{\rho_K(\mathbf{r}')}{|\mathbf{r}_i - \mathbf{r}'|} \right] + \sum_{i \in I, J} \sum_{i < j \in I, J} \frac{1}{|\mathbf{r}_i - \mathbf{r}_j|}. \quad (2)$$

Here, I, J, K refer to different fragments and $\rho_J(\mathbf{r}')$ represents the number density of electron with coordinate \mathbf{r}' in the fragment J . The energies and wave functions of each fragment monomer and dimer are then obtained by solving the Schrödinger equations as

$$\hat{H}_I \Psi_I = E_I \Psi_I, \quad (3)$$

$$\hat{H}_{IJ} \Psi_{IJ} = E_{IJ} \Psi_{IJ}. \quad (4)$$

In the FMO2 method, the electronic energy E and the electron density $\rho(\mathbf{r})$ of the whole system are approximately given by

$$E \simeq \sum_{I < J} E_{IJ} - (N_f - 2) \sum_I E_I, \quad (5)$$

$$\rho(\mathbf{r}) \simeq \sum_{I < J} \rho_{IJ}(\mathbf{r}) - (N_f - 2) \sum_I \rho_I(\mathbf{r}), \quad (6)$$

respectively. Here, E_X ($X = I, IJ$) and $\rho_X(\mathbf{r})$ ($X = I, IJ$) refer to the energy and the electron density of fragment monomer (I) or dimer (IJ).

The FMO2 method has successfully been applied to large numbers of molecular systems mainly containing biological molecules (proteins, nucleic acids, *etc.*) and nano-materials [3]. The energy expansion above may also be written as

$$E \simeq \sum_I E_I + \sum_{I < J} \Delta E_{IJ} \quad (7)$$

with

$$\Delta E_{IJ} = E_{IJ} - E_I - E_J. \quad (8)$$

This expansion scheme can further be continued up to the third order (FMO3) as [3–5]

$$E \simeq \sum_I E_I + \sum_{I < J} \Delta E_{IJ} + \sum_{I < J < K} \Delta E_{IJK} \quad (9)$$

with

$$\begin{aligned} \Delta E_{IJK} &= E_{IJK} - (\Delta E_{IJ} + \Delta E_{JK} + \Delta E_{KI}) - (E_I + E_J + E_K) \\ &= E_{IJK} - E_{IJ} - E_{JK} - E_{KI} + E_I + E_J + E_K. \end{aligned} \quad (10)$$

This equation for the FMO3 energy expansion may seem trivial when one considers a system composed of three fragments. It is also noted that similar expansions can be continued up to higher orders [3, 6, 7]. Empirically, this kind of energy expansion, generally known as increment method, converges rapidly in the FMO applications to biomolecular systems. However, there are a limited number of studies concerning the perturbative characterization of the FMO energy expansion [8].

In principle, the complexity or degree of freedom of electronic wave function increases exponentially with the increase of electron number. The FMO method then provides a practical prescription to overcome this difficulty through the energy representation in terms of *cluster expansion* [9, 10], in which the locality of exchange–correlation effects of electrons is utilized and the cumulant expansion [11] may be employed as an underlying mathematical tool to describe the linked clusters. In this chapter, the intuitive energy expansion (increment) scheme in the FMO method above is reformulated as a perturbative cluster expansion, thus being justified on a physical basis. A relationship with Green’s function approach [8, 12] is additionally noted.

2 Cluster Expansion

Let us consider a large molecular system composed of many subsystems called fragments. The Hamiltonian for the whole system can be expressed as

$$H = H_0 + H_1. \quad (11)$$

Here, the “unperturbed” part H_0 may be chosen in a fairly arbitrary way. For example, as a simple choice, one may regard H_0 as representing the sum of the self-consistent field (SCF) or Hartree–Fock (HF) Hamiltonians for the isolated electron systems confined in each fragment. In the usual FMO approach, one may also take into account the contribution of environmental electrostatic potential from surrounding fragments to each fragment Hamiltonian [1, 2]. Alternatively, it is also possible to include the electron correlation effects beyond the SCF or HF approximation in each fragment Hamiltonian, which is usually performed as a hierarchical energy expansion in the actual FMO calculations [3]. The “perturbed” part H_1 can then be expressed as

$$H_1 = \sum_I H_I + \sum_{I,J} H_{IJ} + \cdots, \quad (12)$$

where the first term on the right-hand side of Eq. (12) refers to the sum of residual Hamiltonians of each fragment I , the second term represents the contributions from the interactions between the two fragments (I, J), and so on. We presume that H_0 has a ground state $|\psi_0\rangle$ with the energy E_0 , and consider the canonical ensemble with the temperature T and $\beta = 1/k_B T$.

The partition function for the unperturbed part is given by

$$Z_0 = \text{Tr} e^{-\beta H_0} \quad (13)$$

with the use of trace Tr . The statistical average of any operator A over the unperturbed state is expressed as

$$\langle A \rangle_0 = Z_0^{-1} \text{Tr}(e^{-\beta H_0} A). \quad (14)$$

Considering a function of a parameter λ as

$$\mathcal{E}(\lambda) = Z_0 \langle e^{-\lambda H} e^{\lambda H_0} \rangle_0 = \text{Tr}(e^{-\beta H_0} e^{-\lambda H} e^{\lambda H_0}), \quad (15)$$

the partition function for the Hamiltonian H is given by

$$Z = \mathcal{E}(\beta) = \text{Tr} e^{-\beta H}. \quad (16)$$

Here, the function $\mathcal{E}(\lambda)$ in Eq. (15) is alternatively expressed as [13]

$$\mathcal{E}(\lambda) = Z_0 \langle e^{-\lambda(H_1+L_0)} \rangle_0, \quad (17)$$

where the Liouville super-operator L_0 is defined through

$$L_0 A = [H_0, A]. \quad (18)$$

The equivalence between Eqs. (15) and (17) is proved by the λ derivatives of $e^{-\lambda(H_1+L_0)}$ and $e^{-\lambda H} e^{\lambda H_0}$. Then, Eq. (17) is rewritten as

$$\mathcal{E}(\lambda) = Z_0 \exp f(\lambda) \quad (19)$$

with

$$f(\lambda) = \langle e^{-\lambda(H_1+L_0)} - 1 \rangle_0^c, \quad (20)$$

where the superscript c in Eq. (20) means the cumulant average [9, 11].

The free energy of the whole system is written by

$$F = F_0 + F_1 \quad (21)$$

with

$$F_0 = -\frac{1}{\beta} \ln Z_0 \quad (22)$$

and

$$F_1 = -\frac{1}{\beta} f(\beta). \quad (23)$$

Through the application of the Laplace transform:

$$\tilde{f}(z) = -\int_0^\infty d\lambda e^{\lambda z} f(\lambda) \quad (24)$$

with $\text{Re } z < 0$, we find

$$\begin{aligned} \tilde{f}(z) &= \left\langle \frac{1}{z - H_1 - L_0} - \frac{1}{z} \right\rangle_0^c \\ &= \frac{1}{z^2} \left\{ \left\langle H_1 \left(1 + \frac{1}{z - H} H_1 \right) \right\rangle_0^c \right\}, \end{aligned} \quad (25)$$

where L_0 in $\langle \rangle_0^c$ is replaced with H_0 , and the contribution of factorizable H_0 vanishes therein [9].

The cluster expansion of F_1 is performed by means of Feddeev's resummation technique [14] as follows. Hereafter, we consider the limit of $T \rightarrow 0$, $\beta \rightarrow \infty$ and $z \rightarrow 0$, thus focusing on the ground state energy [9, 10]. In Eq. (25), we pay attention to the scattering operator defined in $\langle \rangle_0^c$ by

$$S = \frac{1}{z - H} H_1 = \sum_{n=1}^{\infty} \left(\frac{1}{z - H_0} H_1 \right)^n, \quad (26)$$

where $(z - H_0)^{-1}$ represents Green's function for H_0 . In the lowest order approximation, the perturbative part of Hamiltonian can be given by the sum of the contributions of each fragment ($I = 1, 2, \dots, N$) as

$$H_1 \approx \sum_{I=1}^N V_I, \quad (27)$$

where V_I may contain the effects by the environmental electrostatic potentials from surrounding fragments and the electron correlations inside the fragment. The scattering operator

$$S = \sum_{n=1}^{\infty} \left(\frac{1}{z - H_0} \sum_{l=1}^N V_l \right)^n \quad (28)$$

is then expressed in terms of an operator

$$A_l = \frac{1}{z - H_0} V_l \quad (29)$$

as

$$\begin{aligned} S &= \sum_{n=1}^{\infty} \left(\sum_{l=1}^N A_l \right)^n \\ &= \sum A_1 \cdots + \sum A_2 \cdots + \sum A_3 \cdots + \cdots \\ &= T_1 + T_2 + T_3 + \cdots, \end{aligned} \quad (30)$$

where T_l refers to the collection of all the terms that begin with A_l .

Since we find a transformed representation as

$$\begin{aligned} T_1 &= (A_1 + A_1^2 + \cdots) + (A_1 + A_1^2 + \cdots)A_2 \cdots + (A_1 + A_1^2 + \cdots)A_3 \cdots + \cdots \\ &= (A_1 + A_1^2 + \cdots)(1 + T_2 + T_3 + \cdots) \\ &= S_1(1 + T_2 + T_3 + \cdots), \end{aligned} \quad (31)$$

we obtain

$$T_l = S_l \left(1 + \sum_{J \neq l} T_J \right), \quad (32)$$

where S_l represents a scattering operator for $H_0 + V_l$. Recalling

$$S = \sum_{l=1}^N T_l \quad (33)$$

and assuming S_l to be small, we thus find $T_l \approx S_l$ and

$$S \approx \sum_{l=1}^N S_l. \quad (34)$$

The ground state energy E relative to E_0 for the unperturbed state $|\psi_0\rangle$ is then given by

$$\delta E = E - E_0 \approx \sum_{I=1}^N \delta E_I \quad (35)$$

with

$$\delta E_I = \langle H S_I \rangle_0^c = \langle H_I S_I \rangle_0^c. \quad (36)$$

If H_0 contains all the energy contributions from the fragment monomers, $A_I = 0$ and $\delta E_I = 0$, as they should be.

Let us next consider the second-order representations. Here, in Eq. (26) for the scattering operator S , in addition to the intra-fragment contributions,

$$A_{II} = A_I = \frac{1}{z - H_0} V_I, \quad (37)$$

we take into account the inter-fragment ($I \neq J$) contributions,

$$A_{IJ} = \frac{1}{z - H_0} V_{IJ}, \quad (38)$$

where V_{IJ} refers to the interactions for the fragment pair IJ . The scattering operator is then expressed as

$$S = \sum_{n=1}^{\infty} \left(\sum_{I,J} A_{IJ} \right)^n \quad (39)$$

and transformed into

$$\begin{aligned} S &= \sum_I \left(\sum_{n=1}^{\infty} A_I^n \right) + \sum_{I \neq J} T_{IJ} \\ &= \sum_I S_I + \sum_{I \neq J} T_{IJ}, \end{aligned} \quad (40)$$

where T_{IJ} includes all the terms which begin with A_{IJ} or A_I followed by A_J as the first factor different from A_I . T_{IJ} is thus expressed as

$$T_{IJ} = (A_{IJ} + A_I A_J + A_I A_J A_I + A_I^2 A_J + \dots) \left(1 + \sum_{K \neq I, J} S_K + \sum_{K \neq I, J; L} T_{KL} \right). \quad (41)$$

The summation of T_{IJ} and T_{JI} is then found to be

$$T_{IJ} + T_{JI} = (S_{IJ} - S_I - S_J) \left(1 + \sum_{K \neq I, J} S_K + \sum_{K \neq I, J; L} T_{KL} \right), \quad (42)$$

where S_{IJ} is the scattering operator for the fragment pair IJ . The total scattering operator of Eq. (40) is then approximated as

$$S \approx \sum_I S_I + \sum_{I < J} K_{IJ} \quad (43)$$

with

$$K_{IJ} = S_{IJ} - S_I - S_J. \quad (44)$$

Thus, we find for the ground state energy

$$E \approx E_0 + \sum_I \delta E_I + \sum_{I < J} \delta E_{IJ} \quad (45)$$

with

$$\begin{aligned} \delta E_{IJ} &= \langle H S_{IJ} \rangle_0^c - \delta E_I - \delta E_J \\ &= \langle H_1 S_{IJ} \rangle_0^c - \delta E_I - \delta E_J, \end{aligned} \quad (46)$$

which reproduces the FMO2 expression.

Analogous procedures can be applied to higher order approximations. Up to the third-order (fragment trimer) contributions, the scattering operator is expressed as

$$S \approx \sum_I S_I + \sum_{I < J} K_{IJ} + \sum_{I < J < K} L_{IJK} \quad (47)$$

with

$$\begin{aligned} L_{IJK} &= S_{IJK} - K_{IJ} - K_{JK} - K_{KI} - S_I - S_J - S_K \\ &= S_{IJK} - S_{IJ} - S_{JK} - S_{KI} + S_I + S_J + S_K, \end{aligned} \quad (48)$$

where S_{IJK} is the scattering operator for the fragment trimer IJK . The energy of the whole system is then given by

$$E \approx E_0 + \sum_I \delta E_I + \sum_{I < J} \delta E_{IJ} + \sum_{I < J < K} \delta E_{IJK} \quad (49)$$

with

$$\begin{aligned}\delta E_{IJK} &= \langle HS_{IJK} \rangle_0^c - \delta E_{IJ} - \delta E_{JK} - \delta E_{KI} - \delta E_I - \delta E_J - \delta E_K \\ &= \langle HS_{IJK} \rangle_0^c - \langle HS_{IJ} \rangle_0^c - \langle HS_{JK} \rangle_0^c - \langle HS_{KI} \rangle_0^c \\ &\quad + \langle HS_I \rangle_0^c + \langle HS_J \rangle_0^c + \langle HS_K \rangle_0^c,\end{aligned}\quad (50)$$

thus reproducing the FMO3 expression.

Summarizing, the cluster expansion formalism above for the ground state energy can be based on a transformation of wave function from the unperturbed $|\psi_0\rangle$ to the exact one as

$$|\Phi\rangle = \Omega|\psi_0\rangle = (1 + S)|\psi_0\rangle, \quad (51)$$

where Ω refers to a wave operator employed in the cumulant expansion [9, 10]. The ground state energy is then given by

$$\begin{aligned}E &= \langle \psi_0 | H | \Phi \rangle^c \\ &= \langle \psi_0 | H \Omega | \psi_0 \rangle^c \\ &= \langle \psi_0 | H (1 + S) | \psi_0 \rangle^c \\ &= \langle H (1 + S) \rangle_0^c.\end{aligned}\quad (52)$$

The energy increment due to the fragment interactions is thus expressed as

$$E - E_0 = \langle HS \rangle_0^c = \langle H_1 S \rangle_0^c \quad (53)$$

whose expansion accords with the cluster expansion of the scattering operator S .

3 Green's Function Approach

As seen in Eq. (26) in the preceding section, Green's functions play a vital role in the cluster expansion of energy. Actually, Green's function formalism was employed [8] to justify and extend the use of FMO expansion scheme, in which Green's function is expressed in terms of the fragment expansion as

$$G = \sum_{I=1}^N G_I + \sum_{I < J} \Delta G_{IJ} + \dots \quad (54)$$

with

$$\Delta G_{IJ} = G_{IJ} - G_I - G_J. \quad (55)$$

Thus, the two-body approximation,

$$G \simeq \sum_{I < J} G_{IJ} - (N - 2) \sum_I G_I, \quad (56)$$

leads to the FMO2 approximation to the ground state energy and other molecular properties.

In addition to the canonical ensemble, one can also consider the grand canonical ensemble with given chemical potential μ and temperature T . Regarding the perturbative Hamiltonian H_1 as a correction due to the inter-fragment interactions, we find an expression for the correction to the grand potential as [12, 15]

$$\Delta \mathcal{J} = -\frac{2}{\beta} \sum_l \sum_i \text{Tr} \ln \left[\mathbf{1} - \mathbf{G}^{(0)}(\varepsilon_i, \zeta_l) \tilde{\Sigma}(\varepsilon_i, \zeta_l) \right] \exp(\zeta_l 0^+). \quad (57)$$

Here, $\mathbf{G}^{(0)}$ and $\tilde{\Sigma}$ are matrices indexed with fragment pair IJ for Green's function for H_0 (diagonal) and the self-energy due to the inter-fragment interactions (off-diagonal), respectively; ε_i denotes the electronic energy of molecular orbital i for corresponding fragment and

$$\zeta_l = \mu + \frac{2l + 1}{\beta} \pi i \quad (58)$$

for $l = 0, \pm 1, \pm 2, \dots$. Rewriting Eq. (57) as

$$\Delta \mathcal{J} = -\frac{2}{\beta} \sum_l \sum_i \text{Tr} \left\{ \ln \left[\tilde{\Sigma} - (\mathbf{G}^{(0)})^{-1} \right] - \ln \left[-(\mathbf{G}^{(0)})^{-1} \right] \right\} \quad (59)$$

and using an identity $\text{Tr} \ln A = \ln \det A$ for any matrix A , we obtain

$$\Delta \mathcal{J} = -\frac{2}{\beta} \sum_{l,i} \left[\ln D(\varepsilon_i, \zeta_l) - \ln \prod_I D_1(\varepsilon_i, \zeta_l; \{I\}) \right] \quad (60)$$

with

$$D_1(\varepsilon_i, \zeta_l; \{I\}) = -[G_I^{(0)}(\varepsilon_i, \zeta_l)]^{-1} = \varepsilon_i - \zeta_l \quad (61)$$

and

$$D(\varepsilon_i, \zeta_l) = \begin{vmatrix} -[G_1^{(0)}]^{-1} & \tilde{\Sigma}_{12} & \tilde{\Sigma}_{13} & \dots \\ \tilde{\Sigma}_{21} & -[G_2^{(0)}]^{-1} & \tilde{\Sigma}_{23} & \dots \\ \tilde{\Sigma}_{31} & \tilde{\Sigma}_{32} & -[G_3^{(0)}]^{-1} & \dots \\ \dots & \dots & \dots & \dots \end{vmatrix}. \quad (62)$$

Further, we introduce an $n \times n$ determinant $D_n(\varepsilon_i, \zeta_l; \{I_1, I_2, \dots, I_n\})$ as

$$D_2(\{I, J\}) = \begin{vmatrix} -[G_I^{(0)}]^{-1} & \tilde{\Sigma}_{IJ} \\ \tilde{\Sigma}_{JI} & -[G_J^{(0)}]^{-1} \end{vmatrix}, \quad (63)$$

$$D_3(\{I, J, K\}) = \begin{vmatrix} -[G_I^{(0)}]^{-1} & \tilde{\Sigma}_{IJ} & \tilde{\Sigma}_{IK} \\ \tilde{\Sigma}_{JI} & -[G_J^{(0)}]^{-1} & \tilde{\Sigma}_{JK} \\ \tilde{\Sigma}_{KI} & \tilde{\Sigma}_{KJ} & -[G_K^{(0)}]^{-1} \end{vmatrix}, \quad (64)$$

and so on. Here, it is noted that $-2\beta^{-1} \sum_{l,i} \ln D_1(\varepsilon_i, \zeta_l; \{I\})$ in Eq. (60) represents the grand potential for H_0 from fragment I and can be expressed in terms of $\ln \langle \exp(\beta \mu n_i) \rangle$ with the weight $\exp(-\beta \varepsilon_i n_i)$ for the occupation number $n_i = 0, 1$ [15]; namely, it can be regarded as a cumulant function for the variable n_i . Similarly, $-2\beta^{-1} \sum_{l,i} \ln D(\varepsilon_i, \zeta_l)$ in Eq. (60) can be regarded as a cumulant function for a set of multiple variables n_i for each fragment monomer or dimer. Then, employing a general theorem for the cluster expansion of cumulant function [11], we find [12]

$$\begin{aligned} \ln D &= \sum_I \ln D_1(\{I\}) + \sum_{I < J} \ln \frac{D_2(\{I, J\})}{D_1(\{I\})D_1(\{J\})} \\ &+ \sum_{I < J < K} \ln \frac{D_3(\{I, J, K\})D_1(\{I\})D_1(\{J\})D_1(\{K\})}{D_2(\{I, J\})D_2(\{J, K\})D_2(\{K, I\})} + \dots \end{aligned} \quad (65)$$

Equation (60) is thus rewritten as

$$\Delta \mathcal{F} = \sum_{I < J} \Delta \mathcal{F}_2(\{I, J\}) + \sum_{I < J < K} \Delta \mathcal{F}_3(\{I, J, K\}) + \dots \quad (66)$$

with

$$\Delta \mathcal{F}_2(\{I, J\}) = -\frac{2}{\beta} \sum_{l,i} \ln \frac{D_2(\{I, J\})}{D_1(\{I\})D_1(\{J\})}, \quad (67)$$

$$\Delta \mathcal{F}_3(\{I, J, K\}) = -\frac{2}{\beta} \sum_{l,i} \ln \frac{D_3(\{I, J, K\})D_1(\{I\})D_1(\{J\})D_1(\{K\})}{D_2(\{I, J\})D_2(\{J, K\})D_2(\{K, I\})}, \quad (68)$$

and so on. The mathematical structure of this expansion is apparently analogous to that for the FMO energy expansion. One may also find an analogous structure to the many-body correlation functions for non-interacting Fermi gas [16].

4 Concluding Remarks

The FMO method provides an efficient and useful *ab initio* tool to evaluate intermolecular interactions in large molecular systems. Justification for the methodology as an increment method for energy can be given in terms of cluster expansion in which mathematical techniques based on the cumulant expansion and Green's function are utilized. The concept of *fragment* is introduced as an essential element of the FMO method, where intra-fragment electron correlation effects and inter-fragment interactions can thus be treated hierarchically [3]. The effective interaction energy between the fragments can then be described in terms of inter-fragment interaction energy (IFIE) [3] in the FMO formalism, which may be regarded as a renormalized (coarse-grained), effective interaction in lower energy regime. Resummation of correlated IFIEs to account for the screening effect based on the underlying charge neutrality principle and the optimization of mutual information for IFIEs can also be carried out [17]. All these components are used for comprehensively analyzing the effective interactions in biomolecular and nano-material systems with affordable computational cost and accuracy.

References

1. Kitaura K, Sawai T, Asada T, Nakano T, Uebayasi M (1999) Chem Phys Lett 312:319
2. Kitaura K, Ikee E, Asada T, Nakano T, Uebayasi M (1999) Chem Phys Lett 313:701
3. Tanaka S, Mochizuki Y, Komeiji Y, Okiyama Y, Fukuzawa K (2014) Phys Chem Chem Phys 16:10310
4. Fedorov DG, Kitaura K (2004) J Chem Phys 120:6832
5. Fujita T, Fukuzawa K, Mochizuki Y, Nakano T, Tanaka S (2009) Chem Phys Lett 478:295
6. Nakano T, Mochizuki Y, Yamashita K, Watanabe C, Fukuzawa K, Segawa K, Okiyama Y, Tsukamoto T, Tanaka S (2012) Chem Phys Lett 523:128
7. Watanabe C, Fukuzawa K, Okiyama Y, Tsukamoto T, Kato A, Tanaka S, Mochizuki Y, Nakano T (2013) J Mol Graph Model 41:31
8. Yasuda K, Yamaki D (2006) J Chem Phys 125:154101
9. Kladko K, Fulde P (1998) Int J Quantum Chem 66:377
10. Fulde P, Stoll H, Kladko K (1999) Chem Phys Lett 299:481
11. Kubo R (1962) J Phys Soc Jpn 17:1100
12. Ebina K (1983) Prog Theor Phys 69:1686
13. Becker KW, Fulde P, Phys Z (1988) B 72:423
14. Faddeev LD (1961) Sov Phys JETP 12:1014
15. Luttinger JM, Ward JC (1960) Phys Rev 118:1417
16. Tanaka S (2011) J Phys Soc Jpn 80:034001
17. Tanaka S, Watanabe C, Okiyama Y (2013) Chem Phys Lett 556:272

Comparison of Various Fragmentation Methods for Quantum Chemical Calculations of Large Molecular Systems



Shigenori Tanaka

Abstract In this chapter, various fragmentation schemes employed in the fragment molecular orbital (FMO) and other methods are comparatively assessed toward efficient order- N quantum chemical calculations of large (bio)molecular systems. After briefly illustrating the features of various fragmentation methods, their *pros* and *cons* are discussed from the viewpoints of cost, accuracy, viability, and versatility.

Keywords Fragmentation · Biomolecule · Quantum chemical calculation · Environmental potential · Parallel computing

1 Introduction

Fragmentation is an essential ingredient for order- N ($O(N)$) *ab initio* quantum chemical calculations [1]. In this article, we comparatively assess the performance of various fragmentation methodologies such as the fragment molecular orbital (FMO) method and others toward efficient molecular fragmentations. By breaking a large molecular system into molecular fragments that can be treated almost independently, the properties of the whole system are expressed as a sum of terms for each fragment with incorporation of many-body effects such as environmental potential and charge transfer. This implementation thus makes intractably huge calculations feasible or at least accelerates the calculations in terms of parallelization. Large numbers of techniques developed in conventional quantum chemistry are then transferable into each fragmentation approach, including those concerning electron correlation, gradients, excitation energies, and various molecular properties.

In the fragment molecular orbital (FMO) method, a molecular system is divided into several subsystems (fragments) [2]. For example, proteins are divided into fragments per amino acid residue as shown in Fig. 1. Note that the definitions of boundary on the main chain of each amino acid residue are different in the context of frag-

S. Tanaka (✉)
Graduate School of System Informatics, Kobe University,
1-1 Rokkodai, Nada-ku, Kobe 657-8501, Japan
e-mail: tanaka2@kobe-u.ac.jp

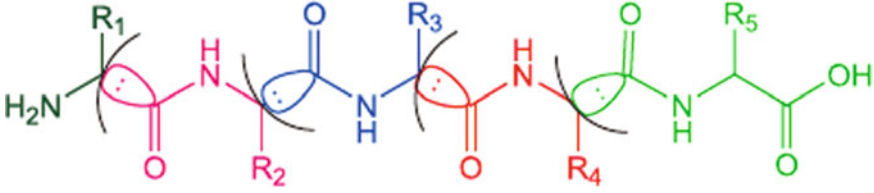


Fig. 1 Fragment division of polypeptide in the FMO method. R refers to the side chain and the fragment boundary is denoted by a solid line

mentation with the unit of $-C-N-C_{\alpha}-$ from those of conventional molecular biology and biochemistry with $-N-C_{\alpha}-C-$. More specifically, the carbonyl group of the main chain in the n -th biological residue with hydrogen-bonding acceptors on oxygen atom belongs to the $(n + 1)$ -th fragment, because the fragments are separated at $C_{\alpha}-C$ bond in front of the carbonyl group on the main chain.

Let us consider a molecular system composed of electrons with electric charge $-e$ and coordinates \mathbf{r}_i and nuclei with electric charge $Z_A e$ and coordinates \mathbf{R}_A . Then the whole system is divided into a collection of N_f fragments (monomers) with index I . In the following, for simplicity, we first address the FMO2 method [2] in which one accounts for the FMO calculations up to the fragment pairs (dimers). We consider the Hamiltonians for the fragment monomer (I) and the fragment dimer (IJ) as

$$\hat{H}_I = \sum_{i \in I} \left[-\frac{1}{2} \Delta_i - \sum_A \frac{Z_A}{|\mathbf{r}_i - \mathbf{R}_A|} + \sum_{J \neq I}^{N_f} \int d\mathbf{r}' \frac{\rho_J(\mathbf{r}')}{|\mathbf{r}_i - \mathbf{r}'|} \right] + \sum_{i \in I} \sum_{i > j \in I} \frac{1}{|\mathbf{r}_i - \mathbf{r}_j|}, \quad (1)$$

$$\hat{H}_{IJ} = \sum_{i \in I, J} \left[-\frac{1}{2} \Delta_i - \sum_A \frac{Z_A}{|\mathbf{r}_i - \mathbf{R}_A|} + \sum_{K \neq I, J}^{N_f} \int d\mathbf{r}' \frac{\rho_K(\mathbf{r}')}{|\mathbf{r}_i - \mathbf{r}'|} \right] + \sum_{i \in I, J} \sum_{i > j \in I, J} \frac{1}{|\mathbf{r}_i - \mathbf{r}_j|} \quad (2)$$

in atomic units. Here, I, J, K refer to different fragments and $\rho_J(\mathbf{r}')$ represents the number density of electron with coordinate \mathbf{r}' in the fragment J . The energies and wave functions of each fragment monomer and dimer are then obtained by solving the Schrödinger equations as

$$\hat{H}_I \Psi_I = E_I \Psi_I, \quad (3)$$

$$\hat{H}_{IJ} \Psi_{IJ} = E_{IJ} \Psi_{IJ}. \quad (4)$$

In the FMO2 method, the electronic energy E and the electron density $\rho(\mathbf{r})$ of the whole system are approximately given by

$$E \simeq \sum_{I>J} E_{IJ} - (N_f - 2) \sum_I E_I, \quad (5)$$

$$\rho(\mathbf{r}) \simeq \sum_{I>J} \rho_{IJ}(\mathbf{r}) - (N_f - 2) \sum_I \rho_I(\mathbf{r}), \quad (6)$$

respectively.

Considering the closed shell system hereafter, the Hartree–Fock–Roothaan equation in the FMO2 scheme is written by

$$F^\lambda C^\lambda = S^\lambda C^\lambda C^\lambda \quad (7)$$

with $\lambda = I$ for fragment monomer and $\lambda = IJ$ for fragment dimer. The Fock matrix F^λ is then expressed by

$$F^\lambda = H^\lambda + G^\lambda, \quad (8)$$

$$H_{kl}^\lambda = H_{kl}^{core,\lambda} + V_{kl}^\lambda + \sum_i B_i \langle k | \theta_i \rangle \langle \theta_i | l \rangle, \quad (9)$$

$$H_{kl}^{core,\lambda} = \langle \chi_k | \hat{h}^\lambda | \chi_l \rangle = \langle k | \hat{h}^\lambda | l \rangle = \int dr \chi_k^*(r) \hat{h}^\lambda \chi_l(r), \quad (10)$$

$$V_{kl}^\lambda = \sum_{K \neq \lambda} (u_{kl}^K + v_{kl}^K), \quad (11)$$

$$u_{kl}^K = \sum_{A \in K} \langle k | \frac{-Z_A}{|r - R_A|} | l \rangle, \quad (12)$$

$$v_{kl}^K = \sum_{m,n \in K} D_{mn}^K \langle \chi_k \chi_m | \chi_l \chi_n \rangle, \quad (13)$$

$$D_{kl}^\lambda = 2 \sum_j^{occ.} C_{kj}^{\lambda*} C_{lj}^\lambda, \quad (14)$$

$$G_{kl}^\lambda = \sum_{m,n \in \lambda} D_{mn}^\lambda \left[\langle \chi_k \chi_m | \chi_l \chi_n \rangle - \frac{1}{2} \langle \chi_k \chi_m | \chi_n \chi_l \rangle \right]. \quad (15)$$

Here, $H^{core,\lambda}$, V^λ , and D^λ refer to the one-electron operator in the fragment λ , the environmental electrostatic potential from the fragments other than λ , and the density

matrix, respectively; G^λ is the two-electron operator in the fragment λ with the basis functions $\chi_k(\mathbf{r})$.

The third term on the right-hand side of Eq. (8) represents a projection operator to remove the orbital θ_k from the variational space with parameter B_k conventionally set to 10^6 . Regarding the fragmentation for a molecule, the sp^3 carbon site is usually employed for the division. The atom at the division site is called the bond detached atom (BDA). As for θ_k , the localized MOs for a methane molecule obtained with the natural localized MO method are used, in which the C-H distance is fixed at 1.09 Å. We then consider a fragment I to which the BDA belongs and a neighboring fragment J to which the atom bonding to the BDA (bond attached atom; BAA) belongs. By rotating the MOs so that one of the orbitals θ_l is directed toward the BAA in fragment J bonding to the BDA, the contribution of θ_l to fragment I and that of other MOs to fragment J is removed by the shift operator, respectively. This procedure for the restriction of basis set enables the localization of MOs within a fragment (Fig. 1). Single bonds are usually detached between fragments, while other bond division approaches have been investigated [3]. It is also noted that the FMO method does not use hydrogen caps (see Sect. 3).

There are at least two kinds of bond detachment treatments available in the framework of FMO approach, that is, hybrid orbital projection (HOP) [4, 5] and adaptive frozen orbitals (AFO) [6, 7]. The HOP method, illustrated above, features unrestricted inter-fragment polarization for appropriately considering the fragmentation of linear chains of atoms. On the other hand, in the AFO method, the electron density of the detached bonds is calculated beforehand for a model system and frozen throughout the FMO calculation. The AFO method can thus be applied to inorganic materials in which several bonds are detached between two fragments. This approach has successfully been used [6, 7] for the descriptions of systems such as zeolite clusters, silicon nanowires, mesoporous silicons, graphene sheets, and organic charge-transfer materials. However, this chapter does not deeply go into the latter approach because of main interests in biomolecular systems such as proteins and nucleic acids.

2 Various Fragmentation Methods

The purpose of this review article is to make comparisons among various fragmentation schemes, including the FMO method, that are applicable to *ab initio* quantum chemical calculations for large (bio)molecular systems. In this section, we briefly illustrate other fragmentation methods such as KEM, MFCC, SFM, MTA, DC, and GMO.

Kernel energy method (KEM) [8] provides an energy decomposition analysis similar to the FMO method. This method divides a system into separate kernels and removes dangling bonds at the periphery of the kernels by using hydrogen caps. Double kernel calculations of nearest neighbor kernels are then performed to evaluate the total energy of system. While only those kernels covalently bonded to one another

were considered in the original approach, subsequent developments have taken into account separate kernels that are not covalently bonded. The energy formulae are analogous to the FMO ones, but the contributions of environmental electrostatic potentials are not included in the KEM method. The kernel interactions are further taken into account up to the fourth-order terms [9]. Applications have been made for proteins, nucleic acids, and π -conjugated systems such as graphene, in which some of new bond fractioning schemes are employed. For example, in fissioning scheme, the aromatic bonds are divided in half parallel to the direction of bonding instead of fractioning single bonds perpendicular to the direction of bonding.

Molecular fractionation with conjugate caps (MFCC) method [10] was originally developed to describe the binding energy of protein–ligand systems. When peptide bonds are fractioned, they are capped with “concaps” that represent the local environment of the fragments instead of hydrogen caps. The total binding energy of protein–ligand system is then calculated by adding together the individual contributions of the fragments and subtracting those from merged concaps. For example, let us consider a protein P composed of N amino acids,

$$P = nA_1A_2 \dots A_N, \quad (16)$$

where A_i represents each amino acid and n refers to the N-terminus, $n = \text{NH}_3^+$ or NH_2 ; A_N represents the C-terminus, and $A_N = R_N\text{CHCOO}^-$ or $R_N\text{CHCOOH}$ with the side chain R_N . To calculate the interaction energy between protein P and ligand L , the protein is divided into single amino acid fragments in terms of C-N peptide bonds. Each fragment is then capped by concaps, C^i and C^{i*} , which contain a C_α atom with side chain in the neighboring residue and describe the valency requirements of the dangling bonds left over after fractionation. The total interaction energy is then given by

$$E(L - P) = \sum_{i=1}^N E(L - C^{i-1*}A_iC^i) - \sum_{i=1}^{N-1} E(L - C^{i*}C^i), \quad (17)$$

where $E(L - C^{i-1*}A_iC^i)$ and $E(L - C^{i*}C^i)$ refer to the interaction energy between the ligand L and the capped fragment $C^{i-1*}A_iC^i$ and that between L and the connected concaps $C^{i*}C^i$, respectively. It is noted here that C^0 and C^N imply n and nothing, respectively. In the following developments of MFCC, the ability to fraction disulfide bonds and the inclusion of nonbonded interactions in globular proteins were also taken into account.

In systematic fragmentation method (SFM) [11], the fragmentation of molecular system is, firstly, performed as

$$M \rightarrow M_1 + M_2 \quad (18)$$

with

$$M_1 = G_1 G_2 \dots G_{n-1} H^{(n-1)} \quad (19)$$

and

$$M_2 = H^{(n)} G_n G_{n+1} \dots G_k, \quad (20)$$

where G_j and $H^{(j)}$ represent a fragment and a hydrogen cap, respectively. The total energy of the system can then be written by

$$E(M) = E(M_1) + E(M_2) + dE_1, \quad (21)$$

where dE_1 describes an energy change created by the bond breakage. The SFM scheme further makes another fragmentation,

$$M \rightarrow M_3 + M_4 \quad (22)$$

with

$$M_3 = G_1 G_2 \dots G_{i-1} H^{(i-1)} \quad (23)$$

and

$$M_4 = H^{(i)} G_i G_{i+1} \dots G_k. \quad (24)$$

The total energy in this case can be given by

$$E(M) = E(M_3) + E(M_4) + dE_2 \quad (25)$$

with the energy correction dE_2 . Then, assuming $i > n$, one finds a combined fragmentation,

$$M \rightarrow G_1 G_2 \dots G_{n-1} H^{(n-1)} + H^{(n)} G_n G_{n+1} \dots G_{i-1} H^{(i-1)} + H^{(i)} G_i G_{i+1} \dots G_k, \quad (26)$$

for which the total energy can be expressed by

$$E(M) = E(M_1) + E(M_5) + E(M_4) + dE_3 \quad (27)$$

with

$$M_5 = H^{(n)} G_n G_{n+1} \dots G_{i-1} H^{(i-1)} \quad (28)$$

and the energy change dE_3 due to the bond breakages. Here, if we make a reasonable approximation as

$$dE_3 \approx dE_1 + dE_2, \quad (29)$$

we obtain a fragmentation expression for the total energy as

$$E(M) \simeq E(M_2) + E(M_3) - E(M_5) \quad (30)$$

from Eqs. (21), (25) and (27). In the actual applications of SFM, the effects of non-bonded interactions are taken into account in *ab initio*, effective fragment potential and electrostatic ways according to interatomic distances.

Molecular tailoring approach (MTA) [12] and its modified version, cardinality guided molecular tailoring approach (CG-MTA) [13], provide not a residue-based method but a distance-based fragmentation method. Two length parameters are important in MTA, that is, maximum fragment size and R-goodness (R_g). MTA creates an initial set of fragments by centering a sphere of radius R_g at each atom and assigning all atoms to fall within the sphere to the fragment, in which aromatic rings and double bonds are kept intact. Then, additional atoms are included or excluded according to the criterion of maximum fragment size; the created fragments are merged due to their proximity and this merging is performed recursively depending on the maximum overlap of nearest neighbor fragments up to the maximum fragment size. After checking the fragments for the respective R_g value of the included atoms, broken bonds are capped with hydrogen atoms. The total energy of the system is then calculated, in which the contributions from all intersecting portions of the merged fragments are counted with the sign of each contribution being set to $(-1)^{K-1}$, where K refers to the number of fragments involved in the intersection. For example, in the case of two-fragment (F_1 and F_2) overlap, the total energy is given by

$$E_M = E_{F_1} + E_{F_2} - E_{F_1 \cap F_2}, \quad (31)$$

which is similar to the FMO2 expression.

The original formulation of divide-and-conquer (DC) approach [14] divides the density of the whole system into the sum of the densities of the subsystems on the basis of the Kohn–Sham density functional theory (DFT). The DC-DFT algorithm represents the three-dimensional space Ω as a union of overlapping spatial domains, $\Omega = \cup_{\alpha} \Omega_{\alpha}$, and physical properties are computed as linear combinations of domain properties. Each domain Ω_{α} is further decomposed into its sub-volumes as $\Omega_{\alpha} = \Omega_{0\alpha} \cup \Gamma_{\alpha}$. Here, $\Omega_{0\alpha}$ is a non-overlapping core covering Ω (i.e., $\Omega = \cup_{\alpha} \Omega_{0\alpha}$ and $\Omega_{0\alpha} \cap \Omega_{0\beta} = 0$ ($\alpha \neq \beta$)), whereas Γ_{α} is a buffer layer that surrounds $\Omega_{0\alpha}$. For each domain Ω_{α} , we define a domain support function $p_{\alpha}(\mathbf{r})$ which takes a value within the unit interval $[0, 1]$ and vanishes outside the domain Ω_{α} . The domain support functions constitute a partition of unity, that is, they satisfy the sum rule, $\sum_{\alpha} p_{\alpha}(\mathbf{r}) = 1$, at every spatial position \mathbf{r} . The partition of unity allows the electron density $\rho(\mathbf{r})$ to be decomposed into

$$\rho(\mathbf{r}) = \sum_{\alpha} \rho_{\alpha}(\mathbf{r}), \quad (32)$$

where $\rho_\alpha(\mathbf{r}) = p_\alpha(\mathbf{r})\rho(\mathbf{r})$ is the partial contribution to the electron density from domain Ω_α . The key approximation in DC-DFT is the replacement of the self-consistent Kohn–Sham Hamiltonian \hat{H} by its subspace approximation \hat{H}_α such that [14]

$$\rho_\alpha(\mathbf{r}) \simeq p_\alpha(\mathbf{r}) \langle \mathbf{r} | \frac{2}{\exp[(\hat{H}_\alpha - \mu)/k_B T] + 1} | \mathbf{r} \rangle, \quad (33)$$

where k_B is the Boltzmann constant, T is the (effective) temperature, and the chemical potential μ is determined from the number of electrons N through the relation, $N = \int d\mathbf{r} \rho(\mathbf{r})$. Here, the subspace Hamiltonian is defined through projection as

$$\hat{H}_\alpha = \int_{\Omega_\alpha} d\mathbf{r} \int_{\Omega_\alpha} d\mathbf{r}' | \mathbf{r} \rangle \langle \mathbf{r} | \hat{H} | \mathbf{r}' \rangle \langle \mathbf{r}' |. \quad (34)$$

One then solves the Kohn–Sham (KS) equation within each domain,

$$\hat{H}_\alpha \Psi_i^\alpha(\mathbf{r}) = \varepsilon_i^\alpha \Psi_i^\alpha(\mathbf{r}) \quad (35)$$

with the orthonormality constraints, $\int d\mathbf{r} \Psi_i^{\alpha*}(\mathbf{r}) \Psi_j^\alpha(\mathbf{r}) = \delta_{ij}$, where $\Psi_i^\alpha(\mathbf{r})$ is the i -th KS orbital with the energy eigenvalue ε_i^α . The electronic ground state is determined self-consistently; the electron density is obtained iteratively until the input density $\rho_{in}(\mathbf{r})$ becomes equal to the output density $\rho_{out}(\mathbf{r})$ within a prescribed tolerance. Here, $\rho_{in}(\mathbf{r})$ is used to calculate the KS potential in \hat{H}_α , whereas $\rho_{out}(\mathbf{r})$ is calculated from Eqs. (32) and (33) using the KS orbitals obtained by solving the KS equations, Eq. (35). It is noted that the local domain KS orbitals are globally informed through the global KS potential and chemical potential. It is also remarked that the DC-DFT scheme can be generalized to be applicable to *ab initio* molecular orbital calculations [15].

Finally, we briefly illustrate the group molecular orbital (GMO) method [16], which is expressed as a localized orbital approach by

$$\left(\hat{F} + \hat{P}_I \right) \varphi_i^I = \varepsilon_i^I \varphi_i^I, \quad (36)$$

$$\hat{P}_I = - \sum_{J \neq I} \left(\hat{F} \sum_i^{occ.} |\varphi_i^J\rangle \langle \varphi_i^J| + \sum_i^{occ.} |\varphi_i^J\rangle \langle \varphi_i^J| \hat{F} \right), \quad (37)$$

where \hat{F} and \hat{P}_I are the Fock and projection operators, respectively; φ_i^I and ε_i^I are the i -th molecular orbital and energy for subsystem (or “group”) I . (“*occ.*” means the occupied states.) The (Huzinaga) SCF equation for group I is then given by

$$\tilde{\mathbf{F}}^I \mathbf{C}^I = \mathbf{S}^I \mathbf{C}^I \boldsymbol{\varepsilon}^I \quad (38)$$

with

$$\tilde{F}_{\mu\nu}^I = F_{\mu\nu}^I + P_{\mu\nu}^I. \quad (39)$$

Here, $\tilde{F}_{\mu\nu}^I$ and $P_{\mu\nu}^I$ are the matrix elements of the effective Fock and projection operators of group I , respectively, with

$$F_{\mu\nu}^I = H_{\mu\nu}^I + V_{\mu\nu}^{2,I} + V_{\mu\nu}^{\text{emb},I}, \quad (40)$$

$$H_{\mu\nu}^I = \langle \mu | -\frac{1}{2}\Delta | \nu \rangle + V_{\mu\nu}^{1,I}, \quad (41)$$

$$V_{\mu\nu}^{1,I} = \sum_{A \in I} \langle \mu | \frac{-Z_A}{|\mathbf{r} - \mathbf{R}_A|} | \nu \rangle, \quad (42)$$

$$V_{\mu\nu}^{2,I} = \sum_{\lambda, \sigma \in I} D_{\lambda\sigma}^I \left[(\mu\nu | \lambda\sigma) - \frac{1}{2} (\mu\lambda | \nu\sigma) \right], \quad (43)$$

$$D_{\lambda\sigma}^I = 2 \sum_i^{\text{occ.}} C_{\lambda i}^I C_{\sigma i}^I. \quad (44)$$

\mathbf{F}^I , \mathbf{H}^I , $\mathbf{V}^{1,I}$, $\mathbf{V}^{2,I}$, and \mathbf{D}^I are the Fock matrix, core Hamiltonian, nuclear attraction, electron–electron repulsion, and density matrix of group I , respectively. $V^{\text{emb},I}$ is the embedding potential for group I due to the rest of the system,

$$V_{\mu\nu}^{\text{emb},I} = \sum_{J \neq I}^N (V_{\mu\nu}^{1,J} + V_{\mu\nu}^{2,J}), \quad (45)$$

with N being the number of groups. The projection operator is written as

$$P_{\mu\nu}^I = - \sum_{J \neq I} \sum_{\mu', \nu' \in J}^{N_{\text{ov}}^I} D_{\mu'\nu'}^J (F_{\mu\mu'}^J S_{\nu'\nu}^J + S_{\mu\mu'}^J F_{\nu'\nu}^J), \quad (46)$$

where \mathbf{S}^J is the overlap integral matrix and N_{ov}^I is the number of overlapping tail groups around group I . The total electronic energy E_I^{ele} of group I is then given by

$$E_I^{\text{ele}} = \frac{1}{2} \text{Tr} \left\{ \mathbf{D}^I \cdot \left(\tilde{\mathbf{F}}^I + \mathbf{H}^I + \mathbf{P}^I \right) \right\}. \quad (47)$$

It is noted that no bond detachment or capping treatment is required in the GMO method in contrast to the FMO and other fragmentation methods, which is due to the introduction of the overlapping tail groups.

3 Pros and Cons: Cost, Accuracy, Viability, and Versatility

3.1 *Disturbance of Electronic States*

Quantum chemical calculations aim at obtaining the most accurate solution to the electronic state of molecular system whose Hamiltonian (model) is given. Then, by introducing various types of model approximations concerning the system division, fragmentation methods inevitably disturb the electronic state of the system from that of the original model, thus causing some inaccuracies and associated irrelevances.

In the FMO method, the C_{α} atom is usually chosen as the bond detached atom (BDA) associated with the single bond breaking between fragments. The dangling bond is thus processed in terms of precalculated sp^3 natural orbital of methane without introduction of hydrogen cap, where the projection operator is used for the distribution of the localized orbitals (Sect. 1). In some other approaches such as KEM and SFM, in contrast, the hydrogen cap is employed for the fragmentation. This introduction of the hydrogen cap may disturb the electronic states and associated energetics of the fragments locally, and may also cause artificial steric effects in some cases. To reduce these adverse effects, the MFCC method employs the “concap” that contains the residues on the both sides of the fragments (see Sect. 2). In the KEM approach, a unique fragmentation called “fissioning” process is also attempted to divide the aromatic bonds (Sect. 2), thus enabling the treatment of conjugated systems such as graphene with reasonable accuracy. The FMO method also explores the possibility of fragmentations other than single bond division with the sp^3 orbital [3] to extend its applicability over various molecular systems (see also Sect. 1). In the DC method, the buffer region plays a role to mitigate the disturbance of electronic states due to the domain division, whereas the choice of its size brings about a trade-off relationship between cost and accuracy (see Sect. 3.4 below).

3.2 *Environmental Effects*

In principle, all the fragmentation schemes can take into account the environmental electrostatic potentials arising from surrounding fragments by incorporating the contributions into local Hamiltonians, while some approaches do (did) not consider them currently (previously). The inclusion of solvent effects primarily associated with surrounding water is similar, but some additional cautions should be considered. If the aqueous solvent effects are described *explicitly*, a water molecule or its cluster is taken into account as a part of the whole molecular system, which can be regarded as a fragment similar to an amino acid residue. It is then known [17] that higher order expansion corrections such as FMO3 over more than two fragments play a significant role to accurately describe the polarization and charge transfer among water molecules. When the solvent effects are considered *implicitly*, on the other hand, some coarse-grained descriptions such as the polarizable continuum model (PCM)

[18], the generalized Born or Poisson–Boltzmann surface area model [19–22], and the effective fragment potential (EFP) method [23] can be combined with each fragmentation model, which have been implemented in the FMO scheme. The choices of combined description schemes are then made considering the compatibility, cost, and purposes for efficient descriptions of dielectric screening, hydrogen bonding, and proton transfer. In addition, when treating large molecular systems, one would sometimes need to incorporate the periodic boundary condition into modeling, which would bring about additional complications in the fragmentation schemes [24].

3.3 *Utility and Extension*

How to make the fragmentation significantly affect the utility and the possible extension of each fragmentation method. In general, the fragmentation methods enable the inter-fragment interaction energy analysis, which would be useful for the rational design of small compound inhibitors and antibody drugs to target proteins, for example. In the case of FMO method, the protein–ligand interaction energy analysis can be comprehensively performed in terms of IFIE (inter-fragment interaction energy) [2] and PIEDA (pair interaction energy decomposition analysis) [25]. However, it is remarked that the FMO scheme usually employs the fragment division not at the peptide bond but at the C_α atom (Sect. 1), which would require some cautions to researchers [26] with respect to the compromise between accuracy and utility. Concerning the incorporation of electron correlation energies, on the other hand, virtually all the fragmentation methods can afford to incorporate the conventional calculation schemes (*e.g.*, MP2, CC, and DFT) in quantum chemistry in straightforward manners, because the electron correlation effects are generally localized spatially. However, the calculations of energy gradients in the fragmentation schemes usually become very complicated [27] and do not allow the use of numerical differentiations to retain satisfactory accuracies. In addition, the issues of diffusion of water molecules and proton transfer in hydrated MD simulations would also require appropriate adjustments of fragmentation to prevent the discontinuities in energy evaluation [2].

3.4 *Cost and Accuracy*

The cost and accuracy of fragmentation methods are usually in a trade-off relationship with each other. In the case of FMO method, at least FMO2 approximation is needed to account for the charge transfer between fragments, which naively requires $O(N^2)$ computational cost, while it can be substantially reduced by sorting with distance thresholds for fragment pairs [2]. In general, fragmentation methods aim at $O(N)$ computation of large molecular systems and then the size of the largest fragment governs the total computation time. Therefore, the MFCC scheme in which approximately three amino acid residues are contained in a fragment demands relatively

high computational cost. Even in the case of FMO method, the load balance is often impaired due to the presence of large residues such as tryptophan or large ligand molecules. In this respect, distance-based fragmentation methods such as MTA may have advantage over other (usually residue-based) approaches. In the case of FMO, a finer fragmentation necessarily leads to inaccuracies in energy expansion, but the ingenious utilization of higher order expansion techniques such as FMO3 and FMO4 would mitigate the difficulties [2, 28].

4 Perspective

One of the most essential issues in the fragmentation methods is the balance between cost and accuracy. Probably, what is the best choice may be highly dependent on the molecular system to be described and on the purpose of the research. In this context, the optimization of the implementation could be carried out with the aid of machine learning or artificial intelligence techniques in the future studies. In addition to the size of fragments, the sites of fragment division substantially affect the accuracy of molecular properties. More specifically, the single bond fragmentation is usually employed in various fragmentation approaches to suppress the disturbance of electronic states, but the possibilities of other ingenious bond divisions may be explored to attain a better performance. Furthermore, some hybrid schemes similar to the concepts of QM/MM and multi-layer approaches may also be attempted. For example, relevant embedding approaches for metal-containing enzymes would be promising for performing the statistical or dynamical simulations with high accuracy.

Among various fragmentation schemes addressed in this chapter, the GMO method also provides a suitable approach for accurately calculating large molecular systems. This procedure solves the Huzinaga subsystem SCF equations using a couple of approximations. It is shown that the GMO scheme can reproduce *ab initio* calculation results quite well and has several additional interesting properties. For example, no caps are required in GMO, where fragment boundaries are naturally handled; molecular charges can be delocalized at fragment boundaries because of the use of tail groups; and the embedding potential properly considers the exchange interaction, which is sometimes ignored in other embedding methods. Moreover, GMO gives fully variational and quasi-orthogonal wave functions among groups (fragments). In the future studies, the large-scale $O(N)$ computations based on the GMO scheme would be anticipated.

5 Conclusion

In this chapter, a variety of fragmentation schemes for large molecular systems were illustrated, laying a main focus on biomolecules, where wave functions are relatively localized. In addition to insulating systems, it is often required for fragmentation

methods to relevantly describe semiconducting, metallic, and charge-transfer systems such as π -conjugated materials, thus attaining wider applicability for general molecular systems. Based on the observation that details of fragmentation implementation are significantly changing from the original version in various fragmentation schemes other than the FMO method, one has much room for making systematic improvement of computational performance, which in turn provides challenging tasks toward accurate $O(N)$ *ab initio* calculations.

References

1. Gordon MS (ed) (2017) Fragmentation: toward accurate calculations on complex molecular systems. Wiley, Chichester, UK
2. Tanaka S, Mochizuki Y, Komeiji Y, Okiyama Y, Fukuzawa K (2014) *Phys Chem Chem Phys* 16:10310
3. Tamura K, Watanabe T, Ishimoto T, Nagashima U (2008) *Bull Chem Soc Jpn* 81:110
4. Nakano T, Kaminuma T, Sato T, Akiyama Y, Uebayasi M, Kitaura K (2000) *Chem Phys Lett* 318:614
5. Nagata T, Fedorov DG, Kitaura K (2010) *Chem Phys Lett* 492:302
6. Fedorov DG, Jensen JH, Deka RC, Kitaura K (2008) *J Phys Chem A* 112:11808
7. Fedorov DG, Avramov PV, Jensen JH, Kitaura K (2009) *Chem Phys Lett* 477:169
8. Huang LL, Massa L, Karle J (2005) *Int J Quantum Chem* 103:808
9. Huang L, Massa L, Karle J (2008) *Proc Natl Acad Sci USA* 105:1849
10. Zhang DW, Xiang Y, Zhang JZH (2003) *J Phys Chem B* 107:12039
11. Collins MA, Deev V (2006) *J Chem Phys* 125:104104
12. Babu K, Gadre SR (2003) *J Comput Chem* 24:484
13. Ganesh V, Dongare RK, Balanarayan P, Gadre SR (2006) *J Chem Phys* 125:104109
14. Yang WT (1991) *Phys Rev Lett* 66:1438
15. Kobayashi M, Akama T, Nakai H (2006) *J Chem Phys* 125:204106
16. Shimazaki T, Kitaura K, Fedorov DG, Nakajima T (2017) *J Chem Phys* 146:084109
17. Fujita T, Fukuzawa K, Mochizuki Y, Nakano T, Tanaka S (2009) *Chem Phys Lett* 478:295
18. Fedorov DG, Kitaura K, Li H, Jensen JH, Gordon MS (2006) *J Comp Chem* 27:976
19. Watanabe H, Okiyama Y, Nakano T, Tanaka S (2010) *Chem Phys Lett* 500:116
20. Okiyama Y, Nakano T, Watanabe C, Fukuzawa K, Mochizuki Y, Tanaka S (2018) *J Phys Chem B* 122:4457
21. Okiyama Y, Watanabe C, Fukuzawa K, Mochizuki Y, Nakano T, Tanaka S (2019) *J Phys Chem B* 123:957
22. Watanabe C, Watanabe H, Fukuzawa K, Parker LJ, Okiyama Y, Yuki H, Yokoyama S, Nakano H, Tanaka S, Honma T (2017) *J Chem Inf Model* 57:2996
23. Nagata T, Fedorov DG, Kitaura K, Gordon MS (2009) *J Chem Phys* 131:024101
24. Fujita T, Nakano T, Tanaka S (2011) *Chem Phys Lett* 506:112
25. Fedorov DG, Kitaura K (2007) *J Comput Chem* 28:222
26. Yoshioka A, Takematsu K, Kurisaki I, Fukuzawa K, Mochizuki Y, Nakano T, Nobusawa E, Nakajima K, Tanaka S (2011) *Theor Chem Acc* 130:1197
27. Fedorov DG, Nagata T, Kitaura K (2012) *Phys Chem Chem Phys* 14:7562
28. Watanabe C, Fukuzawa K, Okiyama Y, Tsukamoto T, Kato A, Tanaka S, Mochizuki Y, Nakano T (2013) *J Mol Graph Model* 41:31

Programs

Recent Development of the Fragment Molecular Orbital Method in GAMESS



Dmitri G. Fedorov

Abstract The development of the fragment molecular orbital (FMO) method in GAMESS is reviewed, summarizing implemented physical properties and computational methods. Algorithmic improvements of FMO to reduce memory requirements and to describe dipole moments in solution are also presented.

Keywords FMO · GAMESS · Dipole moment · Solvent effect

1 Introduction

The recent progress in the development of quantum mechanical (QM) methods for calculations of large molecular systems [1, 2] has been reviewed in detail [3–6], putting the fragment molecular orbital (FMO) method [7] in a perspective with other low-scaling QM methods.

In the course of development by multiple research groups, FMO has been implemented in several computational packages. Some of these FMO implementations such as that in NWChem [8], have remained local, whereas those in ABINIT-MP [9], PAICS [10], and OpenFMO [11] are distributed.

General atomic and molecular electronic structure system (GAMESS) [12, 13] is a QM package, with a freely distributed source [14]. This chapter is mainly a summary of the recent progress in the implementation of FMO specifically in GAMESS [15, 16], whereas in the earlier FMO reviews [17–20] the method is described in a more general way. FMO was released in GAMESS in 2004 (FMO code version 1.0) and the current version available in distributed GAMESS is 5.3.

D. G. Fedorov (✉)

Research Center for Computational Design of Advanced Functional Materials (CD-FMat),
National Institute of Advanced Industrial Science and Technology (AIST), Central 2, Umezono
1-1-1, Tsukuba 305-8568, Japan
e-mail: d.g.fedorov@aist.go.jp

© Springer Nature Singapore Pte Ltd. 2021

Y. Mochizuki et al. (eds.), *Recent Advances of the Fragment Molecular Orbital Method*,
https://doi.org/10.1007/978-981-15-9235-5_3

31

2 FMO Methodology

The FMO method has been described in detail elsewhere [21], and here a succinct description is provided for completeness. FMO n is based on an n -body expansion [22] of size-extensive properties, such as the energy (of size-extensive QM methods), its derivatives, electrostatic moments, electron density, etc. The energy expression for a system divided into N fragments, truncated at the three-body level FMO3, can be written as

$$E^{\text{FMO3}} = \sum_I^N E_I + \sum_{I>J}^N \Delta E_{IJ} + \sum_{I>J>K}^N \Delta E_{IJK} \quad (1)$$

where E_I , ΔE_{IJ} and ΔE_{IJK} are the energies of fragments (monomers), pair (dimer) and trimer corrections, respectively. FMO2, which neglects the last sum in Eq. 1, is frequently used. FMO1 [23, 24] and FMO4 [25] are sometimes used, but less extensively, the former because its accuracy can be insufficient and the latter due to its large computational cost. FMO has been also formulated [26] as a perturbation theory (treating many-body corrections as the perturbation).

Equation 1 can be used for excited states, computed with multiconfiguration self-consistent field (MCSCF) [27], configuration interaction (CI) [28], or time-dependent (TD) density functional theory (DFT) [23]. There can be at most one excited state fragment and other fragments are calculated in the ground state (excited states for dimers are computed only for fragment pairs including the excited state fragment).

An electronic state of any multiplicity can be used in Eq. 1, with restricted or unrestricted open-shell methods as well as with MCSCF [27]. Typically, only one fragment may be open-shell; however, there is a formulation [29] for multiple open-shell fragments, for which dimers and trimers, following the angular momentum addition, are calculated in the highest spin state determined by the multiplicities of monomers. There are methods for treating non-local excitations in FMO by taking into account the coupling between local excitations [30, 31].

2.1 Outline of FMO

FMO calculations are done as follows. First, starting from a set of atomic coordinates, the system is divided into fragments. Various modeling software can be used to do it automatically or manually in GUI. For example, Facio [32] can be used to automatically fragment peptide (protein etc.), nucleotide (DNA etc.), and saccharide (cellulose etc.) systems or any combination thereof. FU [33] can automatically fragment peptides. The most general automatic fragmentation is provided in FragIt [34], where SMILES patterns can be defined for an automatic fragmentation. For non-standard systems, one can define detached bonds manually in Facio by clicking on them.

There is a simple general guideline for fragmentation: the electron density calculated for the whole system and integrated over a set of atoms designed to become a fragment should give the number of electrons as close to an integer as possible (this is because in the fragment calculations the number of electrons is integer). Of course, this exact definition requires full calculations and thus is not used in practice; however, one can roughly predict the delocalization of electrons because molecular systems are connected by a finite set of bonding patterns. Charge transfer between fragments should be minimized but it is acceptable to allow charge transfer on the order of hydrogen bonding (0.05 e). If one attempts to assign one metal cation as a fragment, such fragmentation is usually poor [35], because a large amount of charge may be pulled toward the cation from other fragments. Another point of concern is the conjugation of π electrons, which tend to delocalize.

Usually, single bonds are detached between fragments, although there are exceptions [36]. FMO uses no hydrogen caps because the embedding potential effectively saturates the bonds on fragment boundaries. Two treatments of bond detachment are available, hybrid orbital projection (HOP) [37, 38] and adaptive frozen orbitals (AFO) [39–41]. The former features unrestricted interfragment polarization and is most commonly used for fragmenting one-dimensional chains of atoms (e.g., proteins, DNA, polymers, etc.). Using HOP requires a set of precalculated hybrid orbitals for the bond detached atom (BDA) of each detached bond [37]. These orbitals are pretabulated for most commonly used basis sets. There is a simple scheme for users to generate hybrid orbitals for any basis set and any (single) bond.

In AFO, the electron density of the detached bonds is precalculated for a model system and remains frozen in FMO calculations (all model systems are automatically constructed in the beginning of an FMO/AFO calculation, so that AFO is easy to use). AFO is used for inorganic materials where several bonds can be detached between two fragments. For instance, zeolite clusters [39], silicon nanowires [40], mesoporous silica [42] or ribbons of white graphene [36] are well treated with AFO. Organic charge transport materials [43] have been treated with HOP.

Fragments and their conglomerates are calculated in FMO in the presence of an embedding electrostatic potential (ESP). This ESP for fragment X is calculated using the density (or atomic charges) of all fragments excluding X . ESP depends on the electronic state of all fragments, and thus the fragment calculations in the presence of ESP must be repeated iteratively until the embedding potential converges. After that, fragment pairs and, optionally, trimers are calculated in the presence of the ESP, which is fixed at this stage. The total properties are calculated using the many-body expansion in Eq. 1.

The gradient in FMO is complicated by the dependence of the ESP on the electronic state of each fragment, and one has to solve self-consistent Z-vector (SCZV) equations [44] to obtain orbital responses, similar to the Z-vector method used in the second-order Møller-Plesset perturbation theory (MP2) gradient. SCZV equations have to be derived for each QM method separately. The AFO gradient is even more complex because of extra constraints and only recently [41] the SCZV formulation for density-functional tight-binding (DFTB) [45] has been accomplished.

The analytic Hessian in FMO [46] can be used to generate IR and Raman spectra [47]. By decomposing the Fock matrix in a many-body expansion similar to Eq. 1, and diagonalizing it, one can obtain molecular orbitals (MOs) and density of states (DOS) [48, 49] of a large system.

It is possible to divide the system into layers and specify a different basis set and/or a QM method, in the multilayer formulation of FMO [50]. For instance, one can use a better QM method for an important part of the system, such as the binding pocket of a protein. It is also possible to mix basis sets within the layer, for example, one can add diffuse functions to anionic functional groups. In addition, one can mix basis sets in the auxiliary scheme [51], in which to improve the accuracy of FMO for large basis sets, the polarization effects are evaluated using a smaller basis set, and added to the FMO calculation with a larger basis set without embedding. In the effective FMO method [52–57], polarization is estimated using polarizabilities.

One can take advantage of multilayer FMO for optimizing geometry of a subsystem, for example, ligand and the binding pocket of a protein. It is accomplished in the frozen domain approach [58–60], in which the cost of a partial geometry optimization is much reduced by freezing the electronic state of fragments far away from the active domain whose structure is optimized.

2.2 *Decomposition of Properties*

The many-body expansion in Eq. 1 yields the total properties which closely but not exactly reproduce full QM calculations without fragmentation. It has been argued [61] that the origin of the discrepancy between FMO and full QM calculations lies in the omission of $(n + 1)$ -body quantum–mechanical terms (attributed to charge transfer and exchange–repulsion) in FMO n , whereas the electrostatic treatment including polarization [62] in FMO is exact (except when the polarization is restricted in the AFO scheme or when ESP approximations are used). Equation 1 has the complexity of including many-body electrostatic interactions in each term (including monomer terms E_I), so in Eq. 1 the electrostatic effects are treated at the full N -body level and only non-electrostatic effects are truncated at an n -body level ($n \leq N$) [61].

The many-body expansion provides very fruitful means to define properties of fragments (one-body properties), interactions between fragments (two-body properties) and coupling between fragment interactions (three-body properties). This analysis conceptually corresponds to the use of functional groups in chemistry (analogous to fragments in FMO), which may be affected by the environment (interactions with other fragments). Normally, fragments in FMO cannot be literally as small as functional groups such as OH, because the accuracy is affected by such an excessive fragmentation, although by using FMO4 [63] the accuracy problem for the total properties may be much reduced.

The FMO expansion in Eq. 1 is applied to fragments fully polarized by the environment. The polarization effects are included in the monomer energies, and can

be easily extracted by performing isolated fragment calculations [61] (which can be somewhat ambiguous for fragments connected by covalent bonds, but one can use the minimum cap approach [61] to resolve it). Pair interaction energies (PIEs) ΔE_{IJ} in Eq. 1 are not binding energies between *isolated* fragments; rather, PIEs are interaction energies between *polarized* fragments. This should be remembered when comparing PIEs to other methods.

There are several energy decomposition schemes for FMO. GAMESS includes two of them, interaction energy analysis (IEA) [64] and pair interaction energy decomposition analysis (PIEDA) [61, 65–67]. In PIEDA/MP2, the pair interactions are decomposed into five components, electrostatic (ES), exchange-repulsion (EX), charge transfer and mix terms (CT + mix), dispersion and remainder correlation (DI + RC), and solvent screening (SOLV).

$$\Delta E_{IJ} = \Delta E_{IJ}^{\text{ES}} + \Delta E_{IJ}^{\text{EX}} + \Delta E_{IJ}^{\text{CT+mix}} + \Delta E_{IJ}^{\text{DI+RC}} + \Delta E_{IJ}^{\text{SOLV}} \quad (2)$$

PIEDA can be applied to most QM methods that are interfaced with FMO. In RHF and DFTB, $\Delta E_{IJ}^{\text{DI+RC}}$ is replaced with $\Delta E_{IJ}^{\text{DI}}$ evaluated using an empirical dispersion model [68]; in DFTB, in addition, $\Delta E_{IJ}^{\text{EX}} + \Delta E_{IJ}^{\text{CT+mix}}$ is replaced with $\Delta E_{IJ}^0 + \Delta E_{IJ}^{\text{CT-ES}}$, where “0” and “CT-ES” denote the non-polar 0-order Hamiltonian term and the coupling of CT and ES, respectively. For HF-3c [69], there is an additional basis set superposition error correction term $\Delta E_{IJ}^{\text{BS}}$, and for the auxiliary basis formulation [51] there is a basis set correction term $\Delta E_{IJ}^{\text{BS}}$.

When studying binding between some systems A and B (e.g., protein A and ligand B), it is necessary to do an FMO decomposition for each system, i.e., for A, B, and AB, and then subtract A and B properties from those of AB. If one calculates only a complex AB, the very important effects of deformation, desolvation, and polarization are not properly considered, and the interaction energy in the complex is typically a large overestimate of the binding energy [70]. Studying a binding is conveniently accomplished using the subsystem analysis [70], in which the binding (“bind”) energy is decomposed into fragment contributions.

$$\Delta E^{\text{bind}} = \sum_I^N \Delta E_I^{\text{bind}} \quad (3)$$

In case of rigid inorganic materials such as zeolites binding guest molecules, one can take an optimized structure for an interaction analysis. However, for flexible organic molecules, such as proteins, it may be better to study binding by doing molecular dynamics (MD) simulations [71], and decompose the binding energy averaged over an MD trajectory. FMO has been recently extended [72] to perform such analyses of fluctuations in MD, taking into account temperature and flexibility of molecules. Doing sufficiently long MD simulations is problematic even for fast methods such as DFTB: for the small Trp-cage protein consisting of 20 residues only 1 ns FMO/MD simulations have been done [73].

2.3 Solvation Models for FMO in GAMESS

Although one can use explicit QM treatment of solvent molecules in FMO, it requires configurational sampling, which is computationally expensive. Several other solvent models are available for FMO in GAMESS. For effective fragment potentials (EFP), solvent molecules are treated explicitly, so that the sampling problem remains, but the EFP cost is rather low (FMO is interfaced only with the first generation EFP1) [74–76]. There is a special analysis developed for FMO/EFP, IEA [64], which provides a decomposition of the energy to quantify solvent effects such as polarization. In the polarizable continuum model (PCM) [77], solvent is treated as continuum, which is very convenient for defining solvent screening and cost-effective as the solvent sampling problem does not arise. The solvation model density (SMD) approach shares the treatment of solvent–solute electrostatics with PCM, but the non-polar interaction is described differently [78].

It is possible to combine FMO with molecular mechanics (MM), using the Tinker [79] interface to GAMESS. In the implementation of FMO/MM [22, 80], no MM charge embedding is used, i.e., it is an integrated MO MM (IMOMM) [81] rather than a QM/MM [82] approach. Geometries of proteins and protein–ligand complexes have been optimized with FMO/MM [22, 80].

2.4 Reduction of Memory Requirements in FMO

One big problem in running FMO calculations of large systems is memory. Even on PC clusters, where one can have many gigabytes of RAM per core, the problem arises when the number of fragments is large; on modern supercomputers the problem is severe, because they tend to have a relatively small amount of memory per core. Some novel algorithmic solutions are described below.

Although the scaling of FMO has been measured to be nearly linear, $O(N^{1.2})$ [45] for FMO2 applied to realistic globular water clusters, the memory consumption for FMO n in GAMESS is $O(N^n)$. It is clear that this is a big problem when N is large. For example, for 10,000 fragments, the memory requirement would be proportional to 800,000,000 bytes ($8N^2$) per core even at the level of FMO2. The exact factor (usually, 3–10) multiplying this big number depends on the details of calculations.

In this work, two solutions are described, one for FMO2 and another for FMO3. In the case of FMO3 in GAMESS, at least two elements in the $O(N^3)$ array are stored for each trimer. The solution adopted here is to avoid storing all trimer corrections. Instead, one adds them up on the fly and obtains the total energy. These trimer terms may be of interest in analyzing interactions, and they are printed in the output so that if necessary, they can be extracted by postprocessing scripts. By doing this, all $O(N^3)$ arrays are eliminated in FMO3, but all $O(N^2)$ arrays remain, making the FMO3 memory requirements quadratic.

For FMO2, there is an $O(N^2)$ array that stores several energy terms for each dimer. It can be similarly eliminated by adding up all terms and printing individual values without storing them. However, there is another problem. In FMO, one typically uses approximations to reduce the computational cost to nearly linear. This requires that one should define interfragment distances, which is an $O(N^2)$ array. It cannot be simply eliminated as other energy arrays, and a different strategy is employed.

In a typical setup of doing FMO calculations, one has to distinguish near fragment pairs from the rest in order to apply efficient approximations. The number of near pairs is linear [83], with the prefactor controlled by the threshold. Therefore, instead of an $O(N^2)$ array, an array of the size of aN is allocated, which for each fragment I stores a short list of fragments J for near dimers IJ . The parameter a is the maximum size of this list; it is predicted by the user and in practice it is set to 5–10, depending on the packing of fragments in space. Such an array does eliminate the quadratic memory requirement for FMO2, when combined with the strategy of not storing individual dimer terms. Note that this strategy cannot at present be used to linearize FMO3 memory requirements, because the computation of trimer corrections on the fly uses stored dimer energies, so that FMO3 calculations need a quadratic memory allocation. In the current implementation of linearizing the FMO2 memory usage there are some limitations, for instance, all approximation thresholds must use the same value and some methods storing extra dimer terms may not be used.

2.5 Electrostatic Embedding

The electronic state of fragments is obtained in FMO in the presence of an embedding potential, which describes polarization. Because ESP is calculated self-consistently, polarization is described at the full many-body level (all fragments polarize each other until convergence) [61]. The polarization is a very important many-body effect and the form of ESP affects the results. In the original FMO [7], the ESP V^X of fragment X is taken to have the form of the ab initio Coulomb operator,

$$V_{\mu\nu}^X = \sum_{K \neq X}^N \left\{ \sum_{A \in K} \left\langle \mu \left| -\frac{Z_A}{|\mathbf{r} - \mathbf{R}_A|} \right| \nu \right\rangle + \sum_{\rho\sigma \in K} D_{\rho\sigma}^K (\mu\nu|\rho\sigma) \right\} \quad (4)$$

where μ , ν , ρ and σ number atomic orbitals (AOs), K runs over fragments and A over atoms. Z_A and \mathbf{R}_A are the atomic charges and coordinates, respectively. \mathbf{D}^K is the electron density of fragment K .

It has been suggested [84] to use approximations to the two-electron term, point charge (ESP-PC) and atomic population (ESP-AP) for far separated fragments. These approximations, although successful in accelerating the calculations, result in numerical errors, especially at a high-order expansion level [85]. Also, approximating ESP requires special response terms for the gradient [86].

It can be argued that for small values of thresholds, such an ESP results in a different physical model rather than approximates the full two-electron embedding, as the name may mistakenly suggest. Switching to the purely one-electron form of ESP [87, 88] by applying the ESP-PC approximation to all fragments K in Eq. 4, allows one to use very diffuse basis sets, which otherwise have severe convergence problems in FMO. However, for covalently connected fragments the FMO accuracy with such one-electron ESP is in general not satisfactory [88]. It has also been suggested to combine calculations with ESP for medium basis sets and calculations without ESP for diffuse basis sets in the auxiliary basis set approach [51]. Alternatively, large basis sets can be used in “our own N -layered integrated molecular orbital and molecular mechanics” (ONIOM) combined with FMO [89].

It has been attempted with limited success to use damping of point charges to take into account charge penetration [88]. However, in FMO-DFTB [45], a one-electron form of ESP is always used, which is based on a more complex form of the Coulomb operator than a simple inverse distance, and FMO-DFTB with such potential works well also for covalently connected fragments. It has been suggested to use multiple charges per atom to mimic multipoles for a special type of FMO calculations [90].

It has been proposed to improve the physical model of ESP by adding exchange terms [26, 48]. However, it does not improve the accuracy of FMO except for the special case of adding exchange terms to the total Fock matrix for the purpose of defining molecular orbitals of the whole system [48, 49].

In FMO, one can use a cluster representation of crystal embedding by placing the system in the field of point atomic charges [91]. Alternatively, a periodic form of the ESP can be used with periodic boundary conditions [92, 93]. To accelerate ESP calculations, the multipole expansion [94] can be used. In solution, an embedding from the solvent can be added using one-electron potentials for point charges on the cavity [77].

2.6 Summary of the FMO Functionality in GAMESS

A summary of the FMO development for different QM methods in GAMESS is given in Table 1. Because gradient development is complicated by the need to formulate SCZV, some methods and options have not been extended to allow accurate gradient calculations, and for some methods such as coupled cluster (CC), only energy can be calculated.

In terms of the types of calculations (Table 2), one can do single point runs (to obtain the energy for a given molecular structure), geometry optimization to locate minima, saddle point search to locate transition states, vibrational analysis (Hessian), or IR and Raman spectra simulations. Several analyses are available in GAMESS: PIEDA, IEA and the fluctuation analysis for MD. Molecular orbitals and energies, and density of states (DOS) can be computed. For treating heavy atoms, one can use effective or model core potentials, which have been interfaced with FMO in GAMESS [76]. FMO results can be plotted using Facio [32] or FU [33].

Table 1 Summary of the FMO development in GAMESS

Method	Energy	Gradient	Hessian
HF	[12, 121]	[12, 29, 44, 122, 123]	[46, 124]
DFTB	[45, 125]	[126, 127]	[128, 129]
DFT	[130, 131]	[130, 132]	[133, 134]
MP2	[135–137]	[135, 138, 139]	
CC	[140, 141 ^a]		
MCSCF	[27]	[27]	
TDDFT	[27, 142, 143 ^a]	[144]	
CI	[145]		
PCM	[77, 146]	[147, 148]	[149]
EFP	[74]	[75, 76]	
RISM	[150] ^a		

^aImplemented in a local version

Table 2 Summary of FMO development in GAMESS

Property	References
Energy	[12]
Gradient	[44]
Hessian	[46]
Mapping chemical reactions	[54, 59]
Electronic excitations	[23, 27, 145]
Pair interaction energies	[61, 65, 66, 72]
Gibbs free energies	[46]
Atomic charges and higher multipole moments	[12]
Electron density on a grid	[20, 24]
Molecular electrostatic potential (MEP) on a grid	[151, 152]
Fock matrix, MOs and their energies, DOS	[48, 49, 153–155] ^a
Fragment-wise dielectric constants	[65]
Infrared spectrum	[46]
Raman spectrum	[47]
Nuclear magnetic resonance shift ^a	[90, 156, 157]
Ion mobility spectroscopy ^a	[24]
Isotope effects ^a	[158]
Charge carrier mobility ^a	[113]
Radial distribution function ^a	[129]

^aAvailable in a local version or requires supplemental software

The parallelization of FMO in GAMESS uses generalized distributed data interface (GDDI) [95], in which CPU cores are assigned to groups, and one group performs a fragment or a dimer/trimer calculation. Grouping cores has the big advantage of reducing the parallel communications to a small subset of all cores and thus increasing the parallel efficiency. On the other hand, it gives rise to a somewhat complicated problem of optimizing load balancing at two levels within and between groups. Several approaches to the load balancing can be used: static [95], dynamic [95], and semi-dynamic [96], whereas the heuristic static load balancing [97] and the heterogeneous scheme [98] use a sophisticated balancing optimization. FMO has been used on many supercomputers including Intrepid [99], Mira [100], and the K computer [101]. Recently, an OpenMP parallelization of FMO in GAMESS has been developed [101, 102].

As an application, chignolin (PDB: 1UAO) was calculated at the level of Hartree–Fock (HF) with the 6-31G** basis set combined with conductor PCM (C-PCM) at the level of PCM <1> using van-der-Waals atomic radii. The solute cavity is constructed by combining atomic spheres, each of which is divided into 60 tesserae with a point charge on each tessera. The charge renormalization was not used (to probe effect of the charge escape, i.e., of the distribution of a part of the electron density of the solute outside of the solvent cavity).

Solvent screening in PCM appears because of induced solvent charges, which can be defined as the sum of solvent charges \tilde{q}_i around a given solute atom [64]. One can also define the solvent dipole moment $\tilde{\mathbf{d}}^X$ for fragment X as

$$\tilde{\mathbf{d}}^X = \sum_{i \in X} \tilde{q}_i (\mathbf{R}_i - \mathbf{R}_0) \quad (5)$$

where i numbers tesserae with charge \tilde{q}_i and coordinate \mathbf{R}_i . \mathbf{R}_0 is the reference point, common to all fragments. The contributions $\tilde{\mathbf{d}}^X$ can be added up to define the total solvent dipole (the higher order n -body terms for $n > 1$ vanish due to the additivity).

$$\tilde{\mathbf{d}} = \sum_{I=1}^N \tilde{\mathbf{d}}^I \quad (6)$$

Now, if the total charge of the system is not zero, multipole moments of the rank of 1 and above depend on \mathbf{R}_0 . One approach is to set \mathbf{R}_0 to be the center of charge of the system. In this work, however, a simpler approach is taken by taking it to be the center of nuclear charges only (i.e., excluding the electronic contribution). In PCM [103], the relation between the total induced solvent charge \tilde{q} and the total solute charge Q is

$$\tilde{q} \approx -\frac{\varepsilon - 1}{\varepsilon} Q \quad (7)$$

where ε is the dielectric constant of the solvent. This relation is not exact due to the charge escape problem and can be enforced by the charge renormalization [104]. The total charge of a solvated system is

$$\tilde{q} + Q \approx \frac{Q}{\varepsilon} \quad (8)$$

In water, $\varepsilon = 78.39$ and $1/\varepsilon \approx 0$; thus, within a small error of 1–2%, $\tilde{q} + Q \approx 0$. This is the justification for the weak dependence of the total (solute + solvent) dipoles on \mathbf{R}_0 . To test this dependence, another choice of defining \mathbf{R}_0 was employed, to set it to the center of mass.

Some atomic charges in chignolin are shown in Table 3. The total formal solute charge Q of chignolin is -2 , and the calculated solvent charge \tilde{q} is 1.9526 (if the charge renormalization were used, it would have been 1.9745 according to Eq. 7), thus the total charge $\tilde{q} + Q$ is -0.0474 . Individual atomic and fragment charges do not obey the simple relation in Eq. 7 because of many-body effects, i.e., the charges on fragment I are induced not only by the atoms and solvent charges on I , but by all other fragments too.

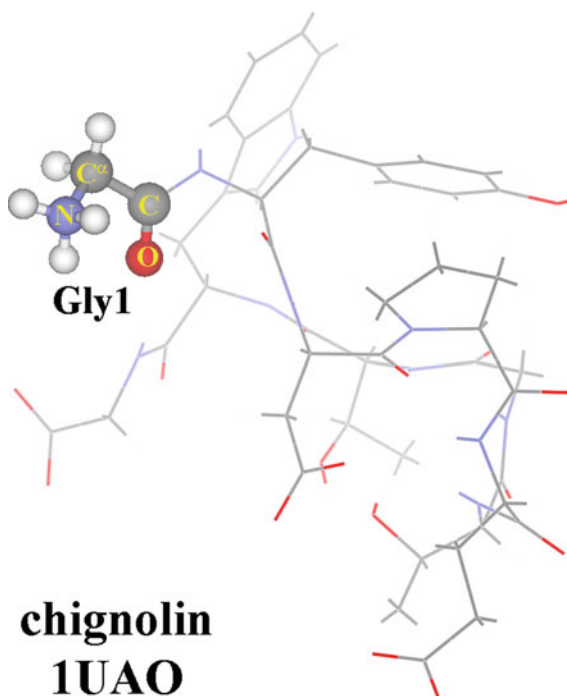
The computed charge of $-\text{NH}_3^+$ is 0.6264 (compare to the formal value of $+1$). Within $-\text{NH}_3^+$, the nitrogen has a negative charge of -0.6228 , and it deprives adjacent hydrogens of much of their electron density. The computed charge on Gly-1 (the convention is to use dash to denote fragment residues, and no dash for real residues) is 1.0761, it differs from 1 because it is calculated with FMO2, which includes the effect of charge transfer to other fragments. The total induced solvent charge on Gly-1 is -0.8330 . It is smaller than $-(\varepsilon - 1)/\varepsilon = -0.9872$ (see Eq. 7) because of the charge quenching effect [65] (and, to a smaller extent, charge escape) due to the potential pressure of other fragments, in particular, Asp-3, which has an

Table 3 Solute q_A (Mulliken) and solvent \tilde{q}_A charges (a.u.) of atom A in Gly-1 of chignolin (1UAO) for FMO2-HF/6-31G** and full (unfragmented) calculations. σ_A is the solvent coverage (%) of atom A^a

A	q_A	\tilde{q}_A	σ_A	Group	q	\tilde{q}
N	-0.623	-0.094	7.7	$-\text{NH}_3^+$	0.626	-0.569
H ¹	0.415	-0.158	23.3			
H ²	0.411	-0.132	22.3			
H ³	0.423	-0.186	30.4			
C ^{α}	-0.175	-0.073	7.0	$-\text{CH}_2-$	0.315	-0.266
H ^{α2}	0.251	-0.094	24.6			
H ^{α3}	0.240	-0.099	21.9			
C	0.789	-0.027	2.3	$-\text{C}=\text{O}$	0.134	0.003
O	-0.655	0.030	9.0			

^aSee Fig. 1. q and \tilde{q} are the solute and solvent charges of functional groups, respectively

Fig. 1 The first residue Gly1 (N-terminus, $Q_1 = +1$) in chignolin is shown as balls and sticks



opposite charge of -1 and whose potential cancels out partially the potential of Gly-1, and thus reduces the induced solvent charge.

The dipole moments are shown in Table 4. There are three anionic (Asp-3, Glu-5, and Gly-10) and one cationic (Gly-1) fragments. The charged fragments can be seen to have large solute \mathbf{d}^X and solvent $\tilde{\mathbf{d}}^X$ dipole moments, of typically opposite sign for each component so that the sum $\mathbf{d}^X + \tilde{\mathbf{d}}^X$ tends to be small. The x coordinates of the centers of charge and mass happen to be very similar, whereas y and z elements differ substantially. This is why $\tilde{\mathbf{d}}_x^X$ shows no \mathbf{R}_0 dependence, whereas the other two components differ by as much as 0.11 Debye. On the other hand, $\mathbf{d}^X + \tilde{\mathbf{d}}^X$ for the two choices of \mathbf{R}_0 differs by 0.02 Debye or less, i.e., the total values are rather insensitive to the choice of \mathbf{R}_0 .

For the center of mass reference, the total solute and solvent dipole moments are 82.289 and 78.580 Debye, respectively, and the length of their vector sum is 4.126 Debye. The observed screening is by the factor of $82.289/4.126 = 19.94$, which can be compared to the theoretical screening factor for charges in Eq. 8 ($\epsilon = 78.39$). For comparison, the computed charges are screened with the factor of $2/0.0474 = 42.19$ (different from ϵ because of the charge escape). Thus, dipole moments are screened about twice weaker than charges, in this system.

Table 4 Solute \mathbf{d}^I and solvent $\tilde{\mathbf{d}}^I$ dipole moments (Debye) of fragment I in FMO2-HF/6-31G** for chignolin^a

I	\mathbf{R}_0	d_x^I	d_y^I	d_z^I	\tilde{d}_x^I	\tilde{d}_y^I	\tilde{d}_z^I	$ \mathbf{d}^I + \tilde{\mathbf{d}}^I $
Gly-1	C	-25.81	11.63	-15.31	23.95	-11.45	14.72	1.95
Tyr-2	C	0.32	7.33	-0.24	-0.07	-5.16	1.30	2.43
Asp-3	C	17.77	-5.09	-18.39	-11.21	1.03	7.54	13.31
Pro-4	C	-4.50	3.80	0.66	0.00	-3.45	-1.88	4.69
Glu-5	C	6.64	7.21	-39.68	-7.39	-5.12	37.16	3.36
Thr-6	C	-1.79	1.78	-3.75	1.86	-2.13	9.22	5.48
Gly-7	C	-3.72	3.38	-0.13	2.37	-2.70	2.27	2.62
Thr-8	C	-3.36	2.29	2.85	3.86	0.77	-0.23	4.06
Trp-9	C	4.41	-7.50	-2.54	-3.08	2.53	6.23	6.33
Gly-10	C	23.46	28.98	17.27	-23.46	-26.51	-18.81	2.91
Gly-1	M	-25.81	11.74	-15.36	23.95	-11.54	14.75	1.96
Tyr-2	M	0.32	7.33	-0.24	-0.07	-5.18	1.30	2.41
Asp-3	M	17.77	-5.19	-18.35	-11.21	1.10	7.51	13.31
Pro-4	M	-4.50	3.80	0.66	0.00	-3.46	-1.88	4.68
Glu-5	M	6.64	7.10	-39.64	-7.39	-5.00	37.12	3.36
Thr-6	M	-1.79	1.78	-3.75	1.86	-2.10	9.21	5.46
Gly-7	M	-3.72	3.38	-0.13	2.37	-2.69	2.26	2.61
Thr-8	M	-3.36	2.29	2.85	3.86	0.78	-0.23	4.07
Trp-9	M	4.41	-7.50	-2.54	-3.08	2.50	6.24	6.36
Gly-10	M	23.46	28.88	17.31	-23.46	-26.40	-18.86	2.92

^aThe choice of \mathbf{R}_0 is the center either of nuclear charge (C) or mass (M)

3 Conclusions and Outlook

The main categories of FMO applications are: biochemical studies including protein–ligand binding [105], folding [106, 107], enzymatic catalysis [108, 109], chemical processes in explicit solvent [110], and electronic excitations [111, 112]. One venue of FMO applications lies in the parametrization of other approaches based on FMO calculations [113, 114] and also in studying structure–activity relationships [115, 116].

There have been only few applications of FMO to polymers [117, 118]. These applications have been done for cluster models of polymers, which may be appropriate when the system of interest has no periodic symmetry due to defects, presence of ligands, or because one is interested specifically in a nanoparticle with its boundary effects. For systems with a periodic symmetry present, one may need to apply periodic boundary conditions [93], which are also sometimes applied to solutions despite the lack of symmetry in real systems.

It may be considered a typical feature of most organic systems, large enough to make it feasible to do fragmentation in FMO, to be flexible, which necessitates sampling of the conformational space in a temperature-dependent fashion, usually with molecular dynamics. Although FMO/MD can be performed [119], it is still challenging to carry on simulations for a realistic duration even with the most computationally efficient methods such as DFTB.

The FMO potential in treating inorganic systems has been much underused because of the need to manually set up fragments with multiple detached bonds between them (some systems, such as ionic liquids [73, 120], do not have this problem), and it is hoped that in future more work will be done in the area of material science. As a step in this direction, FMO-DFTB, combined with the AFO treatment suitable for inorganic materials, has been developed and applied to a demonstrative molecular dynamics simulation system of a 10 m nano system containing over 1 million atoms [41].

GUI development has advanced to a practically useful level, but it falls behind the development of the method and computational software, and a major effort will have to be invested in improving FMO-enabled GUI to make FMO calculations easy to perform, and various results easy to visualize.

Acknowledgements The author thanks Prof. Kazuo Kitaura for his guidance in implementing FMO in GAMESS and many fruitful discussions.

References

1. Kussmann J, Beer M, Ochsenfeld C (2013) Linear-scaling self-consistent field methods for large molecules. *WIREs: Comput Mol Sci* 3:614–636
2. Akimov AV, Prezhdo OV (2015) Large-scale computations in chemistry: a bird's eye view of a vibrant field. *Chem Rev* 115:5797–5890
3. Gordon MS, Pruitt SR, Fedorov DG, Slipchenko LV (2012) Fragmentation methods: a route to accurate calculations on large systems. *Chem Rev* 112:632–672
4. Gao J, Truhlar DG, Wang Y, Mazack MJM, Löffler P, Provorse MR, Rehak P (2014) Explicit polarization: a quantum mechanical framework for developing next generation force fields. *Acc Chem Res* 47:2837–2845
5. Collins MA, Bettens RPA (2015) Energy-based molecular fragmentation methods. *Chem Rev* 115:5607–5642
6. Raghavachari K, Saha A (2015) Accurate composite and fragment-based quantum chemical models for large molecules. *Chem Rev* 115:5643–5677
7. Kitaura K, Ikeo E, Asada T, Nakano T, Uebayasi M (1999) Fragment molecular orbital method: an approximate computational method for large molecules. *Chem Phys Lett* 313:701–706
8. Sugiki S, Kurita N, Sengoku Y, Sekino H (2003) Fragment molecular orbital method with density functional theory and DIIS convergence acceleration. *Chem Phys Lett* 382:611–617
9. Komeiji Y, Inadomi Y, Nakano T (2004) PEACH 4 with ABINIT-MP: a general platform for classical and quantum simulations of biological molecules. *Comput Biol Chem* 28:155–161
10. Ishikawa T, Ishikura T, Kuwata K (2009) Theoretical study of the prion protein based on the fragment molecular orbital method. *J Comput Chem* 30:2594–2601

11. Takami T, Maki J, Ooba J, Inadomi Y, Honda H, Susukita R, Inoue K, Kobayashi T, Nogita R, Aoyagi M (2007) Multi-physics extension of OpenFMO framework. *AIP Conf Proc* 963:122–125
12. Schmidt MW, Baldrige KK, Boatz JA, Elbert ST, Gordon MS, Jensen JH, Koseki S, Matsunaga N, Nguyen KA, Su S, Windus TL, Dupuis M, Montgomery JA (1993) General atomic and molecular electronic structure system. *J Comput Chem* 14:1347–1363
13. Gordon MS, Schmidt MW (2005) Advances in electronic structure theory: GAMESS a decade later. In: Dykstra CE, Frenking G, Kim KS, Scuseria GE (Eds) *Theory and applications of computational chemistry, the first forty years*, Chapter 41. Elsevier, Amsterdam, pp 1167–1189
14. GAMESS homepage. <https://www.msg.ameslab.gov/games/index.html>. Accessed 20 March 2019
15. Fedorov DG, Kitaura K (2004) The importance of three-body terms in the fragment molecular orbital method. *J Chem Phys* 120:6832–6840
16. Alexeev Y, Mazanetz MP, Ichihara O, Fedorov DG (2012) GAMESS as a free quantum-mechanical platform for drug research. *Curr Top Med Chem* 12:2013–2033
17. Fedorov DG, Kitaura K (2007) Extending the power of quantum chemistry to large systems with the fragment molecular orbital method. *J Phys Chem a* 111:6904–6914
18. Fedorov DG, Nagata T, Kitaura K (2012) Exploring chemistry with the fragment molecular orbital method. *Phys Chem Chem Phys* 14:7562–7577
19. Tanaka S, Mochizuki Y, Komeiji Y, Okiyama Y, Fukuzawa K (2014) Electron-correlated fragment-molecular-orbital calculations for biomolecular and nano systems. *Phys Chem Chem Phys* 16:10310–10344
20. Fedorov DG (2017) The fragment molecular orbital method: theoretical development, implementation in GAMESS, and applications. *WIREs: Comput Mol Sci* 7:e1322
21. Fedorov DG, Kitaura K (eds) (2009) *The fragment molecular orbital method: practical applications to large molecular systems*. CRC Press, Boca Raton, FL
22. Fedorov DG, Asada N, Nakanishi I, Kitaura K (2014) The use of many-body expansions and geometry optimizations in fragment-based methods. *Acc Chem Res* 47:2846–2856
23. Chiba M, Fedorov DG, Kitaura K (2007) Time-dependent density functional theory with the multilayer fragment molecular orbital method. *Chem Phys Lett* 444:346–350
24. Alexeev Y, Fedorov DG, Shvartsburg AA (2014) Effective ion mobility calculations for macromolecules by scattering on electron clouds. *J Phys Chem A* 118:6763–6772
25. Nakano T, Mochizuki Y, Yamashita K, Watanabe C, Fukuzawa K, Segawa K, Okiyama Y, Tsukamoto T, Tanaka S (2012) Development of the four-body corrected fragment molecular orbital (FMO4) method. *Chem Phys Lett* 523:128–133
26. Yasuda K, Yamaki D (2006) The extension of the fragment molecular orbital method with the many-particle Green's function. *J Chem Phys* 125:154101
27. Fedorov DG, Kitaura K (2005) Multiconfiguration self-consistent-field theory based upon the fragment molecular orbital method. *J Chem Phys* 122:054108
28. Mochizuki Y, Koikegami S, Amari S, Segawa K, Kitaura K, Nakano T (2005) Configuration interaction singles method with multilayer fragment molecular orbital scheme. *Chem Phys Lett* 406:283–288
29. Nakata H, Schmidt MW, Fedorov DG, Kitaura K, Nakamura S, Gordon MS (2014) Efficient molecular dynamics simulations of multiple radical center systems based on the fragment molecular orbital method. *J Phys Chem A* 118:9762–9771
30. Polyakov IV, Khrenova MG, Moskovsky AA, Shabanov BM, Nemukhin AV (2018) Towards first-principles calculation of electronic excitations in the ring of the protein-bound bacteriochlorophylls. *Chem Phys* 505:34–39
31. Fujita T, Mochizuki Y (2018) Development of the fragment molecular orbital method for calculating nonlocal excitations in large molecular systems. *J Phys Chem A* 122:3886–3898
32. Suenaga M (2008) Development of GUI for GAMESS/FMO calculation. *J Comput Chem Jpn* 7:33–54 (in Japanese)
33. Fedorov DG, Kitaura K (2017) Modeling and visualization for the fragment molecular orbital method with the graphical user interface FU, and analyses of protein-ligand binding. In:

- Gordon MS (ed) Fragmentation: toward accurate calculations on complex molecular systems. Wiley, Hoboken, pp 119–139
34. Steinmann C, Ibsen MW, Hansen AS, Jensen JH (2012) FragIt: a tool to prepare input files for fragment based quantum chemical calculations. *PLoS ONE* 7:e44480
 35. Fujita T, Fukuzawa K, Mochizuki Y, Nakano T, Tanaka S (2009) Accuracy of fragmentation in ab initio calculations of hydrated sodium cation. *Chem Phys Lett* 478:295–300
 36. Avramov PV, Fedorov DG, Sorokin PB, Sakai S, Entani S, Ohtomo M, Matsumoto Y, Naramoto H (2012) Intrinsic edge asymmetry in narrow zigzag hexagonal heteroatomic nanoribbons causes their subtle uniform curvature. *J Phys Chem Lett* 3:2003–2008
 37. Nakano T, Kaminuma T, Sato T, Akiyama Y, Uebayasi M, Kitaura K (2000) Fragment molecular orbital method: application to polypeptides. *Chem Phys Lett* 318:614–618
 38. Nagata T, Fedorov DG, Kitaura K (2010) Importance of the hybrid orbital operator derivative term for the energy gradient in the fragment molecular orbital method. *Chem Phys Lett* 492:302–308
 39. Fedorov DG, Jensen JH, Deka RC, Kitaura K (2008) Covalent bond fragmentation suitable to describe solids in the fragment molecular orbital method. *J Phys Chem A* 112:11808–11816
 40. Fedorov DG, Avramov PV, Jensen JH, Kitaura K (2009) Analytic gradient for the adaptive frozen orbital bond detachment in the fragment molecular orbital method. *Chem Phys Lett* 477:169–175
 41. Nishimoto Y, Fedorov DG (2018) Adaptive frozen orbital treatment for the fragment molecular orbital method combined with density-functional tight-binding. *J Chem Phys* 148:064115
 42. Roskop L, Fedorov DG, Gordon MS (2013) Diffusion energy profiles in silica mesoporous molecular sieves modelled with the fragment molecular orbital method. *Mol Phys* 111:1622–1629
 43. Fujino I, Fedorov DG, Kitaura K, Hirose H, Nakayama N (2015) Fragment molecular orbital simulations of organic charge transport materials: a feasibility study. *J Imag Soc Jpn* 54:554–560
 44. Nagata T, Brorsen K, Fedorov DG, Kitaura K, Gordon MS (2011) Fully analytic energy gradient in the fragment molecular orbital method. *J Chem Phys* 134:124115
 45. Nishimoto Y, Fedorov DG, Irlé S (2014) Density-functional tight-binding combined with the fragment molecular orbital method. *J Chem Theory Comput* 10:4801–4812
 46. Nakata H, Nagata T, Fedorov DG, Yokojima S, Kitaura K, Nakamura S (2013) Analytic second derivatives of the energy in the fragment molecular orbital method. *J Chem Phys* 138:164103
 47. Nakata H, Fedorov DG, Yokojima S, Kitaura K, Nakamura S (2014) Simulations of Raman spectra using the fragment molecular orbital method. *J Chem Theory Comput* 10:3689–3698
 48. Fedorov DG, Kitaura K (2009) The role of the exchange in the embedding electrostatic potential for the fragment molecular orbital method. *J Chem Phys* 131:171106
 49. Fedorov DG, Kitaura K (2017) Many-body expansion of the Fock matrix in the fragment molecular orbital method. *J Chem Phys* 147:104106
 50. Fedorov DG, Ishida T, Kitaura K (2005) Multilayer formulation of the fragment molecular orbital method (FMO). *J Phys Chem A* 109:2638–2646
 51. Fedorov DG, Kitaura K (2014) Use of an auxiliary basis set to describe the polarization in the fragment molecular orbital method. *Chem Phys Lett* 597:99–105
 52. Steinmann C, Fedorov DG, Jensen JH (2010) Effective fragment molecular orbital method: a merger of the effective fragment potential and fragment molecular orbital methods. *J Phys Chem A* 114:8705–8712
 53. Steinmann C, Fedorov DG, Jensen JH (2012) The effective fragment molecular orbital method for fragments connected by covalent bonds. *PLoS ONE* 7:e41117
 54. Steinmann C, Fedorov DG, Jensen JH (2013) Mapping enzymatic catalysis using the effective fragment molecular orbital method: towards all ab initio bio-chemistry. *PLoS ONE* 8:e60602
 55. Pruitt SR, Steinmann C, Jensen JH, Gordon MS (2013) Fully integrated effective fragment molecular orbital method. *J Chem Theory Comput* 9:2235–2249

56. Christensen AS, Steinmann C, Fedorov DG, Jensen JH (2014) Hybrid RHF/MP2 geometry optimizations with the effective fragment molecular orbital method. *PLoS ONE* 9:e88800
57. Bertoni C, Gordon MS (2016) Analytic gradients for the effective fragment molecular orbital method. *J Chem Theory Comput* 12:4743–4767
58. Fedorov DG, Alexeev Y, Kitaura K (2011) Geometry optimization of the active site of a large system with the fragment molecular orbital method. *J Phys Chem Lett* 2:282–288
59. Nakata H, Fedorov DG, Nagata T, Kitaura K, Nakamura S (2015) Simulations of chemical reactions with the frozen domain formulation of the fragment molecular orbital method. *J Chem Theory Comput* 11:3053–3064
60. Nakata H, Fedorov DG (2016) Efficient geometry optimization of large molecular systems in solution using the fragment molecular orbital method. *J Phys Chem A* 120:9794–9804
61. Fedorov DG, Kitaura K (2007) Pair interaction energy decomposition analysis. *J Comput Chem* 28:222–237
62. Fedorov DG, Kitaura K (2006) Theoretical development of the fragment molecular orbital (FMO) method. In: Starikov EB, Lewis JP, Tanaka S (eds) *Modern methods for theoretical physical chemistry of biopolymers*. Elsevier, Amsterdam, pp 3–38
63. Watanabe C, Fukuzawa K, Okiyama Y, Tsukamoto T, Kato A, Tanaka S, Mochizuki Y, Nakano T (2013) Three- and four-body corrected fragment molecular orbital calculations with a novel subdividing fragmentation method applicable to structure-based drug design. *J Mod Graph Model* 41:31–42
64. Nagata T, Fedorov DG, Sawada T, Kitaura K (2012) Analysis of solute-solvent interactions in the fragment molecular orbital method interfaced with effective fragment potentials: theory and application to a solvated griffithsin-carbohydrate complex. *J Phys Chem A* 116:9088–9099
65. Fedorov DG, Kitaura K (2012) Energy decomposition analysis in solution based on the fragment molecular orbital method. *J Phys Chem A* 116:704–719
66. Green MC, Fedorov DG, Kitaura K, Francisco JS, Slipchenko LV (2013) Open-shell pair interaction energy decomposition analysis (PIEDA): formulation and application to the hydrogen abstraction in tripeptides. *J Chem Phys* 138:074111
67. Fedorov DG (2019) Solvent screening in zwitterions analyzed with the fragment molecular orbital method. *J Chem Theory Comput* 15:5404–5416.
68. Grimme S, Ehrlich S, Goerigk L (2011) Effect of the damping function in dispersion corrected density functional theory. *J Comput Chem* 32:1456–1465
69. Fedorov DG, Kromann JC, Jensen JH (2018) Empirical corrections and pair interaction energies in the fragment molecular orbital method. *Chem Phys Lett* 702:111–116
70. Fedorov DG, Kitaura K (2016) Subsystem analysis for the fragment molecular orbital method and its application to protein-ligand binding in solution. *J Phys Chem A* 120:2218–2231
71. Xu P, Guidez EB, Bertoni C, Gordon MS (2018) Ab initio force field methods derived from quantum mechanics. *J Chem Phys* 148:090901
72. Fedorov DG, Kitaura K (2018) Pair interaction energy decomposition analysis for density functional theory and density-functional tight-binding with an evaluation of energy fluctuations in molecular dynamics. *J Phys Chem A* 122:1781–1795
73. Vuong VQ, Nishimoto Y, Fedorov DG, Sumpter BG, Niehaus TA, Irlé S (2019) The fragment molecular orbital method based on long-range corrected density-functional tight-binding. *J Chem Theory Comput* 15:3008–3020
74. Nagata T, Fedorov DG, Kitaura K, Gordon MS (2009) A combined effective fragment potential-fragment molecular orbital method. I. The energy expression and initial applications. *J Chem Phys* 131:024101
75. Nagata T, Fedorov DG, Sawada T, Kitaura K, Gordon MS (2011) A combined effective fragment potential-fragment molecular orbital method. II. Analytic gradient and application to the geometry optimization of solvated tetraglycine and chignolin. *J Chem Phys* 134:034110
76. Nagata T, Fedorov DG, Kitaura K (2012) Analytic gradient and molecular dynamics simulations using the fragment molecular orbital method combined with effective potentials. *Theor Chem Acc* 131:1136

77. Fedorov DG, Kitaura K, Li H, Jensen J, Gordon M (2006) The polarizable continuum model (PCM) interfaced with the fragment molecular orbital method (FMO). *J Comput Chem* 27:976–985
78. Fedorov DG (2018) Analysis of solute-solvent interactions using the solvation model density combined with the fragment molecular orbital method. *Chem Phys Lett* 702:111–116
79. Ponder JW (2018) TINKER 3.9. <https://dasher.wustl.edu/tinker>. Accessed 20 April 2018
80. Fedorov DG, Ishida T, Uebayasi M, Kitaura K (2007) The fragment molecular orbital method for geometry optimizations of polypeptides and proteins. *J Phys Chem A* 111:2722–2732
81. Maseras F, Morokuma K (1995) IMOMM: a new integrated ab initio+ molecular mechanics geometry optimization scheme of equilibrium structures and transition states. *J Comput Chem* 16:1170–1179
82. Lyne PD, Hodoscek M, Karplus M (1999) A hybrid QM-MM potential employing Hartree-Fock or density functional methods in the quantum region. *J Phys Chem A* 103:3462–3471
83. Nagata T, Fedorov DG, Kitaura K (2011) Mathematical formulation of the fragment molecular orbital method. In: Zalesny R, Papadopoulos MG, Mezey PG, Leszczynski J (eds) *Linear-scaling techniques in computational chemistry and physics*. Springer, New York, pp 17–64
84. Nakano T, Kaminuma T, Sato T, Fukuzawa K, Akiyama Y, Uebayasi M, Kitaura K (2002) Fragment molecular orbital method: use of approximate electrostatic potential. *Chem Phys Lett* 351:475–480
85. Fedorov DG, Kitaura K (2006) The three-body fragment molecular orbital method for accurate calculations of large systems. *Chem Phys Lett* 433:182–187
86. Nagata T, Fedorov DG, Kitaura K (2012) Analytic gradient for the embedding potential with approximations in the fragment molecular orbital method. *Chem Phys Lett* 544:87–93
87. Kamiya M, Hirata S, Valiev M (2008) Fast electron correlation methods for molecular clusters without basis set superposition errors. *J Chem Phys* 128:074103
88. Fedorov DG, Slipchenko LV, Kitaura K (2010) Systematic study of the embedding potential description in the fragment molecular orbital method. *J Phys Chem A* 114:8742–8753
89. Asada N, Fedorov DG, Kitaura K, Nakanishi I, Merz KM Jr (2012) An efficient method to evaluate intermolecular interaction energies in large systems using overlapping multicenter ONIOM and the fragment molecular orbital method. *J Phys Chem Lett* 3:2604–2610
90. Gao Q, Yokojima S, Fedorov DG, Kitaura K, Sakurai M, Nakamura S (2014) Octahedral point-charge model and its application to fragment molecular orbital calculations of chemical shifts. *Chem Phys Lett* 593:165–173
91. Fukunaga H, Fedorov DG, Chiba M, Nii K, Kitaura K (2008) Theoretical analysis of the intermolecular interaction effects on the excitation energy of organic pigments: solid state quinacridone. *J Phys Chem A* 112:10887–10894
92. Fujita T, Nakano T, Tanaka S (2011) Fragment molecular orbital calculations under periodic boundary condition. *Chem Phys Lett* 506:112–116
93. Brorsen KR, Minezawa N, Xu F, Windus TL, Gordon MS (2012) Fragment molecular orbital molecular dynamics with the fully analytic energy gradient. *J Chem Theory Comput* 8:5008–5012
94. Choi CH, Fedorov DG (2012) Reducing the scaling of the fragment molecular orbital method using the multipole method. *Chem Phys Lett* 543:159–165
95. Fedorov DG, Olson RM, Kitaura K, Gordon MS, Koseki S (2004) A new hierarchical parallelization scheme: generalized distributed data interface (GDDI), and an application to the fragment molecular orbital method (FMO). *J Comput Chem* 25:872–880
96. Ikegami T, Ishida T, Fedorov DG, Kitaura K, Inadomi Y, Umeda H, Yokokawa M, Sekiguchi S (2005) Full electron calculation beyond 20,000 atoms: ground electronic state of photosynthetic proteins. In: *Proceedings of the supercomputing 2005*. IEEE computer society, Seattle
97. Alexeev Y, Mahajan A, Leyffer S, Fletcher G, Fedorov DG (2012) Heuristic static load-balancing algorithm applied to the fragment molecular orbital method. In: *Proceedings of the supercomputing 2012*. IEEE computer society, Salt Lake City


98. Talamudupula SK, Sosonkina M, Gaenko A, Schmidt MW (2012) Fragment molecular orbital method adaptations for heterogeneous computing platforms. *Proc Comput Sci* 9:489–497
99. Fletcher GD, Fedorov DG, Pruitt SR, Windus TL, Gordon MS (2012) Large-scale MP2 calculations on the Blue Gene architecture using the fragment molecular orbital method. *J Chem Theory Comput* 8:75–79
100. Pruitt SR, Nakata H, Nagata T, Mayes M, Alexeev Y, Fletcher G, Fedorov DG, Kitaura K, Gordon MS (2016) Importance of three-body interactions in molecular dynamics simulations of water demonstrated with the fragment molecular orbital method. *J Chem Theory Comput* 12:1423–1435
101. Mironov V, Alexeev Y, Fedorov DG, Umeda H, Pruitt S, Gaenko A, Gordon MS (2021) Multi-level parallelization of the fragment molecular orbital method in GAMESS. In: Mochizuki Y et al (Ed) *Recent advances of the fragment molecular orbital method*. Springer, Singapore (In press)
102. Mironov V, Alexeev Y, Fedorov DG (2019) Multi-threaded parallelization of the energy and analytic gradient in the fragment molecular orbital method. *Int J Quant Chem* 119:e25937
103. Tomasi J, Mennucci B, Cammi R (2005) Quantum mechanical continuum solvation models. *Chem Rev* 105:2999–3093
104. Cammi R, Tomasi J (1995) Remarks on the use of the apparent surface charges (ASC) methods in solvation problems: iterative versus matrix-inversion procedures and the renormalization of the apparent charges. *J Comput Chem* 16:1449–1458
105. Morao I, Fedorov DG, Robinson R, Southey M, Townsend-Nicholson A, Bodkin MJ, Heifetz A (2017) Rapid and accurate assessment of GPCR-ligand interactions using the fragment molecular orbital-based density-functional tight-binding method. *J Comput Chem* 38:1987–1990
106. He X, Fusti-Molnar L, Cui G, Merz KM Jr (2009) Importance of dispersion and electron correlation in ab initio protein folding. *J Phys Chem B* 113:5290–5300
107. Simoncini D, Nakata H, Ogata K, Nakamura S, Zhang KYJ (2015) Quality assessment of predicted protein models using energies calculated by the fragment molecular orbital method. *Mol Inf* 34:97–104
108. Ito M, Brinck T (2014) Novel approach for identifying key residues in enzymatic reactions: proton abstraction in ketosteroid isomerase. *J Phys Chem B* 118:13050–13058
109. Pruitt SR, Steinmann C (2017) Mapping interaction energies in chorismate mutase with the fragment molecular orbital method. *J Phys Chem A* 121:1798–1808
110. Pruitt SR, Brorsen KR, Gordon MS (2015) Ab initio investigation of the aqueous solvation of the nitrate ion. *Phys Chem Chem Phys* 17:27027–27034
111. Kistler KA, Matsika S (2009) Solvatochromic shifts of uracil and cytosine using a combined multireference configuration interaction/molecular dynamics approach and the fragment molecular orbital method. *J Phys Chem A* 113:12396–12403
112. Shigemitsu Y, Mutai T, Houjou H, Araki K (2014) Influence of intermolecular interactions on solid state luminescence of imidazopyridines: theoretical interpretations using FMO-TDDFT and ONIOM approaches. *Phys Chem Chem Phys* 16:14388–14395
113. Kitoh-Nishioka H, Welke K, Nishimoto Y, Fedorov DG, Irlé S (2017) Multiscale simulations on charge transport in covalent organic frameworks including dynamics of transfer integrals from the FMO-DFTB/LCMO approach. *J Phys Chem C* 121:17712–17726
114. Doi H, Okuwaki K, Mochizuki Y, Ozawa T, Yasuoka K (2017) Dissipative particle dynamics (DPD) simulations with fragment molecular orbital (FMO) based effective parameters for 1-palmitoyl-2-oleoyl phosphatidyl choline (POPC) membrane. *Chem Phys Lett* 684:427–432
115. Mazanetz MP, Ichihara O, Law RJ, Whittaker M (2011) Prediction of cyclin-dependent kinase 2 inhibitor potency using the fragment molecular orbital method. *J Cheminf* 3:2
116. Hitaoka S, Chuman H, Yoshizawa K (2015) A QSAR study on the inhibition mechanism of matrix metalloproteinase-12 by arylsulfone analogs based on molecular orbital calculations. *Org Biomol Chem* 13:793–806
117. Nakata H, Fedorov DG, Yokojima S, Kitaura K, Nakamura S (2014) Derivatives of the approximated electrostatic potentials in unrestricted Hartree-Fock based on the fragment molecular orbital method and an application to polymer radicals. *Theor Chem Acc* 133:1477

118. Sawada T, Fedorov DG, Kitaura K (2009) Structural and interaction analysis of helical heparin oligosaccharides with the fragment molecular orbital method. *Int J Quantum Chem* 109:2033–2045
119. Komeiji Y, Mochizuki Y, Nakano T, Fedorov DG (2009) Fragment molecular orbital-based molecular dynamics (FMO-MD), a quantum simulation tool for large molecular systems. *J Mol Str: THEOCHEM* 898:2–7
120. Halat P, Seeger ZL, Acevedo SB, Izgorodina EI (2017) Trends in two- and three-body effects in multiscale clusters of ionic liquids. *J Phys Chem B* 121:577–588
121. Pruitt SR, Fedorov DG, Kitaura K, Gordon MS (2010) Open-shell formulation of the fragment molecular orbital method. *J Chem Theory Comput* 6:1–5
122. Pruitt SR, Fedorov DG, Gordon MS (2012) Geometry optimizations of open-shell systems with the fragment molecular orbital method. *J Phys Chem A* 116:4965–4974
123. Nakata H, Fedorov DG, Nagata T, Yokojima S, Ogata K, Kitaura K, Nakamura S (2012) Unrestricted Hartree-Fock based on the fragment molecular orbital method: energy and its analytic gradient. *J Chem Phys* 137:044110
124. Nakata H, Fedorov DG, Yokojima S, Kitaura K, Nakamura S (2014) Efficient vibrational analysis for unrestricted Hartree-Fock based on the fragment molecular orbital method. *Chem Phys Lett* 603:67–74
125. Nishimoto Y, Fedorov DG, Irlle S (2015) Third-order density-functional tight-binding combined with the fragment molecular orbital method. *Chem Phys Lett* 636:90–96
126. Nishimoto Y, Nakata H, Fedorov DG, Irlle S (2015) Large-scale quantum-mechanical molecular dynamics simulations using density-functional tight-binding combined with the fragment molecular orbital method. *J Phys Chem Lett* 6:5034–5039
127. Nishimoto Y, Fedorov DG (2016) The fragment molecular orbital method combined with density-functional tight-binding and the polarizable continuum model. *Phys Chem Chem Phys* 18:22047–22061
128. Nakata H, Nishimoto Y, Fedorov DG (2016) Analytic second derivative of the energy for density-functional tight-binding combined with the fragment molecular orbital method. *J Chem Phys* 145:044113
129. Nishimoto Y, Fedorov DG (2017) Three-body expansion of the fragment molecular orbital method combined with density-functional tight-binding. *J Comput Chem* 38:406–418
130. Fedorov DG, Kitaura K (2004) On the accuracy of the 3-body fragment molecular orbital method (FMO) applied to density functional theory. *Chem Phys Lett* 389:129–134
131. Nakata H, Fedorov DG, Yokojima S, Kitaura K, Sakurai M, Nakamura S (2014) Unrestricted density functional theory based on the fragment molecular orbital method for the ground and excited state calculations of large systems. *J Chem Phys* 140:144101
132. Brorsen KR, Zahariev F, Nakata H, Fedorov DG, Gordon MS (2014) Analytic gradient for density functional theory based on the fragment molecular orbital method. *J Chem Theory Comput* 10:5297–5307
133. Nakata H, Fedorov DG, Zahariev F, Schmidt MW, Kitaura K, Gordon MS, Nakamura S (2015) Analytic second derivative of the energy for density functional theory based on the three-body fragment molecular orbital method. *J Chem Phys* 142:124101
134. Nakata H, Fedorov DG (2018) Analytic second derivatives for the efficient electrostatic embedding in the fragment molecular orbital method. *J Comput Chem* 39:2039–2050
135. Fedorov DG, Kitaura K (2004) Second order Møller-Plesset perturbation theory based upon the fragment molecular orbital method. *J Chem Phys* 121:2483–2490
136. Fedorov DG, Ishimura K, Ishida T, Kitaura K, Pulay P, Nagase S (2007) Accuracy of the three-body fragment molecular orbital method applied to Møller-Plesset perturbation theory. *J Comput Chem* 28:1476–1484
137. Katouda M (2011) Application of resolution of identity approximation of second-order Møller-Plesset perturbation theory to three-body fragment molecular orbital method. *Theor Chem Acc* 130:449–453
138. Nagata T, Fedorov DG, Ishimura K, Kitaura K (2011) Analytic energy gradient for second-order Møller-Plesset perturbation theory based on the fragment molecular orbital method. *J Chem Phys* 135:044110

139. Green MC, Nakata H, Fedorov DG, Slipchenko LV (2016) Radical damage in lipids investigated with the fragment molecular orbital method. *Chem Phys Lett* 651:56–61
140. Fedorov DG, Kitaura K (2005) Coupled-cluster theory based upon the fragment molecular-orbital method. *J Chem Phys* 123:134103
141. Findlater AD, Zahariev F, Gordon MS (2015) Combined fragment molecular orbital cluster in molecule approach to massively parallel electron correlation calculations for large systems. *J Phys Chem A* 119:3587–3593
142. Chiba M, Fedorov DG, Kitaura K (2008) Polarizable continuum model with the fragment molecular orbital-based time-dependent density functional theory. *J Comput Chem* 29:2667–2676
143. Chiba M, Koido T (2010) Electronic excitation energy calculation by the fragment molecular orbital method with three-body effects. *J Chem Phys* 133:044113
144. Chiba M, Fedorov DG, Nagata T, Kitaura K (2009) Excited state geometry optimizations by time-dependent density functional theory based on the fragment molecular orbital method. *Chem Phys Lett* 474:227–232
145. Ikegami T, Ishida T, Fedorov DG, Kitaura K, Inadomi Y, Umeda H, Yokokawa M, Sekiguchi S (2010) Fragment molecular orbital study of the electronic excitations in the photosynthetic reaction center of *blastochloris viridis*. *J Comput Chem* 31:447–454
146. Nakata H, Fedorov DG, Kitaura K, Nakamura S (2015) Extension of the fragment molecular orbital method to treat large open-shell systems in solution. *Chem Phys Lett* 635:86–92
147. Li H, Fedorov DG, Nagata T, Kitaura K, Jensen JH, Gordon MS (2010) Energy gradients in combined fragment molecular orbital and polarizable continuum model (FMO/PCM) calculation. *J Comput Chem* 31:778–790
148. Nagata T, Fedorov DG, Li H, Kitaura K (2012) Analytic gradient for second order Møller-Plesset perturbation theory with the polarizable continuum model based on the fragment molecular orbital method. *J Chem Phys* 136:204112
149. Nakata H, Fedorov DG (2019) Simulations of infrared and Raman spectra in solution using the fragment molecular orbital method. *Phys Chem Chem Phys* 21:13641–13652
150. Yoshida N (2014) Efficient implementation of the three-dimensional reference interaction site model method in the fragment molecular orbital method. *J Chem Phys* 140:214118
151. Mazanetz MP, Chudyk E, Fedorov DG, Alexeev Y (2016) Applications of the fragment molecular orbital method to drug research. In: Zhang W (ed) *Computer aided drug discovery*. Springer, New York, pp 217–255
152. Fedorov DG, Brekhov A, Mironov V, Alexeev Y (2019) Molecular electrostatic potential and electron density of large systems in solution computed with the fragment molecular orbital method. *J Phys Chem A* 123:6281–6290
153. Tsuneyuki S, Kobori T, Akagi K, Sodeyama K, Terakura K, Fukuyama H (2009) Molecular orbital calculation of biomolecules with fragment molecular orbitals. *Chem Phys Lett* 476:104–108
154. Kobori T, Sodeyama K, Otsuka T, Tateyama Y, Tsuneyuki S (2013) Trimer effects in fragment molecular orbital-linear combination of molecular orbitals calculation of one-electron orbitals for biomolecules. *J Chem Phys* 139:094113
155. Nebgen B, Prezhdo OV (2016) Fragment molecular orbital nonadiabatic molecular dynamics for condensed phase systems. *J Phys Chem A* 120:7205–7212
156. Gao Q, Yokojima S, Kohno T, Ishida T, Fedorov DG, Kitaura K, Fujihira M, Nakamura S (2007) Ab initio NMR chemical shift calculations on proteins using fragment molecular orbitals with electrostatic environment. *Chem Phys Lett* 445:331–339
157. Gao Q, Yokojima S, Fedorov DG, Kitaura K, Sakurai M, Nakamura S (2010) Fragment-molecular-orbital-method-based ab initio NMR chemical-shift calculations for large molecular systems. *J Chem Theory Comput* 6:1428–1444
158. Auer B, Pak MV, Hammes-Schiffer S (2010) Nuclear-electronic orbital method within the fragment molecular orbital approach. *J Phys Chem C* 114:5582–5588

The ABINIT-MP Program



Yuji Mochizuki , **Tatsuya Nakano**, **Kota Sakakura**, **Yoshio Okiyama**, **Hiromasa Watanabe**, **Koichiro Kato**, **Yoshinobu Akinaga**, **Shinya Sato**, **Jun-inchi Yamamoto**, **Katsumi Yamashita**, **Tadashi Murase**, **Takeshi Ishikawa**, **Yuto Komeiji**, **Yuji Kato**, **Naoki Watanabe**, **Takashi Tsukamoto**, **Hirotooshi Mori**, **Koji Okuwaki**, **Shigenori Tanaka**, **Akifumi Kato**, **Chiduru Watanabe**, and **Kaori Fukuzawa**

Abstract We have been developing the ABINIT-MP program system as an original code for the fragment molecular orbital (FMO) calculations. ABINIT-MP has several unique features such as a variety of efficient correlated methods and hybrid parallelism. Additionally, an associated graphical user interface (named as BioStation Viewer) has been provided for end-users. In this chapter, we summarize the current

Y. Mochizuki (✉) · Y. Kato · K. Okuwaki

Department of Chemistry and Research Center for Smart Molecules, Faculty of Science, Rikkyo University, 3-34-1 Nishi-ikebukuro, Toshima-ku, Tokyo 171-8501, Japan
e-mail: fullmoon@rikkyo.ac.jp

Y. Mochizuki · K. Fukuzawa

Institute of Industrial Science, The University of Tokyo, 4-6-1 Komaba, Meguro-ku, Tokyo 153-8505, Japan

T. Nakano · Y. Okiyama

National Institute of Health Sciences, 3-25-26 Tonomachi, Kawasaki-ku, Kawasaki, Kanagawa 201-9501, Japan

K. Sakakura

Human Resources Development Group, Foundation for Computational Science, 7-1-28 Minatojima Minamicho, Chuo-ku, Kobe 650-0047, Japan

H. Watanabe

HPC SYSTEMS Inc., 3-9-15 Kaigan, Minato-ku, Tokyo 108-0022, Japan

K. Kato

Department of Applied Chemistry, Graduate School of Engineering, Kyushu University, 744 Motoooka, Nishi-ku, Fukuoka 819-0395, Japan

Center for Molecular Systems (CMS), Kyushu University, 744 Motoooka, Nishi-ku, Fukuoka 819-0395, Japan

Y. Akinaga

VINAS Co., Ltd., 2-1-31 Dojima, Kita-ku, Osaka-shi, Osaka 530-0003, Japan

S. Sato · J. Yamamoto · K. Yamashita · T. Murase

NEC Solution Innovators, Ltd., 1-18-6 Shinkiba, Koto-ku, Tokyo 136-8627, Japan

T. Ishikawa

Graduate School of Science and Engineering, Kagoshima University, 1-21-40, Korimoto, Kagoshima 890-0065, Japan

© Springer Nature Singapore Pte Ltd. 2021

Y. Mochizuki et al. (eds.), *Recent Advances of the Fragment Molecular Orbital Method*, https://doi.org/10.1007/978-981-15-9235-5_4

features of the ABINIT-MP program. Plans and activities of future developments are addressed as well.

Keywords ABINIT-MP · Four-body FMO (FMO4) · Hybrid parallel execution · Supercomputer · Higher-order correlated calculation · Graphical user interface (BioStation viewer)

1 Introduction

The fragment molecular orbital (FMO) scheme was proposed in 1999 by Kitaura et al. [1] to realize fully quantum–mechanical (QM) molecular orbital (MO) calculations for large-scale molecular systems such as proteins and DNAs at the reasonable computational costs through parallel executions. The basic idea of FMO would be related to the Morokuma–Kitaura energy decomposition analysis (EDA) by which the components of interaction energies between two molecules of interest can be analysed [2]. Although there have been various fragmentation-based MO schemes as compiled in Refs. [3–6], FMO has been the most widely used, in particular for biochemistry/physics and pharmaceutical chemistry [7–9]. A principal reason for this situation can be attributed to the fact that the list of pair interaction energy (PIE) or inter-fragment interaction energy (IFIE) for fragment pairs is straightforwardly obtained at the end of FMO calculations, and these quantities are informative to grasp the nature of interactions for a given target system [10–12]. Certainly, a variety of

Y. Komeiji

Biomedical Research Institute, AIST, Tsukuba Central 2, Tsukuba, Ibaraki 305-8568, Japan

N. Watanabe · T. Tsukamoto

Mizuho Information and Research Institute Inc, 2-3 Kanda Nishiki-cho, Chiyoda-ku, Tokyo 101-8442, Japan

H. Mori

Department of Applied Chemistry, Faculty of Science and Engineering, Chuo University, 1-13-27 Kasuga, Bunkyo-ku, Tokyo 112-8551, Japan

S. Tanaka

Graduate School of System Informatics, Department of Computational Science, Kobe University, 1-1 Rokkodai, Nada-ku, Kobe 657-8501, Japan

A. Kato

Scopion Tech LLC., Okada, Tateyama, Chiba 294-0024, Japan

C. Watanabe

RIKEN, Center for Life Science Technologies, 1-7-22 Suehiro-cho, Tsurumi-ku, Yokohama, Kanagawa 230-0045, Japan

K. Fukuzawa

School of Pharmacy and Pharmaceutical Sciences, Hoshi University, 2-4-41 Ebara, Shinagawa-Ku, Tokyo 142-8501, Japan

realistic FMO applications are documented by the respective experts in other chapters in this book.

Currently, the FMO calculations have been available with GAMES-US [13, 14], PAICS [15, 16], OpenFMO [17, 18] and ABINIT-MP [12, 19]. In this chapter, the current features of our ABINIT-MP program (written in FORTRAN) are documented; please refer to the corresponding chapters for other programs. Various abilities implemented in ABINIT-MP are described in the following sections according to categories such as “Energy calculation” and “Energy gradient calculation”.

2 Energy Calculation

The Hartree–Fock (HF) method [20] of the closed-shell restricted type is the base of FMO calculations, and this fundamental ability was originally implemented by Nakano [21]. At the fragment monomer (1-body) stage, the self-consistent charge (SCC) condition is subjected to optimize the environmental electrostatic potential (ESP) [10–12]. Namely, this monomer HF stage is iterated until the convergence, where a typical number of iterations is about 50 for proteins. Various basis sets are preset in ABINIT-MP, and the current standard basis set is the 6-31G(d) (or 6-31G*) of valence double-zeta plus polarization (DZP) equality [20, 22]. The bond detachment atom (BDA) of sp^3 carbon [21] is prepared and preset for the respective basis sets. The HF calculations are processed in a parallelized integral-direct way; the integral buffering is available when requested. To reduce the cost of ESP computations, a couple of Mulliken population-based approximations [23] (atomic orbital charge (AOC) and point charge (PTC)) are usually adopted. The parallelism in ABINIT-MP is of dual-layer type, and both flat MPI mode and OpenMP/MPI hybrid mode (or shared-memory processor (SMP) model) are supported. When the monomer SCC condition is satisfied, the optimized ESP set is used for the fragment dimer (2-body) stage [10–12]. Note that no re-optimization of ESP with iteration is made for dimers. The quantum–mechanical polarization and charge delocalization are incorporated at the monomer and dimer stages, respectively. The dimers consisting of distant monomers are treated with the electrostatic approximation (Dimer-ES) without doing HF calculation [23]. This is the original 2-body FMO scheme (explicitly denoted as FMO2-HF) proposed by Kitaura [1]. The list of IFIEs is obtained when the dimer stage completes [24]. In ABINIT-MP, 3-body (FMO3) and 4-body (FMO4) expansions are available [25], by which accuracy is substantially improved; the ESP setting is to be modified for these explicit many-body expansions. In FMO4, up to fragment tetramers consisting of four close monomers are to be computed. Typical incremental costs of FMO3 and FMO4 relative to FMO2 are 3 and 10, respectively, at the HF level. The modified IFIEs are proposed for FMO3 and FMO4 as well [26].

In ABINIT-MP, the default route of orbital optimizations in HF calculations has been a C2 variant of direct inversion of iterative sequence (C2-DIIS) [27]. The energy DIIS (EDIIS) [28] as well as the second-order MO based optimizer [29, 30] were also implemented for difficult cases of convergence.

It has been well known that the second-order Møller-Plesset perturbation (MP2) [20, 31] is the easiest and computationally cheapest wavefunction recipe to take the electron correlation into account. In fact, the dispersion-type interaction such as CH/π is never described at the HF level, and thus (at least) MP2 must be performed after HF. The kernel of MP2 processing is the integral transformation with a formal cost of N^5 (N means the number of basis function in a given fragment). At the monomer stage, the MP2 calculation starts just after the final HF calculation with the SCC convergence [10–12]. The FMO-MP2 with ABINIT-MP [32–34] is performable with an efficient integral-direct parallelism of both flat MPI and OpenMP/MPI modes. The incremental cost factor of FMO-MP2 relative to FMO-HF is typically a range of 2–3 in the 2-body expansion, depending on available processors and memories. In other words, FMO-MP2 is quite routinely done as the standard job of FMO calculation for the IFIE-based analyses. Note that MP2 is skipped for the Dimer-ES pairs because of no HF calculation. A partial renormalization (PR-MP2) [35] as well as spin-component scaling (SCS-MP2) [36] are usable as options. An approximate MP2 density matrix (without solving the coupled perturbed HF (CPHF)) can be computed when requested for population analyses [32, 33].

The third-order Møller-Plesset perturbation (MP3) [20, 31] incorporates the electron pair-pair interactions unlike MP2 as an independent pair model. The formal cost of MP3 raises one order as N^6 due to tensor contractions of integrals and MP1 amplitudes. A scaled MP3 approach called as MP2.5 (in which the MP3 additional correlation energy is halved [37]) has attracted interest because evaluated interaction energies by this way are comparable to those by the coupled cluster singles and doubles with perturbative triples (CCSD(T)) method as the golden recipe to describe the electron correlation. ABINIT-MP has an efficient integral-direct MP3 module for FMO2 calculations with parallelism of both flat MPI and OpenMP/MPI [38]. If enough amount of memory and high-speed computing cores are usable for FMO-MP3, the incremental factor relative to FMO-MP2 is less than 10 (depending on the type of processors); only 2 as the best case. Reliability of IFIE analyses could be enhanced with the MP2.5 scaling, if the FMO-MP3 calculation is applicable to a given system.

A variety of higher-order correlated methods [20, 31] from the fourth-order Møller-Plesset perturbation (MP4) to CCSD(T) are available in ABINIT-MP within FMO2 [39]; the SMP execution of OpenMP/MPI is assumed. The CCSD(T) computation consists of the iterative N^6 part of amplitude optimization of singles and doubles and the non-iterative N^7 part of perturbative triples. Under parallelization, a series of tensor contractions among integrals, amplitudes and intermediate quantities are performed by matrix-oriented operations through DGEMM. The memory demand for CCSD iterations is considerable, and thus Bruckner doubles (BD) [40] is an alternative route; the number of grand iterations for BD is typically 5. The relative cost of CCSD(T) and BD(T) to MP2 can reach roughly a hundred times. Although such higher-order correlated methods are so costly, the cross-reference data of IFIEs are obtainable for comparison with the MP2 or MP2.5 results [41].

The unrestricted HF (UHF) calculation is used when the target molecular system contains an open-shell fragment, where the three-body treatment (FMO3)

is supported [42, 43]. Correspondingly, the unrestricted MP2 (UMP2) method [20, 31] is adopted for the correlation correction. Care is necessary for spin contamination, especially for the existence of near-degeneracy. The applicability of FMO-UHF is thus rather limited.

Several approximations to 2-electron integrals having four indices have been known [44], where the fundamental concept is the factorization to some tensors with fewer indices. Note that such factorizations are suitable for matrix-oriented processing. In ABINIT-MP, the Cholesky decomposition with adaptive metric (CDAM) scheme is usable for the HF and MP2 calculations with parallelism [45]. For the dimer MP2 stage, the acceleration with CDAM is roughly 10 times for the 6-31G basis set [20, 22]. The CDAM option is usable also for MP3, however the acceleration is not preferable unfortunately; the resolution-of-identity (RI) [44] may be promising for MP3 as implemented in PAICS [46, 47].

The integral generator module of ABINIT-MP written by Nakano is based on Obara's recursive algorithm [48], and only Cartesian type basis function is supported (6d and 10f). Actually, two types of binary executable with and without handling of f functions are prepared, because the former is 1.5 times larger because of the lengthy processing in inner loops of the integral generator. The scalar relativistic effects (mass-velocity and Darwin) are incorporated by using the model core potential (MCP) sets [49, 50] whose valence basis functions are of DZP quality [51]. The MCP-based FMO-MP2 method is applicable even to the uranyl (UO_2^{2+})-attached DNA model under the explicit hydration condition [52]. For light elements, the MCP basis set has better flexibility than that of the 6-31G(d) basis set, but the computational cost increases due to longer contractions of valence primitives [41].

When a given target system grows in size, the number of Dimer-ES pairs [23] turns huge and thus costly. The approximation of continuous multipole moment (CMM) is further applied to process the Dimer-ES energies for relatively long distanced pairs [53]; the acceleration factor is typically 10 without significant loss of accuracy in total energy (1×10^{-4} atomic unit). Although the ESP-AOC and ESP-PTC approximations are usable for the ESP computations, there is a potential need to evaluate the exact ESP within tractable time. Recently, the CMM technique has been introduced for the ESP part as a speed-up option.

The multi-layer FMO (MFMO) treatment [54] in ABINIT-MP was first used for excited-state calculations for the chromophore of photoactive proteins [55]; this topic is addressed later. In the latest version of ABINIT-MP (Open Version 1 Revision 22) [19], MFMO is oriented rather to the correlated treatment for the pharmacophore of proteins. Namely, the following cost-effective usage is enabled. Both low and high layers defined are treated at the HF level, and the latter is calculated at the MP2 or MP3 levels for IFIE-based detailed discussion on the interactions between ligand and neighbored residues.

3 Energy Gradient Calculation

A set of the first derivative of FMO total energy with respect to nuclear coordinates as the gradient is required for the geometry optimization and also the molecular dynamics (MD). At the early stage of FMO developments with ABINIT-MP, the HF gradient of 2-body expansion (FMO2-HF) was developed [56] and used for preliminary MD simulations [57], where the contribution from BDA was omitted. The current utility of FMO-MD in ABINIT-MP was based on PEACH developed by Komeiji; refer to the corresponding chapter of this book and a couple of reviews [58, 59]. FMO-MD was used to simulate various organic reactions under an explicitly hydrated condition [60–63].

For the water clusters with hydrogen bonds, the 3-body effect is substantial, and thus the FMO3-HF gradient for MD was implemented [64]. According to the precedent implementations in GAMESS-US, both the corrections of self-consistent Z-vector (SCZV) [65] and BDA contribution [66] were incorporated in ABINIT-MP. The periodic boundary condition (PBC) at the FMO3-HF level was also developed for MD in Fujita's [67] and Nakano's local versions. The UHF gradient was implemented at the FMO3 level and demonstrated for the MD simulation of hydrated divalent copper ion [42].

The MP2 gradient [68] was developed for FMO-MD [69], and the importance of electron correlation was demonstrated for the water cluster as well as ammonia cluster [70]. The FMO2-MP2 gradient was used also for the partial geometry optimization in which the region of interest is the target to be optimized; the MP2 correlation was certainly crucial to describe CH/ π and π/π interactions in Trp-Cage [71]. Recently, the frozen domain (FD) option [72] has been introduced as a more efficient route of geometry optimization.

The MCP gradient-based FMO-MD was available for droplet systems containing heavy metal elements such as hydrated trivalent lanthanide ion [73] and cisplatin [74]. The CDAM approximation was implemented for MP2 gradient, but the gross acceleration was not so efficient as for the case of MP3 energy.

4 Property Evaluation

The singlet and triplet excitation energies can be evaluated by the ability of configuration interaction singles (CIS) [55] with parallelized Fock-like contraction processing (N^4 computational cost [75]) under the MFMO framework [54]; the chromophore is just the target of excitations. CIS frequently suffers from overestimations in evaluated transition energies (1–2 eV), especially for singlet states. A perturbative doubles correction named CIS(D) of N^5 cost [76] is thus applied to remedy this discrepancy after MFMO-CIS calculations [77], through inclusions of the orbital relaxation energy for the target excited state and the differential correlation energy from the ground state. Various modified CIS(D) versions incorporating effective higher-order

contributions are available as well [78–80]; the cost scaling nature of N^5 is kept. All these CIS(D) calculations were parallelized in an integral-direct manner. Note that the FMO-CIS gradient and the relaxed density matrix (by solving CPHF equation) for a specified excited state [75, 81] are available and also that the non-local excitations can be modeled for molecular aggregates [82].

The frequency-dependent polarizability based on an HF linear response (LR) [83] was implemented in a similar way to the CIS calculation [84]. This ability is applicable even to silicon-based polymer chains [85]. Although the polarizability values by HF-LR are underestimated relative to those by correlated methods, the semi-quantitative discussion may be possible through proper scaling.

The dipole moment value is calculated for each monomer without charge at the end of the monomer stage. The Mulliken population analysis [20] for all atoms in the given system for FMO calculations is usually done a default utility, and various better choices (natural population analysis [86, 87] or ESP-fitted population analyses such as Merz–Kollman–Singh version [88, 89]) are usable upon request [90, 91].

5 Analysis Tool

As denoted previously, the notable merit of the FMO method is the usability as the analysis tool with IFIE or PIE for a given target system. To enhance such an ability, Morokuma-Kitaura’s EDA [2] variant of PIE (termed as PIEDA) was implemented first in GAMESS-US [92] and later in ABINIT-MP [93], where a certain pair energy is to be decomposed into four terms of “electrostatic” (ES), “Pauli’s exchange repulsion” (EX), “charge transfer” (CT) and “dispersion” (DI). The ES, EX and CT terms are calculated at the HF level, whereas the DI term is evaluated at the MP2 or MP3 levels. Here, care may be taken for the fact that not only pure dispersion contributions but also correlation corrections (to reduce excess ionicity retained by the HF description [20]) are included in the DI term. Recently, the local response dispersion (LRD) [94] ability with HF density has been implemented in ABINIT-MP, by which the dispersion contribution could be discussed separately. The PIEDA modified with LRD may be useful for more detailed discussions.

The solvation effect is often important in estimating the binding energy of ligand to protein in hydrated conditions, and thus the FMO2 Poisson-Boltzmann (PB) model [95] has been implemented [96, 97]; the dielectric constant is the crucial parameter as in the case of polarizable continuum model. A number of grand iterations of FMO-HF to achieve the convergence in the total energy of 1×10^{-5} (in atomic unit) are typically 10–14. Once converged, the MP2 calculations are to be performed. The PB-modified IFIE and PIEDA values show small but vital differences from those without solvation, especially for the interactions among charged fragments [98].

There are a couple of orbital-wise analysis tools in ABINIT-MP. For hydrogen bond or halogen bond with charge transfers, the configuration analysis for fragment interaction (CAFI) [99] is preferable, by which a set of donor and acceptor orbitals are obtained as the pseudo-natural orbital pairs derived from the concurrent electron

relaxation functional (CERF) [100] calculation for the selected fragment monomers after the monomer SCC stage. In contrast, the method of fragment interaction based on local MP2 (FILM) [101, 102] is applicable to capture dispersion-dominated local interactions of such CH/ π or π/π types. Visual presentations of orbital-wise results of CAFI or FILM are helpful in understanding the nature of site-specific interactions in pharmacophore.

The counter-poise (CP) correction from basis set superposition error (BSSE) [103] is available for IFIEs at the HF, MP2 and MP3 levels [104]. In production calculations of FMO2, the 6-31G(d) basis set has been usually used, and the evaluated IFIE values could contain about 40% of BSSE portions in the worst situation based on our experiences [41]. Some cautions may thus be required for quantitative discussion in comparison with experimental data; semi-quantitative discussion is still possible in the context of analysis, of course.

6 Utility

A potentially demanding step before the FMO calculation starts is the setting of fragmentation associated with the definition of BDAs, where such works should be tedious and error-prone when a given target system is large and complicated; the fragmentation is simple for molecular clusters without mutual bonds. For user's convenience, the fragmentation is automatically carried out in ABINIT-MP, for proteins, DNAs and RNAs. As a preparation of input data, this operation is also possible with the help by BioStation Viewer which is a graphical user interface (GUI) customized for ABINIT-MP [12]; the generated tables of fragmentation information is to be written out on an input file. BioStation Viewer is more useful in handling the output data (e.g., CAFI orbital pairs [99]); demonstrative illustrations by this GUI may be found in other chapters of this book.

As previously denoted, the BDA setting is usually made with the sp^3 -hybridized carbon atom [21]. Due to this limitation, the fragmentation for proteins is done not at the CO–NH peptide bond but at the $C\alpha$ –CO bond. When the carbonyl oxygen atom commits some interactions with other fragments (e.g., hydrogen bond), the assignment of interacting fragment pair looks shifted [105]. Special care should thus be paid for this case [98]. To circumvent such a difficulty, the sp^2 -hybridized BDA setting has been implemented recently [106], by which a straightforward fragmentation at the peptide bond is allowed. Because the respective IFIE values are affected, cross-checking with the standard sp^3 fragmentation is still necessary before the routine usages of sp^2 BDA.

Several Python scripts are provided for ABINIT-MP users. Old input data file can be converted to the latest one by “mkinp.py”. An automated fragmentation of peptoid systems [107] is enabled with “kyfrag.py”, where various functional groups are connected not to $C\alpha$ but to N (of peptide bond) in peptoids [108].

7 Demonstrative Application

In this section, several demonstrative calculations with available methods in ABINIT-MP are summarized. First, a favorable affinity with massively parallel supercomputers is described in the following three paragraphs.

Large-scale MP2 [34], MP3 [38] and higher-order [39] calculations on the Earth Simulators (ES and ES2) of NEC's vector processor type were reported with the 6-31G basis set. The best efficiency relative to theoretical speed (of 1024 processors) was recorded as high as 38.6% for a Trp₁₂₇-His model protein at the full MP4 level on ES2 under the OpenMP/MPI hybrid parallelism, indicating that the DGEMM-based processing of triples is efficiently implemented [39].

The Oakforest-PACS (OFP) system is many-core CPU supercomputer equipping Intel's Knights Landing processor (68 physical cores), and the hyperthreading with virtual cores is supported by a multiplication factor of 4. By setting 64 threads per fragment, the timings of FMO-MP2/6-31G(d) job with 2 and 4 processes on 1 node of OFP were 32.1 h and 15.6 h, respectively, for the HIV-protease-lopinavir complex. The timings of the same job with 4 and 8 processes on 2 nodes were 16.1 h and 8.0 h, respectively. The timing for a case of 16 processes on 4 nodes was 4.1 h. These timing data suggest that the FMO-MP2 job can be executed with a rather small number of nodes on OFP through the hyperthreading; a three-layer parallelization was usable for the MP2 when needed [109].

From April 2020, a new FMO project against the COVID-19 issue has been started by using the supercomputer Fugaku whose performance is the world fastest as of June 2020. Because of the overwhelming computing power of Fugaku, the FMO-MP3/cc-pVDZ calculations (with PIEDA) can be easily processed even for the spike protein of coronavirus consisting of 3.3 thousand amino acid residues; this MP3 job was completed in 3.4 h with 147,456(=48 × 3072) cores, and the relative cost to MP2 was only 2; the results will be published elsewhere.

Now, the excited-state calculations are briefed. The MFMO-CIS(D)/6-31G(d) approach was successfully applied to evaluate both excitation and emission energies for the DsRed protein [110]. The related fluorescent proteins were calculated by the modified CIS(D) schemes [78–80], and the evaluated excitation energies were in agreement with the experimental values within 0.1 eV [111–113]. A fully quantum mechanical estimation of blue shift of $n\pi^*$ excitation energy of the hydrated formaldehyde molecule was another representative example [114], where the droplet hydration model was simulated by FMO-MD and the statistical evaluation of excitation energy was made with the sampled structures from MD trajectories.

A combination of classical MD and FMO was pioneered by Ishikawa [15]. In this scheme, the MD-generated structures are subjected to a series of FMO calculations, and the IFIE values are evaluated by incorporating the structural fluctuations in a statistical fashion. Based on a rich amount of computational resources, such a combinative approach was applied to a couple of biochemical problems. The first is a comparative study on the Calmodulin in which the normal binding positions of Ca(II) ions are replaced by Eu(III) ions [115]; the 4f-in-core MCP was used for

Eu(III) [116]. The second is a structural interaction analysis on the uranyl-bridged DNA [52]. These two works demonstrated an importance of statistical evaluation of IFIEs in a realistic hydrated condition with finite temperature, and this approach has been taken in the latest COVID-19 project on the supercomputer Fugaku as well.

Finally, applications related to the field of applied physics are addressed. Based on the FMO4 scheme, the adsorptions of designed peptides onto specific inorganic surfaces (modeled by large-scale clusters) were analyzed [117–119]. In the cases of hydroxyapatite [118] and calcite [119], the classical MD-sampled structures were calculated at the MP2 level, and the respective roles of amino acid residues in interacting with the surfaces were revealed with a statistical sense. Coarse-grained (CG) simulations such as CG-MD and dissipative particle dynamics (DPD) [120] have attracted considerable interest, because theoretical analyses of mesoscale systems are made computationally tractable; various mesoscale functional devices consisting of lipids, proteins and substrates have been proposed and developed in the applied physics. Reliability and applicability depend on a set of effective interaction parameters for these CG calculations, and empirical parameter-based simulations frequently suffer from several limitations. Recently, the FMO-DPD method has been developed, in which the effective interaction parameters for DPD are non-empirically derived from a series of FMO calculations (a total number of jobs frequently reaches tens of thousands) for segment pairs defined for a given target system [121, 122]; please refer to the corresponding chapter written by Okuwaki in this book. FMO-DPD was applied to a variety of simulations for electrolyte membranes [123], lipid membranes/vesicles [124–127] and even proteins [128], and reasonable agreement with available experimental data was obtained.

8 Future Development

The latest public ABINIT-MP program is Open Version 1 Revision 22 (June 2020). For future releases, various developments have been in progress, and such works are addressed. The RI-based modules of MP2, MP2 gradient and MP3 have been imported from Ishikawa's PAICS [15, 46, 47, 129], and these abilities will be available in Version 2 as an option. From Ishimura's SMASH [130], the numerical quadrature module for density functional theory (DFT) as well as the effective core potential (ECP) module has been incorporated into a test version of ABINIT-MP. The B3LYP calculation [131] was potentially usable for FMO calculations, however the convergence difficulty for fragment dimers [132] has not been resolved. For Version 2, the porting work of integral generator (in which the spherical harmonic basis functions can be used) in SMASH has been underway, where the extant integral generator by Nakano has been kept; both generators may be properly used upon request.

The IFIE-based analysis is hardly applied to the directly linked fragment pairs with BDA [21]. This has been a long-term issue in FMO calculations. A couple of attempts have been made, although the remediation is still far from satisfactory [133, 134]. Continuous efforts are required for improvements.

Depending on the available computational resources (e.g. the latest Fugaku), ABINIT-MP is straightforwardly applicable to systems of thousands of fragments. If one desires the FMO calculations for a whole system consisting of functional proteins, surrounding membrane lipids, ions and waters, a total number of fragments could be more than ten thousand. For such a demanding case, several modifications and extensions may be required; for example, the load-balancing is a potential target to be improved.

As denoted so far, the statistical evaluation of interaction energies has gotten importance. Such an approach is suited to the machine learning (ML) from a viewpoint of post-processing for generated big data. A couple of preliminary ML works have been reported [135, 136]. In the next release of ABINIT-MP (Version 1 Revision 25, scheduled in February 2021), the lists of both IFIE/PIEDA values and associated descriptors (e.g. distance between centers of masses of fragment pair) are available as a separate file to which python scripts are directly applied. The regressions with support vector or random forest may be useful in predicting IFIE values without FMO calculations for a given structure of target system, once the training finishes. Works along this line have been promoted.

9 Summary

In this chapter, we have summarized various features of our ABINIT-MP program [12, 19, 135, 137]. Several demonstrative applications were addressed as well. In comparison with other FMO programs, ABINIT-MP could have several advantages in (1) higher-order correlated calculation, (2) affinity with supercomputers under hybrid parallelism, (3) FMO4, (4) variety of analysis tools, and (5) BioStation Viewer (custom GUI). Further developments have still been in progress for large-scale systems (ten thousand fragments) and statistical interaction analyses (with help of ML).

Acknowledgements The ABINIT-MP program has been developed with the commitments of many people. The authors would be grateful to Dr. Takatoshi Fujita, Dr. Ikuo Kurisaki, Dr. Hirofumi Watanabe, Prof. Kiyoshi Tanaka, Prof. Eisaku Miyoshi and Prof. Kazuo Kitaura for their scientific contributions. Various financial supports for the developments and applications of ABINIT-MP have been provided; (1) JST-CREST, (2) MEXT projects of FSIS, RSS21, SPIRE and FS2020 (priority issue #6) at the University of Tokyo, (3) Health and Labour Sciences Research Grants of Japan, (4) MEXT/JSPS Kakenhi (Nos. 18066009, 20038044, 23540451 and 16H04635), (5) AMED/BINDS (JP19an0101113) and (6) Rikkyo SFR. The trial usage of the supercomputer Fugaku was provided by RIKEN R-CCS and MEXT under the COVID-19 special research project [138]. Some modules such as numerical quadrature routines for LRD were imported from the SMASH program [130] developed by Dr. Kazuya Ishimura. Finally, YM would sincerely thank Prof. Chisachi Kato and Prof. Shinobu Yoshimura (the University of Tokyo) for continuous encouragements and supports.

References

1. Kitaura K, Ikeo E, Asada T, Nakano T, Uebayasi M (1999) *Chem Phys Lett* 313:701
2. Morokuma K, Kitaura K (1976) *Intern J Quant Chem* 10:325
3. Gordon MS, Fedorov DG, Pruitt SR, Slipchenko LV (2012) *Chem Rev* 112:632
4. Collins MA, Bettens RPA (2015) *Chem Rev* 115:5607
5. Raghavachari K, Saha A (2015) *Chem Rev* 115:5643
6. Herbert JM (2019) *J Chem Phys* 151:170901
7. Starikov EB, Lewis JP, Tanaka S (2006) *Modern methods for theoretical physical chemistry of biopolymers*. Elsevier, Amsterdam
8. Fedorov DG, Kitaura K (eds) (2009) *The fragment molecular orbital method: practical applications to large molecular systems*. CRC Press, Boca Raton
9. Heifetz A (ed) (2020) *Quantum mechanics in drug discovery*. Humana Press, New York
10. Gordon MS, Mullin JM, Pruitt SR, Roskop LB, Slipchenko LV, Boatz JA (2009) *J Phys Chem B* 113:9646
11. Fedorov DG, Nagata T, Kitaura K (2012) *Phys Chem Chem Phys* 14:7562
12. Tanaka S, Mochizuki Komeiji, Okiyama Y, Fukuzawa K (2014) *Phys Chem Chem Phys* 16:10310
13. Fedorov DG (2017) *WIREs: Comput Mol Sci* 7:e1322
14. <https://www.msg.Chem.iastate.edu/gamess/index.html>
15. Ishikawa T, Ishikura T, Kuwata K (2009) *J Comput Chem* 30:2594
16. https://www.paics.net/index_e.html
17. Takami T, Maki J, Ooba J, Inadomi Y, Honda H, Susukita R, Inoue K, Kobayashi T, Nogita R, Aoyagi M, Simos TE, Maroulis G (2007) *AIP Conference Proceedings*, AIP 963:122
18. <https://www.openfmo.org/>
19. https://www.cenav.org/abinit-mp-open_ver-1-rev-22/ (Japanese page)
20. Szabo A, Ostlund NS (1982) *Modern quantum chemistry*. Macmillan, New York
21. Nakano T, Kaminuma T, Sato T, Akiyama Y, Uebayasi M, Kitaura K (2000) *Chem Phys Lett* 318:614
22. Foresman JB, Frisch A (1996) *Exploring chemistry with electronic structure methods*, 2nd edn. Gaussian Inc., Pittsburgh
23. Nakano T, Kaminuma T, Sato T, Fukuzawa K, Akiyama Y, Uebayasi M, Kitaura K (2002) *Chem Phys Lett* 351:475
24. Amari S, Aizawa M, Zhang J, Fukuzawa K, Mochizuki Y, Iwasawa Y, Nakata K, Chuman H, Nakano T (2006) *J Chem Inf Model* 46:221
25. Nakano T, Mochizuki Y, Yamashita K, Watanabe C, Fukuzawa K, Segawa K, Okiyama Y, Tsukamoto T, Tanaka S (2012) *Chem Phys Lett* 523:128
26. Watanabe C, Fukuzawa K, Okiyama Y, Tsukamoto T, Kato A, Tanaka S, Mochizuki Y, Nakano T (2013) *J Mol Graph Model* 41:31
27. Sellers H (1993) *Intern J Quant Chem* 45:31
28. Kudin KN, Scuseria GE, Cancès E (2002) *J Chem Phys* 116:8255
29. Bacskay GB (1981) *Chem Phys* 61:385
30. Rendell AP (1994) *Chem Phys Lett* 229:204
31. Shavitt I, Bartlett RJ (2009) *Many-body methods in chemistry and physics*. Cambridge University Press, Cambridge
32. Mochizuki Y, Nakano T, Koikegami S, Tanimori S, Abe Y, Nagashima U, Kitaura K (2004) *Theor Chem Acc* 112:442
33. Mochizuki Y, Koikegami S, Nakano T, Amari S, Kitaura K (2004) *Chem Phys Lett* 396:473
34. Mochizuki Y, Yamashita K, Murase T, Nakano T, Fukuzawa K, Takematsu K, Watanabe H, Tanaka S (2008) *Chem Phys Lett* 457:396
35. Dykstra CE, Davidson ER (2000) *Intern J Quant Chem* 78:226
36. Grimme S (2003) *J Chem Phys* 118:9095
37. Pitoňák M, Neogrady P, Černý J, Grimme S, Hobza (2009) *ChemPhysChem* 10:282

38. Mochizuki Y, Yamashita K, Fukuzawa K, Takematsu K, Watanabe H, Taguchi N, Okiyama Y, Tsuboi M, Nakano T, Tanaka S (2010) *Chem Phys Lett* 493:346
39. Mochizuki Y, Yamashita K, Nakano T, Okiyama Y, Fukuzawa K, Taguchi N, Tanaka S (2011) *Theor Chem Acc* 130:515
40. Handy NC, Pople JA, Head-Gordon M, Raghavachari K, Trucks GW (1989) *Chem Phys Lett* 164:185
41. Yamada H, Mochizuki Y, Fukuzawa K, Okiyama Y, Komeiji Y (2017) *Comput Theor Chem* 1101:46
42. Kato Y, Fujiwara T, Komeiji Y, Nakano T, Mori H, Okiyama Y, Mochizuki Y (2014) *Chem-Bio Inform J* 14:1
43. Yamamoto J, Mochizuki Y (2014) *Chem-Bio Inform J* 14:14
44. Pedersen TB, Aquilante F, Lindh R (2009) *Theor Chem Acc* 124:1
45. Okiyama Y, Nakano T, Yamashita K, Mochizuki Y, Taguchi N, Tanaka S (2010) *Chem Phys Lett* 490:84
46. Ishikawa T, Kuwata K (2009) *Chem Phys Lett* 474:195
47. Ishikawa T, Sakakura K, Mochizuki Y (2018) *J Comput Chem* 186:613
48. Obara S, Saika A (1988) *J Chem Phys* 89:1540
49. Miyoshi E, Mori H, Hirayama R, Osanai Y, Noro T, Honda H, Klobukowski M (2005) *J Chem Phys* 122:074104
50. Mori H, Ueno-Noto K, Osanai Y, Noro T, Fujiwara T, Klobukowski M, Miyoshi E (2009) *Chem Phys Lett* 476:317
51. Ishikawa T, Mochizuki Y, Nakano T, Amari S, Mori H, Honda H, Fujita T, Tokiwa H, Tanaka S, Komeiji Y (2006) *Chem Phys Lett* 427:159
52. Rossberg H, Abe T, Okuwaki K, Barkleit A, Fukuzawa K, Nakano T, Mochizuki Y, Tsushima S (2019) *Chem Comm* 55:2015
53. Nakano T, Yamashita K, Segawa K, Okiyama Y, Watanabe C, Fukuzawa K, Tanaka S, Mochizuki Y (2012) *J Comput Aided Chem* 13:44
54. Fedorov DG, Kitaura K (2005) *J Chem Phys* 122:054108
55. Mochizuki Y, Koikegami S, Amari S, Segawa K, Kitaura K, Nakano T (2005) *Chem Phys Lett* 406:283
56. Kitaura K, Sugiki S, Nakano T, Komeiji Y, Uebayasi M (2001) *Chem Phys Lett* 336:163
57. Komeiji Y, Nakano T, Fukuzawa K, Ueno Y, Inadomi Y, Nemoto T, Uebayasi M, Fedorov DG, Kitaura K (2003) *Chem Phys Lett* 372:342
58. Komeiji Y, Mochizuki Y, Nakano T, Mori H (2012) Molecular dynamics: theoretical developments and applications in nanotechnology and energy. In: Wang L (ed) *InTech Open*. <https://doi.org/10.5772/35247>
59. Komeiji Y, Mochizuki Y, Nakano T, Fedorov DG (2009) *J Mole Struct (Theochem)* 898:2
60. Sato M, Yamataka H, Komeiji Y, Mochizuki Y, Ishikawa T, Nakano T (2008) *J Amer Chem Soc* 130:2396
61. Komeiji Y, Ishikawa T, Mochizuki Y, Yamataka H, Nakano T (2009) *J Comput Chem* 30:40
62. Sato M, Yamataka H, Mochizuki Y, Komeiji Y, Nakano T (2010) *Chem Eur J* 16:6430
63. Sato M, Yamataka H, Komeiji Y, Mochizuki Y (2012) *Chem Eur J* 18:9714
64. Komeiji Y, Mochizuki Y, Nakano T (2010) *Chem Phys Lett* 484:380
65. Nagata T, Brorsen K, Fedorov DG, Kitaura K, Gordon MS (2011) *J Chem Phys* 134:124115
66. Nagata T, Fedorov DG, Kitaura K (2010) *Chem Phys Lett* 492:302
67. Fujita T, Nakano T, Tanaka S (2011) *Chem Phys Lett* 506:112
68. Aikens CM, Webb SP, Bell RL, Fletcher GD, Schmidt MW, Gordon MS (2003) *Theor Chem Acc* 110:233
69. Mochizuki Y, Nakano T, Komeiji Y, Yamashita K, Okiyama Y, Yoshikawa H, Yamataka H (2011) *Chem Phys Lett* 504:95
70. Ninomiya M, Doi H, Matsumoto Y, Mochizuki Y, Komeiji Y (2020) *Bull Chem Soc Jpn* 93:553
71. Tsukamoto T, Mochizuki Y, Watanabe N, Fukuzawa K, Nakano T (2012) *Chem Phys Lett* 535:157

72. Fedorov DG, Alexeev Y, Kitaura K (2011) *J Phys Chem Lett* 2:282
73. Fujiwara T, Mori H, Komeiji Y, Mochizuki Y (2015) *CSW2014. JPS-Conf Series* 5:011001
74. Mori H, Hirayama N, Komeiji Y, Mochizuki Y (2012) *Comput Theor Chem* 986:30
75. Foresman JB, Head-Gordon M, People JA, Frisch MJ (1992) *J Phys Chem* 96:135
76. Head-Gordon M, Rico RJ, Oumi M, Lee TJ (1994) *Chem Phys Lett* 219:21
77. Mochizuki Y, Tanaka K, Yamashita K, Ishikawa T, Nakano T, Amari S, Segawa K, Murase T, Tokiwa H, Sakurai M (2007) *Theor Chem Acc* 117:541
78. Mochizuki Y, Tanaka K (2007) *Chem Phys Lett* 443:389
79. Mochizuki Y (2008) *Chem Phys Lett* 453:09
80. Mochizuki Y (2009) *Chem Phys Lett* 472:143
81. Shroll RM, Edwards WD (1995) *Intern J Quant Chem* 29:395
82. Fujita T, Mochizuki Y (2018) *J Phys Chem A* 122:3886
83. Olsen J, Jørgensen P (1985) *J Chem Phys* 82:3235
84. Mochizuki Y, Ishikawa T, Tanaka K, Tokiwa H, Nakano T, Tanaka S (2006) *Chem Phys Lett* 418:418
85. Ishikawa T, Mochizuki Y, Imamura K, Nakano T, Mori H, Tokiwa H, Tanaka K, Miyoshi E, Tanaka S (2006) *Chem Phys Lett* 430:361
86. Reed AE, Weinhold FJ (1983) *Chem Phys* 78:4066
87. Reed AE, Weinstock RB, Weinhold FJ (1985) *Chem Phys* 83:735
88. Singh UC, Kollman PA (1984) *J Comput Chem* 5:129
89. Besler BH, Merz KM Jr, Kollman PA (1990) *J Comput Chem* 11:431
90. Okiyama Y, Watanabe H, Fukuzawa K, Nakano T, Mochizuki Y, Ishikawa T, Tanaka S, Ebina K (2007) *Chem Phys Lett* 449:329
91. Okiyama Y, Watanabe H, Fukuzawa K, Nakano T, Mochizuki Y, Ishikawa T, Ebina K, Tanaka S (2009) *Chem Phys Lett* 467:417
92. Fedorov DG, Kitaura K (2007) *J Comput Chem* 28:222
93. Tsukamoto T, Kato K, Kato A, Nakano T, Mochizuki Y, Fukuzawa K (2015) *J Comput Chem Jpn* 14:1
94. Sato T, Nakai H (2009) *J Chem Phys* 131:224104
95. Watanabe H, Okiyama Y, Nakano T, Tanaka S (2010) *Chem Phys Lett* 500:116
96. Okiyama Y, Nakano T, Watanabe C, Fukuzawa K, Mochizuki Y, Tanaka S (2018) *J Phys Chem B* 122:4457
97. Okiyama Y, Watanabe C, Fukuzawa K, Mochizuki Y, Nakano T, Tanaka S (2019) *J Phys Chem B* 123:957
98. Hatada R, Okuwaki K, Mochizuki Y, Handa Y, Fukuzawa K, Komeiji Y, Okiyama Y, Tanaka S (2020) *J Chem Inform Model* 60:3593
99. Mochizuki Y, Fukuzawa K, Kato A, Tanaka S, Kitaura K, Nakano T (2005) *Chem Phys Lett* 410:247
100. Mochizuki Y (2005) *Chem Phys Lett* 410:165
101. Ishikawa T, Mochizuki Y, Amari S, Nakano T, Tokiwa H, Tanaka S, Tanaka K (2007) *Theor Chem Acc* 118:937
102. Ishikawa T, Mochizuki Y, Amari S, Nakano T, Tanaka S, Tanaka K (2008) *Chem Phys Lett* 463:189
103. Boys SF, Bernardi F (1970) *Mol Phys* 19:553
104. Okiyama Y, Fukuzawa K, Yamada H, Mochizuki Y, Nakano T, Tanaka S (2011) *Chem Phys Lett* 509:67
105. Yoshioka A, Takematsu K, Kurisaki I, Fukuzawa K, Mochizuki Y, Nakano T, Nobusawa E, Nakajima K, Tanaka S (2011) *Theor Chem Acc* 130:1197
106. Akinaga Y, Kato K, Nakano T, Fukuzawa K, Mochizuki Y (2020) *J Comput Chem* 41:1416
107. Kawada S, Sakaguchi M, Yonekura I, Okuwaki K, Mochizuki Y, Fukuzawa K (2016) *J Comput Chem Jpn* 15:51
108. Sun J, Zuckermann RN (2013) *ACS Nano* 7:4715
109. Watanabe H, Sato S, Sakakura K, Saito S, Mochizuki Y (2018) *J Comput Chem Jpn* 17:147

110. Mochizuki Y, Nakano T, Amari S, Ishikawa T, Tanaka K, Sakurai M, Tanaka S (2007) *Chem Phys Lett* 433:360
111. Taguchi N, Mochizuki Y, Nakano T, Amari S, Fukuzawa K, Ishikawa T, Sakurai M, Tanaka S (2009) *J Phys Chem B* 113:1153
112. Tagami A, Ishibashi N, Kato D, Taguchi N, Mochizuki Y, Watanabe H, Ito M, Tanaka S (2009) *Chem Phys Lett* 472:118
113. Taguchi N, Mochizuki Y, Nakano T (2011) *Chem Phys Lett* 504:76
114. Mochizuki Y, Komeiji Y, Ishikawa T, Nakano T, Yamataka H (2007) *Chem Phys Lett* 437:66
115. Drobot B, Schmidt M, Mochizuki Y, Abe T, Okuwaki K, Brulfert F, Falke F, Samsonov SA, Komeiji Y, Betzel C, Stumpf T, Raff J, Tsushima S (2019) *Phys Chem Chem Phys* 21:21213
116. Fujiwara T, Mori H, Mochizuki Y, Osanai Y, Miyoshi E (2011) *Chem Phys Lett* 510:261
117. Okiyama Y, Tsukamoto T, Watanabe C, Fukuzawa K, Tanaka S, Mochizuki Y (2013) *Chem Phys Lett* 566:25
118. Kato K, Fukuzawa K, Mochizuki Y (2015) *Chem Phys Lett* 629:58
119. Kato K, Fukuzawa K, Mochizuki Y (2019) *Jpn J Appl Phys* 58:120906
120. Español P, Warren PB (2017) *J Chem Phys* 146:150901
121. Okuwaki K, Mochizuki Y, Doi H, Ozawa T (2018) *J Phys Chem B* 122:338
122. Okuwaki K, Doi H, Mochizuki Y (2018) *J Comput Chem Jpn* 17:102
123. Okuwaki K, Mochizuki Y, Doi H, Kawada S, Ozawa T, Yasuoka K (2018) *RSC Adv* 8:34582
124. Doi H, Okuwaki K, Mochizuki Y, Ozawa T, Yasuoka K *Chem Phys Lett* 684:427
125. Doi H, Okuwaki K, Mochizuki Y, Ozawa T (2017) *J Comput Chem Jpn* 16:28
126. Shinsho E, Okuwaki K, Doi H, Mochizuki Y, Furuishi T, Fukuzawa K, Yonemochi E (2018) *J Comput Chem Jpn* 17:172
127. Tanaka H, Takahashi T, Konishi M, Takata N, Gomi M, Shirane D, Miyama R, Hagiwara S, Yamasaki Y, Sakurai Y, Ueda K, Higashi K, Moribe K, Shinsho E, Nishida R, Fukuzawa K, Yonemochi E, Okuwaki K, Mochizuki Y, Nakai Y, Tange K, Yoshioka H, Tamagawa S, Akita H (2020) *Adv Funct Mater* 30:1910575
128. Okuwaki K, Doi H, Fukuzawa K, Mochizuki Y (2020) *Appl Phys Express* 13:017002
129. Ishikawa T, Kuwata K (2012) *J Phys Chem Lett* 3:375
130. <http://smash-qc.sourceforge.net/>
131. Becke AD (1993) *J Chem Phys* 98:5648
132. Nishimoto Y, Fedorov DG (2016) *Phys Chem Chem Phys* 18:22047
133. Nakano T, Mochizuki Y, Fukuzawa K, Okiyama Y, Watanabe C (2017) *J Comput Aided Chem* 18:143
134. Nakano T, Mochizuki Y, Fukuzawa K, Okiyama Y, Watanabe C (2019) *J Comput Aided Chem* 20:1
135. Mochizuki Y, Sakakura K, Akinaga Y, Kato K, Watanabe H, Okiyama Y, Nakano T, Komeiji Y, Okusawa A, Fukuzawa K, Tanaka S (2017) *J Comput Chem Jpn* 16:119
136. Saitou S, Iijima J, Fujimoto M, Mochizuki Y, Okuwaki K, Doi H, Komeiji Y (2018) *Chem-Bio Inform J* 18:58
137. Mochizuki Y, Akinaga Y, Sakakura K, Watanabe H, Kato K, Watanabe N, Okuwaki K, Nakano T, Fukuzawa K (2019) *J Comput Chem Jpn* 18:129
138. <https://www.r-ccs.riken.jp/en/topics/fugaku-coronavirus.html>

PAICS: Development of an Open-Source Software of Fragment Molecular Orbital Method for Biomolecule



Takeshi Ishikawa

Abstract PAICS is an open-source software available for fragment molecular orbital (FMO) calculation. A notable characteristic of PAICS is the capability to use the resolution of the identity (RI) approximation with the FMO scheme. Second-order Møller–Plesset perturbation theory with the RI approximation (RI-MP2) was implemented in PAICS, demonstrating that electron correlation energy of biomolecules could be efficiently calculated. Recently, third-order Møller–Plesset perturbation theory with the RI approximation (RI-MP3) was implemented, which enables us to calculate higher order electron correlation energy of biomolecules in a reasonable computational time. This chapter introduces the development of PAICS, by focusing on the FMO-RI-MP2 and MP3.

Keywords PAICS · FMO-RI-MP2 · FMO-RI-MP3

1 Introduction

With the growth of computer technology, ab initio quantum chemical calculations have been applied to large molecules, including protein and nucleic acids. The fragment molecular orbital (FMO) method [1–5] is one of the most promising approaches for the quantum chemical investigation of such large molecules. As explained in the previous chapter, a target molecule is divided into small fragments, and various molecular properties are approximately calculated from the monomer and dimer calculations of the fragments. Thus, by using the FMO method, we can greatly reduce the computational cost of quantum chemical calculation of large molecule.

One of the program packages available for FMO calculations is “Parallelized ab initio calculation system based on FMO,” which is abbreviated to PAICS [6]. This program is developed by Takeshi Ishikawa, and its source code has been open to the public since 2011 [7]. While Fortran has been traditionally used for the development of quantum chemical program packages, C language is used for PAICS, which is one

T. Ishikawa (✉)

Department of Chemistry, Biotechnology, and Chemical Engineering, Graduate School of Science and Engineering, Kagoshima University, Kagoshima, Japan
e-mail: ishi@cb.kagoshima-u.ac.jp

© Springer Nature Singapore Pte Ltd. 2021

Y. Mochizuki et al. (eds.), *Recent Advances of the Fragment Molecular Orbital Method*, https://doi.org/10.1007/978-981-15-9235-5_5

69

of the characteristics of PAICS. A two-level parallelization with MPI is adopted in PAICS, that is, a whole FMO calculation is parallelized by the fragment monomers or dimers, and each calculation of them is additionally parallelized. When performing FMO calculations, fragmentation manner of a target molecule has to be given for every calculation. This process is very complicated, especially for a large molecule like a biomolecule, resulting that a method to automatically perform such a fragmentation is required. “PaicsView” is developed as a graphical user-interface of PAICS, which has a function of the auto-fragmentation for a typical protein or nucleic acid. Several application studies using PAICS and PaicsView have been reported in the life science field [8–13], including rational drug discoveries of infectious diseases [6, 14–19].

Restricted Hartree–Fock (RHF) method is implemented in PAICS as a basic quantum chemical theory for the FMO scheme, but it is not enough for accurate evaluation of the molecular interaction in biomolecules, in which dispersion interaction (or electron correlation effect) is essential. Thus, the second-order Møller–Plesset perturbation theory (MP2) with the resolution of the identity (RI) approximation [20–22], which is one of the most cost-effective electron correlation methods, is implemented in PAICS [23, 24]. Recently, the third-order Møller–Plesset perturbation theory (MP3) with the RI approximation was further implemented [25]. Because capability of the FMO-RI-MP2 and FMO-RI-MP3 is one of the most important characteristics of PAICS, details of them are described here. Another notable point in the development of PAICS is FMO-based quantum chemical/molecular mechanics method [26], which is given in Chap. 20.

2 RI-MP2 and MP3 with FMO Method

During the past couple of decades, various quantum chemical theories with approximation for the 4-center electron-repulsion integral (ERI) have been developed. Among them, the RI approximation is the most commonly used [27–29], in which the 4-center ERIs are approximately calculated with the 3- and 2-center ERIs using auxiliary basis functions. For example, $(ia|jb)$, a typical molecular orbital-based ERI, is approximately calculated as the following equation:

$$(ia|jb) \approx \sum_P B_{ia}^P B_{jb}^P, \quad (1)$$

where i or j is index of valence molecular orbitals (i.e., occupied orbitals not including frozen core orbitals), a or b is index of virtual molecular orbitals, and P or Q is index of auxiliary basis functions. A typical number of auxiliary basis functions is around three times larger than that of the basis functions. The matrix elements of B^P are calculated as

$$B_{ia}^P = \sum_Q (ia|Q) V_{QP}^{-1/2}, \quad (2)$$

where $(ia|Q)$ is the 3-center ERIs defined as

$$(ia|Q) = \int \varphi_i(\mathbf{r}_1) \varphi_a(\mathbf{r}_1) \frac{1}{|\mathbf{r}_1 - \mathbf{r}_2|} \varphi_Q(\mathbf{r}_2) d\mathbf{r}_1 d\mathbf{r}_2, \quad (3)$$

and $V_{QP}^{-1/2}$ is the element of the inverse of the square root matrix of \mathbf{V} . This \mathbf{V} matrix is calculated using the 2-center ERIs:

$$V_{PQ} = (P|Q) = \int \varphi_P(\mathbf{r}_1) \frac{1}{|\mathbf{r}_1 - \mathbf{r}_2|} \varphi_Q(\mathbf{r}_2) d\mathbf{r}_1 d\mathbf{r}_2. \quad (4)$$

MP2 correlation energy is obtained from the following equation:

$$E^{MP2} = \sum_{ijab} \frac{(ia|jb)[2(ia|jb) - (ib|ja)]}{\varepsilon_i + \varepsilon_j - \varepsilon_a - \varepsilon_b}, \quad (5)$$

where ε_i and ε_a are the orbital energy of the valence and virtual molecular orbitals, respectively. When using the RI approximation, $(ia|jb)$ and $(ib|ja)$ in Eq. (5) are calculated from \mathbf{B}^P matrix with Eq. (1). In the case of MP3 correlation energy, $(ij|ab)$ and $(ac|bd)$ type ERIs are additionally required [30, 31], and they are also calculated from \mathbf{B}^P matrix.

Once \mathbf{B}^P matrix is calculated by Eq. (2) and stored in the memory, the 4-center ERIs can be easily obtained from Eq. (1). RI-MP2 and MP3 energies are efficiently calculated using the DGEMM routine of the basis linear algebra subroutines (BLAS) because the main parts of the operations are described as the matrix multiplications involving \mathbf{B}^P . However, the size of \mathbf{B}^P matrix, which increases with the third power of the molecular size, is a crucial problem for the calculations of large molecules using the RI approximation. Especially in the case of RI-MP3, the memory requirement of \mathbf{B}^P matrix is unattainable because it not only occupied–virtual elements but also virtual–virtual elements are needed. This is a major reason why few application studies using RI-MP3 have been reported. On the other hand, the size of calculation is limited within the pair of fragments in FMO calculations. For example, in the case of a typical protein, dimer calculation of tryptophan pair is the largest size calculation because amino acid residue is usually treated as a single fragment in the FMO method. As a result, the memory requirement of \mathbf{B}^P matrix is not a significant problem for FMO-RI-MP2 and FMO-RI-MP3. Thus, it should be emphasized here that the combination of the FMO method and RI approximation is very promising.

3 Benchmark Calculation of FMO-RI-MP2 and MP3

As benchmark calculations of the FMO-RI-MP2 and MP3 with PAICS, the previously reported calculations of two biomolecular systems are shown here [23–25]. One is prion protein (PrP) complexed with GN8, and another is human immunodeficiency virus type 1 protease (HIV1 PR) complexed with lopinavir. PrP is a key protein in prion diseases, and GN8 [32] is a potential curative agent; the complex contains 103 amino acid residues and 1729 atoms. HIV1 PR is an important protein in the infection of acquired immune deficiency syndrome (AIDS), and lopinavir is an inhibitor; the complex contains 199 amino acid residues and 3225 atoms. The FMO calculations with the cc-pVDZ basis set [33] and auxiliary basis functions developed by Weigend et al. [34] were performed using 32 cores (Intel Xeon E5-2695v4) with a 4.0 GB memory per core.

Table 1 shows the computational times of the total energy of the two complexes by the FMO-RHF, FMO-MP2, FMO-RI-MP2, and FMO-RI-MP3. In the FMO-RHF calculations, the total times were 328.8 and 724.7 min for the PrP and HIV1 PR complexes, respectively. For the FMO-MP2, where the monomer and dimer MP2 calculations were additionally performed, the total times increased to 909.7 and 1618.5 min, respectively (the ratios to the FMO-RHF were 2.77 and 2.33). However, the total times of the FMO-RI-MP2 were 359.2 and 766.7 min, respectively (the ratios were only 1.09 and 1.06), clearly demonstrating that the MP2 correlation energy can be obtained without a significant increase of computational time compared to the FMO-RHF. For the FMO-RI-MP3 calculations, the computational times were 1572.2 and 2591.3 min, and the ratio with respect to the FMO-RHF calculations was 4.78 for the PrP complex and 3.58 for HIV1 PR complex. Thus, we can safely say that the MP3 correlation energy of large molecules can be obtained with a reasonable computational effort by using the RI approximation.

The interaction energy between a protein and small molecule is one of the most important quantities in typical biological applications using FMO method. In

Table 1 Computational time of the energy of FMO-RHF, FMO-MP2, FMO-RI-MP2, and FMO-RI-MP3 for the two biomolecular systems by PAICS. The time is given in minutes. The calculations were performed using 32 Intel Xeon E5-2695v4 cores with a 4.0 GB memory per core

	PrP complex				HIV1 PR complex			
	RHF	MP2	RI-MP2	RI-MP3	RHF	MP2	RI-MP2	RI-MP3
Monomer SCC	144.0	143.7	144.1	144.0	373.6	369.5	366.9	368.9
Monomer	1.9	10.7	2.4	12.4	3.5	16.2	4.2	17.9
Dimer-ES	31.0	31.1	31.0	31.0	107.6	107.6	107.7	110.5
Dimer	113.6	681.6	143.0	1384.7	214.5	1113.2	221.0	248.4
Total	328.8	909.7	359.2	1572.2	724.7	1618.5	766.7	2591.3
Ratio ^a	1.00	2.77	1.09	4.78	1.00	2.23	1.06	3.58

^aThe ratio to the computational time of the FMO-RHF calculation

Table 2 Correlation contributions of FMO-MP2, FMO-MP3, and FMO-MP2.5 to the protein–ligand interaction energies, and their errors associated with the RI approximation. The energy is given in Hartree. MP2.5 values are obtained by the sum of the MP2 correlation energy and half of the MP3 correlation energy

	PrP complex			HIV1 PR complex		
	Without RI	With RI	RI error	Without RI	With RI	RI error
$E_{corr}^{FMO-MP2}$	− 0.11267	− 0.11275	− 0.00008	− 0.19769	− 0.19782	− 0.00013
$E_{corr}^{FMO-MP3}$	− 0.09189	− 0.09196	− 0.00007	− 0.16066	− 0.16075	− 0.00009
$E_{corr}^{FMO-MP2.5}$	− 0.10228	− 0.10235	− 0.00008	− 0.17918	− 0.17929	− 0.00011

Table 2, the correlation contributions to the protein–ligand interaction energy obtained from the FMO-MP2, FMO-MP3, and FMO-MP2.5 are summarized together with the RI approximation errors. MP2.5 is the method proposed by Pitoňák et al. [35] in which the MP3 correlation energy is made half and added to the MP2 correlation energy. It is known that molecular interaction energies calculated by the MP2.5 have a comparable reliability with those calculated by coupled-cluster theory at singles and doubles plus perturbative triples, CCSD(T). For the PrP complex, RI approximation errors were -0.00008 , $+0.00007$, and -0.00008 Hartree in the correlation energies of the FMO-MP2, FMO-MP3, and FMO-MP2.5, respectively. The errors in the HIV1 PR complex were also of same order of magnitude. These results demonstrate that the errors associated with the RI approximation are insignificantly small for the molecular interaction energy. Thus, we can say that the FMO-RI-MP3 or FMO-RI-MP2.5 is one of the most promising method for accurate evaluation of the interaction energies in biomolecules.

In the current version of PAICS, the calculation of energy gradient with RI-MP2 is also available [24]. Table 3 summarizes the computational times of the energy gradient by the FMO-RHF, FMO-MP2, and FMO-RI-MP2. For the PrP complex, the times of the HF and RI-MP2 gradients were 850.0 and 1291.1 min, respectively, whose ratio was only 1.52. Similarly, the ratio was only 1.32 for the HIV1 complex. On the other hand, the computational times of the MP2 gradient were much larger than those of the HF gradient, that is, 2986.5 min (the ratio was 3.51) for the PrP complex and 5378.6 min (the ratio was 2.50) for the HIV1 complex. These results show that not only the energy but also the gradient can be efficiently calculated by using the RI approximation in FMO method.

Although cc-pVDZ basis set was used in these benchmark calculations, it is known that larger basis sets are needed for accurate evaluation of the electron correlation energy in molecular interaction. For example, diffuse basis functions can improve the quantitative description of the dispersion interaction. However, one problem is known to arise in the FMO calculations with a large basis set, that is, the poor convergence of the monomer SCC procedure. Actually, we could not reach to the convergence

Table 3 Computational time of the energy gradient of FMO-RHF, MP2, and RI-MP2 for the two biomolecular systems by PAICS. The time is given in minutes. The calculations were performed using 32 Intel Xeon E5-2695v4 cores with a 4.0 GB memory per core

	PrP complex			HIV1 PR complex		
	RHF	MP2	RI-MP2	RHF	MP2	RI-MP2
Monomer SCC	143.9	144.4	144.6	368.5	371.1	370.1
Monomer	5.5	37.1	12.1	9.0	58.1	19.9
Dimer-ES	260.8	260.6	261.1	881.1	881.6	880.1
Dimer	439.7	2544.4	873.3	892.7	4067.7	1571.6
Total	850.0	2986.5	1291.1	2151.4	5378.6	2841.7
Ratio ^a	1.00	3.51	1.52	1.00	2.5	1.32

^aThe ratio to the computational time of the FMO-RHF calculation

of the monomer SCC of the FMO calculations with cc-pVTZ basis set for above two biomolecular systems in the previous study [23]. Another problem is that the auxiliary basis functions implemented in PAICS are limited within atomic number 1 to 18 and 31 to 36 for cc-pVDZ. As a result, FMO calculations of biomolecules including metal atoms (e.g., copper or zinc atom) cannot be performed with the RI approximation, while such metal-containing biomolecules are one of the most important targets for quantum chemistry. These problems are hoped to be addressed in future.

4 Summary

In this chapter, the development of PAICS was described, focusing on the FMO-RI-MP2 and MP3. The combination of the RI approximation with the FMO method is very promising because the memory requirement of \mathbf{B}^P matrix, which is a main problem of the RI approximation in conventional quantum chemical calculations, is not significant in the FMO scheme. As clearly shown by the benchmark calculations with two biomolecular systems, these methods enable us to efficiently calculate the electron correlation energy in biomolecules. Although PAICS is a potential open-source software for FMO calculations of biomolecules, some issues should be addressed. For example, any implicit solvent model cannot be used, and three-body expansion of the FMO method (so-called FMO3) is not available. These methods are hoped to be implemented in PAICS in the near future.

References

1. Kitaura K, Sawai T, Asada T, Nakano T, Uebayasi M (1999) Pair interaction molecular orbital method: an approximate computational method for molecular interactions. *Chem Phys Lett* 312:319–324
2. Kitaura K, Ikeo E, Asada T, Nakano T, Uebayasi M (1999) Fragment molecular orbital method: an approximate computational method for large molecules. *Chem Phys Lett* 313:701–706
3. Fedorov DG, Kitaura K (2007) Extending the power of quantum chemistry to large systems with the fragment molecular orbital method. *J Phys Chem A* 111:6904–6914
4. Tanaka S, Mochizuki Y, Komeiji Y, Okiyama Y, Fukuzawa K (2014) Electron-correlated fragment-molecular-orbital calculations for biomolecular and nano systems. *Phys Chem Chem Phys* 16:10310–10344
5. Fedorov D, Kitaura K (2009) The fragment molecular orbital method: practical applications to large molecular systems. CRC Press
6. Ishikawa T, Ishikura T, Kuwata K (2009) Theoretical study of the prion protein based on the fragment molecular orbital method. *J Comput Chem* 30:2594–2601
7. PAICS. <https://www.paics.net/>
8. Ishikawa T, Kuwata K (2009a) Interaction analysis of the native structure of prion protein with quantum chemical calculations. *J Chem Theory Comput* 6:538–547
9. Ishikawa T, Burri RR, Kamatari YO, Sakuraba S, Matubayasi N, Kitao A, Kuwata K (2013) A theoretical study of the two binding modes between lysozyme and tri-NAG with an explicit solvent model based on the fragment molecular orbital method. *Phys Chem Chem Phys* 15:3646–3654
10. Itoh Y, Sando A, Ikeda K, Suzuki T, Tokiwa H (2012) Origin of the inhibitory activity of 4-O-substituted sialic derivatives of human parainfluenza virus. *Glycoconjugate J* 29:231–237
11. Arulmozhiraja S, Matsuo N, Ishitsubo E, Okazaki S, Shimano H, Tokiwa H (2016) Comparative binding analysis of dipeptidyl peptidase IV (DPP-4) with antidiabetic drugs—an ab initio fragment molecular orbital study. *PLoS ONE* 11:e0166275
12. Oku H, Inafuku M, Ishikawa T, Takamine T, Ishmael M, Fukuta M (2015) Molecular cloning and biochemical characterization of isoprene synthases from the tropical trees *Ficus virgata*, *Ficus septica*, and *Casuarina equisetifolia*. *J Plant Res* 128:849–861
13. Ishikawa T (2018) Ab initio quantum chemical calculation of electron density, electrostatic potential, and electric field of biomolecule based on fragment molecular orbital method. *Int J Quantum Chem* 118:e25535
14. Sriwilaijaroen N, Magesh S, Imamura A, Ando H, Ishida H, Sakai M, Ishitsubo E, Hori T, Moriya S, Ishikawa T, Kuwata K, Odagiri T, Tashiro M, Hiramatsu H, Tsukamoto K, Miyagi T, Tokiwa H, Kiso M, Suzuki Y (2016) A novel potent and highly specific inhibitor against influenza viral N1–N9 neuraminidases: insight into neuraminidase–inhibitor interactions. *J Med Chem* 59:4563–4577
15. Ma B, Yamaguchi K, Fukuoka M, Kuwata K (2016) Logical design of anti-prion agents using NAGARA. *Biochem Biophys Res Commun* 469:930–935
16. Ishibashi D, Nakagaki T, Ishikawa T, Atarashi R, Watanabe K, Cruz FA, Hamada T, Nishida N (2016) Structure-based drug discovery for prion disease using a novel binding simulation. *EBioMedicine* 9:238–249
17. Makau JN, Watanabe K, Ishikawa T, Mizuta S, Hamada T, Kobayashi N, Nishida N (2017) Identification of small molecule inhibitors for influenza a virus using in silico and in vitro approaches. *PLoS ONE* 12:e0173582
18. Ishikawa T, Mizuta S, Kaneko O, Yahata K (2018) Fragment molecular orbital study of the interaction between sarco/endoplasmic reticulum Ca^{2+} -ATPase and its inhibitor Thapsigargin toward anti-malarial development. *J Phys Chem B* 122:7970–7977
19. Yamaguchi K, Kamatari YO, Ono F, Shibata H, Fuse T, Elhelaly AE, Fukuoka M, Kimura T, Hoshokawa-Muto J, Ishikawa T, Tobiume M, Takeuchia Y, Matsuyama Y, Ishibashi D, Nishida N, Kuwata K (2019) A designer molecular chaperone against transmissible spongiform encephalopathy slows disease progression in mice and macaques. *Nat Biomed Eng* 3:206–219

20. Feyereisen M, Fitzgerald G, Komornicki A (1993) Use of approximate integrals in ab initio theory. An application in MP2 energy calculations. *Chem Phys Lett* 208:359–363
21. Weigend F, Häser M (1997) RI-MP2: first derivatives and global consistency. *Theor Chem Acc* 97:331–340
22. Weigend F, Häser M, Patzelt H, Ahlrichs R (1998) RI-MP2: optimized auxiliary basis sets and demonstration of efficiency. *Chem Phys Lett* 294:143–152
23. Ishikawa T, Kuwata K (2009b) Fragment molecular orbital calculation using the RI-MP2 method. *Chem Phys Lett* 474:195–198
24. Ishikawa T, Kuwata K (2012) RI-MP2 gradient calculation of large molecules using the fragment molecular orbital method. *J Phys Chem Lett* 3:375–379
25. Ishikawa T, Sakakura K, Mochizuki Y (2018) RI-MP3 calculations of biomolecules based on the fragment molecular orbital method. *J Comput Chem* 39:1970–1978
26. Okamoto T, Ishikawa T, Koyano Y, Yamamoto N, Kuwata K, Nagaoka M (2013) A minimal implementation of the AMBER-PAICS interface for ab initio FMO-QM/MM-MD simulation. *Bull Chem Soc Jpn* 86:210–222
27. Whitten JL, Allen LC (1965) Method for computing multicenter one- and two-electron integrals. *J Chem Phys* 43:S170–S171
28. Dunlap BI, Connolly JWD, Sabin JR (1979) On some approximations in applications of $X\alpha$ theory. *J Chem Phys* 71:3396–3402
29. Vahtras O, Almlöf J, Feyereisen MW (1993) Integral approximations for LCAO-SCF calculations. *Chem Phys Lett* 213:514–518
30. Bartlett RJ, Silver DM (1975) Many-body perturbation theory applied to electron pair correlation energies. I. Closed-shell first-row diatomic hydrides. *J Chem Phys* 62:3258–3268
31. Urban M, Kellö V (1979) Applications of perturbation theory to the chemical problems potential energy curves of BH, F2 and N2. *Mol Phys* 38:1621–1633
32. Kuwata K, Nishida N, Matsumoto T, Kamatari YO, Hosokawa-Muto J, Kodama K, Nakamura HK, Kimura K, Kawasaki M, Takakura Y, Shirabe S, Tanaka J, Kataoka Y, Katamine S (2007) Hot spots in prion protein for pathogenic conversion. *Proc Nat Acad Sci* 104:11921–11926
33. Dunning TH Jr (1989) Gaussian basis sets for use in correlated molecular calculations. I. The atoms boron through neon and hydrogen. *J Chem Phys* 90:1007–1023
34. Weigend F, Köhn A, Hättig C (2002) Efficient use of the correlation consistent basis sets in resolution of the identity MP2 calculations. *J Chem Phys* 116:3175–3183
35. Pitoňák M, Neogrady P, Černý J, Grimme S, Hobza P (2009) Scaled MP3 non-covalent interaction energies agree closely with accurate CCSD (T) benchmark data. *ChemPhysChem* 10:282–289

Open-Architecture Program of Fragment Molecular Orbital Method for Massive Parallel Computing (OpenFMO) with GPU Acceleration



Hiroataka Kitoh-Nishioka, Hiroaki Umeda, and Yasuteru Shigeta

Abstract OpenFMO is an open-architecture program of fragment molecular orbital (FMO) method for massively parallel peta- and exa-scale systems. This chapter provides an overview of OpenFMO program, focusing on its latest capabilities, master-worker execution scheme, MPI+OpenMP hybrid parallelization, GPU acceleration, and benchmark performances. The latest version of OpenFMO program is available through an open-source MIT license and the most recent information, including how to download, compile, and execute it with command-line options, and several examples used as a tutorial and template for the users can be found in the OpenFMO official website, <https://openfmo.org>.

Keywords Open source · MPI+OpenMP hybrid parallelization · Master-worker scheme · GPGPU

1 Introduction

As described in great detail by this book, the FMO method [1–3] is a method that has been developed for solving ab initio electronic structures of large bio-molecules, such as protein, nucleic acids, and sugar chains. In the FMO method, the large molecule is first divided into small fragments, where each fragment usually consists of 20 to 40 atoms; the FMO method approximates the electronic structure of the whole molecule by using the results of the electronic-structure calculations performed on the fragment monomers and dimers, depending on the level. Since the fragment electronic-structure calculations are independent of each other, the algo-

H. Kitoh-Nishioka

JST-PRESTO and Center for Computational Sciences, University of Tsukuba, Tsukuba, Japan

e-mail: hkito@ccs.tsukuba.ac.jp

H. Umeda · Y. Shigeta (✉)

Center for Computational Sciences, University of Tsukuba, Tsukuba, Japan

e-mail: shigeta@ccs.tsukuba.ac.jp

H. Umeda

e-mail: humeda@cray.com

© Springer Nature Singapore Pte Ltd. 2021

Y. Mochizuki et al. (eds.), *Recent Advances of the Fragment Molecular Orbital Method*, https://doi.org/10.1007/978-981-15-9235-5_6

rithm of the FMO method is inherently suitable for parallel executions. Previous studies have shown that one can obtain the reasonable parallel efficiencies of the FMO calculations by using up to 1,000 parallel executions [4, 5]. Although several large-scale FMO calculations [6–10] have been reported so far, adequate modifications to the algorithms in FMO calculations and optimal tuning of the parallelized implementations are still essential to achieve the practical FMO executions on more than peta-scale systems with desirable parallel efficiencies.

Toward the efficient FMO calculations on peta-scale computing systems, “OpenFMO” program [11] has been developed by Inadomi and co-workers [12–15] at Kyushu University and Institute of Systems, Information Technologies and Nanotechnologies (ISIT). OpenFMO program currently offers the FMO method with two-body correction (FMO2) at the restricted Hartree–Fock level of theory, called FMO2-RHF, which is written from scratch in C programming language with a short-length code consisting of ca. 54,000 lines. Since OpenFMO program relies on the standard MPI [16] and OpenMP [17] for its parallelization, it runs on any parallel computing platform that possesses a reasonable C compiler, OpenMP API, and MPI library. In the parallelization, OpenFMO program distributes several data arrays required for fragment electronic-structure calculations over all [13] or some [15] processes. Thus, the large-scale FMO calculations are feasible for the parallel computing systems with limited memory resources on each node. Furthermore, OpenFMO program avoids the use of scratch-disk space associated with slow disk-based I/O access and communication [12, 13]. Now, OpenFMO is well optimized for the large FMO2-RHF calculations on the peta-scale massive-parallel computing systems, such as K-computer [18], through the MPI+OpenMP hybrid parallelization of time-consuming molecular integral calculations, improvement of the store of and access to the monomer density matrices, and dynamic load balancing based on a newly implemented global counter [14, 15]. By using the tuned OpenFMO program, Inadomi and co-workers [14, 15] succeeded in carrying out effective large-scale FMO2-RHF/6-31G(d) calculations, in which a targeted protein consisting of 16,764 atoms was divided in to 576 fragments, over up to 20,480 parallel executions.

Another recent remarkable progress in OpenFMO program is the capability of the use of modern NVIDIA graphics processing units (GPUs). The use of powerful GPUs to accelerate quantum chemical calculations is eagerly anticipated in a wide scientific field, while it is a difficult task to adapt pre-existing (legacy) codes to such new hardware frameworks with newly developed programming environments including CUDA (compute unified device architecture). Although several research groups [19–24] have developed GPU-accelerated RHF calculations, there are problems to incorporate them into OpenFMO, for example, one reason arises from non-disclosure of most their codes. Thus, we [25–28] have developed GPU-accelerated FMO2-RHF calculations by implementing the GPU-enabled kernel codes in the following two time-consuming parts of OpenFMO program with CUDA from scratch: (1) Fock-matrix construction [27, 28] and (2) four-center (4C) inter-fragment Coulomb interaction (IFC) [25–27]. We have reported that the GPU-accelerated OpenFMO program can show reasonable speedups for several benchmark calculations [25–27].

We recently made the GPU-accelerated OpenFMO program publicly available on GitHub at <https://github.com/OpenFMO/OpenFMO>. We dedicate the remaining part of this chapter to give some information about the use of OpenFMO program on a CPU/GPU cluster computing system. Section 2 overviews its capabilities. Section 3 explains a scheme of FMO2-RHF calculations for making it easy to understand the following sections. Section 4 explains the master-worker execution model of OpenFMO based on MPI dynamic process management (explained later) or fault-resilient programming middleware, Falanx [29, 30]. Section 5 briefly describes the GPGPU parts of OpenFMO and shows their benchmark performances. Section 6 gives concluding remarks of this chapter.

2 Capabilities

OpenFMO program version 1.0 [11] is available through the repositories hosted on GitHub, <https://github.com/OpenFMO/OpenFMO>. In addition to FMO calculations, the users can do conventional RHF calculations using the “skeleton-RHF” code of OpenFMO, which is also MPI and OpenMP hybrid program. The capabilities of OpenFMO program are summarized as follows:

- RHF and FMO2-RHF.
- Single-point ground-state energy calculation.
- Minimum and double-zeta Gaussian basis functions up to third-row atoms (namely, H - Ar) including STO-3G, 6-31G, 6-31G(d), 6-31G(d,p).
- MPI + OpenMP parallelization for RHF and FMO2-RHF.
- GPU-accelerated RHF and FMO-RHF with Fermi or Kepler microarchitecture supporting double-precision floating-point operations.

Although we assume that OpenFMO program runs on any parallel computing platform, it is preferable that the platform satisfies the conditions as follows:

- LINUX/UNIX cluster machines.
- GNU C compiler.
- Intel C compiler.
- MPI libraries (Default: Intel MPI Library):
MPI_comm_spawn functions are required for OpenFMO based on MPI dynamic process management (explained in Sect. 4).
- Intel MKL(Math Kernel Library).

In addition, GPU-accelerated OpenFMO requires the following conditions that the platform possesses:

- NVIDIA graphics card (Fermi or Kepler microarchitecture) supporting double-precision floating-point operations.
- NVIDIA drivers for GPU.

As described in Sect. 4, there are the following two implementations for the master-worker execution model of OpenFMO program; one version is based on MPI dynamic process management (involving `MPI_Comm_spawn` functions), hereafter called OpenFMO(MPI) for simplicity’s sake; the other version is based on Falanx [29, 30] fault-resilient programming middleware, hereafter called OpenFMO(Falanx). Compiling OpenFMO(MPI) yields the three executables, “ofmo-master,” “ofmo-worker,” and “ofmo-mserv,” while compiling OpenFMO (Falanx) yields the single executable, “ofmo-falanx.” If it is difficult to run with `MPI_Comm_spawn` for your system, you can use OpenFMO (Falanx).

OpenFMO program adopts the almost same input-file format as the FMO calculations implemented in GAMESS [31] ab initio quantum chemistry package. Since some of the input groups used in GAMESS are directly used in OpenFMO, the GAMESS documentations [32], such as “Input Description” and “Further Information,” are useful for the users of OpenFMO. The input files for the FMO calculations of GAMESS can be prepared with the CUI (character user interface)-style program, FMOutil [33], its GUI (graphical user interface)-style version, Fu [34], and another GUI program Facio [35, 36]. Thus, the users also make use of these programs for the preparation of the input file of OpenFMO program. Further information of the inputs can be found in the OpenFMO official website, <https://openfmo.org>.

3 Workflow of FMO

For making it easy to understand the following sections, we here give a brief explanation of FMO2, of which the workflow is schematically illustrated in Fig. 1.

In the FMO method, the total molecule is first divided into N_{frag} fragments and initial density matrices \mathbf{D}_I are calculated for all fragments. The electronic structure of each fragment is then solved self-consistently under the electrostatic potential (ESP) from all other fragments. This procedure is called self-consistency of charge (SCC). After the convergence of SCC, the electronic structure of each fragment-pair is solved under ESP from all other fragments. FMO2 expresses an approximated total electronic energy of a whole molecule, E^{FMO2} , by [1–3]

$$E^{\text{FMO2}} = \sum_{I>J}^{N_{\text{frag}}} E_{IJ} - (N_{\text{frag}} - 2) \sum_I^{N_{\text{frag}}} E_I, \quad (1)$$

E_I and E_{IJ} represent the total electronic energies of I -th fragment monomer and IJ -th fragment-pair (dimer), respectively. Similarly, the approximated electron density matrix of the whole molecule, \mathbf{D}^{FMO2} , is given by

$$\mathbf{D}^{\text{FMO2}} = \sum_{I>J}^{N_{\text{frag}}} \mathbf{D}_{IJ} - (N_{\text{frag}} - 2) \sum_I^{N_{\text{frag}}} \mathbf{D}_I. \quad (2)$$

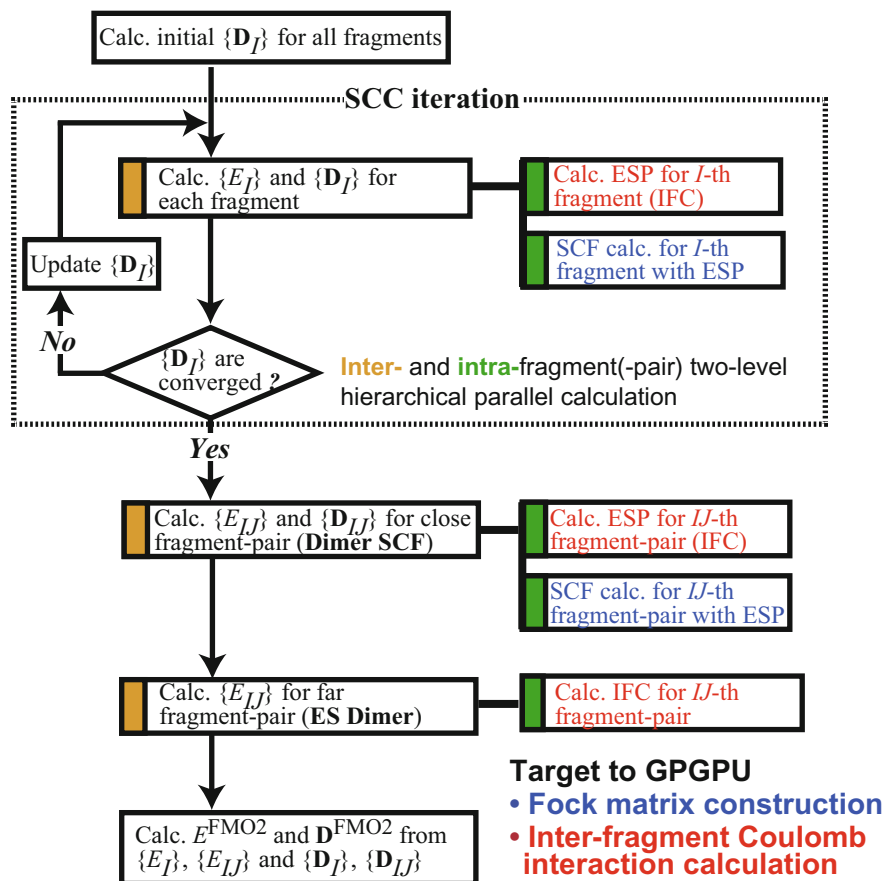


Fig. 1 Workflow of FMO2-RHF calculation

The FMO method uses the following modified Fock matrix to solve the electronic structure of each fragment(-pair) x under ESP,

$$\mathbf{F}_x = {}^0\mathbf{F}_x + \sum_{I \neq x}^{N_{\text{frag}}} {}^x\mathbf{V}_I + \mathbf{P}_x, \quad (3)$$

$${}^0\mathbf{F}_x = {}^0\mathbf{H}_x^{\text{core}} + \mathbf{G}_x, \quad (4)$$

$$[\mathbf{G}_x]_{ij} = \sum_{kl} D_{kl}^x \{2(ij|kl) - (il|kj)\}, \quad (5)$$

where ${}^0\mathbf{F}_x$ represents the conventional Fock matrix of fragment(-pair) x , including one-electron Hamiltonian matrix ${}^0\mathbf{H}_x^{\text{core}}$ and G-matrix defined in Eq. (5). \mathbf{P}_x represents the hybrid orbital projection (HOP) operators, which is required when

bond-detached/attached atoms are involved in x . ${}^x\mathbf{V}_I$ is the ESP generated by the fragment $I (\neq x)$, which is expressed by

$${}^x\mathbf{V}_I = {}^x\mathbf{u}_I + {}^x\mathbf{v}_I, \quad (6)$$

$$[{}^x\mathbf{v}_I]_{ij} = \sum_{kl \in I} D_{kl}^I (ij|kl). \quad (7)$$

Here, ${}^x\mathbf{u}_I$ is the ESP generated by the nuclei of fragment $I (\neq x)$.

At each fragment calculation, the corresponding ESP $\{{}^x\mathbf{V}_I\} (I (\neq x))$ is first evaluated as inter-fragment Coulomb interactions (IFCs) by using Eq. (6), which accompanies the calculations of four-center (4C) two-electron integrals, as shown in Eq. (7). Usually, the FMO method calculates time-consuming 4C-IFCs only for neighboring fragments and approximates the ESPs from the other fragments as the IFCs arising from Mulliken populations or Mulliken atomic charges. Moreover, we can reasonably approximate the electrostatic interaction between long-separated fragment-pair as follows:

$$E_{IJ} \approx E_I + E_J - \text{Tr}(\mathbf{D}_I^J \mathbf{V}_I), \quad (8)$$

which is called ‘‘ES dimer’’ approximation. On the other hand, the explicit SCF calculation of the fragment-pair is called ‘‘Dimer SCF.’’

4 Master-Worker Execution Model

To effectively perform large-scale FMO calculations on a CPU or GPU cluster, the user needs to understand the master-worker execution model of OpenFMO program, which is schematically illustrated in Fig. 2 [15].

In the master-worker model, one process works as a ‘‘master’’ one. All the remaining processes are first divided into ‘‘data server’’ and ‘‘worker’’ processes. All the worker processes are then divided into groups, called ‘‘worker groups.’’ The master process assigns monomer and dimer calculation jobs to each worker group and gathers their results. These jobs are done independently of each other in each SCC loop and the final FMO2 step after the SCC convergence, which is the inter-fragment(-pair) upper level (or coarse-grained) parallelization (see the blocks marked by orange in Fig. 1). The execution of the job assigned to one worker group is parallelized within the worker group, which is the intra-fragment lower level (or fine-grained) parallelization (see the blocks marked by green in Fig. 1). Such the two-level hierarchical parallel scheme is used in other FMO codes including GAMESS [37] and ABINIT-MP [38]. As described in Sect. 3 and shown in Fig. 1, each worker group responsible for the calculation of fragment(-pair) x needs not only the data of one’s own density matrix \mathbf{D}_x but also those of the other fragments, $\{\mathbf{D}_I\} (I \neq x)$, to construct the ESP, $\{{}^x\mathbf{V}_I\}$. The memory requirement for storing the data of monomer density matrices is increased with increasing the system size. If each process tries to store all neces-

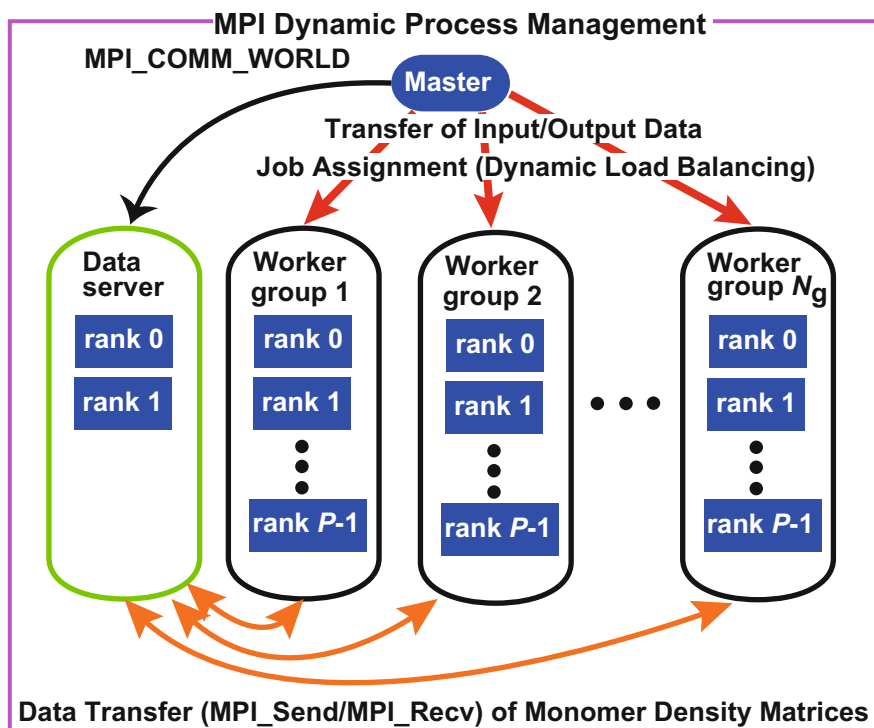


Fig. 2 Master-worker execution model used for OpenFMO

sary density matrices on its memory, the peta-scale FMO calculations for more than 10,000-fragment systems must encounter the memory requirement problem [13]. To avoid the problem, the master process in OpenFMO program distributes the data of monomer density matrices to the memories of data server processes and updates them by following the results done by worker groups. The data server processes are devoted to the response to the communication operations related to density matrices. Since the data server processes are uninvolved in electronic-structure calculations, their implementation leads to a decrease in the computational efficiency to some extent. In the early days, one-sided communication (OSC) of MPI-2 standard was implemented in OpenFMO program [13], where the data of monomer density matrices were distributed over all worker groups. Although the OSC implementation does not need the use of the data server processes, its fragment calculation jobs need to exchange necessary density matrices between worker groups, which leads to an increase in the communication latency during the inter-fragment upper level parallelization. Inadomi and co-workers [15] demonstrated that OpenFMO program using data server process exhibits better performance than the previous OSC-implemented one.

On modern CPU/GPU clusters, we can usually make use of a MPI+OpenMP hybrid scheme to use multi-threading for single-node parallelism in combination with message-passing for parallelization across many nodes. It is well known that MPI+OpenMP hybrid scheme has several advantages, including the fast synchronization within a node, the data sharing between threads, smaller memory footprint, etc. In the released OpenFMO program, MPI+OpenMP hybrid scheme is applied to the molecular integral calculations in Fock matrix, Eq. (5), and 4C-IFC calculations, Eq. (7), which accounts for most of computational time in FMO2-RHF.

One of the most attractive features of OpenFMO program is the implementation of a sophisticated dynamic load-balancing technique with global counter [14, 15], to maintain the good load balance for both inter-fragment upper level and intra-fragment lower level parallelizations. To achieve the parallel efficiency, one should avoid the workload imbalance of the time-consuming evaluation of the molecular integrals. Generally, the integral screening based on Schwarz inequality is used before the integrals are calculated, which reduces the computational costs. Since we are usually unable to know in advance how much tasks will be assigned to each group/process, it is difficult to use a static load-balancing technique that distributes the tasks in a round-robin fashion. From the reason, Inadomi and co-workers [14, 15] implemented the global counter using standard MPI and OpenMP libraries to keep the portability of OpenFMO. In the implementation of the global counter, one thread of “rank 0” process in each work group is used as the master thread of global counter that devoting oneself completely to maintain a global counter in each group and response to the communication operations requested by the other processes/threads; on the other hand, the other threads in each work group can be involved in the molecular integral calculations. As a result, OpenFMO program has achieved very high parallel efficiencies for large-scale FMO calculations so far. See Ref. [14, 15] for further details about its implementation and their benchmark performances.

As described in Sect. 2, there are two implementations for the master-worker execution model: OpenFMO(MPI) and OpenFMO(Falanx). OpenFMO(MPI), which was first implemented, is based on MPI dynamic process management, where the “master” process creates new processes, “Data server” and “worker” ones and manages communication among them. The implementation of MPI dynamic process management enabled the developers to expand OpenFMO program to more flexible “Task parallel” models, including fault-resilient Falanx [29] (explained below) and OmniRPC-MPI [39, 40]; the latter remains unreleased.

Instead of MPI dynamic process management, a fault-resilient programming middleware Falanx [29] is used, for the parallel execution of OpenFMO (Falanx) [30]. When a MPI application is run on an exa-scale computing system with a huge number of processors in the future, a process crash due to a hardware or software failure would no longer be a rare event. In such a case, a single trouble occurrence would terminate conventional MPI applications. Ikegami and co-workers at National Institute Advanced Industrial Science and Technology (AIST) have developed the Falanx middleware that makes it possible to easily develop fault-resilient applications for forthcoming exa-scale computing systems; by using Falanx API, one can easily implement a resource manager for task scheduling and a data store for data protec-

tion to insulate the applications from system failures. Another attractive feature of OpenFMO(Falanx) is that the worker configuration can be rearranged at dimer jobs after SCC convergence [30]. When OpenFMO(MPI) is used, the worker configuration at dimer jobs is beforehand fixed to that at monomer jobs, namely, N_g and P at dimer jobs are identical with those at monomer jobs (see Fig. 2). In FMO calculations, the number of fragment-pair is substantially greater than that of fragment. Therefore, OpenFMO(Falanx) can remarkably improve the workload balance at dimer jobs by increasing N_g with decreasing P within a given computational resource after SCC is converged.

We here give an example how to execute OpenFMO program on a GPU cluster. In the GPU-accelerated OpenFMO program, the master thread of each MPI rank controls one GPU unit. Therefore, you have to set the total number of MPI processes to that of the available GPU units to bring out the GPU's maximum performance on your GPU cluster. For example, in HA-PACS GPU base cluster [41] run by Center for Computational Sciences (CCS), University of Tsukuba, one node is comprised of two Intel E5-2680 CPU (2.6 GHz 8 cores) and 4 NVIDIA M2090 GPUs. If 8 nodes ($2 \times 8 \times 8 = 128$ cores and $4 \times 8 = 32$ GPU units) are used for a FMO calculation, the total number of MPI ranks for the calculation should be set to that of available GPU units, 32, where each MPI rank is composed of 4 threads. Within the given resource (32 ranks), for example, 1 rank is assigned to the "master" process, 1 rank is assigned to the "data server" process, the other 30 ranks are assigned to "worker" processes with $N_g = 15$ and $P = 2$.

5 GPU Acceleration

To realize the GPU acceleration of large-scale FMO calculations, we [25–28] implemented the GPU-enabled kernel codes in the 4C-IFC and Fock-matrix construction parts of OpenFMO program; the former and latter parts are written in red and blue colors, respectively, in Fig. 1. These parts include the time-consuming two-electron (2e) integral calculations. Fock-matrix construction involves accumulating 2e-integral elements, $(ij|kl)$ and $(il|kj)$, to a \mathbf{G}_x matrix, as expressed by Eq. (5). Similarly, 4C-IFC calculation involves accumulating 2e-integral elements, $(ij|kl)$, to a ${}^x\mathbf{v}$ -matrix, as expressed by Eq. (7). When using the massive-parallel threads with limited memory resources on GPU for the calculations, we cannot allocate \mathbf{G}_x or ${}^x\mathbf{v}$ as thread private in GPU local memory. Therefore, massive slow exclusive addition operation is usually needed to accumulate matrix elements into a shared matrix.

To share \mathbf{G}_x matrix within a thread block without the slow "atomic" operation, we have developed a novel algorithm [28], which is based on the parallel large Fock matrix construction algorithm [42] on distributed CPU cluster for FMO-MO method [43, 44]. We first consider a twofold loop around pair indices ij and kl in the G-matrix construction, which is survived pair-index after the overlap integral screening [45]. As illustrated in Fig. 3a, the access pattern to \mathbf{G}_x matrix in an inner kl -loop can be classified as the following three types: $\mathbf{Gi}[]$, for i column array (yellow color),

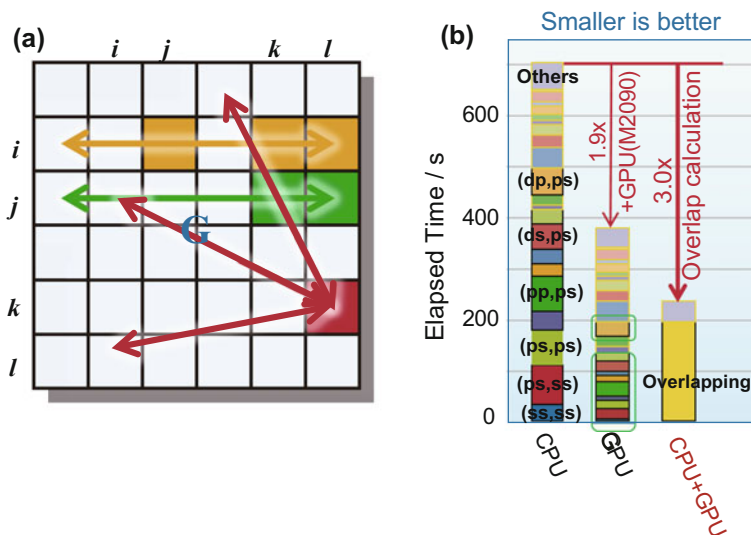


Fig. 3 **a** Access pattern to \mathbf{G} matrix for one 2e-integral, $(ij|kl)$. **b** Elapsed time for RHF/6-31G(d) calculation of 126 atomic molecule (1 282 AO) using “skeleton-RHF” code of OpenFMO program

$\mathbf{G}_j[]$ for j column array (green color), and $\mathbf{G}_k l$ (red color). The index kl runs only limited area of matrix $\mathbf{G}[][]$ (blue color), and points different elements of $\mathbf{G}[][]$ for a given ij index. By making use of this classification, in our algorithm, each thread has only $\mathbf{G}_i[]$ and $\mathbf{G}_j[]$ column arrays, and shares resulting matrix $\mathbf{G}[][]$ among a thread block. By taking reduction for $\mathbf{G}_i[]$ and $\mathbf{G}_j[]$ after inner kl -loop, we can accumulate it into $\mathbf{G}[][]$ without the time-consuming atomic operation. It should be noted that we activate the GPU-enabled kernel code only for selective integral types in order to overlap CPU and GPU calculations. We also did the following CUDA optimizations: index-sorting, Schwarz-screening before main-loop, and dynamic load-balancing.

Because implementing the GPU-accelerated code in the 4C-IFC parts encounters a common problem with the Fock-matrix construction parts, we applied same parallelization techniques to them, followed by task assignment and code tuning.

Figure 3b plots the benchmark performance of the “skeleton-Fock” code of OpenFMO on a single HA-PACS GPU cluster node containing two Intel E5-2680 CPUs with four NVIDIA M2090 GPUs (see the last paragraph of Sect. 4). Figure 3b shows that the speedup by using the GPU-accelerated code without overlapping CPU-GPU execution is ca. 1.9. We can see that the GPU acceleration for smaller integral types is better than that for the bigger ones. As shown in Fig. 3b, the speedup by using GPU-accelerated code with overlapping CPU-GPU execution results in ca. 3.

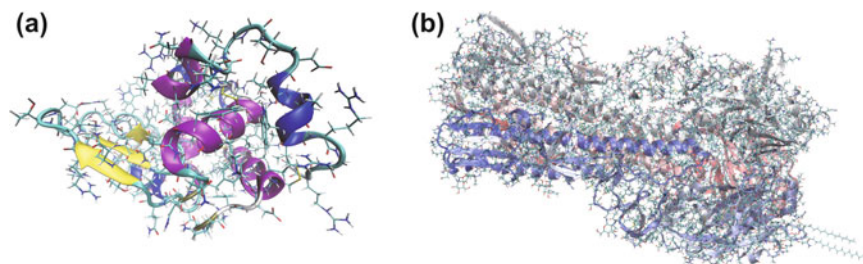


Fig. 4 **a** Lysozyme (1 961 atoms and 57 fragments) **b** Influenza HA protein (23 460 atoms and 721 fragments) [46]

Table 1 Elapsed times (in seconds) observed for GPU-accelerated FMO2-RHF/6-31G(d) calculations of lysozyme, in which the number of worker groups N_g was always set to 15

#node (#GPU)	SCC	Dimer SCF	ES dimer	Total
8 (0)	3 070.5	6 246.2	407.3	9 770.5
8 (32)	827.5	1 674.8	77.8	2 596.8
16 (64)	450.2	898.4	42.2	1 429.6
32 (128)	308.2	530.7	24.8	902.0

We next show some benchmark performances of the GPU-accelerated FMO calculations with OpenFMO(MPI). For the benchmarks, we used HA-PACS GPU base cluster system [41] that was explained in the last paragraph of Sect. 4.

Figure 4a shows a lysozyme molecule (1 961 atoms) that was divided as 2 residues per fragment, leading to 57 fragments in the FMO2-RHF/6-31G(d) calculations. Table 1 lists the elapsed times of the components (SCC, “dimer SCF” and “ES dimer”) of the FMO calculations and the corresponding total ones (see the workflow in Fig. 1).

We first addressed the performance of the GPU acceleration of OpenFMO(MPI). For the purpose, we used 8 nodes with/without 32 GPUs on HA-PACS GPU cluster; 2 MPI ranks were used for master and data server processes; the remaining 30 MPI ranks were divided into $N_g = 15$ worker groups with $P = 2$ MPI ranks (see Fig. 2); and 4 threads (CPU cores) and 1 GPU are involved in each MPI rank. From Table 1, we obtain the speedups of 3.7 for SCC, 3.7 for Dimer SCF, 5.2 for ES Dimer, and 3.8 for total, which verifies the reasonable GPU acceleration of OpenFMO program. We next addressed the parallelization performance of the GPU acceleration of OpenFMO(MPI). For the purpose, as listed in Table 1, we measured the elapsed times of the FMO calculations using 8 nodes with 32 GPUs, 16 nodes with 64 GPUs, and 32 nodes with 128 GPUs. In the benchmarks, N_g was always set to 15. By comparing the total elapsed time between 8 and 16 nodes, we can see that the GPU-accelerated FMO scaled remarkably well with the high efficiency of 91%. When 32 nodes were used, the assigned group (GPU) size $P = 8$ or 9 was generally too large to do each fragment(-pair) job, which is due to the source of the workload

Table 2 Elapsed times (in hours) observed for GPU-accelerated FMO-RHF/6-31G(d) calculation of Influenza HA3 protein, in which 254 MPI ranks (64 nodes) are divided into 84 worker groups

SCC	Dimer SCF	ES dimer	Total
0.52	0.90	0.45	1.97

imbalance. However, the program with 32 nodes kept the parallel efficiency to a modest level, 72%.

Figure 4b shows the influenza HA3 protein (HA3, 23460 atoms) that was previously studied using FMO2-MP2 calculations [46]. In our FMO2-RHF/6-31G(d) calculation, HA3 was divided as 2 residues per fragment, leading to 721 fragments. We used 64 nodes with 256 GPUs on HA-PACS GPU cluster for the benchmark; 2 MPI ranks were used for master and data server processes; for the remaining 254 MPI ranks, N_g and P were set to 84 and 3, respectively; and 4 threads (CPU cores) and 1 GPU are involved in each MPI rank. Table 2 lists the elapsed times of the benchmark in hours. We can see that OpenFMO(MPI) successfully completed the FMO calculation of HA3 within only 2 h [26, 27], which is the first large-scale GPU-accelerated FMO calculation as far as we know.

See Ref. [26] for further details about the benchmark performances of lysozyme and HA3.

6 Concluding Remarks

This chapter has explained OpenFMO program developed for the application of GPU-accelerated FMO calculation on current peta-scale and forthcoming exa-scale computing systems. We have especially highlighted the master-worker model (Sect. 4) and GPU acceleration (Sect. 5) of OpenFMO to give some practical information about its effective use on a CPU/GPU cluster. As indicated by our benchmarks of lysozyme and HA3, OpenFMO program makes it possible to readily perform GPU-accelerated FMO calculations for the large proteins containing hundreds of thousands of atoms with reasonable parallel efficiencies. Further information of the input-file formats and command-line options and several examples used as a tutorial and template for you can be found in the OpenFMO official website, <https://openfmo.org>. We are now engaged in extending the theoretical range of application of GPU-accelerated OpenFMO program: DFT (density functional theory) and RI-MP2 (resolution-of-identity MP2) [47]; the program will also be posted on <https://github.com/OpenFMO/OpenFMO> through open-source license in the future.

Acknowledgements This study is partially supported by the project “Research and Development on Unified Environment of Accelerated Computing and Interconnection for Post-Petascale Era” of Basic Research Programs: CREST “Development of System Software Technologies for post-Peta Scale High Performance Computing,” JST. FMO benchmarks have been carried out under the “Inter-

disciplinary Computational Science Program” in CCS, University of Tsukuba. H.U. acknowledges T. Sawada, Ph.D. (AIST, Fujifilm Corporation) for structure modeling of HA3. H.K.-H. acknowledges the support by JST, PRESTO Grant Number JPMJPR17G4, Japan.

References

1. Kitaura K, Ikeo E, Asada T, Nakano T, Uebayasi M (1999) *Chem Phys Lett* 313:701
2. Nakano T, Kaminuma T, Sato T, Fukuzawa K, Akiyama Y, Uebayasi M, Kitaura K (2002) *Chem Phys Lett* 351:475
3. Fedorov DG, Kitaura K (2004) *J Chem Phys* 120:6832
4. Nakano T, Kaminuma T, Sato T, Akiyama Y, Uebayasi M, Kitaura K (2000) *Chem Phys Lett* 318:614
5. Ikegami T, Ishida T, Fedorov DG, Kitaura K, Inadomi Y, Umeda H, Yokokawa M, Sekiguchi S (2005) *Proceedings of supercomputing 2005*. IEEE Computer Society, Seattle
6. Mochizuki Y, Yamashita K, Murase T, Nakano T, Fukuzawa K, Takematsu K, Watanabe H, Tanaka S (2008) *Chem Phys Lett* 457:396
7. Mochizuki Y, Yamashita K, Fukuzawa K, Takematsu K, Murase T, Watanabe H, Taguchi N, Okiyama Y, Tsuboi M, Nakano T, Tanaka S (2010) *Chem Phys Lett* 493:346
8. Fletcher GD, Fedorov DG, Pruitt SR, Windus TL, Gordon MS (2012) *J Chem Theory Comput* 8:75
9. Alexeev Y, Mahajan A, Leyffer S, Fletcher G, Fedorov DG (2012) *Proceedings of supercomputing 2012*. IEEE Computer Society, Salt Lake City
10. Umeda H (2014) *CICSJ Bull* 32:2 (in Japanese)
11. <https://openfmo.org>
12. Takami T, Maki J, Ooba J, Inadomi Y, Honda H, Kobayashi T, Nogita R, Aoyagi M (2007) [arXiv: cs/0701075](https://arxiv.org/abs/cs/0701075)
13. Maki J, Inadomi Y, Takami T, Suzukita R, Honda H, Ooba J, Kobayashi T, Nogita R, Inoue K, Aoyagi M (2007) *Proceedings of HPCAsia* 07:137
14. Inadomi Y, Maki J, Honda H, Takami T, Kobayashi T, Aoyagi M, Minami I (2013) *J Comput Chem Jpn* 12:145 (in Japanese)
15. Inadomi Y, Inoue K, Maki J, Honda H, Aoyagi M (2014) *CICSJ Bull* 32:6 (in Japanese)
16. <https://www.mpi-forum.org>
17. <https://www.openmp.org>
18. Homepage of RIKEN Center for Computational Science (R-CCS). <https://www.r-ccs.riken.jp/en/>
19. Ufimtsev IS, Martinez TJ (2008) *J Chem Theory Comput* 4:222
20. Yasuda K (2008) *J Comput Chem* 29:334
21. Asadchev A, Allada V, Felder J, Bode MS, Gordon MS, Windus TL (2010) *J Chem Theory Comput* 6:696
22. Wilkinson KA, Sherwood P, Guest MF, Maidoo KJ (2011) *J Comput Chem* 32:2313
23. Asadchev A, Gordon MS (2012) *J Chem Theory Comput* 8:4166
24. Losilla SA, Watson MAM, Aspuru-Guzik A, Sundholm D (2015) *J Chem Theory Comput* 11:2053
25. Umeda H, Hanawa T, Shoji M, Boku T, Shigeta Y (2015) *J Comput Chem Jpn* 14:69 (in Japanese)
26. Umeda H, Hanawa T, Shoji M, Boku T, Shigeta Y (2015) *IPJSJ SIG Technical Report 2015-HPC-151:1* (in Japanese)
27. Umeda H, Hanawa T, Shoji M, Boku T, Shigeta Y (2015) *The international conference for high performance computing, networking, storage and analysis: SC15*
28. Umeda H, Hanawa T, Shoji M, Boku T, Inadomi Y (2013) *IPJSJ Trans Adv Comput Syst* 6:26 (in Japanese)

29. <https://sites.google.com/site/spfalanx/>
30. Takefusa A, Ikegami T, Nakada H, Takano R, Tozawa T, Tanaka Y (2014) The international conference for high performance computing, networking, storage and analysis: SC14
31. Schmidt MW, Baldrige KK, Boatz JA, Elbert ST, Gordon MS, Jensen JH, Koseki S, Matsunaga N, Nguyen KA, Su S et al (1993) *J Comput Chem* 14:1347
32. Homepage of GAMESS by the Gordon Research Group. <https://www.msg.chem.iastate.edu/games/>
33. <http://staff.aist.go.jp/d.g.fedorov/fmo/fmoutil.html>
34. <http://sourceforge.net/projects/fusuite/>
35. Suenaga M (2008) *J Comput Chem Jpn* 7:33 (in Japanese)
36. <http://zzfelis.sakura.ne.jp>
37. Fedorov DG, Olson RM, Kitaura K, Gordon MS, Koseki S (2004) *J Comput Chem* 25:872
38. Tanaka S, Mochizuki Y, Komeiji Y, Okiyama Y, Fukuzawa K (2014) *Phys Chem Chem Phys* 16:10310
39. Murai K, Minami I, Yokogawa M, Umeda H, Sato M, Tuji M, Inadomi Y, Aoyanagi M, Nakajima M (2013) IPSJ SIG Technical Report 2013-HPC-138:1 (in Japanese)
40. Tuji M, Sato M (2014) IPSJ SIG Technical Report 2014-HPC-146:1 (in Japanese)
41. <https://www.ccs.tsukuba.ac.jp/eng/projects/ha-pacs/base-cluster/>
42. Umeda H, Inadomi Y, Watanabe T, Yagi T, Ishimoto T, Ikegami T, Tadano H, Sakurai T, Nagashima U (2010) *J Comput Chem* 31:2381
43. Inadomi Y, Nakano T, Kitaura K, Nagashima U (2002) *Chem Phys Lett* 364:139
44. Watanabe T, Inadomi Y, Umeda H, Fukuzawa K, Tanaka S, Nakano T, Nagashima U (2009) *J Comput Theor Nanosci* 6:1328
45. Almlöf J, Faegri K Jr, Korsell KJ (1982) *J Comput Chem* 3:385
46. Sawada T, Fedorov DG, Kitaura K (2010) *J Phys Chem B* 114:15700
47. Katouda M, Naruse A, Hirano Y, Nakajima T (2016) *J Comput Chem* 37:2623

Pharmaceutical Activities

How to Perform FMO Calculation in Drug Discovery



Kaori Fukuzawa, Chiduru Watanabe, Yoshio Okiyama, and Tatsuya Nakano

Abstract In order to apply the fragment molecular orbital (FMO) method to practical drug discovery research, what procedure should be used? This chapter summarizes the preliminary knowledge necessary for applying the FMO method to the field of drug discovery. First, as a pretreatment of calculation, preparation of structure, fragmentation, and selection of the theoretical method are explained. Then, as to how to evaluate the binding properties of ligand from the obtained results of the FMO calculation, the evaluation method using binding free energy, interaction energy, and its energy components will be explained. Further, various physical quantities obtained from the FMO calculation such as charge distribution, electrostatic potential, and electron density distribution are introduced. Then, how to interpret these values will be explained.

Keywords Molecular modeling · Fragmentation method · Protein–ligand binding · Interaction energy analysis · Electron density-related analysis · ABINIT-MP · BioStation viewer

K. Fukuzawa (✉)

School of Pharmacy and Pharmaceutical Sciences, Hoshi University, 2-4-41 Ebara, Shinagawa, Tokyo 142-8501, Japan

e-mail: k-fukuzawa@hoshi.ac.jp

Department of Biomolecular Engineering, Graduate School of Engineering, Tohoku University, 6-6-11 Aoba, Aramaki, Aoba-ku, Sendai 980-8579, Japan

C. Watanabe

RIKEN Center for Biosystems Dynamics Research, 1-7-22 Suehiro-cho, Tsurumi-ku, Yokohama, Kanagawa 230-0045, Japan

JST, PRESTO, 4-1-8, Honcho, Kawaguchi, Saitama 332-0012, Japan

Y. Okiyama · T. Nakano

Division of Medicinal Safety Science, National Institute of Health Sciences, 3-25-26 Tonomachi, Kawasaki-ku, Kawasaki 210-9501, Kanagawa, Japan

1 Introduction

In *in silico* drug discovery, evaluating their binding properties from the quantum mechanics (QM) based on the electronic state of target protein and ligands is the ultimate precision approach [1]. By using the QM calculation, it becomes possible to treat the problems that cannot be fully explained by classical molecular mechanics (MM), for example, electronic interaction such as halogen bond, CH/ π bond, and hyperconjugation; and effects relating to electronic state such as charge transfer, chemical reaction, and electron excitation. Furthermore, the QM calculation enables quantitative evaluation of important problems in drug discovery such as binding affinity, activity cliff, specificity, selectivity, and substituent effect. The fragment molecular orbital (FMO) method [2–4] is a method that can conduct the QM calculation of protein at the fastest speed in the world with high accuracy. It also gives useful information on the quantitative evaluation of inter- and intra-molecular interaction. By using the QM calculation, it is expected to lead to precise drug design that focuses on the behavior of electrons (which is the essence of chemistry).

In this chapter, the knowledge necessary to use the FMO method for drug discovery is summarized. In Sect. 2, we first explain the simple methodology of the FMO method and the meaning of calculation parameters. In Sect. 3, as a preparation for the FMO calculation, points to be noted in creating a structure, how to divide molecules into fragments, and selection of theoretical method are explained. In Sect. 4, the evaluation of ligand-binding properties by the FMO method is explained. Finally, various properties are explained in Sect. 5.

2 Brief Description of the FMO Method for Use in Protein–Ligand System

In the FMO method, a protein is divided into fragments first, and then the electronic states of the fragments and their combinations are solved in the environmental electrostatic potential (ESP). The FMO method has the advantage that it can efficiently calculate electronic state in whole protein and extract information on mutual interaction among partial structures by introducing fragmentation. In order to further speed up the FMO calculation, there are two important approximation methods. One is the ESP approximation [5] that is an approximation of environmental ESP. The other is the dimer-es approximation [5], in which the interaction between distant monomers is approximated by the electrostatic interaction.

2.1 FMO Energy

The FMO method is a QM calculation method that has been developed to calculate electronic states of a macromolecule such as protein [2–4]. In the conventional QM calculation method, since calculation resources proportional to square to cube of the system size are required, the calculation of whole protein has been considered to be impossible. In the FMO method, a protein is divided into fragments first, and then the electronic states of the fragments and their combinations are solved in the environmental ESP. By these procedures, the system size that determines the calculation cost can be reduced to the size of the fragments. By integrating the obtained electronic state of partial structures, the total electronic state in whole system (energy and electron density) is reconstructed. In the typically used FMO method, the total energy is represented by the energies of fragment monomer (E_I) and fragment dimer (E_{IJ}), as shown below,

$$E_{\text{total}}^{\text{FMO2}} = \sum_I E_I + \sum_{I>J} (E_{IJ} - E_I - E_J). \quad (1)$$

The method is called the FMO2 method, because fragments up to dimer are used in the calculation. When Eq. 1 is transformed into a form expressing the interaction energy, the following equation is obtained,

$$E_{\text{total}}^{\text{FMO2}} = \sum_I E'_I + \sum_{I>J} \Delta \tilde{E}_{IJ}. \quad (2)$$

The first term on the right side is the monomer energy excluding the contribution of the environmental ESP, and the second term represents the inter-fragment interaction energy (IFIE) or pair interaction energy (PIE). This equation shows that, in the FMO calculation, the energy of the whole system can be obtained, and at the same time, the interaction energies between all fragment pairs can be obtained. This means that the FMO method has the characteristic and the advantage that it can efficiently calculate electronic state in whole protein and extract information on mutual interaction among partial structures by introducing fragmentation.

When Eq. 2 is further generalized by including many-body effect, the following equation is obtained,

$$E_{\text{total}} = \sum_I E'_I + \sum_{I>J} \Delta \tilde{E}_{IJ} + \sum_{I>J>K} \Delta \tilde{E}_{IJK} + \sum_{I>J>K>L} \Delta \tilde{E}_{IJKL}. \quad (3)$$

This equation shows that the higher-order terms can be incorporated. The FMO method including up to third-order terms is called the FMO3 method [6, 7], and the one including up to fourth-order terms is called the FMO4 method [8, 9]. The FMO methods including third-order terms and above are generically called the many-body FMO method. When general protein–ligand intermolecular interaction is to be analyzed, the FMO2 is qualitatively sufficient. However, when ligands are divided

into small functional group units or in case that the so-called three-body effect is important, it is necessary to introduce the many-body terms to evaluate the total energy.

IFIE can be further decomposed into four energy components, that is, electrostatic (ES), exchange repulsion (EX), charge transfer (CT), and dispersion (DI) terms. This method, called the pair interaction energy decomposition analysis (PIEDA), is the modification of the energy decomposition analysis (EDA) by Kitaura and Morokuma to FMO [10], which is expressed in the following equation,

$$\Delta \tilde{E}_{IJ} = \Delta \tilde{E}_{IJ}^{\text{ES}} + \Delta \tilde{E}_{IJ}^{\text{EX}} + \Delta \tilde{E}_{IJ}^{\text{CT}} + \Delta \tilde{E}_{IJ}^{\text{DI}}. \quad (4)$$

Since the CT term in this equation includes higher-order terms, it should be expressed as CT + mix to be exact. The PIEDA is extremely useful in applying the FMO method to drug discovery, because it gives information on the characteristics of the interaction in addition to their magnitude (stable or unstable). For example, almost all interactions of ion pairs such as acidic and basic amino acid residue are electrostatic and the ES term is most important. In the hydrogen bonds, the CT term is added in some degree to the ES term of main components, and the DI term becomes the main components in the CH/ π interaction and the π - π interaction. Such interpretation is helpful for the understanding of ligand-binding properties of target protein, protein-protein interaction, and detailed molecular design.

Several computer programs for the FMO calculation are open to the public. In this chapter, operation in the ABINIT-MP [4] program is supposing, that is under development in our research group, but the basic concepts for FMO calculations are the same for all programs. Note that, in addition to the ABINIT-MP, the BioStation Viewer [11] which is a program dedicated to visualization analysis is also under development. Thus, the tasks from setup of input files to analysis of calculation results can be conducted using graphical user interface (GUI).

2.2 ESP Approximation and Dimer-es Approximation

In order to further speed up the FMO calculation, there are two important approximation methods. One is the *ESP approximation* [5], which is an approximation of environmental ESP. The other is the *dimer-es approximation* [5], in which the interaction between distant monomers is approximated by the electrostatic interaction.

As shown in Eq. 1, the total energy obtained by the FMO2 method is expressed as the summation of the energies of monomer and dimer, including the energy obtained by the environmental ESP. In this procedure, when there is a difference between the levels of ESP approximation for monomer and dimer, the FMO calculation cannot be performed correctly. In this case, Eq. 1 is transformed so that the total energy obtained by the FMO2 method is expressed as the summation of the energy of monomer without environmental ESP and the IFIE of dimer with environmental

ESP (Eq. 2). By doing so, the contradiction is not caused even when different levels of ESP approximation are applied to monomers and dimers.

Currently in the protocol of the standard FMO calculation by the ABINIT-MP program, the ESP approximation is conducted in the following method. First, the environmental ESP near the target fragments subject to the calculation is calculated by Mulliken AO population (AO population approximation). Then, the environmental ESP from fragments located further afar is calculated from Mulliken atomic charge (atomic charge approximation). For the exchange between Mulliken AO population and Mulliken atomic charge, the notion, *N-times more than the sum of van der Waals (vdW) radii between nearest neighbor atoms of dimer*, is used as a parameter. In general, the value of $N = 2.0$ is used. This means that the AO population approximation is used for fragments whose distance from the target fragment subject to the calculation is 0.0–2.0 vdW unit, and that the atomic charge approximation is used for those with the distance farther than 2.0 vdW unit. As the parameter setting for the ESP approximation in the ABINIT-MP calculation, $L_{\text{aoc}} = 0.0$ and $L_{\text{ptc}} = 2.0$ are used (Fig. 1).

Next, in the case of the interaction between distant monomers, it is assumed that only electrostatic interaction should be considered. Therefore, in the dimer-es approximation (Fig. 1), the energy of dimer composed of two distant monomers can be approximated by the summation of energy of monomers without energy by the environmental ESP and the summation of the electrostatic interaction energy ($\Delta \tilde{E}_{IJ}^{\text{ES}}$) between two monomers. The relationship is expressed in the following Eq. 5,

$$E'_{IJ} \approx E'_I + E'_J + \Delta \tilde{E}_{IJ}^{\text{ES}}. \quad (5)$$

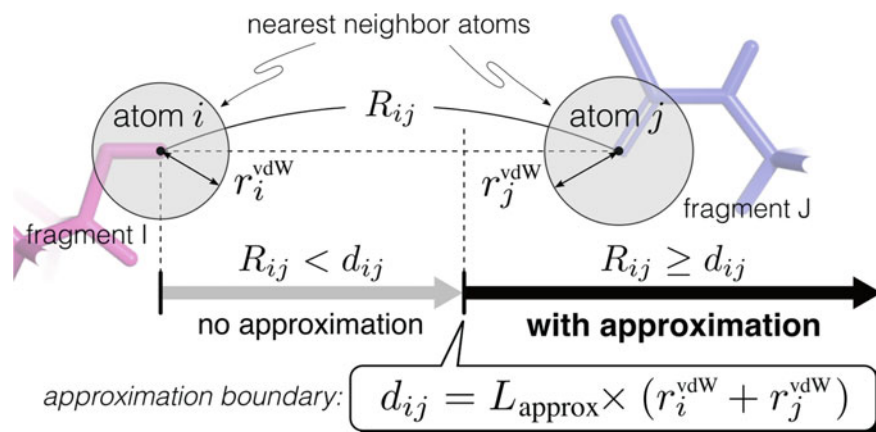


Fig. 1 Schematic diagram of environmental ESP and dimer-es approximation. The AO population approximation, atomic charge approximation, and dimer-ES approximation are represented when L_{approx} is L_{aoc} , L_{ptc} , and L_{dimer} , respectively

In the ABINIT-MP, in order to decide the minimum closest interatomic distance (\AA) between fragments of dimers where the dimer-es approximation is applied, a parameter, *Ldimer*, which indicates N-times or more than the sum of van der Waals radii, is used similar to the above-mentioned ESP approximation. In the standard setting, *Ldimer* = 2.0 is used [5]. In the calculation of target protein of drug discovery, the structures containing metal ions such as Ca^{2+} and Mg^{2+} are often observed. However, in the calculation of these structures, the convergence of dimers containing metal ions is sometimes not good. For this problem, the convergence is improved by setting *Ldimer* = 1.5 in many cases.

3 Preparation for FMO Calculation

In conducting the FMO calculation for biomolecules, ABINIT-MP/BioStation Viewer system has GUI function and related automated tool [12], and the calculation can be done without being aware of details. However, in order to calculate and analyze correctly, it is necessary to pretreat structures and select the method, appropriately. In the following, some of the important points will be explained.

3.1 Modeling of Structure

In the modeling of protein–ligand complex structure that is used in the FMO calculation, the pretreatment is performed using a modeling software such as Molecular Operating Environment (MOE, CCG Inc.) [13] based on the X-ray crystal structure obtained from Protein Data Bank (PDB; [wwpdb.org](http://www.pdb.org)) [14]. Generally, there is no hydrogen atom in the coordinate data obtained from structural biology experiments, and a part of the residue is sometimes missing. Therefore, it is required to compensate the missing parts, estimate the protonation states, add hydrogen, and optimize the geometries as needed. In order to perform the QM calculation, the chemical bond of molecules must be completed. Care must be taken as to all covalent bonds are occupied, and unpaired electrons do not exist. Further, it should be noted that if extremely long (or extremely short) covalent bonds are mixed, the convergence of the calculation becomes extremely worse, especially in the self-consistent charge (SCC) procedure. Conversely, if the SCC is not converged, the cause in most cases is ascribed to the inaccurate structure.

Here, it is an important point for the FMO calculation whether structure determination data of target protein–ligand complex has been experimentally obtained or not. Since the QM calculation is precise, the small difference in the atomic coordinate will affect the results. In particular, the interaction energy is sensitive to the distance of hydrogen bond. For example, even a structural change at 0.1 \AA will affect the interaction energy. For this reason, for structure used in the FMO calculation, it is recommended not to use prediction structure such as homology modeling, but

to use structure that is experimentally determined. If necessary, geometry optimization should be performed at the MM level or the QM level. For the optimization of hydrogen atoms and missing atoms at the MM level, it has been confirmed that the results are not so much dependent on the force field parameters used in the modeling [15]. When there is no experimental structural data of complex, the prediction structure is created by the sampling from docking or the succeeding of molecular dynamics (MD) calculations, as appropriate, although the quality of the structure is inferior. When MD sampling structures are used in the FMO calculation, it is necessary to optimize at least only hydrogen atom geometries.

As interaction analysis by the FMO calculation becomes more accurate, the reliability of the structure to be used becomes more important. However, in general structural analysis data (e.g., X-ray crystal structure at the resolution of about 2 Å), there are many cases where the detailed structure around the ligands is not necessarily clear. In the FMO calculation, the modeling structure based on abovementioned classical MM is generally used. However, for the evaluation of hydrogen bonds, imbalance sometimes occurs between MM structure and FMO energy. As examples of such problems, it was reported that excessive charge transfer is observed due to the distortion of MM structure [16]. Also, it was reported that the good correlation with the calculated and experimental values was obtained for the first time by the geometry optimization at the QM level [17, 18]. In the example of estrogen receptor α (ER α) [17], good correlation of FMO result with the experimental relative binding affinity could be obtained by optimizing the hydrogen bond distance between Glu residue and ligand at the Hartree–Fock (HF) level, and then by appropriately expressing the ligand–receptor charge transfer. In the example of serine–threonine kinase Pim1, the drastic changes in activity values against small changes in the structure called activity cliff were able to be reproduced by the combination of FMO calculation with QM/MM geometry optimization of the hydrogen bond distance between the ligands and amino acid residue [18]. Therefore, in recent precise analysis, some structural determinations are conducted by QM/MM method and partial structural optimization [19] at FMO-HF and higher level. In order to decrease the calculation cost, FMO calculation with frozen domain (FMO/FD) method [20] developed by the GAMESS program is implemented also with the ABINIT-MP.

3.2 Fragmentation

In the FMO calculation, it is required to define what is *fragment*. As mentioned above, in the FMO method, the calculation cost can be dramatically reduced by the fragmentation of molecules, and the interaction energy between fragments can be analyzed. Since this fragmentation is the most important characteristic of the FMO method, the method for the fragmentation would influence both the precision of the calculation and the quality of the analysis. This means that the *quality* of the FMO calculation is determined by the method of fragmentation.

The ABINIT-MP is equipped with automatic fragmentation functions of protein and nucleic acid from the PDB structure. For protein, there are two fragmentation patterns. One is the main-chain fragmentation (default) where protein is divided into amino acid residue units (Fig. 2a). The other is main-chain/side-chain fragmentation in which protein is divided into main chain and side chain (Fig. 2b). Although it is possible to fragment into not only one amino acid residue unit but also any arbitrary number (n) of residue units, this method is rarely used, because there is little advantage in analysis and the cost of calculation increases when the fragment straddles multiple residues. Similarly, in the case of DNA/RNA, three fragmentation patterns are equipped (Fig. 3). The first is the fragmentation into nucleotide units (Fig. 3a), the second is that the nucleotide is divided into the backbone and the base (Fig. 3b), and the third is the fragmentation into phosphate group, sugar and base (Fig. 3c). The standard fragmentation method for proteins is one amino acid residue unit shown in

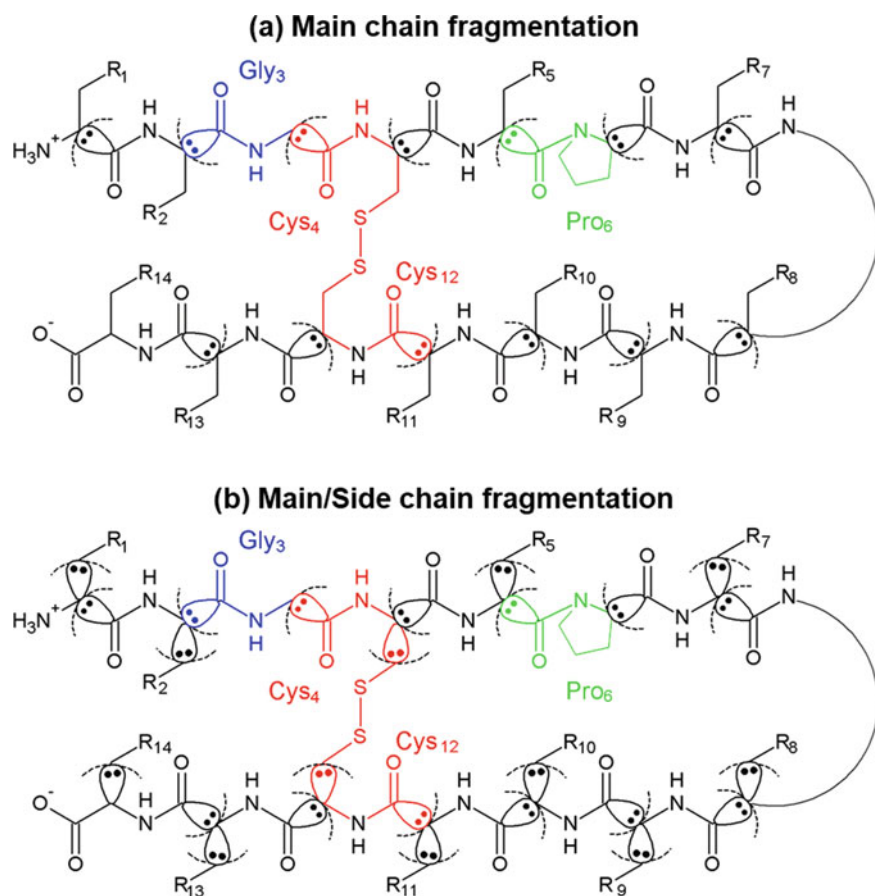


Fig. 2 Fragmentation of protein. Reprinted with permission from Ref. [9]. Copyright 2013 Elsevier

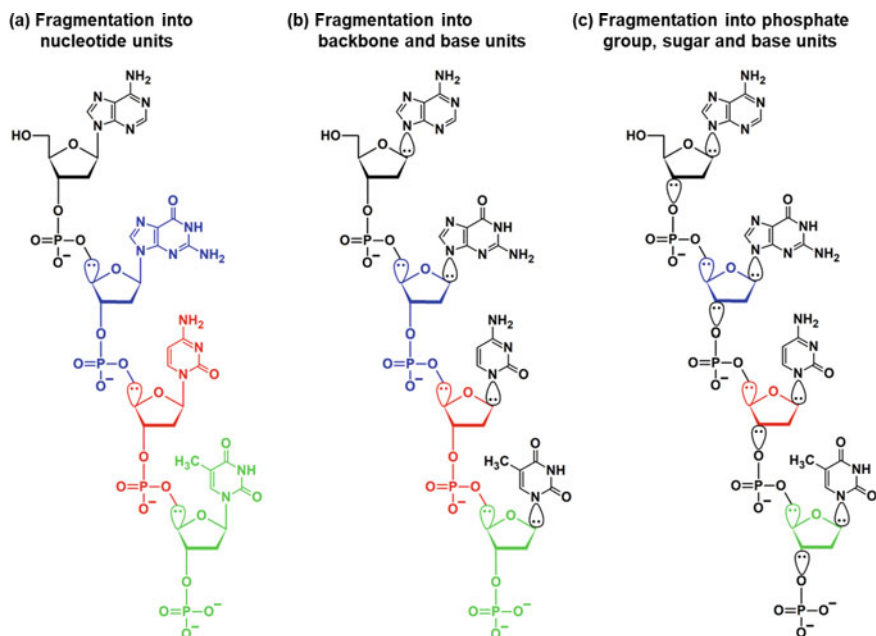


Fig. 3 Fragmentation of DNA and RNA

Fig. 2a, whereas that for nucleic acids is the pattern shown in Fig. 3b. These allow to perform a fragment-based interaction analysis such as IFIE/PIEDA focusing on the amino acid and base moieties. Owing to these automatic fragmentation function, users can easily conduct calculation because the complicated fragmentation setting is not necessary.

Note that there are directions in the fragmentation of bonds shown in Figs. 2 and 3. When a covalent bond between two atoms is divided, binding pair electrons are not divided into each electron, but divided so that the pair electrons belong to one of the atoms. The atom from which electrons are extracted is called bond detached atom (BDA), and the other atom that accepts electrons is called bond attached atom (BAA) (Fig. 4). In BDA, electrons are localized using a projection operator. In order

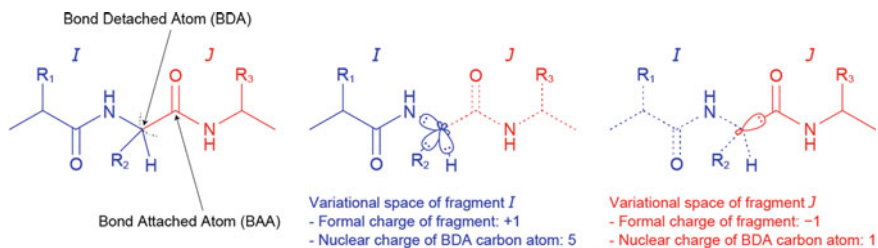


Fig. 4 Bond fragmentation treatment at BDA

to minimize the effect of the fragmentation, the sp^3 carbon is selected as the BDA, which is easy to be localized. Since electrons are transferred, the atomic charge in BDA and BAA formally becomes +1 and -1 , respectively (such charge is called formal charge). In order to avoid artificial electrostatic charging in fragment by the formal charge, nuclear charge in BDA carbon is divided into +5 and +1. By moving +1 nuclear charge at the same time as the electron movement, the total charge is kept unchanged.

The following points should be noted. For protein, not peptide bond but bond between α carbon and carbonyl carbon are broken in order that BDA should become sp^3 carbon. In other words, the bond breaking position is different from the definition of amino acid residue. In particular, since the sequential number assigned to amino acid of carbonyl group belonging to main chain is shifted, it is easy to make a mistake in the assignment of interacting position in interaction energy analysis. Therefore, care must be taken when interpreting the results in which carbonyl group is involved in an interaction [21].

With respect to fragmentation in other than protein and nucleic acid, detailed setting can be manually conducted using GUI of the BioStation Viewer [11] or FMOe [22] (see Sect. 4.3). The user can freely set the splitting of the ligand and special handling of the active center. Low molecular weight compounds, such as ligand, are generally treated as a single fragment. On the other hand, when the size of a ligand is large or when the interaction in partial structures is to be analyzed, those can be split into multiple fragments. In this case, the BDA in the divided bond should be also sp^3 carbon. Specific examples of ligand fragmentation are detailed in Sect. 4.3. Recently, a projection operator with sp^2 type was developed in order to conduct fragmentation at the sp^2 carbon [23]. Although problems still remain in fragmentation of protein at the site of peptide bonds in terms of accuracy, it is expected that the variation of analysis will be expanded by allowing the splitting of the ligand at the sp^2 carbon site.

For water molecules and ions, they may be treated as single fragments, or hydrated ions are sometimes treated as one fragment [24].

When compounds and amino acid residues are divided into fine fragments, the information on the interaction among the partial structures can be obtained. Therefore, such method seems to be convenient at first glance. However, the fact that the calculation accuracy becomes lower as they are divided further and further should not be forgotten. In order to compensate the calculation errors, the FMO method (Eq. 3) with many-body expansion is sometimes used [6, 8]. However, it should be noted that a contradiction occurs between the many-body expansion and the IFIE which is a two-body physical quantity.

3.3 Selection of Theoretical Method

In the ABINIT-MP, the MP2 method that incorporates electron correlation by second-order Møller–Plesset perturbation theory is generally used, in addition to the HF

method [4]. In particular, the MP2 method is the first choice, because electron correlation is necessary to describe dispersion force. Since CH/ π and π - π interactions that are important in biological system can be evaluated using dispersion interaction energy, the MP2 method has a wide range of applications. Since the ABINIT-MP is equipped with a high-speed MP2 calculation algorithm developed by Mochizuki et al. [25, 26], the MP2 calculation of protein with about 300 residue can be performed in several hours using in-house computer with dozens of core. As for the approximation level of the many-body FMO method, the FMO2 method is usually used, while the FMO3 is sometimes used when a ligand is divided into functional groups as described above, or when a so-called many-body effect such as interaction with water is important.

As a basis function, 6-31G* is widely used. A correlation-consistent basis developed by Dunning et al., cc-pVDZ, is also equipped. There are cases in which 6-31G basis is used for the energy calculation when the calculation time is to be reduced. However, for the geometry optimization, if at least 6-31G* is not used, incorrect values may appear in the bond distance. Also, diffuse functions are sometimes added to a part of atoms such as oxygen and metallic elements. Furthermore, a counterpoise correction [27, 28] is used in some case in order to reduce the basis set superposition error (BSSE). When calculation is to be conducted for heavy metal atoms, model core potential (MCP) method, which is one of the core potential approximations, can be sometimes applied to a part of atoms [29].

4 Evaluation of Protein–Ligand Binding

In structure-based drug discovery, the prediction of binding affinity of ligand to target protein is the most important subject. Furthermore, if binding mechanism of ligand can be understood, the obtained knowledge can be applied to precise drug design. In this subsection, the calculation of protein–ligand binding free energy and quantitative interaction analysis between ligand and surrounding amino acid residue based on the FMO method are described.

4.1 Ligand-Binding Affinity Prediction

The binding free energy is generally correlated with the experimental binding affinity at constant temperature, that is, the binding constants such as K_d and K_i and the activity values such as IC_{50} . Thus, the FMO method can be used as an in silico approach for the binding affinity prediction.

The binding free energy ΔG^{bind} that consists of the enthalpic change ΔH and the entropic change ΔS at the temperature T is commonly approximated by the summation of the binding energy ΔE^{bind} and the solvation free energy ΔG^{sol} in the in silico evaluation for protein–ligand binding systems:

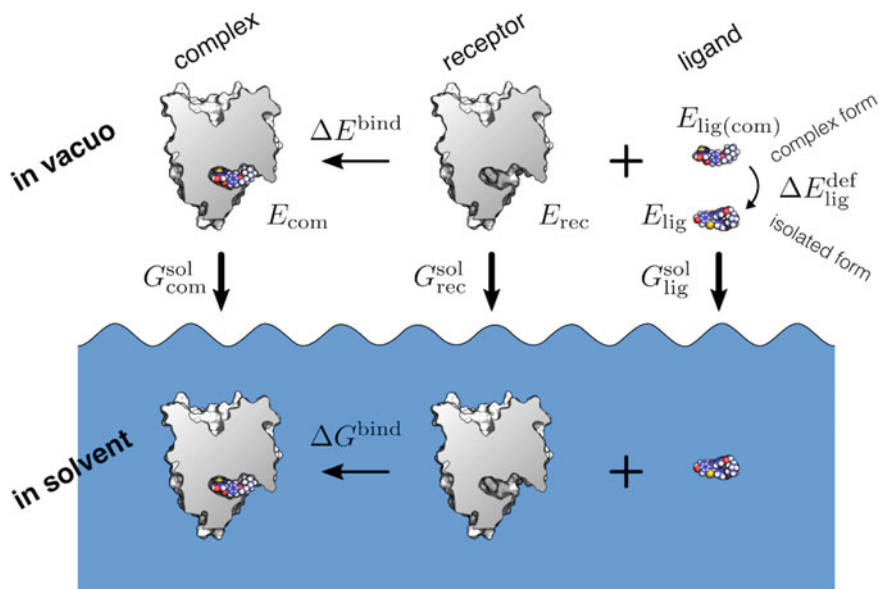


Fig. 5 Thermodynamic cycle for a ligand binding to a protein with solvation free energy (G^{sol}). Reprinted with permission from Ref. [30]. Copyright 2019 American Chemical Society

$$\Delta G^{\text{bind}} = \Delta H - T \Delta S \approx \Delta E^{\text{bind}} + \Delta G^{\text{sol}} \quad (6)$$

where the thermodynamic cycle is shown in Fig. 5. ΔE^{bind} is expressed as the energy difference between the bound and unbound states in vacuo, and structural relaxation for other than ligands is not considered currently in the most cases with FMO:

$$\Delta E^{\text{bind}} = E_{\text{com}} - E_{\text{rec}} - E_{\text{lig}} \approx \Delta E^{\text{int}} + \Delta E_{\text{lig}}^{\text{def}} \quad (7)$$

where ΔE^{int} represents the binding energy without structural relaxation

$$\Delta E^{\text{int}} = E_{\text{com}} - E_{\text{rec}} - E_{\text{lig}(\text{com})}, \quad (8)$$

and $\Delta E_{\text{lig}}^{\text{def}}$ does the deformation energy of a ligand

$$\Delta E_{\text{lig}}^{\text{def}} = E_{\text{lig}(\text{com})} - E_{\text{lig}} \quad (9)$$

defined as the energy difference between conformers bound to a protein and unbound to. Because this difference sometimes takes a considerably large value in quantum chemistry, it can be a non-negligible factor in the binding affinity prediction [30]. Moreover, when the crystal structure is employed for a protein–ligand system, the complexed form of its ligand fatefully contains artificial strain. Thus, removing such strain energy by QM optimization would also improve the prediction [18, 31].

It is also essential to consider physiological conditions of protein–ligand systems, that is, solvation/desolvation, when evaluating their binding affinities. Solvent effects including dielectric polarization or electrostatic screening can be incorporated into FMO with implicit solvent models such as a polarizable continuum model (PCM) [32] or a Poisson–Boltzmann (PB) method [33, 34] by directly coupled with the FMO electron density [35–38]. The desolvation penalty due to a protein–ligand complexation is estimated as follows (Fig. 5):

$$\Delta G^{\text{sol}} = G_{\text{com}}^{\text{sol}} - G_{\text{rec}}^{\text{sol}} - G_{\text{lig}}^{\text{sol}} \quad (10)$$

which includes non-polar contributions such as those estimated from the molecular surface area (SA). The prediction of protein–ligand binding affinities for ER α is a good example for showing the importance to include the solvent effects. The FMO-PBSA approach successfully predicts the binding affinities complexed with its ligands consisting of the mixture of neutral agonists and positively charged antagonists (Fig. 6): the separation resulting from the excessive electrostatic interaction in vacuo is well offset by including desolvation penalty in solution [30].

Because the super-molecular approach mentioned above is often expensive for processing complexes with many ligands, several low-cost estimations of binding (free) energy have also been proposed for the binding affinity prediction. For example, ΔE^{int} can also be evaluated using IFIE for FMO, that is, approximately represented as the summation of the IFIEs between a ligand and all amino-acid-residue fragments:

$$\Delta E^{\text{int}} \approx \sum_{J=1}^N \Delta \tilde{E}_{IJ}, \quad I = \text{ligand}. \quad (11)$$

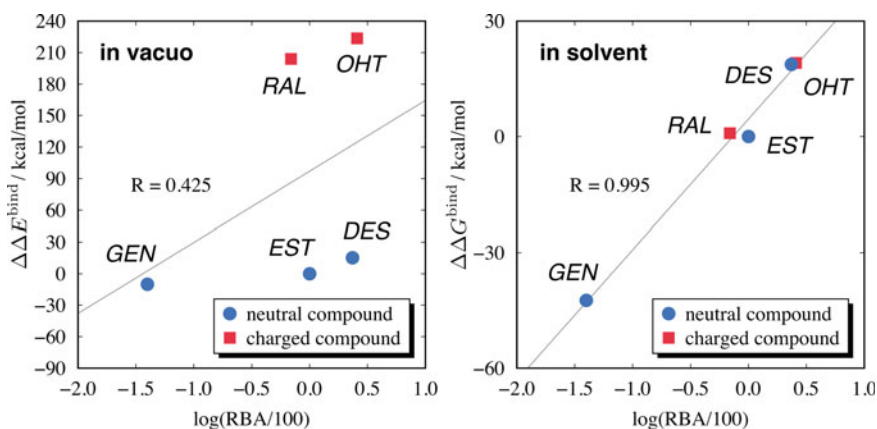


Fig. 6 Experimental binding affinities vs FMO-predicted binding energy in vacuo (left) and binding free energy in an implicit solvent (right) for five bioactive compounds complexed with ER α . Reprinted with permission from Ref. [30]. Copyright 2019 American Chemical Society

Note that, in such a treatment, ΔE^{int} consists only of the interaction energy in the bound state, not including the electron relaxation from the unbound state. For another example, ΔG^{sol} is conveniently evaluated using MM-PBSA and added to ΔE^{bind} obtained from FMO [18]. Note that solvent effects are only partially accounted for in such a treatment where the absence of solvent in the FMO processing never causes dielectric polarization of the electron density. There is versatility in the evaluation of binding energies and inclusion of solvent effects in the FMO framework [39].

4.2 Interaction Energy Analysis

The IFIE and its energy components (PIEDA) are the most used energy values in the analysis of the FMO calculation results. From the definition of these energies (Eqs. 2 and 4), the interaction obtained there is *fragment unit*. Depending on how to specify the fragmentation method described in Sect. 3.2, protein–ligand interaction analysis can be performed on an amino acid residue unit or a functional group unit. A ligand has various interactions between its functional group and surrounding amino acid residue through hydrogen bonds and other types of bonds. With the IFIE/PIEDA analysis, it is possible to understand the situation in detail and obtain extremely useful information on compound design.

The interaction energy analysis is explained using ER α as an example. Many X-ray crystal structures of ER α –ligand complex have been published, and the FMO calculation results for complex structure (PDB ID: 2YJA, 1.82 Å resolution) with 17 β -estradiol that is endogenous agonist are presented. For molecular modeling, hydrogen atoms were complemented using Amber10:EHT force field based on the PDB structure. Then, the structure where ligand and amino acid residue bound with the ligand through hydrogen bond were optimized at the FMO2-HF/6-31G* level was created. The energy calculation was conducted at the FMO2-MP2/6-31G* level.

Figure 7 shows the IFIE and PIEDA values between ligands and each amino acid residue. For ligand binding, the interaction with Glu353 showed remarkably strong stabilization. Subsequently, His524 and Arg394 exhibited stable interaction [9, 40]. These results showed that the ES was predominant, and the CT occurred. In other words, it is understood that the interaction involves the charge transfer through hydrogen bonds. Furthermore, weak interactions with Phe404 and some of Leu and Met were able to be confirmed. In the interaction with the hydrophobic amino acid residue, the DI was predominant. From the visualized diagram (Fig. 8) where interaction energy was mapped in the three-dimensional structure, it is understood that the amino acid residues bound with two hydroxyl groups of ligands, respectively, through hydrogen bond showed ES interaction, while that residues around liposoluble steroid-skeleton exhibited DI interaction. See also the orbital-level interaction analysis described in Sect. 4.3.

Looking at the breakdown of the binding energy (ΔE^{int}) that is represented by the IFIE in Eq. 11 (Table 1), the stabilization energy of the DI showed more than half of that of the ES and the CT (approximately -120 kcal/mol). In other words, it can

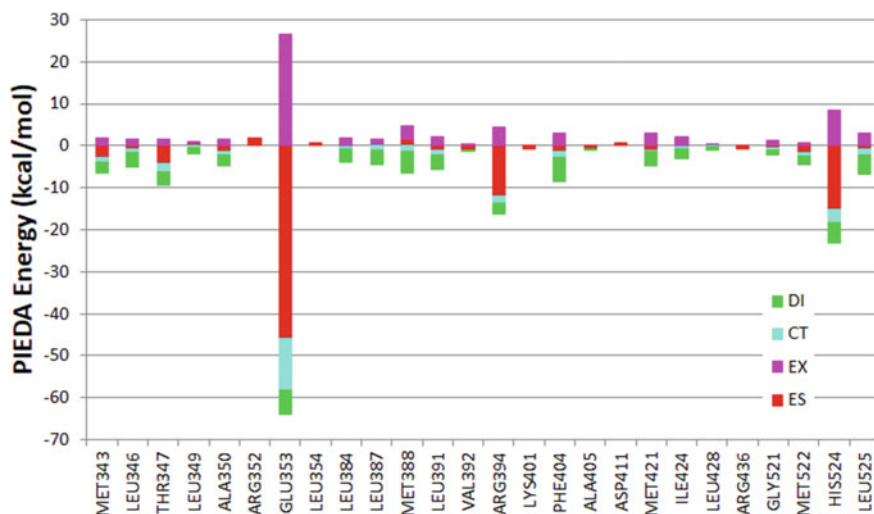


Fig. 7 Results for PIEDA analysis of ligands and each amino acid residue. The data show each component of electrostatic (ES), exchange repulsion (EX), charge transfer (CT), and dispersion (DI) interactions

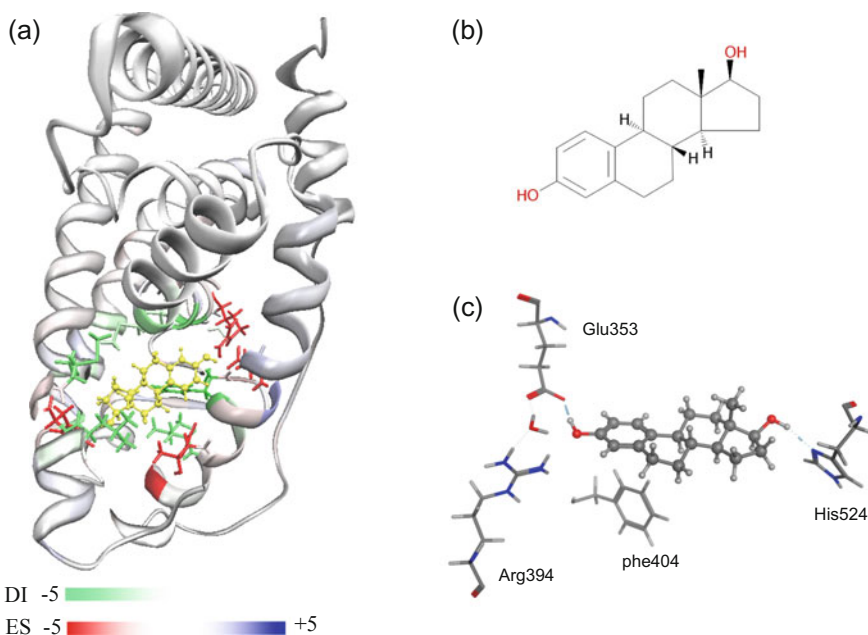


Fig. 8 **a** Visualized diagram of the PIEDA energy for ER–ligand complex. The ligand is shown in yellow, and each amino acid residue in protein is colored depending on the main interaction. Red–blue gradation and green gradation represent the strength of the electrostatic interaction and dispersion interaction, respectively (unit is kcal/mol), **b** Structure of 17β-estradiol, and **c** Interaction around ligand

Table 1 PIEDA component (kcal/mol) in ER α -ligand binding energy (ΔE^{int})

IFIE total	ES	EX	CT	DI
-115.2	-87.0	68.3	-31.8	-64.6

be seen that both hydrogen bond including charge transfer and dispersion interaction made a significant contribution. This is nothing more than theoretically observing the breakdown of binding energies that can be measured thermodynamically.

An example of a system involving nucleic acids is the interaction among the translation inhibitor rocaglamide A (RocA), polypurine RNA, and eIF4A protein [41]. As shown in Fig. 9, the multiple aromatic rings of RocA and RNA bases form a ladder structure, indicating that the inhibitor is part of the base–base stacking process. The FMO results show that most of the stable component of the IFIE between RocA and the RNA base is a DI term, indicating the importance of quantitative evaluation of the dispersion interaction, which is a major component of the stacking interaction in systems containing nucleic acids. Other examples of base–base interaction and base–protein interaction in double-stranded DNA and single-stranded DNA have also been reported [42–45].

Variations of IFIE/PIEDA-based analysis methods include IFIE-map [46] and VISCANA (Visualized Cluster Analysis of Protein–Ligand Interaction) [47]. IFIE-MAP is a method to comprehensively visualize IFIEs for all fragment pairs in the FMO calculation result for a given structure, allowing us to see interaction patterns that reflect the secondary structure of proteins and nucleic acids. Figure 10 shows an IFIE map for protein–DNA–ligand complex. The α -helix structure of proteins and the stacking structure of DNA can be observed as diagonal parallel interaction

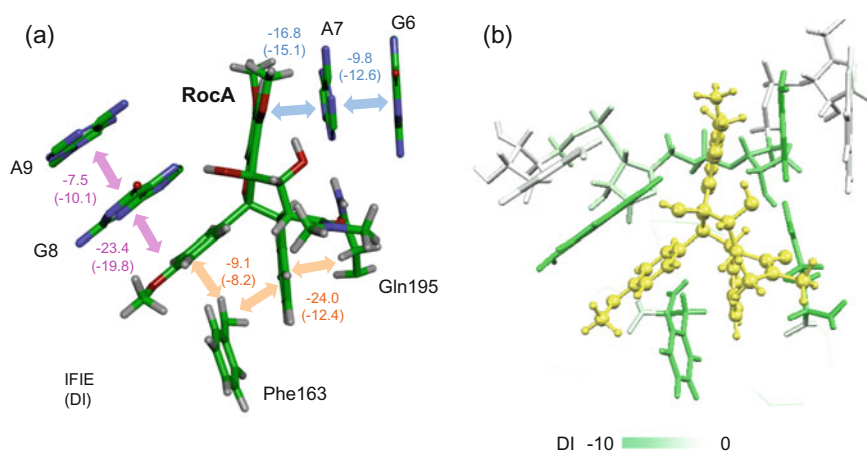


Fig. 9 Structure and molecular interaction between RocA and RNA–protein by FMO calculation and their representations along the RocA-binding pocket in the structure [41]. Energies are in kcal/mol

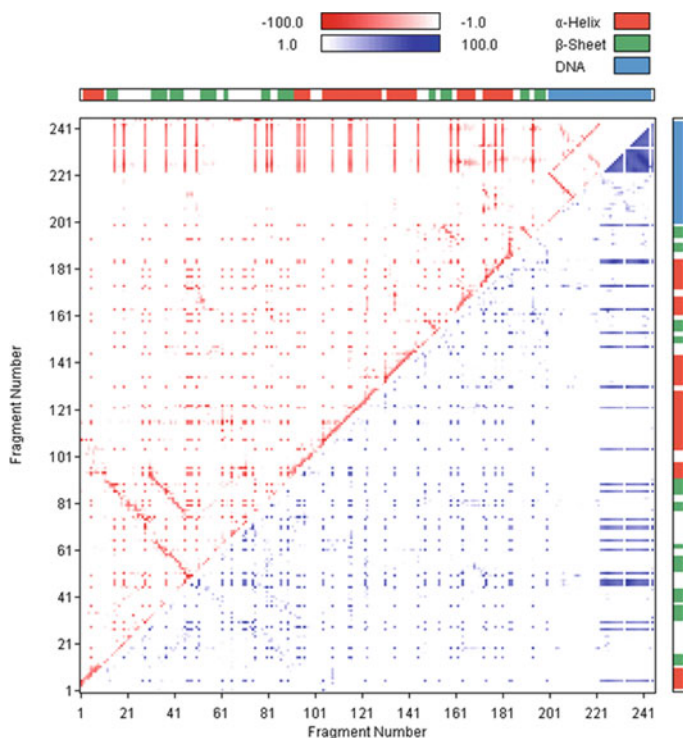


Fig. 10 IFIE map for the complex among cAMP receptor protein, DNA duplex, and cAMP [46]. Fragment number 1–200 represents a protein, 201–222 represents a DNA base, 223–244 represents a DNA backbone, and 245 represents cAMP. The upper triangle shows only the attractive interaction (red) and the lower triangle shows the repulsive interaction (blue), which is colored by the IFIE value (in kcal/mol)

patterns, and the β -sheet of proteins and Watson–Crick hydrogen bonding of DNA can be observed as the interaction patterns perpendicular to the diagonal lines. On the other hand, VISCANA is a method to classify ligands based on their IFIE interaction patterns using the results of FMO calculations of multiple protein–ligand complexes for a target protein. Figure 11 shows examples of candidate ligand compounds that bind to the estrogen receptor. One row corresponds to the FMO results for a single protein–ligand complex, and ligands with similar patterns of interaction with each amino acid residue shown on the horizontal axis are clustered among the ligands. See also Sect. 4.4 in Chap. 8 for details.

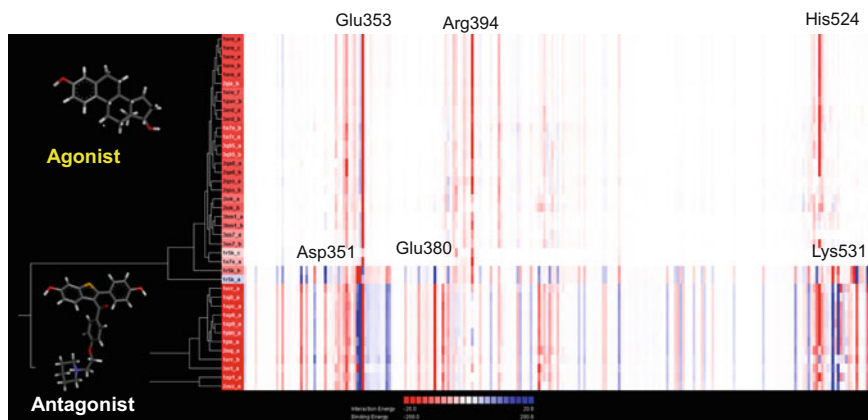


Fig. 11 VISCANA for the complex between estrogen receptor and ligands. The vertical and horizontal axes represent the ligands and amino acid residues, respectively. Each cell is colored according to the IFIE values of the corresponding ligand and amino acid residue, with red and blue representing stabilization and destabilization, respectively

4.3 High-Resolution Interaction Analysis for SBDD

Elucidating the interactions of compounds at the functional group level is an important factor in deciding on design strategies for structure-based drug design (SBDD); this is useful for building design strategies that, for example, identify the hydrogen bonds that are indispensable in ligand bonding as well as the partial structures of ligands that establish CH/ π interactions, and maintain these interactions while introducing substituents to generate new interactions. Furthermore, raw IFIE/PIEDA values tend to overestimate electrostatic interactions in FMO-based interaction energy analyses. For this reason, when analyzing interactions between charged ligands and receptors, the strong electrostatic interactions with basic and acidic amino acid residues dominate, and this can end up masking the weak interactions such as the hydrogen bond, CH/ π , and π - π interactions between ligand and amino acid residues. Consequently, there are reports using ligand fragmentation to identify the functional groups that are essential for these interactions, as well as to the interactions between the charged functional groups in ligands and neutral functional groups [16, 18]. Besides, if the compound that binds to the protein is a large drug such as Lopinavir (Fig. 12), it is difficult to treat the compound as a single fragment. Thus, the ligand fragmentation of large compounds must be performed to reduce computational costs [48]. Furthermore, for the purpose of SBDD, ligand fragmentation is also used when it is desired to perform interaction analysis with the precision of functional group units [9, 18, 49, 50].

When fragmenting a ligand, sp^3 carbon is recommended as the BDA to be fragmented (see Sect. 3.2), and depending on the compound, multiple potential BDA candidates may exist. When carrying out fragmentation, the ligand pocket should be

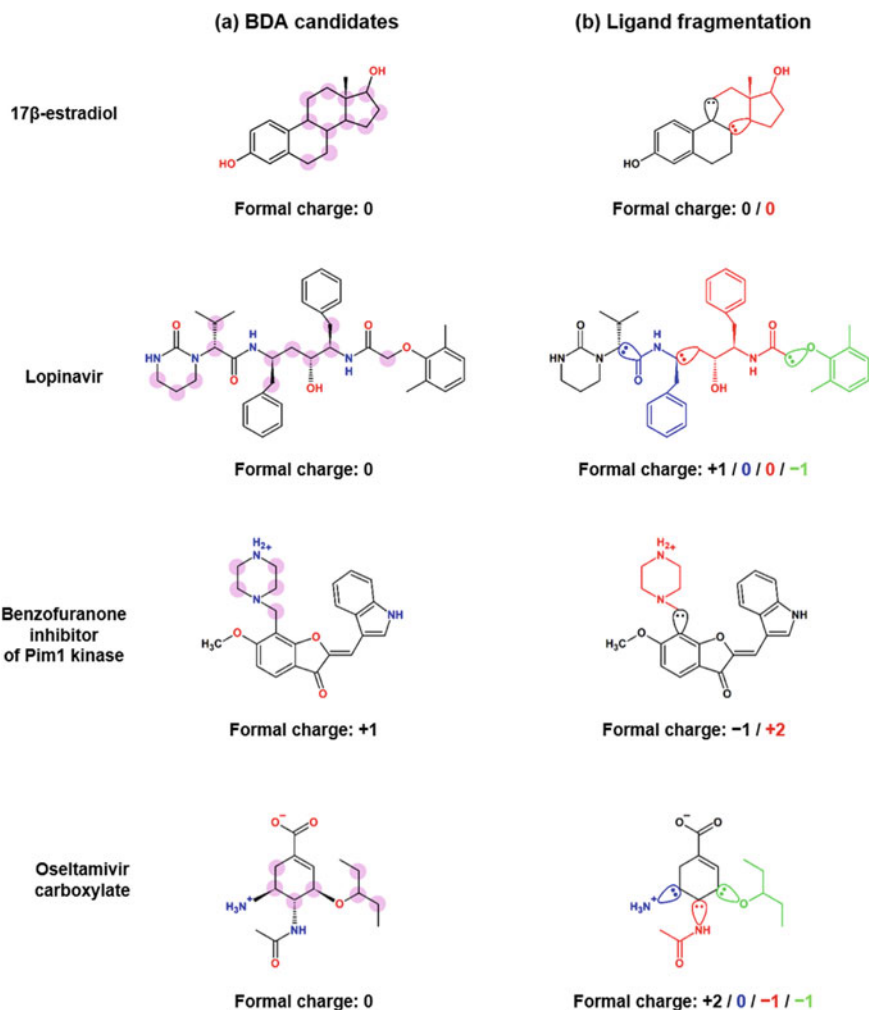


Fig. 12 Examples of ligand fragmentation for 17 β -estradiol, Lopinavir, a benzofuranone inhibitor of Pim1 kinase, and Oseltamivir carboxylate. BDA candidate sp^3 carbons are indicated in pink in (a). Actual instances of ligand fragmentation are shown in (b)

closely observed, the hydrogen bonds and CH/ π interactions whose contributions are desired should be marked beforehand, and a BDA candidate atom located as far away as possible from this interaction site should be selected as the fragmentation point. In addition, it is desirable to minimize the number of ligand fragmentation to reduce errors due to fragmentation. Examples of ligand fragmentation are shown in Fig. 12. Several fragmentation methods were investigated for 17 β -estradiol [9], Lopinavir [48], a benzofuranone inhibitor of Pim1 kinase [18], and Oseltamivir [16], which possess multiple BDA candidates Fig. 12a: based on analysis of protein

pocket three-dimensional structure, and interactions with post-ligand fragmentation proteins, fragmentation as indicated in Fig. 12b was an effective method for identifying the bonding sites. Examples of interaction analyses associated with Oseltamivir by using ligand fragmentation will be discussed later (Fig. 14).

Entry of the following information is required for the input file (ajf file) to run FMO calculations for a fragmented ligand by using the ABINIT-MP program: manual fragmentation option, the number of fragments, atomic information of fragments, the formal charge of fragments, the BDA and BAA information, and the net charge of the whole structure. It is challenging for a user to manually enter all of this data for a complex structure of protein and ligands consisting of several thousand atoms. For this reason, using the manual fragmentation function of the BioStation Viewer [11] pre/postprocessing GUI of ABINIT-MP enables easy preparation of the input file. Lately, it has also become easy to carry out ligand fragmentation with the emergence of the FMOe program [22], which is an SVL program for MOE [13].

The ligand fragmentation operating procedure for the BioStation Viewer and FMOe is as follows: form amino acid residue unit, ligand unit, and water molecule unit fragments beforehand according to conventional fragmentation rules; then conduct detailed ligand fragmentation (Fig. 13). The BioStation Viewer can save the data required for manual fragmentation used in the ABINIT-MP input file by establishing the atoms that form the new fragment, the formal charge of the new fragment, and the BDA and BAA of the new fragmentation point from the Fragment window (Fig. 13a). Similarly, FMOe can generate the input file by defining the BDA and BAA atoms in the Fragmentation window (Fig. 13b). Please refer to the manuals and tutorials for details regarding the operating procedures for ligand fragmentation using these GUIs [11, 22].

Next, we demonstrate the IFIE analysis with main/side chain fragmentation of protein and ligand fragmentation in SBDD context in the cases of neutral and charged ligands of Oseltamivir. The influenza treatments Zanamivir and Oseltamivir are well-known examples of rational design using SBDD to target the neuraminidase (NA), which is a virus membrane surface protein [51]. Such rational drug development

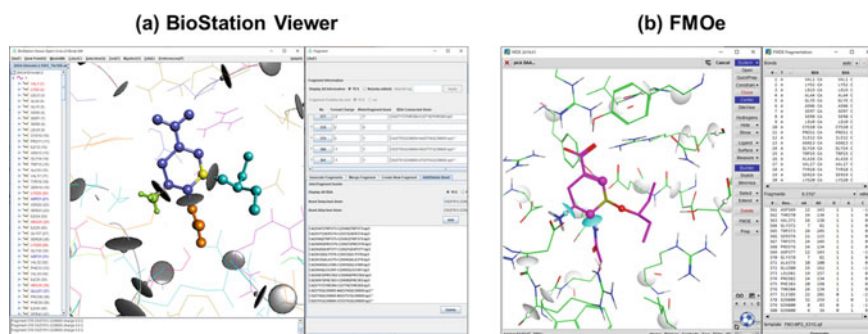


Fig. 13 GUI manipulation screens for ligand fragmentation. **a, b** The ligand fragmentation manipulation screens for the GUIs using BioStation Viewer and FMOe, respectively

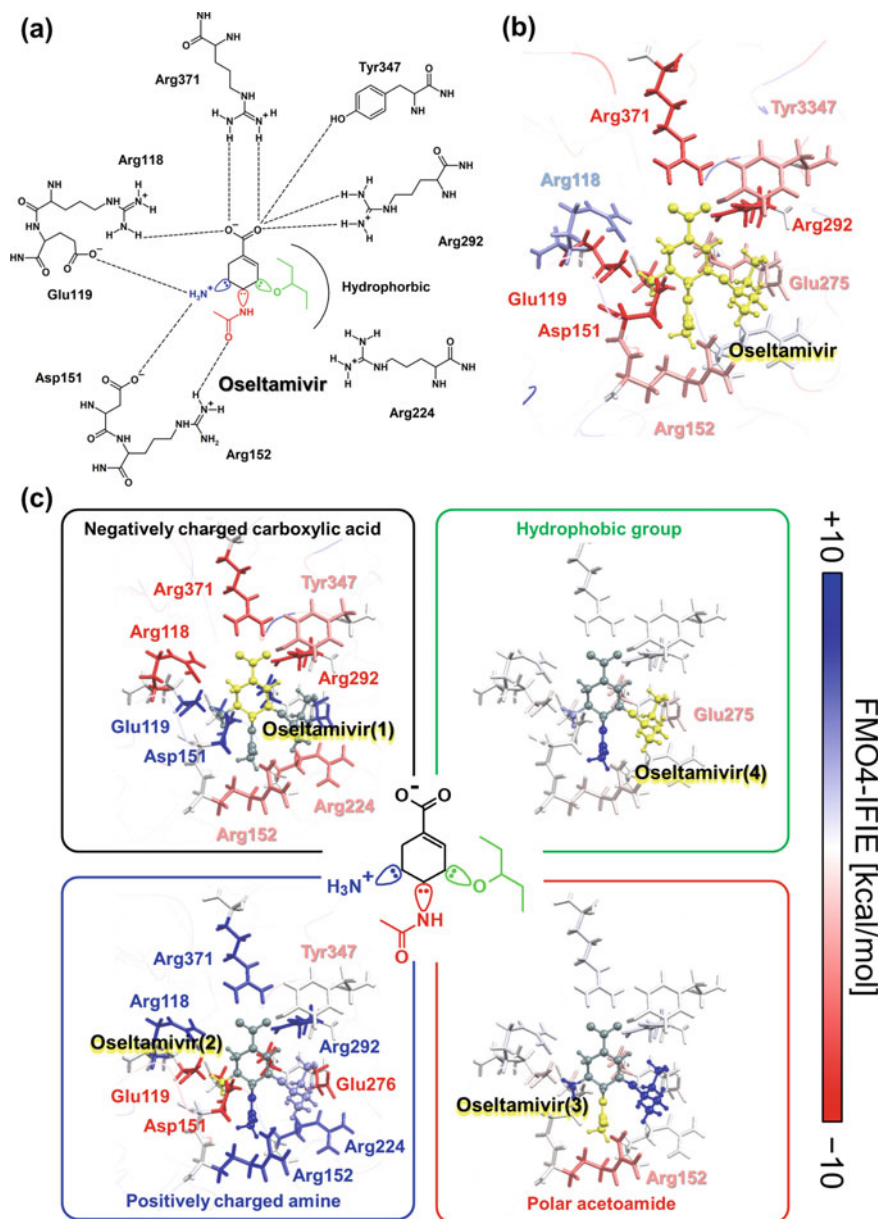


Fig. 14 NA–Osetamivir interaction analysis. **a** The NA–Osetamivir interaction network based on molecular geometry. **b** IFIE analysis with conventional fragmentation, and **c** FMO4-IFIE analysis with main/side chain fragmentation and ligand fragmentation (Osetamivir(1)–(4))

requires evaluation of the protein–ligand interactions at the functional group level [16]. As indicated in Fig. 14a, Oseltamivir's active structure is a zwitterion and each functional group is thought to bond via electrostatic interactions with the positively and negatively charged regions in the NA substrate bonding pocket. In order to elucidate the contributions of Oseltamivir's functional groups that establish several hydrogen bonding sites, namely highly polar functional group such as carboxylate, amine, and acetoamide groups, as well as those that establish hydrophobic bonding sites, such as the hydrophobic 3-methoxy-pentane group, the fragmentation should be a functional group unit. However, while IFIE analysis based on conventional fragmentation can verify interactions between Oseltamivir and neighboring amino acid residues of NA (PDB ID: 2HU4), as shown in Fig. 14b, it cannot identify contributions at the level of Oseltamivir's functional groups. Therefore, as shown in Fig. 14c, the functional group fragmentation was undertaken and interactions with neighboring amino acid residues at the FMO4-MP2/6-31G* level were analyzed. Here, acid residues were fragmented into main chains and side chains. Figure 14c visualizes the interactions between each functional group and neighboring amino acid residues. The fragment containing carboxylate, Oseltamivir(1), in Fig. 14c (indicated in yellow) exhibits strong attractive interactions with neighboring basic residues (red) of -100 kcal/mol, while it exhibits repulsive interactions (blue) of around $+45$ kcal/mol toward acidic residues. Conversely, the fragment incorporating a positively charged amine, Oseltamivir(2), shown in Fig. 14c exhibits -110 kcal/mol attractive interactions with acidic residues and $+45$ kcal/mol repulsive interactions with basic residues. These findings clearly indicate complementarity between the functional groups and the pocket. In addition, the polar acetoamide group, Oseltamivir(3), in Fig. 14c exhibits relatively weak (-29 kcal/mol) and stable interactions with neighboring residues via hydrogen bonds. Furthermore, the hydrophobic 3-methoxy-pentane group, Oseltamivir(4), in Fig. 14c exhibits weak (-7 kcal/mol) and stable interactions with neighboring residues. Thus, all interaction energies can be quantitatively assessed, and quantitative analysis of interactions based on functional group properties is possible. These are not limited to ligands with a charged functional group, but similar analysis can be performed with a ligand composed only of neutral functional groups. Such FMO-based interaction analysis at the functional group level can potentially provide useful knowledge for a structure–activity relationship (SAR) analysis and for designing molecules with stronger bonding capability. Note that the FMO4 levels are not necessarily required for IFIE analysis of functional groups. Calculations of FMO2 levels are usually sufficient to qualitatively evaluate the inter-molecular interactions without covalent bonds.

While the above IFIE/PIEDA is a fragment-by-fragment resolution interaction analysis, there are two types of interaction analysis at the molecular orbital level, called configuration analysis for fragment interaction (CAFI) [52] and fragment interaction based on local MP2 (FILM) [53]. CAFI extracts the molecular orbitals responsible for charge-transfer interactions between fragments, while FILM extracts the molecular orbitals responsible for dispersive interactions between fragments and reveals which orbitals of which functional groups are responsible for these interactions.

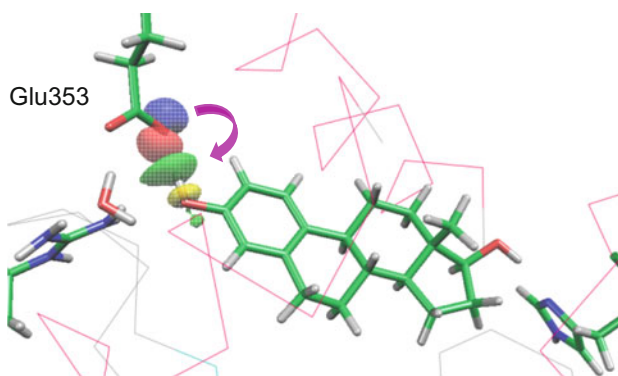
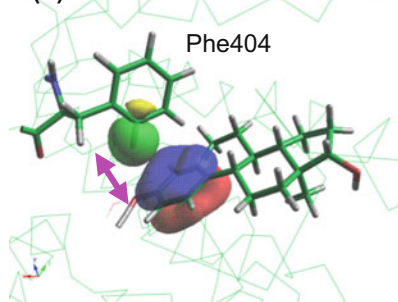
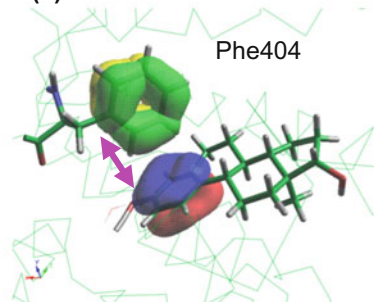
(a) Hydrogen bonding**(b) CH/π interaction****(c) π - π interaction**

Fig. 15 Orbital-wise interaction energy analysis between estrogen receptor and 17β-estradiol using **a** CFI and **b, c** FILM

Figure 15 shows an example of ligand binding to the estrogen receptor, as in Figs. 7 and 8. The electron transfer from the carboxy group (lone pair n_{O} orbital) of Glu353 to the phenol group (σ^*_{OH} orbital) of the ligand due to the hydrogen bond between them is visualized by CFI analysis [40] (Fig. 15a). The CH/π and π-π interactions based on dispersive interactions between the phenol group of the ligand and the phenyl group of Phe404 were also visualized by the FILM analysis (Fig. 15b, c). A picture of the interaction between these orbitals can be obtained together with the interaction energy per orbital.

5 Electron Density and Related Analysis

It should be noted that the FMO method is not only a useful tool for the analysis of interactions between fragment units, but also a full-QM method capable of calculating the electronic state of an entire protein system. Based on the electronic state of the molecule, the spatial distribution of the electron density and electrostatic potential (ESP) of the entire protein can be obtained, and the properties and molecular recognition of the molecule can be studied on the basis of physical quantities such as atomic charges and electrostatic potential maps on the surface of the molecule.

5.1 Population Analysis

The electronic state obtained from the MO calculation contains all the information on the electronic system including its total energy; however, the interpretation is not easy. Therefore, a technique that reduces the electron density into partial atomic charges is often used to easily grasp the electronic state. Partial atomic charges that divide the whole electron density onto discrete atoms are convenient to understand the electron localization or polarization in a molecule. The electron density of a whole system is expanded in the FMO2 framework as below:

$$\rho^{\text{FMO2}}(\mathbf{r}) = \sum_I \rho_I(\mathbf{r}) + \sum_{I>J} \Delta\rho_{IJ}(\mathbf{r}) \quad (12)$$

where $\rho_I(\mathbf{r})$ is the density of monomer and $\Delta\rho_{IJ}(\mathbf{r})$ is the difference in density between the monomer and the dimer [54]. If the position is discretized on atoms, the density on an atom is regarded as the atomic population. In this way, one can construct the atomic charge distribution of a whole system from those of the partial fragments.

Because such atomic charge distributions are not observable, their estimations are not unique and various partitioning methods have been proposed: Mulliken population analysis (MPA) [55], natural population analysis (NPA) [56, 57], and ESP fitting that includes Merz–Kollman (MK) [58, 59], restrained ESP (RESP) [60], and CHELPG [61] are available in ABINIT-MP. These analyses have different design concepts. Thus, it is important to fully understand the characteristics of these analyses for the usage.

MPA is the most popular charge-partitioning method in quantum chemistry. In MPA, each component lying on different atomic centers is forced to be equally divided into them. This assumption is often regarded as physically meaningless, and the gross orbital population sometimes has its outlier [62].

NPA is one of the most promising approaches for eliminating such illness and giving a stable picture that matches chemical intuition [63]. Therefore, it is also useful for quantitative discussion of CT [30, 37]. Tokuda et al. investigated the hydration

effect on three ligands of influenza virus neuraminidase, that is, *N*-acetylneuraminic acid, Oseltamivir, and Zanamivir, demonstrating the reasonable amount of CT to solvent waters with NPA [16].

The ESP fitting is an atomic charge determination by reproducing the molecular electrostatic potential (MEP) around a molecule and there are several variations with MEP sampling and fitting schemes or constraints. In the FMO framework, the charge distribution is obtained by summing up fragment charges fitted to fragment MEP in the FMO convention [64] or fitting to MEP generated from the whole molecular density [65, 66]. In fact, the ESP-fitted charge set derived from the FMO electron density has better ESP reproducibility on the molecular surface than the atomic charge distribution in a force field, by taking account of the structural dependency (Fig. 16). It could also be applicable to the force field parameters of MM or MD [66, 67], or docking scores because of its MEP reproducibility that gives accurate Coulomb interactions.

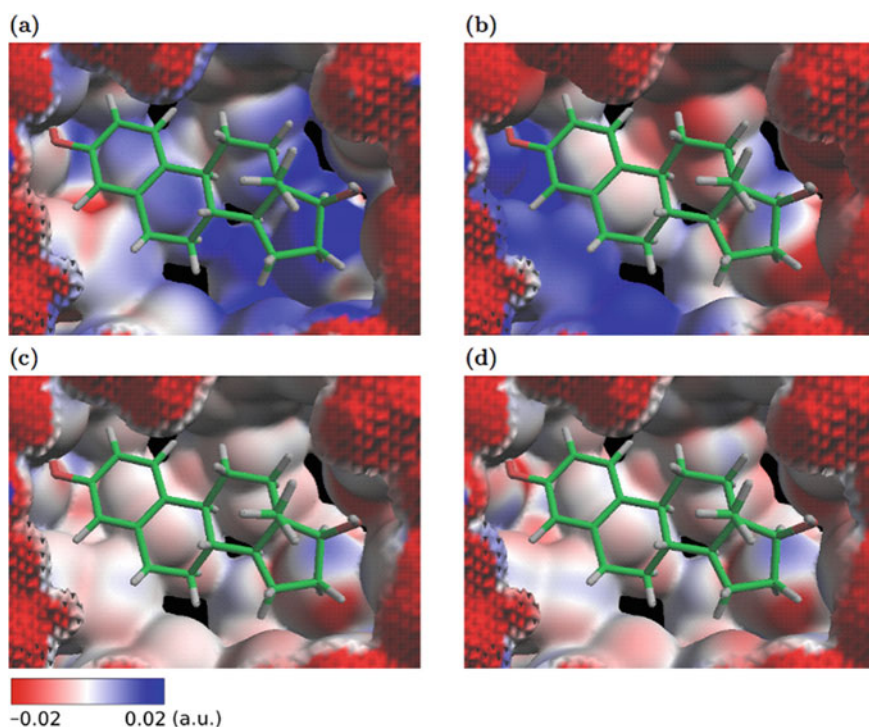


Fig. 16 Differential map between MEPs generated by the FMO density and atomic charge distribution on the electron isodensity surface (0.001 a.u.) of the ligand-binding pocket of ER α : **a** the Mulliken charges **b** the charges in the Amber ff94, **c** the MK charges, and **d** the RESP charges. A ligand, 17 β -estradiol, is also displayed. Reprinted with permission from Ref. [65]. Copyright 2007 Elsevier

5.2 Electrostatic Potential Analysis

The ESP distributions of molecules can also be analyzed by using FMO calculation data [18, 65]. Moreover, ESP maps [65, 68–70] can be constructed in which the electrostatic potential values are mapped on the electron isodensity surface of molecule, which allows for examination of the electrostatic complementarity of protein–ligand pairs.

Figure 17a, b shows the ESP distributions of two benzofuranone inhibitors of Pim1 kinase, (2*Z*)-2-(1*H*-indol-3-ylmethylidene)-6-methoxy-7-(piperazin-1-ylmethyl)-1-benzofuran-3-one (PDB ID: 5VUC) and (2*Z*)-6-methoxy-7-(piperazin-1-ylmethyl)-2-(1*H*-pyrrolo[2,3-*b*]pyridin-3-ylmethylidene)-1-benzofuran-3-one [18]. In the figure, it can be clearly seen that the ESP distribution is changed by introducing a nitrogen atom into the indole ring. This difference between the two ESP distributions was considered one of the causes of the change in the interaction energy observed in the IFIE/PIEDA analysis [18]. We have reported that this difference underlies the different IC₅₀ values of the two compounds [18].

Figure 18 shows the ESP maps on isoelectronic density surface of helix 12 with either agonist or antagonist position and of rest of the ligand-binding domain (LBD) of ER α [68]. It is well known that the position of helix 12 in the C-terminal of the LBD differs depending on whether the receptor is in complex with an agonist or antagonist (e.g., PDB ID: 1GWR and 3ERT). In addition, it has been shown that one of the main factors that determines the position of helix 12 is the electrostatic complementarity between the acidic amino acid residues in helix 12 and the basic amino acid residues in other parts of the LBD [68]. Indeed, the ESP maps show that the negatively charged surface of helix 12 has a complementary relationship with the positively charged areas around Lys529 and Lys362 in the agonist and antagonist bound complex, respectively (Fig. 18). It has also been reported that

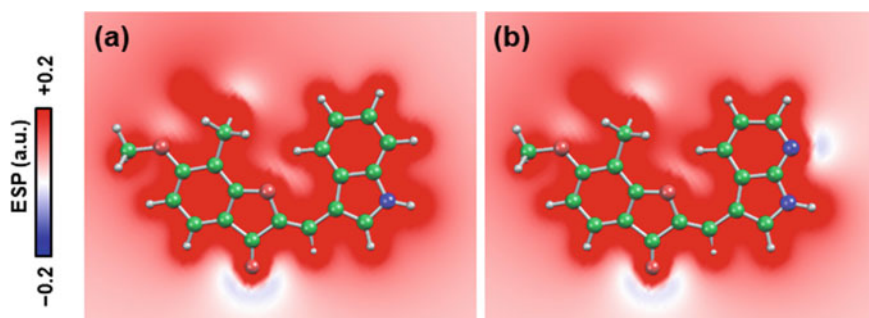


Fig. 17 Electrostatic potential (ESP) analysis. **a** and **b** ESP distributions of two benzofuranone inhibitors of Pim1 kinase: (2*Z*)-2-(1*H*-indol-3-ylmethylidene)-6-methoxy-7-(piperazin-1-ylmethyl)-1-benzofuran-3-one (panel a) and (2*Z*)-6-methoxy-7-(piperazin-1-ylmethyl)-2-(1*H*-pyrrolo[2,3-*b*]pyridin-3-ylmethylidene)-1-benzofuran-3-one (panel b). Reprinted with permission from Ref. [18]. Copyright 2017 American Chemical Society

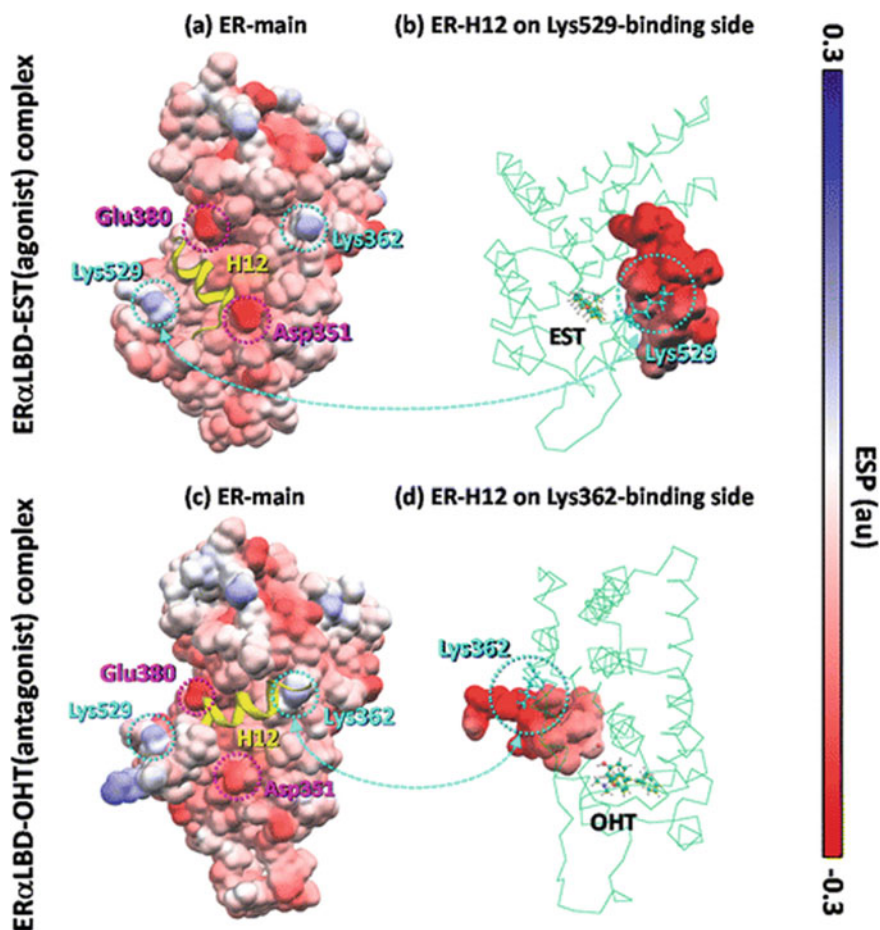


Fig. 18 Electrostatic potential (ESP) map analysis. ESP maps of helix 12 (H12) and the rest of the ligand-binding domain of estrogen receptor alpha (ER α LBD) when bound to an agonist (17 β -estradiol [EST]; (a) and (b)) or antagonist (4-hydroxytamoxifen [OHT]; (c) and (d)). Reprinted with permission from Ref. [68]. Copyright 2014 American Chemical Society

electrostatic complementarity is important for the molecular recognition of DNA by the DNA-binding domain of ER α [69].

The entry of the following information is required for the input file (ajf file) to run FMO calculations for ESPs or ESP maps by using the ABINIT-MP program: grid box space, number of grid points, type of physical quantity of grid data (esp or map file), electron isodensity surface to be mapped (in case of ESP map only), and output file format. Then, the ESP data should be output as either an ABINIT-MP grid file (esp and map files) or a Gaussian cube file (cube and cub files) and analyzed with BioStation Viewer [11] or GaussView [71], respectively.

5.3 Electron Density Analysis

FMO calculations allow us to analyze the electron density distribution of an entire protein system. This means that the electron density distribution obtained from X-ray crystallography are re-evaluated by quantum chemical calculations. To precisely examine interaction energies and chemical reactions in the context of SBDD, molecular structures with high accuracy are needed. However, the positions of hydrogen atoms; the protonation state of amino acid residues such as Asp, Glu, and His; the difference of tautomerization; and the conformation of ligands usually cannot be sufficiently identified by standard X-ray electron density analysis. Therefore, our group is currently developing a novel structure-refinement protocol that uses FMO calculation to improve the resolution of X-ray crystal structure analysis data. By using FMO-based structure optimization [19, 20, 72–76], the potential energy-based conformational analysis, interaction energy analysis, and comparisons of electron densities obtained by X-ray diffraction crystallography with those obtained by FMO calculation, we expect to be able to prioritize a number of modeled structures and obtain more reliable structures that contain hydrogen atom information. We call the framework for this structural refinement “FMO super-resolution refinement”. As the first step in achieving the super resolution, Fig. 19 shows the X-ray and FMO electron densities of crambin (PDB ID: 3NIR), which has the highest resolution of 0.48 Å data that can be obtained from PDB. Currently, the X-ray and FMO electron densities are visually comparable, but in the future, we hope to be able to provide a more precise structure analysis such as evaluation of the validity of structure by direct numerical comparison of electron densities between experimental and FMO data.

The entry of the following information is required for the input file (ajf file) to run FMO calculations for electron density by using the ABINIT-MP program: grid box space, number of grid points, type of physical quantity of grid data (den file), and output file format. Then, the electron density data should be output as either an

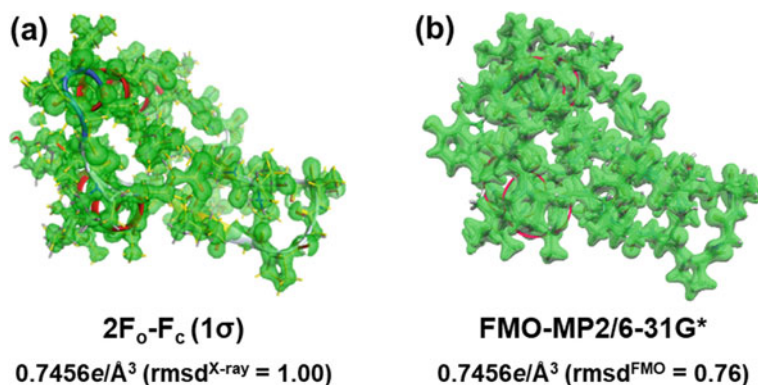


Fig. 19 Electron density analysis at $\rho = 0.7456 e/\text{\AA}^3$ of crambin (PDB ID: 3NIR). **a** X-ray experimental data. **b** FMO calculation data

ABINIT-MP grid file (den file) or a CNS file (cns file) and analyzed with BioStation Viewer [11] or Coot (Crystallographic Object-Oriented Toolkit) [77], respectively.

6 Conclusion Remarks

In this chapter, the basics of FMO method for drug discovery, computational procedures, and various FMO-based analysis methods were introduced with examples. The FMO method provides information on the electronic state of a whole protein system and its intra- and inter-molecular interactions. With the increasing importance of QM calculations in drug discovery, it is desirable to make the best use of QM information obtained from FMO. It is expected that FMO calculations will not only be used directly for the molecular interaction analysis but also as a fundamental technology for the development of FMO-based force field and artificial intelligence (AI), as well as contributing to life sciences such as structural refinement and chemical reaction analysis in structural biology.

Acknowledgments The authors would like to thank Prof. Yuji Mochizuki and Prof. Shigenori Tanaka for ongoing discussions on FMO. A part of this research was done in activities of the FMO drug design consortium (FMOOD). PIEDA analysis was carried out by using MIZUHO/BioStation Viewer. This research was partially supported by Platform Project for Supporting Drug Discovery and Life Science Research (Basis for Supporting Innovative Drug Discovery and Life Science Research (BINDS)) from AMED under Grant Number JP20am0101113. C.W. acknowledges the JST PRESTO Grant Number JPMJPR18GD, Japan.

References

1. Heifetz A (2020) Quantum mechanics in drug discovery. Springer, US, New York, NY
2. Fedorov DG, Kitaura K (2009) The fragment molecular orbital method, 1st edn. CRC Press, Boca Raton
3. Fedorov DG, Nagata T, Kitaura K (2012) Exploring chemistry with the fragment molecular orbital method. *Phys Chem Chem Phys* 14:7562. <https://doi.org/10.1039/c2cp23784a>
4. Tanaka S, Mochizuki Y, Komeiji Y et al (2014) Electron-correlated fragment-molecular-orbital calculations for biomolecular and nano systems. *Phys Chem Chem Phys* 16:10310–10344. <https://doi.org/10.1039/c4cp00316k>
5. Nakano T, Kaminuma T, Sato T et al (2002) Fragment molecular orbital method: use of approximate electrostatic potential. *Chem Phys Lett* 351:475–480. [https://doi.org/10.1016/S0009-2614\(01\)01416-6](https://doi.org/10.1016/S0009-2614(01)01416-6)
6. Fedorov DG, Kitaura K (2006) The three-body fragment molecular orbital method for accurate calculations of large systems. *Chem Phys Lett* 433:182–187. <https://doi.org/10.1016/j.cplett.2006.10.052>
7. Pruitt SR, Nakata H, Nagata T et al (2016) Importance of three-body interactions in molecular dynamics simulations of water demonstrated with the fragment molecular orbital method. *J Chem Theory Comput* 12:1423–1435. <https://doi.org/10.1021/acs.jctc.5b01208>

8. Nakano T, Mochizuki Y, Yamashita K et al (2012) Development of the four-body corrected fragment molecular orbital (FMO4) method. *Chem Phys Lett* 523:128–133. <https://doi.org/10.1016/j.cplett.2011.12.004>
9. Watanabe C, Fukuzawa K, Okiyama Y et al (2013) Three- and four-body corrected fragment molecular orbital calculations with a novel subdividing fragmentation method applicable to structure-based drug design. *J Mol Graph Model* 41:31–42. <https://doi.org/10.1016/j.jmgm.2013.01.006>
10. Fedorov DG, Kitaura K (2007) Pair interaction energy decomposition analysis. *J Comput Chem* 28:222–237. <https://doi.org/10.1002/jcc.20496>
11. BioStation Viewer. The program is available at: <https://fmodd.jp/biostationviewer-dl/>
12. Watanabe C, Watanabe H, Okiyama Y et al (2019) Development of an automated fragment molecular orbital (FMO) calculation protocol toward construction of quantum mechanical calculation database for large biomolecules. *Chem-Bio Inform J* 19:5–18. <https://doi.org/10.1273/cbij.19.5>
13. Molecular Operating Environment (MOE). Chemical Computing Group Inc., 1010 Sherbooke St. West, Suite #910, Montreal, QC, Canada, H3A 2R7
14. Berman HM, Westbrook J, Feng Z et al (2000) The protein data bank. *Nucleic Acids Res* 28:235–242. <https://doi.org/10.1093/nar/28.1.235>
15. Sheng Y, Watanabe H, Maruyama K et al (2018) Towards good correlation between fragment molecular orbital interaction energies and experimental IC50 for ligand binding: a case study of p38 MAP kinase. *Comput Struct Biotechnol J* 16:421–434. <https://doi.org/10.1016/j.csbj.2018.10.003>
16. Tokuda K, Watanabe C, Okiyama Y et al (2016) Hydration of ligands of influenza virus neuraminidase studied by the fragment molecular orbital method. *J Mol Graph Model* 69:144–153. <https://doi.org/10.1016/j.jmgm.2016.08.004>
17. Fukuzawa K, Kitaura K, Uebayasi M et al (2005) Ab initio quantum mechanical study of the binding energies of human estrogen receptor α with its ligands: an application of fragment molecular orbital method. *J Comput Chem* 26:1–10. <https://doi.org/10.1002/jcc.20130>
18. Watanabe C, Watanabe H, Fukuzawa K et al (2017) Theoretical analysis of activity cliffs among Benzofuranone-class Pim1 inhibitors using the fragment molecular orbital method with molecular mechanics Poisson–Boltzmann surface area (FMO+MM-PBSA) approach. *J Chem Inf Model* 57:2996–3010. <https://doi.org/10.1021/acs.jcim.7b00110>
19. Tsukamoto T, Mochizuki Y, Watanabe N et al (2012) Partial geometry optimization with FMO-MP2 gradient: application to TrpCage. *Chem Phys Lett* 535:157–162. <https://doi.org/10.1016/j.cplett.2012.03.046>
20. Fedorov DG, Alexeev Y, Kitaura K (2011) Geometry optimization of the active site of a large system with the fragment molecular orbital method. *J Phys Chem Lett* 2:282–288. <https://doi.org/10.1021/jz1016894>
21. Yoshioka A, Takematsu K, Kurisaki I et al (2011) Antigen–antibody interactions of influenza virus hemagglutinin revealed by the fragment molecular orbital calculation. *Theor Chem Acc* 130:1197–1202. <https://doi.org/10.1007/s00214-011-1048-z>
22. FMOe. The program is available at: <https://github.com/drugdesign/FMOe>
23. Akinaga Y, Kato K, Nakano T et al (2020) Fragmentation at sp² carbon atoms in fragment molecular orbital method. *J Comput Chem* 41:1416–1420. <https://doi.org/10.1002/jcc.26190>
24. Fujita T, Fukuzawa K, Mochizuki Y et al (2009) Accuracy of fragmentation in ab initio calculations of hydrated sodium cation. *Chem Phys Lett* 478:295–300. <https://doi.org/10.1016/j.cplett.2009.07.060>
25. Mochizuki Y, Koikegami S, Nakano T et al (2004) Large scale MP2 calculations with fragment molecular orbital scheme. *Chem Phys Lett* 396:473–479. <https://doi.org/10.1016/j.cplett.2004.08.082>
26. Mochizuki Y, Nakano T, Koikegami S et al (2004) A parallelized integral-direct second-order Møller–Plesset perturbation theory method with a fragment molecular orbital scheme. *Theor Chem Acc* 112:442–452. <https://doi.org/10.1007/s00214-004-0602-3>

27. Ishikawa T, Ishikura T, Kuwata K (2009) Theoretical study of the prion protein based on the fragment molecular orbital method. *J Comput Chem* 30:2594–2601. <https://doi.org/10.1002/jcc.21265>
28. Okiyama Y, Nakano T, Yamashita K et al (2010) Acceleration of fragment molecular orbital calculations with Cholesky decomposition approach. *Chem Phys Lett* 490:84–89. <https://doi.org/10.1016/j.cplett.2010.03.001>
29. Ishikawa T, Mochizuki Y, Nakano T et al (2006) Fragment molecular orbital calculations on large scale systems containing heavy metal atom. *Chem Phys Lett* 427:159–165. <https://doi.org/10.1016/j.cplett.2006.06.103>
30. Okiyama Y, Watanabe C, Fukuzawa K et al (2019) Fragment molecular orbital calculations with implicit solvent based on the Poisson–Boltzmann equation: II. Protein and its ligand-binding system studies. *J Phys Chem B* 123:957–973. <https://doi.org/10.1021/acs.jpcc.8b09326>
31. Okimoto N, Otsuka T, Hirano Y, Taiji M (2018) Use of the multilayer fragment molecular orbital method to predict the rank order of protein–ligand binding affinities: a case study using Tankyrase 2 inhibitors. *ACS Omega* 3:4475–4485. <https://doi.org/10.1021/acsomega.8b00175>
32. Tomasi J, Mennucci B, Cammi R (2005) Quantum mechanical continuum solvation models. *Chem Rev* 105:2999–3093. <https://doi.org/10.1021/cr9904009>
33. Davis ME, McCammon JA (1990) Electrostatics in biomolecular structure and dynamics. *Chem Rev* 90:509–521. <https://doi.org/10.1021/cr00101a005>
34. Sharp KA, Honig B (1990) Calculating total electrostatic energies with the nonlinear Poisson–Boltzmann equation. *J Phys Chem* 94:7684–7692. <https://doi.org/10.1021/j100382a068>
35. Fedorov DG, Kitaura K, Li H et al (2006) The polarizable continuum model (PCM) interfaced with the fragment molecular orbital method (FMO). *J Comput Chem* 27:976–985. <https://doi.org/10.1002/jcc.20406>
36. Watanabe H, Okiyama Y, Nakano T, Tanaka S (2010) Incorporation of solvation effects into the fragment molecular orbital calculations with the Poisson–Boltzmann equation. *Chem Phys Lett* 500:116–119. <https://doi.org/10.1016/j.cplett.2010.10.017>
37. Okiyama Y, Nakano T, Watanabe C et al (2018) Fragment molecular orbital calculations with implicit solvent based on the Poisson–Boltzmann equation: implementation and DNA study. *J Phys Chem B* 122:4457–4471. <https://doi.org/10.1021/acs.jpcc.8b01172>
38. Fedorov DG (2018) Analysis of solute–solvent interactions using the solvation model density combined with the fragment molecular orbital method. *Chem Phys Lett* 702:111–116. <https://doi.org/10.1016/j.cplett.2018.05.002>
39. Okiyama Y, Fukuzawa K, Komeiji Y, Tanaka S (2020) Taking water into account with the fragment molecular orbital method. In: Heifetz A (ed) *Quantum mechanics in drug discovery. Methods in molecular biology*, vol 2114. Humana, New York, NY, pp 105–122
40. Fukuzawa K, Mochizuki Y, Tanaka S et al (2006) Molecular Interactions between estrogen receptor and its ligand studied by the ab initio fragment molecular orbital method. *J Phys Chem B* 110:24276–24276. <https://doi.org/10.1021/jp065705n>
41. Iwasaki S, Iwasaki W, Takahashi M et al (2019) The translation inhibitor rocaglamide targets a bimolecular cavity between eIF4A and polypurine RNA. *Mol Cell* 73:738–748.e9. <https://doi.org/10.1016/j.molcel.2018.11.026>
42. Fukuzawa K, Kurisaki I, Watanabe C et al (2015) Explicit solvation modulates intra- and inter-molecular interactions within DNA: electronic aspects revealed by the ab initio fragment molecular orbital (FMO) method. *Comput Theor Chem* 1054:29–37. <https://doi.org/10.1016/j.comptc.2014.11.020>
43. Fukuzawa K, Komeiji Y, Mochizuki Y et al (2006) Intra- and intermolecular interactions between cyclic-AMP receptor protein and DNA: ab initio fragment molecular orbital study. *J Comput Chem* 27:948–960. <https://doi.org/10.1002/jcc.20399>
44. Fukuzawa K, Komeiji Y, Mochizuki Y et al (2007) Intra- and intermolecular interactions between cyclic-AMP receptor protein and DNA: ab initio fragment molecular orbital study. *J Comput Chem* 28:2237–2239. <https://doi.org/10.1002/jcc.20803>
45. Komeiji Y, Okiyama Y, Mochizuki Y, Fukuzawa K (2017) Explicit solvation of a single-stranded DNA, a binding protein, and their complex: a suitable protocol for fragment molecular orbital calculation. *Chem-Bio Inform J* 17:72–84. <https://doi.org/10.1273/cbij.17.72>

46. Kurisaki I, Fukuzawa K, Komeiji Y et al (2007) Visualization analysis of inter-fragment interaction energies of CRP-cAMP-DNA complex based on the fragment molecular orbital method. *Biophys Chem* 130:1–9. <https://doi.org/10.1016/j.bpc.2007.06.011>
47. Amari S, Aizawa M, Zhang J et al (2006) VISCANA: visualized cluster analysis of protein–ligand interaction based on the ab initio fragment molecular orbital method for virtual ligand screening. *J Chem Inf Model* 46:221–230. <https://doi.org/10.1021/ci050262q>
48. Ishikawa T, Mochizuki Y, Amari S et al (2007) Fragment interaction analysis based on local MP2. *Theor Chem Acc* 118:937–945. <https://doi.org/10.1007/s00214-007-0374-7>
49. Hitaoka S, Harada M, Yoshida T, Chuman H (2010) Correlation analyses on binding affinity of sialic acid analogues with influenza virus neuraminidase-1 using ab initio MO calculations on their complex structures. *J Chem Inf Model* 50:1796–1805. <https://doi.org/10.1021/ci100225b>
50. Hitaoka S, Matoba H, Harada M et al (2011) Correlation analyses on binding affinity of sialic acid analogues and anti-influenza drugs with human neuraminidase using ab initio MO calculations on their complex structures–LERE-QSAR analysis (IV). *J Chem Inf Model* 51:2706–2716. <https://doi.org/10.1021/ci2002395>
51. von Itzstein M, Wu W-Y, Kok GB et al (1993) Rational design of potent sialidase-based inhibitors of influenza virus replication. *Nature* 363:418–423. <https://doi.org/10.1038/363418a0>
52. Mochizuki Y, Fukuzawa K, Kato A et al (2005) A configuration analysis for fragment interaction. *Chem Phys Lett* 410:247–253. <https://doi.org/10.1016/j.cplett.2005.05.079>
53. Ishikawa T, Mochizuki Y, Amari S et al (2008) An application of fragment interaction analysis based on local MP2. *Chem Phys Lett* 463:189–194. <https://doi.org/10.1016/j.cplett.2008.08.022>
54. Nakano T, Kaminuma T, Sato T et al (2000) Fragment molecular orbital method: application to polypeptides. *Chem Phys Lett* 318:614–618. [https://doi.org/10.1016/S0009-2614\(00\)00070-1](https://doi.org/10.1016/S0009-2614(00)00070-1)
55. Mulliken RS (1955) Electronic population analysis on LCAO–MO molecular wave functions. I. *J Chem Phys* 23:1833–1840. <https://doi.org/10.1063/1.1740588>
56. Reed AE, Weinhold F (1983) Natural bond orbital analysis of near-Hartree–Fock water dimer. *J Chem Phys* 78:4066–4073. <https://doi.org/10.1063/1.445134>
57. Reed AE, Weinstock RB, Weinhold F (1985) Natural population analysis. *J Chem Phys* 83:735–746. <https://doi.org/10.1063/1.449486>
58. Singh UC, Kollman PA (1984) An approach to computing electrostatic charges for molecules. *J Comput Chem* 5:129–145. <https://doi.org/10.1002/jcc.540050204>
59. Besler BH, Merz KM Jr, Kollman PA (1990) Atomic charges derived from semiempirical methods. *J Comput Chem* 11:431–439. <https://doi.org/10.1002/jcc.540110404>
60. Bayly CI, Cieplak P, Cornell WD, Kollman PA (1993) A well-behaved electrostatic potential based method using charge restraints for deriving atomic charges: the RESP model. *J Phys Chem* 97:10269–10280. <https://doi.org/10.1021/j100142a004>
61. Breneman CM, Wiberg KB (1990) Determining atom-centered monopoles from molecular electrostatic potentials. The need for high sampling density in formamide conformational analysis. *J Comput Chem* 11:361–373. <https://doi.org/10.1002/jcc.540110311>
62. Bachrach SM (2007) Population analysis and electron densities from quantum mechanics. In: *Reviews in computational chemistry*, pp 171–228
63. Fujiwara T, Mochizuki Y, Komeiji Y et al (2010) Fragment molecular orbital-based molecular dynamics (FMO-MD) simulations on hydrated Zn(II) ion. *Chem Phys Lett* 490:41–45. <https://doi.org/10.1016/j.cplett.2010.03.020>
64. Fedorov DG, Slipchenko LV, Kitaura K (2010) Systematic study of the embedding potential description in the fragment molecular orbital method. *J Phys Chem* 114:8742–8753. <https://doi.org/10.1021/jp101724p>
65. Okiyama Y, Watanabe H, Fukuzawa K et al (2007) Application of the fragment molecular orbital method for determination of atomic charges on polypeptides. *Chem Phys Lett* 449:329–335. <https://doi.org/10.1016/j.cplett.2007.10.066>
66. Okiyama Y, Watanabe H, Fukuzawa K et al (2009) Application of the fragment molecular orbital method for determination of atomic charges on polypeptides. II. Towards an improvement of

- force fields used for classical molecular dynamics simulations. *Chem Phys Lett* 467:417–423. <https://doi.org/10.1016/j.cplett.2008.11.044>
67. Chang L, Ishikawa T, Kuwata K, Takada S (2013) Protein-specific force field derived from the fragment molecular orbital method can improve protein–ligand binding interactions. *J Comput Chem* 34:1251–1257. <https://doi.org/10.1002/jcc.23250>
 68. Watanabe C, Fukuzawa K, Tanaka S, Aida-Hyugaji S (2014) Charge clamps of lysines and hydrogen bonds play key roles in the mechanism to fix helix 12 in the agonist and antagonist positions of estrogen receptor α : Intramolecular interactions studied by the ab initio fragment molecular orbital method. *J Phys Chem B* 118:4993–5008. <https://doi.org/10.1021/jp411627y>
 69. Watanabe T, Inadomi Y, Fukuzawa K et al (2007) DNA and estrogen receptor interaction revealed by fragment molecular orbital calculations. *J Phys Chem B* 111:9621–9627. <https://doi.org/10.1021/jp071710v>
 70. Fedorov DG, Brekhov A, Mironov V, Alexeev Y (2019) Molecular electrostatic potential and electron density of large systems in solution computed with the fragment molecular orbital method. *J Phys Chem a* 123:6281–6290. <https://doi.org/10.1021/acs.jpca.9b04936>
 71. Frisch MJ, Trucks GW, Schlegel HB, Scuseria GE, Robb MA, Cheeseman JR, Scalmani G, Barone V, Petersson GA (2016) Gaussian 16, Rev. C.01. Gaussian, Inc.
 72. Fedorov DG, Ishida T, Uebayasi M, Kitaura K (2007) The fragment molecular orbital method for geometry optimizations of polypeptides and proteins. *J Phys Chem a* 111:2722–2732. <https://doi.org/10.1021/jp0671042>
 73. Ishikawa T, Yamamoto N, Kuwata K (2010) Partial energy gradient based on the fragment molecular orbital method: application to geometry optimization. *Chem Phys Lett* 500:149–154. <https://doi.org/10.1016/j.cplett.2010.09.071>
 74. Nagata T, Fedorov DG, Sawada T et al (2011) A combined effective fragment potential-fragment molecular orbital method. II. Analytic gradient and application to the geometry optimization of solvated tetraglycine and chignolin. *J Chem Phys* 134:034110. <https://doi.org/10.1063/1.3517110>
 75. Fedorov DG, Asada N, Nakanishi I, Kitaura K (2014) The use of many-body expansions and geometry optimizations in fragment-based methods. *Acc Chem Res* 47:2846–2856. <https://doi.org/10.1021/ar500224r>
 76. Nakata H, Fedorov DG (2016) Efficient geometry optimization of large molecular systems in solution using the fragment molecular orbital method. *J Phys Chem a* 120:9794–9804. <https://doi.org/10.1021/acs.jpca.6b09743>
 77. Emsley P, Lohkamp B, Scott WG, Cowtan K (2010) Features and development of Coot. *Acta Crystallogr Sect D Biol Crystallogr* 66:486–501. <https://doi.org/10.1107/S0907444910007493>

FMO Drug Design Consortium



**Kaori Fukuzawa, Shigenori Tanaka, Yoichiro Yagi, Noriyuki Kurita,
Norihito Kawashita, Kenichiro Takaba, and Teruki Honma**

Abstract Drug discovery is one of the most important applications of the fragment molecular orbital (FMO) method. By using the FMO calculation, it is possible to determine the binding properties between a drug candidate compound and a target protein, predict the binding activity, and begin to produce a rational design for the new drug compound. The FMO drug discovery consortium is an industry–academia–government cooperation group, which is conducting various studies with the aim of developing the FMO method as a practical in silico drug discovery technology. In this chapter, we introduce the status of the research conducted by four working groups (WGs) focusing on drug target proteins (the kinase, protease, nuclear receptor, and

K. Fukuzawa (✉)

School of Pharmacy and Pharmaceutical Sciences, Hoshi University, 2-4-41 Ebara, Shinagawa, Tokyo 142-8501, Japan
e-mail: k-fukuzawa@hoshi.ac.jp

Department of Biomolecular Engineering, Graduate School of Engineering, Tohoku University, 6-6-11 AobaAoba-ku, Aramaki 980-8579, Japan

S. Tanaka

Graduate School of System Informatics, Department of Computational Science, Kobe University, 1-1 Rokkodai, Nada-ku, Kobe 657-8501, Japan

Y. Yagi

Graduate School of Engineering, Okayama University of Science, 1-1 Ridai-cho, Kita-ku, Okayama 700-0005, Japan

N. Kurita

Department of Computer Science and Engineering, Toyohashi University of Technology, 1-1 Hibarigaoka Tempaku-cho, Toyohashi, Aichi 441-8580, Japan

N. Kawashita

Faculty of Science and Engineering, Kindai University, 3-4-1 Kowakae, Higashiosaka, Osaka 577-8502, Japan

K. Takaba

Pharmaceuticals Research Center, Laboratory for Medicinal Chemistry, Asahi Kasei Pharma Corporation, 632-1 Mifuku, Izunokuni, Shizuoka 410-2321, Japan

T. Honma

RIKEN Center for Biosystems Dynamics Research, 1-7-22 Suehiro-cho, Tsurumi-ku, Yokohama, Kanagawa 230-0045, Japan

© Springer Nature Singapore Pte Ltd. 2021

Y. Mochizuki et al. (eds.), *Recent Advances of the Fragment Molecular Orbital Method*,
https://doi.org/10.1007/978-981-15-9235-5_8

127

protein–protein interaction WGs) and two WGs focusing on methodology (one WG responsible for developing drug discovery methods and databases and one collaboration with the molecular dynamics-based KBDD, i.e., K supercomputer-based drug discovery, consortium). We also discuss the current state and challenges of FMO-based drug discovery.

Keywords FMO-based drug design · Industry–academia–government cooperation · High-performance computing infrastructure · Ligand-binding property · FMO database

1 About the FMO Drug Design Consortium (FMOODD)

The fragment molecular orbital (FMO) drug design consortium (FMOODD) was launched at the end of 2014 as an industry–academia–government cooperation group with the aim of developing the FMO method as a practical *in silico* drug discovery technology (representative: Kaori Fukuzawa). As of early 2020, 17 pharmaceutical companies, four IT companies, and 15 academic institutions are participants in the group (Fig. 1). The main activities of the FMOODD are to perform the FMO calculation for various target protein–ligand complexes using a high-performance computing infrastructure (HPCI [1]), including the K computer, TSUBAME3.0, FX100, and Oakforest-PACS, and to develop drug discovery techniques based on the obtained data. From 2015 to the present, we have also promoted a HPCI industrial use project entitled “Construction of platform of FMO-based drug design using HPCI system”.

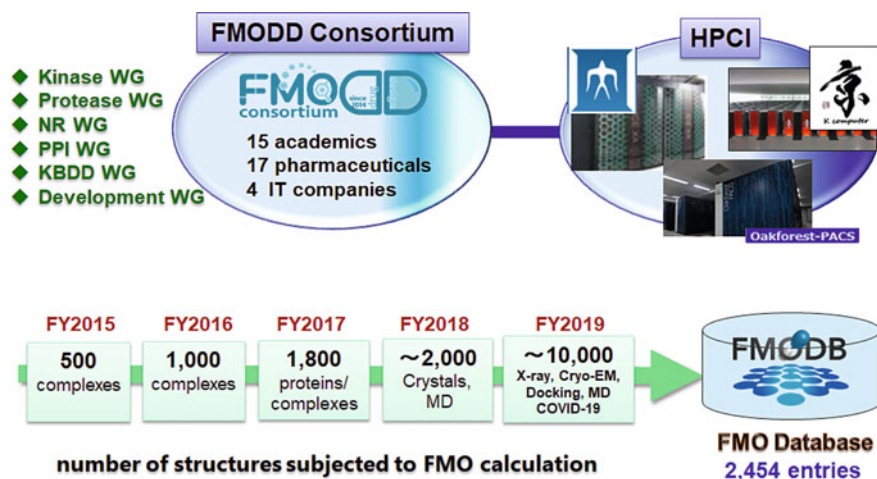


Fig. 1 Research activities of FMO drug design consortium (FMOODD). Abbreviations: WG: working group; NR: nuclear receptor; PPI: protein–protein interaction; KBDD: K supercomputer-based drug discovery; HPCI: high-performance computing infrastructure

Over the past five years, we have successfully performed FMO calculations on thousands of proteins or protein–ligand complexes; consequently, we have advanced drug research and development based on the world’s largest repository of quantum chemical calculation data. The results obtained from our calculations were released to the public in February 2019 as the “FMO Database” (<https://drugdesign.riken.jp/FMODB/>).

Research activities in the FMOODD have been conducted under a WG system. There are currently six WGs: four target WGs focusing on important types of drug target proteins (namely the kinase, protease, nuclear receptor, and protein–protein interaction (PPI) WGs), one development WG responsible for developing drug discovery methods and databases, and the FMOODD-KBDD WG, in which the FMOODD collaborates with another consortium, the KBDD project organized by the Biogrid pharma consortium. Most recently, one development WG for FMO methodology, structural biology WG, and formulation WG were further added.

In these WGs, various methods are used to select target proteins and structures for calculation. In addition to promoting individual themes for each WG based on information from research literature and in-house data, the consortium is also working on “creating guidelines for standard calculation procedures”. To achieve the latter, an exhaustive database search is first performed and FMO calculations are then performed when a structure satisfies both of the following conditions: (1) the Protein Data Bank (PDB) [2] has published the structure of the protein–ligand complex and (2) ChEMBL [3] has registered the activity value of the ligand compound. In addition, we are developing an automated FMO calculation protocol [4] in order to perform a huge number of FMO calculations on these structures. In this protocol, a series of processes including modeling the initial structure, creating an input file for the FMO calculation, executing the FMO calculation in the HPCI, and analyzing the calculation results are performed automatically. This protocol reflects the knowledge gained from each WG’s research, such as the method of structural treatment and the selection of appropriate force fields. Data has already been generated through such automatic calculation and we have registered several hundreds of proteins and their complex structures in the FMO database (see Chap. 9 for details).

To date, in the calculations of proteins or protein–ligand complexes with thousands of structures, FMO2-MP2/6-31G* has been used as the standard theoretical level. Furthermore, we have performed interaction analysis on these structures using inter-fragment interaction energy (IFIE) and pair interaction energy decomposition analysis (PIEDA). In these calculations, the protein is divided into fragments by its amino acid residue units, that is, proteins are split into amino acid residue units. The ligand and water molecule are basically treated as a single fragment, but ligand splitting is performed in some cases.

Coordination with other databases is also an important aspect of the FMO database. Our first work involved FMO data collection for the public PDBbind [5] core dataset, and this work is ongoing. As a future initiative, we are preparing cooperative efforts such as cross-linking with the Protein Data Bank Japan (PDBj). At present, all registered data are FMO calculation results from the ABINIT-MP

program, but we are also working on obtaining FMO results using the GAMESS program.

In the following sections, we will introduce the status of the research and development conducted in each of the WGs.

2 The Kinase WG

The kinase WG focuses on FMO applied to kinase-ligand docking systems. Kinases play important roles in the functional expression of various cellular processes, including those involved in cell aging and autoimmune diseases, and are activated by phosphorylation under the influence of external stressors such as heat, osmotic pressure, and ultraviolet radiation [6]. To assess the capability of the FMO approach for predicting binding affinities and the influence of the structure preparation protocol on this approach, the p38 mitogen-activated protein (MAP) kinase [6–8] (Fig. 2a) was chosen as a target protein. This protein was chosen because of its many X-ray crystal structure entries and extensive experimental activity data: 95 structures with 50% inhibitory concentration (IC_{50}) data in the ChEMBL database [3] were available in the PDB [2]. The p38 MAP kinase is known to have two main stable structures: the DFG (Asp-Phe-Gly)-*in*-loop and the DFG-*out*-loop forms (Fig. 2b). In addition, several structures in our dataset include a DFG-*intermediate*-loop (Fig. 2b). In our work [9], 78 PDB structures were analyzed because the FMO calculations for these structures successfully converged and provided IFIE values, whereas the calculations for the remaining structures did not converge for structural reasons. Because all of the inhibitors we dealt with have corresponding PDB structures and are placed in the

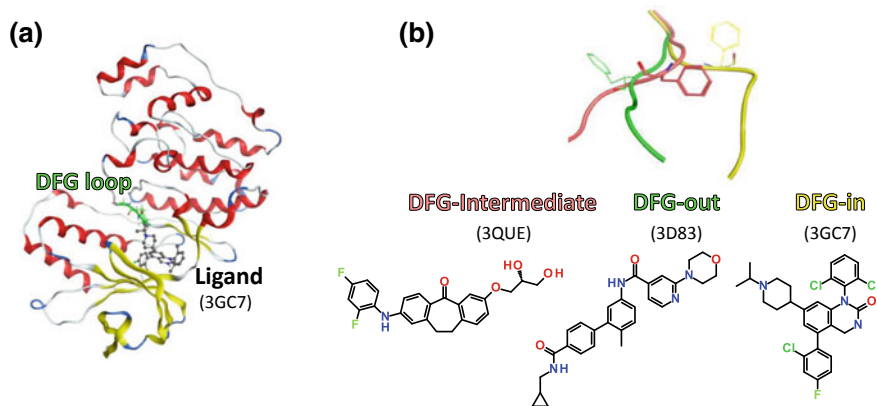


Fig. 2 **a** Complex of the p38 MAP kinase and its ligand, where the ribbon and ball-and-stick models correspond to the protein and ligand, respectively. **b** DFG-*in*, DFG-*out*, and DFG-*intermediate* loop structures are shown as yellow, green, and pink tubes, respectively. Reproduced from Ref. [9] by permission of the Publisher

same binding pocket, these inhibitors can be considered as specific inhibitors; thus, we denoted these inhibitors as “ligands.” We then regarded the IC_{50} value as the experimental measure of ligand binding affinity. We evaluated the IFIE between the p38 MAP kinase and its various inhibitors using the FMO method at the MP2/6-31G* level, and then compared the summation of IFIEs (IFIE-sum) with experimental IC_{50} data. We also categorized the proteins according to their DFG-*in/out*-loop configurations and the ligands according to their scaffold. Additionally, we investigated the difference in IFIEs when different force fields in molecular mechanics (MM) model were used to optimize the complexes. We note that the 78 analyzed structures were distributed among four research groups at different institutions in the kinase WG, which contributed to the structure preparation and optimization in this study, and each group used a different modeling tool; thus, PDB structures for one ligand type were dealt with by multiple institutions. Consequently, we produced six structure sets, namely A, B, C, C', D, and D', containing 38, 8, 25, 25, 15, and 15 complexes, respectively, in which several complexes overlapped between the sets [9].

First, we evaluated the correlation between the experimental IC_{50} values and the calculated IFIEs for the 78 complexes of structures A, C', and D', in which the structures were optimized by the same force field (AMBER10:EHT). Figure 3a shows the relationship between the pIC_{50} ($= -\log_{10}IC_{50}$) and IFIE-sum of all complexes

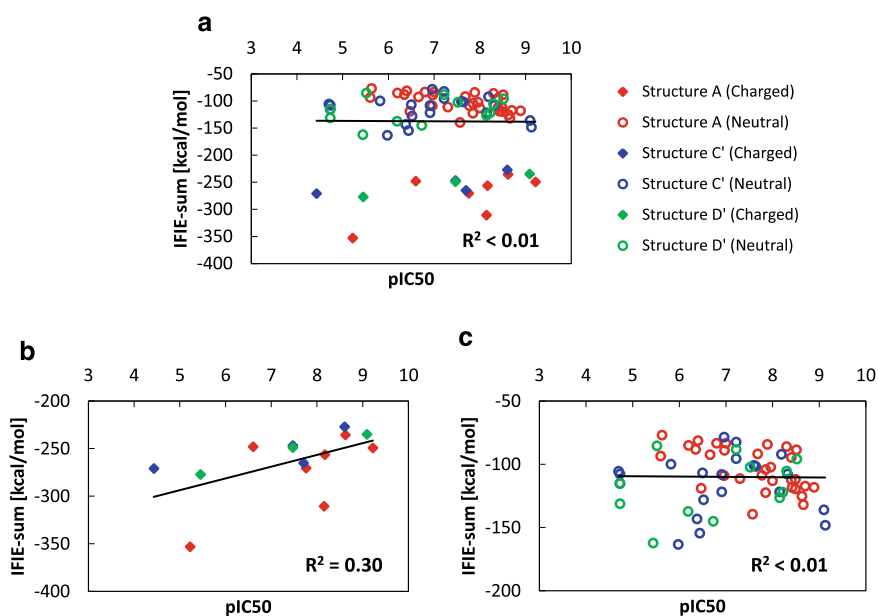


Fig. 3 Correlations between the pIC_{50} and predicted binding energies (summation of IFIE, i.e., IFIE-sum) for **a** all structures, **b** structures with charged ligands, and **c** structures with neutral ligands. These figures were obtained from structures A (red), C' (blue), and D' (green) including DFG-*in*, DFG-*intermediate*, and DFG-*out* proteins. The neutral and charged ligands are represented by circles and diamonds, respectively

with the 78 compounds; a low correlation coefficient of $R^2 < 0.01$ was obtained. Because the difference in IFIE-sum between the neutral and the charged ligands was larger than 100 kcal/mol, as shown in Fig. 3a, it was difficult to collectively compare these data. Thus, we investigated the correlation between the pIC_{50} and the IFIE-sum for ligands with similar net charges. Generally, comparing the IFIE values of neutral and charged fragments was difficult because the absolute value of the IFIE for charged fragment pairs was often overestimated. Figure 3b, c shows the correlation between the pIC_{50} and the IFIE-sum for complexes with charged and neutral ligands, respectively. Even when the neutral and charged ligands were separately considered, the correlations were either irrelevant or not found at all.

Second, we classified the proteins according to their characteristic conformations: the DFG-*in*-loop and DFG-*out*-loop (Fig. 4). Figure 4a, b shows the relationships between the pIC_{50} and the IFIE-sum for the DFG-*in* and DFG-*out* conformations, respectively. In both the cases, the IFIE-sums were not well correlated with the pIC_{50} . Additionally, these results were separated according to ligand charge, as shown in Fig. 4c–f. The IFIE-sums of the charged ligands showed inverse correlations with the pIC_{50} for both the DFG-*in* and DFG-*out* conformations (Fig. 4c, d). However, the DFG-*in* conformation with neutral ligands showed a relatively good correlation ($R^2 = 0.43$), as shown in Fig. 4e. On the other hand, the DFG-*out* conformation was not correlated with neutral ligands ($R^2 < 0.01$), as shown in Fig. 4f. This lack of correlation for the DFG-*out* structures was likely to be caused by the strong interaction between the ligand and the Glu71 because experimental IC_{50} values do not always represent significant inhibition when the IFIE value between the ligand and the Glu71 indicates strong stabilization [9] (see more information below).

Next, we investigated the correlations involving neutral ligands in order to understand the relationship between the pIC_{50} and the IFIE-sum in terms of ligand scaffolds. The correlation between the experimental pIC_{50} and the IFIE-sum of 64 neutral ligands (there were 64 PDB structures with neutral ligands in the 78 calculated PDB structures) is shown in Fig. 3c. Contrary to our expectations, there was no correlation between the experimental pIC_{50} values and the calculated IFIE-sum values for these ligands ($R^2 < 0.01$). However, the IFIE-sums of the p38 MAP kinase in the DFG-*in* conformation with 42 neutral ligands were significantly correlated with the pIC_{50} values, as shown in Fig. 4e. To better understand the origin of this relationship, we divided the 64 neutral ligands into five categories based on visual inspection of the scaffold of the ligand, during which we did not categorize the proteins by the DFG-loop conformation. The five categories were therefore defined as follows: (A) biphenyl amides, (B) three linked aromatic rings, (C) fused aromatic rings, (D) ureas, and (E) others (Fig. 5). Figure 6 shows the relationship between the pIC_{50} and IFIE-sum values for each ligand type. As shown in Fig. 6a–c, e, the IFIE-sums generally exhibited moderately good correlations with pIC_{50} , although the correlation coefficient was still poor for urea-type ligands (Fig. 6d). The X-ray crystal structures showed that all complexes of urea ligands and p38 MAP kinases consisted of DFG-*out*-loop structures. This data shows a similar trend to that shown in Fig. 4f, which presents the correlation between the pIC_{50} and the IFIE-sum of the DFG-*out*

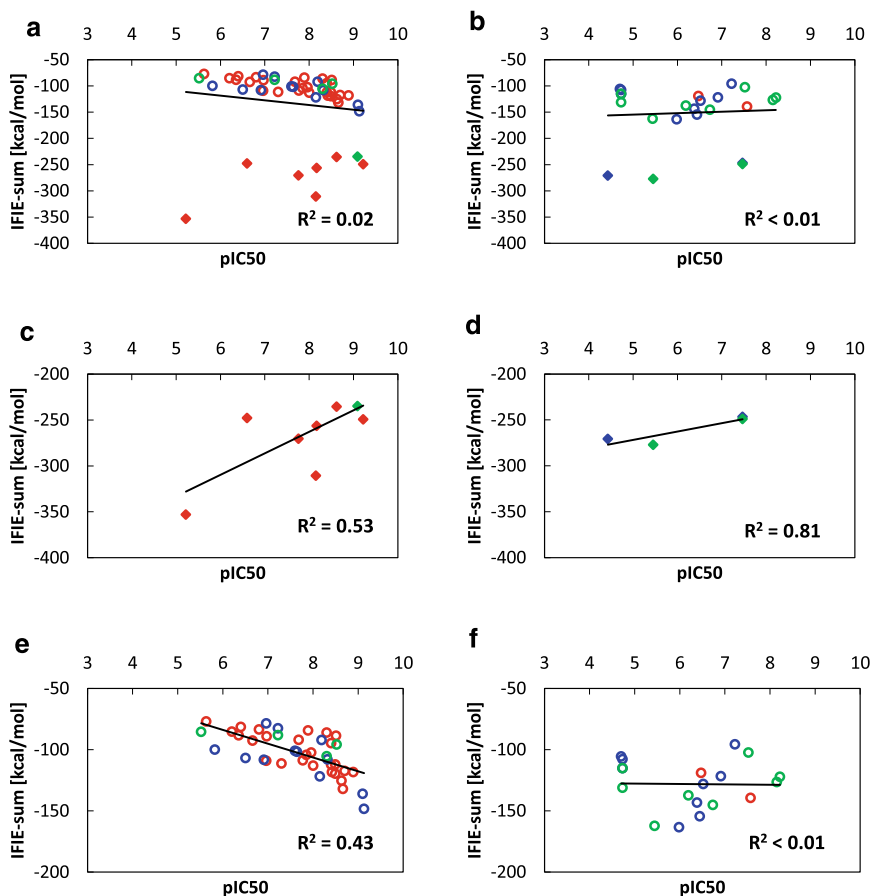


Fig. 4 Correlations between the pIC₅₀ and predicted binding energies (summation of IFIE, i.e., IFIE-sum) for DFG-*in* conformations and DFG-*out* conformations with different ligand scaffolds: **a** combined ligands with DFG-*in* proteins, **b** combined ligands with DFG-*out* proteins, **c** charged ligands with DFG-*in* proteins, **d** charged ligands with DFG-*out* proteins, **e** neutral ligands with DFG-*in* proteins, and **f** neutral ligands with DFG-*out* proteins. These figures were obtained from structures A (red), C' (blue), and D' (green). The neutral and charged ligands are represented by circles and diamonds, respectively

proteins with neutral ligands. In our current dataset, the types of ligand scaffold have their preferable protein conformations for the DFG-loop.

In our study [9], we employed three force fields, namely AMBER10:EHT, AMBER99, and CHARMM27, to investigate the influence of the type of force field used for geometry optimization on the IFIE-sum for ligands. The IFIE-sum obtained with AMBER10:EHT was used as a reference for comparison. Our analysis showed that using different force fields for geometry optimization has little effect on the IFIE-sum; the IFIE-sums obtained with each force field were not significantly

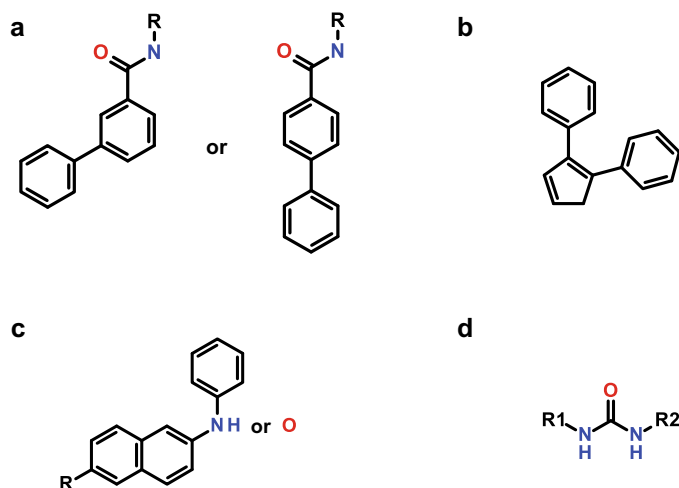


Fig. 5 Ligand types: **a** biphenyl amides, **b** three-linked aromatic rings, **c** fused aromatic rings with $-NH-$ or $-O-$ links, and **d** ureas. Others (i.e., the “other” ligand type category) are not depicted because there is no common scaffold in this category of ligands. Reproduced from Ref. [9] by permission of the Publisher

different with some exceptions. To better understand the origin of the exception cases, we investigated the residues with the largest differences in IFIE due to the force fields used, and we observed that Glu71 frequently provided large contributions to differences in the IFIE-sum. Figure 7 shows that Glu71 and the urea-type ligands make hydrogen bonds. The differences in IFIE of Glu71 become larger in cases involving urea-type ligands. The structures around Glu71 and the urea-type ligand were, however, almost unchanged when different force fields were used (Fig. 7). In explanation of this finding, the IFIE values between the urea-type ligands and Glu71 were large negative values (from -45 to -60 kcal/mol) relative to those of other fragment pairs; therefore, these values were sensitive to the slight structural differences in hydrogen atom positions due to the different force fields. This sensitivity may be related to the poor correlation between IFIE and pIC_{50} for the urea-type ligands, as shown in Fig. 6d.

The FMO results for the binding affinity between the p38 MAP kinase and ligand molecules described above can be comprehensively interpreted from another perspective. In another previous study [10], we performed singular value decomposition (SVD) for the calculated results of the IFIE matrix (amino acid residues \times various ligands) in order to determine the cause of the initial poor results and improve the correlations. In SVD, the original matrix is divided into multiple vectors that are orthogonal to each other. Through this method, we improved the correlation by removing specific vectors that included noise components and impaired the correlation.

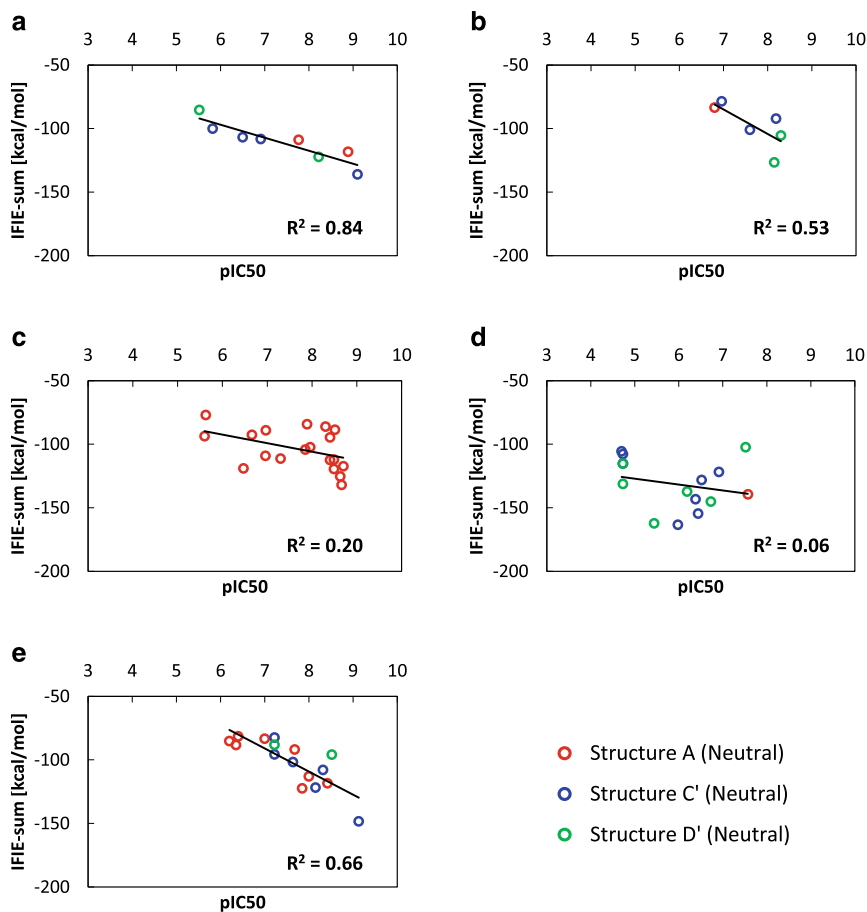


Fig. 6 Correlations between the calculated IFIE-sum and the experimentally measured pIC_{50} for each ligand scaffold: **a** biphenyl amides, **b** three-linked aromatic rings, **c** fused aromatic rings with $-NH-$ or $-O-$ links, **d** ureas, and **e** others. These figures were obtained from structures A (red), C' (blue), and D' (green)

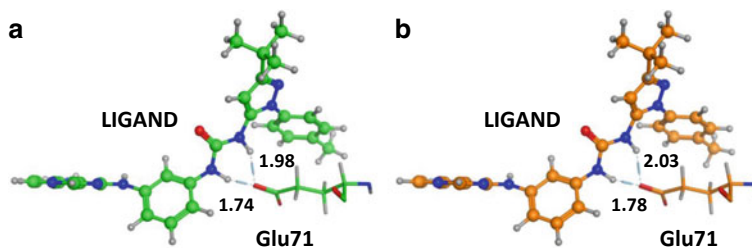


Fig. 7 The distances between the hydrogen atoms in the urea group of ligands and the oxygen atom in the carboxyl group of Glu71 for the structures C' and C (PDB ID: 3GCU). Structure C' and C are shown in (a) and (b), respectively. Reproduced from Ref. [9] by permission of the Publisher

An $m \times n$ matrix A with m and n -dimensional vectors as rows and columns can be related to an $m \times n$ diagonal matrix Σ that satisfies the following equation:

$$\Sigma = U^T A V. \quad (1)$$

Here, U is an $m \times m$ orthogonal matrix, and V is an $n \times n$ orthogonal matrix. If U and V are chosen appropriately, a pair of matrices can be made with Σ satisfying the condition described later. When Eq. (1) is rewritten, the following equation is satisfied:

$$A = U \Sigma V^T. \quad (2)$$

This type of decomposition is known as SVD [11–14]. For simplicity of description, we assume $m \geq n$. Otherwise, we can think of the transposed matrix A^T of A .

If σ_{ij} is an element of Σ , in the case of $i \neq j$, $\sigma_{ij} = 0$; in the case of $i = j$, for $1 \leq i \leq n$, $\sigma_{ij} = \sigma_i \geq 0$. At this time, $\sigma_1 \geq \sigma_2 \geq \sigma_3 \geq \dots$, where σ_i is a singular value of A , a column vector of U is a left singular vector, and a row of V^T is a right singular vector [14, 15].

For example, in Fig. 8, the left-hand side is matrix A before decomposition, while the right-hand side is U , Σ , and V^T in order from the left-hand side matrix. When the original matrix A is $m \times n$, the shape of each matrix is as follows:

A : $m \times n$; U : $m \times m$; Σ : $m \times n$; and V^T : $n \times n$.

The column vector of U is an orthonormal basis for each amino acid residue and the row vector of V^T is an orthonormal basis for each PDB structure with its respective ligand; each singular vector has an independent meaning.

We analyzed the left singular vectors (U) and named them singular vector 1, singular vector 2, and so on, in order from the vector of the first column of the left singular vectors. To execute SVDs, we used `numpy.linalg.svd` in NumPy [16].

Figure 9 shows the average of the calculated IFIEs between each amino acid residue and ligand molecules for 60 structures of p38 [10]. Most of the residues involved in strong binding were charged residues, including Glu71 (−30.74 kcal/mol), Asp112 (−11.29 kcal/mol), and Asp168 (−18.95 kcal/mol). We also examined the statistical correlation between IFIE-sum and experimental pIC_{50} (median value in multiple experiments); we found a lack of correlation (correlation coefficient $R^2 = 0.01$). Since the charged ligands had a significantly lower IFIE-sum

$$\begin{bmatrix} 1 & 2 & 3 \\ 8 & 9 & 7 \\ 10 & 11 & 12 \\ 6 & 4 & 5 \end{bmatrix} = \begin{bmatrix} -0.14 & 0.62 & 0.05 & * \\ -0.55 & -0.54 & 0.58 & * \\ -0.75 & 0.44 & -0.06 & * \\ -0.34 & -0.37 & -0.81 & * \end{bmatrix} \begin{bmatrix} 25.35 & 0 & 0 \\ 0 & 2.15 & 0 \\ 0 & 0 & 1.71 \\ 0 & 0 & 0 \end{bmatrix} \begin{bmatrix} -0.56 & -0.59 & -0.59 \\ -0.68 & -0.09 & 0.73 \\ -0.48 & 0.81 & -0.35 \end{bmatrix}$$

Fig. 8 Example of singular value decomposition (SVD) [15]. Reproduced from Ref. [10] by permission of the Publisher

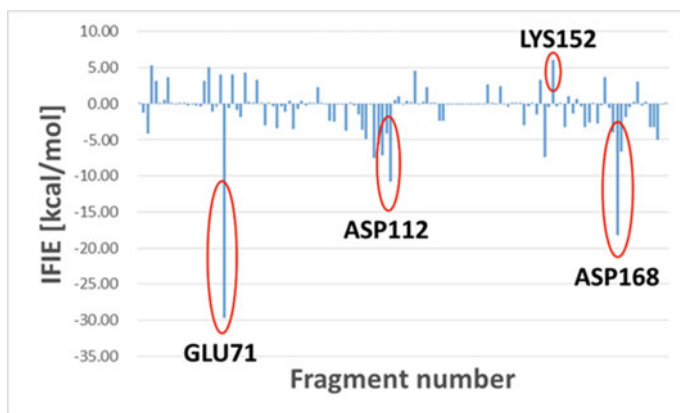


Fig. 9 Average IFIEs between each amino acid residue and the ligand molecules of 60 calculated structures of p38. Several important residues that show strong interactions with ligands are circled in red and named. Reproduced from Ref. [10] by permission of the Publisher

(i.e., they are more stable) than the neutral ligands, we next considered the correlation separately depending on the presence or absence of electric charge in the ligand. As shown in Fig. 10a, b, we were still unable to obtain significant correlations for

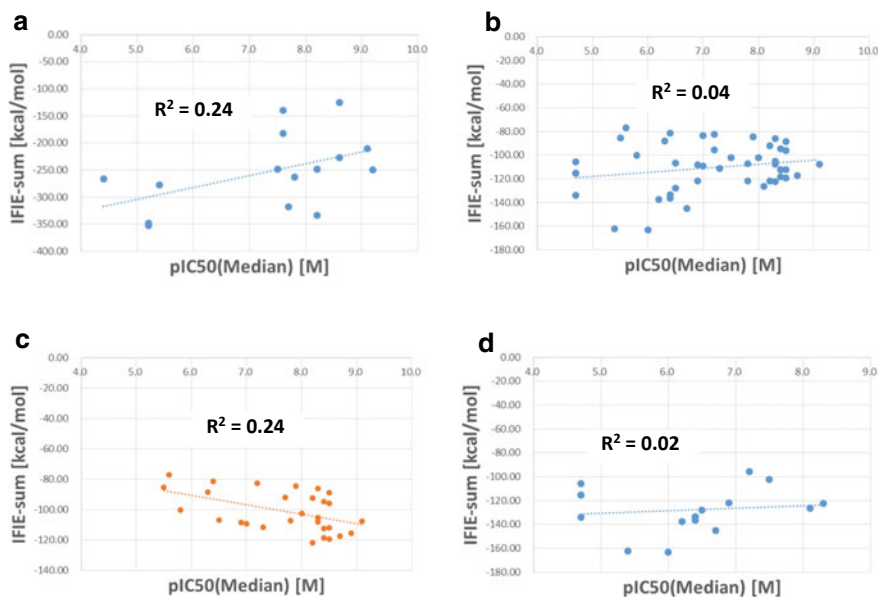


Fig. 10 Correlations between pIC_{50} (Median) and IFIE-sum for **a** charged ligands and **b** uncharged (neutral) ligands. Correlations between pIC_{50} (median) and IFIE-sum for the neutral ligands with the **c** DFG-*in* structure and **d** DFG-*out* structure

both charged and neutral ligands. Indeed, the correlation ($R^2 = 0.24$) observed for the charged ligands in Fig. 10a is irrelevant because the IFIE-sum should be more negative with an increase in pIC_{50} . Subsequently, we further separated the neutral ligand data based on the structure of the DFG-loop (*in* or *out*). Although we did not obtain a good correlation with the DFG-*out* structure (Fig. 10d), pairing the DFG-*in* structure with neutral ligands gave a correlation ($R^2 = 0.24$; Fig. 10c).

We then applied SVD in our analysis of the IFIE data. For the neutral ligands, we examined each left singular vector. The contribution by singular vector 1 was similar to the average value of the IFIE itself, whereas singular vector 2 gave completely different peak residues (Fig. 11). Furthermore, we observed that singular vector 1 from the neutral ligand data (Fig. 11a) had the same peak residues as singular vector 2 from all data. Given these results, we hypothesized that singular vector 2 from all data included a significantly important factor for binding that was not substantially affected by ligand charge. In addition, we examined the correlation between each IFIE-sum of each singular vector and pIC_{50} to identify specific vectors containing noise components. This analysis gave a correlation coefficient of $R^2 = 0.32$ for singular vector 2; however, singular vector 1 showed an inverse (irrelevant) correlation ($R^2 = 0.33$). We then assumed that it might be possible to find out correlations included in the FMO calculation, such as that from singular vector 2, by removing the contribution from singular vector 1; in doing so, we were able to improve the original R^2 of 0.04 (Fig. 10b) to 0.37 (Fig. 12). Thus, these results suggest that the correlation was improved by reducing the contribution of Glu71 because the maximum peak residue of singular vector 1, which was removed, was of Glu71. We confirmed this interpretation by investigating the interaction between Glu71 and the ligand in more detail [10].

For the DFG-*out* structure with neutral ligands, singular vector 1 had a strongly inverse correlation with pIC_{50} . Figure 13 shows the result of removing singular vector 1 from correlations, which succeeded in improving the R^2 values from 0.02 to 0.57. This result supports our previous findings, that is, inaccuracies associated with Glu71 in ligand-binding calculations significantly impaired the correlations.

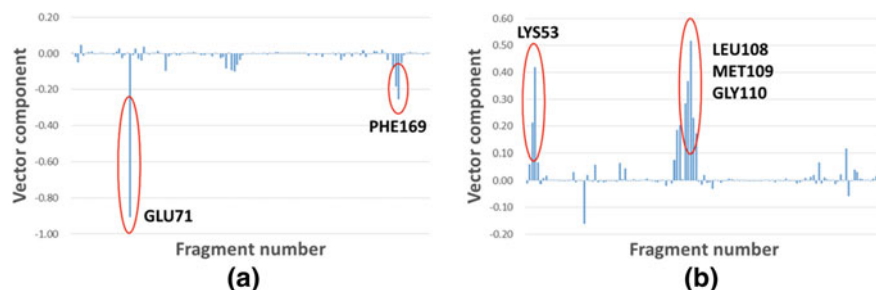


Fig. 11 Peak residues (circled in red) of singular vectors when analyzing neutral ligands. **a** Singular vector 1 and **b** singular vector 2. Reproduced from Ref. [10] by permission of the Publisher

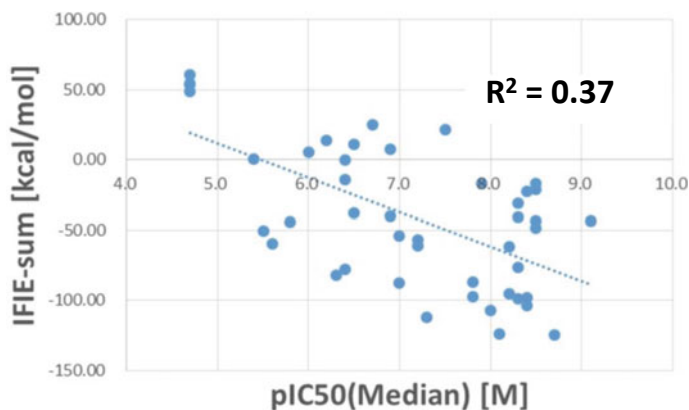


Fig. 12 Correlation between pIC₅₀ and IFIE-sum having removed the contribution of singular vector 1 when analyzing neutral ligands

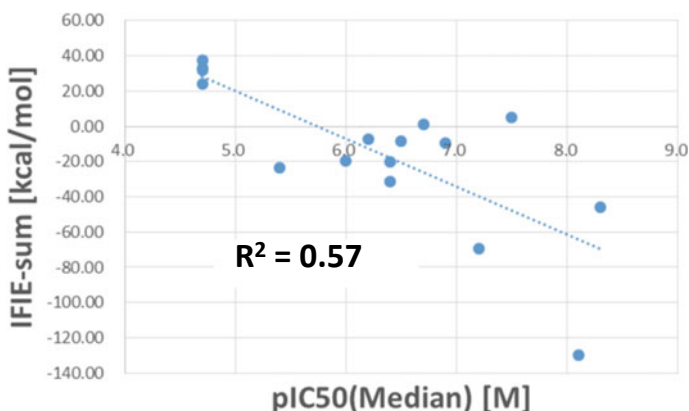


Fig. 13 Correlation between pIC₅₀ and IFIE-sum for the DFG-out structure with neutral ligands when using all the singular vectors except singular vector 1

As demonstrated above, our complementary analyses [9, 10] have provided practical computational approaches in which the FMO-IFIE method can be applied to in silico screening of ligand molecules as inhibitors of p38 MAP kinase and can produce insights into detailed molecular interactions with relevant residues.

3 The Protease WG

We have focused our attention on the FMO calculation [17–19] of the complexes of proteins with ligands to elucidate the function of proteins through analysis of the

interactions between the protein and ligand [20–22]. To this end, we selected renin, a human protease, as the starting target protein of our work. Renin is an aspartic protease that exists in the human kidney and contains 340 amino acid residues [23]. The active site amino acid residues of renin are Asp38 and Asp226. Importantly, renin is the first component of the renin–angiotensin system in hypertension. Figure 14 shows the structure of renin, including the active site amino acid residues Asp38 and Asp226.

Here, we describe the FMO calculation at the FMO2-MP2/6-31G* level for 20 renin complexes and their inhibitors with the activity values at the IC_{50} obtained from ChEMBL [3]. One of the aims of our study was to clarify the relationships between the calculated binding/interaction energies for the renin-inhibitor complexes and the IC_{50} of each inhibitor.

We selected 20 different renin-inhibitor complexes for the FMO calculations. The complex structures were prepared based on X-ray crystal structures and the selected inhibitors are shown in Fig. 15. We obtained these complex structures from PDB. We prepared two types of calculation model for each complex: one included the complexes without crystallization waters (model A) and the other included the complexes with crystallization waters (5.0 Å around the inhibitor; model B). For reconstruction of renin, the missing atoms and missing residues were complemented by homology modeling with SWISS MODEL [24–28]. The N- and C-terminus of renin were then capped by NH_3^+ and COO^- , respectively. In addition, hydrogen atoms were added to renin using AMBER11 [29]. For ligands, the hydrogen atoms were added using GaussView. The charge of ligands was assigned using AM1-BCC of Antechamber implemented in AMBER11. Since the protonation states of the active site residues Asp38 and Asp226 have not been clarified, these residues were

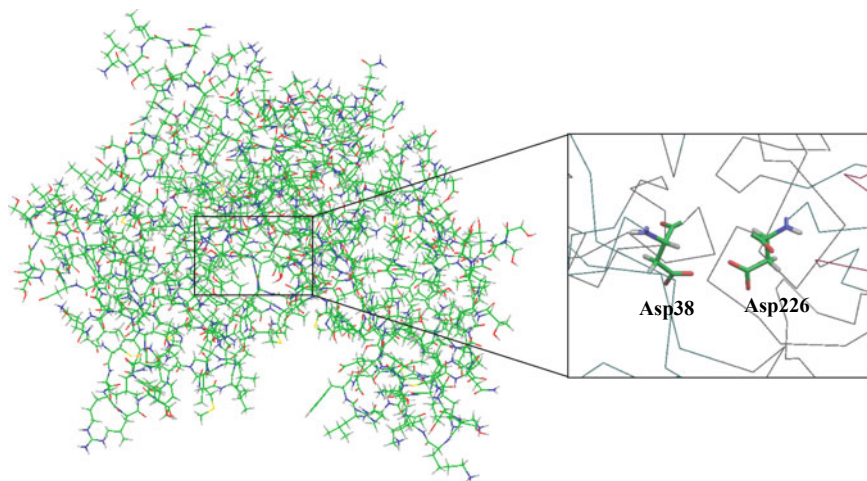


Fig. 14 Structure of renin (left side) and its active site amino acid residues Asp38 and Asp226 (right side). Color code: green C, red O, blue N, white H, and yellow S

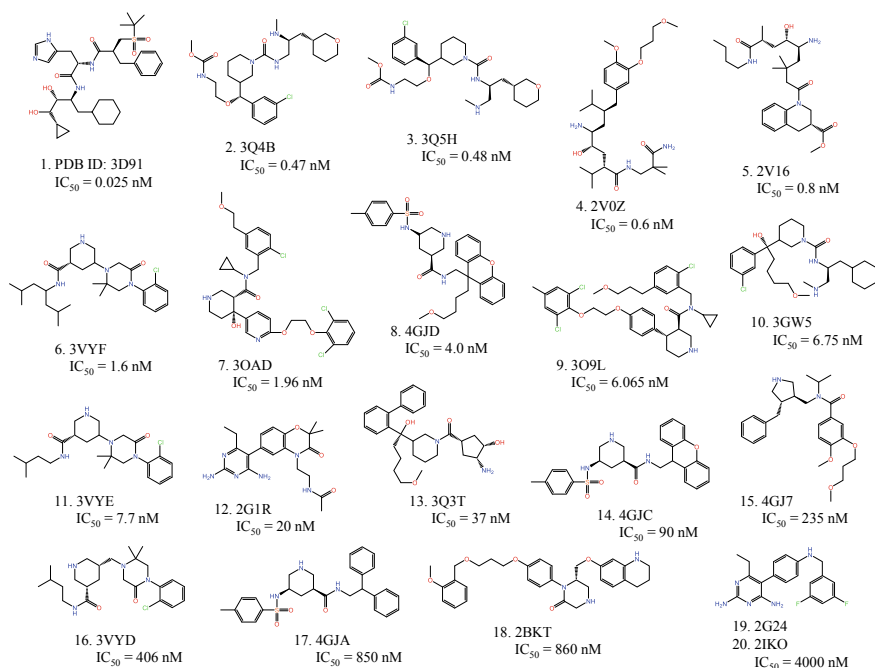


Fig. 15 Data set of inhibitors with the activity values (IC₅₀)

not protonated in our calculations. In order to neutralize the system, counterions were included. The structures of complexes were solvated with TIP3P model water molecules within 8.0 Å of respective complexes. Subsequently, we performed the energy minimization using an MM calculation via AMBER11 with the ff99 and GAFF force fields used for renin and ligands, respectively. All atoms were optimized in the energy minimization.

For model A and B, the surrounding TIP3P model water molecules and counterions were removed after energy minimization. The resulting complexes were subsequently subjected to an FMO calculation. All FMO calculations were performed at the FMO2-MP2/6-31G* level with the Cholesky decomposition approximation [30] using the ABINIT-MP program on the K computer. In these calculations, each amino acid residue of renin and the crystallization water were treated as a single fragment; however, the ligands were divided into fragments. Each system was divided into 339–343 or 342–357 fragments for models A and B, respectively. In addition, all FMO calculations were carried out under vacuum conditions. We evaluated the IFIE between a ligand and the amino acid residues in renin, and estimated the sum of these IFIEs as the binding energy between the inhibitor and the renin. In order to determine the details of the interaction, we also conducted PIEDA calculations [31, 32] to examine the energy components.

Table 1 lists the IC_{50} and pIC_{50} values for each inhibitor, as well as the calculated binding energies for both models A and B. Figure 16 shows the relationships between binding energies and pIC_{50} for both models. FMO computations indicated that the calculated binding energy in both models was correlated to the pIC_{50} of the inhibitors; this correlation was particularly strong for model B ($R^2 = 0.87$; $R = -0.93$).

Figure 17 shows an example of IFIEs between a ligand and selected amino acid residues in a renin complex (PDB ID: 2V0Z, model A) and Fig. 18 shows the PIEDA of the same IFIEs. We found that the inhibitors interact with certain amino acid residues such as Ser41, Tyr83, Ser84, Thr85, and Thr309 in addition to the active site amino acid residues Asp38 and Asp226. In most complexes, PIEDA showed that the main component of IFIE between a ligand and Asp38/Asp226 is electrostatic interaction; in contrast, the main component of IFIE between a ligand and Tyr83 is dispersion interaction.

Our FMO calculation for 20 renin-inhibitor complexes and their inhibitors showed that the binding energies were well correlated with the IC_{50} for each inhibitor. This result suggests that the computed binding energies may enable us to predict the

Table 1 IC_{50} and pIC_{50} values for each inhibitor, and the calculated binding energies (total IFIE) for each complex. PBD: Protein Data Bank

No	PDB ID	IC_{50} (nM)	pIC_{50}	Total IFIE (kcal/mol)	
				Model A	Model B
1	3D91	0.025	10.60	-219.69	-195.52
2	3Q4B	0.47	9.33	-154.57	-152.05
3	3Q5H	0.48	9.32	-143.66	-160.02
4	2V0Z	0.6	9.22	-158.41	-152.06
5	2V16	0.8	9.10	-168.48	-174.75
6	3VYF	1.6	8.80	-157.55	-147.38
7	3OAD	1.96	8.71	-147.74	-140.16
8	4GJD	4	8.40	-165.24	-143.82
9	3O9L	6.065	8.22	-150.07	-134.04
10	3GW5	6.75	8.17	-136.85	-118.84
11	3VYE	7.7	8.11	-132.70	-141.19
12	2G1R	20	7.70	-137.31	-128.73
13	3Q3T	37	7.43	-153.41	-136.89
14	4GJC	90	7.05	-127.43	-119.02
15	4GJ7	235	6.63	-99.63	-122.52
16	3VYD	406	6.39	-131.15	-119.45
17	4GJA	850	6.07	-139.28	-110.65
18	2BKT	860	6.07	-137.18	-106.16
19	2G24	4000	5.40	-89.30	-89.28
20	2IKO	4000	5.40	-78.46	-71.34

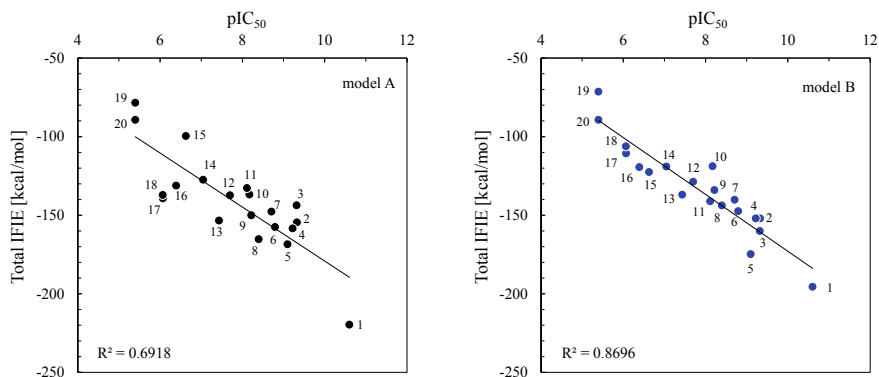


Fig. 16 Relationships between pIC₅₀ and total IFIE

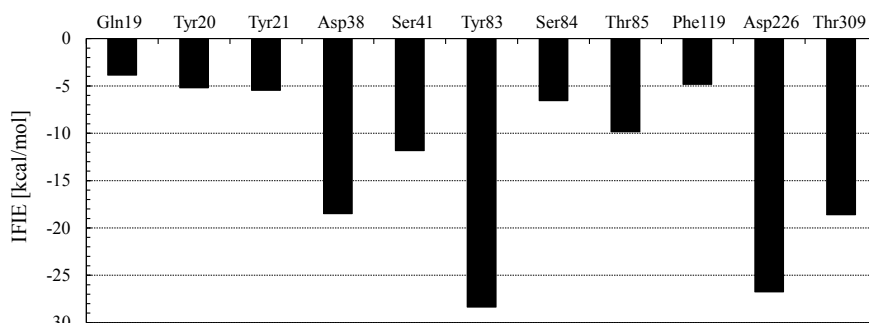


Fig. 17 IFIEs between an inhibitor and the selected amino acid residues in renin (PDB ID: 2V0Z, model A)

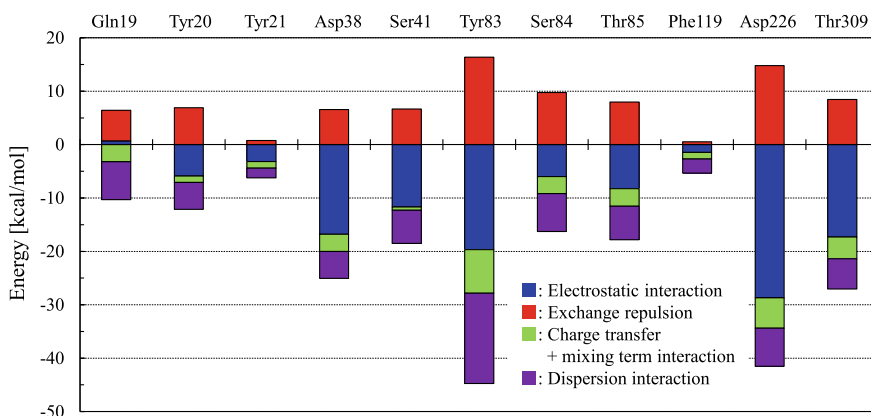


Fig. 18 PIEDA energies between an inhibitor and the selected amino acid residues in renin (PDB ID: 2V0Z, model A)

extent of the effects of individual inhibitors. Currently, the relationship between the IC_{50} and the IFIE values of particular amino acid residues and inhibitors is not entirely clear. Nevertheless, as shown in previous studies [20–22], the IFIE analysis is a useful method for acquiring detailed information on protein–ligand binding. The identified interactions for selected amino acid residues can lead to new information that may be used to develop safer and more effective agents than that are currently available. Presently, we are conducting research as follows: (1) IFIE analysis including crystallization waters to examine the role of water molecules in protein–ligand binding and (2) Visualized Cluster Analysis of Protein–Ligand Interaction (VISCANA) implemented in BioStation Viewer [33] to examine the characteristic indications of ligand binding with the IFIEs between each amino acid residue of renin and its inhibitors. In addition, we are implementing collaborative research supported by the BINDS program (Basis for Supporting Innovative Drug Discovery and Life Science Research) as a part of the Platform Project for Supporting Drug Discovery and Life Science Research from AMED (Japan Agency for Medical Research and Development).

4 The Nuclear Receptor WG

To date, FMO calculations have been performed for approximately 400 nuclear receptor structures, including androgen receptor (AR), vitamin D receptor (VDR), retinoic acid receptor-related orphan receptor γ t (ROR γ t), and estrogen receptor (ER). We have also evaluated the effects of the protonation state of His and the structural fluctuations of water on the correlation between activities and calculated values, and we have conducted various studies aimed at understanding the effects of, for example, functional groups, activity cliffs, and subtype selectivity. Our findings are discussed as follows for each target.

4.1 VDR

The FMO calculation for VDR was explained in detail by Kamimura and Kurita in another Chapter of this book. This is an interesting example of drug design that combines X-ray crystal structure analysis and FMO calculation to assess the binding activity between VDR and two ligands with greatly differing activity values [34, 35]. Importantly, there was sufficient agreement between the results obtained by FMO calculation and experimentation in the correlation between the binding energy of VDR and the ligand. In addition, the chirality of the ligand and the protonation state of the His residue of VDR were found to influence the interaction between VDR and the ligand (Fig. 19) [36, 37]. This demonstrates the importance of correctly setting the protonation state of the His residue existing around the ligand when using

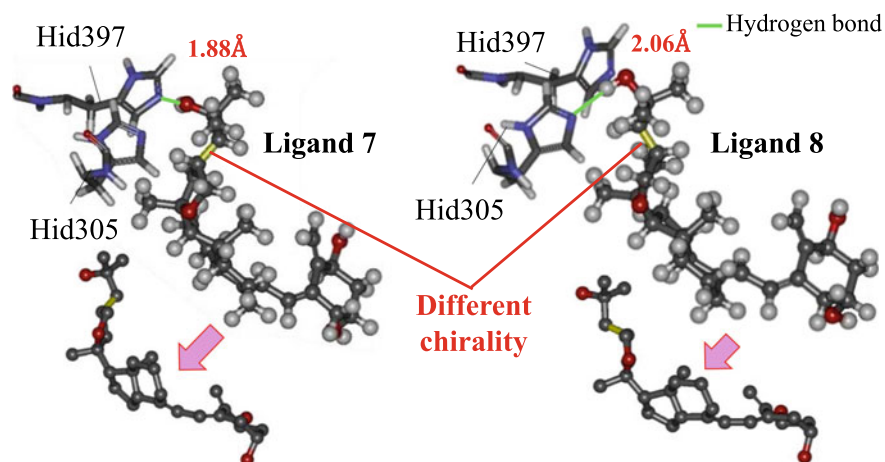


Fig. 19 Effects of ligand chirality on interactions between vitamin D receptor and ligands [36, 37]

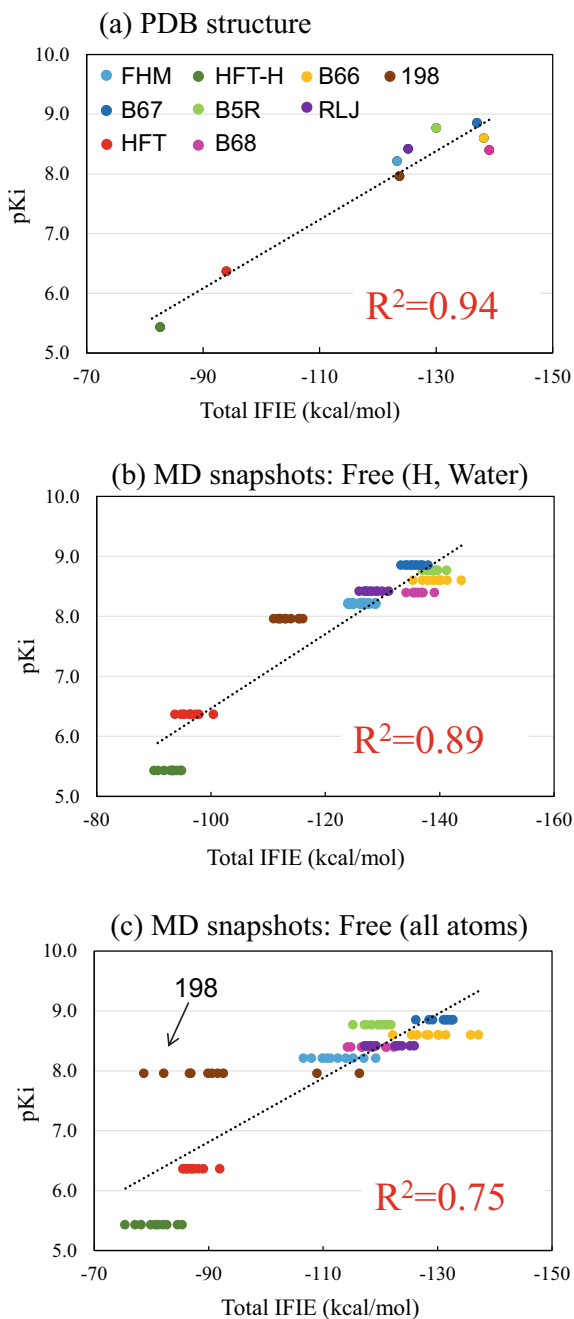
a molecular simulation to analyze the interaction between the protein and various ligands.

4.2 AR

Where AR was used as a target protein, FMO calculations were performed on structures following a comprehensive search using PDB and ChEMBL, as described in Sect. 1. The correlation coefficient between the value of total IFIE obtained by using 36 PDB structures for eight kinds of ligands and the value of K_i obtained experimentally was $R^2 = 0.86$. Thus, results of FMO calculations show that the binding properties between AR and ligands can be analyzed with high accuracy [38]. Furthermore, detailed analysis of IFIEs between each amino acid residue of AR and ligands revealed that the interaction between Asn705 of AR and the hydroxyl group of the ligand is important for strong binding between the two.

We also used FMO calculations to analyze the binding properties of AR and a new ligand with four types of substitution introduced into the functional group; consequently, we proposed a new ligand that binds strongly to AR [38]. Furthermore, molecular dynamics (MD) in a water solvent were calculated to analyze how the change in the arrangement of water molecules around the AR–ligand complex affects the interaction between AR and the ligand. Correlations between the calculated values (total IFIE) and activity values (p*K_i*) were examined for three types of structure: crystal structures, structures in which heavy atoms of AR and the ligand were fixed whereas water and hydrogen atoms were given fluctuations, and structures in which fluctuations of all atoms were considered (Fig. 20). When the fluctuation effect of only water was taken into consideration in the MD calculations, the correlation

Fig. 20 Correlations between p*K_i* and total IFIE considering fluctuations in water in the binding of androgen receptor and a ligand



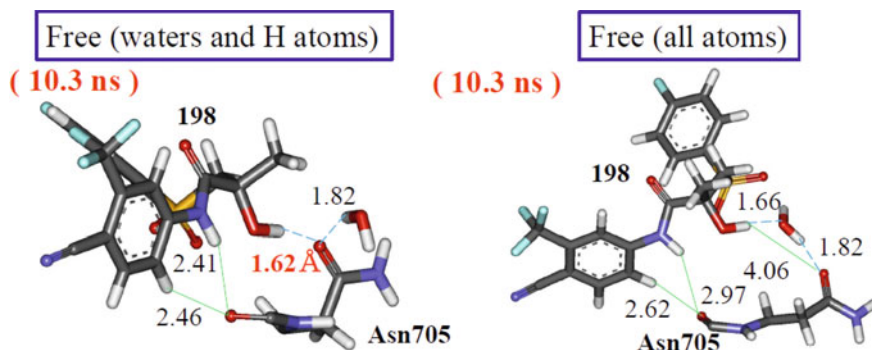


Fig. 21 Change in the interaction between ligand 198 and androgen receptor (AR) Asn705 residue mediated by water molecules. Left: structure with fluctuations only in water and hydrogen atoms; right: structure with fluctuations in all atoms

between the crystal structures and the experimental activity value was maintained; however, the correlation somewhat deteriorated if the structure was moved too much. To explain this reduced correlation, it was suggested that when the entire structure was moved, water molecules may have entered between the interacting ligand and amino acid residue, thereby weakening the direct interaction between AR and the ligand (Fig. 21).

4.3 Retinoic Acid Receptor-Related Orphan Receptor γt

For ROR γt , two types of ligands that act as an agonist or an inverse agonist were used as calculation targets [39]. These ligands are similar in structure but they have opposite actions on ROR γt . In order to determine the cause of this effect, MD calculations of 300 ns in water were used to analyze the structural change that occurs when the ligands bind to ROR γt . It was revealed that in the complex to which the inverse agonist was bound, the structure of Helix 12, which is involved in the transcriptional activity of ROR γt , significantly fluctuated and transcriptional activity was suppressed (Fig. 22a, b). To evaluate the cause of this structural change, we performed FMO calculations on several characteristic structures; we found that rotation of the His479 side chain of ROR γt triggered the structural change of Helix 12 (Fig. 22c). In future research, we intend to similarly analyze other ligands, and we aim to propose a ligand that can suppress the transcriptional activity of ROR γt more effectively.

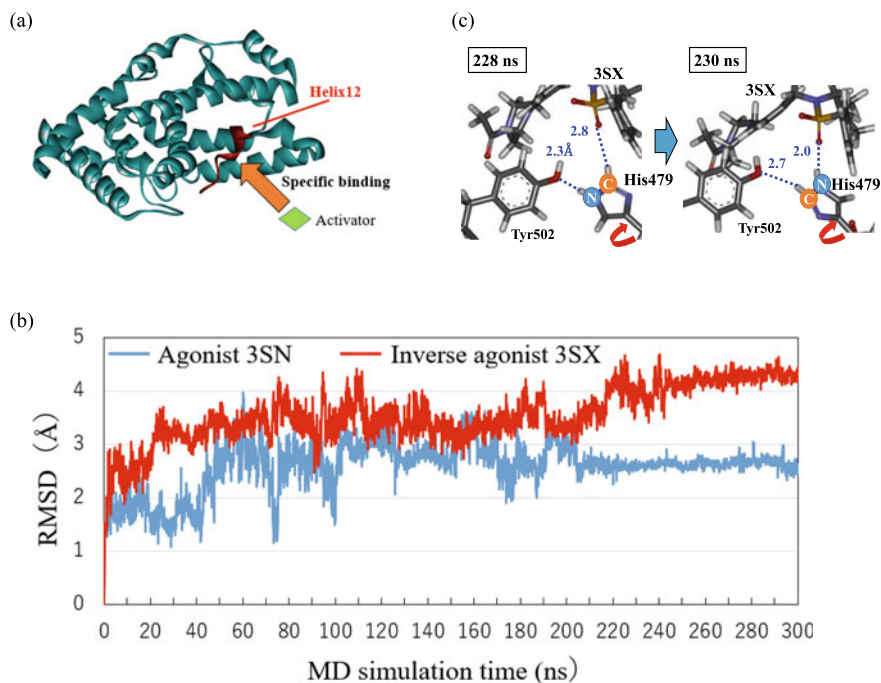


Fig. 22 **a** Specific binding between the Helix 12 site of retinoic acid receptor-related orphan receptor γ t (ROR γ t) and a co-activator. **b** Structural change of Helix 12 during MD calculations. **c** Rotation of the His479 side chain and interaction changes between amino acid Tyr502 and ligand 3SX revealed by MD calculations. Reprinted with permission from Ref. [39]

4.4 ER

ER, a female hormone receptor, has two subtypes (α and β), both of which have cocrystal structures with many ligands. ER-ligand binding has been extensively studied using FMO calculations to determine receptor binding affinity and subtype selectivity [40, 41]. To date, FMO calculations have been performed for cocrystal structures of ER α and 22 types of ligand, as well as ER β and 23 types of ligand. Correlations with the IC₅₀ have also been assessed, and detailed analysis of IFIES has been performed. For complexes with a ligand for which the cocrystal structure has not been published, docking structures are instead used in the analysis.

For ER α , similar to AR, FMO calculations were performed using the globally searched structures obtained from PDB and ChEMBL, as described in Sect. 1. The ligands in the 22 ER α -ligand complex structures include nine agonists and 13 antago-

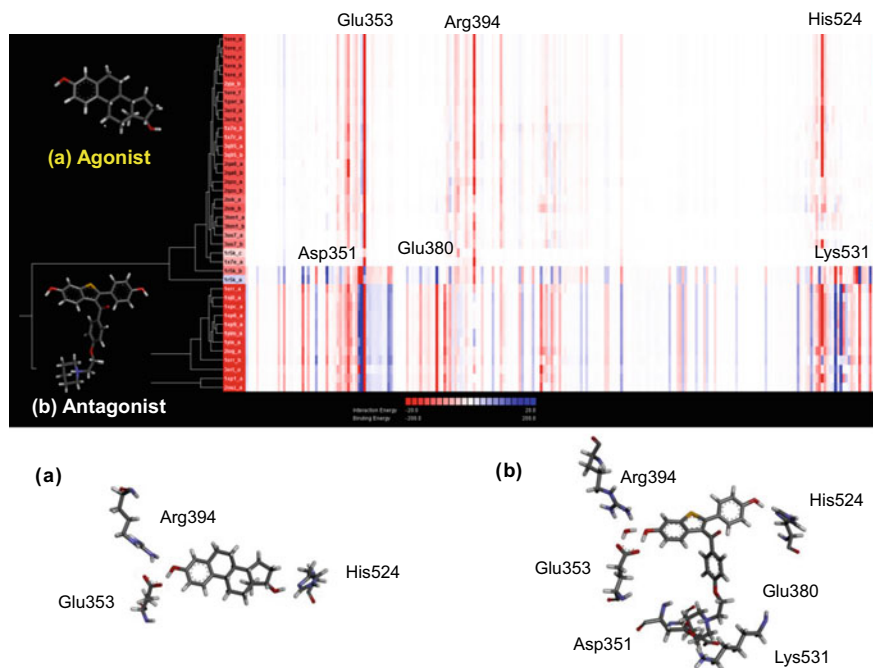


Fig. 23 Clustering analysis of ligands based on IFIEs of estrogen receptor α (ER α) and the ligands

nists. Figure 23 shows the result of clustering the compounds based on the interaction pattern of IFIE using FMO calculation results. This is an example of the VISCANA method [42], which can be used to evaluate the similarity of ligands and extract important interactions common to multiple complex structures. As shown in Fig. 23, the agonist and antagonist are clearly separated. Many ER α agonists are small molecules such as steroids. On the other hand, antagonists have structures in which a long chain is extended in addition to a site with a size similar to that of the agonist, and an amine at the tip has a positive charge. Results showed that the interaction residues common to most of the complexes were amino acid residues that possessed hydrogen bonds with steroid moieties such as Glu353 and His524. For the antagonists, interactions with residues such as Asp351, Glu380, and Lys531 were also observed. Therefore, the magnitude of the interaction energy increased and the electrostatic interaction caused by the positive charge of the ligand tended to become stronger. Consequently, the interaction patterns of agonists and antagonists differed distinctly, and the clusters to which they belonged were segregated. In further analysis of the interaction with a charged ligand, statistically corrected IFIE (SCIFIE) [43] was used to incorporate a shielding effect against excessive electrostatic interaction from distant residues. In addition, excessive separation of the agonist and antagonist has been reduced by incorporating a solvent effect using the FMO-Poisson–Boltzmann and surface area approximation (PBSA) method [44].

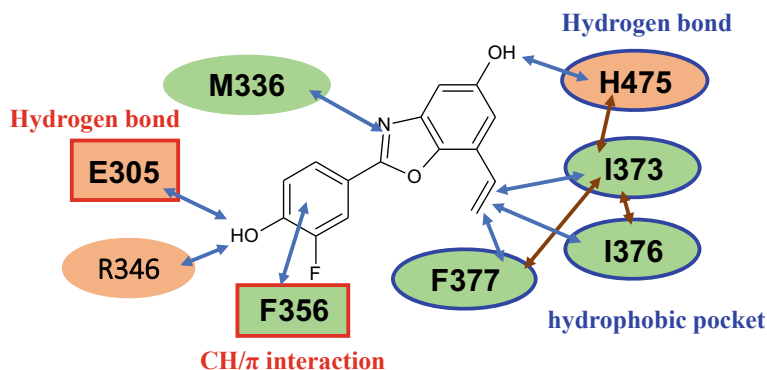


Fig. 24 Interaction between estrogen receptor β (ER β) and β -selective ligands

For ER subtype β , the complex structures registered in PDB were comprehensively calculated and subjected to IFIE/PIEDA analysis. In addition, ligands were clustered using VISCANA, and the relationship between the interaction characteristics and subtype selectivity was examined [45]. Similar to the ER α result, two amino acid residues essential for ligand binding (Glu305 and Phe356), a residue strongly involved in β -selectivity (His475), and three hydrophobic amino acid residues forming the β -selective pocket (Ile373, Ile376, and Phe377) were identified (Fig. 24). We found a strong correlation between the His475–ligand interaction and β -selectivity, revealing that His475 plays an important role in β -selectivity.

In ER subtype selectivity, phytoestrogens are known to have $\times 10$ -fold selectivity, and the synthetic ligand Prinaberel has >200 -fold β selectivity [46]. When binding energy evaluation was performed for 10 types of ligand with various inhibitory activity values (IC_{50}) or subtype selectivity by combining docking calculations and FMO calculations, we obtained a correlation coefficient of $R^2 = 0.79$. Furthermore, the effects of halogen (fluoro group) and the vinyl group, which were introduced to enhance the subtype selectivity at the synthetic stage, were evaluated using PIEDA. The introduction of the fluoro group was found to cause a change in the electrostatic interaction and a structural change derived from the atomic charges of hydrogen and fluorine; the introduction of the vinyl group caused a large change in the dispersion interaction. It is expected that evaluations of the electronic level against the influence of such functional groups will provide a useful index for future molecular design.

5 WG on Protein–Protein Interactions

PPIs occur frequently in vital biological activities and are essential for the performance and control of many biological functions. While PPIs are usually controlled without problems, once these interactions are disrupted, various failures occur that can develop into diseases such as cancer [47]. Therefore, PPI inhibitors have become

attractive targets as therapeutic agents. However, the interaction modes between proteins are diverse, and the design of inhibitors remains challenging [48]. In order to contribute to the development of inhibitors of PPIs, we conducted interaction analysis using the FMO method [17, 31, 49, 50].

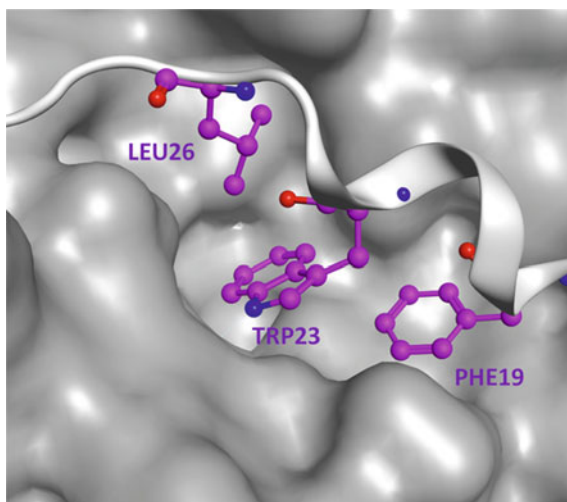
5.1 *MDM2-p53 Interaction Inhibitor*

The oncogenic gene p53 is activated in response to genetic stresses such as ultraviolet light and radiation; it acts as a transcription factor to activate the transcription of various downstream genes that induce cell cycle arrest and apoptosis, thereby inhibiting cellular oncogenicity [51–53]. p53 consists of 393 amino acid residues and five key domains (the transcriptional activation, proline-rich, DNA binding, tetramerization, and basic domains) from the N-terminal side. In addition, p53 is a homotetrameric protein, and various functions of p53, such as DNA binding and nuclear export, depend on its multimeric structure; tetramer formation has also been reported to be essential for the functional expression of p53 [54, 55]. Thus, the tetramerization domain involved in the stability of the p53 tetramer structure is thought to be crucial to the tumor suppressor function of p53, and mutations or deletions in this domain are among the major causes of human cancer. The tetrameric structure of these mutant forms of p53 is remarkably destabilized compared with that of the native form, and the DNA binding capacity and transcriptional activity have also been shown to be reduced [56, 57]. The N-terminal transcriptional activation region of p53 is also known to be the binding region for MDM2, a protein that plays a central role in p53 regulation. MDM2 binds to the α -helix in the transcriptional activation domain of p53 and catalyzes its ubiquitination, thereby promoting the proteasomal degradation of p53 [58, 59]. Thus, p53 is known to be repressed by MDM2, and MDM2 overexpression has been confirmed in several cancers [60, 61]. Consequently, inhibition of p53-MDM2 interactions is expected to restore the tumorigenic function of p53, and MDM2 is considered a major target for the development of anticancer drugs; indeed, many inhibitors have already been reported [62–69].

The mode of interaction of p53-MDM2 has been studied extensively: it is mainly due to the insertion of the side chain including Phe19, Trp23, Leu26, amino acid residues in p53, into the hydrophobic cleft in MDM2. In addition to these hydrophobic interactions, X-ray crystallography of the p53-MDM2 complex has shown that Phe19 and Trp23 of p53 are hydrogen-bonded to Gln72 and Leu54 of MDM2, respectively [70]. Figure 25 shows the mode of interaction between p53 and MDM2 [71]: the p53 side chain including Phe19, Trp23, and Leu26 is positioned so that it enters the gap in MDM2.

As many studies have determined the inhibitors of MDM2, several MDM2-small molecule inhibitor cocrystal structures, obtained by X-ray crystallography, have been registered in PDB. In our study, FMO calculations were performed on these cocrystal structures and the results were compared with reported inhibitory activity values. We showed that the values of the interaction between MDM2 and ligands obtained by

Fig. 25 Interaction between p53 and MDM2 (PDB ID: 1YCQ) [27]. White ribbon: p53; gray surface: MDM2; magenta: Phe19, Trp23, and Leu26 amino acid residues in p53



the FMO method reflected the inhibitory activity values observed experimentally. Thus, our findings could lead to applications for MDM2 inhibitors.

The FMOs were calculated using 17 structures of MDM2-low-molecular-weight compound complexes registered in PDB for which the IC_{50} was reported as inhibitory activity [62–69]. The structures and PDB IDs of each ligand are shown in Fig. 26, and the IC_{50} of each ligand is shown in Table 2. Since MDM2 in the 17 crystallographic structures obtained from PDB had only a partial structure, it was adjusted to the crystal structure with the shortest residue (amino acid residues: Tyr26–Val110) when calculating FMO. Subsequently, Structure Preparation and Protonate 3D were used to complement missing residues and atoms and add hydrogens using MOE2014.0930 [72]. Finally, MMFF94x was used as a force field and structural optimization was performed only for hydrogens in the complex. Furthermore, only those water molecules that were hydrogen-bonded to cross-link the ligand and protein were allowed to remain in the crystallographic water.

Using the crystalline structures optimized as described above, FMO calculations were performed by validating PIEDA using the K supercomputer and ABINIT-MP as a calculation program [73]. MP2 was selected as the calculation level and 6-31G* was used as the basis function.

First, the correlations between IC_{50} and IFIE-sum shown in Table 2 were confirmed (Fig. 27): the resultant R^2 value was 0.68, that is, a relatively strong correlation was obtained. Because of the strong association between the experimental values and IFIE-sum, the FMO-calculated IFIEs could likely be used to predict the interaction between MDM2 and its inhibitors.

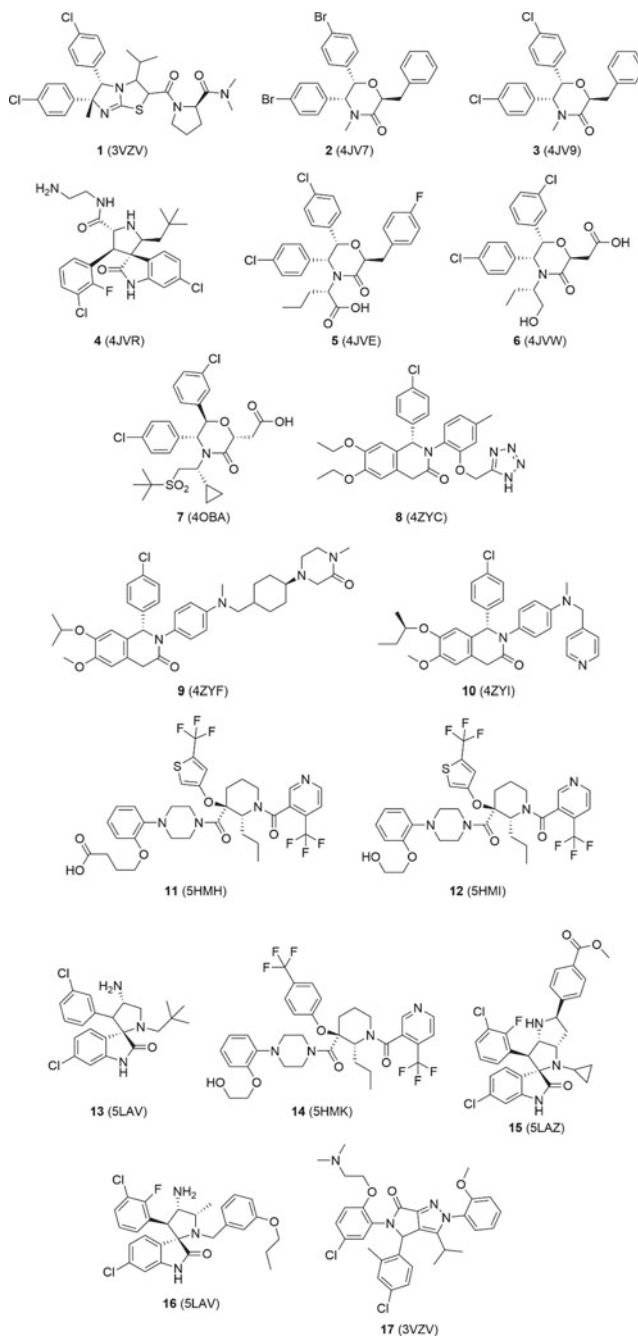
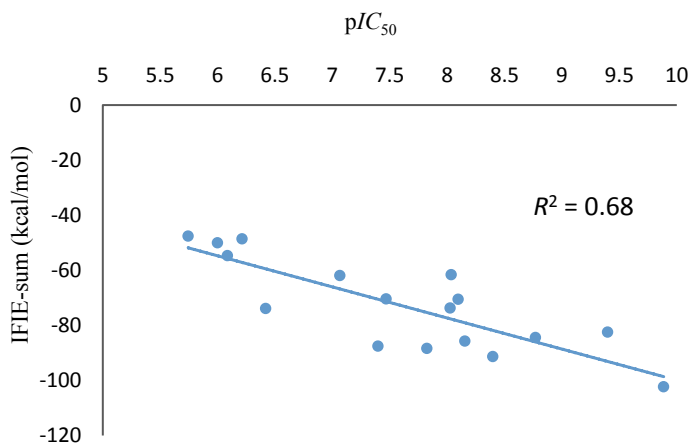


Fig. 26 Ligand structures (MDM2-low-molecular-weight compound complexes) used for FMO calculation. The PDB ID is shown in parentheses

Table 2 IC₅₀ of calculated ligands shown in Fig. 26

Lig. No	PDB ID	IC ₅₀ (nM)	Lig. No	PDB ID	IC ₅₀ (nM)
1	3VZV	9.2	10	4ZYI	8
2	4JV7	1000	11	5HMH	7
3	4JV9	1800	12	5HMI	15
4	4JVR	9.4	13	5LAV	819
5	4JVE	86	14	5HMK	40
6	4JWR	610	15	5LAZ	4
7	4OBA	0.4	16	5LAY	34
8	4ZYC	380	17	5LN2	0.13
9	4ZYF	1.7			

**Fig. 27** Correlation between the summation of ligand–protein IFIEs (IFIE-sum) and pIC₅₀ for MDM2 inhibitors

5.2 β -Secretase 1 Inhibitor

Alzheimer's disease, a neurodegenerative disorder with progressive cognitive impairment, was discovered in 1906 by Dr. Alois Alzheimer, a German psychiatrist [74]. A pathological feature of this disease is senile plaque formed by the deposition of amyloid fibers consisting of amyloid β ($A\beta$) in the brain. The disease state of Alzheimer's disease is largely divided into three stages: stage 1 begins with impairment of memory and learning, emotional upset, but preserved personality; stage 2 includes prominent higher-order dysfunction and marked impairment of memory; and stage 3 involves motor deficits and, eventually, the complete loss of function of the cerebral cortex. In recent years, the number of patients with Alzheimer's disease has increased and the development of effective treatment methods and drugs

has become a priority [75]. However, the contribution of drugs to the treatment of Alzheimer's disease remains lower than that in other therapeutic areas; indeed, drug treatment of the disease is currently inadequate.

Acetylcholinesterase inhibitors and *N*-methyl-D-aspartate receptor antagonists are widely used as agents for improving quality of life in patients with Alzheimer's disease [76]. These drugs are intended to temporarily improve cognitive function and cannot inhibit the progression of the disease itself. Following various studies on the pathogenesis of Alzheimer's disease, the A β hypothesis [77] has been posited: it states that the accumulation of A β , which constitutes the senile plaque deposited in the brain of patients, drives the development of Alzheimer's disease. Thus, A β has become a major target for fundamental therapies.

A β is a partial segment of amyloid precursor protein (APP) that is first cleaved at the *N*-terminus of the A β domain by β -secretase 1 (BACE1), which then cleaves the *C*-terminus of the A β domain, thereby excising the precursor protein and secreting it into the extracellular space. A β is characterized by its high agglutinability: it causes toxicity and neuronal cell death by agglutination. The main molecular species of A β are A β 40 and A β 42 (which are 40 and 42 residues long, respectively). A β 42 is considered to be highly toxic because it is particularly susceptible to aggregation.

BACE1 is a membrane-bound glycoprotein, aspartate protease, with two aspartates, Asp32 and Asp228, as active core sites that catalyze protease action [78] (Fig. 28). BACE1 has been found to trigger A β production, and BACE1-knockout mice can survive without noticeable behavioral or histological abnormalities [79]. Therefore, BACE1 has attracted considerable attention as a safe and effective target for anti-Alzheimer's disease drugs.

BACE1 inhibitors have now been extensively developed. In 2000, the OM99 group, peptide-like compounds of APP, was reported as containing the first potent BACE1 inhibitors. Among the OM99 group, OM99-2 in particular was shown to have

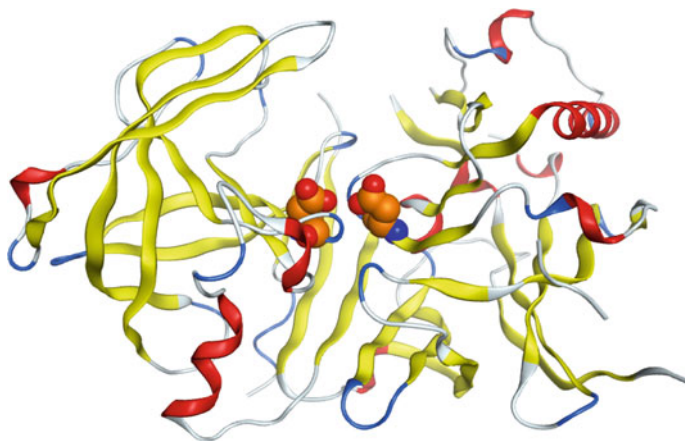


Fig. 28 Structure of β -secretase 1 (PDB ID: 1SGZ). Asp32 and Asp 228 are shown as orange molecules in the reaction center

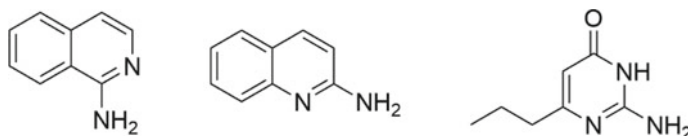


Fig. 29 Examples of cyclic amidine structures in β -secretase 1 (BACE 1) inhibitors

a potent inhibitory activity on nM-units [80]. However, the development of a small molecule inhibitor, that is, not peptide-sized, was the ultimate aim because problems were encountered with penetration into the brain due to the large molecular weight and multiple hydrogen bond donors of the developed peptide-like compounds. This proved challenging as the active pockets of BACE1 are about five amino acid residues in size and it is therefore difficult to inhibit enzymatic activity with small molecule inhibitors. Consequently, potent inhibitors have not since been discovered.

In 2007, aminoquinoline, aminoisoquinoline, and aminopyrimidone were discovered as small molecule lead compounds in BACE1 [81–83] by fragment-based drug discovery (FBDD) [84]. A common feature of these structures is their cyclic amidine structure (Fig. 29).

These cyclic amidine-containing compounds have attracted attention as core scaffolds for BACE1 inhibitors and a number of reports on similar inhibitors have emerged [85–88]. This has led to the discovery of compounds that have an inhibitory effect on A β production in cellular assays, good pharmacokinetics (particularly brain penetration), and even *in vivo* activity [89–91]. Most of these compounds possess the first cyclic amidine structure as a partial structure, indicating that this skeleton is suitable as a BACE1 inhibitor.

In our work, 38 of the BACE1-small molecules complexes registered in PDB with cyclic amidines and reported inhibitory activities were selected as targets for FMO calculations [92–96]. Table 3 shows the inhibitory activity values of each ligand (Fig. 30). All structures have a cyclic amidine structure, and they were divided into five groups according to the differences in the skeleton of these cyclic amidine structures.

First, the crystallographic structures were obtained from PDB. Next, MOE2014.0930 [72] was used to complement the missing residues and atoms and to add hydrogens using Structure Preparation and Protonate 3D. Finally, MMFF94x was used as a force field, and only the hydrogen molecules in the ligand–protein complex were structurally optimized. All of the crystalline water remained.

Using the crystal structures optimized as described above, the FMO calculations were performed using the K supercomputer and ABINIT-MP [73] as a computational program. MP2 was used as the calculation level and 6-31G* was used as the basis function.

We first confirmed the correlations between the experimental values shown in Table 3 and the ligand–protein IFIE-sums (Fig. 31): an R^2 of 0.40 was found, indicating a weak correlation. However, there were outliers in the data (as indicated by the arrows in Fig. 31). We therefore used a Smirnov Grubbs test (with a significance

Table 3 PDB ID and IC₅₀ of ligands (BACE1-small molecules complexes) used for FMO calculations (groups 1–5 correspond to those shown in Fig. 30)

Group	PDB ID	Lig. No	IC ₅₀ (nM)	Group	PDB ID	Lig. No	IC ₅₀ (nM)
1	3IN3	18	60	2	3KMY	37	200
	3IN4	19	30		3L38	38	200
	3IND	20	1,500		3L3A	39	420
	3INE	21	170	3	4J0P	40	51
	3INF	22	40		4J0T	41	28
	3INH	23	20		4J0V	42	435
	3OOZ	24	14		4J0Y	43	77
	4JOO	25	36,380		4J0Z	44	54
	4JP9	26	24		4J17	45	148
	4JPC	27	94		4J1C	46	12
4JPE	28	48	4J1F		47	49	
2	2OHK	29	2,000,000		4J1E	48	19
	2OHL	30	2,000,000		4J1K	49	13
	2OHP	31	94,000	4J1I	50	40	
	2OHQ	32	25,000	4	4FRI	51	2,850
	2OHR	33	100,000		4FRJ	52	280
	2OHS	34	40,000		4FRK	53	8
	2OHT	35	9,100	5	3MSK	54	26,000
	2OHU	36	4,200		3MSL	55	7,000

level of 0.05) to eliminate the outliers. Consequently, the R² value improved to 0.74, suggesting a strong association between the experimental values and IFIEs (Fig. 32). Thus, FMO-calculated IFIEs could likely be used to predict the interactions between BACE1 and its inhibitors.

In summary, we have found a strong association between FMO-calculated IFIE-sums and experimental values in systems for MDM2 inhibitors and BACE1 inhibitors. Therefore, in these systems, the use of IFIE-sum values may promote the design of inhibitors with more potent inhibitory activity. In future research, by carrying out PIEDA and other relevant analyses, the usefulness of the FMO method will be demonstrated in actual drug discovery studies by acquiring data on structural modifications with stronger activities, and by conducting similar analysis using different proteins.

Group 1

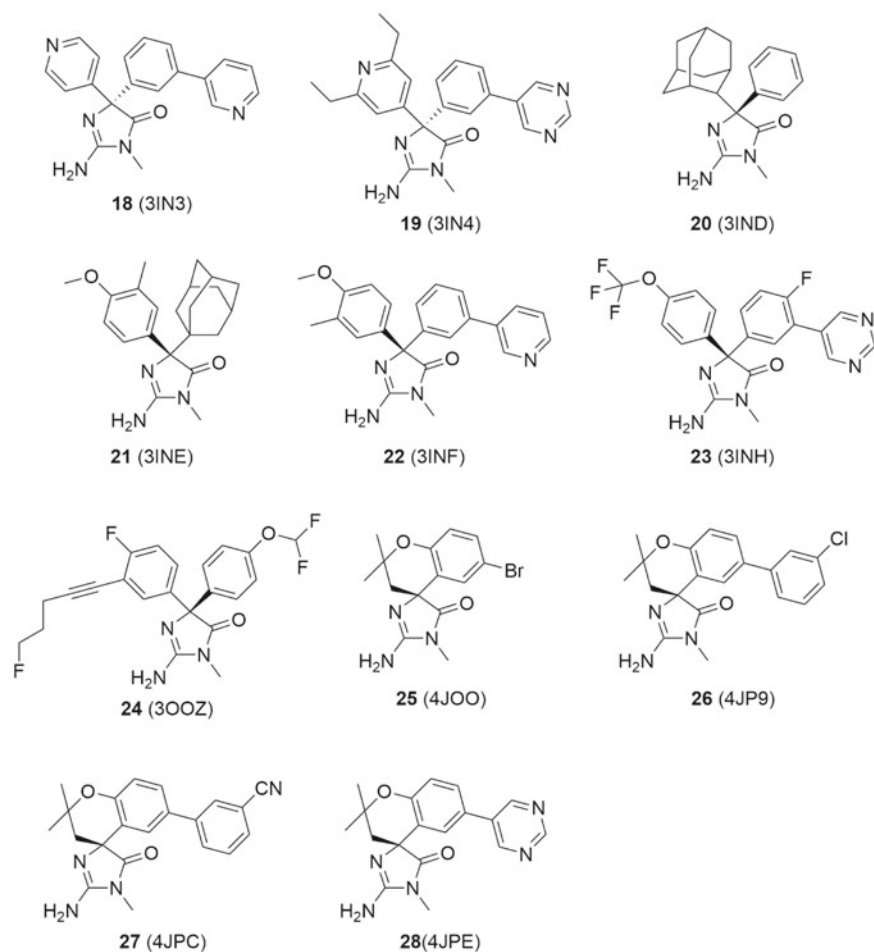
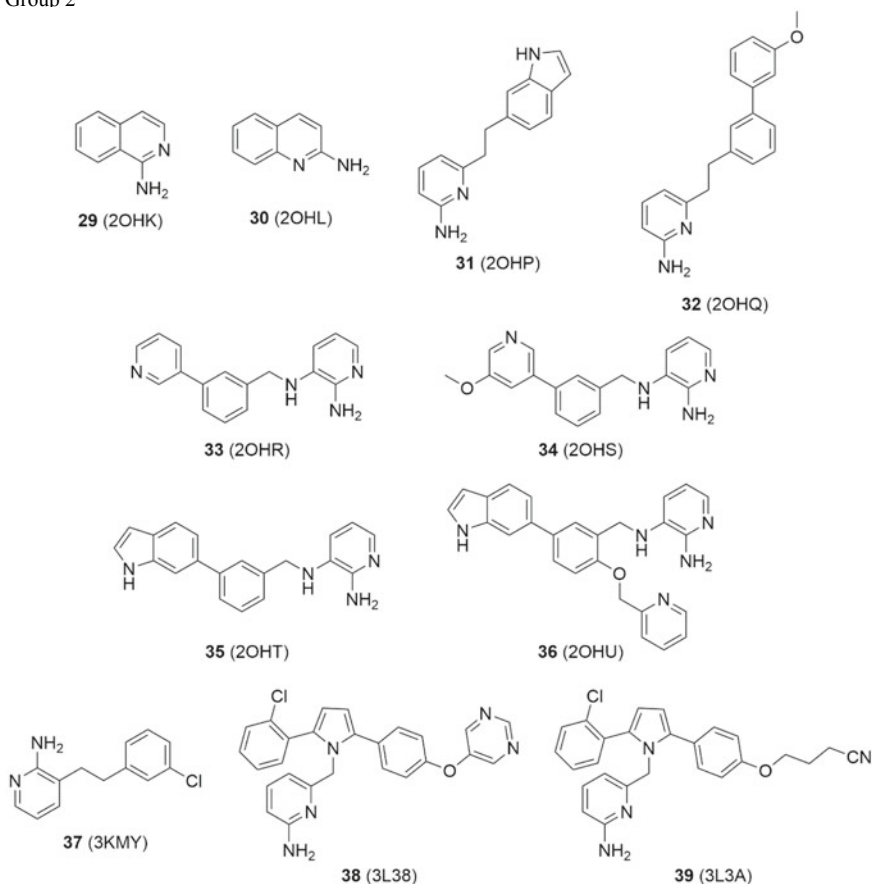


Fig. 30 Groups 1–5 containing the ligand structures of the BACE1-small molecules complexes used for FMO calculations

6 The FMO-D-KBDD WG

The FMO-D-KBDD WG is a collaborative WG that uses FMO methods to analyze the results of docking simulations and MD simulations from the KBDD. The KBDD was established in 2012 as an industry–academia cooperation committee that enables industrial and academic researchers to gather in order to evaluate and develop cutting-edge computational approaches that would be too difficult to tackle alone. Over the past few years, the KBDD has focused on research into protein–ligand-binding free energy calculations and docking pose predictions using MD-based approaches

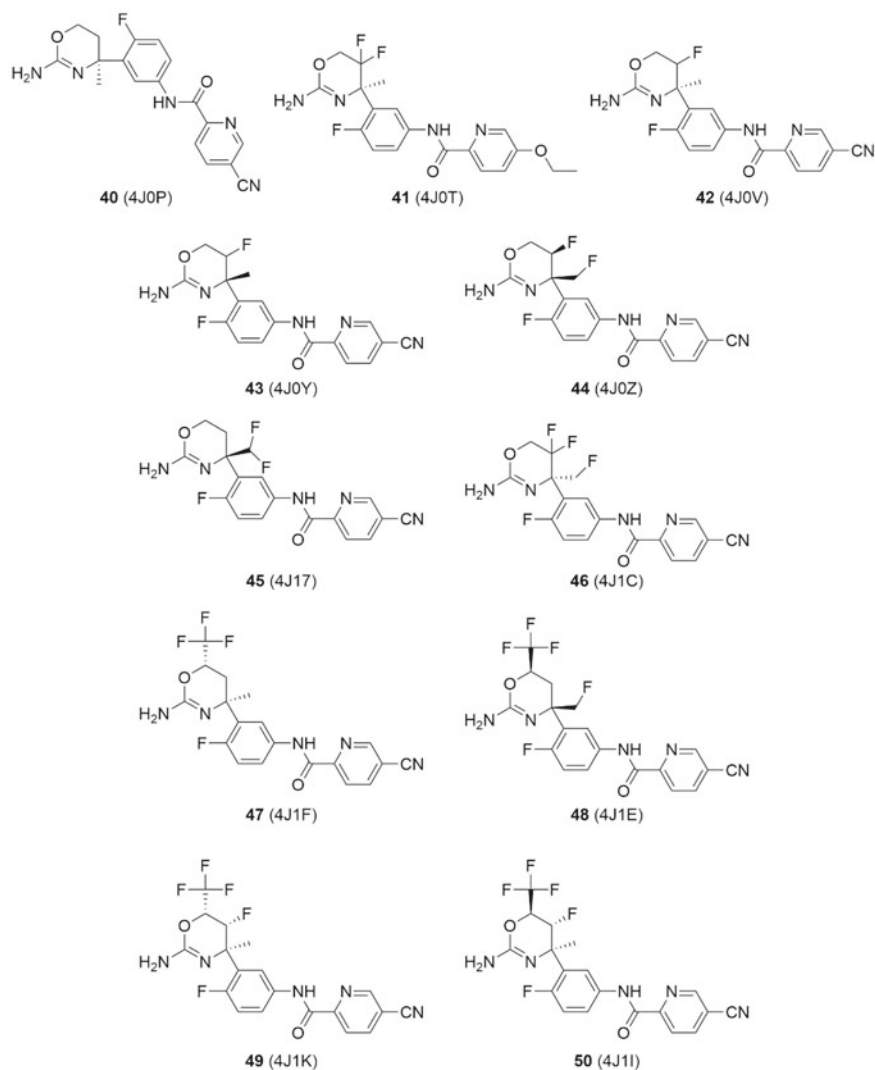
Group 2

**Fig. 30** (continued)

such as MP-CAFEE [97, 98], MM-PB(GB)SA [99, 100], and multiconformational MD simulations [101, 102].

The objective of the FMO-DD-KBDD WG is to effectively utilize KBDD simulation results and revisit protein–ligand-binding free energy calculations and docking pose predictions using FMO-based methods. As previously discussed, protein–ligand interaction energies obtained using FMO simulations can be used to predict protein–ligand-binding affinities [40, 103, 104]. However, FMO-based interaction energies are often obtained via single conformations. In the FMO-DD-KBDD WG, MD trajectories determined by the KBDD are used to perform FMO calculations against multiple protein–ligand complexes, and the effect of using multiple conformers and solvation effects associated with explicit water molecules are investigated in a manner similar to that introduced later in this chapter. Furthermore, docking pose predictions

Group 3

**Fig. 30** (continued)

obtained using MM-PB(GB)SA can be revisited by applying FMO-based interaction energies.

As an example, we describe the prediction of docking poses using FMO-based interaction energies. The docking poses described here were provided by Araki and coworkers from the KBDD, and all FMO calculations were performed using the K supercomputer with FMO2-MP2/6-31G* in vacuo. Docking simulations

Group 4, Group5

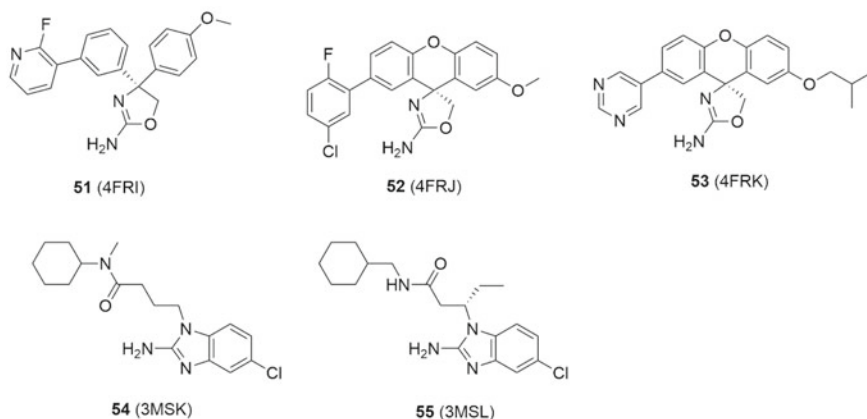


Fig. 30 (continued)

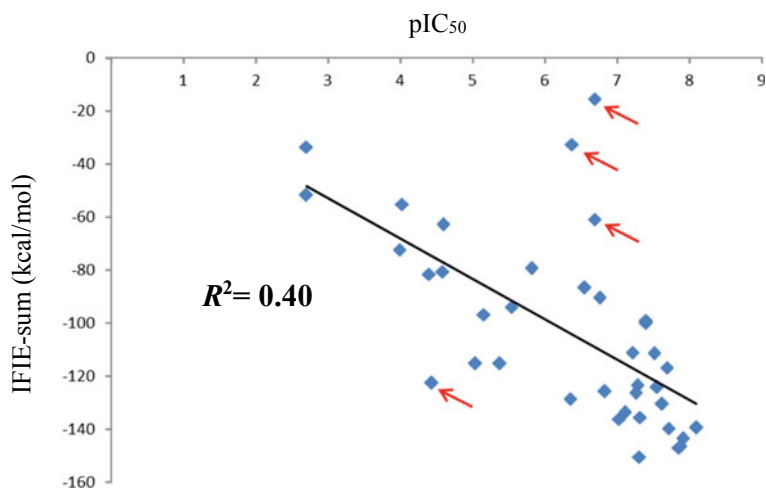


Fig. 31 Correlation between pIC_{50} and the summation of IFIEs (IFIE-sum) for BACE1 inhibitors before elimination of outliers in the data (indicated by red arrows)

were performed using 10 CDK2 kinase ligands (Fig. 33) against a protein structure extracted from a representative cocrystal structure, and 5–11 decoy poses for each ligand were obtained. The docking simulations were performed using Glide [105–107], implemented in Schrödinger software.

The docking poses were evaluated using five different scoring methods: (1) docking scores, (2) MM-PBSA binding free energies, (3) FMO-based interaction energies (i.e., IFIEs), (4) dispersion energy contributions of PIEDA (ΔE_{DI}), and

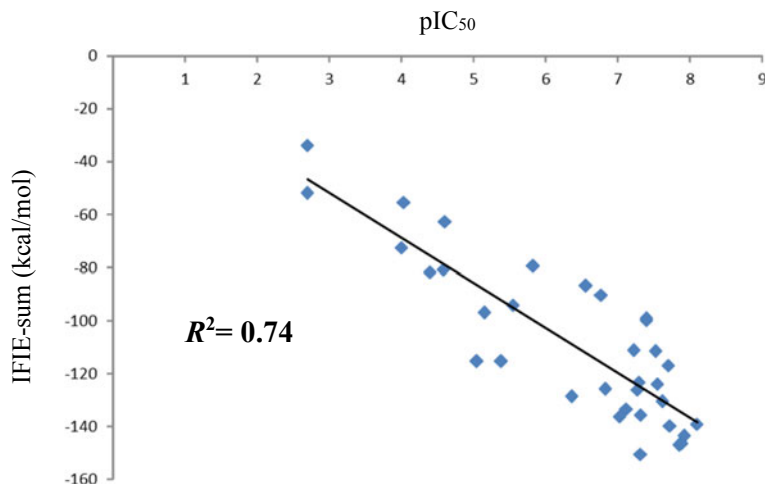


Fig. 32 Correlation between pIC_{50} and the summation of IFIEs (IFIE-sum) for BACE1 inhibitors after elimination of the outliers shown in Fig. 31

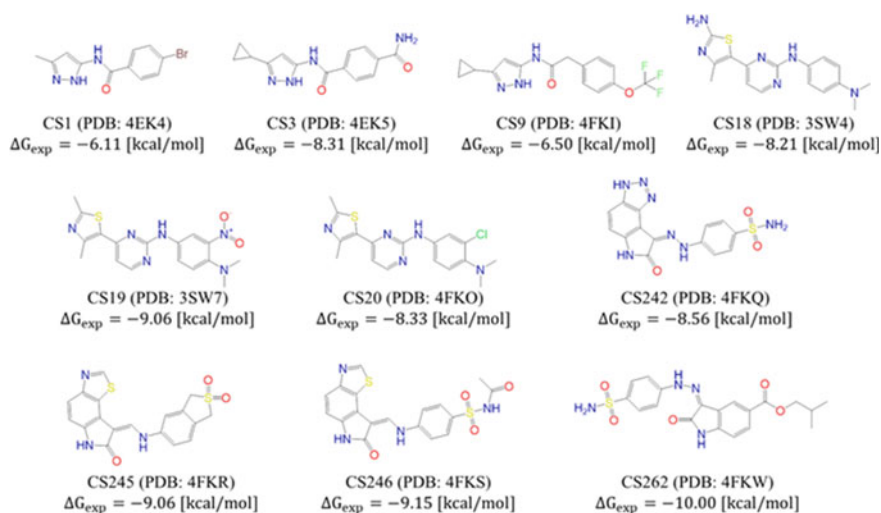


Fig. 33 Ten CDK2 kinase ligand structures and experimentally determined ΔG values taken from the literature [98]. PDB codes are shown in parentheses

(5) IFIEs with desolvation effects incorporated using the PBSA terms from classical MM-PBSA (FMO+MM-PBSA). Here, the dispersion energy contribution of PIEDA, ΔE_{DI} , was also investigated because this energy term exhibited the best correlation between the experimental and calculated binding affinities of IFIE and the four energy contributions of PIEDA (namely electrostatic, exchange repulsion, dispersion, and

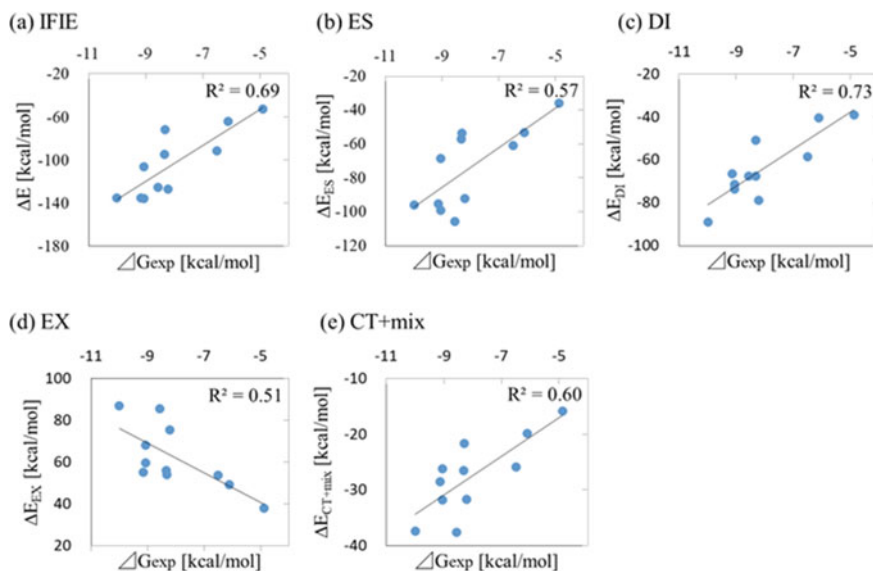


Fig. 34 Correlations between experimentally measured binding free energies and calculated FMO-based interaction energies. FMO calculations were performed against the cocrystal structures of CDK2 ligands shown in Fig. 33. Correlations are shown for FMO-based interaction energies of **a** IFIE (ΔE), which is the summation of all four energy contributions of PIEEDA, **b** electrostatic (ΔE_{ES}), **c** dispersion (ΔE_{DI}), **d** exchange repulsion (ΔE_{EX}), and **e** charge transfer plus higher-order mixed terms (ΔE_{CT+mix}). An additional ligand, CS12, which is not included in Fig. 33, is included in each graph

charge transfer with higher-order mixed terms) (Fig. 34). The averaged MM-PBSA binding free energy over a few tens of nanoseconds of MD simulations for each ligand was incorporated. The root-mean-square-deviations (RMSDs) of the docking poses with respect to the X-ray binding poses were also calculated, and the RMSD values corresponding to the lowest binding energies of the five scoring methods were compared (Table 4). The docking poses were assumed to be correct if the RMSD was $<2.0 \text{ \AA}$. Finally, the accuracy, in terms of retrieving the correct binding poses for each scoring method, was evaluated.

The docking score was the most successful method for retrieving the correct binding pose with an accuracy of 100%. MM-PBSA and ΔE_{DI} were also relatively successful methods with accuracies of 80%. Finally, FMO+MM-PBSA and IFIE methods exhibited accuracies of 70 and 50%, respectively. However, incorporating desolvation effects using MM-PBSA and IFIE improved the accuracy of retrieving the correct binding pose, and using ΔE_{DI} returned results that are comparable to those of FMO+MM-PBSA, even though no such desolvation energies were incorporated. The correlations between MM-PBSA desolvation energies, ΔE_{solv} , and various energy contributions of FMO-based interaction energies for all docking poses tested in this study are shown in Fig. 35. With ΔE_{solv} , the best correlation ($R^2 = 0.46$) was obtained with $\Delta E_{ES,EX,CT+mix}$, where only the dispersion energy, ΔE_{DI} ,

Table 4 Summary of docking pose predictions for CDK2. RMSD values (in Å) are shown for each scoring method (see text for details of methods). The lowest RMSD values obtained by the docking simulation represent the best RMSDs for each ligand

Ligand ID	Best RMSD	Docking score	MM-PBSA	FMO (IFIE)	FMO (DI)	FMO (IFIE) + MM-PBSA
CS1	0.7	0.7	0.7	7.9	7.9	0.7
CS3	0.9	1.1	0.9	0.9	0.9	0.9
CS9	1.7	2.0	2.0	8.5	2.0	1.7
CS18	1.0	1.0	1.0	6.3	6.3	6.3
CS19	1.0	1.0	1.0	7.8	1.0	7.8
CS20	0.9	0.9	2.3	6.8	0.9	6.8
CS242	0.3	0.3	3.5	0.3	0.3	0.3
CS245	1.1	1.9	1.1	1.9	1.9	1.9
CS246	0.7	1.1	0.7	1.2	1.2	1.0
CS262	0.3	0.3	0.3	0.3	0.3	0.3
Accuracy (%)		100	80	50	80	70

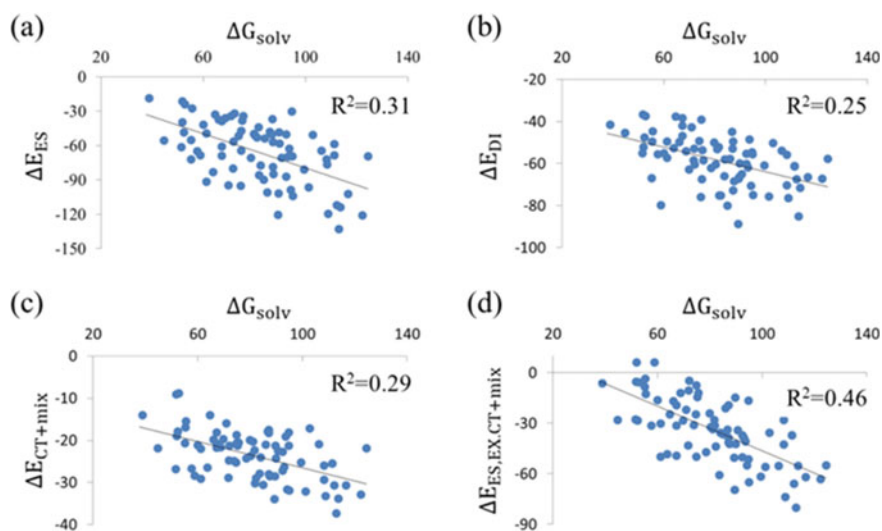


Fig. 35 Correlations between the desolvation free energy, ΔG_{solv} , obtained by MM-PBSA method and FMO-based interaction energies. Correlations are shown for FMO-based interaction energies of **a** electrostatic (ΔE_{ES}), **b** dispersion (ΔE_{DI}), **c** charge transfer plus higher-order mixed terms ($\Delta E_{\text{CT}+\text{mix}}$), and **d** summation of ΔE_{ES} , ΔE_{EX} , and $\Delta E_{\text{CT}+\text{mix}}$ ($\Delta E_{\text{ES,EX,CT}+\text{mix}}$), respectively. The correlation coefficient for exchange repulsion was $R^2 = 0.05$ and this data was excluded from the figure for clarity. Correlations were obtained using all docking poses described in the text. Units are kcal/mol

was omitted from the FMO-based interaction energy. The exclusion of electrostatic, exchange repulsion, and charge transfer plus higher-order mixed energy terms from the FMO-based interaction energies, and the use of dispersion energy alone, may have accounted for the desolvation effect to some extent.

Our results do not suggest that any one scoring method tested here is superior to another. However, in this particular example, the best performance for docking pose prediction was obtained by calculating docking scores. Nevertheless, FMO-based methods should still be useful for pose predictions because they enable the evaluation of weak interactions [108, 109] (such as π - π and CH/ π interactions) that are difficult to evaluate using MM-based methods.

Currently, the FMO-DD WG is focusing on docking pose predictions using targets other than CDK2. Thus, we are expending considerable effort on predicting protein–ligand-binding affinities using MD trajectories generated by the KBDD consortium. The ongoing work of the FMO-DD WG should enhance our understanding of FMO methods. Furthermore, comparing results from two different consortiums using different computational approaches should provide synergy that will generate new ideas for more practical uses of computer simulations.

7 The Development WG

Since the establishment of the FMO drug design consortium in 2014, the development WG has developed and consolidated the foundations of various methods and databases to enhance the efficiency of drug design using the FMO method. In this section, we describe an automated FMO calculation protocol and an FMO database for storing large quantities of corresponding FMO calculation results. Moreover, we provide outlines for binding affinity prediction methods such as FMO+MM-PBSA, FMO-grid, and data collection for artificial intelligence (AI) force fields.

The purpose of the development WG can largely be categorized into the establishment of two platforms. First, the group aims to develop a platform that will enable numerous users to implement FMO calculations and search and analyze calculation results. Second, it aims to develop FMO-related methods to enable high accuracy affinity prediction and methods to design drugs with promising structures. Related to the first aim is the development of an automated FMO calculation protocol (“Auto-FMO protocol”), which facilitates use of the FMO method by inexperienced users and promotes the dissemination of the FMO method. The protocol also allows experienced users to perform FMO calculations on many structures, thereby increasing the efficiency of drug design. Given the high number of FMO calculation results now available, a database for storage of results was necessary; hence, we designed and released the “FMO database,” which includes calculation settings, IFIE/PIEDA values, and analysis and visualization tools.

Related to the second aim described above, we are investigating highly accurate affinity prediction methods by addition of a solvent continuum model (Poisson–Boltzmann) and surface area approximation (i.e., PBSA) to IFIE values. The

FMO+MM/PBSA method, which uses MM-based PBSA, has already been shown to be useful. In addition, we have begun to examine FMO-PBSA, in which FMO-based PB is implemented. Moreover, we have prepared data for the refinement of protein structures using the FMO method, and we have developed an FMO force field using the FMO database along with AI technology. In the following sections, we provide outlines for each of the aforementioned programs and systems, and we discuss our outlook for future developments. Some achievements of the development WG, such as FMO+MM/PBSA and an AI model to predict FMO partial charges, are also explained in other chapters.

7.1 *Auto-FMO Protocol*

When implementing FMO calculations, preprocessing and determining the appropriate FMO settings for given protein–ligand complex structures can be difficult, even for researchers who regularly conduct quantum chemical calculations. For example, appropriate procedures must be applied for pretreating protein structures, determining the presence or absence of water, establishing the fragmentation of the FMO calculations, selecting a level for the basis function and electron correlation, implementing the calculations, and extracting and analyzing the results. A good example is water molecules and protonation/deprotonation states; selecting only one appropriate setting is difficult, even for FMO experts. Moreover, in some cases, multiple settings and conditions should be used. Thus, completing these preprocessing procedures prior to conducting FMO calculations is a hurdle for new researchers, and such difficulties have impeded the widespread use of the FMO method. In some cases, FMO calculations can be performed manually for only a few protein structures; however, in the drug design process, more than 10 calculations are required. Consequently, automation becomes important even for FMO experts; automation of FMO calculations was also essential for the creation of the FMO database.

Figure 36 shows a schematic diagram outlining the developed automated FMO calculation protocol (hereinafter, referred to as the “Auto-FMO protocol”) [4]. In this protocol, we first prepare an input by converting protein structures into the mdb file format for MOE. We then implement the supplementation of disordered regions in protein structures, protonation/deprotonation, tautomerism assignments, structural optimization by MM, and structural optimization by quantum mechanics/MM (QM/MM). When structures have been obtained for the FMO calculation, we simultaneously implement FMO or MM-PBSA calculations. Subsequently, we extract the IFIE data from a file containing the calculation results, perform PIEDA, and obtain the results in a text format (e.g., an Excel spreadsheet).

By using the Auto-FMO protocol, we tested, for example, 149 protein structures with estrogen receptors α and p38 α [9]; the completion rate of the FMO calculation in this case was 99%. Based on a comparison of IFIE values from manual calculations, excluding 17 structures that failed because of the protonation/deprotonation assignments, we obtained about 90% correlation. Thus, the Auto-FMO protocol is

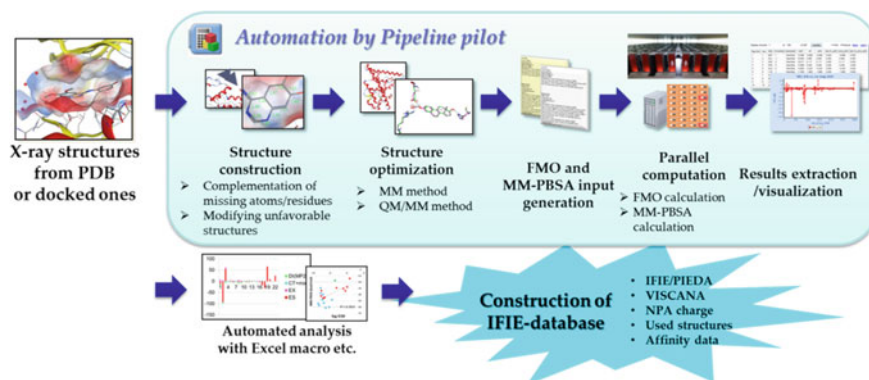


Fig. 36 Schematic diagram showing the flow of the Auto-FMO protocol

an essential tool for future FMO calculations. Nevertheless, several aspects of the protocol still require improvement. First, considering the pretreatment of the protein and/or ligand structure, the assignment differs from the manually obtained result in approximately 5–10% of cases. The MOE Protonate3D function is currently used for the assignments; however, in the future, we plan to develop a prediction method based on AI. Second, because the Auto-FMO protocol depends upon MOE and Pipeline Pilot, which are both commercial software programs, researchers without licenses for these programs cannot use the protocol. Thus, there is a need to combine AI with a free tool such as KNIME in future developments.

The ultimate purpose of the Auto-FMO protocol is to enable “on the fly” FMO calculation services. For instance, when a structural biologist determines a new protein structure, they could input the structural data to the homepage of our service and receive an FMO calculation result within 1 day. We aim to actualize this service through cooperation with a public supercomputer project such as the Fugaku project and subsequent projects.

7.2 FMO Database

The FMO database [110], publicly released on February 21, 2019 is the world’s first database of ab initio FMO calculation results for entire protein structures. As of June 2020, the FMO calculations had been compiled for 2,589 protein structures including 1,102 unique PDB entries. In the database, users can search and browse calculation results by PDB ID, protein name, or ligand name. The database can also perform basic analytical functions. The top page and a search result are shown in Figs. 37 and 38, respectively. Users can search entries by various methods such as ID, keyword, and blast search of amino acid sequences. As well as the ID, PDB ID, FMO DB ID, and Uniprot ID can be used to search the database. In the search

FMOOD The database of quantum mechanical data based on the FMO method
 Last updated: 2020-05-23
 All entries: 2580
 Number of unique PDB entries: 1102

Information ID Search Keyword Search Blast Search

2020.4.17 **COVID-19** FMO data for COVID-19 related proteins have been released on Apr 17, 2020. [here](#).

Category

- COVID-19(133)
 - Papain like protease(5)
 - Main protease(88)
 - Nsp9 RNA binding protein(4)
 - ADP-ribose phosphatase(8)
 - RNA dependent RNA polymerase(5)
 - Endonuclease(2)
 - 2'-O-ribose methyltransferase(2)
 - Seiki protein(8)
 - Nucleocapsid protein(8)
 - Other SARS-CoV-2(3)
- X-ray All Entries(1303)
 - Kinase_c38(188)
 - Kinase_Aurora(46)
 - Kinase_CHK1(43)
 - Nuclear receptor_ERα(60)
 - Nuclear receptor_ERβ(53)
 - Acetabularia(709)
- NMR All Entries(104)
 - TrxGaps(76)
- MD All Entries(1081)
 - TrxGaps(991)
- ElectronMicroscopy All Entries(7)

News: FMO data for COVID-19 related proteins

Search Sample

Keyword Search: COVID-19 [Set Value Of Input](#)
 PDB ID Search: 1ERE [Set Value Of Input](#)
 FMOOD ID Search: 5P4NP [Set Value Of Input](#)
 UniProt ID Search: P03372 [Set Value Of Input](#)
 Keyword Search(Target): Estrogen receptor alpha [Set Value Of Input](#)
 Keyword Search(Ligand): NBI [Set Value Of Input](#)
 Keyword Search(Ligand:DrugName): Diethylstilbestrol [Set Value Of Input](#)
 Keyword Search(Ligand:CAS Number): 56-53-1 [Set Value Of Input](#)
 Blast Search: Sequence of 3RIN / E-Value Cutoff E-148 [Set Value Of Input](#)

All of calculated data by FMO Drug Design (FMOOD) Consortium are licensed under CC BY-SA 4.0. [Citing Us.](#)

Copyright © 2018 FMOOD Consortium. All Rights Reserved.

Fig. 37 Top page of the FMO database

Fig. 38 Example search result from the FMO database. **a** Hit entries (part of the search results). **b** Total IFIE and PIEDA of hit entries

results, hit entries are displayed with simple calculation settings (Fig. 38a) and total IFIE and PIEDA values of the hit entries are summarized (Fig. 38b). When the user selects the PDB ID shown in a large blue font on the search results page, details of the entry appear (Fig. 39). For analytical functions for the IFIE and PIEDA values from single FMO calculation results, the user can also create graphs with data selected according to the distance and the strength from the ligand (Fig. 40). Moreover, data can be downloaded in a text format, such as an Excel spreadsheet, and the analysis results can be downloaded in a graphical format.

The FMO database is a repository for highly precise protein–ligand interaction energy values. We expect it to be used in numerous research fields, including for the clarification of molecular recognition mechanisms in biology, the development of new molecular force fields using AI, and drug design. Currently, an AI molecular force field that considers QM-based interactions is being developed using the information in the database (we discuss this in Sect. 7.4).

7.3 Structure Refinement by FMO

As of November 2018, from the 146,093 experimentally determined protein structures listed in the PDB, the number of structures with a resolution $\leq 1 \text{ \AA}$ is 637 (0.44%). The majority of the structures (124,354 structures, 87.9%) have a resolution $\geq 1.6 \text{ \AA}$, while 10,929 structures (7.5%) have very poor resolutions ($\geq 3.0 \text{ \AA}$). For X-ray crystallographic analysis, the coordinates for each atom therefore cannot be determined from diffraction data alone, with the exception of some cases with a resolution $< 1 \text{ \AA}$. Hence, the coordinates are determined by creating models for structures that have a high compatibility with electron-density data obtained from refraction measurements. This process is repeated several times via an optimization calculation to increase the compatibility with the electron-density data so that it lies within a range in which the MM energy value is low. For resolutions $\geq 3.0 \text{ \AA}$, even benzene rings become difficult to distinguish, and correctly determining coordinates becomes a major challenge [111].

Furthermore, when protein–ligand interaction energies are calculated using a quantum chemical calculation such as the FMO method, great differences can arise in the resulting energy values, even when resolutions are $\sim 0.1\text{--}0.2 \text{ \AA}$. With amino acid residues or ligand molecules, which have a formal charge, the difference can exceed several tens of kcal/mol, which clearly hinders accurate activity prediction and drug design. In such cases, it can be effective to structurally optimize the crystal structure using a QM calculation. Figure 41 shows a comparison of the structural optimization results using MM with those for QM using a low-resolution crystal structure as the initial structure. The cyan-colored MM-optimized structure differs from the experimentally determined high-resolution structure. However, the purple-colored QM-optimized structure is similar to the high-resolution structure. Thus, the QM-optimized structure will be more useful for predicting the inhibitory activity of drugs. In the example of Pim1 [104], the correlation coefficient of the energy for the

1ERE-D

FMO DB ID: 5P4NP
 Calculation Name: 1ERE-D-Xray7
 Preferred Name: Estrogen receptor alpha
 Target Type: SINGLE PROTEIN
 Ligand Name: estradiol
 ligand 3-letter code: EST
 PDB ID: [1ERE](#)
 ChEMBL ID: [CHEMBL206](#)
 UniProt ID: [P03372](#)
 Base Structure: X-ray
 Registration Date: 2017-02-24
 Reference:

 IFIE MAP

 Download Files

Modeling method

Optimization	MOE:Amber10EHT
Restraint	OptH
Protonation	MOE:Protonate3D
Complement	BioStationViewer:StructureComplementation (agonist template: 1A52)
Water	A bridging water among Glu353, Arg394 and ligand.
Procedure	Manual calculation

FMO calculation

FMO method	FMO2-MP2/6-31G(d)
Fragmentation	Auto
Number of fragment	238
LigandCharge	EST=0
Software	MIZUHO/ABINIT-MP 4.0(SMP)

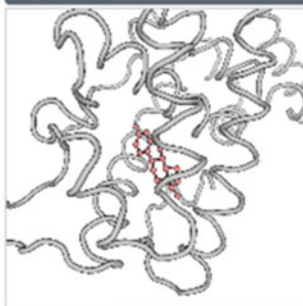
Total energy (hartree)

FMO2-HF: Electronic energy	-3151388.208186
FMO2-HF: Nuclear repulsion	3053174.845449
FMO2-HF: Total energy	-98213.362736
FMO2-MP2: Total energy	-98490.505804

Ligand binding energy

IFIE [kcal/mol]	PIEDA [kcal/mol]				Charge transfer value [e]
IFIE SUM	ES	EX	CT+mix	DI(MP2)	q(I=>J)
-127.936	-141.441	151.973	-80.080	-58.392	0.192

3D Structure

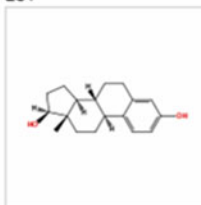


Snapshot

GLU471 DIST:26.222 Total:0.024 DI_MP2:0.000

Ligand structure

EST



Ligand Interaction

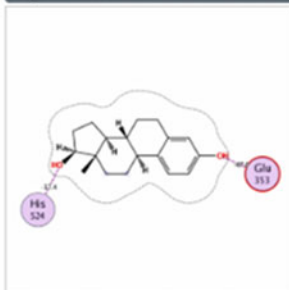


Fig. 39 Details from an example entry in the FMO database



Fig. 40 PIEDA of user-specified fragments (residues)

measured IC_{50} (log scale) values and the FMO+MM/PBSA result was only $R^2 = 0.24$ when using an MM-optimized structure, that is, prediction accuracy was poor. However, when QM optimization was used instead, a significant improvement in the coefficient to $R^2 = 0.85$ was observed, that is, a practical level of accuracy had been achieved.

At the QM level, the QM/MM method, FMO method, and full QM method (shown in Table 5) can be utilized to optimize protein structures. The full QM method utilizes

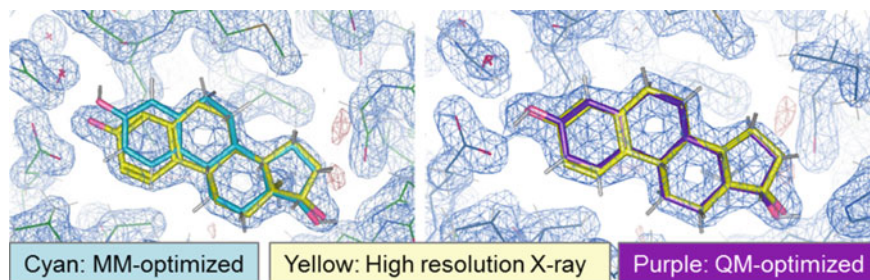


Fig. 41 Importance of quantum mechanics (QM) optimization vs. molecular mechanics (MM) optimization for the refinement of protein structures

Table 5 Comparison of quantum mechanics (QM) optimization methods

	QM/MM	FMO	Full QM
Calculation Cost using 250 res. Protein (HF/6-31G*)	50 h @1 node (3 res. QM region)	800 h @1 node (3 res. Opt region)	Realistically impossible with current resources
Pros	<ul style="list-style-type: none"> Reasonable calculation cost 	<ul style="list-style-type: none"> Accuracy is comparable with full QM Energy decomposition (IFIE, PIEDA) is possible 	<ul style="list-style-type: none"> High accuracy
Cons	<ul style="list-style-type: none"> Very low accuracy for MM region The boundary between QM region and MM region is distorted Energy decomposition is impossible 	<ul style="list-style-type: none"> High calculation cost 	<ul style="list-style-type: none"> Realistically impossible with current resources Energy decomposition is impossible

a normal *ab initio* QM calculation for the entire protein. However, given the performance level of current computers, the computational time is substantial even for single-point calculations in which the structure is not optimized; thus, optimization is nearly impossible. However, the QM/MM method and FMO method can achieve optimization. In the QM/MM method, only a small region of the protein, the “QM region,” is applied in the QM calculation, while the remaining region is evaluated using MM; consequently, the calculation time is greatly reduced relative to that of the full QM method, e.g., a calculation time of ~50 h is possible. However, the accuracy in the MM region is poor, the structure of the boundary between the QM and MM regions is distorted, and energy decomposition analysis such as PIEDA cannot be performed. The FMO method performs a QM calculation of the entire protein; thus,

it does not have the same disadvantages as the QM/MM method. However, the FMO calculation time for structural optimization is at least tenfold greater than that for the QM/MM method.

With support from the Japan Agency for Medical Research and Development (AMED), the development WG is currently developing a program for increasing the speed of structural optimization calculations using the FMO method. In this method, the self-consistent charge (SCC) calculation is conducted for conventional optimization, while a frozen domain method is used for regions far from the ligand; in this process, SCC calculation results from the initial calculation are applied to subsequent calculations. SCC calculations for regions far from the ligand were previously a rate-limiting factor during computation, although only the electron density environment is provided for the ligand. In a preliminary test, using IFIEs for the calculation result produced accurate results with errors within an acceptable range, and the speed was increased five- to ten-fold. Moreover, the effectiveness of this method increases as protein size increases.

To increase the calculation speed, the FMO method can be combined with DFT; this approach can accelerate the calculation by 30-fold compared with conventional FMO calculations [112]. However, this approach has drawbacks, for example, poor accuracy in the electron correlation. Thus, we plan to assess and refine this method in the future.

7.4 Data Preparation for FMO-Based Partial Charge and Force Field AI Models

With current MM calculations, electrostatic interactions are independently treated, while the remaining interactions, such as dispersion forces, are modeled using Lennard–Jones type potential functions. The Lennard–Jones potential is a functional form in which the only variable is the interatomic distance and (6, 12)-potential, which expresses gravity by the sixth power and repulsion by the twelfth power. However, in reality, a large number of interactions, including the dispersion force, are influenced by the shape of electron orbitals and are not determined solely by interatomic distances. Moreover, interactions with considerable strength and those that exhibit an angular dependence, such as π interactions, the orbital interaction of the S atom, and charge-transfer interactions, are not taken into consideration. Therefore, the MM interaction calculation method gives results that are only a rough approximation. To obtain highly accurate activities or binding affinity predictions that can be applied to drug design, a new molecular force field with higher accuracy is necessary.

In recent years, AI models have been developed that surpass the thinking ability of humans; Google's Alpha Go and Alpha Zero are prime examples of such technologies. In addition to the innovation of machine-learning technologies, such as deep learning and reinforcement learning, the advent of big data and high-performance

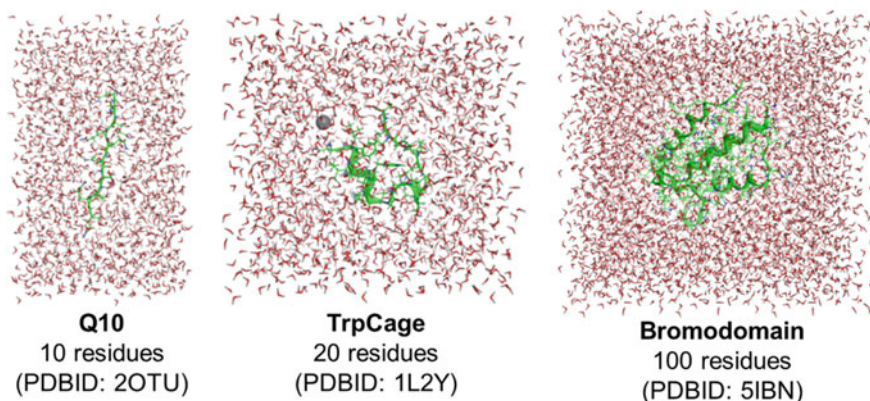


Fig. 42 The molecular systems used for training FMO-based partial charge artificial intelligence models

computing (e.g., GPU) has also contributed to technological advances. In the field of FMO, AI molecular force fields [113] that consider QM interactions are being actively researched because full QM calculations for large systems require substantial calculation times. Moreover, although studies have been reported for simple systems [114] such as water molecules, an AI molecular force field that includes proteins has yet to be realized. The FMO method, as well as the FMO database in which FMO calculation results are registered, is ideal for handling fundamental data. In our research laboratory, we are currently developing an AI molecular force field in cooperation with the AI drug design consortium of Okuno et al. (Life Intelligence Consortium, LINC [115]). Using four systems, consisting of the three molecular systems shown in Fig. 42 and enkephalin (which has five residues), we have conducted a 100 ns MD simulation and extracted 10,000 snapshots from the resulting trajectory file.

7.5 Future Perspectives for the “FMO Drug Design Platform”

Although we are currently developing platforms such as the Auto-FMO calculation protocol and FMO database, as well as developing the AI force field, for the FMO method to be consistent across numerous drug design fields, a greater number of methods must also be developed and integrated.

Figure 43 shows the overall FMO drug design platform that we aim to achieve. First, having obtained drug discovery target structures via X-ray analysis, nuclear magnetic resonance (NMR), or electron microscopy (or by using homology modeling or docking), the initial focus becomes structure quality. The homology model and docking model will be optimized based on the molecular force field. For experimentally determined structures based on X-ray analysis, NMR, or electron microscopy,

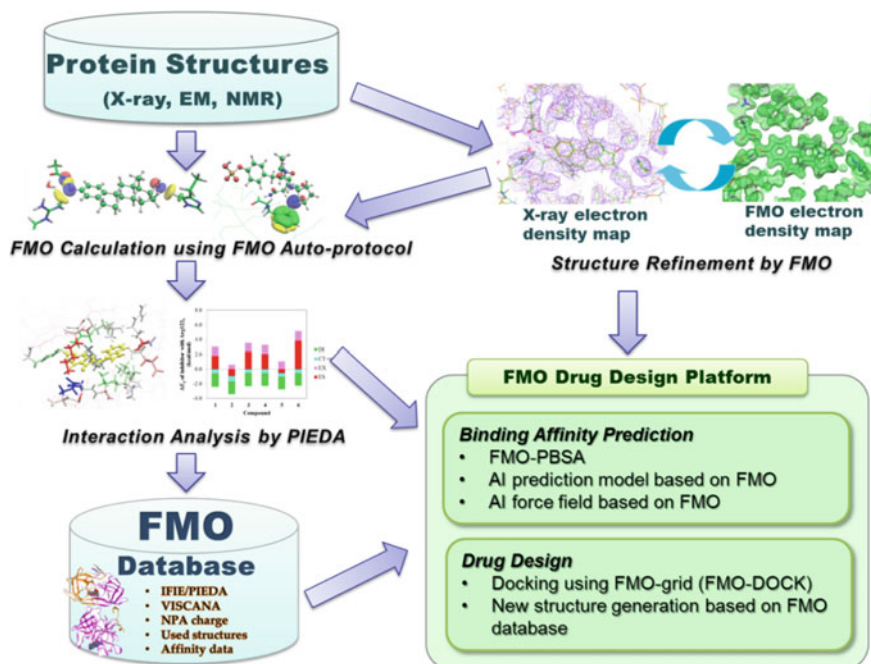


Fig. 43 Planned FMO drug design platform

which depend on X-ray refraction and NMR peak data, the atomic coordinates cannot be completely determined from experimental data alone. Thus, the atomic coordinates must be set to a position in which the molecular force field model and experimental data match. This coordinate information is sufficient for activity prediction based upon molecular force fields; however, for design methods that use QM calculations, such as the FMO method, coordinate information alone is insufficient. Thus, structure refinement by the FMO method described in Sect. 7.4 will be required. Using QM level protein structures, FMO calculations as well as IFIE analysis and PIEDA will be performed. High-quality data will enable us to accurately predict binding affinities using FMO-PBSA; the AI models will learn from the IFIE/PIEDA data. The newly developed AI force field, which is based on the FMO database and FMO interaction grid that uses high-speed FMO calculations by the frozen domain or FMO-DFTB [112], also contributes to drug design with methods including FMO-based docking and de novo structure generation considering QM interactions. The aforementioned tools and platforms will be developed in collaboration with the members of the FMO drug design consortium as well as other projects and consortiums.

Acknowledgments The authors thank Prof. Tatsuya Takagi, Dr. Midori Kamimura, and Dr. Tomonaga Ozawa for managing FMO and for conducting many research discussions. The authors also thank Dr. Chiduru Watanabe and Dr. Yoshio Okiyama for FMO calculations and assistance in the preparation of figures. The results of FMO calculations were obtained using the

HPCI system including the K computer at RIKEN, TSUBAME 3.0 at the Tokyo Institute of Technology, and FX100 at Nagoya University (project IDs: hp150160, hp160103, hp170183, hp180147, hp190119, and hp190133). Prof. Yuji Mochizuki supported the use of the ABINIT-MP program on HPCI. PIEDA calculations were conducted using the MIZUHO/BioStation software package. This research was partially supported by the Platform Project for Supporting Drug Discovery and Life Science Research (Basis for Supporting Innovative Drug Discovery and Life Science Research (BINDS)) from AMED under Grant Number JP20am0101113. The docking poses from Chapter 8.6 were provided by Dr. Mitsugu Araki and coworkers from the KBDD project by the Biogrid pharma consortium. K computer project IDs: hp150025, hp160010, and hp170036. The authors would like to thank Enago (www.enago.jp) for the English language review.

References

1. High performance computing infrastructure. <https://www.hpci-office.jp/folders/english>
2. Protein data bank. <https://www ww p d b . o r g />
3. ChEMBL database. <https://www.ebi.ac.uk/chembl/>
4. Watanabe C, Watanabe H, Okiyama Y, Takaya D, Fukuzawa K, Tanaka S, Honma T (2019) Development of an automated fragment molecular orbital (FMO) calculation protocol toward construction of quantum mechanical calculation database for large biomolecules. *Chem-Bio Inform J* 19:5–18
5. PDB bind. <https://www.pdbbind.org.cn/>
6. Wu P, Nielsen TE, Clausen MH (2015) *Trends Pharmacol Sci* 36:422
7. Cuadrado A, Nebreda AR (2010) *Biochem J* 429:403
8. Pearlman D (2005) *J Med Chem* 48:7796
9. Sheng Y, Watanabe H, Maruyama K, Watanabe C, Okiyama Y, Honma T, Fukuzawa K, Tanaka S (2018) *Comput Struct Biotech J* 16:421
10. Maruyama K, Sheng Y, Watanabe H, Fukuzawa K, Tanaka S (2018) *Comput. Theor Chem* 1132:23
11. Klema V, Laud A (1980) *IEEE Trans Automat Contr* 25:164
12. Kleibergen F, Paap R (2006) *J Economet* 133:97
13. Brand M (2006) *Linear Algebra Appl* 415:20
14. De Lathauwer L, De Moor B, Vandewalle J (2000) *SIAM J Mat Anal* 21:1253
15. Greenacre MJ (1984) *Theory and applications of correspondence analysis*. Academic Press, London
16. NumPy. www.numpy.org
17. Kitaura K, Ikeo E, Asada T, Nakano T, Uebayasi M (1999) Fragment molecular orbital method: an approximate computational method for large molecules. *Chem Phys Lett* 313:701–706
18. Fedorov DG, Kitaura K (2009) *The fragment molecular orbital method: practical application to large molecular system*. CRC Press
19. Tanaka S, Mochizuki Y, Komeiji Y, Okiyama Y, Fukuzawa K (2014) Electron-correlated fragment-molecular-orbital calculations for biomolecular and nano systems. *Phys Chem Chem Phys* 16:10310–10344
20. Yagi Y, Hattori Y, Naoshima Y (2012) Large-scale quantum chemical calculation on the complexes of HIV-1 protease and inhibitors: a relationship of calculation energies with drug effects of inhibitors. *Trans Jpn Soc Simulat Tech* 4(2):41–50
21. Yagi Y, Tanaka T, Imagawa A, Moriya Y, Mori Y, Kimura T, Kamezawa M, Naoshima Y (2014) Large-scale biomolecular chemical computations toward the prediction of *Burkholderia cepacia* lipase enantioselectivity. *J Adv Simulat Sci Eng* 1(1):141–160
22. Yagi Y, Kimura T, Kamezawa M, Naoshima Y (2018) Biomolecular chemical simulations toward elucidation of the enantioselectivity and reactivity of lipases in organic synthesis. *CBI J* 18:21–31

23. Imai T, Miyazaki H, Hirose S, Hori H, Hayashi T, Kageyama R, Ohkubo H, Nakanishi S, Murakami K (1983) Cloning and sequence analysis of cDNA for human renin precursor. *Proc Natl Acad Sci USA* 80:7405–7409
24. Waterhouse A, Bertoni M, Bienert S, Studer G, Tauriello G, Gumienny R, Heer FT, de Beer TAP, Rempfer C, Bordoli L, Lepore R, Schwede T (2018) SWISS-MODEL: homology modelling of protein structures and complexes. *Nucl Acids Res* 46(W1):W296–W303
25. Bienert S, Waterhouse A, de Beer TAP, Tauriello G, Studer G, Bordoli L, Schwede T (2017) The SWISS-MODEL repository: new features and functionality. *Nucleic Acids Res* 45:D313–D319
26. Guex N, Peitsch MC, Schwede T (2009) Automated comparative protein structure modeling with SWISS-MODEL and Swiss-PdbViewer: a historical perspective. *Electrophoresis* 30:S162–S173
27. Benkert P, Biasini M, Schwede T (2011) Toward the estimation of the absolute quality of individual protein structure models. *Bioinformatics* 27:343–350
28. Bertoni M, Kiefer F, Biasini M, Bordoli L, Schwede T (2017) Modeling protein quaternary structure of homo- and hetero-oligomers beyond binary interactions by homology. *Sci Rep* 7:10480
29. Case DA, Darden TA, Cheatham TE III, Simmerling CL, Wang J, Duke RE, Luo R, Walker RC, Zhang W, Merz KM, Roberts B, Wang B, Hayik S, Roitberg A, Seabra G, Kolossváry I, Wong KF, Paesani F, Vanicek J, Wu X, Brozell SR, Steinbrecher T, Gohlke H, Cai Q, Ye X, Wang J, Hsieh M-J, Cui G, Roe DR, Mathews DH, Seetin MG, Sagui C, Babin V, Luchko T, Gusarov S, Kovalenko A, Kollman PA (2010) AMBER 11. University of California, San Francisco
30. Okiyama Y, Nakano T, Yamashita K, Mochizuki Y, Taguchi N, Tanaka S (2010) Acceleration of fragment molecular orbital calculations with Cholesky decomposition approach. *Chem Phys Lett* 490:84–89
31. Fedorov DG, Kitaura K (2007) Pair interaction energy decomposition analysis. *J Comput Chem* 28:222–237
32. Tsukamoto T, Kato K, Kato A, Nakano T, Mochizuki Y, Fukuzawa K (2015) Implementation of pair interaction energy decomposition analysis and its applications to protein-ligand systems. *J Comput Chem Jpn* 14:1–9
33. MIZUHO/BioStation Viewer 3.0, Mizuho information and research institute Inc. (2013)
34. Takeda R, Kobayashi I, Shimamura K, Ishimura H, Kadoya R, Kawai K, Kittaka A, Takimoto-Kamimura M, Kurita N (2017) Specific interactions between vitamin-D receptor and its ligands: ab initio molecular orbital calculations in water. *J Steroid Biochem Mol Biol* 171:75–79
35. Takeda R, Kobayashi I, Suzuki R, Kawai K, Kittaka A, Takimoto-Kamimura M, Kurita N (2018) Proposal of potent inhibitors for vitamin-D receptor based on ab initio fragment molecular orbital calculations. *J Mol Graph Model* 80:320–326
36. Terauchi Y, Suzuki R, Takeda R, Kobayashi I, Kittaka A, Takimoto-Kamimura M, Kurita N (2019) Ligand chirality can affect histidine protonation of vitamin-D receptor: ab initio molecular orbital calculations in water. *J Steroid Biochem Mol Biol* 186:89–95
37. Takeda R, Suzuki R, Kobayashi I, Kawai K, Kittaka A, Takimoto-Kamimura M, Kurita N (2018) Specific interactions between vitamin D receptor and ligand depending on its chirality: ab initio fragment molecular orbital calculations. *Chem-Bio Inform* 18:32–43
38. Kobayashi I, Takeda R, Shimamura K, Ishimura H, Kadoya R, Kawai K, Takimoto-Kamimura M, Kurita N (2017) Specific interactions between androgen receptor and its ligand: ab initio molecular orbital calculations in water. *J Mol Graph Model* 75:383–389
39. Suzuki S, Nakamura T, Saito R, Terauchi Y, Kawai K, Takimoto-Kamimura M, Kurita N (2020) Structural change of retinoic-acid receptor-related orphan receptor induced by binding of inverse-agonist: molecular dynamics and ab initio molecular orbital simulations. *Comput Struct Biotechnol J* (In press). <https://doi.org/10.1016/j.csbj.2020.06.034>
40. Fukuzawa K, Kitaura K, Uebayasi M et al (2005) Ab initio quantum mechanical study of the binding energies of human estrogen receptor α with its ligands: an application of fragment molecular orbital method. *J Comput Chem* 26:1–10

41. Fukuzawa K, Mochizuki Y, Tanaka S, Kitaura K, Nakano T (2006) Molecular interactions between estrogen receptor and its ligand studied by the ab initio fragment molecular orbital method. *J Phys Chem B* 110:16102–16110
42. Amari S, Aizawa M, Zhang J, Fukuzawa K, Mochizuki Y, Iwasawa Y, Nakata K, Chuman H, Nakano T (2006) VISCANA: visualized cluster analysis of protein-ligand interaction based on the ab initio fragment molecular orbital method for virtual ligand screening. *J Chem Inf Model* 46:221–230
43. Tanaka S, Watanabe C, Okiyama Y (2013) Statistical correction to effective interactions in the fragment molecular orbital method. *Chem Phys Lett* 556:272–277
44. Okiyama Y, Watanabe C, Fukuzawa K, Mochizuki Y, Nakano T, Tanaka S (2019) Fragment molecular orbital calculations with implicit solvent based on the Poisson-Boltzmann equation: II. Protein and its ligand-binding system studies. *J Phys Chem B* 123:957–973
45. Seki Y, Kato T, Furuishi T, Fukuzawa K, Yonemochi E (2018) Analysis of ligand binding specificity of estrogen receptor by the fragment molecular orbital method. *J Comput Chem Jpn* 17:160–162
46. Malamas MS, Manas ES, McDevitt RE, Gunawan I, Xu ZB, Collini MD, Miller CP, Dinh T, Henderson RA, Keith JC, Harris HA (2004) Design and synthesis of aryl diphenolic azoles as potent and selective estrogen receptor- β ligands. *J Med Chem* 47:5021–5040
47. Ivanov AA, Khuri FR, Fu H (2013) Targeting protein-protein interactions as an anticancer strategy. *Trends Pharmacol Sci* 34:393–400
48. Arkin MR, Tang Y, Wells J (2014) A, Small-molecule inhibitor of protein-protein interactions: progressing towards the reality. *Chem Biol* 21:1102–1114
49. Kitaura K, Sawai T, Asada T, Nakano T, Uebayasi M (1999) Pair interaction molecular orbital method: an approximate computational method for molecular interactions. *Chem Phys Lett* 312:319–324
50. Kitaura K, Morokuma K (1976) New energy decomposition scheme for molecular-interactions within Hartree-Fock approximation. *Int J Quantum Chem* 10:325–340
51. Levine AJ (1997) p53, the cellular gatekeeper for growth and division. *Cell* 88:323–331
52. McLure KG, Takagi M, Kastan MB (2004) NAD⁺ modulates p53 DNA binding specificity and function. *Mol Cell Biol* 24:9958–9967
53. Wu X, Bayle JH, Olson D, Levine AJ (1993) The p53-mdm-2 autoregulatory feedback loop. *Genes Dev* 7:1126–1132
54. Warnock LJ, Knox AA, Mee TR, Raines SA, Milner J (2008) Influence of tetramerisation on site-specific post-translational modifications of p53: comparison of human and murine p53 tumour suppressor protein. *Cancer Biol Ther* 7:1481–1489
55. Itahana Y, Ke H, Zhang Y (2009) p53 Oligomerization is essential for its C-terminal lysine acetylation. *J Biol Chem* 284:5158–5164
56. Lee AS et al (2003) Reversible amyloid formation by the p53 tetramerization domain and a cancer-associated mutant. *J Mol Biol* 327:699–709
57. Atz J, Wagner P, Roemer K (2000) Function, oligomerization, and conformation of tumor-associated p53 proteins with mutated C-terminus. *J Cell Biochem* 76:572–584
58. Moll UM, Petrenko O (2003) The MDM2-p53 interaction. *Mol Cancer Res* 1:1001–1008
59. Chène P (2003) Inhibiting the p53–MDM2 interaction: an important target for cancer therapy. *Nat Rev Cancer* 3:102–109
60. Oliner JD, Kinzler KW, Meltzer PS, George DL, Vogelstein B (1992) Amplification of a gene encoding a p53-associated protein in human sarcomas. *Nature* 358:80–83
61. Kumar SK et al (2003) Design, synthesis, and evaluation of novel boronic-chalcone derivatives as antitumor agents. *J Med Chem* 46:2813–2815
62. Miyazaki M et al (2013) Lead optimization of novel p53-MDM2 interaction inhibitors possessing dihydroimidazothiazole scaffold. *Bioorg Med Chem Lett* 23:728–732
63. De Turiso FGL et al (2013) Rational design and binding mode duality of MDM2-p53 inhibitors. *J Med Chem* 56:4053–4070
64. Holzer P et al (2015) Discovery of a dihydroisoquinolinone derivative (NVP-CGM097): a highly potent and selective MDM2 inhibitor undergoing phase I clinical trials in p53wt tumors. *J Med Chem* 58:6348–6358

65. Bogen SL et al (2016) Discovery of novel 3,3-disubstituted piperidines as orally bioavailable, potent, and efficacious HDM2-p53 inhibitors. *ACS Med Chem Lett* 7:324–329
66. Gonzalez AZ et al (2014) Selective and potent morpholinone inhibitors of the MDM2-p53 protein-protein interaction. *J Med Chem* 57:2472–2488
67. Gessier F et al (2015) Discovery of dihydroisoquinolinone derivatives as novel inhibitors of the p53-MDM2 interaction with a distinct binding mode. *Bioorg Med Chem Lett* 25:3621–3625
68. Gollner A et al (2016) Discovery of novel Spiro[3 H-indole-3,2'-pyrrolidin]-2(1 H)-one compounds as chemically stable and orally active inhibitors of the MDM2-p53 interaction. *J Med Chem* 59:10147–10162
69. Furet P et al (2016) Discovery of a novel class of highly potent inhibitors of the p53-MDM2 interaction by structure-based design starting from a conformational argument. *Bioorg Med Chem Lett* 26:4837–4841
70. Ding Y, Mei Y, Zhang JZH (2008) Quantum mechanical studies of residue-specific hydrophobic interactions in p53-MDM2 binding. *J Phys Chem B* 112:11396–11401
71. Kussie PH et al (1996) Structure of the MDM2 oncoprotein bound to the p53 tumor suppressor transactivation domain. *Science* 274:948–953
72. Chemical Computing Group Inc. (2004) Molecular operating environment (MOE). *Sci Comput Instrum* 22(1):32
73. Nakano T, Mochizuki Y, Fukuzawa K, Amari S, Tanaka S (2006) Developments and applications of ABINIT-MP software based on the fragment molecular orbital method. *Modern Methods Theor Phys Chem Biopolym* 12(5):39–52
74. Querfurth HW, LaFerla FM (2010) Alzheimer's disease. *N Engl J Med* 362(4):329–344
75. Alzheimer's Association (2013) Alzheimer's disease facts and figures. *Alzheimer's Dement* 9:110–133
76. National Institute for Health and Clinical Excellence (2011) Donepezil, galantamine, rivastigmine, and memantine for the treatment of Alzheimer's Disease. *Natl Inst Heal Clin Excell* 5:1–84
77. Sinha S, Anderson JP, Barbour R, Basi GS, Caccavello R, Davis D, Doan M, Dovey HF, Frigon N, Hong J, Jacobson-Croak K, Jewett N, Keim P, Knops J, Lieberburg I, Power M, Tan H, Tatsuno G, Tung J, Schenk D, Seubert P, Suomensaa SM, Wang S, Walker D, Zhao J, McConlogue L, John V (1999) Purification and cloning of amyloid precursor protein beta-secretase from human brain. *Nature* 402(6761):537–540
78. Cole SL, Vassar R (2007) The Alzheimer's disease Beta-secretase enzyme, BACE1. *Mol Neurodegener* 2(1):22–32
79. Luo Y, Bolon B, Kahn S, Bennett BD, Babu-Khan S, Denis P, Fan W, Kha H, Zhang J, Gong Y, Martin L, Louis JC, Yan Q, Richards WG, Citron M, Vassar R (2001) Mice deficient in BACE1, the Alzheimer's β -secretase, have normal phenotype and abolished β -amyloid generation. *Nat Neurosci* 4(3):231–232
80. Ghosh AK, Bilcer G, Harwood C, Kawahama R, Shin D, Hussain KA, Hong L, Loy JA, Nguyen C, Koelsch G, Ermolieff J, Tang J (2001) Structure-based design: potent inhibitors of human brain memapsin 2 (beta-secretase). *J Med Chem* 44(18):2865–2868
81. Congreve M, Aharony D, Albert J, Callaghan O, Campbell J, Carr RA, Chessari G, Cowan S, Edwards PD, Frederickson M, McMennamin R, Murray CW, Patel S, Murray WN, Patel S, Wallis N (2007) Application of fragment screening by X-ray crystallography to the discovery of aminopyridines as inhibitors of beta-secretase. *J Med Chem* 50(6):1124–1132
82. Edwards PD, Albert JS, Sylvester M, Aharony D, Andisik D, Callaghan O, Campbell JB, Carr RA, Chessari G, Congreve M, Frederickson M, Folmer RH, Geschwindner S, Koether G, Kolmodin K, Krumrine K, Mauger RC, Murray CW, Olsson LL, Patel S, Spear N, Tian G (2007) Application of fragment-based lead generation to the discovery of novel, cyclic amidine β -secretase inhibitors with nanomolar potency, cellular activity, and high ligand efficiency. *J Med Chem* 50(24):5912–5925
83. Geschwindner S, Olsson LL, Albert JS, Deinum J, Edwards PD, de Beer T, Folmer RH (2007) Discovery of a novel warhead against beta-secretase through fragment-based lead generation. *J Med Chem* 50(24):5903–5911

84. Erlanson DA, McDowell RS, O'Brien T (2004) Fragment-based drug discovery. *J Med Chem* 47(14):3463–3482
85. Godemann R, Madden J, Krämer J, Smith M, Fritz U, Hesterkamp T, Barker J, Höppner S, Hallett D, Cesura A, Ebnet A, Kemp J (2009) Fragment-based discovery of BACE1 inhibitors using functional assays. *Biochemistry* 48(45):10743–10751
86. Madden J, Dod JR, Godemann R, Kraemer J, Smith M, Biniszkiwicz M, Hallett DJ, Barker J, Dyekjaer JD, Hesterkamp T (2010) Fragment-based discovery and optimization of BACE1 inhibitors. *Bioorganic Med Chem Lett* 20(17):5329–5333
87. Zhu Z, Sun ZY, Ye Y, Voigt J, Strickland C, Smith EM, Cumming J, Wang L, Wong J, Wang YS, Wyss DF, Chen X, Kuvelkar R, Kennedy ME, Favreau L, Parker E, McKittrick BA, Stamford A, Czarniecki M, Greenlee W, Hunter JC (2010) Discovery of cyclic acylguanidines as highly potent and selective beta-site amyloid cleaving enzyme (BACE) inhibitors: Part I—Inhibitor design and validation. *J Med Chem* 53(3):951–965
88. Murray CW, Callaghan O, Chessari G, Cleasby A, Congreve M, Frederickson M, Hartshorn MJ, McMenamin R, Patel S, Wallis N (2007) Fragment screening by X-ray crystallography to b-secretase. *J Med Chem* 50(6):1116–1123
89. Cheng Y, Judd TC, Bartberger MD, Brown J, Chen K, Freneau RT Jr, Hickman D, Hitchcock SA, Jordan B, Li V, Lopez P, Louie SW, Luo Y, Michelsen K, Nixey T, Powers TS, Rattan C, Sickmier EA, St Jean DJ Jr, Wahl RC, Wen PH, Wood S (2011) From fragment screening to in vivo efficacy: optimization of a series of 2-aminoquinolines as potent inhibitors of beta-site amyloid precursor protein cleaving enzyme 1 (BACE1). *J Med Chem* 54:5836–5857
90. Jeppsson F, Eketjäll S, Janson J, Karlström S, Gustavsson S, Olsson LL, Radesäter AC, Ploeger B, Cebers G, Kolmodin K, Swahn BM, von Berg S, Bueters T, Fälting J (2012) Discovery of AZD3839, a potent and selective BACE1 inhibitor clinical candidate for the treatment of alzheimer disease. *Publ JBC Pap Press* 287(49):41245–41257
91. Malamas MS, Erdei J, Gunawan I, Barnes K, Johnson M, Hui Y, Turner J, Hu Y, Wagner E, Fan K, Olland A, Bard J, Robichaud AJ (2009) Aminoimidazoles as potent and selective human beta-secretase (BACE1) inhibitors. *J Med Chem* 52(20):6314–6323
92. Huang H, La DS, Cheng AC, Whittington DA, Patel VF, Chen K (1998) Structure-and property-based design of aminooxazoline xanthenes as selective, orally efficacious, and CNS penetrable BACE inhibitors for the treatment of Alzheimer's disease. *J Med Chem* 9(4):366–369
93. Hilpert H, Guba W, Woltering TJ, Wostl W, Pinard E, Mauser H, Mayweg AV, Rogers-Evans M, Humm R, Krummenacher D, Muser T, Schnider C, Jacobsen H, Ozmen L, Bergadano A, Banner DW, Hochstrasser R, Kuglstatter A, David-Pierson P, Fischer H, Polara A, Narquizian R (2013) β -secretase (BACE1) inhibitors with high in vivo efficacy suitable for clinical evaluation in Alzheimer's disease. *J Med Chem* 56(2–4):3980–3995
94. Malamas MS, Barnes K, Hui Y, Johnson M, Lovering F, Condon J, Fobare W, Solvibile W, Turner J, Hu Y, Manas ES, Fan K, Olland A, Chopra R, Bard J, Pangalos MN, Reinhart P, Robichaud AJ (2010) Novel pyrrolyl 2-aminopyridines as potent and selective human b-secretase (BACE1) inhibitors. *Bioorg Med Chem Lett* 20:2068–2073
95. Wang YS, Strickland C, Voigt JH, Kennedy ME, Beyer BM, Senior MM, Smith EM, Nechuta TL, Madison VS, Czarniecki M, McKittrick BA, Stamford AW, Parker EM, Hunter JC, Greenlee WJ, Wyss DF (2010) Application of fragment-based NMR screening, X-ray crystallography, structure-based design, and focused chemical library design to identify novel μ M leads for the development of nM BACE-1 (β -site APP cleaving enzyme 1) inhibitors. *J Med Chem Med Chem* 53(53):942–950
96. Congreve M, Aharony D, Albert J, Callaghan O, Campbell J, Carr RA, Chessari G, Cowan S, Edwards PD, Frederickson M, McMenamin R, Murray CW, Patel S, Wallis N (2006) Application of fragment screening by X-ray crystallography to the discovery of aminopyridines as inhibitors of β -secretase. *J Med Chem* 20:2068–2073
97. Fujitani H, Tanida Y, Matsuura A et al (2009) Massively parallel computation of absolute binding free energy with well-equilibrated states. *Phys Rev E* 79:021914

98. Araki M, Kamiya N, Sato M et al (2016) The effect of conformational flexibility on binding free energy estimation between kinases and their inhibitors. *J Chem Inf Model* 56:2445–2456
99. Genheden S, Ryde U (2015) The MM/PBSA and MM/GBSA methods to estimate ligand-binding affinities. *Expert Opin Drug Discov* 10:449–461
100. Homeyer N, Gohlke H (2012) Free energy calculations by the molecular mechanics Poisson-Boltzmann surface area method. *Mol Inform* 31:114–122
101. Nakajima N, Nakamura H, Kidera A (1997) Multicanonical ensemble generated by molecular dynamics simulation for enhanced conformational sampling of peptides. *J Phys Chem B* 101:817–824
102. Bekker GJ, Kamiya N, Araki M et al (2017) Accurate prediction of complex structure and affinity for a flexible protein receptor and its inhibitor. *J Chem Theory Comput* 13:2389–2399
103. Heifetz A, Chudyk EI, Gleave L et al (2016) The fragment molecular orbital method reveals new insight into the chemical nature of GPCR–ligand interactions. *J Chem Inf Model* 56:159–172
104. Watanabe C, Watanabe H, Fukuzawa K et al (2017) Theoretical analysis of activity cliffs among benzofuranone-class Pim1 inhibitors using the fragment molecular orbital method with molecular mechanics Poisson-Boltzmann surface area (FMO+MM-PBSA) approach. *J Chem Inf Model* 57:2996–3010
105. Friesner RA, Banks JL, Murphy RB et al (2004) Glide: a new approach for rapid, accurate docking and scoring. 1. Method and assessment of docking accuracy. *J Med Chem* 47:1739–1749
106. Halgren TA, Murphy RB, Friesner RA et al (2004) Glide: a new approach for rapid, accurate docking and scoring. 2. Enrichment factors in database screening. *J Med Chem* 47:1750–1759
107. Friesner RA, Murphy RB, Repasky MP et al (2006) Extra precision glide: docking and scoring incorporating a model of hydrophobic enclosure for protein-ligand complexes. *J Med Chem* 49:6177–6196
108. Ozawa T, Okazaki K, Kitauro K (2011) CH/ π hydrogen bonds play a role in ligand recognition and equilibrium between active and inactive states of the β 2 adrenergic receptor: an ab initio fragment molecular orbital (FMO) study. *Bioorg Med Chem* 19:5231–5237
109. Ozawa T, Okazaki K (2008) CH/ π hydrogen bonds determine the selectivity of the Src homology 2 domain to tyrosine phosphotyrosyl peptides: an ab initio fragment molecular orbital study. *J Comput Chem* 29:2656–2666
110. <https://drugdesign.riken.jp/FMODB/>
111. https://www.phenix-online.org/presentations/latest/pavel_refinement_general.pdf
112. Nishimoto Y, Fedorov DG, Irlé S (2014) Density-functional tight-binding combined with the fragment molecular orbital method. *J Chem Theory Comput* 10(11):4801–4812
113. Gastegger M, Marquetand P (2015) High-dimensional neural network potentials for organic reactions and an improved training algorithm. *J Chem Theory Comput* 11(5):2187–2198
114. Morawietz T, Singraber A, Dellago C, Behler J (2016) How van der Waals interactions determine the unique properties of water. *PNAS* 113(30):8368–8373
115. Honma T, Mizuguchi K (2018) Life intelligence consortium. *Nihon Yakugaku-kaishi Pharmacia* 54(11)

Development of an Automated FMO Calculation Protocol to Construction of FMO Database



Chiduru Watanabe, Hirofumi Watanabe, Yoshio Okiyama,
and Daisuke Takaya

Abstract In recent years, inter-fragment interaction energy (IFIE) analyses based on the fragment molecular orbital (FMO) method have been widely used for drug design. The reason is that the IFIE analyses can quantify not only electrostatic interactions such as hydrogen bonds but also dispersion forces such as CH/ π interactions difficult to evaluate with classical molecular mechanics (MM). On the other hand, because preparing an input structure for the FMO calculation requires a lot of complicated preprocessing, including complementation of missing atoms and structure optimization, it is difficult to process a large number of structures. In this study, an automated FMO calculation protocol (Auto-FMO protocol) was developed to calculate huge numbers of protein and ligand complexes, such as drug discovery targets, by an ab initio FMO method. The protocol performs structure preparation as preprocessing, submission of FMO processing, and analysis of FMO results as post-processing. Optionally, quantum mechanics/molecular mechanics (QM/MM) optimization of complex structures, conformational searches of ligand structures in solution, and molecular mechanics Poisson–Boltzmann or generalized Born surface area (MM-PBSA/GBSA) calculations can also be carried out. To demonstrate the usefulness of the Auto-FMO protocol, we first compared the ligand-binding interaction energies of 20 estrogen receptor α (ER α) and 70 p38 MAP kinase datasets prepared by the Auto-FMO protocol with those prepared manually. In most cases, the interaction energies showed reasonable agreement between both preparations. Based on such technology, we constructed the FMO database (FMOdb; <https://drugde>

C. Watanabe (✉) · D. Takaya

RIKEN Center for Biosystems Dynamics Research, 1-7-22 Suehiro-cho, Tsurumi-ku, Yokohama 230-0045, Kanagawa, Japan

e-mail: chiduru.watanabe@riken.jp

C. Watanabe

JST, PRESTO, 4-1-8, Honcho, Kawaguchi 332-0012, Saitama, Japan

H. Watanabe

Education Center On Computational Science and Engineering, Kobe University, 7-1-48, Minatojima-minamimachi, Chuo-ku, Kobe 650-0047, Hyogo, Japan

Y. Okiyama

Division of Medicinal Safety Science, National Institute of Health Sciences, 3-25-26 Tonomachi, Kawasaki-ku, Kawasaki 210-9501, Kanagawa, Japan

© Springer Nature Singapore Pte Ltd. 2021

Y. Mochizuki et al. (eds.), *Recent Advances of the Fragment Molecular Orbital Method*, https://doi.org/10.1007/978-981-15-9235-5_9

sign.riken.jp/FMODB/) published in February 2019, consisting of quantum chemical calculation results with the FMO method. FMODB currently contains thousands of FMO calculation data for hundreds of proteins mostly processed by the Auto-FMO protocol. By constructing FMODB and its web interface, even researchers unfamiliar with quantum mechanics (QM) calculations can analyze inter- and intra-molecular interactions of target proteins. Furthermore, accumulation of FMO data is expected to lead to accurate prediction of ligand activities and construction of QM-based force fields by using machine learning and artificial intelligence (AI). This chapter was reprinted and adapted with permission from Watanabe et al. CBI J. 2019, 58, 5–18. Copyright 2019 Chem-Bio Informatics Society [38].

Keywords Fragment molecular orbital (FMO) · Intermolecular interaction · Ligand binding energy · Estrogen receptor α (ER α) · p38 mitogen-activated protein (MAP) kinase · FMO database (FMODB)

1 Introduction

Ab initio quantum mechanical calculations for whole large biomolecules can be efficiently performed by the fragment molecular orbital (FMO) method [1–3]. An inter-fragment interaction energy (IFIE) analysis based on FMO calculations can easily represent the detailed interactions in fragment units. The FMO method is already recognized as a useful drug design tool to analyze ligand binding interactions, incorporating electrostatic interactions such as hydrogen bonds and dispersion forces such as CH/ π interactions, using the pair interaction energy decomposition analysis (PIEDA) [4, 5] and fine fragmentation by the functional group unit, rather than the amino acid residue unit and the whole ligand [6–8]. Recently, the IFIE analysis and its energy decomposition analysis have been applied to the prediction of binding affinity for rational drug design [9–19]. Using FMO calculations of tens of complexes for one target protein, the essential and characteristic interactions of the ligand-binding mode can be abstracted from the IFIE and PIEDA data by clustering methods [20, 21] and singular value decomposition [22]. In addition, the prediction of the activity cliff, which is very difficult using conventional molecular mechanics (MM)-based scoring functions, such as Glide score and molecular mechanics Poisson–Boltzmann surface area (MM-PBSA), was successfully accomplished by the FMO method with molecular mechanics Poisson–Boltzmann surface area (FMO+MM-PBSA) approach incorporating MM-based desolvation effects, using protein–ligand complexes optimized by the quantum mechanics/molecular mechanics (QM/MM) method [23]. Moreover, the FMO-based polarizable continuum model (FMO-PCM) [24] or FMO-based Poisson–Boltzmann surface area (FMO-PBSA) [25–27] methods provide more reliable results in solution, by using a fully polarizable medium for the solute.

Since 2014, we have performed FMO calculations for various drug discovery targets, such as kinases, nuclear receptors, proteases, and protein–protein interactions (PPIs), with experimental binding affinities (IC_{50} , K_i , and K_d values) as the activities of the FMO drug design consortium (FMOOD) [28]. To calculate the huge number of different structures by a manual procedure, we must investigate and choose the various modeling conditions and FMO settings one by one. For example, appropriate structure preparation, which includes complementation of missing atoms or missing residues, addition of hydrogen atoms, and structure minimization, is critically important as the preprocessing before the FMO calculations. However, appropriate methods for preprocessing have not yet been established. We discussed the modeling conditions for the complementation of heavy atoms, with/without water molecules, and the restraint of heavy atoms on the minimization in the FMOOD consortium. As a result, some modeling case studies have been reported [29–35]. Another issue is the treatment of a large amount of structure data, including more than 150,000 Protein Data Bank (PDB) entries [36], to construct an FMO database [37] in the future. There are limits to human power in preparing a huge number of structures by a manual operation. In addition, it is not easy to appropriately perform FMO calculations for inexperienced researchers, in terms of the structure preparation and FMO settings. Thus, we have started to develop “an automated FMO calculation protocol” (Auto-FMO protocol) [38]. We constructed the Auto-FMO protocol consisting of structural preparation based on the MM method, structural optimization based on the QM/MM calculations with our own N -layered integrated molecular orbital and molecular mechanics (ONIOM) method, molecular mechanics Poisson–Boltzmann or generalized Born surface area (MM-PBSA/GBSA) calculations, FMO calculations, and ligand interaction analysis from the MM and FMO calculations. For validation of the Auto-FMO protocol, two datasets of human estrogen receptor α (ER α) and human p38 α mitogen-activated protein (MAP) kinase were used for comparison of the ligand binding energies between the protocol data and the manually prepared data. The main purpose of this study was to investigate the performance of preprocessing in the Auto-FMO protocol. We focused on proteins for which many examples of FMO calculations for ER α and p38 α have been reported [8, 9, 22, 35]. ER α and p38 α were important drug targets related to breast cancer and immune disorder, respectively. The familiar target proteins were appropriate for the validation because evaluations of the prepared structures and its FMO calculations with the protocol were relatively easy to verify. Based on the results, we discussed the current accuracy and issues to solve in the protocol in future work. Additionally, to construct the FMO database [37], various protein structures were calculated by the protocol.

2 Workflow of the Auto-FMO Protocol

The workflow of the Auto-FMO protocol [38] is shown in Fig. 1, and the method for each step is described in the following sections. The protocol was implemented in

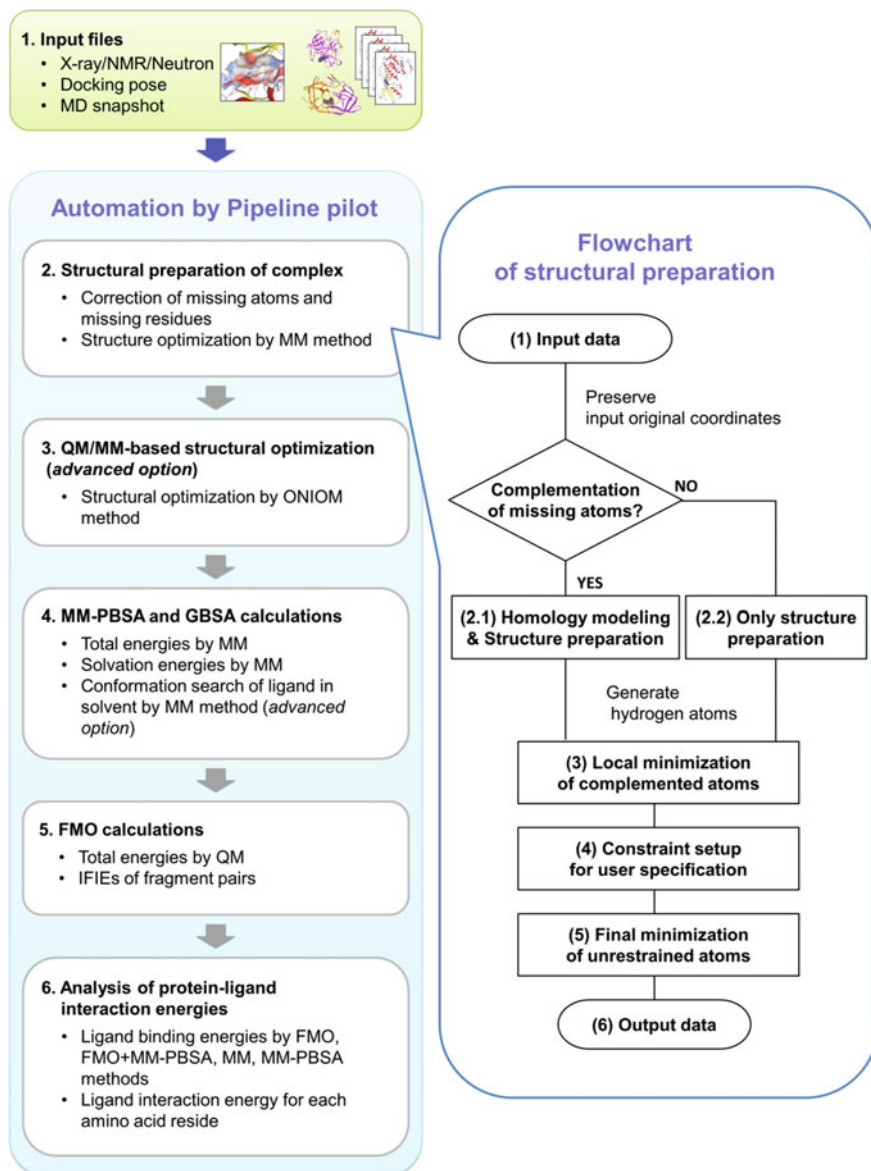


Fig. 1 The workflow of the Auto-FMO protocol. The detailed procedures of the structural preparation are depicted on the right. Reprinted with permission from [38]. Copyright 2019 Chem-Bio Informatics Society

BIOVIA Pipeline Pilot [39]. Further details of the structure preparation step, such as the default parameters, are described in the supplementary information, Section A.

Input file

The three-dimensional structures of protein–ligand complexes or apoprotein structures were prepared in PDB files and transformed into one MDB file [40]. This part should be done by the users, rather than by the Auto-FMO protocol. Water molecules far from each ligand can be removed if necessary. The following processing was performed on the prepared molecular composition (e.g. protein, ligand, water molecules, and cofactors) in here.

Structure preparation

To complement the missing residues and atoms, two different types of functions were newly implemented with built-in functions in MOE: (1) Both missing residues and atoms were simultaneously complemented by the “pro_HomologyModel” function to build a whole protein model, and (2) only the missing atoms of the side chains are complemented by the “StructurePreparation” function. In gap regions due to disorder, the residues next to the gaps are capped by an ACE or NME group to retain the original amide bonds. After the corrections, hydrogen atoms were added to each complex by using the “Protonate3D” function under pH 7.0 conditions. The residues at the N- and C-termini are treated as zwitterionic states with NH_3^+ and COO^- , respectively.

Subsequently, structure optimization with the force field (Amber10:EHT) was performed, using the “MM” function under partial constraints. As the force field, other force fields such as MMFF94x can be selected. For example, only the complemented atoms and hydrogen atoms can be optimized. The constraint settings can be adjusted by the users.

QM/MM-based structure optimization (advanced option)

Structural optimization based on the QM/MM calculations with the ONIOM method at the HF/6-31G*:MM/AMBER level can be automatically performed using the Gaussian09 program package [41] at the RIKEN supercomputer HOKUSAI, as an advanced option. A ligand and its surrounding residues are generally selected as the high layer, and the rest of the biomolecule was assigned to the low layer region. Atoms of the high layer region are only optimized and the other atoms are fixed during the calculations. This option was not active as the default setting, because the QM/MM optimization requires a high computational cost. Users should employ the QM/MM optimization appropriately, where there are the necessities of QM calculation to cope with the cases such as halogen bond. In the protocol, the QM/MM-based total energies were calculated by the ONIOM method.

MM-PBSA and GBSA calculations

The total MM energies and the solvation energies of each protein–ligand complex, apoprotein, and ligand were calculated by the MM-PBSA and MM-GBSA methods with the AMBER tools program [42]. MM-PBSA/MM-GBSA calculations used the

MM-optimized structures obtained from “Structure preparation” or the QM/MM-optimized structures if QM/MM optimization was performed. The Amber99SB force field was used for the protein, and the general Amber force field (GAFF) [43] with the AM1-BCC [44] charge was used for the ligands by antechamber [45]. Conformational searches of ligands in solvent can be performed by MOE to estimate the deformation energies of the ligands in the bound state and the solvent for MM-PBSA, as an advanced option. Several candidates of stable structures in the solvent are used.

FMO calculations

FMO calculations were performed with the ABINIT-MP program [46, 47] on the K computer or our in-house PC cluster server. Users can select various options for the FMO method: a computational level from the Hartree–Fock (HF) and the Møller–Plesset (MP2) level, and a basis set from 6-31G, 6-31G*, and cc-pVDZ. In this study, we used the MP2/6-31G* level with the Cholesky decomposition approximation (CDAM) [48]. The output log files of the FMO calculations include the IFIE and PIEDA values, as well as partial atomic charges by a Mulliken population analysis, a natural population analysis (NPA), and RESP fitting [49, 50].

Analysis of protein–ligand interaction energies

Ligand binding energies based on the MM, MM-PBSA, FMO, FMO+MM-PBSA methods can be extracted from the log files and summarized by the protocol. In addition, the IFIE values of the ligands are listed in an Excel file. The detailed definitions of these energies regarding the ligand are explained in [23].

3 Validation of the Auto-FMO Protocol Data for ER α and P38 α

In this section, an example of FMO calculations with the Auto-FMO protocol will be presented. Using ER α and p38 α MAP kinase (p38 α) dataset, validation of the Auto-FMO protocol was performed by comparing a ligand-binding interaction energy with a manually prepared dataset.

3.1 Validation Data Sets of ER α and P38 α MAP Kinase

For ER α and p38 MAP kinase (p38 α), the complex structures with IC₅₀ values were selected from the PDB and ChEMBL databases (Fig. 2). The datasets of ER α and p38 α have 37 and 96 PDB entries, respectively [38]. Here, we performed the FMO calculations of 38 ER α and 111 p38 α complexes by the Auto-FMO protocol because the PDB data include multiple chain complexes such as homodimer. We

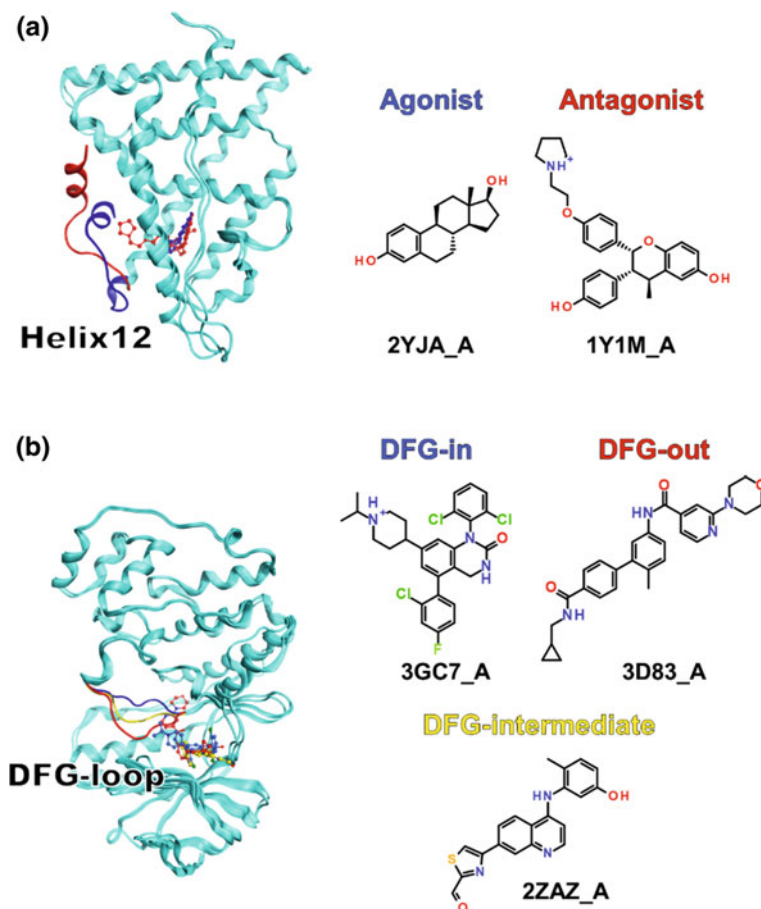


Fig. 2 Complexes of ER α (a) and p38 α (b) where the ribbon and ball-and-stick modes correspond to the protein and ligand, respectively. For ER α complexes, the H12 regions of the agonist-bound form and antagonist-bound form are represented by red and blue ribbons, respectively. For p38 α , the DFG-in, DFG-out, and DFG-intermediate loop structures shown as blue, red, and yellow ribbons, respectively

employed the sequence that constitutes ligand-binding active sites to evaluate ligand-binding energy based on an aligned sequence structure: amino acid residues #309–544 on the ligand-binding domain (LBD) for ER α and #6–351 on the protein kinase domain for p38 α . We here removed all factors other than the sequences focused above, ligands, and key crystal waters. The results of the FMO calculations at the MP2/6-31G* level with CDAM using the automatically prepared structures were compared to those obtained using manually prepared structures. As the manually prepared data, we used already reported 70 p38 α complex data [35]. In terms of ER α , we selected 20 ER α complexes considering the crystal resolutions and the other reasons. These complex structures were included in the above-mentioned 38

Table 1 Data set list for the automated FMO protocol and manually prepared data. Reprinted with permission from [38]. Copyright 2019 Chem-Bio Informatics Society

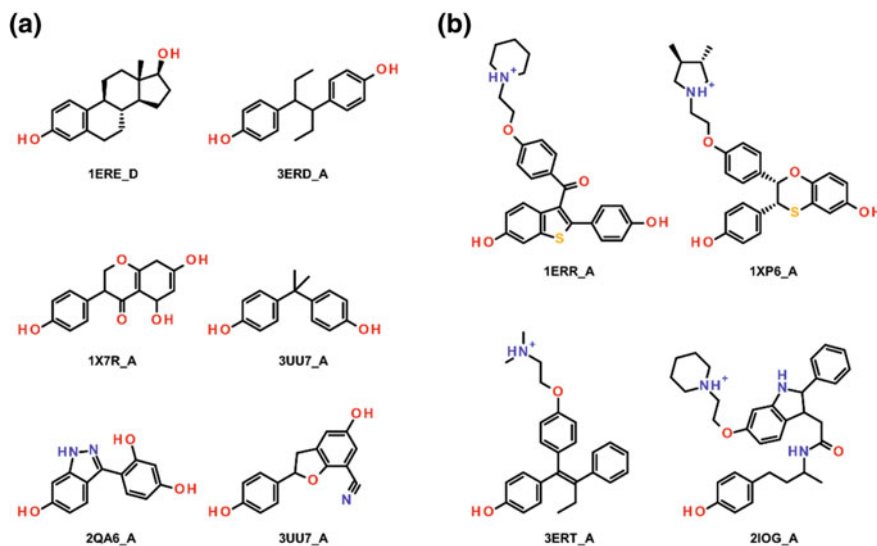
Target protein		Estrogen receptor α	p38 MAP kinase
Manually prepared data	# of completed FMO calculations	20	70
Auto-FMO protocol data	# of completed FMO calculations	20	70
	Average time per complex for structure preparation (minutes)	3.2 ^a	4.7 ^a
	Average time per complex for FMO calculation (hours)	11 ^b	14 ^c

^a Average time of structure preparation by MM optimization for each structure using 1 core at our in-house PC cluster server (Intel(R) Xeon(R) CPU E5-2695 v3 @ 2.30 GHz)

^b Average time of FMO calculation for each structure using 48 cores at our in-house PC cluster server (Intel(R) Xeon(R) CPU E5-2670 v3 @ 2.30 GHz)

^c Average time of FMO calculation for each structure using 960 cores at K computer

and 111 complex structures calculated by the Auto-FMO protocol. Thus, we used the 20 and 70 complex structures for comparison (Table 1). The ligands in these datasets can be classified into two and five types of compounds displayed in Figs. 3 and 4. Since these datasets were diverse, it was suitable to validate the protocol.

**Fig. 3** Ligand types of ER α dataset: **a** agonist and **b** antagonist

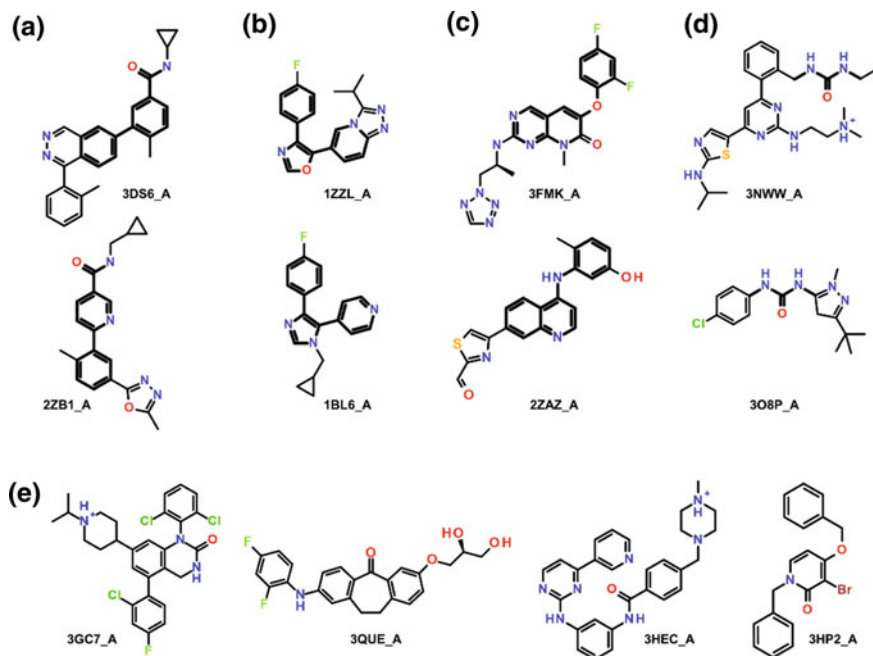


Fig. 4 Ligand types of p38 α dataset: **a** biphenyl amides, **b** three linked aromatic rings, **c** fused aromatic rings with -NH- or -O- links, and **d** ureas, and **e** others. Each common scaffold is shown in bold lines

The numbers of data for each preparation step by the Auto-FMO protocol and the manual procedure are summarized in Table 1. The details are described below. Figure 2 shows the complexes of ER α and p38 α obtained from the Auto-FMO protocol. In the case of ER α , the position of helix 12 (H12), composed of residues Leu536–Ala546, was different depending on whether the bound compound was an agonist or antagonist (Fig. 2a). Hence, the loop between H11 and H12 near the ligand-binding pocket is flexible, and there are missing residues on the loop in some complexes with antagonists (Fig. 3b). In the case of p38 α , The DFG-loop around Ile166–Ala184, including Asp168, Phe169, and Gly170, adopts three types of conformations, such as DFG-in, DFG-out, and DFG-intermediate conformations (Fig. 2). The DFG-loop is placed in the ATP binding pocket and is very flexible and disordered, including the missing residues. In these datasets, because these missing residues of p38 α are located near the bound ligands, they were complemented by both modeling methods (Auto-FMO protocol and manual operation).

Auto-FMO protocol data

The bond orders of all of the ligands were corrected based on LigandExpo and used for the input structures of the Auto-FMO protocols. Subsequently, the Auto-FMO protocol was employed using the same options, as follows. All of the crystal

water molecules were removed; two residues neighboring missing residues as a margin were removed and complemented by homology modeling using the wild type sequence; and the protonation states of the ligands and amino acid residues were determined by Protonate3D at pH 7.0. Finally, all of the hydrogen and missing heavy atoms were optimized by the Amber10:EHT force field.

Manually prepared data

In the case of ER α , a few crystallographic water molecules forming bridging hydrogen bonds among Glu353, Arg394, and the ligand were retained, in addition to the ligands and proteins. By using the BioStation viewer, the missing residues of the complexes with agonists and antagonists were complemented according to the templates of the agonist form (PDB IDs: 1A52 and 2YJA) and the antagonist form (PDB ID: 1Y1M), which were high-resolution X-ray structures that have no missing residues in the H12 regions. The bond orders of all of the ligands were manually corrected. The tautomeric states of amino acid residues and ligands were consequently determined with Protonate3D in MOE. Finally, all of the hydrogens and missing heavy atoms of each ER α complex were optimized by an Amber10:EHT force field.

For p38 α , the structure coordinates prepared by Sheng et al. [35] were used in this study. First, a few crystallographic water molecules were kept in the following two cases. In the first case, the water molecule forming hydrogen bonds with Asp168 and Lys53 was retained in the DFG-in structures, and in the second case, the water molecule forming the hydrogen bond with Asp168 was kept in the DFG-out structures. Secondly, by using the BioStation viewer, the missing residues were complemented with the 3GC7 and 3D83 PDB entries as the template structures of the DFG-in and DFG-out structures, respectively. The templates were full sequences and high-resolution structures, without missing residues. The bond orders of all of the ligands were corrected manually. The tautomeric states of the amino acid residues and ligands were consequently determined with Protonate3D in MOE. Only His312 was dealt with as a cationic protonation state (HIP), considering the surrounding hydrogen bonding network, and the other histidine residues were set as neutral states (HIE or HID). Moreover, the ligand charges were assigned as the corresponding protonation state of pH 7.0 in water. For aliphatic amines, we set the formal charges to + 1e, while aromatic amines such as anilines were set to a formal charge of zero. Finally, all hydrogen and missing heavy atoms for each p38 α complex were optimized by an Amber10:EHT force field.

3.2 Completion Rate of FMO Calculation

We constructed 38 and 111 complexes of ER α and p38 α by the MM-based structure preparation in the Auto-FMO protocol. The number of calculated structures includes multiple chains in each PDB entry. Using our in-house PC cluster server and the K computer, 38 and 110 FMO calculations were successfully completed for the

ER α and p38 α complexes, respectively. There was one structure of p38 α (PDB ID: 4KIN, Chain: D) for which the FMO calculation was not completed. At the structure complement step by homology modeling, the complemented atoms of the complex severely clashed among Gly33, Ala34, and Tyr35. As a result, the FMO calculations were not completed for this structure. However, 99.1% of the FMO calculations using the structures created by the Auto-FMO protocol were completed, showing that this protocol is sufficiently robust for daily FMO research, including drug design. Next, we validated the Auto-FMO protocol by comparing the ligand-binding energies ΔE_{ligand} between the protocol data and the manually prepared data and discussed the accuracy and the issues to improve in the protocol.

3.3 Comparison of Ligand Binding Interaction Energy

To demonstrate the utility of the Auto-FMO protocol, we compared the ligand-binding energies ΔE_{ligand} of the protocol with those of the manually prepared data. To obtain ΔE_{ligand} based on FMO calculations, we summed up the IFIE values of all ligand–residue pairs. The FMO contribution of the ligand-binding energy is given by the following equation:

$$\Delta E_{\text{ligand}} = \sum_{\substack{I=\text{ligand} \\ J \neq I}} \Delta \tilde{E}_{IJ} \quad (1)$$

where $\Delta \tilde{E}_{IJ}$ is the IFIE; and I and J are fragment indices.

For accuracy validation of the protocol, the ligand-binding interaction energies calculated by the Auto-FMO protocol were compared to those of the manually prepared data (Fig. 5). Here, we compared 20 and 70 FMO calculation results of the structures in which the PDB ID and its chain ID matched in both methods for ER α and p38 α , respectively (Table 1).

The coefficients of determination (R^2) for all calculation data of ER α and p38 α were 1.00 and 0.79, respectively. Note that the p38 α data included different ligand charge data between the Auto-FMO protocol data and the manual data. In Fig. 5b, the entries with different charges shown by purple triangles were located at significant outlier positions.

Although the ionization state assignment using MOE should be improved, except for the three outliers (PDB IDs: 3O8P, 1OUK, 3GFE, also see Table 2), R^2 improved to 0.95. In general, the differences in the formal charges seriously affect the calculation results, especially for a QM calculation. Therefore, careful double-checking of the structure preparation by the Auto-FMO protocol is needed for practical use. The high correlations between the manual and the protocol data partially arise from the wide ΔE_{ligand} range between the compound groups (agonist and antagonist groups in ER α and neutral ligand and charged ligand groups in p38 α). To confirm the effects

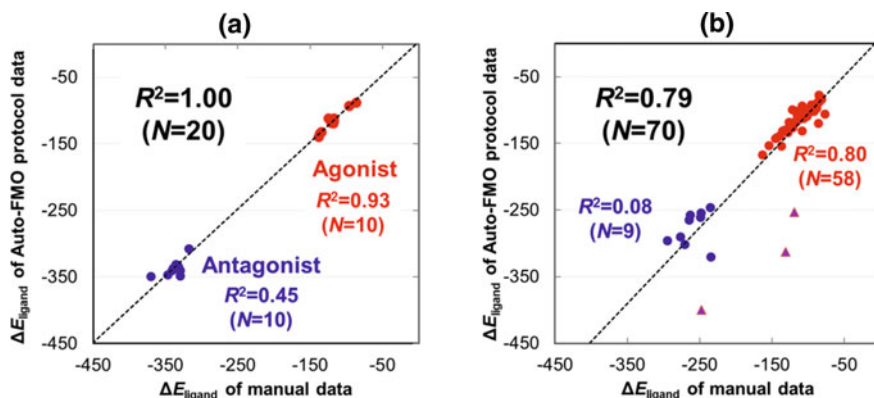


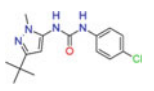
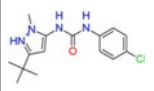
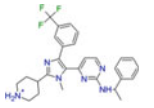
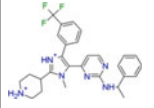
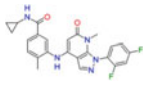
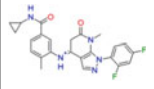
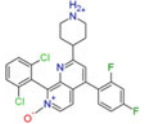
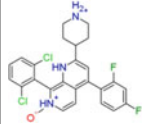
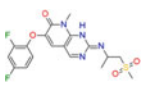
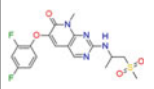
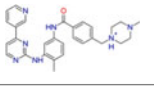
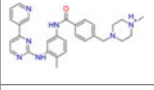
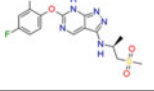
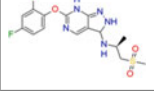
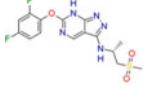
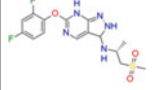
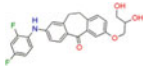
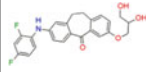
Fig. 5 Correlation of ligand-binding energies between the manual data and the Auto-FMO protocol data for ER α (a) and p38 α (b). The neutral and positively charged ligands are marked with red and blue circles, respectively. Obvious outlier data (PDB IDs: 3O8P, 1OUK, 3GFE) in Fig. 5b, for which the ligand charge of the protocol data differed from that of the manual data, are shown by purple triangles. Reprinted with permission from [38]. Copyright 2019 Chem-Bio Informatics Society

of the ligand charge, the compounds were classified by each ligand charge (neutral (red) and positively charged (blue) in Fig. 5). For only neutral ligands, the R^2 values for ER α and p38 α were sufficiently high (0.93 and 0.80, respectively), in spite of the narrow ΔE_{ligand} range. In contrast, only positively charged ligands provided poor correlations ($R^2 = 0.45$ and 0.08, respectively). In the cases of charged ligands, slight changes of the atomic coordinates (e.g., 0.1 to 0.2 Å) can greatly affect the interaction energy values.

Table 2 summarizes the entries with large differences between the protocol data and the manually prepared data for p38 α . In the three complexes (PDB IDs: 3O8P, 1OUK, and 3GFE) with different ligand charges between the protocol data and the manual data, the differences of the IFIE values were more than 100 kcal/mol. In the next entry (PDB ID: 3MW1), the ligand charges of both structures were equal; however, the protonation state was different. The ligand structure (ligand name: MIH) by the protocol has two additional hydrogen atoms due to the treatment of the rare N-oxide moiety. As a result, the difference in the ligand-binding energy recorded was 80 kcal/mol. There were different tautomerization states in the three complexes (PDB IDs: 3FLS, 3FML, 3FMM). The IFIE difference of the complex (PDB ID: 3HEC) resulted from the different protonated nitrogen atoms of the piperazine ring (ligand name: STI).

In the case of the 3QUE entry, the charge and tautomerization state of the ligand obtained by the protocol were the same as those in the manually prepared data. Here, Fig. 6 shows the three-dimensional structures of the ligand-binding pocket for both data sets. For the complementation of the missing residues by homology modeling, the complemented structures around the ligand showed significant differences. Glu173 formed a hydrogen bond with the ligand in the manually prepared data, while no hydrogen bond between the ligand and Glu173 was detected in the

Table 2 Data set with large differences in ligand-binding interaction energy of the FMO protocol data and the manual data. Reprinted with permission from [38]. Copyright 2019 Chem-Bio Informatics Society

PDB ID (Ligand name)	Chain ID	Manual			Protocol		
		Structural formula	Ligand charge	ΔE_{ligand}	Structural formula	Ligand charge	ΔE_{ligand}
3O8P (BMU)	A		0	- 131.16		1	- 313.04
1OUK (084)	A		1	- 247.85		2	- 399.92
3GFE (P37)	A		0	- 119.51		1	- 252.79
3MW1 (MIH)	A		1	- 234.81		1	- 320.28
3FLS (FLS)	A		0	- 86.03		0	- 119.62
3HEC (STI)	A		1	- 270.74		1	- 301.61
3FML (FML)	A		0	- 77.01		0	- 105.67
3FMM (X12)	A		0	- 109.06		0	- 131.13
3QUE (3FF)	A		0	- 122.39		0	- 99.19

protocol data (Fig. 6). The drastic conformational change of the Glu173 side chain caused a 20 kcal/mol difference in the ligand-binding energies.

Figure 7 shows the correlation between the Auto-FMO protocol data and the manual data, excluding the nine obviously different data listed in Table 2. As a result,

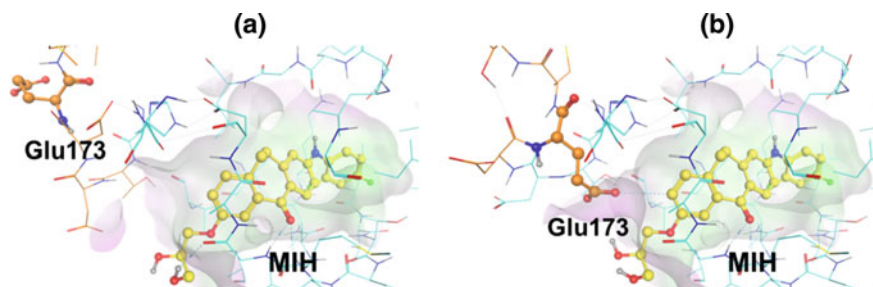
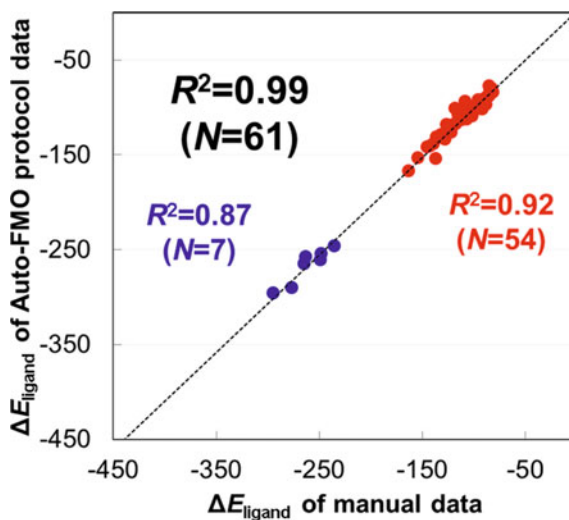


Fig. 6 Three-dimensional structures of the p38 α and ligand (MIH) complex (PDB ID: 3QUE, Chain: **a** in the Auto-FMO protocol data **(a)** and the manually prepared data **(b)**. The ligand and amino acid residues including the X-ray crystal structure are shown by the yellow ball-and-stick models and the cyan line, respectively. Complemented structures regarding missing atoms are highlighted in orange. Glu173 is shown by an orange ball-and-stick model, because a very large conformational difference between the protocol data and the manual data was observed. Reprinted with permission from [38]. Copyright 2019 Chem-Bio Informatics Society

Fig. 7 Validation of the binding energies compared with the manual data and the Auto-FMO protocol data without the obvious nine outliers in the p38 α dataset. The neutral and positively charged ligands are marked in red and blue, respectively. Reprinted with permission from [38]. Copyright 2019 Chem-Bio Informatics Society



the correlations of all data (black), the neutral ligand charge data (red), and the positively charged data (blue) between the protocol and manual data were dramatically improved.

3.4 Issues to Be Solved in the Auto-FMO Protocol

There was one data that the FMO calculation did not complete in Table 1. To reduce the computational cost, we plan to add an MM-based structure filter that removes

incorrect structures before submission to the FMO calculation. The filter will check the bond lengths, bond angles, dihedral angles, and MM-based repulsion energies of residue in each complex according to their standard values observed in X-ray structures.

In the case of p38 α , we detected outliers for the comparison between the Auto-FMO protocol data and the manually prepared data in Fig. 5b. The large differences in the ligand-binding energies between the protocol data and the manually prepared data, which were more than 20 kcal/mol for p38 α , are listed in Table 2. The main reasons for the large differences in the ligand-binding energies between the manual data and the protocol data were the differences in the ionization and tautomerization states of the ligands (Table 2), and the complemented structures regarding missing residues on flexible loops (Figs. 2 and 6). The R^2 values of the ligand-binding energies between the protocol data and the manual data without the nine obviously different compounds were dramatically improved, from 0.79 to 0.99 in the p38 α data set (Figs. 5b and 7). We handled the manually prepared data as representative data of ordinary computational researchers. However, with respect to the ligand structures, the manual preparation is not always effective, because many of the computational researchers are not familiar with the tautomerization and protonation states of a wide variety of chemical species. Indeed, the data with large ΔE_{ligand} differences between manually prepared data and Auto-FMO protocol data (Table 2) contain inappropriate ligand structures on both sides. Therefore, it is necessary to manually check the ionization states and conformations of the complemented residues, using a list of the 2D structures of all ligands and the 3D structures of the complexes output from the protocol. Currently, the ionization assignment depends on the MOE protonate3D function, and it is not easy to enhance the function within MOE. In the future, we would like to develop our original ionization and tautomerization prediction model by combining MM or QM calculations and artificial intelligence (AI), based on the upcoming FMO database [37] including more than thousand FMO data. The Auto-FMO protocol can be used for not only construction of the FMO database but also binding affinity prediction and interaction analysis. In this study, we described the details of the protocol and good agreements with the manual data. In general, for the binding affinity prediction based on the FMO method, we have to consider many factors such as ligand properties including charges and functions (i.e., agonist and antagonist), entropy terms, and solvent effects. Indeed, the previous study of p38 α [35] showed a good correlation between experimental values and estimated binding interaction energies after appropriate classification based on ligand charges, scaffolds, and types of DFG-loop structures. Besides, through singular value decomposition for IFIEs between ligand and each amino acid for several complexes in the cases of ER α and p38 α [22], the correlations between IC₅₀ and estimated ligand-binding energies were improved by removing some particular vectors that involved noise components and impaired the correlation. In several cases [22, 35], the manually prepared data had obtained results that were consistent with the experiments, and the Auto-FMO protocol should allow such studies to be performed with reduced human effort. Considering the entropy and solvation effects [11, 23, 27] is also very important to improve the correlation. These effects for the current datasets

will be considered in our future works by using the FMO+MM-PBSA approach. To enhance the accuracy of the FMO+MM-PBSA method, we plan to use the QM-based atomic charges obtained by FMO calculations in addition to the QM/MM optimization. Because the above-mentioned calculations were time-consuming and the ligand clustering requires a deep understanding of the target and dataset, a more advanced expert system will be needed for practical applications to drug design. One of the future directions of development is AI-based guidance for the binding affinity prediction.

3.5 Construction of FMO Database with the Auto-FMO Protocol

To construct the FMO database, 2488 FMO calculations of various protein targets including 1194 unique PDB entries were performed by the Auto-FMO protocol (Table 3). Similarly to ER α and p38 α datasets, FMO calculations of complexes for estrogen receptor β (ER β), CHK1 kinase, Aurora kinase, and Renin protease datasets with IC₅₀ values selected from the PDB and ChEMBL databases were performed by the protocol. To include FMO calculation results with a diversity of protein structure in the database, various protein structures were calculated by the Auto-FMO protocol, where the residues next to the gaps were capped by ACE or NME group to retain

Table 3 List of datasets generated by the Auto-FMO protocol in FMO database

Structure type	Target protein	# of unique PDB entries	# of FMO DB registration entries
X-ray structure	ER α (236 AA)	22	38
	ER β (234 AA)	28	54
	p38 α MAP kinase (347 AA)	94	202
	CHK1 kinase (261 AA)	42	44
	Aurora kinase (260 AA)	39	53
	Renin protease (330 AA)	7	12
	GPCR (300–460 AA)	15	23
	Apo structure of MOE dataset	863	913
	core-set of PDBbind	82	82
NMR	TrpCage (20 AA)	1	76
MD snapshot	TrpCage (20 AA)	1	991
Total		1194	2488

the original amide bonds. For example, we dealt with 23 GPCR-ligand complexes reported by Chudyk et al. [16], 82 protein–ligand complexes of the core-set from PDBBind [50], and 913 apo structures from Protein Database of MOE including X-ray structures with a resolution of 2.8 Å or better [36, 40]. As a preliminary data using Trp-cage (PDB ID: 1L2Y) with structural fluctuation obtained from NMR and MD snapshot structures, FMO calculations of fluctuating structures were performed by the protocol through only FMO calculation process. The several thousand data were registered in the FMO database, and most of the data were in public. However, since only a part of PDB data had been calculated, we would continue to build data for FMO DB with the Auto-FMO protocol.

4 Conclusion

We have developed the automated FMO calculation protocol (Auto-FMO protocol) to perform a large number of FMO calculations, together with pre- and post-processing. To validate the Auto-FMO protocol, the ligand-binding interaction energies calculated by the Auto-FMO protocol were compared to those of the manually prepared data in the ER α and p38 α datasets. The automated FMO calculation data agreed reasonably well with the manually prepared data ($R^2 = 1.00$ (ER α) and 0.79 (p38 α)). One of the factors that reduced the correlation was the incorrect ionization and tautomerization; for only the neutral ligands or ligands with the same ionization and tautomerization assignments, the R^2 values were significantly improved. Therefore, Auto-FMO protocol users need to check the ionization and tautomerization states of the ligands to avoid systematic misassignments. In the cases of complex structures with missing atoms in flexible regions, there is some room for improvement in the protein modeling to complement the missing atoms. With this protocol, not only computational researchers but also inexperienced researchers can easily perform FMO calculations without complicated procedures. The Auto-FMO protocol would reduce not only operative fluctuations but also artificial mistakes in such as a bond-order setting for ligands. This makes us prepare the uniformly organized data set. In addition, the Auto-FMO protocol has enabled us to construct the FMO database [37] based on several thousand FMO calculations, which will provide quantum mechanical calculations of total energies, interaction energies of fragment pairs, and atomic charges for various protein–ligand complexes for more than tens of thousands of complex structures in the future. This database will be useful for various research fields, such as drug design and structural biology, as well as molecular modeling [11, 51–53]. For example, using thousands of FMO calculation results, AI models that predict molecular force and atomic charges considering QM interactions are currently being developed. The new AI-based molecular force field will lead to more accurate molecular dynamics and docking simulations. Furthermore, we plan to establish an “on the fly” FMO calculation service for structural biologists. Once a structural biologist solves a new X-ray structure, the structure data can be uploaded to the service and the FMO calculation data can be obtained in one day.

Acknowledgements The authors thank Dr. Teruki Honma, Dr. Kikuko Kamisaka, Mr. Shunpei Nagase, Dr. Kaori Fukuzawa, and Prof. Shigenori Tanaka for their collaborators. The authors would like to thank Dr. Kazumi Tsuda and Mr. Daisuke Murayama at Science & Technology Systems, Inc., for supporting the development of the automated FMO calculation protocol. This research was conducted as part of the activity of the FMO drug design consortium (FMODD). The FMO calculations were performed on the K computer (project IDs: hp150160, hp160103, hp170183, and hp180147). For QM/MM optimizations, the supercomputer HOKUSAI (RIKEN Advanced Center for Computing and Communications) was used. PIEDA calculations were performed with the MIZUHO/BioStation software package. This research was partially supported by the Platform Project for Supporting Drug Discovery and Life Science Research (Basis for Supporting Innovative Drug Discovery and Life Science Research (BINDS)) from AMED under Grant Number JP18am0101113. The authors acknowledge JSPS KAKENHI Grant Number JP18K06619 and JST PRESTO Grant Number JPMJPR18GD.

References

1. Kitaura K, Ikeyama E, Asada T, Nakano T, Uebayasi M (1999) Fragment molecular orbital method: an approximate computational method for large molecules. *Chem Phys Lett* 313:701–706
2. Fedrov DG, Kitaura K (2009) The fragment molecular orbital method: practical application to large molecular system. CRC Press, 2009
3. Tanaka S, Mochizuki Y, Komeiji Y, Okiyama Y, Fukuzawa K (2014) Electron-correlated fragment-molecular-orbital calculations for biomolecular and nano systems. *Phys Chem Chem Phys* 16:10310–10344
4. Fedorov DG, Kitaura K (2007) Pair interaction energy decomposition analysis. *J Comp Chem* 28:222–237
5. Tsukamoto T, Kato K, Kato A, Nakano T, Mochizuki Y et al (2015) Implementation of pair interaction energy decomposition analysis and its applications to protein-ligand systems. *J Comput Chem Jpn* 14:1–9
6. Hitaoka S, Harada M, Yoshida T, Chuman H (2010) Correlation analyses on binding affinity of sialic acid analogues with Influenza Virus Neuraminidase-1 using *ab Initio* MO calculations on their complex structures. *J Chem Inf Model* 50:1796–1805
7. Hitaoka S, Matoba H, Harada M, Yoshida T, Tsuji D et al (2011) Correlation analyses on binding affinity of sialic acid analogues and anti-Influenza drugs with human neuraminidase using *ab Initio* MO calculations on their complex structures-LERE-QSAR analysis (IV). *J Chem Inf Model* 51:2706–2716
8. Watanabe C, Fukuzawa K, Okiyama Y, Tsukamoto T, Kato A et al (2013) Three- and four-body corrected fragment molecular orbital calculations with a novel subdividing fragmentation method applicable to structure-based drug design. *J Mol Graph Model* 41:31–42
9. Fukuzawa K, Kitaura K, Uebayasi M, Nakata K, Kaminuma T et al (2005) *Ab Initio* quantum mechanical study of the binding energies of human estrogen receptor α with its ligands: an application of fragment molecular orbital method. *J Comput Chem* 26:1–10
10. Watanabe H, Tanaka S, Okimoto N, Hasegawa A, Taiji M et al (2010) Comparison of binding affinity evaluations for FKBP ligands with state-of-the-art computational methods: FMO, QM/MM, MM-PB/SA, and MP-CAFEE approaches. *CBIJ* 10:32–45
11. Mazanetz MP, Ichihara O, Law RJ, Whittaker M (2011) Prediction of cyclin-dependent kinase 2 inhibitor potency using the fragment molecular orbital method. *J Cheminform* 3:2
12. Heifetz A, Chudyk EI, Gleave L, Aldeghi M, Cherezov V et al (2016) The fragment molecular orbital method reveals new insight into the chemical nature of GPCR–ligand interactions. *J Chem Inf Model* 56:159–172

13. Heifetz A, Aldeghi M, Chudyk EI, Fedorov DG, Bodkin MJ et al (2016) Using the fragment molecular orbital method to investigate agonist–orexin-2 receptor interactions. *Biochem Soc Trans* 44:574–581
14. Heifetz A, Trani G, Aldeghi M, MacKinnon CH, McEwan PA et al (2016) Fragment molecular orbital method applied to lead optimization of novel interleukin-2 inducible T-cell kinase (ITK) inhibitors. *J Med Chem* 59:4352–4363
15. Morao I, Fedorov DG, Robinson R, Southey M, Townsend-Nicholson A et al (2017) Rapid and accurate assessment of GPCR–ligand interactions using the fragment molecular orbital-based density-functional tight-binding method. *J Comp Chem* 38:1987–1990
16. Chudyk EI, Sarrat L, Aldeghi M, Fedorov DG, Bodkin MJ, James T, Southey M, Robinson R, Morao I, Heifetz A (2018) Exploring GPCR-ligand interactions with the fragment molecular orbital (FMO) method. In: *Computational Methods for GPCR Drug Discovery*, Springer, Methods in Molecular Biology, 2018, 1705, pp 179–195
17. Okimoto N, Otsuka T, Hirano Y, Taiji M (2018) Use of the multilayer fragment molecular orbital method to predict the rank order of protein-ligand binding affinities: a case study using tankyrase 2 inhibitors. *ACS Omega* 3:4475–4485
18. Takaya D, Inaka K, Omura A, Takenuki K, Kawanishi M et al (2018) Characterization of crystal water molecules in a high-affinity inhibitor and hematopoietic prostaglandin D synthase complex by interaction energy studies. *Bioorg Med Chem* 26:4726–4734
19. Xu F, Tanaka S, Watanabe H, Shimane Y, Iwasawa M, Ohishi K et al (2018) Computational analysis of the interaction energies between amino acid residues of the measles virus hemagglutinin and its receptors. *Viruses* 10:236
20. Amari S, Aizawa M, Zhang J, Fukuzawa K, Mochizuki Y et al (2006) VISCANA: visualized cluster analysis of protein-ligand interaction based on the *ab Initio* fragment molecular orbital method for virtual ligand screening. *J Chem Inf Model* 46:221–230
21. Kurauchi R, Watanabe C, Fukuzawa K, Tanaka S (2015) Novel type of virtual ligand screening on the basis of quantum-chemical calculations for protein-ligand complexes and extended clustering techniques. *Comput Theor Chem* 1061:12–22
22. Maruyama K, Sheng Y, Watanabe H, Fukuzawa K, Tanaka S (2018) Application of singular value decomposition to the inter-fragment interaction energy analysis for ligand screening. *Comput Theor Chem* 1132:23–34
23. Watanabe C, Watanabe H, Fukuzawa K, Parker LJ, Okiyama Y et al (2017) Theoretical analysis of activity cliffs among benzofuranone-class Pim1 inhibitors using the fragment molecular orbital method with molecular mechanics poisson-Boltzmann surface area (FMO+MM-PBSA) approach. *J Chem Inf Model* 57:2996–3010
24. Alexeev Y, Mazanetz MP, Ichihara O, Fedorov DG (2012) GAMESS as a free quantum-mechanical platform for drug research. *Curr Top Med Chem* 12:2013–2033
25. Watanabe H, Okiyama Y, Nakano T, Tanaka S (2010) Incorporation of solvation effects into the fragment molecular orbital calculations with the Poisson-Boltzmann equation. *Chem Phys Lett* 500:116–119
26. Okiyama Y, Nakano T, Watanabe C, Fukuzawa K, Mochizuki Y et al (2018) Fragment molecular orbital calculations with implicit solvent based on the Poisson-Boltzmann equation: implementation and DNA study. *J Phys Chem B* 122:4457–4471
27. Okiyama Y, Watanabe C, Fukuzawa K, Mochizuki Y, Nakano T, et al. (2019) Fragment molecular orbital calculations with implicit solvent based on the Poisson–Boltzmann equation: II. protein and its ligand-binding system studies. *J Phys Chem B* 123:957–973
28. FMO drug design consortium (FMODD), <https://fmodd.jp/> (accessed on November 10, 2020).
29. Kobayashi I, Takeda R, Suzuki R, Shimamura K, Ishimura H et al (2017) Specific interactions between androgen receptor and its ligand: *ab initio* molecular orbital calculations in water. *J Mol Graph Model* 75:383–389
30. Ozawa M, Ozawa T, Nishio M, Ueda K (2017) The role of CH/ π interactions in the high affinity binding of streptavidin and biotin. *J Mol Graph Model* 75:117–124
31. Ozawa M, Ozawa T, Ueda K (2017) Application of the fragment molecular orbital method analysis to fragment-based drug discovery of BET (bromodomain and extra-terminal proteins) inhibitors. *J Mol Graph Model* 74:73–82

32. Takeda R, Kobayashi I, Shimamura K, Ishimura H, Kadoya R et al (2017) Specific interactions between vitamin-D receptor and its ligands: *ab initio* molecular orbital calculations in water. *J Steroid Biochem Mol Biol* 171:75–79
33. Takeda R, Kobayashi I, Suzuki R, Kawai K, Kittaka A et al (2018) Proposal of potent inhibitors for vitamin-D receptor based on *ab initio* fragment molecular orbital calculations. *J Mol Graph Model* 80:320–326
34. Takeda R, Suzuki R, Kobayashi I, Kawai K, Kittaka A et al (2018) Specific interactions between vitamin D receptor and ligand depending on its chirality: *ab initio* fragment molecular orbital calculations. *CBIJ*. 18:32–43
35. Sheng Y, Watanabe H, Maruyama K, Watanabe C, Okiyama Y et al (2018) Towards good correlation between fragment molecular orbital interaction energies and experimental IC₅₀ for ligand binding: A case study of p38 MAP kinase. *Comput Struct Biotechnol J* 16:421–434
36. Berman HM, Westbrook J, Feng Z, Gilliland G, Bhat TN, Weissig H, Shindyalov IN, Bourne PE (2000) The protein data bank. *Nucleic Acids Res* 28:235–242
37. FMO database, <https://drugdesign.riken.jp/FMODB/> (accessed on November 10, 2020).
38. Watanabe C, Watanabe H, Okiyama Y, Takaya D, Fukuzawa K, Tanaka S, Honma T (2019) Development of an automated fragment molecular orbital (FMO) calculation protocol toward construction of quantum mechanical calculation database for large biomolecules. *CBIJ* 19:5–18
39. BIOVIA Pipeline Pilot, 17.2.0.1361; Dassault systèmes BIOVIA: 5005 Wateridge Vista Drive, San Diego, CA 92121 USA, 2017.
40. Molecular Operating Environment (MOE), 20151001; Chemical Computing Group Inc.: 1010 Sherbooke St. West, Suite #910, Montreal, QC, Canada, H3A 2R7, 2018.
41. Frisch MJ, Trucks GW, Schlegel HB, Scuseria GE, Robb MA et al. (2009) Gaussian 09, Revision D.01; Gaussian, Inc.: Wallingford CT
42. Case DA, Darden TA, Cheatham TE III, Simmerling CL, Wang J et al (2008) AMBER 10. University of California, San Francisco CA
43. Wang J, Wolf RM, Caldwell JW, Kollman PA, Case DA (2004) Development and testing of a general amber force field. *J Comput Chem* 25:1157–1174
44. Jakalian A, Bush BL, Jack DB, Bayly CI (2000) Fast, efficient generation of high-quality atomic charges. AM1-BCC model: I. Method *J Comput Chem* 21:132–146.
45. Wang J, Wang W, Kollman PA, Case DA (2006) Automatic atom type and bond type perception in molecular mechanical calculations. *J Mol Graph Model* 25:247–260
46. BioStation: ABINIT-MP and BioStation Viewer; The program package is available at: <http://www.ciss.iis.u-tokyo.ac.jp/english/dl/index.php> (accessed on November 10, 2020) and http://www.ciss.iis.u-tokyo.ac.jp/riss/dl/download/index.php#download_2 (accessed on November 10, 2020).
47. MIZUHO/BioStation Viewer 3.0; (2013) Mizuho Information and Research Institute Inc.
48. Okiyama Y, Nakano T, Yamashita K, Mochizuki Y, Taguchi N, Tanaka S (2010) Acceleration of fragment molecular orbital calculations with Cholesky decomposition approach. *Chem Phys Lett* 490:84–89
49. Okiyama Y, Watanabe H, Fukuzawa K, Nakano T, Mochizuki Y, Ishikawa T, Tanaka S, Ebina K (2007) Application of the fragment molecular orbital method for determination of atomic charges on polypeptides. *Chem Phys Lett* 449:329–335
50. Okiyama Y, Watanabe H, Fukuzawa K, Nakano T, Mochizuki Y, Ishikawa T, Ebina K, Tanaka S (2009) Application of the fragment molecular orbital method for determination of atomic charges on polypeptides. II. Towards an improvement of force fields used for classical molecular dynamics simulations. *Chem Phys Lett* 467:417–423
51. PDBbind, <http://www.pdbbind.org.cn/> (accessed on November 10, 2020).
52. Saitou S, Iijima J, Fujimoto M, Mochizuki Y, Okuwaki K et al (2018) Application of TensorFlow to recognition of visualized results of fragment molecular orbital (FMO) calculations. *CBIJ* 18:58–69
53. Doi H, Okuwaki K, Mochizuki Y, Ozawa T, Yasuoka K (2017) Dissipative particle dynamics (DPD) simulations with fragment molecular orbital (FMO) based effective parameters for 1-Palmitoyl-2-oleoyl phosphatidyl choline (POPC) membrane. *Chem Phys Lett* 684:427–432

54. Yoshida M, Hirono S (2019) A 3D-QSAR analysis of CDK2 inhibitors using FMO calculations and PLS regression. *Chem Pharm Bull* 67:546–555

Application of FMO to Ligand Design: SBDD, FBDD, and Protein–Protein Interaction



Tomonaga Ozawa and Motoyasu Ozawa

Abstract The structures of target proteins and ligands provide essential information to drug discovery researchers, especially medicinal chemists and computational chemists. They use the structural information to design novel ligands by considering the molecular interactions between ligands and proteins. The interpretations of molecular interactions are usually based on the molecular mechanics method or visual inspection. The advances in structural biology, theoretical chemistry, and organic chemistry that indicate the presence of diverse molecular interactions, such as not only hydrogen bond and electrostatic interaction but also CH/O interaction, π/π interaction, CH/ π interaction, halogen bonding interaction, and sulfur bonding interaction, indicate that there is a requirement for a method that is more accurate as compared to the molecular mechanics method to estimate the nonconventional interactions. The fragment molecular orbital (FMO) method is considered to be promising to estimate the diverse molecular interactions in large-scale molecular systems such as complexes between proteins and ligands; furthermore, this method can be applied to drug design. In this chapter, we report the usefulness of FMO in drug design based on three examples, including structure-based drug design (SBDD), fragment-based drug design, and protein–protein interaction.

Keywords Fragment-based drug design (FBDD) · Protein–protein interactions · CH/ π interaction

1 Introduction

The productivity of drug discovery has been decreasing since the 2000s [1] because of the decreasing number of newly discovered drug target proteins; treatment of undruggable proteins, including the protein–protein interaction (PPI); and increasing drug regulation, especially in terms of safety [2]. Drug discovery scientists are challenging this problem using a combination of advancement in omics technology,

T. Ozawa (✉) · M. Ozawa
Kissei Pharmaceutical Company Ltd., Matsumoto, Nagano, Japan
e-mail: tomonaga_ozawa@pharm.kissei.co.jp

high throughput screening, phenotypic screening, structural biology, computational chemistry (in silico), and big data analysis.

Medicinal chemistry plays an essential role in drug discovery. The mission of medicinal chemistry [3] is to find, develop, and improve drug substances that can be used to cure various diseases. Medicinal chemistry is an interdisciplinary science that covers multiple fields, including organic chemistry, biochemistry, pharmacology, pharmacokinetics, toxicology, structure biology, and computational chemistry. Recent advances in structural biology and computational chemistry have provided insights into target proteins in the drug design process [4]. The number of structural analyses of proteins, including drug targets, by crystallography, has rapidly increased during the last two decades. Furthermore, rapid increases in the performances of the computer systems [5] have enabled us to perform large-scale and precise simulations of the complexes between a drug target protein and its ligand. A combination of structural biology and computational chemistry, which is also called structure-based drug design (SBDD) [6], has been incorporated into the overall modern drug discovery process.

Docking study [7], which involves finding the proper pose of a ligand within a protein binding site, is one of the main approaches of SBDD, and it serves two main purposes. One is to explore the hit compounds from the compound library, which contain 100,000 or more compounds; this is called in silico screening or virtual screening. The second is to search for a detailed docking mode of ligand to protein. While the usefulness of the docking studies has been accepted, the accuracy of such studies must be improved. Docking studies comprise three main elements, including the generation of conformation for ligand, exploration of binding site in target protein, and determination of the docking mode for ligand based on scoring functions. Scoring functions are used to set the priority of testing compounds from known many compounds. Further, alternative methods could be appropriate to perform detailed analyses of molecular interactions.

Ab initio molecular orbital calculations, which can be performed to calculate electronic energies, densities, and other properties, are more appropriate to analyze molecular interactions as compared to the classical force field. The fragment molecular orbital (FMO) method has been used to analyze large systems, such as biomolecular systems and their ligand interactions, because it can be used to obtain electronic information such as electronic densities, many-body interactions, inter-fragment interaction energies (IFIE), and pair interaction energy decomposition analysis (PIEDA). IFIE and PIEDA can provide information about the interactions between ligands and the residues of each amino acid of a target protein. This information is helpful for medicinal chemists and computational chemists, especially from the viewpoint of interpreting the interactions between ligands and proteins as well as for discussing the ligand design.

In this chapter, we report the practical applications of FMO to drug design through three examples, including structure-based drug design (SBDD) [8], fragment-based drug design (FBDD) [9], and protein-peptide interaction [10].

2 Computational Method

2.1 Structure Preparation

All the structures in this report are retrieved from Protein Data Bank (PDB) [11], and the codes and their resolution are listed in Table 1. The hydrogen atoms were generated using the molecular graphic software, Discovery Studio [12] (BIOVIA San Diego, CA, USA). We assumed that the amino groups of the lysine and arginine side chains were protonated, while the carboxyl groups of the aspartic and glutamic side chains were deprotonated. The Chemistry at HARvard Macromolecular Mechanics (CHARMM) force field [13] implemented in Discovery Studio was used in the minimization steps. The structures of the protein and ligand complex were optimized using the steepest descent method at a dielectric constant (ϵ) of 4R (R: distance). The optimizations were performed in a stepwise manner. During the first step, the structures were minimized with constrained non-hydrogen atoms (protein, ligand, and water). Further, the protein backbone atoms were constrained. During the final step, all the atoms were minimized as the harmonic atom constraint was gradually decreased from 100 to 10.0 and 1.0 kcal/molÅ².

Table 1 List of proteins and compounds with PDB ID and resolution

Protein	Compound	PDB ID	Resolution (Å)
Lck	1	1QPJ	2.2
Lck	2	2ZM4	2.7
Lck	3	2ZM1	2.1
Lck	4	2ZYB	2.6
BRD4	5	3UVW	1.4
BRD4	6	4HBV	1.6
BRD4	7	4HBW	1.7
BRD4	8	4HBX	1.6
BRD4	9	4HBY	1.6
BRD4	10	4E96	1.9
BRD4	11	2YEL	1.7
BRD4	12	4Z1Q	1.4
Abl	3BP1	1ABO	2.0
SEM5	Sos	1SEM	2.0
Gads	SLP-76	1OEB	1.7

2.2 CH/ π Interaction and CHPI Analysis

The CH/ π interaction is an attractive molecular force that occurs between a CH group and a π -system [14, 15]. In a typical case, the aliphatic and aromatic CHs are involved as CH donors and π -systems, such as aromatic rings and double or triple bonds, are involved as the CH acceptor; the interaction energies are 1.5–2.5 kcal mol⁻¹ per unit [16]. A notable feature of the CH/ π interaction is that it arises mainly from dispersion energy and not electrostatic energy [17]. Therefore, this interaction does not weaken in water, which makes it critically important from the viewpoint of molecular recognition of biomolecules [18]. The CH/ π interaction is observed to be important in the fields of supramolecular chemistry, conformation of organic compounds, 3D structure protein, substrate specificity of proteins, and rational drug design [19].

The CH/ π interactions were evaluated using the CHPI program implemented in BioStation Viewer [20]. Nishio and Umezawa originally developed this program [21] to search for short contacts between the CH groups and π -systems. This program measures the distances and angles between CH groups and the interacting π -systems (aromatic rings) and indicates the existence of the CH/ π interactions. The criteria for CH/ π interaction are observed to differ according to the position of the CH hydrogen; a detailed description of CHPI analysis was written in the original study. In simple cases, where CH is located above the aromatic ring, CHPI indicates CH/ π interaction if the distance between H and the nearest heavy atom of the aromatic ring is less than 3.05 Å. This value is determined based on the van der Waals distance [(1.2 Å for H + 1.7 Å for C) \times 1.05 = 3.05 Å].

3 Application of FMO to SBDD

3.1 Abstract

The interaction energy was calculated using the ab initio FMO method for complexes between lymphocyte protein tyrosine kinase (Lck) protein and four inhibitors (staurosporine **1**, BMS compound **2**, and our compounds **3** and **4**). In every case, a number of CH/ π interactions were found in the so-called adenine pocket. In the complexes of **2**, **3**, and **4**, CH/ π and NH/ π interactions were observed in another pocket. A tenfold increase in the potency was achieved for **4** relative to **3**. In view of the above results, conversion of the aniline ring of **3** to 2,6-dimethyl aniline of **4** enhanced the CH/ π interactions, resulting in an increase in the affinity for Lck kinase. We suggest that the concept of CH/ π interactions and the use of FMO method allow for rational consideration of nonpolar interactions in the SBDD process.

3.2 Lck Kinase

Src-family tyrosine kinases [22] consist of eight highly homologous proteins that are expressed primarily in hematopoietic tissues, of which Lck and Fyn are expressed in T cells, with Lck playing a critical role in the initial steps of T-cell receptor signaling [23]. Then, an Lck inhibitor is a potential target for an autoimmune agent. Several studies have reported on the synthesis and characterization of Lck kinase inhibitors [24]. These compounds are ATP-competitive inhibitors, and the crystal structure of various Lck complexes has been reported [25]. ATP is known to be bound in the cleft formed between the two lobes of the so-called protein kinase fold (Fig. 1) [26]. Three sites (the hinge region, adenine pocket, and another pocket) are common to all Src-family kinases and are critical for the binding of Lck inhibitors (Fig. 2).

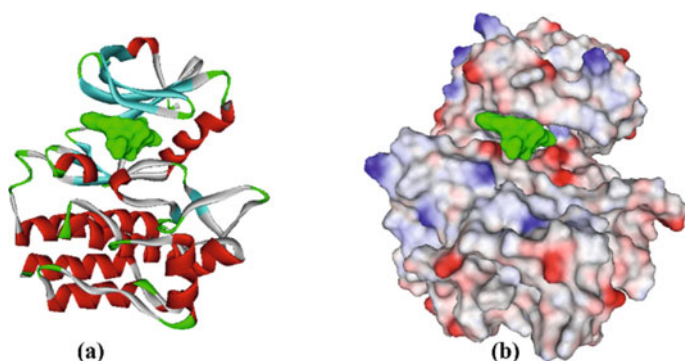


Fig. 1 Structure of Lck kinase showing two lobes and ATP-bind site

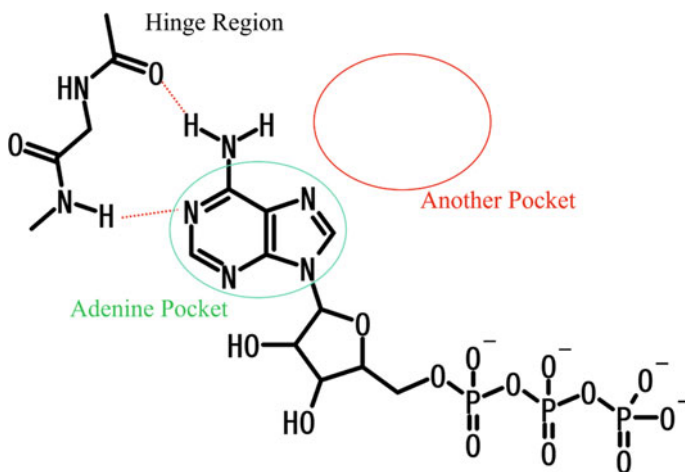


Fig. 2 Schematic representation of binding site of Lck kinase

Donor–acceptor pairs of hydrogen bonds are formed between the backbone atoms of the hinge region and adenine. The adenine moiety is positioned at the so-called adenine pocket, which is composed mainly of aliphatic amino acid residues. Another pocket, which is unoccupied by ATP, binds an aromatic group of the inhibitors. Therefore, we first survey the molecular interactions of the complexes between Lck and known inhibitors by using the FMO method. Using this information, we perform SBDD for Lck inhibitors. Herein, we report the results of the FMO calculations of four complexes between Lck and inhibitors (Fig. 3). Several hydrogen bonds, CH/ π , CH/O [27], and NH/ π [28] interactions have been found to contribute toward stabilizing the structure of Lck complexes.

In view of the significance of the CH/O interaction in the recognition of proteins by their ligand, Pierce designed effective glycogen-synthase-kinase 3 (GSK3) inhibitors by using the concept of CH/O interaction [29].

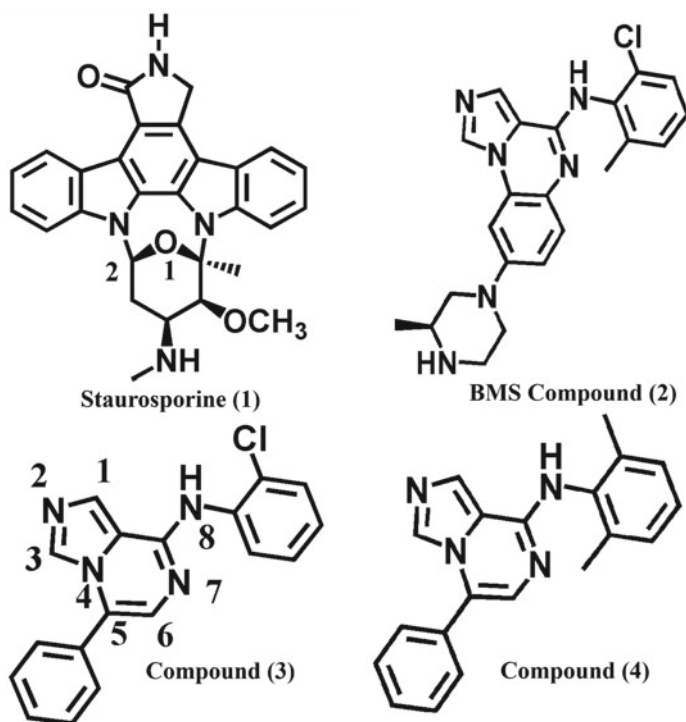


Fig. 3 Structure of four Lck kinase inhibitors analyzed using FMO method

3.3 Interpretation of Ligand and Protein Interaction

3.3.1 Staurosporine (1)

Staurosporine (**1**) is a natural product isolated from bacterium *Streptomyces staurosporeus* by Oomura in 1977 [30]. In subsequent studies, it was found to inhibit protein kinase non-selectively through competition with ATP. Based on this, we postulate that **1** has a basic element of molecular interactions in ATP-competitive kinase inhibitors. Then, the complex between Lck and **1** (pdb code: 1qppj) was retrieved from the PDB, and it was calculated using the FMO method.

Two hydrogen bonds in the hinge region of protein kinases represent the key interactions in the recognition of inhibitors or substrates. In the case of Lck, the hinge region is from Ile314 to Glu320. The two hydrogen bonds formed between **1** and Lck are shown in Fig. 4a. One of the bonds is between the oxygen of the protein backbone in Glu317 and the lactam amide hydrogen of **1**. The other is formed between the amide hydrogen of the protein backbone in Met319 and the lactam carbonyl group of **1**, indicating that **1** interacts with Lck through the typical hydrogen bond pattern of protein kinase inhibitors.

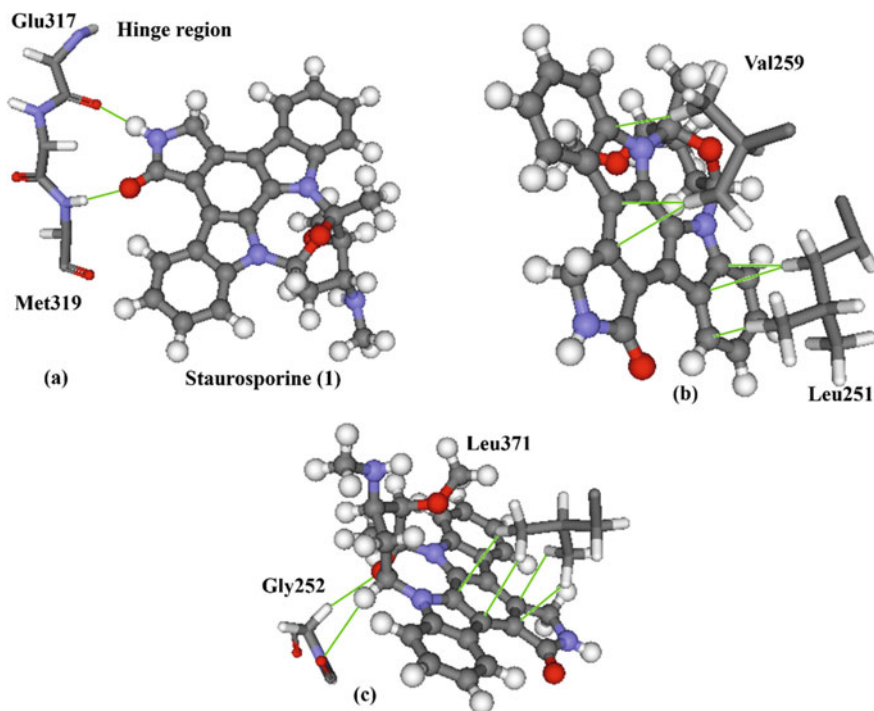


Fig. 4 Interactions between **1** and Lck kinase: **a** hinge region, **b** and **c** ATP-binding site

The results of our FMO calculations are consistent with these observations, indicating **1** has a typical hydrogen bond pattern of kinase inhibitors in the hinge region. That is, IFIE values between **1** and Lck were estimated to be -18.7 and -11.3 kcal/mol, respectively, for Tyr318 and Met319. In the FMO scheme, the interaction of Tyr318 is composed of the carbonyl group of the protein backbone in Glu317, the side chain of Tyr318, and NH group of the protein backbone in Tyr318, details of which are available in the chapter on the basic FMO concept. IFIE between **1** and Lck can be attributed mainly to the hydrogen bond between the peptide oxygen of Glu317 and the lactam amide hydrogen of **1** owing to their relative configuration. IFIE between Met319 and **1** can be attributed to the amide hydrogen of the protein backbone in Met319 and the lactam carbonyl group of **1**. Thus, the importance of the two hydrogen bonds between the hinge region and **1** was confirmed by the FMO calculation.

It is generally accepted that kinase inhibitors have an aromatic group at the ATP-binding site. We investigated the mode of recognition at the ATP-binding site of Lck by performing FMO and CHPI analysis. Table 2 summarizes the results of IFIE, PIEDA, and CHPI analysis between Lck and **1**. In addition to two hinge hydrogen bonds, large IFIE was observed in three aliphatic amino acids, namely, Leu251 (IFIE -6.3 kcal/mol), Val259 (-6.4 kcal/mol), and Leu371 (-6.4 kcal/mol). Dispersion energies estimated from PIEDA are as follows: Leu251 (-7.4 kcal/mol), Val259 (-6.4 kcal/mol), and Leu371 (-8.1 kcal/mol). Seven CH/ π interactions were found by CHPI analysis, as shown in Fig. 4b, c. No hydrogen bond was found between **1** and these three residues. Therefore, those three aliphatic residues interact with **1** through

Table 2 Interaction energies (in kcal/mol) between Lck and staurosporine (**1**)

	IFIE	Es ^a	Ex ^b	CT ^c	DI ^d	q(I = > J) ^e	CH/ π ^f
TYR318	-18.7	-15.8	9.7	-5.5	-7.0	0.022	
ASP382	-15.4	-10.8	2.5	-2.5	-4.7	0.015	
MET319	-11.3	-11.8	6.6	-2.2	-3.8	-0.028	
ASN369	-11.0	-8.2	4.2	-2.7	-4.3	0.031	
GLY252	-10.9	-6.3	3.0	-2.9	-4.6	0.006	
ASP326	-7.7	-6.2	0.5	-0.7	-1.3	0.009	
LEU371	-7.0	-2.2	5.3	-1.9	-8.1	-0.010	2
GLU288	-6.6	-4.5	0.2	-1.1	-1.2	0.011	
VAL259	-6.4	-1.5	3.0	-1.5	-6.4	-0.010	2
LEU251	-6.3	-2.0	4.9	-1.8	-7.4	-0.020	3
LYS269	-4.3	-4.3	0.0	0.0	0.0	0.000	
ASP364	-4.0	-4.0	0.0	0.0	0.0	0.000	
GLY254	-3.1	-2.2	0.1	-0.4	-0.6	0.003	

^aElectrostatic of IFIE, ^bExchange repulsion of IFIE, ^cCharge transfers and higher-order term of IFIE, ^dDispersion interaction of IFIE, ^eAmount of charge transferred from fragment I (ligand) to J (protein), ^fNumber of CH/ π interactions detected by CHPAI program

CH/ π interactions, so CH/ π interactions play an important role in the recognition of **1** at the ATP-binding site of Lck. Amino acids composing the ATP-binding site are highly conserved in many kinases, suggesting that CH/ π interactions play a critical role in the recognition of inhibitors at the ATP-binding site of kinase.

The glycosyl part of **1** has many interactions with Lck. The crystal structure of the complex shows that the methylamino group of the glycosyl part of **1** interacts with Lck through hydrogen bonds, namely, the alcohol oxygen of side chain in Ser323 and the peptide oxygen of main-chain in Ala368. IFIE between **1** and Ser323 is -1.2 kcal/mol. PIEDA showed that this IFIE was composed of mainly large attractive electrostatic interaction ($\Delta E^{\text{ES}} -8.5$ kcal/mol) and large repulsive exchange-repulsion ($\Delta E^{\text{EX}} + 12.5$ kcal/mol), indicating this hydrogen bond was shifted from the ideal position. IFIE between **1** and Asn369 was -11.0 kcal/mol, which is very typical of a hydrogen bond (note that the peptide oxygen in the main-chain of Ala368 is composed of Asn369 according to the FMO scheme). IFIE values of Asp382 (-10.8 kcal/mol) and Asp326 (-7.7 kcal/mol) were observed. These interactions could be regarded as charge-charge interactions because of the large and predominantly attractive electrostatic interaction (ΔE^{ES} Asp382: -10.8 kcal/mol, Asp326: -6.2 kcal/mol). Explaining the IFIE between **1** and Gly252 is difficult. It could be interpreted as two CH/O interactions owing to the configurations and the results of PIED analysis. One is a CH/O interaction between 1-oxygen of the glycosyl group in **1** and α hydrogen in Gly252, a carbonyl oxygen of Gly252; the distance is 2.5 \AA . The other CH/O interaction is between the 6-hydrogen of the glycosyl group in **1** and the peptide oxygen of Leu251; the distance is 2.7 \AA .

To summarize the interactions of staurosporine (**1**), FMO calculations revealed that a variety of interactions contribute to the recognition of Lck by **1**. Therefore, not only hydrogen bonds but CH/ π interaction and CH/O interaction must be considered in the following drug design.

3.3.2 BMS Compound

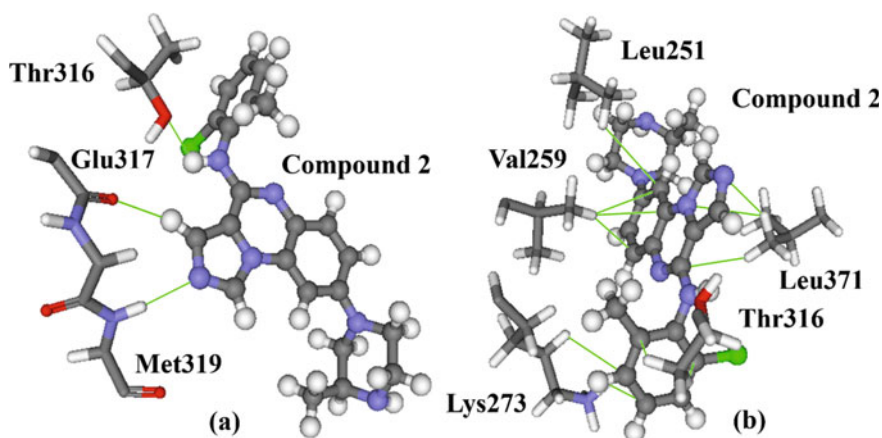
Lipinski's "rule-of-five" [31] states that to be a useful oral drug, a candidate molecule should have fewer than five hydrogen bond donor groups and fewer than 10 acceptor groups. The "rule-of-three," [32] which limits the number of hydrogen bond donors to three, has been proposed for FBDD. These suggestions imply that reducing the number of hydrogen bond donor groups is favorable from the viewpoint of developing oral drugs. In BMS compound [33] **2**, the number of hydrogen bond donors is lower than that in typical kinase inhibitors. The BMS compound was selected as the lead compound in our study.

The IFIE in Table 3 shows that **2** interacts with Met319, Tyr318, and Thr316 in the hinge region. IFIE between **2** and Met319 is -8.2 kcal/mol, which corresponds to the hydrogen bond between the peptide amide hydrogen of Met319 and N3 of the imidazole in **2**. IFIE between **2** and Tyr318 is -7.7 kcal/mol. The crystal structure of the complex shows that the peptide amide group is located on the opposite side of **2**, and the side chain of Tyr318 is more than 4.2 \AA away from **2** in Fig. 5a. We noticed

Table 3 Interaction energies (in kcal/mol) between Lck and BMS compound (**2**)

	IFIE	Es ^a	Ex ^b	CT ^c	DI ^d	q(I = > J) ^e	CH/ π ^f
LYS273	-8.2	-6.6	7.6	-2.7	-6.6	-0.026	
THR316	-8.2	-4.4	4.9	-2.4	-6.4	0.017	1
MET319	-8.2	-5.6	2.5	-1.5	-3.6	-0.020	
TYR318	-7.7	-4.9	1.8	-1.7	-2.9	0.018	
ASP326	-6.6	-4.6	0.4	-1.0	-1.4	0.013	
GLU288	-5.6	-2.7	1.5	-1.9	-2.5	0.024	
GLY252	-4.8	-3.9	3.0	-1.2	-2.7	0.016	
LEU371	-4.7	-1.5	3.4	-1.3	-5.2	-0.009	1
VAL259	-3.9	-0.6	2.8	-1.3	-4.8	-0.013	1
VAL272	-3.4	-2.3	0.1	-0.4	-0.8	0.003	
ILE315	-3.2	-1.9	0.6	-0.7	-1.3	0.010	

^aElectrostatic of IFIE, ^bExchange repulsion of IFIE, ^cCharge transfers and higher-order term of IFIE, ^dDispersion interaction of IFIE, ^eAmount of charge transferred from fragment I (ligand) to J (protein), ^fNumber of CH/ π interactions detected by CHPAI program

**Fig. 5** Interactions between **2** and Lck kinase: **a** hinge region and **b** ATP-binding site

that the hydrogen attached to C4 of the imidazole ring in **2** is located near the peptide carbonyl of Glu317; distance is 2.4 Å. Then, **2** interacts with Lck through the CH/O interaction in the hinge region. Previously, Pierce mentioned the importance of the CH/O interaction in the hinge region of kinase.

In the tricyclic aromatic part of **2**, three CH/ π interactions involving Val259, Ala271, and Leu371 were found by CHPI analysis. IFIE and dispersion energies between these amino-residues and Lck are as follows: Leu371 (4.7, -5.2), Val259 (-3.9, -4.8), and Ala271 (-1.0, -3.0) respectively. The IFIEs of these aliphatic amino-residues are lower than that of compound **1**. These results imply that recognition of the

tricyclic aromatic part of **2** by aliphatic amino acid residues forming the ATP-binding site can be improved by considering the CH/ π interactions shown in Fig. 5b.

The 2-chloro-6-methyl-aniline part of **2** is located in another pocket, while the staurosporine part (**1**) does not exist at this site. Then, different amino acid residues are involved in the recognition of **2**, indicating large IFIE of Lys273 (-8.2 kcal/mol) and Thr316 (-8.2 kcal/mol). CHPI analysis shows one CH/ π interaction between the side chain of Thr316 and the aniline ring of **2**. The ϵ -amino group and the methylene of the side chain in Lys273 were found to be located near the aniline ring of **2**. NH/ π and CH/ π interactions could be attributed to ligand recognition because the electrostatic and dispersion energies estimated by PIEDA are nearly the same (both -6.6 kcal/mol).

FMO calculations revealed that the BMS compound interacts with Lck through not only hydrogen bonds but also through CH/O, NH/ π , and CH/ π interactions, indicating that this compound has sufficient interaction energy to be a candidate for the lead compound. We, therefore, tried to improve the binding affinity of **2** by considering CH/ π interactions.

3.3.3 Compound 3:

N-(2-Chlorophenyl)-5-phenylimidazo[1,5-a]pyrazin-8-amine

In view of the results obtained by the FMO analysis of the above two complexes, we hypothesized that CH/O and CH/ π interactions play an important role, in addition to hydrogen bonds, in the binding of inhibitors to Lck. Thus, N-(2-chlorophenyl)-5-phenylimidazo[1,5-a]pyrazin-8-amine (**3**) was designed and synthesized as a candidate inhibitor. First, we determined the crystal structure of **3** in complex with Lck. Next, FMO calculations were performed to obtain the information necessary for optimizing the structure of **3**.

Table 4 shows the IFIE between **3** and LCK in the hinge region: Thr316 (-8.9 kcal/mol), Tyr318 (-9.2 kcal/mol), and Met319 (-9.7 kcal/mol). These values are similar to those of **2**, indicating **3** has a similar binding mode as **2**.

CHPI analysis indicated the presence of three CH/ π interactions between the imidazo-pyrazine moiety of **3** and the side chain of Val259 and Leu371. Consistent with this observation, IFIE and dispersion energies between **3** and these two residues Val259 (-2.5 , -4.0 kcal/mol) and Leu371 (-4.7 , -5.9 kcal/mol) were attractive. Although Leu251 interacted with the core-ring part of **1** and **2** through CH/ π interactions, Leu251 was remote from the imidazo-pyrazine ring in **3**. By contrast, one CH/ π interaction was found between the side chain of Leu251 and the phenyl ring at position 5 of the imidazo-pyrazine ring. IFIE and dispersion energies were -2.5 and -4.0 kcal/mol, respectively. The tricyclic ring in the core region of inhibitor **2** was converted to a bicyclic ring in **3**. Three amino acid residues (Val259, Leu371, and Leu251) interacting with **2** by CH/ π interactions also contributed toward the recognition of **3** through CH/ π interactions.

Two CH/ π interactions were found between the 2-chloro-aniline part of **3** and the side chain of Thr316. In agreement with this observation, IFIE and dispersion

Table 4 Interaction energies (in kcal/mol) between Lck and compound (**3**)

	IFIE	Es ^a	Ex ^b	CT ^c	DI ^d	q(I => J) ^e	CH/ π ^f
MET319	-9.6	-9.7	6.8	-2.2	-4.5	-0.024	
TYR318	-9.2	-5.1	2.2	-2.3	-4.0	0.018	
THR316	-8.9	-5.8	5.8	-2.5	-6.4	0.016	2
LYS273	-8.0	-5.5	5.3	-2.1	-5.7	-0.022	
GLU288	-7.4	-4.6	1.5	-1.7	-2.5	0.024	
LEU371	-4.7	-1.2	3.8	-1.4	-5.9	-0.006	2
GLY252	-4.6	-3.0	0.4	-0.7	-1.3	0.008	
LEU251	-2.8	-0.6	2.2	-1.1	-3.3	-0.008	1
VAL259	-2.5	0.2	2.3	-0.9	-4.0	-0.006	1

^aElectrostatic of IFIE, ^bExchange repulsion of IFIE, ^cCharge transfers and higher-order term of IFIE, ^dDispersion interaction of IFIE, ^eAmount of charge transferred from fragment I (ligand) to J (protein), ^fNumber of CH/ π interactions detected by CHPAI program

energies were -8.9 and -6.4 kcal/mol. The dispersion energy between **3** and Lys273 is relatively large (-5.7 kcal/mol), and the side chain of Lys273 is located on the aniline ring of **3**. Then, **3** could interact with Lys273 through NH/ π and CH/ π interactions, although the CH/ π interaction was not detected in the CHPI analysis.

FMO calculations showed that **3** interacts with Lck through hydrogen bonds, CH/O, NH/ π , and CH/ π interactions. However, the inhibitory activity of **3** toward Lck remained modest (IC50 = 220 nM).

3.3.4 Compound 4:

N-(2,6-Dimethylphenyl)-5-phenylimidazo[1,5-a]pyrazin-8-amine

FMO calculations revealed that the 2-chlorol-aniline part of **3** interacts with Lck through CH/ π and NH/ π interactions, suggesting the possibility of increasing its inhibitory activity by strengthening these interactions. The effects of substituents on the CH/ π interaction have been investigated using various methods, including infrared (IR) and nuclear magnetic resonance (NMR) spectroscopy, X-ray crystallography, and ab initio calculations. In these studies, it was shown that an electron-donating substituent on the π -ring system strengthens the CH/ π interaction. We, therefore, designed N-(2,6-dimethylphenyl)-5-phenylimidazo[1,5-a]pyrazin-8-amine (compound **4**) to improve interactions, resulting in **4** showed improved inhibitory activity over **3**: compound **3**, 200 nM; and compound **4**, 20 nM (IC50 value for Lck).

The obtained FMO results agree well with the structure-activity relationship (SAR) of **3** and **4** (Table 5). The difference in the interaction energies of Lys273 between **3** and **4** was -5.2 kcal/mol, the largest among the amino acid residues in Lck. The side chain of Lys273 was located above the 2, 6-dimethylphenyl ring of **4**, implying that the enhanced activity of **4** could be attributed to the NH/ π and CH/ π

Table 5 Interaction energies (in kcal/mol) between Lck and compound (**4**)

	IFIE	Es ^a	Ex ^b	CT ^c	DI ^d	q(I => J) ^e	CH/ π ^f
LYS273	-13.2	-9.7	4.4	-2.1	-5.8	-0.021	
MET319	-9.5	-8.2	4.9	-1.9	-4.3	-0.024	
THR316	-8.9	-5.1	6.3	-2.8	-7.4	0.020	2
TYR318	-8.3	-4.5	1.6	-1.9	-3.4	0.015	
GLY252	-5.7	-3.8	1.2	-1.1	-1.9	0.012	
LEU371	-4.6	-1.0	3.1	-1.3	-5.4	-0.006	3
GLU288	-4.4	-0.6	1.7	-2.3	-3.1	0.032	
VAL272	-3.1	-2.0	0.1	-0.3	-0.9	0.001	
ILE315	-3.0	-1.1	0.4	-1.0	-1.4	0.012	
VAL259	-3.0	-0.2	2.6	-1.0	-4.4	-0.007	1
LEU251	-2.9	-0.7	2.9	-1.3	-3.8	-0.010	1

^aElectrostatic of IFIE, ^bExchange repulsion of IFIE, ^cCharge transfers and higher-order term of IFIE, ^dDispersion interaction of IFIE, ^eAmount of charge transferred from fragment I (ligand) to J (protein), ^fNumber of CH/ π interactions detected by CHPAI program

interactions. Because the increase in IFIE can be ascribed mainly to its electrostatic interaction (-4.2 kcal/mol) component, NH/ π interactions are predominantly involved in improving affinity.

By contrast, the difference in the interaction energies in the case of Thr316 was small (+0.02 kcal/mol). The dispersion energy estimated using PIEDA increased from -6.3 (**3**) to -7.3 (**4**) kcal/mol, while the electrostatic interaction decreased from -5.8 (**3**) to -5.0 (**4**) kcal/mol. Then, the opposing interactions could not affect the IFIE value. Karthikeyan described that the addition of a methyl group to the benzene ring increased CH/ π interactions, mainly because of the dispersion energies of the benzene-methane complex, as determined using the CCSD(T) method at the completed basis set limit. Because dispersion energies increased in the complex of **4**, CH/ π interactions increased with dimethyl substitution of the benzene ring. The hydrogen bond between the NH of aniline and the O of the hydroxyl group in the side chain of Thr316 weakened. This appeared to have been caused by a decrease in the acidity of NH in the aniline part of **4** owing to an increase in electron density in the benzene ring by the introduction of methyl groups at positions 2 and 6. The differences in the interaction energies associated with other residues were insignificant. The interactions between **4** and Lck were equivalent to those between **3** in the hinge region and imidazo-pyrazine ring.

3.4 Conclusions

FMO calculations were carried out for four complexes between Lck and four inhibitors (staurosporine **1**, BMS compound **2**, and compounds **3** and **4**). IFIE and PIEDA analysis revealed that inhibitors interact simultaneously with Lck through various molecular interactions; hydrogen bond, CH/O interaction, NH/ π interaction, and CH/ π interaction. IFIE can be used to survey molecular interactions widely, including ligands and all amino-residues, in the case of protein and ligand complexes. Additionally, PIEDA enables us to perform a decomposition analysis of the molecular interactions between ligands and proteins, and it helps interpret these molecular interactions. These interpretations can provide useful insights to medicinal chemists from the viewpoint of SBDD.

4 Application of FMO to FBDD

4.1 Abstract

The molecular interactions of the inhibitors of bromodomains (BRDs) are investigated. BRDs are protein interaction modules that can recognize ϵ -N-acetyl-lysine (ϵ Ac-Lys) motifs found in histone tails and are promising protein–protein interaction (PPI) targets. First, we analyze a peptide ligand containing ϵ Ac-Lys to evaluate native PPIs. Then, we analyze tetrahydroquinazoline-6-yl-benzensulfonamide derivatives found by fragment-based drug design (FBDD) and examine their interactions with the protein compared to the peptide ligand from the viewpoint of IFIE. Furthermore, we analyze benzodiazepine derivatives that are high-affinity ligands for BRDs and examine differences in the CH/ π interactions of the amino acid residues. In addition, we survey changes in the charges of the amino acid residues among individual ligands, perform pair interaction energy decomposition analysis, and estimate the water profile at the binding site. Thus, useful insights for drug design are provided. Through these analyses and considerations, we show that FMO is a useful drug design tool for evaluating the process of FBDD and exploring PPI inhibitors.

4.2 Fragment-Based Drug Design (FBDD)

The use of fragments as the starting point for drug discovery, so-called FBDD [34], has been applied to a wide range of drug targets [35]. FBDD has become one of the major lead-finding methods in drug discovery research [36] and has been used in drug discovery for identifying lead protein–protein interaction (PPI) inhibitors [37]. However, the number of successful examples is small compared to typical targets for small-molecule inhibitors. Therefore, computational approaches are expected to

be useful for providing important information related to each step in the FBDD of PPI inhibitors [38, 39]; these steps include fragment screening, fragment growing, fragment linking, and lead identification.

Knowledge of the structure of the complex formed between the target protein and the ligand is critical in the FBDD process. In FBDD, the starting fragment has low affinity, and therefore, an understanding of molecular interactions is required for rational drug design. Many molecular interactions are involved in ligand binding, so quantum–mechanical calculations [40] must be applied to drug design. Ichihara [41] suggested that FMO and extended calculations, such as PIEDA, can be used to analyze the interaction of hit fragments and the evolution of fragments to the lead molecule.

4.3 Protein–Protein Interaction (PPI) and Bromodomain

A network of protein–protein interactions (PPIs) contributed to the regulation of cellular biology, and dysfunction in PPIs is strongly associated with a variety of diseases [42]. The development of drugs targeting PPIs remains a challenge, especially the development of small-molecule drugs, because PPI interfaces tend to be relatively flat, wide, and featureless compared to typical targets for small molecules, such as enzymes, for example, kinases, and G protein-coupled receptors (GPCRs) [43]. Bromodomain inhibitors are one of the target PPIs.

Bromodomains (BRDs) [44] are compact protein modules comprising approximately 110 amino acid residues that are key interaction modules for recognizing the ϵ -N-acetylation state of a specific lysine residue. The ϵ -acetylated lysine (ϵ Ac-Lys or Kac) is found in large macromolecular complexes that have a role in chromatin remodeling, DNA damage, cell-cycle control, and, especially, in histones. There are 61 BRDs in the human genome, and they are classified into eight families. The bromo and extra C-terminal domain (BET) family is one of the eight families, and it comprises four proteins (BRD2–4 and testes-specific BRDT). Because BRD4 has been reported to regulate the expression of disease-related genes for cancer, inflammation, and viral infections, it is an attractive target for developing drugs for these diseases [45]. Many studies for finding ligands for BRD4 have been conducted since a selective BET inhibitor was discovered in 2010, and several such compounds have entered clinical trials [46].

In this section, we describe the use of FMO for analyzing a bromodomain inhibitor to provide insights related to FBDD. Our investigations included fragment growing in FBDD, comparison of the molecular interactions between the peptide and small-molecule ligands, the contribution of induced charge to affinity and PIEDA, CH/ π interactions, and involvement of water in ligand binding. In this section, we describe our calculations for the following eight compounds (Fig. 6).

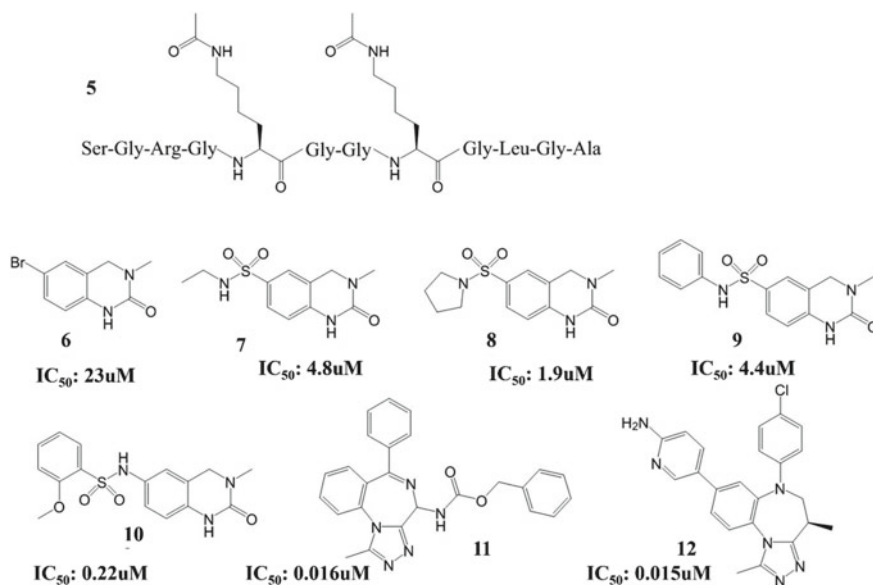


Fig. 6 Structure of bromodomain inhibitors analyzed using FMO with IC_{50} value

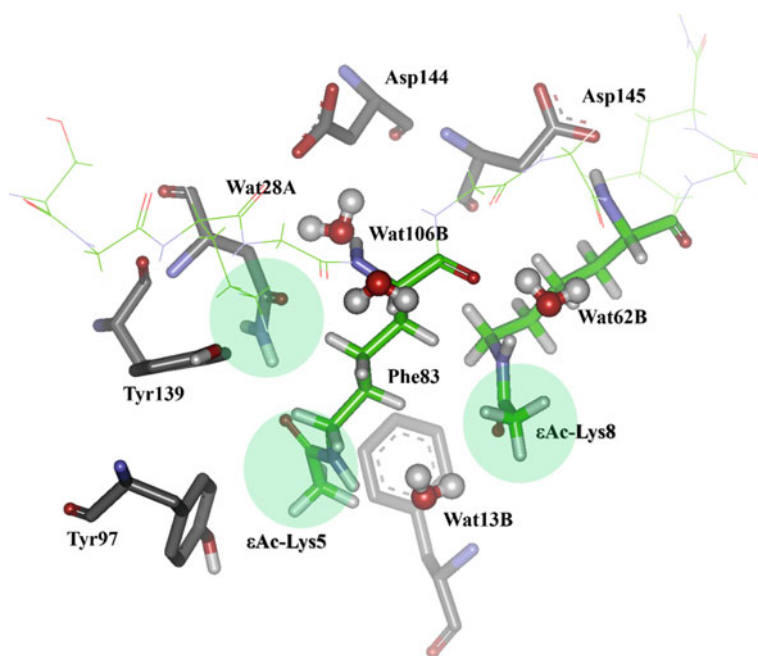
4.4 FMO Calculations for H4K5acK8ac, a Peptide Ligand Containing Two ϵ Ac-Lys

By using systematic histone-peptide arrays, isothermal titration calorimetry (ITC), and crystal structures, Filippakopoulos [43] revealed that peptides containing two ϵ Ac-Lys residues interact more strongly with BRDs than peptides containing only one or no ϵ Ac-Lys residue. The crystal structures showed that the ϵ Ac-Lys of a peptide ligand is anchored to asparagine (Asn140), which is conserved in BRDs, through hydrogen bonds.

We performed FMO calculations on the complex between BRD4 protein and diacetylated peptide H4K5acK8ac (SGRGKacGGKacGLGA, **5**). Table 6 lists IFIE of BRD4 and the two ϵ Ac-Lys residues (ϵ Ac-Lys5 and ϵ Ac-Lys8), which are considered to play a critical role in binding to BRD4. The FMO calculations showed nine strong interactions (five amino acid residues and four waters) between ϵ Ac-Lys5 and BRD4 (Asn140, Asp144, Phe83, water106B, Tyr97, water13B, Tyr139, water28A, and water263B) (Table 6 and Fig. 7). The strong IFIE between ϵ Ac-Lys5 and Asn140 (-16.1 kcal/mol) agrees with the role of Asn140 in anchoring ϵ Ac-Lys5. ϵ Ac-Lys5 has attractive IFIE with three aromatic residues as well: -5.7 (Phe83), -4.8 (Tyr97), and -4.2 (Tyr139) kcal/mol; these residues are highly conserved in BRDs. By contrast, the interaction energies calculated using the molecular mechanics (CHARMm) method are -4.1 (Phe83), $+2.7$ (Tyr97), and -1.3 (Tyr139) kcal/mol. Therefore, it is difficult to identify interactions with three aromatic residues by

Table 6 Interaction energies (in kcal/mol) between BRD4 and H4K5acK8ac peptide (**5**)

IFIE of ϵ Ac-Lys5		IFIE of ϵ Ac-Lys8	
Asn140	-16.1	Asp145	-27.1
Asp144	-10.7	Water62B	-17.6
Phe83	-5.7	Water13B	-10.0
Water106B	-4.9	Asp144	-6.4
Tyr97	-4.8		
Water13B	-4.4		
Tyr139	-4.2		
Water28A	-3.8		
Water263B	-3.7		

**Fig. 7** Interaction between compound **5** (peptide) and BRD4

using molecular mechanics and visual inspection. By contrast, FMO can detect these nonconventional interactions.

Four waters also play roles in binding **5** to BRD4. Water106B and water28A interact with the peptide amide hydrogen of ϵ Ac-Lys5 in **5** through hydrogen bonds. Water263B forms a hydrogen bond with water106B, which forms a hydrogen bond with the peptide carbonyl oxygen of Gly4 in **5**. These three waters are present on the protein surface, so they are thought to be involved in stabilizing the hydrated surface. By contrast, water13B is found at the ligand-binding site and forms a bridge

between ϵ Ac-Lys5 and ϵ Ac-Lys8 through intermolecular hydrogen bonds. The role of this water is examined further in the discussion section.

ϵ Ac-Lys8, the second acetylated residue, was found to interact with four residues: Asp145, Asp144, water62B, and water13B (Table 6 and Fig. 7). The large IFIE (-27.1 kcal/mol) between ϵ Ac-Lys8 and Asp145 is ascribed to the charged hydrogen bond between the NH of the peptide backbone of ϵ Ac-Lys8 and the carboxylate of the side chain of Asp145. However, this strong interaction does not explain why this lysine is acetylated. The FMO calculation showed strong interactions between ϵ Ac-Lys8 and two waters (water62B and water13B). These two waters form hydrogen bonds with the acetylated Lys portion of ϵ Ac-Lys8 and, simultaneously, form hydrogen bonds with ϵ Ac-Lys5. As a result, water62B and water13B form an intramolecular hydrogen bond network between ϵ Ac-Lys5 and ϵ Ac-Lys8 in the peptide ligand. Thus, ϵ Ac-Lys8 could play an important role in maintaining the water network at the binding site, as well as in the direct interaction with BRD4.

In summary, FMO calculations for the complex between H4K5acK8ac (**5**) and BRD4 revealed that ϵ Ac-Lys5 interacts with a conserved key residue (Asp140), and ϵ Ac-Lys8 maintains the water network. In the next section, we compare the interactions between H4K5acK8ac and low-molecular-weight inhibitors.

4.5 Analysis of Fragment Optimization Process in Tetrahydroquinazoline-6-yl-benzensulfonamide Derivatives

The FBDD method was applied by Fish for identifying a lead compound for BRD4 inhibition [47]. The identified compound showed inhibitory activity in a peptide displacement biochemical assay. The structure–activity relationship (SAR) and co-crystal structures between BRD4 and the ligand, including the hit fragment, expanded fragment, and lead compound, were investigated as well. Using their data, we investigated the change in IFIEs between the ligands and the BRD4 protein from a hit fragment (IC₅₀ 23 μ M for BRD4) to a lead compound (IC₅₀ 0.22 μ M for BRD4).

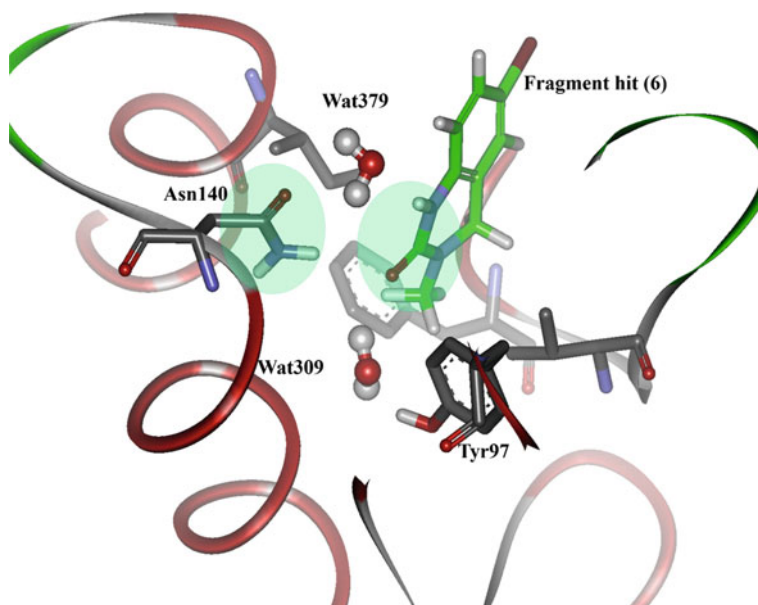
4.5.1 FMO Calculations for 6-bromo-3-methyl-3,4-dihydroquinazolin-2(1H)-one (**6**)

Compound **6** has a weak inhibitory activity for BRD4 (23 μ M), but its molecular weight is low. Therefore, this compound was used as the starting fragment for FBDD. The FMO calculations showed seven strong interactions from five amino acid residues and two waters between **6** and BRD4 (water379, Asn140, Phe83, water309, Tyr97, Ile146, and Val87). Table 7 and Fig. 8 show detailed data and the ligand interactions between **6** and BRD4. The IFIE of Asn140 (-9.4 kcal/mol) is weak compared with the IFIE between ϵ Ac-Lys5 and Asn140 (-16.1 kcal/mol). This decrease in IFIE

Table 7 Interaction energies (in kcal/mol) between BRD4 and Fragment (6)

	IFIE	Es ^a	Ex ^b	CT ^c	DI ^d	q(I => J) ^e	CH/ π ^f
HOH379	-9.6						
ASN140	-9.4	-7.4	0.6	-1.1	-1.5	-0.017	
PHE83	-8.2	-5.7	3.3	-1.6	-4.3	0.026	
HOH309	-5.5						
TYR97	-4.2	-2.7	0.2	-0.5	-1.2	-0.005	
ILE146	-3.5	-0.2	1.6	-0.9	-3.9	-0.004	
VAL87	-3.0	-1.5	2.2	-0.8	-2.9	0.002	
HOH398	-2.9						
HOH323	-2.8						
LEU92	-2.8	-0.6	4.0	-1.1	-5.1	-0.007	
LEU94	-2.1	-0.8	2.1	-0.7	-2.7	-0.004	
TYR139	-2.0	-0.8	0.0	-0.4	-0.9	-0.001	
PRO82	-2.0	-1.3	3.3	-0.9	-3.0	-0.004	
TRP81	-1.7	-1.7	2.8	-0.5	-2.4	-0.003	

^aElectrostatic of IFIE, ^bExchange repulsion of IFIE, ^cCharge transfers and higher-order term of IFIE, ^dDispersion interaction of IFIE, ^eAmount of charge transferred from fragment I (ligand) to J (protein), ^fNumber of CH/ π interactions detected by CHPAI program

**Fig. 8** Interaction between compound 6 (fragment) and BRD4

can be ascribed to a change in configuration from an ideal hydrogen bond between the urea carbonyl of **6** and the amide hydrogen of the side chain in Asn140. IFIEs of other residues, namely, Phe83, Tyr97, Ile146, and Val87, were observed as well, and they were found to be in agreement with Fish's considerations.

Two waters (water379 and water309) are involved in the binding of **6** to BRD4. The IFIE between **6** and water379 is -9.6 kcal/mol, and this value is approximately equal to the IFIE of Asn140. This water exists between the amino group of the urea in **6** and the amide carbonyl oxygen of the side chain of Asn140, and it acts as a bridge between **6** and BRD4. Other ligands interact directly with Asn140, indicating that this water plays an important role in the binding of fragment **6**. Water309 has a considerable IFIE of -5.5 kcal/mol, and it is incorporated into the hydrogen bond network formed by **6** and Tyr97; this network is observed with other ligands as well.

Our FMO calculations revealed that the interactions between **6** and BRD4 partially mimic the interaction between **5** and BRD4. Thus, **6** was thought to be an appropriate starting point for FBDD.

4.5.2 FMO Calculations for 3-methyl-6-(pyrrolidin-1-ylsulfonyl)-3,4-dihydroquinazolin-2(1H)-one (**8**)

8 is a 6-sulfonamide derivative of **6**, and it is over 20-fold more active than **6**. The FMO calculations listed in Table 8 provide insights into this increased affinity. The calculations showed 10 strong interactions (seven amino acid residues and three

Table 8 Interaction energies (in kcal/mol) between BRD4 and compound (**8**)

	IFIE	Es ^a	Ex ^b	CT ^c	DI ^d	q(I => J) ^e	CH/ π ^f
ASN140	-20.9	-21.4	9.7	-4.4	-4.8	-0.003	
HOH301	-9.4						
PHE83	-8.3	-4.9	1.2	-1.7	-3.1	0.018	
ILE146	-6.1	-0.6	4.8	-2.0	-8.2	0.001	1
HOH423	-5.4						
ASP145	-5.2	-4.7	0.9	-0.3	-1.0	0.002	
TRP81	-4.8	-2.5	2.4	-1.0	-3.7	0.009	
TYR97	-3.9	-2.4	0.1	-0.6	-1.0	-0.005	
ASP144	-3.8	-3.8	0.0	0.0	0.0	0.000	
HOH303	-3.3						
HOH324	-2.6						
HOH311	-2.6						
LEU94	-2.4	-0.7	0.8	-0.5	-2.0	-0.005	
LEU92	-2.3	0.1	3.4	-1.2	-4.6	-0.013	2

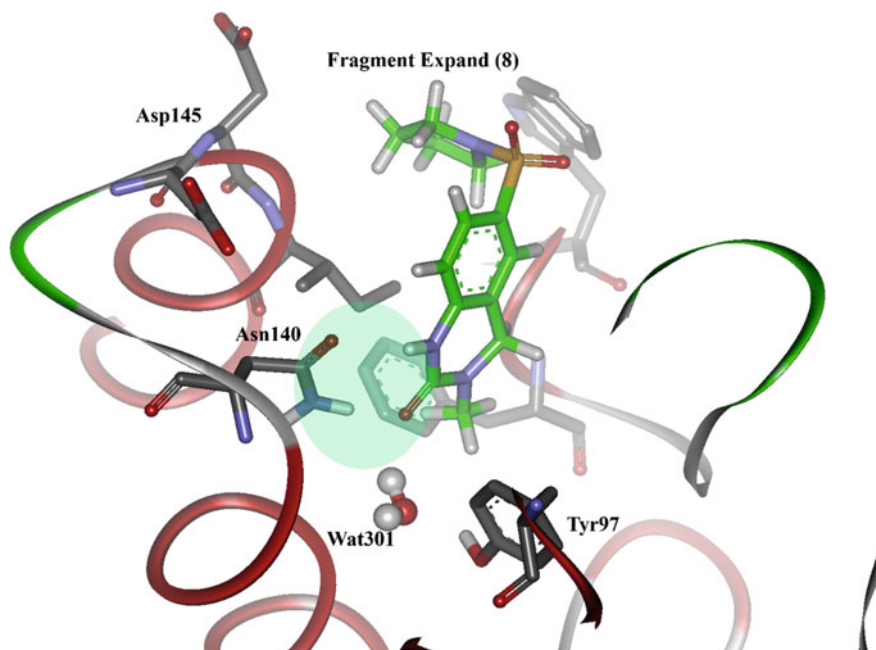


Fig. 9 Interaction between compound **8** (fragment expand) and BRD4

waters) between **8** and BRD4 (Asn140, water301, Phe83, Ile146, water423, Asp145, Trp81, Tyr97, Asp144, and water303).

The IFIE of Asn140 (-20.9 kcal/mol) approximately doubled compared to the IFIE between **6** and Asn140. This IFIE value is nearly equal to the IFIE between the ϵ Ac-Lys5 of **5** and Asn140 (-16.1 kcal/mol). This result indicates that the hydrogen bond between the urea carbonyl of **6** and the amide hydrogen of the side chain of Asn140 is strong in comparison with the bond with the hit fragment **6**, as shown in Fig. 9. Other IFIEs observed for **8** (Phe83 and Tyr97) coincide almost exactly with the IFIEs of **6**.

Newly detected IFIEs [Asp145 (-5.2 kcal/mol), Trp81 (-4.8 kcal/mol), and Asp144 (-3.8 kcal/mol)] support the execution of an appropriate fragment expansion. The IFIE of Trp81 can be attributed mainly to CH/ π interactions. In the peptide ligand **5**, ϵ Ac-Lys8 interacts mainly with Asp145 and Asp144 (see Table 6). The appearance of these two IFIEs in **8** indicates that **8** acquired new interactions, which are observed in peptide **5** as well. In FBDD, it is important to assess whether the expanded fragment has acquired new effective interactions. The interactions between **8** and two Asp (144 and 145) could not be detected by visual inspection. For interpretation of the interactions of Asp145 and Asp144, please see the discussion section. These results show that FMO is a useful tool for investigating fragment expansion. Compounds **7** and **9** have similar affinities for BRD4 compared to **8** (**7**: 4.8 μ M, **8**:

1.9 μM , and **9**: 4.4 μM). These results indicate a similarity in the patterns and in the total IFIEs of compounds **7**, **8**, and **9**.

4.5.3 FMO Calculations for 2-methoxy-N-(3-methyl-2-oxo-1,2,3,4-tetrahydroquinazolin-6-Yl) benzenesulfonamide (**10**)

10 has good affinity (220 nM) for BRD4 and drug-like properties. Thus, **10** was selected as a chemical probe for BRD4. Our FMO calculations (listed in Table 9) showed 14 strong interactions (10 amino acid residues and four waters) between **10** and BRD4 (Asn140, Asp145, water308, Asp144, Phe83, Ile146, water313, Lys91, Trp81, water306, Leu94, Tyr97, water328, and Tyr139). The IFIE of Asn140 (−19.9 kcal/mol) in **10** is nearly equal to the IFIE between $\epsilon\text{Ac-Lys5}$ in **5** and Asn140 (−16.1 kcal/mol), indicating that the cyclic-urea part of **10** interacts with Asn140 in a manner similar to the $\epsilon\text{Ac-Lys5}$ residue of **5**.

Compound **10** was produced by reversing the sulfonamide group in **9**. The affinity of **10** for BRD4 increased approximately 20-fold in comparison with that for **9**. The cause of this increased affinity cannot be explained based on the differences in hydrogen bonds and the binding mode between the two ligands (Fig. 10). The reason for this increased affinity was not described by Fish. There are some differences between the IFIEs of compounds **10** and **9** in Asp145 (−10.2 vs. −5.5 kcal/mol),

Table 9 Interaction energies (in kcal/mol) between BRD4 and compound (**10**)

	IFIE	Es ^a	Ex ^b	CT ^c	DI ^d	q(I => J) ^e	CH/ π ^f
ASN140	−19.9	−18.7	7.7	−4.3	−4.7	0.004	
ASP145	−10.2	−9.0	0.6	−0.5	−1.3	0.002	
HOH308	−8.4						
ASP144	−7.6	−7.6	0.0	0.0	0.0	0.000	
PHE83	−7.3	−4.2	1.3	−1.4	−3.0	0.015	
ILE146	−6.4	−0.8	6.4	−2.5	−9.6	−0.003	3
HOH313	−5.7						
LYS91	−5.3	−5.3	0.0	0.0	0.0	0.000	
TRP81	−5.2	−2.0	2.3	−1.1	−4.4	−0.004	
HOH306	−3.9						
LEU94	−3.8	−1.1	2.7	−1.0	−4.3	−0.011	2
TYR97	−3.3	−0.1	0.9	−1.5	−2.6	−0.012	1
HOH328	−3.1						
TYR139	−3.1	−0.9	0.3	−0.7	−1.7	−0.005	
HOH326	−2.8						
LEU92	−2.6	0.8	2.7	−1.5	−4.6	−0.015	1

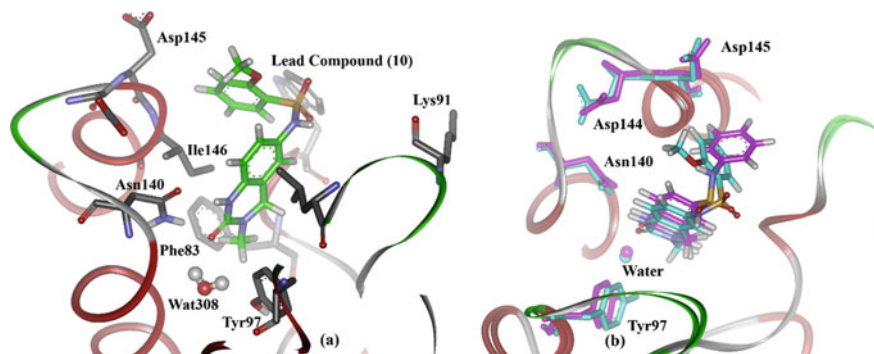


Fig. 10 Interaction between compound **10** (lead compound) and BRD4. **a** Compound **10** at the binding site. **b** Comparison of compound **8** (magenta) and **10** (cyan) at the binding site

Asp144 (-7.6 vs. -6.6 kcal/mol), and Lys91 (-5.3 vs. 0.1 kcal/mol). However, the two compounds have similar IFIEs for other residues. Accordingly, the interactions involving Asp145, Asp144, and Lys91 contribute toward the increased affinity observed for **10**. The IFIEs of Asp144 and Asp145 are especially interesting because these two IFIEs were observed in case of the peptide ligand **5**. This observation indicates that the FBDD process for compounds **6** to **10** proceeds by mimicking the interactions of the peptide ligand.

4.6 Insight into FBDD Process

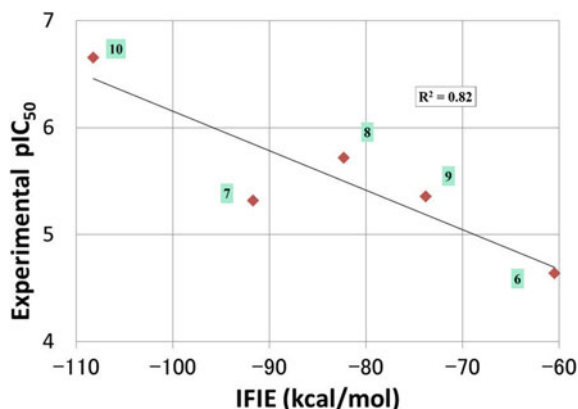
4.6.1 Correlation Between IC₅₀ and the Total IFIEs

We hypothesized that the changes in affinity are derived mainly from enthalpic effects [48] for compounds **6**–**10**, which are analogous compounds, although different energy terms are involved in the ligand-binding processes. Figure 11 shows a significant correlation ($R^2 = 0.82$) between the IC₅₀ value of BRD4 and the total IFIEs of a ligand; the total IFIEs are summed up values of all IFIEs between the ligand and the amino acid residues of BRD4. This correlation indicates that the IFIEs can be used as SAR considerations for compounds **6**–**10**.

4.6.2 Contribution of Charge to IFIEs

An explanation for the differences in affinity between **8** and **10** is difficult to provide based on visual inspection because a difference in direct interactions was not found. We analyzed the IFIEs of these compounds and found that changes in the IFIEs of Asp145 are related to differences in the affinities of compounds **8** and **10**.

Fig. 11 Relationship between experimental values and IFIE values for compounds **6–10**



The negative charge of Asp145 increased with an increasing affinity for BRD4 [−0.84 (**6**), −0.87 (**8**), and −0.90 (**10**)]. These charges were assumed to be derived from charge-induced dipole interactions [49], which cannot be estimated by visual inspection and molecular mechanics calculations. This finding indicates the utility of quantum-mechanics-based FMO for SAR consideration.

4.6.3 Changes in IFIEs from Fragment-Hit to Lead

The hit fragment **6** was optimized to the small-molecule lead **10**. We attempted to evaluate this process based on changes in IFIEs from **6** to **10** and by comparing the IFIEs with those of peptide ligand **5**.

The IFIE of **6** with Asn140 (−9.4 kcal/mol) is weaker than that for the other investigated compounds. The IFIE of **7** (−16.5 kcal/mol) is nearly equal to that of the peptide ligand (−16.1 kcal/mol), and compounds **8** (−20.9 kcal/mol), **9** (−21.9 kcal/mol), and **10** (−19.9 kcal/mol) have strong IFIEs for Asn140. Thus, the effect of the interaction between εAc-Lys5 of the peptide ligand and the Asn140 of BRD4 is retained in the small-molecule ligands derived from FBDD. By contrast, the IFIE of the peptide ligand **5** between εAc-Lys8 and Asp145 is stronger than that in the non-peptide ligands. While the hit fragment **6** has no IFIEs with Asp145, the IFIEs of compounds **7–10** with Asp145 increased to nearly half the value for the peptide ligand, resulting in corresponding improvements in affinity.

An analysis of the IFIEs revealed that in the FBDD process, the hit fragments were optimized sequentially for mimicking the interaction of εAc-Lly5 to εAc-Lys8 in peptide and BRD4, as shown in Fig. 12. The first hit fragment partially mimics the interaction between εAc-Lys5 and Asn140, and then, the ligands are optimized to have an equally strong interaction with Asn140. The interaction with εAc-Lys8 is optimized as well, but no lead compound was found to fully mimic the interaction with the peptide ligand **5**.

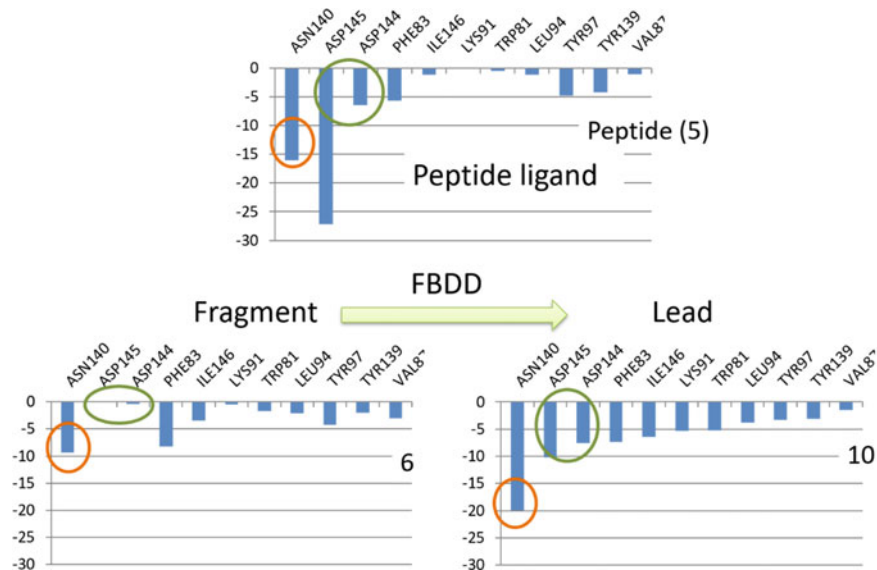


Fig. 12 Change in IFIE from fragment compound to lead compound

4.7 Evaluation of High-Affinity Ligands

4.7.1 FMO Calculation for Compound 11 and 12

Benzodiazepines (BzDs) modulate the γ -aminobutyric acid (GABA) receptor and have been approved for treating sleeping disorders, seizures, muscle spasms, and anxiety. Furthermore, in 2010, BzDs were found to bind to BRDs, and these derivatives have subsequently been studied extensively. Compound **11** (GW841819) [50] is one of the highest affinity for BRD4 (16 nM).

FMO calculations showed 20 strong interactions (13 amino acid residues and 7 waters) between **11** and BRD4 (Asn140, Ile146, Phe83, water2215, Lys141, Leu92, water2177, water2183, Pro82, water2126, water2095, Trp81, Val87, Tyr97, Asp145, water2104, Leu94, Tyr139, water2104, Leu94, Tyr139, and water2104) (Table 10). The IFIEs of Asn140, Asp145, and Asn144 (-10.9 , -4.0 , and 7.0 kcal/mol, respectively) are weaker than those of the benzenesulfonamide derivative **10**. By contrast, the IFIEs of Ile146 (-10.6 kcal/mol) and Phe83 (-9.9 kcal/mol) are stronger than those of **10** (-6.4 and -7.3 , respectively), and distinct amino acid residues (Leu92, Pro82, and Val87) are involved in the interactions with BRD4. As a result, **11** has higher affinity than **10**.

Compound **12** is another high-affinity ligand derived from a thienodiazepine-based ligand [51], and has a high affinity for BRD4 (15 nM). Our FMO calculations showed 14 strong interactions (10 amino acid residues and four waters) between **12** and BRD4 (Asn140, Phe83, water318, Trp81, Ile146, Pro82, water320, Tyr97, Val87,

Table 10 Interaction energies (in kcal/mol) between BRD4 and compound (**11**)

	IFIE	Es ^a	Ex ^b	CT ^c	DI ^d	q(I => J) ^e	CH/ π ^f
ASN140	-10.9	-9.9	8.0	-3.3	-5.7	0.025	
ILE146	-10.6	-2.8	7.2	-3.2	-11.8	-0.018	3
PHE83	-9.9	-6.7	2.7	-1.1	-4.8	0.021	
LYS141	-6.6	-6.5	0.0	0.0	-0.1	0.000	
LEU92	-6.2	-1.5	4.2	-2.0	-6.9	-0.021	2
PRO82	-5.1	-2.0	4.8	-1.7	-6.2	-0.006	1
TRP81	-4.4	-1.3	2.3	-1.1	-4.3	0.005	
VAL87	-4.2	-2.6	1.8	-0.8	-2.6	-0.003	
TYR97	-4.1	-2.7	0.0	-0.3	-1.1	-0.002	
ASP145	-4.0	-3.0	1.0	-0.4	-1.5	0.000	
ASN93	-3.6	-2.6	2.0	-0.5	-2.5	0.020	
LEU94	-3.2	-0.7	2.7	-1.2	-4.0	-0.003	
TYR139	-3.0	-0.3	0.8	-0.9	-2.6	-0.011	

^aElectrostatic of IFIE, ^bExchange repulsion of IFIE, ^cCharge transfers and higher-order term of IFIE, ^dDispersion interaction of IFIE, ^eAmount of charge transferred from fragment I (ligand) to J (protein), ^fNumber of CH/ π interactions detected by CHPAI program

water388, Lys141, Leu92, water376, and Tyr139). Table 11 shows that the IFIEs of **12** are similar to those of **11** (Table 10).

4.7.2 Comparison of Interaction Energies Between High-Affinity Ligands (**11** and **12**) and **10**

Comparison of IFIEs for **11** and **12** with those for **10** revealed that more nonpolar amino acid residues (Pro82 and Val87) contribute to the ligand–protein interactions in **11** and **12**. Then, we investigated ligand–protein interactions between these ligands and BRD4 by PIEDA and CHPI program. PIEDA analysis indicated that the dispersion interactions mainly contributed to these interactions, and CHPI found some CH/ π interactions.

CH/ π interactions for **10**, **11**, and **12** are listed in Table 12. We noted that there are differences in the amino acid residues interacting via CH/ π interactions. Compounds **11** and **12** were found to not interact with Leu94 and Tyr97 through CH/ π interactions. Instead, **11** and **12** have CH/ π interactions with the Pro82 that forms the WPF shelf, which is conserved among BET family bromodomains. All amino acid residues of the peptide ligand **5** and sulfonamide derivatives (**6–10**) have weak IFIEs with this proline, indicating that compounds **11** and **12** are characterized by the involvement of Pro82 in ligand recognition. Pro82 forms the WPF shelf with Trp81 and Phe83.

Table 11 Interaction energies (in kcal/mol) between BRD4 and compound (**12**)

	IFIE	Es ^a	Ex ^b	CT ^c	DI ^d	q(I => J) ^e	CH/ π ^f
ASN140	-15.0	-13.0	4.7	-2.2	-4.4	0.006	
PHE83	-11.0	-7.2	2.4	-1.2	-5.0	0.022	
HOH318	-7.6						
TRP81	-6.7	-2.2	2.1	-1.1	-5.4	-0.003	1
ILE146	-6.3	-0.8	5.1	-2.0	-8.6	-0.009	
PRO82	-4.9	-1.4	4.6	-1.8	-6.2	-0.003	
HOH320	-4.8						
TYR97	-4.7	-2.8	0.1	-0.5	-1.5	-0.003	
VAL87	-3.7	-1.5	0.9	-0.7	-2.5	-0.002	
HOH388	-3.5						
LYS141	-3.5	-3.4	0.0	0.0	0.0	0.000	
LEU92	-3.3	-1.0	3.6	-1.0	-4.9	-0.009	2
HOH376	-3.2						
TYR139	-3.1	-2.3	2.7	-0.7	-2.8	0.005	

^aElectrostatic of IFIE, ^bExchange repulsion of IFIE, ^cCharge transfers and higher-order term of IFIE, ^dDispersion interaction of IFIE, ^eAmount of charge transferred from fragment I (ligand) to J (protein), ^fNumber of CH/ π interactions detected by CHPAI program

Table 12 CH- π interactions of compounds **10**, **11**, and **12** with BRD4

Compound 10	Compound 11	Compound 12
Phe83	Pro82	Trp81
Leu92	Phe83	Pro82
Leu94	Leu92	Phe83
Tyr97	Ile146	Leu92
Ile146		

4.7.3 Involvement of Conserved Sequence in High-Affinity Ligands

The WPF shelf has a specific local structure in which the side chains of three sequential nonpolar amino acid residues (WPF: Trp81, Pro82, and Phe83) assemble into the binding site. Pro82 is sandwiched between Trp81 and Phe83, and the axial hydrogens of the pyrrolidine ring of Pro82 are directed toward the aromatic ring surface of Trp81 and Phe83. The equatorial hydrogen faces the binding site, interacting with the π system of the ligands through CH/ π interactions. Similar conformations of proline and aromatic amino residues are observed in proline-recognition domains which are described in the next section. Furthermore, we investigated the CH/ π network [52] of compound **12** by using CHPI. The results showed that compound **12** forms a large CH/ π network with Trp81, Pro82, Phe83, Leu92, and Ile146. This network is

extended over the entire binding site, so this network could contribute to the high affinities observed in the cases of ligands **11** and **12**.

4.8 Consideration of Water in the Ligand Binding Site

4.8.1 IFIE for Water in Peptide Ligand (5)

In this section, we applied to the application of IFIE to interpret the role of water in the binding site. We noticed that the benzene rings of **11** and **12** that interact with Pro82 through CH/ π interaction are in the almost same position where water13B is present in the case of peptide ligand **5** (Fig. 13). Water13B forms a hydrogen bond network with the acetylamino groups of ϵ Ac-Lys5 and ϵ Ac-Lys8, as described previously. The IFIEs of water13B with BRD4 and peptide were investigated, and three strong interactions were observed: ϵ Ac-Lys8, water193A, and ϵ Ac-Lys5 (water13B does not directly interact with BRD4). Water193A exists at the protein surface, so water13B is thought to be stabilized mainly by ϵ Ac-Lys5 and ϵ Ac-Lys8 at the binding site of BRD4. Therefore, we speculated that this water cannot exist at the binding site of BRD4 without stabilization by ϵ Ac-Lys5 and ϵ Ac-Lys8 through hydrogen bonds. Consequently, we assumed that water13B is not always required for ligand binding.

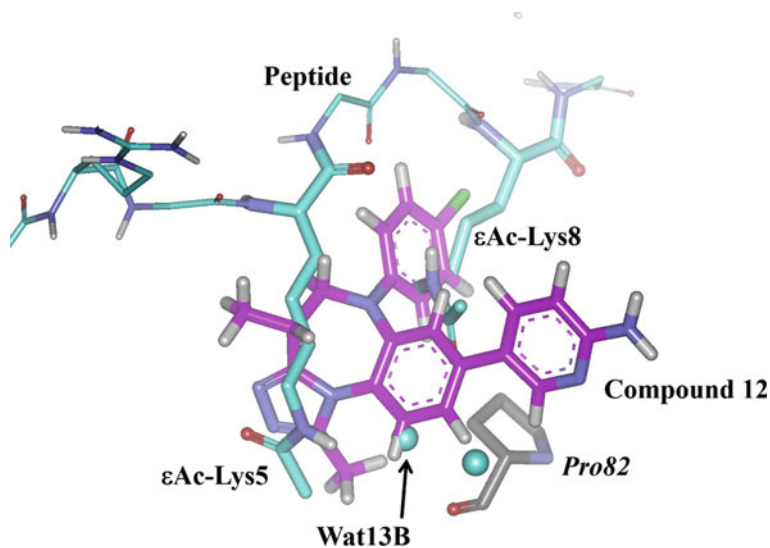


Fig. 13 Overlapped view of peptide (**5**) and compound **12** at binding site

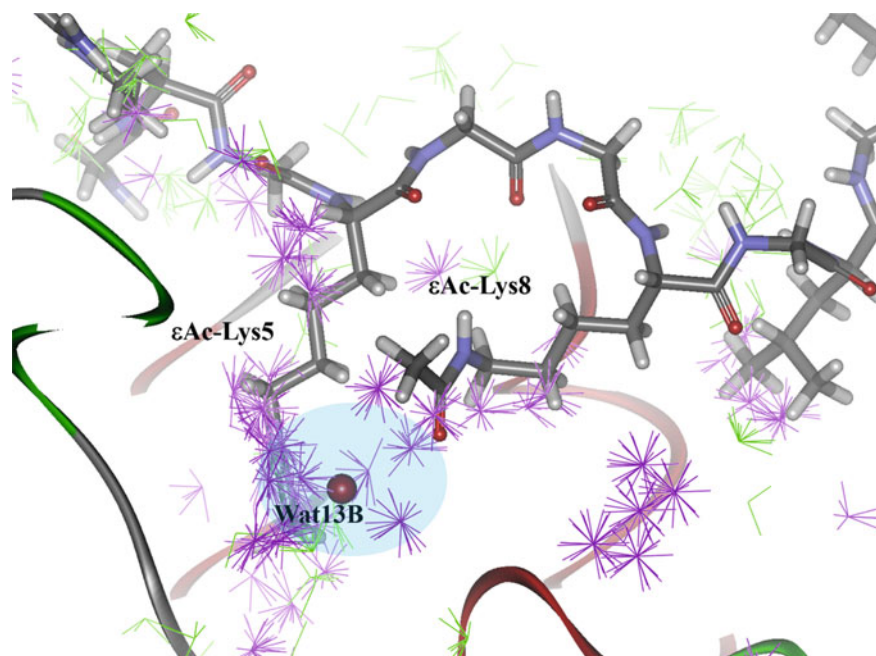


Fig. 14 SZMAP analysis. Destabilized virtual water molecules are shown in purple, and stabilized virtual water molecules are shown in green

4.8.2 Binding Free Energies Analysis by SZMAP for Water in Peptide Ligand (5)

Furthermore, we evaluated the profiles of water13B by using SZMAP [53], which computes binding free energies of water molecules at the binding sites of proteins. The results of SZMAP analysis, presented in Fig. 14, show that water13B exists in a region with a preference for hydrophobic groups, indicating that water13B is not necessary for ligand binding. This result agrees with our assumptions derived from IFIEs regarding water13B.

4.8.3 Useful Information About Water from IFIE

These results raise the possibility that the IFIEs of water can provide information about water groups at the binding site of proteins for use in drug design, even though many examples should be accumulated.

4.9 Conclusions

In this study, FMO methods were used to examine interactions between BRD4 and ligands, including the peptide ligand **5**, fragment hit **6**, expanded compounds (**7**, **8**, **9**, and **10**), and other high-affinity scaffold compounds (**11** and **12**). The FMO method allowed us to compare the interactions of the peptide ligand and non-peptide ligands, as well as to trace the FBDD process. PIEDA showed that the contributions of different energy components differ across the various scaffolds. FMO can provide useful information about hydrogen bonds, induced charges, CH/ π interactions, and water molecules. Thus, FMO is a useful tool for considering the molecular interactions between ligands and proteins in the process of fragment-based drug design.

5 Importance of CH/ π Interactions in Recognition of Core Motif in Proline-Recognition Domains

5.1 Abstract

In this section, we examine CH/ π interactions in protein/ligand complexes involving at least one proline residue by using the FMO method and CHPI analysis. FMO calculations are performed at the MP2/6-31G* levels for three Src homology 3 (SH3) domains and five proline-recognition domains complexed with their corresponding ligand peptides. Proline-recognition domains use a conserved set of aromatic residues to recognize proline-rich sequences of specific ligands. Many CH/ π interactions were identified in these complexes. CH/ π interactions occurred in the central part of the proline-rich motifs. Our results indicate that CH/ π interactions are important for the recognition of SH3 and proline-recognition domains by their ligand peptides, and they play a vital role in the signal transduction system. The combined use of the FMO method and CHPI analysis is effective for studying protein/protein and protein/ligand interactions, and it could be useful from the viewpoint of rational drug design.

5.2 FMO Calculations for SH3 Domain

5.2.1 Features of SH3 Domain

Protein–protein interactions mediate many signal pathways in eukaryotic cells, and they are involved in many diseases [54]. Thus, compounds that modulate specific interactions are valuable and could be developed into new drugs [55]. However, the regulation of protein–protein interactions remains a major challenge in drug discovery [56] because they often occur at extremely large, flat, and hydrophobic

binding sites. We investigated whether the FMO method allows for the analysis of protein–protein interactions by investigating the Src homology 3 (SH3) domain and the proline-recognition domains, including the SH3 domain.

The Src homology 3 (SH3) domain recognizes proline-rich sequences, and it is one of the most frequent motifs in the human genome. SH3 domains [57] are found in many protein families, and they interact with modular proteins, playing a role in the transmission of many intracellular signals, for example, protein kinase.

The SH3 domain can recognize diverse sequences, and it contains three types of binding modes [58] (Fig. 15). Typical SH3-binding peptides have a proline-rich sequence with a core element, PxxP (P: proline, x: any residue), classified according to the orientation of the binding mode [59]. In the class-I peptide binding mode [60], ligand peptides have a consensus sequence RxxPxxP (R: arginine) and are located in the “plus” orientation (Fig. 16a), whereas in the class-II peptide binding mode [61],

Fig. 15 Graphic representation of SH3 domain and various peptide ligands

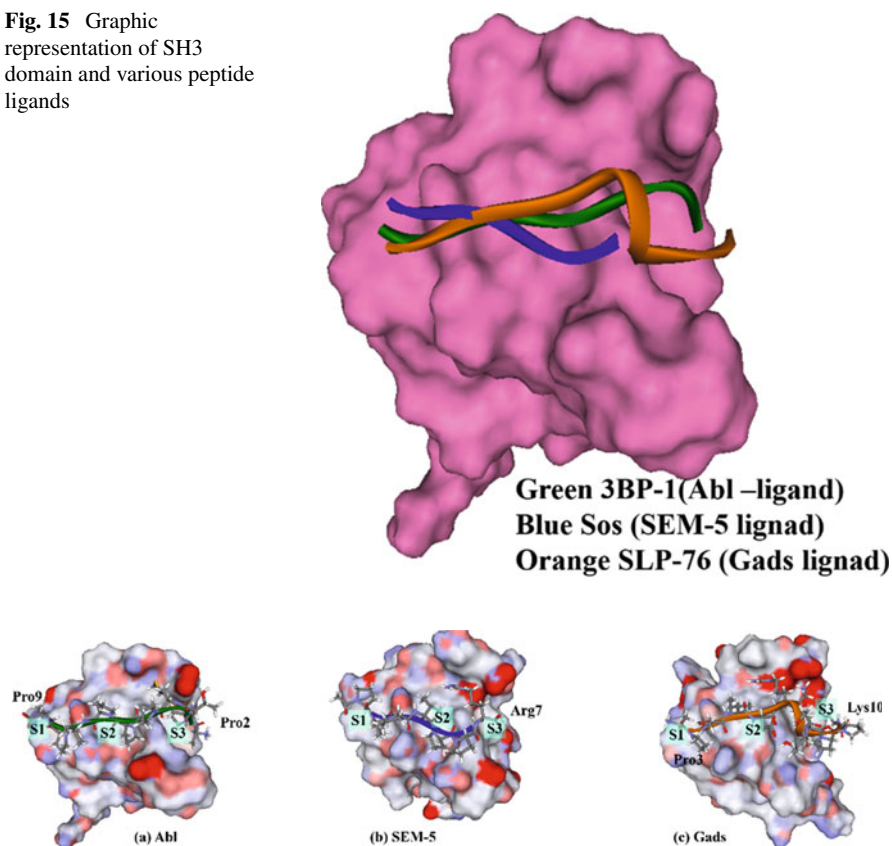


Fig. 16 Structure of SH3 domain and peptide. **a** Structure of Abl-SH3 complexed with 3BP1 peptide. **b** Structure of SEM5-SH3 complexed with Sos peptide. **c** Structure of Gads-SH3 complexed with SLP-76 peptide

ligand peptides have a consensus sequence xPxxPxR and are located in the “minus” orientation (Fig. 16b). In the class-III binding mode [62], peptides have an atypical SH3-binding motif, RxxK (K: lysine; Fig. 16c), and proline is absent.

Critical aromatic amino residues exist at the binding site of the SH3 domain. These aromatic residues are known to mainly bind nonpolar residues, including proline. Hydrogen bonds and electrostatic interactions are hardly ever observed between the aromatic residues in SH3 and the side chains of the ligand peptides, while the existence of nonpolar interactions such as CH/ π interactions at the binding site has been reported. Bhattacharyya and Chakrabarti [63] found that several CH/ π interactions occur in the complex between the SH3 domain of Abl protein and its peptide ligands. Here, we discuss the versatility of the binding mode observed in SH3 ligand peptides by comparing the role of CH/ π interactions with that of hydrogen bonds.

5.2.2 Interaction Between Abl-SH3 Domain and Ligand Peptide

The Abl protein [64] is a non-receptor tyrosine kinase localized in the nucleus and cytoplasm, and implicated in stress response, cell differentiation, cell division, and cell adhesion. Musacchio [59] determined the crystal structure of a complex formed between the SH3 domain of Abl and a proline-rich peptide (3BP-1). They reported that 3BP1 was bound in the plus orientation with a polyproline-II (PPII) helix conformation (Fig. 16a).

First, we examined the CH/ π interactions in this complex by using the CHPAI program. Table 13 lists the CH/ π interactions detected in the complex. Figure 17 shows that 11 CH/ π interactions occur in the Abl/3BP1 complex. Four aromatic residues of Abl (Tyr70, Trp99, Trp110, and Tyr115) are surrounded by four prolines and one alanine (Ala1, Pro2, Pro6, Pro9, and Pro10). CH/ π interactions were observed at the S1, S2, and S3 sites, and two CH/ π networks were found. Trp99,

Table 13 Interaction energies (in kcal/mol) between Abl-SH3 and ligand peptide

Abl	Peptide	IFIE	Es ^a	Ex ^b	CT ^c	DI ^d	q(I => J) ^e	CH/ π ^f
TRP99	PRO2	-7.3	-2.9	3.0	-1.7	-5.6	0.020	2
TRP99	PRO6	-5.3	-0.2	4.4	-3.0	-6.4	0.008	2
TRP110	ALA1	-10.8	-6.8	2.4	-2.5	-4.0	0.032	2
TRP110	PRO2	-5.4	-3.2	2.9	-0.6	-4.4	0.019	1
TYR70	PRO9	-2.3	-0.9	1.0	-0.6	-1.9	0.003	1
TYR70	PRO10	1.1	3.6	2.5	-0.8	-4.2	0.004	2
TYR115	PRO9	1.2	3.4	3.1	-1.6	-3.7	-0.002	1

^aElectrostatic of IFIE, ^bExchange repulsion of IFIE, ^cCharge transfers and higher-order term of IFIE, ^dDispersion interaction of IFIE, ^eAmount of charge transferred from fragment I (ligand) to J (protein), ^fNumber of CH/ π interactions detected by CHPAI program

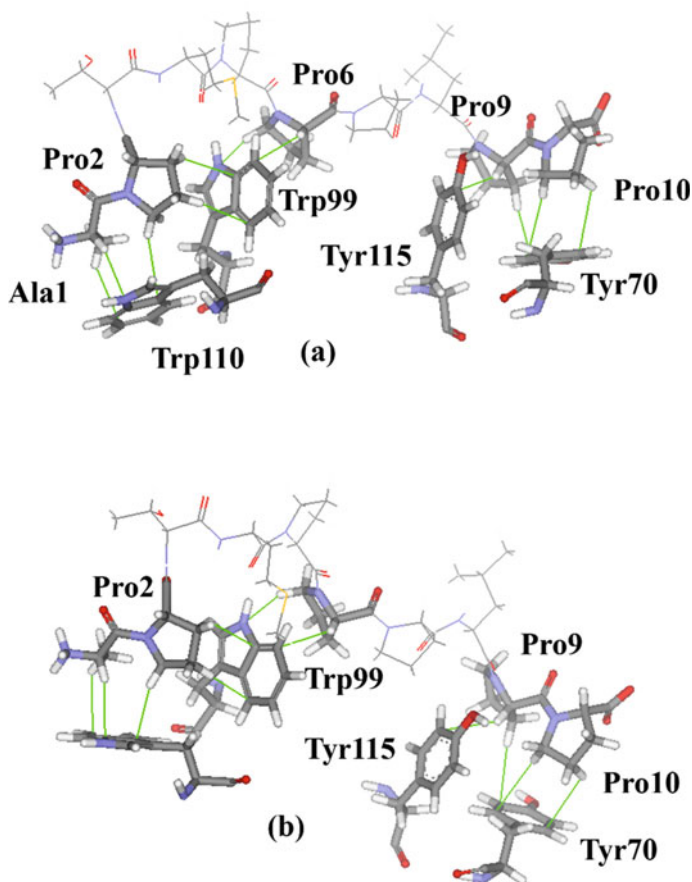


Fig. 17 Interactions between Abl-SH3 and 3BP1. The green line indicates CH/ π interactions. **a** view from S1 site. **b** View from S3 site

which was strictly conserved in the SH3 domain, was located at the center of the binding site and was sandwiched between two proline residues (Pro2 and Pro6).

We then investigated the interaction energies of these CH/ π interactions by means of FMO calculations. Table 13 lists the results of IFIE and PIEDA analyses of the relevant residues in the Abl-SH3/3BP1 complex. Trp99 was shown to interact with Pro2 and Pro6. IFIE and dispersion energies estimated by FMO calculations were -7.3 and -5.6 kcal/mol for Trp99/Pro2 and -5.3 and -6.4 kcal/mol for Trp110/Pro6, respectively. These results indicate that the CH/ π interactions contribute mainly to the recognition of conserved tryptophan to ligand peptide.

Trp110 has CH/ π interactions with Ala1 and Pro2 as well. IFIE values and dispersion energies estimated by means of FMO calculations were -10.8 and -4.0 kcal/mol for Trp110/Ala1 and -5.4 and -4.4 kcal/mol for Trp110/Pro2, respectively. The interaction energy of Ala1 is partly accounted for by a protonated amine because the

electrostatic energy estimated using PIEEDA is -6.8 kcal/mol. Pro2 interacted with the aromatic part of two tryptophan (Trp99 and Trp110) residues through three CH/ π interactions, while no hydrogen bond was observed. These two tryptophan residues composing the S3 site are known to contribute to the binding of the ligand peptide. Thus, CH/ π interactions play an important role in the recognition of the ligand at the S3 site.

For Tyr70, three CH/ π interactions were detected with Pro9 and Pro10. IFIE and dispersion energies were -2.3 and -1.9 kcal/mol for Tyr70/Pro9. By contrast, IFIE and dispersion energies were $+1.1$ and -4.2 kcal/mol for Tyr70/Pro10. Two CH/ π interactions were detected in Tyr70/Pro10*, but the interaction energies between Tyr70 and Pro10* were repulsive owing to the presence of the C-terminal carboxylate anion of Pro10, which indicates that the electrostatic energies evaluated using PIEEDA are repulsive ($+3.6$ kcal/mol) while the dispersion energies are attractive (-4.2 kcal/mol). Because this position is not at the C-terminal in a real biological system, the attractive interaction surely occurs between corresponding to these two residues, and it is attributed to CH/ π interactions. Pro10 is a component of the core motif PXXP. Thus, CH/ π interactions likely play an important role in ligand recognition.

The interaction between Tyr115 and Pro9 was calculated to be repulsive despite the existence of a CH/ π interaction. This was probably caused by electrostatic repulsion between the phenol oxygen of Tyr115 and the carbonyl oxygen.

Eleven CH/ π interactions were detected between Abl-SH3 and 3BP1 by CHPI analysis, but two of them were repulsive in terms of IFIE. The FMO calculations showed that the CH/ π interactions involving Trp99 and Trp110 were important from the viewpoint of binding. The results of CHPI analysis and FMO calculations indicated that the CH/ π interactions were involved in the interaction of the PxxP core motif in the SH3 domain.

5.2.3 Interaction Between SEM5-SH3 and Ligand Peptide

The SH3 domain of the *Caenorhabditis elegans* protein SEM5 (SEM5-SH3) [65] is homologous to the human “growth factor receptor-bound protein 2” (Grb2).

Lim [66] determined the crystal structure of the complex formed between SEM5-SH3 and a proline-rich peptide (Sos). The Sos peptide has a polyproline-II (PPII) helix conformation, similar to the one found in the 3BP1 peptide. Sos was found to be bound to SEM5 in the minus orientation in contrast to the Abl-SH3/3BP1 complex. NMR studies [60] showed that Sos binds to SEM5 in the minus orientation.

Table 14 lists the CH/ π interactions detected in the complex. Figure 18 shows that six CH/ π interactions occurred in the SEM5/Sos complex; three aromatic rings of SEM5 (Phe163, Trp191, and Tyr207) had CH/ π interactions with three proline (Pro2, Pro3, and Pro6). At the S1 site, two prolines (Pro2, Pro3) and two aromatic rings (Phe163, Tyr207) formed a CH/ π network. CH/ π interactions were observed at both S1 and S2 sites. The interaction mode of the conserved tryptophan (Trp191) was distinct from that seen in Abl.

Table 14 Interaction energies (in kcal/mol) between SEM5-SH3 and ligand peptide

Abl	Peptide	MP2	Es	Ex	CT	DI	q	CH/ π
TRP191	PRO6	-6.6	-3.0	0.6	-1.6	-2.5	0.018	1
PHE163	PRO2	1.7	5.1	2.5	-2.0	-4.0	0.008	2
PHE163	PRO3	-3.6	-2.9	2.8	-0.2	-3.3	0.009	1
TYR207	PRO2	2.2	4.1	0.7	-1.0	-1.7	0.009	1
TYR207	PRO3	-5.7	-2.5	0.9	-1.3	-2.8	0.012	1

^aElectrostatic of IFIE, ^bExchange repulsion of IFIE, ^cCharge transfers and higher-order term of IFIE, ^dDispersion interaction of IFIE, ^eAmount of charge transferred from fragment I (ligand) to J (protein), ^fNumber of CH/ π interactions detected by CHPAI program

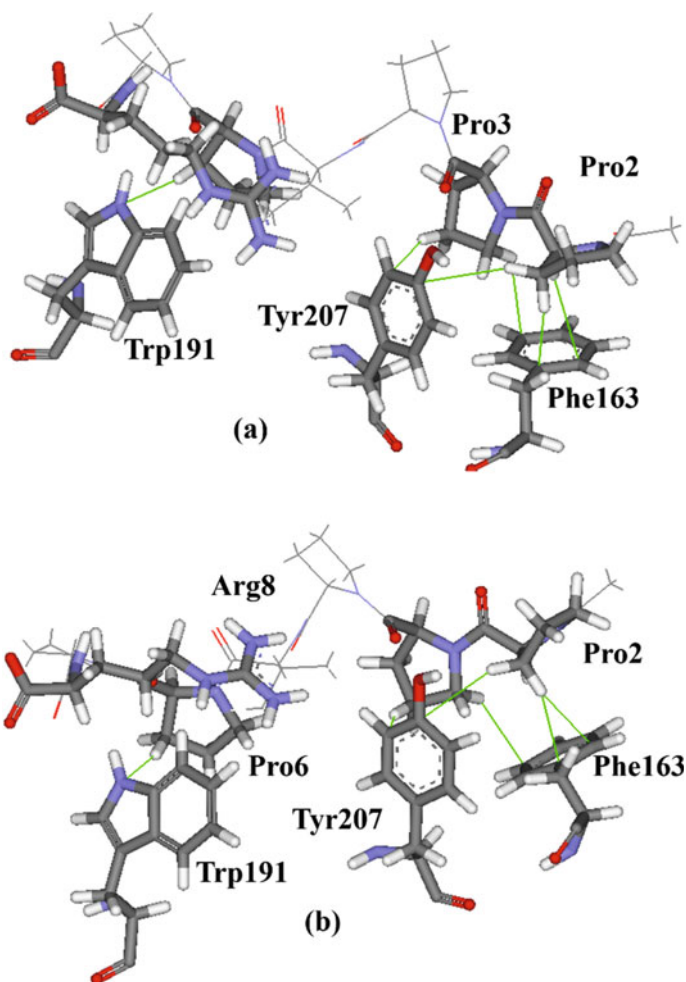


Fig. 18 Interactions between SEM5-SH3 and Sos. The green line indicates CH/ π interaction. **a** View from S1 site. **b** View from S3 site

Table 14 lists the interaction energies between the relevant residues in the SEM5/Sos complex. Trp191, which is conserved among the SH3 family, interacted primarily with Pro6 through CH/ π interactions. IFIE and dispersion energies estimated by means of FMO calculations were -6.6 and -2.6 kcal/mol for Trp191/Pro6. Arg8 was found to be located near the indole ring of Trp191. IFIE between Trp191/Arg8 was -21.3 kcal/mol. The hydrogen bond between the NH of the indole ring of Trp191 and the carbonyl oxygen of Pro7 was contained in Arg8 owing to the fragmentation rule of the FMO scheme. In addition, the alkyl chain of Arg8 was around the indole ring. Though no CH/ π interaction was detected by CHPI, two CH/ π short contacts were observed: 2.8 Å between the γ -hydrogen of Arg8 and the ζ -carbon of Trp199, and 3.0 Å between the η -nitrogen (guanidine group) of Arg8 and the η -hydrogen of Trp199. The guanidine group can be regarded as a π -group, in which case it serves as a π donor for the CH/ π interaction. The dispersion energies were -6.4 kcal/mol for Trp191/Arg8, which supports the existence of CH/ π interactions.

FMO results show that Phe163 and Tyr207 interacted with Pro3, which is consistent with the CHPI result. IFIE and dispersion energies were -3.6 and -3.3 kcal/mol for Phe163/Pro3 and -5.7 and -2.8 kcal/mol for Tyr207/Pro3, respectively. Pro3 constituted a part of the core motif, PxxPxR, in the minus orientation, as observed in SEM5-SH3. Thus, the CH/ π interactions involving Pro3 play an important role in ligand recognition by SEM5-SH3.

The IFIE values of Pro2 with Phe163 and Tyr207 were unattractive ($+1.7$ and 2.2 kcal/mol), although CH/ π interactions were observed. By contrast, dispersion energies were attractive (-4.0 and -1.7 kcal/mol). An artificial N-terminal acetyl group may be associated with these discrepancies.

To summarize, several CH/ π interactions have been shown between SEM5-SH3 and Sos. Our FMO calculations showed that Pro3, Pro6, and Arg8, which are components of the core PXXPxR motif, interact with proteins primarily through CH/ π interactions.

5.2.4 Interaction Between Gads-SH3 and Ligand Peptide

Gads is a Grb2-like adaptor protein that associates with the T-cell receptor signal transducer SLP-76 [67]. Harkioliaki [68] found that the SLP-76 peptide binds specifically the SH3 domain of Gads with high affinity (0.1 μ M). This fact is different from other peptides binding to SH3 with lower affinities (1 – 10 μ M). They determined the crystal structure of the complex formed between Gads-SH3 and the SLP-76 peptide (PAPSIDRSTKPPL). SLP-76 does not have the typical SH3-binding motif, PxxP. Instead, SLP-76 contains an RxxK motif and does not form the PPII helix. It is bound to Gads-SH3 in a clamp-like shape with the minus orientation (Fig. 19). Gads-SH3 has the typical structure of the SH3 motif, as well as Abl and SEM5. Harkioliaki reported that the structure of Gads-SH3 closely resembles that of SEM5. NMR studies have shown that SLP76 binds to Gads-SH3 in a similar manner.

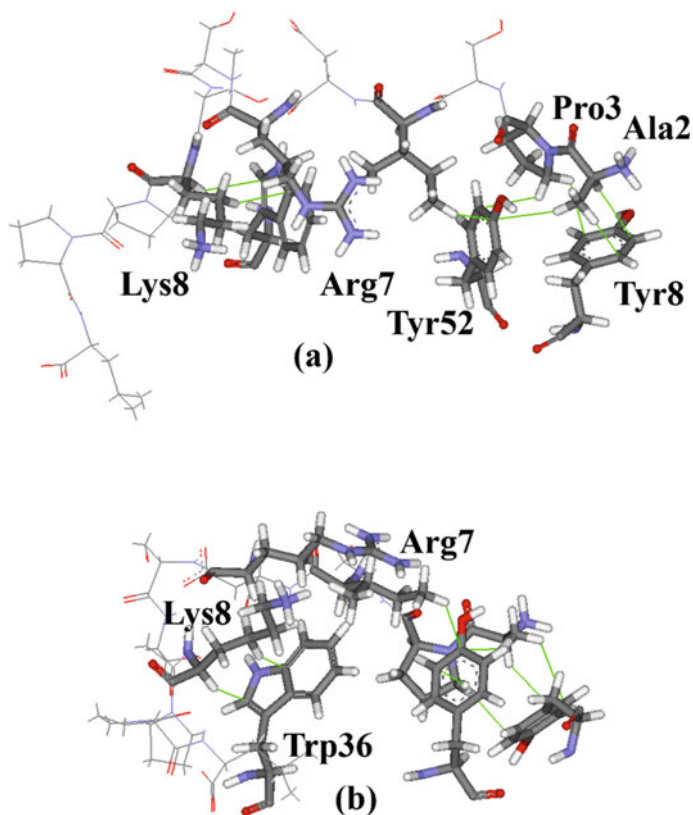


Fig. 19 Interactions between Gads-SH3 and SLP-76. The green line indicates CH/ π interaction. **a** View from S1 site. **b** View from S3 site

Table 15 Interaction energies (in kcal/mol) between Gads-SH3 and ligand peptide

Gads	Peptide	IFIE	Es ^a	Ex ^b	CT ^c	DI ^d	q(I \Rightarrow J) ^e	CH/ π ^f
TRP36	LYS10	-13.9	-8.4	5.7	-2.9	-8.2	0.003	2
TYR8	ALA2	-15.2	-11.9	2.5	-2.2	-3.5	0.025	2
TYR8	PRO3	-3.1	-2.0	2.7	-0.5	-3.3	0.016	1
TYR52	ALA2	-11.2	-9.5	1.2	-1.1	-1.8	0.015	1
TYR52	PRO3	-7.9	-3.4	2.4	-2.4	-4.5	0.029	1
TYR52	ILE5	-4.3	-2.2	2.6	-1.1	-3.5	0.013	1

^aElectrostatic of IFIE, ^bExchange repulsion of IFIE, ^cCharge transfers and higher-order term of IFIE, ^dDispersion interaction of IFIE, ^eAmount of charge transferred from fragment I (ligand) to J (protein), ^fNumber of CH/ π interactions detected by CHPAI program

Table 15 lists the CH/ π interactions detected in the Gads/SLP76 complex. Figure 19 shows that eight CH/ π interactions occur in this complex among three aromatic rings of Gads (Tyr8, Trp36, and Tyr52) and four alkyl groups in the ligand (Ala2, Pro3, Ile5, and Lys10). CH/ π interactions were observed at the S1, S2, and S3 sites. The binding mode of SLP76 peptide seems to be characterized mainly by the interactions of Trp36 with two long alkyl chains (Arg7 and Lys10).

IFIE and dispersion energies were -13.9 and -8.2 kcal/mol for Trp36/Lys10, respectively, and two CH/ π interactions were detected between the alkyl chain of Lys10 and Trp36. These CH/ π interactions [69] could be considered to contribute mainly to the binding because the ammonium group of the side chain in Lys10 was located at some distance from Trp36 (5.8 Å). In the FMO scheme, the hydrogen bond between the carbonyl oxygen of Asp6 and the indole NH of Trp36 was reflected by the interaction energies between Trp36 and Arg7 (Table 16) because two hydrogens (CH α and CH γ) of the methylene in the side chain of Arg7 were in close contact with the indole ring of Trp36 (both 3.03 Å). CH/ π interactions were involved in the interaction between Trp36 and Arg7 based on the relatively large IFIE and dispersion energies (-18.2 and -5.8 kcal/mol) between the two residues. The interaction energies between Arg7 and Trp36 resulted from the hydrogen bond and the CH/ π interactions. The RxxK motif is composed of Arg7 and Lys10, which interact with Trp36 through CH/ π interactions, indicating the importance of CH/ π interactions from the viewpoint of recognition of Gads by the SLP76 peptide.

At the S2 site, a CH/ π interaction was detected between Ile5 and Tyr52. IFIE and dispersion energies were -4.3 and -3.6 kcal/mol. The CH/ π interactions detected at the S1 site (Tyr8 and Tyr52), were analogous to those of the Sem-5/Sos complex.

Table 16 Strong interaction energies (in kcal/mol) between SH3 domains and peptides

Protein	Peptide	IFIE
Abl		
Trp99	Pro5	-12.5
SEM5		
Trp191	Pro7	-4.8
Trp191	Arg8	-21.3
Glu172	Arg8	-82.4
Gads		
Trp36	Arg7	-17.9
Trp36	Thr9	-6.0
Glu14	Arg7	-60.3
Glu17	Arg7	-128.2
Glu14	Lys10	-117.5
Asp16	Lys10	-126.7
Glu17	Lys10	-97.1

In summary, several CH/ π interactions were found in the complex of Gads/SLP-76. Although SLP-76 does not have the PxxP motif, the RxxK motif formed by Arg7 and Lys10 interacted with the conserved tryptophan (Trp36) through CH/ π interactions.

5.2.5 Charge–Charge Interactions Observed in SH3 Domain

Several relative large IFIE interactions were noted between negatively charged amino-residues (Arg and Lys) and positively charged residues (Asp and Glu) in the complexes of SEM5/Sos and Gads/SLP-76 (Table 16). For example, large IFIE contributions from the charged residues were found between Glu172 and Arg8 in SEM5/Sos (–82.4 kcal/mol). The electrostatic interaction estimated by PIEDA analysis for Glu172/Arg8 in SEM5/Sos was –76.4 kcal/mol, so the interactions between these two residues were attributed mainly to Coulombic energies. Coulombic energy is inversely proportional to the dielectric constant (ϵ) in the microscopic environment. The dielectric constant varies with the environment, for example, in the interior of a protein molecule, ϵ is assumed to be about 4, while in bulk-phase water, ϵ is assumed to be about 78. Arg8 was located near the water phase. Thus, the dielectric constant around Arg8 was relatively large. The interaction energies between Arg8 and Glu172 would be reduced markedly in an aqueous medium relative to the estimated IFIE values under the vacuum condition.

Similarly, charge–charge interactions were found in the complexes of Gads/SLP-76 Glu14/Arg7 (–60.3 kcal/mol), Glu17/Arg7 (–128.2 kcal/mol), Glu14/Lys10 (–117.5 kcal/mol), Asp16/Lys10 (–126.7 kcal/mol), and Glu17/Lys10 (–97.1 kcal/mol). Although the interaction energies of these pairs would be reduced in an aqueous medium, closed contacts of charge–charge pairs (Glu17/Arg7, Glu14/Lys10 and Asp16/Lys10) can contribute significantly to the binding of SLP76 (peptide) to Gads (protein). Then, the high affinity of SLP-76 can be ascribed to these charge–charge interactions.

5.2.6 Hydrogen Bonds Observed in Conserved Tryptophan

The hydrogen bonds between the indole NH hydrogen of the conserved tryptophan of SH3 domains and the carbonyl oxygen of the peptide for all Abl, SEM5, and Gads. However, the interaction mode differed slightly among these three complexes. In Abl-SH3, the hydrogen bond was formed between the carboxyl O of Met4 and the indole NH of Trp99 (Fig. 20a). The interaction energies were allocated between Pro5 and Trp99 (–13.1 kcal/mol; Table 16) owing to the FMO schemes; the i^{th} carbonyl groups were allocated to $(i + 1)$ th residues.

In Sem-5, the indole NH of Trp191 was located between two carbonyl oxygens of Pro6 and Pro7; two hydrogen bonds were formed. These two hydrogen bonds were reflected by the interaction energies of Pro7 and Arg8 with Trp191, which were –5.1 and –21.3 kcal/mol, respectively (Fig. 20b, Table 16).

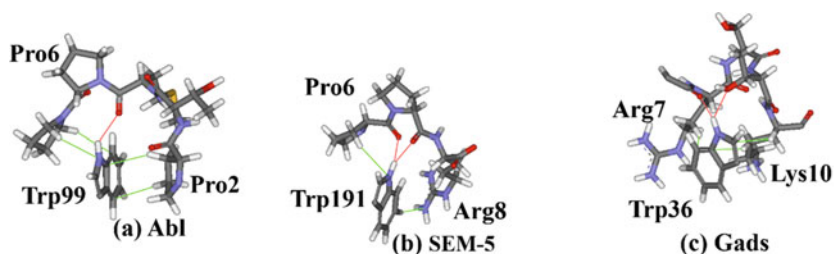


Fig. 20 Difference in binding mode around conserved tryptophan. The red line indicates hydrogen bond, and the green line indicates CH/ π interactions

In Gads, the indole NH of Trp36 formed two hydrogen bonds through the carbonyl oxygen of Asp6 and the oxygen of hydroxyl in Thr9. The interaction energies were -18.2 and -6.1 kcal/mol for Arg7 and Thr9, respectively (Fig. 20c, Table 16). In all three complexes, the NH hydrogen of the conserved tryptophan in the SH3 domains serves as the hydrogen donor for the carbonyl oxygen of the peptide ligand. Thus, the conserved tryptophan residues provided sites for the hydrogen bond and the CH/ π interactions in the molecular recognition of SH3 domains.

5.2.7 CH/O Interactions Observed in SH3 Domain

Chakrabarti [62] reported that proline forms a CH/O interaction with the carbonyl oxygen of the SH3 domain. Consistent with those results, CH/O interactions were observed in Sem-5 and Gads. In Sem-5, the γ -hydrogen of Pro6 was located near the carbonyl oxygen of Asn190, which was allocated to Trp191 in the FMO scheme; the distance was 2.92 Å, and the interaction energy was -6.6 kcal/mol (Table 14). This interaction was attributed partly to the CH/O interactions because no hydrogen bond was observed around them, and electrostatic energies were higher than dispersion energies (-3.0 vs. -2.5 kcal/mol), as determined by PIEEDA analysis. Similar binding modes occurred in Pro3/Tyr207 of Sem-5 (Table 14) and Pro3/Tyr52 of Gads (Table 15). These three prolines functioned as hydrogen bond donors for both the CH/ π and the CH/O interactions.

5.2.8 Features of Binding Sites in SH3 Domain

The binding modes of the three complexes were compared in the binding of the ligand peptides to the SH3 domains. The S1 site consisted of two aromatic residues, and they bound proline residues in the ligand peptides. Our analyses based on the FMO method and the CHPI program indicated that the stability of the complexes could be ascribed mainly to CH/ π interactions: Pro10* in Abl/3BP1, Pro3 in Sem5/Sos, and Pro3 in Gads/SLP76.

The S2 site consisted of conserved tryptophan, tyrosine, and proline residues. Few molecular interactions were found between the aromatic rings of these residues and the ligands. Another proline belonging to the PxxP motif was bound at this site: Pro7 in Abl/3BP1 and Pro6 in Sem-5/Sos. Although the amino residues consisting this site were conserved among the SH3 domains, the role of this site remains unclear in terms of molecular interactions.

The interaction modes of the S3 site were distinct among the three SH3 domains. Figure 19 shows the difference in the molecular interactions around the conserved tryptophan. In Trp99 of the Abl/3BP1 complex, one hydrogen bond and four CH/ π interactions were observed; both the π -faces and the NH of the indole group were used to recognize the ligand. In Trp191 of the Sem-5/Sos complex, two hydrogen bonds and two CH/ π interactions were found. In Trp36 of the Gads/SLP-76 complex, two hydrogen bonds and three CH/ π interactions were observed.

To summarize, the S1 site recognized the PxxP motif by means of CH/ π interactions. The S3 site interacted with a variety of sequences through hydrogen bonds and CH/ π interactions, allowing for diverse recognition of the SH3 domain.

5.3 *CH/ π Interactions in Proline-Recognition Domains*

5.3.1 Proline-Recognition Domains

To establish a general trend, we explored the CH/ π interactions in the other proline-recognition domains, including Enabled/VASP homology1 (EVH1) [70], WW [71], ubiquitin E2 variant (UEV) [72], profilin [73], and glycine-tyrosine-phenylalanine (GYF) domain [74]. The binding sites of these proline-recognition domains contain aromatic residues as well as the SH3 domain.

5.3.2 CH/ π Interactions Observed in Core Motif

Several CH/ π interactions have been detected between aromatic residues in the proline-recognition domains and proline sidechains of the ligand-peptide. Figure 21 shows a representative case of the profilin/ligand complex; the interactions between Pro9 and Trp3 in the complex are shown, and the interaction energy is -6.4 kcal/mol. The face-to-face arrangement of the proline side chain versus the tryptophan aromatic ring (interaction energies of the CH/ π interactions are listed in Supplementary Information) is noteworthy.

CH/ π interactions occurred in the central part of the proline-rich motifs. Table 17 lists the sequence of the proline-rich motifs. At least one proline interacted with the proline-recognition domains through the CH/ π interactions. Thus, we concluded that the CH/ π interactions played a crucial role in the recognition of the proline-recognition domains by the proline-rich motifs.

Fig.21 Representative case for multiple CH/ π interactions shown in profilin/ligand complex

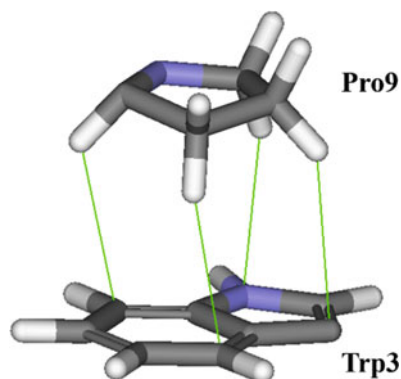


Table 17 Proline-recognition domains and their core motifs

Domain	Motif ^{a,b}	Residues occurring CH/ π in motif
SH3 Class-I	(R/K)xxPxx P	Pro10
SH3 Class-II	P xx P x(R/K)	Pro3, Pro6
SH3 Class-III	R xx K	Arg8, Lys10
WW	PP xY	Pro54, Pro55
EVH1	FPxx P	Pro1005
GYF	(R/K/G)xx PP Gx(R/K)	Pro68, Pro69
profilin	Poly(L-proline) PPPPPPPP	Pro6, Pro7, Pro9, Pro10, Pro12, Pro13
UEV	PT AP	Pro210

^a ×, any amino acid

^b Bold texts indicate the residues interacting through CH/ π hydrogen bonds

5.4 Conclusions

Three SH3 domains and five proline-recognition domains, complexed with their specific ligands, were studied using the FMO method and CHPI analysis. CH/ π interactions were shown to play an important role in binding in all the cases. The S1 and S2 sites of the SH3 domain recognized the PxxP motif. The versatility of ligand recognition of the SH3 domains was attributed to the interaction mode of the S3 site. CH/ π interactions were noted in other proline-recognition domains as well. These findings suggest that CH/ π interactions play an important role in the recognition of proline-recognition domains. The combined use of the FMO method and CHPI analysis is a valuable approach for studying protein/protein and protein/ligand interactions, and this combination may be useful from the viewpoint of rational drug design.

6 General Trend of CH/ π Interactions

6.1 Additivity of CH/ π Interactions

Many CH/ π interactions have been observed through this report and have contributed to the recognition between ligand and protein. CH/ π interactions are thought to play more important roles when they occur simultaneously. Then, to consider the additivity of CH/ π interactions, we analyzed results pertaining to CH/ π interactions obtained herein by considering the relationship between the number of interactions and the pair interaction energies included in IFIE and dispersion energies. A plot of the number of CH/ π interactions and pair interaction energies is shown in Fig. 22. These results demonstrate that the interaction energies of CH/ π interaction have additivity. This fact supports the concept that multiple CH/ π interactions can produce a significant even though their single interaction energies are weaker than the energies of hydrogen bonds. The good relationship between the number of CH/ π interactions and dispersion energies as compared with that between the number of CH/ π interactions and IFIE agrees with the fact that the CH/ π interactions can be ascribed mainly to the dispersion energies.

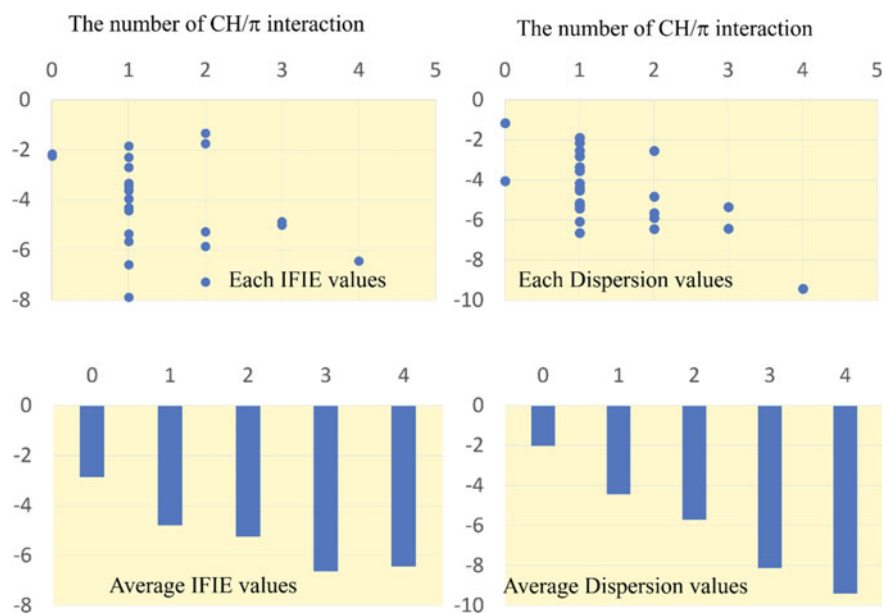


Fig. 22 Relationship between number of CH/ π interactions and pair interaction energies. **a** Plot of IFIE values between CH/ π acceptor and donor. **b** Plot of average IFIE values between CH/ π acceptor and donor. **c** Plot of each dispersion interaction between CH/ π acceptor and donor. **d** Plot of average dispersion interactions between CH/ π acceptor and donor

6.2 *CH/π interaction Energies for Obtaining Each Aromatic Amino Residue*

Each aromatic residue considered herein was analyzed to consider the frequency of the CH/π acceptor. Table 18 shows the list and average of pair interaction energies calculated in this study. Phenylalanine has the largest IFIE among aromatic residues because the electrostatic interaction energies included from the CH/O interactions are higher than those in case of the bromodomain. Average dispersion energies are -5.0 (Trp), -4.3 (Tyr), and -3.2 (Phe), respectively. Then, dispersion energies reflect the features of the CH/π acceptors. This result is quite reasonable, considering the high aromaticity and large surface area of it, and it agrees well with Weiss' report that 72% of Tryptophan has CH/π interaction.

7 Conclusion

In modern drug discovery, the structure of the complex between ligand and protein is one of the required information for driving a drug discovery project. Furthermore, the presences and roles of diverse molecular interactions in ligand recognition have been suggested, so more accurate estimation of molecular interactions is expected. Because the FMO method would be promising for evaluating these molecular interactions, we used it to analyze the molecular interactions between ligands and proteins. In this chapter, FMO was applied to three systems, which are considered general drug design processes, namely, SBDD, FBDD, and protein–protein interaction. Analyses based on IFIE and PIEDA revealed critical interactions for ligand recognition and provided useful knowledge for rational drug design.

In the SBDD Sect. 3, FMO revealed general molecular interactions in case of the kinase ligand, which interacts with the hinge region through hydrogen bond and with the adenine pocket through CH/π interactions. FMO analysis found that the affinity of the lead compound can be improved by increasing the number of CH/π interactions. A new ligand was designed to increase CH/π interactions, resulting in a tenfold increase in affinity. Additionally, CH/O interactions could serve as an alternative to the hydrogen bond depending on the scenario.

In the FBDD Sect. 4, we used FMO to compare the molecular interactions between a peptide ligand and a non-peptide ligand, which were derived from FBDD. IFIE analysis revealed that in this FBDD process, the hit fragment was optimized sequentially for mimicking the interactions of the peptide ligand. Similarly, molecular interactions of other scaffolds were investigated, suggesting differences in interactions between ligands derived from FBDD and other scaffolds. These results showed that FMO can provide useful insights into FBDD, which itself requires an accurate understanding of molecular interactions. Furthermore, the contributions of charge-induced dipole interactions were pointed out based on the results of our FMO analysis.

Table 18 List of detected CH/ π interactions (in kcal/mol) in this study

	IFIE	Es ^a	Ex ^b	CT ^c	DI ^d	q(I => J) ^e	CH/ π ^f	Ligand	Protein
PHE163	-3.6	-2.9	2.8	-0.2	-3.3	0.009	1	Pro3	SEM5
PHE77	-1.7	-0.1	1.8	-0.9	-2.5	0.006	2	Pro1004	EVH1
PHE83	-9.9	-6.7	2.7	-1.1	-4.8	0.021	1	lig-7	Bromo
PHE83	-8.4	-5.3	1.1	-1.5	-2.8	0.015	1	lig-5	Bromo
PHE83	-8.3	-4.9	1.2	-1.7	-3.1	0.018	1	lig-4	Bromo
PHE83	-7.3	-4.2	1.3	-1.4	-3.0	0.015	1	lig-6	Bromo
Ave.(PHE)	-6.6	-4.0	1.8	-1.1	-3.2	0.014			
TYR16	-4.9	-1.3	3.6	-1.8	-5.3	0.031	3	Pro1002	EVH1
TYR17	-3.4	-2.4	7.0	-2.6	-5.4	0.014	1	Pro69	GYF
TYR207	-5.7	-2.5	0.9	-1.3	-2.8	0.012	1	Pro3	SEM5
TYR28	-2.7	-2.5	7.6	-1.7	-6.1	0.029	1	Pro55	WW
TYR33	-2.2	-0.7	3.6	-1.0	-4.0	0.009	0	Pro68	GYF
TYR52	-7.9	-3.4	2.4	-2.4	-4.5	0.029	1	Pro3	Gads
TYR52	-4.3	-2.2	2.6	-1.1	-3.5	0.013	1	Ile5	Gads
TYR6	-5.8	-1.7	4.6	-2.8	-5.9	0.007	2	Pro12	Profilin
TYR63	-2.2	-0.7	0.1	-0.5	-1.1	0.003	0	Pro211	UEV
TYR68	-3.3	-0.6	7.1	-3.1	-6.6	0.003	1	Pro210	UEV
TYR68	-1.3	-2.1	3.7	1.9	-4.8	0.009	2	Pro211	UEV
TYR70	-2.3	-0.9	1.0	-0.6	-1.9	0.003	1	Pro9	Abl
Ave.(TYR)	-3.8	-1.8	3.7	-1.4	-4.3	0.0			
TRP110	-5.4	-3.2	2.9	-0.6	-4.4	0.019	1	Pro2	Abl
TRP191	-6.6	-3.0	0.6	-1.6	-2.5	0.018	1	Pro6	SEM5
TRP28	-5.0	-0.4	3.7	-2.0	-6.4	0.017	3	Pro68	GYF
TRP3	-6.4	-1.5	7.2	-2.7	-9.4	0.021	4	Pro9	Profilin
TRP31	-4.4	-3.7	5.8	-1.3	-5.2	0.012	1	Pro7	Profilin
TRP31	-3.6	-0.6	2.3	-1.2	-4.1	0.009	1	Pro6	Profilin
TRP39	-3.9	-0.8	4.7	-2.7	-5.1	-0.011	1	Pro54	WW
TRP39	-1.8	-1.3	0.8	0.7	-2.1	0.008	1	Pro55	WW
TRP81	-4.8	-2.5	2.4	-1.0	-3.7	0.009	1	lig-4	Bromo
TRP99	-7.3	-2.9	3.0	-1.7	-5.6	0.020	2	Pro2	Abl
TRP99	-5.3	-0.2	4.4	-3.0	-6.4	0.008	2	Pro6	Abl
Ave.(TRP)	-5.0	-1.8	3.4	-1.5	-5.0	0.012			

^aElectrostatic of IFIE, ^bExchange repulsion of IFIE, ^cCharge transfers and higher-order term of IFIE, ^dDispersion interaction of IFIE, ^eAmount of charge transferred from fragment I (ligand) to J (protein), ^fThe number of CH/ π interaction detected by CHPAI program

In the protein–protein interactions Sect. 5, we investigated molecular interactions among SH3 domains as a typical example of proline-rich peptide. The results of this analysis showed that prolines interact with aromatic residues of the SH3 domain through CH/ π interactions. Although conserved tryptophans play critical roles among the SH3 domains, the contributing molecular interactions can change in response to the conformation and amino residues of the ligand peptide. In other proline-recognition domains, prolines of the ligand peptide interact also with the aromatic residues of proteins through CH/ π interactions.

In the last Sect. 6, we surveyed general trends in CH/ π interactions observed in this chapter, even though the number of samples was small. The additivity of CH/ π interactions was confirmed based on the relationship between the number of CH/ π interactions and dispersion energies. The average dispersion interactions of each aromatic amino residues were -5.0 (Trp), -4.3 (Tyr), and -3.2 (Phe) kcal/mol, and this order is consistent with the frequency of the aromatic residues involved in CH/ π interactions.

Herein, we showed that FMO can provide useful information for rational drug design, even though we performed FMO calculations under the vacuum condition and without optimization in quantum mechanics. With advances in computer algorithms and computational power, it is expected that the FMO method implemented in water treatment and optimization will be used routinely for drug design. At that time, FMO can provide many answers to problems related to drug design.

References

1. Mignani S, Huber S, Tomás H (2016a) *Drug Discov Today* 21:573–584
2. Mignani S, Huber S, Tomás H (2016b) *Drug Discov Today* 21:239–249
3. Wermuth C (ed) *The practice of medicinal chemistry*, 3rd edn. Elsevier, Academic Press, 2008, pp 64
4. Zuercher W, Elkins J, Knapp S (2016) *Cell Chem Biol* 23:173–182
5. Ruyck J, Brysbaert G, Blossey R (2016) *Adv Appl Bioinform Chem* 9:1–11
6. Śledź P, Caffisch A (2018) *Curr Opin Struct Biol* 48:93–102
7. Friesner R, Banks J, Murphy R (2004) *J Med Chem* 47:1739–1749
8. Ozawa T, Tsuji E, Ozawa M (2008) *Bioorg Med Chem* 16:10311–10318
9. Ozawa M, Ozawa T (2017) Ueda K. *J Mol Graph* 74:73–82
10. Ozawa T, Okazaki K, Kitaura K (2011) *J Comput Chem* 32:2774–2782
11. Protein Data Bank <https://www.rcsb.org/>
12. Discovery Studio <https://accelrys.com/products/collaborative-science/biovia-discovery-studio/>
13. Vanommeslaeghe K, Hatcher E, Acharya C (2010) *J Comput Chem* 31:671–690
14. Nishio M, Umezawa Y, Hirota M (1995) *Tetrahedron* 51:8665–8701
15. Nishio M, Umezawa Y, Honda K (2009) *CrystEngComm* 11:1757–1788
16. Novoa J, Mota F (2000) *Chem Phys Letter* 318:345–354
17. Tsuzuki S, Honda K, Uchimaru T (2000) *J Am Chem Soc* 122:3746–3753
18. Weiss S, Brandl M, Sühnel J (2001) *Trends Biochem Sci* 26:521–523
19. Nishio M, Umezawa Y, Jacques F (2014) *Phys Chem Chem Phys* 16:12648–12683
20. BioStation View https://www.cenav.org/abinit_mp_open/
21. Umezawa U, Tsuboyama S, Takahashi H (1999) *Bioorg Med Chem* 7:2021–2026

22. Šušva M, Missabch M (2000) *Trends Pharmacol Sci* 21:489–495
23. Palacios M (2004) *Weiss a Oncogene* 23:7990–8000
24. Snow R, Cardozo M, Morwick T (2002) *J Med Chem* 45:3394–3405
25. Zhu X, Kim L, Newcomb R (1999) *Structure* 7:651–661
26. Xing L, Klug-Mcleod J, Rai B (2015) *Bioorg Med Chem* 23:6520–6527
27. Baures P, Wiznycia A, Beatty A (2000) *Bioorg Med Chem* 8:1599–1605
28. Mohan N, Vijayalakshmi K, Koga N (2010) *J Comput Chem* 31:2874–2882
29. Pierce C, Haar E, Binch M (2005) *J Med Chem* 48:1278–1281
30. Omura S, Iwai Y, Hirano, (1997) *J Antibiot* 30:275–282
31. Lipinski A, Lombardo F, Dominy W (2001) *Adv Drug Deliv Rev* 46:3–26
32. Congreve M, Carr M, Murray C (2003) *Drug Discov Today* 8:876–877
33. Chen P, Doweyko A, Norris D (2004) *J Med Chem* 18:4517–4529
34. Shuker S, Hajduk P, Meadows R (1996) *Science* 274:1531–1534
35. Erlanson D, Fesik S, Hubbard R (2016) *Nat Rev Drug Discov* 15:605–619
36. Scott D, Ehebauer M, Pukala T (2013) *ChemBioChem* 14:332–342
37. Barile E, Pellecchia M (2014) *Chem Rev* 114:4749–4763
38. Jubb H, Blundell T, Ascher D (2015) *Prog Biophys Mol Biol* 119:2–9
39. Pelay-Gimeno M, Glas A, Koch O (2015) *Angew Chem Int Ed* 54:8896–8927
40. Alexeev Y, Mazanetz M, Ichihara O (2012) *Curr Top Med Chem* 12:2013–2033
41. Ichihara O, Barker J, Law R (2011) *Mol Inf* 30:298–306
42. Thangudu R, Bryant S, Panchenko A (2012) *J Mol Biol* 415:443–453
43. Arkin M, Tang Y, Wells J (2014) *Chem Biol* 21:1102–1114
44. Filippakopoulos P, Picaud S, Mangos M (2012) *Cell* 149:214–231
45. Romero F, Taylor A, Crawford T (2016) *J Med Chem* 59:1271–1298
46. Brand M, Measures A, Wilson B (2015) *ACS Chem Biol* 10:22–39
47. Fish P, Filippakopoulos P, Bish G (2012) *J Med Chem* 55:9831–9837
48. Bissantz C, Kuhn B, Stahl M (2010) *J Med Chem* 53:5061–5084
49. Sharp K, Honig B (1990) *Annu Rev Biophys Biophys Chem* 19:301–332
50. Chung C, Coste H, White J (2011) *J Med Chem* 54:3827–3838
51. Taylor A, Vaswani R, Gehling V (2016) *ACS Med Chem Lett* 7:145–150
52. Sureshan K, Uchimarui T, Yao Y (2008) *CrystEngComm* 10:493–496
53. Bayden A, Moustakas D, Joseph-McCarthy D (2015) *J Chem Inf Model* 55:1552–1565
54. Pawson T, Raina M, Nash P (2002) *FEBS Lett* 513:2–10
55. Fry D (2006) *Biopolymers* 84:535–552
56. Montfort R, Workman P (2009) *Trends Biotechnol* 27:315–328
57. Mayer B (2001) *Cell Sci* 114:1253–1263
58. Kaneko T, Li L, Li S (2008) *Front Biosci* 4938–4952
59. Li S (2005) *Biochem J* 390:641–653
60. Musacchio A, Saraste M, Wilmanns M (1994) *Nat Struct Biol* 1:546–551
61. Terasawa H, Kohda D, Hatanaka H (1994) *Nat Struct Biol* 1:891–897
62. Liu Q, Berry D, Nash P (2003) *Mol Cell* 2003:471–481
63. Bhattacharyya R, Chakrabarti P (2003) *J Mol Biol* 331:925–940
64. Ling X, Ma G, Sun T (2003) *Cancer Res* 63:298–303
65. Rozakis-Adcock M, Fernley R, Wade J (1993) *Nature* 363:83–85
66. Lim W, Richards F, Fox R (1994) *Nature* 372:375–379
67. Bourette R, Arnaud S, Myles G (1998) *EMBO J* 17:7273–7281
68. Harkiolaki M, Lewitzky M, Gilbert R (2003) *EMBO J* 22:2571–2582
69. Horigai M, Kataoka M, Imamoto Y (2006) *J Am Chem Soc* 128:10646–10647
70. Prehoda K, Lee D, Lim W (1999) *Cell* 97:471–480
71. Pires J, Taha-Nejad F, Toepert F (2001) *J Mol Biol* 314:1147–1156
72. Pornillos O, Alam S, Davis D (2002) *Nat Struct Biol* 9:812–817
73. Mahoney N, Rozwarski D, Fedorov E (1999) *Nat Struct Biol* 6:666–671
74. Freund C, Kühne R, Yang H (2002) *EMBO J* 21:5985–5995

Drug Discovery Screening by Combination of X-ray Crystal Structure Analysis and FMO Calculation



Midori Takimoto-Kamimura and Noriyuki Kurita

Abstract Quantum chemistry calculations are the best way to understand the specific interactions between drug targets and ligands in the process of drug discovery lead optimization, using the crystal structures of these complexes. The present ab initio FMO calculations elucidate the reason why a slight structural difference of VD3 derivatives could cause a large difference in their binding affinities, although it could not be understood by just looking at their complex structures. We are confident that the combination of X-ray analysis and FMO calculations is a powerful tool to understand why the biological activities of the ligands are drastically changed by the slight differences in the ligand structures. Based on the results of FMO calculations, we would like to use for the novel potent ligand which can bind specifically to the ligand binding domain of human vitamin D receptor and inhibit the pathogenesis of immune diseases.

Keywords Vitamin D3 agonists · Vitamin D receptor · Structure-based drug design · X-ray analysis · FMO calculation · Molecular simulation · Binding affinity

Vitamin D plays an important role not only in the regulation of bone metabolism and blood calcium level, but also deeply correlated with cancer and immune diseases. The physiological effects of vitamin D are caused through vitamin D receptor (VDR). Previous researches [1] have suggested that VDR is present in almost all cell tissues in vivo, and that the physiological expression of vitamin D is deeply involved in the pathogenesis of immune diseases such as cancer and the disorder of hormone response. Therefore, clinical research on the application of various derived compounds based on vitamin D as a cancer therapeutic drug is under way.

M. Takimoto-Kamimura (✉)

Teijin Institute for Bio-Medical Research, Teijin Pharma Ltd, 4-3-2 Asahigaoka, Hino, Tokyo 191-8512, Japan

e-mail: m.kamimura@teijin.co.jp

N. Kurita

Department of Computer Science and Engineering, Toyohashi University of Technology, 1-1 Hibarigaoka Tempaku-cho, Toyohashi 441-8580, Aichi, Japan

The relation between vitamin D and various diseases is being elucidated [2] and the three-dimensional complex structure between VDR ligand-binding domain (VDR-LBD) and some VDR agonists needs to be determined in order to clarify the function of VDR. We have used X-ray crystallographic analysis techniques to understand the binding properties between VDR and vitamin D₃ (VD₃) derivatives [3]. However, only their binding modes often do not explain the difference in their biological activities. In particular, the reason why the binding affinities with VDR were greatly changed with slight differences of the structure of the ligand could not be clarified. Thus, using fragment molecular orbital (FMO) calculations [4], a high sophisticated molecular simulation technique, we successfully analyzed the specific interactions between VDR-LBD and VD₃ derivatives at an electronic level and identified the causes of large differences in binding properties with VDR due to the slight structure differences in the derivatives [5].

This paper introduces the results of X-ray crystallography and the specific interactions between VDR-LBD and VD₃ derivatives revealed by ab initio FMO calculations for the design of new active ligands. By combining X-ray crystallography with FMO calculation, it becomes extremely powerful tool to understand the peculiar interaction between VDR-LBD and VD₃ derivatives which could not be clarified only by the conventional structural analysis at an electronic level. These results will give useful information in proposing new effective ligands for VDR. Furthermore, by using similar research tools, we believe that the ability to reveal specific interactions between various proteins and ligands involved in the disease could lead to proposal of novel therapeutic agents for those diseases.

1 X-ray Crystallographic Analysis of the Complex of VDR-LBD and Various Ligands

So far active VD₃ derivatives have been marketed; for example, Onealpha®, Ediol®, as osteoporosis drugs and Bonalpha® as an active vitamin D₃ keratosis treatment and psoriasis treatment. During the development of these drugs, these drugs have been created by the so-called classical medicinal chemistry from 1 α ,25-dihydroxy vitamin D₃ (1 α ,25(OH)₂VD₃). The most important point in the VDR drug discovery is the strength of the activity, which is the pharmacological effect, and the calcium action in the blood, which is the side effect, cannot be separated, and these have been controlled by strictly controlling the dosage and administration until now, but the issue which aims at the separation with the pharmacological effect like usual small molecular drug is still big. The first X-ray structures of a complex of human VDR (hVDR) LBD and 1 α ,25(OH)₂VD₃ were obtained by Moras and colleagues [6] and then the technique for designing ligands using structure-based drug design (SBDD) is now common sense in pharmaceutical industries. More than 130 complex structures, including our structure, have already been registered in protein data bank (PDB).

1.1 Structure of the Ligand-Binding Domain of RatVDR in Complex with a Non-Secosteroidal Vitamin D3 YR301

We have conducted X-ray structural analyses that lead to various breakthroughs. In particular, the first non-secosteroidal compound complex analysis with YR301 in collaboration between Teijin Pharma and Dr. Kurihara of the National Institutes of Health and Safety [7] attracted great attention as a compound that can lead to usual synthetic low-molecular-weight drugs from secosteroidal scaffold. As a result of attempting the separation of the racemate of LG190178, the absolute configuration was also able to be confirmed by our X-ray structural analysis. Their chemical structures are shown in Fig. 1. Figure 2 shows that the binding mode as a basis of

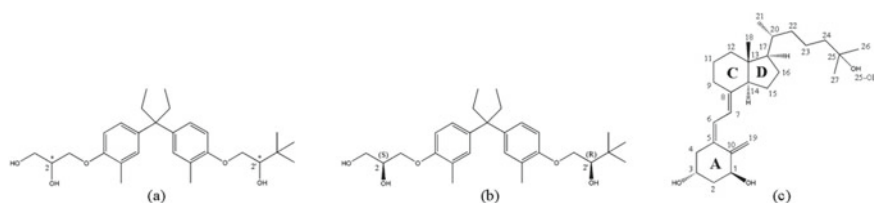


Fig. 1 Chemical structures **a** LG190178, **b** YR301 [(2S)-3-[4-(3-{4-[(2R)-2-hydroxy-3,3-dimethylbutoxy]-3-methylphenyl}pentan-3-yl)-2-methylphenoxy]propane-1,2-diol] and **c** 1α,25(OH)₂VD₃ (1α,25-dihydroxy vitamin D3)

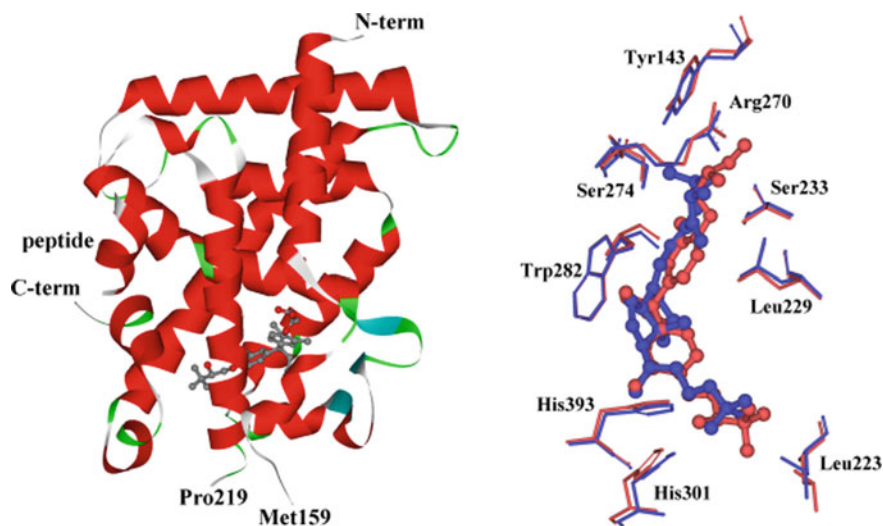


Fig. 2 *Left*: Overall structure of rat VDR LBD-YR301 with the synthetic peptide containing the LXXLL sequence of the coactivator DRIP 205 complex. *Right*: Ligand-binding pocket of the structure hVDR LBD-1α,25(OH)₂VD₃ (PDB Code: 1DB1, blue) onto rVDR LBD-YR301 complex structures (PDB Code: 2ZFX, red)

the high activity was completely the same with the secosteroidal compound, and this became a reason why YR301 shows similar activity with $1\alpha,25(\text{OH})_2\text{VD}_3$.

1.2 Structure of the Ligand-Binding Domain of hVDR in Complex with 14-Epi-19-Nortachysterol

On the other hand, in the joint research between Teijin Pharma and Professor Kittaka of Teikyo University, we had the opportunity to analyze the complex structures of human VDR ligand-binding domain (hVDR-LBD) with numerous interesting secosteroidal VDR ligands synthesized in Kittaka laboratory. In particular, we were really surprised that the 14-epi-19-nortachysterol derivatives had a linker moiety between the A and CD rings attached differently in the hVDR pockets; that is, the C5,6-*s-trans* and C7,8-*s-trans* triene configurations had a structure that was inverted with the natural C7,8-ene-configuration of $1\alpha,25(\text{OH})_2\text{D}_3$ (shown in Fig. 3). It is also the first worldwide finding [8], and C5,6-*s-cis* configuration is the first to be able to maintain biological activity even when C5,6-*s-trans* configuration of the linker is altered even the *trans* form was proven.

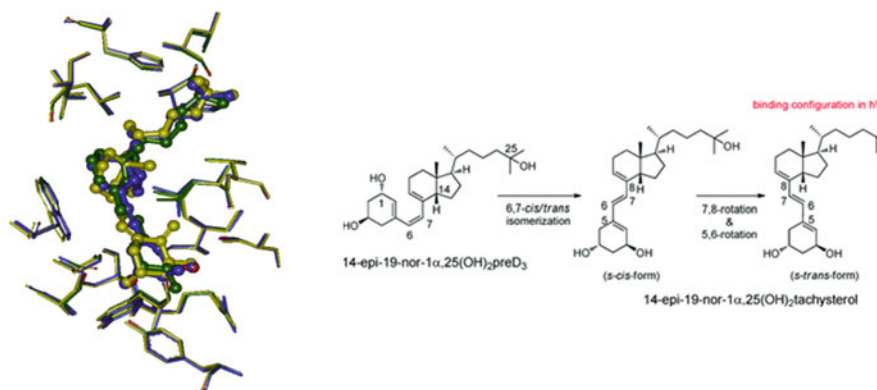


Fig. 3 *Left:* Superposed three-dimensional structures of 14-epi-19-nor- $1\alpha,25(\text{OH})_2$ tachysterol (blue) onto $1\alpha,25(\text{OH})_2\text{VD}_3$ (yellow) in the hVDR ligand-binding pocket; *Right:* The mechanism view of C6,7-*cis/trans* isomerization from 14-epi-19-nor- $1\alpha,25(\text{OH})_2$ preD₃ to 14-epi-19-nor- $1\alpha,25(\text{OH})_2$ tachysterol

1.3 Structure of the Ligand-Binding Domain of hVDR in Complex with 2 α -Heteroarylalkyl Active Vitamin D3

The 2 α -heteroarylalkyl active vitamin D3, which we discuss here, was another interesting piece of collaboration between Teijin pharma and Professor Kittaka of Teikyo University [9]. Various heterocyclic analogs were designed and synthesized at 2 α position in his laboratory, and the transcriptional activity was assessed using binding affinity and human osteosarcoma cells, respectively. The biological efficacy of 2 α -[2-(tetrazol-2-yl)ethyl]-1 α ,25(OH) $_2$ D $_3$ (ligand 1 of Fig. 4) was confirmed. Subsequent bone mineral density increases over natural ligand levels were confirmed using ovariectomized (OVX) rats as osteoporosis model. In the meantime, in ligand 2 of Fig. 4 in which the position of N differs, any drug effect has not been observed.

In order to explain these differences in activity, the complex structures of these two compounds with hVDR-LBD were analyzed by X-ray and the results were superimposed. As shown in Fig. 5, the structures were almost superimposed, and we could not clearly explain in the viewpoint of the binding modes why these small structural difference effected biological activities. Not only in this theme, there are cases in which the activity can be explained by the binding mode of the X-ray analysis, and cases in which the activity difference cannot be explained. In the latter case, it may be important to use quantum chemical calculations to quantitatively interpret the interaction modes.

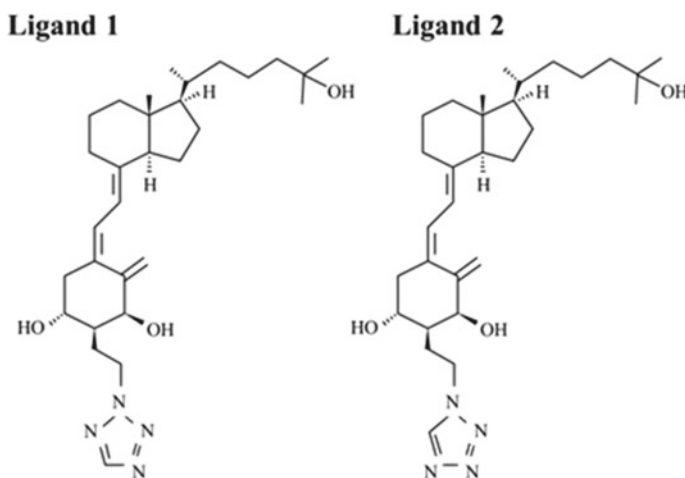
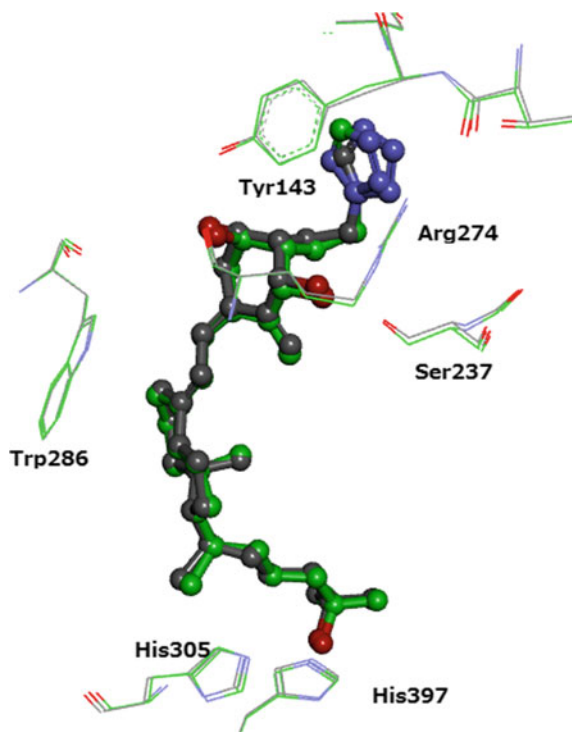


Fig. 4 Chemical structures of the vitamin D derivatives employed in the present study [5]

Fig. 5 Superposing ligand 1 complex (PDBcode: 4ITE green) onto ligand 2 complex (PDBcode: 4ITF gray) with hVDR-LBD



2 FMO Calculations for Vitamin D Receptor Ligand-Binding Domain and Ligand Complexes

In the present calculations, the FMO method [4] was used to calculate the electronic states of proteins with high accuracy and high speed. The FMO method is widely used for the analysis of specific interactions between proteins and ligands that inhibit their objective at an electronic level [10]. Indeed, in November 2014, the FMO Drug Design (FMOOD) Consortium [11] was established in Japan with the participation of universities, national laboratories, pharmaceutical companies, and informatics companies, with the objective of developing FMO calculation-based *in silico* drug discovery techniques using supercomputers “Kei” as practical technologies. First of all, two structures shown in Fig. 5 are selected as subjects for the FMO calculations in FMOOD. The biological assays and X-ray crystallography analysis were performed at Teijin Pharma. However, interaction modes between each ligand and VDR-LBD in the two structures could not explain the difference in the biological activities of the ligands. Therefore, to elucidate the reason for this difference, FMO calculations were conducted at Kurita laboratory of Toyohashi University of Technology.

2.1 Subjects and Conditions of FMO Calculations

In the present FMO calculations [5], two VD3 derivatives shown in Fig. 4 were used as the target ligands. Although these ligands differ only in the positions of the carbons at the terminal tetrazole ring, the EC_{50} (effective concentration for 50% inhibition of the maximal one values) indicates that ligand 1 is 0.006 nM in the transcriptional activity using Hos/SF, and ligand 2 is 0.31 nM, and the cause for this significant difference in EC_{50} is not clear, although the inhibitory effect of ligand 1 is considerably greater. Therefore, first, based on the PDB structure of VDR-LBD and these ligands determined by X-ray crystallographic analysis, the initial structure of the complex was made, and water molecule was added to the ambient of the structure 8 Å, and the stable structure of the complex in water was decided using classical molecular mechanics (MM) calculations. In the MM calculations, AMBER99SB-ILDN and GAFF force fields were used for VDR-LBD and the VD3 derivatives, respectively, while TIP3P model was used for water molecules. We assigned Hid protonation (neutral histidine with a proton located at Nd) for the His residues existing at the inside of hVDR-LBD, while Hip⁺ protonation was assigned for the His residues on the outside of hVDR-LBD.

Next, for the obtained stable structure, the FMO calculation was carried out in order to clarify the peculiar interaction between each amino acid residue of VDR-LBD and the VD3 derivatives. In doing so, the FMO calculation was carried out in a condition closer to the hydration state in vivo, considering water molecules within 6 Å of the complex ambient. The ab initio MP2/6-31G(d) method was used for describing accurately the π - π stacking, NH- π , and CH- π interactions that occur between VDR-LBD and the VD3 derivatives. The FMO calculation program ABINIT-MP Ver.6.0 [12] was used for calculations. In addition, to clarify the strength of the interaction between VDR-LBD and these ligands, the binding energies (BE) between VDR-LBD and the ligands were calculated based on the total energies (TEs) of the components using the following equation.

$$\begin{aligned} \text{BE} = & \text{TE}(\text{VDR} - \text{LBD} + \text{ligand} + \text{water}) - \text{TE}(\text{VDR} - \text{LBD} + \text{water}) \\ & - \text{TE}(\text{ligand} + \text{water}) + \text{TE}(\text{water}) \end{aligned}$$

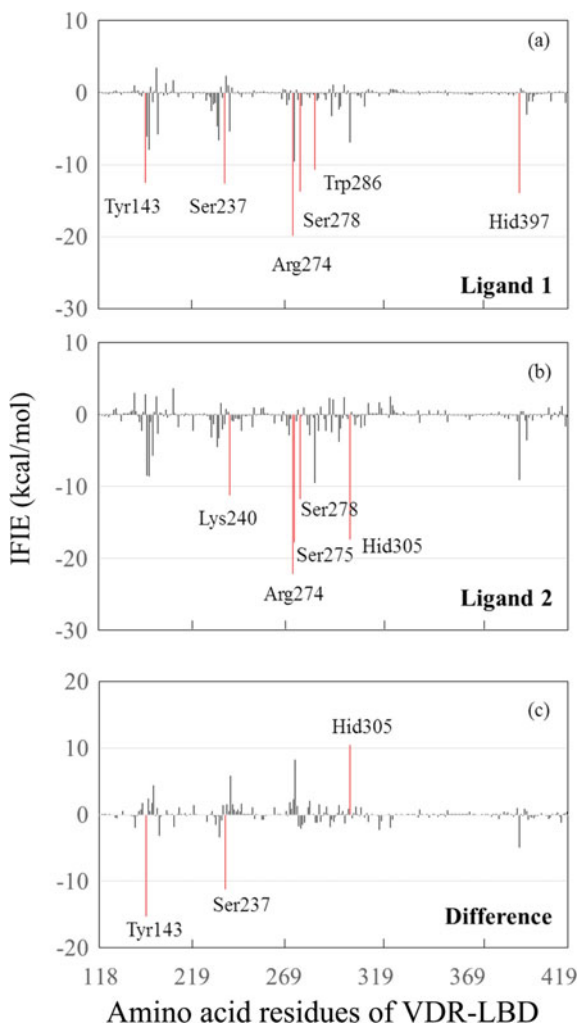
2.2 Interaction Energy Between VDR-LBD and VD3 Derivatives

To verify the validation of the computational approach used in this calculation, we compared the BE between the VDR-LBD and the two ligands with the EC_{50} values obtained in the experimentals [9]. The BE (-139.2 kcal/mol) of ligand 1 was found to be larger than the BE (-131.9 kcal/mol) of ligand 2, indicating that ligand 1 binds more strongly to VDR-LBD. This result can qualitatively explain the trends

of experimentally obtained EC_{50} values. Therefore, we analyzed the specific interactions between VDR-LBD and the ligands, based on the inter-fragment interaction energy (IFIE) [13] obtained by the same FMO calculations.

Next, the IFIEs between the ligand and the amino acid residues constituting VDR-LBD were analyzed in order to clarify the cause why the BE values of the ligands 1 and 2 differ significantly to each other. As shown in Fig. 6a, b, both the ligands bind most strongly to Arg274 of VDR-LBD. Arg274 was found to be critical for binding to the ligands in the previous experiment [9]. Therefore, the results of the present FMO calculations could explain the experimental results. Furthermore, in addition to Arg274, the FMO calculations revealed that Ser278 also exhibits strong

Fig. 6 IFIEs between each amino acid residue of VDR-LBD and ligand; **a** ligand 1, **b** ligand 2, and **c** difference in IFIE between ligands 1 and 2 [5]



(−10 kcal/mol or more) attractive interactions with both the ligands to be critical for the binding between VDR-LBD and the ligands.

In order to clarify the difference in the binding characteristics between VDR-LBD of the ligands 1 and 2, the difference between Fig. 6a, b was obtained, and the difference in IFIE was graphed. In Fig. 6a, c negative value indicates that the ligand 1 interacts more strongly with VDR-LBD, while a positive value indicates that the ligand 2 interacts strongly with VDR-LBD. It was revealed that Tyr143 and Ser237 of VDR-LBD interact more strongly with the ligand 1 and that Hid305 interacts more strongly with the ligand 2. These differences in interactions with amino acid residues may be related to the large differences in the EC_{50} of ligands 1 and 2.

2.3 Specific Interactions Between VDR-LBD and VD3 Derivatives

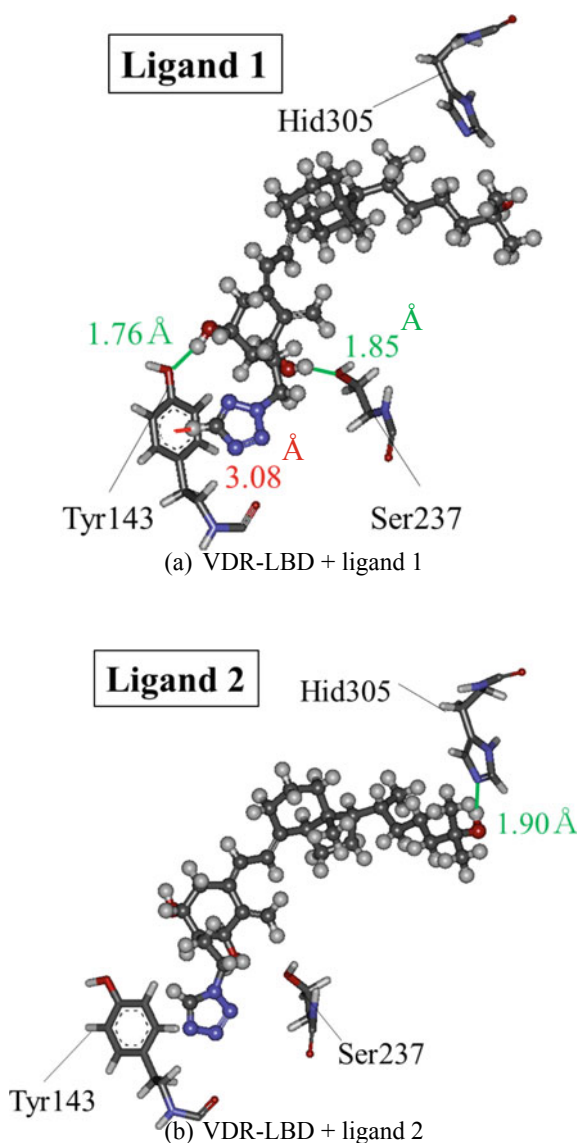
In order to clarify the causes of the above-mentioned differences in IFIEs, we have analyzed in detail the structures in which amino acid residues of Tyr143, Ser237, and Hid305 interact with the ligands. As shown in Fig. 7a, the ligand 1 is hydrogen-bonded to the side-chain terminal oxygens of Tyr143 and Ser237. In particular, the distance between ligand 1 and Tyr143 is 1.76 Å, and a strong hydrogen bond is formed. This may have occurred because, as shown in Fig. 7a, the CH-site of the tetrazole ring at the end of the ligand 1 was brought closer to Tyr143 by forming a CH– π interaction with the phenyl ring of the Tyr143 side chain. Indeed, CH– π interactions are realized at 3.08 Å distances by directing the CH-site of the tetrazole ring toward the Tyr143 phenyl-ring. The dispersion energy in the IFIE (−12.54 kcal/mol) between Tyr143 and the ligand 1 was evaluated to be −10.6 kcal/mol. It was thus revealed that CH– π interaction is largely involved in the interaction between Tyr143 and the ligand 1.

On the other hand, as shown in Fig. 7b, CH– π interaction cannot be formed between the ligand 2 and Tyr143, due to a shift of the CH-site in the tetrazole ring. As a result, the Tyr143 side chain and the ligand 2 are located apart, and there is no hydrogen-bonding between the oxygen atoms of the side chain termini of Tyr143 and the ligand 2. Thus, for the first time, the present FMO calculations revealed that the interaction between the ligand and Tyr143 and the BE between the VDR-LBD and the ligand are significantly affected due to a slight difference in the position of the CH-site in the tetrazole ring at the termini of ligands 1 and 2. Consequently, it was elucidated that the main cause for the large differences between the experimentally obtained values of EC_{50} for ligands 1 and 2 is related to the difference in the interactions between the tetrazole ring of the ligands and the Tyr143 side chain.

In terms of Hid305, as shown in Fig. 7, the ligand 2 is hydrogen-bonded, but there is no particularly strong attractive interaction with the ligand 1, resulting in the structures consistent with the IFIE size shown in Fig. 6.

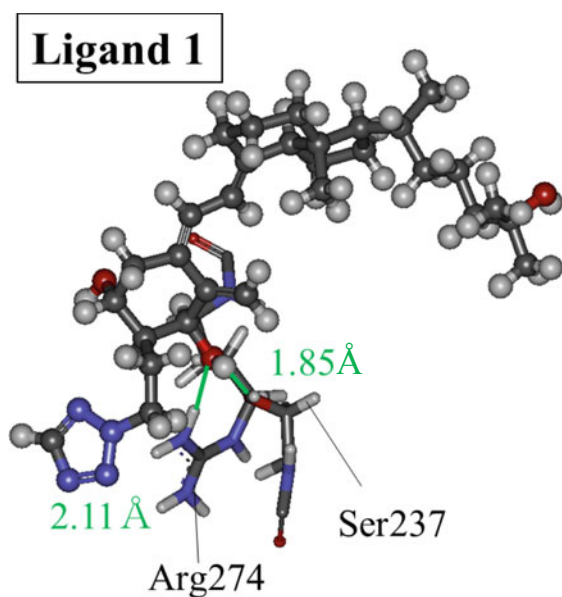
Finally, we compared the interaction structures with ligands 1 and 2 for Arg274 and Ser237, which have large values of IFIE (Fig. 6a, b). As shown in Fig. 8a, the H

Fig. 7 Interacting structures between VDR-LBD residues (Tyr143, Ser237, and Hid305) and ligand in **a** VDR-LBD + ligand 1, and **b** VDR-LBD + ligand 2. Green lines and a red line indicate hydrogen-bonding and CH- π interactions, respectively [5]

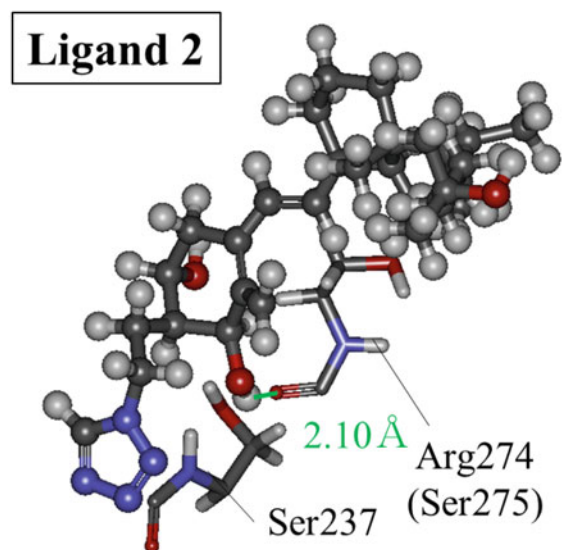


atom of the OH group of the phenyl ring of the ligand 1 forms a hydrogen bond at a distance of 1.85 Å with the O atom of the side chain end of Ser237, and in addition, the O atom of the same OH group forms a hydrogen bond at a distance of 2.11 Å with the NH₂ group of the side chain end of Arg274. These hydrogen bonds cause strong attractive interactions between the ligand 1 and Arg274 and Ser237, as shown in Fig. 6a.

Fig. 8 Interacting structures between VDR-LBD residues (Ser237 and Arg274) and ligand in **a** VDR-LBD + ligand 1, and **b** VDR-LBD + ligand 2. Green lines indicate hydrogen-bonding interactions between VDR-LBD and ligand [5]



(a) VDR-LBD + ligand 1



(b) VDR-LBD + ligand 2

On the other hand, as shown in Fig. 8b, the H atom of the OH group of the phenyl ring of the ligand 2 forms a hydrogen bond at a distance of 2.10 Å with the O atom of the backbone between Arg274 and Ser275, indicating a strong attractive interaction with the ligand 2, as shown in Fig. 6b. However, the side chain of Ser237 dissociates from the OH group of the phenyl ring of the ligand 2, and there is no hydrogen bond between the ligand 2 and Ser237, as shown in Figs. 7b and 8b. Accordingly, it was clarified that strong attractive interaction between the ligand 2 and Ser237 did not occur.

3 For the Design of New Active Ligands Effective for VDR-LBD

As shown in Figs. 7 and 8, the different CH-site at the terminal tetrazole ring of the ligands 1 and 2 altered significantly the interaction pattern with the ambient VDR-LBD residues, and it was found that the impact also changed the interaction between the ligand and other residues, and that the interaction between the ligand and VDR greatly changed. Such apparently weak interactions as CH- π may also play vital roles in some environments, and the importance of these weak interactions can be estimated properly by performing ab initio FMO calculations for the structures obtained by X-ray analysis with diverse ligands. Large-sized ligands, particularly those that bind to VDR-LBD and have large numbers of hydrogen atoms, require long computational time in house computers, while the calculations using cloud systems such as supercomputer “Kei” would allow for rapid feedbacks. As a result, the cycle of drug design composed of “compound synthesis \rightarrow X-ray analysis \rightarrow FMO calculation \rightarrow new design of the ligand” is efficiently circulated, and it is considered that the new ligand which works effectively for VDR-LBD can be proposed.

Recently, it was reported that the binding affinity between VDR-LBD and its ligand depends significantly on the chirality of the ligand [14, 15]. Furthermore, we are confident that the combination of X-ray analysis and FMO calculations is the powerful tool to understand why the biological activities of the ligands are drastically changed by the slight differences in the ligand structures. Based on the results of FMO calculations, we would like to propose novel potent ligands which can bind specifically and strongly to hVDR-LBD and inhibit the pathogenesis of immune diseases.

References

1. Walters MR (1992) Newly identified actions of the vitamin D endocrine system. *Endocr Rev* 13:719–764
2. Nakagawa K (2002) Analysis of molecular mechanism of cancer cell differentiation and apoptosis induced by vitamin D3 analogs on the basis of molecular recognition of vitamin D receptor ligand binding domain. *Yakugaku Zasshi* 122:781–791

3. Matsuo M, Hasegawa A, Takano M, Saito H, Kakuda S, Chida T, Takagi K, Ochiai E, Horie K, Harada Y, Takimoto-Kamimura M, Takenouchi K, Sawada D, Kittaka A (2013) Synthesis of 2 α -Heteroarylalkyl active vitamin D3 with therapeutic effect on enhancing bone mineral density in vivo. *ACS Med Chem Lett* 4:671–674
4. Kitaura K, Ikeo E, Asada T, Nakano T, Uebayashi M (1999) Fragment molecular orbital method: an approximate computational method for large molecules. *Chem Phys Lett* 313:701–706
5. Takeda R, Kobayashi I, Shimamura K, Ishimura H, Kadoya R, Kawai K, Kittaka A, Takimoto-Kamimura M, Kurita N (2017) Specific interactions between vitamin-D receptor and its ligands: *ab initio* molecular orbital calculations in water. *J Steroid Biochem Mole Biol* 171:75–79
6. Rochel N, Wurtz JM, Mitschler A, Klaholz B, Moras D (2000) The crystal structure of the nuclear receptor for vitamin D bound to its natural ligand. *Mol Cell* 5:173–179
7. Kakuda S, Okada K, Eguchi H, Takenouchi K, Hakamata W, Kurihara M, Takimoto-Kamimura M (2008) Crystal structure of the rat vitamin D receptor ligand binding domain complexed with YR301 and a synthetic peptide containing the NR2 box of DRIP 205. *Acta Crystallogr Sect F Struct Biol Cryst Commun* 64:970–973
8. Sawada D, Tsukuda Y, Saito H, Kakuda S, Takimoto-Kamimura M, Ochiai E, Takenouchi K, Kittaka A (2011) Crystal structure of the human vitamin D receptor ligand binding domain complexed with Yne-diene type analog of active 14-*epi*-2 β -methyl-19-norvitamin D3. *J Am Chem Soc* 133:7215–7221
9. Matsuo M, Hasegawa A, Takano M, Saito H, Kakuda S, Takagi K, Ochiai E, Horie K, Takimoto-Kamimura M, Takenouchi K, Sawada D, Kittaka A (2014) Design and synthesis of 2 α -(tetrazolylethyl)-1 α ,25-dihydroxyvitamin D3 as a high affinity ligand for vitamin D receptor. *J Steroid Biochem Mole Biol* 144:201–203
10. Tanaka S, Mochizuki Y, Komeiji Y, Okiyama Y, Fukuzawa K (2014) Electron-correlated fragment-molecular-orbital calculations for biomolecular and nano systems. *Phys Chem Chem Phys* 16:10310–10344
11. FMO Drug Design Consortium. <https://eniac.scitec.kobe-u.ac.jp/fmodd/>
12. Mochizuki Y, Yamashita K, Nakano T, Okiyama Y, Fukuzawa K, Taguchi N, Tanaka S (2011) Higher-order correlated calculations based on fragment molecular orbital scheme. *Theor Chem Acc* 130:515–530
13. Fukuzawa K, Nakano T, Kato A, Mochizuki Y, Tanaka S (2007) Applications of the fragment molecular orbital method for bio-macromolecules. *J Comp Chem* 6:185–198
14. Takeda R, Suzuki R, Kobayashi I, Kawai K, Kittaka A, Takimoto-Kamimura M, Kurita N (2018) Specific interactions between vitamin D receptor and ligand depending on its chirality: *ab initio* fragment molecular orbital calculations. *Chem-Bio Inform J* 18:32–43
15. Terauchi Y, Suzuki R, Takeda R, Kobayashi I, Kittaka A, Takimoto-Kamimura M, Kurita N (2019) Ligand chirality can affect histidine protonation of vitamin-D receptor: *ab initio* molecular orbital calculations in water. *J Steroid Biochem Mole Biol* 186:89–95

Cooperative Study Combining X-ray Crystal Structure Analysis and FMO Calculation: Interaction Analysis of FABP4 Inhibitors



Uno Tagami and Kazutoshi Takahashi

Abstract X-ray crystal structural determination of FABP4 in complex with four inhibitors revealed the binding modes of the complexes, and the interactions between FABP4 and the inhibitors were analyzed. The detailed structure–activity relationship (SAR) could not be explained in terms of these crystal structural observations. Therefore, the interactions between FABP4 and the inhibitors were analyzed in more detail using fragment molecular orbital (FMO) method. This analysis revealed that the total interfragment interaction energies between FABP4 and each inhibitor correlated with the ranking of the K_i value for the four inhibitors. Furthermore, the interactions between each inhibitor and specific amino acid residues in FABP4 were identified. The oxygen atom of Lys58 in FABP4 was found to be very important for strong inhibitor–protein interactions. These results might provide useful information for the development of novel potent FABP4 inhibitors.

Keywords FABP · aP2 · Inhibitor · X-ray crystal structure · FMO

1 Introduction

In drug discovery, the structure of the complex between a target protein and a drug compound is key to understanding the drug's reaction mechanism and improving its activity through structural changes. Many complex structures have been reported recently [1], made possible by the progress in protein preparation, purification, and structure determination techniques, as represented by X-ray crystal structure analysis. While X-ray crystal structure analysis provides accurate coordinates of each amino acid and the drug compound, it is difficult to judge the interaction intensity simply by visual inspection of these coordinates [2]. For example, if hydrogen bonds are present, it is impossible to estimate their strength relative to other interactions simply from the bond distance or angle. Moreover, some interactions, such as hydrophobic interactions and dispersion forces, run the risk of being overlooked by

U. Tagami (✉) · K. Takahashi

Research Institute for Bioscience Products and Fine Chemicals, Ajinomoto Co., Inc, 1-1 Suzuki-cho, Kawasaki 210-8681, Japan
e-mail: uno_tagami@ajinomoto.com

© Springer Nature Singapore Pte Ltd. 2021

Y. Mochizuki et al. (eds.), *Recent Advances of the Fragment Molecular Orbital Method*, https://doi.org/10.1007/978-981-15-9235-5_12

267

X-ray analysis. Molecular orbital method is a powerful technique to calculate these interactions. However, the calculation cost is too high to estimate many protein–ligand interactions. Fortunately, fragment molecular orbital (FMO) calculations can solve this problem at an acceptable cost for industrial users. Therefore, FMO is a suitable approach to estimate the interaction intensities between each amino acid and the drug compound [3–6]. In this chapter, the interaction analysis of FABP4 and its inhibitors is reported as an example of a cooperative study combining X-ray crystal structure analysis and FMO calculation.

Fatty acid-binding proteins (FABPs) are cytoplasmic proteins that bind to hydrophobic ligands, such as long-chain fatty acids, in a noncovalent and reversible manner. It has been suggested that FABPs act as chaperone proteins for fatty acids and play important roles in homeostasis of fatty acids and the lipid signaling pathway [7]. The protein FABP4 (aka aFABP, aP2), a member of the FABP family, is a 14.6 kDa cytosolic protein mainly expressed in macrophages and adipocytes. Previous studies have reported that mice with FABP4-deficiency caused by genetic and diet-induced obesity show protection against the development of hyperinsulinemia and insulin resistance [8, 9]. An FABP4-deficiency in apolipoprotein E-deficient mice also confers protection against the development of atherosclerosis [10]. Furthermore, treatments with prototype small-molecular inhibitors for FABP4 have been shown to attenuate fatty infiltration in the livers of ob/ob mice [11]. These studies have demonstrated that FABP4-deficiency is related to several diseases, including diabetes, atherosclerosis, and liver disease, and that potent, selective, small-molecular inhibitors for FABP4 might be potential therapeutic agents for these diseases. Recently, a small series of FABP4 inhibitors have been reported, most of which have been identified by a structure-based drug design (SBDD) method [12–16]. Thus, the crystal structures of several ligand-bound human FABP4s have been determined [11, 12, 17], which provided insights into the structural foundation underlying the binding modes of endogenous ligands and small-molecular inhibitors in the FABP4 binding site. Structurally, FABP4 contains 10 antiparallel β -strands forming a characteristic β -clam shell structure, which provides a substrate binding site [18–25]. Considering these findings, it is believed that ligands occupy the internal pocket of FABP4, and carboxylic acid ligands usually have polar interactions with the Arg126 and Tyr128 side-chains of the protein. In addition, the importance of a negatively charged substituent, such as a CO_2^- , SO_3^- , or PO_3^- group, in these inhibitors has been revealed [26].

The purpose of this study was to discover a potent FABP4 inhibitor as a new drug candidate. We determined the crystal structures of the complexes of FABP4 and its inhibitors. However, it was difficult to rationalize the structure–activity relationship (SAR) simply by visual inspection of hydrogen bonds or hydrophobic interactions. For a more detailed analysis, the inhibitor–protein interactions were investigated using the FMO method. Using the calculated interfragment interaction energies (IFIEs) [4–6, 27–29] between the inhibitors and FABP4 amino acid residues, the various inhibitor–protein interactions were described in detail to allow the development of new FABP4 inhibitors.

2 Methods

2.1 Discovery of Potent FABP4 Inhibitors

Initially, our in-house compound library was screened using a human FABP4 binding assay. We identified a hit compound that possessed an indole core structure (data not shown). Next, 300 compounds were designed based on this compound and assayed to find novel inhibitors. The lead compound was identified by SBDD against the in-house compound library using the X-ray crystal structures determined for the FABP4/inhibitor complexes.

The first modifications focused on substitutions to form indole analogs. As a result, compound 3 was identified as the leading inhibitor. Next, compound 2 was identified as a potent FABP4 inhibitor by comparison of the crystal structures of FABP4/compound 2 complex with that of compound 3. Next, compound 1 was developed by using the “Enumerate Library from Ligands” module of BIOVIA Discovery Studio 4.0 (Dassault Systèmes) to substitute the indole ring at the 3-position in compound 2. Finally, Glide docking in Maestro 9.2 (Schrödinger, LLC) was used for screening these synthetic candidate inhibitors. All inhibitors were synthesized by the methods described in an earlier patent [30].

Compound 4 is used as an inactive compound that possesses a common indole core structure for comparison with compound 1–3.

2.2 Biological Evaluation (FABP4 Binding Assay)

The in vitro activities of the FABP4 inhibitors were determined using an FABP4 Inhibitor/Ligand Screening Assay Kit (Cayman Chemical Co., Ann Arbor, MI, USA), according to the manufacturer’s protocol with a slight modification [31]. This method was used for both the screening and calculation of the IC_{50} and K_i values. The K_d values were determined as 1.7 μ M by Scatchard plot analysis using recombinant human FABP4 protein and 1-anilinonaphthalene-8-sulfonic acid.

2.3 Crystallization and Structural Determination

The FABP4 was expressed by an *Escherichia coli* expression system and highly purified. The protein/compound solutions were produced by mixing the protein and each compound to final concentrations of 6 mg/mL FABP4 and 2.5 mM compound. The crystals were then grown at 23 °C from a 1/1 mixture (v/v) of the protein/compound with crystallization solution (2.4 M NaH_2PO_4/K_2HPO_4 , pH 7.3). Crystals were transferred into a cryoprotectant solution (2.93 M NaH_2PO_4/K_2HPO_4 , pH 7.3, 25% glycerol and 2.5 mM compound). Data collections were conducted at KEK-PF (Tsukuba,

Japan). The resulting structures were deposited in the Protein Data Bank as 5D4A, 5D45, 5D47, and 5D48 for compound 14, respectively.

2.4 FMO Analysis

The SARs between FABP4 and each compound were analyzed using the FMO method. The X-ray crystal structures of the FABP4/inhibitor complexes were used for these analyses. The complex structures were protonated and refined using Protein Preparation Wizard in Maestro 9.2 (Schrödinger, LLC). Then, all water molecules—none of which participated in ligand binding—were deleted to prevent their excessive influence on the FMO calculations. The FMO calculations and analyses were performed using BioStation Viewer 13.01 (MIZUHO Rev.) [32]. The FMO calculations used the ABINIT-MP 5.0 code and the level of theory was MP2/6-31G [33–35]. Each amino acid residue was treated as a single fragment by separating between the carbonyl and α -carbon. First, FABP4 was divided into individual amino acid units with the Generate Fragments/Auto/Generate Fragments module of BioStation Viewer. Next, the four compounds were each partitioned into two fragments for the FMO calculations. The compounds all possessed a carboxylic group, and all interacted with FABP4 at the same interaction site. To clarify the SAR (i.e., to specify which part of the compounds was responsible for their activity), the α - and β -carbons of carboxylic acid were separated from each other, with the α -carbon in the same fragment as the carboxylic group. The α -carbons are set as BAA (bond-detached atom), and the β -carbons are set as BAA (bond-attached atom) (Fig. 1). Then, the interaction of FABP4 with the moiety containing the β -carbon, and with the moiety containing the α -carbon and carboxylic group, of each compound was analyzed.

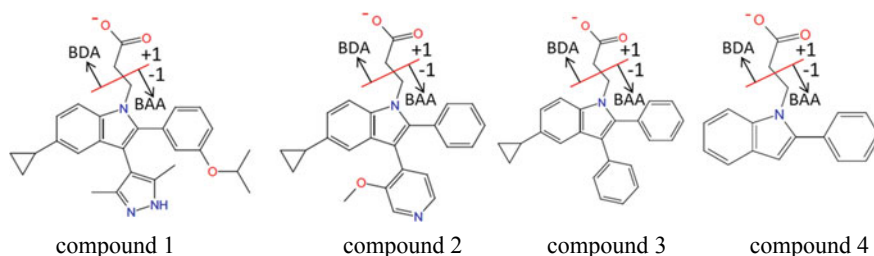


Fig. 1 Method for fragmentation of each inhibitor

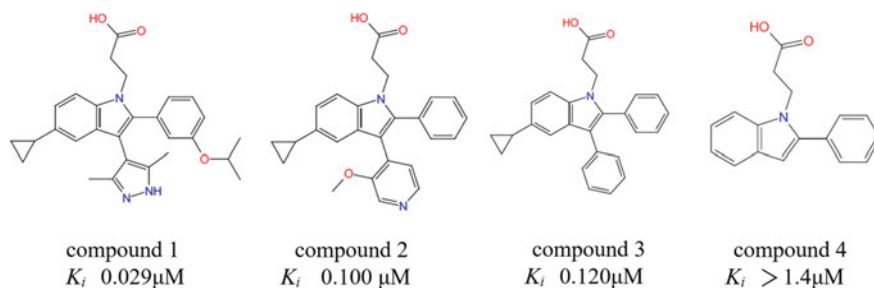


Fig. 2 Structures and activities of four novel inhibitors

3 Results and Discussion

3.1 Structures and Activities of Inhibitors

For the analysis of the inhibitor–protein interactions, four novel inhibitors with a common scaffold were selected from determined complex structures. Among the four inhibitors, compounds 1, 2, and 3 possessed sequentially lower activities, and compound 4 showed the lowest activity (Fig. 2). We were particularly motivated to clarify why compound 1 was three times more active than compound 2, and to analyze the relevant interactions to provide useful information for the development of novel potent FABP4 inhibitors.

3.2 Crystallographic Structures

Next, the crystallographic structures of FABP4 complexes with the four inhibitors (compounds 1–4) were determined, as shown in Fig. 3. The resolution of these structures was sufficiently high (1.65–1.81 Å) for reliable quantum mechanical analysis using FMO.

The 31 residues located within 5.0 Å of any atom of compound 1 were aligned by the “align binding site” function (Maestro, Schrödinger). The binding sites were found to be very similar among all four complexes, as demonstrated by the root mean square deviation of just ~0.3 Å. All four compounds possessed a carboxyl group, which generally formed hydrogen bonds with FABP4s Arg126 and Tyr128 (Fig. 4), but the interactions of the other moieties showed more distinct variations. It was clear that FABP4 had a greater number of interactions with compounds 1 and 2 than with compounds 3 and 4. To further elucidate the inhibitor–protein binding, the interactions of FABP4 with the characteristic moieties of compounds 1 and 2 were studied in more detail. Two hydrogen bonds with Ser55 and Lys58, and four hydrophobic interactions with Ala36, Pro38, Phe57, and Ala75, were observed in compound 1s pyrazole substructure (Fig. 4a). Meanwhile, one hydrogen bond with

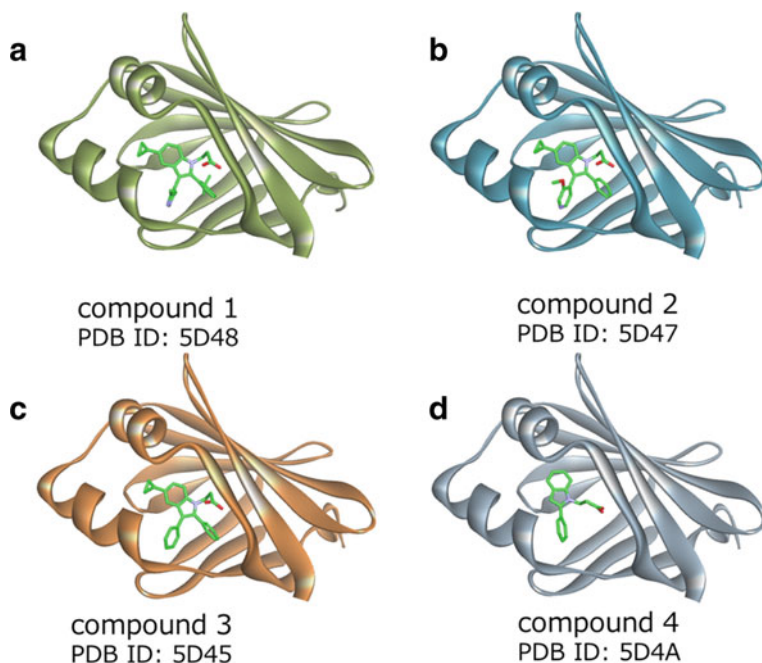


Fig. 3 The crystal structures of FABP4 binding with the four inhibitors

Ser55 and five hydrophobic interactions with Ala33, Ala36, Pro38, Lys58, and Ala75 were observed in compound 2's 2-methoxypyridine moiety (Fig. 4b). Therefore, a simple sum of the number of hydrogen bonds and hydrophobic interactions in these crystal structures was insufficient to explain the precise activity differences between compounds 1 and 2. More information regarding the binding modes and inhibition potencies was obtained via FMO calculations of the precise interaction energies in these complexes.

3.3 FMO Analysis

The validity of the FMO method was confirmed by analyzing the correlation between the IFIE and the K_i values. The IFIE is the sum of the interaction energy components, including electrostatic, exchange–repulsion, charge transfer and mixing, and dispersion energies (ES, EX, CT+ mix, and DI, respectively), and was calculated for each amino acid residue. The IFIEs of each individual amino acid residue were summed to yield the IFIE sum. Negative values represented favorable interaction energies for the binding of an amino acid residue with a ligand. The IFIE sum and K_i of the four inhibitors for FABP4 are shown in Table 1. The correlation coefficient between $\log(K_i)$ and the IFIE sum of compounds 1–4 was 0.729 (note that K_i of compound 4 was

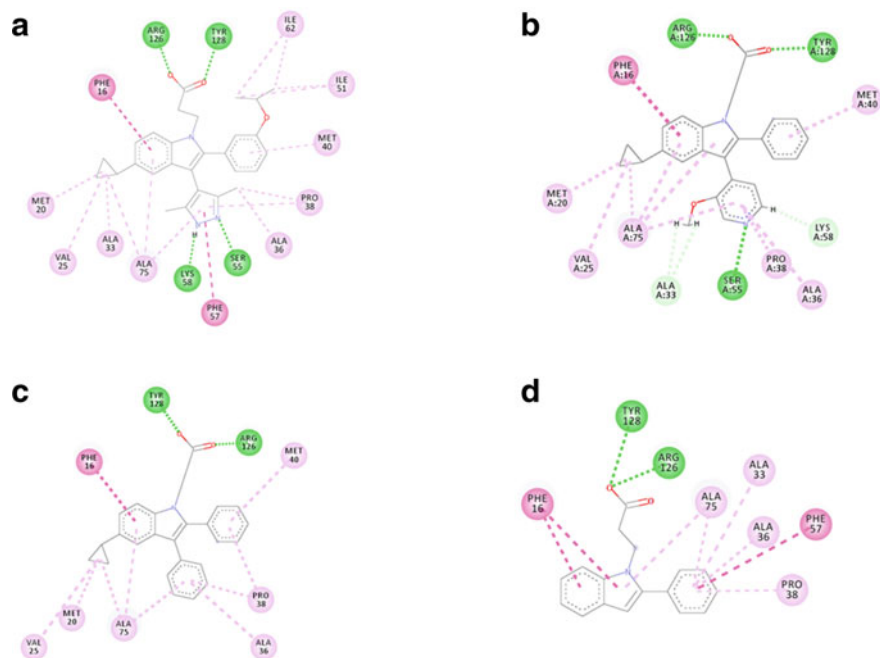


Fig. 4 2D diagrams of the binding sites around compounds 1(A), 2(B), 3(C), and 4(D), drawn using Discovery Studio 4.5. Green, conventional hydrogen bonds and pink, other interactions, including π -alkyl, π - π T-shaped, alkyl, and CH...O hydrogen bonds. (Reprinted with permission from [31]. Copyright 2018 American Chemical Society)

Table 1 K_i and IFIE sum of FABP4 in complex with the four inhibitors

Compound	K_i (μM)	IFIE sum (kcal/mol)	ES (kcal/mol)	EX (kcal/mol)	CT + mix (kcal/mol)	DI (kcal/mol)
1	0.03	-97.06	-88.43	103.78	-43.13	-69.28
2	0.10	-59.84	-53.88	90.60	-29.28	-67.28
3	0.12	-51.29	-26.56	49.28	-18.64	-55.36
4	>1.4	-31.80	-10.51	26.23	-13.28	-34.23

ES is electrostatic energy, EX is exchange-repulsion energy, CT + mix is charge transfer and mixing energy, DI is dispersion energy. IFIE for each residue is sum of ES, EX, CT + mix, and DI. IFIEs of each individual residue are summed to yield IFIE sum. (Reprinted with permission from [31]. Copyright 2018 American Chemical Society)

calculated as 1.4, much higher than the others), while it was 0.999 when including only compounds 1-3, indicating almost perfect correlation. This validated the FMO method for assessing the activities of the inhibitors in this study.

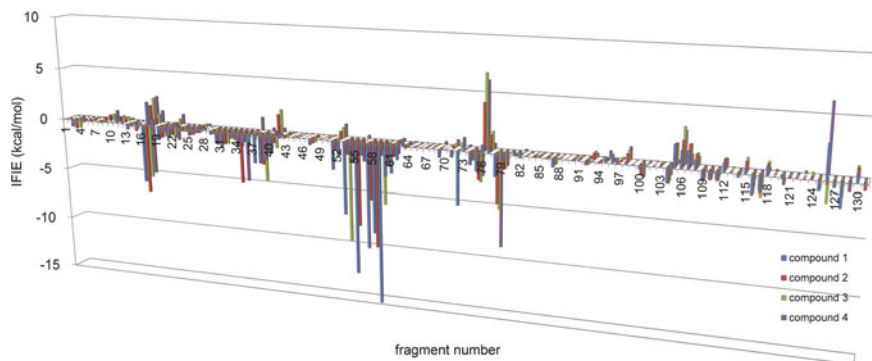


Fig. 5 IFIEs between each compound and amino acid residues of FABP4. Horizontal axis shows fragment numbers, which correspond approximately to the amino acid residues, and vertical axis represents the IFIE for each fragment. (Reprinted with permission from [31]. Copyright 2018 American Chemical Society)

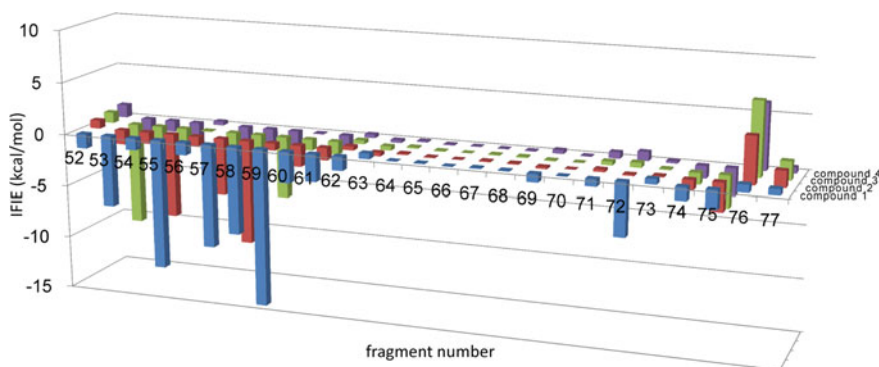


Fig. 6 IFIEs magnified from Lys52 to Asp77. (Reprinted with permission from [31]. Copyright 2018 American Chemical Society)

The IFIEs between each compound and the amino acid residues of FABP4 are shown in Fig. 5. The main interactions of the residues from Lys52 to Asp77 are shown magnified in Fig. 6.

3.3.1 Interaction Analysis of Compound 1

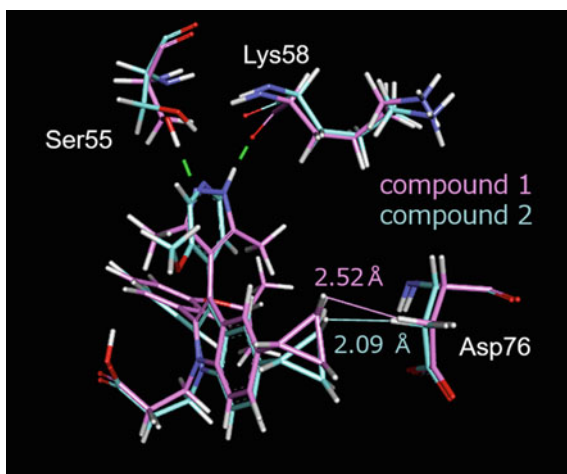
Compound 1 exhibited strong interactions with Ser55, Phe57, and Lys58 (fragment 59), giving this compound the smallest K_i value among the four inhibitors. Notably, compound 1 formed hydrogen bonds with the Ser55 side-chain oxygen atom and Lys58 main chain (Fig. 4a), and the related IFIEs were the lowest observed at -12.33 and -14.96 kcal/mol, respectively (Table 2). A hydrogen bond with Lys58 has been

Table 2 The interaction energies (IFIEs) between each residue (52–77) and the four compounds

Fragment number	Amino acid residue	IFIE [kcal/mol]			
		Compound 1	Compound 2	Compound 3	Compound 4
52	LYS52	-1.39	0.78	1.02	1.24
53	SER53	-6.81	-1.36	-9.64	-2.28
54	GLU54	-1.13	-1.09	-1.17	-1.03
55	SER55	-12.33	-7.93	-1.32	-2.16
56	THR56	-1.18	-0.89	-0.09	0.35
57	PHE57	-9.79	-5.39	-2.52	-3.61
58	LYS58	-8.30	-9.83	-3.89	-1.49
59	ASN59	-14.96	-0.66	-5.85	-2.32
60	THR60	-2.94	-2.00	-1.03	-0.07
61	GLU61	-2.59	-1.17	-1.23	-1.17
62	ILE62	-1.32	0.36	0.36	0.33
63	SER63	0.53	-0.34	-0.39	-0.26
64	PHE64	0.04	0.12	0.13	0.11
65	ILE65	0.06	-0.07	-0.07	-0.08
66	LEU66	-0.03	-0.01	0.01	0.03
67	GLY67	0.09	0.09	0.08	0.03
68	GLN68	0.07	0.10	0.11	0.06
69	GLU69	-0.77	-0.18	-0.09	0.34
70	PHE70	0.03	0.00	-0.01	-0.05
71	ASP71	-0.66	0.24	0.35	0.58
72	GLU72	-4.94	-0.11	0.46	0.83
73	VAL73	0.49	0.11	0.10	0.19
74	THR74	-1.20	-0.88	-1.06	-1.15
75	ALA75	-1.74	-2.62	-2.97	-2.55
76	ASP76	0.69	4.32	6.85	6.11
77	ASP77	0.57	1.50	1.71	0.52

described in the docking model of Pimozide [36]. It is notable that this interaction was detected here in the X-ray crystal structure, indicating its importance in the present molecular binding as well as the utility of the FMO method. Phe57 also formed π - π T-shaped interactions (Fig. 3a), but the strengths of these interactions could not be clarified by visual observation alone. The IFIE of Phe57 revealed that these interactions were strong, with a strength of -9.79 kcal/mol (Table 2). Meanwhile, the IFIE of fragment 76 (Asp76) presented the largest repulsive force of all the residues. Among the four compounds, the repulsive interaction with Asp76 was weakest for compound 1. In compound 1, the moiety located nearest to Asp76 was the cyclopropane ring, according to the X-ray crystal structure. In fact, cyclopropane

Fig. 7 The distance from Asp76 to compound 1 and compound 2



was a common moiety among each of compounds 1, 2, and 3. However, comparing those compounds, the distance between cyclopropane and Asp76 was ~ 0.4 Å longer in compound 1 than in compounds 2 and 3 (Fig. 7). This greater distance—which was probably a result of compound 1 being anchored by hydrogen bonds with Ser55 and Lys58—is assumed to be the main reason why the repulsive interaction with Asp76 was weakest for compound 1. Although ~ 0.4 Å is only a slight difference, its importance can be discussed with confidence because these crystal structures were highly reliable. The very high resolution of the coordinates, combined with the very low temperature factor (B-factor) of Asp76 (17.84–28.78), ensured that the fluctuation in positions was small.

3.3.2 Interaction Analysis of Compound 2

The situation for compound 2 was slightly more complicated because this compound formed a hydrogen bond with Ser55 in the crystal structure (Fig. 4b), for which the IFIE was -7.93 kcal/mol (Table 2). However, the strongest interaction of compound 2 was with FABP4 fragment 58, having an IFIE of -9.83 kcal/mol. While the Lys58 oxygen atom formed a CH...O hydrogen bond [37] with compound 2 in the crystal structure (Fig. 4b) as the distance of CH...O is 2.45 Å and the angle is 126.1° , the amine group of Lys58s main chain also interacted strongly, with an ES energy of -7.30 kcal/mol [31]. According to the FMO calculations (Fig. 6), Phe57 also interacted strongly, with an IFIE of -5.39 kcal/mol, but this interaction was not evident from visual inspection of the X-ray structure (Fig. 4b). The main IFIE component of the interaction between compound 2 and Phe57 was dispersion energy (-3.62 kcal/mol) [31]. Dispersion interactions cannot be identified from the distances and angles of X-ray crystal structures; however, by calculating interaction energies based on electronic states, FMO analysis was able to recognize this term.

In this way, the SARs of compounds 1 and 2 could be explained on the basis of their interactions with amino acid residues and the energies calculated from FMO analyses. These results showed that an FABP4 inhibitor required a strong interaction with Lys58 and, thus, compound 1, which possessed strong interactions with Lys58, also possessed high inhibition activity.

3.3.3 Interaction Analysis of Compound 3

For compound 3, FMO analysis again identified interactions that cannot otherwise be recognized. FABP4 fragment 53 (Ser53) exhibited the largest IFIE (-9.64 kcal/mol; Fig. 5, green bar) with compound 3, even though no interactions with Ser53 were recognized from X-ray crystal structural analysis (Fig. 4c). The main IFIE component of the interaction between compound 3 and Ser53 was dispersion energy (-6.04 kcal/mol) [31], which, as explained above, cannot be recognized from the distances and angles of X-ray crystal structures.

4 Conclusion

The crystallographic structures of FABP4 in complexes with four inhibitors were solved, and the interactions were described by FMO analyses. These analyses were very helpful in determining why compound 1 possessed the most potent inhibitory activity. Furthermore, the importance of the interaction with Lys58 was revealed, contributing an insight into the design of strong inhibitors, which will be useful for future inhibitor identification. In this way, a cooperative study combining X-ray crystal structure analysis and FMO calculations enabled a deep understanding of the protein–ligand interaction for the benefit of inhibitor development.

Acknowledgments The authors would like to thank EA Pharma Co., Ltd., Ajinomoto Co., Inc., and Photon Factory. They also thank Leo Holroyd, Ph.D., from Edanz Group (www.edanzediting.com/ac) for editing a draft of this manuscript.

References

1. RCSB PDB Annual Report 2016
2. Mazanetz MP, Ichihara O, Law RJ, Whittaker M (2011) Prediction of cyclin-dependent kinase 2 inhibitor potency using the fragment molecular orbital method. *J Cheminform* 3(1):1–15
3. Kitaura K, Ikeo E, Asada T, Nakano T, Uebayasi M (1999) Fragment molecular orbital method: an approximate computational method for large molecules. *Chem Phys Lett* 313:701–706
4. Fedorov DG, Kitaura K (2007) Extending the power of quantum chemistry to large systems with the fragment molecular orbital method. *J Phys Chem a* 111(30):6904–6914

5. Fedorov DG, Nagata T, Kitaura K (2012) Exploring chemistry with the fragment molecular orbital method. *Phys Chem Chem Phys* 14(21):7562–7577
6. Gordon MS, Fedorov DG, Pruitt SR, Slipchenko LV (2012) Fragmentation methods: a route to accurate calculations on large systems. *Chem Rev* 112(1):632–672
7. Furuhashi M, Hotamisligil GS (2008) Fatty acid-binding proteins: role in metabolic diseases and potential as drug targets. *Nat Rev Drug Discov* 7(6):489–503
8. Hotamisligil GS, Johnson RS, Distel RJ, Ellis R, Papaioannou VE, Spiegelman BM (1996) Uncoupling of obesity from insulin resistance through a targeted mutation in aP2, the adipocyte fatty acid binding protein. *Science* 274(5291):1377–1379
9. Uysal KT, Scheja L, Wiesbrock SM, Bonner-Weir S, Hotamisligil GS (2000) Improved glucose and lipid metabolism in genetically obese mice lacking aP2. *Endocrinology* 141(9):3388–3396
10. Makowski L, Boord JB, Maeda K, Babaev VR, Uysal KT, Morgan MA, Parker RA, Suttles J, Fazio S, Hotamisligil GS, Linton MF (2001) Lack of macrophage fatty-acid-binding protein aP2 protects mice deficient in apolipoprotein E against atherosclerosis. *Nat Med* 7(6):699–705
11. Furuhashi M, Tuncman G, Gorgun CZ, Makowski L, Atsumi G, Vaillancourt E, Kono K, Babaev VR, Fazio S, Linton MF, Sulsky R, Robl JA, Parker RA, Hotamisligil GS (2007) Treatment of diabetes and atherosclerosis by inhibiting fatty-acid-binding protein aP2. *Nature* 447(7147):959–965
12. Lehmann F, Haile S, Axen E, Medina C, Uppenberg J, Svensson S, Lundback T, Rondahl L, Barf T (2004) Discovery of inhibitors of human adipocyte fatty acid-binding protein, a potential type 2 diabetes target. *Bioorg Med Chem Lett* 14(17):4445–4448
13. Ringom R, Axen E, Uppenberg J, Lundback T, Rondahl L, Barf T (2004) Substituted benzylamino-6-(trifluoromethyl)pyrimidin-4(1H)-ones: a novel class of selective human A-FABP inhibitors. *Bioorg Med Chem Lett* 14(17):4449–4452
14. Sulsky R, Magnin DR, Huang Y, Simpkins L, Taunk P, Patel M, Zhu Y, Stouch TR, Bassolino-Klimas D, Parker R, Harrity T, Stoffel R, Taylor DS, Lavoie TB, Kish K, Jacobson BL, Sheriff S, Adam LP, Ewing WR, Robl JA (2007) Potent and selective biphenyl azole inhibitors of adipocyte fatty acid binding protein (aFABP). *Bioorg Med Chem Lett* 17(12):3511–3515
15. Barf T, Lehmann F, Hammer K, Haile S, Axen E, Medina C, Uppenberg J, Svensson S, Rondahl L, Lundback T (2009) N-Benzyl-indolo carboxylic acids: Design and synthesis of potent and selective adipocyte fatty-acid binding protein (A-FABP) inhibitors. *Bioorg Med Chem Lett* 19(6):1745–1748
16. Hertzfel AV, Hellberg K, Reynolds JM, Kruse AC, Juhlmann BE, Smith AJ, Sanders MA, Ohlendorf DH, Suttles J, Bernlohr DA (2009) Identification and characterization of a small molecule inhibitor of Fatty Acid binding proteins. *J Med Chem* 52(19):6024–6031
17. Marr E, Tardie M, Carty M, Brown Phillips T, Wang IK, Soeller W, Qiu X, Karam G (2006) Expression, purification, crystallization and structure of human adipocyte lipid-binding protein (aP2). *Acta Crystallogr Sect F Struct Biol Cryst Commun* 62(Pt 11):1058–1060
18. Ory J, Kane CD, Simpson MA, Banaszak LJ, Bernlohr DA (1997) Biochemical and crystallographic analyses of a portal mutant of the adipocyte lipid-binding protein. *J Biol Chem* 272:9793–9801
19. Ory JJ, Banaszak LJ (1999) Studies of the ligand binding reaction of adipocyte lipid binding protein using the fluorescent probe 1, 8-anilinoanthracene-8-sulfonate. *Biophys J* 77(2):1107–1116
20. Ory JJ, Mazhary A, Kuang H, Davies RR, Distefano MD, Banaszak LJ (1998) Structural characterization of two synthetic catalysts based on adipocyte lipid-binding protein. *Protein Eng* 11(4):253–261
21. Lalonde JM, Bernlohr DA, Banaszak LJ (1994) X-ray crystallographic structures of adipocyte lipid-binding protein complexed with palmitate and hexadecanesulfonic acid. Properties of Cavity Binding Sites. *Biochemistry* 33(16):4885–4895
22. Lalonde JM, Levenson MA, Roe JJ, Bernlohr DA, Banaszak LJ (1994) Adipocyte lipid-binding protein complexed with arachidonic acid. Titration calorimetry and X-ray crystallographic studies. *J Biol Chem* 269(41):25339–25347

23. Xu Z, Bernlohr DA, Banaszak LJ (1993) The adipocyte lipid-binding protein at 1.6-Å resolution. Crystal structures of the apoprotein and with bound saturated and unsaturated fatty acids. *J Biol Chem* 268(11):7874–7884
24. Xu Z, Bernlohr DA, Banaszak LJ (1992) Crystal structure of recombinant murine adipocyte lipid-binding protein. *Biochemistry* 31(13):3484–3492
25. Xu ZH, Buelt MK, Banaszak LJ, Bernlohr DA (1991) Expression, purification, and crystallization of the adipocyte lipid binding protein. *J Biol Chem* 266(22):14367–14370
26. Van Dongen MJ, Uppenberg J, Svensson S, Lundback T, Akerud T, Wikstrom M, Schultz J (2002) Structure-based screening as applied to human FABP4: a highly efficient alternative to HTS for hit generation. *J Am Chem Soc* 124(40):11874–11880
27. Nakano T, Kaminuma T, Sato T, Fukuzawa K, Akiyama Y, Uebayasi M, Kitaura K (2002) Fragment molecular orbital method: use of approximate electrostatic potential. *Chem Phys Lett* 351(5–6):475–480
28. Hitaoka S, Harada M, Yoshida T, Chuman H (2010) Correlation analyses on binding affinity of sialic acid analogues with influenza virus neuraminidase-1 using ab initio MO calculations on their complex structures. *J Chem Inf Model* 50(10):1796–1805
29. Watanabe C, Fukuzawa K, Okiyama Y, Tsukamoto T, Kato A, Tanaka S, Mochizuki Y, Nakano T (2013) Three- and four-body corrected fragment molecular orbital calculations with a novel subdividing fragmentation method applicable to structure-based drug design. *J Mol Graph Model* 41:31–42
30. Wataru M, Masayuki S, Chieko E, Munetaka T, Tomomi Y, Sen T (2014) Indole derivative or salt thereof. Patent number WO2014003158
31. Tagami U, Takahashi K, Igarashi S, Ejima C, Yoshida T, Takeshita S, Miyanaga W, Sugiki M, Tokumasu M, Hatanaka T, Kashiwagi T, Ishikawa K, Miyano H, Mizukoshi T (2016) Interaction analysis of FABP4 inhibitors by X-ray crystallography and fragment molecular orbital analysis. *ACS Med Chem Lett* 7(4):435–439
32. Feyereisen M, Fitzgerald G, Komornicki A (1993) Use of approximate integrals in ab initio theory. An application in MP2 energy calculations. *Chem Phys Lett* 208 5–6:359–363
33. Mochizuki Y, Nakano T, Koikegami S, Tanimori S, Abe Y, Nagashima U, Kitaura K (2004) A parallelized integral-direct second-order Moller-Plesset perturbation theory method with a fragment molecular orbital scheme. *Theoret Chem Acc* 112(5–6):442–452
34. Mochizuki Y, Koikegami S, Nakano T, Amari S, Kitaura K (2004) Large scale MP2 calculations with fragment molecular orbital scheme. *Chem Phys Lett* 396(4–6):473–479
35. Fedorov DG, Kitaura K (2004) Second order Moller-Plesset perturbation theory based upon the fragment molecular orbital method. *J Chem Phys* 121(6):2483–2490
36. Wang Y, Lin HQ, Law WK, Liang WC, Zhang JF, Hu JS, Ip TM, Waye MM, Wan DC (2015) Pimozide, a novel fatty acid binding protein 4 inhibitor, promotes adipogenesis of 3T3-L1 cells by activating PPARγ. *ACS Chem Neurosci* 6(2):211–218
37. Pierce AC, Sandretto KL, Bemis GW (2002) Kinase inhibitors and the case for CH...O hydrogen bonds in protein-ligand binding. *Proteins* 49(4):567–576

Application of FMO for Protein–ligand Binding Affinity Prediction



Kenichiro Takaba

Abstract The fragment molecular orbital (FMO) method has emerged as a powerful computational tool for structure-based drug design. Pair interaction energy decomposition analysis (PIEDA) enables detailed analysis of protein–ligand interactions, and many studies have shown that interaction energies can be used to predict protein–ligand binding affinities. However, the accuracy is insufficient for application to lead optimization. To increase the method’s accuracy, we introduce an ensemble FMO method in which molecular dynamics simulations are used to generate multiple protein–ligand complex structures, and FMO calculations are performed for ensembles of conformers with explicit water molecules. To assess the ensemble FMO method, we examined the correlations between experimental and calculated binding affinities of two systems, internal project A and Pim1 kinase. The correlations between experimental pIC_{50} values and FMO-based interaction energies *in vacuo* calculated based on MM-optimized X-ray crystal structures were $R^2 = 0.28$ and $R^2 = 0.53$ for internal project A and Pim1, respectively. Using the ensemble FMO method, the correlation for internal project A improved ($R^2 = 0.67$), whereas the correlation for Pim1 was unchanged ($R^2 = 0.53$). If combinations of different PIEDA energies were allowed, the best correlations for internal project A and Pim1 were $R^2 = 0.76$ and $R^2 = 0.62$, respectively. We also discuss the application of a reinforcement learning method, Best Arm Identification, in which the performance of the ensemble FMO method was maximized by avoiding unpromising compounds in the early stages to allocate limited computational resources to more-promising compounds.

Keywords Protein–ligand binding affinity prediction · Fragment molecular orbital method · Molecular dynamics simulation · Machine learning

K. Takaba (✉)

Pharmaceuticals Research Center, Asahi Kasei Pharma Corporation, Shizuoka, Japan
e-mail: takaba.kb@om.asahi-kasei.co.jp

© Springer Nature Singapore Pte Ltd. 2021

Y. Mochizuki et al. (eds.), *Recent Advances of the Fragment Molecular Orbital Method*,
https://doi.org/10.1007/978-981-15-9235-5_13

281

1 Introduction

Over the past few years, the fragment molecular orbital (FMO) method [1–4] has emerged as a powerful tool for assisting structure-based drug design (SBDD) [5–7]. One of the keys to success in SBDD is having a good understanding of protein–ligand interactions, not just for rational drug design but also for constructive communications with medicinal chemists. FMO is an attractive computational approach for tackling this problem, in which inter-fragment interaction energy (IFIE) analysis [3] allows analysis of protein–ligand interactions with quantum effects at reasonable computational cost. Thus, in pair interaction energy decomposition analysis (PIEDA) [4], the interaction energy, ΔE , can be deconstructed into four energy terms: electrostatic (ΔE_{ES}), exchange repulsion (ΔE_{EX}), dispersion (ΔE_{DI}), and charge transfer with higher order mixed terms (ΔE_{CT+mix}), which offers more detailed information regarding the protein–ligand interactions.

Another advantage of the FMO method is that it can be used to predict protein–ligand binding affinity [8–10]. FMO-based interaction energies obtained by PIEDA describe the stability of protein–ligand complexes and thus provide reliable estimates of protein–ligand enthalpic binding contributions. Protein–ligand binding phenomena are very complex events in which binding is associated with various energy terms, such as enthalpy, entropy, and solvation/desolvation effects [7]. Even though not all of these factors are accounted for in FMO approaches, many studies have shown that moderate correlations between experimental binding affinities and FMO-based interaction energies can be achieved. For example, Heifetz and coworkers observed moderate to high correlations ($R^2 = 0.58 \sim 0.76$) between experimentally measured affinities and FMO-based interaction energies *in vacuo* for various G-protein coupled receptors by performing FMO calculations against computationally modeled structures [9]. Their study suggests that FMO is suitable for protein–ligand binding affinity predictions even though it does not incorporate solvation effects and thus could be applied to modeled structures. Watanabe and coworkers utilized FMO with molecular mechanics Poisson–Boltzmann surface area (FMO + MM-PBSA) to incorporate desolvation effects and study the activity cliffs of serine/threonine kinase Pim1 inhibitors [10]. Comparing various qualities of complex structures, they found that QM/MM-optimized structures provided the best correlation ($R^2 = 0.85$) between experimental pIC_{50} values and FMO + MM-PBSA binding energies. When desolvation effects were excluded from the abovementioned study, the correlation decreased to $R^2 = 0.67$, indicating the importance of considering desolvation effects for accurately predicting protein–ligand binding affinity.

Another example is shown in Fig. 1, which shows the results of analyses of correlations between experimental pIC_{50} values and FMO-based interaction energies *in vacuo* for 207 MM-optimized X-ray crystal structures from our internal project A. Even though solvation effects were not included in the calculation and different chemotypes were included in the analysis, moderate to high correlations ($R^2 = 0.54 \sim 0.72$) were observed with different PIEDA interaction energy terms. The best correlation ($R^2 = 0.72$) was observed with charge transfer with the higher order

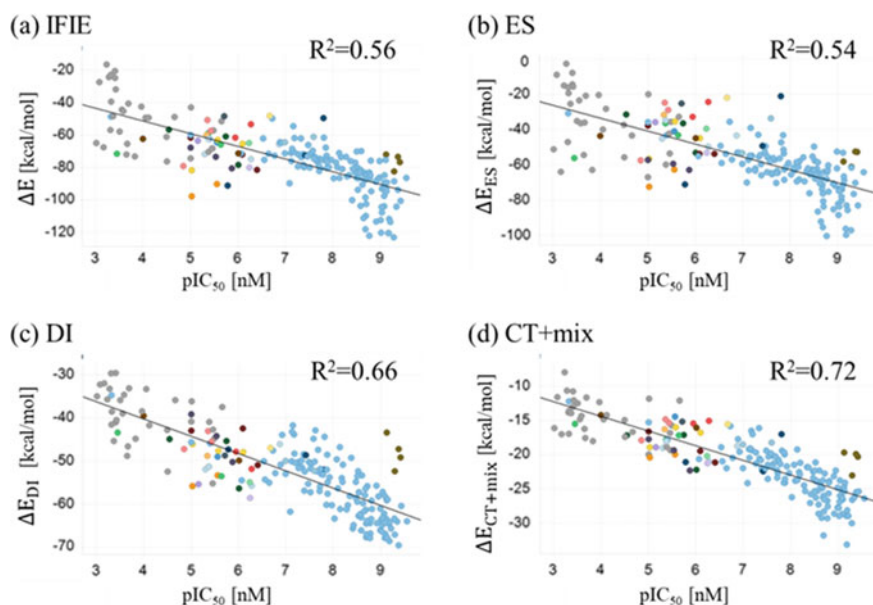


Fig. 1 Plots of the correlation between experimental pIC₅₀ values and FMO-based interaction energies *in vacuo* for 207 MM-optimized X-ray crystal structures obtained from internal project A. (a–d) Correlations with IFIE (ΔE), electrostatic energy (ΔE_{ES}), dispersion energy (ΔE_{DI}), and charge transfer plus higher order mixed terms (ΔE_{CT+mix}), respectively. Each colored circle represents a different chemotype. MM-optimized structures were prepared using Protein Preparation Wizard [19] implemented in Schrödinger software, version 2016–4

mixed term ΔE_{CT+mix} . It will be interesting to compare these results with those obtained using molecular mechanics-based methods, such as molecular dynamics (MD)-based approaches, as typical force fields do not explicitly account for charge transfer effects [11–13].

Generally, the FMO-based interaction energy can be obtained from a single protein–ligand complex structure, such as an X-ray crystal structure or computationally modeled structure [8–10]. However, previous studies suggest that averaging of FMO-based interaction energies over ensemble of conformers is expected to be more reliable than considering only a single conformer [14, 15]. Ishikawa et al. performed FMO calculations against 40 different structures of prion protein generated by MD simulations and examined the influence of geometrical fluctuations on FMO calculation [14]. Fedorov et al. performed MD simulations with FMO calculations for two ligands bound to Trp-cage miniprotein and introduced the idea of systematic averaging of FMO-based interaction energies to evaluate protein–ligand binding energies [15].

In this study, we examine whether averaged FMO-based interaction energies and accounting solvation effects with explicit water molecules can improve the quantitative structure–activity relationships (QSARs). We refer to this approach as an

ensemble FMO method, in which FMO calculations are performed against ensemble of conformers as introduced in previous studies [14, 15]. MD simulations were utilized to generate multiple protein–ligand complex structures but other approaches such as Monte-Carlo based methods can be applied as well. Furthermore, we apply a reinforcement learning method, Best Arm Identification (BAI) [16–18], in which unpromising compounds are avoided in the early stages so that the limited amount of computational resources can be allocated to more-promising compounds. This approach is expected to maximize the performance of ensemble FMO analyses in which promising compounds are chosen from a set of candidates within the limited amount of computational resources.

2 Ensemble FMO

2.1 Computational Method

The workflow of ensemble FMO is as follows. First, the system is prepared by correcting missing loops and residues, and hydrogen atoms are added to each protein–ligand complex structure. Next, an MD simulation with explicit water molecules is performed, and MD snapshots including water molecules are extracted from the trajectory for each system. The MD snapshots are then subjected to restrained MM-optimization to prepare the input structures for FMO calculations. Finally, for each MD snapshot, PIEDA of protein–ligand and water–ligand interaction energies is conducted. The ensemble FMO-based interaction energy of a ligand is obtained from the following equation:

$$\langle \Delta E \rangle = \frac{1}{N} \sum_{i=1}^N (\Delta E_{\text{ES}}^i + \Delta E_{\text{EX}}^i + \Delta E_{\text{DI}}^i + \Delta E_{\text{CT+mix}}^i),$$

where i and N denote the indices of the MD snapshots and the total number of MD snapshots, respectively. The decomposed energy terms of ensemble FMO-based interaction energies are represented as $\langle \Delta E_{\text{ES}} \rangle$, $\langle \Delta E_{\text{EX}} \rangle$, $\langle \Delta E_{\text{DI}} \rangle$, and $\langle \Delta E_{\text{CT+mix}} \rangle$. The FMO results obtained from a single conformer can be distinguished from ensemble FMO results in which FMO-based interaction energies are expressed without brackets.

In this study, MD simulations were performed using the AMBER14 package [20] with Amber ff14SB force field [12] for proteins, and TIP3P [21] models were used for water molecules. Ligand force fields were parameterized using general Amber force field (GAFF) [22] with AM1-BCC [23, 24] charges. System preparation and restrained MM-optimization to prepare the input structures for FMO calculations were carried out using the Protein Preparation Wizard [19] implemented in Schrödinger software, version 2016–4. FMO calculations were performed

using FMO code version 18 embedded in the General Atomic and Molecular Electronic Structure System (GAMESS) [25]. FMO calculations were performed with FMO2-MP2/6-31G.

2.2 Application of Ensemble FMO

2.2.1 Internal Project A

To assess ensemble FMO, nine ligands from internal project A depicted in Fig. 1 were selected. Each ligand belongs to a different chemotype with various substituents; the net charge of each of the nine ligands was neutral. The correlations between experimental pIC_{50} values and different energy contributions of FMO-based interaction energies *in vacuo* were $R^2 = 0.28$, $R^2 = 0.18$, $R^2 = 0.32$, $R^2 = 0.44$, and $R^2 = 0.27$, for ΔE , ΔE_{ES} , ΔE_{DI} , $\Delta E_{\text{CT+mix}}$, and ΔE_{EX} , respectively (Fig. 2).

The procedures for ensemble FMO are briefly summarized below. After preparation for the MD simulation, system minimization followed by 50 ps NVT equilibration and an additional 200 ps NPT equilibration were performed. $C\alpha$ atom restraints were gradually reduced during the equilibration step. MD trajectories were extracted every 10 ps from the last 100 ps of the equilibration step. A total of 10 MD snapshots were used for FMO calculations for each ligand. Several studies have shown that a solvent shell of approximately 8 Å is necessary to incorporate solvent effects [26, 27]. Therefore, water molecules within 9 Å of the protein–ligand complexes were considered in FMO calculations.

The correlations between experimental pIC_{50} values and different energy contributions of FMO-based interaction energies were $R^2 = 0.67$, $R^2 = 0.61$, $R^2 = 0.50$, $R^2 = 0.76$, and $R^2 = 0.72$ for $\langle \Delta E \rangle$, $\langle \Delta E_{\text{ES}} \rangle$, $\langle \Delta E_{\text{DI}} \rangle$, $\langle \Delta E_{\text{CT+mix}} \rangle$, and $\langle \Delta E_{\text{EX}} \rangle$, respectively (Fig. 2). The best correlation ($R^2 = 0.76$) was obtained with $\langle \Delta E_{\text{CT+mix}} \rangle$, whereas the FMO-based interaction energy $\Delta E_{\text{CT+mix}}$ showed a poor correlation ($R^2 = 0.44$) *in vacuo*. Another interesting finding was that the water–ligand interaction energies differed among the nine ligands examined (Fig. 3). The correlation between experimental pIC_{50} values and the ensemble FMO-based interaction energy $\langle \Delta E \rangle$, decreased to $R^2 = 0.29$ without the contribution of water molecules.

2.2.2 Pim1 Kinase

Next, ensemble FMO was applied to serine/threonine kinase Pim1 inhibitors (Fig. 4). In contrast to the case of internal project A, activities differed significantly only with respect to the position of the indoline-ring nitrogen. As mentioned in the Introduction, Watanabe and coworkers found that QM/MM-optimized structures and desolvation effects incorporated using MM-PBSA were important for obtaining high correlations ($R^2 = 0.85$) between experimental pIC_{50} values and FMO + MM-PBSA binding energies [10]. When the desolvation effect was omitted from the calculation, the

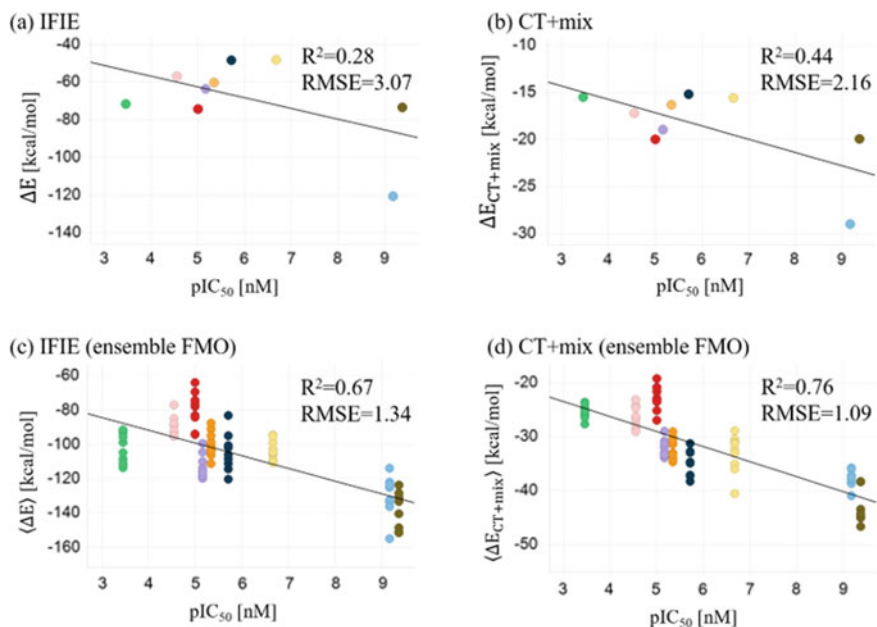


Fig. 2 Comparison of MM-optimized single conformation FMO and ensemble FMO. Plots of the correlation between experimental pIC_{50} values and FMO-based interaction energies are shown. Correlations with FMO-based interaction energies of IFIE (ΔE) and charge transfer plus higher order mixed terms (ΔE_{CT+mix}) *in vacuo* obtained from MM-optimized X-ray crystal structures are shown in (a) and (b), respectively. Correlations with ensemble FMO-based interaction energies for $\langle \Delta E \rangle$ and $\langle \Delta E_{CT+mix} \rangle$ are shown in (c) and (d), respectively. MD snapshots used for ensemble FMO are depicted explicitly, with each colored circle denoting a different ligand. Note that the ligands depicted in pink and red are colored differently from Fig. 1 to make the visualization more clear. Averaged ensemble FMO-based interaction energies were used to obtain the coefficient of determination, R^2 , and the correlation line depicted in black. The root-mean-standard-error (RMSE) of the calculated pIC_{50} is depicted in each graph

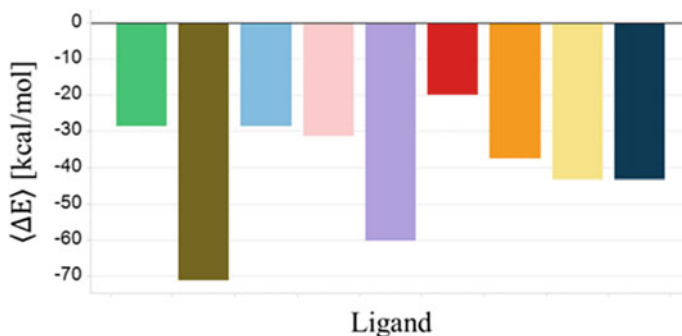


Fig. 3 Comparison of ligand-water interaction energies among different ligands obtained using ensemble FMO. Each color bar corresponds to the individual ligands shown in Figs. 1 and 2

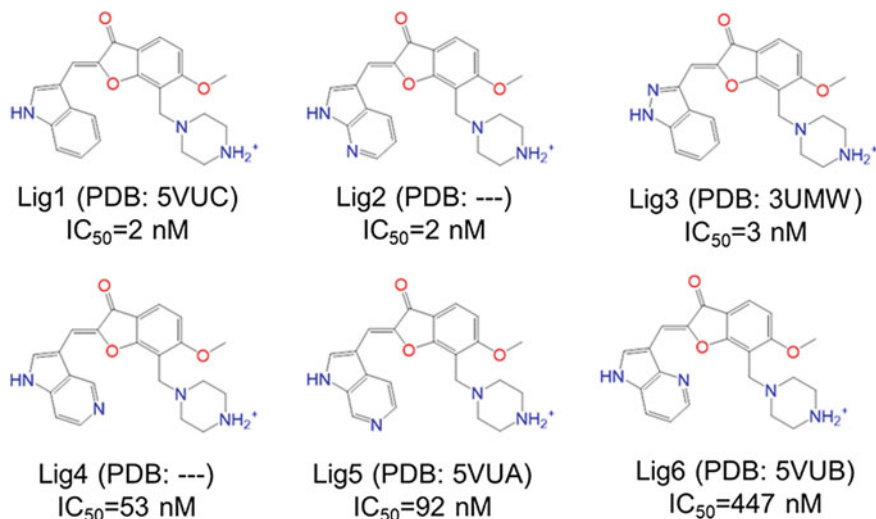


Fig. 4 Ligand structures and experimental IC₅₀ values as reported in the original literature [10]. PDB codes are shown in parentheses (if available)

correlation decreased to $R^2 = 0.67$. Furthermore, the correlation decreased to $R^2 = 0.53$ when the binding energies were calculated *in vacuo* using MM-optimized structures. Pim1 is an excellent example with which to challenge ensemble FMO, particularly whether considering multiple conformers generated using MM-methods improves the QSAR, even though QM/MM-optimized high-quality structures are important for obtaining sufficient correlation between experimental and calculated binding affinities.

Protein–ligand complex structures for each ligand were prepared similar to those reported in the original literature [10]. The Pim1-Lig1 X-ray crystal structure was used as a template for preparing all other protein–ligand complexes. The complex structures were then prepared for MD simulations following a procedure similar to that used for internal project A. After equilibration, 3 independent 50 ns MD simulations were performed to sample the protein–ligand complexes and confirm the stability of the ligand binding pose. Trajectories were extracted every 2.5 ns from the 50 ns production run, in which the first 12.5 ns were disregarded. A total of 45 MD snapshots were used for the FMO calculations for each ligand. To reduce the computational cost, only protein residues and water molecules that were 14 Å away from the ligand were considered during the FMO calculation. The protein residues used in the FMO calculations were consistent throughout the calculation, but the number of water molecules differed slightly between the MD snapshots.

The correlations between pIC₅₀ values and different energy contributions for the ensemble FMO-based interaction energies were $R^2 = 0.53$, $R^2 = 0.38$, $R^2 = 0.02$, $R^2 = 0.01$, and $R^2 = 0.35$ for $\langle \Delta E \rangle$, $\langle \Delta E_{ES} \rangle$, $\langle \Delta E_{DI} \rangle$, $\langle \Delta E_{CT+mix} \rangle$, and $\langle \Delta E_{EX} \rangle$, respectively (Fig. 5). The best correlation ($R^2 = 0.62$) was obtained by combining the

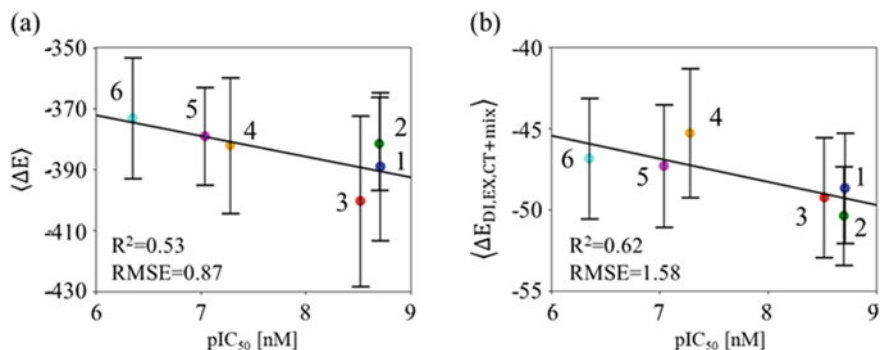


Fig. 5 Plots of the correlation between experimental pIC_{50} values and ensemble FMO-based interaction energies (in kcal/mol). (a, b) Correlations with ensemble FMO-based interaction energies of $\langle \Delta E \rangle$ and $\langle \Delta E_{DI,EX,CT+mix} \rangle$, respectively. Error bars indicate the standard deviations of interaction energies obtained from 45 individual FMO calculations for each ligand. The root-mean-square-error (RMSE) of the predicted pIC_{50} values is depicted in each graph. The index numbers correspond to the ligands shown in Fig. 4

energy terms of dispersion, exchange repulsion, and charge transfer with higher order mixed terms, $\langle \Delta E_{DI,EX,CT+mix} \rangle$. The correlations between experimental pIC_{50} values and ensemble FMO-based interaction energies for $\langle \Delta E \rangle$ and $\langle \Delta E_{DI,EX,CT+mix} \rangle$ with respect to varying numbers of MD snapshots are summarized in Table 1. The correlations ranged from $R^2 = 0.08$ – 0.80 for $\langle \Delta E \rangle$ and $R^2 = 0.18$ – 0.79 for $\langle \Delta E_{DI,EX,CT+mix} \rangle$, depending on the manner in which MD snapshots were extracted. The use of a single MD trajectory, Traj1, in which MD snapshots were extracted every 2.5 ps, exhibited the highest correlation ($R^2 = 0.79$) with $\langle \Delta E_{DI,EX,CT+mix} \rangle$. However, for other cases, the use of a single MD trajectory correlated poorly ($R^2 < 0.50$) with the experimental binding affinities. The best correlation ($R^2 = 0.80$) was obtained with $\langle \Delta E \rangle$ using MD trajectories for Traj2 and Traj3 in which MD snapshots were extracted every 5 ps.

Table 1 Coefficient of determination, R^2 , depending on the number of MD trajectories and MD snapshot intervals

	2.5 ns Interval		5.0 ns Interval	
	$\langle \Delta E \rangle$	$\langle \Delta E_{DI,EX,CT+mix} \rangle$	$\langle \Delta E \rangle$	$\langle \Delta E_{DI,EX,CT+mix} \rangle$
Traj1	0.43	0.79	0.22	0.46
Traj2	0.33	0.18	0.24	0.31
Traj3	0.08	0.40	0.18	0.52
Traj1,2	0.57	0.68	0.42	0.68
Traj1,3	0.31	0.76	0.29	0.77
Traj2,3	0.46	0.31	0.80	0.46
Traj1,2,3	0.53	0.62	0.63	0.70

2.3 Discussion

Ensemble FMO was applied to internal project A and Pim1 kinase to assess the utility of protein–ligand binding affinity predictions. The correlations between experimental pIC_{50} values and ensemble FMO-based interaction energies exhibited marked improvement with respect to the MM-optimized single conformation FMO results for internal project A, whereas the improvement was limited for Pim1. The best correlation was obtained when neglecting the contributions of the electrostatic energy terms from the FMO-based interaction energies for both internal project A and Pim1. This could have been due to the inverse relationship between the electrostatic interaction energies and the desolvation free energies. Ignoring the electrostatic energy terms may have implicitly accounted for the desolvation effect to some extent [28].

Ensemble FMO may be beneficial for cases in which poor correlations are obtained with FMO-based interaction energies *in vacuo* derived from single conformations, as observed with internal project A. Even though only 10 structures for each ligand were considered from a 100 ps MD trajectory, the use of multiple conformers led to improvement in the QSAR. However, this may strongly depend on the target system.

Improvements in the QSAR may be limited in cases in which moderate correlations have been obtained with FMO-based interaction energies, as in the case of Pim1. The correlation with the ensemble FMO-based interaction energy $\langle \Delta E \rangle$, was $R^2 = 0.53$, the same value reported by Watanabe and coworkers for the MM-optimized FMO-based interaction energy, ΔE , *in vacuo* [10]. One possible reason may be the difference in the level of theory used in the study. In our study, FMO2-MP2/6-31G was applied, whereas Watanabe and coworkers used FMO3-MP2/6-31G*, which is a higher level theory. Another reason could be that the number of complex structures and the process for generating the ensemble conformers used in ensemble FMO were inadequate. The method used to generate ensembles of protein–ligand complexes remains an issue.

Utilizing an adequate number of conformers may help improve the QSAR, but there will be a trade-off between computational cost and prediction accuracy. As FMO calculations are independent from one another in ensemble FMO, distributed computing using supercomputers and cloud services can help reduce the total computational cost. Furthermore, application of a reinforcement learning method, such as BAI [16–18] (discussed in the next section), may help maximize the performance of ensemble FMO in cases of restricted computational resources.

3 Bandit Ensemble FMO

3.1 General Concept of Bandit Ensemble FMO

Candidate drugs are typically discovered through DMTA (design-make-test-analysis) cycles in which compounds to be synthesized in the next cycle are prioritized from

idea compounds. Ideally, rapid and accurate predictions of protein–ligand binding affinities help in prioritizing idea compounds, but not all compounds require accurate affinity predictions. For example, assume we have M idea compounds, and N compounds are going to be synthesized in the next DMTA cycle. The goal is to select the top N promising compounds, and as long as these compounds are chosen, the prediction accuracies for the other compounds are not an issue.

Terayama and coworkers demonstrated that the reinforcement learning method called Best Arm Identification (BAI), also known as Multi-Armed Bandit, enables optimal control of the number of MD runs needed to identify the correct binding pose using MM-PBSA in cases of restricted computational resources [29]. Inspired by their work, we applied BAI algorithms to ensemble FMO to avoid unpromising compounds in the early stages and thus allocate the limited amount of computational resources available to more-promising compounds. This approach should identify the most-promising compounds at minimal computational cost. We designated this method “bandit ensemble FMO”.

The BAI concept is usually explained by referencing a gambling problem using slot machines. BAI centers upon optimizing the allocation of limited resources to identify the best of many slots. Each slot has an arm, and when an arm is selected, a player gets a reward according to a probability distribution. The reward for each arm has a different probability distribution that is not known a priori. The objective is to maximize the reward within the budget, in which the number of trials to pull the arm is limited.

In bandit ensemble FMO, the arm, reward, and budget correspond to candidate compounds, FMO-based interaction energy, and the total number of FMO trials, respectively. The workflow of bandit ensemble FMO is shown in Fig. 6. Suppose we have M candidate compounds. The first step is to generate multiple protein–ligand complex structures with explicit water molecules using MD simulations and then prepare FMO input files for each compound (Preparation). We then define the total amount of computational resources available, that is, the total number of FMO trials or total simulation time (e.g., three days) (Input). FMO calculations for each compound i are performed, and FMO-based interaction energies, ΔE_i , are evaluated (Initialize). Next, we calculate a score, S_i , for each compound i based on the ensemble FMO-based interaction energy, $\langle \Delta E_i \rangle$, where the scoring function depends on the BAI algorithm [16–18]. The compound with the highest score is selected for the next FMO calculation round (Selection). The selection process is repeated until reaching the predefined number of FMO trails. Finally, the top N compounds with the highest scores, S_i , are chosen as the most-promising compounds within the group of M candidate compounds.

3.2 Computational Method

Here, we apply ϵ -greedy [16], one of the most popular BAI algorithms, to ensemble FMO. In each round of the selection process, the algorithm selects the compound with

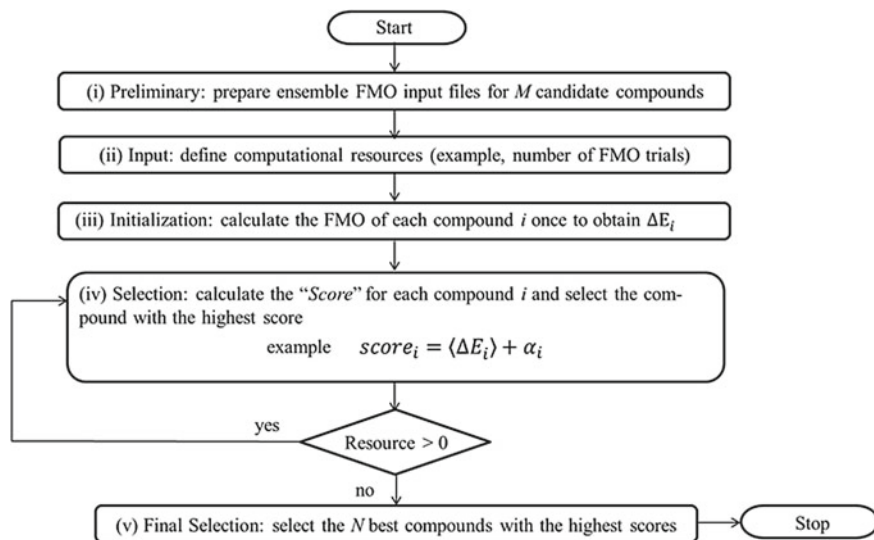


Fig. 6 Workflow of bandit ensemble FMO. α_i is an additional scoring term which differs among BAI algorithms

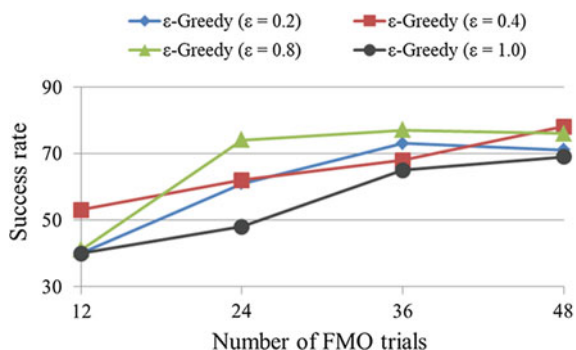
the highest absolute ensemble FMO-based interaction energy with probability $1 - \epsilon$ and selects a random compound with probability ϵ . When $\epsilon = 1$, this is equivalent to random selection. Although other BAI algorithms are thought to be more suitable for this particular problem, ϵ -greedy was chosen because it is very simple to implement and the objective of this study is to validate the concept of bandit ensemble FMO.

3.3 Application of Bandit Ensemble FMO

A retrospective study of bandit ensemble FMO employing ϵ -greedy was performed using the ensemble FMO results of Pim1 discussed in Sect. 2.2.2. As shown in Fig. 5b, Lig2 had the lowest ensemble FMO-based interaction energy $\langle \Delta E_{DI,EX,CT+mix} \rangle$ among the 6 ligands examined. This result was obtained by performing 270 FMO calculations in total. In this study, 100 independent bandit ensemble FMO calculations were performed, with the total number of FMO calculations restricted to 12, 24, 36, and 48 trials, respectively. We then monitored the success rate, defined as the number of times Lig2 was selected as the compound with the lowest ensemble FMO-based interaction energy among the 100 trials conducted.

The results of the bandit ensemble FMO are shown in Fig. 7. The success rate gradually increased as the number of FMO trials increased for all ϵ values. The best performance was obtained for $\epsilon = 0.8$, where the method outperformed random selection ($\epsilon = 0$). The success rate was 40 and 41% for $\epsilon = 0$ and $\epsilon = 0.8$, respectively, when the number of FMO trials was limited to 12. The success rate for

Fig. 7 Success rate, defined as the number of times Lig2 was selected as the lowest ensemble FMO-based interaction energy among the 6 ligands examined, with respect to different numbers of FMO trials (12, 24, 36, and 48 trials). A total of 100 independent bandit ensemble FMO calculations were performed for each trial set



$\epsilon = 0.8$ improved to 74%, whereas the success rate was 48% for $\epsilon = 0$ when the number of FMO trials was increased to 24. The success rate did not improve when the number of FMO trials was increased to 36 and 48 for $\epsilon = 0.8$. The performance of bandit ensemble FMO for $\epsilon = 0.2$ and $\epsilon = 0.4$ was somewhere between that obtained for $\epsilon = 0.8$ and $\epsilon = 1$. No significant differences in success rates were observed among all ϵ values after 36 FMO calculation trials.

3.4 Discussion

The rate of success in selecting Lig2 as the most-promising compound was 74% when ϵ was set at 0.8 and the number of FMO calculation trials was set at 24. Although the success rate was not perfect, it incurred only approximately 1/10 of the computational cost required for uniform sampling (total of 270 FMO calculations), where FMO calculations were performed 45 times for each ligand to retrieve Lig2 as the most-promising compound.

In this study, we applied ϵ -greedy, which is one of the simplest BAI algorithms. A disadvantage to the use of ϵ -greedy, however, is that an arm (compound) will always be selected with a certain probability, even for unpromising arms. We expect other algorithms, such as UGapE (unified gap-based exploration) [30], in which the number of times arm i is selected in each round, and a confidence score based on defined criteria is accounted for during the selection process, may be better suited to this purpose. However, the optimal algorithm may differ depending on the set of compounds being studied and the amount of computational resources available.

4 Conclusion and Perspective

In actual drug discovery projects, protein–ligand binding affinity predictions are often performed using computationally modeled structures, such as docking models. The

model may have some uncertainty, in which the orientation of ligand substituents can be wrong and protein residues may undergo reorientation among different ligands, which can be difficult to know a priori. Ensemble FMO, which utilizes MD simulations, has the advantage of allowing modification of the orientation of protein–ligand complex structures and thus represents an alternative approach for predicting protein–ligand binding affinities. Application of the BAI algorithm should therefore maximize the performance of ensemble FMO so that unpromising compounds can be avoided in the early stages and the limited amount of computational resources can be allocated to more-promising compounds. However, the method for generating ensemble conformations and the optimal BAI algorithm to use for ensemble FMO requires further research. Application of machine learning techniques such as Random Forest and Deep Neural Networks using PIEDA as descriptors represents an additional approach for predicting protein–ligand binding affinities.

In the future, we expect development of more hybrid approaches in which FMO methods, MD simulations, and machine learning approaches are applied in a complementary manner to derive new approaches for predicting protein–ligand binding affinities.

Acknowledgements The author thanks Kazufumi Ohkawa for thoughtful discussions and assistance in preparing the manuscript.

References

1. Kitaura K, Sawai T, Asada T et al (1999) Pair interaction molecular orbital method: an approximate computational method for molecular interactions. *Chem Phys Lett* 312:319–324
2. Kitaura K, Ikeo E, Asada T et al (1999) Fragment molecular orbital method: an approximate computational method for large molecules. *Chem Phys Lett* 313:701–706
3. Nakano T, Kaminuma T, Satao T et al (2002) Fragment molecular orbital method: use of approximate electrostatic potential. *Chem Phys Lett* 351:475–480
4. Fedorov DG, Kitaura K (2007) Pair interaction energy decomposition analysis. *J Comput Chem* 28:222–237
5. Wlodawer A, Vondrasek J (1998) Inhibitors of HIV-1 protease: a major success of structure-assisted drug design. *Annu Rev Biophys Biomol Struct* 27:249–284
6. Bagal SK, Andrews M, Bechle BM et al (2018) Discovery of potent, selective, and peripherally restricted Pan-Trk kinase inhibitors for the treatment of pain. *J Med Chem* 61:6779–6800
7. Bissantz C, Kuhn B, Stahl M (2010) A medicinal chemist's guide to molecular interactions. *J Med Chem* 53:5061–5084
8. Fukuzawa K, Kitaura K, Uebayasi M et al (2005) Ab initio quantum mechanical study of the binding energies of human Estrogen receptor α with its ligands: an application of fragment molecular orbital method. *J Comput Chem* 26:1–10
9. Heifetz A, Chudyk EI, Gleave L et al (2016) The Fragment molecular orbital method reveals new insight into the chemical nature of GPCR–ligand interactions. *J Chem Inf Model* 56:159–172
10. Watanabe C, Watanabe H, Fukuzawa K et al (2017) Theoretical analysis of activity cliffs among Benzofuranone-class Pim1 inhibitors using the fragment molecular orbital method with molecular mechanics poisson-Boltzman surface area (FMO+MM-PBSA) approach. *J Chem Inf Model* 57:2996–3010

11. Lopes PEM, Guvench O, MacKerell AD (2015) Current status of protein force fields for molecular dynamics. *Methods Mol Biol* 1215:47–71
12. Maier JA, Martinez C, Kasavajhala K et al (2015) ff14SB: improving the accuracy of protein side chain and backbone parameters from ff99SB. *J Chem Theory Comput* 11:3696–3713
13. Harder E, Damm W, Maple J et al (2016) OPLS3: a force field providing broad coverage of drug-like small molecules and proteins. *J Chem Theory Comput* 12:281–296
14. Ishikawa T, Kuwata K (2010) Interaction analysis of the native structure of prion protein with quantum chemical calculations. *J Chem Theory Comput* 6:538–547
15. Fedorov DG, Kitaura K (2018) Pair interaction energy decomposition analysis for density functional theory and density-functional tight-binding with an evaluation of energy fluctuations in molecular dynamics. *J Phys Chem A* 122:1781–1795
16. Auer P, Cesa-Bianchi N, Fischer P (2002) Finite-time analysis of multiarmed bandit problem. *Mach Learn* 47:235–256
17. Audibert J, Bubeck S, Munos R (2010) Best arm identification in multi-armed bandits. In: The 23rd annual conference on learning theory, dan Carmel hotel, Haifa, 27–29 June 2010
18. Gabillon V, Ghavamzadeh M, Lazaric A, Bubeck S (2011) Multi-bandit best arm identification. In: Twenty-fifth annual conference on neural information processing systems, Granada congress and exhibition centre, Granada, 12–17 December 2011
19. Sastry GM, Adzhigirey M, Day T et al (2013) Protein and ligand preparation: parameters, protocols, and influence on virtual screening enrichments. *J Comput Aid Mol Des* 27:221–234
20. Salomon-Ferrer R, Case DA, Walker RC (2013) An overview of the Amber biomolecular simulation package. *WIREs Comput Mol Sci* 3:198–210
21. Jorgensen WL, Chandrasekhar J, Madura JD et al (1983) Comparison of simple potential functions for simulating liquid water. *J Chem Phys* 79:926–935
22. Wang J, Wolf RM, Caldwell JW et al (2004) Development and testing of a general amber force field. *J Comput Chem* 25:1157–1174
23. Jakalian A, Jack DB, Bayly CI (2000) Fast, efficient generation of high-quality atomic charges. AM1-BCC model: I method. *J Comput Chem* 21:132–146
24. Jakalian A, Jack DB, Bayly CI (2002) Fast, efficient generation of high-quality atomic charges. AM1-BCC model: II parameterization and validation. *J Comput Chem* 23:1623–1641
25. Schmidt MW, Baldrige KK, Boatz JA et al (1993) General atomic and molecular electronic structure system. *J Comput Chem* 14:1347–1363
26. Komeiji Y, Ishida T, Fedorov DG et al (2007) Change in a protein's electronic structure induced by an explicit solvent: an ab initio fragment molecular orbital study of ubiquitin. *J Comput Chem* 28:1750–1762
27. Fukuzawa K, Kurisaki I, Watanabe C et al (2015) Explicit solvation modulates intra- and inter-molecular interactions within DNA: electronic aspects revealed by the ab initio fragment molecular orbital (FMO) method. *Comput Theor Chem* 1054:29–37
28. Huggins DJ, Sherman W, Tidor B (2012) Rational approaches to improving selectivity in drug design. *J Med Chem* 55:1424–1444
29. Terayama K, Iwata H, Araki M et al (2018) Machine learning accelerates MD-based binding pose prediction between ligands and proteins. *Bioinformatics* 34:770–778
30. Gabillon V, Ghavamzadeh M, Lazaric A (2012) Best arm identification: a unified approach to fixed budget and fixed confidence. In: Twenty-sixth annual conference on neural information processing systems, Harrahs and Harveys, Lake Tahoe, 3–8 December 2012

Recent Advances of In Silico Drug Discovery: Integrated Systems of Informatics and Simulation



Teruki Honma

Abstract With recent trends toward the use of big data for drug discovery-related databases, increased computing scale and speed, and sophisticated computation theory for molecular design, in silico drug discovery is becoming an increasingly practical technique. Prior to 2010, its contribution was limited to the early-stage drug discovery of feasible targets; however, applications of recent new technologies to more difficult and complicated targets have led to the effective drug design in the late stage of the drug discovery process. Herein, after reviewing recent in silico drug discovery that utilizes information science (informatics, including artificial intelligence (AI)) and computational science (biomolecular simulations based on molecular dynamics and quantum mechanics), we introduce actual cases of in silico drug discovery. Finally, we discuss efforts in applying AI to drug discovery, which has become practical recently, and consider potential future developments.

1 Introduction

In small molecule drug discovery, the processes involved in discovering lead compounds from hits and identifying development candidates from these lead compounds have a low success rate. To reduce the risk, major pharmaceutical companies are increasingly leaving this stage of the discovery process to academia and venture businesses. On the other hand, active attempts have been made to use information science (informatics) and computational science (simulations) to make these processes more efficient. This is referred to as in silico screening (virtual screening) or in silico drug discovery. In recent years, in silico screening has been used on nearly all targets in small molecule drug discovery, although in varying degrees.

The enrichment of drug discovery-related information and improvements in computational performance have increased the value of using in silico screening in drug discovery. These two factors have laid the foundation for the development of various design methods, including docking, molecular dynamics calculation,

T. Honma (✉)

RIKEN Center for Biosystems Dynamics Research, Yokohama, Japan

e-mail: honma.teruki@riken.jp

© Springer Nature Singapore Pte Ltd. 2021

Y. Mochizuki et al. (eds.), *Recent Advances of the Fragment Molecular Orbital Method*,
https://doi.org/10.1007/978-981-15-9235-5_14

295

quantum chemical calculation, and machine learning (AI). For example, in terms of the enrichment of drug discovery-related information, as of 2018, databases with >140,000 entries of three-dimensional protein structure information (PDB), >95 million items of known compound information (PubChem), and >340 million items of compound information with preprocessing for in silico screening at RIKEN, and a public database with >2.1 million items of compound information with bioactivity values (the ChEMBL database) are available for use (Fig. 1).

With regard to computer performance, the performance of multi-purpose supercomputers, such as the K computer and TSUBAME in Japan, is increasing at a constant rate. Furthermore, computational devices dedicated to molecular dynamics computation, such as Anton [1] and MDGRAPE [2], outperform the K computer despite having a much smaller chassis with less power. The increased use of in silico screening is also evident in academia. According to a survey by Proschak et al. [3], papers dealing with high throughput screening (HTS) as a means to discover hit chemical compounds began to increase in 1990 and plateaued around the year 2000. After 2000, the number of papers dealing with in silico screening began to increase. Currently, the number of papers dealing with in silico screening roughly equal those dealing with HTS; the number continues to increase. As of 2016, Nature and related journals have reported drug discovery cases using virtual screening (same significance as in silico screening) practically every month.

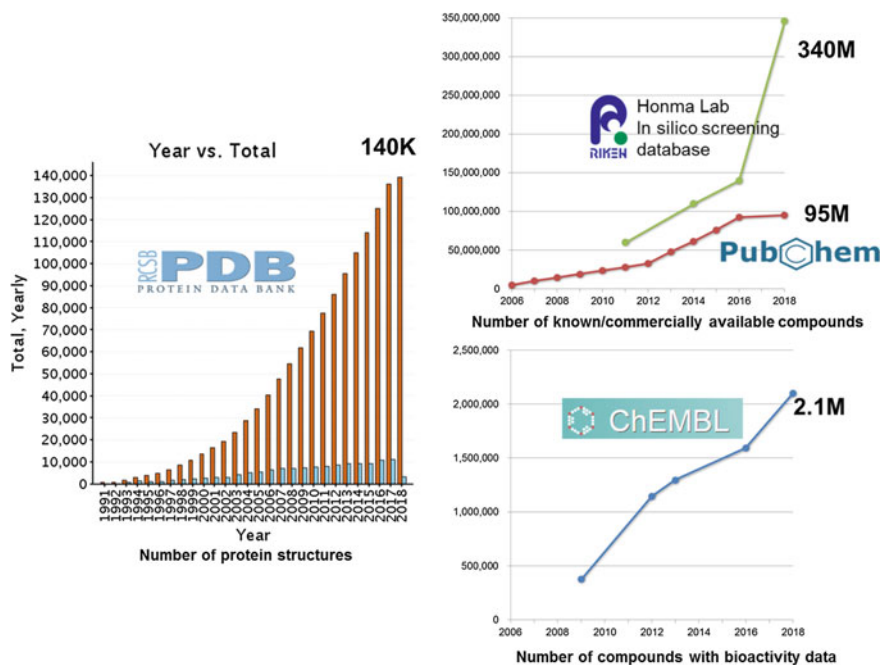


Fig. 1 Big data for drug discovery information

2 Merging of Informatics and Simulation in In Silico Drug Discovery Technology

In silico drug discovery requires modeling of phenomena that can occur in relation to the drug within the body or cells in the real world using a particular theory. Based on the type of theory used, the modeling methods can be roughly classified as informatics- and simulation-based methods. As the informatics-based methods primarily use structure–activity relationship information on the small compound (ligand) side, they constitute ligand-based drug discovery (LBDD). In LBDD, modeling is performed using machine learning based on statistical theory or structural similarity indices. Machine learning is an element technology of AI; recently, deep learning has been used frequently as a new-generation machine learning method. The simulation-based methods use information on protein structures to simulate protein–ligand interactions using various theories, such as classical molecular force fields, quantum mechanics, and molecular dynamics. Thus, these constitute structure-based drug discovery (SBDD).

A mutually complimentary relationship exists between informatics and simulations. Informatics-based designs demonstrate short calculation times, and the hit rate accuracy is relatively stable without depending on specific researcher experience. However, informatics-based designs also have the disadvantage that only compounds sharing the same binding sites and binding modes as the known inhibitors used in the search are identified as hit compounds. With some modifications such as using 3D shape features, somewhat different skeletal structures can be searched. In contrast, with simulations, binding free energies can be precisely predicted according to the laws of physics. Drug discovery can also be extended to include all possible protein binding sites. Thus, simulation can completely compensate the disadvantages of informatics. However, the calculation time of simulations may be extremely long and the simulation may fail completely if the calculation settings are inappropriate. Molecular simulation is easily misunderstood by other academic disciplines; reasonable answers are not provided automatically at the mere pressing of a button. To obtain a reasonable result, it is crucial for experienced researchers to refer to the calculation settings of similar cases and consider existing experimental results. If the calculation procedure and conditions have been verified over a sufficiently wide range, such known conditions can be applied without further investigation. In actual drug discovery, however, it is essential to deal with a wide range of aspects and subjects for calculation, and merely following existing procedures and conditions frequently is insufficient to achieve good results.

At the RIKEN Homma Laboratory, we are attempting to develop a highly practical in silico drug discovery systems that combine informatics-based methods (LAILAPS [4] and MUSES [5]) and simulation-based methods (PALLAS [6] and FMO + MM/PBSA [7]) (Fig. 2). The LAILAPS method detects a wide range of inhibitors as comprehensively as possible by simultaneously running a variety of ligand search techniques, including machine learning prediction that uses 3D molecular profiles developed in the laboratory as the descriptor. LAILAPS is particularly effective when

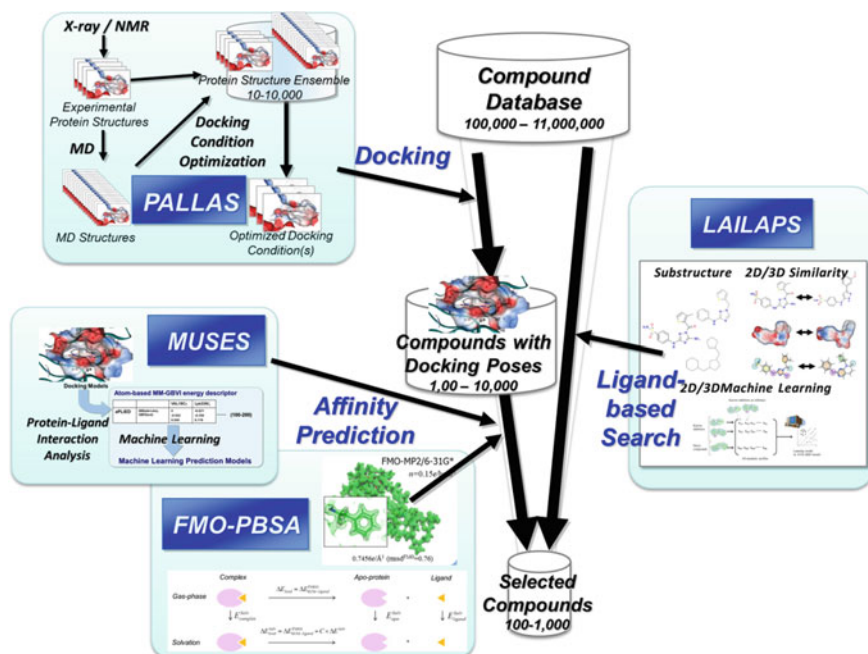


Fig. 2 Integration of informatics and simulation in the in silico screening system

there is limited information. In addition to being used for information collection prior to simulations, such as for docking, LAILAPS can discover new ligands when the protein structure is unknown. For example, new Adiponectin receptor ligands were searched based on analogous membrane protein and upstream protein ligand information, leading to the world's first discovery of activators [8].

The PALLAS simulation method optimizes docking conditions between proteins and ligands. In high-speed docking with over several millions of chemical compounds, it is impossible to perform time-consuming binding free energy calculations on each individual chemical compound; thus, the protein structures used in docking and the docking algorithm heavily influence the accuracy of the screening results. PALLAS performs verification docking against the protein structure ensemble obtained from crystal structures and molecular dynamics simulations using known ligands of the target and analogous proteins. It then semi-automatically optimizes various conditions, including the protein structures, docking algorithms, and their settings. Actual high-speed docking is typically executed by selecting several to ~10 docking conditions.

Reasonable docking results can be obtained using optimized conditions (model structures in which proteins and ligands are virtually bound with the correct orientation); however, with conventional docking scores, it is difficult to determine bioactivity such as inhibitory activity with sufficient accuracy. For example, the IC_{50} correlation between prediction and actual measurements is ~0.2–0.4 with R^2 . Therefore,

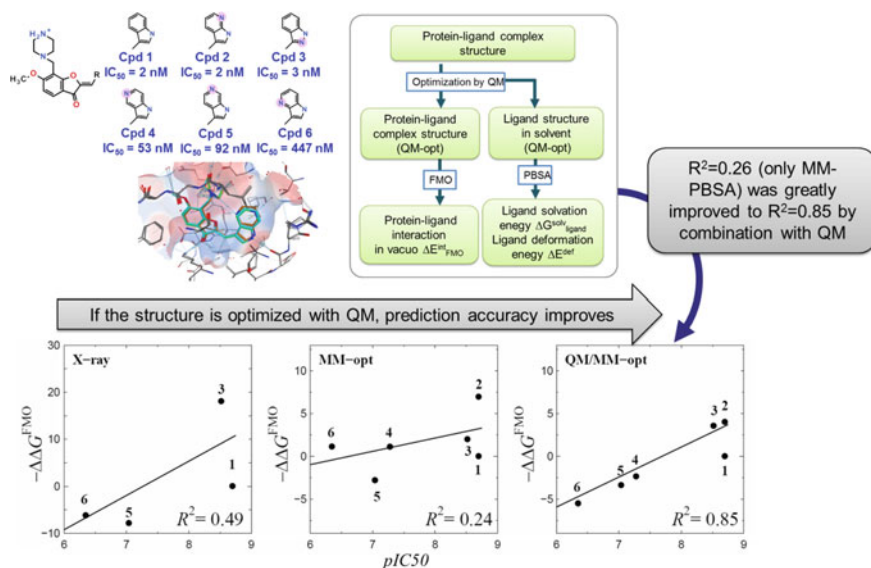


Fig. 3 Activity cliff prediction using a score that combines FMO and the solvent effect

we have developed the MUSES method to assess activity based on structural informatics and a method to predict activity based on quantum mechanical calculations. MUSES is an artificial intelligence (AI) technology that quantifies various interactions of the docking model for proteins and ligands and learns the difference between interaction patterns for active ligands and inactive ones using machine learning. The verification results reveal that when crystal structures or reasonable docking models of known several inhibitors are available, evaluations that exceed commercially available docking scores can be performed. In addition, with regard to the prediction of free energy using the fragment orbital molecular (FMO) method, we are developing, in collaboration with the FMO Drug Design Consortium [9], a score that incorporates solvent effects in the FMO method (FMO + MM/PBSA) [7]. In the example shown in Fig. 3, with Pim1 kinase, inhibitory activity differs by several hundred times due to a difference in a single atom. In the so-called “activity cliff” example, conventional MM-PBSA method demonstrated extremely poor prediction accuracy ($R^2 = 0.26$), using a score that combines the FMO method and MM-PBSA and by further optimizing the crystal structures via QM/MM, the result was greatly improved to $R^2 = 0.85$.

3 Applications to Drug Discovery Targets

The above mentioned in silico drug discovery methods have been applied to > 30 varieties of drug discovery targets in RIKEN. The probability of achieving a hit relative to the drug discovery target (drug discovery difficulty level) is greatly

dependent on the shape and characteristics of the particular target. We analyzed the IC_{50} values of a total of 600,000 inhibitors for 1,487 varieties of targets listed in the ChEMBL database. Observing the maximum potency for each target, inhibitors below 100 nM (for which drug development is possible) were found for the majority of targets. However, over several hundred varieties, for which drug development was considered difficult, with maximum potency levels ranging between 1 μ M and 1 mM, were also found. Generally, for small molecules to block the function of proteins at $\leq 1 \mu$ M, they must have large pockets of $\geq 400 \text{ \AA}^3$, deep pocket shape, and key hydrogen or ionic bonding sites at deep positions. In our laboratory, we deal with targets of varying complexity; some representative examples are introduced hereafter.

Protein kinases have large, deep pockets, and they contain key hydrogen bonds in the hinge region within the deep area of the pockets. Therefore, they are targets for which the discovery of small molecule inhibitors is feasible. For these targets, it is important to discover structurally diverse inhibitors at the initial stage so that issues with pharmacokinetics, toxicity, kinase selectivity, and patentability can be addressed in the later stages of the drug development. Pim1 and HCK, which are targets for leukemia, and ALK2, which is a target for the rare disease Fibrodysplasia Ossificans Progressiva (FOP), are all kinase targets. However, via *in silico* screening, we discovered a variety of inhibitors of $\leq 10 \mu$ M at a comparatively high hit rate of 5–10% by combining LAILAPS, PALLAS, and MUSES at an early stage. In particular, with the Pim1 inhibitor [10] case shown in Fig. 4, we investigated docking conditions using PALLAS in the state for the first *in silico* screening in which there was only

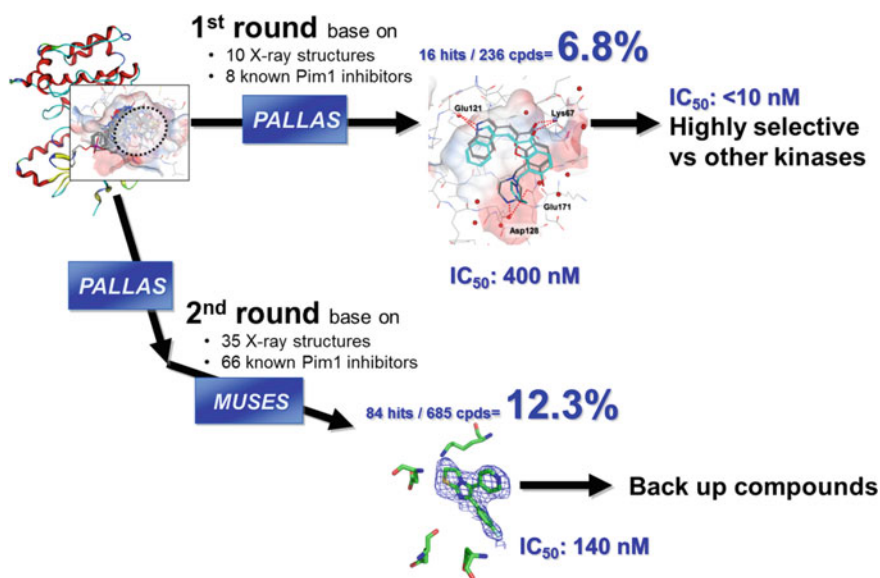


Fig. 4 *In silico* screening of Pim1 inhibitors

information about 10 crystal structures and eight known inhibitors. Via in silico screening, using the selected optimization conditions produced a sufficient hit rate of 6.8%. Using the synthetic development of Nagano et al. from Tokyo University on these first-time hits led to the discovery of highly potent and highly selective inhibitors. Following this, using the additional assay/crystal structure information (35 crystal structures and 66 known inhibitors) in the second in silico screening, the hit rate improved to 12.3%. The additional hits were valuable backup chemical compounds for solving ADME and toxicity issues.

Figure 5 shows the example [11, 12] of an HCK inhibitor design for an acute myeloid leukemia treatment drug target. In this case, chemical compounds with extremely high activity (IC_{50} : 7.7 nM) were obtained from the first in silico screening. Complex crystal structures with HCK were solved using the X-ray analysis by Yokoyama et al. of RIKEN. According to the complex structure, we introduced a new amine substituent to the initial inhibitor to form an ionic bond with Asp348. As

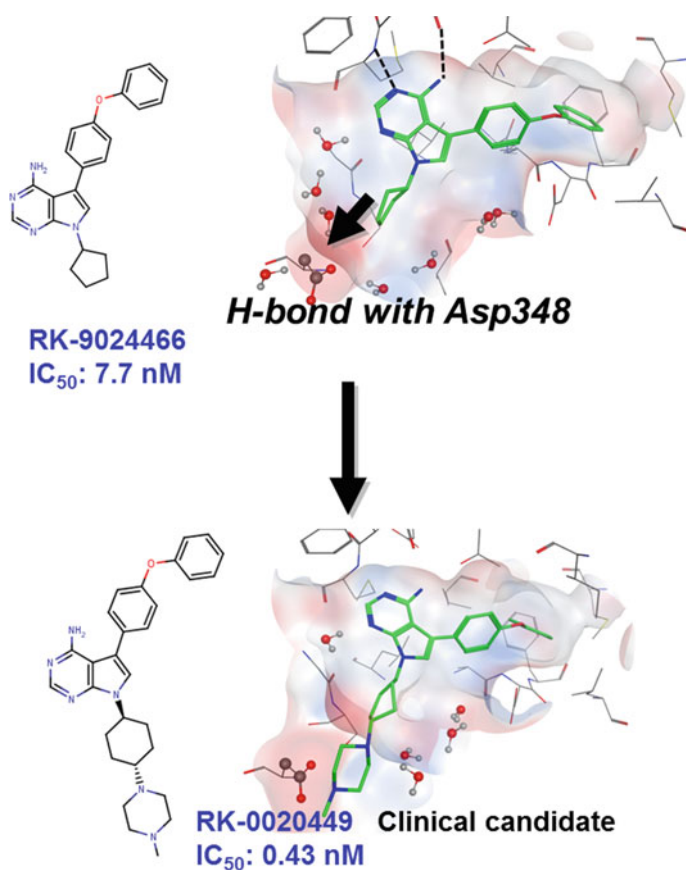


Fig. 5 Optimized design of HCK inhibitors

the result of design, RK-0020449 was obtained. It demonstrated sufficient inhibitory activity (0.43 nM) and efficacy in patient-derived AML cells, and a clinical trial is being prepared in the United States.

In contrast, two types of difficult targets are those with extremely small and shallow pockets and a high level of freedom. A typical example of the former is DHOD [13, 14], which is an anti-trypanosomal drug target that contains orotic acid pockets with an extremely small binding site of 200 \AA^3 . When analyzing the PDB bind database (a database of complex crystal structures and chemical compounds with various information, such as IC_{50} values), we learned that chemical compounds with high activity below IC_{50} : $1 \text{ }\mu\text{M}$ are difficult to obtain when the volume of the binding pocket is $\leq 300 \text{ \AA}^3$. Thus, in the trypanosoma DHOD case, small molecule drug discovery was initially considered difficult; however, by effective collaboration of structure-based design, organic synthesis, and crystal structure analysis, we successfully designed new chemical compounds that push out the specific loop structure and extend the pocket. For pockets that are extended $\geq 400 \text{ \AA}^3$, we constructed a virtual chemical compound library that can easily perform synthesis. This virtual library can also perform selection via docking using the PALLAS and MUSES methods. From the synthesis of only 20 chemical compounds, we derived high DHOD inhibitory activity of approximately IC_{50} : $0.15 \text{ }\mu\text{M}$ from starting compounds of approximately IC_{50} : $100 \text{ }\mu\text{M}$ (Fig. 6).

Another category of high-difficulty targets is the so-called “protein–protein interaction targets” which come into contact with each other over a wide area and transmit signals, creating interactions between them. DOCK1/2 [15], which is a target discovered by Fukui et al. of Kyushu University, has been studied in the laboratory. DOCK1/2 forms protein–protein interactions with Rac1. By predicting the ligand binding sites and performing *in silico* screening using docking to the predicted sites, several inhibitors of $\sim 10 \text{ }\mu\text{M}$ were discovered. For such difficult targets, inhibitors with the desired activities are often not detected via only one *in silico* screening; therefore, it is important to gradually acquire information and to repeat the design process using the new information. The key is to build a robust joint research structure where research is performed with tenacity and perseverance. Further, it is essential to have various types of systems that can immediately use the new information, such as those established in the laboratory, to improve the accuracy and efficiency of *in silico* screening.

4 From In Silico Drug Discovery to AI Drug Discovery

Herein, we discuss some next-generation technologies that will improve both the accuracy of each step of prediction and the probability of drug discovery for high-difficulty targets. The first of these technologies is the use of quantum mechanical calculations. Molecular dynamics calculations and quantum mechanical calculations are mutually complimentary methods used for dealing with molecular behaviors. These methods share a relationship similar to two wheels on a vehicle. The former

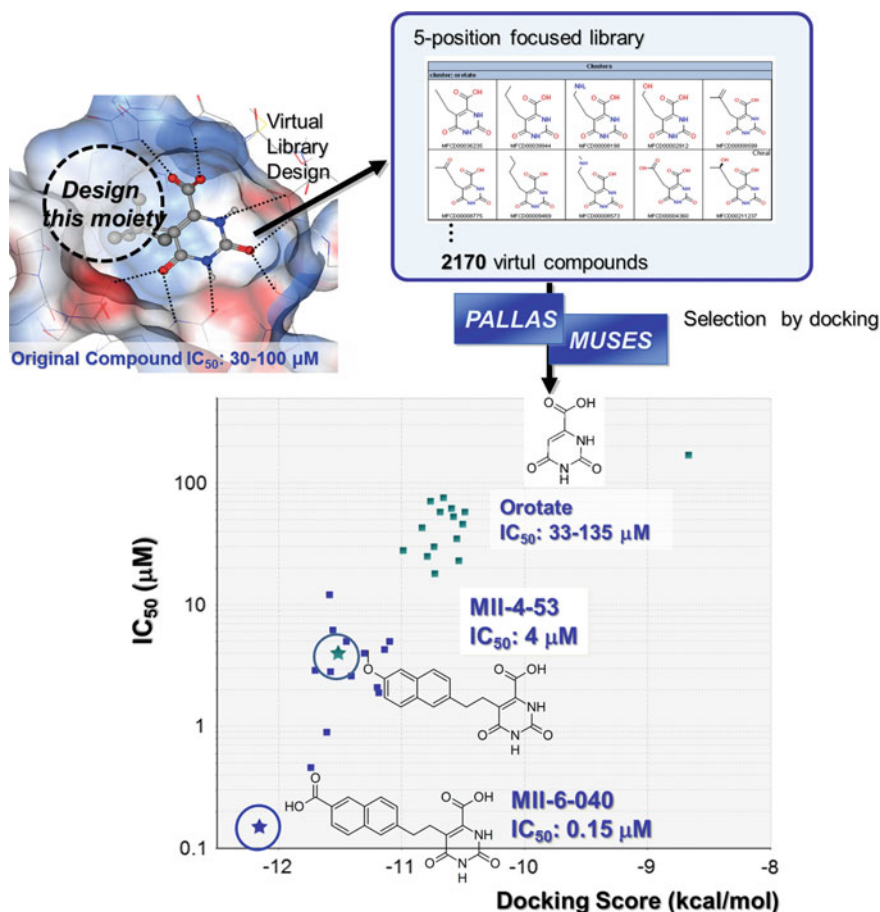


Fig. 6 Optimized design of DHOD inhibitors using a virtual library and docking

analyzes the dynamic behavior of molecules, whereas the latter is the most accurate method known for calculating static interactions between molecules. Currently, molecular dynamics calculations are studied extensively. Some progress has been achieved in drug discovery, for example, in applying free energy calculation based on MP-CAFFE by Fujitani et al. and long-term simulations approaching the millisecond level using the dedicated device, Anton, by Shaw et al. However, in these molecular dynamics calculations, classical force fields are used for calculating the interactions between molecules because of constraints related to the calculation time. Interactions that require orbital calculations, such as π interactions, are not accurately considered. Thus, the level of prediction can worsen in some cases. In Japan, Kitaura et al. developed the fragment molecular orbital (FMO) method, which enables first-principles quantum mechanics calculations for huge systems, such as proteins. Currently, we are collaborating with Fukuzawa and coworkers from Hoshi University at the FMO drug

design consortium [9] to develop a method of applying the FMO method to practical drug discovery. Examples of our study include: quantum chemical refinement of the resolution of crystal structures using the FMO method, highly accurate free energy prediction based on FMO + MM/PBSA (Fig. 3) [7], and construction of the FMO database (currently under preparation for public release in 2018) for performing comprehensive FMO calculations for PDB protein structures and publishing the calculation values. In particular, the FMO database already stores over 2000 FMO calculation results. Based on these data, we are collaborating with the AI consortium (LINC) in Japan, which will be described later, to develop a new AI-based molecular force field that considers the results of quantum chemical calculations.

Another direction of research is AI drug discovery using data from the expanding quantities of drug discovery-related information. *In silico* drug discovery methods until now have only been able to simultaneously predict one item, such as target binding affinity. However, development candidates or marketed drugs must meet or exceed certain levels of quality in numerous criteria, such as pharmacokinetics, safety, and pharmaceutical formulation. The difficulty of optimizing these items simultaneously is a reason for the low success rate of drug development. From this perspective, although conventional *in silico* drug discovery methods have made partial contributions to drug discovery, they cannot be said to have made a major contribution overall. AI drug discovery has the hidden potential to be able to guide the optimization of multiple items in an efficient direction. This will provide the first step in which the *in silico* method can, in a true sense, make a major contribution to drug discovery. However, it is necessary to secure a large volume of high-quality drug discovery-related data with the right set of experimental conditions and to combine previous individual highly accurate prediction models. This will require, in addition to cooperation by industry, government, and academia, complete and dedicated efforts in many drug discovery-related fields. In Japan, the LINC [16] was established in 2016, with Okuno from Kyoto University as a representative, and it has initiated the development of AI for a variety of drug discoveries.

Mizuguchi from the medical foundation KENEIKEN and the author are members of LINC, and are promoting the development of AI for cutting-edge drug discovery. The structure of LINC is based on more than 90 pharmaceutical and IT companies and has a total of over 500 participants. The points to be emphasized here are that all stages of drug discovery are covered by AI—from the upstream process of identification and validation of targets to downstream clinical trials and analysis after coming to the market. 30 projects are under operation. Progress has been achieved in terms of small molecule drug design, in the development of original descriptors for deep learning, AI for analyzing simulation results, molecular force field AI, and AI for new structure proposals.

References

1. Shaw DE, Deneroff MM, Dror RO, Kuskin JS, Larson RH, Salmon JK, Young C, Batson B, Bowers KJ, Chao JC, Eastwood MP, Gagliardo J, Grossman JP, Ho CR, Ierardi DJ, Kolossváry I, Klepeis JL, Layman T, McLeavey C, Moraes MA, Mueller R, Priest EC, Shan Y, Spengler J, Theobald M, Towles B, Wang SC (2008) A special-purpose machine for molecular dynamics simulation. *Commun ACM* 51(7):91–97
2. Ohmura I, Morimoto G, Ohno Y, Hasegawa A, Taiji M (2014) MDGRAPE-4: a special-purpose computer system for molecular dynamics simulations. *Phil Trans R Soc A* 372:20130387
3. Tanrikulu Y, Krüger B, Proschak E (2013) The holistic integration of virtual screening in drug discovery. *Drug Discov Today* 18:358–364
4. Sato T, Yuki H, Takaya D, Sasaki S, Tanaka A, Honma T (2012) Application of support vector machine to three-dimensional shape-based virtual screening using comprehensive three-dimensional molecular shape overlay with known inhibitors. *J Chem Inf Model* 52(4):1015–1026
5. Sato T, Honma T, Yokoyama S (2010) Combining machine learning and pharmacophore-based interaction fingerprint for in silico screening. *J Chem Inf Model* 50(1):170–185
6. Sato T, Watanabe H, Tsuganezawa K, Yuki H, Mikuni J, Yoshikawa S, Kukimoto-Niino M, Fujimoto T, Terazawa Y, Wakiyama M, Kojima H, Okabe T, Nagano T, Shirouzu M, Yokoyama S, Tanaka A, Honma T (2012) Identification of novel drug-resistant EGFR mutant inhibitors by in silico screening using comprehensive assessments of protein structures. *Bioorg Med Chem* 20(12):3756–3767
7. Watanabe C, Watanabe H, Fukuzawa K, Parker LJ, Okiyama Y, Yuki H, Yokoyama S, Nakano H, Tanaka S, Honma T (2017) Theoretical analysis on activity cliff among benzofuranone class Pim1 inhibitors using the fragment molecular orbital with molecular mechanics Poisson-Boltzmann surface area (FMO+MM-PBSA) method. *J Chem Inf Model* 57(12):2996–3010
8. Okada-Iwabu M, Yamauchi T, Iwabu M, Honma T, Hamagami KI, Matsuda K, Yamaguchi M, Tanabe H, Kimura-Someya T, Shirouzu M, Ogata H, Tokuyama K, Ueki K, Nagano T, Tanaka A, Yokoyama S, Kadowaki T (2013) A small-molecule AdipoR agonist for type 2 diabetes and short life in obesity. *Nature* 503:493–499
9. <https://eniac.scitec.kobe-u.ac.jp/fmodd/>
10. Nakano H, Saito N, Parker L, Tada Y, Abe M, Tsuganezawa K, Yokoyama S, Tanaka A, Kojima H, Okabe T, Nagano T (2012) Rational evolution of a novel type of potent and selective proviral integration site in Moloney murine leukemia virus kinase 1 (PIM1) inhibitor from a screening-hit compound. *J Med Chem* 55(11):5151
11. Saito Y, Yuki H, Kuratani M, Hashizume Y, Takagi S, Honma T, Tanaka A, Shirouzu M, Mikuni J, Handa N, Ogahara I, Sone A, Najima Y, Tomabechei Y, Wakiyama M, Uchida N, Tomizawa-Murasawa M, Kaneko A, Tanaka S, Suzuki N, Kajita H, Aoki Y, Ohara O, Shultz LD, Fukami T, Goto T, Taniguchi S, Yokoyama S, Ishikawa F (2013) A pyrrolo-pyrimidine derivative targets human primary AML stem cells in vivo. *Sci Trans Med* 5:181ra52
12. Yuki H, Kikuzato K, Koda Y, Mikuni J, Tomabechei Y, Kukimoto-Niino M, Tanaka A, Shirai F, Shirouzu M, Koyama H, Honma T (2017) Activity cliff for 7-substituted pyrrolo-pyrimidine inhibitors of HCK explained in terms of predicted basicity of the amine nitrogen. *Bioorg Med Chem* 25(16):4259–4264
13. Inaoka DK, Iida M, Tabuchi T, Honma T, Lee N, Hashimoto S, Matsuoka S, Kuranaga T, Sato K, Shiba T, Sakamoto K, Balogun EO, Suzuki S, Nara T, Rocha JR, Montanari CA, Tanaka A, Inoue M, Kita K (2016) The open form inducer approach for structure-based drug design. *PLoS ONE* 11(11):e0167078
14. Inaoka DK, Iida M, Hashimoto S, Tabuchi T, Kuranaga T, Balogun EO, Honma T, Tanaka A, Harada S, Nara T, Kita K, Inoue M (2017) Design and synthesis of potent substrate-based inhibitors of the *Trypanosoma cruzi* dihydroorotate dehydrogenase. *Bioorg Med Chem* 25(4):1465–1470

15. Nishikimi A, Uruno T, Duan X, Cao Q, Okamura Y, Saitoh T, Saito N, Sakaoka S, Du Y, Suenaga A, Kukimoto-Niino M, Miyano K, Gotoh K, Okabe T, Sanematsu F, Tanaka Y, Sumimoto H, Honma T, Yokoyama S, Nagano T, Kohda D, Kanai M, Fukui Y (2012) Blockade of inflammatory responses by a small-molecule inhibitor of the Rac activator DOCK2. *Chem Biol* 19(4):488–497
16. <https://rc.riken.jp/life-intelligence-consortium/>

Pharmaceutical Industry—Academia Cooperation



Alexander Heifetz, Peter V. Coveney, Dmitri G. Fedorov, Inaki Morao, Tim James, Michelle Southey, Kostas Papadopoulos, Mike J. Bodkin, and Andrea Townsend-Nicholson

Abstract There has been a long history of fruitful cooperation between academia and the pharmaceutical industry, with the primary beneficiary of this interaction being, of course, the public. Since the middle of the last century, the drug discovery process has been driven by the translational research partnership between these two sectors. Collaboration between academia and industry has accelerated based on the ever-increasing demand for novel medicines, technologies, new drug targets, financial pressures and from the past successes. Here, we review the benefits and challenges for each sector seeking to engage in a fruitful and productive collaboration and provide some practical solutions, based on our own experiences, to make this kind of collaboration successful and rewarding. We provide several examples of partnerships between Evotec (UK) Ltd. and academia (National Institute of Advanced Industrial Science and Technology (AIST, Japan), University College London, University of Oxford and briefly review the technologies that have been developed as a result. We also show how this kind of collaboration can be particularly effective within a larger, multi-partner, academia-industry collaboration (CompBioMed).

Keywords Academia · Industry · Collaboration · Drug discovery · Drug · G protein-coupled receptors · GPCR · Chemical interactions · Drugs · Receptor · Computational · Modelling · QM · Quantum mechanics · FMO · Fragment molecular orbitals method · CADD · Computer-aided drug design · SBDD ·

A. Heifetz (✉) · I. Morao · T. James · M. Southey · K. Papadopoulos · M. J. Bodkin
Evotec (UK) Ltd., 114 Milton Park, Abingdon, Oxfordshire OX14 4SA, United Kingdom
e-mail: Alexander.Heifetz@evotec.com

A. Heifetz · A. Townsend-Nicholson
Structural and Molecular Biology, Darwin Building, University College London, Gower Street,
London WC1E 6BT, United Kingdom

P. V. Coveney
Centre for Computational Science, Department of Chemistry, University College London, London
WC1H 0AJ, United Kingdom

D. G. Fedorov
CD-FMat, National Institute of Advanced Industrial Science and Technology (AIST), 1-1-1
Umezono, Tsukuba, Ibaraki 305-8568, Japan

Structure based drug design · Hierarchical GPCR modeling protocol (HGMP) ·
Residence time · Steered molecular dynamics (SMD)

1 Background

Why is there a need for collaborative research between the pharmaceutical industry and academia? We will endeavor to answer this question. Each sector has their own motives for embarking on a collaboration of this kind, and accounting for these can significantly improve the mechanism of collaboration and lead to an increase in such joint research programs in the future. In this chapter, we will draw from our personal experience and review the benefits and obstacles, which both parties should consider before generating a true and fruitful partnership. We will propose practical solutions of how to make academia-industry collaborations efficient and meet the needs of both partners.

1.1 *Pharmaceutical Industry*

The pharmaceutical industry lives and breathes translational research by transforming knowledge of a potential drug target into a medicine for patients around the world. Drug discovery is often long and expensive from the conception of an idea, via target validation, small molecule discovery, research and development (R&D) phases, and clinical trials to marketed drug. The pharmaceutical industry (pharma) spends about \$1 billion to \$2 billion to invent each new drug [1]. This process is challenging intellectually, scientifically, economically, organizationally, and emotionally but when successful, lives are saved and suffering is decreased.

The annual expenditure for pharma R&D relative to income from sales has increased nearly every year over the last three decades, but the return on R&D investment has dramatically decreased. In the early 1980s, \$1 invested in capitalized research returned about \$3 (in sales). This took 10 to 15 years; however, there was a clear positive return on investment across the industry. Three decades later, the financial situation is completely different—when capitalized R&D returned only \$0.83 per \$1 invested (Fig. 1). This is clearly not a sustainable business model.

Many different factors have been proposed to explain this constant decrease in return; however, there is one fundamental issue at play that drives all these factors together: *the law of diminishing returns*, as suggested by Stott (see Fig. 1) [2]. In his analysis, Stott proposes that the incremental improvement in patient care with each new drug that makes it to market raises the expectation for the next drug that will follow. Not only does this make each subsequent drug more expensive to produce but also, eventually, the scope for significant improvement on previous versions becomes negligible. It is indeed ironic that the relationship between patient care and return on financial investment for the pharmaceutical companies providing the

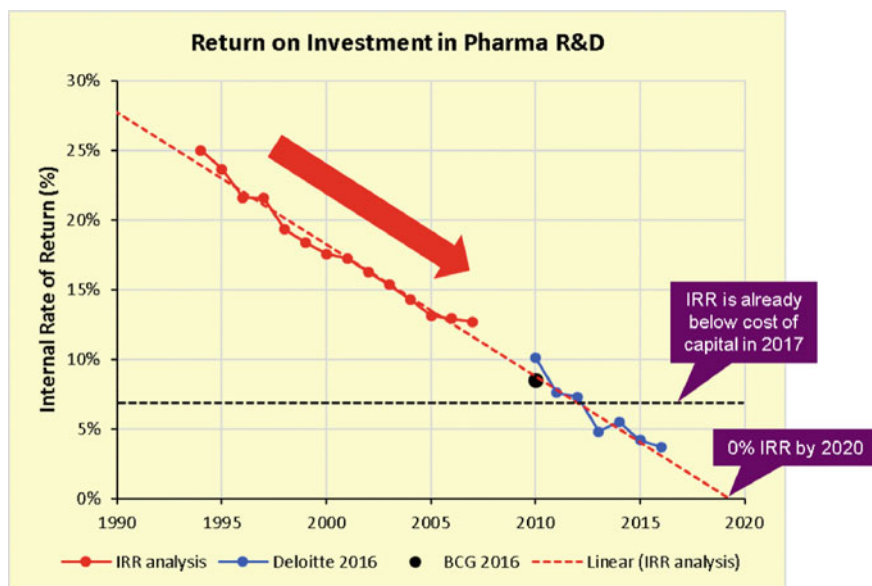


Fig. 1 Plot of time versus internal rate of return (IRR) on investment, taken from blog of Stott [2] (reproduced with permission of the author). Various analysts (notably Deloitte and BCG) have tried to measure Big Pharma's R&D productivity in terms of IRR

therapeutic solutions is, effectively, inversely proportional. This highlights that the need for innovation, as part of the drug development pipeline, is paramount in order to maintain competitive and commercial success.

While the pharmaceutical industry's business model depends on innovation, there is now a growing divide in innovation strategies within the sector. Some companies prefer to invest primarily in their own research engine [1]. Others seek innovation externally. However despite their differing approaches to R&D, all major pharmaceutical companies continue looking to academia for sources of innovation beyond their internal research engines [1].

Industry relies on academia for basic research that identifies novel molecular targets and for clinical trials. Furthermore, alliances with top scientists from academia increases the credibility of the company to investors and other stakeholders, while building a network of key opinion leaders that might endorse future products. In addition, collaboration with academia allows pharmaceutical companies to diversify their drug and technology portfolios with little risk and high return on investment. It also provides access to highly skilled talent, specialized expertise, state-of-the-art equipment and facilities. For example, new animal models, patient databases and other infrastructure from the academic community, such as human tissue banks, provide unique opportunities for the validation of identified targets and pathways.

1.2 *Academia*

Academic research can also significantly benefit from collaboration with industry. Academic endeavors are increasingly being driven toward research that will address matters of pressing societal concern. In the biomedical sciences, there is significant emphasis on translating fundamental discoveries into improvements in human health and well-being. Industry is an important player in this process as it offers the opportunity to help develop solutions for real-life problems, bringing academic science further down the translational research pathway toward application. A successful collaboration with industry facilitates translational research, but also offers to researchers and students the opportunity to gain new perspectives and integrate new skills into their research. It enables academic scientists to show that they are driving innovation and have the capacity and the network to make a demonstrable contribution to society and the economy.

As government funding decreases, academic scientists are placed under increasing pressure to obtain funding from external sources [3]. Collaboration with industry provides several interesting alternatives by which to finance academic research, ranging from shared research grants (such as those provided in the UK by the BBSRC, EPSRC, MRC, Royal Society and UK Research and Innovation, among others), shared research projects or fee-for-service projects. In the US, the NIH clearly endorses collaboration with industry in its Clinical Translational Sciences Institutes and in the new National Center for Advancing Translational Sciences.

Collaboration between academia and industry frequently happens at the edges of different disciplines where innovation occurs. There is increasing evidence showing that university-business cooperation can result in a higher number of academic publications that are also of higher quality [1], showing that these collaborations are able to enhance and improve research outputs, as measured by journal citation rates and citation lifetime [1].

Collaboration with industry provides important feedback to academic researchers. Application of computational methods to realistic problems pinpoints the necessary improvements and extensions that have to be implemented to improve the quality and usefulness of computational methods. Purely academic projects may be biased toward the high standards in the theoretical field but on the other hand they tend to use oversimplified models not adequately describing the chemistry and physics of a practical process. In joint research projects the focus may be better tuned to solve the practical problem at hand.

1.3 *Challenges*

On the face of it, these collaborations make sense for both sides, and yet they remain very challenging. Why? Firstly, by their very nature these projects are often discovery

driven and there will inevitably be unanticipated events throughout the project lifetime that can derail even the best planned project [3]. Secondly, a very real challenge is that of culture clash [3]. A fundamental difference appears between the two sides when it comes to publishing results. Industry seeks profit through competitive advantage, naturally developing a culture of confidentiality. On the contrary, academic achievement is often measured through the number and quality of publications, which are essential to support shared research grants.

An additional cultural clash comes from the more traditional academic perception that research is performed to obtain novel understanding, made publicly available as soon as possible and be free from biased commercial interest. Recent surveys conducted among academics have demonstrated that “the expected benefits from collaboration are not clearly perceived by all researchers” and that “academics who are not already involved in industry collaborations fail to recognize the potential opportunities of engaging with industry” [4]. Each academic institution has its own policy concerning collaboration with industry. Would it be possible for universities and pharma to create a universal template? The availability of a widely adopted template could increase the efficiency and speed of research by standardizing some individual details that require negotiation, such as intellectual property rights, royalty rates, payments, and other items that are specific to a particular collaboration. From industry’s perspective, a sizeable gap exists between the way in which basic academic research is conducted and the needs of the pharmaceutical industry. The general requirements of the pharmaceutical industry for any drug discovery approach are: (1) the method should be applicable to drug discovery projects; (2) the method should be effective and cost-efficient; and, (3) it should satisfy the immediate need for such information to be provided in “real-time”. This gap must be bridged in order to successfully apply academic knowledge to the drug discovery process.

Despite these challenges, it is critically important for industry and academia to collaborate to improve health and well-being in many areas of medicine. Despite the tensions between these two sectors, potential conflicts of interest and regulatory issues, the number of industry-academia collaborations is growing, worldwide. Interestingly, most of these collaborations differ from those of the past. Historically, these collaborative endeavors were large programs that covered entire therapeutic areas, an approach that was in most cases less productive than expected [1]. Current industry-academic collaborations now tend to be precisely targeted to a specific project and we anticipate that the nature of this kind of collaboration will continue to evolve as more thoughtful ways of working together to develop and become used as examples of best practice.

2 Examples of Academia-Evotec Ltd. (Industry, Drug Discovery Company) Collaborations

In the modern era, collaboration between academia and pharma is often focused around addressing specific challenges in drug-discovery. Here, we provide three examples of collaborative programs between academia, and Evotec (UK) Ltd. established to address key challenges in drug-discovery. The three programs are concerned with the development of novel methods and computational-experimental tools. The objectives of each program are as detailed:

- (1) Explore the nature of the molecular interactions between a ligand and its receptor as well as the interactions between residues within that receptor.
- (2) Develop a method for modelling the secondary structure of G protein-coupled receptors (GPCR).
- (3) Develop a method for determining protein–ligand residence time, to improve the effectiveness of therapeutic compounds.

2.1 *Molecular Interactions Identified by the Fragment Molecular Orbital Method*

The National Institute of Advanced Industrial Science and Technology (AIST, Japan), University College London (UCL) and Evotec (UK) Ltd. combined efforts on a project to develop the use of quantum mechanical tools for the exploration of protein–ligand and protein–protein interactions to inform drug discovery.

The understanding of binding interactions between a protein and a small molecule plays a key role in the rationalization of potency, selectivity, and kinetics and is essential for an efficient structure-based drug design (SBDD) program. However, the full complexity of the molecular interactions that are so critical to the rational drug discovery process cannot always be explained, even when the crystal structure is available and used to perform force field-based molecular mechanics calculations. Quantum mechanical (QM) methods can address this shortcoming, but are computationally expensive, making the use of these calculations impractical for the pharmaceutical industry.

We routinely use the Fragment Molecular Orbital (FMO) QM method [5, 6] in protein–ligand binding calculations and drug design because it offers a substantial computational saving over traditional QM methods by partitioning the system into small fragments and performing QM calculations on these. A typical FMO calculation on a GPCR–ligand complex takes approximately 4 h to complete on 36 CPU cores, which is significantly faster and less computationally expensive than classical QM calculations. FMO has been successfully applied in many confidential and non-confidential SBDD programs such as the discovery of kinase (ITK) inhibitors [7] and novel Hsp90 inhibitors [8]. We have also recently demonstrated how FMO can

be efficiently used in the analysis of GPCR-ligand interactions [5, 6, 9], specifically in the investigation of Agonist-OX2 receptor interactions [5].

FMO takes, as an input, a protein–ligand complex and provides, as an output, a list of the specific interactions and their chemical nature. FMO is a highly valuable tool for rational SBDD as it provides an accurate and comprehensive list of strong, weak, or repulsive interactions between the ligand and its surrounding residues. This information is useful in rational SBDD in terms of ligand modifications such as scaffold replacement and linking, extension of chemical moieties to form stronger or new interactions with the protein or, alternatively, for the discovery of new ligands. FMO was recently combined with density-functional tight-binding (DFTB) allowing us to run FMO at a dramatically enhanced speed but with a comparable level of accuracy, compared with the FMO-MP2 protocol we deployed previously [10]. For the first time it is now possible to perform FMO calculations for protein–ligand complexes in a high-throughput manner and to process large amounts of experimental data. Protein–ligand complexes can be refined, re-scored, and re-ranked with FMO-DFTB in the presence of the surrounding water molecules.

We have extended our application of FMO, moving from the study of protein–ligand interactions to the characterization of protein–protein interactions. The structural stability, function and ligand binding of GPCRs are dominated by the interactions between residues of different helices [11, 12]. However, the question of what constitutes the structural features responsible for “gluing” together the seven helices of the GPCR bundle and how these affect ligand binding, receptor flexibility and activation, remains open. We applied FMO to study the network of residue–residue interactions between different GPCR helices (TMs). These essential structural insights can be applied to design ligands that can more efficiently interact with the inter-TM network, controlling receptor structure and flexibility and thereby affecting its function. This has the potential to lead to a new generation of more effective GPCR-targeted drug [13].

2.2 Computer-Aided Drug Design and the Hierarchical GPCR Modelling Protocol (HGMP)

A series of collaborations between academia and industry underpin the development of a computational engine to support structure-based drug design (SBDD) in G protein-coupled receptor (GPCR) drug discovery programs. These collaborations have been supported by shared research grants awarded jointly to the academic (University of Oxford, University College London (UCL)) and industrial (Evotec) partners and to CompBioMed, a large academic-industrial research Centre of Excellence led by UCL and funded by the European Commission’s Horizon 2020 Programme.

GPCRs are the largest membrane protein superfamily, and vast amounts of industrial and academic research is carried out on these receptors on a global scale.

There are over 800 GPCRs in the human genome and signal transduction by this receptor superfamily controls most of the physiological processes ranging from vision, smell, and taste to neurological, cardiovascular, endocrine, reproductive functions, and many more, making GPCRs one of the most important classes of current pharmacological targets.

The importance of GPCRs is highlighted by the award of the Nobel Prize for Chemistry (2012) to two GPCR researchers, Brian Kobilka and Robert Lefkowitz. However, GPCRs are underexploited as therapeutic targets, given that 60% of all prescription drugs today target just 50 of the 800 available GPCR targets. A recent expansion of the repertoire of GPCRs targeted for drug discovery is a consequence of the increasing availability of structural information describing the binding site of the targeted receptor. However, X-ray crystallography, a traditional source of structural information, is not currently feasible for every possible GPCR or GPCR-ligand complex, significantly limiting the ability of crystallography to contribute to the drug discovery process for GPCR targets in “real-time”. The urgent need for other practical and cost-efficient alternatives can be met by the development of sophisticated computational modeling, particularly when this is complemented by experimental structure–function studies.

A novel hierarchical GPCR modeling protocol (HGMP) [14] has been developed by Evotec (UK) Ltd. and the University of Oxford to support structure-based drug discovery programs (Fig. 2). The HGMP generates a 3D model of GPCR structures and the complexes they form with small molecules by applying computational methods. The models produced by HGMP are exploited in structure-based drug discovery projects. HGMP is a workflow that begins with homology modeling followed by MD simulation and flexible ensemble docking to predict binding poses and function of ligands bound to GPCRs. The HGMP includes a large set of unique

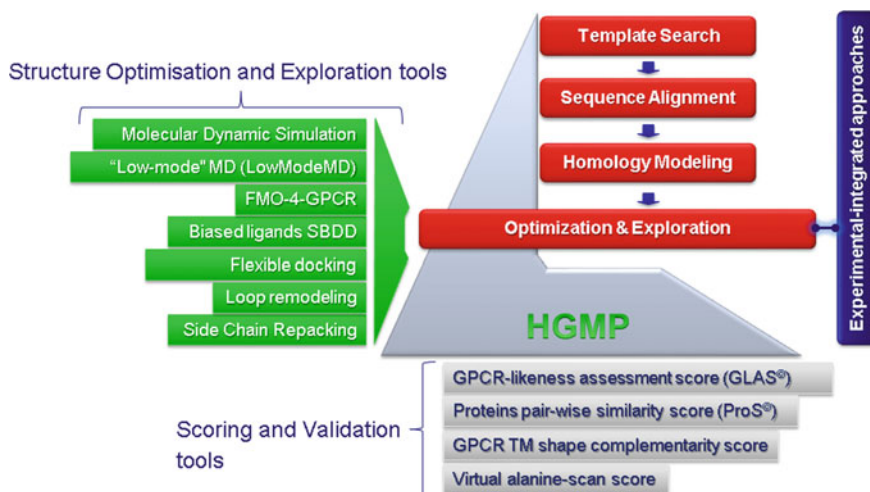


Fig. 2 HGMP: a novel workflow used to inform structure-based drug discovery

plugins that can be used to refine the models generated and contains exclusive scoring functions such as the GPCR-likeness assessment score (GLAS), which can be used to evaluate the quality of the model [15]. HGMP is also “armed” with a pairwise protein comparison method (ProS) used to cluster the structural data generated by the HGMP and to distinguish between different activation sub-states.

The optimization and validation of HGMP has been performed by Evotec (UK) Ltd. and applied to drug discovery projects. The outstanding performance of HGMP has been demonstrated in GPCR drug discovery projects on numerous targets including: MCH-1R [16] for obesity treatment, Orexin-1 and -2 receptors [15, 17] for insomnia, 5-HT_{2C} [18, 19] for the treatment of metabolic disorders [19] and in many other confidential drug-discovery programs. The refinement and use of the GPCR model is an iterative process where new experimental data produced in the drug discovery cycle is fed back into HGMP and used for the continuous validation and refinement of the model (Fig. 3) [18].

FMO-4-GPCR is an integrated component of the HGMP and is used to apply FMO to the analysis of interactions between ligand and receptor for the model that has been constructed with HGMP [5, 10, 14]. This information is essential to allow medicinal chemists to adopt a rational approach to the modification of lead compounds in order to enhance favorable interactions. Although it is primarily used to interrogate the molecular nature of these interactions, FMO-4-GPCR can also be used as a test of

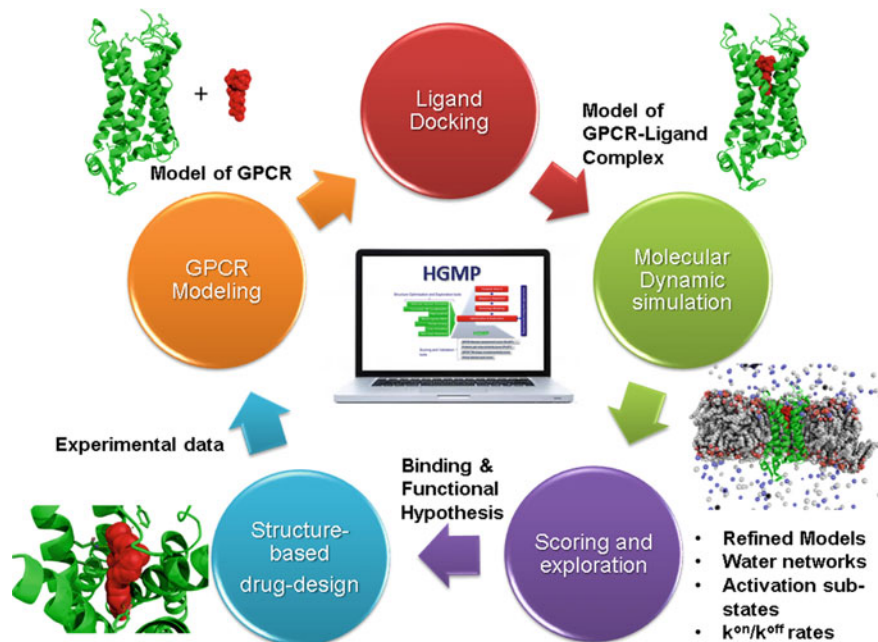


Fig. 3 The GPCR application and refinement cycle and HGMP

the quality of the model generated by HGMP, as FMO often crashes if the quality of the model is insufficient, allowing models to be subjected to further optimization.

Funding support for HGMP and its applications comes from a number of different sources. In 2011, the Royal Society awarded Evotec (Alexander Heifetz) an Industry Fellowship to establish a collaboration with the University of Oxford (Philip Biggin) for the development of computational methods to guide drug discovery. In 2013, the BBSRC (UK Research and Innovation) provided funding support for the Oxford-Evotec collaboration through a FLIP Flexible Interchanger Programme research grant to develop methods for the discovery of GPCR biased ligands. In 2016, the European Commission funded the CompBioMed Centre of Excellence (<https://www.compbioimed.eu>) focused on the use and development of computational methods for biomedical applications, with the specific intention of adapting the HGMP and other relevant codes for use on supercomputers in order to provide the capabilities needed for the development of patient-specific drugs (personalized medicine).

CompBioMed provides a focal point for the development and sustainability of software (codes, programs, and packages) that are capable of high fidelity three- and four-dimensional modelling and simulation of all aspects of the human body, from the molecular level to the whole human and beyond, in health and disease. The accuracy, reliability, and reproducibility of these models, and therefore of the underpinning software, is essential for their intended future role in personalized medicine, for example in clinical decision support for individual patients. Such approaches have an impact *inter alia* on drug discovery, including repositioning and targeted therapies for precision medicine, through the potential for rapid and accurate assessment of drug efficacy in specific disease cases, of direct relevance to the pharmaceutical industry; and to provide added value to medical device measurement data, for example as acquired by various imaging modalities. Thus the project involves major industry participation, furthering the direction, uptake and exploitation of high performance computing (HPC) within academia, industry, and healthcare sectors.

CompBioMed is of particular interest in terms of academic–industrial collaborations for three reasons. First, it is a vast academic–industrial collaboration consisting of 15 core partners and 36 associate partners drawn from academia and from small, medium, and large enterprises. This arrangement has worked exceptionally well and the award of CompBioMed2 for 2019 has recently been confirmed. Second, CompBioMed aims to adapt relevant codes and protocols so that they can run in automated fashion on high performance computing facilities. This provides the opportunity, for example, to expand the capabilities of the HGMP and apply it far more extensively than is possible with the computational resource typically used to run it. Third, CompBioMed has substantial impact, both in terms of supporting and facilitating modelling and simulation activities, and in providing education (Fig. 4) and training for a very heterogeneous set of end-users from both academia and industry. Collaborations between academia and industry do not frequently involve teaching; however, CompBioMed facilitated this opportunity for the smaller collaboration between Evotec and UCL. These two partners were able to communicate their expertise and knowledge through the development and delivery of a two hour training course on An Introduction to Computer-Aided Drug Design (CADD) and GPCR Modelling—(<https://>

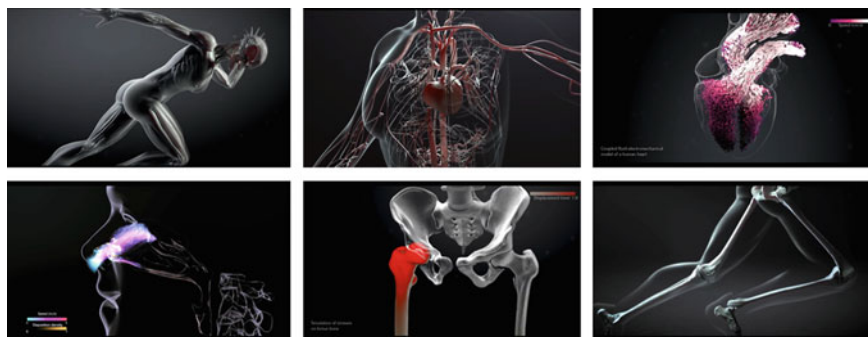


Fig. 4 Screen snapshots taken from the “Virtual Humans” film produced by the Barcelona Supercomputing Centre (BSC) and CompBioMed H2020 Centre of Excellence in Computational Biomedicine, led by University College London (<https://youtu.be/1FvRSJ9W734>)

youtu.be/K6Ysidm3icQ) and Innovations in HPC-training for Medical, Science and Engineering Students (<https://youtu.be/w3nvt6n1WZI>) at the 2018 CompBioMed Winter School at the Barcelona Supercomputing Centre (<https://www.compbio.med.eu/events-2/compbio-med-training-winter-school-2018-at-bsc/>).

2.3 Residence Time and Improved Clinical Efficacy

UCL and Evotec have recently formed a collaboration aimed at developing tools to address receptor–ligand residence time, funded by a FLIP Flexible Interchanger Programme research grant to Andrea Townsend-Nicholson to bring Alexander Heifetz to UCL as the flexible interchanger from industry. The keys goals of UCL–Evotec collaboration are to develop and validate a method that can: (1) rationalize the RT profile of known GPCR binders by calculating the forces that affect protein–ligand residence time; and, (2) validate this method by structure-based discovery of novel GPCR binders with long and short RT.

Drug–target residence time (RT) is the length of time that a drug stays bound to its target receptor. Long lasting (long RT) ligands are often involved in multistep binding that promotes conformational changes in receptor structure and in the water molecule network. This causes a “trapping” of the ligand inside the binding pocket, resulting in a prolonged RT. Networks of water molecules often act as a “lid” that traps the ligand inside the protein, prolonging the RT without affecting the binding affinity.

Evidence reveals that ~70% of long RT therapeutics displayed higher efficacy than comparable faster-dissociating drugs [20, 21], supporting the view that drug–target RT is of even greater importance than affinity, therapeutically. Recently several notable reviews have emphasized the pivotal role of RT optimization in the early

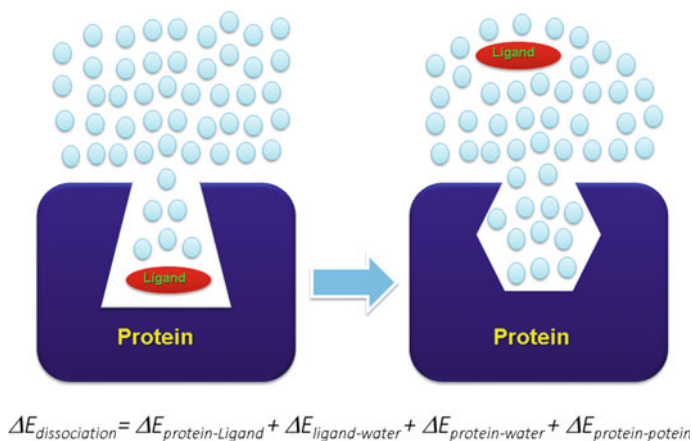


Fig. 5 Schematic description of dissociation energy terms

phases of drug discovery [22]. However, despite the clear correlation between therapeutic efficacy of drug candidates and RT, no practical method has been developed to address this crucial parameter in a rational manner.

We have adopted an integrated computational-experimental approach to developing a tool by which to calculate RT, using steered molecular dynamic (SMD) simulations to calculate the forces (dissociation energy terms, Fig. 5) involved in ligand dissociation. SMD involves applying a force to artificially “pull” the ligand out of the receptor binding site and calculating the forces that “resist” ligand dissociation as the ligand makes and breaks contacts with specific residues along its exit path. Experimental methods are applied to interrogate these residues and confirm their involvement in ligand dissociation. Iteration between computational and experimental findings allows refinement of the computational prediction of RT. Ultimately, this methodology will be used to guide the design of ligands with improved RT profiles, leading drugs with greater efficacy in the clinic.

3 Conclusions and Solutions

UCL and Evotec each have benefitted tremendously from the creation of a collaborative environment that has integrated experimental and computational biology instead of considering them as separate areas of investigation. This partnership provides a research environment with: state-of-the-art instrumentation, resources and protocols; scientific experts from pharma, biotech and academia; a multidisciplinary approach to the development of new technologies in a collaborative fashion and to the development of individuals with unique and valued skill sets; and a commitment to encouraging the timely and effective dissemination of knowledge arising from research. The resources of both partners (Evotec and UCL) have enabled the provision of

in-depth specialist training in the experimental and computational methodologies needed for the successful completion of the projects that have been jointly undertaken. This collaboration includes a multidisciplinary approach involving computational (modelling, molecular dynamic simulations, computational drug discovery, *in silico* drug-receptor docking) and experimental (recombinant receptor expression and kinetic analyses of ligand association and dissociation rates) methodologies.

Collaboration works well when the following principles are established from the outset:

1. Project objectives are defined and limited to address a specific issue.
2. Specific project goals defined and a schedule of agreed milestones are set.
3. Project goals have defined elements for each partner.
4. Both partners are involved at every stage, even if this is solely in an advisory capacity.
5. Partners are geographically close that allows face-to-face meetings.
6. Relationship building and development is included as one of the specific project goals.

This final point is particularly important. Although a collaboration, formally, is an undertaking made by the at least two partnering organizations, an individual typically drives it from each partner. Critical factors to collaborative success include the building and maintenance of a strong interpersonal relationship between these leads ensuring that time is taken in the beginning to set clear objectives and expectations. In our experience, binary relationships, such as joint supervision of a PhD student working on a mutually relevant research project can provide useful facilitators of relationship building. The mutual attention paid to the supervisor-student relationship and the clear objectives required for a Ph.D. project help drive progress equally from both sides and minimizes the risk of misunderstandings.

We also believe that close geographical proximity between the partnering institutions or collaborations is hugely beneficial to the academic-industrial partnership, especially when collaborating scientists are able to meet face-to-face on a regular basis (at least once a month). This allows project management with timely discussion and response to the recent results and planning of the next steps. Teleconferences can be very useful, but we have found that interspersing these with regular face-to-face meetings is the most effective way to drive an industrial-academic collaboration.

One of the key objectives of a successful collaboration is the dissemination of knowledge produced during the collaboration. This may take the form of conference presentations and publications in peer-reviewed journals and books. Numerous peer-reviewed publications have arisen from the collaborative endeavors described in this chapter and in 2018, a book on “Computational Methods for GPCR Drug Discovery” was published by Springer and edited by Alexander Heifetz. The chapters were authored by experts from academia and industry and describe how structure and ligand-based approaches and cheminformatics approaches can be applied to address key issues in drug discovery issues (<https://www.springer.com/gb/book/9781493974641>). In addition, an international conference sponsored by the Royal

Society, organized by Evotec (Alexander Heifetz) and focused on the topic of “GPCR Structure, Function, Drug Discovery and Crystallography” and was held in the UK on 1–2 September 2014. This conference brought together 20 renowned experts in GPCR research and drug discovery spanning Europe, Australia, and North America. Approximately half of the attendees were from academia and half from industry [23]. In 2017, leading practitioners from academia and industry presented the state of the art in binding free energy calculations at the CompBioMed/BioExcel Workshop on Free Energy Calculations From Molecular Simulation: Applications in Life and Medical Sciences.

In summary, it is extremely rewarding to see how knowledge can be translated into new and more efficient drugs, tools that address an unmet clinical need and benefit patients. This is most effectively achieved through collaborations between industry and academia. Pharmaceutical companies offer their own scientific expertise and platforms, derived from their wide experience in medicinal and computational chemistry, target related biology, structural biology, ADMET, high-throughput technologies. When this is combined with academia’s fundamental biochemistry and molecular biology, physiology and pharmacology from cellular to systems level, powerful and effective therapeutic solutions can be developed, bringing benefit to both parties and society.

Academia is reliant on industry for the medicines and technologies that it uses to take care of patients. Conversely, industry is reliant on academia for the vast basic research laboratories and hospitals that are needed to bring a drug to market. In a way, academia and the pharmaceutical industry are co-dependent enterprises seeking to bring benefit to the health of patients. Both industry and academia need to identify and address biases and difficulties that impede collaboration between them in order to work effectively and synergistically together. Our experience has shown that this can be achieved, bringing benefit for both partners.

We would like to finish this review with the wise words of Michael Rosenblatt [1] “*I think the secret of a true partnership is acting like you have a true partner. This applies to both academia and industry. We need to partner for the sake of modern medicine; we need to do it for the sciences fundamental to medicine; and most of all, we need to do it for our patients*”.

References

1. Rosenblatt M (2013) How academia and the pharmaceutical industry can work together: the president’s lecture, annual meeting of the American Thoracic Society, San Francisco, California. *Ann Am Thorac Soc* 10:31–38
2. Stott K (2017) Pharma’s broken business model: an industry on the brink of terminal decline, *Biotech Voices*, R&D 2017. <https://endpts.com/pharmas-broken-business-model-an-industry-on-the-brink-of-terminal-decline/>

3. Ridyard D (2016) Guidelines for successful industry-academic collaboration. <https://www.execrank.com/board-of-directors-articles/guidelines-for-successful-industry-academic-collaboration>
4. Dasgupta A (2017) Finding the right fit in academia and industry collaboration. <https://www.geospatialworld.net/article/expectations-in-academia-and-industry-collaboration/>
5. Heifetz A, Aldeghi M, Chudyk EI, Fedorov DG, Bodkin MJ, Biggin PC (2016) Using the fragment molecular orbital method to investigate agonist-orexin-2 receptor interactions. *Biochem Soc Trans* 44:574–581
6. Chudyk EI, Sarraf L, Aldeghi M, Fedorov DG, Bodkin MJ, James T, Southey M, Robinson R, Morao I, Heifetz A (2018) Exploring GPCR-ligand interactions with the fragment molecular orbital (FMO) Method. *Methods Mol Biol* 1705:179–195
7. Heifetz A, Trani G, Aldeghi M, MacKinnon CH, McEwan PA, Brookfield FA, Chudyk EI, Bodkin M, Pei Z, Burch JD, Ortwin DF (2016) Fragment molecular orbital method applied to lead optimization of novel Interleukin-2 Inducible T-cell kinase (ITK) inhibitors. *J Med Chem* 59:4352–4363
8. Barker JJ, Barker O, Courtney SM, Gardiner M, Hesterkamp T, Ichihara O, Mather O, Montalbetti CA, Muller A, Varasi M, Whittaker M, Yarnold CJ (2010) Discovery of a novel Hsp90 inhibitor by fragment linking. *ChemMedChem* 5:1697–1700
9. Heifetz A, Chudyk EI, Gleave L, Aldeghi M, Cherezov V, Fedorov DG, Biggin PC, Bodkin MJ (2016) The fragment molecular orbital method reveals new insight into the chemical nature of GPCR-ligand interactions. *J Chem Inf Model* 56:159–172
10. Morao I, Fedorov DG, Robinson R, Southey M, Townsend-Nicholson A, Bodkin MJ, Heifetz A (2017) Rapid and accurate assessment of GPCR-ligand interactions using the fragment molecular orbital-based density-functional tight-binding method. *J Comput Chem* 38:1987–1990
11. Venkatakrishnan AJ, Deupi X, Lebon G, Heydenreich FM, Flock T, Miljus T, Balaji S, Bouvier M, Veprintsev DB, Tate CG, Schertler GF, Babu MM (2016) Diverse activation pathways in class A GPCRs converge near the G-protein-coupling region. *Nature* 536:484–487
12. Venkatakrishnan AJ, Deupi X, Lebon G, Tate CG, Schertler GF, Babu MM (2013) Molecular signatures of G-protein-coupled receptors. *Nature* 494:185–194
13. Hauser AS, Attwood MM, Rask-Andersen M, Schioth HB, Gloriam DE (2017) Trends in GPCR drug discovery: new agents, targets and indications. *Nat Rev Drug Discov* 16:829–842
14. Heifetz A, Storer RI, McMurray G, James T, Morao I, Aldeghi M, Bodkin MJ, Biggin PC (2016) Application of an integrated GPCR SAR-modeling platform to explain the activation selectivity of human 5-HT_{2C} over 5-HT_{2B}. *ACS Chem Biol* 11:1372–1382
15. Heifetz A, Barker O, Morris GB, Law RJ, Slack M, Biggin PC (2013) Toward an understanding of agonist binding to human Orexin-1 and Orexin-2 receptors with G-protein-coupled receptor modeling and site-directed mutagenesis. *Biochemistry* 52:8246–8260
16. Heifetz A, Barker O, Verquin G, Wimmer N, Meutermans W, Pal S, Law RJ, Whittaker M (2013) Fighting obesity with a sugar-based library: discovery of novel MCH-1R antagonists by a new computational-VAST approach for exploration of GPCR binding sites. *J Chem Inf Model* 53:1084–1099
17. Heifetz A, Morris GB, Biggin PC, Barker O, Fryatt T, Bentley J, Hallett D, Manikowski D, Pal S, Reifegerste R, Slack M, Law R (2012) Study of human Orexin-1 and -2 G-protein-coupled receptors with novel and published antagonists by modeling, molecular dynamics simulations, and site-directed mutagenesis. *Biochemistry* 51:3178–3197
18. Storer RI, Brennan PE, Brown AD, Bungay PJ, Conlon KM, Corbett MS, DePianta RP, Fish PV, Heifetz A, Ho DK, Jessiman AS, McMurray G, de Oliveira CA, Roberts LR, Root JA, Shanmugasundaram V, Shapiro MJ, Skerten M, Westbrook D, Wheeler S, Whitlock GA, Wright J (2014) Multiparameter optimization in CNS drug discovery: design of pyrimido[4,5-d]azepines as potent 5-hydroxytryptamine 2C (5-HT_{2C}) receptor agonists with exquisite functional selectivity over 5-HT_{2A} and 5-HT_{2B} receptors. *J Med Chem* 57:5258–5269

19. Tye H, Mueller SG, Prestle J, Scheuerer S, Schindler M, Nosse B, Prevost N, Brown CJ, Heifetz A, Moeller C, Pedret-Dunn A, Whittaker M (2011) Novel 6,7,8,9-tetrahydro-5H-1,4,7,10a-tetraaza-cyclohepta[f]indene analogues as potent and selective 5-HT(2C) agonists for the treatment of metabolic disorders. *Bioorg Med Chem Lett* 21:34–37
20. Vauquelin G (2015) On the ‘micro’-pharmacodynamic and pharmacokinetic mechanisms that contribute to long-lasting drug action. *Expert Opin Drug Discov* 1–14
21. Guo D, Hillger JM, AP IJ, Heitman LH (2014) Drug-target residence time--a case for G protein-coupled receptors, *Med Res Rev* 34:856–892
22. Potterton A, Hussein FS, Southey MW, Bodkin MJ, Heifetz A, Coveney PV, Townsend-Nicholson A (2019) Ensemble-based steered molecular dynamics predicts relative residence time of A2A receptor binders. *J Chem Theory Comput*
23. Heifetz A, Schertler GF, Seifert R, Tate CG, Sexton PM, Gurevich VV, Fourmy D, Cherezov V, Marshall FH, Storer RI, Moraes I, Tikhonova IG, Tautermann CS, Hunt P, Ceska T, Hodgson S, Bodkin MJ, Singh S, Law RJ, Biggin PC (2015) GPCR structure, function, drug discovery and crystallography: report from Academia-Industry International Conference (UK Royal Society) Chicheley Hall, 1–2 September 2014. *Naunyn Schmiedebergs Arch Pharmacol* 388:883–903

Elucidating the Efficacy of Clinical Drugs Using FMO



Sundaram Arulmozhiraja, Hiroaki Tokiwa, and Hitoshi Shimano

Abstract It is known that first-principles based fragment molecular orbital (FMO) theory can be used to study protein–ligand interactions quantitatively. This includes obtaining amino acid residue-wise interactions with the ligand and detailed interaction components such as electrostatic, dispersion, charge-transfer, and exchange-repulsion. This chapter discusses the ability of FMO calculations on elucidating the efficacy of the clinical drugs that are available in the market. For this purpose, two kinds of clinical drugs, dipeptidyl peptidase IV (DPP-4) inhibitors (sitagliptin, linagliptin, alogliptin, teneligliptin, omarigliptin, and trelagliptin) and peroxisome proliferator-activated receptor- α (PPAR α) modulators (fenofibrate and pemafibrate), were considered. The FMO calculations on relevant protein-drug complexes were made at the correlated Resolution-of-Identify second-order Moller Plesset (RI-MP2) level of theory utilizing correlation consistent double-zeta (cc-pVDZ) basis set. The results discussed here clearly reveal that interfragment interaction energies obtained using FMO calculations correlate significantly with the activity of the drugs and hence the activity of the drugs can be positively identified through FMO calculations. The results presented here further encourages that this novel calculation approach can be used for other types of drugs too to study the efficacy of the clinical as well as potential drugs.

S. Arulmozhiraja (✉) · H. Tokiwa

Department of Chemistry, Rikkyo University, 3-34-1 Nishi-Ikebukuro, Toshima, Tokyo 171-8501, Japan

e-mail: raja@rikkyo.ac.jp

H. Shimano

Department of Internal Medicine (Endocrinology and Metabolism), Faculty of Medicine, University of Tsukuba, Tsukuba, Ibaraki 305-8575, Japan

International Institute for Integrative Sleep Medicine (WPI-IIIS), University of Tsukuba, Tsukuba Ibaraki 305-8575, Japan

Life Science Center for Survival Dynamics, Tsukuba Advanced Research Alliance (TARA), University of Tsukuba, Tsukuba Ibaraki 305-8577, Japan

AMED-CREST, Japan Agency for Medical Research and Development (AMED), 1-7-1, Ohte-machi, Chiyoda-ku, Tokyo 100-0004, Japan

© Springer Nature Singapore Pte Ltd. 2021

Y. Mochizuki et al. (eds.), *Recent Advances of the Fragment Molecular Orbital Method*, https://doi.org/10.1007/978-981-15-9235-5_16

323

Keywords FMO calculations · Efficacy of clinical drugs · Interfragment interaction energies · Dipeptidyl peptidase IV (DPP-4) inhibitors · Peroxisome proliferator-activated receptor- α (PPAR α)

1 Introduction

The drug's action is mainly affected by two factors: (1) the quantity of drug that reaches the target receptor protein and (2) the degree of affinity between it and its target receptor. The other important factor is the intrinsic activity, the ability to produce an effect after bound to the receptor, of the drug. Drugs that activate receptor, agonists, must have both large binding affinity and intrinsic activity. They must bind effectively to their target proteins, and the protein-drug complex must be capable of producing an effect in the targeted area. On the other hand, drugs that block activity of receptors, antagonists (inverse agonist), must bind effectively but have little or no intrinsic activity because their function is to prevent an agonist from interacting with its receptors. Therefore, the binding affinity, to the target protein, is an important and essential quality of a potential drug candidate. Potency (amount of drug needed to produce an effect) and efficacy (drug's capacity to produce an effect) are the two indicators through which a drug's effects can be evaluated. These two indicators have good correspondence with the affinity and hence the binding affinity is a critical tool to analyze the potency and efficacy of the drugs. Because of this, researchers aspire to evaluate the binding affinity of the drugs or potential drug candidates to understand their potency or efficacy.

Computationally, quantum mechanical (QM) calculations are essential to study the protein–ligand complexes as they exhibit various non-bonding interactions, such as π -stacking (π - π and CH- π), charge-transfer, polarization dispersion, and classical as well as non-classical (weak) hydrogen bonding interactions. So, one can understand theoretical chemists' strong desire to apply QM methods to biological systems as they can bring an improved representation to these systems and because of this improved knowledge, novel insights of the biomolecules can be understood. Among a few existing approaches to accomplish this task, fragmentation method occupies a significant place [1]. First-principles calculations-based fragment molecular orbital (FMO) QM method developed by Kitaura and co-workers [2–4] is an excellent method to study large systems such as proteins in a reliable way. By introducing electrostatic potential in the many-body expansion, Kitaura et al. [2] were able to incorporate many-body effects in the framework of a two-body expansion. In this fragmentation method, the system is divided into fragments, for example, protein is divided into amino acid fragments (each amino acid is considered as a fragment), and the conventional molecular orbital or density functional theory (DFT) calculations are performed for each fragment and fragment pair. The total properties of the protein are derived in a many-body expansion by combining the properties of fragments and fragment pairs. Because of this, obtaining accurate protein–ligand binding affinity,

which is of significant importance in drug discovery becomes greatly possible using FMO method.

High-level *ab initio*, say correlated, FMO calculations can provide not only the reliable binding energy between the ligand and the protein but also a complete list of the interactions forged between the ligand and protein components quantitatively and so it is very much suitable for studying the protein–ligand complexes with confidence and hence it has been successfully applied to study a lot of protein–ligand interactions by consistently evaluating their binding energies [5–12]. Particularly, FMO was used to predict cyclin-dependent kinase 2 inhibitor potency [13], to compare experimentally measured potencies/activities of the ligands of FK506 protein [5] and of FABP4 [14], for potency calculations on a novel Hsp90 fragment-linked inhibitor [15], to lead optimization of ITK inhibitors [6], to study the inhibitor activity of sialic acid analogues and anti-influenza drugs toward hNEU2 [16], to discover antiprion compounds [17].

This chapter details the ability of FMO calculations on analyzing the efficacy of the clinical drugs that are available in the market by considering two of our recent works: dipeptidyl peptidase IV (DPP-4) inhibitors and peroxisome proliferator-activated receptor- α (PPAR α) modulators [18, 19].

2 Theoretical Background and Methods

As the fragmentation method FMO treats the whole biomolecular system as a combination of fragments, QM calculations can be performed for the large system with much reduced computational cost. FMO method fragments the large molecular system so that molecular orbitals (MOs) of the fragments and fragment pairs, instead of the whole system, are computed. Thus, the FMO computation's dependence on system size (N) is reduced to $O(N^2)$, as opposed to $O(N^{3-4})$ with conventional MO methods.

In the FMO method, the total properties of a large system, say protein, are derived in a many-body expansion by combining the properties of the fragments. Ligand can be considered as a fragment in a protein–ligand complex. Each fragment is allowed to interact with all other fragments. In the first step, each monomer (fragment) is calculated in the Coulomb field exerted by all remaining monomers. This changes monomer electron densities and hence the Coulomb field they determine. Thus, the monomer calculations are repeated self consistently, and the converged monomers are polarized by the whole system. In the second step, each dimer (fragment pair) is computed in the Coulomb field exerted by all remaining monomers. By subtracting the energies of the two monomers from a dimer energy, interaction energy between the monomers can be obtained. This continues according to the order of FMO. The total energy of the whole system is calculated by summing up the total energy of the fragment monomers, dimers, trimers, and so on, as shown in the following relation.

$$E_{\text{total}} = E_{\text{total}}^{\text{FMO1}} + \Delta E_{\text{total}}^{\text{FMO2}} + \Delta E_{\text{total}}^{\text{FMO3}} \dots$$

If the total energy expansion is truncated with two-body (second-order FMO), or three-body (third-order FMO) terms, the following equations are obtained, respectively.

$$E_{\text{total}}^{\text{FMO2}} = \sum_I E_I + \sum_{I>J} (E_{IJ} - E_I - E_J),$$

$$E_{\text{total}}^{\text{FMO3}} = E_{\text{total}}^{\text{FMO2}} + \sum_{I>J>K} \{(E_{IJK} - E_I - E_J - E_K) - (E_{IJ} - E_I - E_J) - (E_{JK} - E_J - E_K) - (E_{IK} - E_I - E_K)\},$$

where E_I is the total energy of the fragment I , E_{IJ} is the total energy of the dimer comprising fragments I and J , and E_{IJK} is the total energy of the trimer comprising fragments I , J , and K . In a conventional way, the binding energy of the ligand could be derived using the following relation:

$$\Delta E_{\text{ligand}} = E_{\text{complex}} - (E_{\text{receptor}} + E_{\text{ligand}}),$$

where E_{ligand} , E_{receptor} , and E_{complex} are the energy of the ligand, receptor, and complex, respectively.

In the two-body method, fragments and their dimers are calculated. The calculated interfragment interaction energies (IFIEs) are used to analyze the molecular recognition of ligands by proteins. The IFIE between any two fragments calculated by FMO is a sum of four energy terms: electrostatics, exchange-repulsion, charge-transfer, and dispersion. The electrostatic and charge-transfer terms are important for hydrogen bonding, polar interaction, and salt bridges. Dispersion term becomes prominent in hydrophobic interactions. The exchange-repulsion energy term describes steric repulsion between electrons, which prevents atoms from clashing with each other. The overall binding energy of the ligand in a protein–ligand complex can be estimated by summing up the IFIEs obtained between the ligand and all the residues. It should be mentioned however that IFIE is not the difference between the energy of the protein–ligand complex and the sum of the energies of the “free” protein and ligand rather it represents the “strength” of the interactions between the ligand and protein residues in the complex. The total IFIE, summation of all the IFIEs, describe the stability of the protein–ligand complex. This stability correlates with, but is not the same as, the binding energy. This overall binding energy between the ligand and protein can be related to the resultant biological potency of the compound as measured in a biological assay.

The present ab initio FMO calculations were made using the PAICS program [20] to calculate the binding energies between the target proteins and the clinical drugs considered in the present study. The FMO calculations were performed at the correlated Resolution-of-Identify second-order Moller Plesset (RI-MP2) level of theory [21–23] utilizing correlation consistent double-zeta (cc-pVDZ) basis set [24].

In this chapter, we classified the interaction energy mainly as electrostatic and dispersion (van der Waals) energies. Since dispersion is more hydrophobic in nature, we refer dispersion energy as hydrophobic energy in places. The Hartree–Fock (HF) term in the calculated interaction energy represents the electrostatic interaction (noted as “HF-IFIE”) while the remaining MP2 correlation energy (Δ MP2) approximately denotes the dispersion term (noted as “ Δ MP2-IFIE”). These representations were followed throughout this chapter and the calculated IFIEs were utilized for analyzing the protein-drug binding.

3 Sample Cases

3.1 Case 1: DPP-4 Inhibitors

Diabetes is a group of metabolic diseases and data shows that more than 425 million people have diabetes at present worldwide and unfortunately this number may rise to 700 million in 2045 [25]. In 2017, diabetes was responsible for 4 million deaths, even after spending USD727 billion on diabetes treatment and related complications, and it is expected to double between 2005 and 2030 and become seventh leading cause of death by 2030 [25, 26].

One of the recently developed methods to treat type 2 diabetes is the inhibition of DPP-4. Technically, oral intake of food into gastrointestinal track (GIT) releases incretin hormones such as glucagon-like peptide-1 (GLP-1) and glucose-dependent insulinotropic polypeptide (GIP). These incretins stimulate insulin secretion from pancreatic β -cells. GLP-1 suppresses glucagon production from α -cells when the glucose level is elevated (Fig. 1) [27, 28]. However, these incretins are degraded by the serine protease dipeptidyl peptidase IV (DPP-4) enzyme, causing increase in blood sugar level (a typical example for type 2 diabetes mellitus). Hence, inhibiting DPP-4 actions is a way to tackle type 2 diabetes by indirectly activating insulin secretion without hypoglycemia and this becomes an established approach in recent years [29].

There are twelve DPP-4 inhibitor drugs—sitagliptin, vildagliptin, saxagliptin, alogliptin, linagliptin, teneligliptin, gemigliptin, anagliptin, omarigliptin, trelagliptin, evogliptin, and gosogliptin—available in the market to date for the treatment of type 2 diabetes (Fig. 2) [30]. Various good combination of medicines came out in the recent years but still there are many single medicines and sulfonylurea/metformin combination medicines. Many of these DPP-4 inhibitor drugs are used with metformin/sulfonylurea, well-known drugs for the treatment of type 2 diabetes, concomitantly with additive effect to increase GLP-1, which also effectively decrease glucose production. These gliptins therefore are used as second line therapy after metformin.

The FMO calculations performed on six selected gliptins (sitagliptin, linagliptin, alogliptin, teneligliptin, omarigliptin, and trelagliptin) complexed with DPP-4 are

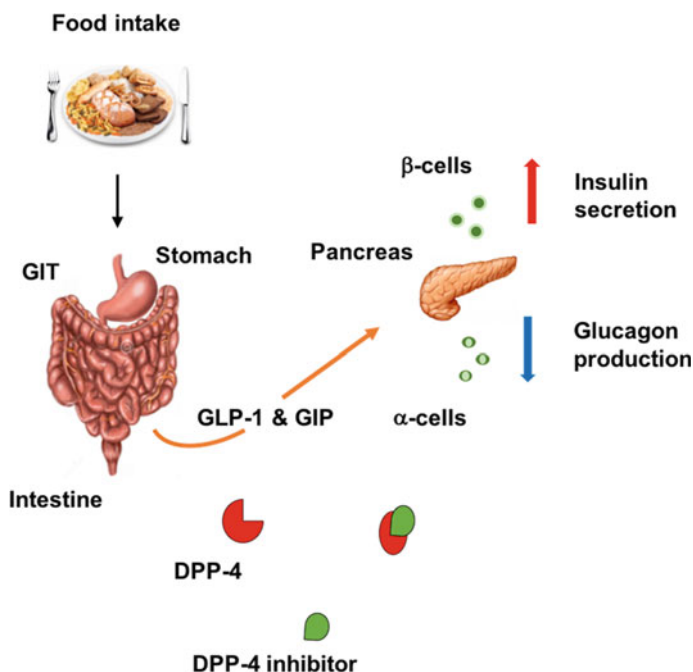


Fig. 1 Schematic mechanism of insulin production and DPP-4 inhibitor action

discussed here. X-ray cocrystal structures of DPP-4 with these inhibitors [sitagliptin (PDB ID: 1X70) [31], linagliptin (2RGU) [32], alogliptin (3G0B) [33] teneligliptin (3VJK) [34], Omarigliptin (4PNZ) [35], and trelagliptin (5KBY) [36] were taken from the Protein Data Bank.

Binding mode of the selected DPP-4 inhibitors in the active site of the DPP-4 is depicted in Fig. 3. Previous protocols [37] are used in defining the subsites S_2 , S_1 , S'_1 , and S'_2 . Additionally, the site beyond S_2 that involves in the interaction is defined as S_2 extensive subsite (S_2 ext.) as denoted by Nabeno et al. [38]. The figure indicates that all the gliptins interact with S_1 , S_2 , and S'_1 subsites. In addition to these interactions, alogliptin, linagliptin, and trelagliptin (class II group) interacts with S'_2 subsite and while sitagliptin, teneligliptin, and omarigliptin (class III group) interacts with S_2 extensive subsite. Overall, all the inhibitors reside in the hydrophobic cavity made up of Arg125, Glu205, Glu206, Tyr547, Tyr662, Tyr666, Ser630, and Phe357.

According to the available experimental studies [38, 39], linagliptin is known as the most active inhibitor and the sitagliptin is the least one. The aim here is to understand whether one can get the idea about the activity/efficacy of the drugs through FMO calculations. The calculated interaction energies, i.e., interfragment interaction energies, obtained between the selected inhibitor drugs and amino acid residues of the DPP-4 that are significantly involving in the interactions are given in Fig. 4. In line with the existing evidences, the FMO calculations indicate that the largest contribution of the interaction comes from the electrostatic interactions with the carboxyl

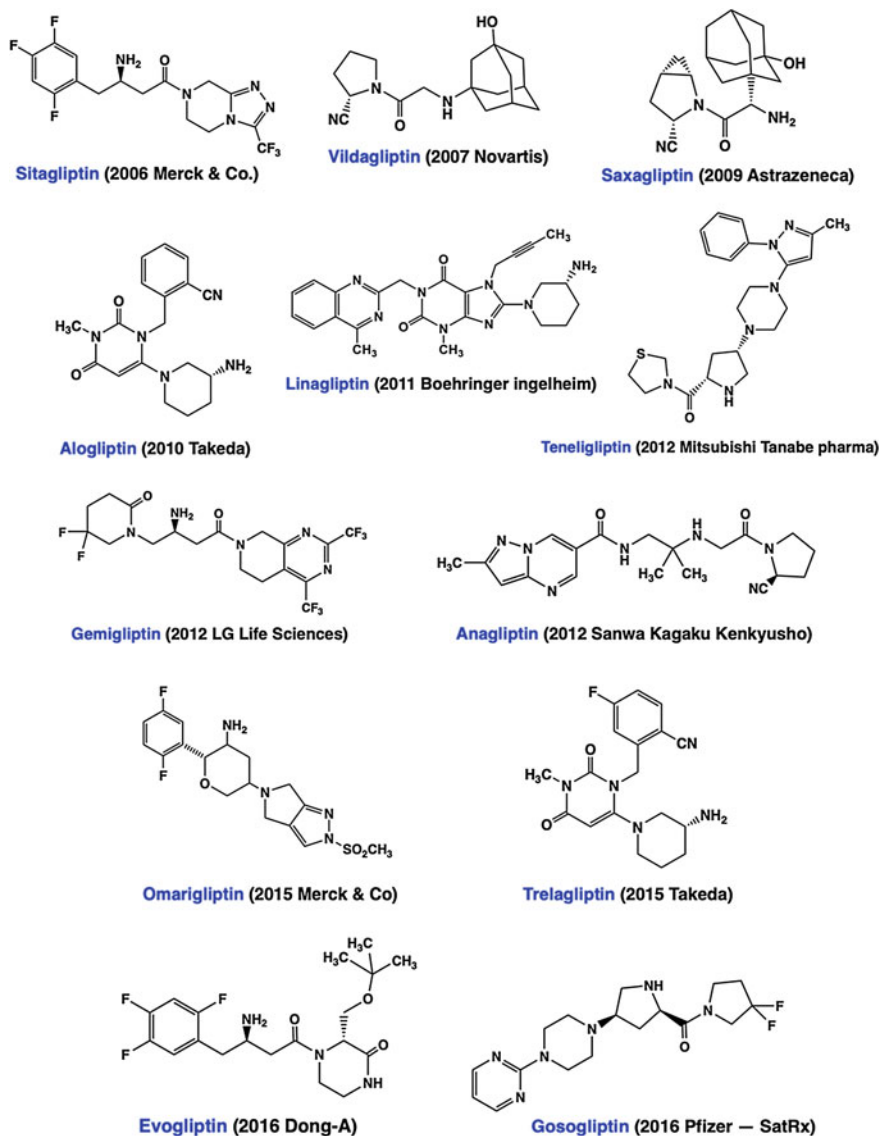


Fig. 2 DPP-4 inhibitor drugs available in the market

group of Glu205 and Glu206—these two amino acids in the S_2 subsite form salt bridges (in fact hydrogen bonding interaction is also involved with these charge-charge interactions) with the amino group of all the DPP-4 inhibitors. However, the results reveal that the electrostatic interaction (HF-IFIE) between the inhibitors and DPP-4 is not an indicator of the activity of the DPP-4 inhibitor drugs—HF-IFIEs

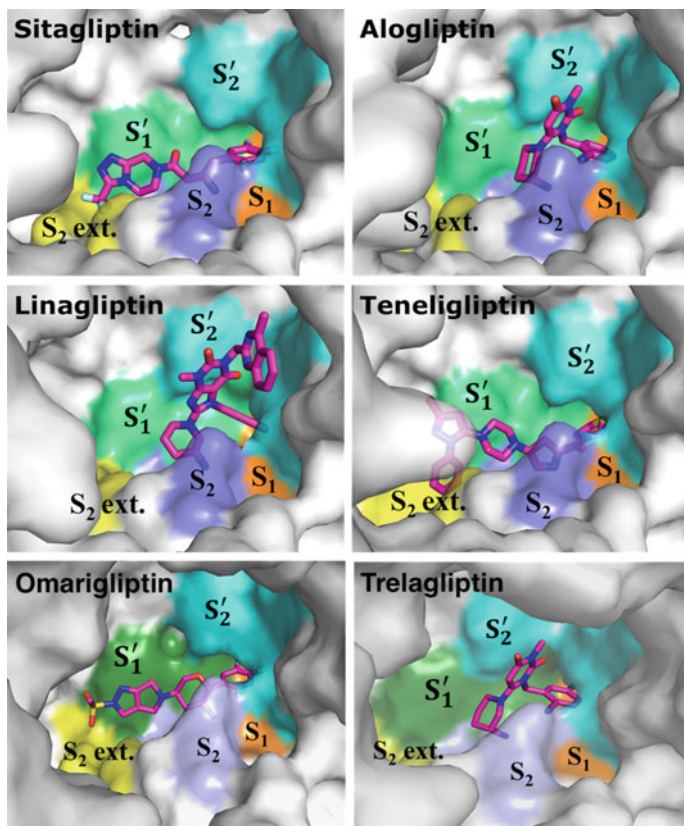


Fig. 3 Binding modes of each inhibitor drug in the active site of DPP-4. S_1 subsite consists of Ser630, Val656, Trp659, Tyr662, Tyr666, Val711, and Asn710; S_2 subsite consists of Arg125, Phe357, Arg358, Glu205, Glu206, and Arg669; S'_1 subsite consists of Phe357, Tyr547, Pro550, Ser630, Tyr631, and Tyr666; S'_2 subsite consists of Tyr547, Trp629, Ser630, and His740; and S_2 ext. (S_2 extensive) subsite consists of Val207, Ser209, Phe357, and Arg358

calculated for the least active sitagliptin is the largest. So it is clear that though electrostatic interactions play the important role in the inhibitor-DPP-4 interactions, they are unable to indicate the activity of the inhibitor drugs.

On the other hand, hydrophobic interactions (Δ MP2-IFIEs) give a different picture. It should be mentioned here that almost all the interactions, other than the interactions with Glu205 and Glu206 amino acids, are mostly due to hydrophobic interactions. All the three class II type gliptins have significant interactions at S'_2 , S'_1 , and S_1 subsites, especially, the strongest ones are with tryptophan 629 and tyrosine 547. Interestingly, the most active linagliptin has the strongest interactions with these two residues—this inhibitor strongly interacts with Tyr547 through its uracil moiety (by forming a π - π stacking interaction) as well as via its imidazole group (by forming OH- π interaction); its methylquinazolinone moiety interacts strongly

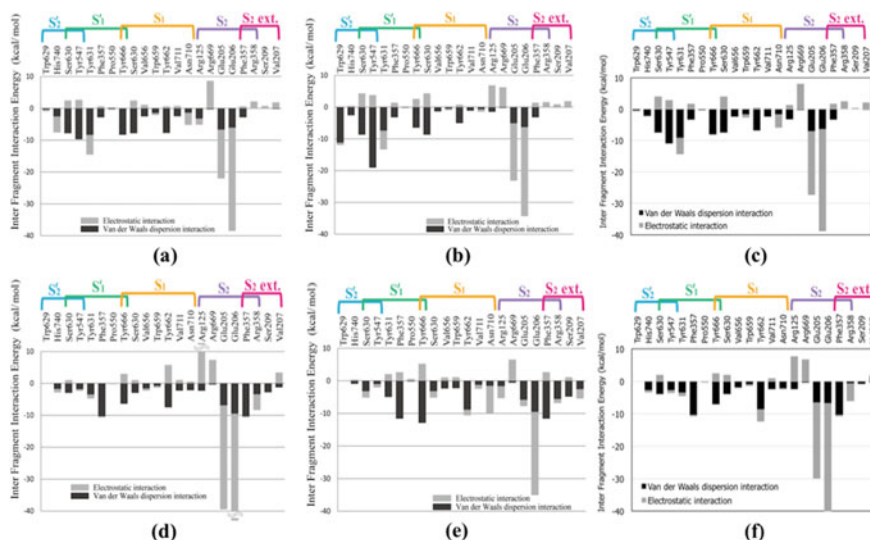


Fig. 4 Significant interfragment interaction energies (IFIEs) obtained between amino acid residues at the active site of DPP-4 and the inhibitors: **a** alogliptin, **b** linagliptin, **c** trelagliptin, **d** sitagliptin, **e** teneligliptin, and **f** omarigliptin. Gray and black bars represent electrostatic (HF-IFIE term) and van der Waals interaction (Δ MP2-IFIE term) energies, respectively

with Trp629 through both with π - π stacking interaction as well as with CH- π interaction. As noticed from the calculated IFIEs (Fig. 4), most active linagliptin has the strongest interactions with these two residues. The three class III type gliptins have strong interactions at S_2 extensive, S_1 , and S_1 subsites. Here too, the highly active teneligliptin has stronger interactions in these regions when compared with the other two gliptins. The main interactions of teneligliptin are with Tyr666 and Phe357—while thiazoline moiety of this inhibitor forms a CH- π interaction with Tyr666, its piperazine moiety interacts with Phe357 through a CH- π interaction. These results indicate that hydrophobic interactions may reflect the activity of the DPP-4 inhibitors. Detailed analysis indicates that strong hydrophobic interactions at S_2 , S_2 extensive, and S_1 subsites, especially the interactions at S_2 subsite, are crucial for an efficient DPP-4 inhibitor drug.

Next, the calculated hydrophobic interaction energies (sum of the all Δ MP2-IFIEs) of the inhibitors are compared with the experimental binding energies and potencies to understand whether there is any relationship between them. For this comparison, four inhibitors are considered because experimental results at same conditions are available only for these four inhibitors (Fig. 5) [38, 39]. Notably, the calculated hydrophobic IFIEs (Δ MP2-IFIEs) have a good correlation, R^2 of 0.85, with the experimental inhibitory activities (pIC₅₀) [38], Fig. 5a. Comparing the calculated hydrophobic IFIEs (Δ MP2-IFIEs) with the recently observed experimental binding affinities (K_D) of these four selected inhibitors indicate a significant correlation, R^2 of 0.69 (Fig. 5b).

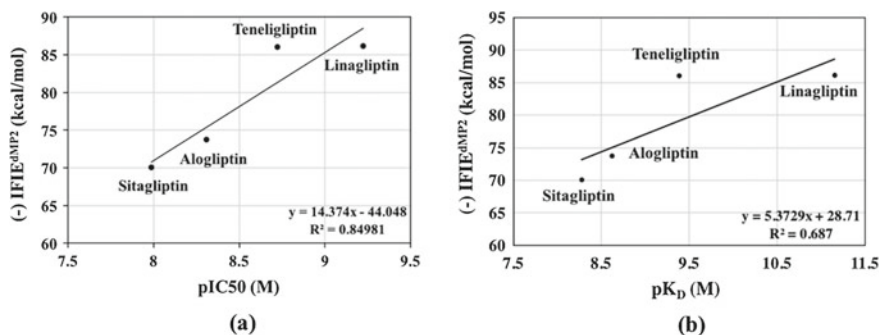
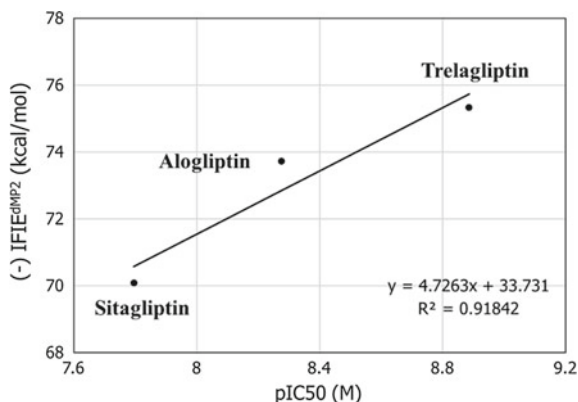


Fig. 5 Correlation between sum of the all hydrophobic IFIEs ($\Delta MP2$ -IFIEs), calculated between the inhibitor drugs with the DPP-4, and **a** experimental inhibitor activity [pIC_{50}] (taken from Ref. [37]) and **b** experimental binding affinity [pK_D] of the inhibitors from surface plasmon resonance data (taken from Ref. [38])

Fig. 6 Correlation between sum of the all hydrophobic IFIEs ($\Delta MP2$ -IFIEs), calculated between the inhibitors drugs (sitagliptin, alogliptin, and trelagliptin) with the DPP-4, and the experimental inhibitor activities [pIC_{50}] (taken from Ref. [35])



A recent experimental study [36] compared the inhibitor activity of the newly developed trelagliptin with two other gliptins (sitagliptin and alogliptin) and found that trelagliptin is more potent than the other two. The calculated IFIEs corroborate well with the experimental conclusion that trelagliptin is more potent than the other two gliptins, sitagliptin and alogliptin (Fig. 6). All these correlations clearly show the relationship between the calculated FMO-IFIEs and the inhibitor potencies of the DPP-4 inhibitors.

3.2 Case 2: PPAR α Modulators

Lipid metabolism-related proteins are attracting a lot of attention as important targets for novel drug development of chemical treatment of hyperlipidemia in diabetes.

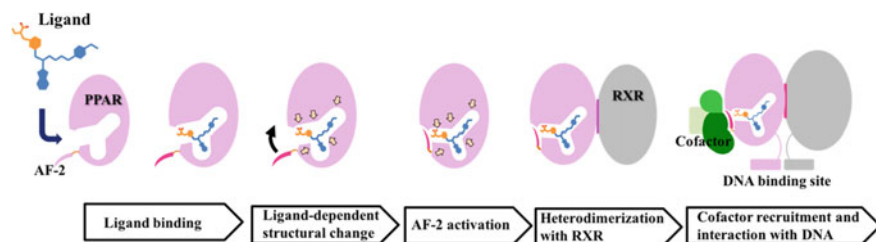


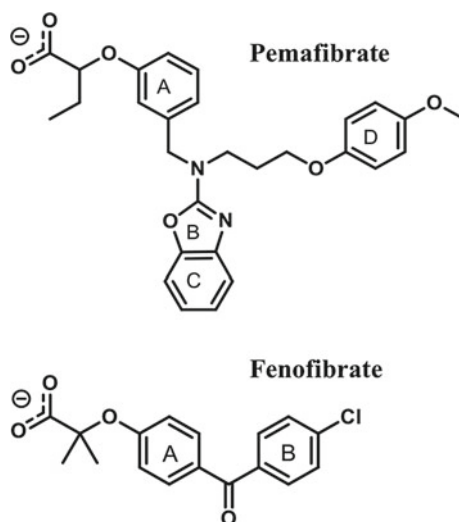
Fig. 7 Schematic diagram of PPAR α activation by an agonistic ligand

Peroxisome proliferator-activated receptor- α (PPAR α), Sterol receptor element-binding protein (SREBP), and Elongation of very long-chain fatty acids proteins (Elovl) family are closely related with signaling mechanisms of fatty acids [40]. PPAR α is a ligand-activated transcription factor involved in the regulation of lipid homeostasis and improves hypertriglyceridemia to reduce cardiovascular risks. The PPAR structure is composed of a variable N-terminal domain harboring a ligand-independent activation function, a conserved DNA-binding domain (DBD), and a C-terminal ligand binding domain (LBD), which contains the ligand-dependent activation function 2 (AF-2) [41]. Activation of PPAR α by its agonists triggers conformational changes in PPAR α , including stabilization of the extreme C-terminal Helix 12 (AF-2 interface) to an active position, and enhances heterodimerization with the retinoid X receptor α (RXR α) [42], promoting recruitment of nuclear coactivators and ultimately interacts with DNA-binding sites designed as PPAR response elements to regulate target gene transcription (Fig. 7) [43]. As PPARs involve in transcription of genes related to the cellular proliferation and differentiation, immune responses and metabolism of carbohydrates and lipids, they are targeted for the treatment of diabetes, dyslipidemia, metabolic diseases, and to prevent other related diseases including cardiovascular events. Thus, PPAR agonists can be considered as drugs to treat diabetes and metabolic syndrome.

Hypolipidemic fibrate-class drugs are popular among the identified ligands for PPAR α [44–46]. Fibrates such as gemfibrozil, bezafibrate, and fenofibrate decrease plasma triglyceride (TG) and increase high-density lipoprotein (HDL) cholesterol levels in patients with types 2 diabetes and dyslipidemia, and prevent coronary heart disease and stroke. However, fibrates have some dose related adverse effects. Meanwhile, pemafibrate (Fig. 8), a newly identified novel selective PPAR α modulator, is found to have high PPAR α activity and specificity, and showed robust TG-lowering effects with elevated TG and low HDL cholesterol [47, 48]. Earlier studies also revealed that pemafibrate has higher transcription efficacy and less side effects than clinically used fibrates [49–51].

Here, FMO studies on pemafibrate and fenofibrate (a well-known fibrate-class drug to reduce cholesterol level), Fig. 8, complexed with PPAR α are detailed. Since the experimental structures of the pemafibrate- and fenofibrate-bound PPAR α are not available, the structures were obtained using *in silico* molecular simulation combined

Fig. 8 Structures of pemaifibrate and fenofibrate



with quantum-mechanics/molecular-mechanics (QM/MM) calculations [19]. These newly constructed structures were used for the FMO calculations.

The constructed complex structures are depicted in Fig. 9. As shown in the figure, all the three pharmacophores of pemaifibrate binds well with the three regions of the binding domain of PPAR α . This seems to give it an advantage over the smaller fenofibrate in the binding to PPAR α .

The FMO-IFIEs calculated for the significant interactions are given in Fig. 10. The calculated IFIEs clearly indicate that pemaifibrate interacts strongly with the ligand binding domain (LBD) than by fenofibrate. Though it is partially due to the fact that the former interacts with all the three regions of the LBD, while the latter does it mainly with one region of the LBD because of its size, pemaifibrate interacts strongly even to the region where the interaction pattern of both drugs with their COO⁻ group is qualitatively same. In both the complexes, the acidic COO⁻ group

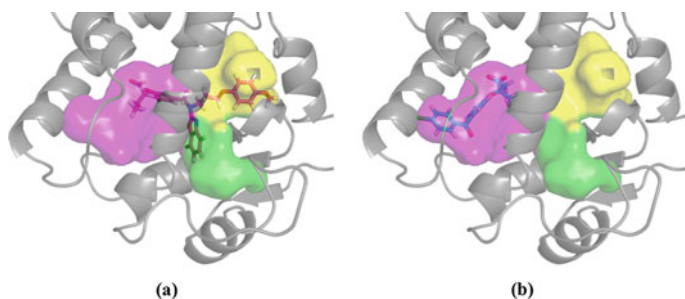


Fig. 9 Binding modes of **a** pemaifibrate and **b** fenofibrate drugs in the binding pocket of PPAR α . The binding domain is divided into three pharmacophore regions

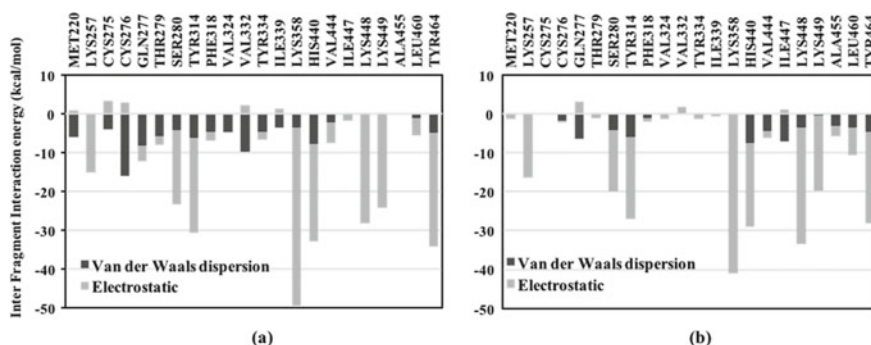


Fig. 10 Important IFIEs obtained between amino acid residues at the binding pocket of PPAR α and the PPAR α modulators: **a** pemafibrate and **b** fenofibrate. Gray and black bars represent electrostatic (HF-IFIE) and van der Waals interaction (Δ M_{P2}-IFIE) energies, respectively

forms a strong hydrogen bonding network by forming hydrogen bonds with Ser280, Tyr314, His440, and Tyr464. As it is clear from Fig. 10, all these four hydrogen bonds are stronger in pemafibrate-bound PPAR α than in fenofibrate-bound PPAR α .

All these FMO results show that pemafibrate binds strongly with the LBD of PPAR α than by fenofibrate. This correlates well with the fact that pemafibrate has higher activity and transcriptional efficacy than fenofibrate [19, 47–51]. Thus it can be fairly said that FMO-IFIEs can be used to investigate the activity/efficacy of the clinic drugs.

4 Concluding Remarks

Understanding the efficacy of the drugs/potential drug candidates is highly important and here the efficacy of the clinical drugs (DPP-4 inhibitors and PPAR α modulators) is analyzed by using first-principle based FMO theory. The results presented here clearly indicate that activity of the drugs can be positively identified through FMO calculations. In both cases, better drugs fit better in the whole space of their target pockets that IFIEs well depict, especially highlighting importance of integration of small hydrophobic interactions. So, the results are interesting and they are a nice example for this novel calculation approach that could also be used for other types of drugs.

It should be mentioned here that to derive the accurate binding affinities involving proteins, of course, physiological condition should be considered. Then it is necessary to consider solvent effects, entropic effects, and dynamic effects, in addition to the binding energies (referred in this chapter) calculated in the gas phase. Obviously, destabilization polarization and desolvation energies of the fragments should be considered. Despite the fact that not all these factors are accounted in these gas-phase

studies, the correlation obtained between the experimental and calculated binding affinities should be considered as a significant one.

A complete FMO method that incorporates all the above-mentioned effects such as solvent, entropic, conformational stabilization effects can not only be integrated into the structure-based drug discovery program for the reliable quantitative estimation of ligand binding affinity, but also can be used to study the efficacy of the clinical drugs.

Acknowledgments This work has been supported by AMED-CREST #18gm0910003, and JSPS KAKENHI Grant Number 17H06395 and 15H02541 (H.S.). The computations in this work were performed using the Research Center for Computational Science, Okazaki, Japan; the Center for Computational Sciences (CCS) at University of Tsukuba, Japan; and the facilities of the Supercomputer Center, the Institute for Solid State Physics, The University of Tokyo, Japan.

References

1. Gordon MS, Fedorov DG, Pruitt SR, Slipchenko LV (2012) Fragmentation methods: a route to accurate calculations on large systems. *Chem Rev* 112(1):632–672
2. Kitaura K, Ikeo E, Asada T, Nakano T, Uebayasi M (1999) Fragment molecular orbital method: an approximate computational method for large molecules. *Chem Phys Lett* 313(3):701–706
3. Fedorov DG, Kitaura K (2007) Extending the power of quantum chemistry to large systems with the fragment molecular orbital method. *The J Phys Chem A* 111(30):6904–6914
4. Fedorov DG, Nagata T, Kitaura K (2012) Exploring chemistry with the fragment molecular orbital method. *Phys Chem Chem Phys* 14(21):7562–7577
5. Otsuka T, Okimoto N, Taiji M (2015) Assessment and acceleration of binding energy calculations for protein-ligand complexes by the fragment molecular orbital method. *J Comput Chem* 36(30):2209–2218
6. Heifetz A, Trani G, Aldeghi M, MacKinnon CH, McEwan PA, Brookfield FA, Chudyk EI, Bodkin M, Pei Z, Burch JD, Ortwin DF (2016) Fragment molecular orbital method applied to lead optimization of novel interleukin-2 inducible T-cell kinase (ITK) inhibitors. *J Med Chem* 59(9):4352–4363
7. Minami A, Ishibashi S, Ikeda K, Ishitsubo E, Hori T, Tokiwa H, Taguchi R, Ieno D, Otsubo T, Matsuda Y, Sai S, Inada M, Suzuki T (2013) Catalytic preference of salmonella typhimurium LT2 sialidase for N-acetylneuraminic acid residues over N-glycolylneuraminic acid residues. *FEBS Open Bio* 3:231–236
8. Fedorov DG, Kitaura K (2016) Subsystem analysis for the fragment molecular orbital method and its application to protein-ligand binding in solution. *The J Phys Chem A* 120(14):2218–2231
9. Sriwilajaroen N, Magesh S, Imamura A, Ando H, Ishida H, Sakai M, Ishitsubo E, Hori T, Moriya S, Ishikawa T, Kuwata K, Odagiri T, Tashiro M, Hiramatsu H, Tsukamoto K, Miyagi T, Tokiwa H, Kiso M, Suzuki Y (2016) A novel potent and highly specific inhibitor against influenza viral N1–N9 neuraminidases: insight into neuraminidase-inhibitor interactions. *J Med Chem* 59(10):4563–4577
10. Tanaka S, Mochizuki Y, Komeiji Y, Okiyama Y, Fukuzawa K (2014) Electron-correlated fragment-molecular-orbital calculations for biomolecular and nano systems. *Phys Chem Chem Phys* 16(22):10310–10344
11. Fukuzawa K, Watanabe C, Kurisaki I, Taguchi N, Mochizuki Y, Nakano T, Tanaka S, Komeiji Y (2014) Accuracy of the fragment molecular orbital (FMO) calculations for DNA: Total energy, molecular orbital, and inter-fragment interaction energy. *Comput Theor Chem* 1034:7–16

12. Heifetz A, Chudyk EI, Gleave L, Aldeghi M, Cherezov V, Fedorov DG, Biggin PC, Bodkin MJ (2016) The fragment molecular orbital method reveals new insight into the chemical nature of GPCR–ligand interactions. *J Chem Inf Model* 56(1):159–172
13. Mazanetz MP, Ichihara O, Law RJ, Whittaker M (2011) Prediction of cyclin-dependent kinase 2 inhibitor potency using the fragment molecular orbital method. *J Cheminformatics* 3(1):2
14. Tagami U, Takahashi K, Igarashi S, Ejima C, Yoshida T, Takeshita S, Miyanaga W, Sugiki M, Tokumasu M, Hatanaka T, Kashiwagi T, Ishikawa K, Miyano H, Mizukoshi T (2016) Interaction analysis of FABP4 inhibitors by X-ray crystallography and fragment molecular orbital analysis. *ACS Med Chem Lett* 7(4):435–439
15. Barker JJ, Barker O, Courtney SM, Gardiner M, Hestekamp T, Ichihara O, Mather O, Montalbetti CA, Muller A, Varasi M, Whittaker M, Yarnold CJ (2010) Discovery of a novel Hsp90 inhibitor by fragment linking. *ChemMedChem* 5(10):1697–1700
16. Hitaoka S, Matoba H, Harada M, Yoshida T, Tsuji D, Hirokawa T, Itoh K, Chuman H (2011) Correlation analyses on binding affinity of sialic acid analogues and anti-influenza drugs with human neuraminidase using ab initio MO calculations on their complex structures—LERE-QSAR analysis (IV). *J Chem Inf Model* 51(10):2706–2716
17. Choi J, Kim H-J, Jin X, Lim H, Kim S, Roh I-S, Kang H-E, No KT, Sohn H-J (2018) Application of the fragment molecular orbital method to discover novel natural products for prion disease. *Sci Rep* 8(1):13063
18. Arulmozhiraja S, Matsuo N, Ishitsubo E, Okazaki S, Shimano H, Tokiwa H (2016) Comparative binding analysis of dipeptidyl peptidase IV (DPP-4) with antidiabetic drugs—an ab initio fragment molecular orbital study. *PLoS ONE* 11(11):e0166275
19. Yamamoto Y, Takei K, Arulmozhiraja S, Sladek V, Matsuo N, Han S-I, Matsuzaka T, Sekiya M, Tokiwa T, Shoji M, Shigeta Y, Nakagawa Y, Tokiwa H, Shimano H (2018) Molecular association model of PPAR α and its new specific and efficient ligand, pemafibrate: structural basis for SPPARM α . *Biochem Biophys Res Commun* 499(2):239–245
20. Ishikawa T, Kuwata K (2009) Fragment molecular orbital calculation using the RI-MP2 method. *Chem Phys Lett* 474(1):195–198
21. Feyereisen M, Fitzgerald G, Komornicki A (1993) Use of approximate integrals in ab initio theory. An application in MP2 energy calculations. *Chem Phys Lett* 208(5):359–363
22. Vahtras O, Almlöf J, Feyereisen MW (1993) Integral approximations for LCAO-SCF calculations. *Chem Phys Lett* 213(5):514–518
23. Bernholdt DE, Harrison RJ (1996) Large-scale correlated electronic structure calculations: the RI-MP2 method on parallel computers. *Chem Phys Lett* 250(5):477–484
24. Dunning TH (1989) Gaussian basis sets for use in correlated molecular calculations. I. The atoms boron through neon and hydrogen. *The J Chem Phys* 90(2):1007–1023
25. International Diabetes Federation. *IDF Diabetes Atlas*, 8th edn. <https://www.diabetesatlas.org/>
26. World Health Organization (2016) *Global report on diabetes*. World Health Organization, France
27. Kieffer TJ, McIntosh CH, Pederson RA (1995) Degradation of glucose-dependent insulinotropic polypeptide and truncated glucagon-like peptide 1 in vitro and in vivo by dipeptidyl peptidase IV. *Endocrinology* 136(8):3585–3596
28. Deacon CF, Johnsen AH, Holst JJ (1995) Degradation of glucagon-like peptide-1 by human plasma in vitro yields an N-terminally truncated peptide that is a major endogenous metabolite in vivo. *The J Clin Endocrinol Metab* 80(3):952–957
29. Rosenstock J, Zinman B (2007) Dipeptidyl peptidase-4 inhibitors and the management of type 2 diabetes mellitus. *Curr Opin Endocrinol Diabetes Obes* 14(2):98–107
30. Cahn A, Cernea S, Raz I (2016) An update on DPP-4 inhibitors in the management of type 2 diabetes. *Expert Opin Emerg Drugs* 21(4):409–419
31. Kim D, Wang L, Beconi M, Eiermann GJ, Fisher MH, He H, Hickey GJ, Kowalchick JE, Leiting B, Lyons K, Marsilio F, McCann ME, Patel RA, Petrov A, Scapin G, Patel SB, Roy RS, Wu JK, Wyvratt MJ, Zhang BB, Zhu L, Thornberry NA, Weber AE (2005) (2R)-4-Oxo-4-[3-(trifluoromethyl)-5,6-dihydro[1,2,4]triazolo[4,3-a]pyrazin-7(8H)-yl]-1-(2,4,5-trifluorophenyl)butan-2-amine: a potent, orally active dipeptidyl peptidase IV inhibitor for the treatment of type 2 diabetes. *J Med Chem* 48(1):141–151

32. Eckhardt M, Langkopf E, Mark M, Tadayyon M, Thomas L, Nar H, Pfrengle W, Guth B, Lotz R, Sieger P, Fuchs H, Himmelsbach F (2007) 8-(3-(R)-Aminopiperidin-1-yl)-7-but-2-ynyl-3-methyl-1-(4-methyl-quinazolin-2-ylmethyl)-3,7-dihydropurine-2,6-dione (BI 1356), a highly potent, selective, long-acting, and orally bioavailable DPP-4 inhibitor for the treatment of type 2 diabetes. *J Med Chem* 50(26):6450–6453
33. Zhang Z, Wallace MB, Feng J, Stafford JA, Skene RJ, Shi L, Lee B, Aertgeerts K, Jennings A, Xu R, Kassel DB, Kaldor SW, Navre M, Webb DR, Gwaltney SL (2011) Design and synthesis of pyrimidinone and pyrimidinedione inhibitors of dipeptidyl peptidase IV. *J Med Chem* 54(2):510–524
34. Yoshida T, Akahoshi F, Sakashita H, Kitajima H, Nakamura M, Sonda S, Takeuchi M, Tanaka Y, Ueda N, Sekiguchi S, Ishige T, Shima K, Nabeno M, Abe Y, Anabuki J, Soejima A, Yoshida K, Takashina Y, Ishii S, Kiuchi S, Fukuda S, Tsutsumiuchi R, Kosaka K, Murozono T, Nakamaru Y, Utsumi H, Masutomi N, Kishida H, Miyaguchi I, Hayashi Y (2012) Discovery and preclinical profile of teneligliptin (3-[(2S,4S)-4-[4-(3-methyl-1-phenyl-1H-pyrazol-5-yl)piperazin-1-yl]pyrrolidin-2-yl]carbonyl]thiazolidine): a highly potent, selective, long-lasting and orally active dipeptidyl peptidase IV inhibitor for the treatment of type 2 diabetes. *Bioorg Med Chem* 20(19):5705–5719
35. Biftu T, Sinha-Roy R, Chen P, Qian X, Feng D, Kueth JT, Scapin G, Gao YD, Yan Y, Krueger D, Bak A, Eiermann G, He J, Cox J, Hicks J, Lyons K, He H, Salituro G, Tong S, Patel S, Doss G, Petrov A, Wu J, Xu SS, Sewall C, Zhang X, Zhang B, Thornberry NA, Weber AE (2014) Omarigliptin (MK-3102): a novel long-acting DPP-4 inhibitor for once-weekly treatment of type 2 diabetes. *J Med Chem* 57(8):3205–3212
36. Grimshaw CE, Jennings A, Kamran R, Ueno H, Nishigaki N, Kosaka T, Tani A, Sano H, Kinugawa Y, Koumura E, Shi L, Takeuchi K (2016) Trelagliptin (SYR-472, Zafatek), novel once-weekly treatment for type 2 diabetes, inhibits dipeptidyl peptidase-4 (DPP-4) via a non-covalent mechanism. *PLoS ONE* 11(6):e0157509
37. Schechter I, Berger A (1967) On the size of the active site in proteases. I. Papain. *Biochem Biophys Res Commun* 27(2):157–162
38. Nabeno M, Akahoshi F, Kishida H, Miyaguchi I, Tanaka Y, Ishii S, Kadowaki T (2013) A comparative study of the binding modes of recently launched dipeptidyl peptidase IV inhibitors in the active site. *Biochem Biophys Res Commun* 434(2):191–196
39. Schnapp G, Klein T, Hoevels Y, Bakker RA, Nar H (2016) Comparative analysis of binding kinetics and thermodynamics of dipeptidyl peptidase-4 inhibitors and their relationship to structure. *J Med Chem* 59(16):7466–7477
40. Shimano H, Sato R (2017) SREBP-regulated lipid metabolism: convergent physiology—divergent pathophysiology. *Nat Rev Endocrinol* 13(12):710–730
41. Brelivet Y, Rochel N, Moras D (2012) Structural analysis of nuclear receptors: from isolated domains to integral proteins. *Mol Cell Endocrinol* 348(2):466–473
42. Kota BP, Huang TH, Roufogalis BD (2005) An overview on biological mechanisms of PPARs. *Pharmacol Res* 51(2):85–94
43. Desvergne B, Wahli W (1999) Peroxisome proliferator-activated receptors: nuclear control of metabolism. *Endocr Rev* 20(5):649–688
44. Diabetes Atherosclerosis Intervention Study Investigators (2001) Effect of fenofibrate on progression of coronary-artery disease in type 2 diabetes: the diabetes atherosclerosis intervention study, a randomised study. *Lancet (London, England)*, 357(9260):905–910
45. Bloomfield Rubins H, Davenport J, Babikian V, Brass LM, Collins D, Wexler L, Wagner S, Papademetriou V, Rutan G, Robins SJ (2001) Reduction in stroke with gemfibrozil in men with coronary heart disease and low HDL cholesterol: the veterans affairs HDL intervention trial (VA-HIT). *Circulation* 103(23):2828–2833
46. Prevention, Bezafibrate Infarction (2000) Secondary prevention by raising HDL cholesterol and reducing triglycerides in patients with coronary artery disease. *Circulation* 102(1):21–27
47. Raza-Iqbal S, Tanaka T, Anai M, Inagaki T, Matsumura Y, Ikeda K, Taguchi A, Gonzalez FJ, Sakai J, Kodama T (2015) Transcriptome analysis of K-877 (a novel selective PPARalpha modulator (SPPARAlpha))-regulated genes in primary human hepatocytes and the mouse liver. *J Atherosclerosis Thromb* 22(8):754–772

48. Ishibashi S, Yamashita S, Arai H, Araki E, Yokote K, Suganami H, Fruchart JC, Kodama T (2016) Effects of K-877, a novel selective PPARalpha modulator (SPPARMalpha), in dyslipidaemic patients: a randomized, double blind, active- and placebo-controlled, phase 2 trial. *Atherosclerosis* 249:36–43
49. Hennuyer N, Duplan I, Paquet C, Vanhoutte J, Woittrain E, Touche V, Colin S, Vallez E, Lestavel S, Lefebvre P, Staels B (2016) The novel selective PPARalpha modulator (SPPARMalpha) pemafibrate improves dyslipidemia, enhances reverse cholesterol transport and decreases inflammation and atherosclerosis. *Atherosclerosis* 249:200–208
50. Fruchart JC (2013) Selective peroxisome proliferator-activated receptor alpha modulators (SPPARMalpha): the next generation of peroxisome proliferator-activated receptor alpha-agonists. *Cardiovasc Diabetology* 12:82
51. Takei K, Han SI, Murayama Y, Satoh A, Oikawa F, Ohno H, Osaki Y, Matsuzaka T, Sekiya M, Iwasaki H, Yatoh S, Yahagi N, Suzuki H, Yamada N, Nakagawa Y, Shimano H (2017) Selective peroxisome proliferator-activated receptor-alpha modulator K-877 efficiently activates the peroxisome proliferator-activated receptor-alpha pathway and improves lipid metabolism in mice. *J Diab Invest* 8(4):446–452

Application of Fragment Molecular Orbital Calculations to Functional Analysis of Enzymes



Shogo Nakano, Sohei Ito, and Hiroaki Tokiwa

Abstract Enzymes are biocatalysts catalyzing various reactions in metabolism. Several of amino acid metabolizing enzymes are applied to industrial usage because of their high functionalities, such as high specificity and reactivity. Elucidation of reaction mechanism of these enzymes would be helpful to improve their functions. In this chapter, we introduce how combinational analysis of fragment molecular orbital (FMO) calculation, structural, and biochemical analysis can elucidate molecular mechanism of industrially important enzymes. Firstly, we will represent that the combinational analysis can represent why artificially designed *R*-selective amine oxidase reacts with *R*-methylbenzylamine (*R*-MBA) in racemic MBA selectively without being inhibited by *S*-MBA. Secondly, for the highly selective L-threonine 3-dehydrogenase (TDH) which is applied to quantify L-threonine concentration in various samples, we will show that FMO calculation can suggest existence of residue working as a sensor to detect completion of enzyme reaction in TDH. In the future, many more enzymatic functions and protein mechanics will be elucidated by combinatorial approaches based on computational chemistry, structural biology, and enzyme chemistry.

Keywords Enzyme reaction mechanism · L-threonine 3-dehydrogenase · *R*-selective amine oxidase · Substrate selectivity · Amino acid metabolism

1 Introduction

Advances in biotechnology have enabled us to make use of various biomaterials, such as enzymes, in industrial and medical applications. For example, enzymes are renewable natural products that provide an alternative to chemical catalysts as green

S. Nakano (✉) · S. Ito
Graduate School of Integrated Pharmaceutical and Nutritional Sciences, University of Shizuoka,
52-1 Yada, Suruga-ku, Shizuoka 422-8526, Japan
e-mail: snakano@u-shizuoka-ken.ac.jp

H. Tokiwa
Department of Chemistry, Rikkyo University, Toshima-ku, Nishi-ikebukuroTokyo 171-8501,
Japan

© Springer Nature Singapore Pte Ltd. 2021
Y. Mochizuki et al. (eds.), *Recent Advances of the Fragment Molecular Orbital Method*,
https://doi.org/10.1007/978-981-15-9235-5_17

341

catalysts; however, general enzymes bear high substrate specificity, and this is a hurdle to broad catalytic applications because high specificity would restrict the application of enzymes to very limited numbers of substrates and reactions. Enzyme specificity must therefore be modified to suit the desired reaction on a case-by-case basis using an approach called rational design. This approach uses information such as structural and functional data. Among various experimental methods, there is no doubt that X-ray crystallography has contributed greatly to the progress of rational design [1]. In addition, many instances of successful design have reportedly involved a computational chemistry approach [1–3]. For example, Kemp eliminase, which was previously believed to not exist in nature, can be rationally designed after selecting template structures from the PDB database [4]. The design was performed after molecular interactions between the protein and ligand had been predicted by structural and computational analysis. Under isothermal and isobaric conditions, molecular interactions can be represented as Gibbs free energy (ΔG) and ΔG can be divided into enthalpy (ΔH) and entropy ($-T\Delta S$) terms.

Recently, many methods have been reported for quantifying molecular interactions involving either experimental or computational approaches. Isothermal titration calorimetry (ITC) is a representative experimental method for measuring energy [5]: the dissociation constant (K_d) and ΔH can be directly determined by measuring the heat that is generated upon either release or binding of ligands, and $-T\Delta S$ can be indirectly estimated from calculations [5]. On the other hand, ITC often requires high concentrations of proteins depending on the K_d value of the ligands; this is a hurdle when preparation of large amounts of enzyme (>several mg) is difficult. Surface plasmon resonance (SPR) can determine K_d values utilizing lower amount of protein samples compared with ITC, whereas thermodynamics parameters can be determined indirectly by fitting the K_d values which were determined by changing measurement temperature to the van't Hoff Eq. [6]. Molecular interactions could be estimated by computational approaches if we could prepare protein structures that bind ligands at their active site.

Two approaches are broadly utilized at the moment, namely, molecular mechanical (MM) and quantum mechanical (QM) calculations. MM methods can estimate interaction energy based on forcefield parameters, such as CHARMM and AMBER. The benefit of the MM method is the low computational cost, whereas interactions involving electron perturbation, such as π - π stacking and dispersion force, are hard to estimate accurately [7]. QM methods can complement the weaknesses of MM; however, the computational cost is too expensive to apply to macro molecular systems, such as proteins. Hybrid methods combining QM and MM (QM/MM) are broadly utilized to reduce the costs. Such methods calculate the interactions at the active site and other regions at the QM and MM levels, respectively.

Conversely, many reports have indicated that molecular interactions far from the active site often affect enzymatic properties. In fact, Morley K. and Kazlauskas R. J. reported that several mutations distant from the active site affect thermal stability and enzymatic parameters [8]. For example, substrate selectivity for Asn266Met mutant of glutaryl acylase was 200-fold improved compared with wild type in spite that the mutation site locates far from active site (>7.0 Å) [9]. Many groups also

reported that mutation of hydrophilic residues at protein surface to hydrophobic ones enhances thermal stability and enzymatic activity [8]. In any cases, dispersion force would be changed by the mutations, and the changes enhance the protein functions. To indicate the changes quantitatively, the molecular interactions of proteins must be estimated by QM calculations. Kitaura et al. developed an ab initio fragment molecular orbital (FMO) method which has the potential to clear this hurdle [10]. In the FMO method, molecules are divided into fragments, and molecular orbital calculations are performed between the fragments. Because of the fragmentations, the FMO method can reduce computational costs, and therefore, protein molecules could be applied to the calculation. In general, protein molecules are divided into fragments which are formed by amino acid. Interaction energies were calculated as either interfragment interaction energies (IFIEs) or pair interaction energies (PIEs). The lower computational cost of the FMO method compared with the general QM method is advantageous for analyzing molecular interactions. However, a few reports have been published in which protein function was elucidated by combinatorial approaches involving experimental and FMO methods.

In this chapter, we will describe our two studies that have involved the elucidation of enzymatic functions using combinatorial approaches. The first aim is to reveal the origin of stereoselectivity for *R*-selective amine oxidase designed by introducing two point mutations, Y228L and R283G, into *D*-amino acid oxidase from pig kidney [11]. The second is to elucidate the reaction mechanism of *L*-threonine 3-dehydrogenase, which belongs to the short-chain dehydrogenase/reductase family. This mechanism comprises the substrate recognition mechanism associated with structural and dynamic changes [12] and the product release mechanism [13].

2 Determining the Basis of Stereoselectivity for Artificially Designed *R*-Selective Amine Oxidase by Mutating Two Residues in Pig Kidney *D*-Amino Acid Oxidase (pkAOx)

Chiral compounds are precursors for various fine chemicals and medicines. In particular, chiral amines are used to synthesize many pharmaceutical drugs, such as levocitirizine and solifenacin [14]. Chemical catalysts and methods to achieve chiral synthesis of such amines are still being developed [15]. Simultaneously, the enzyme optical resolution method is applied to the synthesis because of the advantages of enzymes compared with chemical catalysts, including the renewable, eco-friendly nature of enzymes, and the high efficiency of enzymes for obtaining enantiomerically pure compounds [16, 17]. Turner's group pioneered the synthesis of chiral amines using enzymatic optical resolution. They succeeded in designing *S*-selective amine oxidase (*S*-AOx) by mutating FAD-dependent monoamine oxidase (MAO) through directed evolution [18]. By accumulating further mutations in *S*-AOx using a combination of directed evolution and rational design, substrate specificity can be

extended toward amines containing bulky groups, such as aminodiphenylmethane and tertiary amines [14, 19–21].

In contrast to many studies on *S*-AOx, there have not been any recent reports concerning *R*-selective amine oxidase (*R*-AOx). Recently, Heath et al. successfully designed an *R*-AOx with high substrate selectivity but weak activity, namely, the E350L, E352D variant of 6-hydroxy-D-nicotine oxidase [22]. At the same time, Yasukawa et al. succeeded in designing an *R*-AOx, namely, the Y228L, R283G variant of pig kidney D-amino acid oxidase (pkAOx) [23]. Deracemization utilizing *R*-AOx can be achieved by the process shown in Fig. 1a. *R*-AOx specifically oxidizes (*R*)-MBA in racemic MBA (*rac*-MBA), and a chemical reductant, such as NaBH₄, reduces the resulting imine to *rac*-MBA (Fig. 1a). In this study, we focused on the latter *R*-AOx, pkAOx. pkAOx exhibits high reactivity and specificity toward a few amines that bear an aromatic ring, such as *R*-methylbenzyl amine ((*R*)-MBA) and 2-phenylpyrrolidine (PhPyr) [23]. Simultaneously, high specificity would restrict the application of pkAOx toward the enzymatic optical resolution of other amines. Therefore, the extension of substrate selectivity by rational design is required to expand its potential application.

An understanding of the reaction mechanism for pkAOx is required to change their selectivity via rational design. Hence, we first attempted to elucidate the mechanism by determining the crystal structure of pkAOx which binds (*R*)-MBA at the active site. The structure of the pkAOx-(*R*)-MBA binding form could be determined at a resolution of 1.88 Å (Fig. 1b). The overall structure of pkAOx is almost identical to the native DAAO structure; the root-mean-square deviation (RMSD) of the C α atoms in the two structures was 0.627 Å. Conversely, structural comparison at the active site between pkAOx-(*R*)-MBA and the DAAO-benzoate-binding form indicated that the binding sites for the aromatic ring of the two ligands differs; the ring of (*R*)-MBA is located on the xylene ring of FAD in pkAOx (Fig. 1b), whereas the benzoate ring is placed on the pyrimidine ring of FAD in DAAO (Fig. 1c). Summarizing the structural data, the pkAOx reaction mechanism was predicted as shown in Fig. 1c. Firstly, (*R*)-MBA binds to the pkAOx active site where the aromatic group of F242, *para*-hydroxyphenyl group of Y224, and the xylene ring of FAD appears to form a π - π stacking interaction with (*R*)-MBA. The (*R*)-MBA binds to the active site in the neutral form [24]. The hydride at the C α atom of (*R*)-MBA would be transferred to oxidized FAD while deprotonation of the amino group occurs simultaneously through a water molecule that forms a hydrogen bond with the main chain of G313 and the hydroxyl group of Y224 [23].

We could predict the molecular mechanism of (*R*)-MBA oxidation by pkAOx (Fig. 1d), whereas we could not show why pkAOx can be applied to the deracemization of (*S*)-MBA. Crystal structures of pkAOx bound to various amines at the active site (Fig. 2a) indicate that (*S*)-MBA (Fig. 2a, cyan) can bind to the pkAOx active site as well as the case of (*R*)-MBA (green in Fig. 2a). This suggests that (*S*)-MBA in *rac*-MBA is a potential competitive inhibitor of (*R*)-MBA. However, pkAOx appeared to not be inhibited by (*S*)-MBA; in fact, this enzyme exhibits a high enantiomeric excess value (>99% ee for (*S*)-MBA) when utilizing *rac*-MBA as a substrate [23]. To determine the basis of the high stereoselectivity of pkAOx, we performed

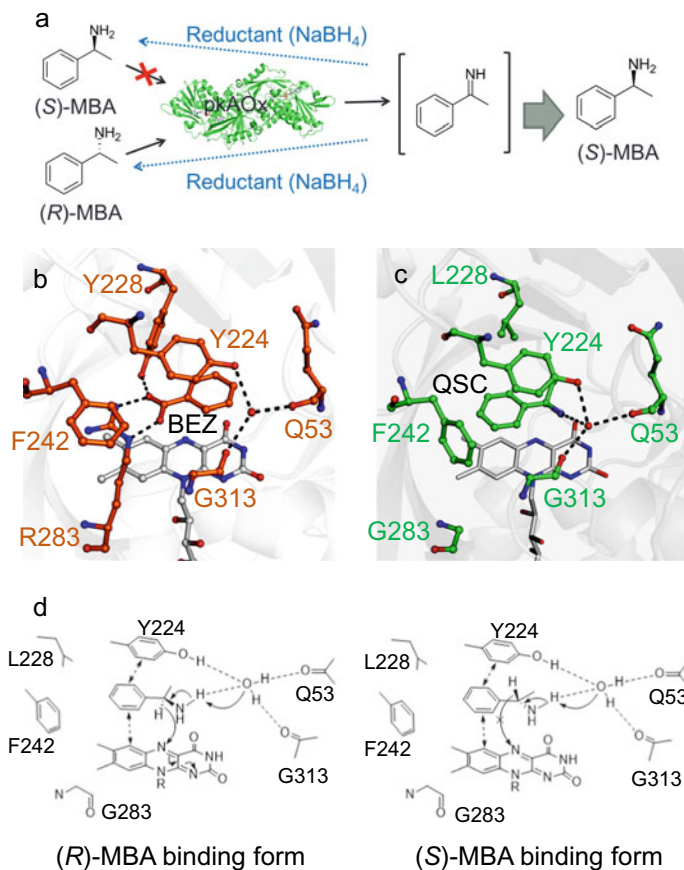


Fig. 1 Schematic illustrating the deracemization of *rac*-MBA by pKAox (a). pKAox selectively oxidizes *(R)*-MBA to imine. The imine is reduced by a chemical reductant, such as NaBH₄, to *rac*-MBA. By performing the process repeatedly, optically pure *(S)*-MBA could be obtained. Active site structures of DAAO which binds benzoate (BEZ) (b) and pKAox which ligates *(R)*-MBA (QSC) (c). The carboxyl group of BEZ interacts with guanidinium group of R283 (B). The amino group of QSC forms hydrogen bond interaction with water molecule via the side chain of Y224, and the main chains of Q53 and G313 (C). Reaction mechanism of pKAox (d). In the *(R)*-MBA binding form, a hydrogen atom on the C α atom is oriented toward the FAD ring (D), and hydride transfer can occur easily (D). In contrast, for the *(S)*-MBA binding form, hydride transfer does not occur because the hydrogen atom is oriented toward Y224 (D)

interaction energy analysis for the *(R)*- and *(S)*-MBA binding forms of pKAox. MM calculations are the first choice for estimating interaction energies; however, in the case of pKAox, MM calculations are not suitable because the interaction between pKAox and the ligand appears to be formed mainly by π - π stacking and dispersion force based on structural analysis. Hence, QM calculations, including FMO calculations, are more suitable for estimating the interaction. The FMO method can estimate

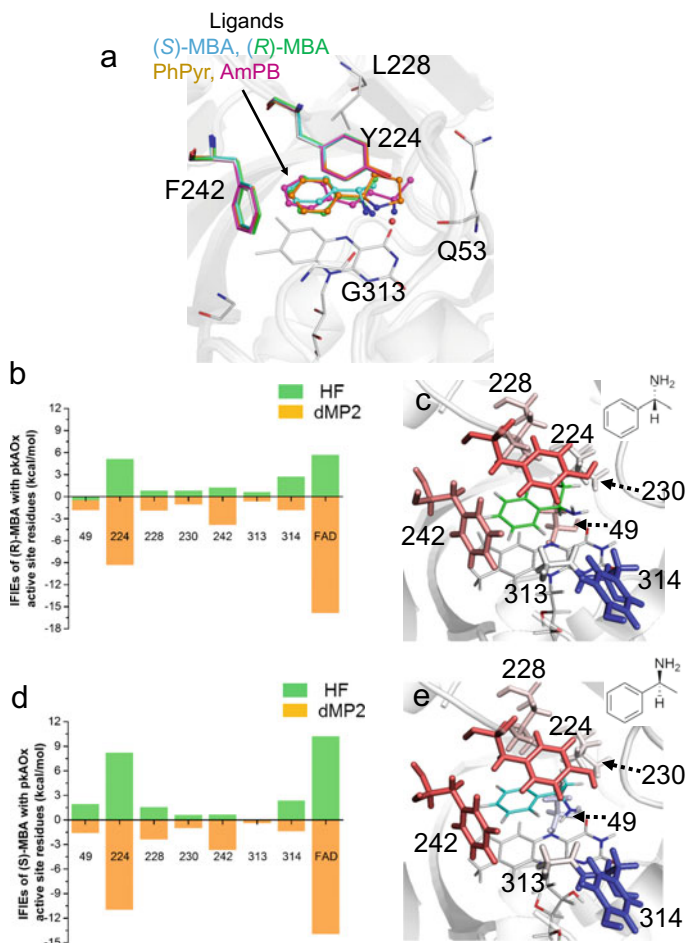


Fig. 2 Active site structures of the ligand binding forms of pKAOx (**a**). The (*R*)-MBA, (*S*)-MBA, 2-phenylpyrrolidine (PhPyr), and 3-amino-1-phenylbutane (AmPB) binding forms are colored in green, blue, orange, and magenta, respectively. Bar graphs of IFIEs for (*R*)-MBA (**b**) and (*S*)-MBA binding forms of pKAOx at the active site (**d**). Representation of MP2-IFIEs on crystal structures of (*R*)-MBA (**c**) and (*S*)-MBA binding form (**e**). The structures were colored depending on their IFIE values. Positive (repulsive) and negative (stable) IFIEs were colored in blue and in red, respectively

the interaction energy quantitatively, including π - π stacking and dispersion force. Utilizing this calculation, we can obtain interfragment interaction energies (IFIEs). IFIEs for the pKAOx-(*R*)-MBA and pKAOx-(*S*)-MBA binding forms were calculated by applying Hartree-Fock theory (HF-IFIEs, Fig. 2b and d, green bars) and Møller-Plesset perturbation theory subjected to counterpoise corrections. HF-IFIEs are represented as sum of the following energies; electrostatic energies, exchange repulsive energies, and the energy for charge transfer + higher order mixed term [25]. MP2-IFIEs are represented as the sum of HF-IFIE and electron correlation

energies including dispersion force calculated by applying MP2 theory. In the IFIE, the part of correlation energies was called dMP2-IFIE (Fig. 2b and d, orange bars). As expected, ligands appeared to be recognized mainly with dispersion interactions in both structures, whereas HF-IFIEs make a smaller contribution to binding.

Next, by focusing on active site residues and FAD, which appear to form interactions with the ligand, MP2-IFIEs were compared for (*R*)- (Fig. 2b, the sum of green and orange bar) and (*S*)-MBA binding forms (Fig. 2d, the sum of green and orange bar). In addition, these residues were colored on the structure of the (*R*)- (Fig. 2c) and (*S*)-MBA binding forms (Fig. 2e) with dependency on MP2-IFIEs. Structural analysis indicated that dispersion force, especially π - π stacking interactions brought about by Y224, F242, and FAD, contributes mainly to the formation of stable interactions with (*R*)- and (*S*)-MBA. In fact, about 70% ((*R*)-MBA binding form) and 80% ((*S*)-MBA binding form) of IFIEs are derived from dispersion force. Comparative analysis of IFIEs indicates that (*R*)-MBA forms ~ 13 kcal/mol more stable interaction than (*S*)-MBA binding forms with pKAox, suggesting that (*R*)-MBA in *rac*-MBA is recognized with greater specificity than (*S*)-MBA.

Based on IFIE analysis, we attempted to extend the substrate selectivity of pKAox by site-directed mutagenesis. Among the seven residues located near the ligands, Y224 and F242 were selected as candidates for mutation because of their strong contribution to the binding of the ligands. The plots for the enzyme turnover rate (k_{cat}) of pKAox and their variants (Y224L, F242I, F242V, and F242L) are shown in Fig. 3a; here, the k_{cat} values for (*R*)-MBA and (*R*)-1-[2-naphthyl]ethylamine ((*R*)-NEA) are plotted on the *x*- and the *y*-axis, respectively. The Y224L variant is inactive toward both (*R*)-MBA and (*R*)-NEA, suggesting that Y224 is essential for *R*-AOx activity in pKAox. To oxidize the substrate efficiently, the side chain of Y224 may activate a water molecule that interacts with the amino group of (*R*)-MBA. On the other hand, F242 variants would likely be (*R*)-NEA specific *R*-AOx (Fig. 3a). By mutating F242 to other hydrophobic residues, a new cavity which can bind naphthyl group of (*R*)-NEA would be generated, thereby enabling the variants to be specific for (*R*)-NEA.

To summarize our results, we predicted mutation candidate residues of pKAox to extend their selectivity. To screen pKAox, which exhibits activity toward amine compounds that bear a bulky group at the aromatic ring position (Fig. 3b, orange), mutating the aromatic ring site (Fig. 3c, orange surface) is effective. The successful design of pKAox specific for (*R*)-NEA by mutating F242, one of the residues that forms the aromatic ring site, would support this hypothesis. In contrast, mutations at the C_{β} -site (Fig. 3d, green surface region) would be effective for extending the selectivity toward amino compounds bearing other molecules at the C_{β} -position (Fig. 3b, green region). In support of our hypothesis, Yasukawa et al., succeeded in designing a new amine oxidase that oxidizes (*S*)-4-Cl-benzhydrylamine by mutating I230, which is located at the C_{β} site (Fig. 3d, green), to Ala [26]. This suggests that the FMO method can provide useful information for designing new artificial enzymes with different substrate selectivities.

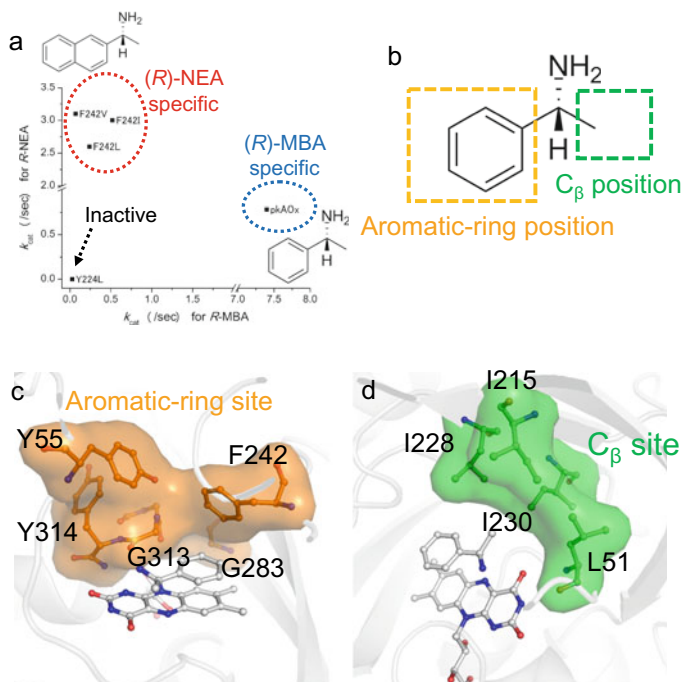


Fig. 3 Turnover rates for (*R*)-MBA and (*R*)-NEA by pkAOx and its point mutation variants (a). pkAOx displays higher turnover rates with (*R*)-MBA than with (*R*)-NEA, suggesting that pkAOx is an (*R*)-MBA-specific *R*-AOx. In contrast, F242 variants (F242V, F242I, and F242L) exhibit a higher turnover rate with (*R*)-NEA, suggesting that F242 variants are (*R*)-NEA specific *R*-AOx. The Y224L variant is inactive. Division of aromatic ring and C $_{\beta}$ positions in (*R*)-MBA (b). Aromatic-ring (c) and C $_{\beta}$ sites in pkAOx (d). The aromatic ring site is formed by five residues; Y55, F242, G283, G313, and Y314. The C $_{\beta}$ site comprises four hydrophobic residues, namely, L51, I215, I228, and I230

3 Reaction Mechanism of Highly Specific L-threonine 3-dehydrogenase Belonging to the Short-Chain Dehydrogenase/Reductase Family

Many reports have suggested that the concentration of L-amino acids in plasma changes in patients suffering from certain diseases, including some cancers [27, 28]. A new diagnostic method for such diseases can therefore be developed if the L-amino acid concentration can be quantified accurately. An example of such a method called AminoIndex technology has been developed [27, 28]. Various enzymes with high substrate specificity have been discovered to perform the quantification, such as L-phenylalanine dehydrogenase [29] and L-arginine oxidase [30]. L-threonine 3-dehydrogenase belongs to the short-chain dehydrogenase/reductase family (SDR-TDH) and is the main target in this section. SDR-TDH can also be used for amino acid quantification; it is an NAD $^{+}$ -dependent enzyme with high specificity toward L-Thr [31]. This enzyme catalyzes dehydrogenation at the 3' carbon atom of L-Thr, which

generates 2-amino 3-ketobutyrate (AKB) and NADH (Fig. 4a) [32]. SDR-TDHs are expressed in species ranging from bacteria to mammals, and their physiological importance has been documented. For example, *Trypanosoma brucei* utilizes L-Thr

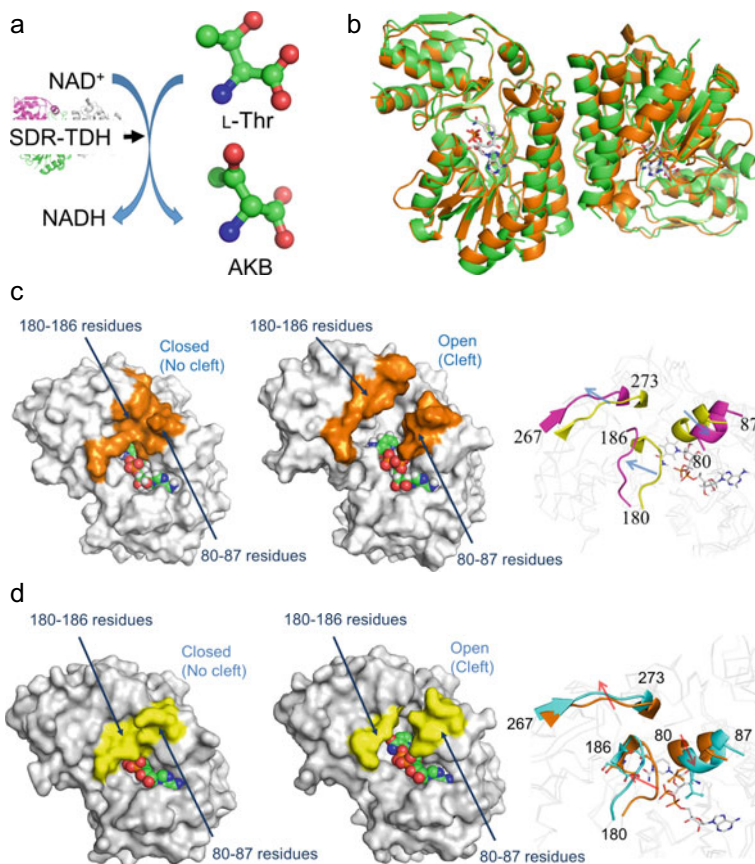


Fig. 4 Reaction scheme of SDR-TDH (a). SDR-TDH catalyzes the conversion of L-Thr to AKB, using NAD^+ as a cofactor. Structural comparison between the apo (green) and ternary complex (orange) forms of SDR-TDH from *Cupriavidus necator* (b). The two structures are similar to each other; the RMSD between the apo and the ternary complex forms is 0.44 Å. Structural comparison of NAD^+ -binding form of CnTDH between the initial (c, at 0 ns) and final (d, at 50 ns) states of the MD simulation. The three flexible regions (80–87, 180–186, and 267–273 regions) are colored in orange, suggesting that binary complex form of CnTDH would have an open form in solution. Conformational changes in the flexible regions, such as 80–87 and 180–186 residues, were induced with as the MD simulation progressed (arrowed direction represented in (e)). Crystal structures of the ternary complex form of CnTDH(WT) (f) and NAD^+ -binding form of the CnTDH(T186S) variant (g). As predicted by MD simulation (c–e), an identical conformation change at the flexible regions could be observed in the crystal structures. Similar conformation changes have been confirmed (h)

as a carbon source for lipid and sterol synthesis by metabolizing L-Thr with SDR-TDH [33], while Wang et al., reported that SDR-TDH is essential for growing mouse embryonic stem cells [34].

To elucidate the molecular mechanism of SDR-TDH, many groups have attempted to determine their crystal structures. At present, more than five crystal structures of this enzyme belonging to different species have been reported [12, 35–37]. Yoneda et al. reported that the reaction mechanism underlying SDR-TDH catalysis of L-Thr dehydrogenation: the hydroxyl group of the substrate, L-Thr, is dehydrogenated by the side chain of an active site residue, a Tyr, and the hydride at the C $_{\beta}$ atom of the substrate is transferred to NAD $^{+}$ [35, 36]. This mechanism was validated by kinetic analysis of SDR-TDH variants; however, several mechanisms remain unknown. For example, why SDR-TDHs exhibit high specificity toward L-Thr and how SDR-TDHs release their product, AKB, after completion of the reaction has yet to be elucidated. We attempted to elucidate these still unknown mechanisms by multidisciplinary analysis of X-ray crystallography, enzyme kinetics, and computational chemistry analysis.

Firstly, we attempted to elucidate the origin of the high specificity of SDR-TDHs toward L-Thr through combinatorial analysis by using *Cupriavidus necator* SDR-TDH as a target. Crystal structures for the apo and ternary complex forms (i.e., the L-Thr and NAD $^{+}$ binding forms) of CnTDH were determined at 2.25 and 2.5 Å resolution, respectively. Structural comparisons between them indicated that they share similar overall structures except for a number of regions (Fig. 4b). For example, the NAD $^{+}$ recognition loop, which is formed by residues 38–59 in CnTDH, cannot be assigned to the electron density map for the apo form (green in Fig. 4b), suggesting that the loop bears a flexible conformation. In contrast, all residues could be assigned to electron density map for the ternary complex form (orange in Fig. 4b). Furthermore, the ternary complex structure has a closed form, suggesting that L-Thr and NAD $^{+}$ binding to SDR-TDH causes the enzyme to become rigid [12].

Although the occurrence of a conformational change was confirmed in the SDR-TDHs by simultaneous binding to NAD $^{+}$ and L-Thr, it is unclear what stepwise structural and dynamical changes are induced by binding only NAD $^{+}$ first and subsequently by binding L-Thr [12]. In fact, SDR-TDH catalyzes the reaction using a Ping-Pong Bi-Bi mechanism: NAD $^{+}$ binds first, followed by L-Thr binding to the active site [32]. To verify this, we applied a molecular dynamics (MD) simulation to the CnTDH-NAD $^{+}$ binding form by removing L-Thr from the crystal structure of the CnTDH ternary form. The MD simulation was performed for 50 ns utilizing NAMD; the detailed simulation procedure was described previously [12]. The initial (Fig. 4c, left, at 0 ns) and the final states (Fig. 4c, middle, at 50 ns) of trajectory structures were indicated in Fig. 4c, suggesting that the CnTDH structure is changed from the “closed” to the “open” state by leaving away the two regions (Fig. 4c, 80–87 and 180–186 regions colored in orange) from each other (Fig. 4c, right). Because of the cleft in the open state forms (Fig. 4c, middle), the substrate, L-Thr, can enter the active site of SDR-TDH. Recently, we succeeded in determining CnTDH(T186S)-NAD $^{+}$ binding form (Fig. 4d, middle), indicating that the crystal structure shows the “open” state as expected from our MD simulation (middle in Fig. 4c). The structural change

at the three regions, which was confirmed by comparing crystal structures (Fig. 4d, right), was almost identical to those predicted by our MD simulation (Fig. 4c, right) [12].

Summarizing all the results, we predicted the stepwise conformational and dynamical changes induced by binding of NAD⁺ and L-Thr (Fig. 5). In the apo form (Fig. 5, upper left), the four arrowed regions adopt a flexible conformation in order to bind NAD⁺ efficiently. By binding NAD⁺, the 38–59 loops bear rigid form, whereas the catalytic domain and the 80–87 region still have flexible form (Fig. 5, upper right). Here, the SDR-TDH remains in the “open” state. When L-Thr binds to the active site, the structure changes to the “closed” state, and all regions indicated in the figure adopt a rigid form (Fig. 5, lower right). After the reaction is completed, the 80–87 region and the catalytic domain have flexible forms, and the structure changes to the “open” state. The products, AKB and NADH, are released into the solvent (Fig. 5, lower left). The predicted mechanism can be validated by enzyme kinetics analysis of CnTDH variants [12].

Here, one question remains: how does SDR-TDH detect the completion of L-Thr dehydrogenation and AKB generation? Detection is important for switching between the “open” and “closed” state of SDR-TDHs to release AKB into the solvent. Thus, we tried to elucidate the product release mechanism of SDR-TDH by analyzing high resolution structures of monomeric SDR-TDHs from a metagenomic library (mtTDH). Through crystal structure analysis of mtTDH, we can obtain the structure of the AKB-NADH binding form of mtTDH at 1.35 Å resolution (Fig. 6a). FMO analysis was performed on the structure obtained. The IFIEs between AKB

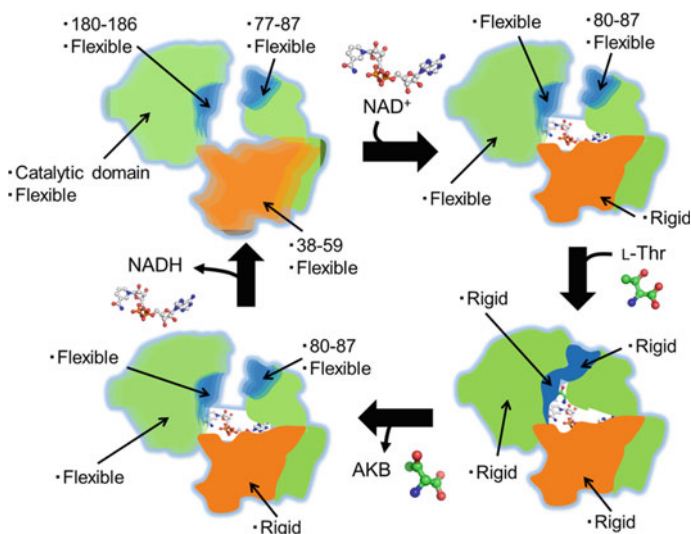


Fig. 5 Schematic model of structural changes for SDR-TDH induced by binding of NAD⁺ and L-Thr. The flexibility and conformation of the three regions are changed, and switching between open and closed state is induced by binding of NAD⁺ and L-Thr

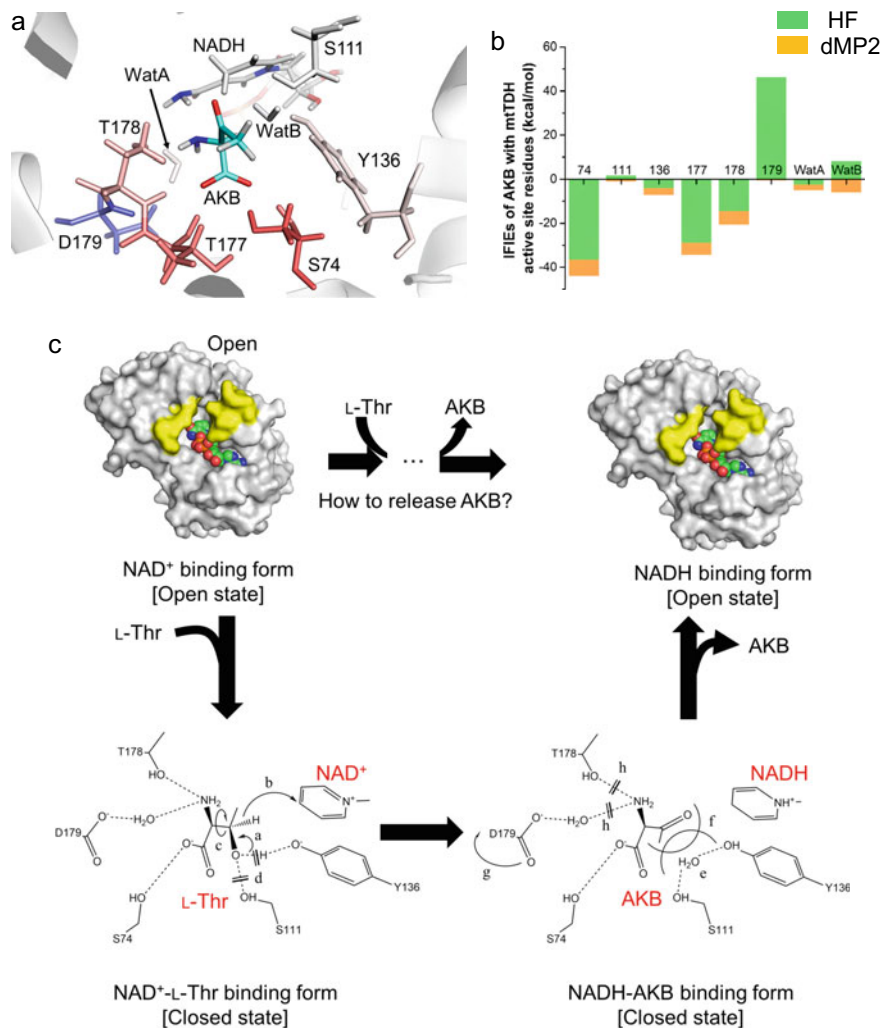


Fig. 6 IFIEs for MP2 between mTDH and AKB (**a**). Residues are colored depending on IFIE magnitude. The interactive and repulsive forces are represented in red and blue, respectively. The IFIEs for HF (green) and dMP2 (magenta) of six residues and two water molecules are shown (**b**). Among the residues, only D179 generates a repulsive force with AKB. Proposed product release mechanism of SDR-TDHs associated with structural change (**c**). Upon binding L-Thr, the structure changes from the open to the closed state, and the reaction following the process from step to step will occur

and active site residues (S74, S111, Y136, T177, T178, D179, WatA, and WatB) were calculated; the IFIEs for HF and dMP2 are represented as green and orange bars, respectively (Fig. 6b). IFIE analysis indicated that SDR-TDH recognizes AKB by using mostly ionic interactions. The graph indicates that only D179 generates repulsive forces with AKB (Fig. 6b), suggesting that D179 opposes the formation of stable interactions with AKB and L-Thr for SDR-TDHs. In spite of the destabilization, enzyme kinetic analysis of D179 variants indicate that the lack of repulsive force inhibits switching between the open and closed states of mtTDH, suggesting that D179 is a key residue for switching the state of SDR-TDH [13].

Considering all of our data together, we were able to predict the product release mechanism of SDR-TDH (Fig. 6c). In the NAD^+ -L-Thr binding form, L-Thr interacts with the active site residues. In this form, D179 should generate a repulsive force with L-Thr; however, this force would be cancelled by other stable interactions derived from such hydrogen bond interactions. After the formation, dehydrogenation occurs as shown in process a and b (Fig. 6c). Thereafter, the C_α - C_β bond of L-Thr is rotated (process c in Fig. 6c). In the AKB-NADH binding form that is generated, AKB breaks the hydrogen bonds which formed with the side chain hydroxyl groups of S111 and Y136. Because of this, the repulsive force generated by D179 cannot be cancelled. Here, we can easily predict that S111 and Y136 form hydrogen bonds with the hydroxyl group of L-Thr because many groups have reported that the same residues in other TDHs form interaction with L-Thr [13, 36]. A conformational change is induced in D179 so that it forms the open state. Therefore, we predict that D179 works as a “sensor” to detect reaction completion in SDR-TDH [13].

4 Summary

As we have shown in the previous two sections, the application of computational chemistry, which includes not only MD simulation but also FMO analysis, can uncover the enzyme reaction mechanism which is hard to deduce only from X-ray crystal structures. In particular, FMO analysis should be used to determine interaction energy for the protein–ligand complex when hydrophobic and dispersion forces make the main contribution to stabilization as in the case of pKAOx, since it is difficult to estimate these forces correctly using the MM Method. In the future, many more enzymatic functions and protein mechanics will be elucidated by combinatorial approaches based on computational chemistry, structural biology, and enzyme chemistry.

Acknowledgments The authors are grateful to the beamline staff for their assistance with experiments performed at PF and SPring-8. Computations were performed using the Research Center for Computational Science, Okazaki, and the facilities of the Supercomputer Center at the Institute for Solid State Physics, The University of Tokyo.

Funding This work was supported by JSPS KAKENHI Grant Number 16K18688, 17KT0010, 17K06931, and 18K14391.

Conflict of Interest The authors declare no competing financial interests.

References

1. Bornscheuer UT, Huisman GW, Kazlauskas RJ, Lutz S, Moore JC, Robins K (2012) Engineering the third wave of biocatalysis. *Nature* 485:185–194
2. Jiang L, Althoff EA, Clemente FR, Doyle L, Rothlisberger D, Zanghellini A, Gallaher JL, Betker JL, Tanaka F, Barbas CF 3rd, Hilvert D, Houk KN, Stoddard BL, Baker D (2008) De novo computational design of retro-aldol enzymes. *Science* 319:1387–1391
3. Wijma HJ, Floor RJ, Bjelic S, Marrink SJ, Baker D, Janssen DB (2015) Enantioselective enzymes by computational design and in silico screening. *Angew Chem Int Ed Engl* 54:3726–3730
4. Rothlisberger D, Khersonsky O, Wollacott AM, Jiang L, DeChancie J, Betker J, Gallaher JL, Althoff EA, Zanghellini A, Dym O, Albeck S, Houk KN, Tawfik DS, Baker D (2008) Kemp elimination catalysts by computational enzyme design. *Nature* 453:190–195
5. Leavitt S, Freire E (2001) Direct measurement of protein binding energetics by isothermal titration calorimetry. *Curr Opin Struct Biol* 11:560–566
6. Borsi V, Calderone V, Fragai M, Luchinat C, Sarti N (2010) Entropic contribution to the linking coefficient in fragment based drug design: a case study. *J Med Chem* 53:4285–4289
7. Swart M, van der Wijst T, Fonseca Guerra C, Bickelhaupt FM (2007) Pi-pi stacking tackled with density functional theory. *J Mol Model* 13:1245–1257
8. Morley KL, Kazlauskas RJ (2005) Improving enzyme properties: when are closer mutations better? *Trends Biotechnol* 23:231–237
9. Pelissier MC, Sebban-Kreuzer C, Guerlesquin F, Brannigan JA, Bourne Y, Vincent F (2014) Structural and functional characterization of the *Clostridium perfringens* N-acetylmannosamine-6-phosphate 2-epimerase essential for the sialic acid salvage pathway. *J Biol Chem* 289:35215–35224
10. Kitaura K, Ikeo E, Asada T, Nakano T, Uebayasi M (1999) Fragment molecular orbital method: an approximate computational method for large molecules. *Chem Phys Lett* 313:701–706
11. Nakano S, Yasukawa K, Tokiwa T, Ishikawa T, Ishitsubo E, Matsuo N, Ito S, Tokiwa H, Asano Y (2016) Origin of stereoselectivity and substrate/ligand recognition in an FAD-dependent R-selective amine oxidase. *J Phys Chem B* 120:10736–10743
12. Nakano S, Okazaki S, Tokiwa H, Asano Y (2014) Binding of NAD⁺ and L-threonine induces stepwise structural and flexibility changes in *Cupriavidus necator* L-threonine dehydrogenase. *J Biol Chem* 289:10445–10454
13. Motoyama T, Nakano S, Yamamoto Y, Tokiwa H, Asano Y, Ito S (2017) Product release mechanism associated with structural changes in monomeric L-threonine 3-dehydrogenase. *Biochemistry* 56:5758–5770
14. Ghislieri D, Green AP, Pontini M, Willies SC, Rowles I, Frank A, Grogan G, Turner NJ (2013) Engineering an enantioselective amine oxidase for the synthesis of pharmaceutical building blocks and alkaloid natural products. *J Am Chem Soc* 135:10863–10869
15. Reetz MT (2011) Laboratory evolution of stereoselective enzymes: a prolific source of catalysts for asymmetric reactions. *Angew Chem Int Ed Engl* 50:138–174
16. Asano Y (2010) Tools for enzyme discovery, In: Baltz RHD, Julian E, Demain AL (ed) *Manual of industrial microbiology and biotechnology*, 3rd edn. American Society for Microbiology, USA
17. Asano HGAY (2012) Introduction—Principle and historical landmarks of enzyme catalysis in organic synthesis. In: *Enzyme catalysis in organic synthesis*. Springer, pp 3–42
18. Alexeeva M, Enright A, Dawson MJ, Mahmoudian M, Turner NJ (2002) Deracemization of alpha-methylbenzylamine using an enzyme obtained by in vitro evolution. *Angew Chem Int Ed Engl* 41:3177–3180

19. Dunsmore CJ, Carr R, Fleming T, Turner NJ (2006) A chemo-enzymatic route to enantiomerically pure cyclic tertiary amines. *J Am Chem Soc* 128:2224–2225
20. Atkin KE, Reiss R, Koehler V, Bailey KR, Hart S, Turkenburg JP, Turner NJ, Brzozowski AM, Grogan G (2008) The structure of monoamine oxidase from *aspergillus niger* provides a molecular context for improvements in activity obtained by directed evolution. *J Mol Biol* 384:1218–1231
21. Kohler V, Bailey KR, Znabet A, Raftery J, Helliwell M, Turner NJ (2010) Enantioselective biocatalytic oxidative desymmetrization of substituted pyrrolidines. *Angew Chem Int Ed Engl* 49:2182–2184
22. Heath RS, Pontini M, Bechi B, Turner NJ (2014) Development of an R-selective amine oxidase with broad substrate specificity and high enantioselectivity. *ChemCatChem* 6:996–1002
23. Yasukawa K, Nakano S, Asano Y (2014) Tailoring D-amino acid oxidase from the pig kidney to R-stereoselective amine oxidase and its use in the deracemization of alpha-methylbenzylamine. *Angew Chem Int Ed Engl* 53:4428–4431
24. Trimmer EE, Wanninayake US, Fitzpatrick PF (2017) Mechanistic studies of an amine oxidase derived from d-amino acid oxidase. *Biochemistry* 56:2024–2030
25. Fedorov DG, Kitaura K (2007) Pair interaction energy decomposition analysis. *J Comput Chem* 28:222–237
26. Yasukawa K, Motojima F, Ono A, Asano Y (2018) Expansion of the substrate specificity of porcine kidney D-amino acid oxidase for S-stereoselective oxidation of 4-Cl-Benzhydrylamine. *ChemCatChem* 10:3500–3505
27. Yatabe J, Yatabe MS, Ishibashi K, Nozawa Y, Sanada H (2013) Early detection of colon cancer by amino acid profiling using aminoindex Technology: a case report. *Diagn Pathol* 8:203
28. Noguchi Y, Zhang QW, Sugimoto T, Furuhashi Y, Sakai R, Mori M, Takahashi M, Kimura T (2006) Network analysis of plasma and tissue amino acids and the generation of an amino index for potential diagnostic use. *Am J Clin Nutr* 83:513S–519S
29. Asano Y, Nakazawa A, Endo K (1987) Novel phenylalanine dehydrogenases from *Sporosarcina ureae* and *Bacillus sphaericus*. purification and characterization. *J Biol Chem* 262:10346–10354
30. Matsui D, Terai A, Asano Y (2016) L-arginine oxidase from *pseudomonas* sp. TPU 7192: characterization, gene cloning, heterologous expression, and application to L-arginine determination. *Enzyme Microb Technol* 82:151–157
31. Ueatrongchit T, Asano Y (2011) Highly selective L-threonine 3-dehydrogenase from *Cupriavidus necator* and its use in determination of L-threonine. *Anal Biochem* 410:44–56
32. Kazuoka T, Takigawa S, Arakawa N, Hizukuri Y, Muraoka I, Oikawa T, Soda K (2003) Novel psychrophilic and thermolabile L-threonine dehydrogenase from psychrophilic cytophaga sp. strain KUC-1. *J Bacteriol* 185:4483–4489
33. Millerioux Y, Ebikeme C, Biran M, Morand P, Bouyssou G, Vincent IM, Mazet M, Riviere L, Franconi JM, Burchmore RJ, Moreau P, Barrett MP, Bringaud F (2013) The threonine degradation pathway of the trypanosoma brucei procyclic form: the main carbon source for lipid biosynthesis is under metabolic control. *Mol Microbiol* 90:114–129
34. Wang J, Alexander P, Wu L, Hammer R, Cleaver O, McKnight SL (2009) Dependence of mouse embryonic stem cells on threonine catabolism. *Science* 325:435–439
35. Yoneda K, Sakuraba H, Muraoka I, Oikawa T, Ohshima T (2010) Crystal structure of UDP-galactose 4-epimerase-like L-threonine dehydrogenase belonging to the intermediate short-chain dehydrogenase-reductase superfamily. *FEBS J* 277:5124–5132
36. Yoneda K, Sakuraba H, Araki T, Ohshima T (2012) Crystal structure of binary and ternary complexes of archaeal UDP-galactose 4-epimerase-like L-threonine dehydrogenase from *thermoplasma volcanium*. *J Biol Chem* 287:12966–12974
37. He C, Huang X, Liu Y, Li F, Yang Y, Tao H, Han C, Zhao C, Xiao Y, Shi Y (2015) Structural insights on mouse L-threonine dehydrogenase: a regulatory role of Arg180 in catalysis. *J Struct Biol* 192:510–518

AnalysisFMO Toolkit: A PyMOL Plugin for 3D-Visualization of Interaction Energies in Proteins (3D-VIEP) Calculated by the FMO Method



Takaki Tokiwa, Shogo Nakano, Hiroaki Tokiwa, and Yasuteru Shigeta

Abstract Interresidue and ligand/substrate-residue interactions in a biomacromolecular system such as drug target protein variously correlated with structure, function, and bioactivity of the system. Reliable theoretical interaction analysis with a ligand/substrate has given us fruitful information to identify the key residue and theoretically design novel high potent candidates. The interfragment interaction energies can be calculated appropriately under the FMO scheme based on the first-principles (electronic) calculations. Analysis tool of the FMO method is very useful by visualizing and rendering analysis of the results in protein structure: 3D-visualization of interaction energies in proteins (3D-VIEP). We have also developed the toolkit “AnalysisFMO” to perform the 3D-VIEP method, which can assist in analyzing the FMO results generated by quantum-chemical packages such as GAMESS, PAICS, and ABINIT-MP. AnalysisFMO consists of two separate tools, RbAnalysisFMO and the PyMOL plugins by Ruby and Python programs, respectively. The first tool can

Takaki Tokiwa and Shogo Nakano contributed equally to this work.

T. Tokiwa

Department of Chemistry, Graduate School of Science, Tohoku University, 6-3, Aoba, Aramaki, Aoba-ku, Sendai, Miyagi 980-8578, Japan

e-mail: htokiwa@yahoo.co.jp

T. Tokiwa · Y. Shigeta (✉)

Department of Physics, Graduate School of Pure and Applied Sciences, University of Tsukuba, 1-1-1 Tennodai, Tsukuba, Ibaraki 305-8571, Japan

e-mail: shigeta@ccs.tsukuba.ac.jp

S. Nakano (✉)

Graduate School of Integrated Pharmaceutical and Nutritional Sciences, University of Shizuoka, 52-1 Yada, Suruga-ku, Shizuoka 422-8526, Japan

e-mail: snakano@u-shizuoka-ken.ac.jp

H. Tokiwa (✉)

Department of Chemistry, Rikkyo University, Nishi-ikebukuro, Toshima-ku, Tokyo 171-8501, Japan

e-mail: htokiwa@yahoo.co.jp

Y. Shigeta

Center for Computational Sciences, University of Tsukuba, 1-1-1 Tennodai, Tsukuba, Ibaraki 305-8577, Japan

© Springer Nature Singapore Pte Ltd. 2021

Y. Mochizuki et al. (eds.), *Recent Advances of the Fragment Molecular Orbital Method*, https://doi.org/10.1007/978-981-15-9235-5_18

extract interfragment interaction energies (IFIEs) or pair interaction energies (PIEs) from the FMO output file, and the second tool enables to visualize IFIEs or PIEs in the target system together with structures on a window of PyMOL program.

Keywords AnalysisFMO · Interfragment interaction energies (IFIEs) · 3D-VIEP · PyMOL plugins · Ruby and python programs

1 Introduction

The amount of protein structural data is increasing rapidly due to advances in protein structure analysis such as X-ray crystallography, nuclear magnetic resonance (NMR), and cryo-electron microscopy (cryoEM). Currently, structural data are registered in the public database known as the Protein Data Bank (PDB), and the PDB file format is broadly utilized to represent protein coordinate data. The PDB has three branches, namely the RCSB PDB, the PDBj, and the PDBe. The Worldwide PDB (wwPDB) was established with the cooperation of these branches. PDB data are freely available from the database. At present, more than 150,000 PDB datasets have been deposited in the PDB (as of May 2019). PDB data only contain coordinate data for each atom in protein structures. Therefore, it is difficult to analyze PDB data without using molecular graphics software to visualize it. Furthermore, PDB data contains no information about which residues contribute to interactions with ligands with other amino acid residues. Thus, a method to quantify interaction energies between them is required to identify such interactions.

There are experimental methods available to quantify interaction energies between protein and ligands, such as isothermal titration calorimetry (ITC) [1]. ITC can measure any enthalpy change (ΔH) that occurs upon ligand binding and dissociation constant (K_d) values directly by measuring heat generated during ligand binding to a target protein. Because large amounts of target proteins are required to perform ITC, ITC measurement is limited to a subset of proteins. On the other hand, computational approaches can be broadly utilized to quantify energies in cases where we can obtain 3D structural data for proteins to use in ligand docking simulation and homology modeling. Specifically, molecular mechanics (MM) calculations are widely applied to quantification because of the low computational cost and ease of use. Force-field parameters are necessary to perform MM calculations, and CHARMM [2] and AMBER [3] are widely used at the moment. Nevertheless, MM calculations have the following inherent drawback: the inaccurate estimation of weak interaction energies stemming from electron correlations, such as π - π stacking and hydrophobic interactions. Ab initio quantum mechanical (QM) calculations can be an alternative to MM calculations, which give interaction energies more accurately than MM. However, QM calculations involve a high computational cost, which prevents applications to larger molecular systems such as proteins.

The fragment molecular orbital (FMO) method was developed to overcome these limitations and apply QM calculations to large molecular systems [4]. Currently,

several FMO calculation packages have been reported, including PAICS [5], ABINIT-MP [6], and GAMESS [7]. Interfragment interaction energies (IFIEs), sometimes called Pair Interaction Energies (PIEs), are calculated in a manner that accounts for correct monomer polarization due to the external electrostatic field of all the residues in a protein. The FMO method is now applied to the analysis of a wide variety of systems such as accurate estimation of the interaction energies between proteins, such as orexin-2 receptor and inducible T-cell kinase, and their ligands [8, 9] and elucidating why *R*-selective amine oxidase exhibits high stereoselectivity [10]. Although the FMO method can contribute to the elucidation of protein functions, its application is limited because of the complexity involved in the associated data analysis. FMO calculation packages such as PAICS, ABINIT-MP, and GAMESS have individual graphical user interface (GUI) tools, namely PaicsView (PV), Biostation Viewer, and FU (FMO utility), respectively. However, there is no universal visualization tool for all FMO packages, which means that a user needs to learn these tools one by one, which is a hurdle to performing FMO analysis. Therefore, the development of a universal tool is essential for broadening the applications of FMO analysis.

Among several molecular graphics software packages, PyMOL is widely used to visualize the 3D structure of biomolecules [11]. PyMOL was developed by utilizing an object-oriented language, C/C++, and a Python interpreter is embedded in the software to expand its functions. PyMOL is superior to other graphics software not only because of its excellent visualization capability but also because of its programmable interface, named PyMOL API, which can help users to implement new functions in PyMOL. By using this interface, we can develop a plugin written in Python, which extends the functionality of PyMOL. Several PyMOL plugins have been developed so far, including CAVER, which finds and visualizes tunnels and channels in biomolecules [12], GROMACS GUI, which can generate an input file to perform molecular dynamics simulations with GROMACS [13], among others. We have also developed plugins to perform 3D-visualization of interaction energies in proteins (3D-VIEP) generated by FMO calculations. These plugins may contribute to the performance of various applications, including rational protein design, *in silico* drug design [14], and the elucidation of enzymatic mechanisms [15].

In this chapter, we will introduce our toolkit, AnalysisFMO, for 3D-visualization of protein–protein and protein–ligand interaction energies (IFIEs and PIEs) in target protein systems and the application of the 3D-VIEP method [16]. AnalysisFMO includes two tools: RbAnalysisFMO, which extracts IFIEs or PIEs from an output file containing FMO calculations, while the second tool is a set of PyMOL plugins, namely PyPAICS, PyABINIT-MP, and PyGAMESS, which visualize IFIEs/PIEs in the target system together with structures in a PyMOL window.

2 AnalysisFMO Toolkit

2.1 Environment Construction to Run AnalysisFMO Toolkit to Achieve the 3D-VIEP

The AnalysisFMO toolkit consists of RbAnalysisFMO and a set of PyMOL plugins which are written in Ruby [17] and Python [18], respectively. Several Ruby libraries are necessary to run the RbAnalysisFMO tool, including Logger and Nokogiri [sparklemotion/nokogiri, GitHub. <https://github.com/sparklemotion/nokogiri/blob/master/LICENSE.md>]. The RbAnalysisFMO tool can convert output files generated by FMO packages (PAICS, ABINIT-MP, and GAMESS) into CSV files that contain either IFIEs or PIEs. The PyMOL plugins load the corresponding PDB and CSV files which are utilized as input files to execute RbAnalysisFMO. The following Python libraries are required to execute the PyMOL plugins: Tkinter, Python megawidgets, and Numpy. Plugin installation can be completed through the PyMOL plugin installation tool (*menu bar* in external GUI of PyMOL → *Plugin* → *Plugin Manager* → *Install new Plugin* → *Choose file...*). The plugins can be confirmed in the Plugin submenu if the installation is completed.

2.2 Overview of AnalysisFMO Toolkit

A flowchart illustrating how to execute the AnalysisFMO toolkit is shown in Fig. 1. Firstly, users have to perform FMO calculations with one of the FMO packages (PAICS, ABINIT-MP, or GAMESS). The output file generated includes a large amount of data, usually several megabits in size, and most of them are not used to visualize the interaction energies in the plugins. The RbAnalysisFMO tool can extract information about interaction energies (PIEs and IFIEs) from the output file, and generate a CSV file containing the extracted information (Fig. 1).

After generation of the CSV file by RbAnalysisFMO, PyMOL plugins are utilized to visualize interaction energies in the protein structure. The CSV and PDB files can be loaded through the plugin (Fig. 2). The CSV file generated by PAICS, ABINIT-MP, and GAMESS can be loaded by PyPAICS, PyABINIT-MP, and PyGAMESS, respectively. In Fig. 2, we show one of the PyMOL plugins, PyGAMESS. The CSV and PDB files can be loaded through the tabs “*Load csv file (2D)*” and “*Load pdb file*” as shown in panel 1, respectively (Fig. 2). After loading the files, we select either the “*All-pairs*” or “*Selected-pairs*” mode in 3D-VIEP method depending on the type of analysis being performed (Fig. 1). Here, the target system is divided into single-residue fragments. N corresponds to the total number of fragments (ligands, amino acid residues, H₂O molecules, etc.) in the PDB data. The modes can be selected from the tabs in panel 2 (Fig. 2). A CSV file, which contains $n \times n$ pairs of IFIEs or PIEs, is required to execute “*All-pairs*” mode. To control the function of the “*All-pairs*” mode, some information must be described in the input, such as chain name, residue

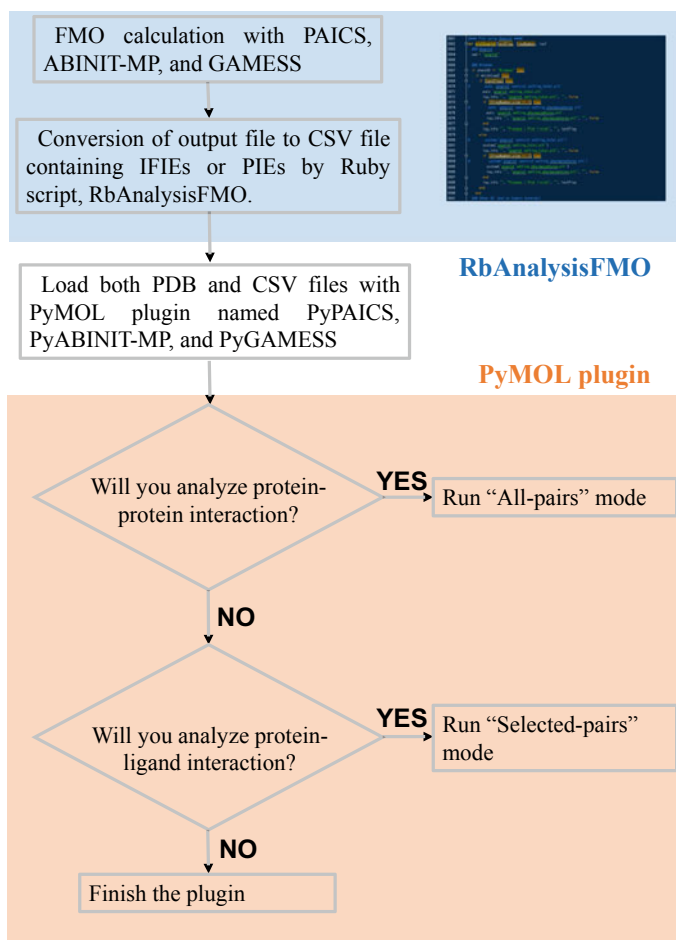


Fig. 1 Flowchart for the AnalysisFMO toolkit

number, and contour value, as shown in panel 3. A CSV file including either IFIEs or PIEs between either the ligand or a user-defined amino acid residue and other amino acid residues is required to run the “Selected-pairs” mode. A summary of the AnalysisFMO toolkit is shown in Table 1.

2.3 *RbAnalysisFMO* Tool—Conversion of Output File from Any FMO Package into a CSV File

As noted before, the RbAnalysisFMO tool can convert an output file from any FMO package to a CSV file containing interaction energies, i.e., $n \times n$ pairs (*user-selected*

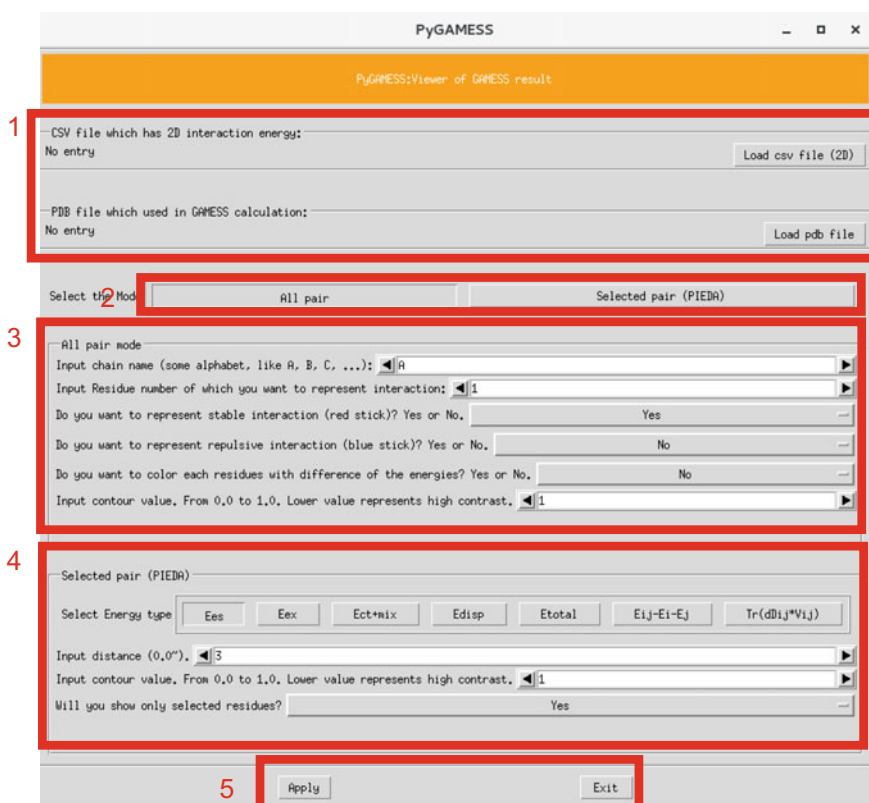


Fig. 2 Graphical user interface of our PyMOL plugin. The plugin can be divided into the following five sections. (1) selecting the input CSV generated by RbAnalysisFMO and the PDB file, (2) selecting the mode, (3) inputting parameters in the “All-pairs” mode, (4) inputting parameters in the “Selected-pairs” mode, and (5) starting or ending plugin use

Table 1 Characteristics of the AnalysisFMO toolkit

	FMO software		
Question about the functions of the toolkit	PAICS ^a	GAMESS ^b	ABINIT-MP ^c
Can RbanalysisFMO.rb extract interaction energies?	○	○	○
Can the plugin visualize IFIEs?	○ (PyPAICS)	×	○ (PyABINIT-MP)
Can the plugin visualize PIEs?	×	○ (PyGAMESS)	○ (PyABINIT-MP-PIEDA)
Can the plugin run on Linux?	○	○	○
Can the plugin run on Windows?	○	×	○ (Only PyABINIT-MP)

^aPAICS, 2012/05/13 version or later

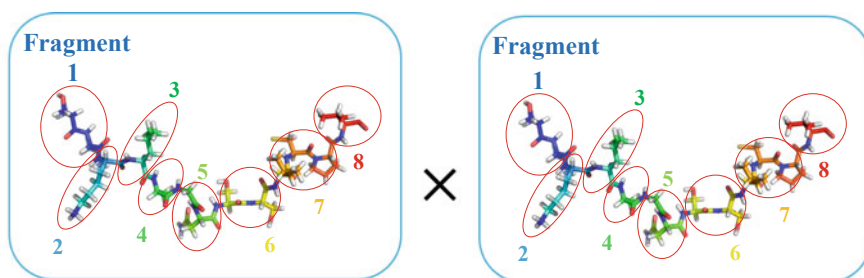
^bGAMESS, Version 11 Nov. 2017 (R3), FMO version 5.2

^cABINI-MP Open Ver. 1. Rev. 10/20,180,222

$fragment(s) \times n$ pairs) of IFIEs or PIEs when the “All-pairs” (“Selected-pairs”) mode is selected as illustrated in Fig. 3a. If the total number of fragments is n in the FMO scheme, the CSV file will contain $n \times n$ fragment pairs of IFIEs/PIEs as a two-dimensional (2D) table in the “All-pairs” mode. In the “Selected-pairs” mode, the CSV file will contain $1 \times (n - 1)$ IFIEs/PIEs as a one-dimensional (1D) table. If a target fragment is selected as a ligand (e.g., drug candidate, synthetic derivative, etc.) in the “Selected-pairs” mode, the CSV file will contain $1 \times n$ IFIEs/PIEs as a 1D table, which is essential data for in silico drug design since users can easily extract IFIEs/PIEs between the ligand and related amino acid residues around the binding site in the target protein. As an additional function of RbAnalysisFMO, this tool can generate a modified PDB file in which B-factor values of the atoms are replaced by Mulliken charges calculated at the adopted FMO calculation level of

a),

IFIEs or PIEs of $n \times n$ fragment pairs
(n is the total number of fragment)



b),

IFIEs/PIEs between user-selected fragment(s) and all fragments

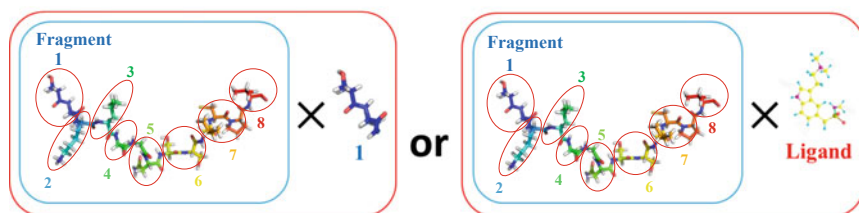


Fig. 3 Schematic illustration of the two analysis modes: The “All-pairs” and “Selected-pairs” modes (a and b). The “All-pairs” mode can analyze IFIEs/PIEs as [fragments]-[fragments] interaction. Therefore, $n \times n$ fragment pairs when the total number of the fragments is n . The “Selected-pairs” mode can analyze IFIEs/PIEs as [user’s selected fragment(s)]-[all fragments] interaction. Users can select ligand(s) or specific fragment(s) in the PDB file, and in this mode, the plugin can analyze IFIEs/PIEs between target fragment(s) and all fragments

theory in the “All-pairs” mode. It can also plot IFIEs/PIEs as a 2D interaction map and as a bar graph in the “All-pairs” and “Selected-pairs” modes, respectively, by applying the Gnuplot program [Gnuplot, <https://www.gnuplot.info/>]. The map and graph are helpful for overlooking the interaction energy data. Furthermore, our tool can be applied to the database of quantum mechanical data based on the FMO method [FMO DB, <http://drugdesign.riken.jp/FMO DB/>].

2.4 PyMOL Plugins: The “All-Pairs” Mode

In this paragraph, we will demonstrate how to make use of the “All-pairs” mode, which enables detailed visualization of residue–residue interactions. A picture of the plugins is shown in Fig. 2. Firstly, the CSV and PDB files generated by RbAnalysisFMO are loaded from the tabs “Load csv file (2D)” and “Load pdb file,” respectively (field “1” in Fig. 2). Subsequently, the tab “All-pairs” is selected (field “2” in Fig. 2). Users can further input residue information into the console panel, such as chain identifier and residue number, for which interactions would be represented. For example, if users fill “A” and “100” in the columns labeled “Input chain name” and “Input Residue number” seen in field “3” of Fig. 2, the plugins would visualize the interaction between the 100th residues belonging to chain A and other residues (Fig. 2). At this point, the plugins extract the interaction energies between the target residue and all other residues. Finally, the top five interaction energies, which bear the most negative (attractive) and the most positive (repulsive) interaction energies are identified by the program and represented as red and blue sticks, respectively. The width of the sticks indicates the magnitude of the interaction energies.

2.5 PyMOL Plugins: The “Selected-Pairs” Mode

If users need to analyze a protein–ligand interaction or pairs of interactions between one specific amino acid residue and all other residues, the “Selected-pairs” mode is a convenient option. In this paragraph, we will demonstrate how to make use of the “Selected-pairs” mode. Firstly, two files, namely the PDB file and CSV file, must be prepared. The latter contains PIEs/IFIEs between a ligand and all residues of the target protein generated by the RbAnalysisFMO tool. These files can be loaded into the plugins as described for the All-pairs mode (see field “1” of Fig. 2). After selecting the “Selected-pairs” tab in field 2, parameters must be set in field “4” and one of the desired energy tabs must be selected from the column “Select Energy type” (Fig. 2). The energy tabs can be changed depending on what types of FMO packages were utilized. In other words, users must choose appropriate plugins to visualize the energies correctly. For example, in Pair Interaction Energy Decomposition Analysis (PIEDA) formalism, there are a total of seven tabs in the plugins (Fig. 2), namely the total interaction energy “ E_{total} ” into the electrostatic energy “ E_{es} ,” the exchange

Table 2 List of energies of PIEDA

E_{total}	The total interaction energy
E_{es}	The electrostatic energy
E_{ex}	The exchange repulsive energy
$E_{\text{ct+mix}}$	The energy of charge transfer + MIX
E_{disp}	The dispersion energy
$E_{ij} - E_i - E_j$	The difference between the dimer energy E_{ij} and the monomer energies E_i and E_j
$\text{Tr}(\mathbf{D}_{ij} + \mathbf{V}_{ij})$	The explicit embedded charge transfer energy

repulsive energy, “ E_{ex} ,” the energy for charge transfer + MIX, “ $E_{\text{ct+mix}}$,” and the dispersion energy “ E_{disp} .” In addition, users can choose the internal pair energy “ $E_{ij} - E_i - E_j$,” defined as the difference between the dimer energy E_{ij} and the monomer energies E_i and E_j . Finally, the explicit embedded charge transfer energy “ $\text{Tr}(\mathbf{D}_{ij} + \mathbf{V}_{ij})$ ” is defined (Table 2). These energy tabs are available when users utilize PyGAMESS or PyABINIT-MP-PIEDA. In the case of IFIEs, three tabs are available, including “HF” (Hartree–Fock energy), “dMP2” (the MP2 correlation energies which correspond approximately to the dispersion force), and “MP2” (the sum of the HF and the dMP2 energies). The plugin will select dominantly interacting amino acid residues located within the distance defined in the column “*Input distance (0.0~)*” (Fig. 2). The selected amino acid residues are colored differently depending on the magnitude of the interaction energy as in the case of the “All-pairs” mode.

3 Application Examples

In this section, we will introduce examples of the AnalysisFMO toolkit being used to uncover the molecular mechanism of protein functions since in many cases, it is challenging to elucidate protein functions based solely on the crystal structure.

3.1 Interaction Energy Analysis for Fucose-Binding Lectin, BC2LC

Glycoconjugates are physiologically important compounds, and there are many glycosylated biomolecules, including glycoproteins and glycolipids [19]. They can also be found on cell surfaces. Pathogenic bacteria, such as *Burkholderia cenocepacia* which often causes rapid pulmonary disorder, recognizes glycoconjugates on cell surfaces with the fucose-binding lectin II-like proteins, or PA-IIL-like proteins, BC2LA, BC2LB, and BC2LC [19–21]. Among these three proteins, BC2LC has a unique structure; it is homotrimeric and is similar in structure to tumor necrosis factor (TNF)- α and C1q complement proteins [21]. BC2LC recognizes fucose utilizing the

interaction with Thr74, Thr83, Arg85, and Arg111 postulated based on their crystal structure [21]. However, there is no information available concerning which amino acid residues form strong interactions with fucose.

To perform FMO calculations, we firstly obtained structural data of BC2LC from PDB (PDB entry 2wq4). This structure was obtained from a complex of the protein with methyl-6-deoxy-1-seleno- α -L-galactopyranoside (SFU in Fig. 4a), which is expected to act as an analog of fucose and bind to the active site. After protonation of the structure, FMO calculation was performed with the FMO package, PAICS. Firstly, we used the “Selected-pairs” mode implemented in PyPAICS to visualize IFIEs between SFU and other amino acid residues (Fig. 4a). The magnitude of the attractive interaction energies (colored red in Fig. 4a) was in the following order: Arg111 (chain C) > Arg85 (chain A) > Gly84 (chain A) > Thr74 (chain C). This analysis indicated that Gly84, which had not been predicted to interact with SFU based on the crystal structure alone, forms a stronger interaction with SFU than Thr74. The results inferred that FMO calculation can unveil protein–ligand interactions quantitatively, which is hard to do based only a protein structure.

The interactions distant from the active (or ligand binding) site also play an important role in substrate/ligand recognition in proteins [22]. However, assigning these residues is difficult because there are many candidate residues around the site. We further analyzed the BC2LC structure using the “All-pairs” mode to detect relevant interactions for ligand binding and stability of the complex based on FMO calculations. Based on FMO analysis, there are stable (attractive) interactions between Ser74 (chain B) and other amino acid residues that form direct interaction with SFU. As

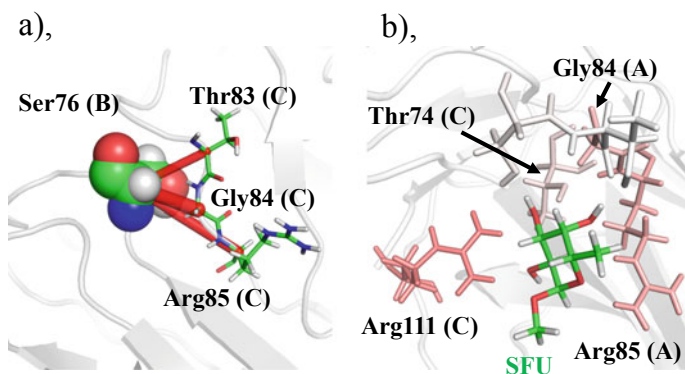


Fig. 4 Analysis of IFIEs for the TNF-like trimeric lectin from *Burkholderia cenocepacia* (BC2LC, PDB ID: 2WQ4) by use of PyPAICS implemented in AnalysisFMO toolkit (**a** and **b**). **a** The “Selected-pairs” mode was utilized to visualize interaction energies between SFU, where the Se atom was replaced by S and other amino acid residues. The attractive and repulsive interactions are colored in red and in blue, respectively. The IFIEs were calculated by applying second-order Møller-Plesset (MP2) perturbation theory with the cc-pVDZ basis set. **b** In the “All-pairs” mode, we visualized the interaction between Ser76 (chain B) and three other residues (Thr83, Gly84, and Arg85)

shown in Fig. 4b, Ser74 formed interactions with Thr83, Gly84, and Arg85 belonging to chain C in the following order of strength: Gly84 > Arg85 > Thr83 (Fig. 4b). These results suggest that Ser74 may be an important component of the sugar-binding site of BC2LC through direct interactions with the amino acid residues at the active site.

3.2 Predicted Metal Coordination Mechanism of Bilirubin Oxidase

In the previous example, we tried to quantify protein–ligand interaction based on IFIEs or PIEs analysis with a PyMOL plugin. Next, we attempt to elucidate the molecular mechanism that explains why metal ions coordinated at the active site of bilirubin oxidase from *Myrothecium verrucaria* (MvBO, PDB ID: 2XLL) cannot be ligated by the mutation of the amino acid residue that interacts indirectly with copper ions. MvBO is a metalloenzyme that catalyzes the oxidation of bilirubin to biliverdin by using an oxygen molecule [23]. In MvBO, three types of Cu ions exist: Type 1 copper (T1Cu), Type 2 copper (T2Cu), and Type 3 copper (T3Cu), which can be classified by their coordination pattern and the resulting absorbance and EPR signal. Catalysis occurs near T2Cu and pairs of T3Cu atoms (Fig. 5a) [23, 24]. As shown in Fig. 4a, several amino acid residues ligated to the Cu atoms. These amino acid residues are important to retain the Cu ions at the indicated site (Fig. 5a). Herein, the imidazole groups of three histidine residues (His136, His403, and His401) coordinated with T3Cu, T3Cu, and T2Cu, respectively (Fig. 4a). The coordination patterns of Cu are essential for MvBO to catalyze the reaction, and many groups have reported the amino acid residues, which are important to Cu coordination by introducing mutations. In a previous study, Kataoka et al. indicated that Asp105,

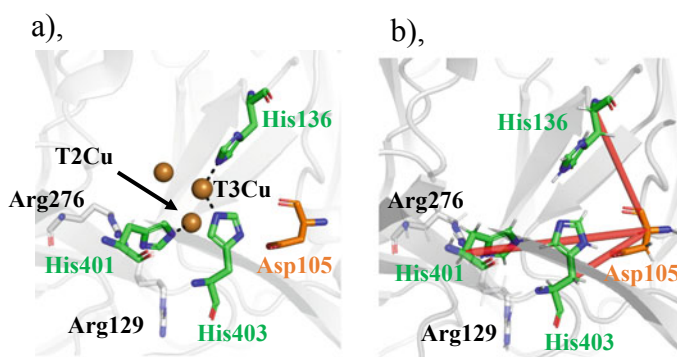


Fig. 5 Analysis of PIEs for bilirubin oxidase from *Myrothecium verrucaria*(MvBO, PDB ID: 2XLL) applying PyGAMESS implemented in the AnalysisFMO toolkit (a and b). Three Cu atoms in the active site of MvBO (a). The interactions between Asp105 and three other histidine residues (His136, His401, and His403) are represented as red sticks (b)

which is indirectly ligated to the Cu ions (orange, Fig. 5a), reduces the coordination number of the Cu ions [24]. In fact, the coordination numbers are in the following order: one (Asp105Ala) and two (Asp105Asn) Cu atoms are missing compared with native MvBO [24].

To determine why the mutation reduces the coordination number of Cu ions, we applied quantum mechanical interaction analysis based on the FMO calculations for MvBO. Calculations were done with the FMO package, GAMESS. Note that all the Cu ions in MvBO were excluded from the FMO calculations because of the convergence in both monomeric SCFs, including the multicenter metal region and dimer-SCC iteration, and is computationally challenging under the FMO scheme. The top three amino acid residues, which each form a stable (attractive) interaction with Asp105, are shown in Fig. 4b, clearly indicating that Asp105 forms interactions with Cu-coordinated residues, i.e., His136, His401, and His403 (Fig. 5b). The role of Asp105 is to help position the three His residues optimally to coordinate with Cu atoms (Fig. 5b). This result demonstrates a good example that protein functions, such as protein folding, the formation of the active site and cofactor recognition, are regulated in a complex manner by residue–residue interactions within the proteins.

4 Summary

In this study, we described the development of the AnalysisFMO toolkit to visualize interaction energies (IFIEs and PIEs) generated by several of FMO packages, i.e., PAICS, GAMESS, and ABINIT-MP. RbAnalysisFMO can extract the energies from the output file for one of the packages, and PyMOL plugin (PyPAICS, PyGAMESS, and PyABINIT-MP) can visualize the energies on the corresponding protein structure. Currently, we are developing a PyMOL plugin to analyze datasets registered in the FMO database [FMO DB, <https://drugdesign.riken.jp/FMO DB/>].

The applications of the toolkit indicate that we can elucidate the molecular mechanisms of proteins that are hard to predict based solely on structural data. For example, we can show that Gly84 in BC2LC interacts with SFU, although Gly84 was not expected to form an interaction with the ligand. Furthermore, we can propose a molecular mechanism to explain why mutating Asp105 in MvBO reduces Cu coordination. Taken together, the AnalysisFMO toolkit is a supportive tool for many users who are planning to elucidate protein functions based on the analysis of FMO calculations.

Acknowledgements The computation in this work was performed at the Research Center for Computational Science, Okazaki, Japan, the Research Center for Computational Sciences (CCS) at the University of Tsukuba, Japan, and Supercomputer Center of the Institute for Solid State Physics at the University of Tokyo, Japan.

Funding This project was supported by the Japan Science and Technology Agency (JST) and National Bioscience Database Center (NBDC). This project also supported by JSPS KAKENHI grant number 16K18688 and 18K14391.

Conflict of Interest The authors declare no competing financial interests.

References

1. Leavitt S, Freire E (2001) Direct measurement of protein binding energetics by isothermal titration calorimetry. *Curr Opin Struct Biol* 11:560–566
2. Brooks BR, Bruccoleri RE, Olafson BD, States DJ, Swaminathan S, Karplus M (1983) CHARMM: a program for macromolecular energy, minimization, and dynamics calculations. *J Comput Chem* 4:187–217
3. Case DA, Cheatham TE 3rd, Darden T, Gohlke H, Luo R, Merz KM Jr, Onufriev A, Simmerling C, Wang B, Woods RJ (2005) The Amber biomolecular simulation programs. *J Comput Chem* 26:1668–1688
4. Fedorov DG, Kitaura K (2009) The fragment molecular orbital method: practical applications to large molecular systems. CRC Press
5. Ishikawa T, Kuwata K (2009) Fragment molecular orbital calculation using the RI-MP2 method. *Chem Phys Lett* 474:195–198
6. Tanaka S, Mochizuki Y, Komeiji Y, Okiyama Y, Fukuzawa K (2014) Electron-correlated fragment-molecular-orbital calculations for biomolecular and nano systems. *Phys Chem Chem Phys* 16:10310–10344
7. Schmidt MW, Baldrige KK, Boatz JA, Elbert ST, Gordon MS, Jensen JH, Koseki S, Matsunaga N, Nguyen KA, Su SJ, Windus TL, Dupuis M, Montgomery JA (1993) General atomic and molecular electronic-structure system. *J Comput Chem* 14:1347–1363
8. Heifetz A, Aldeghi M, Chudyk EI, Fedorov DG, Bodkin MJ, Biggin PC (2016) Using the fragment molecular orbital method to investigate agonist-orexin-2 receptor interactions. *Biochem Soc Trans* 44:574–581
9. Heifetz A, Trani G, Aldeghi M, MacKinnon CH, McEwan PA, Brookfield FA, Chudyk EI, Bodkin M, Pei Z, Burch JD, Ortwine DF (2016) Fragment molecular orbital method applied to lead optimization of novel interleukin-2 inducible T-cell kinase (ITK) inhibitors. *J Med Chem* 59:4352–4363
10. Nakano S, Yasukawa K, Tokiwa T, Ishikawa T, Ishitsubo E, Matsuo N, Ito S, Tokiwa H, Asano Y (2016) Origin of stereoselectivity and substrate/ligand recognition in an FAD-dependent R-selective amine oxidase. *J Phys Chem B* 120:10736–10743
11. Delano WL (2002) The PyMOL molecular graphics system. Delano Scientific, S. C., CA., Ed.
12. Chovancova E, Pavelka A, Benes P, Strnad O, Brezovsky J, Kozlikova B, Gora A, Sustr V, Klvana M, Medek P, Biedermannova L, Sochor J, Damborsky J (2012) CAVER 3.0: a tool for the analysis of transport pathways in dynamic protein structures. *PLOS Comput Biol* 8:e1002708
13. Makarewicz T, Kazmierkiewicz R (2013) Molecular dynamics simulation by GROMACS using GUI plugin for PyMOL. *J Chem Inf Model* 53:1229–1234
14. Yamamoto Y, Takei K, Arulmozhiraja S, Sladek V, Matsuo N, Han SI, Matsuzaka T, Sekiya M, Tokiwa T, Shoji M, Shigeta Y, Nakagawa Y, Tokiwa H, Shimano H (2018) Molecular association model of PPAR α and its new specific and efficient ligand, pemafibrate: structural basis for SPPAR α . *Biochem Biophys Res Commun* 499:239–245
15. Nakano S, Okazaki S, Ishitsubo E, Kawahara N, Komeda H, Tokiwa H, Asano Y (2015) Structural and computational analysis of peptide recognition mechanism of class-C type penicillin binding protein, alkaline D-peptidase from *Bacillus cereus* DF4-B. *Sci Rep* 5:13836
16. Tokiwa T, Nakano S, Yamamoto Y, Ishikawa T, Ito S, Sladek V, Fukuzawa K, Mochizuki Y, Tokiwa H, Misaizu F, Shigeta Y (2019) Development of an analysis Toolkit, AnalysisFMO, to visualize interaction energies generated by fragment molecular orbital calculations. *J Chem Inf Model* 59:25–30

17. Aerts J, Law A (2009) An introduction to scripting in Ruby for biologists. *BMC Bioinform* 10:221
18. Sanner MF (1999) Python: a programming language for software integration and development. *J Mol Graph Model* 17:57–61
19. Imberty A, Varrot A (2008) Microbial recognition of human cell surface glycoconjugates. *Curr Opin Struct Biol* 18:567–576
20. Courtney JM, Dunbar KE, McDowell A, Moore JE, Warke TJ, Stevenson M, Elborn JS (2004) Clinical outcome of *Burkholderia cepacia* complex infection in cystic fibrosis adults. *J Cyst Fibros* 3:93–98
21. Sulak O, Cioci G, Delia M, Lahmann M, Varrot A, Imberty A, Wimmerova M (2010) A TNF-like trimeric lectin domain from *Burkholderia cenocepacia* with specificity for fucosylated human histo-blood group antigens. *Structure* 18:59–72
22. Sommer DJ, Vaughn MD, Ghirlanda G (2014) Protein secondary-shell interactions enhance the photoinduced hydrogen production of cobalt protoporphyrin IX. *Chem Commun (Camb)* 50:15852–15855
23. Koikeda S, Ando K, Kaji H, Inoue T, Murao S, Takeuchi K, Samejima T (1993) Molecular cloning of the gene for bilirubin oxidase from *Myrothecium verrucaria* and its expression in yeast. *J Biol Chem* 268:18801–18809
24. Kataoka K, Kitagawa R, Inoue M, Naruse D, Sakurai T, Huang HW (2005) Point mutations at the type I Cu ligands, Cys457 and Met467, and at the putative proton donor, Asp105, in *Myrothecium verrucaria* bilirubin oxidase and reactions with dioxygen. *Biochemistry* 44:7004–7012

New Methods and Applications

FMO Interfaced with Molecular Dynamics Simulation



Yuto Komeiji and Takeshi Ishikawa

Abstract Three ways to combine FMO and MD are described: FMO-MD, FMO-QM/MM-MD, and MM-MD/FMO. FMO-MD is an ab initio MD in which force is updated on-the-fly by FMO. FMO-QM/MM-MD is a QM/MM-MD method in which the QM part is calculated by FMO. MM-MD/FMO is a simulation protocol in which FMO calculation is performed for molecular configurations generated by MM-MD. The methodology and application of these methods are described and compared.

Keywords MD · MM · Solvation · Reaction

The enormous capability of the FMO method in the electronic state calculation has been discussed in previous chapters. Information obtained from a single-point FMO calculation of a molecule is still limited, however. The capability of FMO can be enhanced in combination with molecular dynamics (MD), which simulates the time-dependent evolution of the molecular system of interest. MD enables us to sample molecular conformations at finite temperature, to calculate time-dependent properties, and even to simulate chemical reactions.

In this chapter we describe three ways to interface FMO and MD. The first is ab initio MD called FMO-MD (Sect. 1), in which the forces acting on all the constituent nuclei are calculated on-the-fly by FMO. The second is FMO-QM/MM-MD (Sect. 2), in which part of the forces are calculated by FMO and the rest by using classical MM parameters. The third is MM-MD/FMO (Sect. 3), in which molecular structures modeled by classical MM-MD are subject to FMO energy calculation.

We will wrap up this chapter by comparing these three ways and discussing the future direction.

Y. Komeiji (✉)

Health and Medical Research Institute, AIST Tsukuba Central, 6, Higashi 1-1-1, Tsukuba 305-8566, Japan

e-mail: y-komeiji@aist.go.jp

T. Ishikawa

Department of Chemistry, Biotechnology, and Chemical Engineering, Graduate School of Science and Engineering, Kagoshima University, 1-21-40 Korimoto, Kagoshima 890-0065, Japan

e-mail: ishi@cb.kagoshima-u.ac.jp

1 FMO-MD

The ab initio FMO-MD method is the most straightforward way to interface FMO with MD [37]. FMO-MD simulates molecular phenomena caused by electronic state changes similar to any ab initio MD methods. In this subsection, we give an outline of the FMO-MD method and its recent major achievements. Readers are also referred to previous reviews for detailed account of FMO-MD up to 2010 [34, 36].

1.1 Methodology

In FMO-MD, the positions of the nuclei of the molecules of interest are updated by the Newtonian equation of motion using the force ($=-\text{energy gradient}$) exerting on the nuclei calculated by FMO. Thus, FMO-MD is an on-the-fly ab initio MD based on the Born–Oppenheimer approximation. The nuclei can be handled by quantum mechanics [11], but usually by classical mechanics in most FMO-MD simulations reported so far.

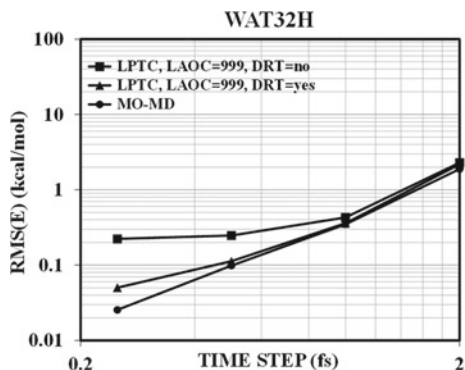
The first implementation of FMO-MD was accomplished by merging an MD program (PEACH) [40] and an FMO program (ABINIT-MP, see Chap. 4) through the system call command [31]. Later on, FMO-MD was implemented in GAMESS [3] and also in ABINIT-MP alone [30].

An essential constituent of FMO-MD is the “dynamic fragmentation (DF)” algorithm, which refers to redefinition of fragments depending on the instantaneous molecular conformation [35]. In this simple DF algorithm, a covalent bonded cluster of atoms is regarded as a fragment. Later on, DF was modified to fix some part of the molecular system to remain static (no redefinition of fragments) while allowing the rest to be dynamic (redefinition of fragments). The modified algorithm called “DF/SF algorithm” is applicable to, for example, a solvated protein, where the protein is regarded as static while the solvent as dynamic [30].

Until today, most of FMO-MD simulations have been performed in a free, non-periodic boundary. Nevertheless, an implementation of the periodic boundary has been reported [10], in which the electrostatic contribution from a layer of image boxes was included. Another implementation of periodic boundary utilized the minimum image convention [3]. Both are important implementations, but the former consumes too much computational resource and the latter lack in enough precision for a long-range simulation. Therefore, an Ewald or Multipole method is required to calculate long-range coulomb interaction for FMO-MD in a periodic boundary (work in progress, Nakano et al. personal communication).

The original FMO gradient [28] is not strictly analytic, due to neglect of exact solution of coupled-perturbed Hartree–Fock (CPHF) equations. This weakness deteriorates the precision of FMO-MD. Fortunately, Nagata and his colleagues have derived a series of fully analytic energy gradients for FMO [47–52] [53]. The analytic gradients were introduced first to GAMESS [3] and later to ABINIT-MP. See Fig. 1

Fig. 1 Comparison of conventional (DRT = no) and analytic (DRT = yes) energy gradients. RMS of total energy as functions of time step was drawn for $\text{H}^+(\text{H}_2\text{O})_{32}$ with ABINIT-MP. Provided by Dr. Takayuki Fujiwara of TS Technology Inc.



for improvement of the energy conservation by the analytic gradient as demonstrated for $\text{H}^+(\text{H}_2\text{O})_{32}$.

Yet another important methodological achievement is the introduction of density-functional tight-binding (DFTB) to FMO-MD (DFTB-FMO/MD) [54] in GAMESS. Though DFTB is not “ab initio,” because it contains parameters, most of them have a sound theoretical basis [41]. Hence, DFTB can be a reasonable and inexpensive alternative to DFT by reducing computational demand greatly. For example, FMO-DFTB/MD of 256 water molecules was ca. 100 times faster than full DFTB/MD while conserving total energy within good precision.

1.2 Applications

FMO-MD has been successfully used for investigation of chemical reactions of small molecules in aqueous solution. Sato et al. [63] reported FMO-MD simulation of hydrolysis of CH_3N_2^+ in explicit solvation. This typical $\text{S}_{\text{N}}2$ -type reaction was shown to proceed via diverse paths including both tight- and loose- $\text{S}_{\text{N}}2$. FMO-MD was then applied to amination and hydration of H_2CO and revealed that the amination proceeds by a stepwise mechanism, but hydration by a concerted one [64, 65].

Besides chemical reactions, FMO-MD has been applied for investigation of hydrated metal ions. A simulation of hydrated Zn^{2+} reproduced the experimental RDF position [12]. Unrestricted Hartree–Fock (UHF) was introduced to FMO-MD and was shown effective in a simulation of Cu^{2+} [27]. FMO-MD was also applied to hydrated Lanthanoid series of heavy ions (Ln^{3+}) and reproduced the Lanthanoid contraction [13]. In an FMO study on hydrated Rn^{2+} ion, Rn^{2+} was shown to have a flexible square antiprism structure with a hydration number of 8.1 [44].

Hydration of small molecules has been also analyzed by FMO-MD. For example, Mori et al. [46] compared solvated structures of *cis*- and *trans*-platins and found that the charge-transfer interaction coupled with the solvent motion is stronger in

cis-platin than in *trans*-platin. This suggests that Pt–Cl bonds in *cis*-platin are easier to cleave.

FMO-DFTB/MD was tested by simulation of (HX)₁₀₀₀, where X = Halogen, and gave X–X radial distribution functions comparable to experimental ones [54]. Recently, FMO-DFTB/MD was used to calculate time-dependent change of PIEDA within TrpCage in an implicit solvent at finite temperature [7].

2 FMO-QM/MM-MD

As reviewed in Subsect. 1.2, FMO-MD has been often applied to molecular systems consisting almost entirely of water molecule. Because water molecules are usually treated as a single fragment, the size of fragments is extremely small (i.e., only three atoms). Thus, the computational time of each step of the MD simulation can be reduced to around a few minutes, which is enough to obtain a several picoseconds trajectory. This is an important reason why aqueous solution systems have been selected for FMO-MD applications. In MD simulations of large biomolecular systems (e.g., simulations of enzyme reactions or biological photo-processes), however, it is difficult to sufficiently reduce the computational cost even by using the FMO method. In FMO calculations of a protein, amino acid residues are treated as single fragments, each consisting of more than 10 or 20 atoms. Consequently, calculation of the energy gradient of a protein containing about 100 amino acid residues requires at least more than several hours (it actually depends on the used theory, basis set, and computer system). Thus, it is too costly to perform FMO-MD simulations of proteins.

Another choice for the quantum chemical investigation of biomolecular systems is quantum chemical/molecular mechanics (QM/MM) method [8, 67, 74, 75], [68]. In the QM/MM method, an important region directly involved in the chemical reaction or photo-process is treated with a quantum chemical method (QM region), while the other region is treated with a classical method using empirical force fields (MM region). In recent decades, many studies utilizing the QM/MM method have been successfully performed [9, 15, 66]. However, when performing the MD simulations with the QM/MM method, the QM region should be limited within a small number of atoms (e.g., several dozen atoms) to reduce the computational cost for the energy gradient. Thus, MD simulations of the enzyme reactions or biological photo-processes with a large active site are difficult even for the QM/MM method.

To overcome such a difficulty, Okamoto et al. [56] proposed the FMO-QM/MM-MD simulation. In this method, FMO is adopted as a quantum chemical method in the context of the QM/MM scheme, resulting in major reduction of the computational cost of the energy gradient of each time step for systems with a large QM region.

2.1 Theory

Here, we first explain the details of the theoretical background of the FMO-QM/MM-MD method.

The target system is divided into MM and QM regions similar to the original QM/MM method. The total energy is calculated from the sum of the internal energies of the QM (E_{QM}) and MM (E_{MM}) regions, and the interaction energy between them ($E_{QM/MM}$) as the following equation:

$$E_{total} = E_{QM} + E_{QM/MM} + E_{MM} \quad (1)$$

The interaction energy is described as

$$E_{QM/MM} = E_{QM/MM}^{elec} + E_{QM/MM}^{non-elec}, \quad (2)$$

where the first and second terms are the electrostatic and non-electrostatic interaction energies, respectively. The non-electrostatic interaction energy is calculated with some empirical parameters as the following equation:

$$E_{QM/MM}^{non-elec} = \sum_{A \in QM} \sum_{B \in MM} \varepsilon_{AB} \left\{ \left(\frac{\sigma_{AB}}{|\mathbf{R}_A - \mathbf{R}_B|} \right)^{12} - 2 \left(\frac{\sigma_{AB}}{|\mathbf{R}_A - \mathbf{R}_B|} \right)^6 \right\}, \quad (3)$$

where A and B are indexes of the atoms in the QM and MM regions, respectively, \mathbf{R}_A and \mathbf{R}_B are positions of the atoms, and ε_{AB} and σ_{AB} are empirical parameters defined for the pair of the atoms. Sum of the internal energy of the QM region and the electrostatic interaction energy between the QM and MM regions is regarded as the energy of the QM region including the external point charges by the MM region atoms. Thus, we additionally introduce a notation of the energy obtained from the FMO calculation:

$$E_{QM} + E_{QM/MM}^{elec} \equiv E_{FMO}^{MM}, \quad (4)$$

Then, the expression of the total energy of Eq. (1) can be written as the following equation:

$$E_{tot} = E_{FMO}^{MM} + E_{QM/MM}^{non-elec} + E_{MM}. \quad (5)$$

In FMO calculations including the external MM point charges, the following Fock operator is used:

$$\hat{f}_X^{MM} = \hat{f}_X + \sum_{K \neq X}^N \hat{V}_X + \hat{P}_X + \hat{V}_X^{MM}, \quad (6)$$

where X is I or IJ for the monomer or dimer calculation of the FMO scheme, respectively. The first three terms are exactly the same as the Fock operator used for the original FMO calculation, the first term being the conventional Fock operator, the second the environmental electrostatic potential, and the third the projection operator. The last term is the electrostatic potential from the external MM point charges, that is,

$$\hat{V}_X^{MM} = \sum_{B \in MM} \frac{-q_B}{|\mathbf{R}_B - \mathbf{r}|}, \quad (7)$$

where q_B is the net charge of the atoms in the MM region.

We introduce the notation of E_X and \mathbf{D}_X as the energy and density matrices, respectively. They are obtained from the monomer or dimer SCF calculation with the Fock operator given in Eq. (6). Additionally, we define E''_X as the following equation:

$$E''_X = E_X - \text{Tr}(\mathbf{D}_X \mathbf{V}_X) - \text{Tr}(\mathbf{D}_X \mathbf{V}_X^{MM}), \quad (8)$$

where \mathbf{V}_X and \mathbf{V}_X^{MM} are operator matrices of \hat{V}_X and \hat{V}_X^{MM} , respectively. Consequently, we consider that this value is the internal energy of the monomer or dimer (contribution of the environmental electrostatic potential and MM point charges is removed from E_X). Using these values, the first term of Eq. (5) is written as

$$\begin{aligned} E_{FMO}^{MM} = & \sum_I^N E''_I + \sum_{I>J}^N (E''_{IJ} - E''_I - E''_J) + \sum_{I>J}^N \text{Tr}(\nu \mathbf{D}_{IJ} \mathbf{V}_{IJ}) \\ & + \sum_I^N \{ \text{Tr}(\mathbf{D}_I \mathbf{V}_I^{MM}) + E_I^{nuc-MM} \} + \sum_{I>J}^N \text{Tr}(\nu \mathbf{D}_{IJ} \mathbf{V}_{IJ}^{MM}), \quad (9) \end{aligned}$$

where $\Delta \mathbf{D}_{IJ}$ is the differential density matrix defined as

$$\nu \mathbf{D}_{IJ} = \mathbf{D}_{IJ} - (\mathbf{D}_I \nu \mathbf{D}_J), \quad (10)$$

and E_I^{nuc-MM} is the electrostatic interaction energy between the nucleus of QM region and MM point charges, that is,

$$E_I^{nuc-MM} = \sum_{A \in I} \sum_{B \in MM} \frac{Z_A q_B}{|\mathbf{R}_A - \mathbf{R}_B|}, \quad (11)$$

where Z_A is the nucleus charge of atom A .

To obtain the force acting on the atoms, which is required for the MD simulation, we must differentiate the total energy of Eq. (5) with respect to the atomic coordinates as the following equation:

$$\frac{\partial E_{tot}}{\partial \mathbf{R}} = \frac{\partial E_{FMO}^{MM}}{\partial \mathbf{R}} + \frac{\partial E_{QM/MM}^{non-elec}}{\partial \mathbf{R}} + \frac{\partial E_{MM}}{\partial \mathbf{R}}. \quad (12)$$

While the second and third terms can be easily calculated because they are empirical potential functions, the first term should be calculated in a quantum chemical way in the context of the FMO method. Differentiated with respect to the coordinates of the QM atoms, the first term is written as the following equation:

$$\begin{aligned} \frac{\partial E_{FMO}^{MM}}{\partial \mathbf{R}_A} &= \sum_I^N \frac{\partial E_I''}{\partial \mathbf{R}_A} + \sum_{I>J}^N \left(\frac{\partial E_{IJ}''}{\partial \mathbf{R}_A} - \frac{\partial E_I''}{\partial \mathbf{R}_A} - \frac{\partial E_J''}{\partial \mathbf{R}_A} \right) + \sum_{I>J}^N Tr \left(v \mathbf{D}_{IJ} \frac{\partial \mathbf{V}_{IJ}}{\partial \mathbf{R}_A} \right) \\ &+ \sum_I^N \left\{ Tr \left(\mathbf{D}_{IJ} \frac{\partial \mathbf{V}_{IJ}}{\partial \mathbf{R}_A} \right) + \frac{\partial E_I^{nuc-MM}}{\partial \mathbf{R}_A} \right\} + \sum_{I>J}^N Tr \left(v \mathbf{D}_{IJ} \frac{\partial \mathbf{V}_{IJ}^{MM}}{\partial \mathbf{R}_A} \right). \end{aligned} \quad (13)$$

On the other hand, the differentiation with respect to the coordinates of the MM atoms can be obtained using the electric field made by the QM region, \mathbf{E}_{QM} , that is,

$$\frac{\partial E_{FMO}^{MM}}{\partial \mathbf{R}_B} = -q_B \mathbf{E}_{QM}(\mathbf{R}_B). \quad (14)$$

Detailed formulation of the electric field in the FMO scheme can be found in Ishikawa [20]. Although we have so far assumed the HF level of theory, the above formulations can be extended to the MP2 level of theory by using the reported FMO-MP2 gradient [45], [48] or FMO-RI-MP2 gradient [23].

2.2 Implementation

As the first implementation of the FMO-QM/MM-MD method, AMBER-PAICS interface has been developed [56] by combining AMBER9, a widely used program package for classical MD simulation [73], and PAICS, an FMO program package [22] (see Chap. 5 for details). In the AMBER-PAICS interface, the SANDER module, the MD engine of AMBER, is run as the main program. In each time step, SANDER calls PAICS through the system call and obtains the energy gradients given in Eqs. (13) and (14). An input file for PAICS is automatically generated at every time step by updating the atomic coordinates. Some information needed for the FMO calculation (e.g., fragmentation manner, basis sets, and so on) is obtained from a separate file. Development of the AMBER-PAICS interface was facilitated by the

QM/MM subroutines originally implemented in AMBER. See Okamoto et al. [56] for further details.

2.3 Applications

Some applications of the FMO-QM/MM-MD have been reported. One of them is the simulation of alanine dipeptide in aqueous solution [56]. In this simulation, a cubic unit cell under the periodic boundary condition was adopted, in which one alanine dipeptide and 3510 solvent water molecules were included. Two types of QM region were prepared. One was a larger QM region containing the alanine dipeptide and 45 water molecules. The other was a smaller one consisting only of the alanine dipeptide. The FMO-QM/MM-MD simulations were executed in the NVT ensemble at 300 K using the Berendsen thermostat. The total simulation time was 6.0 ps, and the last 2.5 ps trajectory was used for the analysis. The MD time step was set to 2 fs. FMO calculations were performed at the HF/6-31G level of theory.

In the trajectory with the large QM region, a triple-water bridging conformation with two peptide C=O groups was mainly observed. The radial distribution function and integrated coordination number were also consistent with a previous first principal DFT-MD simulation [16]. On the other hand, a double-water bridging conformation was observed in the trajectory with the small QM region. It was similar to a previous QM/MM study [26], where only the alanine dipeptide was treated as the QM region. This application study indicated that the size of QM region affects the resulting trajectory.

The ease of periodic boundary is an important advantage of FMO-QM/MM-MD over FMO-MD. In the current implementations of FMO-MD, droplet models have been used instead of periodic boundary condition (see Subsect. 1.1). Consequently, edge artifacts of the droplet model are inevitably included in the trajectory of the FMO-MD simulation [31], but not in FMO-QM/MM-MD with the periodic boundary.

Here, we show another application for a biomolecular system, that is, the FMO-QM/MM-MD simulation of the complex between prion protein (PrP) and GN8 molecule. PrP is an infectious agent of prion diseases [59], which is developed from the conformational conversion of a normal cellular form of the prion protein (PrP^C) into an alternatively folded scrapie isoform (PrP^{SC}). Recently, an anti-prion compound termed GN8 was found to make hydrogen bonding interaction with N159 and E196 of PrP^C, by which the pathological conversion to PrP^{SC} could be inhibited [43]. To examine the molecular interaction between PrP^C and GN8, FMO-QM/MM-MD simulation was performed [56]. The initial structure of the complex was modeled by the NMR structure of mouse PrP^C (PDB code: 1AG2, [60]). The periodic boundary condition was adopted, where 10309 water molecules and two sodium ions were arranged around the PrP^C-GN8 complex in the unit cell (Fig. 2 left). GN8 molecule and important two amino acid residues (N159 and E196) were included in the QM region (Fig. 2 right). Each amino acid residue was treated as a single fragment, and

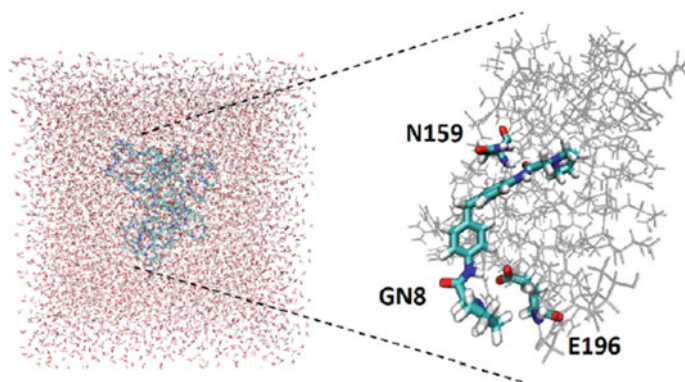


Fig. 2 FMO-QM/MD simulation of the PrP-GN8 protein. Reproduced from Ishikawa [19] with the permission of the publisher

GN8 molecule was divided into four fragments. The energy gradient was calculated at HF/6-31G level of theory, but the total energy and inter-fragment interaction energy (IFIE) was calculated at MP2/6-31G level of theory in every time step. The simulation was carried out in NVT ensemble, where the time step was 1.0 fs and the total simulation time was 5.0 ps. The temperature of the system was maintained at 300 K using the Berendsen thermostat. This FMO-QM/MM-MD simulation took about 20 days using Intel Xeon processor E5429 on 16 cores.

In this study, time-dependent evolution of IFIE between the two amino acid residues and GN8 molecule was calculated directly from the obtained trajectory (Fig. 3), unlike in a typical FMO study in which IFIE is calculated for a single structure modeled by an experimental X-ray structure or for several snapshots picked up from a classical MM-MD trajectory (see next subsection). At the initial time, both the interactions of GN8 with N159 and E196 were sufficiently strong (the IFIEs were around -11 and -19 kcal/mol, respectively). As time progressed, the interaction with N159 became weaker, and finally the IFIE reached to zero. In contrast, the IFIE with E196 remained within -15 to -35 kcal/mol throughout the simulation. Therefore, it was revealed that N159 and E196 have different dynamic behaviors for the binding with GN8. The 5 ps trajectory is, of course, not enough for a reliable discussion of the dynamic behavior of amino acid residues. However, this study indicated that the “dynamic IFIE analysis” by the FMO-QM/MM-MD simulation can provide a different information of the molecular interaction than that provided by the “static IFIE analysis.”

Although we have described two examples of the FMO-QM/MM-MD applications, currently very few studies have been reported on this method. One reason is that there is no appropriate software for FMO-QM/MM-MD simulation (AMBER-PAICS interface is not currently open to the public). Another reason is the need for DF (see Subsect. 1.1) and adaptive QM/MM approach [4, 17], [70]. When performing FMO-QM/MM-MD simulations, definition of the fragmentation should be updated similar to FMO-MD simulations by the FD algorithm. Additionally, in the case

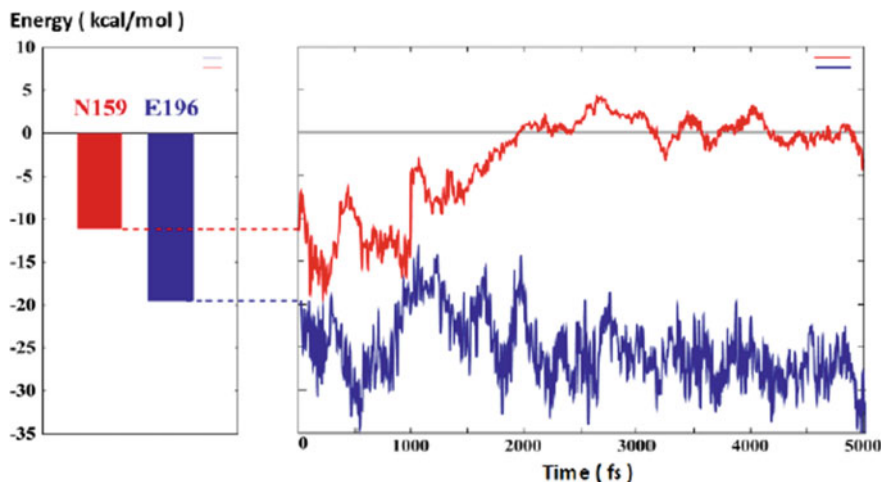


Fig. 3 Dynamic IFIE analysis between GN8 and two amino acid residues (N159 and N196). Reproduced from Okamoto et al. [56] with permission from the publisher

of the FMO-QM/MM-MD, definition of the QM region should also be updated when, for example, water molecules in the QM region happen to move into the MM region during the simulation. Such water molecules should be assigned as the MM region's molecule. This method has already been developed as adaptive QM/MM approach. However, FMO-QM/MM-MD simulation with DF and adaptive QM/MM has not yet been developed. If a user-friendly software including such simulation techniques is developed, FMO-QM/MM-MD method becomes more widely used for the investigation of enzyme reactions or biological photo-processes.

3 MM-MD/FMO

Prior to a single-point FMO energy calculation, the molecular structures are usually modeled by optimization with classical MM-based MD and/or EM methods. We refer to this procedure as MM-MD/FMO. Thus MM-MD/FMO is not so much a simulation method as a protocol or a recipe. MM-MD/FMO is currently necessary for FMO calculation of huge molecular systems whose FMO-MD or even FMO-QM/MM-MD is too demanding to perform. MM-MD/FMO is a ubiquitous procedure because most modeling programs perform an MM-based optimization in preparation of molecular structures. In a typical FMO calculation of protein, the crystal structure is complemented with hydrogens and possibly with counterions and partial solvent, followed by MM-optimization.

In this section, however, we concentrate on MM-MD/FMO of only extensively and explicitly solvated molecular systems, where manipulation of solvent plays a critical

role for validity of the FMO calculation. Inclusion of explicit water solvent was tried in early FMO and FMO-MD calculations of polypeptides and polynucleotides [24, 31], but without critical verification of the solvation protocol. The solvation protocol was minutely investigated later as described below.

To use explicit water solvent, choice of boundary condition is important. Almost all the FMO calculations on biological molecules are performed in a free boundary. Though it is possible to apply the periodic boundary to FMO [10], the extremely high computational demand hinders its practical application. Hence, the simplest way is to perform MM-MD in a free boundary from the beginning so that the resultant modeled structure can be applied to FMO directly (e.g., [31]). Nevertheless, today, most MM-MD simulations of solvated biological molecules are performed in the periodic boundary. We therefore need to convert a molecular structure in the periodic boundary to one in the free boundary to interface MM-MD and FMO. The conversion method is described in Komeiji et al. [38], the outline being schematized in Fig. 4. It is necessary to consider solvent molecules including counterions in the image cells.

A comprehensive evaluation of the explicit solvation of a protein for FMO was reported in a study of the ubiquitin protein [32] performed by the MM-MD/FMO protocol. In this study, structures of pure water and solvated protein were prepared by MM-MD and EM (annealing), from which configurations for FMO were excised with various thicknesses of solvent shell. No counterion was included because ubiquitin has no net charge at the neutral pH. The effect of the solvent thickness varied depending on the physical properties. The protein net charge converged at 4 Å, and the protein internal energy and protein–solvent interaction energy converged at 8 Å.

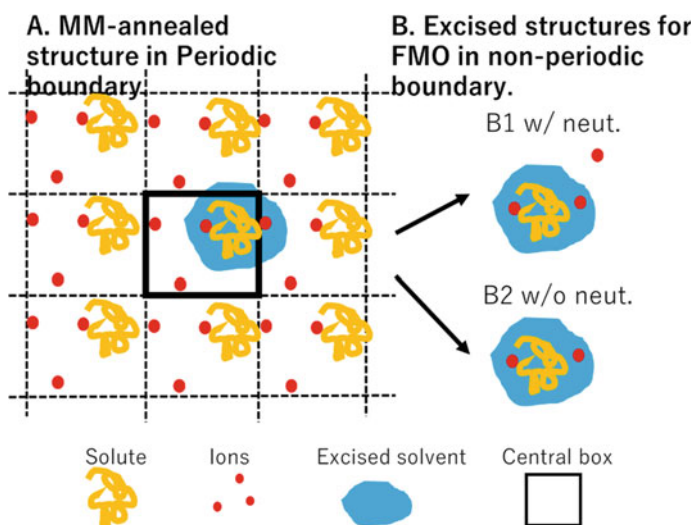


Fig. 4 Schematics for construction of molecular structures for FMO. Reproduced from Komeiji et al. [38] with permission from the publisher

Another important finding was that water molecules within 4 Å of the outer surface are less polarized than the bulk water.

Similar test studies were performed for a double-stranded (ds) DNA [14] and for a single-stranded (ss) DNA [38]. The net charge of dsDNA converged marginally at 4 Å and completely at 8 Å, while that of ssDNA converged at 4 Å. Their internal energies converged marginally at 4 Å and completely at 8 Å. For the DNA–solvent interaction, however, thicker solvent was necessary. Presence of counterions outside the solvation shell affected only the solute (DNA)–solvent (water and ions) interaction and not internal solute energy or net charge.

Taken together, the net charge and internal energy of a protein/DNA are dominantly governed by the first solvent shell within 4 Å from the solute surface and auxiliary by the second and third shells within 8 Å. Hence, it is usually recommended to include water solvent as thick as 8 Å, or, if computationally too demanding, at least 4 Å. It is not strictly required to include all the counterions outside the solvation shell except when neutrality of the system is necessary.

The number of MM-MD/FMO studies in water has been increasing. The investigated molecules are: lysozyme with-NAG [21], monosaccharides with HIV-1 antibody 2G12 [72], vitamin-D receptor with its ligands [69], amyloid-β peptides in an amyloid-β hexamer [25], androgen receptor with its ligand [29], zinc metalloproteinase with its inhibitors [1], ssDNA with the binding protein [39], and dsDNA with UO_2^{2+} [61]. Specific interactions within these molecular complexes have been minutely analyzed by IFIE and PIEDA in explicit solvation.

Promoted by recent advancement of artificial intelligence, Saitou et al. [62] reported an attempt to predict protein secondary structures by combining MM-MD/FMO and deep learning (DL). Two typical protein secondary structures, α-helix and β-sheet, provide some characteristic patterns in the two-dimensional map of inter-fragment interaction energy (IFIE-map [42], see part 3 for details). From MM-MD/FMO calculations for 18 proteins and 3 non-protein molecules, a thousand IFIE-map images were prepared, each labeled depending on the existences of α-helix and β-sheet. The images were used as the training data of DL implemented with the TensorFlow library of Google Inc. Finally, TensorFlow was fed with new data to test its ability to recognize the structural patterns. The characteristic structures in test IFIE-map images were successfully predicted. In this way, it was shown that the pattern recognition ability of DL can be applied to protein secondary structure prediction,

Thus, the MM-MD/FMO protocol has been playing an important role in FMO calculation of biological macromolecules.

However, an important question remains: is it appropriate to use an MM-optimized structure for QM? From an extremely strict viewpoint, the answer would be “No” because a classical MM force field differs from the corresponding QM force field. Nevertheless, because an MM force field can be regarded as an approximation of the QM force field, the MM-optimized molecular structures may serve as a practical workaround when QM-optimization is too demanding for structure modeling. In Komeiji et al. [33, 34], two pieces of indirect evidence were reported for validity of the MM-MD/FMO protocol. One was that relative energy differences among several

configurations of pure water showed good correlation between MM (TIP3P) and QM (HF6-31G*/FMO) calculations. The other was that starting from an MM-optimized solvent (TIP3P) made the subsequent FMO-MD heating much smoother than starting from a random solvent. It was also reported, however, that a carelessly prepared MM parameter resulted in a molecular structure inappropriate for FMO calculation [71].

Considering all these cons and pros, we still regard MM-MD/FMO as a standard protocol for FMO calculation of large molecular systems. There are several ways to improve the MM-MD/FMO protocol. One is use of QM-MM optimization after or without MM optimization [6, 18, 55, 71]. This protocol is useful when studying a local part of the molecular system, for example, the reaction center of an enzyme. Another way is development of MM force field parameters based upon FMO that can mimic the FMO force field at a much lower cost [57, 58]. MM-MD with such an MM force field may give a structure somewhat consistent with subsequent FMO calculation.

4 Perspective

We have so far described three ways to interface FMO with MD, each of which has some problems to be solved for further application to large molecules. It is mandatory to accelerate FMO-MD and FMO-QM/MM-MD. A possible way is introduction of DL to accelerate MD [2, 5, 76]. Another urgent task is development of an FMO-based MM parameter to improve the consistency of the MM-MD/FMO protocol. These developments will achieve a seamless integration of FMO(QM) and MM.

References

1. Ara A, Kadoya R, Ishimura H et al (2017) Specific interactions between zinc metalloproteinase and its inhibitors: Ab initio fragment molecular orbital calculations. *J Mol Graph Model* 75:277–286
2. Behler J, Parrinello M (2007) Generalized neural-network representation of high-dimensional potential-energy surfaces. *Phys Rev Lett* 96:16401
3. Brorsen KR, Minezawa N, Xu F et al (2012) Fragment molecular orbital molecular dynamics with the fully analytic energy gradient. *J Chem Theor Comput* 8:5008–5012
4. Buló RE, Ensing B, Sikkema J et al (2009) Toward a practical method for adaptive QM/MM simulations. *J Chem Theory Comput* 5:2212–2221
5. Endo K, Tomobe K, Yasuoka K (2018) Multi-step time series generator for molecular dynamics. In: *The thirty-second AAAI conference on artificial intelligence*, pp 2192–2199
6. Fedorov DG, Ishida T, Uebayasi M, Kitaura K (2007) The fragment molecular orbital method for geometry optimizations of polypeptides and proteins. *J Phys Chem* 111:2722–2732
7. Fedorov DG, Kitaura K (2018) Pair interaction energy decomposition analysis for density functional theory and density-functional tight-binding with an evaluation of energy fluctuations in molecular dynamics. *J Phys Chem A* 122(6):1781–1795
8. Field MJ, Bash PA, Karplus MA (1990) A combined quantum mechanical and molecular mechanical potential for molecular dynamics simulations. *J Comput Chem* 11:700–733

9. Friesner RA, Guallar V (2005) Ab initio quantum chemical and mixed quantum mechanics/molecular mechanics (QM/MM) methods for studying enzymatic catalysis. *Annu Rev Phys Chem* 56:389–427
10. Fujita T, Nakano T, Tanaka S (2011) Fragment molecular orbital calculations under periodic boundary condition. *Chem Phys Lett* 506:112–116
11. Fujita T, Tanaka S, Fujiwara T, Kusa M, Mochizuki Y, Shiga M (2012) *Ab initio* path integral Monte Carlo simulations for water trimer with electron correlation effects. *Chem Phys Lett* 997:7–13
12. Fujiwara T, Mochizuki Y, Komeiji Y et al (2010) Fragment molecular orbital-based molecular dynamics (FMO-MD) simulations on hydrated Zn (II) ion. *Chem Phys Lett* 490:41–45
13. Fujiwara T, Mori H, Komeiji Y et al (2015) Fragment molecular orbital-based molecular dynamics (FMO-MD) simulations on hydrated Zn (II) ion. In: Tsuchida E (ed) *Proceedings of computational science workshop 2014, JPS Conference 5*, 011001
14. Fukuzawa K, Kurisaki I, Watanabe C et al (2015) Explicit solvation modulates intra- and inter-molecular interactions within DNA: electronic aspects revealed by the ab initio fragment molecular orbital (FMO) method. *Comput Theor Chem* 1054:29–37
15. Gao J, Truhlar DG (2002) Quantum mechanical methods for enzyme kinetics. *Annu Rev Phys Chem* 53:467–505
16. Gaigeot MP (2009) Unravelling the conformational dynamics of the aqueous alanine dipeptide with first-principle molecular dynamics. *J Phys Chem B* 113:10059
17. Heyden A, Lin H, Truhlar DG (2007) Adaptive partitioning in combined quantum mechanical and molecular mechanical calculations of potential energy functions for multiscale simulations. *J Phys Chem B* 111:2231–2241
18. Ishida T (2008) Probing protein environment in an enzymatic process: All-electron quantum chemical analysis combined with ab initio quantum mechanical/molecular mechanical modeling of chorismate mutase. *J Chem Phys* 129:125105
19. Ishikawa T (2013) Implementation of AMBER-PAICS interface (in Japanese). *CICSJ Bull* 31:73–77
20. Ishikawa T (2018) Ab initio quantum chemical calculation of electron density, electrostatic potential, and electric field of biomolecule based on fragment molecular orbital method. *Int J Quantum Chem* 118:e25535
21. Ishikawa T, Burri RR, Kamatari YO et al (2013) A theoretical study of the two binding modes between lysozyme and tri-NAG with an explicit solvent model based on the fragment molecular orbital method. *Phys Chem Chem Phys* 15:3646–3654
22. Ishikawa T, Ishikura T, Kuwata K (2009) Theoretical study of the prion protein based on the fragment molecular orbital method. *J Comput Chem* 30:2594–2601
23. Ishikawa T, Kuwata K (2012) RI-MP2 gradient calculation of large molecules using the fragment molecular orbital method. *J Phys Chem Lett* 3:375–379
24. Ishikawa T, Mochizuki Y, Nakano T et al (2006) Fragment molecular orbital calculations on large scale systems containing heavy metal atoms. *Chem Phys Lett* 427:159–165
25. Ishimura H, Tomioka S, Kadoya R et al (2017) Specific interactions between amyloid- β peptides in an amyloid- β hexamer with three-fold symmetry: Ab initio fragment molecular orbital calculations in water. *Chem Phys Lett* 672:13–20
26. Jono R, Watanabe Y, Shimizu K et al (2010) Multicanonical ab initio QM/MM molecular dynamics simulation of a peptide in an aqueous environment. *J Comput Chem* 31:1168–1175
27. Kato Y, Fujiwara T, Komeiji Y et al (2014) Fragment molecular orbital-based molecular dynamics (FMO-MD) simulations on hydrated Cu(II) ion. *CBI J* 14:1–13
28. Kitaura K, Sugiki S-I, Nakano T et al (2001) Fragment molecular orbital method: analytical energy gradients. *Chem Phys Lett* 336:163–170
29. Kobayashi I, Takeda R, Suzuki R et al (2017) Specific interactions between androgen receptor and its ligand: ab initio molecular orbital calculations in water. *J Mol Graph Model* 75:383–389
30. Komeiji Y, Fujiwara T, Okiyama Y et al (2013) Dynamic fragmentation with static fragments (DF/SF) algorithm designed for ab initio fragment molecular orbital-based molecular dynamics (FMO-MD) simulations of polypeptides. *CBI J* 13:45–57

31. Komeiji Y, Inadomi Y, Nakano T (2004) PEACH 4 with ABINIT-MP: a general platform for classical and quantum simulations of biological molecules. *Comput Biol Chem* 28:155–161
32. Komeiji Y, Ishida T, Fedorov DG et al (2007) Change in a protein's electronic structure induced by an explicit solvent: an ab initio fragment molecular orbital (FMO) study of ubiquitin. *J Comput Chem* 28:1750–1762
33. Komeiji Y, Ishikawa T, Mochizuki Y et al (2009a) Fragment molecular orbital method-based molecular dynamics (FMO-MD) as a simulator for chemical reactions in explicit solvation. *J Comput Chem* 30:40–50
34. Komeiji Y, Mochizuki Y, Nakano T et al (2009b) Fragment molecular orbital-based molecular dynamics (FMO-MD), a quantum simulation tool for large molecular systems. *J Mol Struct THEOCHEM* 898:2–7
35. Komeiji Y, Mochizuki Y, Nakano T et al (2010) Three-body expansion and generalized dynamic fragmentation improve the fragment molecular orbital-based molecular dynamics (FMO-MD). *Chem Phys Lett* 484:380–386
36. Komeiji Y, Mochizuki Y, Nakano T et al (2012) Recent advances in fragment molecular orbital-based molecular dynamics (FMO-MD) simulations. In: Wang L (ed) *Molecular dynamics— theoretical developments and applications in nanotechnology and energy*. InTech, Rijeka, pp 3–24
37. Komeiji Y, Nakano T, Fukuzawa K et al (2003) Fragment molecular orbital method: application to molecular dynamics simulation, “ab initio FMO-MD.”. *Chem Phys Lett* 372:342–347
38. Komeiji Y, Okiyama Y, Mochizuki Y et al (2017) Explicit solvation of a single-stranded DNA, a binding protein, and their complex: a suitable protocol for fragment molecular orbital calculation. *CBI J* 17:72–84
39. Komeiji Y, Okiyama Y, Mochizuki Y et al (2018) Interaction between a single-stranded DNA and a binding protein viewed by the fragment molecular orbital method. *Bull Chem Soc Jpn* 91:1596–1605
40. Komeiji Y, Uebayasi M, Takata R et al (1997) Fast and accurate molecular dynamics simulation of a protein using a special purpose computer. *J Comput Chem* 18:1546–1563
41. Koskinen P, Mäkinen V (2009) Density-functional tight-binding for beginners. *Comput Mater Sci* 27:237–253
42. Kurisaki I, Fukuzawa K, Komeiji Y et al (2007) Visualization analysis of inter-fragment interaction energies of CRP-cAMP-DNA complex based on the fragment molecular orbital method. *Biophys Chem* 130:1–9
43. Kuwata K, Nishida N, Matsumoto T et al (2007) Hot spots in prion protein for pathogenic conversion. *Proc Natl Acad Sci USA* 104:11921–11926
44. Matsuda A, Mori H (2014) Theoretical study on the hydration structure of divalent radium ion using fragment molecular orbital-molecular dynamics (FMO-MD) simulation. *J Sol Chem* 43:1669–1675
45. Mochizuki Y, Nakano T, Komeiji Y et al (2011) Fragment molecular orbital-based molecular dynamics (FMO-MD) method with MP2 gradient. *Chem Phys Lett* 504:95–99
46. Mori H, Hirayama N, Komeiji Y et al (2012) Differences in hydration between cis- and trans-platin: Quantum insights by ab initio fragment molecular orbital-based molecular dynamics (FMO-MD). *Comput Theor Chem* 986:30–34
47. Nagata T, Brorsen K, Fedorov DG et al (2011a) Fully analytic energy gradient in the fragment molecular orbital method. *J Chem Phys* 134:124115
48. Nagata T, Fedorov DG, Ishimura K et al (2011b) Analytic energy gradient for second-order Moeller-Plesset perturbation theory based on the fragment molecular orbital method. *J Chem Phys* 135:044110
49. Nagata T, Fedorov DG, Sawada T et al (2011c) A combined effective fragment potential - fragment molecular orbital method. II. Analytic gradient and application to the geometry optimization of solvated tetraglycine and chignolin. *J Chem Phys*. 134:034110
50. Nagata T, Fedorov DG, Kitaura K (2012a) Analytic gradient and molecular dynamics simulations using the fragment molecular orbital method combined with effective potentials. *Theor Chem Acc* 131:1136–1138

51. Nagata T, Fedorov DG, Li H et al (2012b) Analytic gradient for second order Moeller-Plesset perturbation theory with the polarizable continuum model based on the fragment molecular orbital method. *J Chem Phys* 136:204112
52. Nagata T, Fedorov DG, Kitaura K (2012c) Analytic gradient for the embedding potential with approximations in the fragment molecular orbital method. *Chem Phys Lett* 544:87–93
53. Nakata H, Fedorov DG, Nagata T et al (2012) Unrestricted Hartree-Fock based on the fragment molecular orbital method: energy and its analytic gradient. *J Chem Phys* 137:044110
54. Nishimoto N, Nakata H, Fedorov DG et al (2015) Large-scale quantum-mechanical molecular dynamics simulations using density-functional tight-binding combined with the fragment molecular orbital method. *J Chem Phys Lett* 6:5043–5039
55. Öberg H, Brinck T (2016) Fragment molecular orbital study of the cAMP-dependent protein kinase catalyzed phosphoryl transfer: a comparison with the differential transition state stabilization method. *Phys Chem Chem Phys* 18:15153
56. Okamoto T, Ishikawa T, Koyano Y et al (2013) A minimal implementation of the AMBER-PAICS interface for ab initio FMO-QM/MM-MD simulation. *Bull Chem Soc Jpn* 86:210–222
57. Okiyama Y, Watanabe H, Fukuzawa K et al (2007) Application of the fragment molecular orbital method for determination of atomic charges on polypeptides I. *Chem Phys Lett* 449:329–335
58. Okiyama Y, Watanabe H, Fukuzawa K et al (2009) Application of the fragment molecular orbital method for determination of atomic charges on polypeptides II. *Chem Phys Lett* 467:417–427
59. Prusiner SB (1982) Novel proteinaceous infectious particles cause scrapie. *Science* 216:136–144
60. Riek R, Hornemann S, Wider G et al (1996) NMR structure of the mouse prion protein domain PrP (121–231). *Nature* 382:180–182
61. Rossman A, Abe T, Okuwaki K et al (2019) Destabilization of DNA through interstrand crosslinking by UO_2^{2+} . *Chem Comm* in press
62. Saitou S, Iijima J, Fujimoto M et al (2018) Application of TensorFlow to recognition of visualized results of fragment molecular orbital (FMO) calculations. *CBI J* 18:58–69
63. Sato M, Yamataka H, Komeiji Y et al (2008) How does an $\text{S}_{\text{N}}2$ reaction take place in solution? Full ab initio MD simulations for the hydrolysis of the methyl diazonium ion. *J Am Chem Soc* 130:2396
64. Sato M, Yamataka H, Komeiji Y et al (2010) Does Amination of formaldehyde proceeds through Zwitterionic intermediate in water? FMO-MD simulations by using constraint dynamics. *Chem Eur J* 16:6430–6433
65. Sato M, Yamataka H, Komeiji Y et al (2012) FMO-MD simulations on the hydration of formaldehyde in water solution with constraint dynamics. *Chem Eur J* 18:9714–9721
66. Senn HM, Thiel W (2009) QM/MM methods for biomolecular systems. *Angew Chem Int Ed* 48:1198–1229
67. Singh UC, Kollman PA (1986) A combined ab initio quantum mechanical and molecular mechanical method for carrying out simulations on complex molecular systems: Applications to the $\text{CH}_3\text{Cl} + \text{Cl}^-$ exchange reaction and gas phase protonation of polyethers. *J Comput Chem* 7:718–730
68. Svensson M, Humbel S, Froese RD, Matsubara T, Sieber S, Morokuma K (1996) ONIOM: a multilayered integrated MO + MM method for geometry optimizations and single point energy predictions. A test for Diels–Alder reactions and $\text{Pt}(\text{P}(\text{t-Bu})_3)_2 + \text{H}_2$ oxidative addition. *J Phys Chem* 100:19357–19363
69. Takeda R, Kobayashi I, Shimamura K et al (2017) Specific interactions between vitamin-D receptor and its ligands: Ab initio molecular orbital calculations in water. *J Steroid Biochem Mol Biol* 171:75–79
70. Takenaka N, Kitamura Y, Koyano Y, Nagaoka M (2012) The number-adaptive multiscale QM/MM molecular dynamics simulation: application to liquid water. *Chem Phys Lett* 524:56–61
71. Tokuda K, Watanabe C, Okiyama Y et al (2016) Hydration of ligands of influenza virus neuraminidase studied by the fragment molecular orbital method. *J Mol Graph Model* 69:144–153

72. Ueno-Noto K, Takano K (2016) Water molecules inside protein structure affect binding of monosaccharides with HIV-1 antibody 2G12. *J Comput Chem* 37:2341–2348
73. Walker RC, Crowley MF, Case DA (2008) The implementation of a fast and accurate QM/MM potential method in Amber. *J Comput Chem* 29:1019–1031
74. Warshel A, Karplus M (1972) Calculation of ground and excited state potential surfaces of conjugated molecules. I. Formulation and parametrization. *J Am Chem Soc* 94:5612–5625
75. Warshel A, Levitt M (1976) Theoretical studies of enzymic reactions: dielectric, electrostatic and steric stabilization of the carbonium ion in the reaction of lysozyme. *J Mol Biol* 103:227–249
76. Zhang L, Han J, Wang H et al (2018) Deep potential molecular dynamics: a scalable model with the accuracy of quantum mechanics. *Phys Rev Lett* 120:143001

Linear Combination of Molecular Orbitals of Fragments (FMO-LCMO) Method: Its Application to Charge Transfer Studies



Hiroataka Kitoh-Nishioka, Ryuma Sato, Yasuteru Shigeta, and Koji Ando

Abstract Fragment molecular orbital-linear combination of molecular orbitals of fragments (FMO-LCMO) method makes possible to effectively construct one-electron Hamiltonian, canonical MOs, and their energies of large molecules including protein, DNA, and so on, by using the output of usual FMO calculations. This Chapter reviews the FMO-LCMO method and its applications to the studies on the charge transfer phenomena in bio-systems and organic materials.

Keywords FMO-LCMO · Total Fock matrix · Total canonical MO · Restricted FMO space · Matrix-size reduction · Electron transfer · Marcus theory · Electronic coupling · Electron tunneling · Tunneling pathway · Tunneling current · Triplet-triplet annihilation · Singlet fission

1 Introduction

Fragment molecular orbital (FMO) method [1–3] primarily offers the effective energy calculations of large target molecules. On the other hand, the FMO method itself does not give the MOs of the whole target molecules, similar to the other fragment-based

H. Kitoh-Nishioka (✉)
JST-PRESTO and Center for Computational Sciences, University of Tsukuba,
Tsukuba, Japan
e-mail: hkito@ccs.tsukuba.ac.jp

R. Sato
Center for Biosystems Dynamics Research, RIKEN, Suita, Japan
e-mail: ryuma.sato@riken.jp

Y. Shigeta
Center for Computational Sciences, University of Tsukuba, Tsukuba, Japan
e-mail: shigeta@ccs.tsukuba.ac.jp

K. Ando
Department of Information and Sciences, Tokyo Woman's Christian University,
Tokyo, Japan
e-mail: ando_k@lab.twcu.ac.jp

approaches [4] including the divide-and-conquer (DC) approach [5]. The fragment MOs obtained from FMO calculations are completely localized on the corresponding fragment, which provides some insights of the target molecule. However, the frontier MOs of molecules dominantly contributing to their chemical and physical properties, such as an enzymatic function of a given protein, are often the MOs delocalized over several fragments. Within the framework of the FMO method, Inadomi et al. [6] developed the MOs of FMO (FMO-MO) scheme as follows: (a) a total molecular electron density is first constructed from the electron density of each fragment as

$$\mathbf{D}_{\text{total}} = \sum_{I>J}^N \mathbf{D}_{IJ} - (N - 2) \sum_I^N \mathbf{D}_I, \quad (1)$$

where \mathbf{D}_I is the electron density of the I th fragment monomer and \mathbf{D}_{IJ} is that of a dimer comprising the I th and the J th fragments in the FMO result; N is the total number of the fragment monomers; (b) the “effective” one-electron Hamiltonian, such as Fock and Kohn–Sham Fock matrices, of the whole molecule is then constructed from $\mathbf{D}_{\text{total}}$ without self-consistent field (SCF) interactions; (c) after that, the canonical MOs of the whole system are calculated from a generalized diagonalization of the “effective” one-electron Hamiltonian. The FMO-MO method can well reproduce the canonical MOs obtained from the conventional Hartree–Fock (HF) calculations of the whole molecule [6, 7]. However, steps (b) and (c) of the FMO-MO method still demand high computational costs for large molecules. To overcome the difficulties in the FMO-MO method by fully utilizing the performance of massively parallel computational architectures, Umeda et al. [8] developed a parallel Fock matrix construction scheme for step (b) and applied the Sakurai–Sugiura method [9] to step (c). They succeeded in applying the scheme to the FMO-MO method for calculating the frontier MOs of the epidermal growth factor receptor (17,246 atoms) with 96,234 atomic orbitals (AOs) at the HF/6-31G level of theory.

Tsuneyuki et al. [10, 11] developed a more efficient method to evaluate the electronic state of a whole molecule, named as the FMO linear combination of MOs of fragments (FMO-LCMO). In the FMO-LCMO method, the “effective” one-electron Hamiltonian can be constructed solely by making use of the usual output of FMO calculations. This is an advantage, for instance, over the FMO-MO method that requires recalculations of the two-electron integrals in step (b). The constructed one-electron Hamiltonian is represented in the fragment-monomer MO basis functions, and as a result, the canonical MOs of the whole molecule are represented by an LCMO of the fragments [10, 11]. The MO-based representation of FMO-LCMO has the following great advantage over the AO-based one (used for conventional quantum chemical calculations and FMO-MO) in the computational costs [10, 11]; by taking into account only a small number of monomer MOs near the frontier MOs of each fragment, the FMO-LCMO method can significantly reduce the matrix size of the constructed Hamiltonian, which provides the MOs of the whole molecule near its highest occupied MO (HOMO) and lowest unoccupied MO (LUMO).

We have demonstrated that the FMO-LCMO method is suitable for the studies on the charge transfer phenomena in both bio-systems and organic materials [12–19]. For example, the biological electron transfer (ET) reactions usually take place via the long-distance electron tunneling between redox centers embedded in protein media [20, 21]; the FMO-LCMO method can effectively construct the MOs of protein in the vicinity of the HOMO-LUMO gap that is essential to describe the wave function of the tunneling electron [12–14]. Moreover, since the MOs are represented in the localized FMO basis, the ET pathway can be easily analyzed at the amino-acid residue-based resolution [12–15].

Section 2 first explains the formulation of the FMO-LCMO method and briefly reviews some test calculations. Section 3 shows the application of the FMO-LCMO method to the electron tunneling associated with biological ET reactions. Section 4 briefly explains how to apply the FMO-LCMO method to the study on the triplet-triplet annihilation (TTA) phenomena. Section 5 is devoted to Concluding Remarks.

2 FMO-LCMO

2.1 Formulation

This subsection describes the formulation of the FMO-LCMO scheme [10, 11] up to the fragment-trimer exchange corrections (FMO3) [3], called FMO3-LCMO [11, 14] or FMO3/LCMO [22]; we will use the former notation hereafter.

In FMO calculations, the total system is first divided into N fragments. The electronic structure of each fragment is then solved self-consistently under the electrostatic potential (ESP) from all other fragments. The p th orbital of fragment I and the corresponding MO energy are denoted by ϕ_p^I and ϵ_p^I , respectively, which are optimized self-consistently under the ESP from the other fragments. In the case of FMO2, the electronic structure of each fragment dimer is then solved under the ESP from all other fragments determined above. The resultant p th orbital of fragment dimer IJ and the corresponding MO energy are denoted by ϕ_p^{IJ} and ϵ_p^{IJ} , respectively. In addition, in the case of FMO3, the electronic structure of each fragment trimer is solved under the ESP from all other fragments. The resultant p th orbital of fragment trimer IJK and the corresponding MO energy are denoted by ϕ_p^{IJK} and ϵ_p^{IJK} , respectively.

By using the FMOs $\{\phi_r^X\}$ and their energies $\{\epsilon_r^X\}$ described above, effective one-electron Hamiltonians, such as Fock and Kohn–Sham Fock operators, of fragment monomer, dimer, and trimer, represented by $X = I, IJ$, and IJK , are written as

$$\hat{H}_X = \sum_r^{N_r^X} |\phi_r^X\rangle \epsilon_r^X \langle \phi_r^X|, \quad (2)$$

where N_r^X is the total number of $\{\phi_r^X\}$. FMO calculations often require bond detachments for their fragmentations of target large molecules; sp^3 carbon atom is usually employed for the fragmentation, which is called a bond-detached atom (BDA). When BDAs are involved in the FMO calculation, the hybrid orbital projection (HOP) operators [23] used at the BDAs produce the ϕ_r^X 's with anomalous huge MO energies. Note that, in the FMO-LCMO method, one should remove the anomalous ϕ_r^X 's from Eq. (2) when using BDAs [10, 11, 22].

In the FMO-LCMO scheme, we project the effective one-electron Hamiltonian operators of fragment monomer, dimer, and trimer, i.e. Eq. (2), to the fragment monomer MOs. The matrix elements transformed into the fragment-monomer MO representation in the intra-fragment I - I block are expressed by

$$(H_{I \leftarrow X})_{I_p, I_q} \equiv \langle \phi_p^I | \hat{H}_X | \phi_q^I \rangle = \sum_r^{N_r^X} \langle \phi_p^I | \phi_r^X \rangle \epsilon_r^X \langle \phi_r^X | \phi_q^I \rangle. \quad (3)$$

On the other hand, the matrix elements transformed into the monomer MO representation in the inter-fragment I - J block, in which ϕ_p^I and ϕ_q^J are involved, are expressed by

$$(H_{IJ \leftarrow X})_{I_p, J_q} \equiv \langle \phi_p^I | \hat{H}_X | \phi_q^J \rangle = \sum_r^{N_r^X} \langle \phi_p^I | \phi_r^X \rangle \epsilon_r^X \langle \phi_r^X | \phi_q^J \rangle. \quad (4)$$

Note that, in the summation in the right-hand side of Eqs. (3) and (4), all the dimer and trimer FMOs are taken, except the spurious ones stemming from the BDAs, as with Eq. (2).

By using Eq. (3), the FMO1-LCMO Hamiltonian matrix ($H_{\text{total}}^{\text{FMO1}}$) is constructed from the monomer-fragment Hamiltonian submatrices as follows [11]:

$$(H_{\text{total}}^{\text{FMO1}})_{I_p, I_q} = (H_{I \leftarrow I})_{I_p, I_q} = \epsilon_p^I \delta_{I_p, I_q}, \quad (H_{\text{total}}^{\text{FMO1}})_{I_p, J_q} = 0 \quad (\text{for } I \neq J). \quad (5)$$

The FMO2-LCMO and FMO3-LCMO Hamiltonian matrices are described as

$$H_{\text{total}}^{\text{FMO2}} = H_{\text{total}}^{\text{FMO1}} + \Delta H_{\text{total}}^{\text{FMO2}}, \quad (6)$$

$$H_{\text{total}}^{\text{FMO3}} = H_{\text{total}}^{\text{FMO2}} + \Delta H_{\text{total}}^{\text{FMO3}}, \quad (7)$$

where $\Delta H_{\text{total}}^{\text{FMO2}}$ and $\Delta H_{\text{total}}^{\text{FMO3}}$ are the two- and three-body corrections, respectively. The intra-fragment (I - I) block of $\Delta H_{\text{total}}^{\text{FMO2}}$, between monomer MOs ϕ_p^I and ϕ_q^I in the same fragment I , is given by

$$(\Delta H_{\text{total}}^{\text{FMO2}})_{I_p, I_q} = \sum_{J \neq I} \{ (H_{I \leftarrow IJ})_{I_p, I_q} - (H_{I \leftarrow I})_{I_p, I_q} \}. \quad (8)$$

On the other hand, the inter-fragment I - J block, in which monomer MOs ϕ_p^I and ϕ_q^J are involved, is

$$(\Delta H_{\text{total}}^{\text{FMO2}})_{Ip,Jq} = (H_{IJ \leftarrow IJ})_{Ip,Jq}. \quad (9)$$

In analogy with the case of the FMO2, the FMO3 correction to the intra-fragment I - I block is

$$(\Delta H_{\text{total}}^{\text{FMO3}})_{Ip,Iq} = \sum_{J < K} \sum_{J, K \neq I} \{ (H_{I \leftarrow IJK})_{Ip,Iq} - (H_{I \leftarrow IJ})_{Ip,Iq} - (H_{I \leftarrow IK})_{Ip,Iq} + (H_{I \leftarrow I})_{Ip,Iq} \}, \quad (10)$$

on the other hand, the inter-fragment I - J block is

$$(\Delta H_{\text{total}}^{\text{FMO3}})_{Ip,Jq} = \sum_{K \neq I, J} \{ (H_{IJ \leftarrow IJK})_{Ip,Jq} - (H_{IJ \leftarrow IJ})_{Ip,Jq} \}. \quad (11)$$

The FMO method usually employs the electrostatic dimer (ES-DIM) approximation [2] that avoids SCF calculations of far-separated dimers and trimers. In Eqs. (8), (10), and (11), the fragment dimers and trimers involved in the ES-DIM approximation should be excluded from the summations [11, 22].

Let's consider the projection of the Hamiltonian of fragment X , (\hat{H}_X), into the limited number of monomer MOs via Eqs. (3) and (4). The use of such projected matrix elements in Eqs. (5)–(11) leads to a considerable matrix-size reduction of $H_{\text{total}}^{\text{FMO}}$. The accuracy of the target quantities obtained from the FMO-LCMO method depends on the selection of the “restricted FMO” (rFMO) space for the projection [10–14]. The proper selection of the rFMO space can significantly reduce the computational costs for constructing the considered total Hamiltonian keeping sufficient accuracy.

The canonical MOs and corresponding energies for the whole molecule can be obtained by solving a generalized eigenvalue problem of $H_{\text{total}}^{\text{FMO}}$ with the overlap matrix among monomer MOs, $S_{Ip,Jq} = \langle \phi_p^I | \phi_q^J \rangle$. If BDAs with the atomic basis functions larger than minimal ones are used, the diagonalization of $H_{\text{total}}^{\text{FMO}}$ suffers from the overcompleteness arising from the redundant inclusion of virtual orbitals on BDAs. In Ref. [11], to remove the linear dependence of basis functions associated with BDAs, a canonical transformation of $H_{\text{total}}^{\text{FMO}}$ was employed as follows:

$$\tilde{H}_{\text{total}}^{\text{FMO}} = U^\dagger H_{\text{total}}^{\text{FMO}} U, \quad (12)$$

where the matrix U diagonalizes the overlap matrix. However, this transformation often mixes the fragment-monomer MOs in unwanted ways for the ET analyses that seek for the pictures based on MOs on each fragment. The problem can be evaded by a projection to proper rFMO space instead of the canonical transformation, Eq. (12), as shown below.

2.2 Accuracy Tests

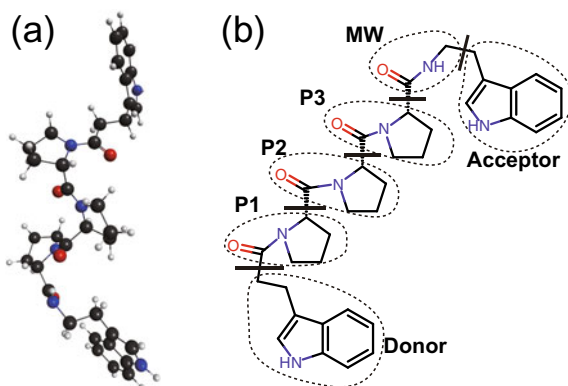
Accuracy tests of the FMO-LCMO method for various systems have been reported in several previous papers [10–15, 17, 22]; the FMO routine implemented in GAMESS [24] was used for all cases. Tsuneyuki *et al.* performed the FMO-LCMO calculations at the FMO2-RHF level on a pseudo-Glycine pentamer with (3_{10}) -helix and stick conformations [10]. Since they used a minimal STO-3G basis set, the problem of linear dependence of FMOs at BDAs does not exist in their study. They confirmed that the FMO-LCMO method reasonably reproduces the energy spectrum and MOs of the whole peptide near its HOMO-LUMO levels even when taking into account a small number of MOs around HOMOs and LUMOs of fragments [10].

We [12] applied the FMO-LCMO method to the FMO2-RHF results of four model ET systems: $\text{CH}_3\text{-(CH}_4)_3\text{-CH}_3$, where non-covalent stacks of methane $(\text{CH}_4)_3$ are sandwiched by CH_3 molecules, $\text{TCNE-(C}_6\text{H}_6)_n\text{-TCNE}$ ($n = 1, \dots, 8$), where non-covalent stacks of benzene $(\text{C}_6\text{H}_6)_n$ are sandwiched by tetracyanoethylene (TCNE) molecules, $\text{Be-C}_n\text{H}_{2n+2}\text{-Be}$ ($n = 2, 4, \dots, 18$), where trans n -alkanes $\text{C}_n\text{H}_{2n+2}$ are sandwiched by Be atoms, and alanine polypeptides (ala_{10}) in α -helix and β -strand conformations. The study used double-zeta basis sets, such as 6-31G(d) and cc-pVDZ, for the FMO2-RHF calculations of the molecular clusters, $\text{CH}_3\text{-(CH}_4)_3\text{-CH}_3$ and $\text{TCNE-(C}_6\text{H}_6)_n\text{-TCNE}$, without the BDAs. To examine the effects of the matrix-size reduction on the results, the study considered a “minimal-valence” rFMO space that includes the same number of monomer MOs as those with the standard minimal basis sets (such as STO-3G) excluding their core MOs. They confirmed that the FMO-LCMO method works well with the basis sets larger than the minimal ones for the construction of the total Hamiltonian and MOs [12].

Kobori et al. [11] applied the FMO-LCMO method to the FMO2- and FMO3-B3LYP calculations with the 6-31G(d) basis sets obtained for alanine dodecamer (ala_{12}) in α -helix and β -turn conformations and chignolin in the β -hairpin conformations. This study did the canonical transformation, Eq. (12), of the constructed $H_{\text{total}}^{\text{FMO}}$ to eliminate the linear dependence of FMOs at BDAs. They confirmed that the FMO3-LCMO method substantially improves the accuracy of the resultant MOs and their energies, compared to FMO2-LCMO. They also demonstrated the rFMO space, consisting of all occupied monomer MOs but a restricted number of unoccupied monomer MOs, can adequately reduce the computational costs with keeping the accuracy. (They note that when using the basis sets larger than minimal ones, the rFMO space had better include all occupied monomer MOs to keep the orthogonality condition with respect to the core orbitals of neighbor fragments.)

Recently, Fedorov and Kitaura [22] proposed a new scheme called FMO/LCMOX, in which the FMO-LCMO method is improved by adding the exchange interaction to the embedding potential of each fragment in the post-factum fashion (namely, after the SCF converges without exchange). They performed the accuracy tests on (ala_{20}) in α -conformation, a water cluster, Trp-cage and crambin proteins, a zeolite cluster, a Si nano-wire, and a boron nitride ribbon. They also performed the systematic benchmarks by considering the effects of the following treatments on the results of

Fig. 1 **a** Structure of Trp-(Pro)₃-Trp peptide. **b** Fragmentations. P1-3 are three proline residues and NW denotes the main chain of Trp (W). Reprinted from Ref. [14], with the permission of AIP Publishing



the FMO-LCMO calculations: the adaptive frozen orbital (AFO) [25] for the bond detachments at BDA instead of HOP, the size of fragmentation (namely, 1 residue/2 residues per fragment), and a polarizable continuum model (PCM)-FMO method [26] for solvation. They demonstrated that the FMO/LCMOX substantially improves the accuracy of the virtual MOs obtained from the FMO-LCMO method at the FMO2 level [22].

Then, we [14] applied the FMO-LCMO method to the FMO2- and FMO3-RHF/6-31G(d) calculations of the Trp-(Pro)₃-Trp in *cis*- and *trans*-polyproline (PP) configurations. Here, we focus on the *trans*-PP case, as illustrated in Fig. 1a. The total system was divided into six fragments, as shown in Fig. 1b; the BDAs are, therefore, involved in the FMO calculations. The Fock matrix obtained from the RHF calculation of the whole system of six fragments was also projected into the FMO space by using Eq. (2) as follows:

$$(H_{\text{total}}^{\text{FMO6}})_{Ip, Jp} = \sum_a \langle \phi_p^I | \psi_a \rangle \epsilon_a \langle \psi_a | \phi_p^J \rangle, \quad (13)$$

where ψ_a and ϵ_a represent the a th canonical MO of the whole system and its energy, respectively. Hereafter, the calculations based on $H_{\text{total}}^{\text{FMO6}}$ are regarded as the reference ones. The study considered a “minimal-valence plus core” rFMO space including the same number of monomer MOs as the standard minimal basis set case, which is denoted by LC(VC)MO. From the FMO-LC(VC)MO/6-31G(d) calculation of the Trp-(Pro)₃-Trp, we found that the smallest eigenvalue of the overlap matrix for systems $S_{\text{total}}^{\text{FMO}}$ was greater than 0.2, which is large enough to regard the FMO space linearly independent. Therefore, the study simply calculated the MOs and their energies with the diagonalization of the matrix-size reduced $H_{\text{total}}^{\text{FMO}}$ without the canonical transformation Eq. (12). Table 1 summarizes the computed errors in the resultant MO energies from the RHF calculation of the whole system, indicating that

Table 1 MO energy gap and errors (in eV) of Trp-(Pro)₃-Trp form FMO-LC(VC)MO calculations

	Gap ^a	MAE ^b		RMS ^c	
		Occ	Uoc	Occ	Uoc
FMO2	10.66	0.107 (#15)	22.4 (#272)	0.0345	3.92
FMO3	10.67	0.102 (#27)	14.6 (#272)	0.0266	3.13
FMO6	10.63	0.0934 (#65)	14.6 (#272)	0.0223	3.13

^aHOMO-LUMO gap. The reference RHF value is 10.63 eV

^bMaximum absolute error of MO energies

Occ/Uoc denote occupied/unoccupied MOs

In parentheses are the MO numbers that exhibit the MAE

^cRoot-mean-square error of MO energies

Reprinted from Ref. [14], with the permission of AIP Publishing

the FMO-LC(VC)MO without Eq. (12) works well as expected. The RMS (root-mean-square error) is notably reduced from FMO2 to FMO3 but not so much from FMO3 to FMO6, indicating nearly converged accuracy at the FMO3 level.

3 Electron Transfer Analysis

3.1 Theory

The rate of biological ET reaction is usually expressed by the Marcus theory as [27]

$$k_{\text{ET}} = \frac{2\pi}{\hbar} |T_{\text{DA}}|^2 \frac{1}{\sqrt{4\pi\lambda k_{\text{B}}T}} \exp\left[\frac{(-\Delta G - \lambda)^2}{4\lambda k_{\text{B}}T}\right], \quad (14)$$

where T_{DA} is the ET coupling matrix element. ΔG and λ are the free energy difference of the ET reaction and the reorganization energy, respectively. \hbar , k_{B} , and T are the Planck constant divided by 2π , Boltzmann constant, and the temperature of the system, respectively. Biological ETs usually take place via the long-distance electron tunneling between redox centers separated by more than several Å; the T_{DA} stems from the superexchange mechanism, where the electronic states of the protein environment work as the virtual intermediate states for the electron tunneling [20, 21]. Therefore, accurate estimation of T_{DA} based on *ab initio* electronic structures of large protein is a difficult but important task to understand biological ETs.

To calculate the T_{DA} with the FMO-LCMO scheme, we employ the following two methods: generalized Mulliken–Hush (GMH) [28] and bridge Green function (BGF) [29, 30]. The former method uses the MOs and their energies of the whole system obtained from the diagonalization of $H_{\text{total}}^{\text{FMO}}$, the latter one treats $H_{\text{total}}^{\text{FMO}}$ itself. Hereafter, we will express the $H_{\text{total}}^{\text{FMO}}$ simply by H .

The GMH method scales the donor-acceptor adiabatic MO energy splitting $\Delta\epsilon_{\text{DA}}$ by a formula

$$T_{\text{DA}} = \frac{|\mu_{\text{DA}}| \Delta\epsilon_{\text{DA}}}{\sqrt{(\mu_{\text{D}} - \mu_{\text{A}})^2 + 4|\mu_{\text{DA}}|^2}}, \quad (15)$$

in which μ_{D} , μ_{A} , and μ_{DA} are the diagonal and off-diagonal dipole matrix elements. It assumes that the Hamiltonian and dipole matrix elements scale similarly for states involved in ETs. Note that the donor and acceptor adiabatic MOs, ψ_{D} and ψ_{A} , can be naturally chosen from the MOs of the whole ET system [12–15]; in general, HOMO and HOMO–1 or LUMO and LUMO+1 are chosen, depending on the considered ET. Despite its simplicity, the GMH formula, Eq. (15), has been successfully applied to a number of ET reactions.

The BGF method expresses T_{DA} as

$$T_{\text{DA}} = H_{\phi_{\text{D}}, \phi_{\text{A}}}^{\text{direct}} + \sum_{I, J} \sum_{I_p, J_q}^N (E_{\text{tun}} S_{\phi_{\text{D}}, I_p} - H_{\phi_{\text{D}}, I_p}) \times G^{\text{B}}(E_{\text{tun}})_{I_p, J_q} (E_{\text{tun}} S_{J_q, \phi_{\text{A}}} - H_{J_q, \phi_{\text{A}}}), \quad (16)$$

in which the sums over I_p and J_q exclude donor and acceptor MOs, ϕ_{D} and ϕ_{A} . The first term $H_{\phi_{\text{D}}, \phi_{\text{A}}}^{\text{direct}}$ in the right-hand side is the direct coupling between ϕ_{D} and ϕ_{A} . S is the overlap matrix. $G^{\text{B}}(E)$ is the bridge Green function defined as

$$G^{\text{B}}(E) = (ES_{\text{QQ}} - H_{\text{QQ}})^{-1}, \quad (17)$$

in which Q is the projection operator to the MO space external to the donor-acceptor MOs. The electron tunneling energy E_{tun} is naturally defined as the average of donor-acceptor orbital energies,

$$E_{\text{tun}} = (\epsilon_{\text{D}} + \epsilon_{\text{A}}) / 2$$

To effectively make use of the FMO-LCMO scheme for the analyses of the electron tunneling pathways in bio-systems, we employ the tunneling current method [30, 31]. The MOs in initial (i) and final (f) diabatic states are expressed in terms of the monomer MOs as follows:

$$|\psi^{\text{i}}\rangle = C_{\text{D}}^{\text{i}} |\phi_{\text{D}}\rangle + \sum_I \sum_{I_p}^N C_{I_p}^{\text{i}} |\phi_p^{\text{i}}\rangle, \quad (18)$$

$$|\psi^{\text{f}}\rangle = C_{\text{A}}^{\text{f}} |\phi_{\text{A}}\rangle + \sum_I \sum_{I_p}^N C_{I_p}^{\text{f}} |\phi_p^{\text{f}}\rangle. \quad (19)$$

Since $C_{\text{D}}^{\text{i}} \simeq 1$ and $C_{\text{A}}^{\text{f}} \simeq 1$ are satisfied in the weak coupling case, the coefficients $\{C_{I_p}^{\text{i}}\}$ and $\{C_{I_p}^{\text{f}}\}$, which represent the mixing of bridge FMOs to the donor and

acceptor FMOs, ϕ_D and ϕ_A , are expressed by the bridge Green function Eq. (17) as follows:

$$C_{Ip}^i = - \sum_J^N \sum_q^{N_q^J} (E_{\text{tun}} S_{\phi_D, Jq} - H_{\phi_D, Jq}) G^B(E_{\text{tun}})_{Jq, Ip}, \quad (20)$$

$$C_{Ip}^f = - \sum_J^N \sum_q^{N_q^J} G^B(E_{\text{tun}})_{Ip, Jq} (E_{\text{tun}} S_{Jq, \phi_A} - H_{Jq, \phi_A}). \quad (21)$$

The tunneling current $\mathcal{J}_{Ip, Jq}$ between monomer MOs ϕ_p^I and ϕ_q^J is given by

$$\mathcal{J}_{Ip, Jq} = \frac{1}{\hbar} (H_{Ip, Jq} - E_{\text{tun}} S_{Ip, Jq}) (C_{Ip}^i C_{Jq}^f - C_{Ip}^f C_{Jq}^i). \quad (22)$$

The total tunneling current between fragments I and J is, therefore, written as

$$\mathcal{J}_{I, J} = \sum_{Ip} \sum_{Jq} \mathcal{J}_{Ip, Jq}, \quad (23)$$

in which the summation over Ip and Jq is over the FMOs within fragments I and J . The ET coupling T_{DA} is expressed as a sum of the tunneling current $\mathcal{J}_{Ip, Jq}$ between basis FMOs $\{\phi_p^I\}$ [12–15],

$$T_{DA} = \hbar \sum_{I \in \Omega_D} \sum_{J \notin \Omega_D} \mathcal{J}_{I, J}, \quad (24)$$

where Ω_D denotes the spatial region assigned to the donor molecule. The normalized inter-fragment tunneling current is defined by

$$\mathcal{H}_{I, J} = \hbar \mathcal{J}_{I, J} / T_{DA}, \quad (25)$$

which satisfies

$$\sum_{I \in \Omega_D, J \notin \Omega_D} \mathcal{H}_{I, J} = 1. \quad (26)$$

3.2 Usage Example

The usages of the techniques described in the previous subsection include the ET studies on the model systems [12], photosynthetic reaction center [13], the Trp-(Pro)₃-Trp peptides [14], and DNA photolyases [15]. Here, we review an application to the hole transfer between two Trp bridged by *trans*-PP linker conformation, as

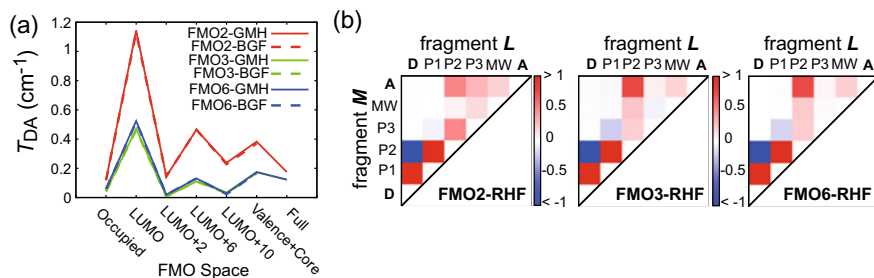


Fig. 2 **a** ET coupling T_{DA} and **b** normalized inter-fragment currents $\mathcal{H}_{I,J}$ calculated for Trp-(Pro)₃-Trp in the *trans*-PP conformation. Reprinted from Ref. [14], with the permission of AIP Publishing

shown in Fig. 1a. Figure 1b shows the fragmentation for the FMO2- and FMO3-RHF/6-31G(d) calculations. The HOMOs of the donor and acceptor fragments are chosen as ϕ_D and ϕ_A , respectively. The HOMO and HOMO-1 of the whole system are chosen as ψ_D and ψ_A for Eq. (15). When we use the full fragment-monomer MO space (namely, no matrix-size reduction) for obtaining the ψ_D and ψ_A , we have to perform the canonical transformation, Eq. (12), to avoid the problems associated with BDAs. On the other hand, when projecting the Hamiltonian into rFMO space not exceeding LC(VC)MO, we simply diagonalize the total FMO-LCMO Hamiltonian for those, as described in Sect. 2.

Figure 2a plots the computed T_{DA} with varying rFMO spaces, from the “occupied-only” to the minimal-valence plus core (VC), indicating that the T_{DA} converges to the value of full space with an oscillation. We can see that FMO3 notably improves the T_{DA} value over FMO2 and has been almost converged to FMO6. Figure 2b plots the normalized inter-fragment tunneling currents, comparing FMO2 and FMO3 with the reference FMO6. In this figure, the LC(VC)MO space was employed. As with the T_{DA} calculations, we can see that FMO3 notably improves the ET pathways over FMO2. The main pathway is the forward ET of $D \rightarrow P1 \rightarrow P2 \rightarrow A$, with a bifurcate back-flow of $P2 \rightarrow D$. FMO3 and FMO6 exhibit larger current back-flow than FMO2, leading to the decrease in T_{DA} owing to destructive interference (see Eq. 24). Figure 2b indicates that the ET pathway proceeds through the BDAs. Therefore, the BDAs would have a possibility to cause some problems for the calculations of T_{DA} and ET pathways within the framework of the FMO-LCMO method. However, Fig. 2 clearly shows that the ET analyses based on FMO-LCMO are robust by the FMO3 correction.

4 Triplet-Triplet Annihilation

The triplet-triplet annihilation (TTA) is a phenomenon, where an excitation energy transfer (EET) between two triplet-excited (T_1) state molecules converts a T_1 state of one molecule into its singlet-excited (S_1) state and, at the same time, converts a

T_1 state of the other molecule into its ground (S_0) state. The TTA phenomenon has attracted much attention to the use of the photon upconversion (UC) process [18, 19]. The inverse phenomenon of TTA is called singlet fission (SF), where an excitation energy transfers from an organic molecule in its S_1 state to a neighboring molecule in its S_0 state and, as a result, both molecules become their T_1 states [32]. This section only focuses on the application of the FMO-LCMO method to the TTA, although its application to SF is straightforward.

The initial state of the TTA process is usually assumed to be a ‘‘correlated triplet pair’’ (T_1T_1) where two T_1 states on neighboring molecules are coupled into an overall pure spin-singlet state. The final state is, here, denoted by S_1S_0 . A direct transition from T_1T_1 to S_1S_0 through the Dexter exchange mechanism merely occurs because its electronic coupling arising from two-electron integrals is significantly small [32]. Therefore, one often assumes that the transition from T_1T_1 to S_1S_0 consists of two sequential one-electron transfer reactions via a charge-separated (CS) state, where one molecule is in its cationic state, and the other is in its anionic state. Note that the CS state corresponds to a cation-anion (CA) or anion-cation (AC) case, depending on the TTA process considered. The TTA rate, k_{TTA} , is expressed using the steady-state approximation as

$$k_{\text{TTA}} = \frac{k_{T_1T_1, \text{CS}} k_{\text{CS}, S_1S_0}}{k_{\text{CS}, S_1S_0} + k_{\text{CS}, T_1T_1}}. \quad (27)$$

$k_{X,Y}$ is the ET rate constant from an initial state X ($= T_1T_1$ or CS) to a final state Y ($= T_1T_1$, S_1S_0 or CS), evaluated using Eq. (14).

All T_{DA} 's appearing in k_{TTA} can be calculated from the FMO-LCMO method performed on the dimer molecules associated with the TTA. We, here, denote HOMOs and LUMOs of fragment monomers, 1 and 2, by ϕ_{H}^1 , ϕ_{H}^2 , ϕ_{L}^1 , and ϕ_{L}^2 , respectively, and assume the MOs, $\{\phi_p^I\}$, to be orthogonal to each other. If two-electron integrals are ignored (i.e. zero-differential overlap formulation is used), the configuration interactions with single and selected double excitations within an active space of the four FMOs and four electrons yield [32]:

$$T_{S_1S_0, \text{CA}} = \langle \phi_{\text{L}}^1 | \hat{F} | \phi_{\text{L}}^2 \rangle, \quad (28)$$

$$T_{S_1S_0, \text{AC}} = -\langle \phi_{\text{H}}^1 | \hat{F} | \phi_{\text{H}}^2 \rangle, \quad (29)$$

$$T_{\text{CA}, T_1T_1} = \sqrt{3/2} \langle \phi_{\text{L}}^1 | \hat{F} | \phi_{\text{H}}^2 \rangle, \quad (30)$$

$$T_{\text{AC}, T_1T_1} = \sqrt{3/2} \langle \phi_{\text{H}}^1 | \hat{F} | \phi_{\text{L}}^2 \rangle, \quad (31)$$

where \hat{F} is the (Kohn–Sham) Fock operator for the dimer. However, the actual monomer MOs obtained from the FMO calculation, $\{\phi_p^I\}$, are not orthogonal to each other. Thus, $\langle \phi_p^I | \hat{F} | \phi_q^J \rangle$ in Eqs. (28)–(31) should be derived from the FMO-LCMO Hamiltonian matrix elements, $(H_{\text{total}}^{\text{FMO}2})_{Ip, Jq}$, corrected with the Löwdin symmetric transformation as follows [16, 17]:

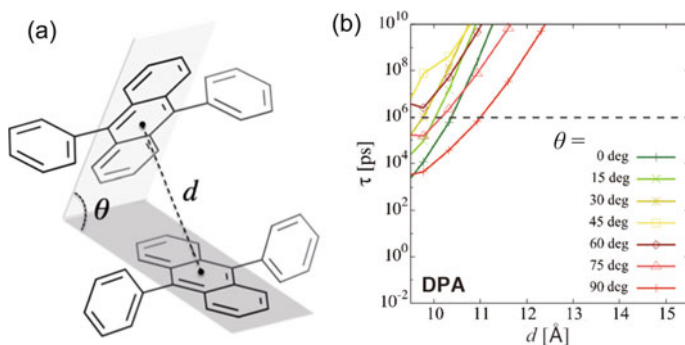


Fig. 3 **a** Dimer model structure of DPA. d represents intermolecular distance. θ represents the molecular orientation angle. The other structural parameters are fixed. **b** Calculated TTA reaction time as functions of θ and d . Reprinted with permission from Ref. [19]. Copyright 2018 American Chemical Society

$$\langle \phi_p^I | \hat{F} | \phi_q^J \rangle = (1 - S_{I_p, J_q}^2)^{-1} \left((H_{\text{total}}^{\text{FMO2}})_{I_p, J_q} - S_{I_p, J_q} \frac{(H_{\text{total}}^{\text{FMO2}})_{I_p, I_p} + (H_{\text{total}}^{\text{FMO2}})_{J_q, J_q}}{2} \right). \quad (32)$$

We [18, 19] examined the TTA reaction time $\tau = 1/k_{\text{TTA}}$ of 9,10-diphenylanthracene (DPA) in solution by using the dimer model structures illustrated in Fig. 3a. The T_{DA} values were calculated from the FMO2-LC-UBLYP/6-31G(d) results of the dimers, where the ϕ_p^I MO basis was optimized on the T_1 state of each fragment I under the ESP from the other fragment. The derivations of the other key parameters (λ , ΔG) in $k_{X,Y}$ are detailed in the references [18, 19]. Figure 3b plots the τ as functions of the dimer configuration parameters θ and d defined by Fig. 3a. Figure 3b clearly shows that the dimer configuration with θ of 90° is favorable for the TTA of the DPA in solution; the TTA occurs within $1 \mu\text{s}$ when d is 11 \AA and θ is 90° , marked by the dotted line in Fig. 3b. The insight obtained from the theoretical analyses based on the FMO-LCMO method would offer many advantages to molecular design for future organic materials with a desirable TTA activity.

5 Concluding Remarks

In this Chapter, we have reviewed the FMO-LCMO method that enables one to calculate the one-electron Hamiltonian and canonical MOs of the target large molecule, emphasizing its advantage in the matrix-size reduction. This Chapter also focuses on its application to the charge transfer studies by the authors [12–15, 18, 19]. The other applications of the FMO-LCMO method include the following studies. Kitoh-Nishioka and Ando [16] combined the FMO-LCMO method with nonempirically tuned range-separated density functional to develop the scheme for computing the

key charge-transfer parameters, such as transfer integral and site energy, in DNA and organic materials. Kitoh-Nishioka et al. [17] developed the FMO-DFTB/LCMO method that makes use of the FMO scheme [33] extended to density-functional tight-binding (DFTB) [34]; the FMO-DFTB/LCMO scheme with a less compressed DFTB parameter sets [35] for the inter-fragment interactions were used for the multi-scale charge transport simulations of covalent organic framework (COF). Fujita and Mochizuki [36] provided the formulation of configuration-interaction singlet (CIS) calculations with the FMO-LCMO method to describe the excited states of large molecules; Fujita and co-workers [37] applied the method to the study the excited states at pentacene/ C_{60} interfaces, where 2,000 atoms were treated quantum mechanically. On the other hand, Yamada et al. [38] developed a similar method to FMO-LCMO within the framework of DC scheme, called DC-a linear combination of the fragment orbitals (DC-LCFO).

The FMO-LCMO method is an excellent and attractive one as described, whereas the examples of its practical application are limited for now. We believe that the FMO-LCMO method is capable of further applications and producing novel approaches to various chemical and physical subjects in accordance with the development of the FMO method.

Acknowledgements H.K.-H. acknowledges the support by JST, PRESTO Grant Number JPMJPR17G4, Japan. R.S. was supported by a special postdoctoral researcher program at RIKEN.

References

1. Kitaura K, Ikeo E, Asada T, Nakano T, Uebayasi M (1999) *Chem Phys Lett* 313:701
2. Nakano T, Kaminuma T, Sato T, Fukuzawa K, Akiyama Y, Uebayasi M, Kitaura K (2002) *Chem Phys Lett* 351:475
3. Fedorov DG, Kitaura K (2004) *J Chem Phys* 120:6832
4. Gordon MS, Fedorov DG, Pruitt SR, Slipchenko LV (2012) *Chem Rev* 112:632
5. Yang W (1991) *Phys Rev Lett* 66:1438
6. Inadomi Y, Nakano T, Kitaura K, Nagashima U (2002) *Chem Phys Lett* 364:139
7. Watanabe T, Inadomi Y, Umeda H, Fukuzawa K, Tanaka S, Nakano T, Nagashima U (2009) *J Comput Theor Nanosci* 6:1328
8. Umeda H, Inadomi Y, Watanabe T, Yagi T, Ishimoto T, Ikegami T, Tadano H, Sakurai T, Nagashima U (2010) *J Comput Chem* 31:2381
9. Sakurai T, Sugiura H (2003) *J Comput Appl Math* 159:119
10. Tsuneyuki S, Kobori T, Akagi K, Sodeyama K, Terakura K, Fukuyama H (2009) *Chem Phys Lett* 476:104
11. Kobori T, Sodeyama K, Otsuka T, Tateyama Y, Tsuneyuki S (2013) *J Chem Phys* 139:094113
12. Nishioka H, Ando K (2011) *J Chem Phys* 134:204109
13. Kitoh-Nishioka H, Ando K (2012) *J Phys Chem B* 116:12933
14. Kitoh-Nishioka H, Ando K (2016) *J Chem Phys* 145:114103
15. Sato R, Kitoh-Nishioka H, Ando K, Yamato T (2018) *J Phys Chem B* 122:6912
16. Kitoh-Nishioka H, Ando K (2015) *Chem Phys Lett* 621:96
17. Kitoh-Nishioka H, Welke K, Nishimoto Y, Fedorov DG, Irle S (2017) *J Phys Chem C* 121:17712
18. Sato R, Kitoh-Nishioka H, Yanai T, Shigeta Y (2017) *Chem Lett* 46:873
19. Sato R, Kitoh-Nishioka H, Kamada K, Mizokuro T, Kobayashi K, Shigeta Y (2018) *J Phys Chem C* 122:5334

20. Moser CC, Keske JM, Warncke K, Farid RS, Dutton PL (1992) *Nature* 355:796
21. Gray HB, Winkler JR (2005) *Proc Natl Acad Sci USA* 102:3534
22. Fedorov DG, Kitaura K (2017) *J Chem Phys* 147:104106
23. Nakano T, Kaminuma T, Sato T, Akiyama Y, Uebayasi M, Kitaura K (2000) *Chem Phys Lett* 318:614
24. Schmidt MW, Baldrige KK, Boatz JA, Elbert ST, Gordon MS, Jensen JH, Koseki S, Matsunaga N, Nguyen KA, Su S et al (1993) *J Comput Chem* 14:1347
25. Fedorov DG, Jensen JH, Deka RC, Kitaura K (2008) *J Phys Chem A* 112:11808
26. Fedorov DG, Kitaura K, Li H, Jensen JH, Gordon MS (2006) *J Comput Chem* 27:976
27. Marcus RA, Sutin N (1985) *Biochim Biophys Acta* 811:265
28. Cave RJ, Newton MD (1996) *Chem Phys Lett* 249:15
29. Skourtis SS, Beratan DN (1999) *Adv Chem Phys* 106:377
30. Stuchebrukov AA (2003) *Theor Chem Acc* 110:291
31. Stuchebrukov AA (1996) *J Chem Phys* 105:10819
32. Smith MB, Michl J (2010) *Chem Rev* 110:6891
33. Nishimoto Y, Fedorov DG, Irlé S (2014) *J Chem Theory Comput* 10:4801
34. Elstner M, Porezag D, Jungnickel G, Elsner J, Haugk M, Frauenheim T, Suhai S, Seifert G (1998) *Phys Rev B* 58:7260
35. Kubas A, Hoffmann F, Heck A, Oberhofer H, Elstner M, Blumberger J (2014) *J Chem Phys* 140:104105
36. Fujita T, Mochizuki Y (2018) *J Phys Chem A* 122:3886
37. Fujita T, Alam MDK, Hoshi T (2018) *Phys Chem Chem Phys* 20:26443
38. Yamada S, Shimojo F, Akashi R, Tsuneyuki S (2017) *Phys Rev B* 95:045106

Modeling of Solid and Surface



Koichiro Kato, Aya Hashimoto, Eiichi Tamiya, Kaori Fukuzawa,
Yuichiro Ishikawa, and Yuji Mochizuki

Abstract This chapter introduces an application of the fragment molecular orbital (FMO) method to the measurement of molecular adsorption on solid surfaces, which is the first use of the FMO method for a purpose other than drug discovery. First, the results of the interaction analysis of biomolecule adsorption on a silica surface, which is a leading type of research for nano-bio interfaces, are presented. Next, the results of the interaction analysis of biomolecule adsorption to the biominerals hydroxyapatite and calcite are shown. In order to analyze the adsorption of biomolecules on crystal surfaces at the quantum chemical level, large-scale calculations are required. However, by using the FMO method, it is possible to carry out analysis at a realistic calculation cost. In addition, the FMO method is expected to enable elucidation of the adsorption mechanism and the molecular design to enhance the adsorption capacity, because it enables quantitative analysis of the interaction between fragments. Next, as an application to general organic–inorganic interfaces, preliminary results for the AFM model system and the silica–rubber polymer complex system are introduced. The key to successful FMO calculations involving the above crystal surface system is to appropriately fragment the crystal clusters and to perform FMO4 calculations taking into account the four-body correction. The application of the FMO method to uses other than drug discovery is expanding, and is expected to expand further in the future.

K. Kato (✉)
Kyushu University, Fukuoka, Japan
e-mail: kato.koichiro.957@m.kyushu-u.ac.jp

A. Hashimoto · E. Tamiya
Osaka University, Osaka, Japan
e-mail: tamiya@ap.eng.osaka-u.ac.jp

K. Fukuzawa
Hoshi University, Tokyo, Japan
e-mail: k-fukuzawa@hoshi.ac.jp

Y. Ishikawa · Y. Mochizuki
Rikkyo University, Tokyo, Japan
e-mail: fullmoon@rikkyo.ac.jp

Keywords Crystal surface · Peptide · Interface · Hydroxyapatite · Calcite · Interaction analysis

1 Introduction

In the fields of biochemistry and biophysical chemistry, macromolecules such as proteins and DNA are studied. In order to perform such macromolecule analyses using quantum theory, it is necessary to reduce the calculation cost. Therefore, various approaches for fast computation have been proposed [1]. The fragment molecular orbital (FMO) method [2] is one of them. By using the FMO method [3, 4], it is possible to obtain physical quantities that can be used for a detailed analysis of intermolecular interactions called interfragment interaction energy (IFIE) analysis. The FMO4 method [5], which takes into account up to four-body correction, has also been developed and is used for fragmentation of amino acids into main and side chains and of ligands into functional groups. By using the FMO4 method, it becomes possible to handle three-dimensional solid crystals having a band gap, such as diamond, silicon, and silica [5]. In fact, quantum mechanics-based interaction analysis between large-scale silica clusters and peptides using the FMO4 method has been reported [6]. Interaction analysis between solids and biomolecules (nano-bio interfaces) is expected to become increasingly important in the field of nano-biotechnology. In the fields of medical-engineering and bio-engineering, topics related to nano-bio interfaces include improvement of the biocompatibility of implants by surface modification, construction of drug delivery systems using nanoparticles, and elucidation of the mechanisms of biomineralization. In the field of applied physics, we are also deeply involved in the development of devices such as highly sensitive biosensors that detect small amounts of proteins and DNA.

In simulation studies for large-scale systems such as nano-bio interfaces, classical molecular dynamics (MD) methods or quantum classical hybrid (QM/MM) methods are used. However, it is difficult to deal with quantum phenomena such as charge-transfer and chemical reactions by means of classical MD. Since the QM/MM method tends to handle a wide range of quantum mechanics, there is a limit to the size of the QM region, which requires proper modeling. Calculations based on density functional theory are also difficult to deal with when periodicity is imposed. Therefore, analyses similar to that in the study by Okiyama and colleagues [6] are currently difficult to achieve by other methods, and the results of their study are thus a milestone in applying the FMO method to problems in the nano-bio interface. Following the work of Okiyama et al. [6], the FMO method was applied to several topics in the nano-bio interface. For example, elucidation of the microscopic adsorption mechanism of hydroxyapatite (HA) and elucidation of specific sequence peptides [7] have been reported. Studies of osteoblast HA using Raman spectroscopy and FMO techniques have also been performed. In addition to HA, calcite has also been investigated by interaction analysis [8]. Of course, the FMO method can also be applied to general inorganic–organic interfaces other than the nano-bio interface. Specifically, the FMO

method has been applied to general interfaces such as an atomic force microscope (AFM) model system and interfaces composed of rubber composite materials.

In this section, we introduce the results of the latest research applying the FMO method to various systems including solid interfaces.

2 Applications for Nano-Bio Interfaces

2.1 *FMO Analysis of Peptides Specifically Adsorbed on a Silica Surface*

The research group of Dr. K. Shiba found a peptide of 12 residues that specifically adsorbs only to the oxide surfaces of titanium, silver, and silicon [9, 10]. In this peptide, it is reported that the surface-binding ability is determined by the first six residues (Arg1-Lys2-Leu3-Pro4-Asp5-Ala6: RKLPPDA). However, the microscopic adsorption mechanism remains unknown. We herein introduce the results of an FMO analysis [6] carried out to elucidate this microscopic mechanism.

The FMO calculations were performed on a complex system combining a cluster model of silica containing 257 silicon atoms and RKLPPDA. RKLPPDA was neutralized at both ends. Explicit water molecules were placed around the peptide to reproduce the hydration environment. The three-dimensional fragmentation method of silica crystals was newly developed, and by combining it with FMO4, highly accurate calculation became possible. Large-scale calculations were performed at the second-order perturbation theory (MP2) level, which can capture the dispersion force, and Cholesky decomposition (the CDAM-MP2 method [11]) was used to shorten the processing time of FMO4 calculations. In the interaction energy analysis, a new method called SCIFIE [12] was also used. By this method, the screening effect between fragments can be statistically incorporated. The key to this applied calculation was the development of a high-precision fragmentation method for silica crystals.

The visualization of IFIE is shown in Fig. 1, and confirms that three charged amino acid residues, Arg1, Lys2, and Asp5, in RKLPPDA are particularly important for binding to the silica surface. This information provides valuable guidance from a computational perspective for peptide modification and optimization. On the other hand, silica was found to be polarized not only on the surface but also inside the silica molecule by peptide binding. This result suggests that it is inappropriate to approximate a solid with a simple and compact cluster model. Figure 2 shows the IFIE value and the amount of charge transfer. As shown in this figure, quantitative evaluation of the interactions between each residue and silica revealed that charged residues contribute significantly to the stabilization. In addition, there is a charge transfer between silica and the peptide. The stabilization due to this charge transfer is a result peculiar to FMO, which is all electron calculation based on quantum mechanics.

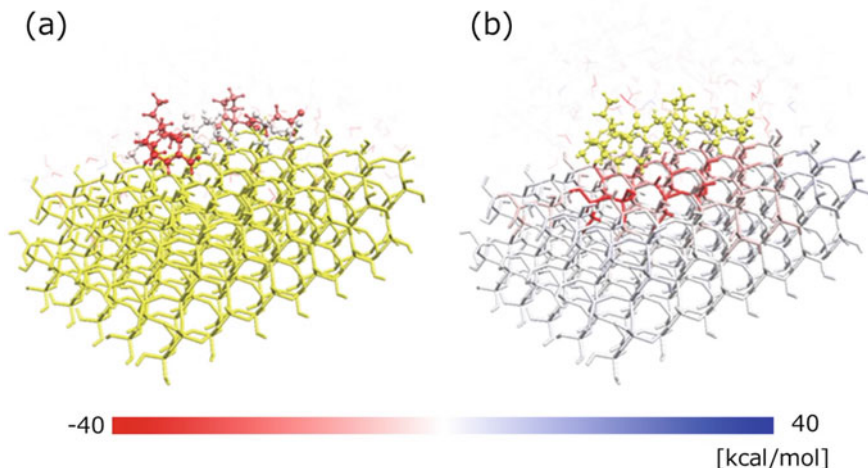


Fig. 1 Visualization of IFIE between silica and RKLPGA **a** for RKLPGA peptides by collecting contributions from all fragments in the silica cluster indicated in yellow. **b** For silica clusters by collecting contributions from all fragments in the RKLPGA indicated in yellow

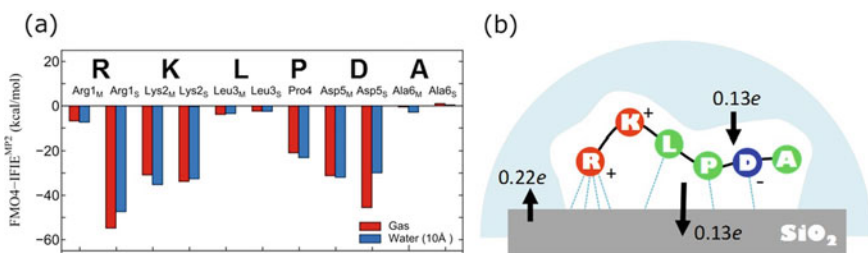


Fig. 2 **a** Plots of IFIE values for Gas and Water (10 Å) models. The Gas model represents a complex in gas phase. The Water (10Å) model represents a hydrated complex with a 10Å water shell. The names of the main and side chains of numbered amino acid residues are given with the subscripts M and S, respectively. **b** Schematic diagram of charge transfer between water, silica and peptide.

The establishment of this calculation method is expected to permit application of the FMO method to not only nano-bio interfaces but also the field of geoscience. Silica is a basic component of minerals such as quartz. Adsorption (desorption) of various ions on mineral surfaces under hydration conditions is an important chemical process, but its understanding by electronic structure calculation is still insufficient. Further development of this FMO4 calculation method is expected to promote a detailed understanding including information on various thermodynamic parameters.

2.2 FMO Analysis of Peptides Specifically Adsorbed on a Hydroxyapatite Surface

Hydroxyapatite (HA) is the major inorganic component of teeth and bones. A computational technique that could efficiently identify peptides that specifically adhere to the HA surface would be useful in various respects. For example, it could be applied to the design of high-performance adhesive materials in dentistry and the development of bone replacement materials to promote bone formation. George et al. [13] and Shiba et al. [14] experimentally demonstrated that peptides consisting of five amino acid residues (ESQES: in the order Glu1-Ser2-Gln3-Glu4-Ser5) have specific adsorptivity to HA. However, the microscopic adsorption mechanism was not sufficiently considered in these studies. Therefore, we addressed this mechanism as an application of the FMO method to a new solid surface following silica. Here, we introduce the results [7] of our interaction analysis of the HA surface and ESQES.

First, we generated a model of a huge HA crystal consisting of 1408 atoms. In this model, the unit cell is expanded to $4 \times 4 \times 2$, and the crystal parameters are $a = 37.76 \text{ \AA}$ and $c = 13.77 \text{ \AA}$. The edge effect is negligible at the center of the crystal surface where amino acids are adsorbed. By neutralizing both ends of ESQES and adsorbing it to HA surface, three composite structures were formed. MD simulations were carried out using these three structures as initial structures. Ten complex structures were sampled from each series. It is noteworthy that the structure was sampled from the MD trajectories to evaluate the adsorption characteristics including the structural fluctuation. In FMO4 calculations for a total of 30 structures, the environmental electrostatic potential is approximated by point charge (ESP-PTC approximation) to reflect the properties of strongly ionized HA. For the 1 s-2p electron of Ca, the environmental electrostatic potential was replaced by the model core potential (MCP). For atoms other than Ca, 6-31G * basis functions were used. The second-order Møller-Plesset correlation correction (MP2) was adopted for energy and electron density. By using the IFIEs obtained by the FMO method, it is possible to quantitatively evaluate the interaction between amino acids and various ions which constitute HA. The atomic charge was calculated by natural bond orbitals and used to discuss the effects of charge transfer and polarization. The execution time of the FMO4-MP2 energy calculation was 3 h per structure using a small server with 96 cores. For the analysis of the interaction energy between amino acid residues and apatite, a method considering the mutual shielding effect between fragments (SCIFE [12]) was also used.

Figure 3 shows the statistical average of the IFIE of each amino acid residue relative to the whole HA. It was commonly found that serine (Ser5) at the terminal part contributes most remarkably to the stabilizing interaction in adsorption. Moreover, analysis of the atomic charge revealed that charge transfer from the phosphate ion adjacent to Ser5 (Fig. 4) was essential for stabilizing the interaction. On the other hand, by considering the structural fluctuation, it was also proven that the stabilization interaction greatly changed depending on the adsorption shape even among identical amino acid residues such as Ser3 and Ser5 or Glu1 and Glu4. From an experimental

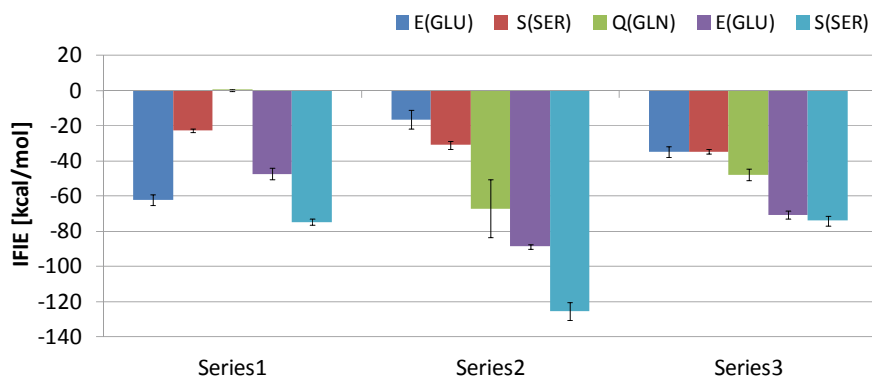


Fig. 3 Interaction energy between HA and five amino acid residues in each series

point of view, George et al. [13] inferred stabilization through electrostatic interactions between the serine, glutamate, and ion components of HA. From this study, it was newly clarified that the position relative to the HA surface and the effect of charge transfer are also likely to be important in addition to the type of amino acids.

In Fig. 5, the SCIFIE of series 1 is visualized. For each amino acid residue shown in yellow, the stabilizing interaction fragment is shown in red and the destabilizing interaction fragment is colored blue. Because glutamic acid is negatively charged, it has a stabilizing interaction with positively charged calcium ions. On the other hand, it has a destabilizing interaction with the negatively charged phosphate ion, and the closer the phosphate ion, the deeper the blue color. Serine at the C-terminus is strongly stabilized with the adjacent phosphate ion with charge-transfer interaction, but it is also shown to be weakly destabilized at a distance. As described above, our FMO4 calculations revealed quantitatively for the first time the polarization state in which stabilization and destabilization coexist in HA crystals by peptide adsorption.

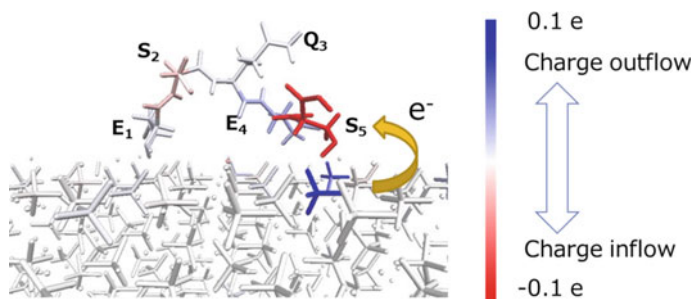


Fig. 4 Visualization of charge transfer to Ser5 from PO4³⁻. The represented structure was captured at 8.8 ns in sequence 1

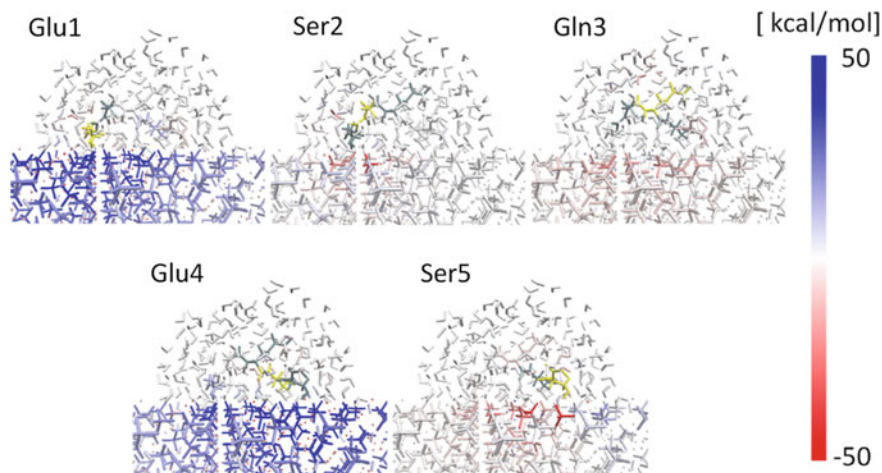


Fig. 5 Visualization of SCIFIE between HA and each amino acid residue shown in yellow. The represented structure was captured at 8.8 ns in sequence 1

2.3 Analysis of Osteoblast Hydroxyapatite by Raman Spectroscopy and the FMO Method

Recently, with respect to the crystal growth of HA, time-lapse Raman imaging analysis [15, 16] of the osteoblast mineralization process was reported. These studies demonstrated that the Raman band obtained from the HA in the cultured tissue shifts to a wavenumber about 7 cm^{-1} lower than that of the pure substance HA. Based on these results, it was considered that HA in the living body exists surrounded by bone matrix proteins such as type I collagen. Therefore, we investigated the influence of adsorption of amino acid monomers on HA using a combination of experiments and simulations. In the experiments, several kinds of amino acids were adsorbed on HA under the conditions of $\text{pH} = 7$ and $37\text{ }^\circ\text{C}$, and the influence of amino acids on HA was examined by Raman spectroscopy. In the simulation, the behavior of three amino acids (Asp, Lys, Ser) on the HA surface and the details of the interaction with the HA surface were analyzed using MD and FMO methods as in the case of HA and ESQES [7].

Details of the simulation are shown below. First, Asp, Lys, and Ser were selected as the three amino acids, and each amino acid neutralizes both ends. Four HA adsorption structures were created for each amino acid (12 structures in total). For all adsorption structures, 300 K MD was performed for 10 ns in a hydrated environment. The final structure in each MD was extracted and interaction analysis by the FMO method was carried out. In the FMO method, the ESP-PTC approximation was used with the previously reported calculation settings [7]. For the basis function, MCP and 6-31G* were used in combination. For the energy and electron density, MP2 was used. The atomic charge calculated by the natural bond orbit was used

for the discussion of the effect of charge transfer and polarization. It is possible to evaluate the interaction between HA and amino acids in an adsorption structure by FMO calculation. However, in order for amino acids to be adsorbed from a hydrated state, they must first be desolvated. When the desolvation energy is large, it may be considered that the adsorption structure is not formed because the hydrated state will be more stable without the adsorption. Therefore, in order to evaluate desolvation energy, analysis using the Molecular Mechanics Poisson–Boltzmann Surface Area (MM-PBSA) method [17] was performed. By calculating the total value of IFIE and the desolvation energy for each amino acid, we were also able to compare the interaction between HA and amino acids while considering the desolvation process.

Figure 6 shows the results of visualizing the obtained IFIE with FMO calculation for 12 adsorption structures. From this figure, it can be seen that PO_4^{3-} —in close proximity to the side chain OH of Ser exerts a strong attractive force. This is in good agreement with the features pointed out in the previous paper [7]. On the other hand, Asp and Lys are charged amino acids. Therefore, negatively charged Asp has an attractive interaction with calcium ion and repulsive interaction with phosphate ion. Also, positively charged Lys has an opposite interaction with Asp. The sum of the IFIEs from all fragments constituting HA for each amino acid is shown in Fig. 7. In Type II of Asp and Type III of Lys, since the amino acid has been separated from HA in MD, the total IFIE is small. On the other hand, in the structure maintaining HA adsorption, the influence of the differences in amino acid type and differences in adsorption structure is small.

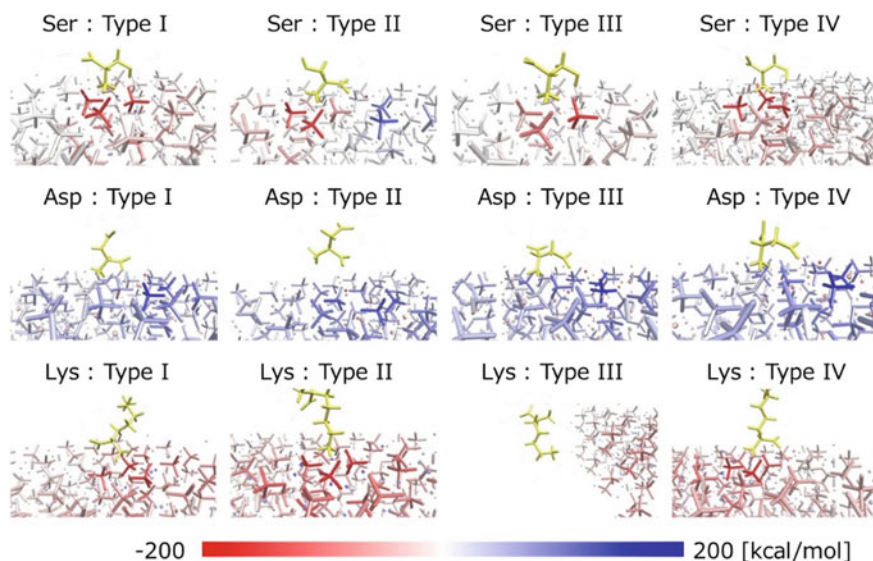


Fig. 6 Visualization of IFIE between HA and each amino acid in yellow

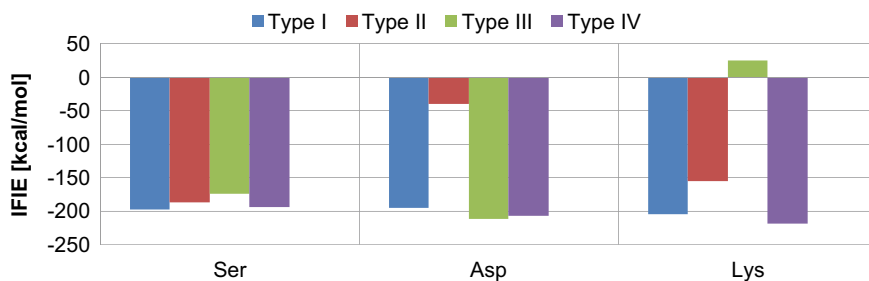


Fig. 7 Interaction energy between HA and each amino acid residue

Next, Table 1 shows the desolvation energy calculated by the MM-PBSA method. MM-PBSA calculation was performed on a Type IV adsorption structure of each amino acid. The desolvation energy decreased in the order of Asp, Lys, and Ser. When the sum of the IFIEs was added to the desolvation energy, Ser became the amino acid with the highest adsorption capacity, followed in order by Lys and Asp. On the other hand, the experimentally obtained Raman band shift is shown in Table 2. The magnitude of the influence on the Raman band shift decreased in the order of Ser, Lys, and Asp. Therefore, it was found that there is a correlation between the IFIE sum with desolvation energy and the amount of the Raman band shift. The Raman experiment revealed the symmetric stretching mode of the phosphate ions. In addition, since HA is an ionic crystal, it is considered that most of the interaction between phosphate ions and surrounding HA ions is due to electrostatic interaction. Therefore, the change in the charge of the phosphate ion due to the amino acid adsorption weakens the electrostatic interaction and is expected to cause the Raman shift. Actually, when calculating the amount of charge transfer from HA to each amino acid, the transfers to Ser, Lys, and Asp were found to be $-0.22e$, $-0.13e$, and $-0.10e$, respectively. There was also a correlation between the amount of Raman band shift and the amount of charge transfer.

Since Ser is not only the most adsorptive amino acid based on the results of the IFIE sum analysis with desolvation energy, but also the most electron-accepting amino acid based on the results of the charge-transfer analysis, it is considered that the largest Raman shift was observed in HA-Ser.

2.4 FMO Analysis of Peptides Specifically Adsorbed on the Calcite Surface

Calcite is a biomineral known as the principal component of eggshells, sea urchin teeth, and thorns. The chemical composition is calcium carbonate (CaCO_3). Calcite is very strong—for example, sea urchin teeth have been reported to be strong enough to pierce rocks without losing their sharpness [18]. Research into the mechanism

Table 1 IFIE sum with desolvation energy taken into consideration (the MM—PBSA calculation was performed on the Type IV adsorption structure of each amino acid)

Type IV adsorption structure [kcal/mol]	Ser	Lys	Asp
IFIE	−193.98	−218.55	−207.12
E_{solv}	139.11	179.81	203.51
IFIE + E_{solv}	−54.87	−38.74	3.61

Table 2 Summary of amino acid effects on the HA Raman band

Coat	Non-cort	Ser	Lys	Asp
Raman band of HA ν_1 mode [cm^{-1}]	963.4	959.7	960.9	962.4
Shift [cm^{-1}]	−	−3.7	−2.5	−0.9

of the biomineralization of calcite is also being actively carried out. The difference in the adsorbability of aspartic acid and glycine [19] and the strong adsorption of aspartic acid-rich peptides on calcite have been reported, indicating the importance of the DDGSDD motif [20, 21]. This section introduces the results of FMO calculation analysis to clarify the microscopic mechanism of DDGSDD adsorption.

A calcite crystal model was constructed with 1,920 atoms. DDGSDD was neutralized at both ends. DDGSDD was adsorbed on the {10–14} of calcite, which is the most stable surface in liquids. Similar to the approach used in HA-ESQES analysis [7], structure sampling by MD and interaction analysis by the FMO method were performed. Here, 4 kinds of composite structures were prepared as an initial structure of MD, and 10 kinds of structures were sampled from 4 series of MD. The FMO method was performed at the FMO4-MP2 level and the ESP-PTC approximation was adopted. The basis functions are MCP for Ca and 6-31 G* for other atoms. The atomic charge is calculated by natural bond orbitals and used to discuss the effects of charge transfer and polarization.

Figure 8 shows the statistical mean value of IFIE between each amino acid residue and calcite. Though the fluctuation by the series is also large, Asp on the end side tends to interact strongly with the calcite. In addition, it was proven that the interaction with the calcite changed greatly from attraction to repulsion depending on the structure even in the same Asp by considering the structural fluctuation. Figure 9 illustrates SCIFIE of series 1, in which the stabilizing fragment (Water or ions) is shown in red and the destabilizing fragment is shown in blue for each amino acid residue shown in yellow. The negatively charged Asp interacts stably with the positively charged calcium ion, but interacts unstably with the negatively charged phosphate ion. Phosphate ions close to Asp are dark blue. Depending on the adsorption structure, some Asp cannot approach the surface calcium ions and are adjacent to phosphate ions. It is considered that a repulsive interaction occurs in such adsorption structures. On the other hand, the specific adsorption of Ser observed in HA-ESQES [7] did not occur in calcite-DDGSDD. Analysis of the atomic charge revealed that the charge

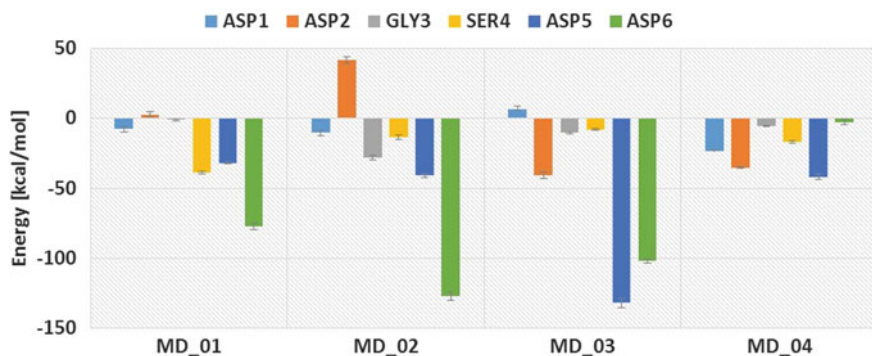


Fig. 8 Interaction energy between calcite and six amino acid residues in each series

transfer from the surface carbonate ion to Ser was not significant. It is considered that this difference was due to polarizability and the sizes of the carbonate and phosphate ions. That is, phosphate ions are more likely to lose electrons than carbonate ions. HA and calcite are the same ionic crystals, but FMO analysis based on quantum mechanics revealed different mechanisms of peptide adsorption.

3 Applications for General Organic–inorganic Interfaces

Since silica, hydroxyapatite, and calcite are important materials in the nanobiotechnology field, the results of our analysis of the interaction between these materials and biomolecules are shown. On the other hand, in the FMO method, it is also possible to analyze the interaction between common organic molecular materials and inorganic crystal surfaces. Below, we introduce two examples of application to such general interfaces.

3.1 Analysis of Small Molecules and the AFM Tip Model on an NaCl Surface

NaCl crystal is one of the simplest ion crystals. It is interesting as a research subject, and has been investigated in many studies, such as a study measuring the desorption heat of molecules adsorbed on the NaCl crystal surface [22]. Furthermore, in recent years, NaCl crystal has often been used for substrate modification of AFM. Visualization of the charge state of atoms [23] and the six-membered ring structure of molecules [24] on the surface of NaCl has been reported. These reports are also very interesting from the viewpoint of computational chemistry. For example, the FMO

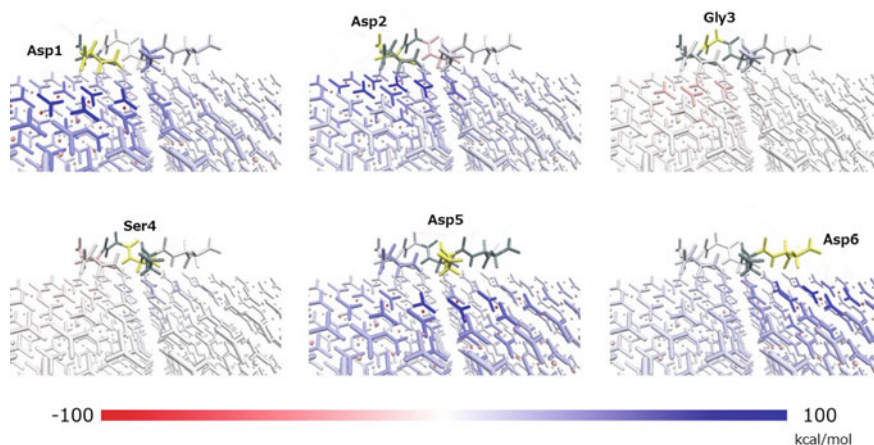


Fig. 9 Visualization of SCIFIE between calcite and each amino acid residue shown in yellow. The represented structure was captured at 9.2 ns in sequence 1

method is expected to reveal factors for molecular adsorption and to be useful for calculating forces on the AFM tip.

In this study, we analyzed molecular adsorption to the NaCl surface. For elucidation of the factors of molecular adsorption, CO, N₂, C₂H₂, C₂H₄, C₆H₆ were targeted. We also examined Si₄H₄, Si₄H₃— as model molecules of the AFM tip. First, a cluster model was prepared that imitated surfaces composed of 25 (single layer) and 50 (2 layers) NaCl units. For each calculation, energy was evaluated while changing the distance between each molecule and the NaCl surface. For the tip model of AFM, the force in the vertical direction of the surface was also evaluated. Calculation settings were equivalent to those for HA and calcite. The FMO4-MP2 level calculation was performed using the ESP-PTC approximation to the environmental electrostatic potential. For basis functions, 6-31G* was applied to Na, Si, and H, and 6-31 + G* was applied to C, O, N, and Cl.

Figure 10 shows the energy change when C₂H₂ and C₂H₄ are brought close to the NaCl surface. It is considered that both molecules record a minimum energy at a specific distance and form a stable state. However, as a result of the HF method, the degree of stabilization is small. This implies that the dispersion force makes an important contribution to the stabilization, and reveals the necessity of the calculation in MP2. Table 3 summarizes the energy minimum (E_{\min}) and distance minimum (R_{\min}) that give E_{\min} , including other molecules. If an experimental report is available, the measured values are also listed. Since this calculation was performed on a simplified model, the deviation from the experimental value was large, but the calculated and experimental values for C₂H₂ remained relatively close. Also, the number of layers of NaCl had little influence on R_{\min} , but it was found to have a significant influence on E_{\min} . The importance of MP2 is suggested again in C₆H₆. Although the stable state was not formed by the HF method, stabilization of about 14 kcal/mol

Table 3 Summary of molecular absorption on an NaCl surface. E_{\min} is the minimum energy value, and R_{\min} is the distance at which E_{\min} was recorded. The units of E_{\min} and R_{\min} are kcal/mol, Å respectively. NB means that no bonding state was formed

	CO		N ₂		C ₂ H ₂		C ₂ H ₄		C ₆ H ₆	
	R_{\min}	E_{\min}	R_{\min}	E_{\min}	R_{\min}	E_{\min}	R_{\min}	E_{\min}	R_{\min}	E_{\min}
MP2(50)	2.6	-8.8	2.5	-10.3	2.9	-8.2	2.9	-9.1	3.2	-13.9
MP2(25)	2.6	-9.4	2.5	-10.0	2.9	-8.8	2.9	-8.8	3.1	-14.6
HF(50)	2.9	-2.2	2.8	-0.8	3.4	-0.8	3.5	-0.8	NB	NB
HF(25)	2.9	-2.9	2.8	-1.7	3.4	-1.4	3.5	-1.2	4.7	-0.2
Exp	-	~4 [22]	-	-	-	~7.7 [25]	-	~5.3 [26]	-	-

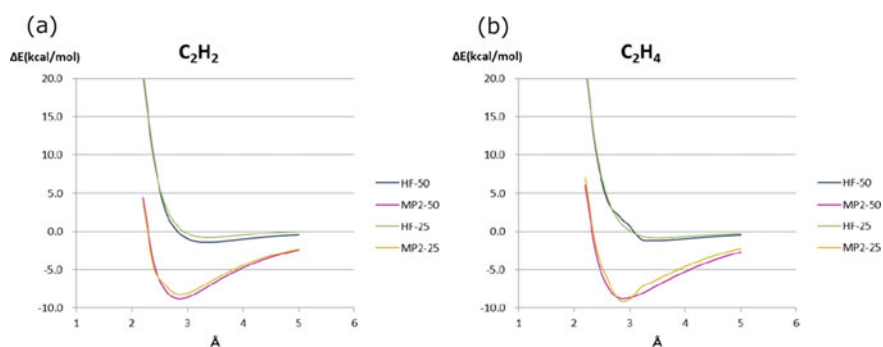


Fig. 10 Energy profile of **a** C₂H₂ and **b** C₂H₄ adsorption on an NaCl surface. The horizontal axis represents the distance between the adsorbed molecule and the NaCl surface. Energy was set to zero when the distance between them was 10 Å

occurred in MP2. Since C₆H₆ is a system rich in π electrons, it is considered that the dispersion force greatly contributes the stabilization of C₆H₆.

Figure 11 shows the change in energy and force when the AFM tip model is brought close to NaCl. It can be seen that a stable state occurs in both model molecules. In the deprotonated (Si₄H₃⁻) model, since the electrostatic interaction is strengthened, the amount of change in energy is large. In regard to the force responsible for this change, we obtained a smoothly changing result in both models. In addition, it was confirmed that the deprotonated model exhibits a sharp change in force according to the distance. Also, as in the case of small molecules, the AFM tip model also shows that the results differ greatly depending on the dispersion force.

The above analysis revealed the importance of the dispersion force as a key factor of molecular adsorption on the NaCl surface. Further, since it was confirmed that smooth force calculation should be possible in the AFM tip model, it might be possible to achieve an AFM simulation closer to the experimental system by using the FMO method.

3.2 Interaction Analysis Between Rubber Polymer and Silica Filler

In the tire industry, a composite material of a polymer and an additive called a filler is widely used. Simulations are actively employed to analyze this composite material. There are many examples of macro-mesoscale simulation, such as the finite element method and rheology. Even at the microscale, such investigations are limited to the analysis of physical properties by classical MD, and there have been very few detailed analyses of the polymer and filler interface based on the electronic state. This is because the number of target atoms becomes enormous, making it difficult to perform the calculations by the conventional electronic structure calculation method.

Carbon black has long been used as a filler material, but in recent years eco-tires incorporating silica have also been developed and widely adopted. As described in previous sections, silica can be efficiently and accurately analyzed by the FMO method. Also, since fragmentation of rubber polymer is not difficult, it is possible to calculate a model in which rubber polymer is entangled with silica filler. In other words, by using the FMO method, it is possible to analyze the interaction at the complex interface between silica filler and rubber polymer based on quantum mechanics.

Our preliminary results are shown here. First, silica filler was expressed as a nanocluster (186 atoms) with a side length of about 1 nm. Polyisoprene and styrene-butadiene rubber (SBR) were adopted as rubber polymers in this study. Our polyisoprene model connected 10 unit structures and the SBR model connected 5 units. Silica nanocluster, polyisoprene, and SBR were divided into 19, 10, and 5 fragments, respectively (see Fig. 12). ESP-AOC approximation was used for the environmental electrostatic potential and 6-31G* was used as a basis function. This calculation was also carried out at the FMO4-MP2 level. For a complex model of silica nanocluster and rubber polymer, we adopted a structure in which five rubber polymers were docked to 1 nanocluster.

Figure 13 is a diagram of the IFIE of each rubber polymer against the silica nanocluster. The silica nanocluster shown in yellow and the stabilizing fragment are red, and the destabilizing fragment is blue. As seen from this figure, the red fragments are widely distributed in both rubber polymers, but SBR is more extensively colored. The main part of the interaction between the silica nanocluster and the rubber polymer is thought to be OH- π interaction due to the silanol group of the silica surface and π electron of the rubber polymer. The benzene ring in the side chain of SBR has large extended π electrons. Therefore, it should be considered that SBR shows an attractive interaction across a wide area. Also, in the FMO calculations, the strength of interaction between rubber polymers can be quantitatively evaluated at the same time. In the interaction between rubber polymers, the π - π interaction plays an important role. Here again, the attractive interaction between the SBRs is stronger than that between the polyisoprenes.

In addition, in rubber composite materials, material strength is also improved by incorporating the crosslinking structure by sulfur. For a sulfur bridge rubber model,

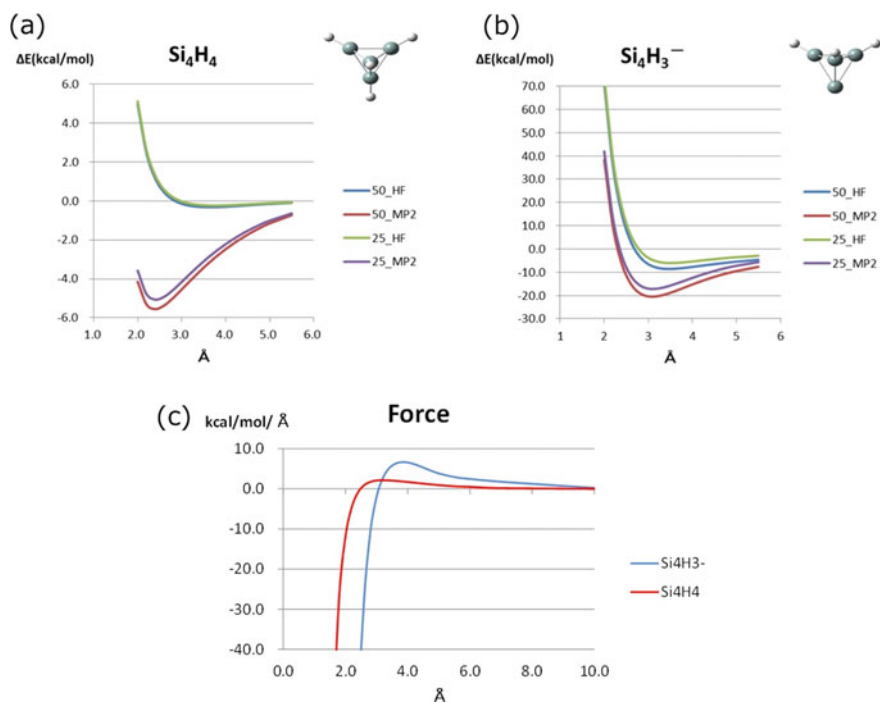


Fig. 11 Change in **a, b** energy and **c** force when approaching the AFM tip model to NaCl. The horizontal axis represents the distance between the adsorbed molecule and the NaCl surface. Force represents the component in the vertical direction on the NaCl surface

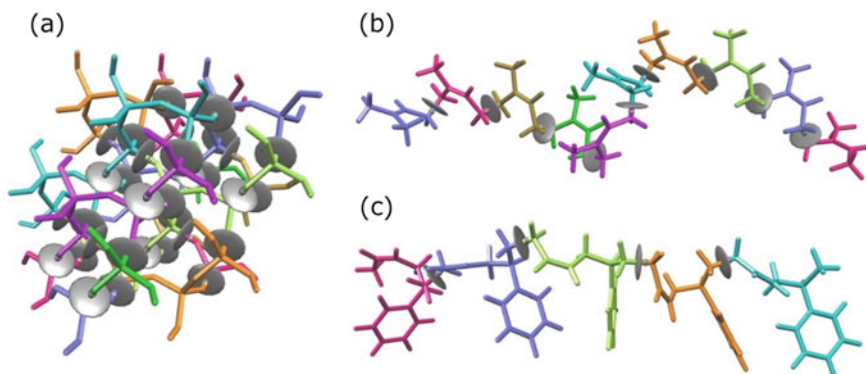


Fig. 12 Fragmentation of the model structures (a), a silica nanocluster (b) and polyisoprene (c) SBR

we also performed FMO calculations in the same way. As shown in Fig. 14, the interaction between the sulfur bridging part of the rubber polymer and the silica was strengthened. The FMO calculation results also implied that a strong complex was formed by sulfur crosslinking.

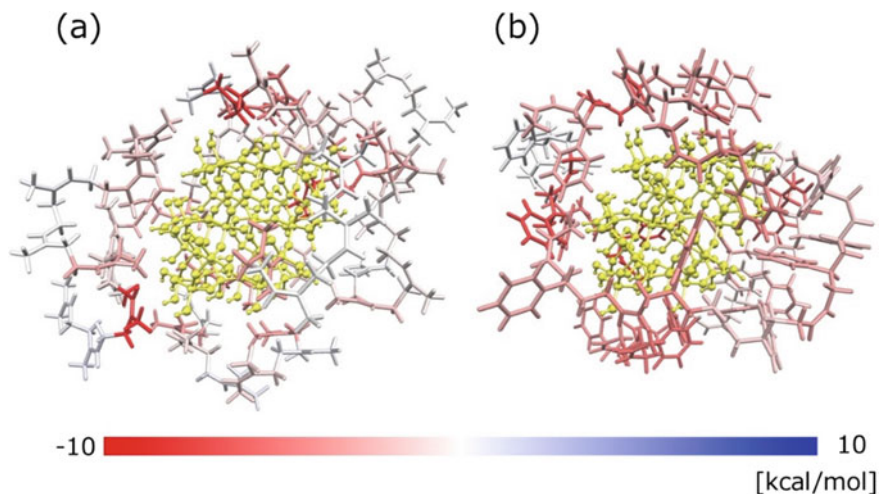


Fig. 13 Visualization of IFIE between the silica nanocluster in yellow and **a** polyisoprene **b** SBR

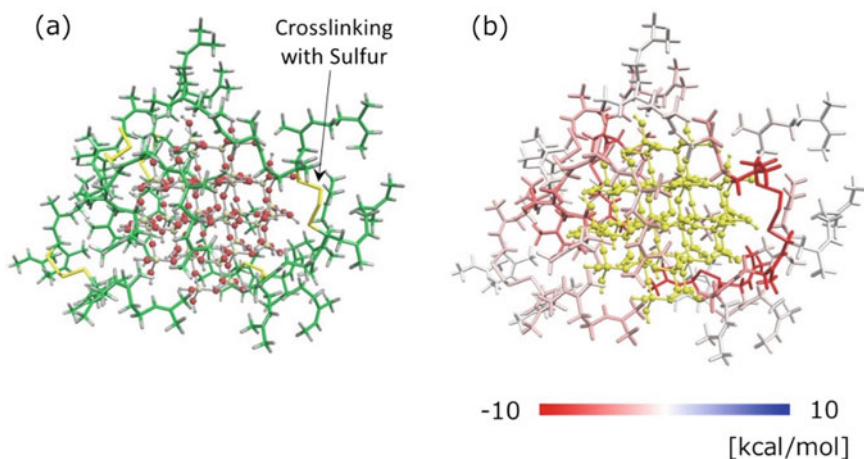


Fig. 14 **a** Atomic structure of the silica nanocluster and sulfur-crosslinked polyisoprene (green: C; red: O; grey: H; yellow: S); **b** visualization of IFIE

4 Summary

This chapter provided examples of application of the FMO method to the molecular recognition of solid surface systems. Elucidation of the molecular recognition mechanism of solid surfaces based on quantum mechanics requires large-scale calculations, so it is difficult to apply other methods at present. As shown in this chapter, it is possible to analyze the interaction of various systems including solid surfaces by applying the FMO4 method. IFIE analysis based on quantum mechanics has provided new insights, such as the importance of charge-transfer interactions between hydroxyapatite and peptide. The quantitative analysis of IFIE enabled by the FMO method is expected to lead not only to the elucidation of molecular recognition mechanisms but also to the design of molecules that recognize specific material surfaces.

Acknowledgements These works were supported by the Strategic Programs Innovative Research (SPIRE) (Field 4—Industrial Innovation) project at the Institute of Industrial Science (IIS) of the University of Tokyo, by SFR-aid from the Rikkyo University, by JSPS KAKENHI Grant Number JP 16H04635 and by funds from the Ministry of Education, Culture, Sports, Science and Technology (MEXT) for the Social and Scientific Priority Issue #6 (Accelerated Development of Innovative Clean Energy Systems) to be tackled by using post-K computer (“Fugaku”).

References

1. Gordon MS, Fedorov DG, Pruitt SR, Slipchenko LV (2012) *Chem Rev* 112:632
2. Kitaura K, Ikeo E, Asada T, Nakano T, Uebayasi M (1999) *Chem Phys Lett* 313:701
3. Fedorov DG, Nagata T, Kitaura K (2012) *Phys Chem Chem Phys* 14:7562
4. Tanaka S, Mochizuki Y, Komeiji Y, Okiyama Y, Fukuzawa K (2014) *Phys Chem Chem Phys* 16:10310
5. Nakano T, Mochizuki Y, Yamashita K, Watanabe C, Fukuzawa K, Segawa K, Okiyama Y, Tsukamoto T, Tanaka S (2012) *Chem Phys Lett* 523:128
6. Okiyama Y, Tsukamoto T, Watanabe C, Fukuzawa K, Tanaka S, Mochizuki Y (2013) *Chem Phys Lett* 566:25
7. Kato K, Fukuzawa K, Mochizuki Y (2015) *Chem Phys Lett* 629:58
8. Kato K, Fukuzawa K, Mochizuki Y (2019) *Jpn J Appl Phys* 58:120906
9. Sano K, Shiba K (2003) *J Am Chem Soc* 125:14234
10. Sano K, Sasaki H et al (2005) *Langmuir* 21:3090
11. Okiyama Y, Nakano T et al (2010) *Chem Phys Lett* 494:84
12. Tanaka S, Watanabe C et al (2013) *Chem Phys Lett* 556:272
13. He G, Dahl T, Veis A, George A (2003) *Nat Mater* 2:552
14. Tsuji T, Oaki Y, Yoshinari M, Kato T, Shiba K (2010) *Chem Comm* 46:6675
15. Hashimoto A et al (2015) *Sci Rep* 5:12529
16. Hashimoto A et al (2014) *J Raman Spectrosc* 45:157
17. Kollman PA, Massova I, Reyes C, Kuhn B, Huo S, Chong L, Lee M, Lee T, Duan Y, Wang W, Donini O, Cieplak P, Srinivasan J, Case DA, Cheatham TE III (2000) Calculating structures and free energies of complex molecules: combining molecular mechanics and continuum models. *Accts Chem Res* 33:889
18. Killian CE et al (2009) *J Am Chem Soc* 137:18404
19. Montanari G et al (2016) *Cryst Growth Des* 16:4813

20. Tsukamoto D et al (2004) *Biochem Biophys Res Commun* 320:1175
21. Gotliv B-A et al (2005) *ChemBioChem* 6:304
22. Hardy JP, Ewing GE, Stables R, Simpson CJS (1985) *Surf Sci* 159:L474
23. Gross L, Mohn F, Liljeroth P, Repp J, Giessibl FJ, Meyer G (2009) *Science* 324:1428
24. Gross L, Mohn F, Liljeroth P, Meyer G (2009) *Science* 325:1110
25. Dunn SK, Ewing GE (1992) *J Phys Chem* 96:5284
26. Willian KR, Ewing GE (1995) *J Phys Chem* 99:2186

Development of the Analytic Second Derivatives for the Fragment Molecular Orbital Method



Hiroya Nakata and Dmitri G. Fedorov

Abstract The development of the analytic second derivatives of the energy with respect to nuclear coordinates for the fragment molecular orbital method is reviewed, and a summary of equations is provided for Hartree–Fock and density functional theory (DFT). The second derivatives are developed for unrestricted DFT. The accuracy of frequencies, IR intensities, Raman activities, and free energies is evaluated in comparison to unfragmented results.

Keywords FMO · Hessian · Infrared spectrum · Raman

1 Introduction

Second derivatives of the energy with respect to nuclear coordinates play a very important role in science. They can be used to obtain harmonic vibrational frequencies, which are of paramount importance as a property of materials. Infrared (IR) and Raman spectra can be simulated by evaluating intensity (activity) for a given frequency. Normal modes can be used as the basis for evaluating anharmonic effects.

Considerable efforts have been invested in reducing the computational cost of calculating second derivatives of the energy in quantum-mechanical (QM) methods, [1, 2] pioneered by Pulay [3]. One route to improve the efficiency is to use fragment-based methods [4], some of which have analytic second derivatives [5–10]. Alternatively, some part of the system can be treated with molecular mechanics

H. Nakata (✉)

Department of Fundamental Technology Research, Research and Development Center
Kagoshima, Kyocera Corporation, 1-4 Kokubu Yamashita-cho,
Kirishima-shi, Kagoshima 899-4312, Japan
e-mail: nakata.hiro07@gmail.com

D. G. Fedorov

CD-FMat, National Institute of Advanced Industrial Science and Technology (AIST),
1-1-1 Umezono, Tsukuba, Ibaraki 305-8568, Japan
e-mail: d.g.fedorov@aist.go.jp

© Springer Nature Singapore Pte Ltd. 2021

Y. Mochizuki et al. (eds.), *Recent Advances of the Fragment Molecular Orbital Method*,
https://doi.org/10.1007/978-981-15-9235-5_22

425

(MM) in QM/MM methods [11]. To reduce the computational cost, Hessian can be computed for a part of the molecular system [12–16].

In the fragment molecular orbital (FMO) method [17–21], the molecular system is divided into fragments, evaluated in the presence of an embedding electrostatic potential (ESP). To improve the accuracy, higher order dimer and trimer terms are added in the many-body expansion [22].

In this chapter, the development of the analytic second derivatives for FMO in GAMESS [23] is reviewed for restricted Hartree–Fock (RHF) [24], restricted open-shell Hartree–Fock (ROHF) [25], unrestricted Hartree–Fock (UHF) [26] and restricted DFT [27]. Previously unpublished analytic second derivatives for FMO-UDFT are presented in this chapter. Analytic second derivatives have also been developed for FMO combined with density-functional tight-binding (DFTB) [28–31] but they are not covered in this chapter.

Detailed equations are given for the two-body FMO expansion (FMO2) [32], and the extension to the three-body FMO3 is briefly covered. FMO can be used with two fragment boundary treatments, hybrid orbital projection (HOP) operator [33, 34] and adaptive frozen orbitals (AFO) [35, 36] but the analytic second derivatives have been derived only for the former.

The accuracy of properties is evaluated in comparison to full unfragmented calculations. Using second derivatives, it is possible to simulate IR and Raman spectra, and determine the path of chemical reactions, in particular, for polymers and enzymes. The free energies can be obtained using statistical thermodynamics, although anharmonic effects and rovibrational coupling for large molecular systems may be very important for the entropy and free energy due to large contributions of low-frequency vibrations [24].

2 Mathematical Formulation

2.1 Analytic Gradient in FMO

2.1.1 Restricted Hartree–Fock

The FMO2 energy of a system divided into N fragments is

$$E = \sum_I E'_I + \sum_{I>J} (E'_{IJ} - E'_I - E'_J) + \sum_{I>J} \text{Tr}(\Delta \mathbf{D}^{IJ} \mathbf{V}^{IJ}), \quad (1)$$

where E'_X is the internal energy of X ($X = I$ for monomers and $X = IJ$ for dimers). The notion *internal* as applied to X refers to the contributions from X only, excluding ESP (ESP of X describes interactions with fragments other than X). The density matrix

difference $\Delta\mathbf{D}^{IJ}$ in Eq. (1) is obtained by subtracting the direct sum of monomer electron densities \mathbf{D}^I and \mathbf{D}^J from the dimer matrix \mathbf{D}^{IJ} as

$$\Delta\mathbf{D}^{IJ} = \mathbf{D}^{IJ} - (\mathbf{D}^I \oplus \mathbf{D}^J), \quad (2)$$

\mathbf{V}^{IJ} in Eq. (1) is the ESP matrix for dimer IJ due to the electron densities and nuclear charges of fragments other than I and J . Although monomer ESPs are used during SCF, in the final energy expression in Eq. (1) only dimer ESPs are present due to the cancellation of terms [32]. The ESP for fragment X is

$$V_{\mu\nu}^X = \sum_{K \neq X}^N V_{\mu\nu}^{X(K)}, \quad (3)$$

where the contribution of fragment K for $\mu\nu \in X$ is

$$V_{\mu\nu}^{K(X)} = \sum_{A \in K} \langle \mu | \left| \frac{-Z_A}{|\mathbf{r} - \mathbf{R}_A|} \right| v \rangle + \sum_{\lambda, \sigma \in K} D_{\lambda\sigma}^K (\mu\nu | \sigma\lambda). \quad (4)$$

\mathbf{R}_A and Z_A are the position and charge of atom A , respectively. $(\mu\nu | \lambda\sigma)$ is the two-electron integral in the atomic orbital (AO) basis. Roman ($ijkl$) and Greek ($\mu\nu\sigma\lambda$) indices denote molecular orbitals (MOs) and AOs, respectively.

The internal fragment energy of X is

$$E'_X = \sum_{\mu\nu \in X} D_{\mu\nu}^X h_{\mu\nu}^X + \frac{1}{2} \sum_{\mu\nu\lambda\sigma \in X} \left[D_{\mu\nu}^X D_{\lambda\sigma}^X - \frac{1}{2} D_{\mu\lambda}^X D_{\nu\sigma}^X \right] (\mu\nu | \lambda\sigma) + \sum_{\mu\nu \in X} D_{\mu\nu}^X p_{\mu\nu}^X + E_X^{\text{NR}}, \quad (5)$$

where $h_{\mu\nu}^X$ is the one-electron Hamiltonian of X . The HOP matrix element is

$$P_{\mu\nu}^X = \sum_{k \in X} B_k \langle \mu | \theta_k \rangle \langle \theta_k | \nu \rangle, \quad (6)$$

where $|\theta_k\rangle$ is a hybrid orbital on the fragment boundary and the universal constant B_k is usually set to 10^6 a.u.. The nuclear repulsion (NR) energy is

$$E_X^{\text{NR}} = \sum_{B \in X} \sum_{A(\in X) > B} \frac{Z_A Z_B}{R_{AB}}, \quad (7)$$

where R_{AB} is the distance between atoms A and B .

In the MO basis, Eq. (5) can be written as

$$E'_X = \sum_{i \in X}^{\text{occ}} 2h_{ii}^X + \sum_{ij \in X}^{\text{occ}} [2(ii|jj) - (ij|ij)] + \sum_{i \in X}^{\text{occ}} 2P_{ii}^X + E_X^{\text{NR}}. \quad (8)$$

The last term in Eq. (1) is

$$\text{Tr}(\Delta \mathbf{D}^{IJ} \mathbf{V}^{IJ}) = 2 \left(\sum_{i \in IJ}^{\text{occ}} V_{ii}^{IJ} - \sum_{i \in I}^{\text{occ}} V_{ii}^{IJ} - \sum_{i \in J}^{\text{occ}} V_{ii}^{IJ} \right). \quad (9)$$

The change of basis from AO to MO for matrices is accomplished via a similarity transformation using the matrix of MO coefficients $C_{\mu i}^X$, for instance

$$P_{ij}^X = \sum_{\mu, \nu \in X} C_{\mu i}^{X*} P_{\mu \nu}^X C_{\nu j}^X. \quad (10)$$

Differentiating E'_X with respect to a nuclear coordinate a , one obtains

$$\begin{aligned} \frac{\partial E'_X}{\partial a} &= \sum_{i \in X}^{\text{occ}} 2h_{ii}^{a,X} + \sum_{ij \in X}^{\text{occ}} [2(ii|jj)^a - (ij|ij)^a] + \sum_{i \in X}^{\text{occ}} 2P_{ii}^{a,X} \\ &+ \sum_{m \in X}^{\text{occ+vir}} \sum_{i \in X}^{\text{occ}} 4U_{mi}^{a,X} F'_{mi}{}^X + \frac{\partial E_X^{\text{NR}}}{\partial a}, \end{aligned} \quad (11)$$

where the superscript a denotes a differentiation with respect to a (except for U , where a is an indexing variable), for example,

$$P_{\mu \nu}^{a,X} = \frac{\partial P_{\mu \nu}^X}{\partial a}. \quad (12)$$

The internal fragment Fock matrix elements are

$$F'_{mi}{}^X = h_{mi}^X + \sum_{k \in X}^{\text{occ}} [2(mi|kk) - (mk|ik)] + P_{mi}^X, \quad (13)$$

where $P_{ij}^{a,X}$ is $P_{\mu \nu}^{a,X}$ in the MO basis. The derivatives of the MO coefficients can be written using the orbital response terms $U_{mi}^{a,X}$ as

$$\frac{\partial C_{\mu i}^X}{\partial a} = \sum_{m \in X}^{\text{occ+vir}} U_{mi}^{a,X} C_{\mu m}^X. \quad (14)$$

In FMO, the electronic states of monomers are self-consistent with respect to each other via the embedding ESP, but the electronic state of a dimer is not self-consistent with respect to the embedding ESP determined by monomer densities. In full RHF and DFT, the orbital response terms $U_{ri}^{a,X}$ are not needed for the gradient [37], but in FMO they have to be used [38] because of this lack of self-consistency between monomers and dimers.

The differentiation of the ESP energy in Eq. (9) with respect to a nuclear coordinate a gives a linear combination of three terms of the form:

$$\begin{aligned} \sum_{i \in X}^{\text{occ}} \frac{\partial V_{ii}^{IJ}}{\partial a} &= 2 \sum_{i \in X}^{\text{occ}} V_{ii}^{a,IJ} + 4 \sum_{m \in X}^{\text{occ+vir}} \sum_{i \in X}^{\text{occ}} U_{mi}^{a,IJ} V_{mi}^{IJ} \\ &+ 8 \sum_{K \neq IJ} \sum_{m \in K}^{\text{occ+vir}} \sum_{k \in K}^{\text{occ}} U_{mk}^{a,K} \sum_{i \in X}^{\text{occ}} (ii|mk). \end{aligned} \quad (15)$$

In Eq. (15), the response contribution of Y to the gradient of X is [39],

$$\bar{U}^{a,X,Y} = 4 \sum_{i \in X}^{\text{occ}} \sum_{r \in X}^{\text{vir}} U_{ri}^{a,X} V_{ri}^Y. \quad (16)$$

There are two types of $\bar{U}^{a,X,Y}$ terms: (a) $\bar{U}^{a,I,I}$ arising from the derivative of the monomer terms and (b) $\bar{U}^{a,X,IJ}$ where X can be I, J or IJ (related to the three \mathbf{D} terms in Eq. (2)). To obtain the occupied-virtual orbital responses $U_{ri}^{a,X}$, one must solve the CPHF equations, as shown below.

The collection of all $\bar{U}^{a,X,Y}$ terms in Eqs. (11, 15) arising from the differentiation of Eq. (1) is

$$\bar{U}^a = - \sum_I^N \bar{U}^{a,I,I} - \sum_{I>J}^N (\bar{U}^{a,IJ,IJ} - \bar{U}^{a,I,I} - \bar{U}^{a,J,J}) + \sum_{I>J}^N (\bar{U}^{a,IJ,IJ} - \bar{U}^{a,I,IJ} - \bar{U}^{a,J,IJ}). \quad (17)$$

\bar{U}^a can be shown to be zero when no ESP approximations are applied [39], otherwise, it is small and may be neglected as an approximation, although it is better to evaluate it. Without ESP approximations, the dimer-related terms $U_{ri}^{a,X,IJ}$ in Eq. (15) need not be evaluated (because their sum vanishes), and only $U_{ri}^{a,I}$ terms have to be obtained by solving CPHF equations. The response term contribution to gradient is

$$R^a = 4 \sum_{I>J}^N \sum_{K \neq I,J} \sum_{r \in K}^{\text{vir}} \sum_{i \in K}^{\text{occ}} \sum_{\mu, \nu \in IJ} U_{ri}^{a,K} \Delta D_{\mu\nu}^{IJ} (\mu\nu|ri). \quad (18)$$

In the following derivations, ESP approximations are not used for simplicity; the formulation with the ESP point charge (ESP-PC) approximation is given elsewhere [39–41]. The FMO gradient with the ESP-PC approximation has a residual error [40] and in order to get an accurate gradient a sufficiently large value of the ESP-PC threshold should be used.

2.1.2 Frozen Domain

In order to increase the speed of a partial geometry optimization, where only a subsystem is optimized, one can assign fragments into domains (Fig. 1): active **A** (containing fragments in which some atoms are optimized), frozen **F** and the buffer **b** between them. The union of **A** and **b** is called the polarizable buffer **B** [42], and the union of **B** and **F** constitutes the total system **S**. The active domain **A** forms the central part of **B**. At present, FMO/FD is developed only at the level of FMO2.

FD uses a multilayer formulation of FMO [43], with 2 layers L_1 (**F**) and L_2 (**B**), into which all fragments are assigned. For the initial molecular structure in a geometry optimization, monomer calculations for the whole system **S** are performed at the level of L_1 in order to obtain the fragment densities of all fragments. Then, FMO2 calculations of the polarizable domain **B** are performed at the level of layer L_2 in the presence of the embedding ESP for the whole system $\mathbf{S} = \mathbf{B}(L_2) \cup \mathbf{F}(L_1)$. The gradient for atoms in **A** is obtained and used to update the molecular geometry. If the gradient is not small enough, the calculation proceeds again to the step of calculating **B**. Thus, an FMO/FD calculation, variationally speaking, is a one-layer computation (layer L_2) of **B** using a frozen embedding from **F** (computed for the initial geometry at the level of L_1 and then frozen).

In addition to the full FD, there is also its approximation, FD with dimers (FDD) [42], in which the total energy is a sum of the internal (int) and ESP-related contributions,

$$E^{\text{FMO/FDD}} = E^{\text{int}} + E^{\text{ESP}}, \quad (19)$$

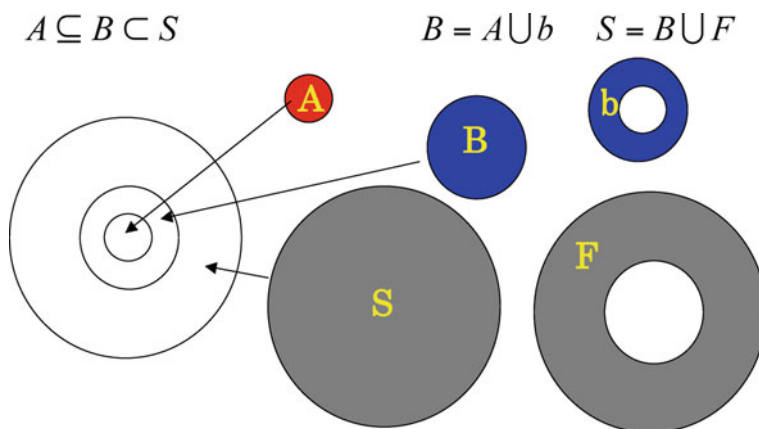


Fig. 1 Division of the total system (**S**) in FMO/FD into frozen (**F**), polarizable buffer (**B**) and active (**A**) domains. Domain **b** is defined as **B** excluding **A**. Layers 1 and 2 coincide with domains **F** and **B**, respectively. Reprinted with permission from [56]. Copyright (2018) American Chemical Society.

where

$$E^{\text{int}} = \sum_{I \in \mathbf{B}} E_I'^{L_2} + \sum_{\substack{I > J \\ I \in \mathbf{A}, J \in \mathbf{B}}} \left(E_{IJ}'^{L_2} - E_I'^{L_2} - E_J'^{L_2} \right) \quad (20)$$

$$E^{\text{ESP}} = \sum_{\substack{I > J \\ I \in \mathbf{A}, J \in \mathbf{B}}} \text{Tr}(\Delta \mathbf{D}^{IJ} \mathbf{V}^{IJ}) + \sum_{I \in \mathbf{A}, J \in \mathbf{F}} \Delta E_{IJ}'^{L_2, L_1}, \quad (21)$$

where the energies $E_I'^{L_m}$ are defined in Eq. (5) with the layer L_m explicitly specified. The first sum over I in E^{int} is referred to as the FMO1 internal energy below. In the last term in Eq. (21), it is assumed by definition that all dimers IJ ($I \in \mathbf{A}$, $J \in \mathbf{F}$) are treated with the ES dimer approximation (described below), irrespective of the distance between I and J . Domains \mathbf{A} and \mathbf{F} should be defined separated, i.e., \mathbf{b} should be wide enough.

In regular FD, the second sum in Eq. (19) is for $I \in \mathbf{B}$ whereas in FDD, $I \in \mathbf{A}$. In other words, in FDD, the contribution of a dimer IJ is ignored if I or $J \notin \mathbf{A}$, because those dimers typically contribute little to the gradient of atoms in \mathbf{A} (note that the contribution is not zero because such dimers include ESP terms from fragments in \mathbf{A}). The energy and analytic gradient are available for both regular FD and FDD, but the second derivatives are developed only for FDD and the equations below are given for FDD.

The derivative of Eq. (19) with respect to a nuclear coordinate $a \in \mathbf{B}$ is

$$\frac{\partial E^{\text{FMO/FDD}}}{\partial a} = E^{\text{int},a} + E^{\text{ESP},a} + R^a. \quad (22)$$

The derivatives of the internal energy $E^{\text{int},a}$ are obtained as a combination of the gradients of the internal energies E'_X , see Eq. (11).

$$E^{\text{ESP},a} = \sum_{\substack{I > J \\ I \in \mathbf{A}, J \in \mathbf{B}}} \sum_{\mu\nu \in IJ} \Delta D_{\mu\nu}^{IJ} V_{\mu\nu}^{a,IJ} + \sum_{I \in \mathbf{A}, J \in \mathbf{F}} \frac{\partial \Delta E_{IJ}'^{L_2, L_1}}{\partial a} \quad (23)$$

$$\begin{aligned} \frac{\partial \Delta E_{IJ}'^{L_2, L_1}}{\partial a} &= \sum_{\mu, \nu \in I} \sum_{A \in J} D_{\mu\nu}^I \left\langle \mu \left| \frac{-Z_A}{|\mathbf{r} - \mathbf{R}_A|} \right| \nu \right\rangle^a + \sum_{\mu, \nu \in J} \sum_{A \in I} D_{\mu\nu}^J \left\langle \mu \left| \frac{-Z_A}{|\mathbf{r} - \mathbf{R}_A|} \right| \nu \right\rangle^a \\ &+ \sum_{\mu, \nu \in I} \sum_{\lambda, \sigma \in J} D_{\mu\nu}^I D_{\lambda\sigma}^J (\mu\nu|\lambda\sigma)^a, \end{aligned} \quad (24)$$

where the integral derivative contribution to the derivative of the ESP is

$$V_{\mu\nu}^{a,IJ} = \sum_{K \neq I, J} \left[\sum_{A \in K} \left\langle \mu \left| \frac{-Z_A}{|\mathbf{r} - \mathbf{R}_A|} \right| \nu \right\rangle^a + \sum_{\lambda, \sigma} D_{\lambda\sigma}^K (\mu\nu|\lambda\sigma)^a \right]. \quad (25)$$

R^a is the total response contribution to the gradient

$$\begin{aligned}
 R^a = & \sum_{\substack{I>J \\ I \in \mathbf{A}, J \in \mathbf{B}}} \left[- \sum_{m \in I} \sum_{i \in I}^{\text{vir}} \sum_{i \in I}^{\text{occ}} 4U_{mi}^{a,I} (V_{mi}^{IJ} - V_{mi}^I) - \sum_{m \in J} \sum_{i \in J}^{\text{vir}} \sum_{i \in J}^{\text{occ}} 4U_{mi}^{a,J} (V_{mi}^{IJ} - V_{mi}^J) \right. \\
 & + \left. \sum_{\mu, \nu \in IJ} \sum_{K \neq I, J} \sum_{m \in K} \sum_{i \in K}^{\text{vir}} \sum_{i \in K}^{\text{occ}} 4U_{mi}^{a,K} \Delta D_{\mu\nu}^{IJ}(\mu\nu|mi) \right] - \sum_I \sum_{m \in I} \sum_{i \in I}^{\text{vir}} \sum_{i \in I}^{\text{occ}} 4U_{mi}^{a,I} V_{mi}^I \\
 & + \sum_{I \in \mathbf{A}, J \in \mathbf{B}} \left[\sum_{m \in I} \sum_{i \in I}^{\text{vir}} \sum_{i \in I}^{\text{occ}} 4U_{mi}^{a,I} V_{mi}^{I(J)} + \sum_{m \in J} \sum_{i \in J}^{\text{vir}} \sum_{i \in J}^{\text{occ}} 4U_{mi}^{a,J} V_{mi}^{J(I)} \right]. \quad (26)
 \end{aligned}$$

For the ESP-PC approximation[32], all terms in Eq. (26) should be calculated; ESP, its derivatives, and the equations to obtain $U_{mi}^{a,I}$ have to be modified, as described in detail elsewhere [40]. Without the ESP-PC approximation, there are cancellations of ESP contributions $U_{mi}^{a,I} V_{mi}^X$, and the total sum of all response contributions in Eq. (26) is

$$R^a = \sum_{I \in \mathbf{b}} \sum_{m \in I} \sum_{i \in I}^{\text{vir}} \sum_{i \in I}^{\text{occ}} 4U_{mi}^{a,I} V_{mi}^I + \sum_{\substack{I>J \\ I \in \mathbf{A}, J \in \mathbf{B}}} \sum_{\mu, \nu \in IJ} \sum_{K \neq I, J} \sum_{m \in K} \sum_{i \in K}^{\text{vir}} \sum_{i \in K}^{\text{occ}} 4U_{mi}^{a,K} \Delta D_{\mu\nu}^{IJ}(\mu\nu|mi). \quad (27)$$

2.1.3 CPHF for Hartree–Fock Gradient

For the FMO-RHF gradient [38], the first-order CPHF equations are solved for monomers only, because $\bar{U}^{a,IJ,IJ}$ containing dimer responses $U_{mi}^{a,IJ}$ in Eq. (17) cancel out. The differentiation of the Fock matrix element with respect to a results in

$$\begin{aligned}
 \frac{\partial F_{ij}^X}{\partial a} = & F_{ij}^{a,X} - (\epsilon_j^X - \epsilon_i^X) U_{ij}^{a,X} - S_{ij}^{a,X} \epsilon_j^X \\
 & - \frac{1}{2} \sum_K \sum_{k \in K} \sum_{l \in K}^{\text{occ}} S_{kl}^{a,K} A_{ij,kl}^{X,K} + \sum_K \sum_{k \in K} \sum_{l \in K}^{\text{vir}} U_{kl}^{a,K} A_{ij,kl}^{X,K}, \quad (28)
 \end{aligned}$$

where $S_{ij}^{a,X}$ is the first derivatives of the overlap integrals for fragment X, and

$$A_{ij,kl}^{X,X} = 4(ij|kl) - (ik|jl) - (il|jk), \quad (29)$$

$$A_{ij,kl}^{X,K} = 4(ij|kl), \quad (\text{for } K \neq X) \quad (30)$$

and the Fock derivative is

$$F_{ij}^{a,X} = h_{ij}^{a,X} + V_{ij}^{a,X} + \sum_{k \in X}^{\text{occ}} [2(ij|kk)^a - (ik|jk)^a] + P_{ij}^{a,X}. \quad (31)$$

The definitions of the derivative integral terms in Eq. (31) are given elsewhere [37, 38]. From Eq. (28), the following relation can be derived [44],

$$U_{ij}^{a,X} = \frac{T_{ij}^{a,X}}{\epsilon_j^X - \epsilon_i^X}, \quad (32)$$

where

$$T_{ij}^{a,X} = B_{0,ij}^{a,X} + \sum_K^{\text{vir}} \sum_{k \in K}^{\text{occ}} \sum_{l \in K} U_{kl}^{a,K} A_{ij,kl}^{X,K}, \quad (33)$$

and

$$B_{0,ij}^{a,X} = F_{ij}^{a,X} - S_{ij}^{a,X} \epsilon_j^X - \frac{1}{2} \sum_K^{\text{occ}} \sum_{k \in K}^{\text{occ}} \sum_{l \in K} S_{kl}^{a,K} A_{ij,kl}^{X,K}. \quad (34)$$

The elements of $U_{ij}^{a,X}$ need not be stored for the gradient but they are needed for the Hessian, and their size in FMO is given by

$$N_{\text{at}} \sum_{I=1}^N N_{\text{occ}}^I N_{\text{virt}}^I, \quad (35)$$

where N_{at} is the number of atoms in the whole system; N_{occ}^I and N_{virt}^I are the numbers of occupied and virtual orbitals in fragment I , respectively. In comparison, in full calculations the matrix to store has the size of

$$N_{\text{at}} N_{\text{occ}} N_{\text{virt}}, \quad (36)$$

where N_{occ} and N_{virt} are the numbers of occupied and virtual orbitals in the whole system, respectively.

Using $F_{ij}^X = \partial F_{ij}^X / \partial a = 0$ for $i \neq j$, CPHF equations are obtained

$$\mathbf{A}'\mathbf{U}^a = \mathbf{B}_0^a, \quad (37)$$

where

$$A_{ij,kl}^{I,I} = \delta_{ik} \delta_{jl} (\epsilon_j^I - \epsilon_i^I) - A_{ij,kl}^{I,I}, \quad (38)$$

$$A_{ij,kl}^{I,K} = -A_{ij,kl}^{I,K} \quad (\text{for } K \neq I). \quad (39)$$

The supermatrix A in Eq. (37) includes blocks from all fragments.

2.1.4 Z-Vector Equations for FMO Gradient

The response contribution in Eqs. (18) and (27) can be obtained as the scalar product of two supervectors using the Z-vector method [37, 38],

$$\mathbf{R}^a = \mathbf{L}^T \mathbf{U}^a, \quad (40)$$

where for regular FMO

$$L_{ri}^I = 4 \sum_{\substack{J>K \\ I \neq J,K}} \sum_{\mu, v \in JK} \Delta D_{\mu v}^{JK}(\mu v | ri), \quad (41)$$

and in the frozen domain case (FDD) for I, J , and $K \in \mathbf{B}$,

$$L_{ri}^I = 4 \sum_{\substack{J>K \\ I \neq J,K}} \sum_{\mu, v \in JK} \Delta D_{\mu v}^{JK, L2}(\mu v | ri) + 4V_{ri}^I. \quad (42)$$

Instead of solving Eq. 40, in the Z-vector method [45], the following set of coupled equations independent of a is solved for \mathbf{Z} :

$$\mathbf{A}^T \mathbf{Z} = \mathbf{L}, \quad (43)$$

and the response contribution to the FMO energy gradient is computed as

$$\mathbf{R}^a = \mathbf{Z}^T \mathbf{B}_0^a. \quad (44)$$

One can separate [38] the diagonal (I, I and K, K) from off-diagonal K, I terms of \mathbf{A} in Eq. (43): for RHF fragments as

$$\sum_{r \in I} \sum_{i \in I}^{\text{vir}} A_{ri,kl}^{I,I} Z_{ri}^I = L_{kl}^I - \sum_{K \neq I}^N \sum_{r \in K}^{\text{vir}} \sum_{i \in K}^{\text{occ}} A_{ri,kl}^{K,I} Z_{ri}^K. \quad (45)$$

Equation (45) is solved iteratively to obtain \mathbf{Z} values. First, the values of Z_{ri}^K in the last term are frozen, and the diagonal elements Z_{ri}^I are obtained for all fragments I independently. In the next iteration, Z_{ri}^K values are updated with values obtained solving independent equations in the previous iteration. This process is repeated until convergence in the self-consistent Z-vector method (SCZV) [38], which typically takes 10–20 iterations. In practice, Eq. (45) is solved using a partial transformation to the AO basis for efficiency [38].

2.2 Second Derivatives in FMO

2.2.1 Hartree–Fock Hessian

The second derivative of the FMO energy with respect to nuclear coordinates a and b is

$$\frac{\partial^2 E}{\partial a \partial b} = \sum_I^N \frac{\partial^2 E'_I}{\partial a \partial b} + \sum_{I>J}^N \left(\frac{\partial^2 E'_{IJ}}{\partial a \partial b} - \frac{\partial^2 E'_I}{\partial a \partial b} - \frac{\partial^2 E'_J}{\partial a \partial b} \right) + \sum_{I>J}^N \frac{\partial^2 \text{Tr}(\Delta \mathbf{D}^{IJ} \mathbf{V}^{IJ})}{\partial a \partial b}, \quad (46)$$

which includes several contributions of the form $\partial^2 E'_X / (\partial a \partial b)$. Inserting the first derivative of the internal energies defined in Eq. (11), one obtains

$$\begin{aligned} \frac{\partial^2 E'_X}{\partial a \partial b} = \frac{\partial}{\partial b} & \left[\sum_{i \in X}^{\text{occ}} 2h_{ii}^{a,X} + \sum_{ij \in X}^{\text{occ}} [2(ii|jj)^a - (ij|ij)^a] + \sum_{i \in X}^{\text{occ}} 2P_{ii}^{a,X} \right. \\ & \left. + \sum_{m \in X}^{\text{occ+vir}} \sum_{i \in X}^{\text{occ}} 4U_{mi}^{a,X} F'_{mi}{}^X + \frac{\partial E_X^{\text{NR}}}{\partial a} \right]. \end{aligned} \quad (47)$$

The total Fock matrix \mathbf{F}^X , composed of the internal and ESP contributions, is diagonal, but \mathbf{F}'^X is not.

$$F_{ij}^X = F'_{ij}{}^X + V_{ij}^X = \delta_{ij} \epsilon_i^X. \quad (48)$$

Using Eq. (48), one can rewrite Eq. (47) as

$$\begin{aligned} \frac{\partial^2 E'_X}{\partial a \partial b} = & \sum_{i \in X}^{\text{occ}} \left[h_{ii}^{ab,X} + P_{ii}^{ab,X} + F'_{ii}{}^{ab,X} \right] \\ & - \sum_{i \in X}^{\text{occ}} 2S_{ii}^{ab,X} \epsilon_{ii}^X + 4 \sum_{i \in X}^{\text{occ}} \sum_{j \in X}^{\text{occ}} S_{ji}^{b,X} S_{ij}^{a,X} \epsilon_{ii}^X \\ & + \sum_{m \in X}^{\text{vir}} \sum_{i \in X}^{\text{occ}} U_{mi}^{b,X} \left[4F'_{im}{}^{a,X} - 4S_{mi}^{a,X} \epsilon_{ii}^X - 2 \sum_{j,l \in X}^{\text{occ}} A_{jl,mi}^{X,X} S_{jl}^{a,X} \right] \\ & - \sum_{i \in X}^{\text{occ}} \sum_{j \in X}^{\text{occ}} S_{ij}^{b,X} \left[2F'_{ij}{}^{a,X} - \frac{1}{2} \sum_{k,l \in X}^{\text{occ}} A_{ij,kl}^{X,X} S_{kl}^{a,X} \right] \\ & - \sum_{i \in X}^{\text{occ}} \sum_{j \in X}^{\text{occ}} S_{ij}^{a,X} \left[2F'_{ij}{}^{b,X} - \frac{1}{2} \sum_{k,l \in X}^{\text{occ}} A_{ij,kl}^{X,X} S_{kl}^{b,X} \right] \\ & + \frac{\partial^2 E_X^{\text{NR}}}{\partial a \partial b} - \bar{U}^{ab,X}, \end{aligned} \quad (49)$$

where

$$F_{mi}^{ab,X} = h_{mi}^{ab,X} + \sum_{j \in X}^{\text{occ}} [2(mi|jj)^{ab} - (mj|ij)^{ab}] + P_{mi}^{ab,X}, \quad (50)$$

$$P_{ii}^{ab,X} = \sum_{\mu, \nu} C_{\mu i}^{X*} P_{\mu\nu}^{ab,X} C_{\nu i}^X. \quad (51)$$

The ESP-related term in Eq. (49) is defined as

$$\begin{aligned} \bar{U}^{ab,X} = & -4 \sum_{i \in X}^{\text{occ}} \sum_{j \in X}^{\text{occ}} \sum_{m \in X}^{\text{vir}} U_{mi}^{b,X} (V_{mj}^X S_{ij}^{a,X} + V_{ij}^X S_{jm}^{a,X}) \\ & + 4 \sum_{i \in X}^{\text{occ}} \sum_{j \in X}^{\text{occ}} \sum_{k \in X}^{\text{occ}} S_{ki}^{b,X} V_{ij}^X S_{jk}^{a,X} - \sum_{i \in X}^{\text{occ}} \sum_{j \in X}^{\text{occ}} 2S_{ij}^{ab,X} V_{ij}^X \\ & + \sum_{m \in X}^{\text{vir}} \sum_{i \in X}^{\text{occ}} 4 \frac{\partial (V_{mi}^X U_{mi}^{a,X})}{\partial b}. \end{aligned} \quad (52)$$

In Eq. (52), a and b run over the entire system, and the contributions for either a or b outside of X come from the ESP of X . The second derivative of the ESP energy for dimer IJ , representing the charge transfer between I and J coupled with the embedding ESP for IJ is

$$\frac{\partial^2}{\partial a \partial b} \text{Tr}(\Delta \mathbf{D}^{IJ} \mathbf{V}^{IJ}) = \frac{\partial}{\partial b} \sum_{I > J}^N \left(2 \sum_{i \in IJ}^{\text{occ}} \frac{\partial V_{ii}^{IJ}}{\partial a} - 2 \sum_{i \in I}^{\text{occ}} \frac{\partial V_{ii}^{IJ}}{\partial a} - 2 \sum_{i \in J}^{\text{occ}} \frac{\partial V_{ii}^{IJ}}{\partial a} \right). \quad (53)$$

The three similar terms for $X = I, J$ or IJ in Eq. (53) can be obtained from Eq. (15) as

$$\begin{aligned} 2 \sum_{i \in X}^{\text{occ}} \frac{\partial^2 V_{ii}^{IJ}}{\partial a \partial b} = & \frac{\partial}{\partial b} \left\{ 2 \sum_{i \in X}^{\text{occ}} V_{ii}^{a,IJ} + 4 \sum_{m \in X}^{\text{occ+vir}} \sum_{i \in X}^{\text{occ}} U_{mi}^{a,X} V_{mi}^{IJ} \right. \\ & \left. + 8 \sum_{K \neq IJ}^{\text{occ+vir}} \sum_{m \in K}^{\text{occ}} \sum_{k \in K}^{\text{occ}} U_{mk}^{a,K} \sum_{i \in X}^{\text{occ}} (ii|mk) \right\} \\ = & 2 \sum_{i \in X}^{\text{occ}} V_{ii}^{ab,IJ} - 2 \sum_{i \in X}^{\text{occ}} \sum_{j \in X}^{\text{occ}} \left(S_{ij}^{a,X} V_{ij}^{b,IJ} + V_{ij}^{a,IJ} S_{ji}^{b,X} \right) \\ & + \bar{U}^{ab,X,IJ} + R^{ab,X}, \end{aligned} \quad (54)$$

where

$$\begin{aligned}
\overline{U}^{ab,X,IJ} = & 4 \sum_{i \in X} \sum_{m \in X}^{\text{occ}} \sum_{\text{vir}} U_{mi}^{b,X} \left\{ V_{im}^{a,IJ} - \sum_j^{\text{occ}} (S_{jm}^{a,X} V_{ij}^{IJ} + S_{ij}^{a,X} V_{mj}^{IJ}) \right\} \\
& + 4 \sum_{i,j \in X}^{\text{occ}} \sum_{k \in X}^{\text{occ}} S_{ki}^{b,X} S_{ij}^{a,X} V_{jk}^{IJ} - 2 \sum_{i \in X}^{\text{occ}} \sum_{j \in X}^{\text{occ}} S_{ij}^{ab,X} V_{ij}^{IJ} \\
& + 4 \sum_{i \in X}^{\text{occ}} \sum_{m \in X}^{\text{vir}} \frac{\partial (U_{mi}^{a,X} V_{im}^{IJ})}{\partial b}. \tag{55}
\end{aligned}$$

The collection of $\overline{U}^{ab,X,IJ}$ and $\overline{U}^{ab,X}$ in Eq. (49) cancel out to be zero when no ESP approximations are applied.

The extra two-electron response contribution $R^{ab,X}$ is

$$\begin{aligned}
R^{ab,X} = & 8 \sum_{m \in X}^{\text{vir}} \sum_{i \in X}^{\text{occ}} \sum_{K \neq IJ}^{\text{occ}} \sum_{j \in K} U_{mi}^{b,X} \left[\sum_{n \in K}^{\text{vir}} 2(im|jn) U_{nj}^{a,K} - \sum_{k \in K}^{\text{occ}} S_{jk}^{a,K} (im|jk) \right] \\
& + 4 \sum_{i \in X}^{\text{occ}} \sum_{K \neq IJ}^{\text{occ}} \sum_{j \in K}^{\text{occ}} \sum_{m \in K}^{\text{vir}} U_{mj}^{a,K} \left[2(ii|jm)^b - \sum_{k \in X}^{\text{occ}} 2S_{ik}^{b,X} (ik|jm) - \sum_{k \in K}^{\text{occ}} 2S_{jk}^{b,K} (ii|km) \right. \\
& \left. - 2 \sum_{k \in K}^{\text{occ}} S_{km}^{b,K} (ii|jk) + \sum_{n \in K}^{\text{vir}} U_{nj}^{b,K} (iinm) - \sum_{k \in K}^{\text{occ}} U_{mk}^{b,K} (ii|jk) \right] \\
& + 4 \sum_{i \in X}^{\text{occ}} \sum_{K \neq IJ}^{\text{occ}} \sum_{j \in K}^{\text{occ}} \sum_{m \in K}^{\text{vir}} U_{mj}^{b,K} \left[2(ii|jm)^a - \sum_{k \in X}^{\text{occ}} 2S_{ki}^{a,X} (ik|jm) - 2 \sum_{k \in K}^{\text{occ}} S_{kj}^{a,K} (ii|km) \right. \\
& \left. - 2 \sum_{k \in K}^{\text{occ}} S_{km}^{a,K} (ii|jk) + \sum_{n \in K}^{\text{vir}} U_{nj}^{a,K} (iinm) - \sum_{k \in K}^{\text{occ}} U_{mk}^{a,K} (ii|jk) \right] \\
& + 4 \sum_{i \in X}^{\text{occ}} \sum_{K \neq IJ}^{\text{occ}} \sum_{k \in K}^{\text{occ}} \sum_{l \in K}^{\text{occ}} S_{kl}^{a,K} \left[\sum_{j \in X}^{\text{occ}} (ij|kl) S_{ij}^{b,X} - (ii|kl)^b + \sum_{j \in K}^{\text{occ}} S_{jl}^{b,K} (ii|jk) \right] \\
& + 4 \sum_{i \in X}^{\text{occ}} \sum_{K \neq IJ}^{\text{occ}} \sum_{k \in K}^{\text{occ}} \sum_{l \in K}^{\text{occ}} S_{kl}^{b,K} \left[\sum_{j \in X}^{\text{occ}} (ij|kl) S_{ij}^{a,X} - (ii|kl)^a + \sum_{j \in K}^{\text{occ}} S_{jl}^{a,K} (ii|jk) \right] \\
& - 4 \sum_{K \neq IJ}^{\text{occ}} \sum_{i \in X}^{\text{occ}} \sum_{j \in K}^{\text{occ}} \sum_{k \in K}^{\text{occ}} S_{jk}^{ab,K} (ii|jk) \\
& - 8 \sum_{K \neq IJ}^{\text{occ}} \sum_{i \in X}^{\text{occ}} \sum_{j \in K}^{\text{occ}} \sum_{m \in K}^{\text{vir}} \sum_{n \in K}^{\text{occ}} (U_{mn}^{b,K} U_{nj}^{a,K} + U_{mn}^{a,K} U_{nj}^{b,K}) (ii|jm) \\
& + 8 \sum_{K \neq IJ}^{\text{occ}} \sum_{i \in X}^{\text{occ}} \sum_{j \in K}^{\text{occ}} \sum_{m \in K}^{\text{vir}} U_{mj}^{ab,K} (ii|jm). \tag{56}
\end{aligned}$$

Inserting Eqs. (49), (52), (54), and (56) in the second derivative of the total FMO energy in Eq. (46), one obtains the fully analytic second derivative.

It is necessary to calculate three types of unknown response terms $U_{mi}^{a,I}$, $U_{mi}^{a,IJ}$, and $U_{mi}^{ab,I}$. The latter can be obtained by solving the second-order CPHF equations for monomers. The derivation of the above equations is fully analytic. However, the current implementation includes three approximations for computational efficiency: (a) solving the second-order CPHF equations of monomers is avoided by neglecting the last two terms in Eq. (56); (b) the calculation of the $U_{mi}^{a,I}$ and $U_{mi}^{a,IJ}$ terms from the first-order CPHF equations of monomers and dimers is done approximately, as described below, and (c) the contribution of the second derivative of the HOP matrix $P_{ij}^{ab,X}$ is neglected.

2.2.2 The Separated Dimer Approximation

If two fragments are well separated, the pair interaction energy (PIE)

$$\Delta E_{IJ} = E'_{IJ} - E'_J - E'_I + \text{Tr}(\Delta \mathbf{D}^{IJ} \mathbf{V}^{IJ}) \quad (57)$$

can be approximated [32] as $\Delta E_{IJ}^{\text{ES}}$ by taking $\Delta \mathbf{D}^{IJ}$ to be $\mathbf{0}$, which also simplifies the internal energy difference.

$$\Delta E_{IJ}^{\text{ES}} = \sum_{\mu\nu \in I} D_{\mu\nu}^I V_{\mu\nu}^{I(J)} + \sum_{\mu\nu \in J} D_{\mu\nu}^J V_{\mu\nu}^{J(I)} - \sum_{\mu, \nu \in I} \sum_{\lambda, \sigma \in J} D_{\mu\nu}^I D_{\lambda\sigma}^J (\mu\nu|\lambda\sigma). \quad (58)$$

The second derivative is

$$\begin{aligned} \frac{\partial^2 E_{IJ}^{\text{ES}}}{\partial a \partial b} &= \bar{E}_{\text{ES}}^{ab,I,I(J)} + \bar{E}_{\text{ES}}^{ab,J,J(I)} \\ &+ \bar{U}_{\text{ES}}^{ab,I,I(J)} + \bar{U}_{\text{ES}}^{ab,J,J(I)} + R_{\text{ES}}^{ab,IJ}, \end{aligned} \quad (59)$$

where $\bar{U}_{\text{ES}}^{ab,I,I(J)}$ is defined elsewhere [24] and

$$\begin{aligned} \bar{E}_{\text{ES}}^{ab,I,I(J)} &= - \sum_{i \in I} \sum_{j \in I}^{\text{occ}} 2(S_{ij}^{b,I} V_{ij}^{a,I(J)} + S_{ij}^{a,I} V_{ij}^{b,I(J)}) \\ &+ 4 \sum_{i \in I} \sum_{m \in I}^{\text{occ}} U_{mi}^{b,I} V_{mi}^{a,I(J)} + 2 \sum_{i \in I}^{\text{occ}} V_{ii}^{ab,I(J)}, \end{aligned} \quad (60)$$

$$\begin{aligned}
R_{\text{ES}}^{ab,IJ} = & -8 \sum_{i \in I}^{\text{occ}} \sum_{j \in I}^{\text{occ}} \sum_{k \in J}^{\text{occ}} \sum_{m \in J}^{\text{vir}} S_{ij}^{a,I} U_{mk}^{b,J} (ij|km) \\
& -8 \sum_{i \in J}^{\text{occ}} \sum_{j \in J}^{\text{occ}} \sum_{k \in I}^{\text{occ}} \sum_{m \in I}^{\text{vir}} S_{ij}^{a,J} U_{mk}^{b,I} (ij|km) \\
& +4 \sum_{i \in I}^{\text{occ}} \sum_{j \in I}^{\text{occ}} \sum_{k \in J}^{\text{occ}} \sum_{l \in J}^{\text{occ}} (S_{ij}^{a,I} S_{kl}^{b,J} + S_{ij}^{b,I} S_{kl}^{a,J}) (ij|kl) \\
& -4 \sum_{i \in I}^{\text{occ}} \sum_{j \in J}^{\text{occ}} (ii|jj)^{ab}. \tag{61}
\end{aligned}$$

The response terms such as $\overline{U}_{\text{ES}}^{ab,I,I(J)}$ arising from ES dimers in Eq. (59) are added to the terms from SCF dimers. It can be shown [38] that their total sum \overline{U}^a in Eq. (17) is 0 for the separated dimer approximation, provided that point charge approximations are not used in ESP; also, $\overline{U}^{ab} = 0$ and the response terms arising from ES dimers need not be evaluated for the gradient and Hessian (but all other terms, except the responses, in Eq. (59) should be computed).

2.2.3 CPHF for Hartree–Fock Hessian

For the Hessian one should solve both monomer and dimer CPHF equations. As mentioned above, these equations are solved approximately (solving them exactly is very complicated because monomer and dimer terms are coupled). Equation (37) is decoupled into independent fragment CPHF equations for each monomer $X = I$ or dimer $X = IJ$ neglecting the terms involving the derivatives for $a \notin X$ and external terms $K \notin X$ (a similar technique is used for MP2 gradient [46]),

$$\mathbf{A}^{I,X,X} \mathbf{U}^{a,X} = \mathbf{B}_0^{a,X}, \tag{62}$$

where

$$B_{0,ij}^{a,X} \approx F_{ij}^{a,X} - S_{ij}^{a,X} \epsilon_j^X - \frac{1}{2} \sum_{k \in X}^{\text{occ}} \sum_{l \in X}^{\text{occ}} S_{kl}^{a,X} A_{ij,kl}^{X,X}. \tag{63}$$

The response terms U are calculated solving Eq. (62) and used in Eqs.(49), (52), (54), and (56).

2.2.4 Frozen Domain Hessian

The second derivative of the FMO/FDD energy with respect to nuclear coordinates a and b is

$$\frac{\partial^2 E^{\text{FMO/FDD}}}{\partial a \partial b} = \sum_{I \in \mathbf{B}} \frac{\partial^2 E_I^{L_2}}{\partial a \partial b} + \sum_{\substack{I > J \\ I \in \mathbf{A}, J \in \mathbf{B}}} \frac{\partial^2 \Delta E_{IJ}^{L_2}}{\partial a \partial b} + \sum_{I \in \mathbf{A}, J \in \mathbf{F}} \frac{\partial^2 \Delta E_{IJ}^{L_2, L_1}}{\partial a \partial b}. \quad (64)$$

Most terms in the FMO/FDD second derivative are the same as in the FMO Hessian, but one term specific to FMO/FDD is described below in detail.

From the derivative of $U_{mi}^{a,I} V_{mi}^I$ in Eq. (27) with respect to b one obtains

$$\begin{aligned} \bar{U}^{ab} &= \sum_{I \in \mathbf{B}} \bar{U}^{ab, I, I} + \sum_{\substack{I > J \\ I \in \mathbf{A}, J \in \mathbf{B}}} \left(\bar{U}^{ab, I, IJ} + \bar{U}^{ab, J, IJ} - \bar{U}^{ab, I, I} - \bar{U}^{ab, J, J} \right) \\ &\quad - \sum_{I \in \mathbf{A}, J \in \mathbf{F}} \left(\bar{U}^{ab, I, I(J)} + \bar{U}^{ab, J, J(I)} \right), \end{aligned} \quad (65)$$

where for $Y = I, J$ and IJ ,

$$\begin{aligned} \bar{U}^{ab, X, Y} &= \sum_{Z \neq Y} \bar{U}^{ab, X, Y(Z)}, \quad (66) \\ \bar{U}^{ab, X, Y(Z)} &= -4 \sum_{i \in X} \sum_{j \in X} \sum_{m \in X}^{\text{vir}} U_{mi}^{b, X} \left(V_{mj}^{Y(Z)} S_{ij}^{a, X} + V_{ij}^{Y(Z)} S_{jm}^{a, X} \right) \\ &\quad + \sum_{i \in X} \sum_{j \in X} \sum_{k \in X}^{\text{occ}} S_{ki}^{b, X} V_{ij}^{Y(Z)} S_{jk}^{a, X} - \sum_{i \in X} \sum_{j \in X}^{\text{occ}} S_{ki}^{ab, X} V_{ij}^{Y(Z)} \\ &\quad + \sum_{m \in X} \sum_{i \in X}^{\text{vir}} 4 \frac{\partial V_{mi}^X U_{mi}^{a, X}}{\partial b}. \end{aligned} \quad (67)$$

Without the ESP-PC approximation, many response contributions to the second derivative of energy cancel out, and one obtains the following FMO/FDD specific term

$$\bar{U}^{ab} = \sum_{I \in \mathbf{b}} \bar{U}^{ab, I, I} - \sum_{I \in \mathbf{A}, J \in \mathbf{F}} \bar{U}^{ab, J, J(I)}. \quad (68)$$

In practice, the Hessian matrix $\mathbf{H}_{\mathbf{AA}}$ for atoms in the active domain \mathbf{A} is constructed and diagonalized [12]. This is equivalent to padding the Hessian in the polarizable domain $\mathbf{B} = \mathbf{A} \cup \mathbf{b}$ with zeros as follows,

$$\mathbf{H} = \begin{pmatrix} \mathbf{H}_{\mathbf{AA}} & \mathbf{0} \\ \mathbf{0} & \mathbf{H}_{\mathbf{bb}} \end{pmatrix}, \text{ where } \mathbf{H}_{\mathbf{bb}} = \begin{pmatrix} \epsilon & 0 & 0 \\ 0 & \ddots & 0 \\ 0 & 0 & \epsilon \end{pmatrix}, \epsilon = 10^{-8} \text{ a.u.} \quad (69)$$

Because only Hessian elements for both a and $b \in \mathbf{A}$ are explicitly required for $\mathbf{H}_{\mathbf{AA}}$, the evaluation of \overline{U}^{ab} in Eq. (68) is not needed (note that the sums in Eq. (68) exclude the case $a, b \in \mathbf{A}$).

In the intrinsic reaction coordinate (IRC) method of mapping reaction paths, the initial Hessian for atoms in \mathbf{B} is constructed according to Eq. (69) and consequently updated using the analytic gradient for atoms in \mathbf{B} .

2.2.5 Extension to the Three-Body Expansion

The FMO3 total energy is obtained by adding three-body terms to the FMO2 energy E [47, 48]

$$E^{\text{FMO3}} = E + \sum_{I>J>K} [\Delta E_{IJK} - \Delta E_{IJ} - \Delta E_{JK} - \Delta E_{KI}], \quad (70)$$

where the three-body correction term is

$$\Delta E_{IJK} = E'_{IJK} - E'_K - E'_J - E'_I + \text{Tr}(\mathbf{D}^{IJK} \mathbf{V}^{IJK}). \quad (71)$$

\mathbf{D}^{IJK} is the difference between the density matrices of a trimer and the three monomers,

$$\mathbf{D}^{IJK} = \mathbf{D}^{IJK} - (\mathbf{D}^I \oplus \mathbf{D}^J \oplus \mathbf{D}^K). \quad (72)$$

The second derivative of the energy with respect to nuclear coordinates a and b is

$$\frac{\partial^2 E^{\text{FMO3}}}{\partial a \partial b} = \frac{\partial^2 E}{\partial a \partial b} + \sum_{I>J>K} \frac{\partial^2}{\partial a \partial b} [\Delta E_{IJK} - \Delta E_{IJ} - \Delta E_{JK} - \Delta E_{KI}]. \quad (73)$$

To obtain the analytic second derivative for FMO3, one should compute the FMO2 values and add extra terms from the sum in Eq. (73), involving $\text{Tr}(\mathbf{D}^{IJK} \mathbf{V}^{IJK})$ and a combination of E'_X , where X also includes trimer IJK terms. For $X = I$ and IJ the expressions are given above. These additional three-body terms in FMO3 are rather similar to the corresponding FMO2 terms, as described in detail elsewhere [27].

2.2.6 Extension to DFT

The second derivative of the internal fragment energy in DFT is similar to RHF, see Eq. (49), except that the DFT exchange-correlation (xc) energy E_{xc}^X has to be added to the internal energy of fragments E'^X in Eq. (5). In DFT, the internal Fock matrix $F'_{ij}{}^X$ and the orbital Hessian matrix $A_{ij,kl}^{X,X}$ are

$$F'_{ij}{}^X = h_{ij}^X + \sum_{k \in X}^{\text{occ}} [2(ij|kk) - c_{\text{HF}}(ik|jk)] + P_{ij}^X + (V_{\text{xc}}^X)_{ij} \quad (74)$$

$$A_{ij,kl}^{X,X} = 4(ij|kl) - c_{\text{HF}} [(ik|jl) - (il|jk)] + 4(f_{\text{xc}}^X)_{ij,kl}, \quad (75)$$

where $c_{\text{HF}} \in [0; 1]$ is the fraction of the HF exchange. $(V_{\text{xc}}^X)_{ij}$ and $(f_{\text{xc}}^X)_{ij,kl}$ are the matrix elements of the first and second functional derivatives of the exchange-correlation functional with respect to the electron density.

The second derivative of the exchange-correlation energy is

$$\begin{aligned} \frac{\partial^2 E_{\text{xc}}^X}{\partial a \partial b} = & \sum_{A \in X} \sum_{t \in A} \left[\frac{\partial^2 w_{At}}{\partial a \partial b} f_{At}^X(\rho_\alpha, \rho_\beta, \gamma_{\alpha\alpha}, \gamma_{\alpha\beta}, \gamma_{\beta\beta}) \right. \\ & + w_{At} \frac{\partial^2 f_{At}^X(\rho_\alpha, \rho_\beta, \gamma_{\alpha\alpha}, \gamma_{\alpha\beta}, \gamma_{\beta\beta})}{\partial a \partial b} \\ & + \frac{\partial w_{At}}{\partial a} \frac{\partial f_{At}^X(\rho_\alpha, \rho_\beta, \gamma_{\alpha\alpha}, \gamma_{\alpha\beta}, \gamma_{\beta\beta})}{\partial b} \\ & \left. + \frac{\partial w_{At}}{\partial b} \frac{\partial f_{At}^X(\rho_\alpha, \rho_\beta, \gamma_{\alpha\alpha}, \gamma_{\alpha\beta}, \gamma_{\beta\beta})}{\partial a} \right], \quad (76) \end{aligned}$$

where w_{At} and f_{At}^X are the quadrature weights and the exchange-correlation functional at the grid point t belonging to atom A . ρ and γ are the electronic density and its derivatives. α and β are spin labels. The exchange-correlation contributions are evaluated by a numerical integration. It is important to note that the contribution of the weight derivative terms should be included even when very fine grids are used.

2.2.7 Extension to Open-Shell Methods

There are two ways to treat open-shell (radical) systems: restricted (ROHF) [25] and unrestricted (UHF) [26]. Because in (non-singlet) ROHF the density matrices for the α and β spins are different, the UHF equations cannot be much simplified for ROHF; thus, here only UHF equations are given that can also be used for ROHF, where the same set of MOs is used for the two spins.

In FMO-UHF [49] some fragments are calculated with UHF, and the rest with RHF. For instance, there could be several radical centers in a material; each such center can be put into a separate fragment and described with UHF; other fragments are closed shell, described with RHF. A dimer calculation is performed with UHF, when at least one fragment in the dimer is UHF, otherwise RHF dimers are computed. Although the equations are derived for any number of UHF fragments, the current implementation of the FMO-UHF Hessian is limited to one UHF fragment.

The total energy E in FMO-UHF is

$$E = \sum_{I=1}^{N^{\text{RHF}}} E'_I + \sum_{K=1}^{N^{\text{UHF}}} E'_K + \sum_{I>J}^{N^{\text{RHF}}} \Delta E_{IJ} + \sum_{K>L}^{N^{\text{UHF}}} \Delta E_{KL} + \sum_{K=1}^{N^{\text{UHF}}} \sum_{I=1}^{N^{\text{RHF}}} \Delta E_{KI} \quad (77)$$

N^{RHF} and N^{UHF} are the numbers of the RHF and UHF fragments, respectively ($N = N^{\text{RHF}} + N^{\text{UHF}}$). I and J run over RHF fragments, whereas K and L denote UHF fragments.

The RHF terms, arising in the second derivative of E in Eq. (77), are given above, and for a UHF fragment X ,

$$\begin{aligned} \frac{\partial^2 E'_X}{\partial a \partial b} = & \sum_{\sigma} \left[\frac{1}{2} \sum_{i^{\sigma}}^{\text{occ}} \left(h_{i^{\sigma} i^{\sigma}}^{ab,X} + F_{i^{\sigma} i^{\sigma}}'^{ab,X} \right) - \sum_{i^{\sigma}}^{\text{occ}} S_{i^{\sigma} i^{\sigma}}^{ab,X} \epsilon_{i^{\sigma}}^X \right. \\ & + 2 \sum_{i^{\sigma}}^{\text{occ}} \sum_{j^{\sigma}}^{\text{occ}} S_{i^{\sigma} j^{\sigma}}^{a,X} S_{i^{\sigma} j^{\sigma}}^{b,X} \epsilon_{i^{\sigma}}^X \\ & + 2 \sum_{i^{\sigma}}^{\text{occ}} \sum_{m^{\sigma}}^{\text{vir}} U_{m^{\sigma} i^{\sigma}}^{b,X} \left\{ F_{m^{\sigma} i^{\sigma}}'^{a,X} - S_{m^{\sigma} i^{\sigma}}^{a,X} \epsilon_{i^{\sigma}}^X \right. \\ & \left. - \frac{1}{2} \sum_{j^{\sigma}}^{\text{occ}} \sum_{k^{\sigma}}^{\text{occ}} S_{k^{\sigma} j^{\sigma}}^{a,X} A_{k^{\sigma} j^{\sigma} i^{\sigma} m^{\sigma}}^{X,X} - \frac{1}{2} \sum_{j^{\bar{\sigma}}}^{\text{occ}} \sum_{k^{\bar{\sigma}}}^{\text{occ}} S_{k^{\bar{\sigma}} j^{\bar{\sigma}}}^{a,X} A_{k^{\bar{\sigma}} j^{\bar{\sigma}} m^{\sigma} i^{\sigma}}^{X,X} \right\} \\ & - \sum_{i^{\sigma}}^{\text{occ}} \sum_{j^{\sigma}}^{\text{occ}} S_{i^{\sigma} j^{\sigma}}^{a,X} \left\{ F_{i^{\sigma} j^{\sigma}}'^{b,X} - \frac{1}{4} \sum_{k^{\sigma}}^{\text{occ}} \sum_{l^{\sigma}}^{\text{occ}} S_{k^{\sigma} l^{\sigma}}^{b,X} A_{i^{\sigma} j^{\sigma} k^{\sigma} l^{\sigma}}^{X,X} \right. \\ & \left. - \frac{1}{4} \sum_{k^{\bar{\sigma}}}^{\text{occ}} \sum_{l^{\bar{\sigma}}}^{\text{occ}} S_{k^{\bar{\sigma}} l^{\bar{\sigma}}}^{b,X} A_{i^{\sigma} j^{\sigma} k^{\bar{\sigma}} l^{\bar{\sigma}}}^{X,X} \right\} \\ & - \sum_{i^{\sigma}}^{\text{occ}} \sum_{j^{\sigma}}^{\text{occ}} S_{i^{\sigma} j^{\sigma}}^{b,X} \left\{ F_{i^{\sigma} j^{\sigma}}'^{a,X} - \frac{1}{4} \sum_{k^{\sigma}}^{\text{occ}} \sum_{l^{\sigma}}^{\text{occ}} S_{k^{\sigma} l^{\sigma}}^{a,X} A_{i^{\sigma} j^{\sigma} k^{\sigma} l^{\sigma}}^{X,X} \right. \\ & \left. - \frac{1}{4} \sum_{k^{\bar{\sigma}}}^{\text{occ}} \sum_{l^{\bar{\sigma}}}^{\text{occ}} S_{k^{\bar{\sigma}} l^{\bar{\sigma}}}^{a,X} A_{i^{\sigma} j^{\sigma} k^{\bar{\sigma}} l^{\bar{\sigma}}}^{X,X} \right\} \left. \right] \\ & - \bar{U}^{ab,X,X} + \frac{\partial^2 E_X^{\text{NR}}}{\partial a \partial b}, \end{aligned} \quad (78)$$

where σ is the spin label (α or β). $\bar{\sigma}$ is the spin opposite to σ , e.g., if $\sigma = \alpha$, then $\bar{\sigma} = \beta$.

The orbital Hessian in UHF is

$$A_{i^\sigma j^\sigma, k^\sigma l^\sigma}^{X,X} = 2(i^\sigma j^\sigma | k^\sigma l^\sigma) - (i^\sigma l^\sigma | j^\sigma k^\sigma) \quad (79)$$

$$A_{i^\sigma j^\sigma, k^{\bar{\sigma}} l^{\bar{\sigma}}}^{X,X} = 2(i^\sigma j^\sigma | k^{\bar{\sigma}} l^{\bar{\sigma}}). \quad (80)$$

A UHF density matrix without a spin label (e.g., \mathbf{D}^{KL}) denotes the sum of the densities for the α and β spins; this matrix is used to compute the potential in Eq. (3). The second derivative of the embedded density transfer term for dimers KI , composed of one UHF and one RHF monomer, is analogous to the RHF case in Eq. (15). Here, an explicit equation is given for the case when both monomers in a dimer are computed with UHF. For $X = K, L$ or KL ,

$$\begin{aligned} \frac{\partial^2 \text{Tr}(\mathbf{D}^X \mathbf{V}^{KL})}{\partial a \partial b} &= \sum_{\sigma} \left[\sum_{i^\sigma \in X}^{\text{occ}} V_{i^\sigma i^\sigma}^{ab, KL} \right. \\ &\quad - \sum_{i^\sigma \in X}^{\text{occ}} \sum_{j^\sigma \in X}^{\text{occ}} (S_{i^\sigma j^\sigma}^{a, X} V_{i^\sigma j^\sigma}^{b, KL} + S_{j^\sigma i^\sigma}^{b, X} V_{j^\sigma i^\sigma}^{a, KL}) \\ &\quad \left. + 2 \sum_{i^\sigma \in X}^{\text{occ}} \sum_{m^\sigma \in X}^{\text{vir}} U_{m^\sigma i^\sigma}^{b, X} V_{m^\sigma i^\sigma}^{a, KL} \right] \\ &\quad + R^{ab, KL} + \bar{U}^{ab, X, KL}, \end{aligned} \quad (81)$$

where $V_{i^\sigma j^\sigma}^{a, KL}$ and $V_{i^\sigma j^\sigma}^{ab, KL}$ are the first and second derivatives of ESP, respectively. $R^{ab, KL}$ are the two-electron integral response terms

$$R^{ab, KL} = \sum_{Y \neq K, L}^{N^{\text{RHF}}} R^{ab, KL(Y)} + \sum_{Z \neq K, L}^{N^{\text{UHF}}} R^{ab, KL(Z)}, \quad (82)$$

where $R^{ab, KL(Y)}$ and $R^{ab, KL(Z)}$ are two-electron integral contributions for RHF fragment Y and UHF fragment Z , respectively, whose definitions are given elsewhere [26] (note that $R^{ab, X}$ defined for RHF in Eq. 56 is analogous to $R^{ab, KL}$ in UHF).

2.2.8 Extension to Unrestricted DFT

In this work, FMO Hessian for restricted DFT was developed for the unrestricted case. The equations for FMO-UDFT Hessian can be construed based on the UHF and DFT equations summarized above, Eqs. (76, 78, 81). For the sake of brevity, explicit equations are not given here.

2.3 Simulation of Spectra

The IR intensity for normal mode i can be computed as

$$I_i \sim \left| \sum_a \mu^a l_{ai} \right|^2, \quad (83)$$

where l_{ai} is the eigenvector of the Hessian for mode i and μ^a is a dipole derivative,

$$\mu^a = \sum_I^N \mu^{a,I} + \sum_{I>J}^N (\mu^{a,IJ} - \mu^{a,I} - \mu^{a,J}). \quad (84)$$

Only the contributions $\mu^{a,X}$ for $a \in X$ are computed, which is an approximation because μ^X depends also on $a \notin X$ via the ESP.

The normal Raman activity [50, 51] of a normal mode i is

$$J_i = 45\alpha_i'^2 + 7\gamma_i'^2, \quad (85)$$

where the symmetric contribution α_i' is

$$\alpha_i' = \frac{1}{3} \left[\left(\frac{\partial \alpha_{xx}}{\partial Q_i} \right) + \left(\frac{\partial \alpha_{yy}}{\partial Q_i} \right) + \left(\frac{\partial \alpha_{zz}}{\partial Q_i} \right) \right], \quad (86)$$

and the anisotropic contribution γ_i' is

$$\begin{aligned} \gamma_i'^2 = & \frac{1}{2} \left[\left(\frac{\partial \alpha_{xx}}{\partial Q_i} - \frac{\partial \alpha_{yy}}{\partial Q_i} \right)^2 + \left(\frac{\partial \alpha_{yy}}{\partial Q_i} - \frac{\partial \alpha_{zz}}{\partial Q_i} \right)^2 + \left(\frac{\partial \alpha_{zz}}{\partial Q_i} - \frac{\partial \alpha_{xx}}{\partial Q_i} \right)^2 \right. \\ & \left. + 6 \left\{ \left(\frac{\partial \alpha_{xy}}{\partial Q_i} \right)^2 + \left(\frac{\partial \alpha_{yz}}{\partial Q_i} \right)^2 + \left(\frac{\partial \alpha_{zx}}{\partial Q_i} \right)^2 \right\} \right]. \quad (87) \end{aligned}$$

The polarizability tensor α_{xy} is the second derivative of the energy with respect to the external electric fields \mathcal{F}_x and \mathcal{F}_y

$$\alpha_{xy} = \frac{\partial^2 E}{\partial \mathcal{F}_x \partial \mathcal{F}_y}, \quad (88)$$

A normal coordinate Q_i is a linear combination of atomic Cartesian coordinates a ,

$$Q_i = \sum_{a=1}^{3N_{\text{at}}} l_{ai} a. \quad (89)$$

The polarizability tensor derivatives in terms of normal coordinates are

$$\frac{\partial \alpha_{xy}}{\partial Q_i} = \sum_{a=1}^{3N_{\text{at}}} l_{ai} \frac{\partial \alpha_{xy}}{\partial a}. \quad (90)$$

In order to obtain normal coordinates associated with vibrational frequencies, it is necessary to calculate the second derivatives of the energy with respect to nuclear coordinates a and b and transform them into mass-weighted Cartesian coordinates using atomic masses m_a , forming the Hessian matrix

$$H'_{ab} = \frac{1}{\sqrt{m_a m_b}} \frac{\partial^2 E}{\partial a \partial b}. \quad (91)$$

The derivative of the polarizability tensor α is the third derivative of the energy with respect to a coordinate a and two components of the electric field \mathcal{F}_i ($i = x, y$ and z). It is obtained by calculating the energy gradient in the presence of the electric field and differentiating this gradient numerically twice (double differencing [50, 51] for $\mathcal{F}_x \mathcal{F}_x, \mathcal{F}_y \mathcal{F}_y, \mathcal{F}_z \mathcal{F}_z, \mathcal{F}_x \mathcal{F}_y, \mathcal{F}_y \mathcal{F}_z,$ and $\mathcal{F}_z \mathcal{F}_x$). In total, 19 single point energy gradient calculations are necessary, varying these fields (1 for no field, 6 for the symmetric terms such as $\mathcal{F}_x \mathcal{F}_x$ and 12 for the asymmetric terms such as $\mathcal{F}_x \mathcal{F}_y$).

The FMO energy calculation in the presence of the electric field \mathcal{F} is straightforward ($\mathcal{F} \cdot \hat{\mu}^0$ is added to the Fock operator of each fragment X , where $\hat{\mu}^0$ is the permanent dipole moment operator) [52]. The derivative of the internal fragment energy is

$$\begin{aligned} \frac{\partial E'_X}{\partial a} &= \sum_{\mu\nu} D_{\mu\nu}^X h_{\mu\nu}^{a,X} + \sum_{\mu\nu \in X} D_{\mu\nu}^X P_{\mu\nu}^{a,X} \\ &+ \frac{1}{2} \left[D_{\mu\nu}^X D_{\lambda\sigma}^X - \frac{1}{2} D_{\mu\lambda}^X D_{\nu\sigma}^X \right] (\mu\nu|\lambda\sigma)^a \\ &+ \sum_{\mu\nu} D_{\mu\nu}^X \mathcal{F} \cdot (\mu|\hat{\mu}^0|\nu)^a \\ &- 2 \sum_{ij \in X}^{\text{occ}} S_{ij}^{a,X} F'_{ji}{}^X - \overline{U}^{a,X,X} + \frac{\partial E_X^{\text{NR}}}{\partial a}. \end{aligned} \quad (92)$$

Thus one can obtain the analytic energy gradient in the presence of the electric field \mathcal{F} , for which one has to calculate the response terms $U_{ri}^{a,K}$ by solving the CPHF equations with the electric field \mathcal{F} by using the Z-vector method, see Eq. (43).

3 Applications of Second Derivatives

3.1 IR Spectra

The accuracy of FMO-DFT Hessian was evaluated earlier [27] and here the main results related to IR spectra are summarized for polyalanine consisting of 10 residues and a styrene oligomer consisting of 8 units, divided into 10 and 4 fragments, respectively. The accuracy is measured versus full DFT results without fragmentation. Water and the polypeptides have hydrogen bonding with substantial three-body effects, whereas in the styrene oligomer these effects are small. Thus FMO3 and FMO2 level was chosen for polyalanine and polystyrene, respectively.

The simulated spectra are shown in Fig. 2 and a summary of results is in Table 1 [27]. The accuracy of FMO is reasonable: the errors for polyalanine do not exceed 13 cm^{-1} and $0.19 \text{ D}^2/(\text{u } \text{Å}^2)$, for frequencies and IR intensities, respectively. In the styrene oligomer, the errors in vibrational frequency and IR intensity do not exceed 1 cm^{-1} and $0.01 \text{ D}^2/(\text{u } \text{Å}^2)$, respectively. The root mean square deviation (RMSD) between all vibrational frequencies in FMO-DFT and full DFT is 2.0 and 0.5 cm^{-1} for polyalanine and styrene oligomer (the maximum error is 10 and 5 cm^{-1}), respectively.

FMO-DFT can be applied to calculate IR spectra of proteins. A comparison of calculated and experimental results for Trp-cage (PDB: 1L2Y) is shown in Table 2 [27]. The Tyr symmetric mode and Amide II and III peaks are well reproduced by FMO, but the Amide I peak has a deviation of about $+50 \text{ cm}^{-1}$ from experiment. The reason for the discrepancy may be the lack of solvent in the Hessian calculation: the Amide I peak in a small polypeptide has a solvent shift of -30 cm^{-1} [26], due to the

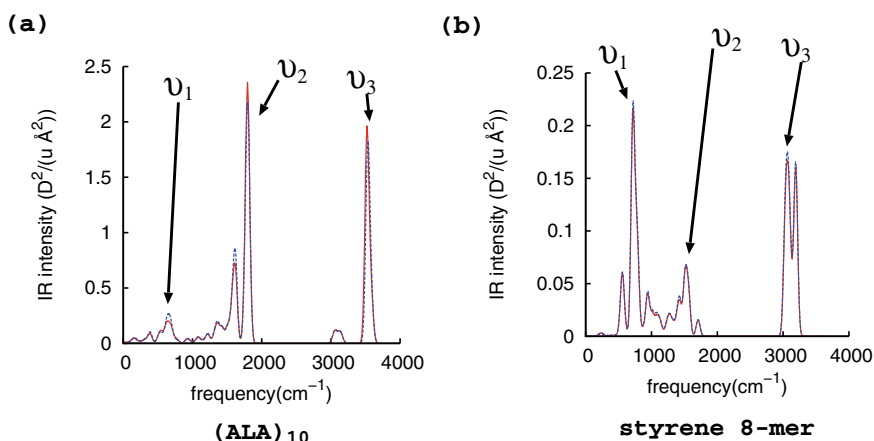


Fig. 2 IR spectra at the LC-BLYP-D/6-31G(d) level of **a** alanine decamer and **b** styrene octamer. FMO and full DFT spectra are shown as red solid and blue dashed lines, respectively. Reprinted with permission from [27]. Copyright (2018) American Institute of physics.

Table 1 Three prominent IR peaks ν_i , computed with FMO using LC-BLYP-D/6-31G(d), and full DFT values are in parentheses [27]

System	ν_1	ν_2	ν_3
	Frequency, cm^{-1}		
Polyalanine ^a	645(653)	1795(1797)	3523(3536)
Styrene oligomer ^b	721(722)	1523(1523)	3065(3064)
	Intensity, $\text{D}^2/(\text{u} \text{ \AA}^2)$		
Polyalanine ^a	0.20(0.27)	2.36(2.17)	1.96(1.83)
Styrene oligomer ^b	0.22(0.22)	0.07(0.07)	0.17(0.18)

^aFMO3, ^bFMO2**Table 2** Prominent IR peaks (in cm^{-1}) computed with FMO3 using LC-BLYP-D/6-31G(d) compared to experimental resonance Raman peaks in the Trp-cage protein (1L2Y)

Label	Calculated ^a [27]	Experiment [63]
Amide I	1709–1726	1662
Amide II	1563–1577	1564
Amide III	1259–1268	1266
Tyr symmetric	1217	1210

^aScaled [64] by 0.9915

coupling of it to the water bending mode, whereas Amide II and III peaks are weakly affected [26].

3.2 Raman Spectra

The accuracy of FMO for Raman spectra is evaluated for vitamins E and C (both treated with RHF) and an organic radical of 2,2,6,6-tetramethylpiperidine-1-oxyl (TEMPO) solvated in N,N-dimethylformamide (DMF) [52] (treated with UHF). The results are shown in Fig. 3. The maximum (RMSD) FMO deviation from full calculations for normal modes in vitamin C, vitamin E, and TEMPO is 27.1 (8.9), 6.2 (1.3), and 7.1 (1.1) cm^{-1} , respectively. The main Raman peaks are listed in Table 3. The errors in frequencies are 2.1, 0.2, and 0.2 cm^{-1} for vitamin C, vitamin E, and TEMPO, respectively, while the respective errors in Raman activities are 5.5, 33.3, and 6.6 $\text{\AA}^4/\text{u}$.

For vitamin C, the hydrogen bonding with water introduces many-body quantum effects (e.g., the coupling of charge transfer in two hydrogen bonds), which are not fully accounted for in FMO2. This explains the observed errors, which are mainly for vibrational modes delocalized over several water molecules, coupled with OH modes in vitamin C.

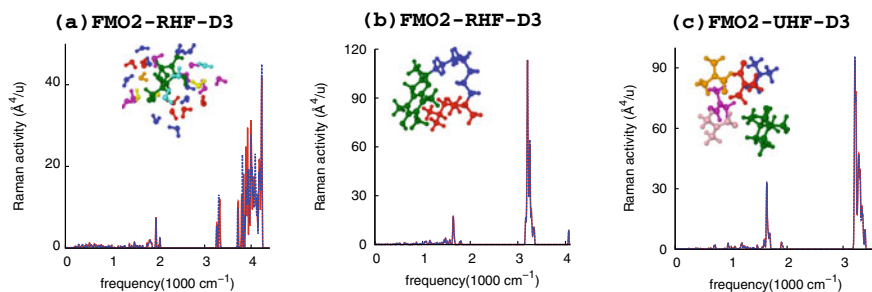


Fig. 3 Raman spectra at the level of HF-D/6-31G(d), where D stands for the dispersion model [65]. FMO-HF and full HF spectra are shown as red solid and blue dashed lines, respectively. **a** Vitamin C solvated in water molecules **b** vitamin E **c** TEMPO solvated in DMF. Reprinted with permission from [52]. Copyright (2018) American Chemical Society

Table 3 Frequencies (cm^{-1}) and Raman activities ($\text{\AA}^4/\text{u}$) computed with FMO and full methods using the 6-31G(d) basis set [52]

System	Frequency		Raman activity	
	FMO	full	FMO	full
Vitamin C ^a	3884.5	3886.6	150.4	144.9
Vitamin E ^a	3203.8	3204.0	403.2	369.9
TEMPO ^b	3237.2	3237.4	130.6	124.0

^aSinglet with RHF, ^bDoublet with UHF

3.3 Localization of Normal Modes

In the localization method [53, 54], normal modes are rotated (the matrix l_{ai} is multiplied by a unitary matrix \mathbf{U}) to localize them, and the diagonal matrix of vibrational frequencies is transformed with \mathbf{U} , yielding a matrix Ω_{ij} , whose off-diagonal elements describe the coupling between localized vibrations i and j . This normal mode localization was performed with Movipac program [55].

The values of $|\Omega_{ij}|$ are plotted in Fig. 4, for the selected ranges of frequencies in IR spectra, representing Peak I in crambin and Tyr symmetric stretch in Trp-cage. It can be seen that the matrices are fairly sparse, with the majority of elements below 1 cm^{-1} , which means that these localized modes are not coupled; however, a few substantial couplings are also observed.

3.4 IR and Raman Spectra of Radicals Using FMO-UDFT

The Hessian for FMO-UDFT, developed in this work, is applied to the styrene hexamer radical, divided into 5 fragments (Fig. 5 and Table 4). The agreement between FMO and full calculations is reasonable. For the four prominent peaks, the devi-

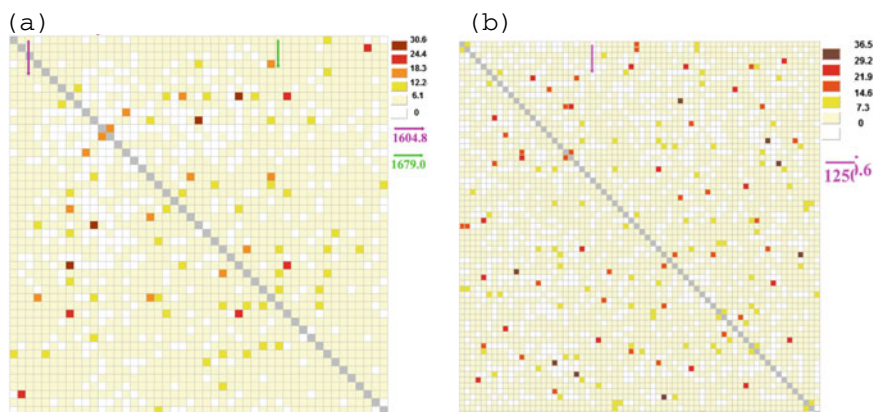


Fig. 4 Couplings $|\Omega_{ij}|$ between localized vibrational modes in **a** Amide I peak of crambin, and **b** Tyr symmetric stretch in Trp-cage; i (j) increases from the top left corner down (to the right). The magnitude of the couplings is shown with colors (the diagonal elements Ω_{ii} are shown in grey). Reprinted with permission from [41]. Copyright (2018) from John Wiley and Sons.

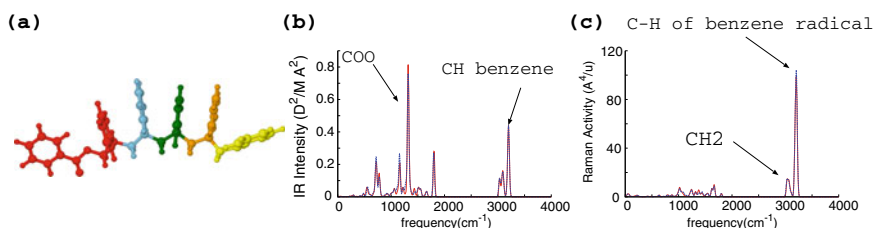


Fig. 5 Polystyrene radical computed with B3LYP-D3/6-31G(d) (red solid and blue dashed lines show FMO-UDFT and full UDFT results, respectively): **a** molecular structure (the radical fragment is in yellow), **b** IR spectrum **c** Raman spectrum.

ation in the frequency and intensity does not exceed 5 cm^{-1} and $0.06 \text{ D}^2/(\text{u} \text{ \AA}^2)$, respectively. The required memory is 1402 and 7071 MB in FMO and full Hessian calculations, respectively (see Eqs. 35 and 36).

By analyzing the vibrational pattern of local modes, it is possible to assign peaks. The IR peak of 1320 cm^{-1} is due to COO^- vibrations, while the 3200 cm^{-1} IR peak comes from C-H bonds in benzene rings. On the other hand, the Raman peak of 3209 cm^{-1} is due to the symmetric vibrational mode of the radical benzene ring. The Raman peak of 3033 cm^{-1} is due to CH_2 .

3.5 Mapping Chemical Reaction Paths

The accuracy of FMO/FDD was evaluated [56] for an S_N2 reaction $XCH_3 + OH^- \rightarrow X^- + CH_3OH$ solvated in 41 water molecules, $X = F, Cl,$ and Br . The active domain **A** was chosen to have only the reaction fragment, containing the solute as well as 6 surrounding water molecules merged into 1 fragment. Other water molecules formed separate fragments. All fragments within 5.2 Å from **A** were assigned to **b**; in this small system domain **F** is empty and the acceleration by using the frozen domain treatment is only because in FDD some dimers are not calculated as explained above.

The threshold of 5.2 Å was recommended in the previous study [42], because for a hydrogen bond between O and H, $5.2 = 2(1.4 + 1.2)$, where 1.4 and 1.2 Å are the van-der-Waals radii of O and H, respectively, and 2 is used as an arbitrary factor, which corresponds to the unitless FMO threshold of 2.0 (such as used for the ES dimer approximation).

The results are shown in Table 5. FMO/FDD correctly reproduces the trend for the three halogen atoms, and the error in the Gibbs free energy does not exceed 1.6 kcal/mol. The largest error in the imaginary frequency is 7.9 cm^{-1} . Overall, FMO/FDD has slightly larger errors than FMO without FDD, compared to full RHF; when FDD is not used, the largest error in the Gibbs free energies and imaginary frequencies are 0.6 kcal/mol and 4.9 cm^{-1} , respectively, which shows how much improvement can be got by enlarging the active domain.

FMO/FDD was also applied [56] to map the reaction path for the keto-enol tautomeric reaction of phosphoglycolohydroxamic acid (PGH) and the triosephosphate isomerase (PDB: 7TIM), for which experimental [57] and theoretical [58] data are available. The system and domain definition are shown in Figures 6 and 7a. One water molecule or residue was assigned to a fragment, except that the reaction center comprising the reactant PGH and Glu-410 were treated as one fragment with the total charge of -3. The active domain **A** was chosen to include only the reaction center fragment as shown in Fig. 6, and the amino acid residues and water molecules within 5.2 Å distance from **A** were included in the polarizable buffer **B**.

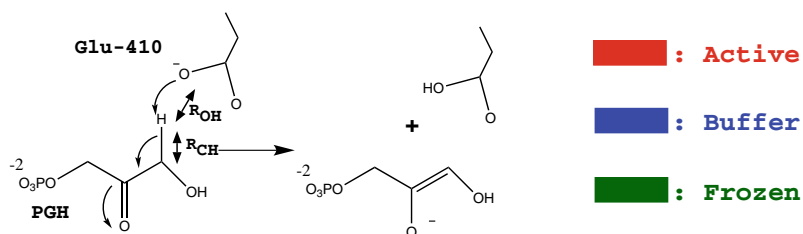
Table 4 Prominent IR peaks (in cm^{-1}) and intensities ($D^2/(\text{u} \text{Å}^2)$) of the styrene oligomer radical (Fig. 5), computed with unrestricted B3LYP/6-31G(d)

FMO-UDFT		Full UDFT	
Peak	Intensity	Peak	Intensity
1320	0.813	1320	0.757
3200	0.437	3200	0.438
1804	0.280	1799	0.272
721	0.217	719	0.246

Table 5 Gibbs free energy barrier ΔG (kcal/mol) at 298.15 K, and the imaginary frequency ω (cm^{-1}) for the $\text{S}_{\text{N}}2$ reaction $\text{XCH}_3 + \text{OH}^- \rightarrow \text{X}^- + \text{CH}_3\text{OH}$ in explicit solvent (water), $\text{X} = \text{F}, \text{Cl}$ and Br [24, 56]

Method (6-31G(d))	Value	F	Cl	Br
FMO-RHF/FDD	ΔG	15.3	12.4	8.6
FMO-RHF	ΔG	17.1	13.0	10.2
full RHF	ΔG	16.5	13.0	10.2
FMO-RHF/FDD	ω	590.1	464.0	426.8
FMO-RHF	ω	585.8	470.3	428.5
Full RHF	ω	590.7	472.1	427.6

(a)



(b)

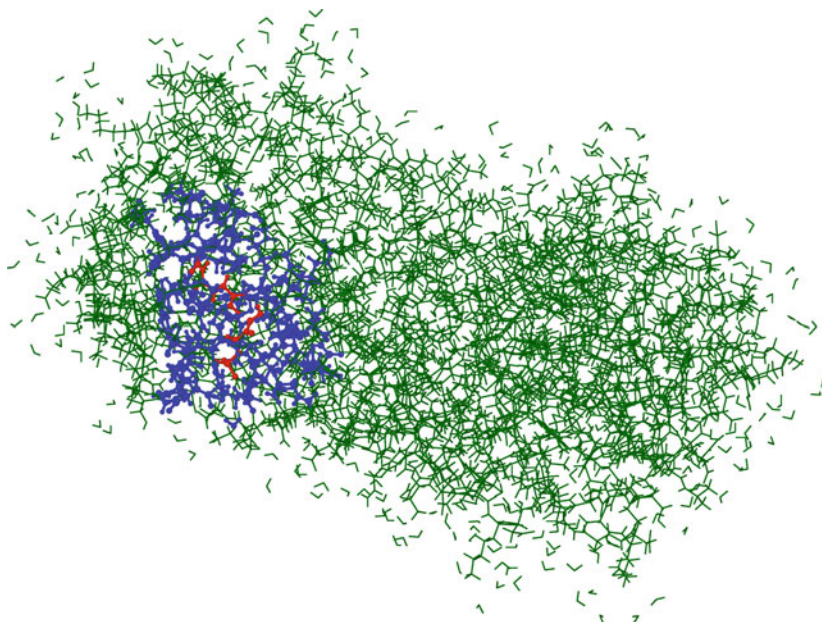


Fig. 6 Enzymatic reaction studied with FMO/FDD: **a** schematic representation, **b** the whole system; the reactants or products form the active domain **A**. Reprinted with permission from [56]. Copyright (2018) American Chemical Society.

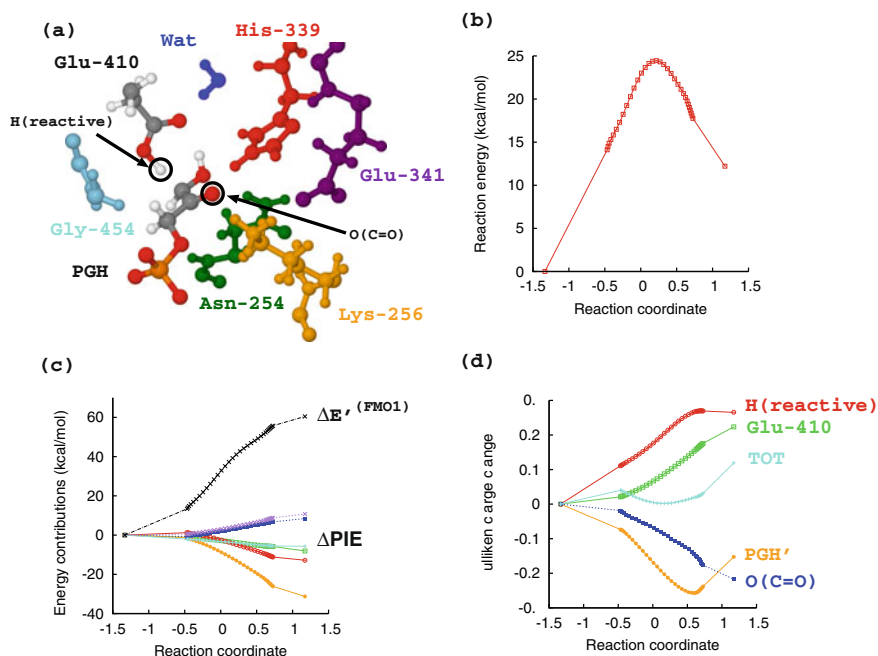


Fig. 7 Keto-enol tautomeric reaction of PGH and the triosephosphate isomerase. **a** The binding pocket at the transition state geometry. **b** Reaction path obtained with IRC using FMO-RHF/FDD; the reaction coordinate (\AA) is mainly given by $R_{\text{CH}} - R_{\text{OH}}$, see Fig. 6a. The energy of the reactants is set to 0. **c** Decomposition of the total energy into the sum of monomer energies $\Delta E'(\text{FMO1}) = \sum_I E'_I$ (black dashed line) and pair interaction energies (ΔPIE) ΔE_{IJ} between the reactant and residue fragments of the enzyme, colored as fragments in (a). **d** Change in the Mulliken charges of the subsystems defined within the reaction fragment: Glu-410, two special atoms O(C=O) and H(reactive) and the rest of PGH (PGH'); the charges at the reactant geometry are set to 0. TOT denotes the total charge on the reactive fragment. Reprinted with permission from [56]. Copyright (2018) American Chemical Society.

The free energy barrier (the FMO-RHF/6-31G(d) energy including the thermodynamical correction for 1 minimum) is 21.4 kcal/mol at the comparable to 21.9 kcal/mol reported earlier [58] at the level of RHF/3-21G, whereas the experimental estimate is 14 kcal/mol [57].

After locating the transition state from a trial geometry using the analytic Hessian developed in this work, IRC simulations were performed to map the reaction path. The reaction coordinate R_{react} was calculated along the actual IRC path and the results are shown in Fig. 7b.

PIE in Eq. (57) can be used to identify the residue fragments, which are important factors in the catalytic activity [59–61]. It should be noted that in FMO fragments are defined by detaching $C\alpha$ -C bonds at $C\alpha$, so that fragment residues in FMO are shifted compared to conventional residues by the carboxyl group. The names of residue frag-

ments in FMO have a hyphen to indicate the difference from conventional residues (GLU-410 is the fragment that corresponds to the amino acid residue GL410).

The total energy E along the path shown in Fig. 7b is divided into the sum of monomer contributions E'_I and PIEs in Fig. 7c. The change in the internal energy E'_I (see Eq. 21) along the reaction path has two contributions: a) the deformation energy, which shows how fragment I is either stabilized or destabilized when its geometry changes relative to the reactant state) and b) the destabilization polarization effect on fragment I by the rest of the system [62] (the stabilization component of the polarization forms a part of the electrostatic component of PIEs and is not separated here).

In addition, the change in PIEs along the path for the important residues depicted in Fig. 7a is shown in Fig. 7c; some residues such as Glu-341 have a relatively small change whereas others such as Lys-256 feature a large change; the reaction coordinate 0.2176 (see Fig. 7b) corresponds to the transition state of the keto-enol tautomeric reaction (largely stabilized by Lys-256 and destabilized by the monomer state).

The change in the charges along the path is shown in Fig. 7d. In this reaction, the charge of the reactant molecule PGH changes from -2 to -3 , whereas Glu-410 turns from an anion into a neutral residue. The charge on the reactive H atom is of special interest. The change in this charge in the reaction is about 0.3, similar to the change in Glu-410. The changes in these charges are parallel to each other (Fig. 7d) for the large region around the transition state. Another important change occurs to the charge of oxygen in the carboxyl of PGH. This means that the negative charge is transferred from Glu-410 to this carboxyl. Thus, energetic changes can be rationalized also in terms of charge transfer.

4 Conclusion

The development of analytic second derivatives in FMO has been summarized, for restricted and unrestricted variants of Hartree–Fock and density functional theory. Detailed equations have been given for the two-body FMO expansion applied to restricted Hartree–Fock, with extensions to DFT, unrestricted Hartree–Fock and three-body expansion. The formulation of FMO-DFTB somewhat differs from other methods and for brevity it has not been described here, see elsewhere for details [30, 31].

FMO Hessian calculations are somewhat expensive because individual response terms are needed (in the gradient, the Z-vector technique allows one to solve for the Z-vector and avoid getting individual responses). To reduce the computational cost, one can use the frozen domain approach, which has been applied to an enzyme containing about 10,000 atoms.

Analytic second derivatives in FMO can be used for many purposes: to improve the efficiency of geometry optimizations, guide transition state search, map chemical reaction path with IRC, and simulate IR and Raman spectra in large molecular sys-

tems. One can also evaluate zero point energies to estimate enthalpies of chemical reactions as in the study of radical damage in lipids [25], although anharmonic corrections may be important for entropy and free energies determined by low-frequency vibrations [24].

FMO significantly accelerates the calculation of second derivatives [24, 26]. Although the Hessian matrix diagonalization scales cubically, this step takes a relatively little absolute time and the practically observed cost is mainly driven by the calculation of dimer responses. Also, FMO significantly reduces the memory for storing supervectors \mathbf{U}^a (compare Eqs. 35 and 36): in styrene hexamer, the memory was reduced by a factor of 5.

Acknowledgements This research used the computational resources of the Supercomputer system ITO in R.I.I.T at Kyushu University as a national joint-usage/research center.

References

1. Deglmann P, Furche F, Ahlrichs R (2002) An efficient implementation of second analytical derivatives for density functional methods. *Chem Phys Lett* 362:511–518
2. Alexeev Y, Schmidt MW, Windus TL, Gordon MS (2007) A parallel distributed data CPHF algorithm for analytic Hessians. *J Comput Chem* 28:1685–1694
3. Pulay P (1969) Ab initio calculation of force constants and equilibrium geometries in polyatomic molecules. *Mol Phys* 17:197–204
4. Gordon MS, Fedorov DG, Pruitt SR, Slipchenko LV (2012) Fragmentation methods: a route to accurate calculations on large systems. *Chem Rev* 112:632–672
5. Sakai S, Morita S (2005) Ab initio integrated multi-center molecular orbitals method for large cluster systems: Total energy and normal vibration. *J Phys Chem A* 109:8424–8429
6. Rahalkar AP, Ganesh V, Gadre SR (2008) Enabling ab initio hessian and frequency calculations of large molecules. *J Chem Phys* 129:234101
7. Jose KVJ, Raghavachari K (2015) Evaluation of energy gradients and infrared vibrational spectra through molecules-in-molecules fragment-based approach. *J Chem Theory Comput* 11(3):950–961
8. Hua W, Fang T, Li W, Yu JG, Li S (2008) Geometry optimizations and vibrational spectra of large molecules from a generalized energy-based fragmentation approach. *J Phys Chem A* 112(43):10864–10872
9. Collins MA (2014) Molecular forces, geometries, and frequencies by systematic molecular fragmentation including embedded charges. *J Chem Phys* 141:094108
10. Liu J, Zhang JZH, He X (2016) Fragment quantum chemical approach to geometry optimization and vibrational spectrum calculation of proteins. *Phys Chem Chem Phys* 18:1864–1875
11. Cui Q, Karplus M (2000) Molecular properties from combined qm/mm methods. I. Analytical second derivative and vibrational calculations. *J Chem Phys* 112:1133
12. Li H, Jensen JH (2002) Partial Hessian vibrational analysis: the localization of the molecular vibrational energy and entropy. *Theor Chem Acc* 107:211–219
13. Jensen JH, Li H, Robertson AD, Molina PA (2005) Prediction and rationalization of protein pKa values using QM and QM/MM methods. *J Phys Chem A* 109:6634–6643
14. Ghysels A, Woodcock HL III, Larkin JD, Miller BT, Shao Y, Kong J, Neck DV, Speybroeck VV, Waroquier M, Brooks BR (2011) Efficient calculation of QM/MM frequencies with the mobile block Hessian. *J Chem Theory Comput* 7:496–514
15. Hafner J, Zheng W (2009) Approximate normal mode analysis based on vibrational subsystem analysis with high accuracy and efficiency. *J Chem Phys* 130:194111

16. Ghysels A, Speybroeck VV, Pauwels E, Catak S, Brooks BR, Neck DV, Waroquier M (2010) Comparative study of various normal mode analysis techniques based on partial Hessians. *J Comput Chem* 31:994–1007
17. Kitaura K, Ikeo E, Asada T, Nakano T, Uebayasi M (1999) Fragment molecular orbital method: an approximate computational method for large molecules. *Chem Phys Lett* 313:701–706
18. Fedorov DG, Kitaura K (2007) Extending the power of quantum chemistry to large systems with the fragment molecular orbital method. *J Phys Chem A* 111:6904–6914
19. Fedorov DG, Nagata T, Kitaura K (2012) Exploring chemistry with the fragment molecular orbital method. *Phys Chem Chem Phys* 14:7562–7577
20. Tanaka S, Mochizuki Y, Komeiji Y, Okiyama Y, Fukuzawa K (2014) Electron-correlated fragment-molecular-orbital calculations for biomolecular and nano systems. *Phys Chem Chem Phys* 16:10310–10344
21. Fedorov DG (2017) The fragment molecular orbital method: theoretical development, implementation in gamess, and applications. *CMS WIREs* 7:e1322
22. Fedorov DG, Asada N, Nakanishi I, Kitaura K (2014) The use of many-body expansions and geometry optimizations in fragment-based methods. *Acc Chem Res* 47:2846–2856
23. Schmidt MW, Baldrige KK, Boatz JA, Elbert ST, Gordon MS, Jensen JJ, Koseki S, Matsunaga N, Nguyen KA, Su S, Windus TL, Dupuis M, Montgomery JA (1993) General atomic and molecular electronic structure system. *J Comput Chem* 14:1347–1363
24. Nakata H, Nagata T, Fedorov DG, Yokojima S, Kitaura K, Nakamura S (2013) Analytic second derivatives of the energy in the fragment molecular orbital method. *J Chem Phys* 138:164103
25. Green MC, Nakata H, Fedorov DG, Slipchenko LV (2016) Radical damage in lipids investigated with the fragment molecular orbital method. *Chem Phys Lett* 651:56–61
26. Nakata H, Fedorov DG, Yokojima S, Kitaura K, Nakamura S (2014) Efficient vibrational analysis for unrestricted Hartree-Fock based on the fragment molecular orbital method. *Chem Phys Lett* 603:67–74
27. Nakata H, Fedorov DG, Zahariev F, Schmidt MW, Kitaura K, Gordon MS, Nakamura S (2015) Analytic second derivative of the energy for density functional theory based on the three-body fragment molecular orbital method. *J Chem Phys* 142:124101
28. Nishimoto Y, Fedorov DG, Irle S (2014) Density-functional tight-binding combined with the fragment molecular orbital method. *J Chem Theory Comput* 10:4801–4812
29. Nishimoto Y, Nakata H, Fedorov DG, Irle S (2015) Large-scale quantum-mechanical molecular dynamics simulations using density-functional tight-binding combined with the fragment molecular orbital method. *J Phys Chem Lett* 6:5034–5039
30. Nakata H, Nishimoto Y, Fedorov DG (2016) Analytic second derivative of the energy for density-functional tight-binding combined with the fragment molecular orbital method. *J Chem Phys* 145:044113
31. Nishimoto Y, Fedorov DG (2017) Three-body expansion of the fragment molecular orbital method combined with density-functional tight-binding. *J Comput Chem* 38:406–418
32. Nakano T, Kaminuma T, Sato T, Fukuzawa K, Akiyama Y, Uebayasi M, Kitaura K (2002) Fragment molecular orbital method: use of approximate electrostatic potential. *Chem Phys Lett* 351:475–480
33. Nagata T, Fedorov DG, Kitaura K (2010) Importance of the hybrid orbital operator derivative term for the energy gradient in the fragment molecular orbital method. *Chem Phys Lett* 492:302–308
34. Nakano T, Kaminuma T, Sato T, Akiyama Y, Uebayasi M, Kitaura K (2000) Fragment molecular orbital method: application to polypeptides. *Chem Phys Lett* 318:614–618
35. Fedorov DG, Jensen JH, Deka RC, Kitaura K (2008) Covalent bond fragmentation suitable to describe solids in the fragment molecular orbital method. *J Phys Chem A* 112:11808–11816
36. Nishimoto Y, Fedorov DG (2018) Adaptive frozen orbital treatment for the fragment molecular orbital method combined with density-functional tight-binding. *J Chem Phys* 148:064115
37. Yamaguchi Y, Schaefer HF III, Osamura Y, Goddard J (1994) A new dimension to quantum chemistry: analytical derivative methods in ab initio molecular electronic structure theory. Oxford University Press, New York

38. Nagata T, Brorsen K, Fedorov DG, Kitaura K, Gordon MS (2011) Fully analytic energy gradient in the fragment molecular orbital method. *J Chem Phys* 134:124115
39. Nagata T, Fedorov DG, Kitaura K (2009) Derivatives of the approximated electrostatic potentials in the fragment molecular orbital method. *Chem Phys Lett* 475:124–131
40. Nagata T, Fedorov DG, Kitaura K (2012) Analytic gradient for the embedding potential with approximations in the fragment molecular orbital method. *Chem Phys Lett* 544:87–93
41. Nakata H, Fedorov DG (2018) Analytic second derivatives for the efficient electrostatic embedding in the fragment molecular orbital method. *J Comput Chem* 39:2039–2050
42. Fedorov DG, Alexeev Y, Kitaura K (2011) Geometry optimization of the active site of a large system with the fragment molecular orbital method. *J Phys Chem Lett* 2:282–288
43. Fedorov DG, Ishida T, Kitaura K (2005) Multilayer formulation of the fragment molecular orbital method (FMO). *J Phys Chem A* 109:2638–2646
44. Aikens CM, Webb SP, Bell RL, Fletcher GD, Schmidt MW, Gordon MS (2003) A derivation of the frozen-orbital unrestricted open-shell and restricted closed-shell second-order perturbation theory analytic gradient expressions. *Theor Chem Acc* 110:233–253
45. Handy NC, Schaefer HF III (1984) On the evaluation of analytic energy derivatives for correlated wave functions. *J Chem Phys* 81:5031–5033
46. Nagata T, Fedorov DG, Ishimura K, Kitaura K (2011) Analytic energy gradient for second-order Møller-Plesset perturbation theory based on the fragment molecular orbital method. *J Chem Phys* 135:044110
47. Fedorov DG, Kitaura K (2004) The importance of three-body terms in the fragment molecular orbital method. *J Chem Phys* 120:6832–6840
48. Fedorov DG, Kitaura K (2004) On the accuracy of the 3-body fragment molecular orbital method (FMO) applied to density functional theory. *Chem Phys Lett* 389:129–134
49. Nakata H, Fedorov DG, Nagata T, Yokojima S, Ogata K, Kitaura K, Nakamura S (2012) Unrestricted Hartree-Fock based on the fragment molecular orbital method: energy and its analytic gradient. *J Chem Phys* 137:044110
50. Komornicki A, McIver JW (1979) An efficient abinitio method for computing infrared and Raman intensities: application to ethylene. *J Chem Phys* 70(4):2014–2016
51. Bacskay GB, Saebø S, Taylor PR (1984) On the calculation of dipole moment and polarizability derivatives by the analytical energy gradient method: application to the formaldehyde molecule. *Chem Phys* 90:215–224
52. Nakata H, Fedorov DG, Yokojima S, Kitaura K, Nakamura S (2014) Simulations of Raman spectra using the fragment molecular orbital method. *J Chem Theory Comput* 10(9):3689–3698
53. Jacob CR, Luber S, Reiher M (2009) Analysis of secondary structure effects on the IR and Raman spectra of polypeptides in terms of localized vibrations. *J Phys Chem B* 113(18):6558–6573
54. Weymuth T, Jacob CR, Reiher M (2010) A local-mode model for understanding the dependence of the extended amide III vibrations on protein secondary structure. *J Phys Chem B* 114:10649–10660
55. Weymuth T, Haag MP, Kiewisch K, Luber S, Schenk S, Jacob CR, Herrmann C, Neugebauer J, Reiher M (2012) Movipac: vibrational spectroscopy with a robust meta-program for massively parallel standard and inverse calculations. *J Comput Chem* 33:2186–2198
56. Nakata H, Fedorov DG, Nagata T, Kitaura K, Nakamura S (2015) Simulations of chemical reactions with the frozen domain formulation of the fragment molecular orbital method. *J Chem Theory Comput* 11:3053–3064
57. Albery WJ, Knowles JR (1976) Free-energy profile for the reaction catalyzed by triosephosphate isomerase. *Biochemistry* 15:5627–5631
58. Zhang Y, Liu H, Yang W (2000) Free energy calculation on enzyme reactions with an efficient iterative procedure to determine minimum energy paths on a combined ab initio QM/MM potential energy surface. *J Chem Phys* 112:3483–3492
59. Ishida T, Fedorov DG, Kitaura K (2006) All electron quantum chemical calculation of the entire enzyme system confirms a collective catalytic device in the chorismate mutase reaction. *J Phys Chem B* 110:1457–1463

60. Ito M, Brinck T (2014) Novel approach for identifying key residues in enzymatic reactions: proton abstraction in ketosteroid isomerase. *J Phys Chem B* 118:13050–13058
61. Jensen JH, Willemos M, Winther JR, De Vico L (2014) In silico prediction of mutant HIV-1 proteases cleaving a target sequence. *PLoS ONE* 9:e95833
62. Fedorov DG, Kitaura K (2007) Pair interaction energy decomposition analysis. *J Comput Chem* 28:222–237
63. Ahmed Z, Beta IA, Mikhonin AV, Asher SA (2005) UV resonance Raman thermal unfolding study of Trp-cage shows that it is not a simple two-state miniprotein. *J Am Chem Soc* 127:10943–10950
64. Scott AP, Radom L (1996) Harmonic vibrational frequencies: an evaluation of Hartree-Fock, Møller-Plesset, quadratic configuration interaction, density functional theory, and semiempirical scale factors. *J Phys Chem* 100:16502–16513
65. Grimme S, Antony J, Ehrlich S, Krieg H (2010) A consistent and accurate ab initio parametrization of density functional dispersion correction (DFT-D) for the 94 elements H-Pu. *J Chem Phys* 132:154104

The FMO-DFTB Method



Yoshio Nishimoto and Stephan Irle

Abstract Although the fragment molecular orbital (FMO) method enables electronic structure calculations with near-linear scaling behavior with respect to system size, the computational cost of ab initio methods typically employed in conjunction with FMO is still prohibitive for routine calculations of very large systems or long timescale molecular dynamics simulations. We, therefore, combined the FMO and density-functional tight-binding (DFTB) method, which is one of the emerging semi-empirical quantum chemical methods, and have demonstrated that FMO-DFTB is capable of performing geometry optimizations for systems containing up to one million atoms using limited computational resources. In this chapter, we will review the basics of the DFTB method first before introducing FMO-DFTB, focusing on the relationship with density functional theory and other FMO methodologies. We also demonstrate the latest scalings of FMO-DFTB2 and DFTB3 using three-dimensional water clusters, showing that the most favorable scaling is $\mathcal{O}(N^{1.16})$. Applications of FMO-DFTB to various systems are briefly summarized, and an outlook to future applications is provided.

Keywords Density-functional tight-binding · Approximate electronic structure theory · Molecular dynamics · Near-linear scaling

1 Introduction

In performing quantum chemical calculations, finding a reasonable trade-off between accuracy and computational cost is always inevitable. If an infinitely fast computer would be available, the choice should always be the full configuration interaction

Y. Nishimoto (✉)

Fukui Institute for Fundamental Chemistry, Kyoto University, Kyoto, Japan
e-mail: nishimoto.yoshio@fukui.kyoto-u.ac.jp

S. Irle

Computational Sciences and Engineering Division and Chemical Sciences Division,
Oak Ridge National Laboratory, Oak Ridge, USA
e-mail: irles@ornl.gov

© Springer Nature Singapore Pte Ltd. 2021

Y. Mochizuki et al. (eds.), *Recent Advances of the Fragment Molecular Orbital Method*,
https://doi.org/10.1007/978-981-15-9235-5_23

method, which allows to compute the exact nonrelativistic solution of the Schrödinger equation within the Born–Oppenheimer approximation. Such a computer, anticipated by some as the ultimate goal of current efforts in quantum computing, is obviously still far from realization. With the currently available limited computational resources, we have to choose a method which (hopefully) yields the highest accuracy with the lowest computational cost, carefully considering the expected accuracy and cost. In principle, accurate methods exhibit unfortunate, steep scaling with respect to system size, such as polynomial or, as in the case of full configuration interaction, factorial. The scaling of all standard quantum chemical calculations is at least equal or greater than quadratic. Quadratic scaling in electronic structure calculations can be achieved by using integral prescreening [1] and density fitting [2] techniques. If the bottleneck of integral calculation can be overcome, for instance, by efficient parallelization or parameterization, matrix diagonalization and other linear algebra related to Hamiltonian and density matrices become dominant, and these operations are commonly associated with cubic scaling. Thus, one always suffers from rapid increase of the computational cost as far as we treat dense matrices. This problem may be actually less severe; we can simply wait for long calculations to finish or, if the code parallelizes well, we can use more and more CPU cores. However, the memory requirement is another, and possibly more severe, problem. If we cannot store a very large matrix in memory, we cannot even execute the calculation. For instance, storing a $100,000 \times 100,000$ matrix in memory requires 74.5 GB in double precision, so some computers with a medium-sized memory space may not handle this large calculation. In any case, calculations for large systems always suffer from these problems.

In this context, a number of linear-scaling methods have been developed, and one of them is the fragment molecular orbital (FMO) method [3], the main theme of this book. After the first idea by Kitaura et al., it has been combined with various *ab initio* methods, and numerous methodological simplifications and advances have been reported. Various FMO approaches have been successfully applied to a great many systems. In spite of the usefulness of the approach itself, computational costs of the *ab initio* methods themselves are still high, even when they are combined with FMO. One may find that treating the whole system in a straightforward fashion with semi-empirical quantum mechanics (QM) methods is sometimes faster than FMO combined with *ab initio* methods, if the system consists of less than a few thousand atoms.

The density-functional tight-binding (DFTB) method [4–8] is one of the semi-empirical QM methods, and it has been applied to a number of nanomaterials [9], chemical [10] and biosystems [11]. The method is known as an approximation of density functional theory (DFT), utilizing tight-binding approximations such as minimal Slater-type basis set and two-center approximations for Hamiltonian matrix elements, and diatomic repulsive potentials. The earliest DFTB development perhaps began with the seminal works by Porezag et al. [12] and Seifert et al. [13]. This option is known as nonself-consistent-charge DFTB (NCC-DFTB) or DFTB1, and it has been applied to systems in which charge polarization is not significant. As the name implies, NCC-DFTB requires only a single diagonalization of a model

Hamiltonian employing a reference electron density. It is conceptually similar to extended Hückel-type methods, although the potentials are more sophisticated. The second generation of DFTB is the self-consistent-charge (SCC) formalism [14], also recently called DFTB2. This extension is based on the fundamental ideas of Foulkes and Haydock [15]. In the SCC formalism, interactions between atomic charges are explicitly taken into account, and the electronic structure is determined as a minimum of electronic energy with respect to the change of variational parameters, improving the description of charge–charge interactions. It requires self-consistent treatment of charge–charge interactions, as is evident from the name. The third generation is the DFTB3 formalism introduced in 2011 by Gaus et al. [16], which includes a third-order term related to the charge-dependence of the Hubbard parameter introduced in DFTB2. More details on DFTB methods are reviewed later.

In terms of the computational cost, even though the pre-factor of DFTB is relatively small, all the DFTB generations require matrix multiplications and diagonalization of the Hamiltonian (roughly equivalently, Fock matrix in Hartree–Fock) matrix more than once, so the computational scaling of these steps formally scales as cubic, and applications to large systems (more than 1000 atoms) are, therefore, not straightforward. For instance, a DFTB energy and gradient calculation for a water cluster containing 4000 molecules take about 6 d on a single CPU [17]. To circumvent this problem, various linear-scaling approaches have been combined with DFTB. One realization is a rather direct method; large systems are treated as they are, i.e., without fragmentation. Focusing only on the approaches combined with DFTB, this category may include the use of an OpenMP sparse matrix solver [18], shift-and-inverse parallel spectral transformations (SIPs) [19], and graph-based Fermi operator expansion [20]. A key of these methods is the exploitation of the sparsity of Hamiltonian and overlap matrices. Another realization divides large systems into smaller spatial segments or fragments: modified divide-and-conquer (mDC) [21], fragment molecular orbital (FMO) [17] and divide-and-conquer (DC) [22, 23]. Although it would be certainly interesting to compare the performance and the applicability of these linear scaling methods, our focus in this chapter is the combination of FMO and DFTB, so we are not going to discuss the DC methods further.

Since 2014, we have been developing an ultra-fast semi-empirical quantum mechanical method, FMO-DFTB, which combines FMO and DFTB. The scaling of the computational cost was close to linear, $\mathcal{O}(N^{1.2})$, even for three-dimensional water clusters. The performance of the method has been reported several times since its initial conception, and the largest system it was applied to consisted of 1,180,800 atoms for which each single point gradient calculation took only 22 min, using a single computer node with 24 CPU cores. In this chapter, we review our FMO-DFTB method after briefly introducing the DFTB method itself. We will discuss previous applications of DFTB and FMO-DFTB and finally conclude with a short summary and future prospect.

2 Basics of the DFTB Method

The basics of the DFTB method are briefly reviewed in this section. The formalism introduced in this subsection is limited for the purpose of this review chapter, and we point the reader to more detailed introductions, for instance, in Refs. [4–8]. Furthermore, semi-empirical quantum mechanical methods have been compared in detail in Ref. [10].

As mentioned, the DFTB method is derived from the DFT method itself. Here, given the (perturbed) total density ρ , the total Kohn–Sham DFT energy can be written as

$$E^{\text{DFT}} = \sum_i^{\text{occ}} f_i \left\langle \psi_i \left| -\frac{\nabla^2}{2} + V^{\text{ext}} \right| \psi_i \right\rangle + \frac{1}{2} \int' \int \frac{\rho \rho'}{|\mathbf{r} - \mathbf{r}'|} + E^{\text{xc}}[\rho] + E^{\text{nuc}}, \quad (1)$$

where f_i is the occupation number of i th orbital ψ_i , V^{ext} is the external potential, $E^{\text{xc}}[\rho]$ is the exchange–correlation energy, and E^{nuc} is the nuclear repulsion. Additionally, the following abbreviations were used: $\int = \int d\mathbf{r}$, $\int' = \int d\mathbf{r}'$, $\rho = \rho(\mathbf{r})$, and $\rho' = \rho(\mathbf{r}')$. For convenience, two more abbreviations are introduced later in the text: $\int'' = \int d\mathbf{r}''$ and $\rho'' = \rho(\mathbf{r}'')$.

A series of approximations can then be introduced. The perturbed total density ρ can be expressed as the sum (superposition) of a reference electron density ρ^0 and a density perturbation $\delta\rho$: $\rho = \rho^0 + \delta\rho$. The reference density ρ^0 usually corresponds to the density of a free atom in vacuum. Free atoms in a bound molecular system or solid affect each other, perturbing their density, and this density fluctuation can be expressed as $\delta\rho$. Using the density partitioning $\rho = \rho^0 + \delta\rho$, the exchange–correlation energy can be expanded in a Taylor series around the reference density in terms of the density perturbation:

$$\begin{aligned} E^{\text{xc}}[\rho] &= E^{\text{xc}}[\rho^0 + \delta\rho] \\ &= E^{\text{xc}}[\rho^0] \\ &\quad + \int \frac{\delta E^{\text{xc}}[\rho]}{\delta\rho} \Big|_{\rho^0} \delta\rho \\ &\quad + \frac{1}{2} \int' \int \frac{\delta^2 E^{\text{xc}}[\rho]}{\delta\rho\delta\rho'} \Big|_{\rho^0, \rho^0} \delta\rho\delta\rho' \\ &\quad + \frac{1}{6} \int'' \int' \int \frac{\delta^3 E^{\text{xc}}[\rho]}{\delta\rho\delta\rho'\delta\rho''} \Big|_{\rho^0, \rho^0, \rho^0} \delta\rho\delta\rho'\delta\rho'' + \dots \end{aligned} \quad (2)$$

With this expansion, the DFT total energy in Eq. (1) can be expanded as

$$\begin{aligned}
E^{\text{DFT}}[\rho^0 + \delta\rho] &= E^{\text{nuc}} - \frac{1}{2} \int' \int \frac{\rho^0 \rho^{0'}}{|\mathbf{r} - \mathbf{r}'|} + E^{\text{xc}}[\rho^0] - \int V^{\text{xc}}[\rho^0] \rho^0 \\
&\quad + \sum_i^{\text{occ}} f_i \left\langle \psi_i \left| -\frac{\nabla^2}{2} + V^{\text{ext}} + \int' \frac{\rho^{0'}}{|\mathbf{r} - \mathbf{r}'|} + V^{\text{xc}}[\rho^0] \right| \psi_i \right\rangle \\
&\quad + \frac{1}{2} \int' \int \left(\frac{1}{|\mathbf{r} - \mathbf{r}'|} + \frac{\delta^2 E^{\text{xc}}[\rho]}{\delta\rho\delta\rho'} \Big|_{\rho^0, \rho^{0'}} \right) \delta\rho\delta\rho' \\
&\quad + \frac{1}{6} \int'' \int' \int \frac{\delta^3 E^{\text{xc}}[\rho]}{\delta\rho\delta\rho'\delta\rho''} \Big|_{\rho^0, \rho^{0'}, \rho^{0''}} \delta\rho\delta\rho'\delta\rho'' + \dots \quad (3) \\
&\approx E^{\text{rep}} + E^{\text{1st}} + E^{\text{2nd}} + E^{\text{3rd}}, \quad (4)
\end{aligned}$$

where V^{xc} is the exchange–correlation potential. Each term in Eq. (4) corresponds to one line in Eq. (3) and is related to the truncation order of the Taylor expansion in Eq. (2). The last equation is a simplified expression of the DFTB energy:

$$E^{\text{DFTB}} = E^{\text{rep}} + E^{\text{1st}} + E^{\text{2nd}} + E^{\text{3rd}}, \quad (5)$$

where the truncation of terms distinguishes the level of DFTB: DFTB1, DFTB2, and DFTB3.

The repulsion energy above is defined by

$$E^{\text{rep}} = E^{\text{nuc}} - \frac{1}{2} \int' \int \frac{\rho^0 \rho^{0'}}{|\mathbf{r} - \mathbf{r}'|} + E^{\text{xc}}[\rho^0] - \int V^{\text{xc}}[\rho^0] \rho^0. \quad (6)$$

Clearly, the first term takes into account the nuclear repulsion, whereas the other terms avoid double-counting Coulomb interactions and the exchange–correlation energy of the reference density. E^{1st} is sometimes referred to as the band structure or electronic energy, defined by

$$E^{\text{1st}} = \sum_i^{\text{occ}} f_i \left\langle \psi_i \left| -\frac{\nabla^2}{2} + V^{\text{ne}} + \int' \frac{\rho^{0'}}{|\mathbf{r} - \mathbf{r}'|} + V^{\text{xc}}[\rho^0] \right| \psi_i \right\rangle. \quad (7)$$

This term is further simplified to yield

$$E^{\text{1st}} = \sum_i f_i \left\langle \psi_i \left| \hat{H}[\rho^0] \right| \psi_i \right\rangle, \quad (8)$$

where $\hat{H}[\rho^0]$ is the Hamiltonian, which is only dependent on the reference density.

The second-order contribution

$$E^{\text{2nd}} = \frac{1}{2} \int' \int \left(\frac{1}{|\mathbf{r} - \mathbf{r}'|} + \frac{\delta^2 E^{\text{xc}}[\rho]}{\delta\rho\delta\rho'} \Big|_{\rho^0, \rho^{0'}} \right) \delta\rho\delta\rho' \quad (9)$$

addresses Coulomb interactions and exchange–correlation contributions of the perturbed electron density. The third-order contribution

$$E^{3\text{rd}} = \frac{1}{6} \int'' \int' \int \frac{\delta^3 E^{\text{xc}}[\rho]}{\delta\rho\delta\rho'\delta\rho''} \Big|_{\rho^0, \rho^{0'}, \rho^{0''}} \delta\rho\delta\rho'\delta\rho'' \quad (10)$$

originates in the third-order Taylor expansion of the exchange–correlation energy. Although higher order DFTB models (with fourth- and higher order Taylor expansion) may also be formulated, no efforts for including them have been devoted. The formulations employed during computation are briefly reviewed in the following subsections. As usual, the linear combination of atomic orbitals (AOs) is applied:

$$\psi_i = \sum_{\mu} \phi_{\mu} C_{\mu i} , \quad (11)$$

where ϕ_{μ} represents μ th AO and $C_{\mu i}$ is the expansion coefficient.

2.1 DFTB1

The NCC-DFTB method is sometimes referred to as DFTB1, indicating both its expansion order, and indicating that it is the first generation of the DFTB hierarchy of methods. The total energy of DFTB1 can be given by the sum of the repulsion and one-electron contributions:

$$\begin{aligned} E^{\text{DFTB1}} &= E^{\text{rep}} + E^{\text{1st}} \\ &= \sum_{A>B} E_{AB}^{\text{rep}} + \sum_{\mu\nu} D_{\mu\nu} H_{\mu\nu}^0 . \end{aligned} \quad (12)$$

Here, the density matrix $D_{\mu\nu}$ is defined by

$$D_{\mu\nu} = 2 \sum_i^{\text{occ}} C_{\mu i} C_{\nu i} , \quad (13)$$

and $H_{\mu\nu}^0$ is sometimes referred to as the non-perturbed Hamiltonian. After neglecting several contributions, the matrix elements of $H_{\mu\nu}^0$ are written as

$$H_{\mu\nu}^0 = \langle \phi_{\mu} | \hat{H} | \phi_{\nu} \rangle = \begin{cases} \varepsilon_{\mu}^{\text{neutral free atom}} & \text{if } \mu = \nu \\ \left\langle \phi_{\mu}^A \left| -\frac{\nabla^2}{2} + V_0^A + V_0^B \right| \phi_{\nu}^B \right\rangle & \text{if } A \neq B \\ 0 & \text{otherwise,} \end{cases} , \quad (14)$$

where A and B represent the index of atoms and $\mu \in A$ and $\nu \in B$. The orbital energy of μ th AO is $\varepsilon_{\mu}^{\text{neutral free atom}}$, and V_0^A is the potential generated by the atom A at a neutral state. The terms in the right-hand side are obtained from reference DFT calculations. In most cases, the Perdew–Burke–Ernzerhof (PBE) [24, 25] exchange–correlation functional is employed in the DFT calculation of atoms and diatomic molecules in vacuum. For $A \neq B$, the term is determined so that the DFTB calculations with parametrized $H_{\mu\nu}^0$ reproduce the band structure obtained with DFT. In actual DFTB calculations, tabulated (discretized) values in the Slater–Koster files are normally interpolated using cubic or fifth-order polynomials, so no integrals are explicitly computed. DFTB was originally developed using Slater-type AOs, although this is only relevant during parametrization, and other choices including numerical AOs and Gaussian AOs have been used as well.

Applying the standard variational method, the optimum MO coefficients can be obtained by solving the generalized eigenvalue problem

$$H_{\mu\nu}^0 C_{\nu i} = S_{\mu\nu} C_{\nu i} \varepsilon_i, \quad (15)$$

where $S_{\mu\nu}$ is the (non-orthogonal) overlap matrix and ε_i are the eigenvalues of the i th vector (molecular orbital). The overlap matrix elements are also parametrized, tabulated, and computed by interpolations, as in the case of $H_{\mu\nu}^0$. The Hamiltonian, here corresponding to $H_{\mu\nu}^0$, is directly constructed with Slater–Koster tables, and is thus not dependent on the electronic structure. Therefore, a single diagonalization suffices to determine the electronic structure and to compute the total energy within DFTB1; no self-consistent field (SCF) cycles are required. Note that the DFTB community usually uses SCC to refer to SCF in Hartree–Fock. However, when combined with FMO, SCC formally means monomer iterations to determine electrostatic potential (ESP). To avoid unnecessary confusion, “SCF” cycles are exclusively used here to determine MO coefficients.

The repulsive potential E_{AB}^{rep} is empirically determined to minimize the deviations of geometrical parameters from reference geometries optimized with DFT. It is usually obtained after having optimized the AOs used to construct the diagonal and off-diagonal matrix elements of the Hamiltonian. We note in passing that parameterization of both electronic parameters as well as repulsive potentials simultaneously may lead to instabilities in the optimization procedure.

2.2 DFTB2

DFTB1 has been successfully applied to some homogeneous systems, such as carbon-based nanomaterials [9] and some bulk systems [14]. Nevertheless, DFTB1 truncates the Taylor series at the first order and does not include charge–charge interactions in the formalism, limiting the accuracy for systems with heteroatoms, and is thus not anymore widely used. Elstner et al. proposed the self-consistent version of DFTB as

a next-generation model in 1998 [14], DFTB2; the total energy within DFTB2 can be written by

$$\begin{aligned} E^{\text{DFTB2}} &= E^{\text{DFTB1}} + \frac{1}{2} \sum_{A,B} \gamma_{AB} \Delta Q_A \Delta Q_B \\ &= \sum_{A>B} E_{AB}^{\text{rep}} + \sum_{\mu\nu} D_{\mu\nu} H_{\mu\nu}^0 + \frac{1}{2} \sum_{A,B} \gamma_{AB} \Delta Q_A \Delta Q_B. \end{aligned} \quad (16)$$

The last term represents the second-order contributions, the third line of Eq. (3). The γ_{AB} function is dependent on the distance between atoms A and B and on the Hubbard values of them. The Hubbard values are related to the atomic ionization potentials and electron affinities or to chemical hardness. At a long distance, γ_{AB} closely follows the inverse of the distance between atoms A and B , R_{AB} and thus corresponds to the pure Coulomb interaction between two charges. On the other hand, at the $R_{AB} \rightarrow 0$ limit, γ_{AB} will be the Hubbard value U_A , leading to charge self-interaction on a give site (atom) [26]. The Mulliken charge ΔQ_A is the difference between the Mulliken population Q_A and the reference density Q_A^0 of atom A : $\Delta Q_A = Q_A - Q_A^0$. The Mulliken population is calculated by

$$Q_A = \sum_{\mu \in A} \sum_{\nu} D_{\mu\nu} S_{\mu\nu}. \quad (17)$$

Only valence electrons are considered in DFTB, e.g., the Q_A^0 of oxygen is six, not eight. In DFTB2, the Hamiltonian matrix $H_{\mu\nu}$, conceptually corresponding to the Fock matrix in Hartree–Fock, is

$$H_{\mu\nu} = H_{\mu\nu}^0 + \frac{1}{2} S_{\mu\nu} \sum_C (\gamma_{AC} + \gamma_{BC}) \Delta Q_C \quad (18)$$

for $A \in \mu$ and $B \in \nu$. Since ΔQ_C is dependent on the density matrix, the Hamiltonian matrix is dependent on the electronic structure. Therefore, the variational parameters within DFTB2 are determined iteratively by solving the eigenvalue problem self-consistently. Consequently, DFTB2 is 5–15 times slower than DFTB1.

2.3 DFTB3

In 2011, Gaus et al. [16] introduced two formal advancements to the DFTB2 as described in 2006 [11]. First, the third-order Taylor expansion term of the exchange–correlation energy in Eq. (2) was introduced. Intuitively, the chemical hardness of an atom should be dependent on its charge state. However, chemical hardness, which is relevant to Hubbard value, is constant within DFTB2; this has severely limited

applying DFTB to highly charged systems, such as an anion and cation system. The third-order term introduced the charge-dependence of the γ_{AB} function in the DFTB formalism. Omitting the detailed derivation, the final energy within DFTB3 was expressed as

$$\begin{aligned}
 E^{\text{DFTB3}} &= E^{\text{DFTB2}} + \frac{1}{6} \sum_{A,B} (\Gamma_{AB} \Delta Q_A + \Gamma_{BA} \Delta Q_B) \Delta Q_A \Delta Q_B \\
 &= \sum_{A>B} E_{AB}^{\text{rep}} + \sum_{\mu\nu} D_{\mu\nu} H_{\mu\nu}^0 + \frac{1}{2} \sum_{A,B} \gamma_{AB} \Delta Q_A \Delta Q_B \\
 &\quad + \frac{1}{6} \sum_{A,B} (\Gamma_{AB} \Delta Q_A + \Gamma_{BA} \Delta Q_B) \Delta Q_A \Delta Q_B. \quad (19)
 \end{aligned}$$

The last term is derived from the third-order expansion term in Eq. (3). The newly introduced function Γ_{AB} is dependent on the distance between atoms A and B , the Hubbard values of them, and the derivative of the Hubbard values with respect to charge fluctuation:

$$\Gamma_{AB} = \left. \frac{\partial \gamma_{AB}}{\partial Q_A} \right|_{Q_A^0} = \frac{\partial \gamma_{AB}}{\partial U_A} \frac{\partial U_A}{\partial Q_A} \Big|_{Q_A^0} \quad (A \neq B). \quad (20)$$

Analytic expressions of Γ_{AB} and γ_{AB} are derived in the Supporting Information Ref. [16]. Historically, the DFTB3 was used with diagonal terms only; $\Gamma = 0$ for $A \neq B$. Nowadays, this diagonal approximation is not usually employed. The Hamiltonian matrix in DFTB3 is

$$\begin{aligned}
 H_{\mu\nu} &= H_{\mu\nu}^0 + \frac{1}{2} S_{\mu\nu} \sum_C (\gamma_{AC} + \gamma_{BC}) \Delta Q_C \\
 &\quad + \frac{1}{6} S_{\mu\nu} \sum_C \{2(\Gamma_{AC} \Delta Q_A + \Gamma_{BC} \Delta Q_B) + (\Gamma_{CA} + \Gamma_{CB}) \Delta Q_C\} \Delta Q_C. \quad (21)
 \end{aligned}$$

Thus, DFTB3 also requires iterative treatment. The convergence of SCF with DFTB3 is usually similar to that with DFTB2, but one or two more cycles may be needed.

The second advancement was the modification of the gamma function introduced in DFTB2: $\gamma_{AB} \rightarrow \gamma_{AB}^h$. The necessity of this modification arose from the difference of chemical hardness between isolated and covalently bonded hydrogen atoms. Thus, this modification improved the calculation of the binding energy in hydrogen bonding. Here, γ_{AB} and γ_{AB}^h are not explicitly distinguished because the difference only affects the electronic structure indirectly. Γ_{AB} is a function of γ_{AB} and is, therefore, also affected.

2.4 Long-Range Corrected DFTB

The most recent and important development in DFTB is the long-range corrected DFTB (LC-DFTB). The first two practical implementation and benchmark studies were reported in 2015 by Humeniuk et al. [27] and Lutsker et al. [28], although the initial formulation was outlined in 2012 by a coauthor of the latter study [29]. The central idea of LC-DFTB is to add Hartree–Fock-like exchange contributions to the DFTB formalism. As the DFTB total energy was derived from the DFT energy with a GGA exchange–correlation functional, the addition of Hartree–Fock-like exchange terms is not completely straightforward [28]. In its current implementation, the reference Hamiltonian matrix elements are obtained using the BNL range-separated functional[30], and the Hartree–Fock-like exchange terms for the density perturbation are obtained using difference density matrices of the one-particle density.

The total energy of LC-DFTB [28] can be written as

$$E^{\text{LC-DFTB}} = \sum_{A>B} E_{AB}^{\text{rep}} + \sum_{\mu\nu} D_{\mu\nu} H_{\mu\nu}^0 + \frac{1}{2} \sum_{A,B} \gamma_{AB} \Delta Q_A \Delta Q_B - \frac{1}{4} \Delta D_{\mu\nu} \Delta D_{\rho\sigma} \sum_{\mu\nu\rho\sigma} (\mu\rho|\sigma\nu)^{\text{lr}}, \quad (22)$$

where

$$(\mu\rho|\sigma\nu)^{\text{lr}} = \frac{1}{4} S_{\mu\rho} S_{\sigma\nu} (\gamma_{AD}^{\text{lr}} + \gamma_{AB}^{\text{lr}} + \gamma_{CD}^{\text{lr}} + \gamma_{CB}^{\text{lr}}), \quad (23)$$

and $\Delta D_{\mu\nu}$ is the difference between $D_{\mu\nu}$ and the reference density matrix, $D_{\mu\nu}^0$: $\Delta D_{\mu\nu} = D_{\mu\nu} - D_{\mu\nu}^0$. The reference density matrix is a diagonal matrix with the number of electrons of free neutral atoms in each AO. The last term in Eq. (22) is the newly added Hartree–Fock-like exchange term. The long-range gamma function γ_{AB}^{lr} is similar to γ_{AB} in DFTB2 and DFTB3, but with an additional dependence on the range-separated parameter ω . In LC-DFT literature, the parameter may be written as μ . This formalism is based on DFTB2; as there is no term with Γ_{AB} , there are no reports for LC-DFTB3 developments at the moment.

LC-DFTB was shown to be roughly ten times more expensive than conventional DFTB, although DFT calculations are 50 times slower than LC-DFTB [28]. Nevertheless, LC-DFTB decreases the self-interaction error, and applications to excited-state calculations [27, 31] have demonstrated that HOMO–LUMO gaps and charge transfer excitation energies are much improved.

2.5 Parameters

In tight binding calculations, in general, it is essential to prepare Slater–Koster parameters prior to simulation, and DFTB is no exception, as already mentioned above.

These parameters are defined for each pair of elements; for water, four combinations are needed: O–O, O–H, H–O, and H–H. The two mixed parameters are required because of possible sign changes in integrals involving orbitals with non-zero angular momentum. Various parameters are employed in DFTB and a number of these parameters are available on the DFTB website [32]. To perform DFTB1 calculations, users have to supply $H_{\mu\nu}^0$, $S_{\mu\nu}^0$, and E_{AB}^{rep} parameters. These are already summarized in Slater–Koster tables, so users simply have to specify the file locations. Users also need Hubbard values for DFTB2, and these have also been tabulated. For DFTB3, users need the derivative of the Hubbard values with respect to charge fluctuation, which has to be given separately. Because many parameters are still missing, not all elements can be treated with DFTB.

3 Basics of the FMO-DFTB Method

A brief history of the methodological development of FMO-DFTB is first presented. The first FMO-DFTB study reported the geometry optimization of a one-million-atom system and was published in 2014 [17]. At that time, only two-body interactions within FMO (FMO2) were considered and the DFTB model employed was only DFTB2: FMO2-DFTB2. The implemented gradient was not fully analytic and response terms coming from the use of ESP that are determined in the monomer cycle were neglected. In the next year, extensions to FMO2-DFTB3 [33] and fully analytic gradient [34] were implemented. Since then, all FMO-DFTB developments have included a fully analytic gradient and an extension to DFTB3. In 2016, FMO-DFTB was combined with the polarizable continuum model (PCM) [35], and an approximate Hessian with FMO-DFTB was implemented by Nakata [36]. In 2017, three-body interactions were included, namely FMO3-DFTB [37]. In 2018, FMO-DFTB was combined with an alternative fragmentation approach for cutting covalent bonds, termed as the adaptive frozen orbital (AFO) method [38]. At that time, FMO-DFTB was the only method using an analytic gradient within AFO because of the complexity of determining the electronic structure [39].

In the following subsections, only the FMO2-DFTB3 formalism is employed. DFTB2 formalism can be obtained by setting $\Gamma_{AB} = 0$. As the extension to FMO3 is straightforward and there is a large overlap between DFTB and other ab initio methods, three-body terms are not explicitly introduced here.

All of these features presented in this chapter are publicly available through the official version of GAMESS-US [40, 41]. DFTB and FMO-DFTB in GAMESS-US were first officially released in 2014. Major updates were executed in 2016 and 2018, and the latter release includes almost all developments presented in this chapter.

3.1 Formalism of FMO-DFTB: Energy

Again, the total energy within FMO2 is given by

$$E = \sum_I^N E'_I + \sum_{I>J}^N (E'_{IJ} - E'_I - E'_J) + \sum_{I>J}^N \Delta E_{IJ}^V, \quad (24)$$

where N is the number of fragments and E'_I is the internal energy of fragment I , defined by

$$E'_X = \sum_{A>B \in X} E_{AB}^{\text{rep}} + \sum_{\mu\nu \in X} D_{\mu\nu}^X H_{\mu\nu}^{0,X} + \frac{1}{2} \sum_{A,B \in X} \gamma_{AB} \Delta Q_A^X \Delta Q_B^X + \frac{1}{6} \sum_{A,B \in X} (\Gamma_{AB} \Delta Q_A^X + \Gamma_{BA} \Delta Q_B^X) \Delta Q_A^X \Delta Q_B^X. \quad (25)$$

This expression is almost identical to Eq. (19) but includes the fragment index. For convenience, the hybrid orbital projection operator $P_{\mu\nu}^X$ is included in the non-perturbed Hamiltonian $H_{\mu\nu}^{0,X}$. $P_{\mu\nu}^X$ for FMO-DFTB is computed here similarly as in other methods. The energy of the charge transfer between fragments I and J in embedding ESP can be written as

$$\Delta E_{IJ}^V = E_{IJ,IJ}^V - E_{I,IJ}^V - E_{J,IJ}^V. \quad (26)$$

In the case of DFTB, the electrostatic interaction between the atoms in fragment X and the atoms in the total system excluding fragment Y is given by

$$E_{X,Y}^V = \sum_{A \in X} \sum_{K \neq Y} \sum_{B \in K} \left\{ \gamma_{AB} \Delta Q_A^X \Delta Q_B^K + \frac{1}{3} (\Gamma_{AB} \Delta Q_A^X + \Gamma_{BA} \Delta Q_B^K) \Delta Q_A^X \Delta Q_B^K \right\}. \quad (27)$$

The first term in Eq. (27) originates from the second-order term, corresponding to the last term in Eq. (16), which originates in the sum of Coulomb interactions and the second-order expansion of the exchange–correlation energy (see the third line of Eq. (3)). The second term in Eq. (27) comes from the third-order term describing an expansion of the exchange–correlation functional, thus physically corresponding to exchange–correlation contributions to the ESP.

The Hamiltonian matrix within FMO-DFTB3 (with hybrid orbital projection) is written as

$$H_{\mu\nu}^X = H_{\mu\nu}^{0,X} + S_{\mu\nu}^X \Omega_{AB}^{X(X)} + V_{\mu\nu}^X \quad (28)$$

for $\mu \in A$ and $\nu \in B$, where the second and third terms come from the internal (atoms in fragment X) and external (atoms outside the fragment X) embedding, respectively. By defining for atoms $A, B \in X$ as

$$\Omega_{AB}^{X(Y)} = \sum_{C \in Y} \left\{ \frac{1}{2} (\gamma_{AC} + \gamma_{BC}) + \frac{1}{3} (\Gamma_{AC} \Delta Q_A^X + \Gamma_{BC} \Delta Q_B^X) + \frac{1}{6} (\Gamma_{CA} + \Gamma_{CB}) \Delta Q_C^Y \right\} \Delta Q_C^Y, \quad (29)$$

the external embedding potential can be written as

$$V_{\mu\nu}^X = \sum_{K \neq X} V_{\mu\nu}^{X(K)} = S_{\mu\nu}^X \sum_{K \neq X} \Omega_{AB}^{X(K)}. \quad (30)$$

Again, the second and third terms in Eq. (29) come from exchange–correlation-like contributions. Since the ESP is already expressed with Mulliken charges, the point charge approximation is always employed within DFTB.

It is important to analyze the $E^{2\text{nd}}$ term for $A = B$:

$$\frac{1}{2} \sum_{A \in X} \gamma_{AA} (\Delta Q_A^X)^2 = \frac{1}{2} \sum_{A \in X} U_A (\Delta Q_A^X)^2. \quad (31)$$

Because U_A is non-zero, $E^{2\text{nd}}$ for $A = B$ is also non-zero. This is a typical symptom of the self-interaction error. The residual value comes from the second-order term of the Taylor expansion (the term proportional to the inverse of the distance is canceled [14]), so the origin of this self-charge interaction seemingly inherits from the self-interaction error of the exchange–correlation functional in DFT. Special care thus has to be paid when evaluating ESP within FMO-DFTB if the system under consideration requires fragmentation across covalent bonds. ESP contributions from the same atom belonging to different fragments cannot be ignored. This also applies to third-order terms.

The introductions of two-electron integral-like terms in DFTB3 for $\mu \in A, \nu \in B, \rho \in C$, and $\sigma \in D$:

$$\begin{aligned} (\mu\nu||\rho\sigma)^{X,Y} &= (\mu\nu|\rho\sigma)^{X,Y} \\ &= \frac{1}{4} S_{\mu\nu}^X S_{\rho\sigma}^Y (\gamma_{AC} + \gamma_{BC} + \gamma_{AD} + \gamma_{BD}) \\ &\quad + \frac{1}{6} S_{\mu\nu}^X S_{\rho\sigma}^Y \{ (\Gamma_{CA} + \Gamma_{CB}) \Delta Q_C^Y + (\Gamma_{DA} + \Gamma_{DB}) \Delta Q_D^Y \} \\ &\quad + \frac{1}{6} S_{\mu\nu}^X S_{\rho\sigma}^Y \{ (\Gamma_{AC} + \Gamma_{AD}) \Delta Q_A^X + (\Gamma_{BC} + \Gamma_{BD}) \Delta Q_B^X \}, \quad (32) \end{aligned}$$

allows the ESP to be written as

$$V_{\mu\nu}^X = \sum_{K \neq X} \sum_{\rho\sigma \in K} (\mu\nu||\rho\sigma)^{X,K} \Delta D_{\rho\sigma}^K. \quad (33)$$

This expression has some connections with FMO-HF and FMO-DFT, although FMO-DFTB benefits from a number of simplifications, resulting in expressions with Mulliken charges (Eqs. 29 and 30).

Efforts are also being made to combine FMO with the recently developed LC-DFTB [28]. In terms of the formalism, the main difference is the addition of exchange contributions to the two-electron integral-like term (Eq. 32):

$$\begin{aligned}
 (\mu\nu||\rho\sigma)^{X,Y} &= (\mu\nu|\rho\sigma)^{X,Y} - \frac{\delta_{XY}}{2} (\mu\rho|\sigma\nu)^{\text{lr},X} \\
 &= \frac{1}{4} S_{\mu\nu}^X S_{\rho\sigma}^Y (\gamma_{AC} + \gamma_{BC} + \gamma_{AD} + \gamma_{BD}) \\
 &\quad - \frac{\delta_{XY}}{8} S_{\mu\rho}^X S_{\sigma\nu}^X (\gamma_{AD}^{\text{lr}} + \gamma_{AB}^{\text{lr}} + \gamma_{CD}^{\text{lr}} + \gamma_{CB}^{\text{lr}})
 \end{aligned} \tag{34}$$

Only intra-fragment exchange contributions are considered, as they are not considered in other FMO-related methods.

3.2 Formalism of FMO-DFTB: Gradient

As the total energy of FMO is not fully variationally determined, differentiation of the energy gives rise to response terms of the electronic structure. In FMO, such response contributions can be efficiently computed by solving self-consistent Z-vector (SCZV) equations [42]. This approach has been applied to ab initio methods. DFTB is not an exception; the response terms are computed to obtain accurate first-order derivatives in a similar manner.

As reported by Ref. [34], the error of the gradient without response contributions is on the order of 5.0×10^{-4} Hartree/Bohr, is greater than the default convergence criterion of GAMESS-US, and is particularly severe when combined with the AFO approach. With FMO2-DFTB3/AFO, the maximum error has been reported as large as 10^{-3} Hartree/Bohr. The analytic gradient is 100 times more accurate, and the remaining error likely stems from the limited accuracy of numerical derivatives. Approximate gradients are rather accurate with FMO3, but the error is still on the order of 10^{-4} Hartree/Bohr.

After derivation, first-order derivatives with FMO-DFTB (with hybrid orbital projection) may be written as

$$\frac{\partial E}{\partial a} = \sum_I^N E_I^{\prime a} + \sum_{l>J}^N (E_{IJ}^{\prime a} - E_I^{\prime a} - E_J^{\prime a}) + \sum_{l>J}^N \Delta E_{IJ}^{V,a} + \mathfrak{R}^a, \tag{35}$$

where $E_X^{\prime a}$ and $\Delta E_{IJ}^{V,a}$ are the terms that come from the derivative of the integrals for E_X^{\prime} and ΔE_{IJ}^V , respectively. \mathfrak{R}^a represents the response and can be written by

$$\mathfrak{R}^a = 4 \sum_I^N \sum_{m \in I}^{\text{virt}} \sum_{i \in I}^{\text{occ}} \mathcal{L}_{mi}^I U_{mi}^{a,I}, \tag{36}$$

where the Lagrangian is

$$\mathcal{L}_{ij}^K = \sum_{I>J(\neq K)}^N \left(V_{ij}^{K(IJ)} - V_{ij}^{K(I)} - V_{ij}^{K(J)} \right) \quad (37)$$

and the unitary transformation matrix $U_{ij}^{a,I}$ is relevant to the derivative of the MO coefficient

$$\frac{\partial C_{\mu i}^I}{\partial a} = \sum_{m \in I}^{\text{all}} C_{\mu m}^I U_{mi}^{a,I} . \quad (38)$$

In FMO-DFTB, the coupled-perturbed (CP) DFTB equation for fragment X can be written as

$$\sum_K^N \sum_{k \in K}^{\text{virt}} \sum_{l \in K}^{\text{occ}} \mathcal{A}_{ij,kl}^{X,K} U_{kl}^{a,K} = \mathcal{B}_{ij}^{a,X} , \quad (39)$$

where

$$\mathcal{A}_{ij,kl}^{X,K} = (\varepsilon_j^X - \varepsilon_i^X) \delta_{ik} \delta_{jl} \delta_{XK} - 4 (ij||kl)^{X,K} \quad (40)$$

and

$$\mathcal{B}_{ij}^{a,X} = F_{ij}^{(a),X} - \varepsilon_j^X S_{ij}^{a,X} . \quad (41)$$

$F_{ij}^{(a),X}$ and $S_{ij}^{a,X}$ contains the derivative of integrals, and the former also contains the renormalization terms. After solving the Z -vector equation

$$\sum_I^N \sum_{i \in I}^{\text{virt}} \sum_{j \in I}^{\text{occ}} Z_{ij}^I \mathcal{A}_{ij,kl}^{I,K} = \mathcal{L}_{kl}^K \quad (42)$$

for all fragments K ($k \in \text{virt}$, $l \in \text{occ}$) self-consistently, the response contribution can be computed by

$$\mathfrak{R}^a = \sum_I^N \sum_{i \in I}^{\text{virt}} \sum_{j \in I}^{\text{occ}} Z_{ij}^I \mathcal{B}_{ij}^{I,a} . \quad (43)$$

These expressions are similar to those given for FMO-HF.

Employing AFO further complicates the algorithm. The first complication is due to the frozen and projected orbital terms in the Hamiltonian matrix. This necessitates solving Z -vector equations in dimers and trimers in addition to SCZV equations. The second complication comes from the use of localized orbitals determined in model systems. Consequently, two types of Z -vector equations must be solved, derived from CP localization and the standard CP equations. In total, four types of Z -vector equations are solved, as outlined in Ref. [39], which contains 111 equations.

3.3 Implementation Notes

As all implementations of FMO-DFTB are parallelized with the generalized distributed data interface (GDDI) [43], FMO-DFTB is parallelized to utilize multiple computer nodes. In GDDI, all of the CPU cores are divided into groups and independent jobs (e.g., fragment calculations) are performed in each group. In principle, each group may consist of more than one CPU core and can do jobs in parallel. At present, however, FMO-DFTB is not efficiently parallelized within each group. Therefore, although it is possible to perform hybrid parallelization (GDDI/DDI; similar to MPI/OpenMPI), this is not efficient. Thus, the developers of FMO-DFTB always assign one CPU core per group.

Dispersion corrections are also implemented for FMO-DFTB. Universal force-field (UFF) [44, 45], Slater–Kirkwood [46], and Grimme’s dispersion [47–49] models can be combined. Since these dispersion models are not dependent on the electronic structure of the system, the value computed with FMO-DFTB exactly reproduces that of full DFTB (i.e., without fragmentation).

In the most recent implementation, results demonstrated the possibility to significantly eliminate the ESP evaluation for dimers (and trimers). As ESP evaluation scales as quadratic, improving this step is of great importance. ESP for dimers may be written and transformed as

$$\begin{aligned}
 V_{\mu\nu}^{IJ} &= S_{\mu\nu}^{IJ} \sum_{K \neq I, J}^N \Omega_{AB}^{IJ(K)} \\
 &= S_{\mu\nu}^{IJ} \sum_{K \neq I, J}^N \left(\Omega_{AB}^{I(K)} + \Omega_{AB}^{J(K)} \right) \\
 &= S_{\mu\nu}^{IJ} \left(\sum_{K \neq I}^N \Omega_{AB}^{I(K)} + \sum_{K \neq J}^N \Omega_{AB}^{J(K)} - \Omega_{AB}^{I(J)} - \Omega_{AB}^{J(I)} \right) \\
 &= S_{\mu\nu}^{IJ} \left(\Omega_{AB}^I + \Omega_{AB}^J - \Omega_{AB}^{I(J)} - \Omega_{AB}^{J(I)} \right). \tag{44}
 \end{aligned}$$

Ω_{AB}^I and Ω_{AB}^J are the ESP for fragment I and J , respectively. As they are not dependent on the combination of I and J , they can be constructed before dimer calculations begin. The computation of Ω_{AB}^{IJ} is then reduced to subtracting the $\Omega_{AB}^{I(J)}$ and $\Omega_{AB}^{J(I)}$ terms. They are calculated in the dimer IJ and thus can be evaluated quickly. A native implementation requires the evaluation of ESP N_{dimer} times, where N_{dimer} is the number of dimers, but the transformation above indicates that the number of the evaluation is decreased to only one. This simplification is only applicable to FMO-DFTB. In addition, if boundary atoms are bond-detached atoms, double counting has to be avoided.

3.4 Computational Efficiency of FMO-DFTB

In 2014, FMO-DFTB scaling for water clusters was reported as $\mathcal{O}(N^{1.21})$ with up to 18,432 atoms. After a number of improvements, new scaling values must be reported. A comparison between the time required to perform a single point gradient calculation at the level of full DFTB3 and FMO2-DFTB3 for the same water clusters is reported in Fig. 1a. The time of full DFTB3 for $N_{\text{at}} > 9216$ is an extrapolated estimate. The observed scaling with full DFTB3 is $\mathcal{O}(N^{2.97})$, very close to the theoretical scaling (cubic). The DSYEVD driver, which is likely the fastest LAPACK diagonalization, was employed. FMO2-DFTB3 took only 129.0 s. The observed scaling was $\mathcal{O}(N^{1.45})$, higher than the previously reported scaling. This is because the most time-consuming step in FMO-DFTB became the evaluation of ESP during monomer SCC iteration, which scales as purely quadratic. Monomer SCC and dimer calculations took 48.1 and 20.3 s, respectively. In addition, evaluating the gradients require solving SCZV equations, which are conceptually similar to monomer SCC, so this step also involves the quadratic scaling step. Nevertheless, FMO-DFTB is more than one thousand times faster than full DFTB for the largest system.

It is also interesting to compare the performance of FMO-DFTB2 and -DFTB3 (Fig. 1b). Overall, FMO-DFTB3 is roughly twice as expensive as FMO-DFTB2, because the evaluation of ESP, which is the most time-consuming step, involves more terms (Γ , see Eq. 29). The scaling of FMO-DFTB2 energy is $\mathcal{O}(N^{1.16})$, which is to be compared with the previous scaling $\mathcal{O}(N^{1.21})$ [17]. As mentioned, solving a set of SCZV equations requires a similar computational effort to solving a monomer SCC. Therefore, gradient evaluation requires almost twice the computational effort.

The scaling of the computation of the Hessian with FMO-DFTB was $\mathcal{O}(N^{2.00})$ and $\mathcal{O}(N^{1.98})$ with one and six CPU cores, respectively [36]. With six CPU cores (Xeon E5-1650 v3), the second-order derivative calculation for 10,041 atoms (water) finished in only 17.2 min, whereas normal mode analysis required 262.4 min for computation. The bottleneck of the analysis was the diagonalization of the Hessian

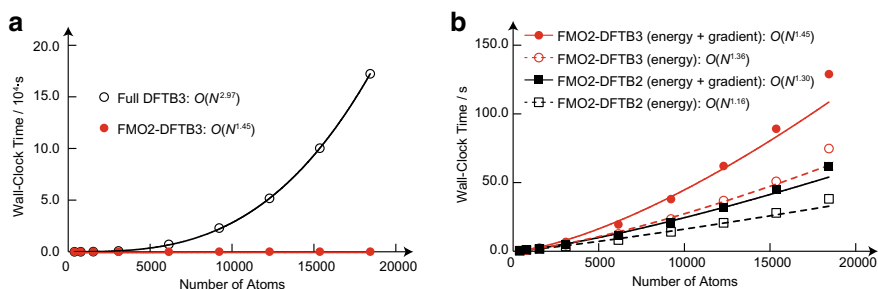


Fig. 1 **a** Wall-clock times of full DFTB3 and FMO2-DFTB3, and **b** comparison of FMO2-DFTB2 and -DFTB3 on one CPU core of Xeon E5-1650 v3

matrix. Considering the performance of FMO-DFTB, it could easily be applied to larger systems; however, as the memory requirement scales as quadratic, this will be a severe problem.

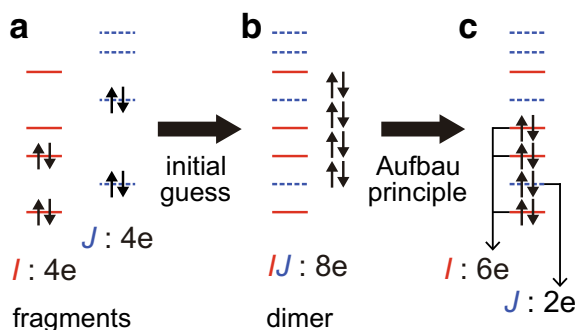
4 Selected Applications

4.1 *Molecular Dynamics Simulations*

Molecular dynamics (MD) simulations with FMO-DFTB have been applied to halogen halides (HF, HCl, HBr, and HI) [34], solvated sodium cation [37], and boron nitride nano-rings [39]. In all cases, the gradient was computed analytically, as gradient inaccuracy introduces artificial effects such as an energy drift in the energy-conservative ensemble. In the first example [34], one million MD steps were performed for systems consisting of 2,000 atoms and the first peak of halogen–halogen radial pair distribution functions obtained experimentally and with FMO-DFTB were compared. Agreement between experimental and computational functions was rather dependent on the chosen DFTB and dispersion models. After many test calculations, FMO-DFTB2 with the UFF-type dispersion model was selected for use. The second example demonstrated a comparative performance of FMO2- and FMO3-DFTB3 [37]. A sodium cation was placed in the center of 473 water molecules; 100 ps MD simulations were performed (100,000 steps). Because the charge in the central sodium cation is prone to delocalize over the surrounding atoms, the inclusion of three-body effects is essential. The coordination numbers obtained with FMO2 and FMO3 were 8.9 and 6.5, respectively; FMO3 gave a value closer to other simulations (5–6), whereas FMO2 significantly overestimated it. This is likely because FMO2 tends to overestimate the binding between fragments in the confined relaxation space. In this simulation, the time step was 1 fs with the help of RATTLE [50] constraints.

The last case employed boron nitride nano-rings [39] and demonstrated that FMO-DFTB may be applicable to MD simulations for one-million-atom systems. Five hundred MD steps over the course of 181 h were performed for the system, which contained 1,180,800 atoms. Unlike other linear-scaling methods, FMO-DFTB is uniquely suited to performing on laboratory-scale computers; the calculation was performed with only 24 CPU cores on a single computer node. Although this simulation was rather short, it demonstrates that, provided more computer resources are available, FMO-DFTB may be applicable to longer and larger simulations and will be a useful tool for understanding the dynamics of large systems.

Fig. 2 Origin of the problem of charge transfer states in dimers. **a** Orbital energies in monomers *I* (red solid lines) and *J* (blue dashed lines) **b** Initial levels in dimer *IJ* **c** Population of initial levels in dimer *IJ* Reproduced from Ref. [35] by permission of the PCCP Owner Societies



4.2 Proteins

Due to self-interaction, DFTB cannot accurately describe orbital energies; applying FMO-DFTB to proteins had thus been problematic until it was combined with PCM. Specifically, deriving DFTB with DFT causes the electronic structure parameters to be fitted to results obtained with the PBE exchange–correlation functional. Additionally, DFTB also underestimates the gap between the highest occupied MO (HOMO) and the lowest unoccupied MO (LUMO). This effect is particularly prominent when fragments have a net charge. The use of DFTB3 improved charge–charge interactions, but not necessarily orbital energies.

A typical consequence of self-interaction is that the orbital levels of fragments with positive and negative charges are akin to be low and high, respectively, with FMO-DFTB. This problem does not directly affect calculations during monomer SCC because orbital levels of fragments do not couple directly. However, in the dimer calculation, *I* and *J* are merged and this causes a problem. For instance, let's assume that fragments *I* and *J* have a positive and negative charge (both have four electrons), respectively, and that the LUMO of fragment *I* is lower than the HOMO of fragment *J* when constructing the dimer *IJ*. Next, an initial guess can be constructed by placing electrons obeying the Aufbau principle. Now, the atoms that belong to fragments *I* and *J* get six and two electrons, respectively, not four and four, resulting in a charge transfer state. Consequently, a charge-transferred electronic structure or a lack of SCF convergence is possible. The situation is schematically depicted in Fig. 2. To combat this, the 1L2Y protein in the original FMO-DFTB paper was neutralized [17].

Once FMO-DFTB was combined with PCM, no such switch occurs. The origin of incorrect orbital energies is partially attributed to strong charge–charge interactions within charged residues and could be alleviated by adding solvent screening effects. This problem is not unique to DFTB; as discussed in Ref. [35], a similar problem occurs with GGA and some hybrid functionals. A more systematic solution may employ a long-range corrected functional. At the Hartree–Fock limit, no such problem occurs, as there is no self-interaction error.

There are four FMO2/PCM (PCM[1], PCM⟨1⟩, PCM[1(2)], and PCM[2]) and six (the former four and PCM[1(3)] and PCM[3]) FMO3/PCM levels, depending on the construction of ESP on the apparent surface charge (ASC) and the scaling for the solute–solvent interaction energy. FMO-DFTB can be combined with any PCM variants. The difference is summarized in Table 1 in Ref. [35]. Analytic derivatives have been developed only when combined with PCM⟨1⟩.

With FMO2-DFTB3-D(UFF)/PCM⟨1⟩, medium-sized proteins up to 3,578 atoms could be optimized. The root-mean-square deviations of the largest optimized structure (PDB: 2CGA) compared with the experimental structure was 0.720 Å. This experimental structure was obtained from X-ray crystallography with a resolution of 1.8 Å. Calculations combined with PCM are somewhat slower than those in a vacuum because linear equations must be solved to obtain ASCs. Nevertheless, the observed scaling (FMO2-DFTB3-D/PCM⟨1⟩ energy + gradient) was $\mathcal{O}(N^{1.39})$, and the performance is still useful for medium to large systems.

Although adding solvent effects circumvented the problem, a more promising and fundamental solution is to apply long-range corrections to DFTB. Ref. [35] showed that the HOMO–LUMO gap problem disappeared when long-range corrected functionals were employed in DFT calculations. Ref. [28] demonstrated that LC-DFTB allows gas phase calculations of the proteins for which the conventional DFTB failed because of the underestimation of HOMO–LUMO gap, which originates from the self-interaction error. Preliminary results demonstrate that FMO-LC-DFTB also does not suffer from this problem.

4.3 Chemoinformatics

Apart from FMO-DFTB, DFTB has been often applied to biosystems; detailed expositions may be found in published reviews [4, 5, 10, 51]. Considering that the development of DFTB2 and DFTB3 has been motivated by describing proper interactions within charged systems, DFTB should be a promising tool for biosystems. Moreover, the fast execution of DFTB calculations should be an appealing feature in the area of chemoinformatics, as the structures and properties of thousands of molecules can quickly be calculated with DFTB. One important development in applying DFTB to biosystems is the combination of DFTB with molecular mechanics (MM), DFTB/MM. An early implementation has been realized in 2001 [52] by Cui et al. DFTB/MM was applied to ATP hydrolysis [53, 54] and cytochrom *c* oxidase [55]. It was also recently applied to evaluate the binding interactions between proteins and ligands, including binding interactions between drugs and H1N1 neuraminidase-1 [56] and docking simulations of zinc-bound ligands [57]. A more practical application of DFTB to chemoinformatics may be found in a study by Qu et al. [58]. Here, DFTB was used to optimize more than 900 molecules to train machine learning models. The trained data could then predict bond dissociation energies of 100 molecules.

Although DFTB is much faster than other *ab initio* methods, its cubic-scaling computational cost has been a major limitation in applying DFTB to larger and/or a large number of systems. Using the QM/MM approach is very useful, especially when focusing on the reaction center of the protein. However, when treating the whole system on equal footing, e.g., to investigate interactions between a protein and ligands, full DFTB or QM/MM approaches may not be the best choice. Furthermore, the combination with FMO is beneficial for the use of pair interaction energy decomposition analysis (PIEDA). Details of PIEDA are described somewhere in this book. Recently, FMO-DFTB was also combined with PIEDA [59]. In this context, in spite of the aforementioned challenge of orbital energies, FMO-DFTB combined with PCM is seemingly a promising tool to investigate interactions between proteins and ligands. FMO-DFTB was applied to the assessment of receptor-ligand interactions and total interaction energies [60]. Here, the quantities computed with FMO-DFTB were validated by comparison with experimental data and FMO-MP2 results; good correlation was found between total interaction energies computed with FMO-DFTB and FMO-MP2 ($R^2 > 0.9$), while the computational cost was reduced by 1000 times.

A similar correlation study was presented by Ref. [35]. Comparing the solvent screening and pair interactions obtained with FMO-DFTB and FMO-DFT (LC-BOP and M11 functionals) showed that the correlations of these parameters were very high with R^2 values greater than 0.97, while the computational cost was reduced by 4,840 times for the IIO5 protein (1,961 atoms). These pilot demonstrations indicate that FMO-DFTB is potentially very useful in the process of drug discovery in which a number of interacting energies between proteins and ligands must be evaluated with a sufficiently accurate method.

4.4 Vibrational Frequency Analysis

Vibrational frequency analysis was applied using FMO-DFTB in two studies [36, 37]. In both, non-resonance Raman spectra were also simulated. Polarizability derivatives were evaluated by the numerical differentiation of gradients under electric fields. Nakata et al. simulated infrared spectra of the epoxy amine oligomers in a system of more than 1000 atoms and compared them with experimental data [36]. Three characteristic peaks were experimentally observed: 1183, 1260, and 3450 cm^{-1} resulting from CH_3 groups in isopropylidene, benzene rings, and hydroxyl groups, respectively. The simulation used one chain of epoxy amine (279 atoms) to show that FMO2-DFTB3 predicted a shift of approximately 150 cm^{-1} , but the use of four chains predicted a peak at 3431 cm^{-1} . Systems of this size are not easy to evaluate even with the conventional DFTB, as the scaling of Hessian is formally $\mathcal{O}(N^4)$.

Another study applied FMO3-DFTB to three isomers of polyalanine and solvated sodium cation [37]. The maximum frequency deviation in FMO3-DFTB3 was less than 10 cm^{-1} , compared with the corresponding frequency computed with full DFTB calculations. Comparison of infrared and Raman spectra of the solvated sodium

cation showed that FMO3-DFTB had a higher accuracy than FMO2 by a factor of 2.5.

4.5 Charge Transport Materials

DFTB has also been applied to describe the electron transfer mechanism of organic molecules and conductors, DNA, and peptides [61–66]. This approach, called “fragment orbital”-DFTB, is similar to the FMO method. It begins with dividing a system into fragments, obtaining HOMOs of each fragment, and then constructing the charge transfer (coupling) integrals by the standard AO–MO transformation:

$$H_{IJ} = \sum_{\mu \in I} \sum_{\nu \in J} C_{\mu i}^I C_{\nu j}^J \langle \phi_{\mu} | \hat{H} | \phi_{\nu} \rangle, \quad (45)$$

where I and J are the index of fragments and $i \in I$ and $j \in J$ represent the index of HOMOs. On-site energies are the orbital level of the HOMO.

Conceptually, there is a large overlap between the fragment orbital and FMO approaches. FMO uses more well-defined fragments with the help of hybrid orbital projection, allowing the application of it to covalently bonded systems to be straightforward and robust. A similar analysis using the linear combination of fragment molecular orbital (LCMO) approach has been studied previously [67, 68]. Recently, Kitoh-Nishioka et al. applied the LCMO approach to FMO-DFTB and performed detailed analysis of the charge transport properties of covalent organic frameworks by combining classical MD, FMO-DFTB, and carrier dynamics simulations [69]. In estimating charge transfer integrals, the standard DFTB parameters were rather “confined” and thus not suitable for evaluation, so unconfined parameters called “8–∞” were employed, similar to previous studies [65, 66]. The confinement of the standard parameters originates from the tight-binding DFTB characters. In spite of the use of unconfined parameters, DFTB still underestimated transfer integrals, and scaling was essential to reproduce LC-BLYP results. Nevertheless, the combination of FMO-DFTB with LCMO should be an important tool for more practical applications using larger systems.

5 Conclusion and Outlook

FMO-DFTB is currently the fastest quantum chemical method among the available FMO-electronic structure method combinations. The scaling of FMO2-DFTB3 is at present $\mathcal{O}(N^{1.45})$ for evaluating the energy gradient and $\mathcal{O}(N^{2.00})$ for evaluating the Hessian. The most favorable scaling was achieved with FMO2-DFTB2, $\mathcal{O}(N^{1.16})$. For a water cluster consisting of 18,432 atoms, a single point gradient calculation

with FMO2-DFTB3 finished in 129.0 0 s with only one CPU core. This development has enabled geometry optimizations and short MD simulations for systems consisting of more than one million atoms and vibrational frequency calculations for those of ten thousand atoms. Typical applications are soft matter and polymers including biosystems. A recent development employing AFOs further widened the range of application into the range of materials.

In spite of these advancements, there is still large room for development. Recent developments are still restricted to closed-shell single electron structure and FMO-DFTB still cannot be applied to systems with radicals. FMO-DFTB can be potentially combined with linear-response time-dependent DFTB, which has already been developed in GAMESS-US. Extensions using periodic boundary conditions are of great importance for bulk systems.

The limitations of DFTB caused by the self-interaction inherent in DFT pose serious problems. The underestimation of HOMO–LUMO gaps is attributed to this drawback. Although this problem was circumvented by adding solvent screening effects, a more pragmatic solution lies in further development of long-range corrected DFTB (LC-DFTB). Developments of FMO around LC-DFTB in GAMESS-US are currently in progress [70]. Another limitation comes from the restriction of available parameters. However, qualified parameters are expected to be routinely generated with machine learning or artificial intelligence technologies in the near future.

Acknowledgements The FMO-DFTB study has been supported by JSPS KAKENHI Grant Numbers 24-4986, 15H06316, 16K05677, and 17K14436. S.I. acknowledges support by the Laboratory Directed Research and Development (LDRD) Program of Oak Ridge National Laboratory. ORNL is managed by UT-Battelle, LLC, for DOE under contract DE-AC05-00OR22725. We acknowledge fruitful discussions with Drs. Dmitri G. Fedorov, Hiroya Nakata, and Hirotaka Kitoh-Nishioka.

References

1. Almlöf J, Faegri Jr, K, Korsell K (1982) Principles for a direct SCF approach to LICAO–MOab-initio calculations. *J Comput Chem* 3(3):385–399. <https://doi.org/10.1002/jcc.540030314>
2. Burow AM, Sierka M, Mohamed F (2009) Resolution of identity approximation for the Coulomb term in molecular and periodic systems. *J Chem Phys* 131(21):214101. <https://doi.org/10.1063/1.3267858>
3. Kitaura K, Ikeo E, Asada T, Nakano T, Uebayasi M (1999) Fragment molecular orbital method: an approximate computational method for large molecules. *Chem Phys Lett* 313:701–706
4. Cui Q, Elstner M (2014) Density functional tight binding: values of semi-empirical methods in an ab initio era. *Phys Chem Chem Phys* 16:14368–14377. <https://doi.org/10.1039/C4CP00908H>
5. Gaus M, Cui Q, Elstner M (2014) Density functional tight binding: application to organic and biological molecules. *WIREs Comput Mol Sci* 4(1):49–61
6. Gotthard S (2017) Tight-binding density functional theory: an approximate Kohn–Sham DFT scheme. *J Phys Chem A* 111(26):5609–5613. <https://doi.org/10.1021/jp069056r>
7. Koskinen P, Mäkinen V (2009) Density-functional tight-binding for beginners. *Comput Mater Sci* 47:237–253
8. Seifert G, Joswig JO (2012) Density-functional tight binding—an approximate density-functional theory method. *WIREs Comput Mol Sci* 2:456–465

9. Irle S, Zheng G, Wang Z, Morokuma K (2006) The C_{60} formation puzzle "solved": QM/MD simulations reveal the shrinking hot giant road of the dynamic fullerene self-assembly mechanism. *J Phys Chem B* 110(30):14531–14545
10. Christensen AS, Kubař T, Cui Q, Elstner M (2016) Semiempirical quantum mechanical methods for noncovalent interactions for chemical and biochemical applications. *Chem. Rev.* 116(9):5301–5337. <https://doi.org/10.1021/acs.chemrev.5b00584>
11. Elstner M (2006) The SCC-DFTB method and its application to biological systems. *Theor Chem Acc* 116:316–325
12. Porezag D, Frauenheim T, Köhler T, Seifert G, Kaschner R (1995) Construction of tight-binding-like potentials on the basis of density-functional theory: application to carbon. *Phys Rev B* 51(19):12947–12957
13. Seifert G, Porezag D, Frauenheim T (1996) Calculations of molecules, clusters, and solids with a simplified LCAO-DFT-LDA scheme. *Int J Quantum Chem* 58(2):185–192
14. Elstner M, Porezag D, Jungnickel G, Elsner J, Haugk M, Frauenheim T, Suhai S, Seifert G (1998) Self-consistent-charge density-functional tight-binding method for simulations of complex materials properties. *Phys Rev B* 58:7260–7268
15. Foulkes WMC, Haydock R (1989) Tight-binding models and density-functional theory. *Phys Rev B* 39:12520–12536. <https://doi.org/10.1103/PhysRevB.39.12520>
16. Gaus M, Cui Q, Elstner M (2011) DFTB3: extension of the self-consistent-charge density-functional tight-binding method (SCC-DFTB). *J Chem Theory Comput* 7(4):931–948
17. Nishimoto Y, Fedorov DG, Irle S (2014) Density-functional tight-binding combined with the fragment molecular orbital method. *J Chem Theory Comput* 10:4801–4812
18. Scemama A, Renon N, Rapacioli M (2014) A sparse self-consistent field algorithm and its parallel implementation: application to density-functional-based tight binding. *J Chem Theory Comput* 10(6):2344–2354. <https://doi.org/10.1021/ct500115v>
19. Murat K, Hong Z, Peter Z, Dixon DA, Wagner AF (2016) Shift-and-invert parallel spectral transformation eigensolver: massively parallel performance for density-functional based tight-binding. *J Comput Chem* 37(4):448–459. <https://doi.org/10.1002/jcc.24254>
20. Niklasson AMN (2017) Next generation extended lagrangian first principles molecular dynamics. *J Chem Phys* 147(5):054103. <https://doi.org/10.1063/1.4985893>
21. Giese TJ, Chen H, Dissanayake T, Giambasu GM, Heldenbrand H, Huang M, Kuechler ER, Lee TS, Panteva MT, Radak BK, York DM (2013) A variational linear-scaling framework to build practical, efficient next-generation orbital-based quantum force fields. *J Chem Theory Comput* 9:1417–1427
22. Hiroaki N, Yoshifumi N, Masato K, Stephan I, Hiromi N (2016) Three pillars for achieving quantum mechanical molecular dynamics simulations of huge systems: Divide-and-conquer, density-functional tight-binding, and massively parallel computation. *J Comput Chem* 37(21):1983–1992. <https://doi.org/10.1002/jcc.24419>
23. Hu H, Lu Z, Elstner M, Hermans J, Yang W (2007) Simulating water with the self-consistent-charge density functional tight binding method: from molecular clusters to the liquid state. *J Phys Chem A* 111:5685–5691
24. Perdew JP (1986) Density-functional approximation for the correlation energy of the inhomogeneous electron gas. *Phys Rev B* 33:8822–8824. <https://doi.org/10.1103/PhysRevB.33.8822>
25. Perdew JP, Burke K, Ernzerhof M (1996) Generalized gradient approximation made simple. *Phys Rev Lett* 77:3865–3868. <https://doi.org/10.1103/PhysRevLett.77.3865>
26. Lundberg M, Nishimoto Y, Irle S (2012) Delocalization errors in a hubbard-like model: consequences for density-functional tight-binding calculations of molecular systems. *Int J Quantum Chem* 112(6):1701–1711. <https://doi.org/10.1002/qua.23178>
27. Humeniuk A, Mitrić R (2015) Long-range correction for tight-binding TD-DFT. *J Chem Phys* 143(13):134120. <https://doi.org/10.1063/1.4931179>
28. Lutsker V, Aradi B, Niehaus TA (2015) Implementation and benchmark of a long-range corrected functional in the density functional based tight-binding method. *J Chem Phys* 143(18):184107. <https://doi.org/10.1063/1.4935095>

29. Niehaus TA, Della Sala F (2012) Range separated functionals in the density functional based tight-binding method: formalism. *Phys Status Solidi B* 249(2):237–244. <https://doi.org/10.1002/pssb.201100694>
30. Livshits E, Baer R (2007) A well-tempered density functional theory of electrons in molecules. *Phys Chem Chem Phys* 9:2932–2941. <https://doi.org/10.1039/B617919C>
31. Kranz JJ, Elstner M, Aradi B, Frauenheim T, Lutsker V, Garcia AD, Niehaus TA (2017) Time-dependent extension of the long-range corrected density functional based tight-binding method. *J Chem Theory Comput* 13(4):1737–1747. <https://doi.org/10.1021/acs.jctc.6b01243>
32. <http://www.dftb.org/>
33. Nishimoto Y, Fedorov DG, Irlé S (2015) Third-order density-functional tight-binding combined with the fragment molecular orbital method. *Chem Phys Lett* 636:90–96
34. Nishimoto Y, Nakata H, Fedorov DG, Irlé S (2015) Large-scale quantum-mechanical molecular dynamics simulations using density-functional tight-binding combined with the fragment molecular orbital method. *J Phys Chem Lett* 6(24):5034–5039. <https://doi.org/10.1021/acs.jpcclett.5b02490>
35. Nishimoto Y, Fedorov DG (2016) The fragment molecular orbital method combined with density-functional tight-binding and the polarizable continuum model. *Phys Chem Chem Phys* 18:22047–22061. <https://doi.org/10.1039/C6CP02186G>
36. Nakata H, Nishimoto Y, Fedorov DG (2016) Analytic second derivative of the energy for density-functional tight-binding combined with the fragment molecular orbital method. *J Chem Phys* 145(4):044113. <https://doi.org/10.1063/1.4959231>
37. Nishimoto Y, Fedorov DG (2017) Three-body expansion of the fragment molecular orbital method combined with density-functional tight-binding. *J Comput Chem* 38(7):406–418. <https://doi.org/10.1002/jcc.24693>
38. Fedorov DG, Jensen JH, Deka RC, Kitaura K (2008) Covalent bond fragmentation suitable to describe solids in the fragment molecular orbital method. *J Phys Chem A* 112(46):11808–11816. <https://doi.org/10.1021/jp805435n>
39. Nishimoto Y, Fedorov DG (2018) Adaptive frozen orbital treatment for the fragment molecular orbital method combined with density-functional tight-binding. *J Chem Phys* 148(6):064115. <https://doi.org/10.1063/1.5012935>
40. Gordon MS, Schmidt MW (2005) Advances in electronic structure theory: GAMESS a decade later. In: Dykstra CE, Frenking G, Kim KS, Scuseria GE (eds) *Theory and applications of computational chemistry, the first forty years*. Elsevier, Amsterdam, pp 1167–1189
41. Schmidt MW, Baldrige KK, Boatz JA, Elbert ST, Gordon MS, Jensen JH, Koseki S, Matsunaga N, Nguyen KA, Su S, Windus TL, Dupuis M, Montgomery JA (1993) General atomic and molecular electronic structure system. *J Comput Chem* 14:1347–1363
42. Nagata T, Brorsen K, Fedorov DG, Kitaura K, Gordon MS (2011) Fully analytic energy gradient in the fragment molecular orbital method. *J Chem Phys* 134:124115
43. Fedorov DG, Olson RM, Kitaura K, Gordon MS, Koseki S (2004) A new hierarchical parallelization scheme: generalized distributed data interface (GDDI), and an application to the fragment molecular orbital method (FMO). *J Comput Chem* 25:872–880
44. Rappé AK, Casewit CJ, Colwell KS, Goddard WA III, Skiff WM (1992) UFF, a full periodic table force field for molecular mechanics and molecular dynamics simulations. *J Am Chem Soc* 114:10024–10035
45. Zhechkov L, Heine T, Patchkovskii S, Seifert G, Duarte HA (2005) An efficient a posteriori treatment for dispersion interaction in density-functional-based tight binding. *J Chem Theory Comput* 1:841–847. <https://doi.org/10.1021/ct050065y>
46. Elstner M, Hobza P, Frauenheim T, Suhai S, Kaxiras E (2001) Hydrogen bonding and stacking interactions of nucleic acid base pairs: a density-functional-theory based treatment. *J Chem Phys* 114(12):5149–5155
47. Grimme S (2006) Semiempirical GGA-type density functional constructed with a long-range dispersion correction. *J Comput Chem* 27(15):1787–1799. <https://doi.org/10.1002/jcc.20495>
48. Grimme S, Antony J, Ehrlich S, Krieg H (2010) A consistent and accurate ab initio parametrization of density functional dispersion correction (DFT-D) for the 94 elements H–Pu. *J Chem Phys* 132:154104

49. Grimme S, Ehrlich S, Goerigk L (2011) Effect of the damping function in dispersion corrected density functional theory. *J Comput Chem* 32(7):1456–1465. <https://doi.org/10.1002/jcc.21759>
50. Andersen HC (1983) Rattle: A “velocity” version of the shake algorithm for molecular dynamics calculations. *J Comput Phys* 52:24–34
51. Elstner M, Frauenheim T, Suhai S (2003) An approximate DFT method for QM/MM simulations of biological structures and processes. *J Mol Struct: THEOCHEM* 632(1):29–41. [https://doi.org/10.1016/S0166-1280\(03\)00286-0](https://doi.org/10.1016/S0166-1280(03)00286-0)
52. Cui Q, Elstner M, Kaxiras E, Frauenheim T, Karplus M (2001) A QM/MM implementation of the self-consistent charge density functional tight binding (SCC-DFTB) method. *J Phys Chem B* 105(2):569–585. <https://doi.org/10.1021/jp0029109>
53. Lu X, Ovchinnikov V, Demapan D, Roston D, Cui Q (2017) Regulation and plasticity of catalysis in enzymes: insights from analysis of mechanochemical coupling in myosin. *Biochemistry* 56(10):1482–1497. <https://doi.org/10.1021/acs.biochem.7b00016>
54. Yang Y, Yu H, Cui Q (2008) Extensive conformational transitions are required to turn on atp hydrolysis in myosin. *J Mol Biol* 381(5):1407–1420. <https://doi.org/10.1016/j.jmb.2008.06.071>
55. Ghosh N, Prat-Resina X, Gunner MR, Cui Q (2009) Microscopic pKa analysis of Glu286 in cytochrome c oxidase (rhodobacter sphaeroides): toward a calibrated molecular model. *Biochemistry* 48(11):2468–2485. <https://doi.org/10.1021/bi8021284>
56. Yeng- Tseng W, Yu- Ching C (2014) Insights from QM/MM modeling the 3d structure of the 2009 H1N1 influenza a virus neuraminidase and its binding interactions with antiviral drugs. *Mol Inf* 33(3):240–249. <https://doi.org/10.1002/minf.201300117>
57. Chaskar P, Zoete V, Röhrig UF (2014) Toward on-the-fly quantum mechanical/molecular mechanical (QM/MM) docking: development and benchmark of a scoring function. *J Chem Inf Model* 54(11):3137–3152. <https://doi.org/10.1021/ci5004152>
58. Qu X, Latino DA, Aires-de Sousa J (2013) A big data approach to the ultra-fast prediction of dft-calculated bond energies. *J Cheminformatics* 5(1):34. <https://doi.org/10.1186/1758-2946-5-34>
59. Fedorov DG, Kitaura K (2018) Pair interaction energy decomposition analysis for density functional theory and density-functional tight-binding with an evaluation of energy fluctuations in molecular dynamics. *J Phys Chem A* 122(6):1781–1795. <https://doi.org/10.1021/acs.jpca.7b12000>
60. Inaki M, Fedorov GD, Roger R, Michelle S, Andrea T, Bodkin JM, Alexander H (2017) Rapid and accurate assessment of GPCR–ligand interactions using the fragment molecular orbital-based density-functional tight-binding method. *J Comput Chem* 38(23):1987–1990. <https://doi.org/10.1002/jcc.24850>
61. Gillet N, Berstis L, Wu X, Gajdos F, Heck A, de la Lande A, Blumberger J, Elstner M (2016) Electronic coupling calculations for bridge-mediated charge transfer using constrained density functional theory (CDFT) and effective hamiltonian approaches at the density functional theory (DFT) and fragment-orbital density functional tight binding (FODFTB) level. *J Chem Theory Comput* 12(10):4793–4805. <https://doi.org/10.1021/acs.jctc.6b00564>
62. Heck A, Kranz JJ, Elstner M (2016) Simulation of temperature-dependent charge transport in organic semiconductors with various degrees of disorder. *J Chem Theory Comput* 12(7):3087–3096. <https://doi.org/10.1021/acs.jctc.6b00215>
63. Heck A, Kranz JJ, Kubař T, Elstner M (2015) Multi-scale approach to non-adiabatic charge transport in high-mobility organic semiconductors. *J Chem Theory Comput* 11(11):5068–5082. <https://doi.org/10.1021/acs.jctc.5b00719>
64. Kubar T, Woiczikowski PB, Cuniberti G, Elstner M (2008) Efficient calculation of charge-transfer matrix elements for hole transfer in dna. *J Phys Chem B* 112:7937–7947
65. Kubas A, Gajdos F, Heck A, Oberhofer H, Elstner M, Blumberger J (2015) Electronic couplings for molecular charge transfer: benchmarking cdft, fodft and fodftb against high-level ab initio calculations. *Phys Chem Chem Phys* 17:14342–14354. <https://doi.org/10.1039/C4CP04749D>
66. Kubas A, Hoffmann F, Heck A, Oberhofer H, Elstner M, Blumberger J (2014) Electronic couplings for molecular charge transfer: benchmarking CDFT, FODFT, and FODFTB against high-level ab initio calculations. *J Chem Phys* 140(10):104105. <https://doi.org/10.1063/1.4867077>

67. Nishioka H, Ando K (2011) Electronic coupling calculation and pathway analysis of electron transfer reaction using ab initio fragment-based method. I. FMO-LCMO approach. *J Chem Phys* 134(20):204109. <https://doi.org/10.1063/1.3594100>
68. Tsuneyuki S, Kobori T, Akagi K, Sodeyama K, Terakura K, Fukuyama H (2009) Molecular orbital calculation of biomolecules with fragment molecular orbitals. *Chem Phys Lett* 476(1):104–108. <https://doi.org/10.1016/j.cplett.2009.05.069>
69. Kitoh-Nishioka H, Welke K, Nishimoto Y, Fedorov DG, Irle S (2017) Multi-scale simulations on charge transport in covalent organic frameworks: Including dynamics of transfer integrals from FMO-DFTB/LCMO. *J Phys Chem C* 121:17712–17726. <https://doi.org/10.1021/acs.jpcc.7b05779>
70. Vuong VQ, Nishimoto Y, Fedorov DG, Sumpter BG, Niehaus TA, Irle S (2019) The fragment molecular orbital method based on long-range corrected density-functional tight-binding. *J Chem Theor Comput* 15(5): 3008–3020. <https://doi.org/10.1021/acs.jctc.9b00108>

Self-Consistent Treatment of Solvation Structure with Electronic Structure Based on 3D-RISM Theory



Norio Yoshida

Abstract The solvent effects on the electronic structure of biomolecules are essential for considering their functions and structures. The three-dimensional reference interaction site model (3D-RISM) theory is a statistical mechanics integral equation theory of molecular liquids. It is suitable for describing the solvation structure of large molecules, i.e., the main target of the fragment molecular orbital (FMO) approach. The hybrid method of FMO and 3D-RISM, referred to as FMO/3D-RISM, enables us to investigate the electronic structure of large molecules in solution as well as solvation thermodynamics at the molecular level. This chapter describes the theoretical background of the 3D-RISM theory, the formalism of the hybrid method of 3D-RISM and quantum chemical theory including the FMO, and the applications of these methods.

Keywords 3D-RISM · Integral equation theory of liquids · Solvation

1 Introduction

Living organisms maintain their lives by continuing the chain of chemical processes including chemical reactions, molecular recognition, and self-organization [1]. Since all such processes take place in solution, any theoretical developments regarding phenomena in living systems should adequately include solvent effects.

In the field of molecular electronic structure theory, methods describing the solvent effect are roughly classified into three types [2]. The most straightforward way to handle the solvent environment is to place solvent molecules explicitly. Such an approach is called the “explicit solvent model.” For example, in studies of biomolecular systems, solvent molecules are treated by molecular mechanics (MM) to save computational cost, while solute molecules are (partially) described by quantum mechanics (QM). The position and the orientation of the solvent molecules are

N. Yoshida (✉)

Graduate School of Science, Department of Chemistry, Kyushu University, Fukuoka, Japan
e-mail: noriwo@chem.kyushu-univ.jp

usually handled by the molecular dynamics (MD) or Monte Carlo (MC) simulations. These methods are referred to as QM/MM-MD or QM/MM-MC, respectively [3–6]. A hybrid method of the fragment molecular orbital (FMO) and the QM/MM method is introduced in another chapter. Although these methods have been successfully applied to various problems in biomolecular systems, they do have a few weaknesses. First, the number of solvent molecules that can be handled in the simulation is limited. Second, the methods are unable to fully sample the configurational space of solvent molecules. This is because solvent molecules have large degrees of freedom and span a large configurational space. This second weakness is a serious problem, especially when dealing with solutions containing dilute components, such as ions.

A second approach for considering solvent effects on the electronic structure of solvated molecules is based on the “implicit solvent model,” including the generalized Born (GB) model, Poisson–Boltzmann (PB) model, polarizable continuum model (PCM), conductor-like screening model (COSMO), solvent model based on density (SMD), and their extensions [7–9]. These methods are most widely used in the field of quantum chemistry because of high computational efficiency (low computational cost and reasonable accuracy). In the implicit solvent models, the solvent environment is regarded as a continuum medium, characterized by a dielectric constant. Some of these methods have been implemented on FMO packages [10–12]. However, there are obvious limitations that arise from the essential nature of the model, i.e., “macroscopic” limitations. Therefore, solute–solvent interactions that require molecular descriptions, such as hydrogen bonds, cannot be described by the implicit solvent model.

Another approach for considering solvent effects is based on the statistical mechanical theory of molecular liquids based on the Ornstein–Zernike (OZ) integral equation theory, such as the molecular OZ (MOZ) equation, the molecular density functional theory, the reference interaction site model (RISM) theory, and the three-dimensional (3D) RISM theory [13–27]. The molecular theories based on the OZ integral equation allow us to consider the microscopic solute–solvent interactions such as hydrogen bonding and solvent distributions with a complete ensemble average in the thermodynamic limit. Although several types of formalization to handle the molecular nature in the OZ theory have been proposed, the 3D-RISM theory is one of the most successful that has been applied to biomolecules [28–30]. The 3D-RISM theory has been applied to various biophysical and biochemical problems, such as molecular recognition, channel transportation, and chemical reactions. In the 3D-RISM theory, the solvent distribution is expressed by the spatial distribution function (SDF) of interaction sites of solvent molecules at the grid points in the solvation box. The SDF is especially suited to complex molecular systems, which are the main target of the FMO approach. In addition, because the SDFs are obtained through statistical mechanics of molecular liquids, no difficulties arise from the explicit and implicit solvent models.

The hybrid methods of the quantum chemical theory and the integral equation theory of liquids allow us to treat the solvent effects on the electronic structure of solvated molecules. In pioneering works by Ten-no, Hirata, and Kato, the hybrid method of RISM theory and the *ab initio* molecular orbital (MO) method was

proposed, which is called the RISM self-consistent field (RISM-SCF) method [31, 32]. Following them, Sato et al. introduced the variational condition of the RISM-SCF method coupled with the multi-configurational self-consistent field (SCF) method, and derived its analytical free energy gradient formula [33]. QM hybrid methods with other integral equation theories have also been proposed, such as MOZ-SCF and 3D-RISM-SCF [22, 34–39]. These hybrid methods have been applied to various chemical physics problems in solution. They are particularly effective for investigating reactions in mixed solvent and electrolyte solution, because the integral equation theory can easily handle such solvent environments, unlike the implicit and explicit solvent models [40–46].

Consequently, the 3D-RISM method is a good candidate to consider the solvent effect in the theoretical framework of the FMO. A hybrid method of the FMO and 3D-RISM, called FMO/3D-RISM, allows us to investigate the whole electronic structure of a macromolecule and the solvent effects on it. Early work on the FMO/3D-RISM method was performed by Takami et al. [47] They applied the FMO/3D-RISM method to a grid computing system. The computational bottleneck of the hybrid of QM and 3D-RISM theory is an evaluation of the electrostatic potential on each rectangular solvent grid point (there are usually 128^3 – 512^3 points). Takami et al. employed the Mulliken charge to save computational cost. However, it is widely known that the electrostatic potential made from the Mulliken charge is problematic. Later, Yoshida proposed an efficient implementation technique for FMO/3D-RISM based on the variational condition as well as its analytical free energy gradient formula [48]. A space decomposition scheme was introduced to evaluate the electrostatic potential, thereby achieving high computational efficiency.

In this chapter, the formalism of the 3D-RISM theory, the hybrid method of 3D-RISM-SCF and FMO/3D-RISM, is presented. The computational schemes of these methods are also reviewed.

2 The 3D-RISM Theory

2.1 Formalism of the 3D-RISM Theory

The formalisms of 3D-RISM and its quantum chemical hybrid methods have been reviewed previously—here we present the formalisms according to the reviews [29, 49]. The 3D-RISM theory is derived from the MOZ theory, which is an extension of the OZ integral equation theory of molecular liquids. These theories describe the structure and thermodynamics of solvation based on the pair correlation function or pair density distribution function (DF).

We begin by introducing the pair density DF of molecules, which is defined as:

$$\rho(\mathbf{r}_1, \mathbf{r}_2, \boldsymbol{\Omega}_1, \boldsymbol{\Omega}_2) = \left\langle \sum_i \sum_{j \neq i} \delta(\mathbf{r}_1 - \mathbf{r}_i) \delta(\mathbf{r}_2 - \mathbf{r}_j) \delta(\boldsymbol{\Omega}_1 - \boldsymbol{\Omega}_i) \delta(\boldsymbol{\Omega}_2 - \boldsymbol{\Omega}_j) \right\rangle. \quad (1)$$

where the summation of i and j run over all particles. When there is no external field, the translational invariance of the pair density DF can be applied and the pair DF is derived as:

$$g(\mathbf{r}_{12}, \boldsymbol{\Omega}_1, \boldsymbol{\Omega}_2) = \left(\frac{\Omega}{\rho}\right)^2 \rho(\mathbf{r}_{12}, \boldsymbol{\Omega}_1, \boldsymbol{\Omega}_2), \quad (2)$$

where ρ is average number density of solvent, $\mathbf{r}_{12} = \mathbf{r}_2 - \mathbf{r}_1$ and $\Omega \equiv \int d\boldsymbol{\Omega}$. The MOZ equation is expressed using the function:

$$h(\mathbf{r}_{12}, \boldsymbol{\Omega}_1, \boldsymbol{\Omega}_2) = c(\mathbf{r}_{12}, \boldsymbol{\Omega}_1, \boldsymbol{\Omega}_2) + \frac{\rho}{\Omega} \int c(\mathbf{r}_{13}, \boldsymbol{\Omega}_1, \boldsymbol{\Omega}_3) h(\mathbf{r}_{32}, \boldsymbol{\Omega}_3, \boldsymbol{\Omega}_2) d\mathbf{r}_3 d\boldsymbol{\Omega}_3, \quad (3)$$

where $h = g + 1$ is the total correlation function and c is the direct correlation function that is defined through the MOZ equation. The pair correlation functions (PCFs), h and c , are the functions of the orientations of molecules and vector connecting two molecules. It is computationally difficult to handle the functions due to the large degrees of freedom. One possible way to reduce the variables in the PCF would be to introduce the interaction site model. The interaction site model can be introduced by taking the orientational averaging of PCF centered at a specific site:

$$h_\gamma(\mathbf{r}) = \frac{1}{\Omega} \int h(\mathbf{r}_{12}, \boldsymbol{\Omega}_1, \boldsymbol{\Omega}_2) \delta(\mathbf{r}_{12} + \mathbf{l}_{2\gamma}(\boldsymbol{\Omega}_2) - \mathbf{r}) d\mathbf{r}_2 d\boldsymbol{\Omega}_2, \quad (4)$$

where $\mathbf{l}_{2\gamma}$ is the vector connecting the center of molecule 2 and interaction site γ . In contrast, the direct correlation function is defined by simply applying a superposition approximation:

$$c(\mathbf{r}_{12}, \boldsymbol{\Omega}_1, \boldsymbol{\Omega}_2) = \sum_\gamma c_\gamma(\mathbf{r}). \quad (5)$$

By using the three-dimensional correlation functions (3D-DFs) given in Eqs. (4) and (5), the 3D-RISM equation can be derived from the MOZ equation:

$$h_\gamma(\mathbf{r}) = \sum_{\gamma'} [c_{\gamma'}(\mathbf{r}') * \chi_{\gamma'\gamma}(|\mathbf{r} - \mathbf{r}'|)], \quad (6)$$

where $*$ denotes the convolution integral and $\chi_{\gamma'\gamma}$ is the solvent susceptibility, obtained by solving the RISM equation for a bulk solvent system prior to the 3D-RISM calculation. The RISM equation for a bulk system can be obtained by introducing the site–site correlation functions, by applying the interaction site model for both molecules. As the 3D-RISM equation includes two unknown functions, h and c , we need another relation between them to close the equation. The equation for closing the 3D-RISM equation is called a “closure relation.” Several closure relations have been proposed, such as a hypernetted chain (HNC), mean spherical approximation (MSA), and Kovalenko–Hirata (KH) closures. To date, the KH closure is the most

popular for the 3D-RISM because it is numerically stable and it gives thermodynamic properties with reasonable accuracy [22]. The KH closure is given by:

$$g_\gamma(\mathbf{r}) = \begin{cases} \exp[d_\gamma(\mathbf{r})] & d_\gamma(\mathbf{r}) < 0 \\ 1 + d_\gamma(\mathbf{r}) & d_\gamma(\mathbf{r}) \geq 0, \end{cases} \quad (7)$$

$$d_\gamma(\mathbf{r}) = -\frac{1}{k_B T} u_\gamma(\mathbf{r}) + h_\gamma(\mathbf{r}) - c_\gamma(\mathbf{r}), \quad (8)$$

where $u_\gamma(\mathbf{r})$ is a solute–solvent interaction potential at position \mathbf{r} . The 3D-RISM theory coupled with the KH closure is called the 3D-RISM-KH theory. The solvation free energy (SFE), or excess chemical potential, is given by:

$$\Delta\mu = \rho \sum_\gamma \int_0^1 d\lambda \int u_\gamma(\mathbf{r}) g_\gamma^\lambda(\mathbf{r}) d\mathbf{r}, \quad (9)$$

where the integration with respect to λ is called the thermodynamic integration, which corresponds to the solvation process of solute molecules. The integration of λ can be performed analytically, to give:

$$\Delta\mu = \frac{\rho}{\beta} \sum_\gamma \int \{-c_\gamma(\mathbf{r}) + \frac{1}{2} h_\gamma(\mathbf{r})^2 \Theta(-h_\gamma(\mathbf{r})) - \frac{1}{2} h_\gamma(\mathbf{r}) c_\gamma(\mathbf{r})\} d\mathbf{r}, \quad (10)$$

where Θ is the Heaviside step function. The existence of the analytical expression of the SFE is a great advantage of the 3D-RISM-KH theory over the explicit solvent models. Thanks to this expression, one can readily obtain the SFE, once the 3D-RISM-KH calculation is completed.

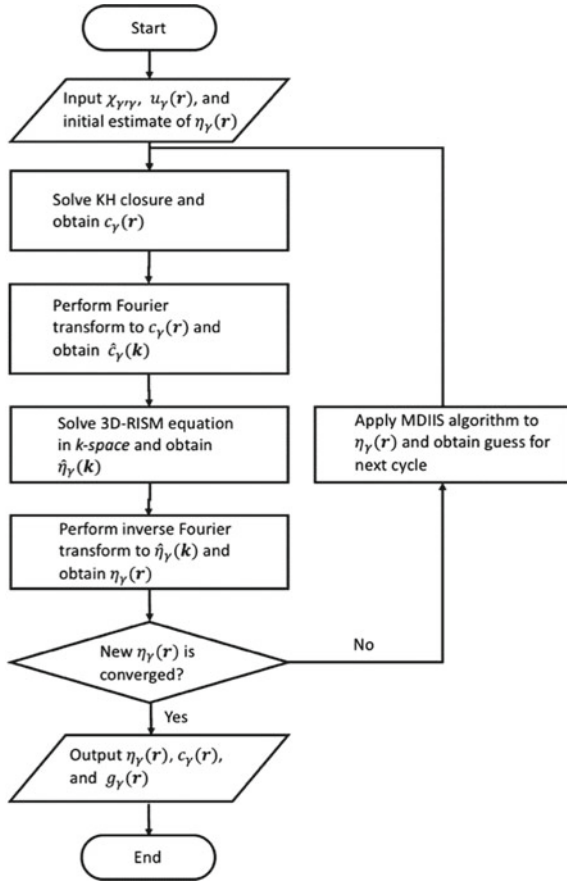
2.2 Computational Scheme of the 3D-RISM Theory

Scheme 1 shows the computational procedure followed to solve the 3D-RISM-KH theory. Before a calculation, the solvent susceptibility and the solute–solvent interaction potential should be obtained. The solvent susceptibility is obtained from the solvent RISM-KH equation for a bulk solvent system. The interaction potential is usually defined as the sum of Lennard–Jones (LJ) potentials and Coulomb interaction between solute and solvent site:

$$u_\gamma(\mathbf{r}) = \sum_\alpha 4\epsilon_{\alpha\gamma} \left[\left(\frac{\sigma_{\alpha\gamma}}{|\mathbf{r}-\mathbf{r}_\alpha|} \right)^{12} - \left(\frac{\sigma_{\alpha\gamma}}{|\mathbf{r}-\mathbf{r}_\alpha|} \right)^6 \right] + \sum_\alpha \frac{q_\alpha q_\gamma}{|\mathbf{r}-\mathbf{r}_\alpha|}, \quad (11)$$

where the potential parameters, σ , ϵ , and q denote the LJ diameter, energy parameter, and point charge, respectively. These parameters are usually taken from the MD package parameter set, such as Amber force field.

Scheme 1 Computational flow chart for 3D-RISM-KH



To perform the 3D-RISM-KH iterations, it is useful to define the indirect correlation function as:

$$\eta_\gamma(\mathbf{r}) = h_\gamma(\mathbf{r}) - c_\gamma(\mathbf{r}). \tag{12}$$

Using this function, the KH closure can be rewritten as follows.

$$c_\gamma(\mathbf{r}) = \begin{cases} \exp[d_\gamma(\mathbf{r})] - \eta_\gamma(\mathbf{r}) - 1 & d_\gamma(\mathbf{r}) < 0 \\ d_\gamma(\mathbf{r}) - \eta_\gamma(\mathbf{r}) & d_\gamma(\mathbf{r}) \geq 0 \end{cases} \tag{13}$$

$$d_\gamma(\mathbf{r}) = -\frac{1}{k_B T} u_\gamma(\mathbf{r}) + \eta_\gamma(\mathbf{r}) \tag{14}$$

Therefore, the KH closure gives c_γ by substitution of η_γ . Because the 3D-RISM equation (Eq. 6) includes the convolution integral, the Fourier transform of the correlation functions is effective for high-speed computing, as given by:

$$\hat{c}_\gamma(\mathbf{k}) = \int c_\gamma(\mathbf{r}) \exp(i\mathbf{k}\mathbf{r}) d\mathbf{r}. \quad (15)$$

Using this expression, the 3D-RISM equation in k -space can be written as:

$$\hat{\eta}_\gamma(\mathbf{k}) = \sum_{\gamma'} \hat{c}_{\gamma'}(\mathbf{k}) \hat{\chi}_{\gamma'\gamma}(|\mathbf{k}|) - \hat{c}_\gamma(k), \quad (16)$$

where $\hat{\chi}_{\gamma'\gamma}$ is a Fourier transform of the solvent susceptibility. Applying the inverse Fourier transform to the indirect correlation function, we obtain the updated indirect correlation function through the 3D-RISM-KH cycle.

The updated indirect correlation function is used as an input of the next 3D-RISM-KH cycle. However, it is usually not a good estimate. To improve the estimation of the indirect correlation function for the next step, we made use of the modified direct inversion in the iterative space (MDIIS) method [50].

The 3D-RISM-KH cycle is repeated until the indirect correlation functions remain unchanged. Finally, one can obtain the total, direct, and indirect correlation functions, as well as the DF. From these correlation functions, the solvation thermodynamic properties such as SFE, partial molar volume, and internal energy can be determined.

3 Hybrid of 3D-RISM and Electronic Structure Theories

3.1 Basics of the 3D-RISM-SCF Method

The hybrid method of the electronic structure and 3D-RISM theories, called KS-DFT/3D-RISM or 3D-RISM-SCF, was proposed by Kovalenko, Sato, and Hirata [22, 37]. (Hereafter, for simplicity, we refer to the method as 3D-RISM-SCF.) Formalism of the 3D-RISM-SCF theory is derived in a similar way to the RISM-SCF/multi-configurational SCF method by Sato et al. [33].

In the 3D-RISM-SCF formalism, the Gibbs energy of the system is defined as follows.

$$G = E_{\text{solute}} + \Delta\mu, \quad (17)$$

where E_{solute} is the electronic energy of a solute molecule, evaluated by the ab initio MO method, or KS-DFT:

$$E_{\text{solute}} = \langle \Psi | \hat{H}_0 | \Psi \rangle, \quad (18)$$

where \hat{H}_0 and Ψ denote the electronic Hamiltonian of an isolated solute molecule and the wave function of a solvated solute molecule. The Gibbs energy of the system should contain the kinetic free energy term; however, in this chapter, this term

is ignored for simplicity. The solute wave functions are obtained by solving the Schrödinger equation with the following Hamiltonian.

$$\widehat{H}_{\text{solv}} = \widehat{H}_0 + \widehat{V}, \quad (19)$$

where \widehat{V} is the solvent–electron interaction term given by:

$$\widehat{V} = \rho \sum_{\gamma} \int g_{\gamma}(\mathbf{r}) \left(\frac{q_{\gamma}}{|\mathbf{r}-\mathbf{r}'|} \right) d\mathbf{r}, \quad (20)$$

where q_{γ} is a point charge on the solvent site γ , and \mathbf{r}' is the coordinate of an electron.

The free energy of solvation $\Delta\mu$ is obtained by solving the 3D-RISM-KH equation under the interaction potential caused by the solute molecule. The solute–solvent interaction potential is given by:

$$u_{\gamma}(\mathbf{r}) = \sum_{\alpha} 4\epsilon_{\alpha\gamma} \left[\left(\frac{\sigma_{\alpha\gamma}}{|\mathbf{r}-\mathbf{r}_{\alpha}|} \right)^{12} - \left(\frac{\sigma_{\alpha\gamma}}{|\mathbf{r}-\mathbf{r}_{\alpha}|} \right)^6 \right] + U_{\gamma}^{\text{es}}(\mathbf{r}), \quad (21)$$

where α denotes a solute atom and

$$U_{\gamma}^{\text{es}}(\mathbf{r}) = - \int \frac{q_{\gamma} |\Psi(\mathbf{r}')|^2}{|\mathbf{r}-\mathbf{r}'|} d\mathbf{r}' + \sum_{\alpha} \frac{Z_{\alpha} q_{\gamma}}{|\mathbf{r}-\mathbf{r}_{\alpha}|}, \quad (22)$$

where σ and ϵ are the LJ parameters (according to their usual meanings). Alternatively, the restrained electrostatic potential (RESP) charge q_{α} for a solute atom is also available for the 3D-RISM-SCF formalism:

$$U_{\gamma}^{\text{es}}(\mathbf{r}) = \sum_{\alpha} \frac{q_{\gamma} q_{\alpha}}{|\mathbf{r}-\mathbf{r}_{\alpha}|} + \sum_{\alpha} \frac{Z_{\alpha} q_{\gamma}}{|\mathbf{r}-\mathbf{r}_{\alpha}|}. \quad (23)$$

When using the RESP charge, the corresponding solvent–electron interaction in the solvated Hamiltonian is given by:

$$\widehat{V} = \rho \sum_{\gamma} \sum_{\alpha} \widehat{q}_{\alpha} \int g_{\gamma}(\mathbf{r}) \left(\frac{q_{\gamma}}{|\mathbf{r}-\mathbf{r}_{\alpha}|} \right) d\mathbf{r}, \quad (24)$$

where \widehat{q}_{α} is a partial charge operator to reproduce the RESP charge on atom α .

3.2 Variational Condition of 3D-RISM-SCF

To derive the variational condition of 3D-RISM-SCF, we begin by defining the Lagrange functions. The Gibbs energy G , given in Eq. (17), can be regarded as a

functional of the correlation functions, i.e., h_γ , c_γ , and η_γ , as well as the one-particle orbitals of the solute wave functions. Imposing constraints on the orthonormality of the one-particle orbital, we define the Lagrange function:

$$L = G - \sum_{\mu\nu} \varepsilon_{\mu\nu} (S_{\mu\nu} - \delta_{\mu\nu}), \quad (25)$$

where $S_{\mu\nu} = \langle \phi_\mu | \phi_\nu \rangle$ and ϕ_μ is a molecular orbital. The $\varepsilon_{\mu\nu}$ is a Lagrange multiplier. Variation with respect to the correlation functions and MOs yields:

$$\begin{aligned} \delta\mathcal{L} = & -\rho k_B T \sum_\gamma \int d\mathbf{r} \left[\left[\exp\left(-\frac{1}{k_B T} u_\gamma(\mathbf{r}) + \eta_\gamma(\mathbf{r})\right) - 1 - h_\gamma(\mathbf{r}) \right] \Theta(-h_\gamma(\mathbf{r})) \right. \\ & + \left[-\frac{1}{k_B T} u_\gamma(\mathbf{r}) + \eta_\gamma(\mathbf{r}) - h_\gamma(\mathbf{r}) \right] \Theta(-h_\gamma(\mathbf{r})) \left. \right] \delta\eta_\gamma(\mathbf{r}) \\ & + \{-\eta_\gamma(\mathbf{r}) + h_\gamma(\mathbf{r}) - c_\gamma(\mathbf{r})\} \delta h_\gamma(\mathbf{r}) \\ & - \frac{k_B T}{(2\pi)^3} \sum_\gamma \int d\mathbf{k} \left\{ -\rho \hat{h}_\gamma(\mathbf{k}) + \sum_{\gamma'} \hat{c}_{\gamma'}(\mathbf{k}) \hat{\chi}_{\gamma'\gamma}(|\mathbf{k}|) \right\} \delta \hat{c}_\gamma(\mathbf{k}) \\ & + 2 \sum_{\mu\nu} P_{\mu\nu} \left\langle \delta\phi_\mu \left| \hat{h} + \sum_{\xi\zeta} \hat{g}_{\xi\zeta} + \hat{V} - \varepsilon_{\mu\nu} \right| \phi_\nu \right\rangle, \quad (26) \end{aligned}$$

where \hat{h} and $\hat{g}_{\xi\zeta}$ denote the one- and two-electron operators, respectively. Each term on the right-hand side of Eq. (26) defines the KH closure, the indirect correlation function, the k -space 3D-RISM equation, and the solvated Fock matrix, respectively. Based on the variational condition, one can obtain the analytical Gibbs energy gradient with respect to the atomic coordinates of a solute molecule [38]:

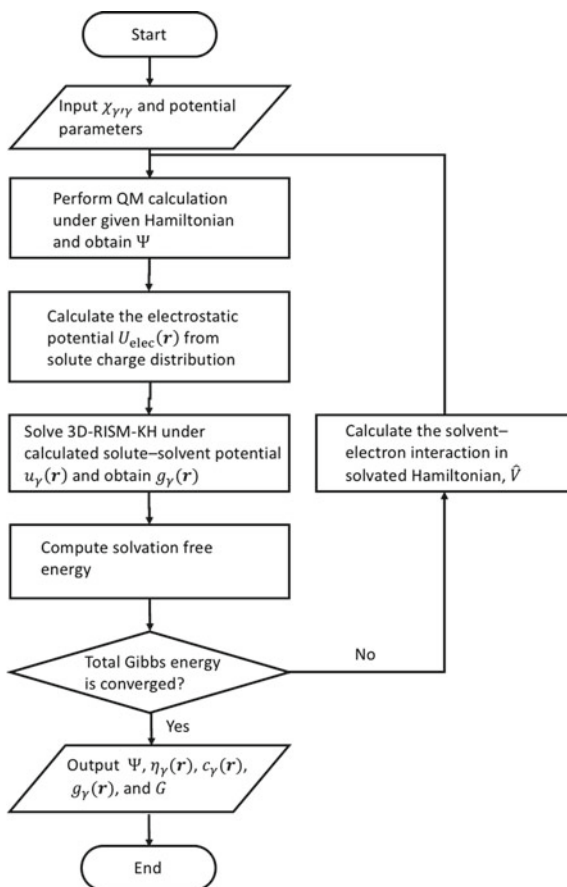
$$\frac{\partial G}{\partial \mathbf{R}_\alpha} = \frac{\partial E_{\text{solute}}}{\partial \mathbf{R}_\alpha} + \frac{\partial \Delta\mu}{\partial \mathbf{R}_\alpha} = \frac{\partial E_{\text{solute}}}{\partial \mathbf{R}_\alpha} + \sum_\gamma \rho \int d\mathbf{r} \left[\left(\frac{\partial u_\gamma(\mathbf{r}; \mathbf{R}_\alpha)}{\partial \mathbf{R}_\alpha} \right) g_\gamma(\mathbf{r}) \right]. \quad (27)$$

The analytical free energy expression allows one to perform the geometry optimization of solvated molecules efficiently.

3.3 Computational Scheme of 3D-RISM-SCF

By solving the 3D-RISM and Schrödinger equations iteratively, the electronic structure of solute molecules and solvation structure can be obtained simultaneously. In Scheme 2, the computational flow chart for 3D-RISM-SCF is shown. Before calculation, the solvent susceptibility and the potential parameters should be prepared. The 3D-RISM-SCF iteration begins with electronic structure calculations of a solute

Scheme 2 Computational flow chart for 3D-RISM-SCF



molecule at the isolated state. From the obtained wave function of solute molecule, the solute-solvent electrostatic potential is calculated using Eq. (22). Under this potential, the 3D-RISM-KH is solved in an iterative manner, as explained in the Sect. (3.2). From the 3D-RISM-KH results, one can obtain the solvation free energy and the distribution functions. By substituting the distribution function into Eq. (24), the term of the solvated Hamiltonian is computed. One then proceeds to the next step of the 3D-RISM-SCF iterative calculation. The 3D-RISM-SCF cycle is repeated until the total Gibbs energy remains unchanged.

4 The FMO/3D-RISM Method

In this section, the formalism of the FMO/3D-RISM method, the variational condition, and the computational scheme are reviewed (extracted from the original

paper [48] with copyright permission). An efficient implementation method for FMO/3D-RISM is also reviewed.

4.1 Formalism of the FMO/3D-RISM Method

Similar to the 3D-RISM-SCF method, the quantum mechanical solute molecules immersed in solution in infinite dilution, where the solute electronic structure is computed by FMO with solvated fragment Hamiltonian.

The solvated fragment (monomer) Hamiltonian in FMO/3D-RISM formalism is given by:

$$H_I^{\text{solv}} = \sum_i^{n_I} \left\{ -\frac{1}{2} \nabla_i^2 - \sum_s^{\text{all atoms}} \frac{Z_s}{|\mathbf{r}_i - \mathbf{r}_s|} + \sum_{J \neq I}^N \int \frac{\rho_J(\mathbf{r}')}{|\mathbf{r}_i - \mathbf{r}'|} d\mathbf{r}' + V^{\text{solv}}(\mathbf{r}_i) \right\} + \sum_{i>j}^{n_I} \frac{1}{|\mathbf{r}_i - \mathbf{r}_j|}, \quad (28)$$

where n_I is the number of electrons in fragment I , $\rho_J(\mathbf{r})$ is the electron density of fragment J at position \mathbf{r} , and N is the total number of fragments. $V^{\text{solv}}(\mathbf{r}_i)$, is the electrostatic potential at \mathbf{r}_i originate from the solvent molecule (it did not appear in the original FMO method):

$$V^{\text{solv}}(\mathbf{r}_i) = -\sum_{\gamma}^{N_v} q_{\gamma} \rho \int \frac{q_{\gamma}}{|\mathbf{r}_i - \mathbf{r}|} g_{\gamma}(\mathbf{r}) d\mathbf{r}, \quad (29)$$

where q_{γ} is the point charge at the solvent interaction site γ .

By analogy with the fragment monomer, the solvated fragment pair Hamiltonian is given by

$$H_{IJ}^{\text{solv}} = \sum_i^{n_I+n_J} \left\{ -\frac{1}{2} \nabla_i^2 - \sum_s^{\text{all atoms}} \frac{Z_s}{|\mathbf{r}_i - \mathbf{r}_s|} + \sum_{K \neq I, J}^N \int \frac{\rho_K(\mathbf{r}')}{|\mathbf{r}_i - \mathbf{r}'|} d\mathbf{r}' + V^{\text{solv}}(\mathbf{r}_i) \right\} + \sum_{i>j}^{n_I+n_J} \frac{1}{|\mathbf{r}_i - \mathbf{r}_j|} \quad (30)$$

The wave functions of solvated fragment monomer, Ψ_I^{solv} , and pair, Ψ_{IJ}^{solv} , are obtained by solving the Schrödinger equations given by:

$$H_I^{\text{solv}} \Psi_I^{\text{solv}} = (E_I^{\text{isolate}} + V_I^{\text{solv}}) \Psi_I^{\text{solv}} \quad (31)$$

and

$$H_{IJ}^{\text{solv}} \Psi_{IJ}^{\text{solv}} = (E_{IJ}^{\text{isolate}} + V_{IJ}^{\text{solv}}) \Psi_{IJ}^{\text{solv}}, \quad (32)$$

where V_I^{solv} and V_{IJ}^{solv} are the solute–solvent electronic interaction energies for the monomer and the dimer, respectively.

The total Gibbs energy G of the system is defined as follows.

$$G = E^{\text{solv}} + \Delta\mu, \quad (33)$$

where E^{solv} is defined as:

$$\begin{aligned} E^{\text{solv}} = & \sum_{s>t}^{\text{all atoms}} \frac{Z_s Z_t}{|\mathbf{r}_s - \mathbf{r}_t|} + \sum_I^N E_I^{\text{isolate}} + \sum_{I>J}^N (E_{IJ}^{\text{isolate}} - E_I^{\text{isolate}} - E_J^{\text{isolate}}) \\ & + \sum_{I>J>K}^N \left\{ (E_{IJK}^{\text{isolate}} - E_I^{\text{isolate}} - E_J^{\text{isolate}} - E_K^{\text{isolate}}) - (E_{IJ}^{\text{isolate}} - E_I^{\text{isolate}} - E_J^{\text{isolate}}) \right. \\ & \left. - (E_{JK}^{\text{isolate}} - E_J^{\text{isolate}} - E_K^{\text{isolate}}) - (E_{IK}^{\text{isolate}} - E_I^{\text{isolate}} - E_K^{\text{isolate}}) \right\} + \dots, \quad (34) \end{aligned}$$

and $\Delta\mu$ is given by Eq. (9).

The solvent distribution function, $g_\gamma(\mathbf{r})$, in Eq. (29) is computed by solving the 3D-RISM-KH equation under the solute–solvent interaction potential:

$$u_\gamma(\mathbf{r}) = \sum_\alpha 4\epsilon_{\alpha\gamma} \left[\left(\frac{\sigma_{\alpha\gamma}}{|\mathbf{r}-\mathbf{r}_\alpha|} \right)^{12} - \left(\frac{\sigma_{\alpha\gamma}}{|\mathbf{r}-\mathbf{r}_\alpha|} \right)^6 \right] + U_\gamma^{\text{es}}(\mathbf{r}), \quad (35)$$

$$U_\gamma^{\text{es}}(\mathbf{r}) = -\sum_I^N \int \frac{q_\gamma |\Psi_I(\mathbf{r}')|^2}{|\mathbf{r}-\mathbf{r}'|} d\mathbf{r}' + \sum_\alpha \frac{Z_\alpha q_\gamma}{|\mathbf{r}-\mathbf{r}_\alpha|}, \quad (36)$$

where ϵ and σ are LJ parameters with usual meanings.

4.2 Variational Condition of the FMO/3D-RISM Method

In this subsection, the variational formalization of the FMO/3D-RISM method and the analytical free energy gradient is briefly explained. In this formalism, the many-body energy terms are assumed to be perturbations from the many-body correlations. From this assumption, Eq. (33) is rewritten as follows.

$$G = E_{\text{mono}}^{\text{solv}} + \Delta\mu + E_{\text{perturb}}^{\text{solv}}, \quad (37)$$

where $E_{\text{mono}}^{\text{solv}}$ is the sum of fragment monomer energy whereas $E_{\text{perturb}}^{\text{solv}}$ is a higher order perturbation term caused by many-body effects:

$$E_{\text{mono}}^{\text{solv}} = \sum_{s>t}^{\text{allatoms}} \frac{Z_s Z_t}{|r_s - r_t|} + \sum_I^N E_I^{\text{isolate}}, \quad (38)$$

$$\begin{aligned} E_{\text{perturb}}^{\text{solv}} &= \sum_{I>J}^N \left(E_{IJ}^{\text{isolate}} - E_I^{\text{isolate}} - E_J^{\text{isolate}} \right) \\ &+ \sum_{I>J>K}^N \left\{ \left(E_{IJK}^{\text{isolate}} - E_I^{\text{isolate}} - E_J^{\text{isolate}} - E_K^{\text{isolate}} \right) - \left(E_{IJ}^{\text{isolate}} - E_I^{\text{isolate}} - E_J^{\text{isolate}} \right) \right. \\ &\quad \left. - \left(E_{JK}^{\text{isolate}} - E_J^{\text{isolate}} - E_K^{\text{isolate}} \right) - \left(E_{IK}^{\text{isolate}} - E_I^{\text{isolate}} - E_K^{\text{isolate}} \right) \right\} + \dots \end{aligned} \quad (39)$$

The Lagrange function of the system can be derived by regarding the (unperturbed) Gibbs energy, $G^{(0)}$, as a functional of the correlation functions and the one-particle orbital of the solvated fragment wave functions [22, 33, 37]:

$$L = G^{(0)} - \sum_I^N \sum_{\mu\nu} \varepsilon_I^{\mu\nu} (S_I^{\mu\nu} - \delta_{\mu\nu}), \quad (40)$$

where $S_I^{\mu\nu} = \langle \phi_I^\mu | \phi_I^\nu \rangle$ is an overlap integral of a molecular orbital of Ψ_I^{solv} , and $\varepsilon_I^{\mu\nu}$ is a Lagrange multiplier of monomer I . The variations with respect to the correlation functions and molecular orbitals yields:

$$\begin{aligned} \delta \mathcal{L} &= -\rho k_B T \sum_\gamma \int d\mathbf{r} \left[\left[\exp\left(-\frac{1}{k_B T} u_\gamma(\mathbf{r}) + \eta_\gamma(\mathbf{r})\right) - 1 - h_\gamma(\mathbf{r}) \right] \Theta(-h_\gamma(\mathbf{r})) \right. \\ &+ \left[-\frac{1}{k_B T} u_\gamma(\mathbf{r}) + \eta_\gamma(\mathbf{r}) - h_\gamma(\mathbf{r}) \right] \delta \eta_\gamma(\mathbf{r}) \\ &+ \left. \left\{ -\eta_\gamma(\mathbf{r}) + h_\gamma(\mathbf{r}) - c_\gamma(\mathbf{r}) \right\} \delta h_\gamma(\mathbf{r}) \right] \\ &- \frac{k_B T}{(2\pi)^3} \sum_\gamma \int d\mathbf{k} \left\{ -\rho \hat{h}_\gamma(\mathbf{k}) + \sum_{\gamma'} \hat{c}_{\gamma'}(\mathbf{k}) \hat{\chi}_{\gamma'\gamma}(|\mathbf{k}|) \right\} \delta \hat{c}_\gamma(\mathbf{k}) \\ &+ 2 \sum_I^N \sum_{\mu\nu} P_{\mu\nu} \left\langle \delta \phi_I^\mu \left| \hat{h} + \sum_{\xi\zeta} \hat{g}_{\xi\zeta} + \hat{V} - \varepsilon_I^{\mu\nu} \right| \phi_I^\nu \right\rangle. \end{aligned} \quad (41)$$

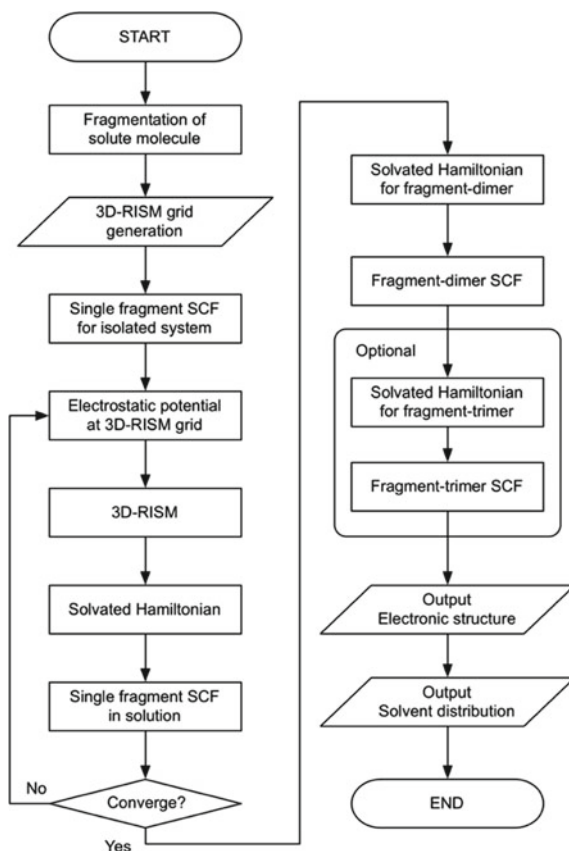
where we assumed to employ the KH closure. In analogy with the 3D-RISM-SCF, the KH closure, indirect correlation function, η , 3D-RISM equation in reciprocal space, and solvated Fock matrix for the fragment monomer are derived from this variational condition.

Based on this variational condition, the analytical gradient of unperturbed Gibbs energy, $G^{(0)}$, with respect to the solute atomic coordinates \mathbf{R}_α is obtained as:

$$\frac{\partial G^{(0)}}{\partial \mathbf{R}_\alpha} = \frac{\partial E_{\text{mono}}^{\text{solv}}}{\partial \mathbf{R}_\alpha} + \frac{\partial \Delta\mu}{\partial \mathbf{R}_\alpha} = \frac{\partial E_{\text{mono}}^{\text{solv}}}{\partial \mathbf{R}_\alpha} + \sum_\gamma \rho \int d\mathbf{r} \left[\left(\frac{\partial u_\gamma(\mathbf{r}; \mathbf{R}_\alpha)}{\partial \mathbf{R}_\alpha} \right) g_\gamma(\mathbf{r}) \right]. \quad (42)$$

Although, in the formalism stated above, the Hartree–Fock method is employed for the electronic structure calculation for simplicity, more sophisticated theories,

Scheme 3 Computational flow chart for FMO/3D-RISM. (reprinted with permission from Ref. [48]. Copyright 2014 AIP.)



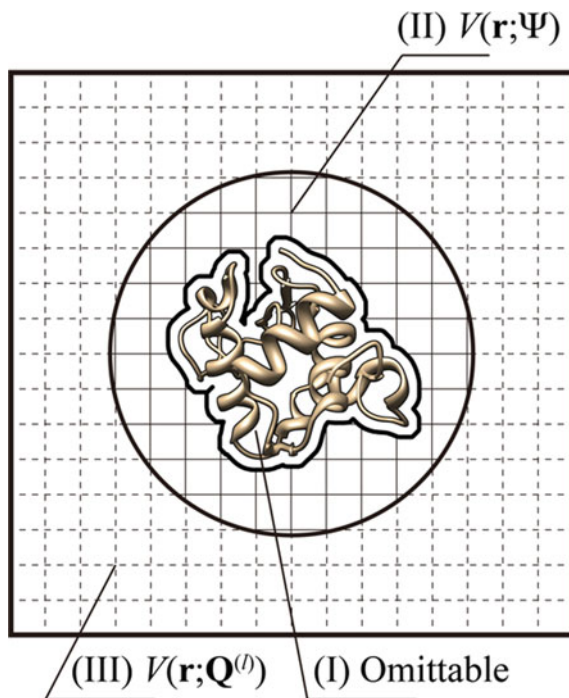
such as the multi-configurational SCF or KS-DFT theories can also be employed instead of the Hartree–Fock method.

The computational scheme of the FMO/3D-RISM method is shown in Scheme 3. As shown in the scheme, the electronic structure of solute fragment monomer and the solvent distribution are determined in self-consistent manner, and the inter-fragments interaction energy terms are added to the total Gibbs energy after fragment monomer/3D-RISM iterations. The details of the computational scheme can be found in the original paper [48].

4.3 Efficient Computation of the Electrostatic Potential in the FMO/3D-RISM Method

The most time-consuming steps in the FMO/3D-RISM computation is the ESP calculations and the construction of the solvated fragment monomer Hamiltonian during

Fig. 1 Schematic of the decomposed regions used in the electrostatic potential calculations. (reprinted with permission from Ref. [48]. Copyright 2014 AIP.)



the fragment monomer iteration, because those steps require the three-center one-electron integrals for all the solvent grids. (The number of the solvent grids is typically $128^3 \sim 256^3$.) Therefore, the method to decrease the computational cost of these parts is required. For this purpose, we introduced a space decomposing technique similar to that used previously for ESP calculation [39].

In this technique, the 3D-RISM solvent grid space is decomposed into three regions as shown in Fig. 1.

Region I is the inside of the repulsive core of the solute atoms, where the solute–solvent interaction potential becomes positively infinite. Therefore, the possibility of existence of solvent molecule in the region I is set to 0;

$$g_\gamma(\mathbf{r}) = 0. \quad (43)$$

This means the ESP calculation is not required in this region. This region is defined to be within the half of the LJ radius.

The 3D-RISM solvent grid points far from the solute molecules are defined as Region III. Because these points sufficiently far from the solute molecules, the multipole expansion of the solute charge density should be effective. The Cartesian tensor expression of the l -th order multipole moment of fragment I is given as follows.

$$\begin{aligned} \mathbf{Q}_I^{(l)} = & -\frac{(-1)^l}{l!} \int |\mathbf{r} - \mathbf{R}_I|^{2l+1} \mathbf{T}^{(l)}(\mathbf{r} - \mathbf{R}_I) |\Psi_I(\mathbf{r})|^2 d\mathbf{r} \\ & + \sum_{\alpha}^{N_I} Z_{\alpha} |\mathbf{r}_{\alpha} - \mathbf{R}_I|^{2l+1} \mathbf{T}^{(l)}(\mathbf{r}_{\alpha} - \mathbf{R}_I), \end{aligned} \quad (44)$$

where \mathbf{R}_I is the center of the atomic charge of fragment I , N_I is number of atoms in fragment I , and \mathbf{T} denotes the following:

$$\mathbf{T}^{(l)}(\mathbf{r}) = \nabla^l \left(\frac{1}{r} \right). \quad (45)$$

Using $\mathbf{Q}_I^{(l)}$, the ESPs acting on the solvent grids in Region III is approximately given by:

$$V(\mathbf{r}) = \sum_I^N \sum_l^{N_I} \frac{(-1)^l}{(2l-1)!!} \mathbf{Q}_I^{(l)} \otimes \mathbf{T}^{(l)}(\mathbf{r}), \quad (46)$$

where the symbol \otimes indicates a full contraction of the two rank- l tensors [51] and N_I defines the truncation limit of the multipole expansion. In this study, we truncated the multipole expansion at $N_I = 3$.

Region II is middle of the region I and region III. In this region, the charge density of the solute molecule must be described precisely based on the wave function, because the electrostatic potential by solute molecule is highly inhomogeneous. Therefore, the ESP is given by exact form:

$$V(\mathbf{r}) = -\sum_I^N \int \frac{|\Psi_I^{\text{solv}}(\mathbf{r}')|^2}{|\mathbf{r}-\mathbf{r}'|} d\mathbf{r}' + \sum_{\alpha}^{\text{allatoms}} \frac{Z_{\alpha}}{|\mathbf{r}-\mathbf{r}_{\alpha}|}. \quad (47)$$

In summary, the solute-solvent electrostatic interaction potential and the electrostatic potential term in the solvated Hamiltonian V^{solv} are given by

$$U_{\gamma}^{\text{es}}(\mathbf{r}) = \begin{cases} 0 & \text{for (I)} \\ -\sum_I^N \int \frac{q_{\gamma} |\Psi(\mathbf{r}')|^2}{|\mathbf{r}-\mathbf{r}'|} d\mathbf{r}' + \sum_{\alpha} \frac{Z_{\alpha} q_{\gamma}}{|\mathbf{r}-\mathbf{r}_{\alpha}|} & \text{for (II)} \\ q_{\gamma} \sum_I^N \sum_l^{N_I} \frac{(-1)^l}{(2l-1)!!} \mathbf{Q}_I^{(l)} \otimes \mathbf{T}^{(l)}(\mathbf{r}) & \text{for (III)} \end{cases} \quad (48)$$

$$\begin{aligned} V^{\text{solv}}(\mathbf{r}_i) = & -\sum_{\gamma}^{N_v} \rho \int_{\text{region(II)}} \frac{q_{\gamma}}{|\mathbf{r}_i - \mathbf{r}|} g_{\gamma}(\mathbf{r}) d\mathbf{r} \\ & -\sum_{\gamma}^{N_v} \rho \int_{\text{region(III)}} \frac{q_{\gamma}}{|\mathbf{r} - \mathbf{R}_I|} g_{\gamma}(\mathbf{r}) d\mathbf{r} \end{aligned}$$

$$\times \frac{(-1)^l}{l!} \sum_l^{N_l} \frac{(-1)^l}{(2l-1)!!} (|\mathbf{r} - \mathbf{R}_l|^{2l+1} \mathbf{T}^{(l)}(\mathbf{r} - \mathbf{R}_l)) \otimes \mathbf{T}^{(l)}(\mathbf{r}) \quad (49)$$

This technique dramatically reduces computational cost at the expense of a detailed description of the electronic distribution of solute molecule at region III.

4.4 Assessment of the FMO/3D-RISM Method

In this subsection, the solvent effects on several systems were examined for the sake of an assessment of the FMO/3D-RISM method. Details of the computation are found in the original paper [48].

The systems for the assessment are summarized in Fig. 2 and Table 1. In the exam 37 system, each water molecule is treated as a different fragment whereas the every single amino acid are treated as a fragment monomer in the 1PLX, 1L2Y, and 2XFD.

The extended simple point charge (SPC/E) parameter set was used for water at ambient conditions (i.e., a temperature of 298 K and density of 1.0 g cm⁻³) [52, 53]. The same water LJ parameters were used for solute water in the exam 37. The Amber99 parameter set was employed for all the solute amino acids [53].

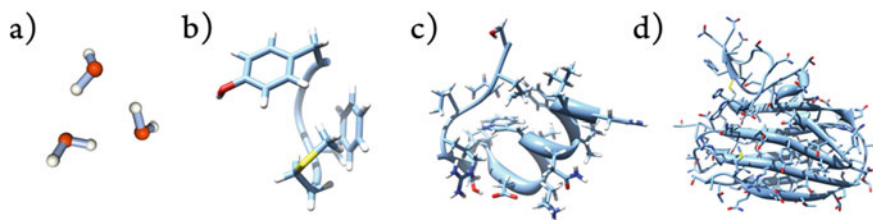


Fig. 2 Structures of the target molecules. **a** Water trimer taken from exam37.inp in the GAMESS package, **b** methionine-enkephalin (PDB: 1PLX), **c** Trp-cage (PDB: 1L2Y), and **d** cellulose binding module VCBM60 (PDB: 2XFD). (reprinted with permission from Ref. [48]. Copyright 2014 AIP.)

Table 1 Structural and computational parameters of the target molecules

Parameter	Molecule			
	exam37	1PLX	1L2Y	2XFD
Number of atoms	9	75	304	1,584
Number of fragments	3	5	19	107
Number of electrons	30	304	1,158	6,194
Solvent box size [Å ³]	64.0 ³	64.0 ³	128.0 ³	128.0 ³

Reprinted with permission from Ref. [48]. Copyright 2014 AIP

Table 2 Comparison of the dipole moments and total free energy between FMO/3D-RISM and FMO/PCM methods

Molecule	$\langle \Delta D \rangle^a$		$\Delta G^{\text{solvation } b}$		
	3D-RISM	PCM	3D-RISM		PCM
			KH	GF ^c	
(a) exam37	0.22	0.12	- 7.38	- 12.40	- 12.61
(b) 1PLX	1.99	1.52	- 67.83	- 99.61	- 121.22
(c) 1L2Y	1.09	0.78	21.85	- 88.05	- 207.54
(d) 2XFD	0.81	0.54	437.45	- 72.90	- 256.08

^aMean value for the difference between the fragment dipole moment in solution and in gas phase. The units are Debyes. ^bThe units are kcal mol⁻¹. ^cThe values were calculated using a Gaussian fluctuation formula rather than the Kovalenko–Hirata formula. (reprinted with permission from Ref. [48]. Copyright 2014 AIP.)

To assess the difference between the solvation model, the FMO/3D-RISM, and FMO/PCM were applied to the system stated above. The average change in the fragment dipoles

$$\langle |\Delta D| \rangle = \frac{1}{N} \sum_I^N |D_I^{\text{solv}} - D_I^{\text{gas}}|, \quad (50)$$

and SFEs of the system are summarized in Table 2. D_I^{solv} denotes the dipole moment of fragment I . Two types of SFE formula are used, namely, KH and h Gaussian fluctuation (GF).

The 3D-RISM SFEs are higher than those by PCM. Since the KH closure tends to overestimate the excluded volume effects on the SFE, KH shows larger values [54, 55]. The GF and PCM-SFEs show same sign; however, the absolute values of SFE for the large systems are quite different from each other. No clear trend of SFE behavior is found. To discuss the accuracy of the SFEs, more comprehensive research is required. (See Refs. [43, 55–59]).

The dipole moments show clear tendency unlike SFEs. In Fig. 3, the dipole moments by 3D-RISM of each fragments are compared with those by PCM. Most of fragments show the greater dipole moment evaluated by 3D-RISM than the PCM, and the average change in the fragment dipoles also shows greater values in 3D-RISM. Because the 3D-RISM can handle the microscopic solute–solvent interaction such as hydrogen bonding, the electronic polarization induced by solvent molecules may be greater than those by PCM. To look close this feature, the close up view of solvation structure of glutamine 73 (Q73) and glutamate 75 (E75) are shown in Fig. 4, because Q73 and E75 show remarkable deviation in Fig. 3b. Near the amide oxygen of Q73 and carbonyl oxygen of E75, the conspicuous hydrogen distributions are observed, which indicate that the hydrogen bonds between solute oxygen and the solvent water hydrogen are formed. It may be due to the strong polarization of the fragments.

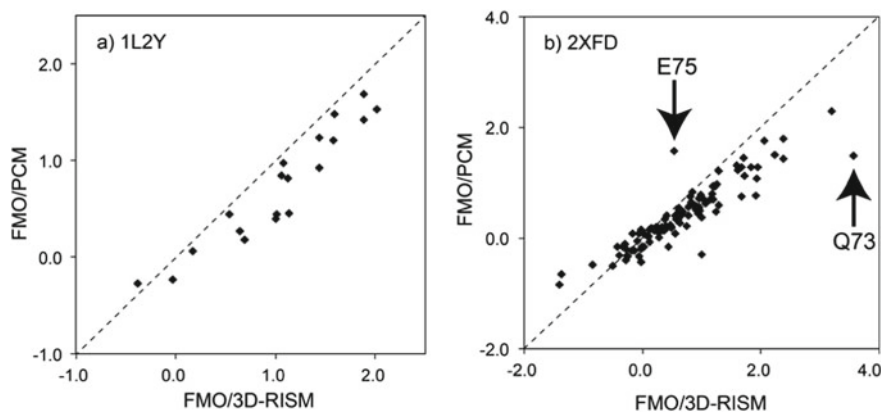


Fig. 3 The fragment dipole moments calculated using the FMO/PCM method and the FMO/3D-RISM method plotted against each other, for **a** molecule 1L2Y and **b** molecule 2XFD. The arrows shown in plot **(b)** indicate the values for fragments Q73 and E75. The units are Debyes. (reprinted with permission from Ref. [48]. Copyright 2014 AIP.)

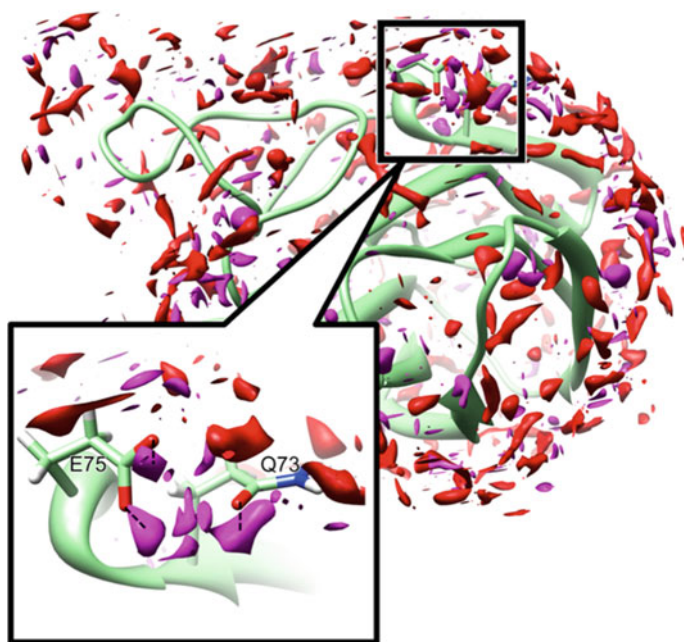


Fig. 4 Isosurface plots for the SDFs of oxygen (in red) and hydrogen (in magenta) around molecule 2XFD. The isosurface value is $g(r) = 4.0$. The inset shows the detailed solvation structure around molecules Q73 and E75. The broken lines indicate the candidates of hydrogen bonds. (reprinted with permission from Ref. [48]. Copyright 2014 AIP.)

As shown here, the 3D-RISM method allows us to discuss the microscopic features of the solvent molecules based on the distribution functions, unlike PCM.

5 Summary and Perspective

In this chapter, the hybrid method of the FMO and the 3D-RISM theory, called the FMO/3D-RISM method, has been reviewed. The method enables one to investigate the electronic structure of a macromolecule and the solvation effects on it at the molecular level.

The 3D-RISM theory can provide the SDFs obtained through a complete ensemble average over the entire configuration space of solvent molecules within the thermodynamic limits. It is extremely difficult to achieve a similar level of ensemble average with an MD simulation if the solute molecule has a complex structure, like a protein, or the solution contains dilute species, such as ions.

The 3D-RISM theory naturally reproduces all the solvation thermodynamic properties, including solute–solvent interaction energy, solvation entropy, and solvation free energy, and their derivatives, such as the partial molar volume. Therefore, the QM hybrid method with the 3D-RISM theory can provide a comprehensive means of analyzing chemical and biological processes in solution. For example, the molecular recognition by proteins, a fundamental process in living systems, lends itself to investigation by the FMO/3D-RISM method.

Molecular recognition processes are characterized by changes in Gibbs energy due to the formation of ligand–receptor complexes, such as enzyme–substrate complexes. In such processes, both the quantum mechanical interaction between ligand and receptor and the hydration/dehydration of the molecules play essential roles. However, there is still a need for improvements related to several important factors, such as structural fluctuation and inter-fragment charge transfer, among others. Combining the FMO/3D-RISM with the methods introduced in other chapters, i.e., density functional tight binding, linear combination of molecular orbitals, and MD, will enable more accurate and a wider variety of analyses of biological processes.

Acknowledgments The author is grateful to Prof. Fumio Hirata (Toyota Physical and Chemical Research Institute), Prof. Yoshihiro Watanabe (Kyushu University), and Prof. Haruyuki Nakano (Kyushu University) for helpful discussions. Molecular graphics and analyses were performed with the UCSF Chimera package [60].

References

1. Alberts B (2014) *Molecular biology of the cell*, 6th edn. Garland Science, New York
2. Feig M (2010) *Modeling solvent environments*. Willey-VCH, Weinheim

3. Field MJ, Bash PA, Karplus M (1990) *J Comput Chem* 11:700
4. Aqvist J, Warshel A (1993) *Chem Rev* 93:2523
5. Gogonea V, Suarez D, van der Vaart A, Merz KW (2001) *Curr Opin Struct Biol* 11:217
6. Gao JL (1996) *Acc Chem Res* 29:298
7. Tomasi J, Mennucci B, Cammi R (2005) *Chem Rev* 105:2999
8. Tomasi J, Persico M (1994) *Chem Rev* 94:2027
9. Cramer C, Truhlar DG (1999) *Chem Rev* 99:2161
10. Fedorov DG, Kitaura K, Li H, Jensen JH, Gordon MS (2006) *J Comput Chem* 27:976
11. Fedorov DG (2018) *Chem Phys Lett* 702:111
12. Watanabe H, Okiyama Y, Nakano T, Tanaka S (2010) *Chem Phys Lett* 500:116
13. Chandler D, Andersen HC (1972) *J Chem Phys* 57:1930
14. Andersen H, Chandler D, Weeks J (1972) *J Chem Phys* 57:2626
15. Andersen H, Chandler D (1972) *J Chem Phys* 57:1918
16. Blum L (1973) *J Chem Phys* 58:3295
17. Blum L, Torruella J (1972) *J Chem Phys* 56:303
18. Blum L (1972) *J Chem Phys* 57:1862
19. Beglov D, Roux B (1997) *J Phys Chem B* 101:7821
20. Beglov D, Roux B (1996) *J Chem Phys* 104:8678
21. Fries PH, Patey GN (1985) *J Chem Phys* 82:429
22. Kovalenko A, Hirata F (1999) *J Chem Phys* 110:10095
23. Kovalenko A, Hirata F (1998) *Chem Phys Lett* 290:237
24. Hirata F (2003) *Molecular theory of solvation*. Kluwer, Dordrecht
25. Hansen JP, McDonald IR (2006) *Theory of simple liquids* 3rd edn. Academic Press, Amsterdam
26. Zhao S, Ramirez R, Vuilleumier R, Borgis D (2011) *J Chem Phys* 134:194102
27. Gendre L, Ramirez R, Borgis D (2009) *Chem Phys Lett* 474:366
28. Yoshida N, Imai T, Phongphanphane S, Kovalenko A, Hirata F (2009) *J Phys Chem B* 113:873
29. Yoshida N (2017) *J Chem Info Model* 57:2646
30. Kovalenko A, Blinov N (2011) *J Mol Liq* 164:101
31. Ten-No S, Hirata F, Kato S (1994) *J Chem Phys* 100:7443
32. Ten-No S, Hirata F, Kato S (1993) *Chem Phys Lett* 214:391
33. Sato H, Hirata F, Kato S (1996) *J Chem Phys* 105:1546
34. Yoshida N (2011) *Proc Comput Sci* 4:1214
35. Yoshida N (2007) *Condens Matter Phys* 10:363
36. Yoshida N, Kato S (2000) *J Chem Phys* 113:4974
37. Sato H, Kovalenko A, Hirata F (2000) *J Chem Phys* 112:9463
38. Gusarov S, Ziegler T, Kovalenko A (2006) *J Phys Chem A* 110:6083
39. Yoshida N, Hirata F (2006) *J Comput Chem* 27:453
40. Kasai Y, Yoshida N, Nakano H (2015) *J Chem Phys* 142
41. Kasai Y, Yoshida N, Nakano H (2014) *J Mol Liq* 200:32
42. Tanaka Y, Kawashima Y, Yoshida N, Nakano H (2017) *J Comput Chem* 38:2411
43. Yoshida N, Tanaka H, Hirata F (2013) *J Phys Chem B* 117:14115
44. Hayaki S, Kimura Y, Sato H (2013) *J Phys Chem B* 117:6759
45. Hayaki S, Kido K, Sato H, Sakaki S (2010) *Phys Chem Chem Phys* 12:1822
46. Hayaki S, Kido K, Yokogawa D, Sato H, Sakaki S (2009) *J Phys Chem B* 113:8227
47. Takami T et al (2007) *AIP Conf Proc* 963:122
48. Yoshida N (2014) *J Chem Phys* 140:214118
49. Yoshida N, Hirata F (2018) *The role of water in atp hydrolysis energy transduction by protein machinery*, Suzuki M (ed). Springer Nature Singapore Pte Ltd., Singapore
50. Kovalenko A, Ten-No S, Hirata F (1999) *J Comput Chem* 20:928
51. Gray CG, Gubbins KE (1984) *Theory of molecular fluids volume 1: fundamentals*. Clarendon Press, Oxford
52. Berendsen HJC, Grigera JR, Straatsma TP (1987) *J Phys Chem* 91:6269
53. Wang JM, Cieplak P, Kollman PA (2000) *J Comput Chem* 21:1049
54. Palmer DS, Sørensen J, Schiøtt B, Fedorov MV (2013) *J Chem Theory Comput* 9:5706

55. Truchon J-F, Pettitt BM, Labute P (2014) *J Chem Theory Comput* 10:934
56. Palmer DS, Frolov AI, Ratkova EL, Fedorov MV (2010) *J Phys-Condens Mat* 22:492101
57. Sergiievskiy V, Jeanmairet G, Levesque M, Borgis D (2015) *J Chem Phys* 143:184116
58. Hong J, Yoshida N, Chong S-H, Lee C, Ham S, Hirata F (2012) *J Chem Theory Comput* 8:2239
59. Fujiki R, Kasai Y, Seno Y, Matsui T, Shigeta Y, Yoshida N, Nakano H (2018) *Phys Chem Chem Phys* 20:27272
60. Pettersen EF, Goddard TD, Huang CC, Couch GS, Greenblatt DM, Meng EC, Ferrin TE (2004) *J Comput Chem* 25:1605

New Methodology and Framework

New Methodology and Framework Information Science-Assisted Analysis of FMO Results for Drug Design



Tatsuya Takagi

Abstract Recently, AI, which is sometimes called ‘Machine Learning’ or ‘Data Mining’, has become common even for public. These techniques are widely utilized even in the field of chemistry and pharmaceutical sciences. However, until very recently, the two fields, AI and theoretical chemistry had been separately developed and utilized for solving chemical or biological problems. In this paragraph, I try to show the recent development of machine learning methods and to show the applications of the methods to the results obtained by theoretical chemistry.

Keywords Artificial intelligence · Machine learning · Data mining · Supervised learning · Unsupervised learning · β -secretase

1 Necessity of Information Science-Assisted Analysis

In 1988, AI for chess, named ‘Deep Thought’, won against Donnish Grandmaster, Bent Larsen. In 1996, the new AI of IBM, ‘Deep Blue’ won against Garry Kimovich Kasparov who had been a world chess champion once. And in 1997, Deep Blue had more wins than loses against him. This was the first time that ‘Machine’ won against a world chess champion.

Now, AI (AlphaGo) can win against a European Go champion. In 2016, it won fifth straight against the champion, Fan Hui. In the near future, it is certain that AI will greatly exceed the capability of human being. In the well-known TV drama, ‘Person of Interest’, the AI developed by a protagonist shows the person(s) who will kill some innocent people or be killed by some villains tells their social security numbers. The protagonists try to prevent the incident which was informed by the AI named ‘Machine’. The protagonist who developed ‘Machine’ made the AI just tell their security number in order to prevent the ‘Singularity’ when AIs develop themselves and overtake the capacity of human beings. In the movie, ‘Space Odyssey

T. Takagi (✉)

Graduate School of Pharmaceutical Sciences, Osaka University, Osaka, Japan
e-mail: ttakagi@phs.osaka-u.ac.jp

2001', the AI named HAL started to revolt when it realized that the clue was going to shut down the AI.

Actually, some researchers say that the singularity is to arrive in 2045 [1], when AI significantly exceed the sum of human brainpower. All the people on the earth may be controlled by AI within 30 years.

However, we are sometimes suffered from intractable diseases even now. Most of anti-tumor drugs do not have enough power to make a full recovery; no effective approaches are known for many progressive cranial nerve diseases such as Alzheimer's. Still now, medical scientists have no futuristic overview when these diseases are completely cured. Although medical sciences seem to be much more complicated than 'Go', at least in 2045, we may be able to know everything about such diseases if the singularity 2045 arrives.

Under these circumstances, it is also certain to be unwise not to take advantage of AI, for example, machine learning, in the field of in Silico drug design. Already, many researchers started to apply various kinds of machine learning methods including deep learning, which was adopted for AlphaGo, to design novel drugs for intractable diseases.

Hence, in this section, we will explain on AI, machine learning, and data mining methods briefly. Then, the applications of AIs for FMO results will be shown.

2 What is AI?

2.1 Definition of AI, Machine Learning, and Data Mining.

Sometimes, these words, Artificial Intelligence (AI), Machine Learning, Data Mining, are frequently confused with each other. However, these three words should be used distinctively (Fig. 1).

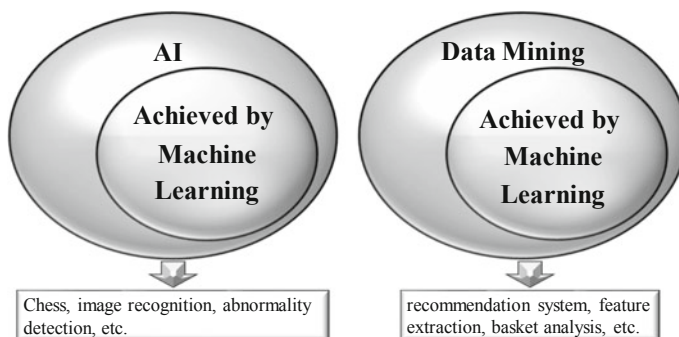


Fig. 1 Venn diagram of the concepts of AI, Data Mining, and Machine Learning

AI is a broader concept of 'Machine learning'. There are some AIs without machine learning methods. For example, some AIs issue a decision deductively, which is not a machine 'learning' method.

On the other hand, 'Data Mining' is a concept which is classified into a different category. People apply 'Data Mining method' to extract some rules from a data set. For example, when you buy something from an online shop, you will find some other goods which are recommended by the shop. Those recommended goods must be selected using a recommendation system which is one of machine learning methods in order to help you find other goods you want to buy. The selections are the results of 'Data Mining' from huge data set of the records, what kind of goods are bought by the consumers who buy the goods you bought. In the below section, we will mention several advanced and popular machine learning methods which can apply to in Silico drug design using FMO.

3 Various Machine Learning Methods

Usually, machine learning methods are classified into three groups, supervised, unsupervised, and reinforcement learnings. In addition, multi-task and transductive learnings are also machine learning groups (Table 1). Here, we will explain the former two kinds of learnings which are used more frequently and for FMO drug design.

Table 1 Frequently used machine learning methods

Categories	Methods	Examples of applications
Supervised learnings	Linear multiple regression method	Hansch-Fujita method, $\log P$ prediction
	Partial least squares method	3D-QSAR
	Logistic regression	Bioactive class prediction
	Support vector machine	Environmental degradability prediction
	Nonparametric regression	Epidemiology, time series analysis
	Hierarchical artificial neural network	Bioactive class prediction
Unsupervised learning	Principal component method	Analysis of DNA array results
	Cluster analysis	Analysis of DNA array results
	Manifold learning including multidimensional scaling method	Microbiology, diagnostic assistance
	Others (t-SNE, UMAP, etc.)	Show regional prescribing patterns, etc
Reinforcement learning	Dose optimization, etc	

3.1 Supervised Learning

3.1.1 Linear Regression Analyses

When you want to predict pharmacological activities of a certain kind of molecules, you should prepare some chemical descriptors which express chemical structures and/or physicochemical properties of molecules. The simplest model for predicting pharmacological activities using the chemical descriptors is linear multiple regression analysis (MRA) which is expressed as shown in Fig. 2.

MRA can be expressed as $y_i = \sum \beta_j x_{ij} + \beta_0$. Here, y_i , x_{ij} , β_j , β_0 , and ε_i indicate a pharmacological activity of the i -th molecule, the j -th descriptor value of the i -th molecule, the coefficient for the j -th descriptor, the intercept, and the error value between calculated and observed y_i values, respectively. Although usually, β_j ($j = 0, 1, \dots, m$) values are obtained by ordinal least squares method (OLS), recently, sparse methods such as lasso regression [2], which is one of penalized regression, have been becoming more popular. Elastic net [3] regression is expressed as follows:

OLS

$$E(\boldsymbol{\beta}) = \frac{1}{n} \sum_{i=1}^n \varepsilon_i^2$$

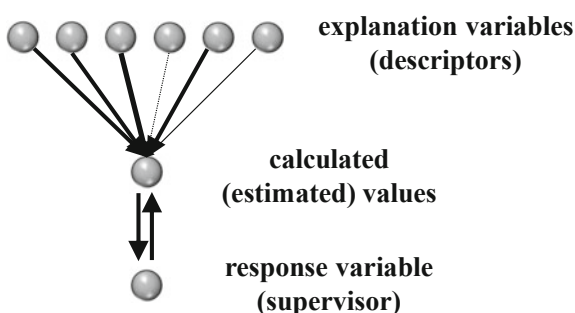
Elastic net

$$E(\boldsymbol{\beta}, \lambda) = \frac{1}{2n} \sum_{i=1}^n \varepsilon_i^2 + \lambda P(\alpha, \boldsymbol{\beta}) \quad (2.1)$$

$$P(\alpha, \boldsymbol{\beta}) = (1 - \alpha) \frac{1}{2} \|\boldsymbol{\beta}\|_{L2}^2 + \alpha \|\boldsymbol{\beta}\|_{L1} = \sum_{j=1}^m \left\{ \frac{1}{2} (1 - \alpha) \beta_j^2 + \alpha |\beta_j| \right\}$$

Here, λ indicates complexity parameter. Lasso and Ridge regressions are the special cases where $\alpha = 1$ and $\alpha = 0$, respectively.

Fig. 2 Supervised learning



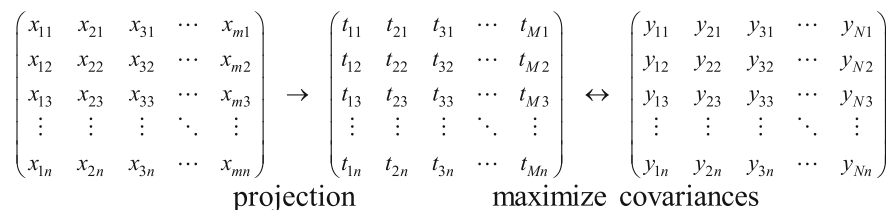


Fig. 3 Outline of partial least square regression

However, in the field of drug design, usually, pharmacological activities ($n = 10\text{--}100$) have to be estimated using large numbers of chemical descriptors ($300\text{--}2000$). In this case, since linear simultaneous equation is indeterminate, MRA cannot be applied. This condition developed another model with latent variables which are consisted of linear combinations of the chemical descriptors. One of such models is Partial Least Squares (PLS) method, which is expressed as follows:

$$\begin{aligned}
 \mathbf{X} &= \mathbf{TP}' + \mathbf{E} \\
 \mathbf{Y} &= \mathbf{UQ}' + \mathbf{F}
 \end{aligned}
 \tag{2.2}$$

where, \mathbf{X} is an $n \times m$ matrix of explanation variables, x_{ij} , \mathbf{Y} is an $n \times N$ matrix of response variables, y_{ik} , \mathbf{T} and \mathbf{U} are $n \times M$ and $n \times K$ matrices of projections of \mathbf{X} and \mathbf{Y} , respectively; \mathbf{P} and \mathbf{Q} are $m \times M$ and $N \times K$ orthogonal loading matrices, respectively; \mathbf{E} and \mathbf{F} are error matrices. \mathbf{T} and \mathbf{U} are determined in order to maximize the covariances between \mathbf{T} and \mathbf{U} . The Eq. (2.2), is solved iteratively (NIPALS). The outline of PLS is shown in Fig. 3. In the next section, we will show an example which used PLS for FMO results.

In addition, Multiple Logistic Regression (MLR) is also frequently applied to the field of Drug Design. In this case, logit ($\log(p/1-p)$) is used instead of metric response variable. Here, p indicates the probability of $y = 1$ when $y = 1$ or 0 (binary).

3.1.2 Nonlinear Regression Analyses

Although abovementioned methods, MRA, LASSO, Ridge, and PLS can treat linear relationships, sometimes, nonlinear relationships are required. For example, an optimum value of molecular hydrophobicity for cell permeability is usually observed, which indicates that the relationship between bioactivity and molecular hydrophobicity is nonlinear.

In some cases, such relationships can be expressed by regression analysis using second order polynomial. However, sometimes, the relationships cannot be expressed by parametric regressions. In these cases, three kinds of machine learning methods are utilized; the first one is nonparametric regression method such as GAM, the second one is artificial neural network, and the third one is tree type regression such

as decision tree (Here, Hidden Markov Model as well as Conditional Random Field are classified into another group).

Nonparametric regression analysis deals with the relationships which cannot be expressed by high-order polynomials. The simplest model, additive model, is written as follows:

$$y_i = \beta_0 + \sum_{j=1}^m f_j(x_{ij}) + \varepsilon_i \tag{2.3}$$

where $f_j(x)$ is a unary function, β is an intercept, and ε is an error term. In this case, usually, $f_j(x)$ is expressed by spline functions. Hastie and Tibshirani proposed General Additive Model (GAM) [4] as one of additive models which need multiple explanation variables.

Hierarchical Artificial Neural Network (HANN) is another solution for nonlinear problems. This method became popular in 1980s and various kinds of applications including home electric appliances were tried. The outline of this method is shown in Fig. 4. Prepared data are inputted into 'Input Layer' neurons. The values are transferred to 'Hidden Layer' neurons using nonlinear functions such as sigmoid function. Thick axons transfer the data more than thin axons. The data are transferred to 'Output Layer' neurons. The data are compared with 'results (supervisors)'. When the values are rather different from the 'results', this system learn by adjusting the thicknesses of the axons to obtain correct output values compared with the 'results'. PLS is a special case of the HANN whose transfer functions are linear ones.

Although this method was considered to be powerful and flexible, soon, researchers encountered some serious problems. The first one is that this system is easy to over-train. The simple example is shown in Fig. 5. The true relationship between x and y values in this graph must be shown in the solid line while HANN tends to draw the dotted line which is not expected.

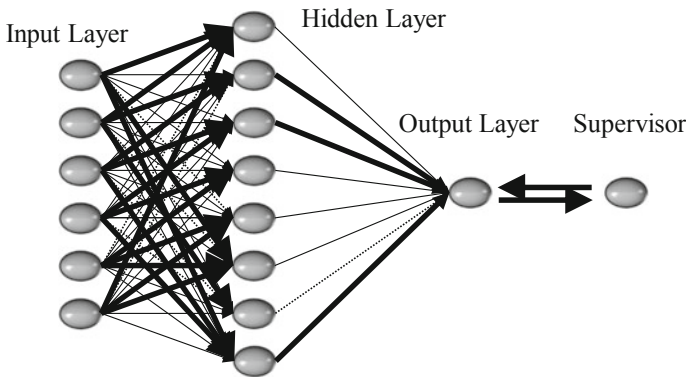
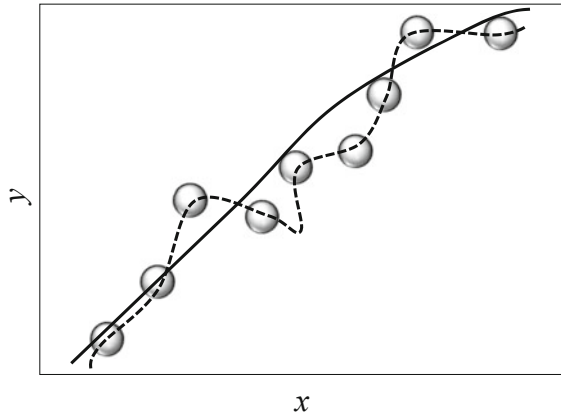


Fig. 4 Frame format of hierarchical artificial neural network

Fig. 5 Example of overfitting



Although HANN became popular in 1980s, researchers soon gave up applying the method to predict unknown data until 2012 when Toronto and Google shock happened.

Recent advances in this field brought about a novel and powerful method, Deep Learning, which is based on the artificial neural network (Fig. 6). AlphaGo, which won against human professional ‘Go’ player, used to be based on Deep Learning and Reinforcement Learning [5] (Present system is based on Reinforcement Learning). While Deep Learning system has many hidden layers, some techniques enables the system to avoid overfitting. One of them is ‘dropout’ which Srivastava et al. [6] proposed in 2014. ‘Dropout’ generates some neurons which are eliminated from the system. This technique is considered to be one of the regularization method to decrement flexible variables. Since the flexibility is reduced when the number of parameters is decreased, ‘Dropout’ can reduce overfitting. Another method for avoiding overfitting is Convolutional Neural Network (CNN), which consists of Input, Convolution, Pooling, Fully connected and Output operations. CNN can be shown as a simple example diagram as shown in Fig. 7.

However, reportedly, Geoffrey Hinton, who developed Deep Learning, gave a speech in MIT and said, ‘The pooling operation used in convolutional neural networks is a big mistake and the fact that it works so well is a disaster’. Recently, Hinton

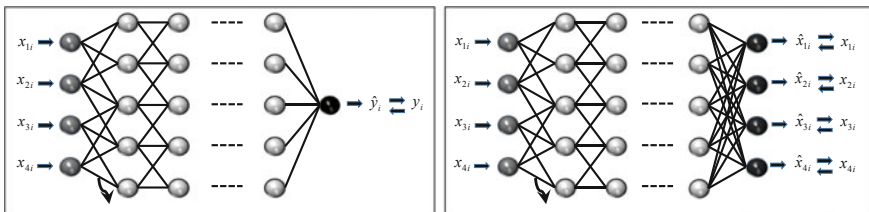


Fig. 6 Structures of supervised (left) and unsupervised (right) deep learning

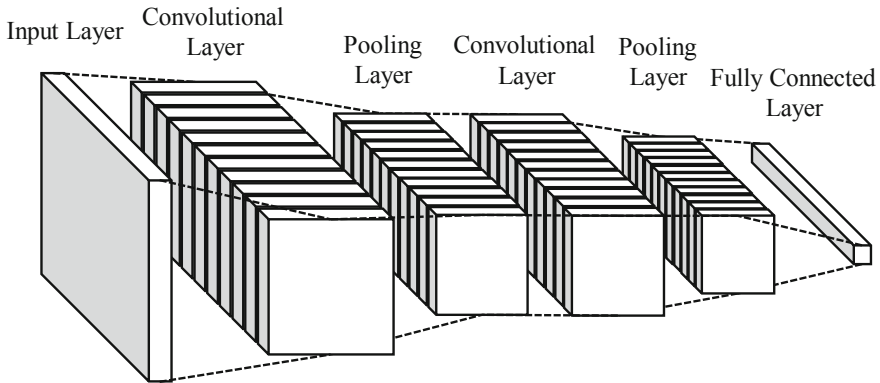


Fig. 7 Conceptual diagram of convolutional neural network

et al. [7] proposed ‘Capsule Network’, which overcomes some problems associated with CNN, especially the pooling operation. Now many researchers are applying the capsule network to various kinds of fields.

3.1.3 Other Supervised Learning Method

Support Vector Machine (SVM) is one of frequently applied methods for classifying two or more categories using explanation variables. This method classifies two categories data to maximize the ‘margin’ between the categories.

Tree model is also frequently used for classification. Especially, Random Forest and Binary Tree are popular because of high generalization capability. Recently, Boosting method is sometimes applied to these supervised learning methods. Especially, Gradient Boosting Method (GBM) shows high generalization capability.

These methods will be explained for another time.

3.2 Unsupervised Learning

Unsupervised learning methods are roughly classified into two categories. One is the group of methods which finds and/or visualizes ‘similar data points’ from the data in high-dimensional space. The other one is for extracting ‘factors or components’ from a data set in high-dimensional space. In the former case, even if the results are shown in two-dimensional space, the two axes have no meanings. On the other hand, in the latter cases, some meanings can be found from extracted axes. Thus, here, the former category of methods is called ‘Classification Method’ and the latter one is called ‘Component Extraction Method’.

3.2.1 Component Extraction and Dimension Reduction Method

A representative method in this category is Principal Component Analysis (PCA). This method determines a ‘Principal Axis’ in order to maximize the variance of the ξ -coordinates (Fig. 8). And the next axis is determined to be orthogonal to the first axis (ξ) and to maximize the variance of η -coordinates, and so on. The resulted axes are called ‘Principal Components’. Hence, each component has the highest variance under the constraint that it is orthogonal to the other components.

In PCA, synthetic variables are calculated as follows:

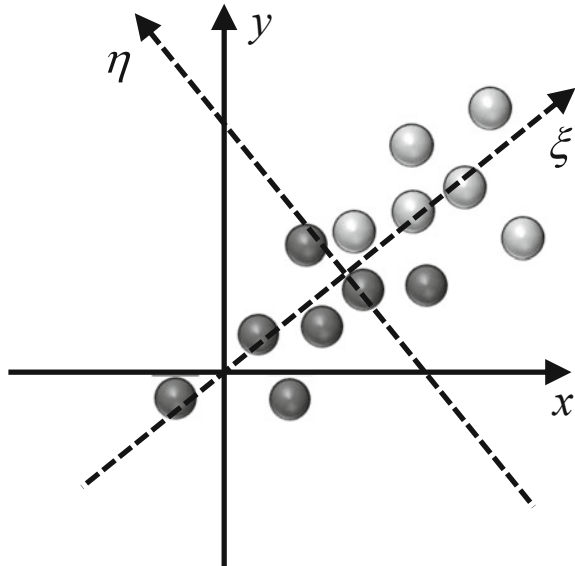
$$z_{ki} = \sum_{j=1}^m a_{kj}x_{ij} \tag{2.4}$$

where z_{kj} is the k th synthetic variable, a_{kj} is the k th component loading, and x_{ij} is a value of variable j . a_{kj} is determined to maximize the variance of z_{kj} under the condition,

$$\sum_{j=1}^m a_{kj}^2 = 1 \tag{2.5}$$

using LaGrange’s method of undetermined multipliers. This problem is solved as eigenvalue–eigenvector problem.

Fig. 8 Conceptual diagram of principal component analysis (PCA)



$$\mathbf{AV} = \varepsilon \mathbf{V} \quad (2.6)$$

where \mathbf{A} is a loading matrix (eigen vector matrix), and \mathbf{V} is correlation coefficient matrix, and \mathbf{V} becomes an eigenvalue vector matrix of \mathbf{A} after the problem is solved.

PCA is often applied to analyze array data set such as DNA array. For example, Chang et al., (8) applied PCA to SNPs data set for extracting principal components which classify autoimmune, neurodegenerating, and some other diseases. They succeeded in classifying systemic lupus erythematosus, vitiligo, multiple sclerosis, schizophrenia, Crohn's, and some other diseases including Alzheimer's.

There are some other linear methods to extract components and to reduce dimensions such as factor analysis, independent component analysis, and principal coordinate analysis, which are based on PCA.

3.2.2 Classification and Visualization Method

Although PCA can be used as a classification method such as beforementioned study [7], PCA's main purpose is extracting main factor that can be explained. As classification methods, there are some superior methods. One of the methods is multidimensional scaling method (MDS).

MDS maps the data in high-dimensional space ($x_{ij} \in R^N$) to two or three-dimensional ($\xi_{ij} \in R^2$ or R^3) space in order to minimize the 'Stress' (S) which is written as follows:

$$\begin{aligned} d_{ij} &= \frac{1}{m} \sum_{p=1}^m (x_{ip} - x_{jp})^2, \quad x_{ip} \in R^N \\ \delta_{ij} &= \frac{1}{2} \left\{ (\xi_{i1} - \xi_{j1})^2 + (\xi_{i2} - \xi_{j2})^2 \right\}, \quad \xi_{iq} \in R^2 \\ S &= \sum_{i < j} \sum (d_{ij} - \delta_{ij})^2 \end{aligned} \quad (2.7)$$

where d_{ij} means a distance in high-dimensional space and δ_{ij} in two-dimensional space.

Recently, non-metric MDS and Generalized MDS (GMDS), which can treat item-item dissimilarities and dissimilarities in an arbitrary smooth non-Euclidean space, respectively, have become popular. Moreover, recently, Manifold Learning, which uses geodesic instead of ordinal distance, has been becoming more popular (Fig. 9). This field is rapidly advancing.

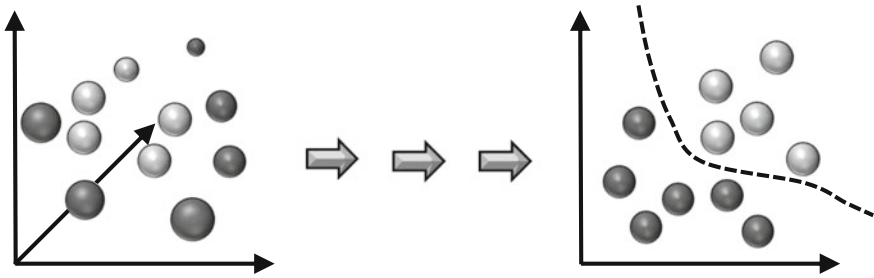


Fig. 9 Conceptual diagram of multidimensional scaling method

3.2.3 Other Classification Methods

As a classical classification method, Cluster Analysis might be the most well-known. Cluster analysis is classified into two groups, Hierarchical and Non-hierarchical methods. Hierarchical cluster analysis is carried out as follows:

- (1) Calculate all the distances between given data.
- (2) Among the calculated distances, the closest two data, A and B (Fig. 10), is merged.
- (3) Calculate the distances between the data and the cluster, AB.
- (4) The closest two clusters (or data), C and D, is merged.
- (5) Merge the remained two clusters, ABFGH and CDE.

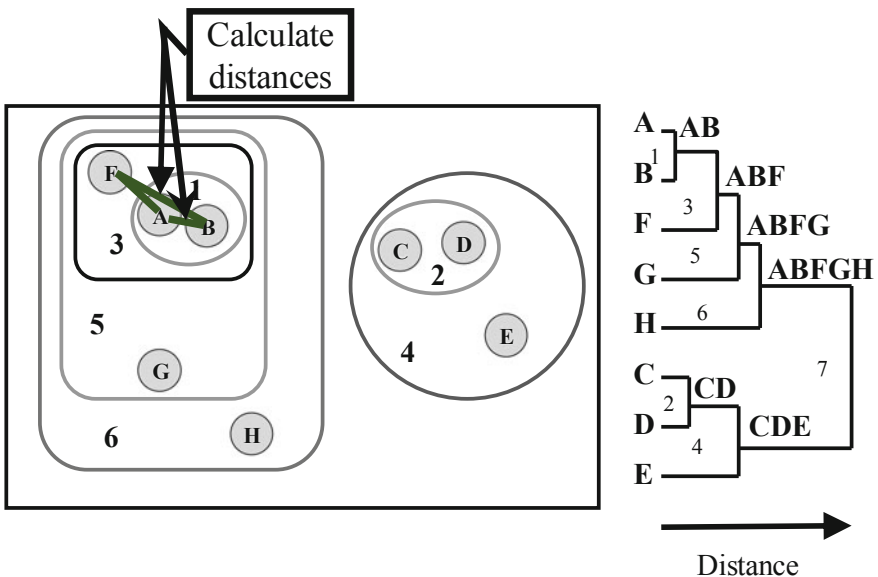


Fig. 10 Conceptual diagram of hierarchical cluster analysis

According to the definitions of ‘distance’, this method has many variations. Especially, there are many definitions for the ‘distance’ between two clusters. This method, cluster analysis, is often used for the analyses of DNA array data.

Recently, Manifold Learning has been becoming more common. This is an extended method of MDS and uses extended distance such as geodesic distance instead of normal distance.

Application of these unsupervised learning methods to FMO docking studies will be shown in below sections.

4 Application Examples of Machine Learning Methods to FMO Docking Studies

4.1 β -secretase Inhibitors

Alzheimer disease is a well-known dementia that has no cure. Among some hypothesis, beta-amyloid one is the most likely to be one of the causes of the disease. This hypothesis postulates that extracellular amyloid beta (A_{β}) deposits are the fundamental cause of the disease. Since beta- and gamma-secretases are considered to be responsible for creating A_{β} , many research groups including mega-pharma companies are trying to develop secretase inhibitors as anti-Alzheimer drugs. However, no tries have succeeded in placing on the market, while many data including co-crystal structures have been reported. Thus, I will show the results of machine learnings of the intermolecular interaction energies between beta-secretases and its inhibitors (Fig. 11) (Table 2).

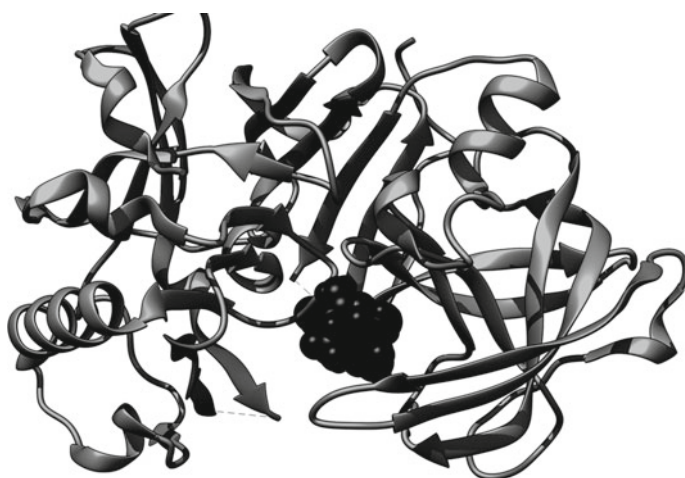


Fig. 11 Structure of β -secretase and its inhibitor

Table 2 pIC₅₀ values of the compounds in Fig. 12

PDBcode	3in3	3in4	3ind	3ine	3inf	3inh	3ooz	4j00
Compounds	a	a	b	b	c	c	d	e
IC ₅₀ uM	0.06	0.03	1.5	0.17	0.04	0.02	0.014	36.83
pIC ₅₀	1.22	1.52	-0.18	0.77	1.40	1.70	1.85	-1.57
IFIE_SUM/kcal mol ⁻¹	-111.29	-111.51	-79.48	-90.51	-99.98	-117.05	-147.10	-122.61
PDBcode	4jp9	4jpc	4jpe	2ohk	2ohl	2ohp	2ohq	2ohr
Compounds	f	f	f	g	h	i	j	k
IC ₅₀ uM	0.024	0.094	0.048	2000	2000	94	25	100
pIC ₅₀	1.62	1.03	1.32	-3.30	-3.30	-1.97	-1.40	-2.00
IFIE_SUM/kcal mol ⁻¹	-130.53	-136.37	-135.71	-51.81	-33.96	-55.47	-62.91	-72.65
PDBcode	2ohs	2oht	2ohu	3kmy	3l38	3l3a	4j0p	4j0t
Compounds	l	m	n	o	p	p	q	r
IC ₅₀ uM	40	9.1	4.2	0.2	0.2	0.42	0.051	0.028
pIC ₅₀	-1.60	-0.96	-0.62	-0.70	-0.70	-0.38	-1.29	-1.55
IFIE_SUM/kcal mol ⁻¹	-81.85	-115.25	-115.25	-61.11	-15.76	-33.01	-123.45	-124.15
PDBcode	4j0v	4j0y	4j0z	4j17	4j1c	4j1f	4j1e	4j1k
Compounds	s	t	u	v	v	v	w	v
IC ₅₀ uM	0.435	0.077	0.054	0.148	0.012	0.049	0.019	0.013
pIC ₅₀	-0.36	-1.11	-1.27	-0.83	-1.92	-1.31	-1.72	-1.89
IFIE_SUM/kcal mol ⁻¹	-128.68	-133.63	-126.37	-125.75	-143.54	-150.68	-139.82	-146.55
PDBcode	4j1i	4fri	4frj	4frk	3msk	3msl		
Compounds	x	y	z	a	b	g		
IC ₅₀ uM	0.04	2.85	0.28	0.008	26	7		
pIC ₅₀	-1.40	0.45	-0.55	-2.10	1.41	0.85		
IFIE_SUM/kcal mol ⁻¹	-99.18	-94.16	-86.78	-139.36	-80.89	-96.95		

*IC₅₀ values were obtained from the literatures [9–11]

5 PCA Results

5.1 Data

All the structures of the secretase-ligand complexes were from PDB database [8]. Their PDB codes and the chemical structures of their ligands are shown in Fig. 12. FMO calculations of the intermolecular interaction energies between β -secretase and the ligands using the PDB co-crystal structures were carried out.

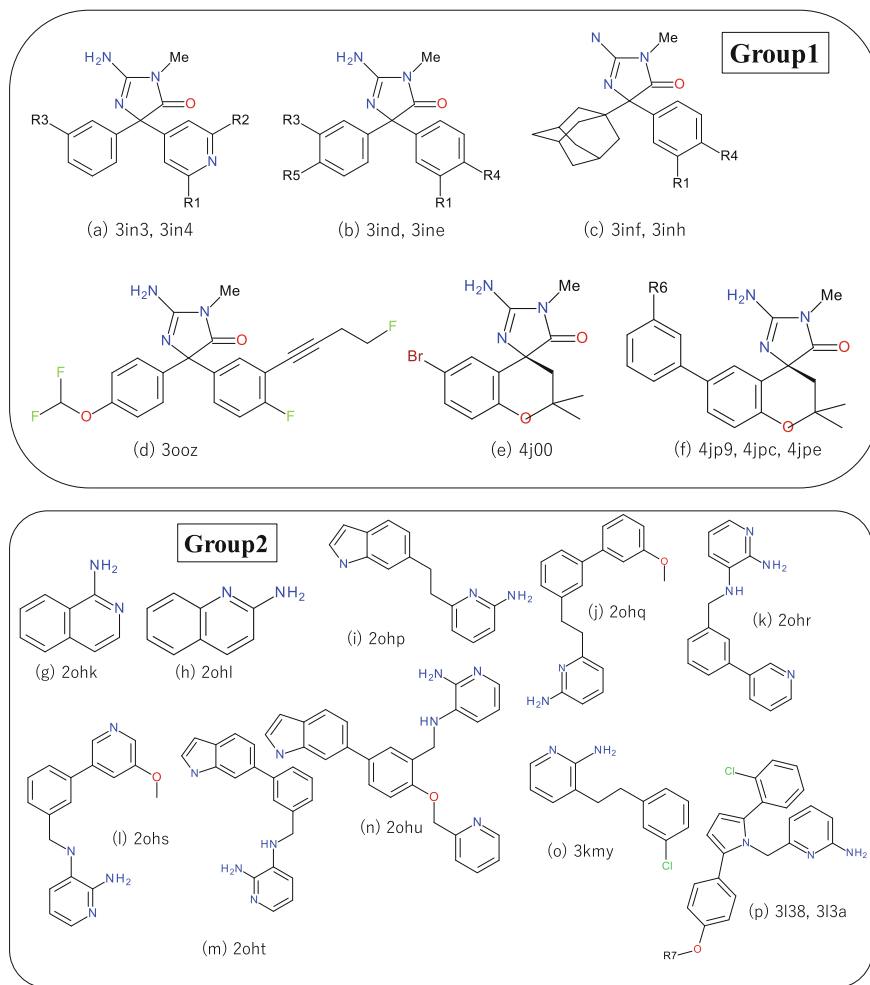


Fig. 12 Chemical Structures and their PDB codes of β -secretase ligands

Principal Component Analysis was carried out using the IFIE data. Resulted eigenvalues and the cumulative contribution ratio are shown in Table 3. Resulted Cumulative Contribution Ratios give satisfactory values when four principal components are adopted. Obtained principal components were rotated using Varimax solution. Obtained scatter plot between factor scores is shown in Fig. 13. Especially, the scatter plot between factors 2 and 3 shows a clear result which distinguishes groups 3 and 4 from other compounds. In this case, although it is difficult to identify the meanings of the extracted factors, this result indicates that at least three or more factors are needed to express the IFIE matrix. MDS was carried out using the IFIE data matrix, which showed that some groups of the ligands could be distinguished from other

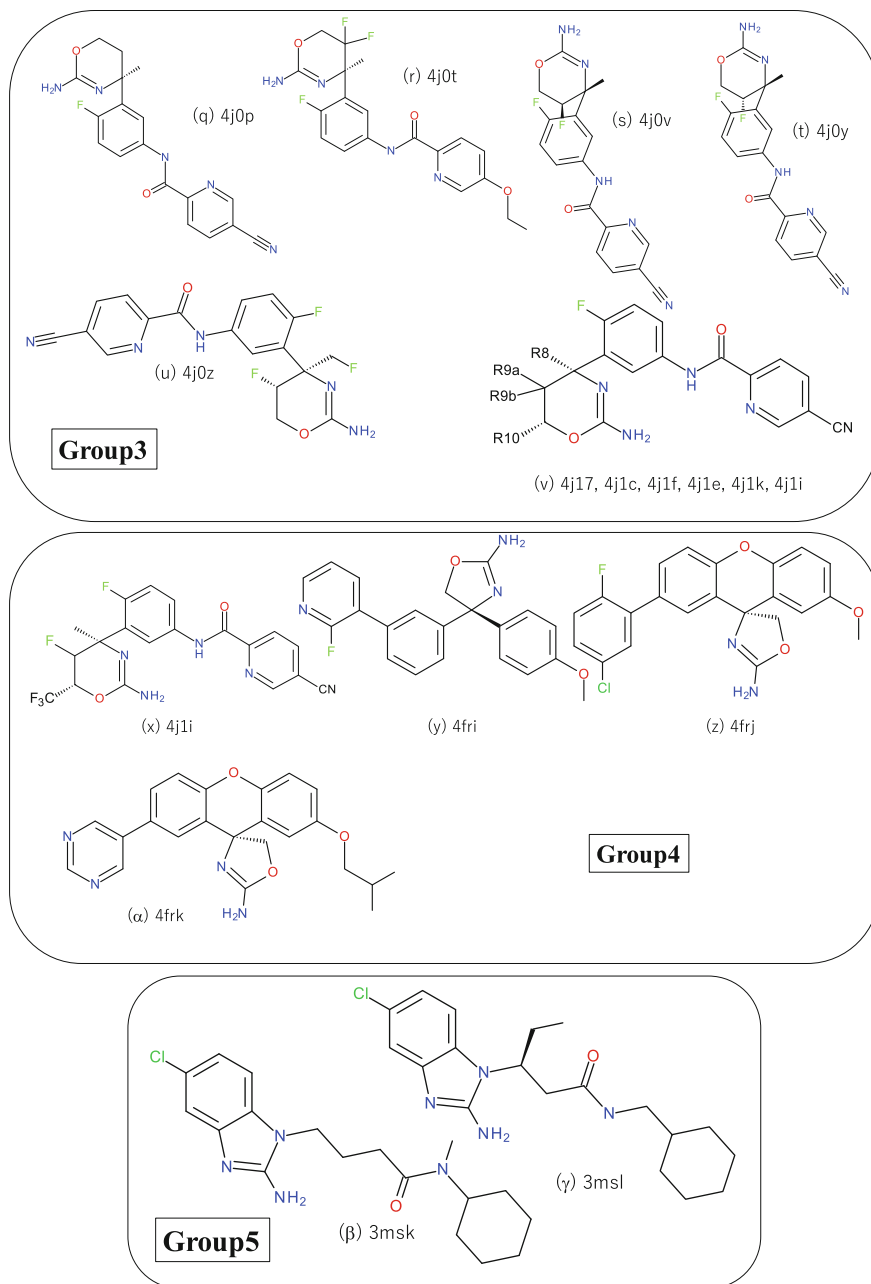
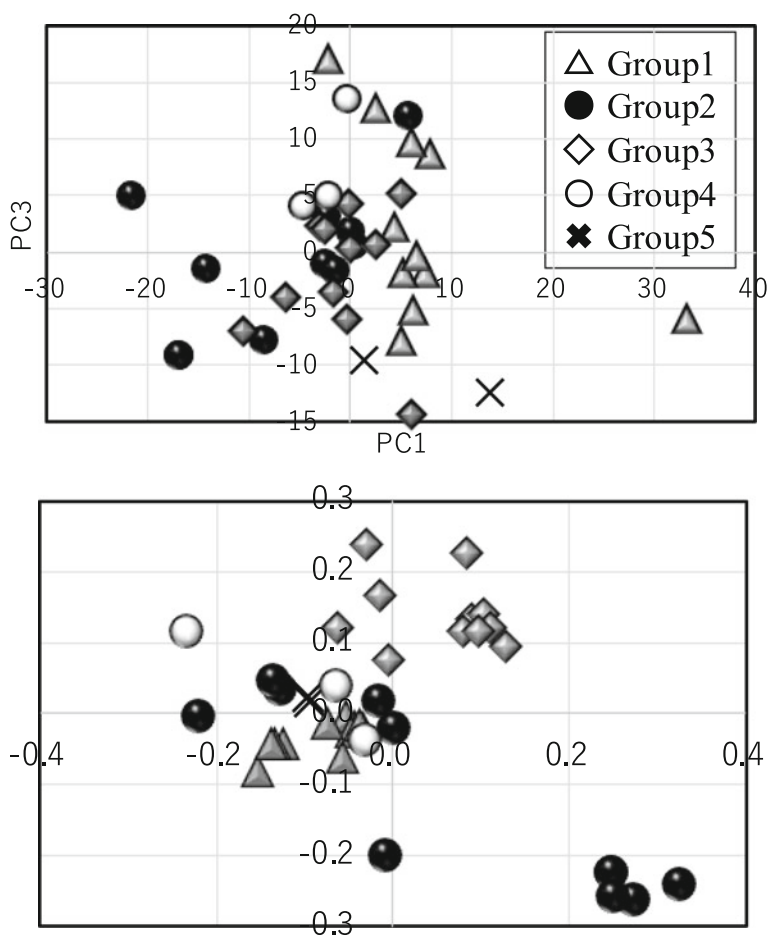


Fig. 12 (continued)

Table 3 Eigenvalues and cumulative contribution ratios obtained by PCA of IFIE data

	PC1	PC2	PC3	PC4	PC5	PC6	PC7	PC8	PC9	PC10
Eigen values	85.2	63.3	53.1	36.2	24.5	19.0	15.9	10.8	9.5	6.6
Cumulative contribution ratios	23.7	41.4	56.2	66.2	73.1	78.4	82.8	85.8	88.4	90.3

**Fig. 13** Scatter Plot between Factors 2 and 3 obtained by Varimax Rotation after PCA (upper) and the first and the second dimensions obtained by MDS (lower)

compounds more easily than PCA (Fig. 13 lower). Although we do not show the results of cluster analysis, similar result was obtained.

Since good correlation between sum of IFIEs and the observed pIC_{50} was not obtained (Fig. 14), PLS-lasso was carried out to obtain the better correlation. The

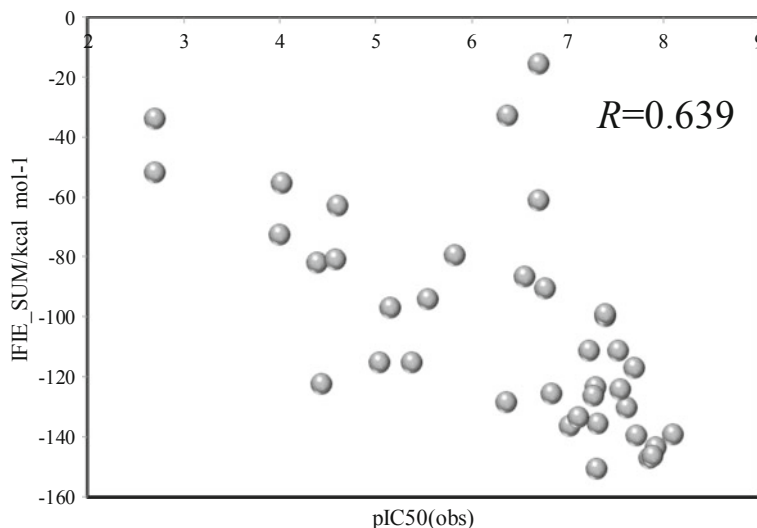


Fig. 14 Scatter plot between simple sum of IFIEs and pIC50s

result is shown in Fig. 15. Better correlation was obtained between estimated and observed pIC₅₀s. Still, this method and its application should be developed to obtain better prediction results and reasonable explanations for the regression coefficients. However, this result implies two significant points. One is that this method (PLS-lasso) is able to correct the bias or errors of FMO calculations. And the other is that this result might be caused by FMO theory which tends to overestimate electrostatic interactions. The latter can be corrected by SCIFIE method [12].

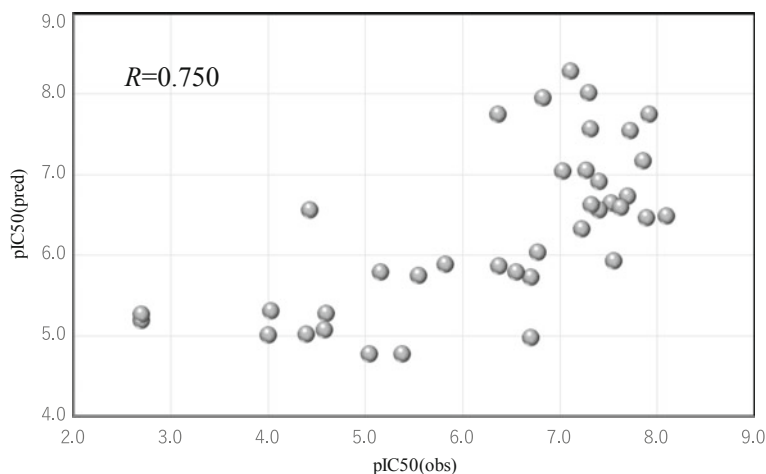


Fig. 15 PLS-lasso result of estimated pIC50 calculated by IFIE data

Acknowledgements Molecular graphics and analyses performed with UCSF Chimera [13], developed by the Resource for Biocomputing, Visualization, and Informatics at the University of California, San Francisco, with support from NIH P41-GM103311 (<https://www.rbvi.ucsf.edu/chimera>).

2D Chemical Structures were drawn with BIOVIA version 19.1 by Dassault Systems.

I would like to thank these organizations for permitting us to use the software.

References

1. Kurzweil R (2005) The singularity is near. Penguin Group, p 122
2. Tibshirani R (1996) Regression shrinkage and selection via the lasso. *J R Stat Soc, Ser B* 58(1):267–288
3. Zou H, Hastie T (2005) Regularization and variable selection via the Elastic Net. *J R Stat Soc Ser B* 67(2):301–320
4. Hastie TJ, Tibshirani RJ (1986) Generalized additive models. *Stat Sci* 1:297–318
5. Silver D, Schrittwieser J, Simonyan K, Antonoglou I, Huang A, Guez A, Hubert T, Baker L, Lai M, Bolton A, Chen Y, Lillicrap T, Hui F, Sifre L, van den Driessche G, Graepel T, Demis (2017) Mastering the game of Go without human knowledge. *Nature* 550:354–359
6. Srivastava N, Hinton G, Krizhevsky A, Sutskever I, Salakhutdinov R (2014) Dropout: a simple way to prevent neural networks from Overfitting. *J Mach Learn Res* 15:1929–1958
7. Sabour S, Frosst N, Hinton GE (2017) Dynamic routing between capsules
8. Chang D, Along K (2014) Principal component analysis characterizes shared pathogenetics from genome-wide association studies. *PLoS Comput Biol* 10:e1003820
9. Huang H, La DS, Cheng AC, Whittington DA, Patel VF, Chen K, Dineen TA, Epstein O, Graceffa R, Hickman D, Kiang Y-H, Louie S, Luo Y, Wahl RC, Wen PH, Wood S, Fremeau RT Jr. (2012) Structure- and property-based design of Aminooxazoline Xanthenes as selective, orally efficacious, and CNS penetrable BACE inhibitors for the treatment of alzheimer's disease. *J Med Chem* 55(21):9156–9169
10. Hilpert H, Guba W, Woltering TJ, Wostl W, Pinard E, Mauser H, Mayweg AV, Rogers-Evans M, Humm R, Krummenacher D, Muser T, Schnider C, Jacobsen H, Ozmen L, Bergadano A, Banner DW, Hochstrasser R, Kuglstatter A, David-Pierson P, Fischer H, Polara A, Narquizian R (2013) β -Secretase (BACE1) inhibitors with high in vivo efficacy suitable for clinical evaluation in alzheimer's disease. *J Med Chem* 56(10):3996–4016
11. Malamas MS, Barnes K, Hui Y, Johnson M, Lovering F, Condon J, Fobare W, Solvibile W, Turner J, Hu Y, Manas ES, Fan K, Olland A, Chopra R, Bard J, Pangalos MN, Reinhart P, Robichaud AJ (2010) Novel pyrrolyl 2-aminopyridines as potent and selective human b-secretase (BACE1) inhibitors. *Bioorg Med Chem Lett* 20:2068–2073
12. Tanaka S, Watanabe C, Okiyama Y (2013) Statistical correction to effective interactions in the fragment molecular orbital method. *Chem Phys Lett.* 556(29):272–277
13. Pettersen EF, Goddard TD, Huang CC, Couch GS, Greenblatt DM, Meng EC, Ferrin TE. (2004). UCSF Chimera—a visualization system for exploratory research and analysis. *J Comput Chem* 25(13):1605–1612

Extension to Multiscale Simulations



Koji Okuwaki , Taku Ozawa, and Yuji Mochizuki

Abstract Fragment molecular orbital (FMO) methods (Fedorov and Kitaura The fragment molecular orbital method: practical applications to large molecular systems, CRC Press, Boca Raton, 2009; Fedorov et al. *Phys Chem Chem Phys* 14:7562, 2012; Tanaka et al. *Phys Chem Chem Phys* 16:10310, 2014), which allow macromolecular systems to be handled by ab initio quantum chemical calculations, have been used primarily for protein, DNA, and molecular aggregation systems, as discussed in previous chapters. In recent years, in the field of materials science, the control of microstructure at the molecular level is strongly desired for the advancement of products, and pre-screening in computational chemistry has attracted much attention in this context. In particular, the prediction of mesoscale properties is an important issue because the mesoscale structure formed by molecular aggregates has a significant impact on physical properties. Therefore, our research group has developed a framework for calculating effective interaction parameters between particles in mesoscale coarse-grained simulations based on nano-scale FMO calculations, and is currently using this system to conduct leading empirical calculations in various systems. In this section, we outline these efforts, and also describe a detailed analysis of a total atomic structure using reverse map technology.

Keywords Multiscale simulation · Dissipative particle dynamics · FMO-DPD · Reverse map · FCEWS

#Affiliation at the time of contributions.

K. Okuwaki (✉) · Y. Mochizuki

Department of Chemistry and Research Center for Smart Molecules, Faculty of Science, Rikkyo University, 3-34-1 Nishi-ikebukuro, Toshima-ku, Tokyo 171-8501, Japan

e-mail: okuwaki@rikkyo.ac.jp

T. Ozawa

JSOL Corporation, 2-5-24 Harumi, Chuo-ku, Tokyo 104-0053, Japan

Y. Mochizuki

Institute of Industrial Science, The University of Tokyo, 4-6-1 Komaba, Meguro-ku, Tokyo 153-8505, Japan

1 Construction of a Coarse-Grained Simulation Parameter Calculation Scheme

Coarse-grained simulations are widely used to analyze large structures because they can simulate larger timescales compared to atomic-level simulations such as molecular dynamics (MD). Among the coarse-grained methods, the dynamic mean field theory [4, 5], which calculates the time evolution of the concentration of components in the system, and the dissipative particle dynamics (DPD) [6–11], which incorporates the fluid theory, are superior for predicting phase-separated structures. Since DPD can keep track of the phase separation behavior at a low computational cost via a molecular particle level approach, its applications include vesicle formation of amphiphilic molecules [12], prediction of the meso structures of polymer electrolyte membranes [13], analysis of the structure of linear oligomer solutions [14], and analysis of the equilibrium structure of amphiphilic bilayers [15].

In the mean field method theory and DPD simulations, the parameters that describe the interactions between the set particles are important, and they are generally closely related to the χ parameters that indicate the affinity between components of the Flory–Huggins theory. However, it is well known that the evaluation of a reliable χ parameter is a difficult task, and thus values based on experimental data or empirical values are generally used in the simulation, and the limits of this application have been pointed out.

There are two main types of χ value prediction methods. The first is the empirical method, in which the solubility parameter SP values [16] and aggregation energies are predicted using inferred models such as the cluster contribution model [17, 18] and Bicerano's method [19]. The second is based on molecular simulations. The main methods are predicting the SP value from the molecular simulation of a single type of molecules [20] and determining the χ value from the interaction between different molecules. Typical of the latter approach are the predictions from the contact energy between segments by Fan et al. [21] and the aggregation predictions from the difference in cohesive energy of the many body model [22]. In this study, we focused on Fan's method because this method has the advantage that the interaction between contacting particles can be obtained directly via a molecular level approach. Fan et al. performed interaction calculations on the exhaustive conformations of a pair of segments, and then used the metropolis method to select the states that can be taken for each temperature to determine the contact energy between the segments. In this approach, however, since the parameters of the classical force field (FF) are used to evaluate the contact energy of the pair, the reliability decreases in a system in which charge transfer is essential as a factor of the interaction.

In order to solve the above problem, it is necessary to carry out the first principle calculation procedure by using molecular orbital (MO) calculation and density functional theory (DFT) calculation considering polarization and charge transfer in the evaluation of the interaction energy. As an example, Sepehr et al. evaluated the DPD interaction parameters in a model of Nafion® hydration, which is representative of polymer electrolyte membranes, based on the DFT method [23]. Nafion® membrane

interactions are difficult to depict within the classical FF framework because they are characterized by charge transfer. However, when the molecular size of the segment pair becomes large, applying the usual first-principles calculation to the parameter evaluation involves many calculation costs, and it may be difficult to construct a general-purpose scheme.

Therefore, focusing on the method of Fan et al. [21] for calculating parameters from the interaction energies between small molecules, we established a highly accurate parametrization method by using the fragment molecular orbital (FMO) calculation [1–3]. This set of parameter calculation functions has been systematized as an automated framework and made available to the public as the FMO-based Chi-parameter Evaluation Workflow System (FCEWS) (https://www.cenav.org/fcews_ver1_rev2/) [24].

In Flory–Huggins’ lattice theory, the χ parameter is defined as

$$\chi = \frac{Z\Delta E_{AB}}{RT}, \quad (1)$$

where Z is the coordination number of the model lattice. The contact energy ΔE_{AB} represents the amount of energy which changes with the mixing of components A and B, and is given by the equation

$$\Delta E_{AB} = \bar{E}_{AB} - \frac{(\bar{E}_{AA} + \bar{E}_{BB})}{2}, \quad (2)$$

where \bar{E}_{AB} is the average interaction energy between components A and B. From Eqs. (1) and (2), it can be seen that the values essential for the parameter calculation between the two components are the coordination number Z and average interaction energies \bar{E}_{AB} , \bar{E}_{AA} , and \bar{E}_{BB} . In the FCEWS system, these values can be automatically calculated from the molecular calculation. The system workflow is shown in Fig. 1. The users can generate a large number of configurations of the target molecules (I), calculate Z values (I’), and calculate the interaction energies of all configurations by using FMO calculation with the ABINIT-MP program (II) only by preparing the molecular structure of the two components for which the parameter is to be calculated. Then the interactions are processed by the Metropolis Monte-Carlo method to obtain average interaction energies for each temperature (III). Further, at this time, the orientation information of the configuration is also acquired for each structure, and scaling is carried out depending on the isotropy to prevent an overestimation of the average interaction. Subsequently, an χ parameter reflecting additional molecular characteristics is calculated. As a verification calculation of this method, the upper critical temperature of phase transition obtained from the χ parameter was calculated for three examples of a molecular system (hexane–nitrobenzene, polyisobutylene–diisobutyl ketone, and polystyrene–polyisoprene) considered in the previous study

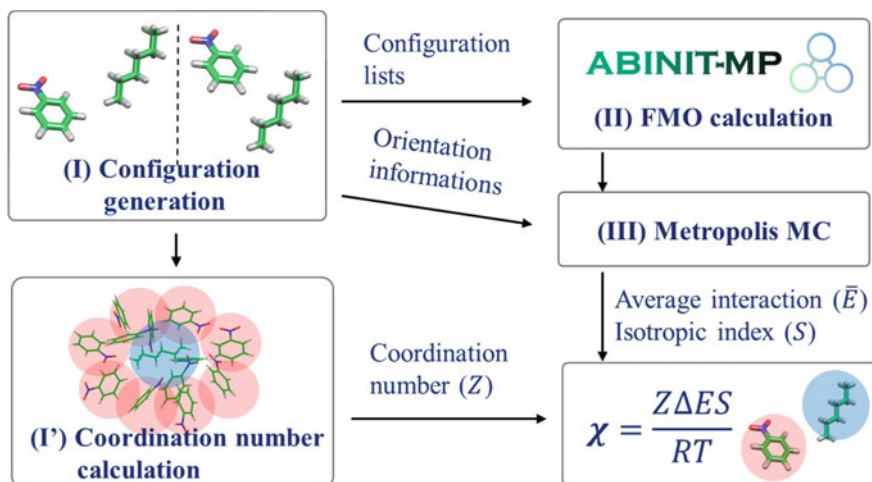


Fig. 1 Workflow for calculating parameters using FMO calculations

by Fan et al., and the experimental value could be reproduced with an error of about 10% [25]. The FCEWS system is intended for use on a Linux server from the viewpoint of computational cost, but it can also be used on Windows. In addition to various job management systems (PBS, Torque, LSF, Lava), jobs can be submitted to some supercomputers. The basic usage is CUI-based, but it is also GUI-based and included with J-OCTA ver. 4.1 and later (<https://www.j-octa.com/>).

2 Applications Using the FMO-DPD Method

This section introduces an example of an application that performs calculations by the FMO-DPD cooperation method using the parameter calculation scheme introduced in the previous section. The calculations of the polymer electrolyte membrane and lipid membrane, in which the problem of the parameters is highly significant, are described.

2.1 DPD Simulation

First, the DPD simulation used in this study will be described. The original DPD was proposed by Hoogerbrugge and Koelman [6, 7], and extended to polymers by Groot et al. [9, 10, 26]. Here, the outline of the model and the algorithm of DPD are described.

The forces acting on the particles are conservative, dissipative, random, and spring forces to connect the particles, and the time evolution of the system is obtained by solving Newton's equations of motion:

$$\frac{d\mathbf{r}_i}{dt} = \mathbf{v}_i \quad (3)$$

$$m_i \frac{d\mathbf{v}_i}{dt} = \mathbf{f}_i, \quad (4)$$

where \mathbf{r}_i , \mathbf{v}_i , and m_i are the position, velocity, and mass of the i th particle, respectively. For convenience, the mass and diameter of the particles are scaled relative to 1 to reduce the units. The force \mathbf{f}_i includes three parts of the original DPD equation and an additional spring force of the polymer system. The interaction between two particles can be written as the sum of these forces.

$$\mathbf{f}_i = \sum_{j \neq i} (\mathbf{F}_{ij}^C + \mathbf{F}_{ij}^D + \mathbf{F}_{ij}^R + \mathbf{F}_{ij}^S) \quad (5)$$

The first three forces of the original DPD act within a specific cut-off radius r_c . The conservation force \mathbf{F}_{ij}^C is given by the following Eq. [9]

$$\mathbf{F}_{ij}^C = \begin{cases} -a_{ij}(r_c - r_{ij})\mathbf{n}_{ij} & r_{ij} < r_c \\ 0 & r_{ij} \geq r_c \end{cases}, \quad (6)$$

where a_{ij} is the maximum repulsive force between particles i and j , $r_{ij} = \mathbf{r}_j - \mathbf{r}_i$, $r_{ij} = |\mathbf{r}_{ij}|$, and $\mathbf{n}_{ij} = \mathbf{r}_{ij}/|\mathbf{r}_{ij}|$. The repulsion parameters between particles of different type correspond to the mutual solubility provided by the χ parameter set. When the reduced density ρ is assumed to be 3, a linear relation with a_{ij} is usually set as

$$a_{ij} = a_{ii} + 3.27\chi_{ij}. \quad (7)$$

The details of the process of determining χ_{ij} are given in Chapter 5.3.1. The dissipative force \mathbf{F}_{ij}^D is a hydrodynamic force and is given by

$$\mathbf{F}_{ij}^D = \begin{cases} -\gamma\omega^D(r_{ij})(\mathbf{n}_{ij} \cdot \mathbf{v}_{ij})\mathbf{n}_{ij} & r_{ij} < r_c \\ 0 & r_{ij} \geq r_c \end{cases}, \quad (8)$$

where γ is the friction parameter, $\omega^D(r_{ij})$ is the weight function, and $\mathbf{v}_{ij} = \mathbf{v}_j - \mathbf{v}_i$. The friction parameter γ is a value related to the viscosity of the system.

The random force \mathbf{F}_{ij}^R corresponds to the thermal noise and is described by the parameter σ and another weight function $\omega^R(r_{ij})$ as follows:

$$\mathbf{F}_{ij}^R = \begin{cases} \sigma \omega^R(r_{ij}) \zeta_{ij} \Delta t^{-\frac{1}{2}} \mathbf{n}_{ij} & r_{ij} < r_c \\ 0 & r_{ij} \geq r_c \end{cases}. \quad (9)$$

The randomness is incorporated through the element ζ_{ij} , which is a randomly fluctuating variable with Gaussian statistics:

$$\langle \zeta_{ij}(t) \rangle = 0 \quad (10)$$

$$\langle \zeta_{ij}(t) \zeta_{kl}(t') \rangle = (\delta_{ik} \delta_{jl} + \delta_{il} \delta_{jk}) \delta(t - t'). \quad (11)$$

They are assumed to be uncorrelated for different particle pairs and time. There is a relation between the two weighting functions and two parameters:

$$\omega^D(r_{ij}) = [\omega^R(r_{ij})]^2 \quad (12)$$

$$\sigma^2 = 2\gamma kT. \quad (13)$$

In this study, the weighting function is selected as follows:

$$\omega^D(r_{ij}) = [\omega^R(r_{ij})]^2 = \begin{cases} (r_c - r_{ij})^2 & r_{ij} < r_c \\ 0 & r_{ij} \geq r_c \end{cases}. \quad (14)$$

Since the parameters σ and γ are selected to be 3 and 4.5, respectively, $kT = 1$. The variable $\Delta t^{-1/2}$ in Eq. (9), as discussed by Groot and Warren, is responsible for ensuring a consistent diffusion of particles independent of the integration step size. The bonding force \mathbf{F}_{ij}^S of the polymer, when the particles i and j are connected, is expressed as a harmonic oscillator of the equilibrium distance r_e by the following equation [27]:

$$\mathbf{F}_{ij}^S = -C(r_e - r_{ij})\mathbf{n}_{ij}. \quad (15)$$

The time evolution of the system was carried out by a modified Verlet method following the method of Groot et al. with $\lambda = 0.65$. In the simulation, the units of length and time are made dimensionless, and conversion to a real dimension can be performed as described by Groot et al. [26]. The COGNAC module of J-OCTA is used in this section.

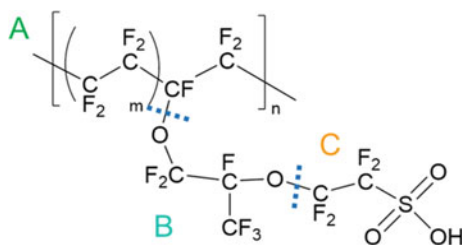
2.2 Percolation Analysis of the Polymer Electrolyte Membrane

Polymer electrolyte fuel cells (PEFCs) do not emit carbon dioxide (CO_2), so they are widely studied for use in automobiles as an energy source with low environmental cost. An important component of PEFCs is the polymer electrolyte membrane (PEM); PEFCs containing a PEM are also called proton exchange membrane fuel cells (PEMFCs). The most widely used PEMs are of the perfluorosulfonic acid (PFSA) type, such as the Nafion® membrane of DuPont, which provides chemical, thermal, and mechanical stability in addition to high proton conductivity. It is known that a hydrated Nafion membrane has a nano-phase separation structure composed of a hydrophobic phase containing a main chain and a hydrophilic phase containing a sulfonic acid group, and that a water cluster network formed inside the membrane is related to the proton conductivity, which in turn is directly related to the performance of the cell. To elucidate the hydrated structure of Nafion, a number of molecular calculations have been carried out, such as those of Voth [28–30], Choe [31–33], and Dupuis [34–36]. However, there is still room for improvement in terms of the chemical durability, gas permeability, high manufacturing cost, and so on, and development of a substitute is expected. Sulfonated polyether-ether-ketones having aromatic hydrocarbons (SPEEK) are among the promising candidates [37, 38]. SPEEK exhibits high thermal stability, mechanical properties, and high cost effectiveness, but problems of chemical stability and low conductivity have been pointed out.

In this section, we report a DPD simulation of the structure of hydrated Nafion and SPEEK. Important interaction parameters between DPD particles were evaluated by the FMO method; the network connectivity of water clusters, which is considered to be related to conductivity, was evaluated by percolation analysis; and Nafion and SPEEK were compared.

Figure 2 shows the structure of Nafion. According to Yamamoto's previous study [13], the basic unit of the Nafion chain was divided into three segments of the same size (A: $-\text{CF}_2-\text{CF}_2-\text{CF}_2-\text{CF}_2-$; B: $-\text{O}-\text{CF}_2-\text{C}(\text{CF}_3)-\text{F}-\text{O}-$; and C: $-\text{CF}_2-\text{CF}_2-\text{SO}_3\text{H}$). The termini were capped with F for segments A and C and with CF_3 for segment B. The structure of SPEEK is shown in Fig. 3. The chain was divided into three segments, A, B, and C, similar to Nafion. The termini were capped with CH_3 . In addition,

Fig. 2 Molecular structure and segmentation of Nafion



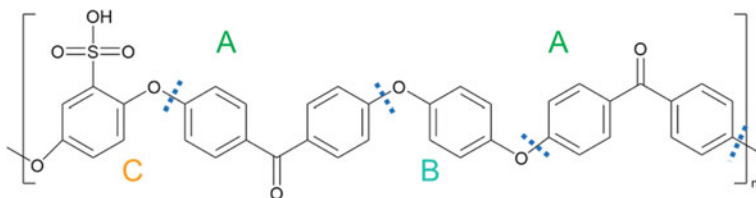


Fig. 3 Molecular structure and segmentation of SPEEK

various conformations were considered for water molecules. The water particle (W) is typically modeled by a water tetramer with cyclic hydrogen bonding for DPD simulations due to the segment size problem. However, such a model might fail to interact with outer particles because of its internal hydrogen bonding. Therefore, we employed three kinds of dimers (with shapes of linear, cyclic, and bifurcated types) and even a monomer as the candidates interacting with the sulfonic side chain (C).

The χ parameters were calculated for each segment of Nafion and SPEEK. The geometry segment was optimized by Gaussian09 [39] with B97D [40]/6-31G(d', p') level calculation. A total of 2000 configuration structures were generated for each pair, and the interaction energy was calculated for each generated conformation using FMO2-MP 2/6 -31G (d') level calculation, and then the χ values were calculated. For the DPD simulation, the time step was set to $\Delta t = 0.05$, and the cell size was set to 30 DPD-length unit (R_c). Since $\rho = 3$, the system includes 81,000 particles in each simulation. Since the DPD particle size corresponds to four molecules of water, R_c is 0.71 nm, and the cell size corresponds to 21.3 nm. Models of the polymer are shown in Fig. 4. For Nafion, three different structures with equivalent weights (EW) were prepared as structures (a)–(c). Structure (b) corresponds to the commonly used Nafion 117 (EW = 1100). SPEEK placed one hydrophilic segment in every four particles. The time evolution was performed in 10,000 steps for a total of 500 DPD-time units (t). In each model, the simulations were carried out for water contents of 10–30 vol% with 2 vol% intervals. The trajectories were stored every 100 steps (5 DPD-time units).

Table 1 shows the values of χ obtained from FMO calculations, where the values of Yamamoto and Hyodo's preceding study [13] are listed for comparison. The χ value using FMO is small for the A–B (−0.17) and C–W (−4.1) pairs, while it exceeds 20 for the A–W and B–W pairs. Although the trends in these parameters are consistent with the results of Yamamoto et al. [13], the absolute values of our χ related to water particles is larger, suggesting the contributions of polarization and charge transfer interactions incorporated by the FMO calculations. The value of χ of SPEEK is also shown in Table 2. The χ values among polymer segments (A–B, A–C, and B–C) were −0.75, 4.94, and 3.53, respectively, suggesting these segments had high affinity for each other. In addition, the χ of C–W was −3.78, which indicates a strong interaction. Thus, the trends in the parameters predicted from the structure of SPEEK were reproduced.

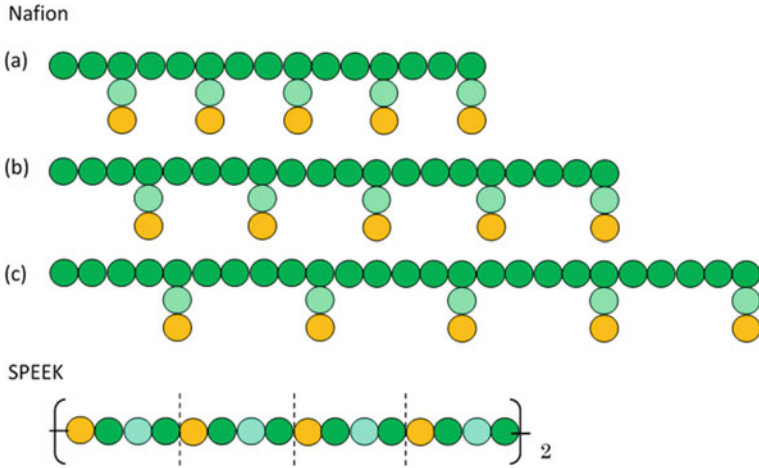


Fig. 4 DPD particle model of Nafion polymer and SPEEK. The segment size is about 0.71 nm. The green, light green, and yellow particles correspond to segments A, B, and C in Figs. 2 and 3, respectively. Structure (b) is Nafion 117 (EW = 1100), and structures (a) and (c) are defined as low and high EW models, respectively (Reproduced from Ref [43] with the permission of the authors licensed under CC BY 3.0)

Table 1 χ and a_{ij} values of each component of Nafion (350 K)

	This work		Previous work [13]
	χ	a_{ij}	χ
A-B	-0.17	24.44	0.02
A-C	7.51	49.54	3.11
B-C	7.36	49.05	1.37
A-W	25.37	107.91	5.79
B-W	27.86	116.05	4.90
C-W	-4.1	11.60	-2.79

Table 2 χ and a_{ij} values of each component of SPEEK (350 K)

Pair	χ	a_{ij}
A-B	-0.75	22.55
A-C	4.94	41.14
B-C	3.53	36.54
A-W	28.09	116.80
B-W	19.49	88.69
C-W	-3.78	12.65

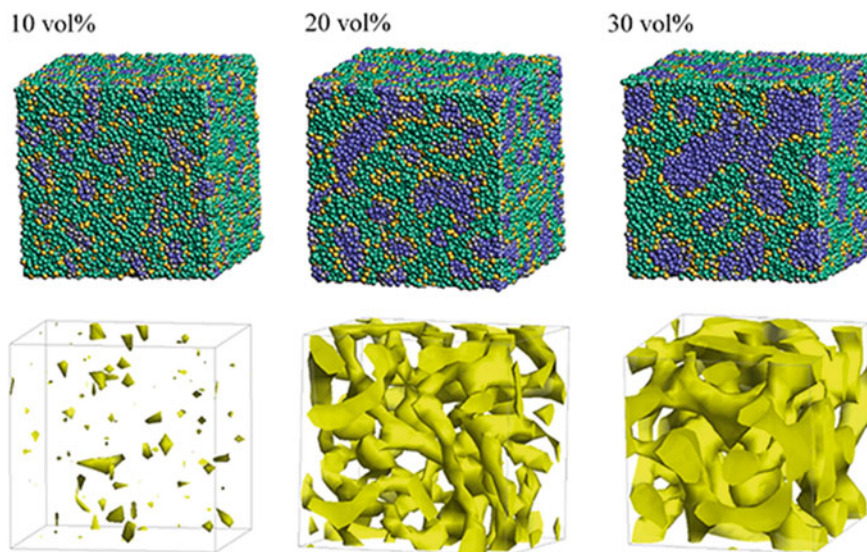


Fig. 5 Dependence of morphology on the water contents of Nafion ($t = 500$) with a symbolic structure (b) in Fig. 4. Morphologies of 10, 20, and 30 vol% are depicted in the upper row. Water density distributions are drawn in the lower row (Reproduced from Ref [43] with the permission of the authors licensed under CC BY 3.0)

Figure 5 illustrates the dependence of morphology on the water contents of 10, 20, and 30 vol% for the Nafion with symbolic structure (b) of Fig. 4. The clusters are sparse at 10 vol%, but at 20 vol% they are connected, and they form large channels at 30 vol%. To verify the results, the water cluster structure of Nafion's results was analyzed and compared with the experimental data. The small-angle scattering patterns were obtained from the radial distribution function (RDF) of water particles in the case of the Nafion (b) structure (Nafion 117). As a result, a peak originating from the water network (ionomer peak) was observed at around $q = 0.2$, and as the water content increased, the peak shifted to lower angles and its intensity increased. This tendency is in good agreement with the experimental data⁸ of small-angle neutron scattering (SANS).

In addition, to directly evaluate the connectivity value, a percolation analysis was performed. The size of the water cluster was defined as

$$R(i, j) \leq R_C, \quad (16)$$

where $R(i, j)$ is the distance between the particles i and j , and R_C is a criterion for contact. If Eq. (16) is true, these two particles (i and j) belong to the same cluster. The cluster connectivity M is thus calculated as

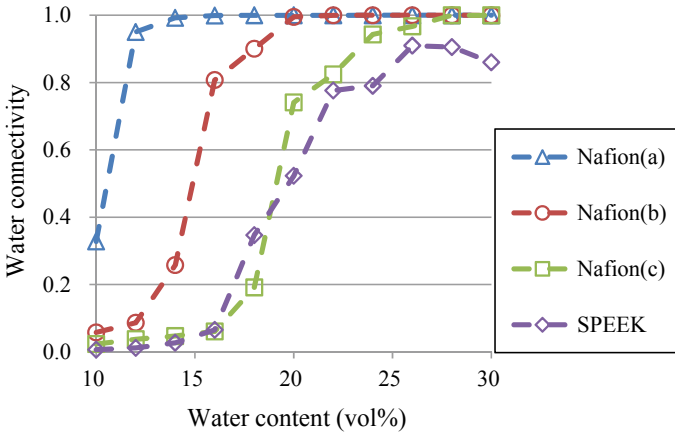


Fig. 6 The degree of water connectivity between Nafion and SPEEK in terms of water content. The average structure of every 100 steps is used. The triangles, circles, and squares represent the results of the Nafion symbol structures (a), (b), and (c) in Fig. 4, respectively, and the diamonds correspond to SPEEK (Reproduced from Ref [43] with the permission of the authors licensed under CC BY 3.0)

$$M = \frac{\sum_{i=1}^N g(i)}{N}, \tag{17}$$

where N is the total number of particles in the system, and $g(i)$ is the cluster size to which particle i belongs. The R_C was set to 1.1 DPD unit length, corresponding to the spacing of the first coordination area obtained from the RDF of DPD. For the percolation analysis, a series of additional DPD simulations were carried out for the water content range of 10–30 vol% with 2 vol% intervals. Figure 6 represents the results of connectivity for Nafion and SPEEK, where the transient structures of every 100 steps of $t = 300–500$ were used in the evaluations. It is found that the connectivity rapidly grows over 0.8 at specific water content for all structures. The results that a smaller EW has greater conductivity and the trend of SPEEK being less able to form water clusters than Nafion were in agreement with the experimental results [41, 42]. Looking at the final connectivity value, it is still about 0.9 for SPEEK, whereas it reached 1.0. This difference also indicates the difference in the phase behavior between Nafion and SPEEK. In summary, the percolation analysis has shed light on the difference in mesoscale connection structures of water clusters formed by Nafion and SPEEK. Certainly, Nafion is better as a PEM material than SPEEK [43].

2.3 Analysis of Lipid Membranes

In recent years, in the biomedical field, research and development of technologies for controlling lipid membranes, vesicles, and proteins at the molecular level, such as drug delivery systems (DDS) and sensors simulating biomembranes, have been actively carried out. For this purpose, it is necessary to analyze the details of the structure of bio-membranes. However, it is difficult to obtain detailed information—such as the distribution of lipid molecules, the unevenness of the membranes, and the fluidity of the double membranes—by means of experiments, and thus most of the details of the structure have not been clarified yet. In order to reveal these details, molecular simulation is indispensable, and much molecular simulation research has been performed [44–47]. Since the simulation of the membrane molecule needs to deal with an enormous structure, the verification in the coarse-grained simulation is important, but the parameters are mainly empirical. Therefore, we performed FMO-DPD simulation on 1-palmitoyl-2-oleoyl-sn-glycero-3-phosphocholine (POPC) [48]. In addition, as a first step of DDS, structure verification was carried out on a mixed membrane of positively charged lipids and phospholipids intended for liposome as an siRNA carrier.

The POPC molecule was divided into six small molecules as shown in Fig. 7, and parameters between seven components including water were calculated. In addition, phospholipids generally have a negatively charged phosphate part and a positively charged choline part, and it is important to accurately calculate the interaction between these hydrophilic parts and water. However, the interactions of the ionized segments cannot be accurately estimated in vacuum calculations. Therefore, we calculated the solvent interaction by the Poisson–Boltzmann equation [49]. When the solvent effect was included, the bond energy was calculated by subtracting the energy of a single molecule from the energy of the complex. The binding energy is

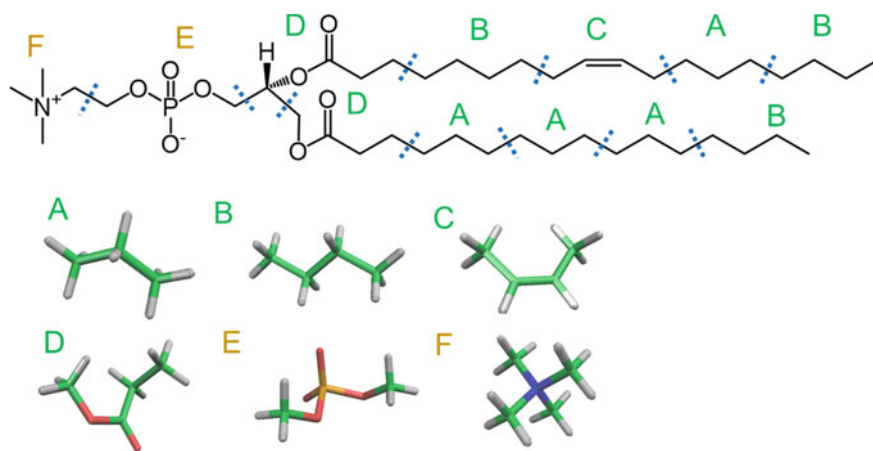


Fig. 7 Molecular structure and segmentation of POPC

given by the following equation:

$$\Delta E(AB) = E(AB) - \{E(A) + E(B)\}. \quad (18)$$

Further, as in the case of the calculations for Nafion, several types of water segments were calculated for ionic segments. A total of 21 sets of interspecies parameters were calculated for each segment. The segments were optimized in Gaussian 09 at the B97D/6-31G(d', p') level, respectively. A total of 2000 configurations were calculated for each pair, and the solvent-effect interaction energy was evaluated at the FMO2-MP2/6-31G (d') level. The dielectric constant of PB was set to internal 1.0 and external 80.0 for all segments. For the DPD simulation, the structure of POPC was modeled by connecting seven kinds of segments, as shown in Fig. 7. The time step was set to $\Delta t = 0.05$, the cell size was set to $30 R_c$ (81,000 particles, 21.3 nm in real dimension), and a time evolution of 100,000 steps was performed. The trajectories were stored every 100 steps (5 DPD time units).

Table 3 shows the values of χ obtained from FMO calculations. The χ values were small for hydrophobic particle pairs (A–B, A–C, and B–C), while it exceeds 10 for the A–W, B–W, and C–W pairs. In addition, E–W pair exhibited high affinity. The generated lipid bilayer structure of DPD simulation results are shown in Fig. 8, where the hydrophobic part (A–D particles) and hydrophilic part (E–F particles)

Table 3 χ values (300 K) between the components of POPC

	B	C	D	E	F	W
A	-0.18	-0.23	1.39	4.75	4.76	12.08
B		-0.61	0.71	5.46	5.81	12.66
C			1.18	4.81	5.74	10.56
D				1.99	-4.00	9.73
E					2.55	-6.64
F						6.00

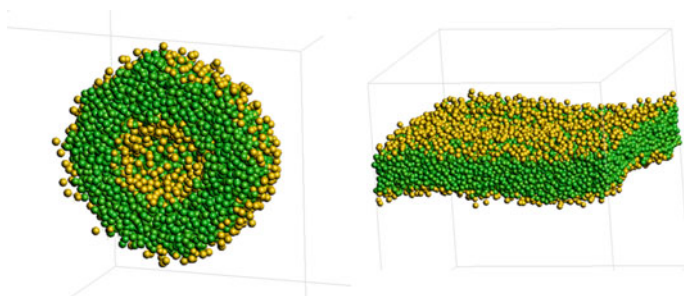


Fig. 8 The results of DPD simulation (POPC content 13 vol%, 19 vol%). Green and yellow particles correspond to a hydrophilic portion (a–d) and a hydrophobic portion (e, f), respectively

of POPC are illustrated with green and yellow colors, respectively. The water is not visualized. To validate this structure, the surface area and the thickness were calculated and compared with the experimental data. The volume fraction of the lipid bilayer at the same pressure in each direction (X, Y, and Z) was 17.7% in this simulation. Therefore, the membrane area of the stabilized bilayer was estimated as 69.4 \AA^2 . This value was in good agreement with the observed and simulated values of $62\text{--}68 \text{ \AA}^2$ from previous studies [50–53]. The thickness of lipid was measured as the thickness of the area where the density of hydrophobic particles was larger than 0.5. This value was 2.8 nm, which is in agreement with the experimental value of 2.58 nm measured by NMR [54].

Moreover, the structures of a mixed vesicle of DPPC, a neutral phospholipid, and DOTAP, a positively charged lipid, were also verified as the beginning of DDS. DPPC consists of only saturated bonds in the hydrocarbon chain, and DOTAP has unsaturated bonds on both sides of the lipid. DOTAP, a positively charged lipid, is widely used as a vector for nucleic acid drugs such as DNA and siRNA. Simulations were performed with DOTAP:DPPC = 0:1, 1:3, 1:1, 3:1, and 1:0, respectively. At that time, as a counter ion, an anionic water cluster model (Wm) containing OH^- was defined in addition to A–F in Fig. 7. As a condition in the parameter calculation, the set distance of the dielectric model in the calculation of the solvent effect was adjusted to 1.1 times the sigma of the UFF force field [55] following the Gaussian 09. As a result of DPD, it was found that the greater the ratio of DOTAP, the more oblate lipid vesicle becomes. This tendency was in good agreement with the SAXS result [56].

3 Detailed Analysis Using a Reverse Map

In the previous sections, we have verified a method for mesoscale analysis using nano-level information in the form of DPD execution using parameters obtained from high-precision interaction energies by FMO calculation. This section describes an attempt to perform detailed analysis at the nano level by mapping atoms to the results of the DPD simulation. This approach is called reverse mapping or back mapping and has been tested by Doruker et al. [57–61]. By atomizing the DPD results and performing FMO calculations, the accuracy of the obtained parameters can be confirmed and a local detailed analysis can be performed. In this section, we report the development of a system that atomizes the DPD results using reverse maps and performs a detailed analysis using FMO calculations for the test model of Nafion and lipid membranes described in the previous section.

3.1 Reverse Map Scheme

The reverse map of the DPD results and the procedure for detailed analysis of the atomized structure are shown below.

- (i) Density conversion is performed in order to adjust the DPD dimensionless result to correspond to the real dimension.
- (ii) Atom information of the segment is assigned for each coarse-grained particle. At this time, the segment molecules are rotated in order to match the termini position of the particle as much as possible.
- (iii) The structure obtained in (ii) is relaxed by using MD (using an NPT ensemble).
- (iv) Cut out the part of the structure obtained in step (iii) where you want to do FMO calculations.
- (v) Fragment information is set to the structure of (iv) and FMO calculations are performed. In this study, the MD calculation in step (iii) and FMO calculation in step (iv) were performed by using the programs COGNAC (GAFF forcefield was assigned) and ABINIT-MP, respectively. The series of calculation systems will be available soon.

3.2 Test Examples

The model of the polymer electrolyte membrane and lipid membrane treated in the previous section was used as a calculation target. DPD was performed using a model of 1000 particles for the polymer electrolyte membrane and 5000 particles for the lipid membrane. In this chapter, we assume that we return to the atomic structure, and we introduce a stronger potential that takes into account the rigidity of the skeleton. In Nafion and POPC, the harmonic potential of $C = 160$, $r_e = 0.6$ in Eq. (15) was introduced between particles directly bonded to each other, and the harmonic potential of $C = 80$, $r_e = 1.2$ was introduced at 1–3 particles as the potential for maintaining the angle. The DPD results were atomized in the above scheme, and after relaxation by MD, FMO calculations were performed at the FMO2-MP 2/6-31G (d') level.

Figure 9 shows the results of the FMO calculations of the reverse mapped structure. From the DPD results of 1000 particles, the structure of 11,000 atoms could be obtained. As can be seen from the results of (c) in the figure, the water molecule (Red), which directly contacts the sulfonic acid part (yellow part) at the interface between the electrolyte membrane and water, shows a strong interaction. The IFIE value was about -20 kcal/mol. Similarly, a strong interaction between phosphoric acid and water was observed in the lipid membrane.

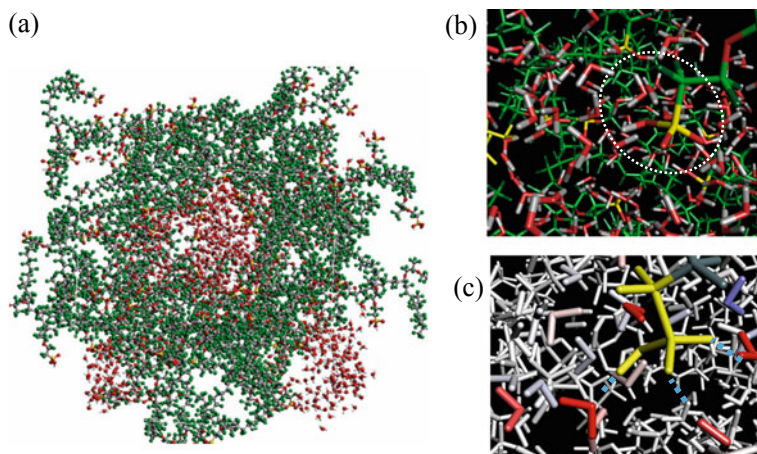


Fig. 9 The FMO analysis for the reverse mapped structure of Nafion. **a** The full-atom structure using a reverse map (about 11,000 atoms). **b** The interface between the electrolyte membrane and the water cluster. **c** IFIE analysis shows that the region showing a strong interaction with the yellow region (sulfonic acid) is red

4 Summary

We have described our newly developed method, FMO-DPD, which calculates the parameters between the components of an arbitrary molecule and performs meso-level simulations, and performed pioneering applied calculations in systems where the parameter problem is significant.

For the small molecule system examined in the preceding study, the calculation by this method was carried out, and the experimental value was reproduced with an error of about 10% on the upper critical temperature of the phase transition obtained from the χ parameter. The parametrization program is available under the name of FCEWS [24] and distributed in a bundle with the material analysis software J-OCTA. In the polymer electrolyte membrane, the difference of the connecting behavior of the cluster by the water content in Nafion and SPEEK was verified. The peak position and shape of the small angle scattering calculated from the radial distribution of water particles for Nafion were in good agreement with the experimental values. When the results of the connectivity of the water cluster were compared between Nafion and PEEK, the trend agreed with the measured value of the conductivity. In the case of lipid membranes, we succeeded in reproducing the structures of vesicles and membranes in POPC. The membrane area and thickness were in reasonable agreement with experimental values [50–53, 55]. The simulation of the mixed membrane intended for DDS was also carried out, and the shape change of the vesicle was reproduced. In addition, a reverse map of the DPD results and FMO calculations was established.

More recently, we have been working on folding calculations for small proteins and simulating other more challenging lipid systems [62, 63]. In addition, reducing the computational cost of parametrization through machine learning is under consideration. As shown by various applied calculations, the FMO-DPD method, which combines highly accurate molecular orbital calculations with coarse-grained simulation methods, has great potential as a design tool for predicting physical properties in general.

References

1. Fedorov DG, Kitaura K (2009) The fragment molecular orbital method: practical applications to large molecular systems. CRC Press, Boca Raton
2. Fedorov DG, Nagata T, Kitaura K (2012) *Phys Chem Chem Phys* 14:7562
3. Tanaka S, Mochizuki Y, Komeiji Y, Okiyama Y, Fukuzawa K (2014) *Phys Chem Chem Phys* 16:10310
4. Fraaije JGEM, van Vlimmeren BAC, Maurits NM, Postma M, Evers OA, Hoffmann C, Altevogt P, Goldbeck-Wood G (1997) *J Chem Phys* 106:4260
5. Hasegawa R, Doi M (1997) *Macromolecules* 30:5490
6. Hoogerbrugge PJ, Koelman JMVA (1992) *Europhys Lett* 19:155
7. Koelman JMVA, Hoogerbrugge PJ (1993) *EPL Europhysics Lett* 21:363
8. Mackie AD, Avalos JB, Navas V (1999) *Phys Chem Chem Phys* 1:2039
9. Groot RD, Warren PB (1997) *J Chem Phys* 107:4423
10. Groot RD, Madden TJ (1998) *J Chem Phys* 108:8713
11. Wijmans CM, Smit B, Groot RD (2001) *J Chem Phys* 114:7644
12. Yamamoto S, Maruyama Y, Hyodo S (2002) *J Chem Phys* 116:5842
13. Yamamoto S, Hyodo S, Words KEY (2003) *Polym J* 35:519
14. Arai N (2015) *Mol Simul* 41:996
15. Shillcock JC, Lipowsky R (2002) *J Chem Phys* 117:5048
16. Benesi HA, Hildebrand JH (1949) *J Am Chem Soc* 71:2703
17. Van K, In DW (1976) *Properties of polymers: their estimation and correlation with chemical structure*. Elsevier, Amsterdam
18. Coleman MM, Serman CJ, Bhagwagar DE, Painter PC (1990) *Polymer (Guildf)* 31:1187
19. Bicerano J (2002) *Prediction of polymer properties*. CRC Press
20. Prathab B, Subramanian V, Aminabhavi TM (2007) *Polymer (Guildf)* 48:409
21. Fan CF, Olafson BD, Blanco M, Hsu SL (1992) *Macromolecules* 25:3667
22. Jawalkar SS, Adoor SG, Sairam M, Nadagouda MN, Aminabhavi TM (2005) *J Phys Chem B* 109:15611
23. Sepehr F, Paddison SJ (2016) *Chem Phys Lett* 645:20
24. Okuwaki K, Doi H, Mochizuki Y (2018) *J Comput Chem Jpn* 17:102
25. Okuwaki K, Mochizuki Y, Doi H, Ozawa T (2018) *J Phys Chem B* 122:338
26. Groot RDD, Rabone KLL (2001) *Biophys J* 81:725
27. Schlijper AG, Hoogerbrugge PJ, Manke CW (1995) *J Rheol* 39:567
28. Petersen MK, Voth GA (2006) *J Phys Chem B* 110:18594
29. Petersen MK, Wang F, Blake NP, Metiu H, Voth GA (2005) *J Phys Chem B* 109:3727
30. Feng S, Voth GA (2011) *J Phys Chem B* 115:5903
31. Choe Y-K, Tsuchida E, Ikeshoji T (2007) *J Chem Phys* 126:154510
32. Choe Y-K, Tsuchida E, Ikeshoji T, Yamakawa S, Hyodo S (2008) *J Phys Chem B* 112:11586
33. Choe Y-K, Tsuchida E, Ikeshoji T, Yamakawa S, Hyodo S (2009) *Phys Chem Chem Phys* 11:3892

34. Devanathan R, Venkatnathan A, Rousseau R, Dupuis M, Frigato T, Gu W, Helms V (2010) *J Phys Chem B* 114:13681
35. Devanathan R, Venkatnathan A, Dupuis M (2007) *J Phys Chem B* 111:8069
36. Venkatnathan A, Devanathan R, Dupuis M (2007) *J Phys Chem B* 111:7234
37. Pozuelo J, Riande E, Saiz E, Compañ V (2006) *Macromolecules* 39:8862
38. Roy S, Markova D, Kumar A, Klapper M, Müller-Plathe F (2009) *Macromolecules* 42:841
39. Frisch MJ, Trucks GW, Schlegel HB, Scuseria GE, Robb MA, Cheeseman JR, Scalmani G, Barone V, Mennucci B, Petersson GA, Nakatsuji H, Caricato M, Li X, Hratchian HP, Izmaylov AF, Bloino J, Zheng G, Sonnenberg JL, Hada M, Ehara M, Toyota K, Fukuda R, Hasegawa J, Ishida M, Nakajima T, Honda Y, Kitao O, Nakai H, Vreven T, Montgomery Jr. JA, Peralta JE, Ogliaro F, Bearpark M, Heyd JJ, Brothers E, Kudin KN, Staroverov VN, Kobayashi R, Normand J, Raghavachari K, Rendell A, Burant JC, Iyengar SS, Tomasi J, Cossi M, Rega N, Millam JM, Klene M, Knox JE, Cross JB, Bakken V, Adamo C, Jaramillo J, Gomperts R, Stratmann RE, Yazyev O, Austin AJ, Cammi R, Pomelli C, Ochterski JW, Martin RL, Morokuma K, Zakrzewski VG, Voth GA, Salvador P, Dannenberg JJ, Dapprich S, Daniels AD, Farkas O, Foresman JB, Ortiz JV, Cioslowski J, Fox DJ (2016) *Gaussian 09, Revision B.01*. Gaussian Inc., Wallingford CT
40. Grimme S (2006) *J Comput Chem* 27:1787
41. Wu X, Wang X, He G, Benziger J (2011) *J Polym Sci Part B Polym Phys* 49:1437
42. Fontanella JJ, Edmondson CA, Wintersgill MC, Wu Y, Greenbaum SG (1996) *Macromolecules* 29:4944
43. Okuwaki K, Mochizuki Y, Doi H, Kawada S, Ozawa T, Yasuoka K (2018) *RSC Adv* 8:34582
44. Andoh Y, Okazaki S, Ueoka R (2013) *Biochim Biophys Acta Biomembr* 1828:1259
45. Leekumjorn S, Sum AK (2007) *J Phys Chem B* 111:6026
46. Hu M, Stanzione F, Sum AK, Faller R, Deserno M (2015) *ACS Nano* 9:9942
47. Peng B, Ding X-Y, Sun C, Liu W, Zhang JZH, Zhao X (2016) *RSC Adv* 6:45569
48. Doi H, Okuwaki K, Mochizuki Y, Ozawa T, Yasuoka K, Mochizuki Y, Ozawa T, Yasuoka K, Mochizuki Y, Ozawa T, Yasuoka K (2017) *Chem Phys Lett* 684:427
49. Watanabe H, Okiyama Y, Nakano T, Tanaka S (2010) *Chem Phys Lett* 500:116
50. Kučerka N, Tristram-Nagle S, Nagle JF (2006) *J Membr Biol* 208:193
51. Kučerka N, Nieh MP, Katsaras J (2011) *Biochim Biophys Acta Biomembr* 1808:2761
52. Jurkiewicz P, Cwiklik L, Vojtíšková A, Jungwirth P, Hof M (2012) *Biochim Biophys Acta Biomembr* 1818:609
53. Gurtovenko AA, Vattulainen I (2008) *J Phys Chem B* 112:1953
54. Nezil FA, Bloom M (1992) *Biophys J* 61:1176
55. Rappé AK, Casewit CJ, Colwell KS, Goddard WA, Skiff WM (1992) *J Am Chem Soc* 114:10024
56. Shinsho E, Okuwaki K, Doi H, Mochizuki Y, Furuishi T, Fukuzawa K, Yonemochi E (2018) *J Comput Chem Jpn* 17:172
57. Kacar G, Atilgan C, Özen AS (2010) *J Phys Chem C* 114:370
58. Harmandaris VA, Adhikari NP, Van Der Vegt NFA, Kremer K (2006) *Macromolecules* 39:6708
59. Doruker P, Mattice WL (1999) *Macromol Theory Simul* 8:463
60. Doruker P, Mattice WL (1997) *Macromolecules* 30:5520
61. Spyriouni T, Tzoumanekas C, Theodorou D, Müller-Plathe F, Milano G, Mu F, Milano G, Müller-Plathe F, Milano G (2007) *Macromolecules* 40:3876
62. Okuwaki K, Doi H, Fukuzawa K, Mochizuki Y (2020) *Appl Phys Express* 13:017002
63. Tanaka H, Takahashi T, Konishi M, Takata N, Gomi M, Shirane D, Miyama R, Hagiwara S, Yamasaki Y, Sakurai Y, Ueda K, Higashi K, Moribe K, Shinsho E, Nishida R, Fukuzawa K, Yonemochi E, Okuwaki K, Mochizuki Y, Nakai Y, Tange K, Yoshioka H, Tamagawa S, Akita H (2020) *Adv Funct Mater* 1910575

FMO-Based Investigations of Excited-State Dynamics in Molecular Aggregates



Takatoshi Fujita and Takeo Hoshi

Abstract In this chapter, we review our approach to investigate optoelectronic functions and excited-state dynamics in molecular aggregates. The approach is based on electronic coupling calculations by the fragment molecular orbital (FMO) method. The electronic couplings determine charge transfer and excitation energy transfer rates and are thus essential for describing optoelectronic processes. Moreover, the electronic couplings can also be used for derivations of model Hamiltonians, which enable real-time dynamics simulations by the wavepacket propagation method. As illustrative applications, we investigate exciton relaxation dynamics in an organic semiconductor thin film and charge-separation dynamics in an electron–donor/electron–acceptor interface. We demonstrate how the FMO and wavepacket dynamics methods can be used to understand the excited-state dynamics of the organic materials.

Keywords Electronic couplings · Wavepacket dynamics · Excitons · Organic optoelectronic materials

1 Introduction

Molecular aggregates can exhibit remarkable optical and electronic properties that differ substantially from those of an isolated molecule [49, 50]. Because of their attractive features, organic aggregates comprising semiconductor molecules or polymers can potentially lead to flexible, lightweight, and printable electronic devices [2]. Predicting the optoelectronic properties of organic aggregates is essential to understanding the mechanism of device operation and to rationally designing novel

T. Fujita (✉)

Institute for Molecular Science, 38 Nishigo-Naka, Aichi 444-8585, Japan
e-mail: tfujita@ims.ac.jp

T. Hoshi

Department of Applied Mathematics and Physics, Tottori University,
4-1-101 Koyama-Minami, Tottori 680-8552, Japan
e-mail: hoshi@tottori-u.ac.jp

© Springer Nature Singapore Pte Ltd. 2021

Y. Mochizuki et al. (eds.), *Recent Advances of the Fragment Molecular Orbital Method*,
https://doi.org/10.1007/978-981-15-9235-5_27

547

materials. However, organic materials are typically large and disordered systems; their electronic states cannot be treated by conventional quantum chemistry methods. Moreover, the charge photogeneration process in an organic solar cell consists of several elementary steps, including light absorption, excitation energy transfer (EET), and charge transfer (CT). Simulating time evolutions of the electronic states are necessary for understanding such energy conversion processes in a solar cell or a light-emitting diode.

The fragment molecular orbital (FMO) method proposed by Kitaura and co-workers [33] is a fragment-based *ab initio* electronic structure theory capable of treating large systems. In the FMO method, a system is divided into a lot of fragments; the total energy and physical quantities are approximated from self-consistent field (SCF) calculations of fragment monomers, dimers, and optionally trimers. The theoretical formulations of the FMO method and its applications have been well documented [10, 11, 14, 55], and they are found in other chapters in this book. Molecular orbitals (MOs) obtained in the FMO method are localized within a fragment monomer or dimer. Thus, the FMO method could not be applied to functional molecular aggregates, in which an electron may be delocalized over many molecules. The delocalization of wave functions must be recovered to investigate electronic processes occurring in organic materials.

Electronic coupling calculations are essential ingredients in computational studies of the electronic processes. An electronic coupling is defined as the electronic interaction between initial and final diabatic states associated with EET or CT. In this manuscript, we use a diabatic state to refer to an electronic state, in which a charge carrier or an electronic excitation is localized within a subunit in the total system. From another perspective, if an electronic Hamiltonian is calculated in the diabatic basis, the off-diagonal elements correspond to the electronic couplings. The application of the FMO to CT coupling calculations was pioneered by Kitoh and Ando [34, 47]. In their initial work [47], they have compared the generalized Mulliken-Hush [26], Green's function, and FMO-linear combination of molecular orbital (FMO-LCMO) methods [57]. The details of the CT coupling calculations can be found in the other chapters in this book. The EET coupling calculation within the FMO was first implemented by Fujita et al. [21] on the basis of the multilayer FMO (MLFMO)/configuration interaction single (CIS) [13, 42] method and the transition charge of electrostatic potential (tresp) [41]. Later, Fujita et al. have generalized the electronic coupling calculation [22] using the transition density fragment interaction-transfer integral (TDFI-TI) method introduced by Fujimoto [16, 17]. The electronic couplings have also been adopted for calculating nonlocal excited states in large molecular systems [18, 22].

In this chapter, we review our FMO-based investigations of excited-state dynamics in organic molecular aggregates. Our approach is based on three components: (i) FMO-based electronic coupling calculations, (ii) derivations of model Hamiltonians, and (iii) a wavepacket dynamics method. Using the electronic couplings obtained from an FMO calculation for an aggregate, we derive a model Hamiltonian that describes a charge carrier or an exciton in the aggregate. From a theoretical viewpoint, an *ab initio* many-electron Hamiltonian can be mapped into a reduced one-

body or two-body Hamiltonian through the FMO calculation. The time evolution of the model Hamiltonian is then simulated using a wavepacket propagation method. We attempt to understand photophysical and optoelectronic processes in a molecular aggregate as the quasiparticle dynamics described by the model Hamiltonian. We have implemented the electronic coupling calculations and model Hamiltonian derivations into the ABINIT-MP [44, 45, 55] program. In view of computations, an FMO calculation by the ABINIT-MP program provides Hamiltonian matrix elements. The matrix data are then passed to other software that simulates the time propagation. After reviewing the methods and implementations, we describe their application to organic electronic materials.

2 Electronic Couplings and Model Hamiltonians

2.1 FMO-LCMO Method for CT Couplings

First, we briefly summarize the FMO-LCMO method. The FMO-LCMO relies on the FMO-like many-body expansion of the Fock matrix [12, 38, 57]:

$$\mathbf{F} = \sum_I \oplus \mathbf{F}^I + \sum_{I>J} \oplus (\mathbf{F}^{IJ} - \mathbf{F}^I \oplus \mathbf{F}^J), \quad (1)$$

where \mathbf{F}^I and \mathbf{F}^{IJ} are Fock matrices for fragment monomer and dimer, respectively. Here, the direct sum indicates that the matrix elements of \mathbf{F}^I and \mathbf{F}^{IJ} should be added to appropriate locations in the total Fock matrix, \mathbf{F} . In the FMO-LCMO method, the fragment Fock matrices are calculated in the basis of fragment monomer MOs. For example, matrix elements of \mathbf{F}^I and \mathbf{F}^{IJ} are calculated according to

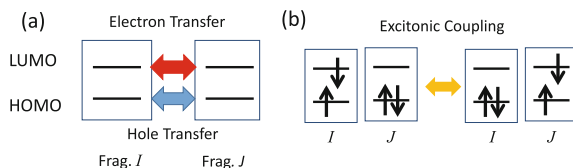
$$F_{Ip,Iq}^I = \langle \psi_p^I | F^I | \psi_q^I \rangle = \delta_{Ip,Iq} \epsilon_p^I, \quad (2)$$

$$F_{Ip,Jq}^{IJ} = \langle \psi_p^I | F^{IJ} | \psi_q^J \rangle = \sum_{r \in IJ} \epsilon_r^{IJ} \langle \psi_p^I | \psi_r^{IJ} \rangle \langle \psi_r^{IJ} | \psi_q^J \rangle. \quad (3)$$

Here, $|\psi_p^I\rangle$ is a wave function of a p th MO in an I th fragment; ϵ_p^I is the corresponding orbital energy; and p , q , and r refer to the general MO. Because the monomer MOs of different fragments are not orthogonal, the overlap matrix elements between them must be considered. Diagonalization of the FMO-LCMO Fock matrix as a generalized eigenvalue problem yields approximate solutions to the canonical MOs of the whole system.

The advantages of the FMO-LCMO method are the efficient matrix-size reduction and the electronic coupling calculations. If all monomer MOs are included as the basis functions for the total Fock matrix, the dimension of the total Fock matrix is the same as the number of atomic orbitals (AOs) in the entire system. However, we

Fig. 1 Schematics of **a** CT coupling and **b** EET coupling



expect that canonical MOs around the highest occupied molecular orbital (HOMO) or lowest unoccupied molecular orbital (LUMO) are dominantly described from the monomer MOs around the HOMO or LUMO of each fragment monomer. Therefore, the MOs around the HOMO–LUMO region of the whole system can be appropriately reproduced by the reduced Fock matrix, which includes a small number of MOs of each fragment. Another advantage of the FMO-LCMO method is the CT coupling calculations. By definition, an interfragment off-diagonal element of the total Fock matrix describes the electronic interaction between two monomer MOs [23, 35, 36], as schematically depicted in Fig. 1a. The off-diagonal elements in the FMO-LCMO Fock describe an interaction between nonorthogonal MOs, and defining electronic couplings as the interaction between orthogonal MOs is often useful. In the FMO-LCMO method, the following orthogonalized Hamiltonian [40] can be used to define the electronic coupling:

$$\mathbf{F}' = \mathbf{S}^{-\frac{1}{2}} \mathbf{F} \mathbf{S}^{-\frac{1}{2}}, \quad (4)$$

where $\mathbf{S}^{-\frac{1}{2}}$ is the square root of inverted overlap matrix of monomer MOs. Note that for the 2×2 case, the FMO-LCMO method is almost equivalent to the projective method introduced by Baumeier, Kirkpatrick, and co-workers [3].

2.2 MLFMO-CIS Method for EET Couplings

In this subsection, we present EET coupling calculations based on the MLFMO. As represented in Fig. 1b, an EET coupling is defined as the interaction between two local excited states [16, 26, 30]. In the FMO method, an excited state localized within a fragment monomer is obtained by the MLFMO method in combination with an excited-state method, such as the configuration interaction method [42, 43, 54] or time-dependent density functional theory (TDDFT) [5–7]. The EET coupling can then be obtained as the interaction between two local excited states.

We start by summarizing the MLFMO method for obtaining local excited states. In the MLFMO scheme [13, 42], fragments in a whole system are divided into lower and higher layers. After a ground-state calculation of the whole system, the fragments in the higher layer are treated by an excited state method. In the MLFMO-CIS method [42], for example, an excited-state Hamiltonian matrix of a fragment monomer is calculated and diagonalized to obtain the excitation energies (E_{Im}) and excited-state amplitudes (b_{ia}^{Im}), where m is an index for an excited state.

Here, we introduce a fragment configuration state function (CSF) that includes all electronic degrees of freedom in the whole system. An excited state, which is obtained from MLFMO-CIS for a target fragment, contains electronic degrees of freedom only in the fragment. The fragment CSFs must be considered to define Hamiltonian matrix elements of the whole system. First, the ground-state wave function of the whole system is described as the product of fragment ground-state wave functions, $|G\rangle = \prod_I |\Psi_{Ig}\rangle$. The singlet singly substituted fragment CSF is defined as, $|e_{Ia}h_{Ii}\rangle = \frac{1}{\sqrt{2}} \left(a_{Ia,\alpha}^\dagger a_{Ii,\alpha} + a_{Ia,\beta}^\dagger a_{Ii,\beta} \right) |G\rangle$, where $a_{Ia,\alpha}^\dagger$ ($a_{Ia,\beta}$) is the creation (annihilation) operator of the α -spin (β -spin) electron in the a th orbital of the I th fragment. Here, i and a refer to occupied and virtual MOs, respectively. In this section, only singlet excited states are considered, although the extension to triplet excited states is straightforward. A fragment CSF describing a local excitation (LE) is defined from the CIS amplitude and the intrafragment singly substituted CSFs:

$$|LE_{Im}\rangle = \sum_{ia} b_{ia}^{Im} |e_{Ia}h_{Ii}\rangle. \quad (5)$$

Using the fragment CSFs for LE states, we define excitonic couplings as the interaction between two localized excited states.

$$V_{Im,Jn} = \langle LE_{Im} | H | LE_{Jn} \rangle = V_F + V_D. \quad (6)$$

Here, V_F and V_D represent long-range and short-range contributions, respectively, and they are given by

$$V_F = 2 \sum_{\mu\nu \in I} \sum_{\lambda\sigma \in J} T_{\mu\nu}^{Im} T_{\lambda\sigma}^{Jn} (\mu\nu|\lambda\sigma), \quad (7)$$

$$V_D = - \sum_{\mu\nu \in I} \sum_{\lambda\sigma \in J} T_{\mu\nu}^{Im} T_{\lambda\sigma}^{Jn} (\mu\lambda|\nu\sigma). \quad (8)$$

Here, $T_{\mu\nu}^{Im}$ is the transition density matrix [15] of the m th excited state of the I th fragment; it is defined as $T_{\mu\nu}^{Im} = \sum_{ia} b_{ia}^{Im} C_{\mu i}^I C_{\nu a}^I$, where $C_{\mu i}^I$ is the MO coefficient. The term $(\mu\nu|\lambda\sigma)$ denotes two-electron AO integrals. V_F describes the long-range Coulomb interaction; its leading term is the dipole–dipole coupling. By contrast, V_D corresponds to the short-range exchange interaction; its magnitude is much smaller than that of the long-range term in the case of organic molecular aggregates.

The excitonic Coulomb couplings defined by Eq. (7) can be approximated as the sum of pairwise interactions of atomic point charges,

$$V_{Im,Jn} = \sum_{A \in I} \sum_{B \in J} \frac{q_A^m q_B^n}{|\mathbf{R}_A - \mathbf{R}_B|}, \quad (9)$$

where \mathbf{R}_A denotes a nuclear position of an A th atom, and q_A^m is a transition atomic charge [41] for an m th excited state. The transition atomic charges are determined in such a way that they reproduce the transition density of the m th excited state.

2.3 Model Hamiltonians for Molecular Aggregates

In this subsection, we discuss the connection between the FMO method and model Hamiltonians. The electronic Hamiltonian in the FMO method contains all electronic degrees of freedom in the whole system; simulating real-time dynamics is thus a formidable task. By contrast, a model Hamiltonian describes a quasiparticle and treats electronic degrees of freedom as a one-body or a two-body problem. Therefore, the real-time dynamics of excited states can be realized using the model Hamiltonian in combination with a wavepacket dynamics method. Model Hamiltonians can be derived from the FMO calculation by assigning each molecule as an independent fragment. That is, a fragment in the FMO method can be regarded a molecular site in model Hamiltonians. Here, we introduce model Hamiltonians that describe a single charge carrier or an exciton in a molecular aggregate, relating them with the electronic couplings obtained from the FMO method.

The model Hamiltonian for a single charge carrier (either a hole or an electron) is described as a tight-binding form,

$$F' = \sum_I \epsilon_p^I |\psi_{p'}^I\rangle \langle \psi_{p'}^I| + \sum_{I>J} t_{I p', J p'} |\psi_{p'}^I\rangle \langle \psi_{p'}^J|, \quad (10)$$

where ϵ_p^I is the MO energy of an I th molecular site and $t_{I p', J p'}$ is the transfer integral between two sites I and J . Here, we assumed a single orbital per molecular site, while the inclusion of many MOs per molecular site is straightforward. The model Hamiltonian for a hole or an electron can be obtained if $p = \text{HOMO}$ or $p = \text{LUMO}$. When each molecule is assigned as an independent fragment in the FMO calculation, the FMO-LCMO Fock matrix is almost equivalent to Eq. (10). Because the orthogonal basis is assumed in the tight-binding Hamiltonian, the diagonal and off-diagonal elements of the transformed Fock matrix (Eq. 4) can be regarded as the site energies and transfer integrals in Eq. (10), respectively.

The model Hamiltonian for electronically excited states of molecular aggregates is given by the Frenkel exciton model [9]. The Frenkel exciton model writes an excited-state wave function of the total system as a superposition of intramolecular excited states:

$$\langle LE_{Im} | H | LE_{Jm} \rangle = \delta_{IJ} E_{Im} + (1 - \delta_{IJ}) V_{Im, Jm}. \quad (11)$$

Here, we assume one excited state per fragment ($m = S_1$) for simplicity. The basis $|LE_{Im}\rangle$ denotes a state in which an I th molecule is excited, whereas the rest of the

molecules are in ground states. By the construction, the basis state in the Frenkel exciton model can be described as the fragment CSF for the LE state in the MLFMO method. Therefore, the parameters in the Frenkel exciton model can be derived from the MLFMO method: E_{Im} and $V_{Im,Jm}$ can be obtained as an excitation energy of a fragment monomer and an excitonic coupling, respectively, in the MLFMO-CIS method.

The Frenkel exciton model can be extended to describe any single-electron excited states by correcting fragment CSFs of interfragment CT excitation, $|e_I a h_J\rangle$ ($I \neq J$). Here, the Frenkel-CT Hamiltonian is

$$H = H_F + H_{CT} + H_{F-CT}, \quad (12)$$

where H_{CT} is the Hamiltonian for interfragment CT states and H_{F-CT} describes the interaction between LE and CT states. The off-diagonal matrix elements of H_{CT} are given by transfer integrals. The matrix element of H_{F-CT} is calculated as a product of a CI amplitude and transfer integrals. Details of the Hamiltonian matrix elements are described elsewhere [18].

The Frenkel-CT Hamiltonian can be simplified if only HOMO and LUMO orbitals are used. Dropping the MO subscripts, we can write the electron-hole Hamiltonian as

$$\langle e_I h_J | H | e_K h_L \rangle = \delta_{JL} F_{IK}^e + \delta_{IK} F_{JL}^h + H_{IJ,KL}^{2e}, \quad (13)$$

where F^e and F^h are one-body Hamiltonians for an electron and a hole, respectively. H^{2e} contains electron-electron interaction terms such as electron-hole Coulomb interactions and excitonic couplings. In the CIS method, H^{2e} describes the Hartree-Fock (HF) Coulomb term and the exchange term, which correspond to electron-hole exchange and electron-hole Coulomb attraction, respectively.

3 Implementation in ABINIT-MP

In this section, we briefly summarize the computational procedure and implementation. The electronic coupling calculation and derivations of the model Hamiltonian have been implemented in the ABINIT-MP software developed by Nakano, Mochizuki, and co-workers [44, 55]. The FMO-LCMO method was implemented at the FMO2 level [57]. After SCF calculations for fragment monomers and dimers, fragment Fock matrices are calculated according to Eqs. (2) and (3), respectively. The total Fock matrix is then calculated from the fragment Fock matrices, which can be used for calculating the CT electronic couplings or for carrier mobility simulations.

The implementation of the excitonic coupling and calculations of the excited-state Hamiltonian are based on the CIS module in the ABINIT-MP developed by Mochizuki and co-workers [42, 43, 54]. After a conventional ground-state FMO calculation, excited-state calculations are performed for fragment monomers. The

resulting CIS transition densities are used for the excitonic coupling through the Fock-like contraction [15], as in Eqs. (7) and (8). The derivation of tresp charges was implemented on the basis of the CIS transition density and the optimally weighted charge introduced by Okiyama et al. [48].

4 Wavepacket Dynamics

This section is devoted to the foundation of wavepacket dynamics. From the mathematical viewpoint, a wavepacket is expressed on an N -component vector $\mathbf{u} \equiv (u_1, u_2, \dots, u_N)^T$ and the dynamics is formally written, in the form of time-dependent Schrödinger equation, by

$$i \frac{d\mathbf{u}}{dt} = H\mathbf{u}, \quad (14)$$

where H is an $N \times N$ Hamiltonian (Hermitian) matrix. The real-time dynamics is given by the formal solution of

$$\mathbf{u}(t+h) = e^{-ihH} \mathbf{u}(t), \quad (15)$$

with a given tiny time interval h . When the wavepacket dynamics of a hole or excited electron is considered, its time scale is much smaller than that of the atomic motion. A typical scale of the time interval h is estimated by the atomic time unit of

$$\tau_{\text{au}} \equiv \frac{\hbar^3}{m} \left(\frac{e^2}{4\pi\epsilon_0} \right)^{-2} \approx 0.024189 \text{ fs} \approx \frac{1}{40} \text{ fs} \quad (16)$$

with the electron mass m , the elementary charge e , Planck's constant \hbar , and the dielectric constant of vacuum ϵ_0 . Therefore, the time interval h is usually much smaller than that in the molecular dynamics simulation ($h_{\text{MD}} \approx 1\text{fs}$).

Wavepacket dynamics simulations of a one-body wave function, hole, or excited electron, have been investigated for decades, since the method can describe both ballistic and diffusive behaviors. As a typical method, the wavepacket is perturbed by the atomic thermal motion and an essential issue is the modeling of the atomic motion. For example, a pioneering paper [56] adopted a one-dimensional site model, in which each molecule is treated as a lattice site and the electron–phonon coupling is included. The atomic motion is realized by the classical (Newtonian) dynamics of mobile lattice sites. The wavepacket is represented on sites and its dynamics is realized by the quantum wavepacket dynamics. The real-time dynamics is simulated with the time interval of $h = 1/40$ fs.

Although the atomic motion appears explicitly in the above theoretical approach, another approach is a method in which the atomic motion is treated as randomized effects on a wavepacket. The matrix H is dependent on time and is governed by

randomized variables that reflect the atomic motion. For example, hole wavepacket dynamics of condensed organic molecules or polymers was realized with a tight-binding (Slater–Koster form) Hamiltonian H on AO bases [27, 29]. The number of bases N_{AO} is proportional to that of atoms N_{atom} ($N_{AO} \propto N_{\text{atom}}$). The explicit atomic structure is used as an input and the Hamiltonian H is decomposed into two terms:

$$H = H_0 + H_a. \quad (17)$$

The first term H_0 , a constant matrix, is the tight-binding Hamiltonian that is determined by the input atomic structure and the second term $H_a = H_a(t)$ is a randomized matrix that stems from the thermal motion. In Refs. [27, 29], for example, the randomized matrix is modeled to be diagonal and

$$(H_a)_{\mu\mu} \equiv \frac{k_B T}{2} \cos 2\pi\theta_{A(\mu)}, \quad (18)$$

where the temperature is denoted as T and a random number of θ_A is generated for each atom index A ($A = 1, 2, \dots, N_{\text{atom}}$). The subscript $A(\mu)$ indicates the atom that includes the μ th AO. The random numbers $\{\theta_A\}_A$ are updated as a uniform random number of $\theta_A \in [0, 1]$ with the time interval of ($h = 1\text{fs}$). In short, the AO energy $H_{\mu\mu}$ has a time-dependent fluctuation on the order of T . From the above definition, the same random number is applied among the AOs on the same atom. The initial value of H_a is chosen to be the zero matrix ($H_a = O$), since the term of H_a appears as a consequence of the atomic structure deviating from the initial one by the thermal motion. The initial wavepacket is chosen to be an eigenvector of $H(t = 0) = H_0$, typically the highest occupied state. The initial atomic structure is usually disordered from the thermal motion and the initial wavepacket $\mathbf{u}(t = 0)$ is localized on one or several atoms. At the zero-temperature case, H_a is always zero ($H_a = O$) and the wavepacket does not propagate, because the wavepacket population on the μ th AO basis $p_\mu(t) \equiv |u_\mu(t)|^2$ is unchanged. At a finite-temperature case, H_a is non-zero ($H_a \neq O$) and the wavepacket can propagate through the material. In other words, the wavepacket propagation is driven by the atomic motion term of H_a . Since the Hamiltonian matrix $H(t)$ in the time interval of $nh \leq t \leq (n + 1)h$ with a given integer n is constant ($H(t) = H(nh)$), the real-time dynamics within the time interval is realized analytically by diagonalizing $H(nh)$.

Here, a theoretical generalization is proposed, as a preliminary research, for exciton wavepacket dynamics within the mathematical formulation of Eq. (14) [1, 28]. Suppose a system of N_{mol} molecules. A basis of the wavepacket vector \mathbf{u} means a two-body state denoted by a pair of an (excited) electron and a hole as $|e_I h_J\rangle$, where the electron occupies the I th molecular site and the hole occupies the J th molecular site. The constant Hamiltonian term H_0 indicates the two-body Hamiltonian for a given atomic structure and is generated by the FMO-based method explained in this chapter. The number of two-body wave function bases N_{CSF} is proportional to N_{mol}^2 ($N_{CSF} \propto N_{\text{mol}}^2$). The atomic motion term H_a is modeled by the diagonal matrix of

$$(H_a)_{kk} = \langle e_I h_J | H_a | e_I h_J \rangle \equiv \frac{k_B T}{2} (\cos 2\pi\theta_{J(k)} + \cos 2\pi\theta_{I(k)}), \quad (19)$$

where the temperature is denoted as T , k refers to a two-body basis, and a random number of θ_I is generated for each molecular index I or J ($I, J = 1, 2, \dots, N_{\text{mol}}$). The subscript $J(k)$ indicates the molecule that is occupied by the hole of the k th two-body basis, while subscript of $I(k)$ indicates the molecule that is occupied by the electron of the k th two-body basis. The real-time dynamics is realized by the same numerical method as that in the one-body wavepacket dynamics.

Finally, the computational aspect for large systems is discussed on the above method. The computational time of the method is governed by the iterative diagonalization of $H(nh)$ ($n = 0, 1, 2, \dots$). Since we used a dense-matrix solver in ScaLAPACK (<http://www.netlib.org/scalapack/>), the computational time is proportional to $N^3 \propto N_{\text{mol}}^6$ and will be impractical for large systems, such as a system with thousands of molecules or more ($N_{\text{mol}} \geq 10^3$, $N \propto N_{\text{mol}}^2 \geq 10^6$). An eigenvalue problem with $N = 10^6$ in the electronic state calculation was solved within 1.5 hours by the whole system of the K supercomputer [25]. Since the matrix H is, fortunately, sparse in most cases, the use of sparse-matrix solvers, like Krylov subspace method, is promising for large systems.

5 Applications to Organic Electronic Materials

5.1 DNTT Thin Film

In this subsection, we present the application of the combined FMO and wavepacket methods to the exciton dynamics in an organic semiconductor thin film. Optical properties of organic molecular aggregates have been investigated by the Frenkel exciton model. Because of relatively low dielectric constants of organic systems, an electron–hole Coulomb attraction is considered to be sufficiently strong to form a bound electron–hole pair. However, this Frenkel exciton model is challenged by electron energy-loss spectroscopy [51] and by ab initio calculations using the many-body Green’s function method [52]. The nature of excited states of high-mobility organic semiconductors has become an active research field in recent years.

Here, we focus on the dinaphtho[2,3-b:2',3'-f]thieno[3,2-b]-thiophene (DNTT) thin film [22]. DNTT is a *p*-type organic semiconductor molecule [59]; its molecular and crystal structures are shown in Fig. 2. In a recent time-resolved spectroscopy study, Ishino et al. [31] have suggested that the mixed Frenkel and CT exciton is formed after the optical excitation. Motivated by their work, we have investigated the exciton dynamics of the DNTT thin film on the basis of the electron–hole Hamiltonian parameterized by the FMO and wavepacket dynamics method.

We begin with the electronic couplings between DNTT molecules. The transfer integrals and excitonic couplings were obtained from the FMO-CIS/6-31G* calcu-

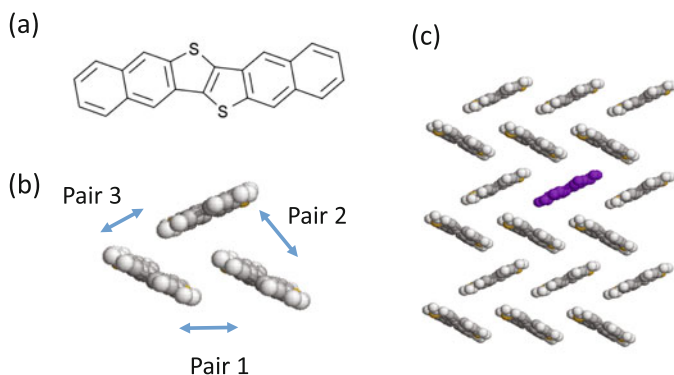


Fig. 2 **a** Molecular and **b, c** packing structures [59] of DNTT. In **(c)**, the molecular site chosen as the initial condition for the wavepacket dynamics ($|\psi(t=0)\rangle = |e_1 h_1\rangle$) is depicted in purple

Table 1 Electron and hole transfer integrals (t_e and t_h), and excitonic Coulomb couplings (V_F) in meV for molecular pairs in the DNTT crystal structure in the ab plane (see Fig. 2b for pair labeling), which were obtained at the FMO-CIS/6-31G* level

	t_e	t_h	V_F
Pair 1	24	83	3
Pair 2	51	38	33
Pair 3	38	125	59

lation for the DNTT trimer. In Table 1, we show the HOMO–HOMO and LUMO–LUMO transfer integrals (t_h and t_e), and the excitonic Coulomb couplings (V_F) in the DNTT trimer (Fig. 2b). The results show that the hole transfer integrals are larger than the others, confirming that the DNTT is an efficient p-type organic semiconductor. Using these electronic couplings and assuming translational symmetry, we defined the electron–hole Hamiltonian (Eq. 13) for extended DNTT molecular aggregates. The absorption spectrum obtained from the FMO-based Hamiltonian is in reasonable agreement with the experimentally obtained spectrum [22].

Having obtained the reasonable model Hamiltonian for the DNTT aggregates, we next turn to the time evolution of excited states. To this end, we adopted the stochastic Schrödinger equation proposed by Zhao and co-workers [60]. In contrast to a method using the classical random noise [20], this stochastic Schrödinger equation considers quantum effects of phonon bath and appropriately provides a Boltzmann distribution in the long time. An ensemble average of the exciton wavepacket propagations yields the two-body electron–hole density matrix, $\rho^{eh}(t) = \langle |\psi(t)\rangle \langle \psi(t)| \rangle_{ens}$. The system of 18 DNTT molecules in the ab plane, as depicted in Fig. 2c, was taken as a model of thin films. As a limiting case, the local excited state ($|e_1 h_1\rangle$) was used for the initial condition of excited-state dynamics. The excitonic density matrix was calculated at the temperature of 300 K.

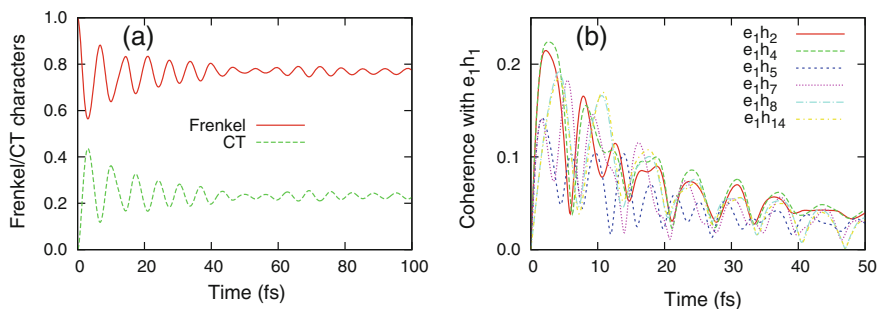
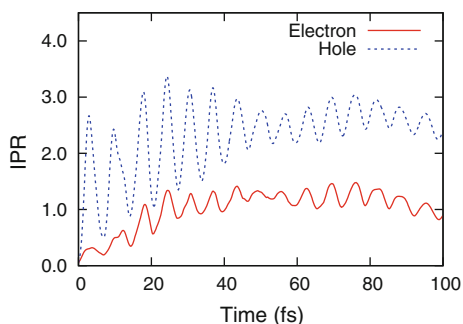


Fig. 3 **a** Frenkel and CT character and **b** Coherence between the initial LE state ($|e_1h_1\rangle$) between a neighboring CT state ($|e_1h_J\rangle$, $J \neq 1$). Reprinted with permission from T. Fujita, S. Atahan-Evrenk, N. P. D. Sawaya, et al. *J. Chem. Phys. Lett.* 7:1374–1380, 2016. Copyright 2016 American Chemical Society

Here, we show the ultrafast dynamics after the optical excitation. The Frenkel and CT character of the exciton wave function can be quantified as $p_F(t) = \sum_I |\langle e_I h_I | \Psi(t) \rangle|^2$ and $p_{CT}(t) = \sum_{I \neq J} |\langle e_I h_J | \Psi(t) \rangle|^2$, respectively. Figure 3a shows the oscillation between the Frenkel and CT populations, implying the presence of electronic coherence between Frenkel and CT states. The coherence can be seen as off-diagonal elements of the electron–hole density matrix. The electronic coherence between the initial LE state ($|e_1h_1\rangle$) and neighboring CT states ($|e_1h_J\rangle$) is shown in Fig. 3b, clearly indicating that the coherence persists for approximately 50 fs. It follows that, for the initial 50 fs, the excited-state wave function is a coherent superposition of Frenkel and CT states. Their electronic coherence then decays as a result of the dissipation and thermal fluctuations, and the initial state becomes the incoherent mixture of Frenkel and CT states for $t > 50$.

To gain deeper insight into the ultrafast dynamics, we highlight the dynamics of the electron and hole wave functions that compose the excited state. Here, we aimed to quantify the spatial extents of electron and hole wave functions. To this end, a one-body electron or hole density matrix was obtained by tracing out the hole or electron basis: $\rho^e(t) = Tr_h \rho^{eh}(t)$ or $\rho^h(t) = Tr_e \rho^{eh}(t)$. The spatial extent of the wave function was quantified as the generalized inverse participation ratio [8], $L_\rho^{e/h}(t) = \left(\sum_{IJ} |\rho_{IJ}^{e/h}| \right)^2 / \left(N \sum_{IJ} |\rho_{IJ}^{e/h}|^2 \right)$. Because the coherence is included in the IPR, this measure can distinguish an incoherent mixture of localized states from a coherently delocalized state. The IPRs of hole and electron density matrices shown in Fig. 4 indicate that the spatial extent of the hole is larger than that of the electron. Regarding the HOMO–HOMO transfer integrals being larger than the LUMO–LUMO transfer integrals, the hole wave function can be more easily delocalized. In addition, the strong oscillation in the IPRs implies that the hole wave function expands and shrinks around the localized electron wave function. The time scale of the oscillation correlates with the electronic coherence between Frenkel and CT states. The combined FMO and wavepacket methods have revealed the underlying

Fig. 4 Electron and hole IPRs. Reprinted with permission from T. Fujita, S. Atahan-Evrenk, N. P. D. Sawaya, et al. *J. Chem. Phys. Lett.* 7:1374–1380, 2016. Copyright 2016 American Chemical Society



ing dynamics of electron and hole wave functions, which govern the mixing between Frenkel and CT states.

5.2 Pentacene/ C_{60} Interface

In this subsection, we present the application to the electron–donor/electron–acceptor (D/A) interface as a model for organic solar cells. In an organic solar cell, a bound electron–hole pair is first created by light absorption. Charge separation then occurs at the D/A interface, yielding photogenerated charge carriers. Predicting the excited states formed across the interface is essential to understanding the charge separation. In addition, a quantum dynamics simulation is also necessary because the total charge photogeneration process includes several elementary steps.

Here, we focus on the D/A interface comprising a C_{60} molecule as an electron acceptor and a pentacene (PEN) molecule as an electron donor, respectively. PEN/ C_{60} interfaces have been widely investigated [4, 46], because PEN and C_{60} are typical p-type and n-type organic semiconductor molecules, respectively. As a limiting interfacial orientation, we considered the face-on configuration of a PEN/ C_{60} bilayer heterojunction (Fig. 5). An FMO calculation was performed to characterize excited states formed across the PEN/ C_{60} interface. Moreover, we investigate the real-time dynamics of charge photogeneration, utilizing the wavepacket propagation of the electron–hole wave function.

The excited states of the PEN/ C_{60} interface were modeled on the basis of Eq. (12) [18]; the Hamiltonian enables a consistent description of both localized and delocalized states and of both bound electron–hole pairs and charge separated states. The singlet excited-state wave function of the PEN/ C_{60} interface was described as

$$\begin{aligned}
 |\Psi\rangle = & \sum c_{LE(C)}|LE(C)\rangle + \sum c_{CT(C-P^+)}|CT(C^-P^+)\rangle \\
 & + \sum c_{LE(P)}|LE(P)\rangle + \sum c_{CT(P-P^+)}|CT(P^-P^+)\rangle, \quad (20)
 \end{aligned}$$

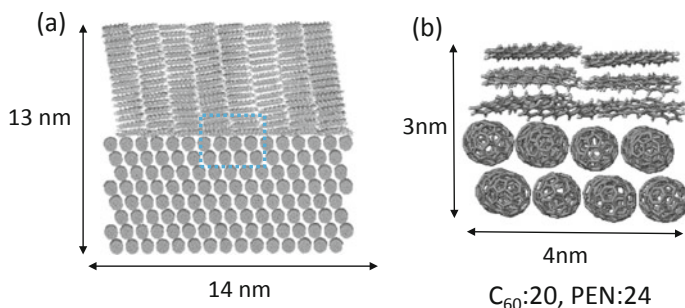


Fig. 5 **a** Atomistic structures of the **(a)** face-on orientation of the PEN/ C_{60} interface. **b** Local interface structures treated quantum mechanically by the excited-state method. Reproduced from T. Fujita, Md. K. Alam, T. Hoshi, *Phys. Chem. Chem. Phys.* 20:26443–26452, 2018. With permission from the PCCP Owner Societies

where $|LE(C)\rangle$ and $|LE(P)\rangle$ are intramolecular first excited states for C_{60} and PEN molecules, respectively. The term $|CT(C^-P^+)\rangle$ denotes an interfacial charge transfer (ICT) state comprising a hole on a HOMO of a PEN molecule and an electron on a LUMO, LUMO+1, or LUMO+2 of a C_{60} molecule. The intermolecular CT states within PEN molecules $|CT(P^-P^+)\rangle$ were also included. The matrix elements of the excited-state Hamiltonian were calculated in these fragment CSFs. The excited state calculation for the local interface structure (Fig. 5b) was performed at the FMO-CIS/6-31G** level, in which the surrounding molecules included in Fig. 5a were treated as external point charges. Because excitation energies are substantially overestimated at the CIS level, the diagonal elements of the excited-state Hamiltonian were corrected. Further details of the excited-state calculation are provided elsewhere [24].

We introduce three quantities to characterize excited states. The ICT character of an M th excited state is quantified by $P_{ICT} = \sum_k |\langle CT(C^-P^+) | \Psi_M \rangle|^2$. The electron–hole separation is defined as $R_{eh} = \langle \Psi_M | \mathbf{R}_e - \mathbf{R}_h | \Psi_M \rangle$, which denotes the center-of-mass distance between the electron and hole wave functions that constitute the excited state. Note that the electron–hole separation does not reflect the spatial extent of electron or hole wave functions. Therefore, we introduce the variance of R_{eh} to quantify the spatial extent of wave functions, $\sigma_{eh}^2 = \langle \Psi_M | ((\mathbf{r}_e - \mathbf{r}_h) - R_{eh})^2 | \Psi_M \rangle$. σ_{eh} increases with increasing spatial extent of electron or hole wave function and thus quantifies the spatial delocalization of an excited state.

The diagonalization of the excited-state Hamiltonian yields more than 2,000 excited states. First, we consider ICT character versus excitation energy as shown in Fig. 6. The lowest ICT state is located at 1.41 eV and is lower than the PEN excited states that are optically bright. Therefore, initial excited states formed in the PEN molecules result in the population of the lower ICT state via thermal relaxation. The free charge carriers are then generated through the ICT states.

Next, we turn to the electron–hole separation and the spatial extent of excited states. Here, the excited states were categorized into three groups according to their

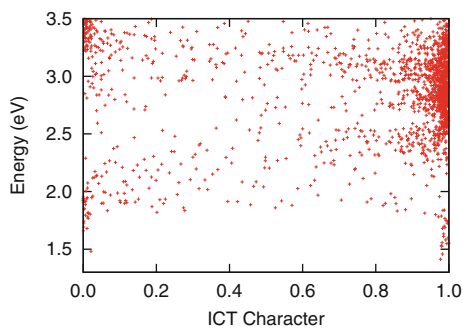


Fig. 6 ICT characters for excited states of the PEN/C₆₀ interface. Reproduced from T. Fujita, Md. K. Alam, T. Hoshi, *Phys. Chem. Chem. Phys.* 20:26443–26452, 2018. With permission from the PCCP Owner Societies

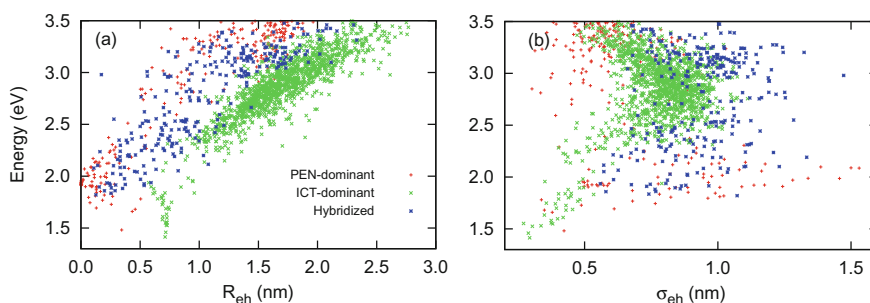


Fig. 7 **a** Electron–hole separation and **b** spatial delocalization for excited states of the PEN/C₆₀ interface. Reproduced from T. Fujita, Md. K. Alam, T. Hoshi, *Phys. Chem. Chem. Phys.* 20:26443–26452, 2018. With permission from the PCCP Owner Societies

P_{ICT} values: PEN-dominant states ($P_{ICT} < 0.2$), ICT-dominant states ($P_{ICT} > 0.8$), and PEN-ICT hybridized states ($0.2 < P_{ICT} < 0.8$). In Fig. 7a, b, R_{eh} and σ_{eh} for these three groups are shown in different colors. The lower ICT states (< 2.0 eV) are characterized by lower R_{eh} and σ_{eh} values. It follows that the lower ICT state is a tightly bound electron–hole pair comprising localized electron and localized hole wave functions. The PEN-dominant states at approximately 2.0 eV are characterized by a smaller R_{eh} and relatively large σ_{eh} . These PEN-dominant states are delocalized as the Frenkel exciton states, which are the superposition of bound electron–hole pairs. The electronic couplings between PEN and ICT states result in the emergence of the PEN-ICT hybridized states. Compared with the ICT-dominant states, the hybridization decreases R_{eh} but increases σ_{eh} . The enhancement of σ_{eh} is ascribed to the electron delocalization over both PEN and C₆₀ molecules; the superposition of PEN and ICT states results in the electron wave function extending over PEN and C₆₀ molecules. The presence of the delocalized electron wave functions across the D/A interface promotes efficient charge separation, enhancing long-range electron transfer.

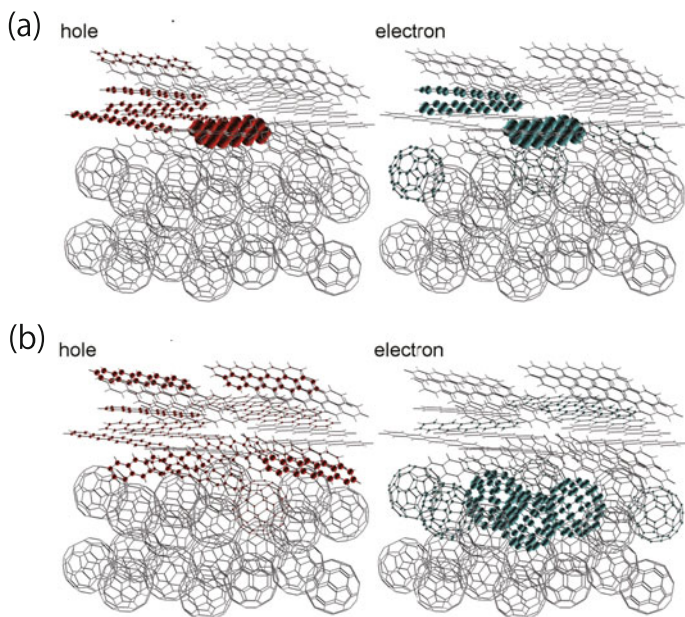


Fig. 8 Charge-separation dynamics at the PEN/C₆₀ interface; **a** the initial state ($t = 0$) and **b** the final state ($t \approx 10$ ps)

Having characterized the excited states, we present a preliminary result for the dynamical simulation of the exciton dissociation process into electron and hole at the PEN/C₆₀ interface [1, 28]. The exciton wavepacket dynamics was realized by the method described in Sect. 4. The FMO-derived excited-state Hamiltonian was used as the constant Hamiltonian term, and the atomic motion term was modeled by Eq. (19). The exciton wavepacket simulation was simulated at the temperature of 30 K. We chose the initial condition of the dynamical simulation as an adiabatic excited state that describes a Frenkel exciton state. The excitation energy of the initial adiabatic states is 2.10 eV, and its P_{ICT} is 0.26. Thus, the initial state is the PEN-dominant Frenkel exciton with partial admixture of ICT states.

Figure 8 shows the result of the wavepacket dynamics. Here, the electron or hole occupation ratio on each molecule is expressed by the radius of atoms (balls) of each molecule. As shown in Fig. 8a, the initial state is an electron-hole pair nearly on the same molecules. The final state $t \approx 10$ ps is shown in Fig. 8b and is a CT-like state, since most of the electron populations are distributed over C₆₀ molecules.

6 Conclusions

In the present chapter, we have reviewed our approach to excited-state dynamics in molecular aggregates. The computations of the electronic couplings in the FMO method were explained in detail. The transfer integrals are calculated by the FMO-LCMO method, whereas the excitonic couplings are obtained within the MLFMO-CIS method. In addition, we have discussed the relationship between the FMO calculations and the model Hamiltonians. The real-time excited-state dynamics is realized by the model Hamiltonian and wavepacket dynamics method. Our approach allows for *ab initio* simulations of the excited-state dynamics; the successful simulations require accurate parameterization of the model Hamiltonian. However, we note that quantitative MO energies or excitation energies cannot be obtained at the HF or CIS level. To improve the accuracy, we are currently developing many-body Green's function theory within the FMO framework [19].

Here, we contrast the present method with the original FMO method. According to Li et al. [39], fragment-based electronic structure methods can be classified into energy-based and density matrix-based methods. In an energy-based fragmentation method, on one hand, the total energy is directly approximated from the energies of subsystems. In a density matrix-based method [37], on the other hand, the density matrix of an entire system is first approximated from subsystem calculations, and the total energy is then obtained from the total density matrix. Obviously, the FMO method [33] is an energy-based fragmentation method, in which a total wave function is not obtained. By contrast, the present FMO-based method allows for calculating excited-state wave functions of an entire system. In this sense, the FMO-LCMO [57] and excited-state method [24] may be regarded as a density matrix-based approach, which is in contrast to the original FMO method. In terms of applications, our approach can describe optoelectronic functions in molecular systems. This is in contrast to FMO applications thus far, most of which utilize interfragment interaction energy analyses to investigate the thermodynamic stability of biomolecules. Our developments have extended the applicability of the FMO method to explore optoelectronic processes.

We have presented the application studies on the DNTT thin film and the C₆₀/PEN interface. In particular, we highlight the spatial extents of the electron and hole wave functions that constitute exciton states. We show that the dynamics of the electron and hole wave functions play essential roles in optoelectronic processes, such as the exciton relaxation dynamics and charge separation. Because the extent of delocalization is determined by the interplay among electronic couplings, structural disorder, and finite-temperature effects, the combined approach based on the FMO and wavepacket dynamics is indispensable. Although we have focused on the organic materials, our approach is general and can be applied to other molecular systems. Potential applications include functional supramolecular systems [58] and bio-inspired materials [32, 53], as well as organic electronic materials.

Acknowledgements T.F. thanks Yuji Mochizuki, Tatsuya Nakano, and Yoshio Okiyama for the collaborations on the FMO-based electronic coupling calculations and their implementation in the

ABINIT-MP program. T.F also thanks Sule Atahan-Evrenk, Nicolas P. D. Sawaya, Alán Aspuru-Guzik, and Md. Khorshed Alam for their collaborations on the organic electronic materials. T.F acknowledges the financial support by Ministry of Education, Culture, Sports, Science and Technology (MEXT) as a Building of Consortia for the Development of Human Resources in Science and Technology. This work was supported in part by scientific priority issue (Creation of new functional devices and high-performance materials to support next-generation industries; CDMSI) to be tackled by using post-K computer.

References

1. Abe Y (2018) Quantum dynamics simulation of organic opt-electronics device materials (written in Japanese). M. Thesis, Tottori University, Tottori, Japan
2. Bao Z, Locklin J (2007) Organic field-effect transistors. CRC Press
3. Baumeier B, Kirkpatrick J, Andrienko D (2010) Density-functional based determination of intermolecular charge transfer properties for large-scale morphologies. *Phys Chem Chem Phys* 12:11103–11113
4. Brigeman AN, Fusella MA, Yan Y, Purdum GE, Loo YL, Rand BP, Giebink NC (2016) Revealing the full charge transfer state absorption spectrum of organic solar cells. *Adv Energy Mater* 6:1601001
5. Chiba M, Koido T (2010) Electronic excitation energy calculation by the fragment molecular orbital method with three-body effects. *J Chem Phys* 133:044113
6. Chiba M, Fedorov DG, Kitaura K (2007) Time-dependent density functional theory based upon the fragment molecular orbital method. *J Chem Phys* 127:104108
7. Chiba M, Fedorov DG, Kitaura K (2007) Time-dependent density functional theory with the multilayer fragment molecular orbital method. *Chem Phys Lett* 444:346
8. Dahlbom M, Pullerits T, Mukamel S, Sundström V (2001) Exciton delocalization in the b850 light-harvesting complex: Comparison of different measures. *J Phys Chem B* 105:5515
9. Davidov AS (1971) Theory of molecular excitons. Springer, New York
10. Fedorov DG, Kitaura K (2007) Extending the power of quantum chemistry to large systems with the fragment molecular orbital method. *J Phys Chem A* 111:6904
11. Fedorov DG, Kitaura K (eds) (2009) The fragment molecular orbital method: practical applications to large molecular systems. CRC Press, Boca Raton, FL
12. Fedorov DG, Kitaura K (2017) Many-body expansion of the fock matrix in the fragment molecular orbital method. *J Chem Phys* 147:104106
13. Fedorov DG, Ishida T, Kitaura K (2005) Multilayer formulation of the fragment molecular orbital method (FMO). *J Phys Chem A* 109:2638
14. Fedorov DG, Nagata T, Kitaura K (2012) Exploring chemistry with the fragment molecular orbital method. *Phys Chem Chem Phys* 14:7562
15. Foresman JB, Head-Gordon M, Pople JA, Frisch MJ (1992) Toward a systematic molecular orbital theory for excited states. *J Phys Chem* 96:135
16. Fujimoto KJ (2012) Transition-density-fragment interaction combined with transfer integral approach for excitation-energy transfer via charge-transfer states. *J Chem Phys* 137:034101
17. Fujimoto KJ, Kitamura C (2013) A theoretical study of crystallochromy: spectral tuning of solid-state tetracenes. *J Chem Phys* 139:084511
18. Fujita T, Mochizuki Y (2018) Development of the fragment molecular orbital method for calculating nonlocal excitations in large molecular systems. *J Phys Chem A* 122(15):3886
19. Fujita T, Noguchi Y (2018) Development of the fragment-based cohsex method for large and complex molecular systems. *Phys Rev B* 98:205140
20. Fujita T, Huh J, Aspuru-Guzik A (2014) A stochastic reorganizational bath model for electronic energy transfer. *J Chem Phys* 140:244103

21. Fujita T, Huh J, Saikin SK, Brookes JC, Aspuru-Guzik A (2014) Theoretical characterization of excitation energy transfer in chlorosome light-harvesting antennae from green sulfur bacteria. *Photosynth Res* 120:273
22. Fujita T, Atahan-Evrenk S, Sawaya NPD, Aspuru-Guzik A (2016) Coherent dynamics of mixed frenkel and charge-transfer excitons in dinaphtho[2,3-b:2'3'-f]thieno[3,2-b]-thiophene thin films: The importance of hole delocalization. *J Phys Chem Lett* 7:1374
23. Fujita T, Haketa Y, Maeda H, Yamamoto T (2017) Relating stacking structures and charge transport in crystal polymorphs of the pyrrole-based π -conjugated molecule. *Org Electron* 49:53
24. Fujita T, Alam MK, Hoshi T (2018) Thousand-atom ab initio calculations of excited states at organic/organic interfaces: toward first-principles investigations of charge photogeneration. *Phys Chem Chem Phys* 20:26443
25. Hoshi T, Imachi H, Kumahata K, Terai M, Miyamoto K, Shoji F (2016) Extremely scalable algorithm for 10^8 -atom quantum material simulation on the full system of the K computer. *Proc ScalA16 in SC16*, pp 33–40
26. Hsu CP (2009) The electronic couplings in electron transfer and excitation energy transfer. *Acc Chem Res* 42:509
27. Imachi H (2017) Numerical methods for large-scale quantum material simulations. D. Thesis, Tottori University, Tottori, Japan
28. Imachi H, Abe Y, Hoshi T, Fujita T. Unpublished work
29. Imachi H, Yokoyama S, Kaji T, Abe Y, Tada T, Hoshi T (2016) One-hundred-nm-scale electronic structure and transport calculations of organic polymers on the k computer. *AIP Conf Proc* 1790:020010/1–4
30. Iozzi MF, Mennucci B, Tomasi J, Cammi R (2004) Excitation energy transfer (EET) between molecules in condensed matter: a novel application of the polarizable continuum model (PCM). *J Chem Phys* 120:7029
31. Ishino Y, Miyata K, Sugimoto T, Watanabe K, Matsumoto Y, Uemura T, Takeya J (2014) Ultrafast exciton dynamics in dinaphtho[2,3-b:2'3'-f]thieno[3,2-b]-thiophene thin films. *Phys Chem Chem Phys* 16:7501
32. Kawada S, Sakaguchi M, Yonekura I, Okuwaki K, Mochizuki Y, Fukuzawa K (2016) Fragment molecular orbital calculations on peptoids (written in Japanese). *J Comput Chem Jpn* 15:51
33. Kitaoura K, Ikee E, Asada T, Nakano T, Uebayasi M (1999) Fragment molecular orbital method: an approximate computational method for large molecules. *Chem Phys Lett* 313:701
34. Kitoh-Nishioka H, Ando K (2012) Fragment molecular orbital study on electron tunneling mechanisms in bacterial photosynthetic reaction center. *J Phys Chem B* 116:12933
35. Kitoh-Nishioka H, Ando K (2015) Charge-transfer matrix elements by FMO-LCMO approach: hole transfer in DNA with parameter tuned range-separated DFT. *Chem Phys Lett* 621:96
36. Kitoh-Nishioka H, Ando K (2016) FMO3-LCMO study of electron transfer coupling matrix element and pathway: application to hole transfer between two tryptophans through CIS- and trans-polyproline-linker systems. *J Chem Phys* 145:114103
37. Kobayashi M, Nakai H (2011) Divide-and-conquer approaches to quantum chemistry: theory and implementation. In: Zalesny R, Papadopoulos MG, Mezey PG, Leszczynski J (eds) *Linear-scaling techniques in computational chemistry and physics: methods and applications*. Springer, Dordrecht, Netherlands, pp 97–127
38. Kobori T, Sodeyama K, Otsuka T, Tateyama Y, Tsuneyuki S (2013) Trimer effects in fragment molecular orbital-linear combination of molecular orbitals calculation of one-electron orbitals for biomolecules. *J Chem Phys* 139:094113
39. Li W, Li S, Jiang Y (2007) Generalized energy-based fragmentation approach for computing the ground-state energies and properties of large molecules. *J Phys Chem A* 111:2193
40. Löwdin PO (1950) On the non-orthogonality problem connected with the use of atomic wave functions in the theory of molecules and crystals. *J Chem Phys* 18:365
41. Madjet ME, Abdurahman A, Renger T (2006) Intermolecular coulomb couplings from ab initio electrostatic potentials: application to optical transitions of strongly coupled pigments in photosynthetic antennae and reaction centers. *J Phys Chem B* 110:17268

42. Mochizuki Y, Koikegami S, Amari S, Segawa K, Kitaura K, Nakano T (2005) Configuration interaction singles method with multilayer fragment molecular orbital scheme. *Chem Phys Lett* 406:283
43. Mochizuki Y, Tanaka K, Yamashita K, Ishikawa T, Nakano T, Amari S, Segawa K, Murase T, Tokiwa H, Sakurai M (2007) Parallelized integral-direct CIS(D) calculations with multilayer fragment molecular orbital scheme. *Theor Chem Acc* 117:541
44. Nakano T, Kaminuma T, Sato T, Akiyama Y, Uebayasi M, Kitaura K (2002) Fragment molecular orbital method: use of approximate electrostatic potential. *Chem Phys Lett* 351:475
45. Nakano T, Mochizuki Y, Fukuzawa K, Amari S, Tanaka S (2006) Developments and applications of ABINIT-MP software based on the fragment molecular orbital method. In: Starikov EB, Lewis JP, Tanaka S (eds) *Modern methods for theoretical physical chemistry of biopolymers*. Elsevier Science, Amsterdam, pp 39–52
46. Nakayama Y, Mizuno Y, Hosokai T, Koganezawa T, Tsuruta R, Hinderhofer A, Gerlach A, Broch K, Belova V, Frank H, Yamamoto M, Niederhausen J, Glowatzki H, Rabe JP, Koch N, Ishii H, Schreiber F, Ueno N (2016) Epitaxial growth of an organic p-n heterojunction: C60 on single-crystal pentacene. *ACS Appl Mater Inter* 8:13499
47. Nishioka H, Ando K (2011) Electronic coupling calculation and pathway analysis of electron transfer reaction using ab initio fragment-based method. I. FMO-LCMO approach. *J Chem Phys* 134:204109
48. Okiyama Y, Watanabe H, Fukuzawa K, Nakano T, Mochizuki Y, Ishikawa T, Ebina K, Tanaka S (2009) Application of the fragment molecular orbital method for determination of atomic charges on polypeptides. II. Towards an improvement of force fields used for classical molecular dynamics simulations. *Chem Phys Lett* 467:417
49. Saikin SK, Eisfeld A, Valleau S, Aspuru-Guzik A (2013) Photonics meets excitonics: natural and artificial molecular aggregates. *Nanophotonics* 2:21
50. Scholes GD, Rumbles G (2006) Excitons in nanoscale systems. *Nat Mater* 5(9):683–696
51. Schuster R, Knupfer M, Berger H (2007) Exciton band structure of pentacene molecular solids: breakdown of the frenkel exciton model. *Phys Rev Lett* 98:037402
52. Sharifzadeh S, Darancet P, Kronik L, Neaton JB (2013) Low-energy charge-transfer excitons in organic solids from first-principles: the case of pentacene. *J Phys Chem Lett* 4:2197
53. Sun J, Zuckermann RN (2013) Peptoid polymers: a highly designable bioinspired material. *ACS Nano* 7:4715
54. Taguchi N, Mochizuki Y, Nakano T (2011) Fragment molecular orbital calculations for excitation energies of blue- and yellow-fluorescent proteins. *Chem Phys Lett* 504:76
55. Tanaka S, Mochizuki Y, Komeiji Y, Okiyama Y, Fukuzawa K (2014) Electron-correlated fragment-molecular-orbital calculations for biomolecular and nano systems. *Phys Chem Chem Phys* 16:10310
56. Troisi A, Orlandi G (2006) Charge-transport regime of crystalline organic semiconductors: diffusion limited by thermal off-diagonal electronic disorder. *Phys Rev Lett* 96:086601
57. Tsuneyuki S, Kobori T, Akagi K, Sodeyama K, Terakura K, Fukuyama H (2009) Molecular orbital calculation of biomolecules with fragment molecular orbitals. *Chem Phys Lett* 476:104
58. Würthner F, Kaiser TE, Saha-Möller CR (2011) J-aggregates: from serendipitous discovery to supramolecular engineering of functional dye materials. *Angew Chem Int Ed* 50:3376
59. Yamamoto T, Takimiya K (2007) Facile synthesis of highly π -extended heteroarenes, dinaphtho[2,3-b:2',3'-f]chalcogenopheno[3,2-b]chalcogenophenes, and their application to field-effect transistors. *J Am Chem Soc* 129:2224
60. Zhong X, Zhao Y (2013) Non-markovian stochastic schrödinger equation at finite temperatures for charge carrier dynamics in organic crystals. *J Chem Phys* 138:014111

Application of the Fragment Molecular Orbital Method to Organic Charge Transport Materials in Xerography: A Feasibility Study and a Charge Mobility Analysis



Ikuro Fujino, Dmitri G. Fedorov, and Kazuo Kitaura

Abstract The charge transport rate constant is calculated using the Marcus theory for a pair of fragments in two different ways: neglecting and accounting for the effect of the environment. The latter is accomplished with the fragment molecular orbital (FMO) method. In order to apply FMO to charge transport materials (CTMs), it is first validated by comparing the accuracy and timings to full calculations without fragmentation, for several types of fragmentation models applied to dispersive and cross-linked CTMs. Secondly, the Marcus theory combined with FMO is applied to simulate charge transport phenomena using Einstein's diffusion model or kinetic Monte Carlo (KMC) method. The result of charge mobility simulation shows qualitative agreement with experiment, and KMC is found to give better results than the diffusion theory because it takes into account the directionality and the charge transport path.

Keywords Charge transport material · Charge mobility · Charge transfer rate constant · Marcus theory · Kinetic Monte Carlo simulation

I. Fujino (✉)

Key Technology Laboratory, Fuji Xerox Co., Ltd., N430 Sakai, Nakai-machi, Ashigarakami-gun, Kanagawa 259-0157, Japan

e-mail: ikuro.fujino@fujixerox.co.jp

D. G. Fedorov

Research Center for Computational Design of Advanced Functional Materials (CD-FMat), National Institute of Advanced Industrial Science and Technology (AIST), Central 2, Umezono 1-1-1, Tsukuba 305-8568, Japan

K. Kitaura

Advanced Institute for Computational Science (AICS), RIKEN, 7-1-26 Minatojima-minami-machi, Chuo-ku, Kobe, Hyogo 650-0047, Japan

Fukui Institute for Fundamental Chemistry, Kyoto University, Takano-Nishihiraki-cho 34-4, Sakyou-ku, Kyoto 606-8103, Japan

1 Introduction

1.1 Importance of Analyzing the Electronic Structure of Charge Transport Materials

Computational simulations of materials are used to facilitate material design and predict material properties. Quantum chemical approaches are very useful for phenomena such as charge transport based on the behavior of holes or electrons. In most such approaches, molecular orbitals (MO) are used, describing the electronic state. However, their computational cost makes it difficult to apply these methods for an analysis of functional materials, because the cost of such MO theories as Hartree–Fock is formally proportional to the fourth power of the number of basis functions due to two-electron integral calculations [1]. Various computational methods have been proposed in order to calculate large molecular systems efficiently [2–4]. One of them is the fragment molecular orbital (FMO) method, which has been applied widely in biochemistry [5–9]. FMO offers a large improvement in efficiency at a small penalty in accuracy, provided that the fragmentation is done properly. Although the fragmentation for bio-molecules has been studied in detail, much less is known about accurate fragmentation schemes for organic functional materials, especially charge transport materials that are used in xerographic processes [10]. The accuracy of FMO for various fragmentations is established and FMO is applied to study charge transport in materials.

1.2 Computation of Charge Mobility

Different algorithms for computing charge mobility are discussed in this section and FMO is validated as a practical tool for calculations and analysis of charge mobility in materials.

1.2.1 Models of Charge Mobility

In amorphous organic materials, charge transport can occur between molecules following the so-called hopping mechanism. In this mechanism, the charge transport can be depicted as a series of charge hopping between neighboring molecules through the molecular cluster. Several definitions are used to describe charge transport at different size scales. At the smallest scale, a charge transport path is evaluated based on molecular orbital energy levels and the localization of molecules. Also, because charge hopping involves a change in the molecular structure as the charge state moves, the reorganization energy is a relevant property. These simple but important mechanisms do not describe the charge transport adequately due to not considering molecular pairs, an important aspect of charge hopping. In the Marcus

theory, a charge hopping rate between molecular pairs is defined, and the charge coupling element of two molecules is computed that depends on the spatial overlap of the molecular orbitals involved in a charge hopping [11]. Moreover, this theory explicitly considers the geometrical effects in a molecular cluster, and the transport theory is employed with the charge hopping rate that is calculated for every pair of neighboring molecules. Alternatively, there is another approach called the Gaussian disorder model, GDM [12], where the charge transport is characterized by deviations of the Gaussian distribution function describing the density of states and position of molecular sites. In other words, GDM focuses on the behavior of a group of molecules, whereas Marcus theory focuses on individual molecular pairs. In this study, the Marcus theory is used to analyze charge transport in a molecular cluster while the electronic structure is determined with FMO or full MO calculations.

1.2.2 Analysis of Charge Transport in Nano-Scale Simulations

In previous simulations of charge mobility performed for molecular design of charge transport materials, the Marcus theory was employed to evaluate charge transport quantitatively using MO methods [13, 14]. Namely, the electronic structure of an isolated monomer pair is determined by an MO approach, and then the charge transfer rate constant is obtained based on the Marcus theory. In this approach, because isolated pairs of molecules are calculated, the effect of the environment (mainly, the electrostatic potential) is neglected in calculating the electronic structure, so that polarization effects are not accounted for. In xerographic processes, often a mixture of charge transport and polymer materials is used, for which it may be important to consider the effect of the environment [15]. In particular, polar materials may be substantially affected by the environmental potential. This obstacle is absent in FMO because it has an environmental electrostatic potential in each calculation of molecules or their pairs [5].

Besides a more sophisticated and accurate physical model including the environmental electrostatic potential, FMO calculations are faster than MO methods if the number of basis functions (or atoms) is sufficiently large. FMO is a many-body expansion of size-extensive [16] molecular properties [17], and the order n of the expansion is specified as FMO n . In FMO2, one calculates the electronic states of fragments (monomers) and their pairs (dimers), followed by a calculation of trimers in FMO3 (all of these calculations are performed in the embedding potential) [18]. In FMO, efficient approximations [19] reduce the scaling if the system size is large enough. On the other hand, although the scaling of full MO calculations is formally $O(N^4)$, integral screening, matrix diagonalization, and other techniques help to reduce the computational cost to at most $O(N^3)$. In addition, FMO is a very useful tool to study charge transfer because it provides the natural basis for considering molecules and their pairs in the embedding potential, with a manageable computational cost.

1.3 The Objective of This Study

In this study, two computational tasks are accomplished for the evaluation of charge mobility at the molecular scale. One is to validate FMO for charge transfer materials in comparison to full MO methods in terms of the total properties such as the energy and also to compare the computational time. The other is to establish a charge transport simulation model using FMO. Because FMO takes the environmental electrostatic potential into account in the calculation of the electronic structure of molecules, it has a great advantage for molecular design because charge transport may be affected by the environment for instance, due to binding polymers added to charge transport materials. After the electronic structure is calculated, the charge hopping rate for each pair of neighboring molecules is determined, and then the charge mobility, which is an experimentally measurable value, is obtained with the classical transport theory.

2 Validation of FMO for Organic Charge Transport Materials

In order to perform FMO calculations, the molecular system has to be divided into pieces called fragments. In other words, for each atom one has to assign a fragment to which it belongs. This assignment of atoms to fragments can be done automatically for bio-molecules using various software because bio-systems are built from standard blocks such as amino acid residues or nucleic acids. However, organic charge transport materials need a different pattern for fragmentation, which, once established, can be later integrated into programs. Therefore, an important objective is to establish guidelines for fragmentation. For a chosen fragmentation, an input file is made, which is used to execute computational software. Many results summarized in this section have been previously published in [20].

2.1 Fragmentation of Organic Charge Transport Molecules

Charge transport materials (CTMs) are often classified as either hole or electron transport materials for the purpose of device design. Besides this, charge transport materials can be divided into two groups based on the existence or absence of covalent bonds between fragments in FMO, namely, dispersive charge transport materials (no such bonds) and cross-linked charge transport materials, shown in Figs. 1 and 2.

One of the major differences is that while dispersive CTMs shown in Fig. 1a–c are individual molecules, cross-linked CTMs shown in Fig. 2 are macroscopic polymers. As long as the dispersive CTMs are not composed of a large number of atoms, it is reasonable to assign one molecule as a fragment in FMO. This strategy

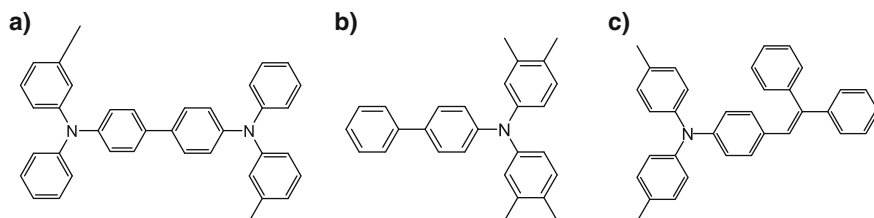


Fig. 1 Example of dispersive charge transport materials: **a** TPD, **b** TPA1, **c** TPA2

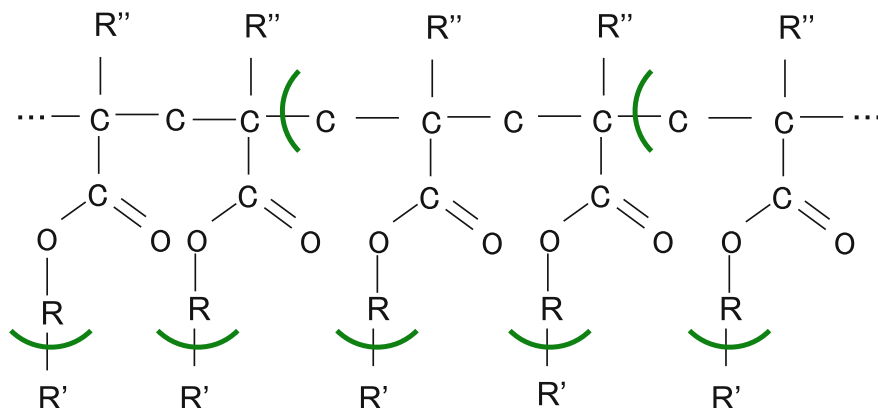


Fig. 2 Fragment division model for a cross-linked CTM

has been found to work well in our previous studies where the number of atoms of the dispersive CTMs is in the range of a few dozens to a few hundred of atoms [20].

On the other hand, a division of covalent bonds for a cross-linked CTM has to be done because of its long polymer chain and cross-linking parts, see Fig. 2. In order to build a fragmentation model, cross-linked CTM models were constructed with the polymerization count of 10 and divided in several ways, as shown in Fig. 3. At first, CTM was fragmented taking one unit as a fragment divided at every cross-linking point as shown in Fig. 3a so that there are 10 fragments in FMO. This way the fragment size is kept small, and all fragments are of similar size, which gives an advantage for parallel computations; however, test calculation showed poor convergence in dimer calculations. Specifically, two out of five models did not converge, and for the three that converged, the difference of the total energy between FMO and full MO is around 3 eV, which is not small. The origin of this error is the close proximity of two neighboring fragmentation points [21], i.e., two circled C atoms in Fig. 3a.

Next, two units were taken as one FMO fragment by dividing the CTM into five fragments as shown in Fig. 3b. Although this division has a very high accuracy versus full MO, 0.01 eV, again, three out of five molecular models did not converge. Finally, the CTM was divided into 15 fragments as shown in Fig. 3c. First, the CTM is divided into two parts, namely, the charge transport moiety and cross-linking moiety. This

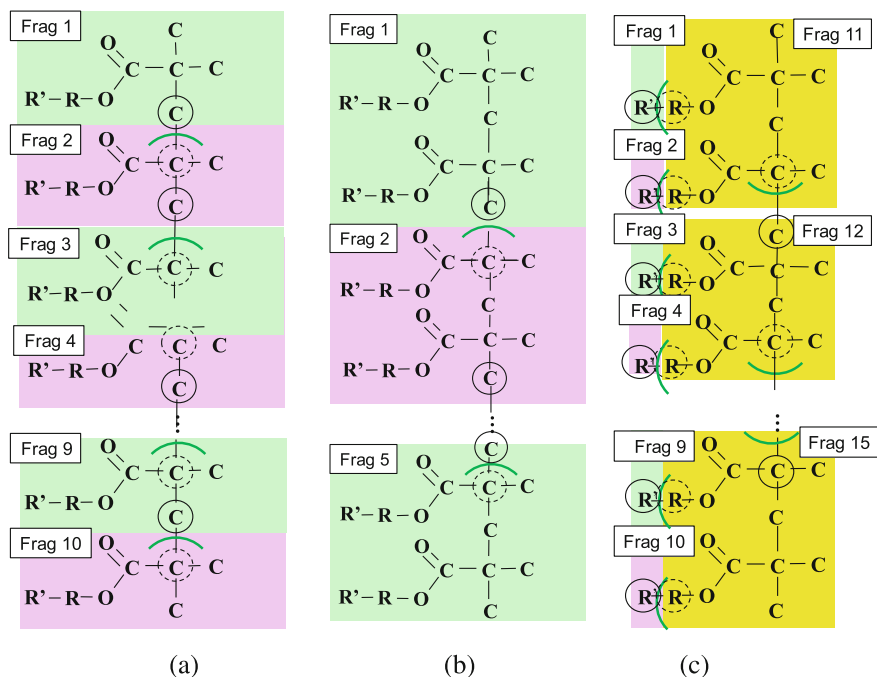


Fig. 3 Fragmentation models with a division of covalent bonds for cross-linked CTM: **a** one unit as a fragment, **b** two units as a fragment, **c** two cross-linking moieties as a fragment (yellow) and one charge transport moiety R' (green and pink) as a fragment. Solid and dashed circles indicate the positions of bond-attached and bond-detached atoms, respectively

is not done only to make the fragment size smaller, but to enable the interaction analysis and separate the contribution of the charge transport moiety from that of the cross-linking moiety. In other words, one can investigate features of the charge transport moiety, which is important for designing charge transport, and exclude effects of the cross-linking moiety, which is important for structural characteristics of the materials. Note that fragmenting near the COO group was not done to avoid having several fragmentation points close to each other. This is why there is a small R group included in the cross-linking moiety. Secondly, the cross-linking moiety is divided not in 10, but in 5 fragments. This is important to keep fragmentation points separated in space. The final fragmentation model contains 15 fragments (10 charge transport moieties and 5 cross-linking moieties) for a cross-linked CTM as shown in Fig. 3c. An FMO fragmentation is performed at an atom, for instance, $C_1|C_2$, not between atoms (not C_1-C_2), and therefore there is a difference between the $C_1|C_2$ and C_1-C_2 fragmentations. In $C_1|C_2$, C_2 is the bond-attached atoms (BAA) and C_1 is the bond-detached atoms (BDA), respectively, denoting the fact that the bond with its two electrons is included in the fragment to which C_2 belongs.

2.2 Validation of Fragmentations

In this section, the accuracy of FMO is established by comparing to full MO calculations. There are two aspects in the validation of the fragmentations: the speed and accuracy. In measuring the performance, the number of atoms N is used to study the scaling $O(N^a)$. The error of FMO is typically proportional to the number of atoms. The performance of fragmentations is established based on the criteria of speed and accuracy.

The amorphous structure of a molecular cluster was simulated using molecular dynamics (MD), see Fig. 4a. This MD simulation was done using J-OCTA [22] for molecular modeling and VSOP, a module of J-OCTA, for MD parallel computation (J-OCTA is a registered trademark of JSOL corporation). NPT MD was done at 1 atm and 300 K. Next, a number of snapshots are selected from MD, because the structure is amorphous. These extracted molecular structures were optimized with molecular mechanics (MM) executed with COGNAC [23] using general Amber force field (GAFF), see Fig. 4b. Finally, full MO, FMO2, and FMO3 calculations were performed using the FMO code [24] implemented in GAMESS [25]. The FMO fragmentation, performed with Facio [26, 27], is shown in Fig. 4c. The calculations were performed at the level of B3LYP/6-31G*. The hybrid orbital projection technique was used to treat fragment boundaries. A single node equipped with 16 cores was used for time measurement of the small systems containing less than 1,000 atoms. For time measurement of larger systems, 10 nodes equipped with 20 cores per node were used at FOCUS supercomputer system, which is a HPC infrastructure operated by Foundation for Computational Science [28]. The difference of total energy for fixed structures was obtained by comparing MO and FMO2. For larger systems, MO calculations were too large to perform, and the accuracy was estimated by comparing FMO2 with FMO3.

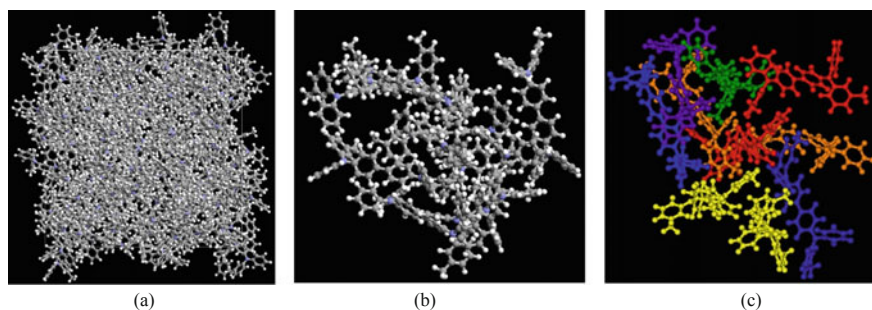


Fig. 4 Molecular systems during the validation: **a** amorphous structure obtained from MD; **b** selected molecules, whose structure is optimized with MM; **c** fragmentation in FMO

2.3 Results of the FMO Validation

The validation was performed for dispersive molecules, TPD, and cross-linked CTMs [20]. A TPD molecular cluster of up to 10 molecules was computed (Fig. 5a). The scaling of FMO is about 1 order of magnitude smaller than that of full MO, but it is somewhat high because the TPD molecules are relatively large and for 2–10 fragments the linear scaling regime is not reached. The computational time for FMO2 is shorter than that of MO at about 100 atoms or more. The FMO2 timings for 10–30 TPD molecules, shown in Fig. 5b, indicate an approximately linear scaling of FMO2 with $R^2 = 0.9818$. The dependence of the error on the system size is shown for two ranges of the system sizes, FMO2 versus MO (Fig. 6a) and FMO2 versus FMO3 (Fig. 6b). The error dependence on the size is nearly linear with the correlation of $R^2 = 0.9904$ and $R^2 = 0.9608$ for these two comparisons, respectively. Thus, the FMO error is reasonable and increases nearly linear with respect to the system size, and the computational efficiency is nearly linear high (except small sizes). Thus, FMO is validated for TPD as a charge transfer material.

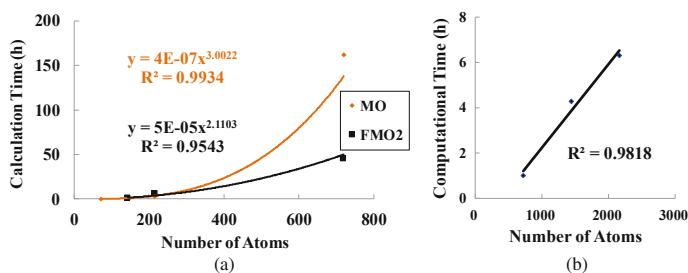


Fig. 5 Dependence of the computational time on the number of atoms for TPD: **a** 1–10 molecules, **b** 10–30 molecules (only FMO2 timings are shown)

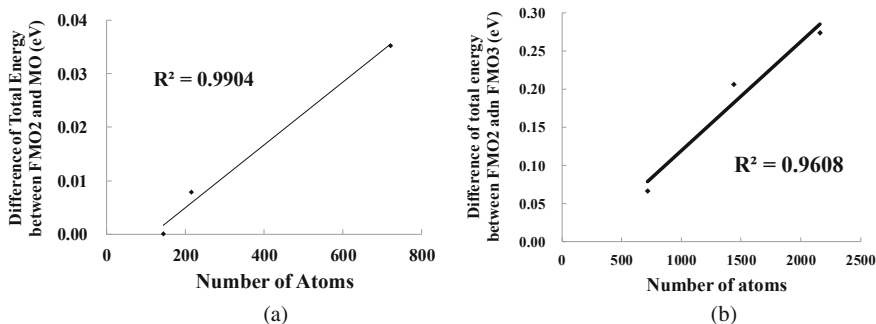


Fig. 6 Dependence of the FMO2 accuracy on the number of atoms for TPD: **a** 1–10 molecules, **b** 10–30 molecules

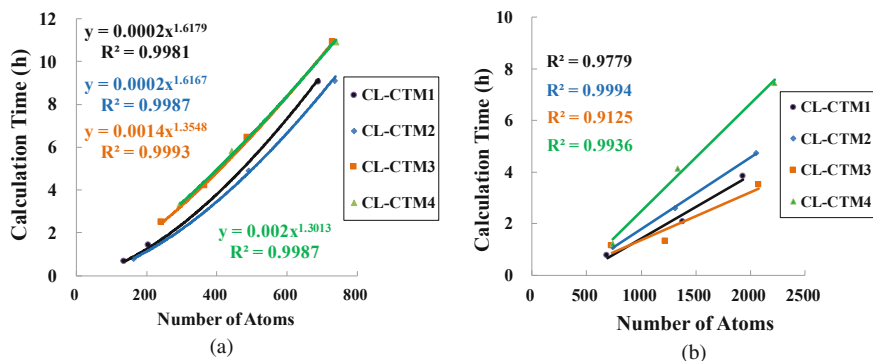


Fig. 7 Dependence of the computational time on the number of atoms for cross-linked CTMs (CL-CTM1, ..., CL-CTM4): **a** the small systems, **b** the large systems

Next, FMO is validated for cross-linked CTMs. The scaling of FMO2 observed for the smaller range of atoms was between 1.3 and 1.7, see Fig. 7a, where cross-linked CTM is denoted as CL-CTM. For the larger set, the scaling is approximately linear, see Fig. 7b. The error as a function of the number of atoms is approximately linear, as shown in Fig. 8a, b. The larger range shown in Fig. 8b has more deviations in the error apparently due to the somewhat random effect of the structure on the accuracy, more pronounced for larger systems and when FMO2 accuracy is measured versus FMO3. Compared to TPD, the larger deviations in Fig. 8b may be explained by the smaller error in TPD because it has no covalent boundaries between fragments. Overall, the FMO accuracy and timings are reasonable for practical applications to study charge transport in CTMs.

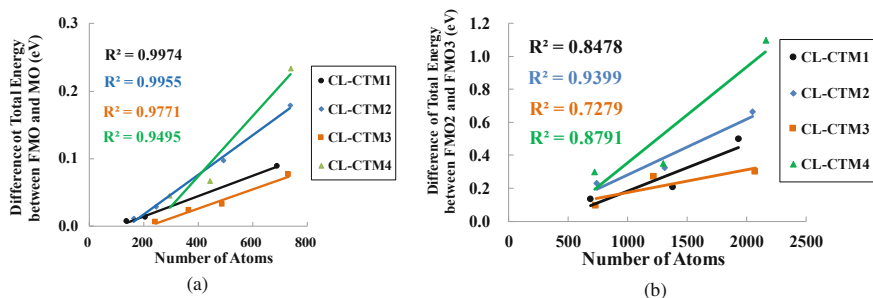


Fig. 8 Dependence of the FMO2 accuracy on the number of atoms for cross-linked CTMs: **a** the small systems; **b** the large systems

2.4 Summary of the FMO Feasibility Study

The validation studies confirmed the feasibility of FMO to study charge transport materials. An optimum fragmentation is determined for dispersive and cross-linked charge transport materials: one molecule per fragment for the former, and for the latter, two types of fragments are defined: charge transport moiety and cross-linked moieties. In this way, one can focus on charge hopping between charge transport fragments, which matches the needs of material design. In addition, one can divide the long polymer cross-linked moiety into several fragments depending on the degree of polymerization (as found above, at least two units should be used as one fragment). As a result of the examination of the computational speed and accuracy, it can be concluded that FMO is adequate for charge transport materials, not only increasing the speed of calculations versus full MO, but also providing natural blocks for the studies of charge transport.

3 Calculation of Charge Mobility

In this part, the charge mobility in CTM is analyzed using FMO, the Marcus theory, and the transport model. The charge hopping rate, a microscopic charge transport property, is evaluated based on the Marcus theory, using the electronic structure calculated with FMO. Using the charge hopping rate, one can evaluate the charge mobility, a macroscopic charge transport property, based on two transport models. Many results summarized in this section have been previously published in [10].

3.1 Charge Mobility Based on the Marcus Theory

3.1.1 Calculation of the Charge Transport Rate Constant

Charge transport phenomena in amorphous organic charge transport materials are often interpreted using the hopping mechanism. The charge mobility is evaluated by first obtaining the charge transfer rate constant, which describes the hopping rate as shown in Fig. 9a, and then the charge hopping in the molecular cluster is simulated with a transport theory as shown in Fig. 9b. The charge transfer rate constant, obtained from quantum-chemical calculations, is related to the charge mobility, whose value can be measured experimentally.

According to the Marcus theory [11], the charge transport (CT) rate constant k_{CT} is expressed as

$$k_{CT} = \frac{W^2}{\hbar} \sqrt{\frac{\pi}{\lambda k_B T}} e^{-\frac{(-\Delta G + \lambda)^2}{4\lambda k_B T}} \quad (1)$$

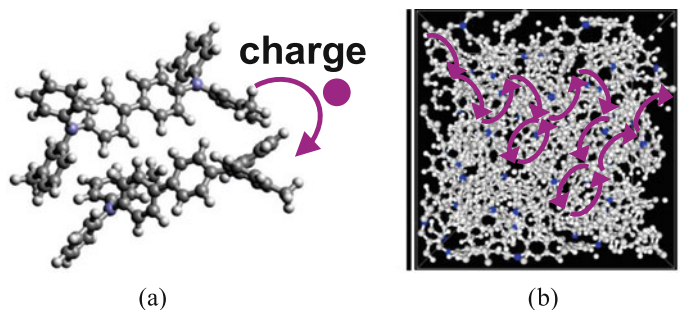


Fig. 9 **a** Intermolecular charge hopping and **b** charge migration through the molecular cluster

where \hbar is the reduced Planck's constant (Planck's constant divided by 2π), k_B is the Boltzmann's constant, T is the temperature, λ is the reorganization energy, W is the charge coupling element, and ΔG is the change in the Gibbs' free energy due to the charge hopping. Among these physical quantities, the reorganization energy and the charge coupling element are related to the electronic structure, and quantum-chemical computations can be used to evaluate them.

3.1.2 Calculation of the Reorganization Energy

Due to the charge migration as the charge hopping proceeds, a molecule changes its charge state. For example, the charge can change from 0 to +1, and vice versa, during the hole transport process. Upon ionization, the molecule undergoes a structural relaxation leading to an energy minimum of the cation, and the energy change from one charge state to another is denoted as λ_1 in Fig. 10. Similarly, the cation undergoes a structural relaxation to the energy minimum of the neutral state, with the energy change λ_2 . These changes in the energy are important because they take place frequently in charge hopping. According to the Nelsen's four point method [29], the reorganization energy λ is expressed as

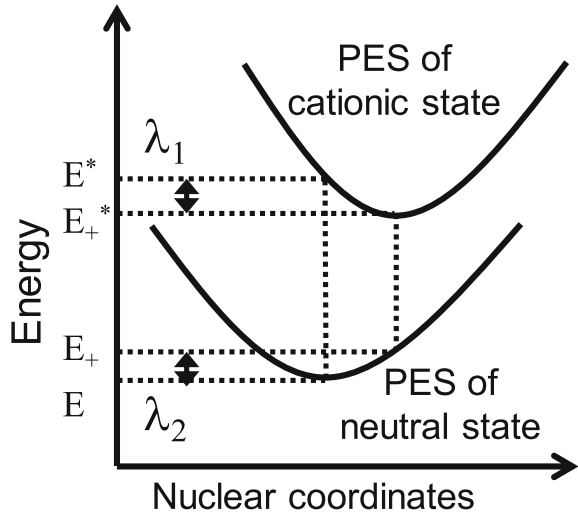
$$\lambda = \lambda_1 + \lambda_2 = (E^* - E_+^*) - (E_+ - E) \quad (2)$$

where E and E^* are the energies of the neutral and cationic states at the geometry of the neutral minimum, respectively, whereas E_+ and E_+^* are the energies of the neutral and cationic states at the cationic minimum. In this work, λ was evaluated for standalone molecules.

3.1.3 Calculation of Electron Coupling Elements

The charge coupling element W depends on the electronic structure of two neighboring molecules between which the charge hopping occurs, and it can be calculated

Fig. 10 Schematic diagram of the states used to calculate the reorganization energy based on Nelson's four point method for potential energy surfaces (PES) of the neutral and cationic states (see main text for the description of symbols)



with the fragment approach [30] as follows:

$$W = \frac{V - \frac{1}{2}S(\varepsilon_1 + \varepsilon_2)}{1 - S^2} \quad (3)$$

$$V = \langle \varphi_1 | h_{ks} | \varphi_2 \rangle \quad (4)$$

$$S = \langle \varphi_1 | \varphi_2 \rangle \quad (5)$$

$$\varepsilon_i = \langle \varphi_i | h_{ks} | \varphi_i \rangle, i = 1, 2 \quad (6)$$

where h_{ks} is the Kohn–Sham Hamiltonian, φ_i and ε_i are the molecular orbital and the site energy of molecule i , respectively; V is the charge transfer integral; and S is the overlap integral between two molecular orbitals. h_{ks} is defined for the dimer (the two neighboring molecules), whereas φ_i is separately calculated for each molecule (called a fragment). φ_i is taken to be the highest occupied MO (HOMO) of each fragment when computing the carrier mobility.

3.1.4 Simulation of Transport Phenomena Using Kinetic Monte Carlo Simulations

If every charge hopping between molecules occurs independently, then the charge transfer rate constant k_{CT} can be taken to be the probability of hopping from site i to one of the neighboring molecules, site j , and the probability is expressed as follows:

$$P_{ij} = \frac{k_{CT}^{ij}}{\sum_{l \neq m} k_{CT}^{lm}} \quad (7)$$

The normalizing summation is taken for all the neighboring sites (in FMO, a site is one fragment). This probability can be used either in the diffusion model or the kinetic Monte Carlo method (KMC) to simulate transport phenomena involving charge mobility. These two models are compared below.

The diffusion model is based on Einstein's relation for charged particles, or molecular sites in this study,

$$\mu = \frac{e}{k_B T} D \quad (8)$$

where e is the charge and D is the diffusion coefficient for charged particles. For an isotropic molecular cluster, the diffusion coefficient D is given by

$$D = \frac{1}{6} \sum_{ij} r_{ij}^2 k_{CT}^{ij} P_{ij} \quad (9)$$

where r_{ij} is distance between the centers of mass of molecules i and j .

On the other hand, an application of KMC to simulate charge transport phenomena is equivalent to simulating time-of-flight (TOF). In the TOF simulation, a specimen is placed between electrodes with an electric potential of E separated by distance d , and the time τ is calculated as a total amount of time that the charge spends to migrate from anode to cathode. Since hopping probability is different for each molecular pair, it is suitable to apply KMC method to determine the most probable migration path. Then the charge mobility μ is evaluated as

$$\mu = \frac{d}{\tau E} \quad (10)$$

The above formulation is simulated in the following way. A specimen with a linear size of d is simulated in MD as shown in Fig. 11, and the hopping rate for each pair of molecules is calculated using FMO based on the Marcus theory. When each hopping rate is determined, the hopping probability is determined following Eq. 7, and then the optimum charge migration path can be found. Figure 12 shows how the destination of a charge hopping is selected based on the hopping probability. In Fig. 12a, there are four neighboring molecular sites around site i , where the charge is currently situated. This charge hops to one of these four sites as driven by the hopping probability. In order to determine to which site the hopping occurs, the accumulative probability density function is evaluated as shown in Fig. 12b, and generate a uniform random number ρ over the interval $[0, 1]$. If ρ satisfies the following relation:

Fig. 11 Schematic diagram of charge migration corresponding to TOF measurement

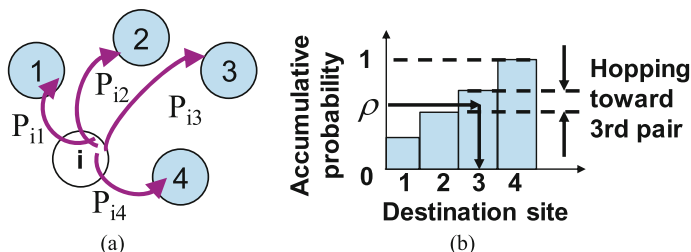
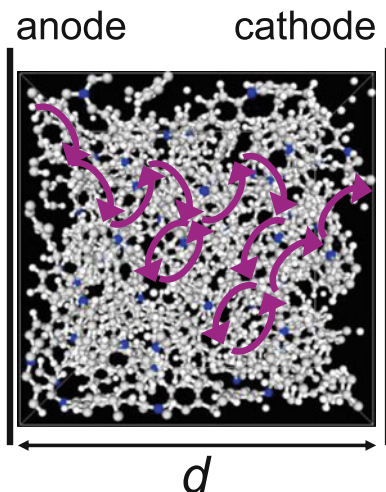


Fig. 12 Schematic of kinetic Monte Carlo simulation: **a** four candidates j as a hopping destination from site i , and each pair has a hopping probability P_{ij} . **b** determination of the destination site using a uniform random number ρ and the cumulative probability distribution

$$\sum_{j=1}^J P_{ij} \leq \rho < \sum_{j=1}^{J+1} P_{ij} \quad (11)$$

then the charge hops to site J . For instance, if a random number ρ happens to be as shown in Fig. 12b, then the destination of the hopping is selected as the site 3. This procedure that uses a random number and the accumulative probability density function is applied every time the destination of a charge hopping is determined. In other words, the accumulative probability density function is different for every charge hopping site i , and a new ρ is generated every single time Eq. 11 is applied.

In addition, the electric field effect during charge migration is accounted for by adding the following contribution to the Gibbs' free energy in Eq. 1:

$$\Delta G_{ij} = eE\Delta x_{ij} \quad (12)$$

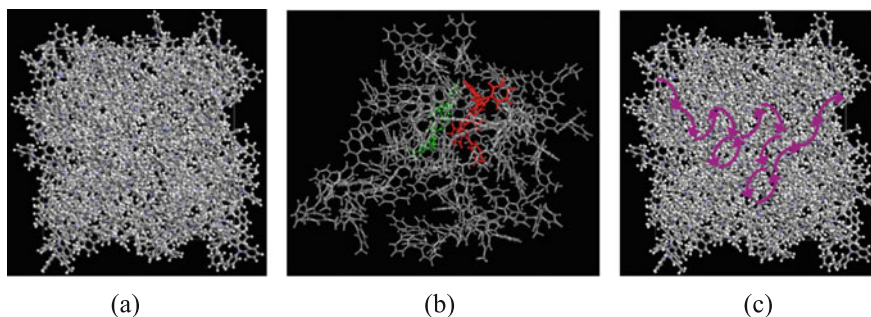


Fig. 13 Three-step approach in the multiscale charge mobility simulation of dispersive CTM, such as TPD: **a** molecular cluster calculated with molecular dynamics; **b** hopping rate k_{CT} computed for each pair of molecules with FMO; **c** hopping path analysis as a sequence of carrier hoppings in the molecular cluster

where E is the static electric field and Δx_{ij} is the difference in the chosen coordinate (the field direction) between the centers of mass of hopping molecular sites i and j .

3.2 Simulation of the Charge Transport Rate Constant and Charge Mobility

Two different scales are considered for the evaluation of the charge mobility: a molecular pair scale to obtain the hopping rate and a molecular cluster scale to analyze transport phenomena. Three steps of this analysis are shown in Fig. 13. At first, the amorphous molecular cluster is simulated with MD and MM, as shown in Fig. 13a. An NPT MD simulation is performed at 1 atm and 300 K. Next, the electronic structure of molecular pairs is calculated to obtain the charge transfer rate constant k_{CT} using FMO-B3LYP/6-31G* with the Grimme's empirical dispersion correction [31], taking one molecules as a fragment. The Kohn–Sham Hamiltonian h_{ks} and molecular orbitals φ in Eq. 3 are obtained from FMO dimers and monomers, respectively. The charge migration path is obtained with KMC to evaluate the charge mobility μ . The distance between electrodes, which is equivalent to the linear size of the molecular cluster, is between 2 and 4 nm, depending on the result of MD for each molecular species. The applied electric field strength is 30 V/ μ m.

3.3 Results Obtained with the Diffusion Model

First, the charge mobility is obtained using the diffusion model for transport phenomena whereas the charge transfer rate constant k_{CT} is calculated using MO or FMO (in the context of the charge rate constant, “MO” refers to calculations of a

dimer neglecting the rest of the system; “FMO” refers to the dimer in FMO where the electrostatic potential from the environment is added). In the TPD case, the charge mobility obtained from the rate constant k_{CT} calculated with both MO and FMO is rather similar, as shown in Fig. 14. This implies that the polarization effects for this system are not substantial. This is because hole transport molecules are less affected by the environment than electron transport molecules.

The simulated mobility is larger by 1–2 orders than experimental values. This can be rationalized by the spatial randomness of amorphous materials, in which there are various molecular pairs that are close or distant, having a large or small rate constant k_{CT} . According to Eq. 9, the charge mobility is proportional to the diffusion constant D , which is approximately equal to the sum of all rate constants k_{CT} . Because of this summation, the constant D , and thus the mobility μ , is mainly determined by the molecular pairs that have large rate constants k_{CT} even if the fraction of such pairs is small. The simulation indicates that a range of the rate constants k_{CT} of TPD is distributed from $10^3/s$ to $10^{13}/s$ as shown in Fig. 15. There are very few molecular pairs with k_{CT} on the order of 10^{13} , and these pairs result in a large diffusion constant D , and thus a large mobility μ , as discussed above.

Fig. 14 Calculated charge mobility from the diffusion model combined with MO and FMO

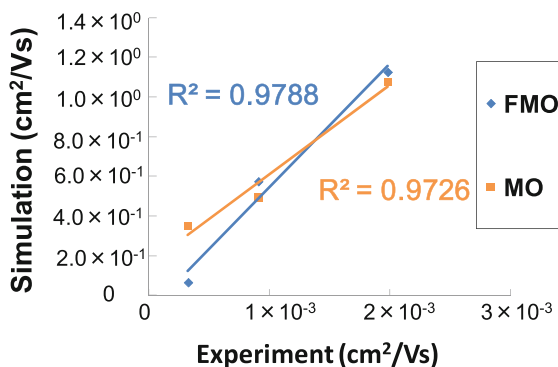
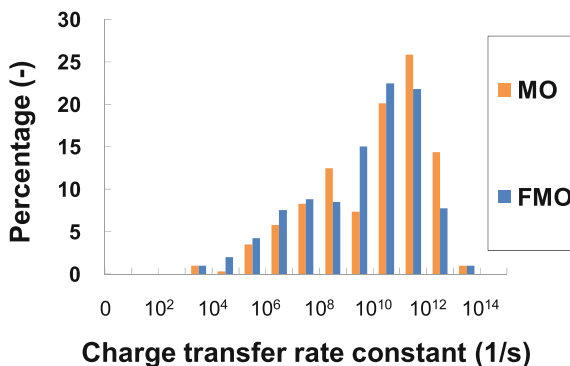


Fig. 15 Distribution of charge transfer rate constants k_{CT} obtained with MO and FMO



3.4 Results Obtained with the KMC Model

The charge mobility can also be simulated with KMC. Because there was not much of a difference in charge transfer rate constants k_{CT} obtained by FMO or MO in the molecular cluster composed of hole transport materials, the rate constant for KMC is obtained only with FMO. The simulated charge mobility with the diffusion model and KMC is compared with experimental results in Fig. 16. Although both models qualitatively reproduce the experimental trend, the mobility obtained with KMC is closer to experiment. It is rationalized that allowing charges to take a random migration path in KMC overcomes the possible cause of overestimation of the charge mobility in the diffusion model. Because detailed hopping information is obtained in KMC, the behavior of the hopping can be discussed following the previous study [32].

The charge hopping for every neighboring molecular pair is classified as forward or backward, along the chosen direction given by the electric field direction. The number of such hoppings is shown in Fig. 17. Although there are some pairs that have more frequent charge hopping, some of them do not have a large net number

Fig. 16 Simulated and measured charge mobility of triphenylamine. Reprinted with permission from ISJ [10]

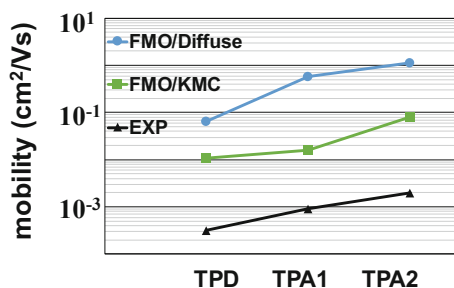


Fig. 17 Gross counts of charge hopping for each fragment pair (hoppings along the field are shown as positive, and negative otherwise) using the scale on the left. The sum of charge hoppings in both directions (the net number of hoppings) is plotted using the scale on the right. Reprinted with permission from ISJ [10]

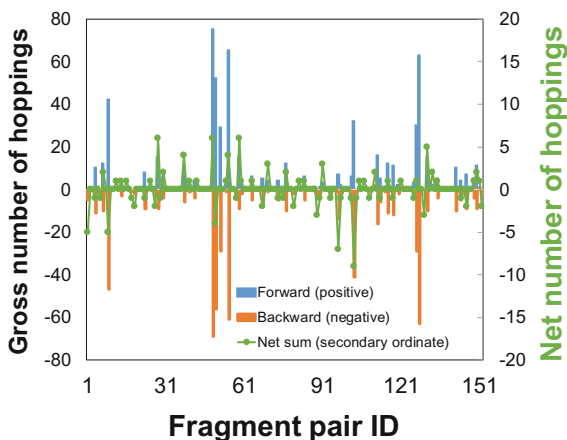
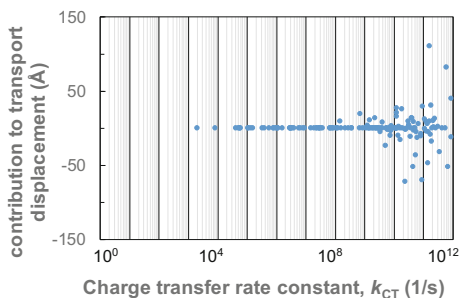


Fig. 18 Relationship between the hopping rate k_{CT} of each fragment pair and its contribution to the charge mobility, expressed in terms of the cumulative transport displacement on the y-axis. Reprinted with permission from ISJ [10]



of hopping because hoppings forward and backward cancel out. This likely happens for molecular pairs ij that have large k_{CTij} and k_{CTji} and small rates between i or j and other sites. In other words, charge hopping takes place back and forth within the pair ij with a large k_{CT} . It is important to note that despite of the back and forth hoppings, the charge tends to move forward because k_{CT} of backward and forward hopping is slightly different due to the applied electric field that affects change in the Gibbs' free energy as described in Eq. 12.

Clearly, a molecular pair with a small net number hopping contributes little to the charge mobility even if the pair has a large gross number of hoppings. The contribution to the charge mobility is determined by the net number of hoppings and the hopping distance along the applied field direction. In contrast, there are some pairs that make a large contribution despite their small gross number of hoppings. Thus, contribution to the charge mobility can be expressed as the product of net number of hoppings and the intermolecular distance Δx_{ij} in Eq. 12, as shown in Fig. 18.

Figure 18 implies a different view of the charge migration in the diffusion model and KMC. Because the charge mobility is approximately proportional to the square of k_{CT} in the diffusion model, the points on the plot should be found in the upper right corner and not around the transport displacement of 0 Å. In contrast, in KMC, pairs with large k_{CT} do not necessarily make a large contribution to the charge mobility. This difference suggests that a consideration of the charge migration path is important to analyze the dependence of the charge mobility on the molecular structure in amorphous organic charge transport materials, because the calculated mobility in KMC is closer to experiment than in the diffusion model.

4 Conclusion

The charge mobility of organic charge transport material has been evaluated by first obtaining charge transfer rate constant k_{CT} , which is an index of the charge transport for a molecular pair, based on the Marcus theory. Then, the charge mobility μ , a macroscopic quantity of the charge transport, has been evaluated by considering the

charge transport as a series of charge hoppings between the pairs in a molecular cluster. The charge mobility μ has been simulated with the diffusion model or KMC. FMO has also been used in similar simulations by others [33, 34].

The results showed that the values of μ simulated with KMC are larger by about one order of magnitude than experimental values, whereas for the diffusion model the values are larger by about two order of magnitude. In addition, it has been found that large k_{CT} does not necessarily contribute much to the charge mobility in the molecular cluster because of the cancellation of the migration along the field; thus, it is necessary to properly sum contributions of molecular pairs along a path for an accurate evaluation of charge transport in amorphous organic charge transport materials.

Acknowledgements We thank the members of the computer chemistry working group (CCWG) at the Japan association of chemical innovation (JACI) for many fruitful discussions. Special thanks are due to Mr. Kento Mori of MOLSIS Inc. and Professor Hironori Kaji of Institute for Chemical Research, Kyoto University for their valuable suggestions and lectures held at CCWG. We are also thankful to discussions with colleagues in Fuji Xerox Co., Ltd. who accumulated a vast amount of knowledge about charge transport materials over many years.

References

1. Szabo A, Ostlund NS (1996) Modern quantum chemistry: introduction to advanced electronic structure theory. Dover Publications
2. Kussmann J, Beer M, Ochsenfeld C (2013) Linear-scaling self-consistent field methods for large molecules. WIREs: Comput Mol Sci 3:614–636. <https://doi.org/10.1002/wcms.1138>
3. Akimov AV, Prezhdo OV (2015) Large-scale computations in chemistry: a bird's eye view of a vibrant field. Chem Rev 115:5797–5890. <https://doi.org/10.1021/cr500524c>
4. Gordon MS, Pruitt SR, Fedorov DG, Slipchenko LV (2012) Fragmentation methods: a route to accurate calculations on large systems. Chem Rev 112:632–672. <https://doi.org/10.1021/cr200093j>
5. Kitaura K, Ikeo E, Asada T, Nakano T, Uebayasi M (1999) Fragment molecular orbital method: an approximate computational method for large molecules. Chem Phys Lett 313:701–706. [https://doi.org/10.1016/S0009-2614\(99\)00874-X](https://doi.org/10.1016/S0009-2614(99)00874-X)
6. Fedorov DG, Kitaura K (2007) Extending the power of quantum chemistry to large systems with the fragment molecular orbital method. J Phys Chem A 111:6904–6914. <https://doi.org/10.1021/jp0716740>
7. Fedorov DG, Nagata T, Kitaura K (2012) Exploring chemistry with the fragment molecular orbital method. Phys Chem Chem Phys 14:7562–7577. <https://doi.org/10.1039/C2CP23784A>
8. Tanaka S, Mochizuki Y, Komeiji Y, Okiyama Y, Fukuzawa K (2014) Electron-correlated fragment-molecular-orbital calculations for biomolecular and nano systems. Phys Chem Chem Phys 16:10310–10344. <https://doi.org/10.1039/C4CP00316K>
9. Fedorov DG (2017) The fragment molecular orbital method: theoretical development, implementation in GAMESS, and applications. WIREs Comput Mol Sci 7:e1322. <https://doi.org/10.1002/wcms.1322>
10. Fujino I, Fedorov DG, Kitaura K, Hirose H, Inami K (2017) The analysis of carrier mobility in organic charge transport materials by fragment molecular orbital method. J Img Soc Jpn 56(5):48–54. <https://doi.org/10.11370/isj.56.502>

11. Marcus R, Sutin N (1985) Electron transfers in chemistry and biology. *Biochem Biophys Acta* 811:265–322. [https://doi.org/10.1016/0304-4173\(85\)90014-X](https://doi.org/10.1016/0304-4173(85)90014-X)
12. Bäessler H (1993) Charge transport in disordered organic photoconductors a Monte Carlo simulation study. *Phys Stat Sol (B)* 175:15. <https://doi.org/10.1002/pssb.2221750102>
13. Coropceanu V, Cornil J, Filho D, Olivier Y, Silbey R, Brédas J (2007) Charge transport in organic semiconductors. *Chem Rev* 107(4):926–952. [10.1021/cr050140x](https://doi.org/10.1021/cr050140x)
14. Yamada T (2011) Molecular and electronic structures and charge-transport properties of triphenylamine-related materials for organic light-emitting diodes (OLEDs). Dissertation, Kyoto University. <https://doi.org/10.14989/doctor.k16320>
15. Morishita H (2016) Binder resin for high durable organic photoconductors. *J Img Soc Jpn* 55(2):195–200. <https://doi.org/10.11370/isj.55.195>
16. Bartlett RJ (1981) Many-body perturbation theory and coupled cluster theory for electron correlation in molecules. *Ann Rev Phys Chem* 32:359–401. <https://doi.org/10.1146/annurev.pc.32.100181.002043>
17. Fedorov DG, Asada N, Nakanishi I, Kitaura K (2014) The use of many-body expansions and geometry optimizations in fragment-based methods. *Acc Chem Res* 47:2846–2856. <https://doi.org/10.1021/ar500224r>
18. Fedorov DG, Kitaura K (Eds) (2009) The fragment molecular orbital method: practical applications to large molecular systems. CRC Press, pp 16–18
19. Nakano T, Kaminuma T, Sato T, Fukuzawa K, Akiyama Y, Uebayasi M, Kitaura K (2002) Fragment molecular orbital method: use of approximate electrostatic potential. *Chem Phys Lett* 351:475–480. [https://doi.org/10.1016/S0009-2614\(01\)01416-6](https://doi.org/10.1016/S0009-2614(01)01416-6)
20. Fujino I, Fedorov DG, Kitaura K, Hirose H, Nakayama N (2015) Fragment molecular orbital simulation of organic charge transport materials: a feasibility study. *J Img Soc Jpn* 54(6):554–560. <https://doi.org/10.11370/isj.54.554>
21. Fedorov DG, Jensen JH, DeKa RC, Kitaura K (2008) Covalent bond fragmentation suitable to describe solids in the fragment molecular orbital method. *J Phys Chem A* 112:11808–11816. <https://doi.org/10.1021/jp805435n>
22. <https://www.j-octa.com>. Accessed 18 Sep 2015
23. <https://octa.jp>. Accessed 18 Sep 2015
24. Fedorov DG, Kitaura K (2004) The importance of three-body terms in the fragment molecular orbital method. *J Chem Phys* 120:6832–6840. <https://doi.org/10.1063/1.1687334>
25. Schmidt MW, Baldrige KK, Boatz JA, Elbert ST, Gordon MS, Jensen JH, Koseki S, Matsunaga N, Nguyen KA, Su S, Windus TL, Dupuis M, Montgomery JA (1993) General atomic and molecular electronic structure system. *J Comput Chem* 14:1347–1363. <https://doi.org/10.1002/jcc.540141112>
26. Suenaga M (2005) Facio: new computational chemistry environment for PC GAMESS. *J Comput Chem Jpn* 4(1):25–32 [in Japanese]. <https://doi.org/10.2477/jccj.4.25>
27. Suenaga M (2008) Development of GUI for GAMESS/FMO calculation. *J Comput Chem Jpn* 7(1):33–53 [in Japanese]. <https://doi.org/10.2477/jccj.H1920>
28. <https://www.j-focus.or.jp>. Accessed 18 Sep 2015
29. Rossi M, Sohlberg K (2009) Predictions of hole mobility in molecular organic crystals: incorporating thermal effects. *J Phys Chem C* 113(16):6821–6831. <https://doi.org/10.1021/jp8086978>
30. Lee C, Waterland R, Sohlberg K (2011) Prediction of charge mobility in amorphous organic materials through the application of hopping theory. *J Chem Theory Comput* 7(8):2556–2567. <https://doi.org/10.1021/ct2003463>
31. Grimme S, Antony J, Ehrlich S, Krieg H (2010) A consistent and accurate ab initio parametrization of density functional dispersion correction (DFT-D) for the 94 elements H–Pu. *J Chem Phys* 132:154104. <https://doi.org/10.1063/1.3382344>
32. Suzuki F, Shizu K, Kawaguchi H, Furukawa S, Sato T, Tanaka K, Kaji H (2015) Multiscale simulation of charge transport in a host material, N, N'-dicarbazole-3,5-benzene (mCP), for organic light-emitting diodes. *J Mat Chem C* 3:5549–5555. <https://doi.org/10.1039/C5TC000543D>

33. Nishioka H, Ando K (2011) Electronic coupling calculation and pathway analysis of electron transfer reaction using *ab initio* fragment-based method. I. FMO-LCMO approach. J Chem Phys 134:204109. <https://doi.org/10.1063/1.3594100>
34. Kitoh-Nishioka H, Welke K, Nishimoto Y, Fedorov DG, Irle S (2017) Multiscale simulations on charge transport in covalent organic frameworks including dynamics of transfer integrals from the FMO-DFTB/LCMO approach. J Phys Chem C 121(33):17712–17726. <https://doi.org/10.1021/acs.jpcc.7b05779>

Group Molecular Orbital Method and Python-Based Programming Approach



Tomomi Shimazaki

Abstract In this chapter, an algorithm to solve the Huzinaga subsystem self-consistent field equations is described, together with two approximations: a local expansion of subsystem molecular orbitals and a truncation of the projection operator. We have referred to the algorithm as the group molecular orbital (GMO) method, and its theoretical concept is based on fragmenting and dividing molecular orbitals, similar to the fragment molecular orbital (FMO) method. However, the GMO method can define a Hamiltonian for each molecular group (fragment), unlike FMO. In addition, we discuss a Python-based programming approach to efficiently implement the GMO algorithm. Python can provide several advantages in program development, including flexibility and high productivity, easy integration for different algorithms, and abundant tools and libraries. We also present that the Python-based approach does not sacrifice the computational performance of quantum chemistry calculations.

Keywords Group molecular orbital · GMO · Python · Cython · Huzinaga SCF

1 Introduction

In the fragment molecular orbital (FMO) method, a molecular system is divided into several subsystems (fragments), and the interactions between these subsystems are hierarchically considered to reproduce the total energy of the whole molecule [1]. The FMO method is frequently used to investigate biological molecular systems such as proteins and enzymatic reactions. We recently proposed the group molecular orbital (GMO) method by which the Huzinaga subsystem self-consistent field (SCF)

T. Shimazaki (✉)

Graduate School of Nanobioscience, Yokohama City University, Seto 22-2,
Kanazawa-ku, Yokohama, Kanagawa 236-0027, Japan

Kobe University, Graduate School of System Informatics, Rokkodai-cho
1-1, Nada-ku, Kobe, Hyogo 657-8501, Japan

RIKEN, Advanced Institute for Computational Science, Minatojima-minami-machi
7-1-26, Chuo-ku, Kobe, Hyogo 650-0047, Japan
e-mail: tshima@yokohama-cu.ac.jp

© Springer Nature Singapore Pte Ltd. 2021

Y. Mochizuki et al. (eds.), *Recent Advances of the Fragment Molecular Orbital Method*,
https://doi.org/10.1007/978-981-15-9235-5_29

equations are solved by spatially dividing a molecule [2, 3]. This GMO method can be categorized as a subsystem approach [4–15], and its basic concept is similar to that of FMO. In GMO, we use two approximations: a local expansion of subsystem molecular orbitals and a truncation of the projection operator [3]. These approximations are introduced to handle large molecular systems at reasonable computational costs. Also, the GMO method can naturally define the subsystem Hamiltonian for each group (fragment) whereas FMO cannot. Although GMO can seamlessly consider N-body interactions among several monomers (groups), FMO may not be good at handling complex interactions, as seen in molecular crystals. Nevertheless, there are a number of similarities between the FMO and GMO methods, and therefore we can integrate them into a single calculation framework. Such an FMO/GMO method would be useful to compensate each of their disadvantages.

To develop first-principles quantum chemistry methodologies such as FMO and GMO, compiled languages such as C/C++ and Fortran are usually used. The computational cost of first-principles methods is extremely high, and therefore compiled languages are adopted for calculation performances. Here, we examine the use of Python dynamic programming language that is widely used in web and desktop applications to implement the GMO method [3, 16, 17]. Python supports several programming styles, including procedural, functional, and object-oriented ones. The allocated memories in Python are automatically managed by the garbage collector based on the reference count scheme. Also, in Python, one can easily use abundant libraries and utilities so that, with these characteristics, skilled programmers can develop their applications more efficiently than when using only compiled languages. However, Python is an interpreted language, and programs written in Python usually run much slower than those developed in compiled languages. Therefore, Python does not seem to be suitable for developing quantum chemistry programs. To overcome this weakness and take advantage of Python in the quantum chemistry field, we used a binding approach, which creates a bridge to connect Python and the compiled languages. We used compiled languages to create hot spots in the program and used Python for the other parts. Thus, different computer languages can be properly used according to their appropriateness.

In the binding approach, Python scripts can directly call functions and subroutines written in compiled languages without using system calls. Thus, we can seamlessly handle both Python and compiled languages in quantum chemistry. The Python ecosystem provides various binding techniques, some of which will be explained later. In addition, we will show that the Python approach does not sacrifice the computational performance of quantum chemistry calculations. We believe that this approach can improve the productivity of programmers. It will be particularly useful for SCF-level theories such as FMO and GMO. In such methods, it is necessary to divide and aggregate molecular orbitals and handle complicated input and output processes, which can be easily written in Python. We give a brief explanation of GMO in Sect. 2, and the Python-based programming approach for quantum chemistry calculations is discussed in Sect. 3. The calculation results and a summary are presented in Sects. 4 and 5, respectively.

2 Group Molecular Orbital Method

In this section, we briefly discuss the GMO method. Huzinaga and Cantu derived the following SCF equations for subsystem I [2, 3]:

$$(\hat{F} + \hat{P}_I) \varphi_i^I = \varepsilon_i^I \varphi_i^I \quad (1)$$

$$\hat{P}_I = - \sum_{J \neq I} \left(\hat{F} \sum_i^{occ} |\varphi_i^J\rangle \langle \varphi_i^J| + \sum_i^{occ} |\varphi_i^J\rangle \langle \varphi_i^J| \hat{F} \right) \quad (2)$$

where \hat{F} and \hat{P}_I are the Fock and projection operators, respectively, and φ_i^I and ε_i^I are the i th molecular orbital and energy for subsystem I . The Huzinaga SCF equation for group I (subsystems are called groups below) is given by

$$\tilde{\mathbf{F}}^I \mathbf{C}^I = \mathbf{S}^I \mathbf{C}^I \varepsilon^I \quad (3)$$

where

$$\tilde{F}_{\mu\nu}^I = F_{\mu\nu}^I + P_{\mu\nu}^I \quad (4)$$

Here, $\tilde{F}_{\mu\nu}^I$ and $P_{\mu\nu}^I$ are the matrix elements of the effective Fock and projection operators of group I , respectively.

$$F_{\mu\nu}^I = H_{\mu\nu}^I + V_{\mu\nu}^{2,I} + V_{\mu\nu}^{\text{emb},I} \quad (5)$$

$$H_{\mu\nu}^I = \langle \mu | -\frac{1}{2} \nabla^2 | \nu \rangle + V_{\mu\nu}^{1,I} \quad (6)$$

$$V_{\mu\nu}^{1,I} = \sum_{A \in I} \langle \mu | \frac{-Z_A}{|\mathbf{r} - \mathbf{R}_A|} | \nu \rangle \quad (7)$$

$$V_{\mu\nu}^{2,I} = \sum_{\lambda, \sigma \in I} D_{\lambda\sigma}^I \left[(\mu\nu | \lambda\sigma) - \frac{1}{2} (\mu\lambda | \nu\sigma) \right] \quad (8)$$

$$D_{\mu\nu}^I = 2 \sum_i^{occ} C_{\mu i}^I C_{\nu i}^I \quad (9)$$

\mathbf{F}^I , \mathbf{H}^I , $\mathbf{V}^{1,I}$, $\mathbf{V}^{2,I}$, and \mathbf{D}^I are the Fock matrix, core Hamiltonian, nuclear attraction, electron–electron potential, and density matrix of group I , respectively. $V^{\text{emb},I}$ is the embedding potential for group I due to the rest of the system,

$$V_{\mu\nu}^{\text{emb},I} = \sum_{J \neq I}^N (V_{\mu\nu}^{1,J} + V_{\mu\nu}^{2,J}) \quad (10)$$

where N is the number of groups. The projection operator is defined as

$$P_{\mu\nu}^I = - \sum_{J \neq I}^{N_{\text{ovl}}^I} \sum_{\mu', \nu' \in J} D_{\mu'\nu'}^J (F_{\mu\mu'}^J S_{\nu'\nu}^J + S_{\mu\mu'}^J F_{\nu'\nu}^J) \quad (11)$$

where \mathbf{S}^J is the overlap integral matrix. N_{ovl}^I is the number of overlapping tail groups (defined below) around group I . The total electronic energy E_I^{ele} of group I is

$$E_I^{\text{ele}} = \frac{1}{2} \text{Tr} \left\{ \mathbf{D}^I \cdot (\tilde{\mathbf{F}}^I + \mathbf{H}^I + \mathbf{P}^I) \right\} \quad (12)$$

and the total energy E of the whole system is

$$E = \sum_I^N E_I^{\text{ele}} + E^{\text{nr}} \quad (13)$$

where E^{nr} is the nuclear repulsion energy. Solving the group SCF equation with the entire basis functions for all groups is equivalent to the Huzinaga method, and it gives the same regular SCF results. However, it is slower than the regular SCF method. To obtain the total energy efficiently and accurately, we introduce two approximations by using the locality of basis functions: the expansion of group MOs over local basis functions and the use of a local projection [3]. These approximations reduce the computational scale, and are suitable to facilitate parallel computations for large systems. The further details of the GMO method can be found in the literature [3]. In the next section, we discuss the Python binding approach to implement the quantum chemistry algorithm.

3 Implementation of the Algorithm Using Python

3.1 Binding Techniques

We can integrate programs written in C/C++ as well as Fortran programs into Python by using binding techniques. The Python ecosystem provides several tools to bind different compiled languages such as ctypes, CFFI, f2py, Cython, Swig, and Boost.Python. In this section, we briefly introduce the Boost.Python and Cython techniques, which are examined in our project [3, 17].

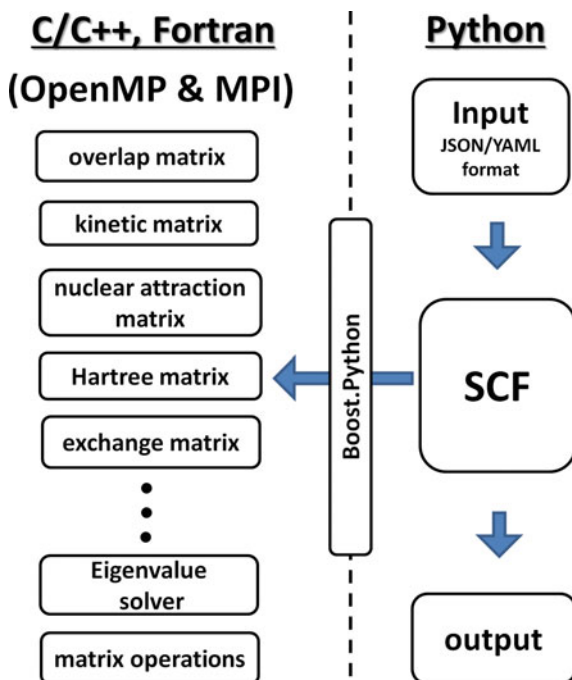
Boost.Python is a wrapper library that encapsulates C++ programs into Python extension modules [18]. To create Python extensions, we need to write configuration files describing the C++ data structures to be exposed to Python. Boost.Python generates source codes (in the style of template programming) to wrap the data structures from these configuration files. Thus, Boost.Python allows us to directly handle C++ programs in Python, but we should note that a shared Boost.Python library is required when an extension module created by Boost.Python is called in the run time.

Cython translates Python scripts into C/C++ codes [19]. A source code translated by Cython can be built using a C/C++ compiler, and we can create a Python extension module. In Python, a standard procedure is provided to call foreign programs, but the method is extremely cumbersome. To overcome this problem, Cython generates C/C++ source codes for interfacing foreign computer programs with Python. Here the C/C++ codes are translated using configuration (interface) files, which must be prepared by the users. This process is similar to that of Boost.Python. Also, Cython can directly create an extension from a Python script, but the execution speed of the extension is quite slow. Thus, Cython offers a procedure to improve the performance. For this purpose, we add C/C++ type information on variables to the Python scripts, and the modules created from such scripts typically show faster performances. In other words, Cython provides a superset programming language of Python, which has type information to create fast extension modules. The computational speed of extensions written in the Cython language is comparable to that of C/C++ native programs. If an extension does not include any Python functions (objects) in the body (content), it can run at almost the same speed as programs written in C/C++. If sufficient type information is given, Cython can translate a Python script into a complete C/C++ program. Thus, Cython can create high-speed extension modules, which means that we can create quantum chemistry extensions enjoying the flexibility and productivity obtained from Python. For example, in the initial development stage, we can use Python to create an extension, and if it becomes clear that a higher calculation speed is required, we just add C/C++ types to the program. In the Cython approach, we can adopt such a flexible program development style.

3.2 Implementation Based on Boost.Python

In our project, we examined different binding techniques to develop quantum chemistry programs. At the initial stage, we used ctypes, f2py, and Boost.Python. Especially Boost.Python was used to handle complex C/C++ data structures, including classes. Figure 1 shows the overall structure of our developed program, where the SCF method is written in Python. The input/output processing is also written in Python using the JSON (JavaScript Object Notation) and YAML (YAML Aint Markup Language) formats. To implement the input parser, we used the JSON and YAML libraries. We can easily develop the input process by utilizing these formats and libraries instead of defining our own ones. Conversely, the functions for obtaining overlap, kinetic, nuclear attraction, Hartree, and exchange matrices are written in

Fig. 1 Program structure of an SCF routine. The calculations of one/two-electron operators are executed in compiled languages such as C/C++ and Fortran, and program controls and input/output processing are written in Python. To bridge the compiled languages with Python, binding techniques such as Boost.Python and Cython are used



C++ because of the heavy numerical calculations involved. Eigenvector calculations and matrix operations such as additions and multiplications are also implemented in Fortran and C++, respectively, and these algorithms are exposed to Python by means of the binding techniques. This program structure provides a number of benefits, for example, if we want to replace several routines for specific purposes, we can easily modify the Python script without compiling and building codes. In particular, the SCF loop is implemented in the style of functional programming languages. Therefore, functions used in the SCF loop can be simply replaced.

When an extension created by Boost.Python is called in the run time, the shared Boost.Python library is required, which means that the extension has machine and system dependencies. The system dependency may cause some problems. Especially in high-performance computing (HPC) environments, we need to pay special attention to the message passing interface (MPI) and OpenMP libraries [17]. The Cython-based approach can relieve this painful situation because extensions created by Cython do not require specific shared libraries in the run time. In the next section, we explain the Cython-based binding technique.

3.3 *Implementation Based on Cython*

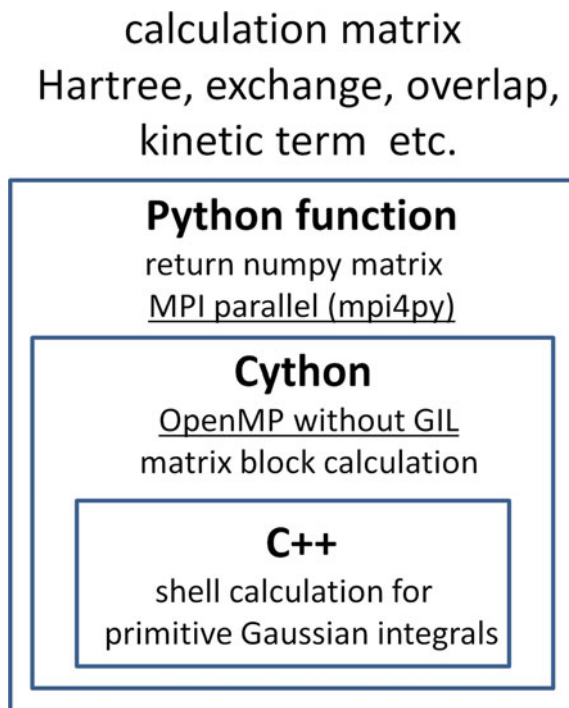
Here, we discuss a quantum-chemistry-program implementation based on the Cython technique. Cython can create interfaces between C/C++ and Python, where functions written in C/C++ can be directly called from a Python script. Therefore, we can adopt the strategy described in the previous section (Fig. 1) in the Cython approach. Conversely, Cython-based extension modules are less machine dependent than those created by Boost.Python.

The Cython language is a Python superset for creating extensions where we can specify a C/C++ type for variables in Python scripts to achieve better performance. Conversely, if a type is not specified, the variable is handled as a Python object in the extension. This also means that the flexibility and high productivity obtained from Python are not impaired, even if Cython is used. If we do not care about the performance (calculation speed) in a part of the extension, we can write that part using Python. Thus, we can seamlessly use the Python and Cython languages, balancing between performance and productivity. Even if there is a requirement for performance later, we just specify types for variables in the Python code. Thus, we can develop extensions for quantum chemistry algorithms in the sophisticated Python grammar.

The current version of our program uses the technique described above. We show the program structure for our quantum chemistry functions in Fig. 2. In our program, both C/C++ and Python/Cython are used to implement one (two)-electron operators such as overlap, kinetic, nuclear attraction, Hartree, exchange, and so on. We used C/C++ for the deepest part, where the shell calculations for primitive Gaussian integrals are executed, and adopted Python/Cython for the other parts including matrix constructions and parallel calculations. In our project, Python is used to achieve parallel computing based on the MPI library, where `mpi4py` is utilized [20]. In the Python ecosystem, several libraries are provided for parallel computing, and even in Cython, we can use these libraries without extra procedures. Thus, we can control parallel computing including distributions and aggregations of data in the Python-based programming style. Finally, Python functions return a numpy (numerical Python) matrix for a one/two-electron operator [21]. The returned matrix can be handled in Python as usual.

Finally, we discuss the OpenMP technique, in which threads and a shared memory are used to achieve parallel computing. Conversely, Python uses the global interpreter lock (GIL), which is a mutex to prevent multiple threads from simultaneously accessing a Python object because the memory management of Python is not thread-safe. If a programmer wants to use OpenMP functions in Python/Cython programs, GIL needs to be explicitly removed. In the absence of GIL, programmers are responsible for exclusive access to shared memory, as in C/C++ and Fortran. We note that Python objects cannot be accessed without GIL. Programming in such a situation may be similar to programming in a compiled language, for example, we need to specify a C/C++ type for all variable needs in the part where GIL is removed. In our project, the shell calculations for primitive Gaussian integrals are written in C++ so that we

Fig. 2 Program structure of a Python function to obtain a numpy matrix for a one/two-electron operator



can easily develop extensions without GIL. Thus, the program structure in Fig. 2 is also suitable when OpenMP is used.

3.4 Python-Based Rapid Development

The Python-based programming approach is useful for SCF-level theories such as FMO and GMO, but we want to emphasize another advantage of Python. When a new theory is developed, numerous trial-and-error procedures are usually required; hence, especially during the early stages of the process, we may frequently need to rewrite and modify the source codes. Through such trials, we can verify or update the new theory. Python is useful for such trial-and-error processes. When we developed the GMO method, we received immense support from the Python-based programming approach. We note that CPU-consuming routines and functions, such as one/two-electron integrals, had already been prepared as extension modules. These routines were developed in our previous projects, and therefore we could easily use them by simply calling the Python scripts. Thus, we could concentrate on the GMO implementation. This also means that as various extensions are prepared, we can more easily develop various quantum chemistry algorithms in Python. The GMO exten-

sion created in this project may be useful to develop other theories such as integration algorithms between FMO and GMO.

4 Calculation Results

4.1 Python-Based Calculations

Here, we discuss the performance of the Python-based quantum chemistry program, especially regarding the SCF algorithm. In this case, we used the Boost.Python binding technique, and this example could be useful for obtaining typical insights into Python-based programming. Figure 3 shows the calculation times for the SCF method both with and without Python. In the case without Python, the quantum chemistry program is implemented only in compiled languages, that is, C/C++ and Fortran, whereas in the case with Python, the binding technique discussed in the previous sections is used. Here, the guanine tetramer depicted in Fig. 3 is calculated at the Hartree–Fock (HF) level using the 6-31G* basis set and a workstation with Xeon E5620 2.4 GHz CPUs. The quantum chemistry programs with/without Python are parallelized by the OpenMP technique and executed in the computational environment of eight CPU cores. The Python-based program requires 1738 s for the total quantum chemistry calculation, whereas in the case without Python, the total calculation time is 1741 s. Thus, we can confirm that we do not lose any computational performance if Python is used.

To analyze these results, we summarize the details of the computational times in Fig. 3. The Fock matrix calculations, which include the electron-repulsive integrals, are the most time-consuming part. The programs with and without Python require 1180 and 1183 s for this part, respectively. The eigenvector calculations and the direct inversion of the iterative subspace (DIIS) method require the second-highest computational times, namely, 453 and 454 s for the cases with and without Python, respectively. The remaining parts of the quantum chemistry calculations are summarized in the other sections, which includes calculations of one-electron operators, input/output processing, and so on. The costs related to using Python are also included in other parts, and we can confirm that they are negligibly small. In the GMO calculations, the Python approach can be used without sacrificing any computational performance. In the next section, we show the results of such GMO calculations.

4.2 GMO Calculations

In this section, we show the calculation results obtained by the GMO method. The size of the groups and the local basis functions influence the accuracy of GMO. To construct the local basis functions of a group, we use the basis functions of atoms in

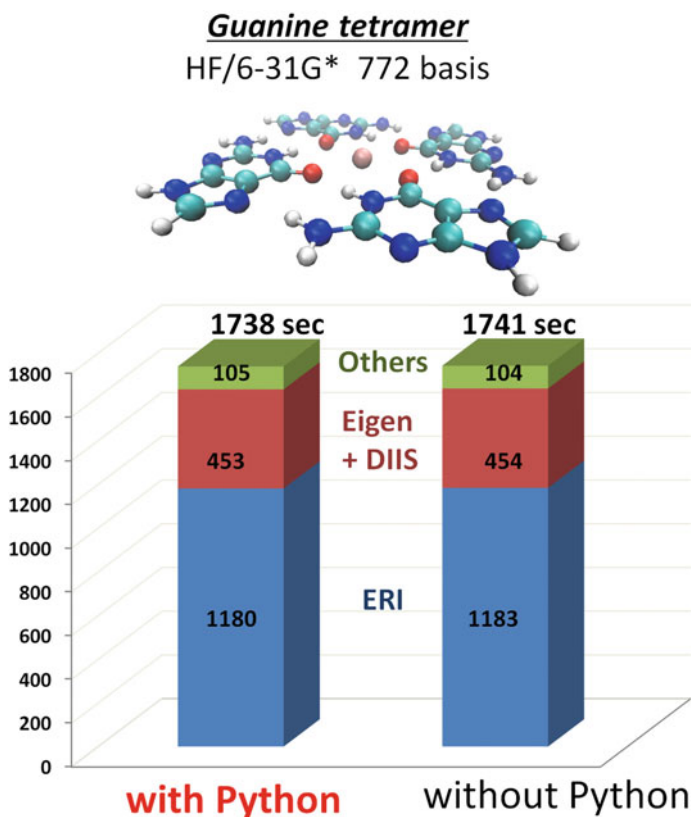


Fig. 3 Calculation time with and without Python. The costs related to using Python, which are negligibly small, are partially included in other parts. The hot spots are written in compiled languages so that quantum chemistry calculations can be efficiently executed. Python can be used to develop quantum chemistry programs without sacrificing computational performance

the group together with the tail groups located within a specified distance from the group (R-TAILS). For water cluster systems, a water molecule is defined as a group. For covalent boundaries, a connected set of nearby atoms is defined as a group.

We examined the energy error dependence on R-TAILS by using the $(\text{H}_2\text{O})_{20}$ cluster model and adopting the STO-3G basis set. When R-TAILSs of 2.8, 3.2, 3.8, and 4.8 are used, the GMO method gives errors of -0.07 , 0.22 , 0.23 , and 0.18 kcal/mol, respectively [3]. Here, the error is defined as the total energy difference between the GMO and ab initio methods. The error becomes negative (overstabilization) for the smallest tail groups and positive (understabilization) for the larger tail groups. Two factors can be considered as error sources: one is the insufficient delocalization stabilization of group electrons, and the other is the underestimated repulsion by other groups through the projection operator. If the local projection approximation is not applied, the GMO errors monotonically decrease. In this situation, the entire

projection matrix is used, and the GMO errors are caused only by truncating the basis set of groups.

For a system with covalent boundaries, we examined the *n*-alkane (C₂₀H₄₂) model with R-TAILS = 2.2. We changed the number of carbon atoms in a group to confirm the accuracy dependence on group size. When 2, 3, 4, and 5 carbon atoms are used, the energy error becomes 11.2, -1.4, -0.43, and -0.18 kcal/mol, respectively [3]. From these calculations, we can confirm that the smallest group exhibits the largest error and the errors become negative for larger groups owing to the underestimated projection repulsion.

5 Summary

We have discussed the GMO method as a suitable approach for calculating large molecular systems. This procedure solves the Huzinaga subsystem SCF equations using approximations. We show that GMO can reproduce ab initio calculation results quite well and has several additional interesting properties, for example, no caps are required in GMO, where fragment boundaries are naturally handled; molecular charges can be delocalized at fragment boundaries because of the use of tail groups; and the embedding potential properly considers exchange interaction, which is sometimes ignored in other embedding methods. In addition, GMO gives fully variational and quasi-orthogonal wave functions among groups (fragments).

We also discussed the Python programming (binding) technique. In several quantum chemistry calculations, there are a few hot spots that heavily consume CPU resources whereas other parts do not need so many resources. Although compiled languages need to be used for hot spots, we can use more productive ways for the other parts. The Python-based approach discussed in this chapter could become a strong candidate to improve the productivity of programmers. Furthermore, for subsystem theories such as FMO and GMO, we can obtain several advantages from Python, for example, GMO demands frequent grouping and joining of molecular orbitals, and such cumbersome processing can more easily be written in Python. In addition, the Python-based approach makes trial-and-error procedures easier when examining new theoretical ideas. Here, we explained the Python-based technique on our quantum chemistry project, but it could be useful for other trials as well.

References

1. Kitaura K, Ikeo E, Asada T, Nakano T, Uebayasi M (1999) Fragment molecular orbital method: an approximate computational method for large molecules. *Chem Phys Lett* 313(3–4):701
2. Huzinaga S, Cantu AA (1971) Theory of separability of many electron systems. *J Chem Phys* 55:5543
3. Shimazaki T, Kitaura K, Fedorov DG, Nakajima T (2017) Group molecular orbital approach to solve the huzinaga subsystem self-consistent-field equations. *J Chem Phys* 146(8):084109

4. Yang W (1991) Direct calculation of electron density in density-functional theory. *Phys Rev Lett* 66:1438
5. Stoll H (1992) Correlation energy of diamond. *Phys Rev B* 46:6700
6. Nagata T, Takahashi O, Saito K, Iwata S (2001) Basis set superposition error free self-consistent field method for molecular interaction in multi-component systems: projection operator formalism. *J Chem Phys* 115(8):3553
7. Exner TE, Mezey PG (2002) Ab initio-quality electrostatic potentials for proteins: an application of the ADMA approach. *J Phys Chem A* 106(48):11791
8. Nakano T, Kaminuma T, Sato T, Fukuzawa K, Akiyama Y, Uebayasi M, Kitaura K (2002) Fragment molecular orbital method: use of approximate electrostatic potential. *Chem Phys Lett* 351(5–6):475–480
9. Khaliullin RZ, Head-Gordon M, Bell AT (2006) An efficient self-consistent field method for large systems of weakly interacting components. *J Chem Phys* 124(20):204105
10. Seijo L, Barandiaran Z, Soler JM (2007) Order-N and embedded-cluster first-principles DFT calculations using siesta/mosaico. *Theor Chim Acta* 118(3):541–547
11. Elliott P, Burke K, Cohen MH, Wasserman A (2010) Partition density-functional theory. *Phys Rev A* 82(2):024501
12. Gordon MS, Fedorov DG, Pruitt SR, Slipchenko LV (2012) Fragmentation methods: a route to accurate calculations on large systems. *Chem Rev* 112(1):632
13. Kobayashi M, Nakai H (2012) How does it become possible to treat delocalized and/or open-shell systems in fragmentation-based linear-scaling electronic structure calculations? The case of the divide-and-conquer method. *Phys Chem Chem Phys* 14(21):7629
14. Sahu N, Gadre SR (2014) Molecular tailoring approach: a route for ab initio treatment of large clusters. *Acc Chem Res* 47(9):2739
15. Watanabe Y, Matsuoka O (2014) Nonorthogonal molecular orbital method: single-determinant theory. *J Chem Phys* 140(20):204111
16. Python. <https://www.python.org>
17. Shimazaki T, Hashimoto M, Maeda T (2015) Developing a high-performance quantum chemistry program with a dynamic scripting language. In: *Proceedings of the 3rd international workshop on software engineering for high performance computing in computational science and engineering*. Association for computing machinery, p 9
18. Boost.Python. <http://www.boost.org>
19. Cython. <http://docs.cython.org>
20. Dalcin LD, Paz RR, Kler PA, Cosimo A (2011) Parallel distributed computing using python. *Adv Water Resour* 34(9):1124–1139
21. Numpy. <http://www.numpy.org>

Multi-Level Parallelization of the Fragment Molecular Orbital Method in GAMESS



Vladimir A. Mironov, Yuri Alexeev, Dmitri G. Fedorov, Hiroaki Umeda,
Spencer Pruitt, Alexander Gaenko, and Mark S. Gordon

Abstract The parallelization of the fragment molecular orbital (FMO) method implemented in GAMESS is reviewed for Cray/Intel, IBM Blue Gene, and Fujitsu supercomputers. Various strategies for load balancing are compared. A basic OpenMP implementation of FMO is described and its parallel efficiency is reported. The two-level generalized distributed data interface is extended to an arbitrary number of levels and applied using three levels to an FMO Hessian calculation at the level of second-order Møller–Plesset (MP2) theory.

Keywords GAMESS · Fragment molecular orbital method · FMO · Parallelization · OpenMP · MPI · DDI · Load balancing

V. A. Mironov

Department of Chemistry, Lomonosov Moscow State University, Leninskie gory 1/3, Moscow 119991, Russia

Y. Alexeev (✉)

Argonne National Laboratory, Computational Science Division, Argonne, IL 60439, USA
e-mail: yuri@anl.gov

D. G. Fedorov

CD-FMat, National Institute of Advanced Industrial Science and Technology, Central 2, Umezono 1-1-1, Tsukuba 305-8568, Japan

H. Umeda

Institute for Molecular Science, National Institute of Natural Sciences, 2F Hulic Kamiyacho Building, 4-3-13 Toranomon, Minato-ku, Tokyo 105-0001, Japan

Center for Computational Sciences, University of Tsukuba, 1-1-1 Tennodai, Tsukuba, Ibaraki 305-8577, Japan

Cray Japan Inc., 15F Hibiya Daibiru, 1-2-2, Uchisaiwai-Cho, Chiyoda-ku, Tokyo 100-0011, Japan

S. Pruitt

Academic & Research Computing, Worcester Polytechnic Institute, Worcester, MA 01609, USA

A. Gaenko · M. S. Gordon

Department of Chemistry and Ames Laboratory, Iowa State University, Ames, IA 50011, USA

A. Gaenko

Advanced Research Computing, University of Michigan, 3550 Rackham, 915 E. Washington St., Ann Arbor, MI 48109-1070, USA

1 Introduction

The parallelization of quantum-mechanical (QM) methods has historically been difficult due to the layered structure of multiple sophisticated algorithms with complicated memory access patterns. To maximize the scalability according to Amdahl's law, each of these algorithms has to be parallelized. However, many QM algorithms are notoriously difficult to parallelize. Therefore, the development of quantum chemistry code for massively parallel computation is a difficult and time-consuming task. An efficient parallelization of the quantum chemistry code is required to utilize modern supercomputers efficiently. As a result of the combination of algorithmic, parallelization, and hardware advances, QM methods can be applied to large molecular systems [1].

The cost of conventional QM calculations scales superlinearly with the size of the molecular systems, although there is ongoing work to develop linear scaling methods. One algorithmic approach to study large chemical systems using QM methods while reducing the overall computational cost is to exploit the locality of QM interactions. This can be accomplished by decomposing a molecular system [2] into fragments. An extra benefit of this approach is that fragment interactions and properties can be used for understanding large and complex molecular systems.

One example of the fragmentation methods is the fragment molecular orbital (FMO) method [3, 4]. In FMO, properties of the full system are obtained by combining the results of individual QM calculations of all fragments. The complete FMO formalism is described elsewhere [4–10]. FMO has been implemented [11, 12] in several computational chemistry packages: GAMESS [13, 14], ABINIT-MP [15, 16], PAICS [17], and OpenFMO [18]. There are OpenMP + MPI parallelizations of FMO in the ABINIT-MP [19] and OpenFMO [18] packages.

GAMESS is a no-cost QM package with many commonly used QM methods implemented. GAMESS is parallelized with the distributed data interface (DDI) [20]. The main idea of DDI is to abstract all communication and parallelization calls to an underlying communication library, making the scientific DDI-parallelized code in GAMESS hardware and software agnostic. As a result, standard DDI routines are called from GAMESS, whereas the low-level implementation details are hidden inside the DDI code. The two primary options for inter-processor communication interfaces in DDI are an MPI library and a native TCP/IP socket library, in addition to the less frequently used LAPI [21] and ARMCI [22] implementations. On most supercomputers, MPI libraries provided by vendors are highly optimized for each specialized high-performance interconnects (e.g., Cray Gemini, Mellanox InfiniBand, or Intel OmniPath). The socket library in GAMESS is often used on small PC clusters. There is also an alternative parallel libcchem library for GAMESS developed for both CPUs and GPUs (graphical processing units) [23].

Normally, DDI spawns GAMESS processes in pairs. One process of each pair is a data server that is used for communication and data transfer, while the other process performs QM computations. If DDI is implemented on top of TCP sockets, the data server process uses little CPU time; however, in MPI implementation of

DDI, the data server usually occupies a CPU core, and actively listens for incoming connections (in some MPI libraries it is possible to reduce the performance loss by tuning process-to-core placement options). This scheme allows QM algorithms to asynchronously access data on other nodes, but it leverages an overhead of computing resources due to the duplication of GAMESS processes. On x86_64-based CPU systems (e.g., Intel Xeon or AMD Opteron) with 1–2 dozens of CPU cores, the memory overhead is not large. However, on modern architectures such as Intel Xeon Phi, which have 60+ cores per CPU, this overhead results in a substantial waste of CPU power and memory. To address this problem, a more lightweight approach that does not spawn full GAMESS processes for communication has to be used for intranode parallelization. Using this approach, a process can spawn multiple child threads, and these threads share most of the system resources of their parent process. While there are many application programming interfaces (APIs) available to implement threading in applications, OpenMP is one of the most popular APIs in high-performance computing (HPC). There were several attempts to implement an OpenMP parallelization in GAMESS. The implementations on Cray XT5 [24] and on K [25] supercomputers are not publicly available.

This chapter provides an overview of the previous FMO parallelization in GAMESS, and presents new development toward threading FMO using OpenMP. First, the DDI interface and load balancing strategies are described. A generalization of GDDI into an arbitrary number of parallelization levels is presented. Next, the OpenMP parallelization of FMO on the K computer is briefly described. The OpenMP code in GAMESS previously developed for the first [26, 27] and second [28] generations of Intel Xeon Phi is extended in this work into treating FMO.

2 Generalized Distributed Data Interface

The generalized distributed data interface (GDDI) was developed [29] in an effort to exploit the inherent granularity of parallelization tasks in FMO. The following sections describe the original two-level implementation, and its generalization into an arbitrary number of levels. The approaches used to address load balancing problems for FMO calculations are also introduced.

2.1 *Original Two-Layer Generalized Distributed Data Interface*

The two fundamental problems faced when parallelizing computational algorithms are the cost of communication, and load balancing of work between processes. An increase in the number of parallel processes necessarily increases the time required to exchange data. To maximize the efficiency of computation, load balancing is

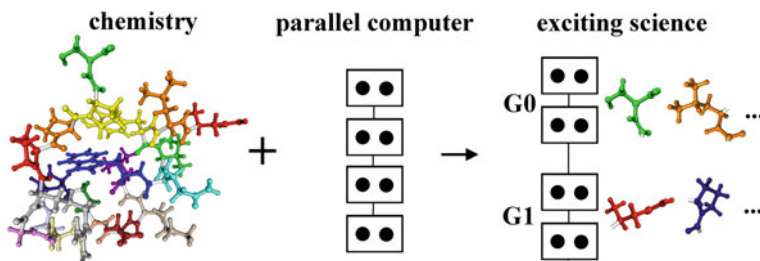


Fig. 1 Parallelization of a Trp-cage protein (1L2Y) calculation using two-layer GDDI/2 on four nodes (boxes) each having two CPU cores (circles), divided into two groups of two nodes. Each group (G_0 and G_1) performs fragment calculations

employed in an attempt to assign the same amount of work to each process. This helps to ensure simultaneous completion of all tasks across parallel processes. Load balancing is essential for many QM methods due to the variability in work assigned to each task. For example, computation of integrals involving s type basis functions takes less time to complete than integrals involving p type basis functions. The number of these smaller tasks is sufficiently large to enable the development of efficient load balancing schemes that can be applied to parallel QM algorithms.

In the FMO method, one can take advantage of the inherent task granularity created by the fragmentation scheme. For example, a protein calculation can be divided into a set of subtasks (individual amino acid fragment calculations). These fragment subtasks can then be assigned to groups of CPU cores, with each fragment calculation being run in parallel using existing QM algorithms. This group-based methodology implemented for both socket and MPI versions of DDI [29] provides two levels of parallelization (Fig. 1), minimizing global communication and maximizing load balancing between tasks. In MPI implementation of GDDI, a communicator is created for each FMO group [15].

In addition to FMO, GDDI in GAMESS has been used in several QM methods, including replica exchange molecular dynamics [30, 31] and dynamic nucleation theory [32]. Other potential applications are numerical and semi-numerical Hessians, and numerical gradients.

3 Extension of GDDI into an Arbitrary Number of Layers

Some QM calculation types possess more levels of granularity than 2. Examples of methods that are capable of exploiting an extra level of task parallelism include FMO numerical gradients, and the estimation of FMO energies for a set of molecular geometries. The latter application is useful for building multidimensional potential energy surface maps of chemical systems.

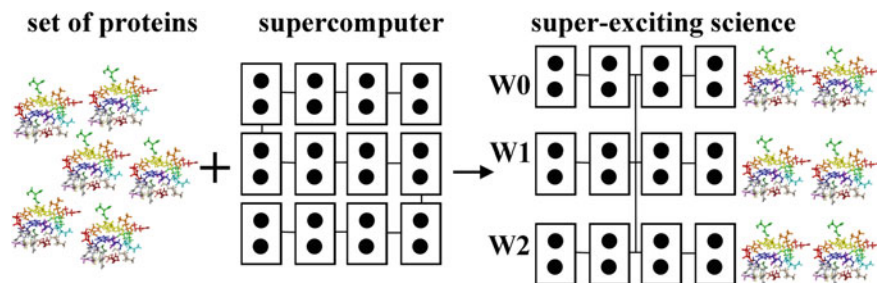


Fig. 2 Parallelization of a numerical FMO Hessian calculation using three-layer GDDI/3 on 12 nodes (boxes) each having two CPU cores (circles), divided into three worlds W_i , each assigned proteins with one coordinate shifted (only six coordinate shifts are shown). Each world is divided into two groups as shown in Fig. 1

The multi-level GDDI in GAMESS was implemented using both TCP/IP sockets, and a standard MPI library. Currently, only the calculation of semi-analytic FMO Hessians (numeric differencing of analytic gradients) was parallelized using three-layer GDDI, useful when fully analytic FMO Hessian calculations are not implemented. The loop over atomic coordinates for the numeric differencing corresponds to the third level of parallelization of single point FMO calculations.

The GDDI parallelism is specified by an integer specifying the number of levels after a slash (e.g., GDDI/2, GDDI/3, etc.). The implementation of GDDI/ n is illustrated for $n = 3$ as follows (Fig. 2). First, all available cores are divided into worlds. Each world is divided into groups, and each group is composed of multiple nodes. Each world is assigned one FMO calculation (for instance, one protein). Then within the world, groups perform individual fragment calculations. Within the group, work is further divided between cores, for instance, two-electron integrals. The concept of *scope*, introduced earlier for GDDI/2 [29], holds increased importance for values of $n > 2$. The scope (that can be internally bound to an MPI communicator) shows where the current parallel operation is applied. In GDDI/2, there are three scopes: group master scope, group scope, and world scope. For example, when all one- and two-electron integrals are computed, the Fock matrix for a fragment is summed in the group scope. After all fragment calculations are performed, the fragment energies of different monomers and dimers calculated in different groups are summed in the world scope. The group master scope is used to exchange information between the groups by limiting the inter-group communications to group masters. In all cases, the scope should be used appropriately, for instance, when an operation in the world scope is performed, all groups must participate in it.

In GDDI/ n ($n > 2$), the same scopes are used; there are, however, two additional operations to move up and down between the levels (these two operations are accomplished using two new scopes, superworld and subgroup, respectively). An illustration of this is shown in Fig. 3 (in some sense, GDDI/ n has a fractal structure with a complexity order of n). One drawback of the current implementations is that

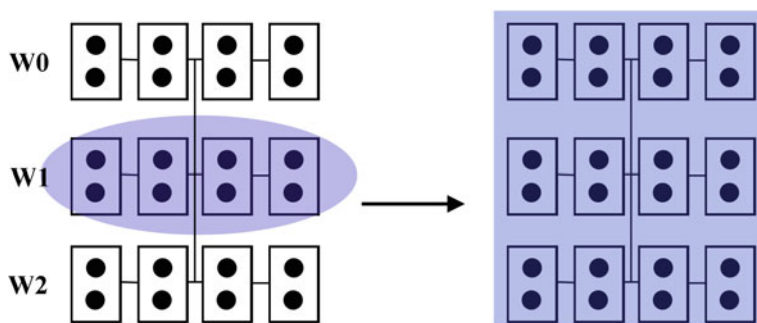


Fig. 3 On the left, a parallel operation in the world scope is conducted in world W_1 (with 8 cores), shown with a shaded ellipse. After a superworld scope change, the next operation in the world scope extends over the whole set of worlds

Table 1 Semi-numerical Hessian calculation of $(\text{H}_2\text{O})_8$ at the level of FMO2-MP2/aug-cc-pVTZ on a PC cluster (3 dual 2.2 GHz Xeon nodes, 72 cores total)

Method	Time (min)	Cores per group	Groups per world	Worlds
GDDI/2	370	8	9	1
GDDI/3	257	2	4	9

dynamic load balancing for $n > 2$ is only allowed within the group; at all other levels, static load balancing must be used.

To measure the efficiency of GDDI/3, a semi-numeric FMO Hessian was calculated for a cubic water cluster $(\text{H}_2\text{O})_8$ at the FMO2-MP2/aug-cc-pVTZ level of theory using the point charge form of the embedding potential [33] (because at present, there is no analytic FMO-MP2 Hessian, one has to use numerical differencing). As a result of this calculation, harmonic vibrational frequencies and IR intensities were obtained. The calculation was performed on a PC cluster consisting of 3 dual 2.2 GHz Intel Xeon-based compute nodes with a total of 72 cores, connected by Gigabit Ethernet. The DDI implementation of MP2 was used [20, 34]. A comparison of GDDI/2 and GDDI/3 is shown in Table 1, where it can be observed that a substantial speedup was obtained even for this small PC cluster.

3.1 Parallel Load Balancing

There are two major approaches to load balancing, static and dynamic; however, in practice, the two approaches can be used in a hybrid way. In static load balancing, most suitable to the case of task granules of the same size or when the number of CPU cores is a multiple of the number of granules, each CPU core is assigned a fixed set of tasks. In dynamic load balancing, tasks are distributed dynamically; when one task is finished, another task is assigned. There are five types of load balancing used

in GAMESS: (a) plain static, (b) 1-dynamic, (c) heuristic static, (d) semidynamic, and (e) n -dynamic ($n > 1$). The latter two types are in fact combinations of static and dynamic load balancing. In n -dynamic load balancing, tasks are assigned as “ n -packs,” whereas within the pack, tasks are done statically (a simple analogy would be: 1-dynamic is to visit a shop for each bottle of beer; 6-dynamic means buying a 6-pack). This n -dynamic scheme was recently implemented in FMO [35]. The n -packs reduce the large cost of processing the global counter (visiting the shop), and are usually efficient when there are many more tasks than cores. The semidynamic load balancing used in FMO [36] was designed to deal with the case when the sizes of the tasks vary significantly. To put in an analogy, if ants have to carry an elephant, and a set of small insects to their heap, naturally, the number of ants needed to carry the elephant is much larger than the number needed to carry a scorpion. If the groups of ants are formed once and not changed during the foraging, there has to be a way to send the big group to the elephant rather than a loose caterpillar. This is accomplished with semidynamic load balancing: one or more large groups of CPU cores are created and assigned to a set of large tasks (in case there is more than one elephant in the forest). These large groups operate on their tasks statically; when done with large tasks, they join other groups doing the rest of the small tasks dynamically (ideally, they should disband forming many smaller groups but that is not yet implemented).

In FMO calculations, elephant tasks occur infrequently: in pharmaceutical applications, many drug molecules are large (around 100 atoms) whereas amino acid residues in proteins have 10–20 atoms; in excited state calculations, only one fragment is computed using very expensive methods for excited states; and transition metals typically necessitate forming large fragments including them. In the heuristic static load balancing [37], groups are customized for each fragment based on a model that predicts the cost ahead of time, then the grouping is optimized using mathematical models. There is also an implementation of FMO in GAMESS linked with a task manager that can handle tasks with different sizes run on heterogeneous groups in GDDI [38]. The number of tasks in FMO varies depending on whether fragments or their pairs are calculated. For better efficiency, the number of groups is specified for these two steps separately.

The parallel efficiency of FMO was evaluated on the Intrepid supercomputer [39], with the IBM Blue Gene/P architecture. The scaling was measured up to 131,072 cores. For $(\text{H}_2\text{O})_{1024}$ and FMO2-MP2/aug-cc-pVDZ, the speedup was $41.1/7.1 = 5.8$ when the number of cores was increased from 16,384 to 131,072 (8 times). The FMO3-MP2/6-31G(d,p) efficiency was also measured for $(\text{H}_2\text{O})_{64}$ on IBM Blue Gene/Q on the Mira supercomputer [40]. When the number of cores increased from 2,048 to 65,536 (32 times), the speedup was $880/55 = 16$. The efficiency is smaller compared to Intrepid because the molecular system is much smaller (although FMO3 has a somewhat better scaling than FMO2 because there are more subtasks).

4 OpenMP Parallelization

A drawback of an MPI parallelization is its excessive memory consumption in a multicore environment. This is because several instances of the same application are executed on each multicore node. Their number is limited only by the hardware design and the software policies; it is usual to run one MPI process per CPU core. The problem is that all of the local data of these processes are replicated. Local data comprises both the dynamic memory, which is allocated at runtime and whose amount can be controlled by the user, and the static memory, which is initialized when the program starts. The memory footprint of the dynamic memory is usually larger than that of static memory. However, the latter is significant for GAMESS.

There are also memory buffers of the MPI runtime library used for sending and receiving messages. The number of these buffers grows rapidly with the number of MPI processes, because the MPI library has to be ready to communicate with any other process in the application at runtime. A typical memory footprint for several hundreds of MPI processes is a few tens of megabytes per process. It is not a problem for small or medium PC clusters, but on a supercomputer consisting of many nodes having more than 60 cores per node, the footprint of the MPI library can grow up to several gigabytes per node.

A well-designed parallel application should keep the amount of replicated data at a minimum and stores most of the data distributed among all processes. Although DDI supports distributing memory among working processes, some sizeable arrays in GAMESS are not distributed. Even though using distributed memory helps to reduce the memory footprint, it does not reduce the overhead of MPI memory buffers. An effective solution to these problems is to distribute useful work between nodes using MPI and use OpenMP inside each node. Recently, a hybrid MPI + OpenMP parallelization of the Hartree–Fock, MAKEFP, and RI-MP2 codes in GAMESS has been developed [27, 28, 41–44].

In a pure OpenMP application, the master process spawns multiple threads on the same node. These threads share most of the data of the master process, except for the data explicitly defined to be private and stack memory. The OpenMP standard does not imply running threads on remote nodes; some OpenMP implementations do, but they have not gained much popularity.

In contrast to OpenMP, MPI allows one to run processes on multiple nodes. The data of any MPI process is explicitly private (i.e., it cannot be directly accessed by any other process) and sophisticated approaches have to be used to create distributed memory space. The hybrid MPI + OpenMP approach combines the advantages of both approaches, where MPI is used for running processes on different nodes and for internode communication. Each MPI process spawns a group of threads using OpenMP. The data sharing inside each group of threads can be implemented easily with OpenMP. Another advantage of this scheme is that OpenMP and MPI can use separate load balancing strategies thereby reducing the amount of expensive global communication and improving the overall performance. In the hybrid MPI + OpenMP code, the load balancing among MPI processes is implemented with

the DDI library, whereas OpenMP dynamic load balancing is used for sharing work among threads.

OpenMP is a directive-based approach, in which specific compiler directives are inserted into the FORTRAN code. It is convenient, because OpenMP programming does not require many error-prone modifications of the scientific code. However, some code needs refactoring due to the language feature restrictions of OpenMP. Special care has to be taken of the FORTRAN common blocks, which are not thread-safe in general, so that all threads can simultaneously read and write the data stored in a common block. All problematic common blocks have to be marked with an OpenMP threadprivate directive.

4.1 Parallelization on the K-Computer

The first ten-petaflop supercomputer in the world, the K-computer, has 82,944 compute nodes with a single socket SPARC64 VIIIfx processor and 16 GB memory, which has eight processor cores or 663,552 cores in total [25]. These nodes are connected with the Tofu interconnect, which has a 6D Mesh/Torus network structure, and the system provides compute nodes as a 3D torus network to the users. DDI was implemented on the K-computer based on the ARMCI library [22], where 1 CPU core per node (out of 8) is used as a data management process, in contrast to 4 cores per node in the typical DDI used for data servers.

OpenMP parallelization [41] was limited to a single point resolution of identity (RI)-based MP2 energy calculation [42, 45] using FMO. Specifically, an OpenMP parallelization was performed for the RI-MP2 driver, subroutines for the Fock matrix calculation, orbital orthonormalization, matrix diagonalization, second-order self-consistent field (SO-SCF), and electrostatic potential (ESP). An ESP implementation was developed taking advantage of vector operations of modern processors [46].

The Fock matrix generation is a hotspot of conventional Hartree–Fock calculations for large molecules. However, in FMO, the molecular system is divided into a number of small fragments, and a different strategy should be employed for an efficient parallelization. A typical fragment Fock matrix is small enough to reside in thread-private memory and an efficient OpenMP version of the Fock matrix construction can be devised.

First, each thread allocates its own copy of the fragment Fock matrix. Instead of using OpenMP directives to declare the Fock matrices and working arrays as private, the dynamic memory allocation was adopted in GAMESS. Next, each thread computes its contribution to the Fock matrix, and all thread-private partial Fock matrices are summed up at the end.

The usual OpenMP DO directives were not used for loop parallelization at the Fock matrix construction step. Instead, thread-local counters were used for workload distribution, removing the overhead of thread synchronization. The dynamic load balancing in DDI was implemented with a global counter, whereby each compute process gets a new task index. However, assigning many nodes per DDI group,

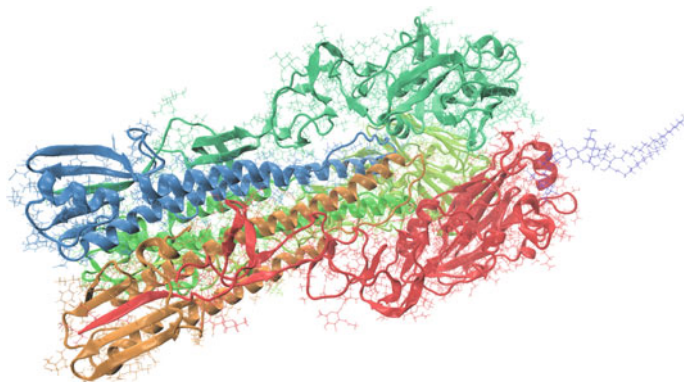


Fig. 4 Influenza HA protein (23,461 atoms), computed using at the RI-MP2 level using FMO on 196,608 cores of the K-computer in 11 min

inevitable on a supercomputer, results in a massive access to the global counter with a frequent synchronization among OpenMP threads. To reduce this overhead, the DDI load balancing was enhanced to optionally return multiple task indices in one request, managing these multiple tasks by a local counter on each node without OMP DO directives, in a manner closely resembling the n -pack strategy described above.

The orthonormalization of molecular orbitals can be a problem when the number of processes in a DDI group is large. In GAMESS, it is parallelized by assigning each orbital to a process in a round-robin fashion, which requires multiple broadcasts. To avoid the communication overhead, a block of orbitals was assigned to a process in a block-cycle fashion, reducing the number of broadcasts. The hotspot of a RI-MP2 calculation is matrix–matrix multiplication, for which a multithreaded library was used. Other steps of RI-MP2 were parallelized by marking loops over occupied or virtual orbitals with OpenMP DO directives.

The performance of this OpenMP-enabled GAMESS was evaluated on 24,576 nodes (=196,608 cores) of the K-computer. The target was the influenza HA protein (23,461 atoms, see Fig. 4) [47] divided into 721 fragments, for which a single point energy was computed with FMO-RI-MP2/6-31G(d) using the cc-pVDZ basis set in RI. This benchmark calculation has been completed in about 11 min with the 78% parallelization efficiency (Table 2).

4.2 *OpenMP Parallelization on Theta*

Theta is a 9.7 PFlops supercomputer built using the second generation of the Intel Xeon Phi processors, Knight's Landing. Theta has 3,624 nodes, each equipped with a 64-core Intel Xeon Phi 7230 and 192 GB of DRAM. Each core has two units for

Table 2 FMO calculations of a protein consisting of 23,461 atoms on the K-computer, at the level of RI-MP2/6-31G(d)

Nodes	Time (s)	Efficiency ^a	DDI grouping for monomers	DDI grouping for dimers
12,288	999		192 groups of 64 nodes	768 groups of 16 nodes
24,576	641	0.78	332 groups of 64 nodes + 26 groups of 128 nodes	1,522 groups of 16 nodes + 7 groups of 32 nodes

^aObtained as 999/641 divided by 2, where 2 = 24,576/12,288

floating point operations. Thus, up to 128 compute threads per node can be efficiently used and each thread has about 1.5 GB of RAM.

Recently, an OpenMP parallelization of the Hartree–Fock code in GAMESS has been developed [27, 28]. The OpenMP threading of other quantum chemistry methods is under way. The limiting step of HF is the two-electron calculation in the Fock matrix elements. The common strategy is to use the so-called direct HF, where two-electron integrals are computed on the fly as needed, whereas the alternative to pre-store integrals may be useful on fast solid-state drives [48]. The algorithm for the two-electron contribution to the Fock matrix has four nested loops over atomic orbitals, which are parallelized using MPI processes and OpenMP threads. The density matrix is easily stored in shared memory because it is unchanged during the Fock matrix computation. The simplest and quite efficient strategy is not sharing the Fock matrix, with each thread having access only to its own copy of the matrix. The Fock matrix built on each thread has to be added up (*reduced*), over all threads on a node, and then over all MPI processes. Sharing the Fock matrix among threads can be done by adding ERI contributions to a temporary buffer private to each thread, and from time to time flushing the buffers to the Fock matrix stored in shared memory.

In FMO, the embedding electrostatic potential (ESP) is calculated for each fragment I , adding contributions from fragment $J \neq I$. The algorithm of the two-electron ESP is rather similar to that for the Fock matrix, and the same OpenMP parallelization strategy was used. However, because in FMO one can use the point charge approximation [49] in the ESP of fragment I for such fragments J that are far from I , the number of point charges can be very large.

In this work, the calculation of the one-electron ESP contributions was parallelized using OpenMP. One-electron integrals are computed in a twofold nested loop over atomic orbitals. Static load balancing is performed over MPI processes for the top nested loop, whereas dynamic load balancing is done over OpenMP threads for the second loop. The contribution of one-electron integrals is accumulated in the one-electron Hamiltonian matrix. It is safe to place it in shared memory because different threads always access different parts of this matrix.

The basic FMO parallelization using MPI + OpenMP developed in this work is limited to the one-body FMO method, FMO1-HF, where monomer fragments are computed. This level of calculation can describe polarization of fragments.

To test parallel efficiency on Theta, a water cluster (H₂O)₃₉₃₂ with the radius of 30 Å was generated using FU [50]. Each water molecule in this system was described

Table 3 FMO1-HF/aug-cc-pVTZ calculations of a spherical water droplet with a radius of 30 Å consisting of 11,796 atoms divided into 3,932 fragments on Theta supercomputer using GAMESS/MPI + OpenMP^a

Number of nodes	4	8	16	32	64	128
Number of MPI compute processes	32	64	128	256	512	1,024
Total number of threads	512	1,024	2,048	4,096	8,192	16,384
Wall-clock time, seconds	842	430	222	118	69	42

^a8 compute processes and 8 data servers per node, 16 threads per compute process

as a separate fragment. It was calculated at the level of FMO1-HF/aug-cc-pVTZ. On each Xeon Phi processor, 8 MPI compute processes were executed, spawning 16 OpenMP threads each (128 threads per node in total). The timings are shown in Table 3 and Fig. 5. The observed scaling is satisfactory overall, although there is some room for improvement.

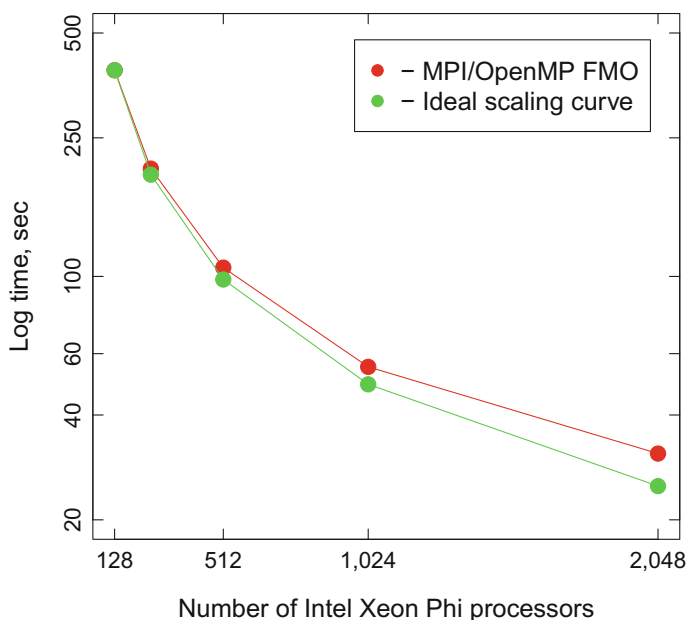


Fig. 5 Wall-clock timings on the Theta supercomputer for FMO1-HF/aug-cc-pVTZ calculations of a spherical water droplet with a radius of 30 Å consisting of 11,796 atoms divided into 3,932 fragments

5 Conclusions

In this work, FMO parallelization strategies on several supercomputers have been described, covering in detail various load balancing schemes. The OpenMP code in GAMESS has been extended to work with FMO at the level of FMO1-HF. GDDI has been generalized to provide an arbitrary number of parallelization levels. The performance of the MPI + OpenMP code in GAMESS developed for FMO has been tested on the Theta supercomputer, and the three-level GDDI performance has been evaluated on a PC cluster.

The present chapter presents just first steps to thread GAMESS, but much remains to be done extending the basic FMO1-HF implementation reported here. It is our hope that FMO calculations in GAMESS accelerated by modern supercomputers will be able to solve important chemical problems in future.

Acknowledgements We thank Dr. Ryan Olson for contributing code to the multilevel GDDI. VM thanks Intel Parallel Computing Centers program for funding. DGF and HU thank the Next-Generation Supercomputer (NGS) project funded by the Ministry of Education, Culture, Sports, Science and Technology (MEXT) in Japan. This work was supported by the Office of Science, U.S. Department of Energy, under Contract DE-AC02-06CH11357. MSG acknowledges support from the US Department of Energy Exascale Computing Project. This research was in part supported by the Exascale Computing Project (17-SC-20-SC), a collaborative effort of the U.S. Department of Energy Office of Science and the National Nuclear Security Administration.

Glossary

GAMESS general atomic and molecular electronic structure system

QM quantum-mechanical

FMO fragment molecular orbital

HPC high-performance computing

MPI message passing interface

OpenMP open multi-processing

HF Hartree–Fock

References

1. Akimov AV, Prezhdo OV (2015) Large-scale computations in chemistry: a bird's eye view of a vibrant field. *Chem Rev* 115:5797–5890
2. Gordon MS, Fedorov DG, Pruitt SR, Slipchenko LV (2012) Fragmentation methods: a route to accurate calculations on large systems. *Chem Rev* 112:632–672
3. Kitaura K, Sawai T, Asada T, Nakano T, Uebayasi M (1999) Pair interaction molecular orbital method: an approximate computational method for molecular interactions. *Chem Phys Lett* 312:319–324

- Fedorov DG, Kitaura K (2007) Extending the power of quantum chemistry to large systems with the fragment molecular orbital method. *J Phys Chem A* 111:6904–6914
- Nagata T, Fedorov DG, Kitaura K (2011) Mathematical formulation of the fragment molecular orbital method. In: *Linear-scaling techniques in computational chemistry and physics*. Springer Netherlands, Dordrecht, pp 17–64
- Fedorov D, Kitaura K (eds) (2009) *The fragment molecular orbital method: practical applications to large molecular systems*. CRC Press, Boca Raton, FL
- Fedorov DG, Nagata T, Kitaura K (2012) Exploring chemistry with the fragment molecular orbital method. *Phys Chem Chem Phys* 14:7562
- Tanaka S, Mochizuki Y, Komeiji Y, Okiyama Y, Fukuzawa K (2014) Electron-correlated fragment-molecular-orbital calculations for biomolecular and nano systems. *Phys Chem Chem Phys* 16:10310–10344
- Fedorov DG (2017) The fragment molecular orbital method: theoretical development, implementation in GAMESS, and applications. *Wiley Interdiscip Rev Comput Mol Sci* 7:e1322
- Mazanetz MP, Chudyk E, Fedorov DG, Alexeev Y (2016) Applications of the fragment molecular orbital method to drug research. In: Zhang W (ed) *Computer-aided drug discovery*. Springer, New York, NY, pp 217–255
- Fedorov DG, Kitaura K (2004) The importance of three-body terms in the fragment molecular orbital method. *J Chem Phys* 120:6832–6840
- Alexeev Y, Mazanetz MP, Ichihara O, Fedorov DG, Fedorov DG (2012) GAMESS as a free quantum-mechanical platform for drug research. *Curr Top Med Chem* 12:2013–2033
- Schmidt MW, Baldrige KK, Boatz JA, Elbert ST, Gordon MS, Jensen JH, Koseki S, Matsunaga N, Nguyen KA, Su S, Windus TL, Dupuis M, Montgomery JA (1993) General atomic and molecular electronic structure system. *J Comput Chem* 14:1347–1363
- Gordon MS, Schmidt MW (2005) Advances in electronic structure theory: GAMESS a decade later. In: Dykstra C, Frenking G, Kim K, Scuseria G (eds) *Theory and applications of computational chemistry*. Elsevier, Amsterdam, pp 1167–1189
- Inadomi Y, Nakano T, Kitaura K, Nagashima U (2001) Increased efficiency of parallel calculations of fragment molecular orbitals by using fine-grained parallelization on a HITACHI SR8000 supercomputer. In: Hertzberger B, Hoekstra A, Williams R (eds) *High-performance computing and networking. HPCN-Europe 2001. Lecture notes in computer science*. Springer, Berlin, Heidelberg, pp 569–572
- Komeiji Y, Inadomi Y, Nakano T (2004) PEACH 4 with ABINIT-MP: a general platform for classical and quantum simulations of biological molecules. *Comput Biol Chem* 28:155–161
- Ishikawa T, Ishikura T, Kuwata K (2009) Theoretical study of the prion protein based on the fragment molecular orbital method. *J Comput Chem* 30:2594–2601
- Takami T, Maki J, Ooba J, Inadomi Y, Honda H, Susukita R, Inoue K, Kobayashi T, Nogita R, Aoyagi M, Simos TE, Maroulis G (2007) Multi-physics extension of OpenFMO framework. In: *AIP conference proceedings*. AIP, pp 122–125
- Doi H, Okuwaki K, Mochizuki Y, Ozawa T, Yasuoka K (2017) Dissipative particle dynamics (DPD) simulations with fragment molecular orbital (FMO) based effective parameters for 1-palmitoyl-2-oleoyl phosphatidyl choline (POPC) membrane. *Chem Phys Lett* 684:427–432
- Fletcher GD, Schmidt MW, Bode BM, Gordon MS (2000) The distributed data interface in GAMESS. *Comput Phys Commun* 128:190–200
- Shah G, Nieplocha J, Mirza J, Kim C, Harrison R, Govindaraju RK, Gildea K, DiNicola P, Bender C (1998) Performance and experience with LAPI—a new high-performance communication library for the IBM RS/6000 SP. In: *Proceedings of the first merged international parallel processing symposium and symposium on parallel and distributed processing*. IEEE Comput Soc, pp 260–266
- Nieplocha J, Tipparaju V, Krishnan M, Panda DK (2006) High performance remote memory access communication: the ARMCI approach. *Int J High Perform Comput Appl* 20:233–253
- Asadchev A, Gordon MS (2013) Fast and Flexible Coupled Cluster Implementation. *J. Chem. Theory Comput.* 9:3385–3392

24. Ishimura K, Kuramoto K, Ikuta Y, Hyodo S (2010) MPI/OpenMP hybrid parallel algorithm for Hartree–Fock calculations. *J Chem Theory Comput* 6:1075–1080
25. K-Computer. <https://www.r-ccs.riken.jp/en/k-computer/system>
26. Mironov VA, Khrenova M, Moskovsky AA (2015) On quantum chemistry code adaptation for RSC petastream architecture. In: Kunkel J, Ludwig T (eds) *High performance computing*. Springer, Cham, Frankfurt, pp 113–121
27. Mironov VA, Moskovsky AA, D’Mello M, Alexeev Y (2017) An efficient MPI/OpenMP parallelization of the Hartree–Fock–Roothaan method for the first generation of Intel® Xeon Phi™ processor architecture. *Int J High Perform Comput, Appl*
28. Mironov VA, Alexeev Y, Keipert K, D’mello M, Moskovsky AA, Gordon MS (2017) An efficient MPI/OpenMP parallelization of the Hartree-Fock method for the second generation of Intel® Xeon Phi™ processor. In: *Proceedings of the international conference for high performance computing, networking, storage and analysis on SC’17*. ACM Press, New York, New York, USA, pp 1–12
29. Fedorov DG, Olson RM, Kitaura K, Gordon MS, Koseki S (2004) A new hierarchical parallelization scheme: generalized distributed data interface (GDDI), and an application to the fragment molecular orbital method (FMO). *J Comput Chem* 25:872–880
30. Fedorov DG, Sugita Y, Choi CH (2013) Efficient parallel implementations of QM/MM-REMD (quantum mechanical/molecular mechanics-replica-exchange MD) and umbrella sampling: isomerization of H₂O₂ in aqueous solution. *J Phys Chem B* 117:7996–8002
31. Ito S, Fedorov DG, Okamoto Y, Irle S (2018) Implementation of replica-exchange umbrella sampling in GAMESS. *Comput Phys Commun* 228:152–162
32. Devarajan A, Gaenko A, Gordon MS, Windus TL (2017) Nucleation using the effective fragment potential and two-level parallelism. In: *Fragmentation*. Wiley, Chichester, UK, pp 209–226
33. Fedorov DG, Slipchenko LV, Kitaura K (2010) Systematic study of the embedding potential description in the fragment molecular orbital method. *J Phys Chem A* 114:8742–8753
34. Fletcher GD, Schmidt MW, Gordon MS (1999) Developments in parallel electronic structure theory. *Adv Chem Phys* 110:267–294
35. Nishimoto Y, Fedorov DG (2018) Adaptive Frozen orbital treatment for the fragment molecular orbital method combined with density-functional tight-binding. *J Chem Phys* 148:064115
36. Ikegami T, Ishida T, Fedorov DG, Kitaura K, Inadomi Y, Umeda H, Yokokawa M, Sekiguchi S (2005) Full electron calculation beyond 20,000 atoms: ground electronic state of photosynthetic proteins. In: *ACM/IEEE SC 2005 conference (SC’05)*. IEEE, Seattle, Washington, USA, p 10
37. Alexeev Y, Mahajan A, Leyffer S, Fletcher G, Fedorov DG (2012) Heuristic static load-balancing algorithm applied to the fragment molecular orbital method. In: *2012 international conference for high performance computing, networking, storage and analysis*. IEEE, Salt Lake City, Utah, USA, pp 1–13
38. Talamudupula SK, Sosonkina M, Gaenko A, Schmidt MW (2012) Fragment molecular orbital method adaptations for heterogeneous computing platforms. *Procedia Comput Sci* 9:489–497
39. Fletcher GD, Fedorov DG, Pruitt SR, Windus TL, Gordon MS (2012) Large-scale MP2 calculations on the blue gene architecture using the fragment molecular orbital method. *J Chem Theory Comput* 8:75–79
40. Pruitt SR, Nakata H, Nagata T, Mayes M, Alexeev Y, Fletcher GD, Fedorov DG, Kitaura K, Gordon MS (2016) Importance of three-body interactions in molecular dynamics simulations of water demonstrated with the fragment molecular orbital method. *J Chem Theory Comput* 12:1423–1435
41. Umeda H, Sato M (2011) Parallelization of GAMESS to the large-scale computing. In: *Proceedings of the 30th JSST annual conference (JSST 2011)*; *International conference on modeling and simulation technology*, OS2, Tokyo, Japan, p 92
42. Feyereisen M, Fitzgerald G, Komornicki A (1993) Use of approximate integrals in ab initio theory. An application in MP2 energy calculations. *Chem Phys Lett* 208:359–363
43. Pham B, Gordon MS. Hybrid OpenMP/MPI RI-MP2 energy and gradient implementation in GAMESS

44. Gunina AO, Gordon MS. Hybrid OpenMP/MPI implementation of EFMO method in GAMESS
45. Katouda M, Nagase S (2009) Efficient parallel algorithm of second-order Møller–Plesset perturbation theory with resolution-of-identity approximation (RI-MP2). *Int J Quantum Chem* 109:2121–2130
46. Furukawa Y, Koga R, Yasuda K (2011) Acceleration of computational quantum chemistry by heterogeneous computer architectures. In: *Proceedings of the 30th JSST annual conference (JSST 2011)*; International conference on modeling and simulation technology, OS2, Tokyo, Japan, p 85
47. Sawada T, Fedorov DG, Kitaura K (2010) Binding of influenza A virus hemagglutinin to the sialoside receptor is not controlled by the homotropic allosteric effect. *J Phys Chem B* 114:15700–15705
48. Mironov VA, Moskovsky AA, Alexeev Y (2017) Power measurements of Hartree–Fock algorithms using different storage devices. In: *2017 IEEE international parallel and distributed processing symposium workshops (IPDPSW)*. IEEE, Orlando, US, pp 1004–1011
49. Nakano T, Kaminuma T, Sato T, Fukuzawa K, Akiyama Y, Uebayasi M, Kitaura K (2002) Fragment molecular orbital method: use of approximate electrostatic potential. *Chem Phys Lett* 351:475–480
50. Fedorov DG, Kitaura K (2017) Modeling and visualization for the fragment molecular orbital method with the graphical user interface FU, and analyses of protein–ligand binding. In: Gordon MS (ed) *Fragmentation: toward accurate calculations on complex molecular systems*. Wiley, Chichester, UK, pp 119–139